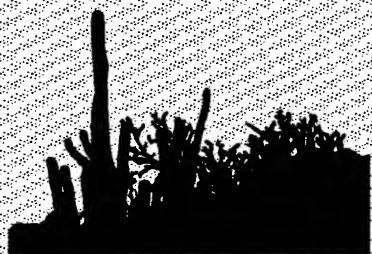




***14th International Symposium  
Military Aspects of Blast  
and Shock (MABS)  
Las Cruces, New Mexico, U.S.A.  
10 -15 September 1995***

**PROCEEDINGS**



20011031 090



Statement A  
Approved for public release;  
Distribution unlimited.....

# Table of Contents

## Section 1 - Airblast and Shock Phenomenology

<b>A Study of the Boundary Layer in a Large Scale Blast Wave over a Natural Surface,</b> Dewey, McMillin, van Netten, Canada and Ethridge, Keefer, Needham, USA .....	1
<b>Airblast Propagation in Tunnels with Obstacles: Experimental Investigation and</b> Numerical Calculations, Binggeli, Anet, Schläpfer, Switzerland .....	29
<b>Collateral Effects of Confined Blast Events, Mazzola, Myers, Fry, USA .....</b>	39
<b>Experimental Study of Turbulent Baroclinic Boundary Layers, Neuwald,</b> Reichenbach, Germany and Kuhl, USA .....	61
<b>Influence of Rock Disintegration in High-Loading-Density Underground</b> Explosions on Peak Overpressure, Bücking, Germany .....	73
<b>Oblique Reflection of Decaying Pressure Waves, Heilig, Germany .....</b>	85
<b>Source Characteristics of Aluminized Explosives, Rinehart, Babcock, USA .....</b>	109

## Section 2 - Structures and Blast Effects

<b>An Experimental Study of Damage to Scale Model Cylinders from Near Field</b> Underwater Explosions, Brett, van der Schaaf, Barclay, Australia .....	129
<b>Analysis of Blast Loads on Commercial Buildings, Birnbaum, Clegg, Fairlie,</b> Hayhurst, Francis, USA and UK .....	139
<b>Blast Wave Attenuation in Tunnels and Expansion Chambers Containing</b> Discrete Roughness Elements, Smith, Vismeg, Tingey, UK .....	163
<b>Intermediate-Scale Underground Magazine Tests: Results of Airblast Studies</b> from an Idealized Detonation Experiment, Joachim, Davis, USA .....	171
<b>Measurement and Simulation of Air Blast Hazards Associated with Door</b> Breaching Operations, Winter, Thornton, Learmonth, Jones, Kemister, Ritzel, Australia .....	183
<b>Nonlinear Analysis of Tunnel-Section Subjected to Explosion Loading,</b> Høiseth, Nauta, Norway and The Netherlands .....	207
<b>Reduction of Muzzle Blast by Barriers, Absil, Kodde, Weerheijm, The Netherlands .....</b>	231
<b>Techniques Developed for Accurate Scale Modelling of Reinforced Concrete</b> Structures and the Results for a Generic Model, Seeds, UK .....	249
<b>Use of CFD/CSD Capability for Design of Blast Deflectors for a Mine Resistant</b> Vehicle, Lottati, Dillon, Sergi, Strittmatter, Sousk, Eidelman, USA .....	259
<b>Blast Resultants behind Cantilever Walls: Comparison between Full-Scale and Model-</b> Scale Experiments, Hulton, Smith, Rose, UK .....	275

## Section 3 - Measurement Techniques

<b>Anomalies in Pressure-Time Recordings Caused by Water Drops on a Pencil</b> Blast Pressure Probe, Medin, Axelsson, Selin, Sweden .....	287
<b>Development of a Transducer for the Measurement of Temperature of Airblast</b> Flow Fields, Muller, Schraml, Mihalcin, USA .....	305
<b>Intermediate-Scale Underground Magazine Tests: Analysis of Thermal</b>	



<b>Instrumentation and Prediction Techniques, Joachim, USA</b> .....	315
<b>Internal Pressure Measurements from Explosively Loaded Cubicles,</b> <b>Yiannakopoulos, Australia</b> .....	327
<b>The Characterization of a New Explosive Using Smoke Trail Photo-Diagnostics,</b> <b>McMillin, Dewey, Canada</b> .....	345
<b>New Measurement Techniques to Determine Material Properties for the</b> <b>Calculation of Temperature Distributions, Simon, Bein, Eggers, Köhler,</b> <b>Neurath, Pelzl, Germany</b> .....	365
<b>The Development of Blast Wave Cantilever Gauges, van Netten, Dewey, Canada</b> .....	389

#### Section 4 - Large Blast Simulators

<b>Propagation and Attenuation of Blast Waves in a Long Model Blast-Simulator,</b> <b>Amann, Germany</b> .....	415
<b>LB/TS Predictive Tool, Sevier, Needham USA</b> .....	435

#### Section 5 - Non-Ideal Airblast and Thermal Effects

<b>Simulation of Non-Ideal Blast with a Shock Tube Exit Jet, Loucks, Muller, Thane,</b> <b>Cline, Ferguson, Mermagen, USA</b> .....	459
<b>Precursor Simulation Using a Flow Simulator, Klaus, Duckerschein, Germany</b> .....	485
<b>Simulation of Non-Ideal Blast Waves Produced by the Thermal Precursor in</b> <b>Nuclear Explosions, Mergnat, Tournemine, Gratias, France</b> .....	499
<b>Thermal Radiation Transmission through Composite Material, Loucks, USA</b> .....	513
<b>Turbulent Boundary Layers in Airblast Precursors, Kuhl, Bell, Ferguson, Chien,</b> <b>Collins, USA</b> .....	535

#### Section 6 - Biological Effects of Airblast

<b>Biological Effects of Blast on Sheep: Comparison of Shock Tube Exposure to</b> <b>Free Field Exposure , Vassout, France and Mayorga, Argyros, Topper, USA</b> .....	565
<b>Auditory and Nonauditory Damage-Risk Assessment for Simulated Weapons</b> <b>Fired from an Enclosure, Johnson, Yelverton, Hicks, Doyal, USA</b> .....	577

#### Section 7 - Julius J. Meszaros Memorial Lecture

<b>A Projected History of Sensing Technology for Earth Kinetics (J. Meszaros</b> <b>Memorial Monograph), Ingram, USA and Madshus, Norway</b> .....	603
<b>Blast Wave Measurements Techniques, Structural Response and Calibration,</b> <b>Reisler, Keefer, Ethridge, USA</b> .....	645

#### Section 8 - Workshops

<b>Experimental and Numerical Study of Flow in Multi-Driver Large Blast Simulators,</b> <b>Schraml, USA and Mergnat, Gratias, France</b> .....	681
---	-----

# A STUDY OF THE BOUNDARY LAYER IN A LARGE SCALE BLAST WAVE OVER A NATURAL SURFACE

J. M. Dewey, D. J. McMillin, A. A. van Netten  
Dewey McMillin & Associates Ltd, 1741 Feltham Road, Victoria  
BC V8N 2A4, Canada

N. Ethridge, J. Keefer  
Applied Research Associates, Inc., 30 Centennial Lane, Aberdeen, MD 21001

C. Needham  
Applied Research Associates, Inc., 4300 San Mateo Blvd. NE, Albuquerque, NM  
87110

## 1. SUMMARY

A study has been made of the boundary layer above the ground surface in the blast wave produced by the explosion of a hemispherical surface-burst 2,431 ton charge of ammonium nitrate and fuel oil (MINOR UNCLE). Numerical simulation and a variety of measurement techniques were used in the study.

A two-dimensional numerical simulation was carried out using the SHARC code to predict the variation of the physical properties in the blast wave as functions of height above the ground surface at several distances from the centre of the explosion. The simulation assumed a ground roughness of 0.63 cm, which was the average of measurements made at several places on the graded radials along which diagnostic measurements of the blast wave were made. A shock-following grid was used to maintain high resolution at and near the shock front. A version of the  $K-\epsilon$  turbulence model, in conjunction with a rough law-of-the-wall, was used to describe the formation and growth of the real-surface boundary layer. The calculation was carried out from booster detonation to a time of 1.5 seconds. This time corresponds approximately to the end of the positive duration at the 5 psi level<sup>1</sup>.

Attempts were made to observe and measure the boundary layer characteristics using various methods. These included high speed photography of the displacement of vertical smoke trails, displacement cubes placed on and elevated above the ground, and vertical arrays of horizontal cantilevers.

An array of smoke trails was established at the 5 psi level, produced by launchers placed in buried silos so that the trails extended from the ground surface. The motion of the trails in the blast wave was recorded by a high speed camera. Analysis of the recorded motion indicated a boundary layer that had grown to a height of 25 cm after a flow time of 100 ms. This result agreed with the prediction of the numerical simulation for this overpressure level.

Cubes made from several different materials and of several sizes have been exposed to a large number of blast waves, and the displacement of the cubes serves as a passive

---

<sup>1</sup>Measurement stations were established along radial lines for the MINOR UNCLE event at positions where the peak hydrostatic overpressure was predicted to reach certain levels, measured in psi. These stations will be referred to by their nominal 'psi' values

diagnostic measure of the dynamic pressure forces in the blast wave. For the boundary layer experiment cubes with edge lengths of 152 mm, 51 mm and 44 mm were placed on the ground and raised above the ground on short pedestals. Some of the cubes placed at the 5 psi level were in the field of view of a high speed camera, and the initial displacements and velocities of these cubes were measured. Because of the different mode of initial movement of the cubes on the ground versus those on pedestals and the apparently low effective height of the boundary layer, a significant reduction of cube displacements was observed only for the small cubes on the surface, and primarily for stations at 10 psi and above.

Seven vertical arrays of horizontal cantilevers were used to measure the variation of dynamic pressure with height: five along the North radial over graded ground at the 50, 30, 20, 10 and 5 psi levels, and two over ungraded ground at the 50 and 30 psi levels. Steel cantilevers were used at the higher pressure levels and aluminum at the lower levels. The effect of the boundary layer was observed in all cases, and excellent agreement was obtained when the time-resolved dynamic pressure profiles from the numerical simulation were used to calculate the expected deformation of the cantilevers. The boundary layer over the ungraded ground was shown to be significantly higher than that over the graded ground.

Based on the comparisons between results of the numerical simulation and the measured properties of the blast wave, it is concluded that, within the limits of the spatial resolution of the measurement techniques, the simulation gave a good description of the boundary layer between the nominal 150 psi and 5 psi levels.

## 2. INTRODUCTION

This study of the boundary layer produced by the MINOR UNCLE explosion was conceived and directed by Arnfinn Jenssen of the Norwegian Defence Construction Service in order to answer some of the questions raised after previous large scale explosive tests concerning the nature of the boundary layer in a blast wave and its probable effects on measured blast properties and on the loading of structures. The project was started at a relatively late stage in the planning process so that it was necessary to rely on passive measurement techniques which did not depend on electronic recording.

The literature on boundary layers in blast waves is not extensive, although there are a number of theoretical studies, e.g. Mirels and Hamman, 1962; Liu and Mirels, 1980; Du *et al*, 1982, and Dymant, 1982). There are even fewer reports on the physical measurement of boundary layers in blast waves, and the most significant is probably that of Carpenter (1973), which describes static pressure, pitot pressure, surface shear and flow temperature measurements at the 60 psi and 30 psi stations on the MIDDLE GUST 100 ton TNT test over a clean hard surface. The excellent measurements reported by Carpenter reinforce the conclusion of the present project that a comprehensive study of the boundary layers produced by blast waves over real surfaces, using numerical and measurement techniques, is urgently needed to fill a void in our knowledge of the physical properties of blast waves and their effects.

at a height of about 2 m, and reached heights of about 20 m or higher, as required.

In order to study the boundary layer in the blast wave from the MINOR UNCLE explosion a miniature version of the launcher was built on approximately a one-third scale using a 2 cm diameter barrel tube, 20 cm long, and a 1.25 cm diameter projectile tube: 20 cm long for black smoke and 40 cm long for white. The sizes of the other components of the mini-launcher and the amounts of gunpowder propellant and black and white smoke powders were similarly reduced. The mini-launchers were initiated using detonators and a 12-volt battery in a circuit which was closed by a remotely controlled relay. The launchers were designed to generate straight vertical smoke trails about 15 cm wide, to a height of about 2 m.

The miniature launchers were fired from below ground level by mounting each one inside a silo made from a 10 cm diameter plastic tube, 1 m long. The silo was inserted into a hole in the plywood cover of an underground chamber and lowered until the muzzle end of the assembly was level with the surrounding ground surface. A flanged ring was used to secure the silo to the chamber cover. Figure 1 shows a mini-launcher and its silo before assembly and emplacement. In order for the launchers to produce smoke trails beginning below ground level, it was important for the lower ends of the silos to remain open to the air in the chamber. Five launchers were used in a single chamber and all were fired with the same battery and relay at 1 sec after the charge detonation.

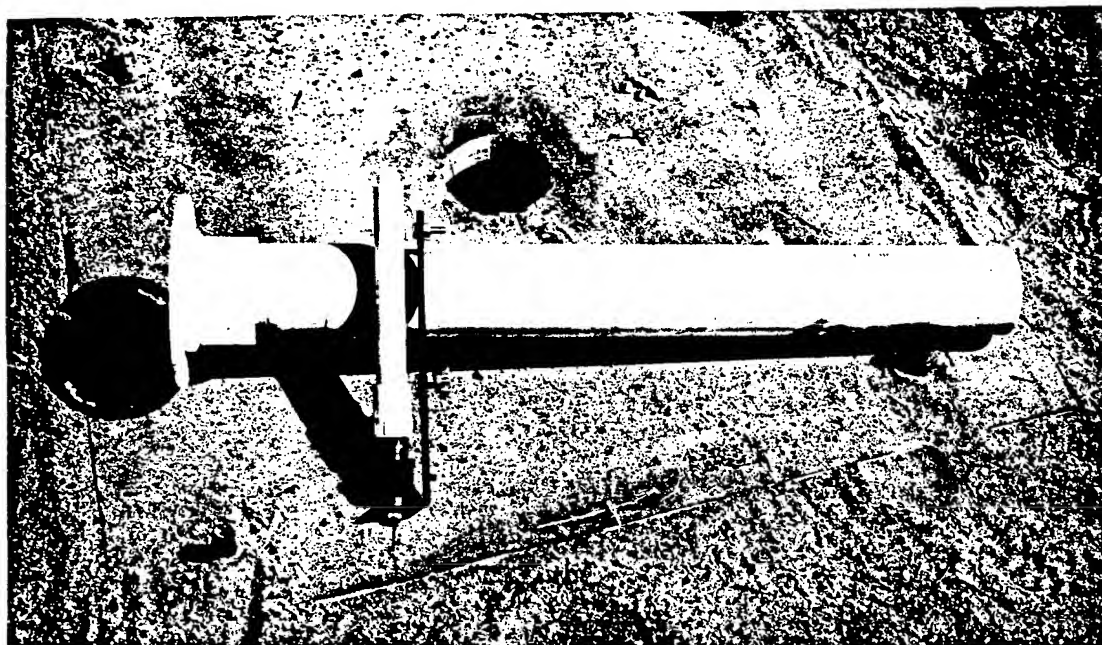


Figure 1. Miniature smoke launcher and firing silo. The launcher was placed in the lower end of its silo after being loaded and armed. The silo was then lowered into a hole in the plywood cover of the underground chamber so that the top flange was flush with the ground surface. The silo was approximately 1 m long.

The launcher site was located at the 5 psi station to the side of, and adjoining, a graded measurement radial. The five launchers were positioned along a radial line through ground zero. The closest to ground zero was at a distance of 715.2 m, where the peak hydrostatic overpressure was predicted to be 34.5 kPa (5 psi). The launchers were spaced 66 cm apart, using alternating black and white smoke so as to maximize the contrast between adjacent trails.

A 35mm camera running at a nominal speed of 300 pictures per second was used to record the movement of the trails in the blast wave. To enhance the visibility of the smoke trails a white back board, 2.6 m high and 16 m long, was erected as a background to the trails when viewed from the camera position. The camera was 27.5 m from the smoke trails, and the back board was 14.5 m behind the trails. The line of sight from the camera was perpendicular to the radial from ground zero to the launchers. The field of view was such that the motion of the smoke trails could be followed for about 10 m. Five accurately surveyed fiducial markers were placed in the field of view: three on the back board, and two in the foreground between the camera and the smoke trails. The two foreground markers were made strong enough so that they would not move during the passage of the blast wave. The site, and the region extending towards ground zero, were graded and a dust suppressant was used. White lime, in addition to dust suppressant, was spread on the ground between the smoke launchers and the back board to increase the contrast and visibility of the lowermost portion of the mini-trails, where the boundary layer might be seen.

#### **4.2 Displacement Cubes**

Extensive use has been made of cubes of various sizes and materials, placed on or slightly above the ground, and exposed to blast waves so that their resulting displacements can be used as a diagnostic technique to monitor the dynamic forces of the blast waves (Ethridge and Dixon 1988, Dixon-Heister et al 1990, Ethridge 1992, Ethridge et al 1995).

On MINOR UNCLE cubes were placed at the 50, 30, 20, 15, 10 and 5 psi measurement stations on a graded measurement radial. The cubes for each station were selected according to size and mass such that they would displace a useful distance for the expected blast environments. The large and small cubes placed at the same station were chosen to have about the same area-to-mass ratio. At each station some of the cubes were placed on the ground while others were elevated 17.75 cm or 22.85 cm on small platforms, depending on the size of the cube, so that the centres of the elevated cubes were at a height of 25.4 cm..

At the 5 psi station an additional nine cubes were placed in the field of view of the high speed camera which was used to record the smoke trail displacement, as described above. Detailed information about these cubes and their placement is given in table 3.7 of Ethridge et al (1995). Four of the cubes were placed on the ground surface, and the bases of the others were elevated 10.2 cm, 17.8 cm or 22.9 cm.

#### **4.3 Cantilever Arrays**

When a circular cross-section ductile rod, clamped at one end, is exposed to a blast wave its normal mode of deformation is to bend about the clamped end. The rest of



in the mean flow kinetic energy of the zone. The turbulent kinetic energy dissipated during a time step was added to the internal energy of the zone.

### 3.2 The Calculation

The shock propagation calculation was initiated from an earlier calculation of the detonation of 2.4 kiloton of ammonium nitrate/fuel oil (ANFO) in an atmosphere equivalent to the US Standard Atmosphere at 1,617 m above sea level, the altitude of the White Sands Test Site. The charge was assumed to be a centre-detonated hemisphere on the ground surface. A two dimensional, high explosive burn calculation using SHARC, served as the initial conditions for the MINOR UNCLE shock and boundary layer calculation. The shock calculational zone sizes in the region of the shock front were 5 cm in the vertical direction by 15 cm. in the horizontal. The calculation started just outside the charge and continued until the positive phase was complete at the 5 psi level, approximately 1.5 seconds after detonation. The zone size was retained in the shock-following subgrid throughout the calculation. The roughness parameters for the wall function model included a roughness element size of 6.35 mm and a fractional coverage of 50%. These numbers were obtained from a large number of measurements along the measurement radials at the test site. The measurement radials had been graded, rolled, and dust stabilized, thus accounting for the relatively smooth surface.

The calculation included the detonation products, and air with a real-air equation of state. The full  $K - \epsilon$  turbulence model and rough wall model were included throughout the calculation. A number of stations were included in the calculation at which the hydrodynamic parameters as functions of time were recorded. These stations corresponded to the positions at which measurements were made along the radials. In addition, space profiles of the hydrodynamic variables were recorded at selected times.

Post processing of the space profiles allowed plotting of histograms and contours of any hydrodynamic variable at any of the selected times. Post processing of the station records provided time histories of any hydrodynamic variables and the associated impulses at any of the several hundred pre-selected positions. The hydrodynamic variables included: pressure, density, energy density, turbulence level, rate of turbulence dissipation, and particle velocity. In addition, temperature, momentum, dynamic pressure, stagnation pressure, turbulent diffusion velocity, turbulent viscosity, and their gradients could be calculated. Special routines allowed the plotting of histograms, contours, vectors, interferograms, projections and overlays of many of these parameters.

## 4. MEASUREMENT TECHNIQUES

### 4.1 Flow Tracer Photography

High speed photography of the displacement of smoke trails in blast waves has been used extensively as a blast wave diagnostic technique (e.g. Dewey and McMillin 1988, 1991, 1993, 1995a). The smoke trails used in those experiments were formed by launchers mounted on the ground surface. The trails were about 75 cm wide, began

### 3. NUMERICAL SIMULATION

#### 3.1 The Numerical Model

The boundary layer in the blast wave produced by the MINOR UNCLE explosion was simulated using the Second Order Hydrodynamic Advanced Research Code (SHARC), which is a state of the art, first principles, finite difference, time marching computer code. The code is fully conservative of mass, momentum, and energy and uses a two phase approach to solve the hydrodynamic conservation equations for compressible flow using an Eulerian grid. The code was developed to allow the solution of complex unsteady flow problems which may include the effects of turbulence. The inviscid version of the code was developed to reduce the numerical viscosity to a minimum, well below the real viscosity of air. This was necessary in order to add a realistic turbulence model in which the numerical errors would not dwarf the effects of real turbulence and viscosity. The two equation model of Launder and Spalding (1972), known as the  $K - \epsilon$  turbulence model, was incorporated.

The original  $K - \epsilon$  turbulence model was developed for incompressible steady state flows. The model in SHARC has been significantly modified and uses variable coefficients in the equations for development and dissipation of turbulence. The model retains the ability to accurately calculate the effects of turbulence in steady state jet problems, for instance, and permits the solution in the presence of decaying shock waves and other transient phenomena. The model is similar to that described by Barthel (1985). The model handles turbulence generated by both Rayleigh-Taylor and Kelvin-Helmholtz type instabilities, and has proved satisfactory for solving a large class of problems, including jets, shocks, and fireball rise over a wide range of length scales.

Using this form of the model as the starting point, a boundary layer law of the wall was added. The wall function is based on the work of Clauser (1954), and of Viegas and Rubesin (1983, 1985). The history of the development of the boundary layer law-of-the-wall model is described by Pierce (1986). This model was further extended by the inclusion of a shear stress mechanism for dust sweep-up from smooth surfaces, where the shear stress is a natural outcome of the law-of-the-wall calculation.

The model has been implemented in SHARC with both an explicit and implicit form of solution. The surface roughness was characterized by a roughness height and a percentage of coverage. Some restrictions on zone size were necessary to allow the proper functioning of the rough wall condition. At least 20 zones were used to define the boundary layer in order to capture the vertical gradients in the developed layer. The zone size was set to at least three times the roughness height of the boundary surface. For example, a 10 mm roughness required at least a 3 cm zone size. If the zones are smaller, the sub-scale assumptions of the law of the wall are invalid. If the zones are too large, the velocity gradients are not well defined and the resolution of the boundary layer is lost.

Turbulence and turbulent dissipation rate were carried as zone parameters at the zone centres, and were fluxed from zone to zone using the same second order differencing as that for the other conserved quantities of mass, momentum and energy. The turbulent kinetic energy generated in a given time step was balanced by a reduction

Height Above Ground: 25 mm

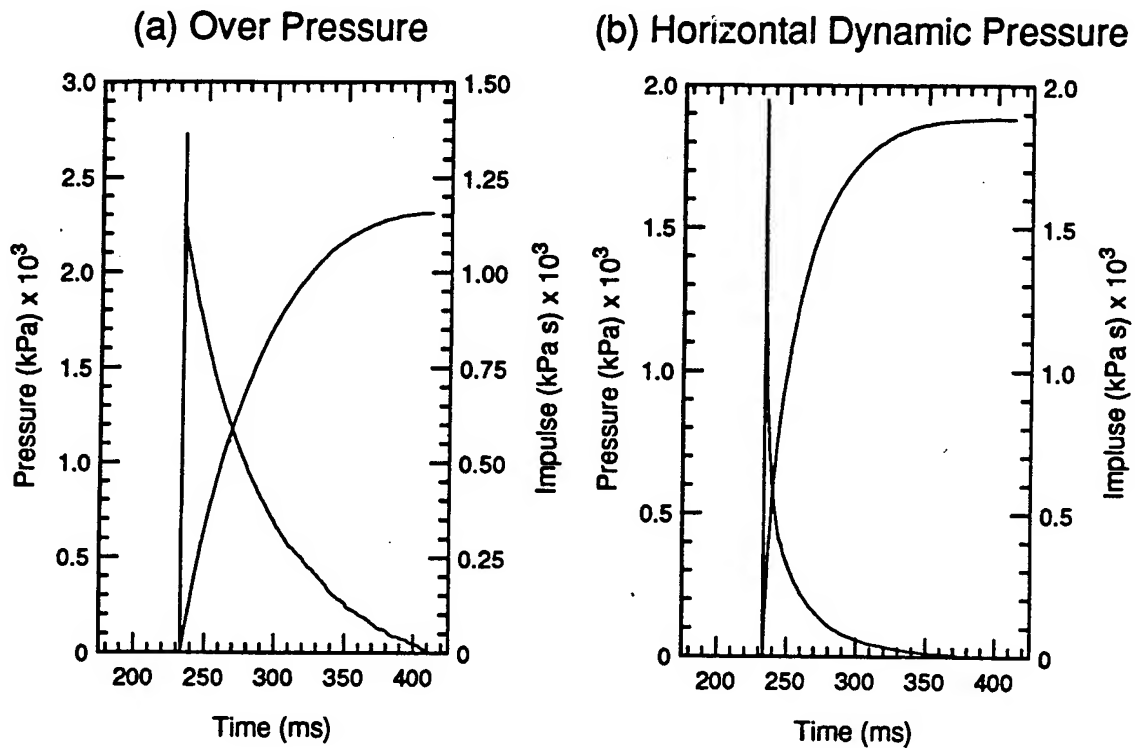


Figure 2. Typical time histories of (a) hydrostatic overpressure and (b) horizontal dynamic pressure at a radial distance of 270 m. The fine zoning in the calculation produced some overshoot at the shock front and the peak value was calculated by averaging the maximum and the first minimum after that maximum. Time histories such as these were obtained from 2.5 cm to 1.5 m above the ground at intervals of 5 cm to provide vertical profiles of blast properties.

the cantilever remains straight. Such deformable cantilevers can be used as economical blast gauges if the angle of deformation can be related to the physical properties of the blast wave. Extensive arrays of such gauges were used to monitor the blast waves from the DISTANT IMAGE (van Netten and Dewey, 1992) and MINOR UNCLE (van Netten and Dewey, 1995) explosions. In addition, on the MINOR UNCLE event seven vertical arrays of horizontal cantilevers were used to measure the variation of dynamic pressure with height: five on a measurement radial over graded ground at the 50, 30, 20, 10 and 5 psi stations, and two over ungraded ground at the 50 and 30 psi levels. Steel cantilevers were used at the higher pressure levels and aluminum at the lower levels.

The horizontal cantilevers on the graded radial were supported by five streamlined mounts: 0.6 m in chord, 2.44 m long and 0.05 m wide. These mounts were positioned in holes approximately 0.9 m deep and set in concrete, with the remaining 1.54 m above the ground used to support a series of horizontally mounted cantilevers aligned perpendicular to the blast. 8 or 15 cantilevers were mounted on both sides of each mount at heights above the ground from 3.0 cm to 1.43 m. These were either made of steel 1018, aluminum 6061 or aluminum 4043, with diameters which ranged from 1.27 cm to 0.155 cm, and lengths from 0.7 m to 0.2 m. All cantilevers on one side of a mount were of the same length, and in some cases a different length was used on the other side. Details of the cantilevers and the positions of the mounts are given by van Netten and Dewey (1995).

An attempt was also made to observe the boundary layer above ungraded ground. Streamlined concrete structures, which remained from a previous experiment (Ethridge et al, 1990), were used to mount vertical arrays of horizontal cantilevers at the nominal hydrostatic overpressure levels of 30 and 10 psi. The sizes and materials of these cantilevers were the same as those at the corresponding overpressure levels on the graded measurement radial. The undisturbed rough ground surrounding the cantilever mounts was covered by scattered bushes approximately 30 cm to 60 cm in height.

## 5. RESULTS

### 5.1 Numerical Simulation

Figures 2 (a) and (b) illustrate the typical time histories which were obtained at all the selected stations and at the different heights above the ground. The fine zoning used for the calculation produced some shock-front overshoot, which can be seen in the figures. The peak value was therefore estimated by calculating the arithmetic average of the maximum value and the first minimum after the maximum. The resulting peak values of overpressure and dynamic pressure were plotted as functions of height above the ground, and typical profiles are shown in figures 3 and 4.

The impulses of hydrostatic and dynamic pressure during the positive phase were calculated from the time histories, and are shown in figures 5 and 6. The variation of dynamic pressure impulse with height above the ground demonstrates the most significant effect of the boundary layer. The vertical profiles of dynamic pressure impulse as a percentage of the free-stream value, are illustrated in figures 7, and are

# PEAK HYDROSTATIC OVERPRESSURE VERTICAL PROFILES

Height (mm) vs  
Pressure (kPa)

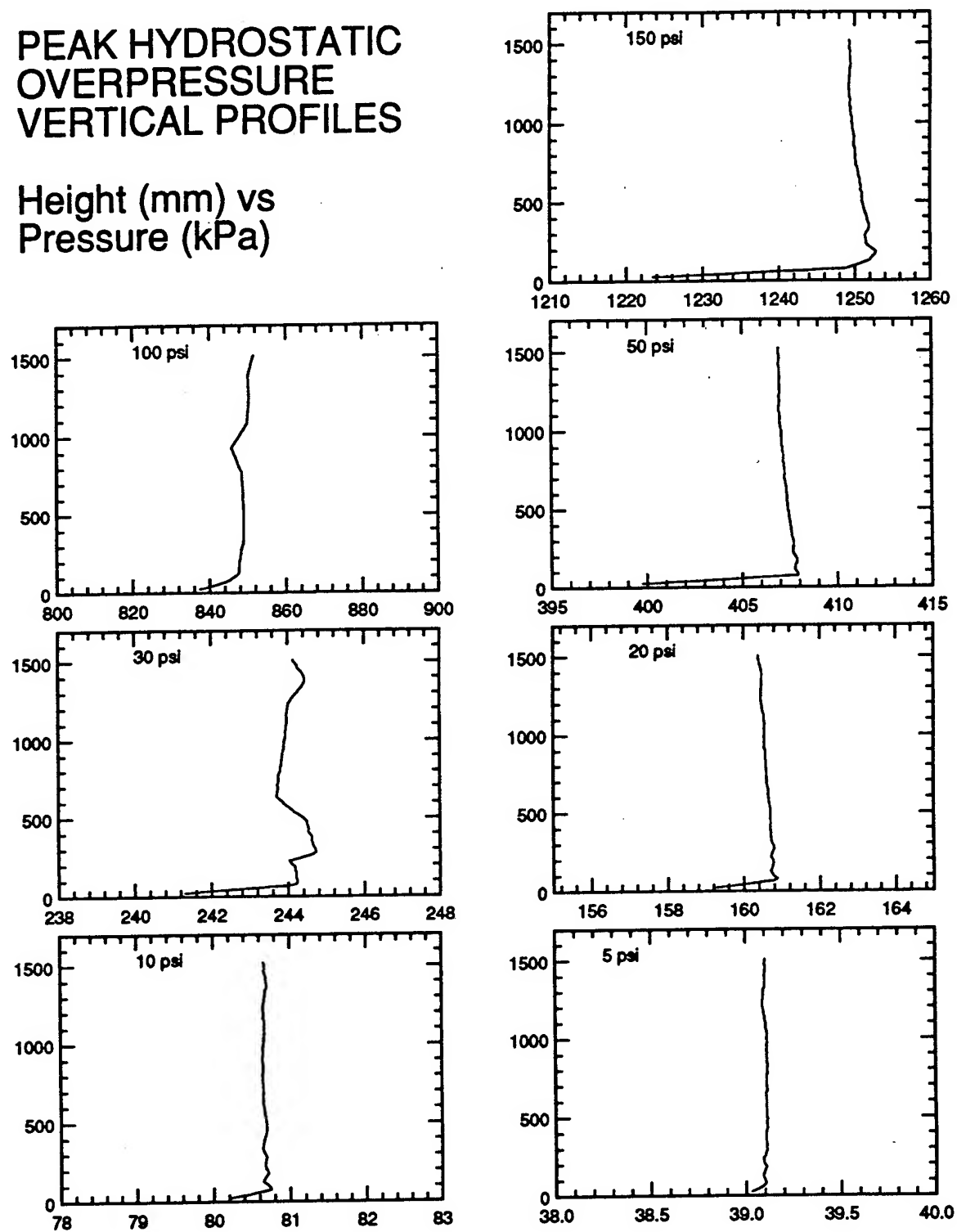


Figure 3. Vertical profiles of peak hydrostatic pressure at several 'psi' stations, obtained from the numerical simulation.



# PEAK DYNAMIC PRESSURE VERTICAL PROFILES

Height (mm) vs  
Pressure (kPa)

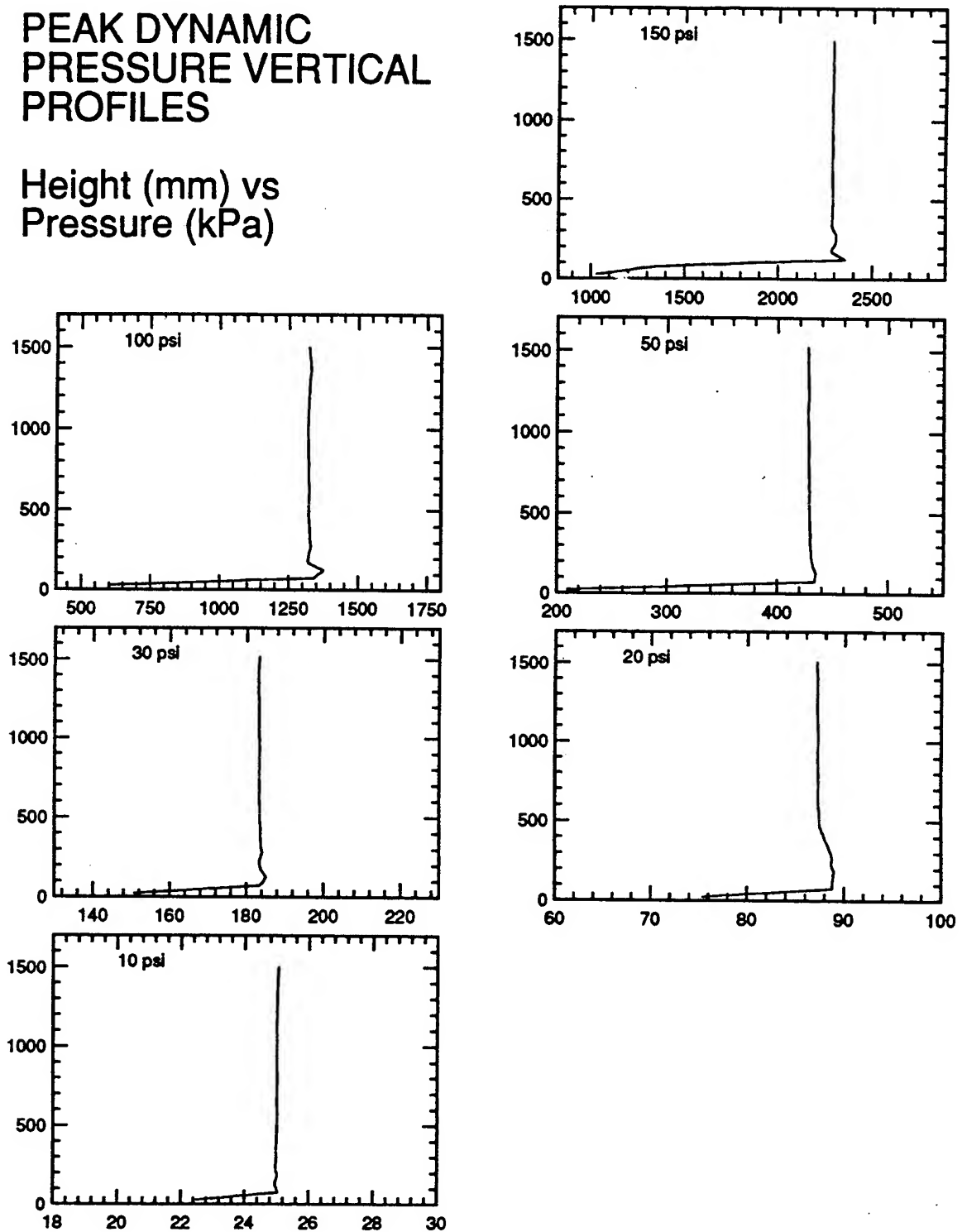


Figure 4. Vertical profiles of peak dynamic pressure at several 'psi' stations, obtained from the numerical simulation.

# HYDROSTATIC OVERPRESSURE IMPULSE VERTICAL PROFILES Height (mm) vs Overpressure Impulse (kPa s)

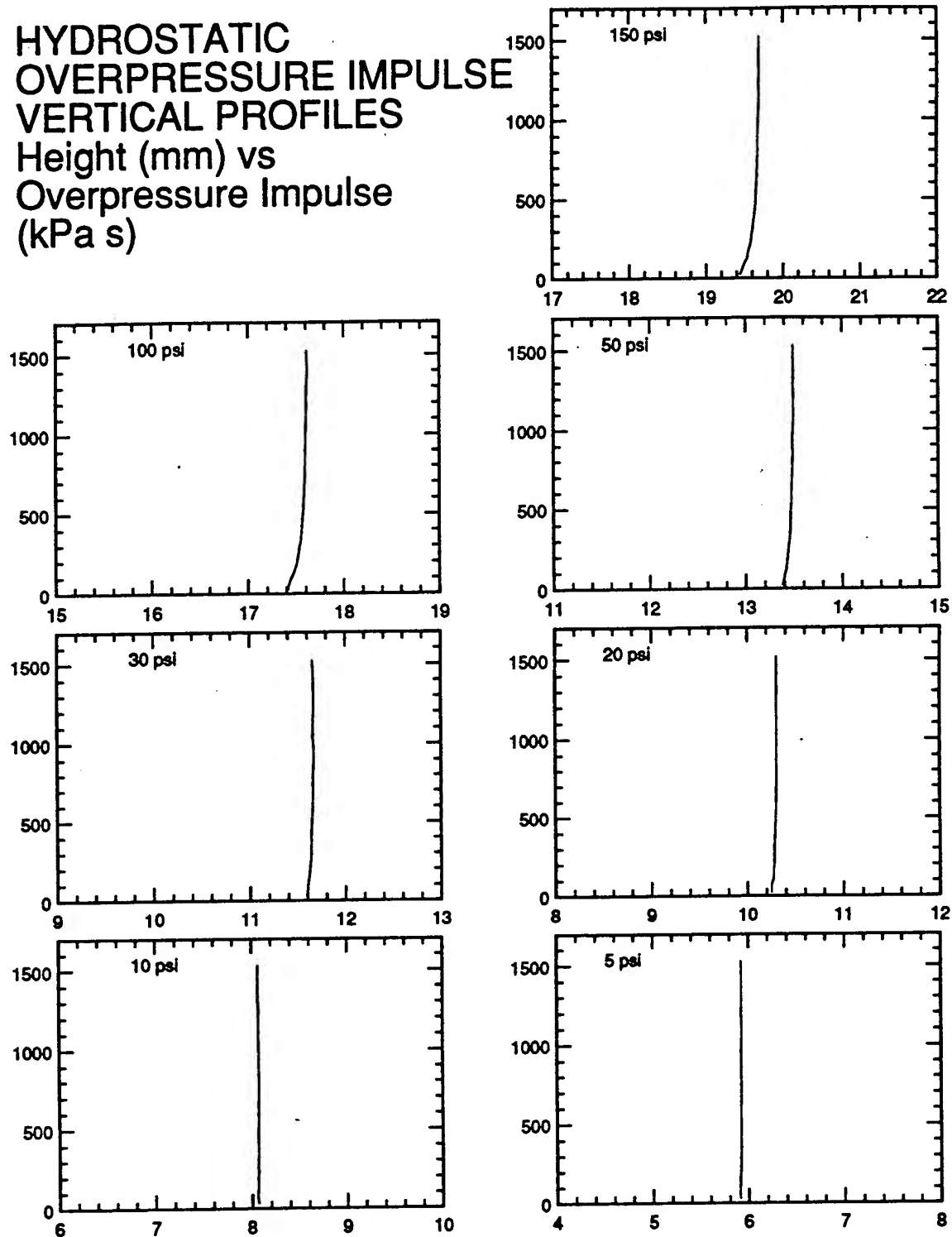


Figure 5. Vertical profiles of hydrostatic overpressure impulse during the positive phase at several 'psi' stations, obtained from the numerical simulation.

# DYNAMIC PRESSURE IMPULSE VERTICAL PROFILES

Height (mm) vs Dynamic  
Pressure Impulse (kPa s)

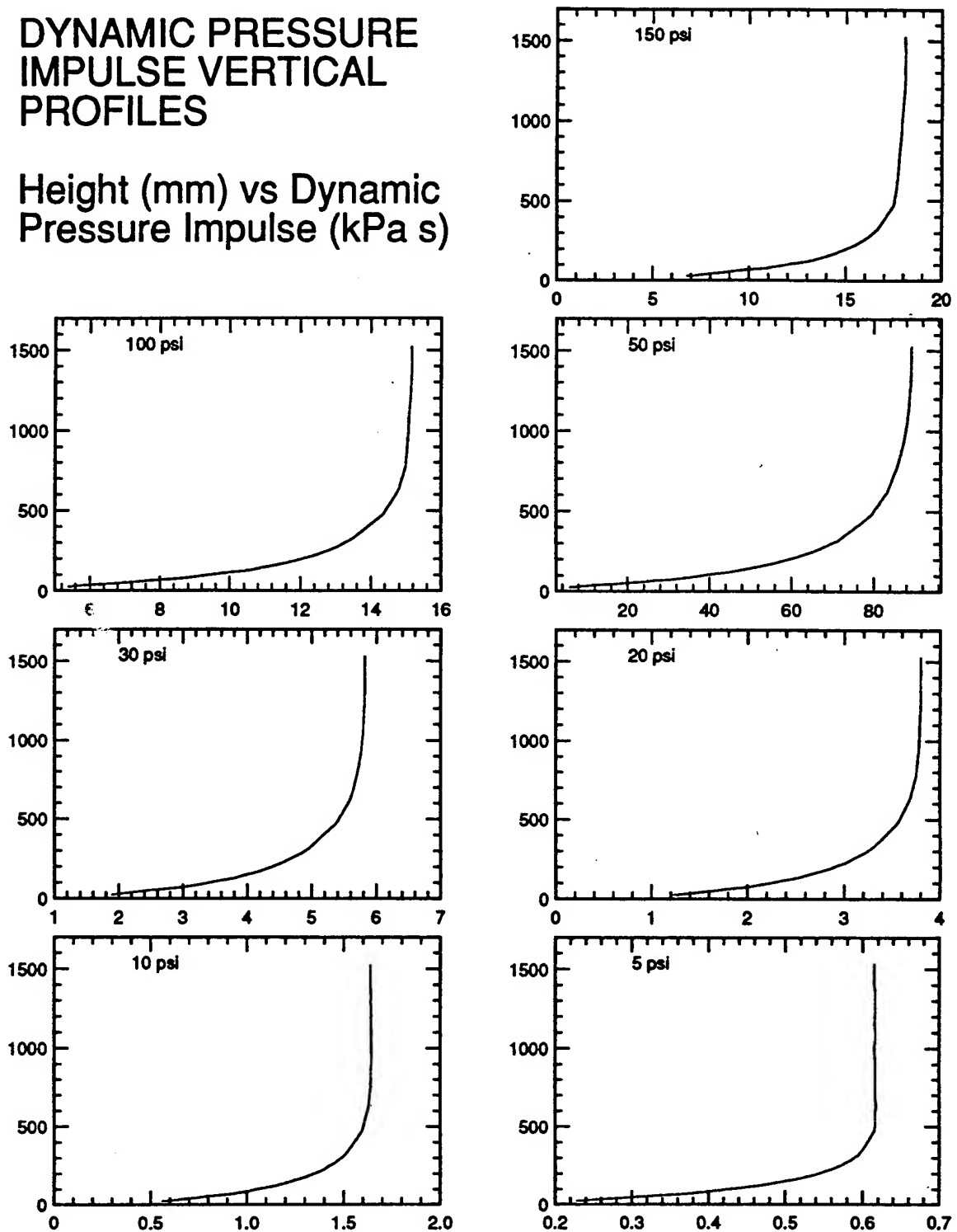


Figure 6. Vertical profiles of horizontal dynamic pressure impulse during the positive phase at several 'psi' stations, obtained from the numerical simulation.

# DYNAMIC PRESSURE IMPULSE

Height (mm) vs  
Percent Free Stream

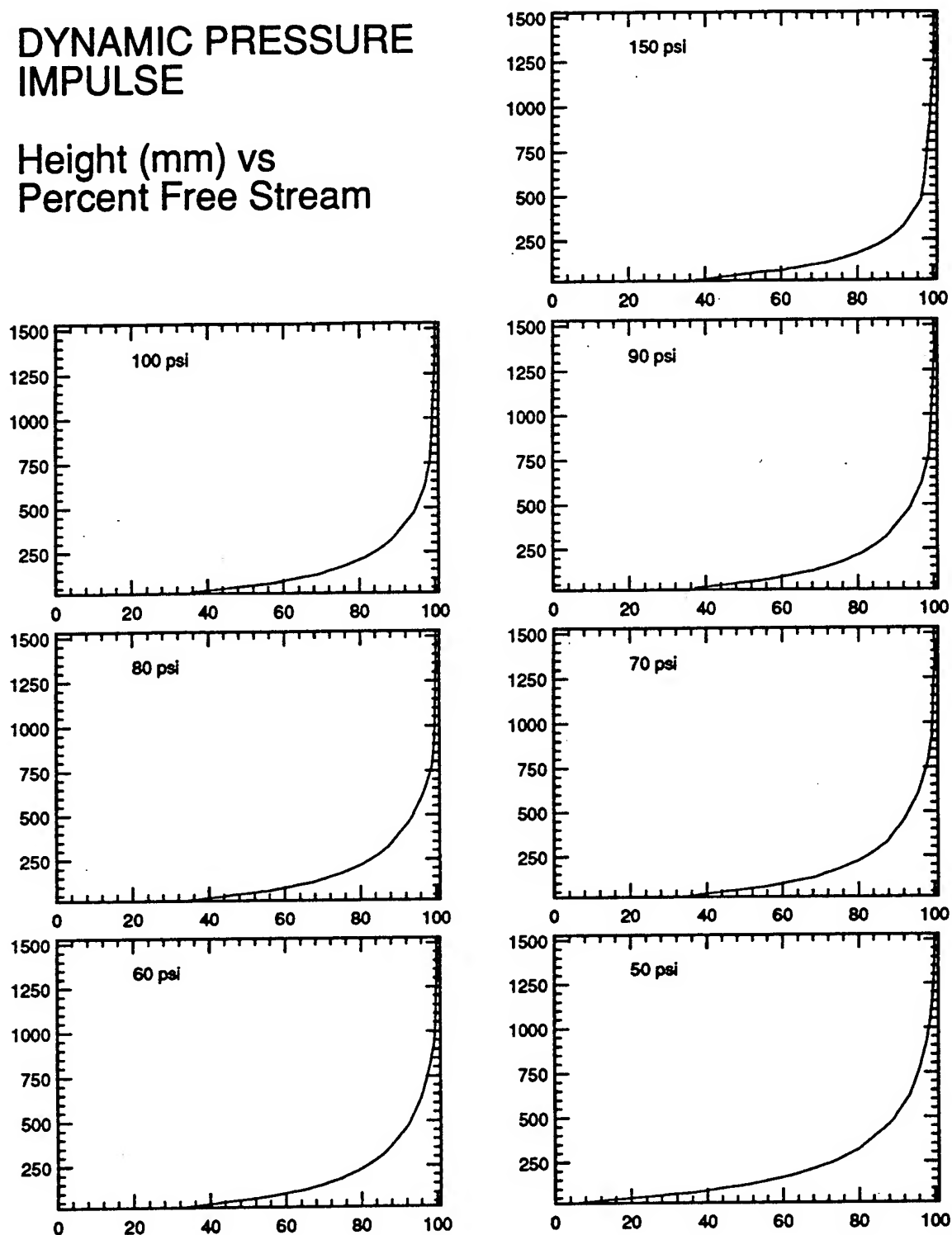


Figure 7. Vertical profiles of horizontal dynamic pressure impulse as a percentage of the free-stream value, obtained from the numerical simulation.

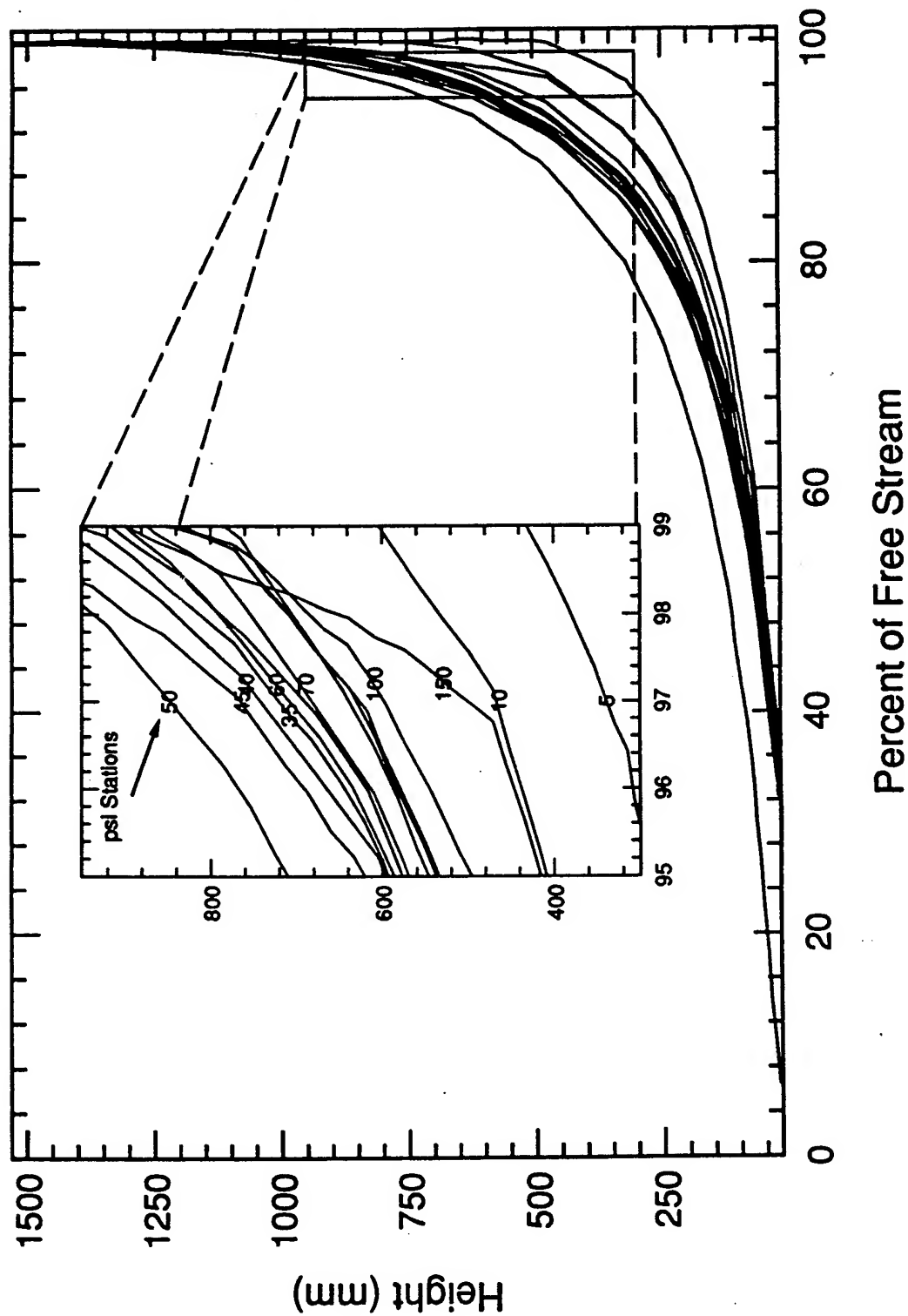


Figure 8. Overlaid vertical profiles of horizontal dynamic pressure impulse at the indicated 'psi' stations.



overlaid in figure 8 to illustrate how the shape of the boundary layer profile changes with overpressure level.

The height of the boundary layer was defined as the height at which the dynamic pressure impulse was 98% of the free-stream value, and this height is plotted as a function of peak overpressure level in figure 9.

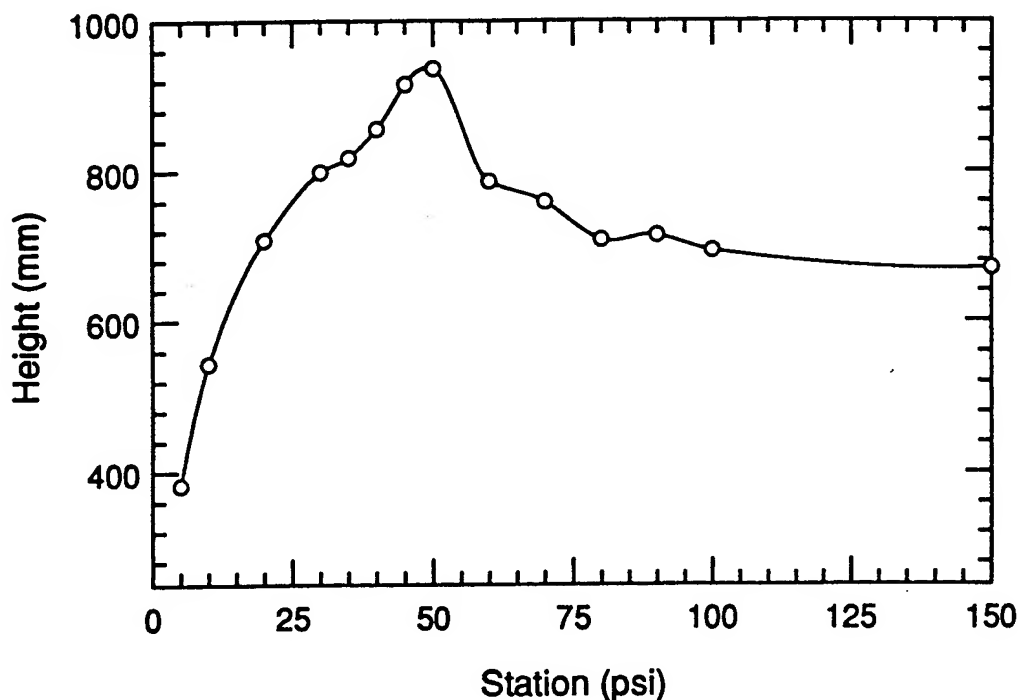


Figure 9. Boundary layer height as a function of peak hydrostatic overpressure level.

## 5.2 Flow Tracer Measurements

The five smoke trails were formed as planned, except that two of the black trails reached a height of only about 1 m instead of the intended 2 m. All the trails started at ground level, and at the time of the shock front arrival had not been dispersed by ambient wind. Just before being hit by the blast wave the trails were straight, vertical, and the required width.

The movement of the trails was recorded successfully on the film, with good contrast and resolution. Figure 10 is a frame from the film just before the arrival of the shock front. The two white smoke trails were not seen as clearly as the black trails against the white back board and ground surfaces, but this was expected. The main purpose of the white trails was to separate the black trails in the event that they approached one another too closely and merged in the compressive blast wave flow. Figure 11 is another frame from the film, about 100 ms after the shock, as the trails were leaving the field of view.

Each frame of the film was projected at a magnification of about 30:1 for analysis. IRIG timing codes recorded on the edge of the film enabled the exposure time of each frame to be determined relative to the charge detonation. The fiducial markers and the centre lines of the smoke trails were digitized using an x-y digitizer. The surveyed

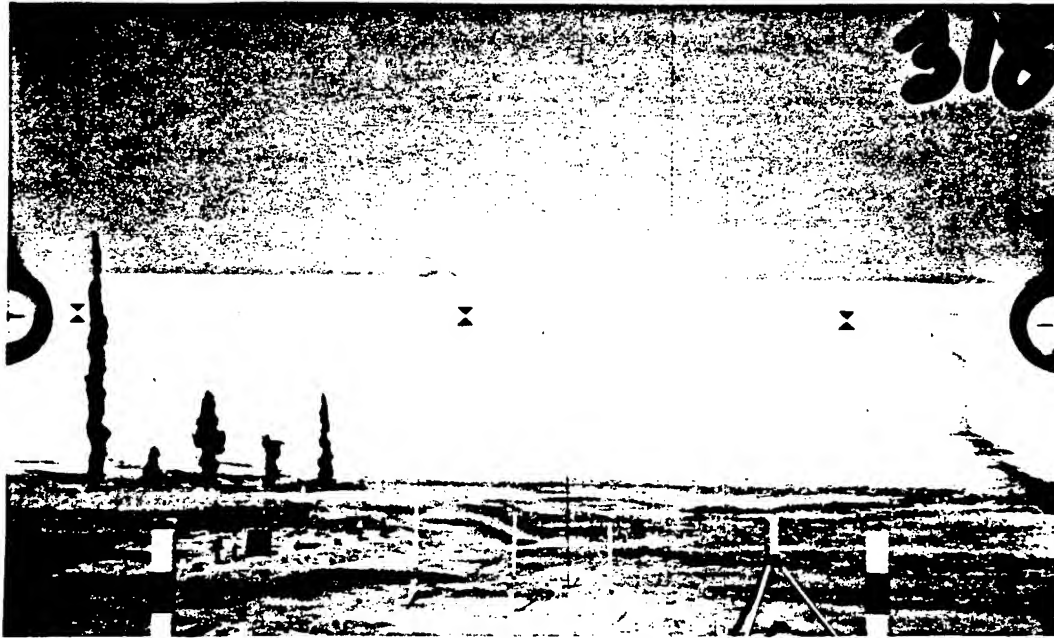


Figure 10. Frame from the high speed film showing the miniature smoke trails just before the arrival of the shock front. The approaching shock is casting a shadow on the back-ground board. There are three fiducial markers on the back-ground board, and two foreground markers on black and white columns at the bottom of the frame. A number of displacement cubes can also be seen in the foreground.

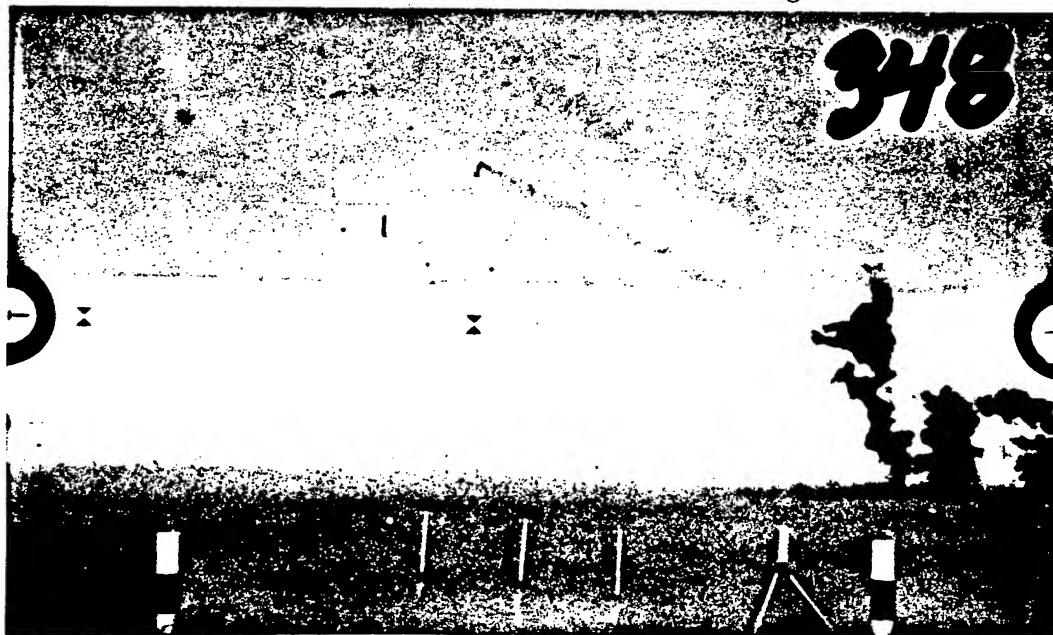


Figure 11. Frame from the high speed film approximately 100 ms after that shown in figure 10. In addition to the smoke trails, the displacement cubes can be seen at the beginning of their motion. The early rotation of the larger cubes can be seen clearly, particularly that of the cube initially on the ground.

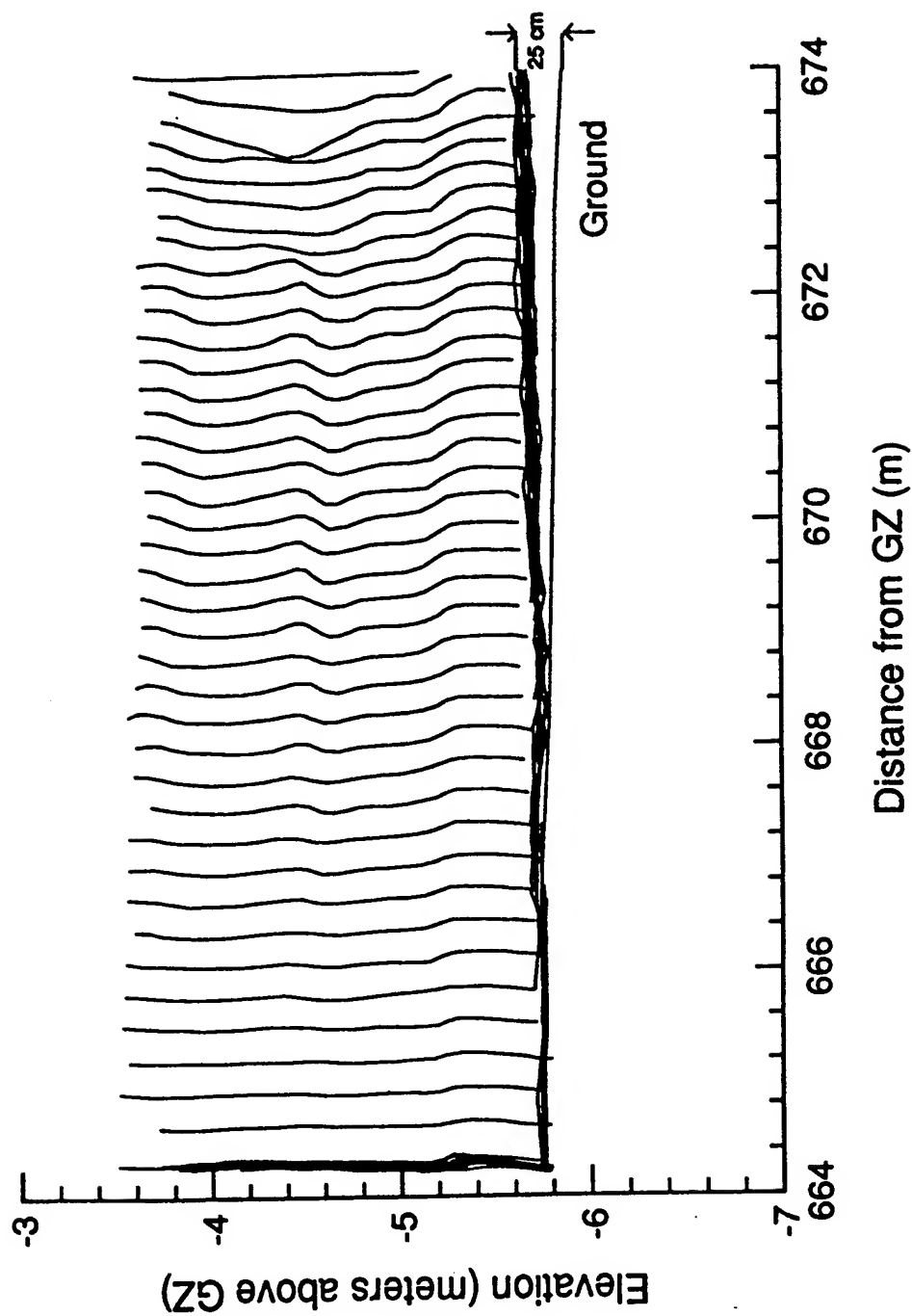


Figure 12. Digitized image of the center line of the black smoke trail closest to the charge at the 5 psi station. The interval between successive images was approximately 3.3 ms. After approximately 100 ms, as the trail leaves the field of view, the height of the boundary layer was approximately 25 cm.

positions of the fiducial markers were used to determine the scaling relationship between distances measured in the plane of the projected film and those in the vertical plane through ground zero containing the smoke trails.

Figure 12 shows the sequence of positions in the object plane of the first smoke trail for all of the frames digitized. Also shown is the intersection between the object plane and the ground surface, which had been surveyed after it had been graded and rolled, and the dust suppressant and white lime applied. The ground surface fell away slightly with increasing distance from ground zero along the radial line passing through the smoke trails and ground zero. Similar results were obtained for all the trails and these are reported by McMillin and Dewey (1995b)

From the digitized images of the smoke trails it was clear that there was an abrupt change in the direction of each trail close to the ground surface which identified the top of the boundary layer. This gradually increased in height, and was about 25 cm above the ground surface when the smoke trails moved from the camera's field of view. This was about 100 ms after the first smoke trail had been hit by the blast wave, during which time it had been displaced almost 10 m.

The velocities of the smoke trails were computed at several heights above the abrupt change in slope which identified the top of the boundary layer. No significant variation of particle velocity with height could be detected above that point.

### 5.3 Cube Displacement

When struck by the blast wave, the cubes on pedestals travel a distance in free flight before contacting the ground. Using the time required to fall the height of the pedestal, an empirical function for displacement over the ground for the cubes versus launch velocity, and the measured total displacement, estimates are made of the distances travelled in the air and after contact with the ground (Ethridge *et al*, 1995, figure 2-1). Table 1 shows the ratios of the estimated distance travelled by the elevated cubes after contact with the ground to the displacement of the ground level cubes. The ratios are for average values at each station. The values listed for 5 psi are for single cubes at the photographic station.

At the 50, 30, and 20 psi stations the cubes were sandblasted so that paint was removed from the fronts of all cubes. Elevated cubes had only a slight removal from the bottom and almost none on the other surfaces, which indicates that they maintained their original orientation during almost all the sandblasting period. Ground-level cubes typically had a clean front, a large loss of paint on the bottom, partial removal on the rear, and slight removal on the top, which indicates rotation away from ground zero. These two modes of motion were recorded at the 5 psi station by high-speed photography.

Table 1. Ratios of Displacements of Elevated and Ground Level Cubes

Station	Cube Type	Height	Ratio
50 psi	152 mm Steel	25.4 cm†	0.97
	51 mm Steel	25.4 cm†	1.82
30 psi	152 mm Steel	25.4 cm†	0.89
	51 mm Steel	25.4 cm†	2.42
	152 mm Aluminum	25.4 cm†	1.06
20 psi	51 mm Steel	25.4 cm†	1.83
	152 mm Aluminum	25.4 cm†	1.10
10 psi	152 mm Oak	25.4 cm†	0.92
	51 mm Aluminum	25.4 cm†	1.89
5 psi	44 mm Oak	10.2 cm‡	1.31
		22.9 cm‡	1.81
	51 mm Aluminum	10.2 cm‡	1.25
		22.9 cm‡	1.29
	152 mm Pine	17.8 cm‡	0.71

†- Height of centre of cube    ‡- Height of base of cube

#### 5.4 Cube Trajectories

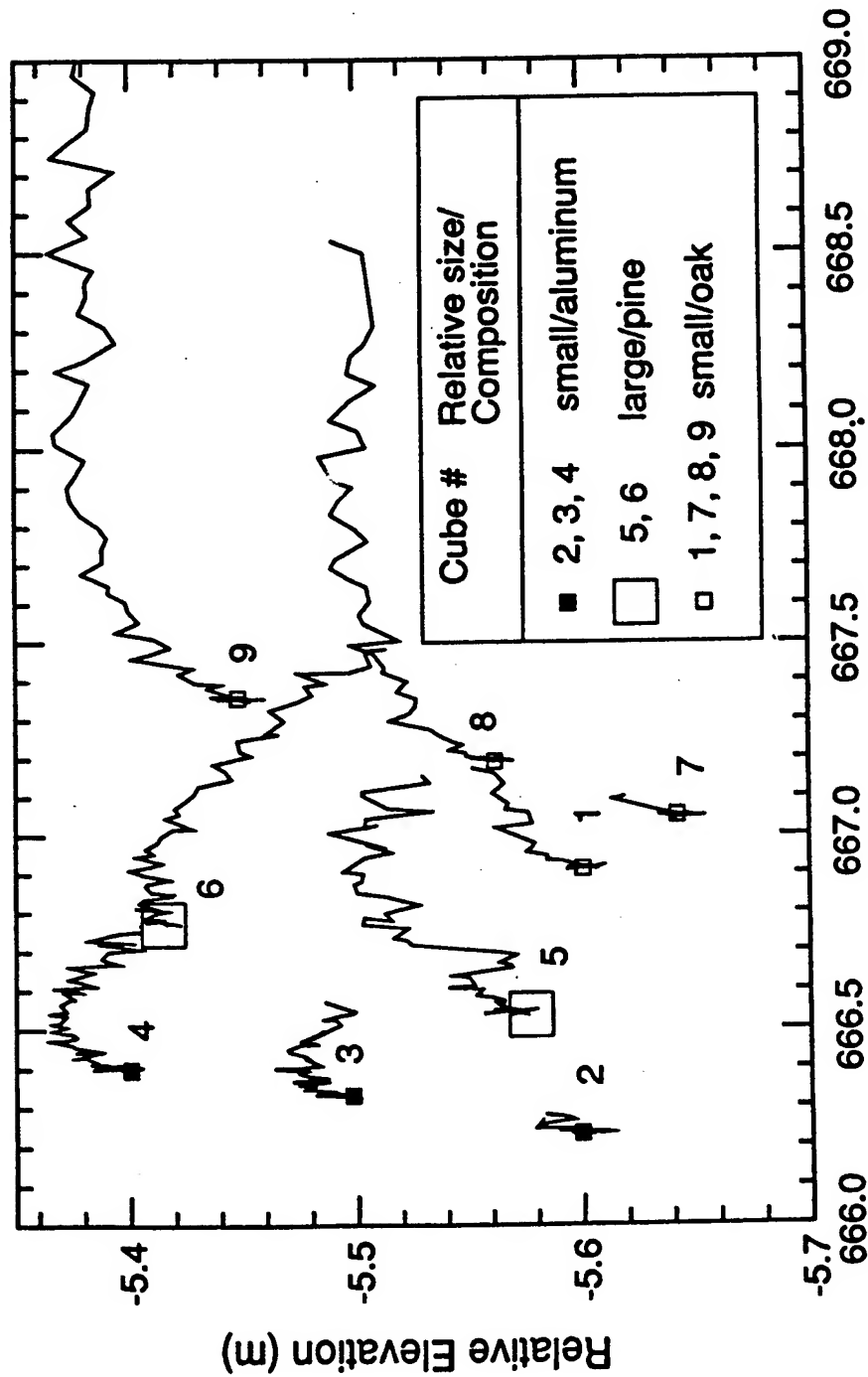
The nine cubes at the 5 psi station were placed so that they were in the field of view of the camera used to record the trajectories of the smoke trails. The individual frames of the film were projected at a magnification of approximately 30:1, and the apparent positions of the centres of the cubes were measured in the projection plane. These positions, for each cube, were transformed to the assumed plane of motion of that cube, *viz.* a vertical plane containing ground zero and the cube's initial surveyed position.

The trajectories of the apparent cube centers were calculated as a series of (x,y,t) values, where x is horizontal distance from GZ, y is the elevation relative to GZ and t is time after charge detonation obtained from the IRIG timing code on the edge of the film. Cube trajectories were measured from t = 1061 ms to t = 1302 ms, corresponding to 71 film frames. Measurements were made for several frames prior to the cubes being hit by the shock front and then for as long as they remained visible. All the cubes were eventually obscured by dust raised from the ground surface. The cubes initially placed on the ground usually disappeared from sight before those initially placed on raised platforms.

The x-y trajectories of the cubes are shown in figure 13. The initial motions of the cubes have an upward component, and this is particularly so for the cubes initially resting on the ground. When the blast interacts with the cubes it causes them to slide and rotate. A cube then presents an inclined base to the blast flow so that lifting forces are generated. The cubes on the ground rotate faster than those on the platforms, producing larger vertical components to their motions.

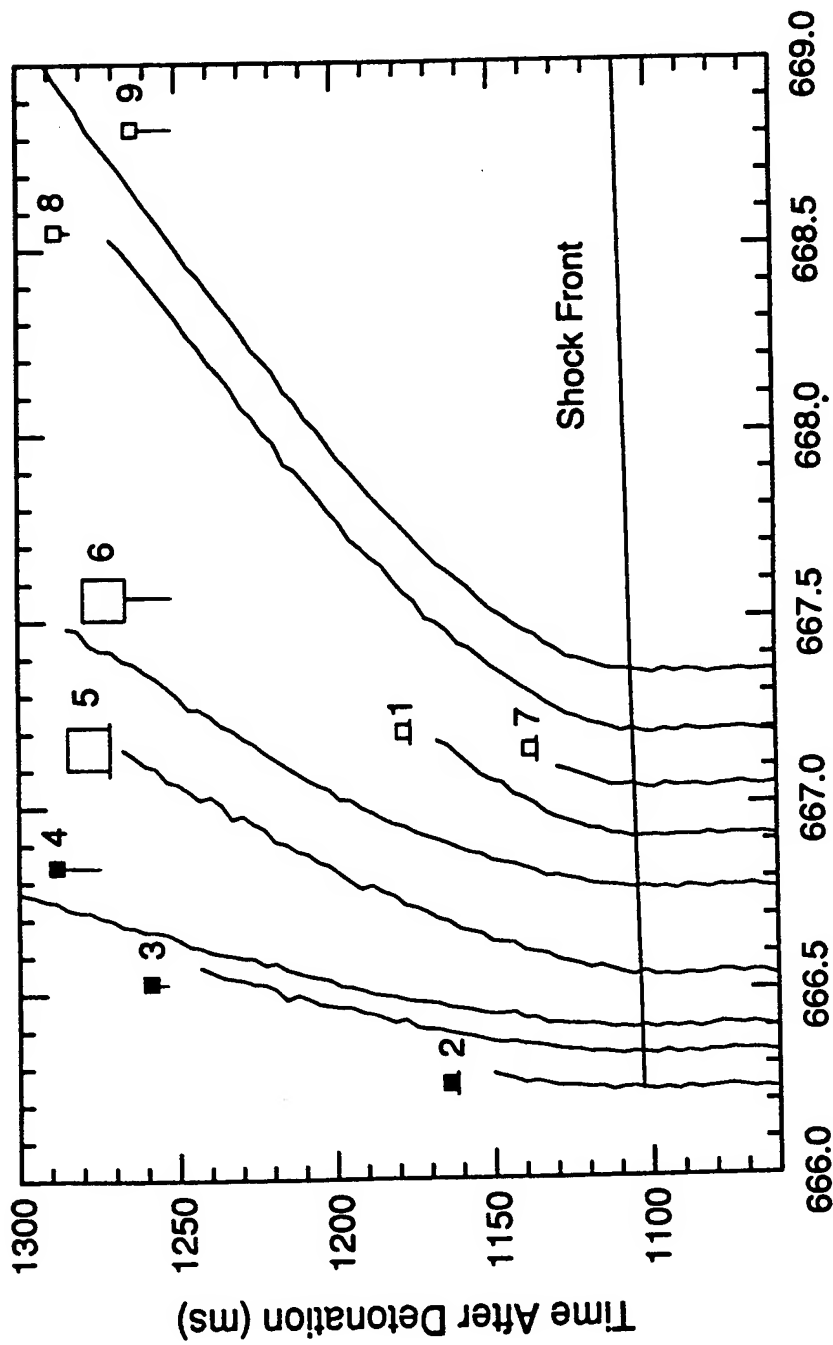
The x-t trajectories of the cubes and the shock front are shown in figure 14. The cubes accelerate relatively slowly, and in most cases may not have reached their maximum velocity by the time they were obscured by the dust. The 44 mm oak





Horizontal Distance from GZ (m)

Figure 13. Trajectories of the nine displacement cubes in the field of view of the camera at the 5 psi station. Heights and distances are relative to ground zero. The 'noise' in the trajectories is due to the difficulty of identifying the centres of the cubes in the projected images, and not an indication of erratic motions of the cubes.



Horizontal Distance from GZ (m)

Figure 14. Horizontal displacement vs time (x-t) trajectories of the nine displacement cubes in the field of view of the camera at the 5 psi station. The shock front trajectory is also shown. The slopes of the trajectories are the horizontal velocities, and it can be seen that there is little difference between the final velocities of the cubes of the same size and material which were initially at different elevations. The type of cube is identified in figure 13.

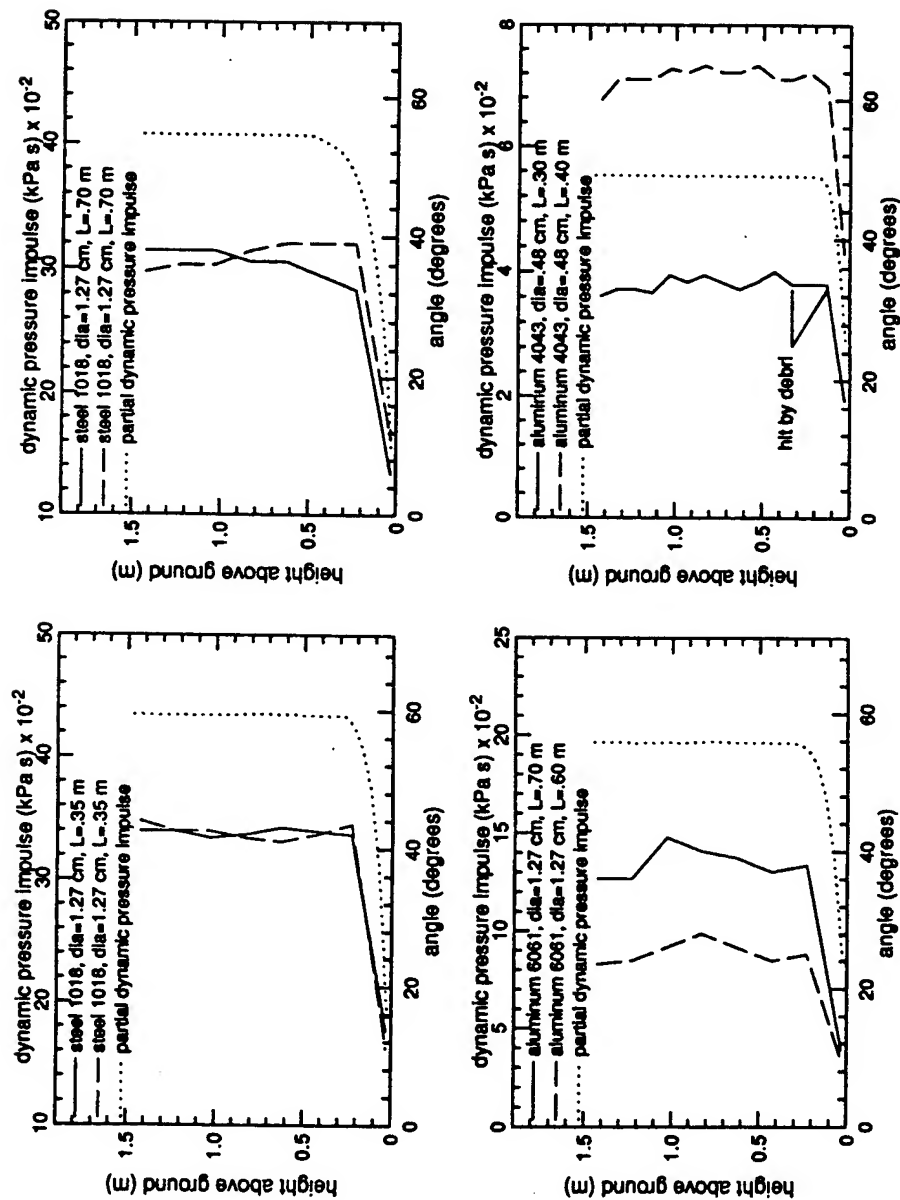


Figure 15. Variation of cantilever bending with height at four of the measurement stations. The dotted lines show the variation of dynamic pressure impulse predicted by the numerical simulation, up to the time at which the dynamic pressure had decayed below the value which would produce further permanent deformation of the cantilever.

cubes, labelled 1, 7, 8 and 9 in figure 14, attain the highest velocities, and the 51 mm aluminum cubes, labelled 2, 3 and 4, the lowest velocities. The 152 mm pine cubes have intermediate velocities. There appear to be no significant differences between the velocities of the cubes on the ground and those elevated on platforms. This is probably because the cubes on the elevated platforms have only a slight upward motion, and soon begin to fall under gravity, whereas the cubes initially on the ground develop larger upward motions so that there is little difference between the heights of the different cubes during the time they are being accelerated by the blast.

### **5.5 Cantilever Deformation**

A variation of cantilever bending with height above the ground was observed at all the vertical arrays, except at the 5 psi station where the lowest cantilevers were damaged by debris. The angles of bend as functions of height at four of the stations are plotted in figure 15. Over the graded ground at the 30 psi station differential bending was observed to a height of 0.23 m. The fact that no variation in bending was observed above a certain height does not mean that the boundary layer did not extend above this height, but that by the time the boundary layer reached that height the blast wave had decayed to a level that it no longer contributed to the bending of the cantilevers, as discussed below.

Over the rough ground differential bending was observed up to a height of 43 cm at the 30 psi station as compared to 23 cm at the same radial distance over the graded area. At the 10 psi stations the corresponding heights were approximately 20 cm over the rough ground and 13 cm over the graded area.

## **6. DISCUSSION AND CONCLUSIONS**

### **6.1 Discussion**

The numerical simulation using the SHARC code has provided a detailed description of all the physical properties of the blast wave in the region immediately above the ground, as functions of time after passage of the shock front. Figure 3 shows that the boundary layer produces a small effect on the peak hydrostatic pressure, although steady state theory normally assumes that the hydrostatic pressure remains constant through a boundary layer. A review of the results from the simulation shows that the shock front in the region close to the ground was slower than that at a metre or so above the ground, and a reduced pressure behind the slower shock is therefore to be expected. The conditions in the blast wave behind the shock front are unsteady. The speed of the shock is faster than the speed of sound behind the shock so that the vertical gradient in hydrostatic pressure does not have time to reach an equilibrium state. This effect is more significant at the higher overpressure levels where there is a greater difference between the shock speed and the local speed of sound behind the shock, as illustrated in table 2.

Table 2		
Overpressure	Shock Speed	Sound Speed
(psi)	(m/s)	(m/s)
100	889	511
30	564	407
5	387	355

The results of the simulation have been compared with measurements made using high speed photography of flow tracers, displacement cubes and cantilever gauges. In comparing the simulated and measured results it is necessary to take into account the time dependence of the growth of the boundary layer. For example, when the smoke tracers moved out of the field of view of the camera the observed height of the boundary layer was approximately 25 cm, after a flow time of 100 ms. For that flow time the numerical results predict a dynamic pressure of 2.5 kPa, at a height of 32 cm, which is the same as the free-field value, and a dynamic pressure of only 0.075 kPa at a height of 2.5 cm. In other words, the boundary layer was growing but had not yet reached a height of 32 cm, as confirmed by the smoke tracer photography.

A comparison of the results of the numerical simulation with those from the arrays of horizontal cantilevers also requires a consideration of the time dependent nature of the growth of the boundary layer. When a cantilever is bent by a blast wave it continues to bend as long as the loading moment is greater than a yield-point value. Within the blast wave the loading moment constantly decreases due to the decay of the dynamic pressure and the decreasing drag coefficient as the cantilever begins to bend. Once the limiting loading moment has been reached the cantilever is not affected by the remaining blast wave. For each vertical array of cantilevers the limiting loading moment was calculated, and the height of the boundary layer was determined from the numerical simulation at the time when that limit would have been reached. The resulting comparisons between the bend angles of the cantilevers as functions of height and the dynamic pressure impulse up to the time of the limiting loading moment derived from the numerical simulation are shown in figure 15. The agreement was excellent at all the stations at which the comparison was possible.

The ratios of the estimated displacements of the elevated cubes, after contact with the ground, to the displacements of the same cubes on the ground surface, listed in table 1, show a boundary layer effect for the small cubes at 10 psi and above. The displacements of the elevated small cubes are factors of 1.82 to 2.42 larger than the displacements of cubes on the ground. However, the ratios for the large cubes are near 1.0. The cross-section of these 152 mm cubes is large compared to the scale of the boundary layer. As a cube on the ground rotates it presents an obstruction with a height that increases to 21.5 cm. An elevated cube, with its bottom surface at a height of 17.5 cm, falls into the rising boundary layer as it moves off the pedestal and presents only its frontal area to the flow. Thus these cubes ultimately experience similar loading. The dimensions of the small cubes, however, are such that the elevated cubes experience a different flow for a longer time than the same cubes on the ground.

At the 5 psi photographic station, when the cubes are first hit by the blast they

begin to rotate and expose a lifting surface to the blast flow, which results in a vertical component to their motion. The cubes on the ground tend to rotate faster than those on the relatively smooth elevated platforms, and so rise more rapidly. As a result, for much of the period during which they are accelerating they are at a similar height to the elevated cubes, as shown in figure 13, and they may also be exposing a larger drag surface to the blast flow.

The dynamic pressure impulse, as determined by the numerical simulation, is probably the most effective measure of the boundary layer height, which is defined as that height at which the positive phase impulse reached 98% of the free-stream value. The variation of boundary layer height with the peak hydrostatic overpressure is given in figure 9, which shows a maximum height close to the 345 kPa (50 psi) region. The height at that point was approximately 95 cm. At higher overpressure levels the boundary layer height ranged from 70 to 80 cm, and at lower levels the height monotonically decreased to 40 cm at the 34.5 kPa (5 psi) station. This type of variation of boundary layer height with distance from ground zero is to be expected. The height of the boundary layer is dependent on two features: the magnitude of the velocity shear and the duration of the flow. The first of these properties decreases with distance from the source and the second increases, thus producing the observed maximum.

## 6.2 Conclusions

The good agreement between the results of the numerical simulation and the measurements made using flow tracer photography, displacement cubes and cantilevers, within the limits of the spatial resolution of the measurement techniques, indicates that the simulation provided an excellent description of the physical properties within the boundary layer produced by the MINOR UNCLE blast wave over a graded surface. In future experiments, now that the nature of the boundary layer is better understood, more exact measurements will be possible, so that the precision of a numerical simulation can be better evaluated.

The simulation gave a detailed description of the blast wave in the range from the 1034 kPa (150 psi) to the 34.5 kPa (5 psi) peak hydrostatic overpressure levels. The results show how the boundary layer at individual locations changes with time, and how the physical properties vary with distance from the explosive source. The study described here has provided results for a single sized explosion over one type of ground surface. The validity of the simulation has been established by the present study, but to make it generally applicable, a matrix of simulations is required using a range of charge sizes and various degrees of ground roughness.

## ACKNOWLEDGEMENTS

The boundary layer project was conceived, funded and coordinated by Arnfinn Jenssen of the Norwegian Defence Construction Service. The authors gratefully acknowledge his leadership and his desire to understand the underlying physical principles which influence the effects of blast waves. The authors wish to thank S. Watkins for her contribution to the preparation of this paper.

## REFERENCES

- Barthel, J.R., 1985. 2D Hydrocode Computations using a  $K - \epsilon$  Turbulence Model: Model Description and Test Calculation, S-CUBED, a Division of Maxwell Laboratories, Inc., SSS-R-85-7115 R-1.
- Carpenter, H.J., 1973. Blast Wave Boundary Layer Measurements, Air Force Weapons Laboratory Rept., AFWL-TR-73-211, pp31.
- Clauser, F.H., 1954. Turbulent Boundary Layer Analysis in Adverse Pressure Gradients, J.Aerosp. Science, 21, 91-108.
- Dewey, J.M. and McMillin, D.J., 1988. Smoke Puff Diagnostics, Proc. MISTY PICTURE Symposium, Def. Nucl. Agency POR 7187-5, 14, 1-64.
- Dewey, J.M. and McMillin, D.J., 1991. Smoke Trail Photo-Diagnostics, MISERS GOLD Symposium Rept, Def. Nucl. Agency POR 7352-2, 207-387.
- Dewey, J.M. and McMillin, D.J., 1993. Smoke Trail Photo-Diagnostics, DISTANT IMAGE Symposium Rept, Def. Nucl. Agency POR 7379-2, 5, 1-46.
- Dewey, J.M. and McMillin, D.J., 1995a. Smoke Trail Photo-Diagnostics, MINOR UNCLE Symposium Rept, Def. Nucl. Agency POR 7453-2, 2, 1-48.
- Du, X., Liu, W.S. and Glass, I.I., 1982. Laminar Boundary Layers behind Blast and Detonation Waves, Univ. Toronto Inst. Aerospace Studies, UTIAS Rept. 259, pp73.
- Dyment, A., 1982. The boundary layer behind the blast wave generated by a very intense explosion on flat ground, Phys. Fluids, 25, 11, 1968-1969.
- Liu, S.W. and Mirels, H., 1980. Numerical solutions for unsteady laminar boundary layers behind blast waves, Phys. Fluids, 23, 4, 681-688.
- McMillin, D.J. and Dewey, J.M., 1995b. Boundary Layer Measurements Using Miniature Smoke Trails, MINOR UNCLE Symposium Rept, Def. Nucl. Agency POR 7453-5, 5, 1-22.
- Mirels, H. and Hamman, J., 1962. Laminar Boundary Layer behind Strong Shock Moving with Nonuniform Velocity, Phys. Fluids, 5, 1, 91-97.
- Dixon-Heister, L., Ethridge, N.H. and Peterson, R.S., 1990. Cube Displacement, MISERS GOLD Symposium Rept, Def. Nucl. Agency POR 7352-3, 1, 1-176.
- Ethridge, N., 1992. Displacement of Cubes by Blast, DISTANT IMAGE Symposium Rept, Def. Nucl. Agency POR 7379-3, 10, 1-61.
- Ethridge, N.H. and Dixon, L., 1988. Displacement Cubes, Proc. MISTY PICTURE Symposium, Def. Nucl. Agency POR 7187-2, 3, 1-79.
- Ethridge, N.H., Dixon-Heister, L.A., Jackson, W.F. and Peterson, R.S., 1990. Dust Measurements, MISERS GOLD Symposium Rept, Def. Nucl. Agency POR 7352-3, 219-363.

Ethridge, N.H., Flory, R.A. and Keefer, J.H. 1995. Cube Displacements, MINOR UNCLE Symposium Rept, Def. Nucl. Agency POR 7453-5, 6, 1-62.

Launder, B.E. and Spalding, D.B., 1972. Mathematical Models of Turbulence, Academic Press, New York.

Pierce, T.H., 1986. Numerical Boundary Layer Analysis with the  $K - \epsilon$  Turbulence Model and Wall Functions, S-CUBED, a Division of Maxwell Laboratories, Inc., SSS-R-87-8138.

van Netten, A.A. and Dewey, J.M., 1992. Cantilever Gauges, DISTANT IMAGE Symposium Rept, Def. Nucl. Agency POR 7379-5, 5, 1-49.

van Netten, A.A. and Dewey, J.M., 1995. Horizontal Cantilever Gauges and Cantilever Gauges, MINOR UNCLE Symposium Rept, Def. Nucl. Agency POR 7453-5, 4, 1-68.

Viegas, J.R., and Rubesin, M.W., 1983. Wall Function Boundary Conditions in the Solution of the Navier-Stokes Equations for Complex Compressible Flows, Proc. 16th AIAA Fluid and Plasma Dynamics Conf. AIAA-83-1694, pp45.

Viegas, J.R., Rubesin, M.W., Horstman, C.C., 1985. The Use of Wall Functions as Boundary Conditions for Two-Dimensional Separated Compressible Flows, Proc. 23rd AIAA Aerospace Sciences Meeting, AIAA-85-0180, pp34.



- basic data to validate the AUTODYN-2D numerical calculations.

These results will be included in the Swiss Design Manual for Protective Structures (LS 2000)

### 3. EXPERIMENTAL SETUP

The test series have been conducted on a shock tube. To generate conventional blast profiles a very short driver was used. Additionally, a so-called dumptank with special openings was mounted at the end of the tube in order to avoid disturbances of the incident blast wave.

**Figure 3-1** shows the schematic outline of the experimental setup used for this test series, whereas in **Figure 3-2** the geometrical parameters of the obstacles investigated are given. For all the investigations the tunnel cross-section was square.

**Figure 3-3** presents the three different obstacle configurations tested.

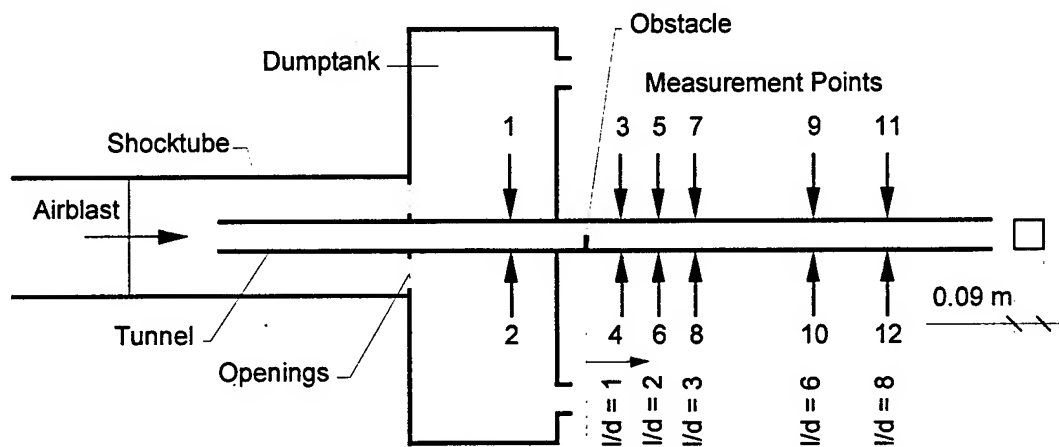


**Figure 3-1:** Experimental setup

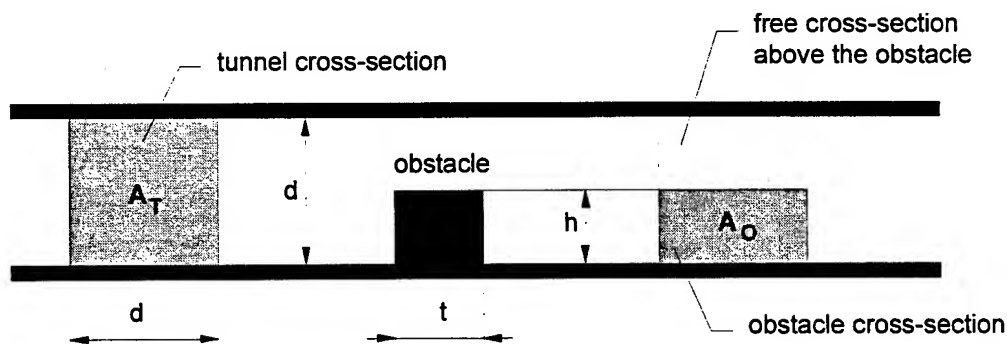


**Figure 3-2:** Geometrical parameters of the experimental setup

# **AIRBLAST PROPAGATION IN TUNNELS WITH OBSTACLES**

## **EXPERIMENTAL INVESTIGATION AND NUMERICAL CALCULATIONS**

Ed. Binggeli, B. Anet  
NC Laboratory Spiez, CH-3700 Spiez, Switzerland

Dr. D. Schläpfer  
E. Basler & Partner, CH-8702 Zollikon, Switzerland

### **ABSTRACT**

This paper investigates by means of small scale models the influence of obstacles on the propagation of a short duration blast in straight tunnels. Three different cross sectional ratios of the obstacles were used. Side-on pressure time histories have been measured at different locations after one as well as two obstacles in series, where the obstacles were either in a row or opposite.

Additionally, numerical calculations with the two dimensional FD-hydrocode AUTODYN-2D were performed. The comparison of the numerical results with the experimental ones shows an acceptable agreement for the peak-overpressure of the ongoing airblast but is disappointing with respect to the impulse. Generally speaking we observed that obstacles like baffles, all kinds of plates and screens, cause a reduction of the impulse, whose numerical value is mainly determined by the ratio between the blocked cross section and the total cross section. However, such obstacles provoke also reflections which lead to recovery and even amplification of the peak-overpressure of the ongoing airblast.

### **1. INTRODUCTION**

The rapid developments in non-nuclear weapons technology in the near past emphasize the importance of considering the threat to protective structures due to conventional weapons effects.

For the case of the detonation of a conventional weapon at the entrance of a tunnel or in the tunnel itself, knowledge about the propagation of short duration blasts in tunnel and tunnel systems is rather scarce. Therefore the NC Laboratory Spiez started an experimental and numerical research program in order to investigate such configurations more thoroughly.

### **2. OBJECTIVES**

The main goal of the test series described in this paper was to work out

- the behavior of short duration blast waves of conventional explosions passing over tunnel obstacles by measuring peak-overpressure and impulse at various distances downstream of the obstacles.

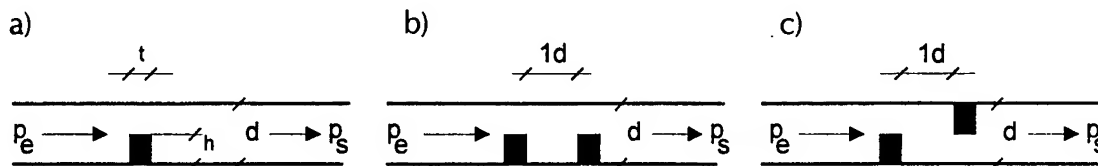


**Figure 3-3:** Obstacle configurations investigated; a) single obstacle  
b) two obstacles in a row, c) two obstacles opposite

#### 4. TEST PROGRAM

**Figure 4-1** shows the chosen set of the main parameters for the experimental investigations. The thickness  $t$  of the obstacles is  $0.1d$ ,  $0.5d$  and  $1d$  with area cross-section ratios  $A_O/A_T$  of 25%, 50% and 75%. The peak-overpressure of the incident blast wave varied between 0.5 bar and 3 bar. To check the reproducibility at least 3 identical tests were performed for each configuration.

$p_e$ [bar]	0.5, 1.0, 2.0, 3.0
$h/d$ [-]	0.25, 0.5, 0.75
$t/d$ [-]	0.1, 0.5, 1.0
$A_O/A_T$ [%]	25, 50, 75

**Figure 4-1:** Test parameters

#### 5. RESULTS

##### 5.1 EXPERIMENTAL RESULTS

In order to get a better insight in the complex diffraction process which occurs in the vicinity of the obstacles, the flow field has been visualized by means of optical techniques. Both shadowgraphs as well as watertable pictures were used for this purpose. Some results are presented in **Figure 5-1**.

The reflection of the incident blast wave at the obstacles and the formation of strong vortices at the edges are typical for such diffraction type obstacles. The pictures shown in the right part of **Figure 5-1** document that the watertable is still a useful and efficient tool for visualization purposes and a great help mainly for providing a fast and low cost analysis especially in the case, where a large number of geometrical parameters is involved.

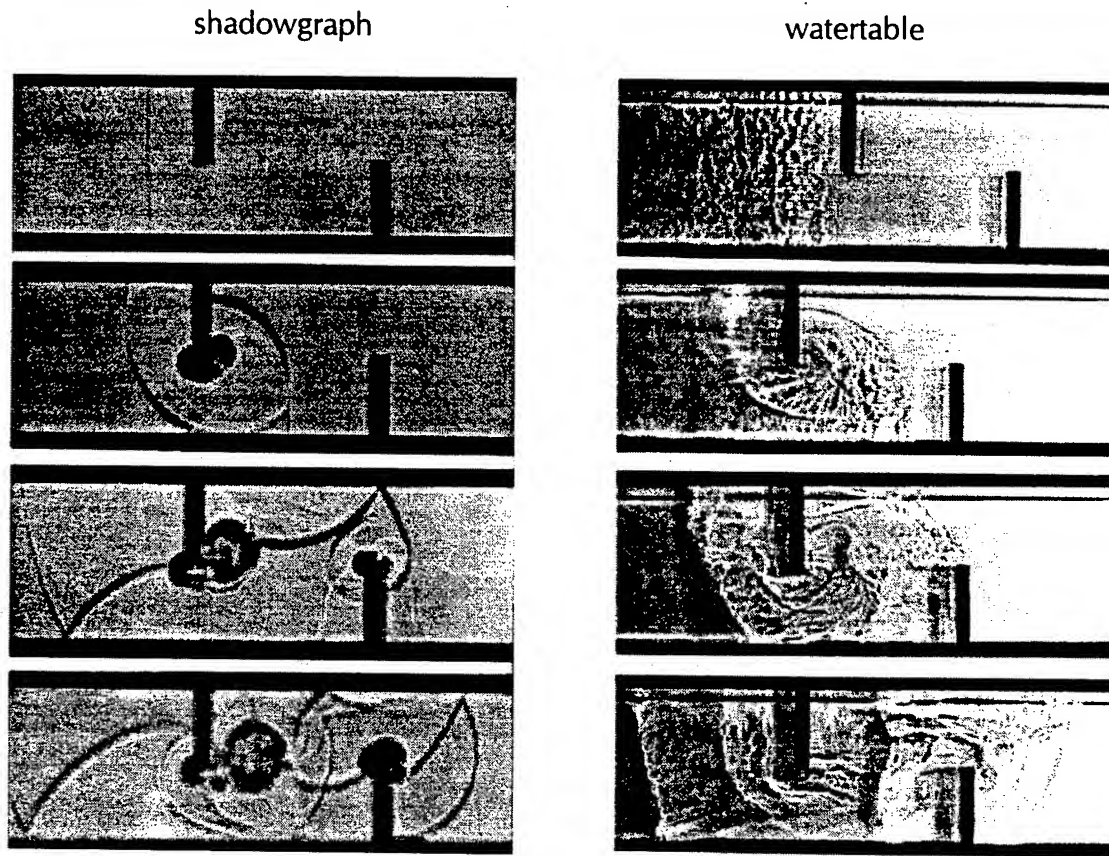


Figure 5-1: Visualization of the blast wave passing obstacles

As an example Figure 5-2 shows pressure-time histories for a single obstacle with an area ratio of 75%, measured at a distance of  $2d$ , respectively  $6d$  after the obstacle. The peak-overpressure of the incident blast wave is 0.5 bar. The pressure profile at the measuring point MP 3 ( $l/d = 2$ ) is characterized by a first weak shock front followed by a stronger reflected shock as well as by large pressure oscillations caused by the many reflections of the blast at the obstacle itself and at the sidewalls of the tunnel.

At MP 4 (opposite MP 3) the reflection effects are already damped but due to the reflections mentioned above, the peak-overpressure of the ongoing blast is almost identical to the one of the incident blast wave. However, after the shock front the pressure decreases sharply, leading to a greatly reduced impulse. Further down at  $l/d = 6$  (MP 9 and MP 10) the blast wave is almost recovered and smoothed.

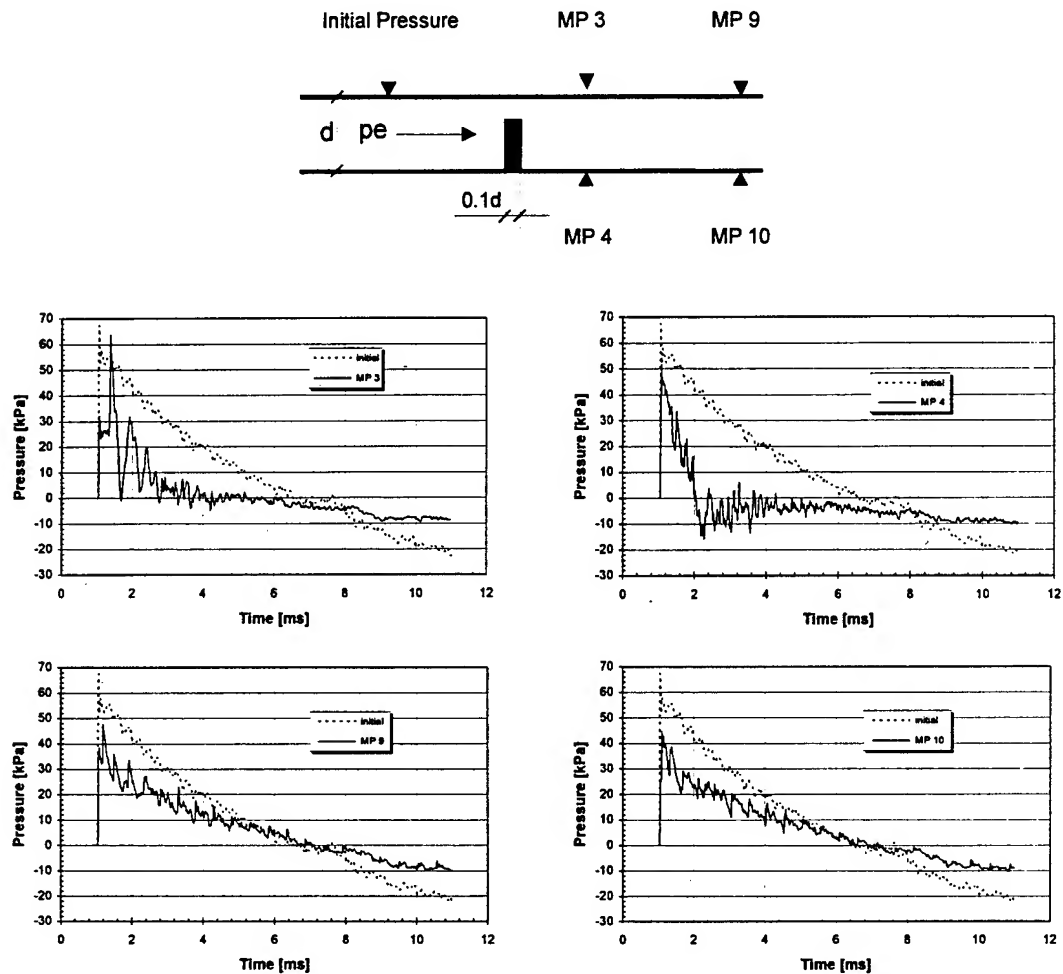


Figure 5-2: Pressure profiles at  $l/d = 2$  and  $l/d = 6$

## 5.2 NUMERICAL RESULTS

The numerical calculations have been performed with the AUTODYN-2D computercode. The AUTODYN is a two dimensional FD hydrocode which is running in our Laboratory on a Personal Computer. The number of nodes is limited to 30'000. In Figure 5-3 vectorplots (left row) and contourplots (right row) for a blast wave passing obstacles at different times are presented as a typical example of such calculations.

In comparison with the shadowgraphs presented in Figure 5-1 the numerical results show that the diffraction process of the blast wave at the obstacle is modeled fairly well. As a code for inviscid fluid flows, AUTODYN is of course not able to handle the flow separation and the vortex formation at the edges of the obstacle properly.

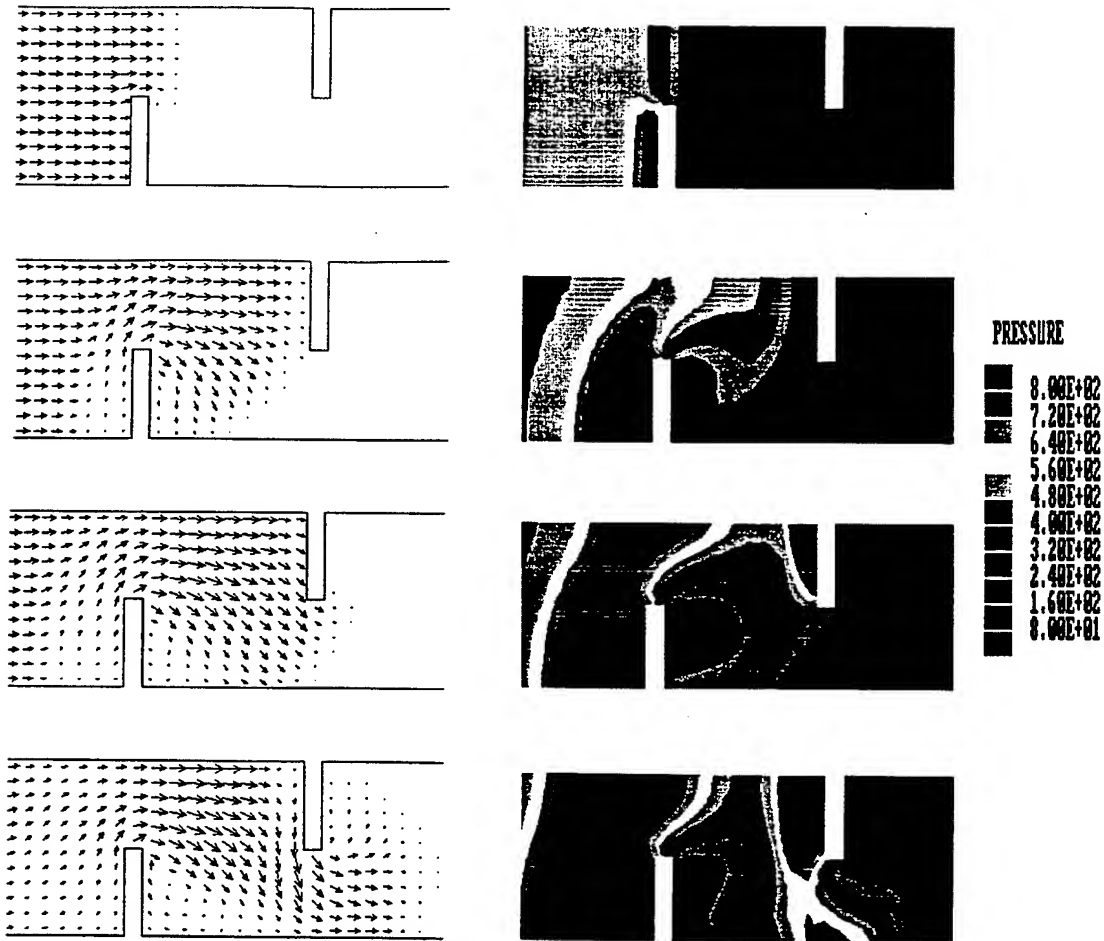


Figure 5-3: Vector and contour plots

### 5.3 COMPARISON BETWEEN NUMERICAL AND EXPERIMENTAL RESULTS

Based on some representative pressure-time histories the numerical data provided by AUTODYN-2D calculations are compared to the corresponding experimental ones, this for the measurement points MP 3 and MP 4 located at  $l/d=2$  and for MP 9 and MP 10 located at  $l/d=6$  after the obstacles considered.

Figures 5-6 and 5-7 show typical pressure-time histories from tests with one obstacle and two obstacles opposite, for peak-overpressures  $p_e$  of the incident blast waves of 2.0 bar and 3.0 bar respectively.

Although the numerical model matches the experimental shock tube arrangement as closely as possible, the incident numerical blast profiles (MP 1) for both tests show a slightly higher peak-overpressure than the ones from the experiment.

Comparing the profiles at MP 3 and MP 4 just after the obstacle one can say, that the agreement is quite satisfying. Even the oscillations of the pressure-time histories, caused by the many reflections of the blast at the obstacles and the tunnel side walls, are correctly modeled, but they are strongly damped in the numerical calculations probably due to the fact that the vortex-blast interaction (see **Figure 5-6**) is not properly taken into account.

In some distance after the obstacle (MP 9, MP 10) the initial parts of the pressure-time histories, where diffraction effects dominate, correspond excellently. In a later time, where viscosity effects become increasingly important higher pressures are observed in the experiment which lead to higher impulse values as compared to the numerically calculated ones.

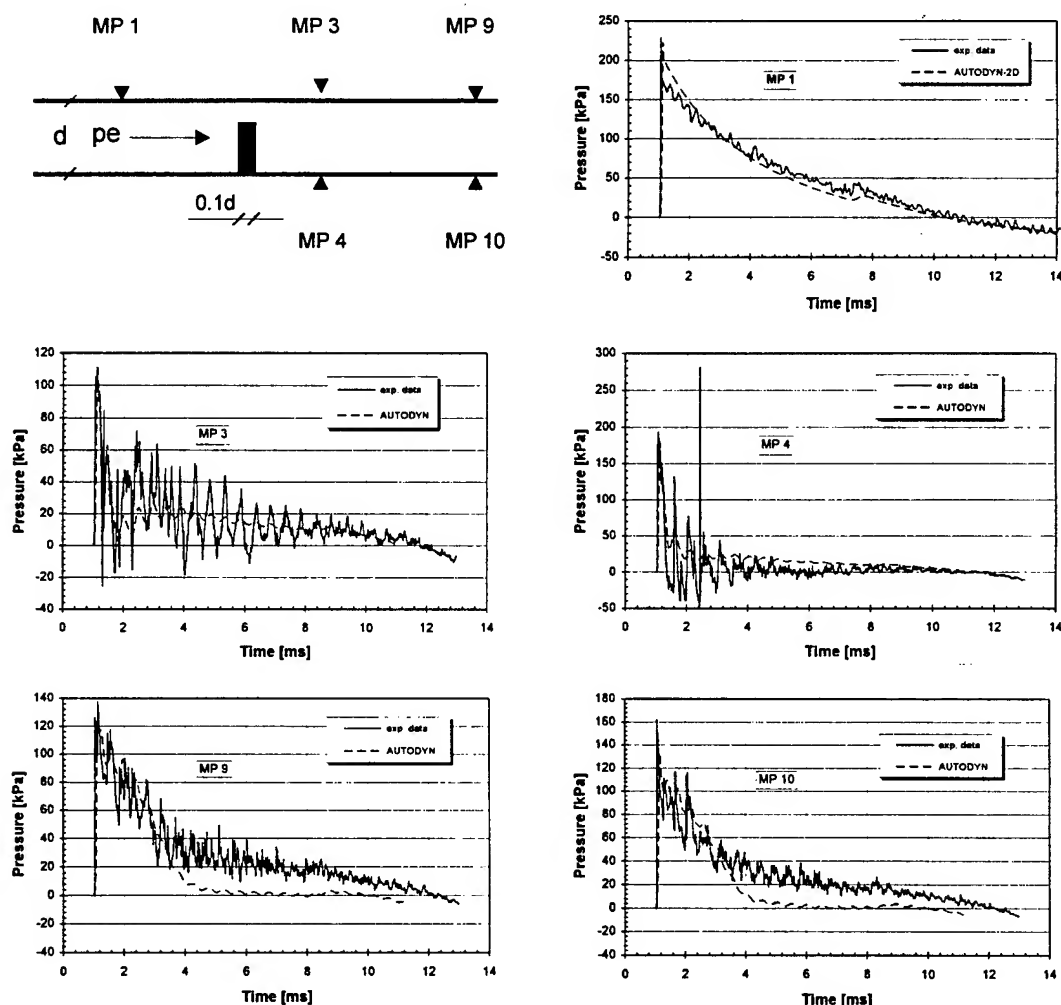


**Figure 5-6:** Comparison of calculated and measured pressure time histories

For the profiles shown in **Figure 5-7**, the agreement in the very earliest loading phase is again satisfying. In the later phase, however, the numerical results are rather disappointing and in such a form hardly usable for engineering purposes. The modeling approximations which had to be done to solve this problem and the inability of the AUTODYN-2D to handle viscous flow fields might be responsible for the poor agreement observed after the initial diffraction of the shock front. Further calculations will clarify this point.

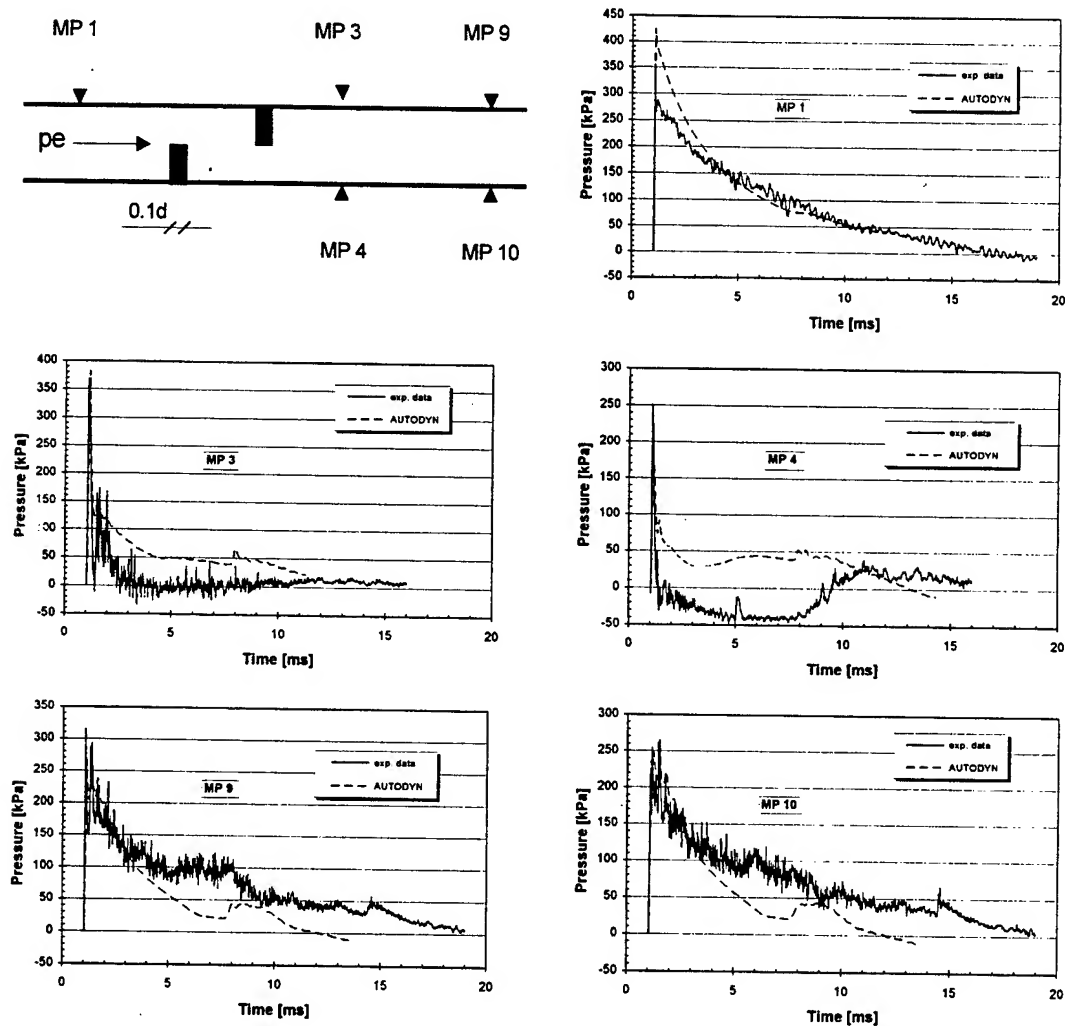


**Figure 5-7:** Comparison of calculated and measured pressure time histories



## 6. EFFECTIVENESS OF OBSTACLES IN TUNNELS

### 6.1 A SINGLE OBSTACLE CONFIGURATION

Based on the experimental results **Figure 6-1** shows the effectiveness of a single obstacle in terms of peak-overpressure and impulse related to the values of the incident blast wave for different cross-sectional area ratios of the obstacles at  $l/d = 2$ . The thickness of the obstacle is  $0.1d$ .

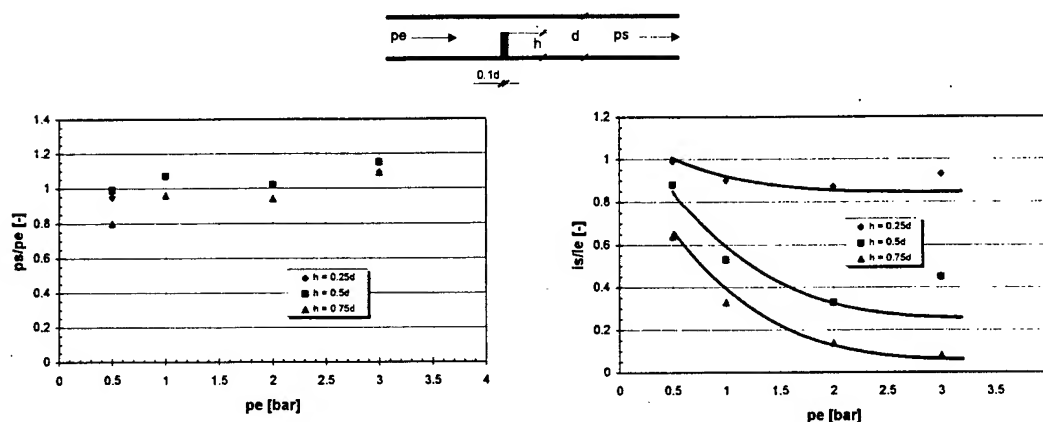


**Figure 6-1:** Influence of the area ratio

Cross-section area ratios of the obstacles up to 50% do surprisingly not attenuate the peak pressure of the ongoing blast, even a slight increase can be observed. Only for area ratios of 75% an attenuation of the peak-overpressure occurs. On the other hand the impulse is strongly influenced by the obstacles. The attenuation of the impulse can reach values up to 90% depending on the peak-overpressure of the incident blast wave.

### 6.2 OTHER OBSTACLE CONFIGURATIONS

The diagrams in **Figure 6-2** show the effects of the three obstacle configurations investigated on the peak-overpressure of the blast wave at  $l/d = 2$ ; this for an area ratio of 50% and a thickness of the obstacle of  $0.1d$ .

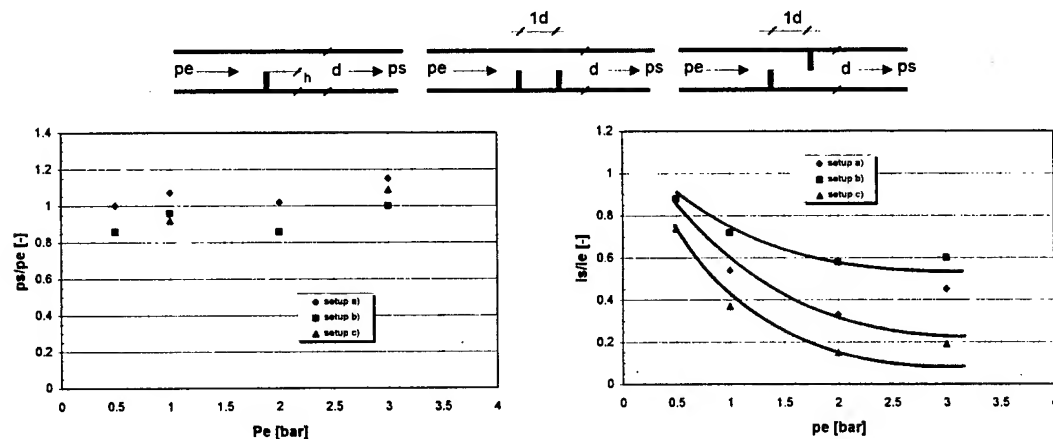


**Figure 6-2:** Influence of the obstacle configuration

The same tendency with respect to the peak-overpressure and impulse, as described above for the case of a single obstacle, can also be observed with other obstacle configurations.

### 6.3 INFLUENCE OF THE OBSTACLE THICKNESS

In Figure 6-3 the influence of the thickness of the obstacle on the peak-overpressure and impulse at  $l/d = 2$  is displayed for a single obstacle configuration with an area ratio of 50%.

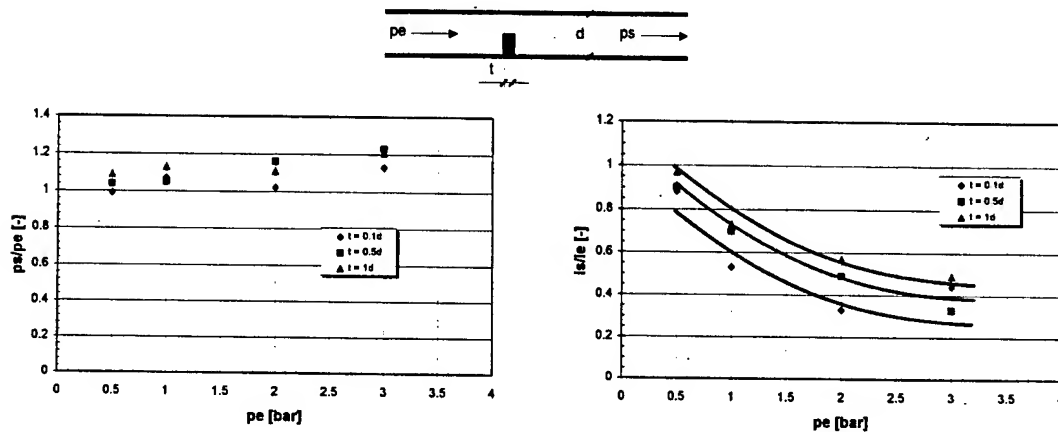


Figure 6-3: Influence of the single obstacle thickness

With increasing obstacle thickness the peak-overpressure increases too, whereas the damping factor for the impulse decreases.

## 7. SUMMARY AND CONCLUSIONS

The propagation of a short duration blast wave in a tunnel with different obstacle configurations has been investigated experimentally with small scale models on a shock tube. Furthermore, the results were used as a base for the validation of numerical calculations with the AUTODYN-2D code.

A first set of numerical results is presented in this paper. Although encouraging, at the time being the numerical results provide only qualitative but very valuable information on the flow field characteristics but are not able to match the experimental results. Especially in the later time phase of the diffraction, where viscosity effects become dominant a great discrepancy can be observed. Thus, further calculations and improvements in the modeling technique are needed.

Generally speaking we observed that obstacles like baffles, all kind of plates and screens, primarily cause a reduction of the impulse of the ongoing blast wave, whose value is largely determined by the ratio between blocked cross section and total cross section. However, such obstacles provoke also reflections which lead to recovery and amplification of the peak-overpressure of the ongoing blast.

## **COLLATERAL EFFECTS OF CONFINED BLAST EVENTS**

**Thomas Mazzola, Logicon RDA**

**Dave Myers, MAJ USA, Defense Nuclear Agency**

**Rick Fry, Defense Group, Inc.**

Customary safety considerations of explosive events are focused primarily on the prompt hazards associated with blast, thermal and fragmentation. However, other, more subtle, collateral effects from the explosion may result from the release of hazardous materials to the atmosphere and the subsequent transport. In a realistic military scenario, we may be concerned with the release of toxic materials associated with the production or storage of weaponry. In a blast trial, we may be concerned with transport of simulated toxic materials or simply with atmospheric pollutants which may be a nuisance in the neighborhood of the test. In this paper, we explore those event parameters which are most significant for collateral effects.

We consider a range of explosive charges within confined facilities of varying internal volumes and with a variety of openings to the atmosphere. The focus here is to estimate the plausible range of plumes released to the atmosphere. For this we use the quasi-steady blowdown model STEP1, developed for DNA in which we characterize the released containment mass, plume dimensions, plume duration, and other parameters. In parallel, we consider the atmospheric transport and surface deposition sensitivities to plume parameters, as well as to the background meteorology using DNA-sponsored SCIPUFF atmospheric transport model. We consider both local and long-range effects. Through these parametric calculations, the most significant parameters for collateral effects are determined.

Based upon the calculational findings, the most important plume parameters are isolated and approximate correlations with blast event conditions are derived. This provides a quick estimation tool for use in estimating downwind collateral effects hazards.

## **Introduction**

In the MABS community, investigation of blast damage effectiveness or of aspects of explosive blast hardening is fairly common. These subjects are often primary objectives of blast research projects. Study of the unintended or undesired by-products of blast events, sometimes called collateral effects, is less frequently reported. In the current study, we will focus on the lofting of hazardous pollutants into the atmosphere. Instead of focusing on details of the transient shock phenomena, we study those physical phenomena which are most important to the injection of hazardous materials into the atmosphere.

The reason for studying the collateral effects of blast events derive from the military need to responsibly plan for and operate around the possible release of hazardous materials into the environment. The release of such materials, particularly nuclear, biological, and chemical (NBC) materials, into the atmosphere may result from attacks upon or accidents at military or industrial facilities. As part of the DNA Hazard Prediction and Assessment Capability (HPAC), we are adapting for operational users computer models to credibly predict the release, transport, and effects on personnel of NBC materials. Such computer models may also be useful to those studying the safety and environmental impact aspects of blast field trials.

This paper will first describe the modeling approach for predicting the expulsion of hazardous materials from hard facilities due to the venting of internal explosion products. Parametric results from such models will be presented and discussed. The analysis of these results leads to a proposed simplified engineering model for estimating the expulsion of hazardous material as a source for downwind transport. We conclude with a discussion of the validity of these models and identification of those source parameters most important to the downwind transport.

## **Structural Expulsion and Plume Model (STEP1)**

STEP1 is designed to model the expulsion of material from inside a structure after it is attacked by a weapon. Currently STEP can handle the debris created by a concrete structure and stored dry biological agent only. This concrete structure can have many rooms and the damage can range from a weapon penetration to a wall or roof failure. The future model will have the ability to handle hard and soft structures, and deal with all types of stored materials. Clearly STEP1 can be used for more than just weapon sources, but the program has focused on Counterproliferation (CP) type scenarios.

The model consists of three pieces: a multi-room blowdown model (MBLM), a jet expansion model (JEM), and an initial plume model (PTOP). STEP is not an atmospheric transport model, but it must handle the initial plume since this is a violent environment not well described by any current atmospheric transport model.

MBLM has similarities to the BLASTX model, but was extended to handle the specific problems associated with collateral effects. It is an engineering-format interior flow code that calculates the time varying conditions within a rigid-walled structure. Currently the model handles 15 rooms, but it is trivial to modify if the need arises to handle as many rooms as necessary. The code treats each computational zone as a room. The advection between rooms is calculated by applying integrated solutions for quasi-steady frictional gas dynamic flow from a reservoir to a receiver. This allows MBLM to handle complex connectivity in a simplified manner. The code calculates the anaerobic and aerobic reactions. The current code accepts detonation characteristic of any weapon desired. Particulates, both reactive and non-reactive, and vapors can be added to the structure and included in the process. Gravitational settling of the particulate is also modeled. Heat transfer to the walls is considered and modeled for both convective and conductive heat transfer.

The JEM model uses semi-empirical relationships developed primarily for jet engines and rocket exhaust plumes. It takes the output from MBLM describing flow at the vent area and calculates the jet produced. The modeling considers exit pressure that exceeds ambient level, and the flow is said to be underexpanded. In underexpanded sonic conditions, the arrangement of expansion and shock waves cause an increase in the diameter of the jet as the flow returns to ambient pressure. The jet alternates between supersonic and subsonic flow with Mach disks separating the two. The jet then returns to sonic flow where local pressure equals ambient. The Mach number in the jet decreases monotonically as distance from the vent increases.

PTOP calculates the initial plume from a jet of particles from a vent. The model at first represents a plume top that incorporates the materials from the rising jet. The jet momentum contributes significantly to the early plume growth. Entrainment of the surrounding cold air is considered and plays a large role in determining the buoyancy of the initial plume. PTOP takes the results of JEM and uses the same basic concepts developed for the Low Altitude Multi-Burst (LAMB) code to develop the initial plume. PTOP assumes that all the jet material overtakes the plume top and become permanently entrained in the plume top. The material equilibrates thermally and mechanically with the material already present in the plume. The motion of the plume top considers the effects of air entrainment, drag, buoyancy, adiabatic expansion, and the inertial effect of motion in the surrounding atmosphere. The amount of air entrained is proportional to the rise velocity of the plume top, augmented by the internal toroidal vortex. This is modeled by a submodel (Hill's vortex). Initially the plume rise is dominated by momentum in the jet, and then the dominating physical process is buoyancy and effects of the surrounding air.

## Comparison with Experiment

The modeling effort was conducted in conjunction with an experimental program. The experimental program provided scaled experiments at 1/17, 1/6 and 1/3 scale. Additional full scale experiments were conducted by other programs, but the data available was readily useable to help improve and check the performance of the model. In the scaled experiments varied fractions of the initial dry particles mass were expelled as shown in Figure 1. From comparison with such data, the fraction lofted and available for expulsion has been deduced to be about 40%, an empirical factor we use.

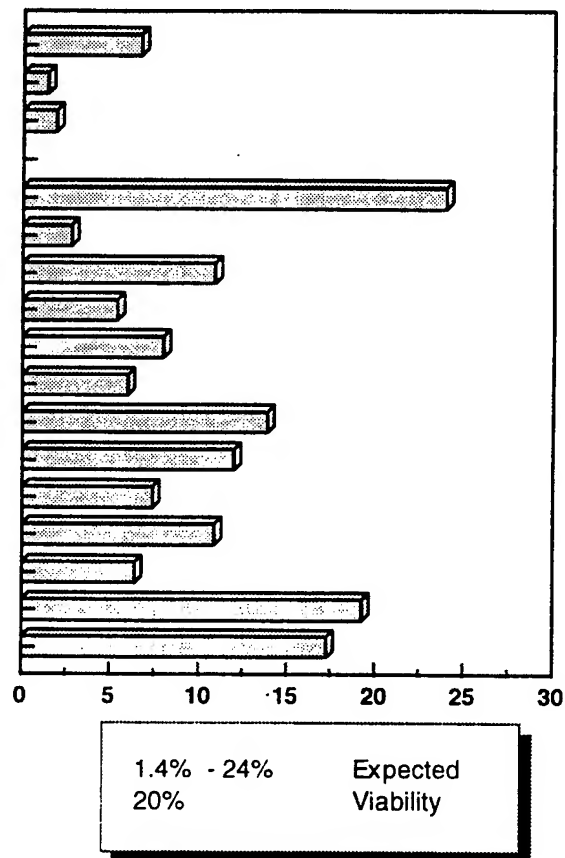


**Figure 1. Dry particle expulsion percentages from a series of experiments conducted at Waterways Experiment Station (WES).**

The amount of the material expelled is the most important element of the source for downwind hazard prediction. Therefore, it is extensively studied during the modeling effort. We also studied the plume rise to get an empirical check point for STEP. Below is a comparison with two full scale data sets, one from DIPOLE EAST 51 conducted at White Sands Missile Range (WSMR), and the other from DIPOLE IDLE 2 also at WSMR.

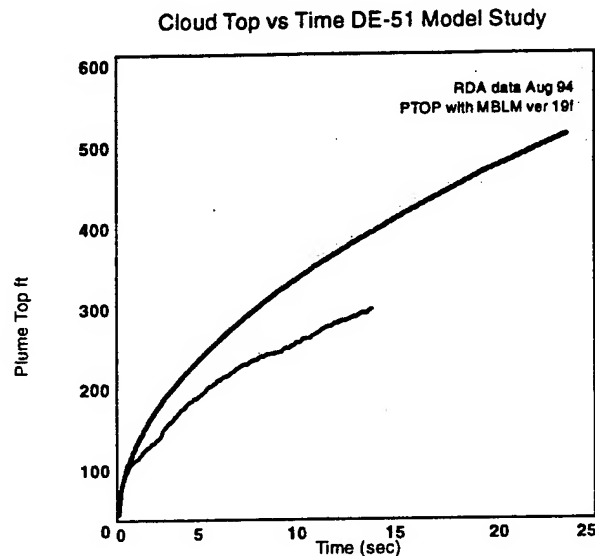


**Figure 2:** DIPOLE EAST 51 plume rise versus time, experimental data and model comparison.

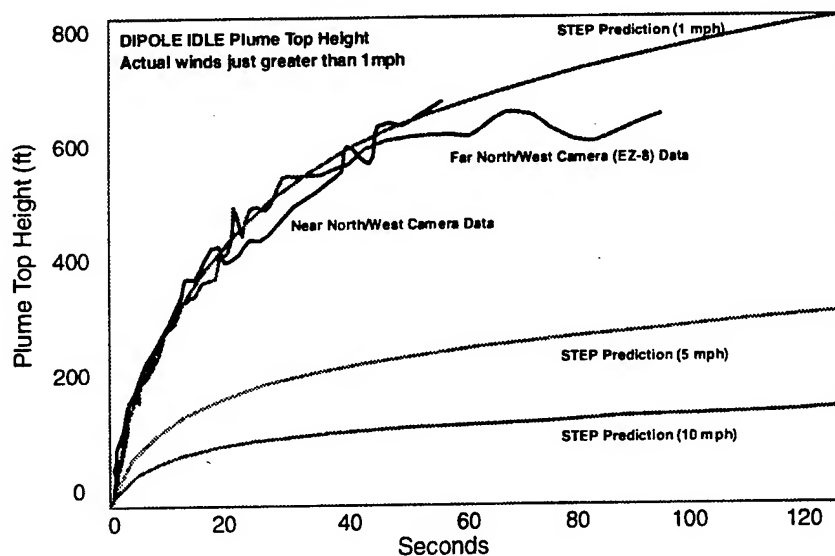


**Figure 3.** DIPOLE IDLE 2 plume rise versus time, experimental data versus model comparison.

These comparisons are interesting considering DE51 used a penetrating weapon as the source and the DI2 used four JATO rockets as a source of energy in the structure. The model is still being developed, but is quite versatile even in the early stages.

## Parametric Results of Expulsion Calculations and Models

It is useful for reference to numerical solutions and for evaluating scaling parameters to consider analytic solutions. It turns out that for an ideal gas assumption and for a single room chamber, an analytic solution exists for the expulsion problem (Srinivasa, 1994). In this case, the amount of expelled mass, as a fraction of the initial mass in the room, is given by

$$f_e = 1 - (E_i/E_o)^{-1/\gamma},$$

where sub-i and sub-o refer to initial (post-explosion) energy in the gas in the room and ambient energy in the gas in the room, respectively.  $\gamma$  is the ideal gas ratio of specific heats, and must be the ratio of two integers,  $(n+1)/n$ . Here, the primary implied variables are the room volume, effecting the total ambient energy, the charge size, affecting the initial total energy, and the amount and type of high explosive, which with the ambient air define an effective  $\gamma$ . A parametric plot of this equation is given in Figure 4. For large energy ratios, the fraction quickly approaches one. For dry, small particulate, one can assume a similar behavior for the particle mass expelled as a fraction of the amount well mixed in the gasses after the explosion.

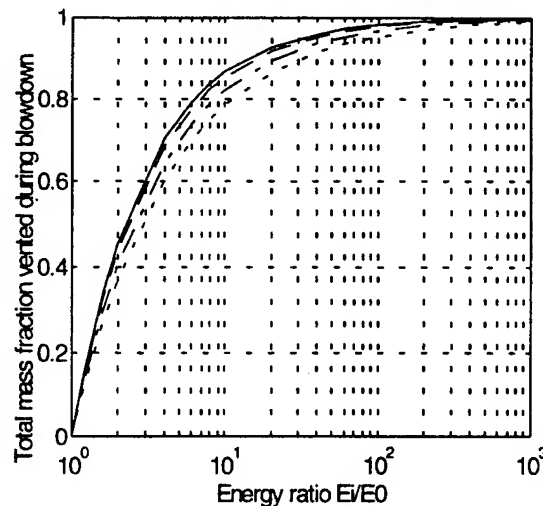


**Figure 4.** Variation of the fraction of total mass vented during blowdown with the energy ratio and  $\gamma$ .

Solid line  $\gamma=8/7$ ; Dashed line  $\gamma=6/5$ ; Chain line  $\gamma=4/3$ ; Dotted line  $\gamma=3/2$

In a blast event with a realistic weapon, case fragments along with the blast induced stresses result in a significant amount of dust creation within the enclosed structure. In addition, internal stores may produce dust as a result of the blast event. The



small particulate associated with such dust can readily absorb heat from the surrounding gasses, thereby reducing the effective gas energy and associated room pressurization. Using the STEP1 numerical computer code described in the previous paragraphs, such effects have been examined. Sensitivity blowdown of venting time and expelled masses to total dust mass are shown in Figures 5 and 6. Effectively, the dust has reduced the energy released to the gasses for expulsion. For fine dust, one can assume thermal equilibrium within the structure to approximately account for such energy sharing.

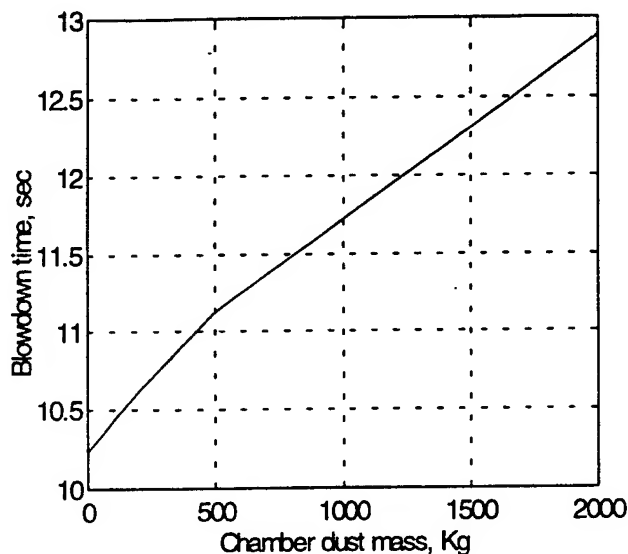


**Figure 5.** Total vent time vs. mass of dust in chamber. Single chamber-single vent configuration. Chamber volume =  $300\text{m}^3$ . Charge weight = 245 kg.

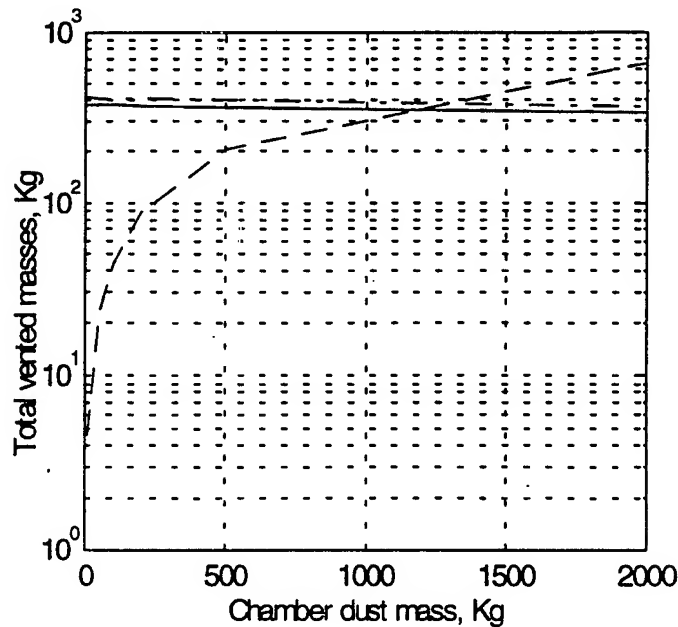


**Figure 6. Dependence of total vented masses of hazardous tracer particles (solid line), dust (dashed line), and explosion gases (dash-dot line) on mass of dust in the chamber. Single chamber - single vent configuration. Chamber volume = 300 m<sup>3</sup>; Charge weight 245 kg.**

As the targeted structure becomes more complex in internal geometry, the one room analytic solutions no longer apply. Nevertheless, they provide guidance for interpreting results from more complex numerical models. A four room and hallway floor plan is depicted in Figure 7a. STEP1 calculation results for such a geometry are shown in Figure 8, where the weapon penetration hole is into one of the rooms and the penetration hole diameter is the parameter. Here we see that the expulsion fraction increases as the hole diameter increases. The analytic result had no diameter dependence, yet these results do. This is due to the doorways interconnecting rooms, presenting another characteristic area to the blowdown physics. The doorway areas correspond in area to the 1.58m diameter area. It is perhaps not surprising that when the doorway out of the burst room is larger than the penetration hole in area, the expulsion fraction is reduced.

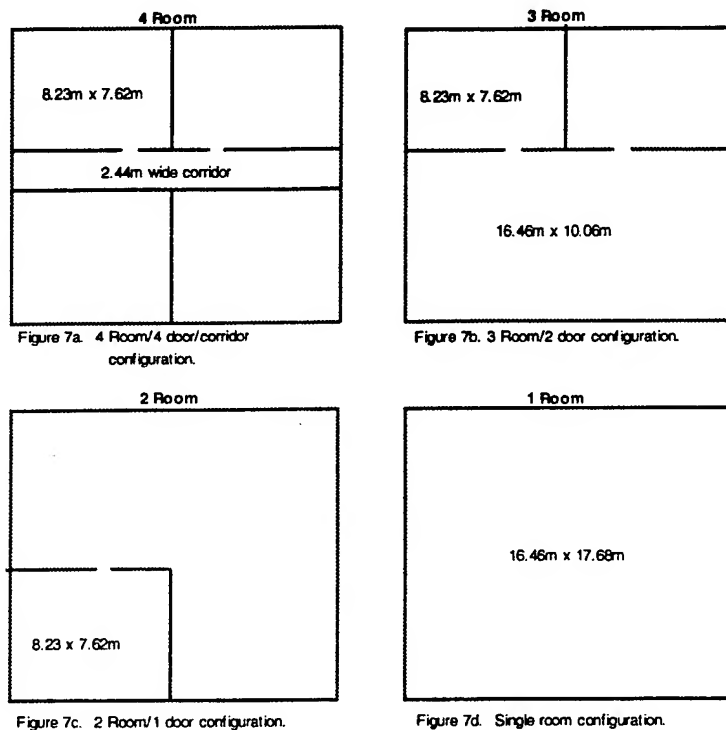


**Figure 7: (a - d) Schematic plan views of four different configurations occupying the same volume. The overall dimensions are 16.4592m x 17.6824m x 3.048m. All doors are 3' x 7'. The strike room with the charge, the tracer particles and the vent is in the lower left quadrant in all cases. The input lofted tracer particle mass is 8.3462kg.**

When the penetration hole is large compared to other leak areas from the burst room, the initial energy is mostly confined to the burst room. If one has knowledge of the burst room size versus the facility size, then an improved approximate model can perhaps be invoked. To test this hypothesis, additional STEP1 results are consulted. The 4 room results for a 2m diameter hole are contrasted with a single room facility of the same total plan area in Figure 9. Clearly more expulsion occurs in the 4 room facility when the explosion energy is assumed spread over the whole facility. On the other hand, when the explosion energy is apportioned ONLY to the burst room, the four room energy ratios are effectively larger as indicated. In this way, the 4 room and 1 room results can be made to correspond, at least for large hole diameters.

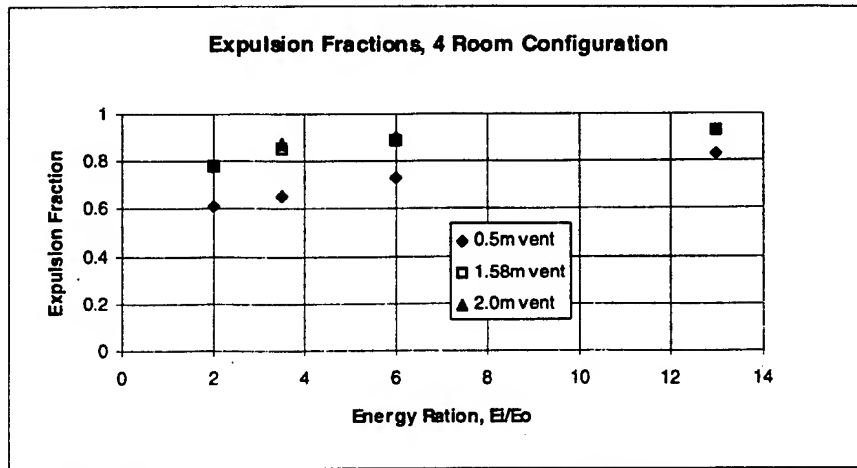


Figure 8. Expelled mass fraction for 4-room configuration.

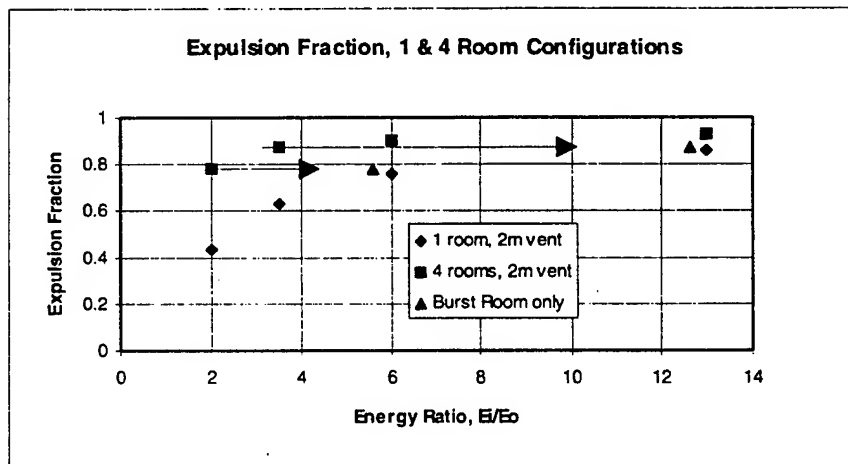
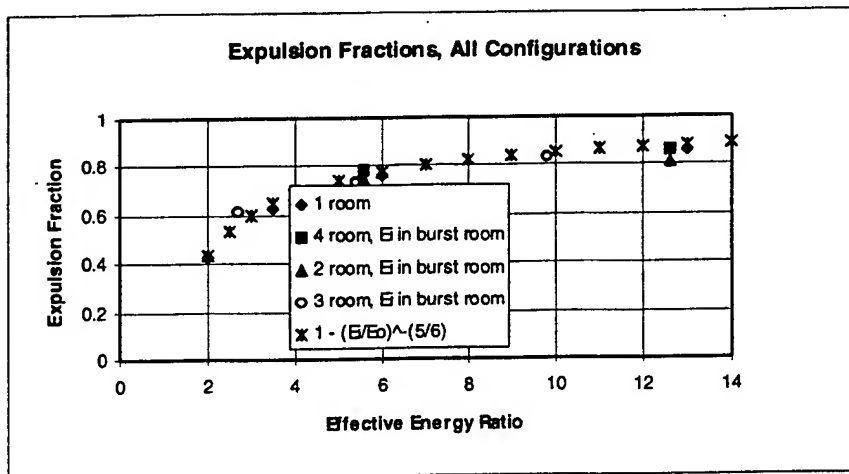


Figure 9. Expelled mass fractions with 2 m vent diameter, 1 room and 4 room plans.

To further test this approximate modeling of complex floor plans, all 4 floor plans shown in Figure 7 were modeled with STEP1 calculations, using a 2 meter hole diameter. Attributing the explosion energy to only the "burst room" of each case, resulted in the expulsion fraction versus effective energy ratio plot shown in Figure 10. For comparison, an analytic result for a  $\gamma$  of 6/5 is shown as well. Clearly, there are some simplified engineering model possibilities indicated.



**Figure 10. Expelled mass fractions with 2 m vent diameter, all configurations.**

Simplified models of the mass expelled from facilities is suggested by the foregoing results. When only a few details of the facility are known, such that only total facility internal volume can be estimated, an upper bound on the expulsion fraction can be approximated. The upper bound depends upon the facility volume, the charge weight and the penetration hole diameter. Comparisons with STEP1 results are shown in Figures 11. A lower bound can also be provided which is independent of hole diameter as shown on the figure. Here, figures 11a, 11b and 11c correspond to results for all four floor plans with vent diameters of 0.5, 1.58 and 2.0m, respectively. If internal fine dust is expected and can be estimated, the reduced energy in the gas can be estimated assuming thermal equilibrium to refine such estimates. Further comparisons with dust are given in Figure 12. In this case, the amount of dust in the room is varied for the four room configuration only and vent diameters of 0.5 and 2.0m in figures 12a and 12b, respectively. If further details on the facility layout are available, the associated estimates may be further refined by consideration of the burst room only as suggested in Figure 10, above.

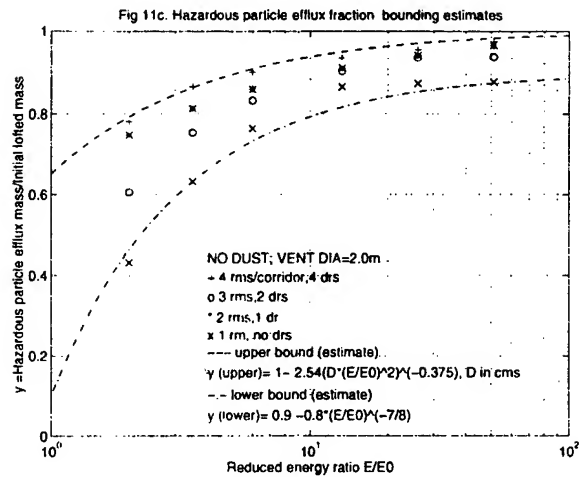
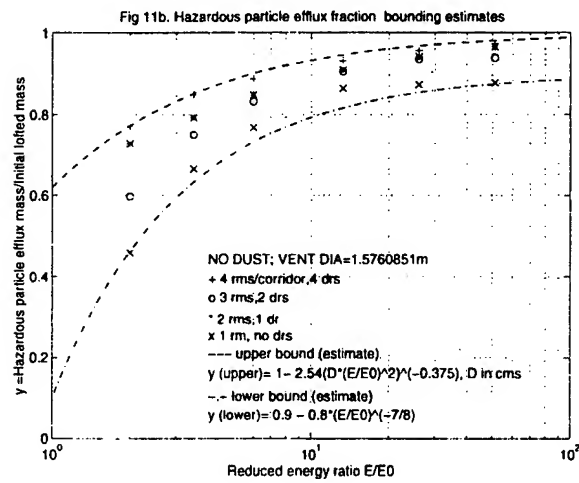
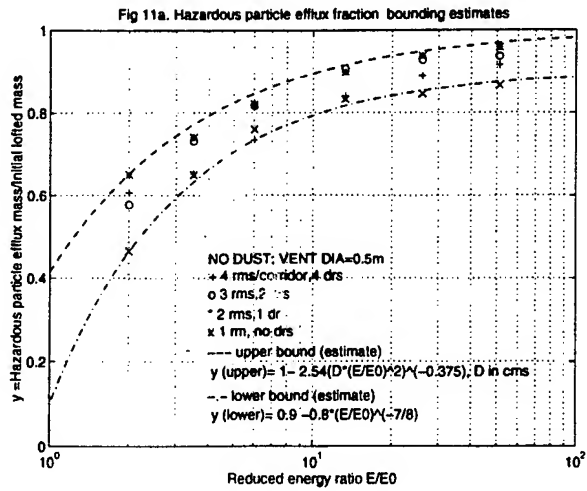


Figure 11. (a-c) Expelled mass fractions assuming no concrete dust.

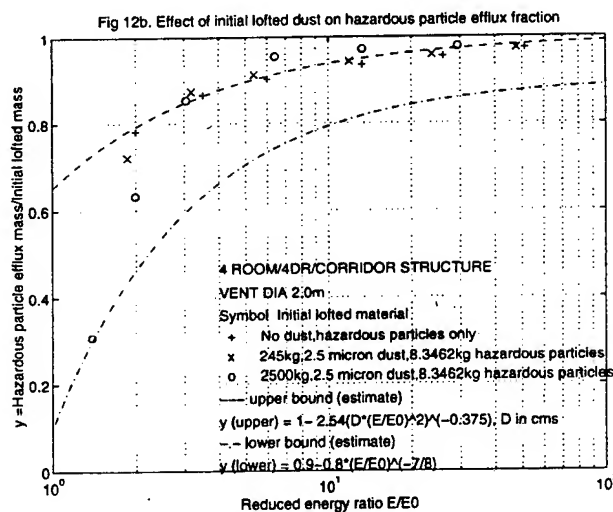
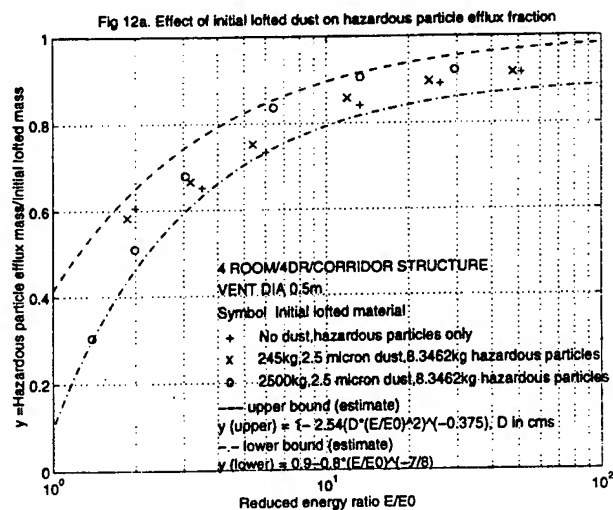


Figure 12. (a-b) Expelled mass fractions with concrete dust and assuming thermal equilibrium.

### Transport Sensitivities

Particulate and gaseous transport through the atmosphere is of great importance in the assessment of nuclear, biological and chemical release hazards. In order to predict accurate downwind effects, the source of these hazardous releases must be adequately characterized. We will discuss here the effects that changes in various parameters, such as particle size, release height, cloud dimensions, etc., have on the resulting plume.

We will use as a baseline the case of a 4.54kg indium sesquioxide ( $\text{In}_2\text{O}_3$ ) release at ground level ( $h=0$ ), initial cloud dimensions of  $15 \times 15 \times 100\text{m}$ , and a uniform particle size of

10 $\mu$ m. The weather we will use for our baseline is a windfield generated by a mass-consistent weather model called MINERVE which includes terrain features and is generated from actual weather observations on 13 April 1995. The location for these cases is White Sands Missile Range.

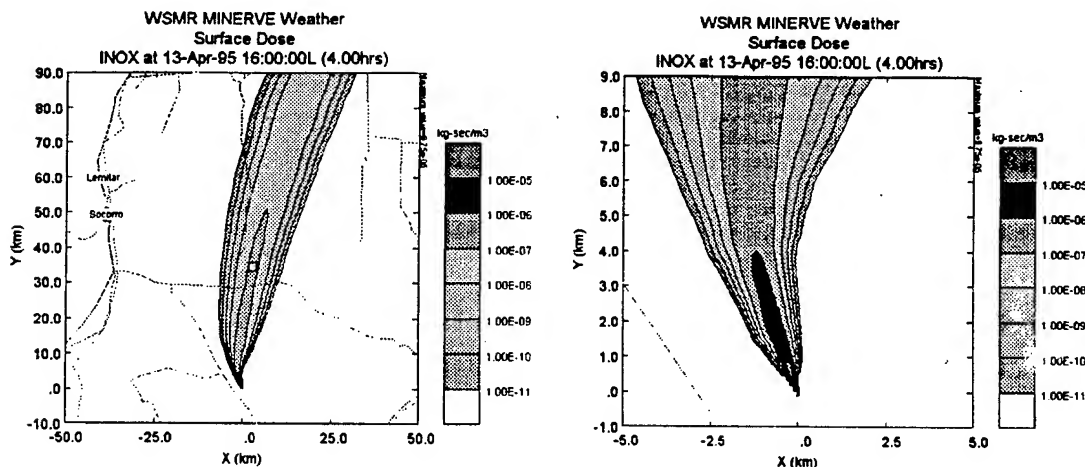


**Figure 13. Integrated Surface Dose of Indium at 4 hours after release for BaselineCase.**

The plume generated with these input parameters is demonstrated in Figure 13. The variable plotted is the integrated surface dose which is a mass per inhalation rate and is integrated over the time of cloud passage at the ground surface.

The first parameter to be changed is the mass; we raise the mass one order of magnitude to 45.4kg. As expected, the values for surface dose increase one order of magnitude in Figure 14.



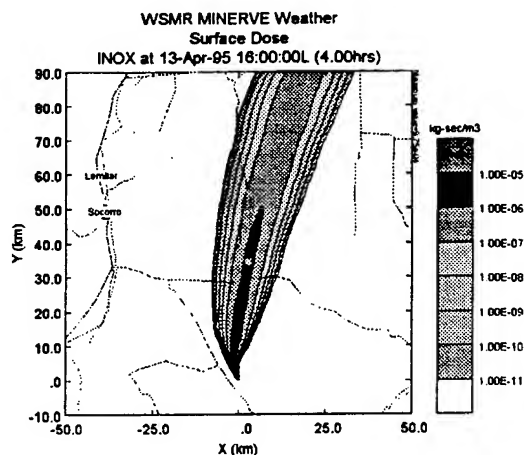


**Figure 14. Integrated Surface Dose of Indium for 45.4kg Release.**

Increasing the diameter of the initial cloud size to 100m and bringing the mass back down to 4.54kg, the resulting plume spreads out considerably within a short range, as can be seen by comparison of Figures 13b and 15b.

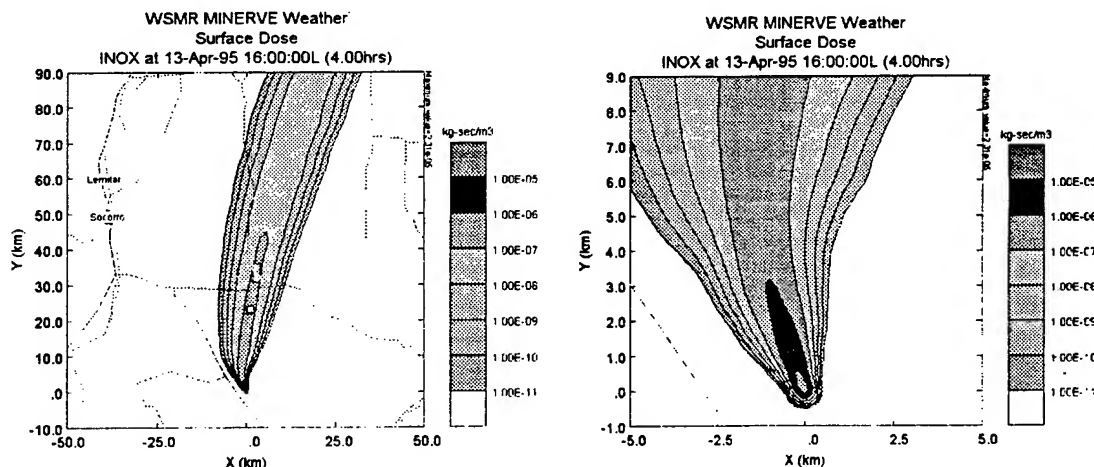


**Figure 15a & b. Surface Dose for Indium w/ 100m Cloud Diameter, and 4.54kg Mass.**

Comparing Figure 13a to 15a, we can see that farther out the turbulence in the winds mix the cloud such that the source diameter has no more effect.

Much larger variations in results are seen by changing particle size. A particle size of  $1\mu\text{m}$  was used to generate the results in Figure 16. As expected, with this small particle size, the plume travels much farther since the smaller particles take longer to fall out.

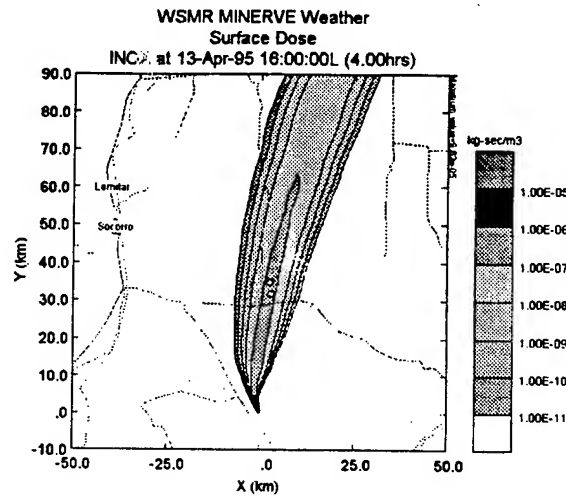


**Figure 16. Surface Dose of Indium w/ 1 micron Particle Size.**

By increasing the original particle size one order of magnitude to  $100\mu\text{m}$  the resulting plume is shown in Figure 17.

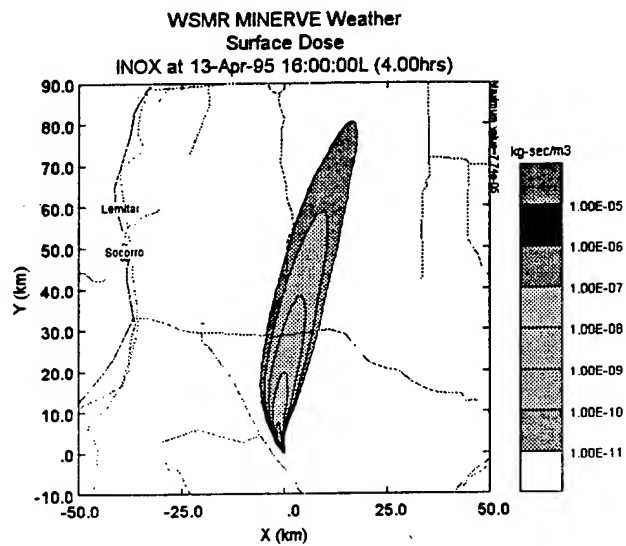


**Figure 17. Surface Dose of Indium w/ 100 micron Particle Size.**

In this case, the larger particles fell out of the cloud much earlier. Now changing to a log-normal particle size distribution with a mean mass diameter (MMD) of  $10\mu\text{m}$  and distribution  $\sigma_G=1.8$ , Figure 18 shows a very similar plume to Figure 13.

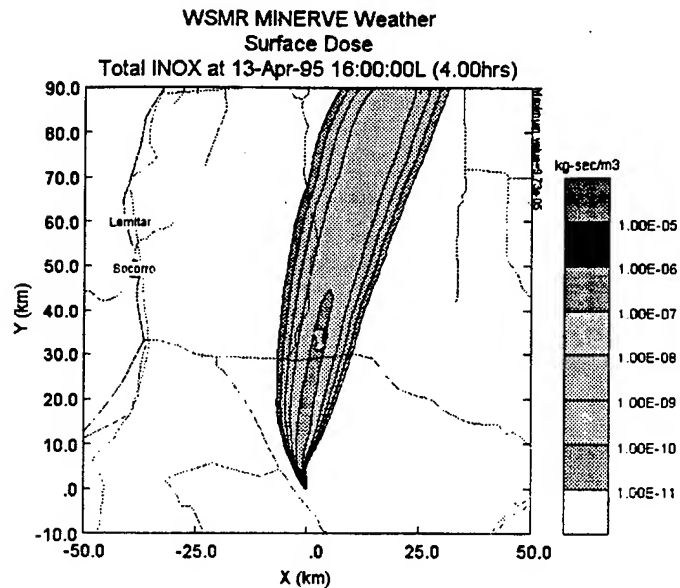


**Figure 18. Surface Dose of Indium w/ Log-Normal Particle Distribution.**

This similarity is to be expected, though, since the majority of the particles are near 10 microns in size. About 95% of the mass is between 3 and 32 $\mu$ m.

In increasing the release height, no really dramatic change is seen until the height reaches an altitude sufficient to either push the top of the cloud above the boundary layer or is high enough to just take a long time to fall. This last possibility is what happened in Figure 19. Here the release is at 500m height.

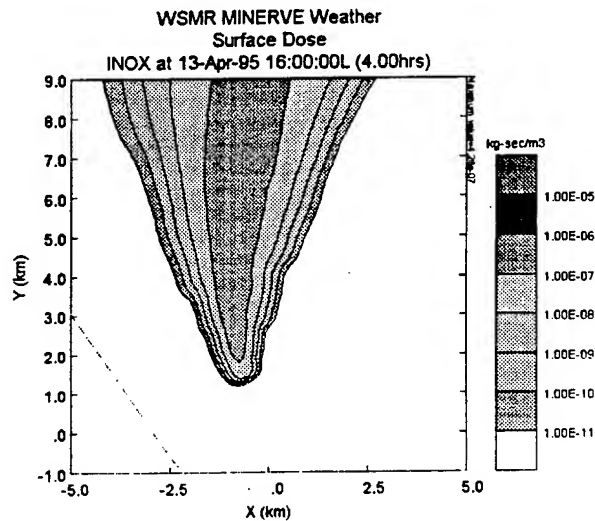


**Figure 19. Surface Dose of Indium for Release Height of 500m.**

In cases involving changes in release height, the weather and time of day will have a major effect on the resulting plume. The weather and time of day will influence the amount of vertical mixing in the boundary layer and the boundary layer height. The time of day for this case was 1200 local, which results in a very thick boundary layer and a lot of vertical mixing.

The variable that most effects the result, obviously is the weather. The cases above were all run using the MINERVE generated windfield which included the terrain. Now, Figure 20 depicts a run using only the raw weather observations with no terrain.

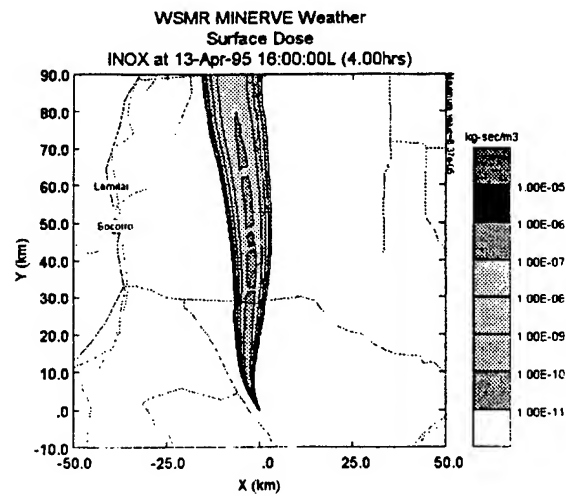


**Figure 20. Surface Dose of Indium w/ Observational Winds.**

This plume is clearly much different between Figures 13 and 20 in not only direction, but also concentration.

### Conclusions

Based upon physical modeling of internal detonations collateral effects expulsion into the atmosphere has been studied. Downwind transport of hazardous materials depends significantly on the total mass expelled and this parameter has been modeled for engineering estimation purposes.

## References

Srinivasa, D., T. Mazzola, and J. Kyme, "Venting from Blast in a Responding Chamber," Proceedings Vol. 2, MAB-13, September 1993.

Srinivasa, D. "Efflux from a Single Chamber: Analysis of Sensitivity", to be published.

Sykes, R. Ian, et al., "PC-SCIPUFF Version 0.2, Technical Documentation," DNA technical report, to be published.

Sykes, R. I., W.S. Lewellen, and S.F. Parker., "A Turbulent-Transport Model for Concentration Fluctuations and Fluxes," JFM, Vol. 139, pp 193-218, 1984.

Sykes, R.I., S. F. Parker, and D.S. Henn, "Numerical Simulation of ANATEX Tracer Data Using a Turbulence Closure Model for Long-Range Dispersion," J of Appl. Met., Vol. 32, No. 5, May 1993.

# EXPERIMENTAL STUDY OF TURBULENT BAROCLINIC BOUNDARY LAYERS

**P. Neuwald and H. Reichenbach**

*Ernst Mach Institut*

*D-79104 Freiburg i. Br., Germany*

**A. L. Kuhl**

*Lawrence Livermore National Laboratory*

*Livermore, California, USA*

## Abstract

The interaction of a  $M = 1.4$  air shock wave with a dense-gas wall layer was studied in the EMI shock tube. A 10-mm thick 1000-mm long layer was created by injecting Freon through the porous floor of the test section. As the incident shock front propagates along the layer, it is retarded there due to its reduced sound speed and reflected obliquely from the floor of the test section. This sets up a series of alternating compression and expansion waves which strongly perturb the interface shear layer and cause it to evolve rapidly to a turbulent boundary layer flow. In this case, vorticity is created at the air-Freon interface by an inviscid, baroclinic mechanism, namely, the misalignment of pressure and density gradients.

Shadow-schlieren photography was used to visualize the turbulent mixing in this baroclinic boundary layer. Laser-Doppler Velocimetry (LDV) was used to measure the streamwise velocity histories at 14 heights. After transition, the boundary layer profiles may be approximated by a power-law function  $u \sim y^\alpha$  where  $\alpha \approx 3/8$ . This value lies between the clean flat plate value ( $\alpha = 1/7$ ) and the dusty boundary layer value ( $\alpha \approx 0.7$ ), and is controlled by the gas density near the wall.

## 1. Introduction

For some time part of the numerical experiments in nonsteady fluid dynamics have focused on the problem of a normal shock propagating along a dense-gas wall layer. This problem is strongly related to a simplified modelling of a planar shock propagating along a bed of loose dust. Besides this, it is interesting how turbulence evolves in this boundary layer type, since the mechanisms are essentially inviscid. The incident shock is retarded in the dense-gas (Freon) layer due to its reduced sound speed and reflected obliquely from the floor. The wave reflections within the dense layer strongly perturb the interface shear layer, which rolls up into a turbulent boundary layer. This is not surprising, e.g., the interface is first subjected to shock accelerations, and is thus susceptible to Richtmyer-



Meshkov instabilities (Richtmyer 1960, Meshkov 1960). Later, it can be viewed as a Kelvin-Helmholtz mixing layer with strong density effects. In this respect, it can be viewed as a boundary layer version of the Brown and Roshko free shear problem (1974). Vorticity is deposited at the layer interface mainly by a baroclinic mechanism  $\nabla \rho \times \nabla p$ , the misalignment of pressure gradients and density gradients. In contrast to viscous boundary layers, baroclinic boundary layers evolve according to inviscid mechanisms which are eminently amenable to gasdynamic simulations. They also allow us to study the inviscid aspects of turbulent boundary layers at all scales larger than the Kolmogorov scale — without the unnecessary complication of viscosity. In particular, detailed measurements are needed to check direct numerical simulations of such boundary layers ( e.g., Greenough et al., 1993 ). Described here are the results of shock tube experiments performed at the EMI. The diagnostics included LDV measurements of streamwise velocity histories in the boundary layer, and companion shadow photography of the development of the mixing layer. The experiments are described in the next section.

## 2. Experiment Description

A schematic of the shock tubes test section is shown in Figure 1. A fixture was used that consisted of a narrow plenum chamber covered by a porous surface forming the floor of the test section. Through this floor Freon gas was injected at constant pressure into the shock tube that was initially filled with ambient air. The injection duration and the diaphragm rupture delay were computer-controlled.

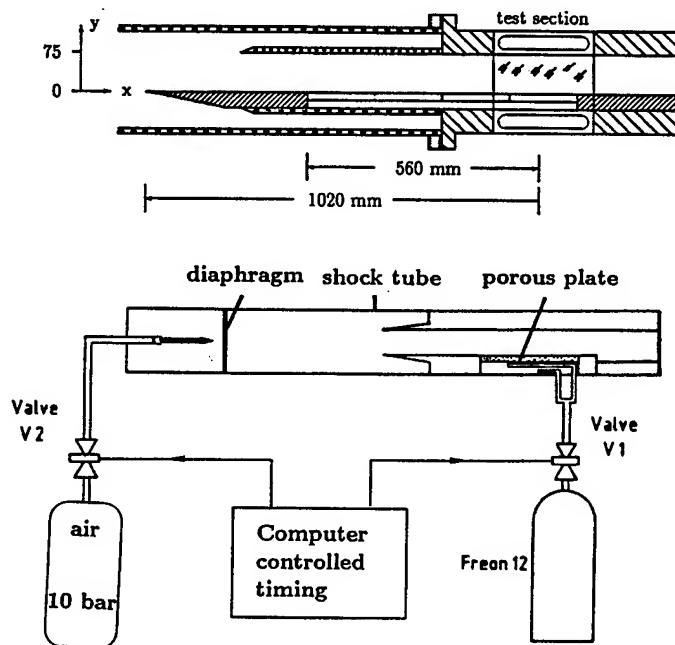


Figure 1: Schematic of the test section (lengths in mm).

A differential laser interferometer was used to visualize the preshock density gradient normal to the floor. Repeated tests showed that the computer controlled injection procedure led to very reproducible preshock density profiles. The leading edge of the Freon layer was approximately 1000 mm ahead the center of the test section; the actual preshock density profile is shown in Figure 2; for numerical simulations it can be modelled as tanh-profile:

$$\rho/\rho_{\text{air}} = 2.8 - 1.8 \tanh [(y-y_c)/h], \quad (1)$$

where  $y_c = 6.5$  mm and  $h = 9$  mm.

Shadow photographs from the 24-spark Craz-Schardin high-speed camera made visible the essential features of the shock-induced flow and the turbulent mixing processes. The primary diagnostic consisted of a dual-beam Laser-Doppler Velocimeter (LDV) in combination with 100-MHz transient recorders that eliminate the need for real-time signal processing and make it possible to perform Doppler burst spectrum analysis in a post-processing mode. The LDV system allows one to simultaneously measure the streamwise velocity component at four different heights. The probe volumes — about 125  $\mu\text{m}$  in diameter and 1.2 mm in spanwise extension — were located in the center of both the streamwise and spanwise width of the test section. The characteristics of the spectrum analysis were a compromise between accuracy and data rate. The average data rate was of the order of 180 kHz. The accuracy of the velocity measurements can only be estimated to be around 2 % ( because it depends significantly on the signal-to-noise ratio of the optical signal, which can vary over a wide range). Besides this, one must remember that the collected data represent the velocity of tracer particles; thus the accuracy of velocity fluctuations depends upon the frequency response of the particles. The velocity measurements were accompanied by pressure measurements at the roof of the test section. In addition, pressure histories at different heights were obtained with pressure gauges mounted flush into an aluminium plate that was substituted for one of the test section windows in some experiments.

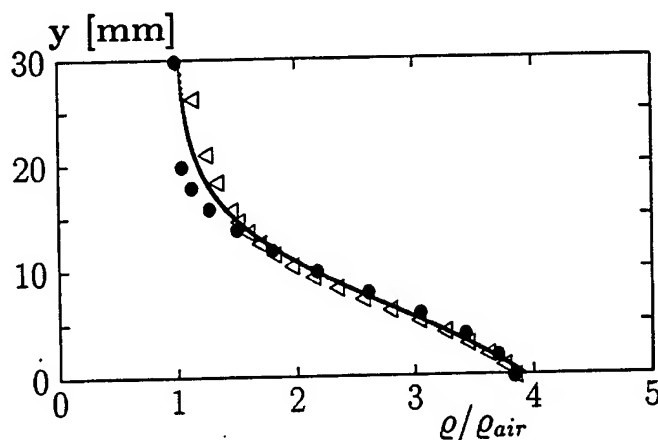


Figure 2: Pre-shock density profile of the Freon layer.

### 3. Flow Visualization

The first frames in Figure 3 show the initial interaction of a  $M_s = 1.4$  shock with the dense-gas layer and the deposition of vorticity at the interface. The shock front is curved (i.e., retarded) near the wall because of the smaller sound speed in the Freon layer that causes a slower propagation of the shock front. The periodic deformation of the interface observed in the first frames of the shadowgraphs can be explained as follows:

the dense gas layer acts like waveguide, whereby the shock reflects between the wall and the interface, and sets up a series of compression and expansion waves that radiate

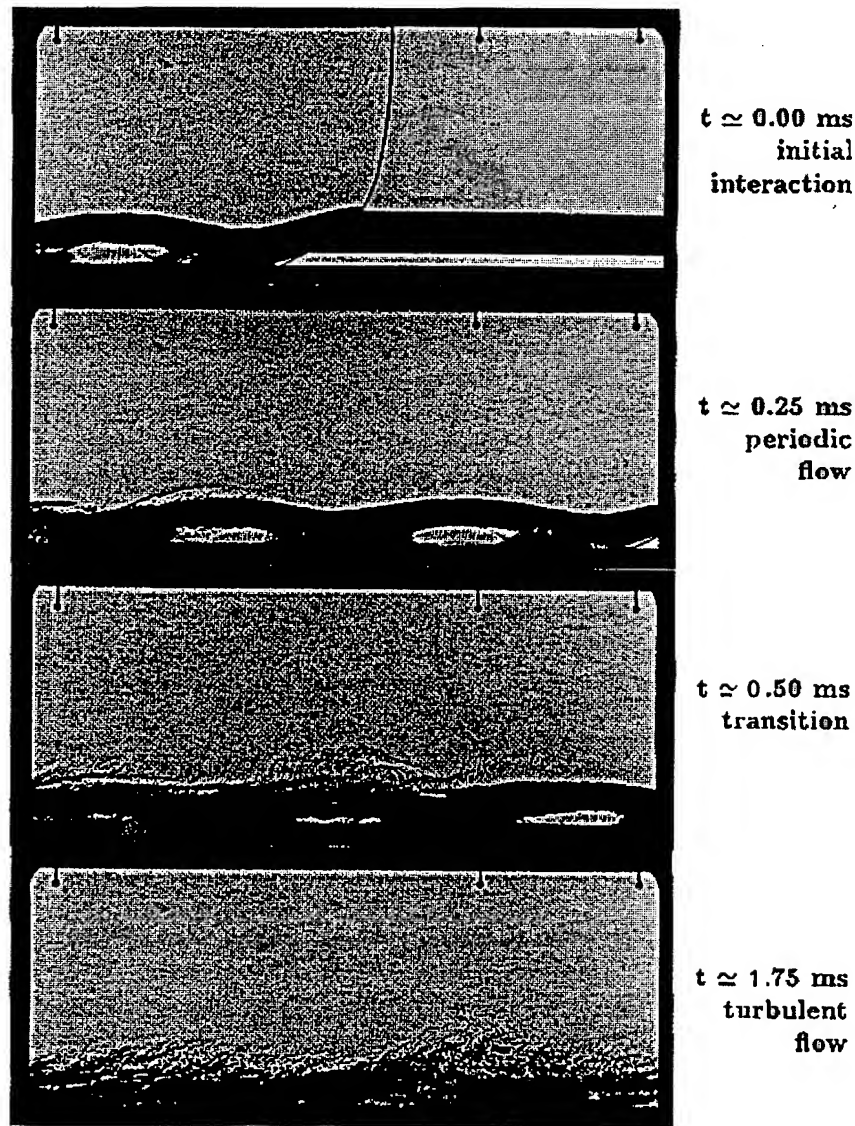
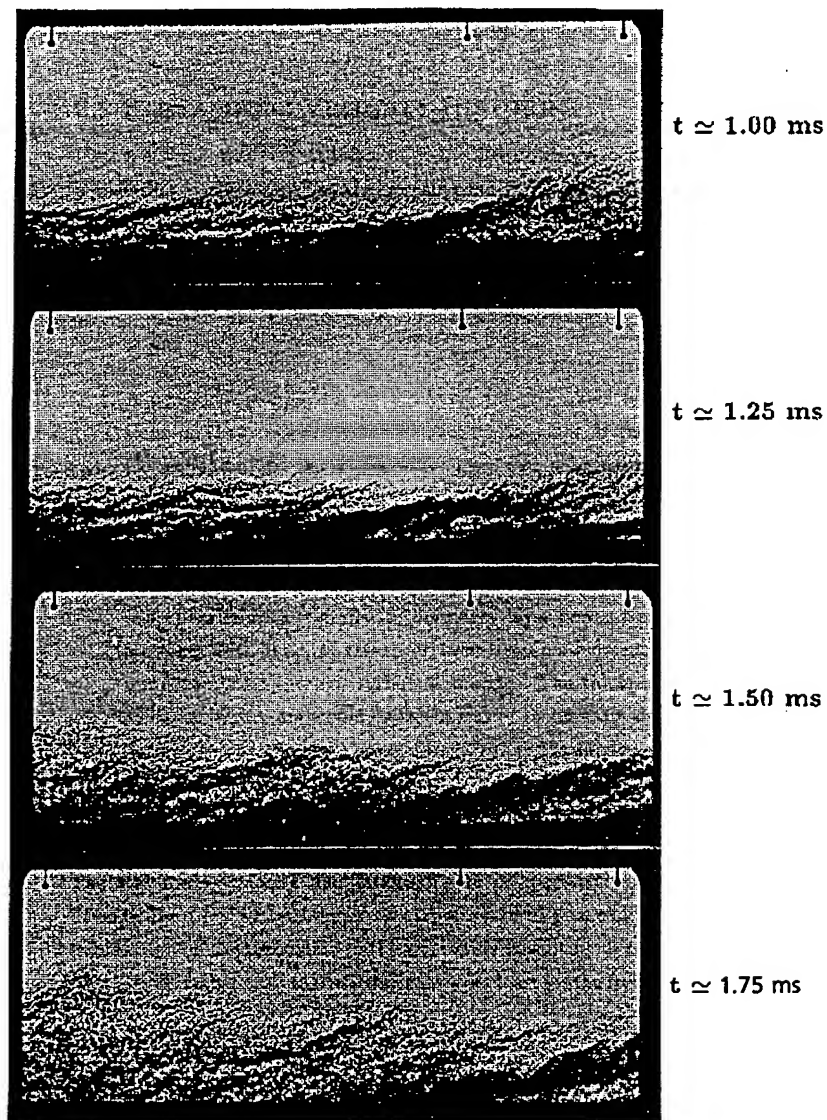


Figure 3: Shadow photography of the flow.

from the layer. The smooth undulated surface of the interface layer is soon broken up into regions characterized by small scale structures in the shadowgraphs; they rapidly spread over the whole interface, indicating the transition to turbulent boundary layer flow.

The second set of frames in Figure 4 show the evolution of the turbulent shear flow. The layer interface is no longer undulated; small scale structures become predominant and first spread from the interface into the boundary layer and at later times also into the freestream region.



**Figure 4:** Shadow photography of the evolution of the turbulent boundary layer.

#### 4. Streamwise Velocity Histories

Figure 5 shows five sample histories of the streamwise velocity. The height  $y = 45$  mm corresponds to the freestream condition; at  $y = 30$  mm the probe is located in the transition region, while probes at  $y = 20$  mm, 10 mm and 4 mm are in the boundary layer. The pressure and LDV measurements suggest that there are two characteristic regimes in the development of the shear flow:

1. A periodic regime ( $\Delta t \leq 0.75$  ms) — distinguished by large oscillations of the pressure due to the wave reflections in the Freon layer. Corresponding oscillations of the streamwise velocity indicate strong perturbations of the shear layer (e.g., as much as 100 % in the interface region).
2. A shear flow regime ( $\Delta t > 0.75$  ms) — where the streamwise velocity  $u(y,t)$  varies with  $y$  similar to boundary layer flows. Near the wall  $u$  increases with time, as the shear layer acquires momentum from the freestream flow through turbulent mixing. The thickness  $\delta_{st}$  of the sublayer (where one could expect a loss of momentum due to viscous drag arising at the wall) grows like  $4 \sqrt{\nu \cdot t}$ , and is smaller than 0.3 mm in Freon for times less than 2 ms. Thus the main part of the boundary layer is not influenced by wall drag.

The streamwise velocity fluctuations  $u'$  are comparatively weak ( $\pm 5$  %). Though the LDV system might be inappropriate to give exact quantitative information on the turbulence in this nonsteady flow, it tends to overestimate fluctuations rather than to underestimate — at least for the frequencies below 20 kHz. The weak fluctuations can be interpreted in combination with the shadowgraphs that show very-fine-scale structures (i.e., smaller than 1 mm) are immediately present. Contrary to previous numerical simulations, no predominant 2-D rotational structures were observed. This suggests that:

- (i) the complete 3-D turbulence spectrum — including Kolmogorov scales — is set up immediately after transition,
- (ii) dissipation acts immediately to keep  $u'$  small; and
- (iii) it probably takes more time for large-scale structures to grow.

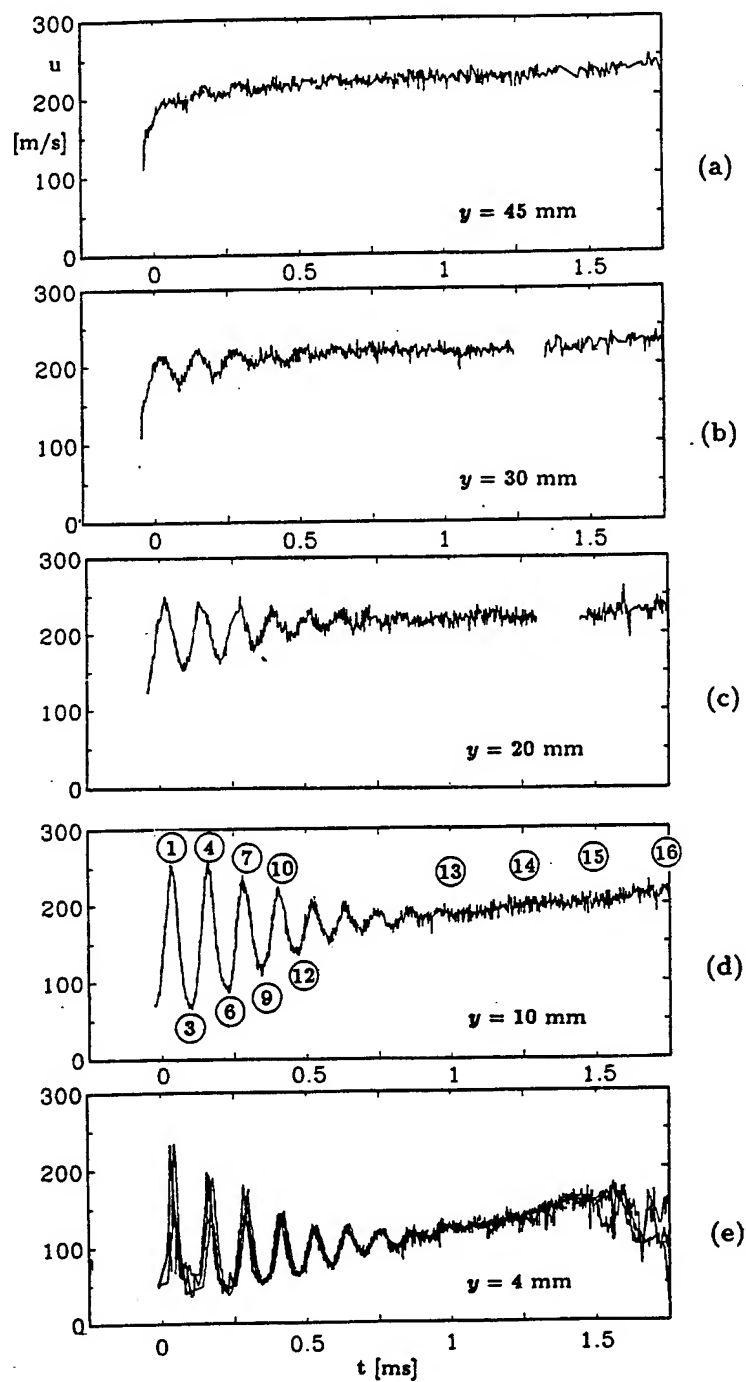
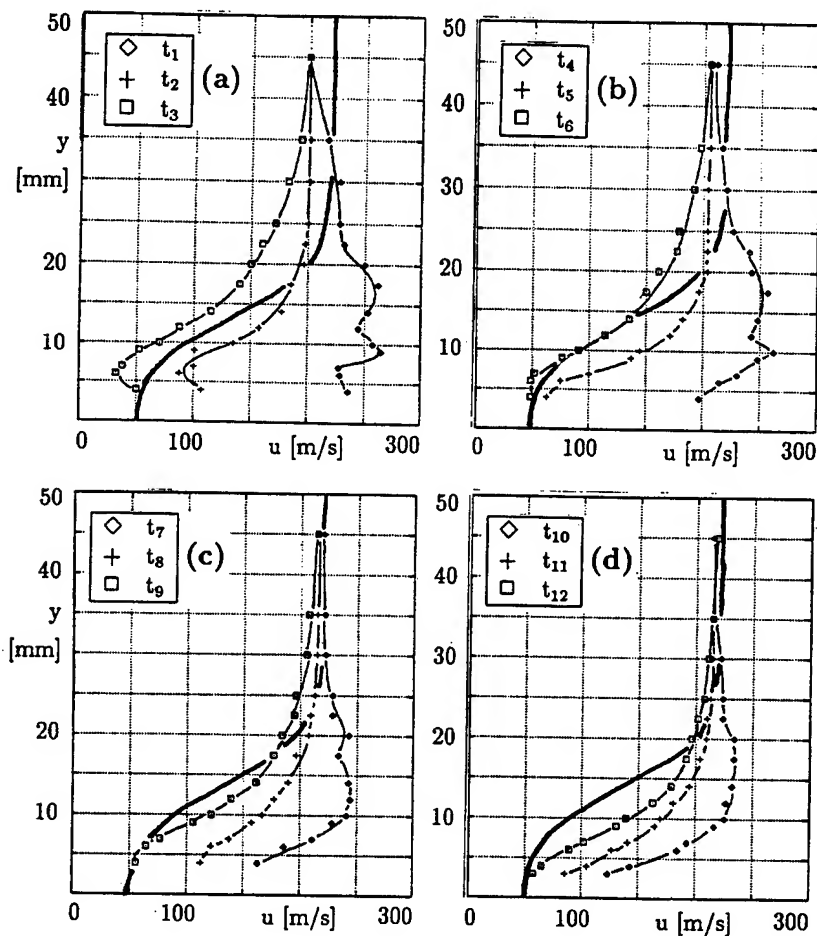


Figure 5: Streamwise velocity at different heights.

## 5. Evolution of the Velocity Profiles

Figure 6 shows the evolution of the velocity profiles during the periodic regime for the first four cycles. During each cycle three times are depicted: -- the instant of peak velocities ( $t_1, t_4, t_7, t_{10}$ ), -- the mid-point of each cycle ( $t_2, t_5, t_8, t_{11}$ ), -- and the instant of minimum velocities ( $t_3, t_6, t_9, t_{12}$ ). Also a curve from a previous numerical simulation is shown (Kuhl et al., 1992), averaged during the same time period (0 to 1 ms). This calculated curve is most similar to the profiles at the minimum fluctuation times.



**Figure 6:** Instantaneous streamwise velocity profiles during the periodic regime:  
 (a) first cycle; (b) second cycle; (c) third cycle; (d) fourth cycle.  
 Solid lines without symbols from the numerical simulation (Kuhl et al., 1992).

Figure 7 presents a semi-logarithmic plot of the velocity profiles: in (a) the evolution of the mid-cycle values during the periodic regime, which converge at later times, in (b) four instantaneous profiles in the shear flow regime, which show a logarithmic law behaviour in the range from  $y = 4$  mm to  $y = 20$  mm. The profiles may be fit with a logarithmic function

$$u/U_\infty = 1 + b \log y/y_0 \quad (2)$$

where the constants are listed in Table 1. At late times, the logarithmic slope converges to a value of  $b \approx 0.45$ , similar to other turbulent boundary layers.

Time	b	$y_0$ [mm]
$t_{13}$	0.58	19.6
$t_{14}$	0.48	16.9
$t_{15}$	0.44	18.7
$t_{16}$	0.45	17.5

Table 1

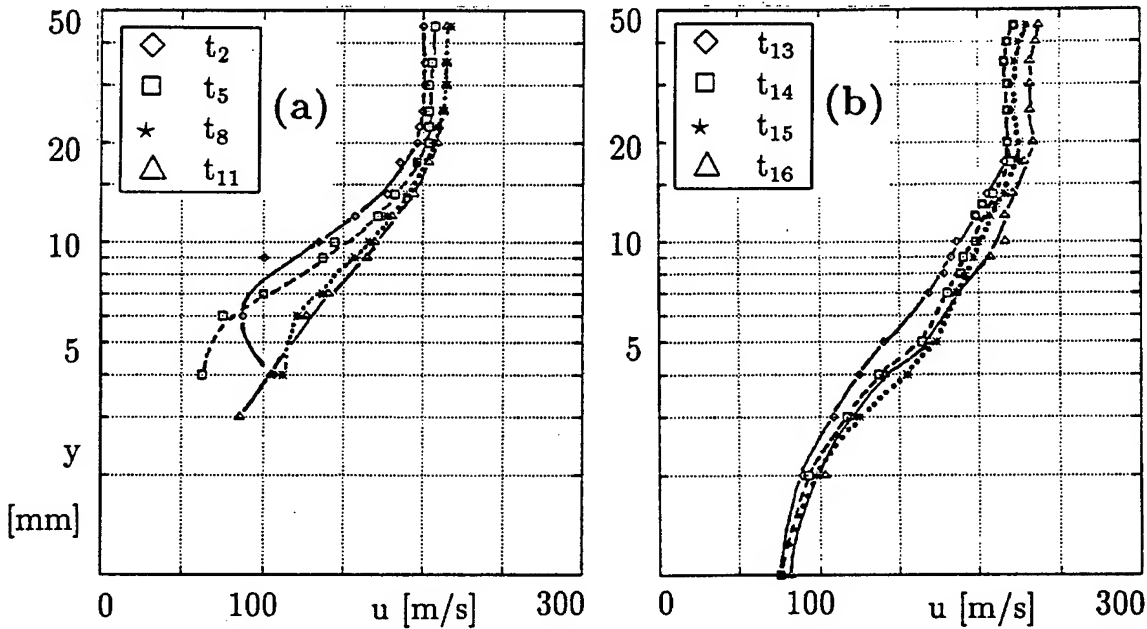


**Figure 7:** Semi-logarithmic profiles of streamwise velocity:  
(a) evolution of mid-cycle values;  
(b) shear flow regime.



## 6. Boundary Layer Profiles

In the shear flow regime, it is useful to scale the experimental data — in order to facilitate comparisons with other boundary layer flows. In Figure 8 we have plotted the boundary layer profiles:

$$u/U_\infty = f(\eta) \quad (3)$$

where  $U_\infty \approx 230$  m/s,  $\eta = y/\delta$  and  $\delta = y$ , where  $u/U_\infty = 0.98$ . Approximating the profiles by a power law function

$$u/U_\infty = \eta^\alpha \quad (4)$$

yields exponents  $\alpha$  between  $2/8$  and  $3/8$ . The baroclinic boundary layer profiles are thus midway between a clean flat plate ( $\alpha = 1/7$ ) and a dusty boundary layer behind a normal shock. This illustrates that there are density effects (i.e., the profiles are lower than the clean flat plate case), though less than in the dusty boundary layer. The density profile tends to control the shear flow profile  $u(y)$ : Specifically the density ratios of the different cases (e.g.  $\langle \rho \rangle / \rho_{\text{air}} \approx 10$  for the normal shock over a dust bed,  $\langle \rho \rangle / \rho_{\text{air}} \approx 4$  for the Freon layer, and  $\langle \rho \rangle / \rho_{\text{air}} \approx 1$  for the clean flat plate) explain why the present results are midway between the flat plate and the dusty boundary layer case.

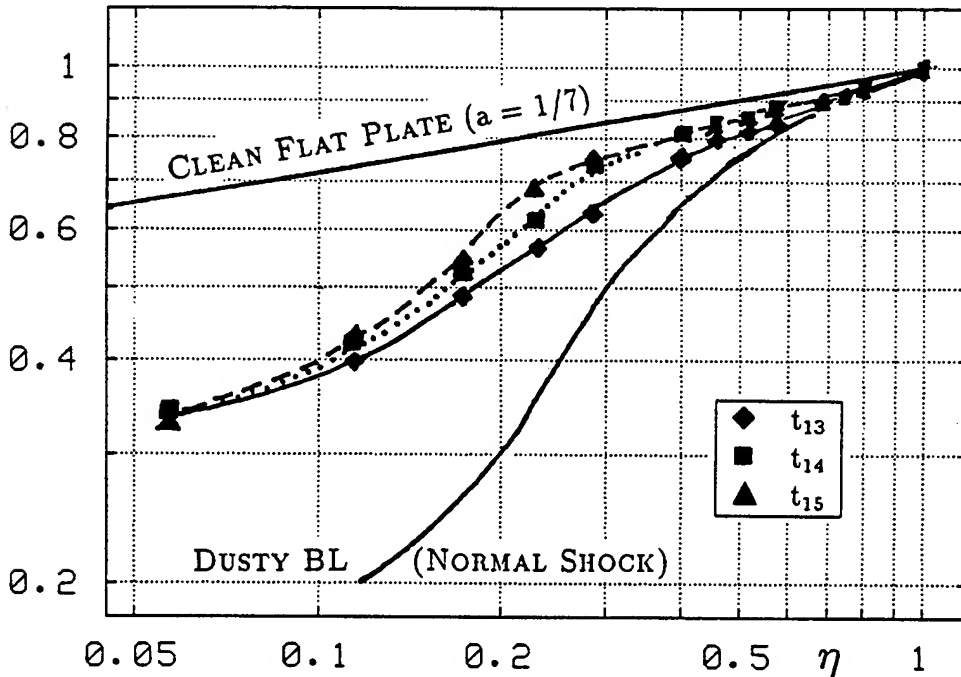


Figure 8: Boundary layer profiles.

## 7. Conclusions

Two characteristic regimes were observed in the boundary layer evolution: an initial periodic regime that was dominated by wave reflections within the Freon layer, and later, a turbulent shear flow regime. Near the wall, the boundary layer profiles exhibited a logarithmic law-of-the-wall region  $u/U_\infty = 1 + 0.45 \log (y/y_0)$  similar to viscous turbulent boundary layers. Away from the wall, the profiles had a power-law character:  $u/U_\infty = \eta^\alpha$  where  $2/8 \leq \alpha < 3/8$ . These values lie between the clean flat plate value of  $\alpha = 1/7$  and the dusty flow value of  $\alpha \approx 0.7$ . The velocity profiles are controlled by the gas density near the wall.

## Acknowledgement

Work performed under the auspices of the U.S. Department of Energy by the Lawrence Livermore National Laboratory under Contract number W-7405-ENG-48. Also sponsored by the Defense Nuclear Agency under DNA IACRO #92-824 and Work Unit 00001 and under Contract number DNA 001-91-C-0039.

## References

- Batt RG, Kulkarny VA, Behrens HW, Rungaldier H (1988) Shock induced boundary layer dust lofting. In: Grönig H (ed) Shock Tubes and Waves: Proc. 16th Int. Symp. on Shock Tubes and Waves, VCH press, Weinheim, Germany, pp 209-215
- Brown GL, Roshko A (1974) On density effects and large structures in turbulent mixing layers. *J. Fluid Mech.* 64:775-816
- Greenough JA, Bell JB, Kuhl AL, Reichenbach H (1993) Direct Simulation of Shock Induced Mixing, 4th Int. Workshop on the Physics of Compressible Turbulent Mixing, Cambridge, England (in press).
- Kuhl et al (1990) Simulation of a turbulent dusty boundary layer behind a shock. In: Kim Y (ed) Current Topics in Shock Waves, Proc 17th Int Symp on Shock Waves and Shock Tubes, AIP Conf Proc 208, pp 762-769
- Kuhl AL, Reichenbach H, Ferguson RE (1992) Shock interactions with a dense-gas wall layer. In: Takayama T (ed), Shock Waves: Proc 18th Int Symp on Shock Waves, Springer, Berlin Heidelberg New York, pp 159-166
- Meshkov EE (1960) Instability of the interfaces of two gases accelerated by a shock wave. *Izv, AN SSSR Mekhanika Zhidkosti i Gaza* 4(5):151-157
- Neuwall P, Reichenbach H et al. (1992) Preliminary Measurements Applying the LDV system at the EMI Shock Tube. Technical report T6/92, Ernst-Mach-Institut, Freiburg, Germany
- Richtmyer RD (1960) Taylor instability in shock acceleration of compressible fluids. *Comm. Pure and Applied Math.*, 13:297-319
- Schlichting H (1958) Grenzschichttheorie. Verlag G. Braun, Karlsruhe

# Influence of rock disintegration in high-loading-density underground explosions on peak overpressure.

Paul W. Bücking

Fraunhofer-Institut für Kurzzeitdynamik  
-ERNST MACH INSTITUT-  
Eckerstr. 4  
D-79104 Freiburg, Germany

## 1. Introduction

In 1994 a 2563.7 kg Comp-B charge was detonated in the Linchburg mine tunnel system, Magdalena, New Mexico, USA. This corresponds to a loading density of  $38.8 \text{ kg/m}^3$  TNT - a volume increase by rock breakout due to a preceding smaller detonation taken into account.

The experimental results and *Sharc*-Code predictions computed in the USA and Germany under the assumption of ideal reflecting boundaries differed considerably. The question arose what caused the disagreement between a well-defined experiment and a validated and established code.

Numerical investigations by Ch. Needham (ARA, Albuquerque) on possible energy dissipating effects: turbulence, water vapor, dust, ground motion and thermal conductivity showed a synergetic effect of max. 10% in peak overpressure reduction. But the "no excuse" calculations were a factor of about two and more too high.

The fact that *Sharc* predicted too high overpressures and, because of this, too early arrival times relative to the experimental data in a high-loading-density contained detonation does not mean that the hydrocode is not a valid calculational tool. It does mean that some physical mechanism or mechanisms that are significant for this type of problem were not included in the calculational approach when treating the walls as ideal reflecting.

A mechanism that can cause a strong effect is a considerable disintegration of rock material in a high-loading-density detonation.

The effects due to rock disintegration are a function of loading density and also of rock properties. Accordingly the computational results with ideal reflecting inactive boundaries will differ more and more from those with activated boundaries when the loading density increases. During the reflection phase peak pressures are diminished as a function of rock disintegration in comparison to those computed under the assumption of ideal reflection. This effect will be practically zero for low loading densities and very significant for high-loading conditions. However it is unknown at what loading density (problem dependent) the effect is so important that a rock model has to be applied. These considerations may be of importance because the computation time goes up by about a factor of ten.

It is the aim of this numerical investigation to find out if the application of *Sharc*'s granit model shows the described tendency - and if it does if the computed pressure time histories come close to the ones recorded in the experiments with special emphasis on shock arrival time and the level of the first peak pressures.

Thus in the efforts to predict pressures for high-loading-density underground detonations a step backward had to be done in the sense that the results of a series of

experiments with increasing charge weight are used as a reference for the numerical results when studying the effects of the numerical granit model and the different ways to apply it.

## 2. Numerical simulation and global considerations

The calculations presented apply the Tillotson equation of state model for granit. The material constants were adjusted to those of sand stone rock samples taken at different positions within the explosion chamber. To adjust the overburden pressure and temperature to the conditions at the Magdalena test site some constants in the rock model had to be changed. The model also contains a porosity which allows air to mix into rock. Besides rock material can be pushed aside. The additional small volume is quite significant because the gas is under very high pressure. The heating of the rock is also taken into account. The *Sharc-Code* as a descendant of the *Hull* code inherited this granit equation of state formulation which is a numerical artefact to globally simulate on a physical basis such a material.

The Magdalena experiments were conducted for Comp-B charges of 71.2 kg, 341.67 kg, 938 kg and 2563.7 kg assembled from 8" cubes of about 14.3 kg each (density of HE is about  $\rho = 1.7 \text{ g/cm}^3$ ). This corresponds to loading densities of  $1.15 \text{ kg/m}^3$ ,  $5.7 \text{ kg/m}^3$ ,  $15.6 \text{ kg/m}^3$  and  $38.8 \text{ kg/m}^3$  TNT equivalent. The computations simulate these experiments applying the granit model in all cases. Up to three different approaches were performed doing this:

1. a. granit cells active at all times
2. granit cells activated by shock if the compressive or shear stress of the rock material is exceeded, limited regime of disintegration according to loading density
3. as before - but additionally ground shock to infinity taken into account

While the initial ideal reflecting computation was done for the whole tunnel-chamber system the influence of rock was computed for a much smaller part including only the detonation chamber, the access tunnel to the chamber and about 10 m of the main drift to one side. Because of symmetry conditions within the time window investigated the line of symmetry was straight through the middle of the detonation chamber, charge and access tunnel with station #32 in the main drift mirrored on left to right. Thus in the numerical model we have four representative stations close to the detonation which correspond to experimental ones (fig. 1). A comparison between experiments and calculations is made for these stations and a match or mismatch will be necessarily valid at stations downstream.

For experiments of underground explosions in complex geometries a match between experiment and calculation does not mean that a close correspondence of overpressure histories in every peak can be expected. This is - to a smaller extend - due to a 2D-approximation of a 3D-event but mainly to the fact that there is a cascade

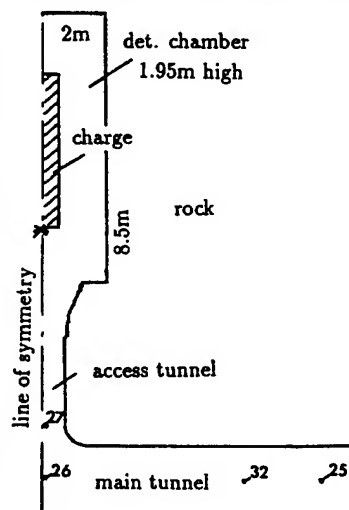


Figure 1 Problem geometry

of shock reflections and interactions. Thus initial small differences in geometry or the assumed and actual detonation behaviour can rapidly lead to *locally* quite different pressure peaks. This was numerically shown for the four stations in the  $5.7 \text{ kg/m}^3$  detonation when the exit tunnel from the detonation chamber was made narrower in the 2D-calculation than in reality in order to match the jump of the actual cross-sectional area between detonation chamber and tunnel ( $A_1/A_2=3.82$ ). This about 36% contraction (from 1.43m to 1.05m) resulted in a considerable change in the singular peak pressure values and the time of their occurrence. For the closest station #27 this is shown in fig. 2. As expected the contraction also influences the arrival time and the outflow behaviour.

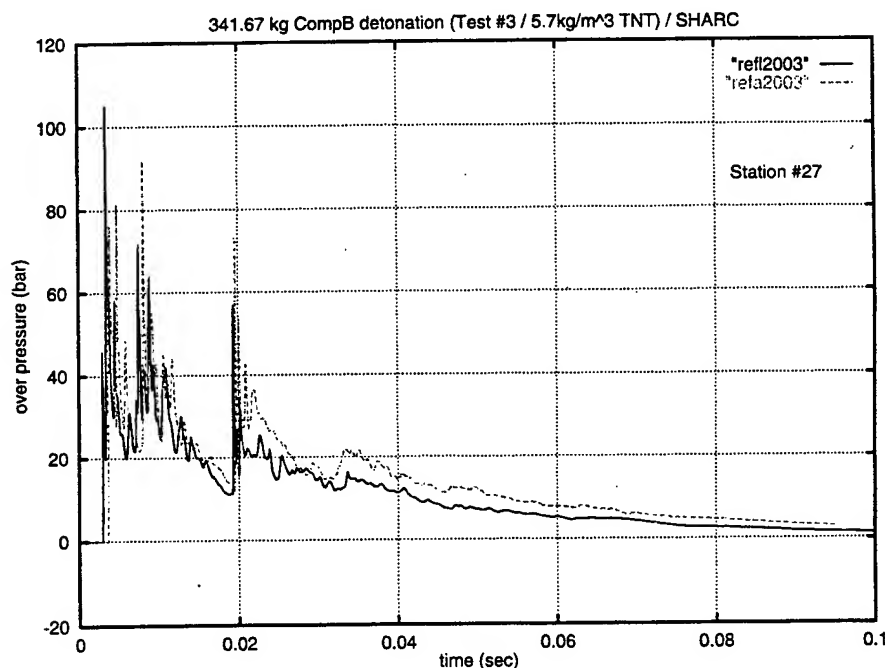


Figure 2 Influence of tunnel contraction according to cross-sectional area ratios (refa) on overpressures (both ideal reflecting).

This change resulted in differences of about the same order that may exist between the computational and experimental results.

Consequently the best thing would be to have in an experiment and a calculation a cluster of gages distributed around a location (also off the wall) and compare the whole ensemble in an averaging or weighting way. Unfortunately, for practical and economical reasons, the experiments could not provide such data clusters.

On the other hand the first pressure pulse and its arrival time determine the degree of correspondence between experiment and calculation.

In order to determine the influence of rock disintegration relative to conditions with perfect reflecting walls all loading-density cases were computed also ideal reflecting. For the highest loading density an ideal reflecting computation had been done already in the original "no excuse" computation of the whole chamber - tunnel system intended to give an overpressure prediction. Thus it was possible to compare the

results of the reduced system with the extended model. As expected there were some minor differences caused by the fact that the assumed symmetry in the small model does not so perfectly exist in the big one because of slightly different rock break-outs at corners of chamber - tunnel junctions. Thus such deviations will be inherent when comparing the numerical results with the experiments. But the enormous reduction in computational efforts made it inevitable to make use of the symmetry.

Because the pressure histories of the experiments in all cases show at times of about greater than 50 msec a tendency of a very slowly decaying pressure level it was thought that this behaviour could be handled by properly taking into account the jumps in the cross-sectional area. But computations showed that the long-term high pressure level could not be predicted by a correct representation of the outflow conditions though from fig. 2 a certain effect is obvious. Thus the relatively high pressure level at later times must be due to the interaction of shock waves and rock material. This seems to be proved by the surprising fact - it was only intended to look for effects on the arrival time and peak pressure level - that it was possible to numerically simulate this long-term behaviour for high loading densities up to 200 msec quite accurately (better with growing loading density).

## 2.1 Computational details

All computations had to be performed in some successive steps:

1. Computation of the long beam-like charge - 100 cm to 406 cm long and initiated at the whole surface end towards the tunnel exit. The amount of mass of the wooden charge support is taken into account. These computations are stopped after some hundred microseconds when the whole charge has detonated and the shock front has spread close up to the computational grid boundaries.
2. The computed state of the detonation process is injected into the computational grid for the whole problem including the granit model. The further development of the process is computed including shock interaction with the granit, granit cell activation, rock disintegration and ground shock (latter not done for smallest loading density). The computations were done up to 20 ms. At these times the shock-granit interactions seem to be completed and influences from these interactions satisfyingly taken into account.
3. Extraction of granit from multi-material cells with proper corrections necessary and turning all disrupted granit of still high density to inactive 'island'-cells. This is done to speed up the calculation considerably in order to proceed up to 200 ms.

## 2.2 Test #2 / 71.2 kg Detonation / 1.15 kg/m<sup>3</sup>

1.15 kg/m<sup>3</sup> is quite a small loading density. This means that in this case possibly no disintegration of rock will occur. Thus a computation with perfect reflecting detonation chamber walls should give the same results as an application of the granit model and both should agree with the experimental results.

This expected agreement was actually found in the computation with took into account possible rock disintegration. A computation which additionally includes ground shock has not yet been done. The results are close to the experimental data as is shown by some numerical values (ref=reflective; gr=granit; e=experiment):

station #27:  $t_{a_{ref}}=5.2\text{ms}$  /  $p_{a_{ref}}=23.8\text{bar}$   $t=5.31\text{ms}$   
 $t_{a_{gr}}=5.2\text{ms}$  /  $p_{a_{gr}}=25.0\text{bar}$   $t=5.3\text{ms}$   
 $t_{a_e}=4.68\text{ms}$  /  $p_{a_e}=25.7\text{bar}$   $t=5.3\text{ms}$

station #26:  $t_{a_{ref}}=6.53\text{ms}$  /  $p_{a_{ref}}=6.2\text{bar}$   $t=15.25\text{ms}$   
 $t_{a_{gr}}=6.53\text{ms}$  /  $p_{a_{gr}}=6.23\text{bar}$   $t=15.4\text{ms}$   
 $t_{a_e}=6.4\text{ms}$  /  $p_{a_e}=4.95\text{bar}$   $t=15.4\text{ms}$

station #25:  $t_{a_{ref}}=15.1\text{ms}$  /  $p_{a_{ref}}=6.2\text{bar}$   $t=15.25\text{ms}$   
 $t_{a_{gr}}=15.23\text{ms}$  /  $p_{a_{gr}}=6.23\text{bar}$   $t=15.4\text{ms}$   
 $t_{a_e}=15.23\text{ms}$  /  $p_{a_e}=4.95\text{bar}$   $t=15.4\text{ms}$

Figure 3 shows the good agreement found for arrival times and overpressure peaks.

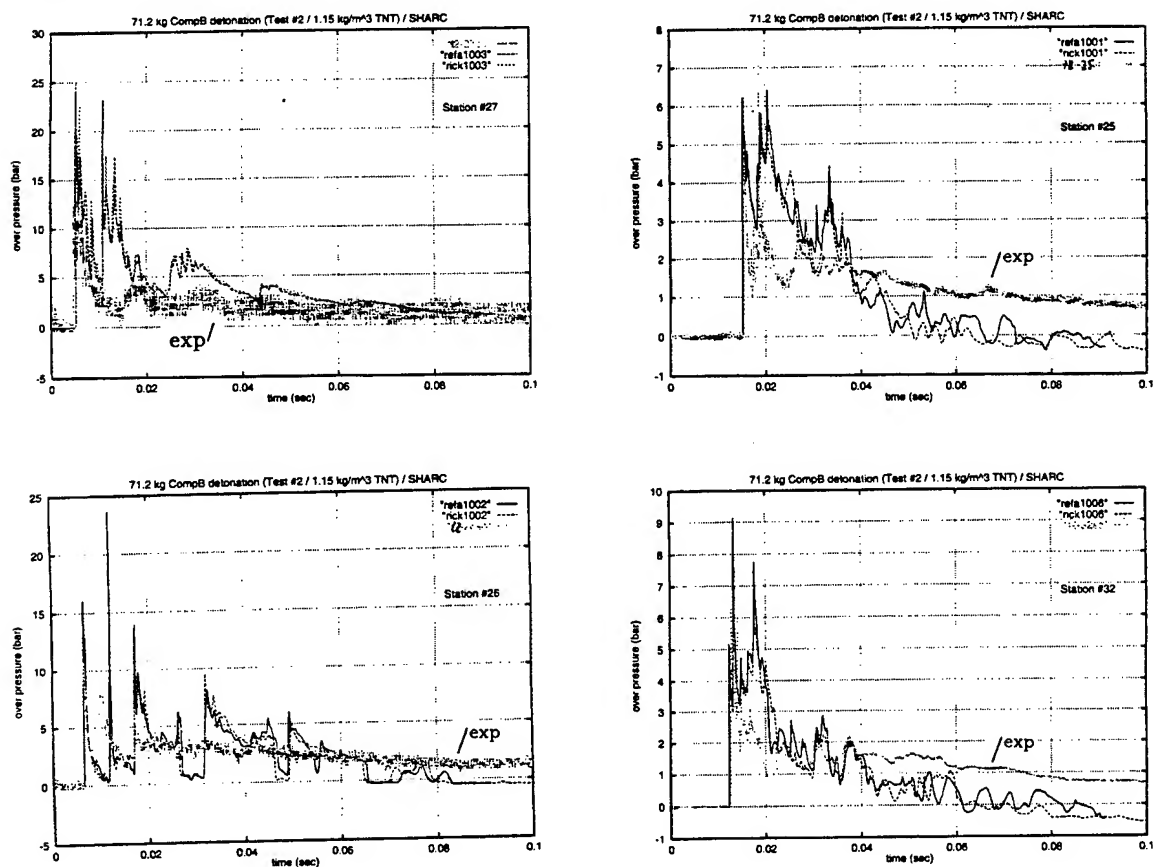


Figure 3 Comparison of experimental (t2-station #) pressure time histories reflecting (refa...) and rock (ri.. rock turned to island; no ground shock);

Especially for stations further downstream (#32 and #25) it is obvious that the pressure level decays much slower than computed. After about 40 ms the computed and experimental outflow-phase overpressures histories diverge. The computed behaviour is blast-like with a negative phase whereas in the experiment the overpressure never drops below ambient.

A similar tendency as described is valid for all experiments and computations. For the loading-density cases of  $5.7 \text{ kg/m}^3$ ,  $15.6 \text{ kg/m}^3$  and  $38.8 \text{ kg/m}^3$  another computational approach was able also to simulate this longer term measured pressure level correctly. This approach is also about to be applied to the small detonation.

### 2.3 Test #3 / 341.67 kg Detonation / $5.7 \text{ kg/m}^3$

Figure 4 shows the pressure distribution inside the detonation chamber which has a new boundary according to shock wave - rock interaction in the case of a computation with active granit cells at all times. This way of computation was used initially and gave satisfying results with respect to the desired peak pressure reduction only in the highest loading-density case. In all other cases also a strong effect in reduction of peak pressures was found. This shows that the gas-rock interaction is responsible for a considerable peak overpressure reduction, but that it is necessary to trigger this reduction process by activating the granit cells according to the strength of the detonation and rock material.

Besides in the initial computational approach after some milliseconds numerical difficulties killed the computations. These difficulties initiated program development to get rid of the granit and turn it to islands after some time of shock - rock interaction (fig. 4) - a method which later was used to speed up the computation in granit-cell-activated computations.

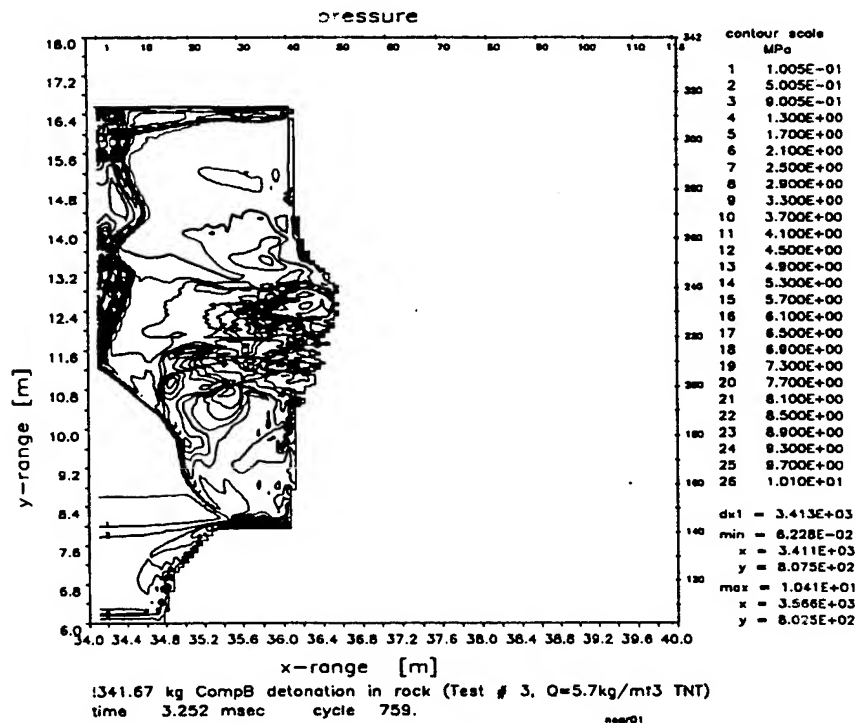


Figure 4 Pressure distribution in detonation chamber with ragged new boundary after shock - rock interaction

This switch to inactive cells instead of granit is done after some time regarded to be long enough to allow the main shock-rock interactions to take place and have their



influence on the gasdynamics inside the chamber-tunnel system.

The initial computational approach was skipped and will not be considered further.

In the shock-activated granit cell computation the geometrical effect to the explosion chamber wall is very small for this loading density and comprises only some cells.

A comparison between the peak pressures of an ideal reflecting computation and experiment shows that pressures are already computed considerably too high for the stations closest to the explosion. This means that though the loading density is still relatively small already a pressure reduction is caused by shock-rock interaction. For station #27 initial peaks of about 80 bar are computed but only of 55 bar measured with some excessive peaks afterwards but none in the experiment. Fig. 5 also shows the comparison for the other stations.

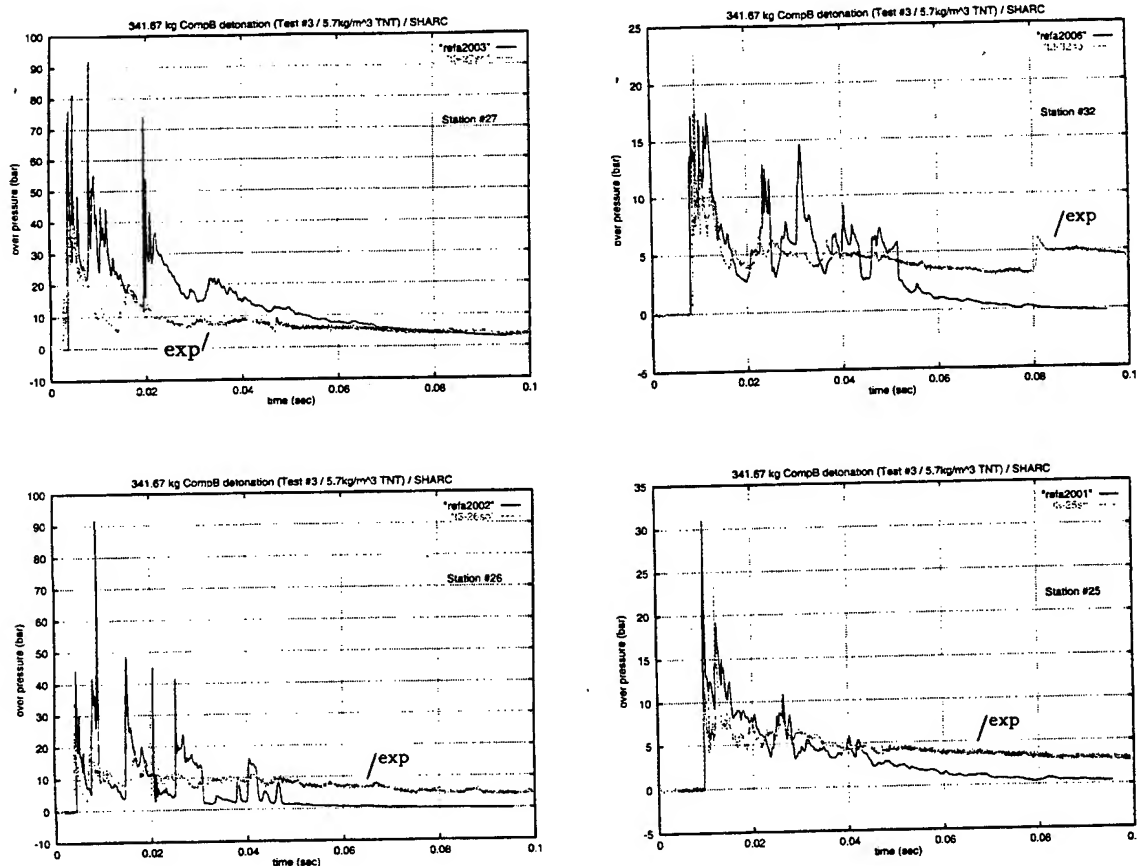


Figure 5 Comparison of overpressures: computed ideal reflecting and experiment for a loading density of 5.7 kg/m<sup>3</sup>

Except for station #27 the pressure level after about 50 ms is computed much lower than in the experiment. On the other hand arrival times are about exact at all stations. This shows that exact arrival times do not necessarily imply a correct pressure peak level in the pressure history shortly after the initial shock.

Quite a good agreement is found when *Sharc's* granit model including ground shock is applied. The arrival time computed is only about 1.5 ms delayed. The experimental records contain some singular needle-shaped peaks about  $45\ \mu\text{s}$  wide which are about 30% higher than the computed pressure level. Discarding these Figure 6 shows then quite a good correspondence of overpressures between experiment and computation. Additionally the measured relatively high pressure level at longer times up to about  $140\ \mu\text{s}$  is met quite well by this and only this way of computation.

#### 2.4 Test #5 / 938 kg Detonation / $15.6\ \text{kg/m}^3$

The computations performed included rock disintegration and ground shock. The application of the rock model in the computation for this loading density gives a quite significant effect in peak overpressure reduction associated with a delayed shock arrival time (fig. 7). Additionally the effect computed has just the right amount to fit very well with the measured pressure time history levels at the closest stations #27 and #26. This is valid not only for the initial instationary shock dominated phase but also up to the computed 160 ms which are dominated by outflow conditions (fig 8). A rigid boundary computation gives a more 'blast-like' behaviour in which the pressure level decreases more rapidly with time and thus does not show the measured relatively high pressure at longer time.

Computations with rock disintegration only (case a) and additionally with ground shock (case b) show different influences on the over pressure histories. Fig. 9 shows the differences for the closest and farthest stations #27 and #25 (rgck..= a) ; rock..=b ). Case b) causes an additional peak pressure reduction during the shock-dominated phase and a considerable over pressure increase at later times - a behaviour which results in a quite good agreement with experiment as shown in fig. 8.

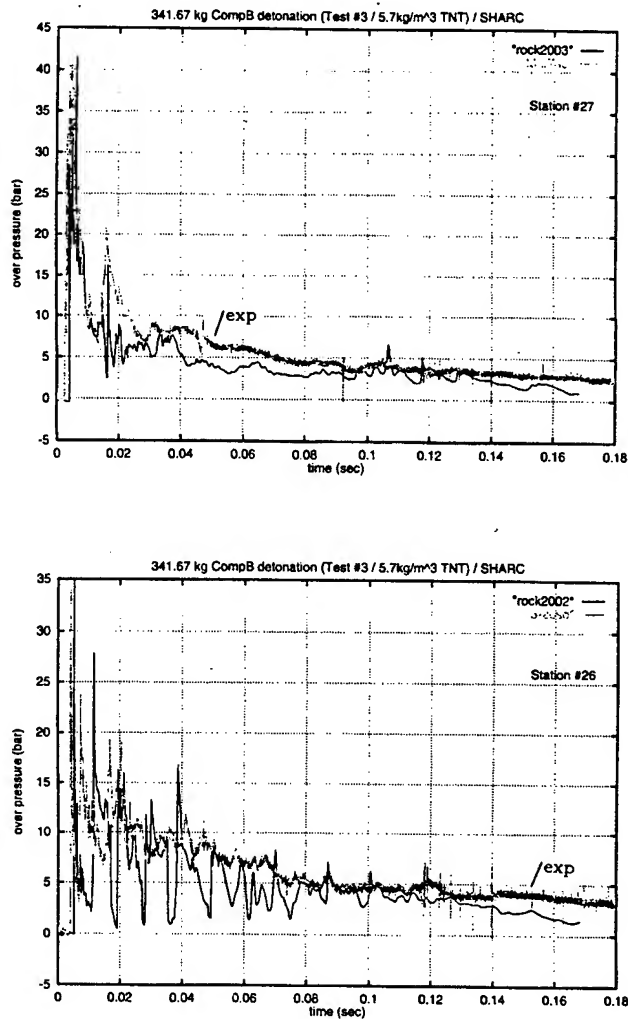


Figure 6 Comparison of overpressures: Sharc granit model with ground shock and experiment for a loading density of  $5.7\ \text{kg/m}^3$

Before the shock wave through the tunnel arrives at stations #32 and #25 the computed overpressure histories show small disturbances. These are caused by the

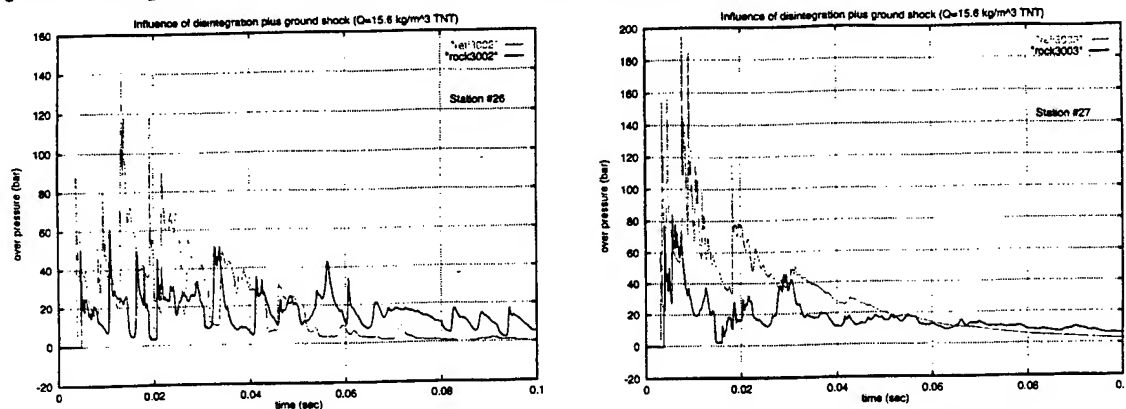


Figure 7 Comparison of overpressures: computed ideal reflecting (refl..) versus rock disintegration and ground shock (rock..) for a loading density of  $15.6 \text{ kg/m}^3$

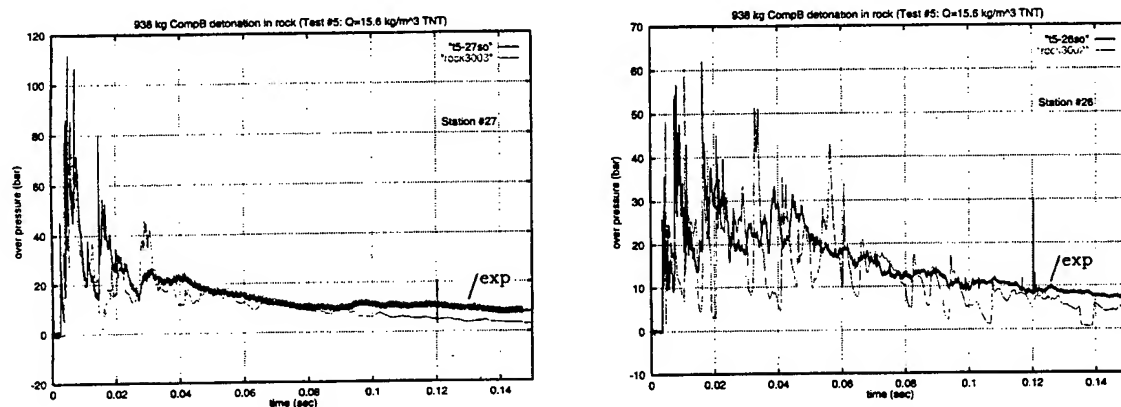


Figure 8 Comparison of overpressures: experiment (t5...) versus rock disintegration and ground shock (rock..) for a loading density of  $15.6 \text{ kg/m}^3$

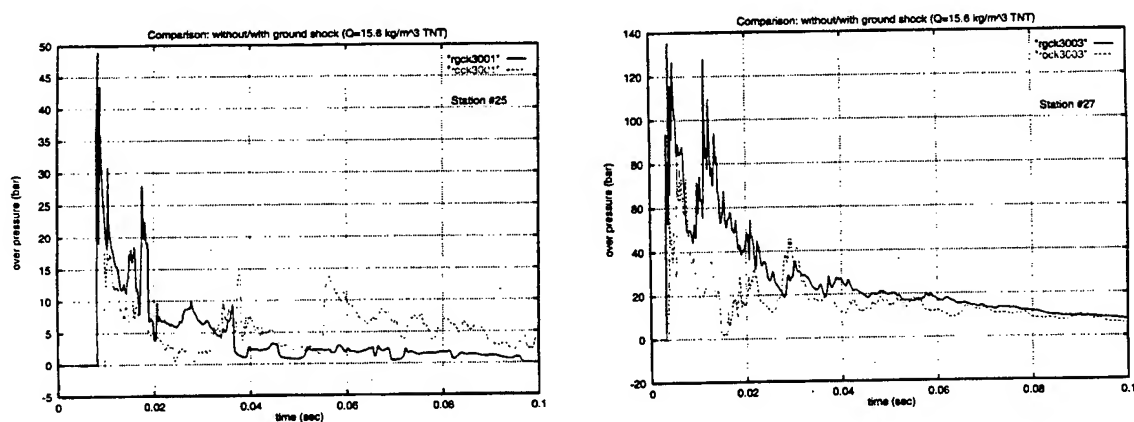


Figure 9 Comparison of overpressures: computed rock disintegration (rgck..) versus rock disintegration plus ground shock (rock..) for a loading density of  $15.6 \text{ kg/m}^3$

ground shock through the rock generating a weak disturbance in the tunnel air due to a great impedance mismatch. These disturbances show up also in the experimental records. Fig. 10 shows the pressure wave expanding into the rock medium in case b) whereas fig. 11 shows a region of disrupted rock of nearly unchanged density and a crater region with a very steep gradient at the crater lips bulging into the detonation chamber.

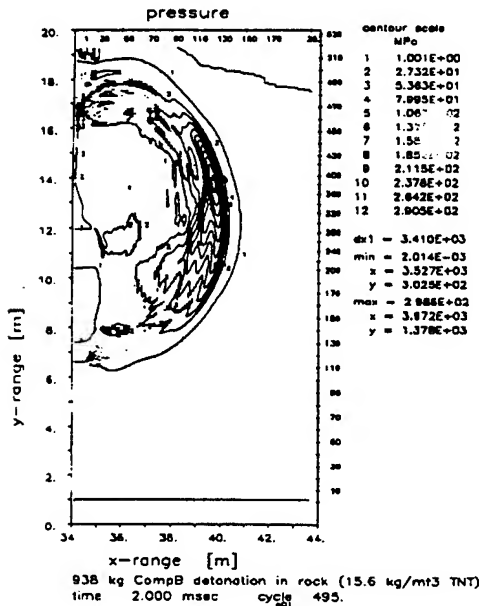


Figure 10 Ground shock expanding into rock. Rock disintegration plus ground shock for a loading density of  $15.6 \text{ kg/m}^3$

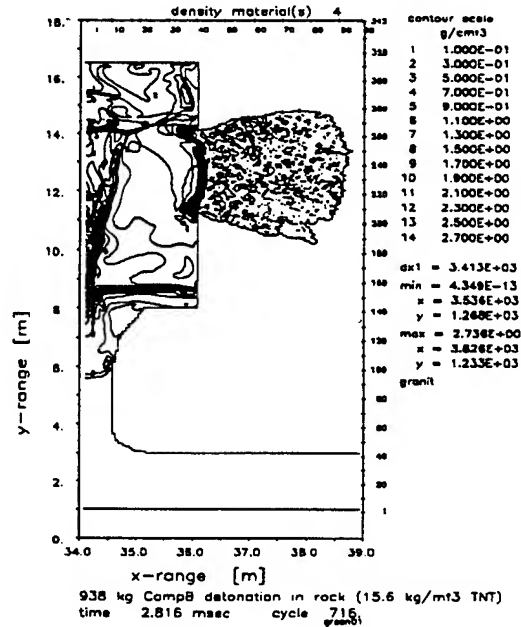


Figure 11 Region of disintegrated rock with crater. No ground shock taken into account. Loading density of  $15.6 \text{ kg/m}^3$

## 2.5 Test #6 / 2563.7 kg Detonation / $38.8 \text{ kg/m}^3$

Figures 12 give the comparison between experiment and a perfect reflective calculation (case a) at the four given stations. These should be compared with figures 13 computed with rock disintegration and ground shock (case b). While for station #27 being closest to the detonation in case a) and b) the arrival time and the very first peak are nearly identical and coincide quite exactly with the experiment the following peak pressures in case a) are computed much too high whereas for b) we have a very close correspondence between measured and computed peak pressures:  $ta_c=2.34\text{ms}$  /  $pa_c=40.1\text{bar}$  /  $ta_e=2.01\text{ms}$  /  $pa_e=32.4\text{bar}$  /  $pmax_c=203\text{bar}_{t=5.7\text{ms}}$  /  $pmax_e=197\text{bar}_{t=5.6\text{ms}}$ .

Though the computed incident shock with 40.1 bar is stronger than the measured one it arrives .33ms later. This is in contradiction to physics and shows that in some cases it may happen that in an experiment the exact zero-time for a gage is not given correctly.

A very good correspondence between experiment and calculation (b) is also found for station #26 which is hit by multiple shock reflections from the main drift's tunnel wall. That is why it is a sensitive indicator and especially apt for an experimental / numerical data check. As for station #27 the up to 200 ms computed longer time

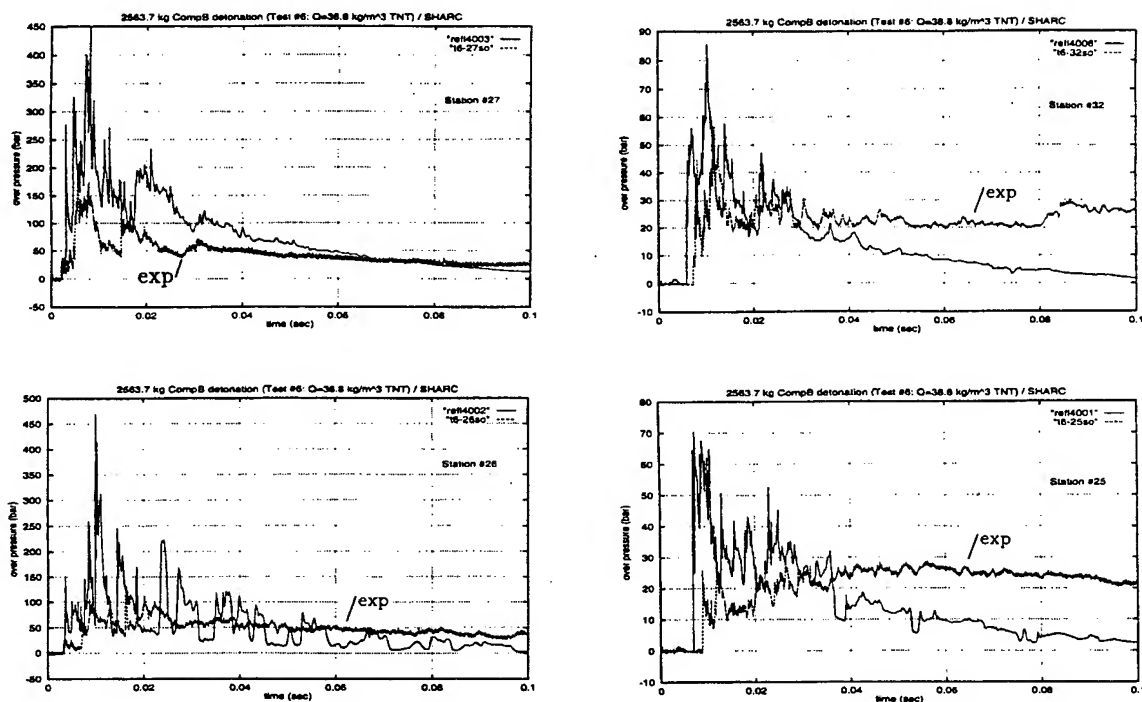


Figure 12 Comparison of overpressures: Ideal reflective computation versus experiment for a loading density of  $38.8 \text{ kg/m}^3$

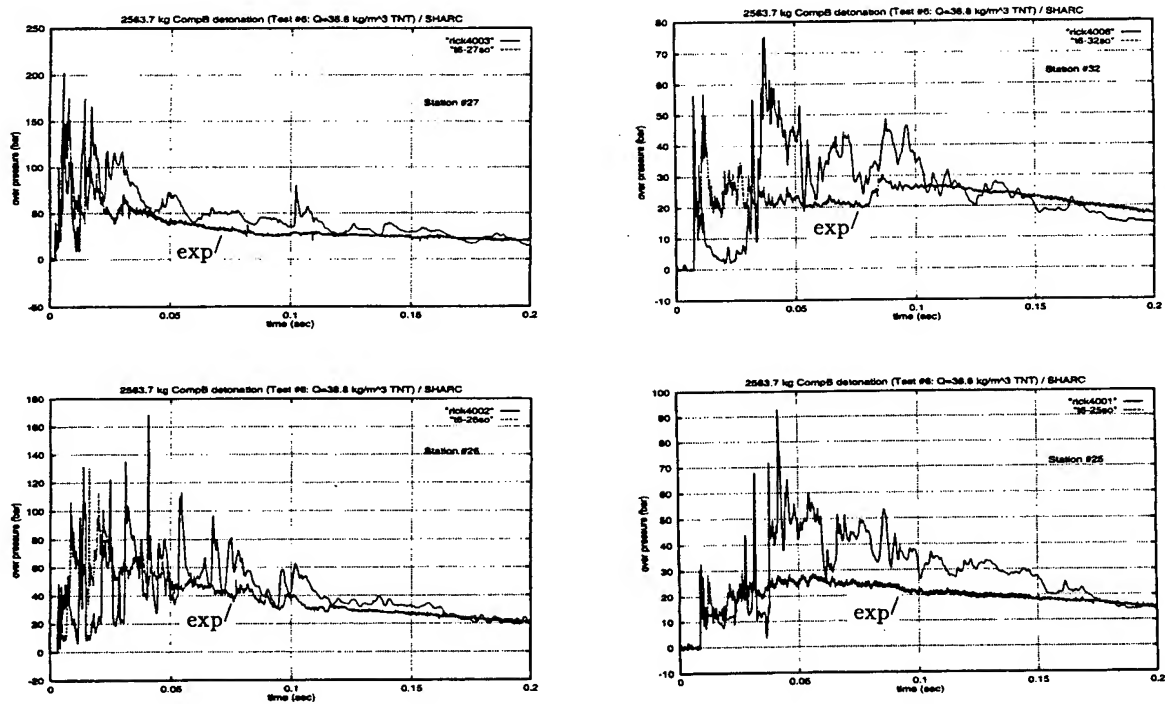


Figure 13 Comparison of overpressures: rock disintegration plus ground shock versus experiment for a loading density of  $38.8 \text{ kg/m}^3$

pressure level of about 20 bar is in very good correspondence with the experiment. It was quite unexpected that it would be possible to also simulate this behaviour, because all other ways of applying the granit model could not simulate this level and resulted in a much faster decay to low pressure values.

Thus taking into account rock disintegration and ground shock in the calculation gives the correct arrival times and peak overpressures as well as the pressure decay for longer times far beyond the instationary phase of shock interactions. From this it is concluded that the calculation now takes into account the relevant physical effect in a high-loading-density detonation which was missing in the ideal-reflecting approach.

This computational approach giving satisfying results was first found for this high-loading-density case. It was then applied to the  $15.6 \text{ kg/m}^3$  and  $5.7 \text{ kg/m}^3$  cases with the same good results.

### 3. Conclusion

Numerical predictions of underground detonations will result in much too high overpressures when not taking into account shock-rock interactions.

With increasing loading density the shock-rock interactions become more and more important. The effects due to rock disintegration are a function of loading density and also of rock properties. Accordingly the computational results with ideal reflecting inactive boundaries will differ more and more from those with activated boundaries when the loading density increases. During the reflection phase peak pressures are diminished as a function of rock disintegration. This effect will be practically zero for low loading densities and very significant for high-loading conditions. However it is unknown at what loading density (problem dependent) the effect is so important that a rock model has to be applied. Only for small loading densities a calculation with ideal-reflecting walls may give correct values when the charge was stored off the enclosing walls. For a loading density of  $5.7 \text{ kg/m}^3$  already significant influences were found (charge room-centered)

Computations showed that additionally to rock disintegration another effect has to be considered: ground shock. By this overpressures are reduced even more and are then in close correspondence with experimental results up to the highest loading-density of  $38.8 \text{ kg/m}^3$  investigated.

Taking into account rock disintegration and ground shock in the calculation gives the correct arrival times and peak overpressures during the initial instationary shock-dominated phase as well as the pressure level at longer times at outflow conditions. The latter was quite unexpected because all other ways of applying the granit model could not simulate this level and resulted in a much faster blast-like decay to low pressure values.

From this it is concluded that the relevant physical effects in underground detonations are rock disintegration and ground shock. The calculational method offered by the *Sharc* code allows to trigger the computational process of rock-cell activation according to the strength of the detonation and rock material.

The result of the experimental and calculational efforts in this American/European cooperation is that a numerical procedure was found and tested which - when applying the *Sharc* Code - gives reliable predictions of overpressures for detonations in underground storages by taking into account shock-rock interactions.

# Oblique Reflection of Decaying Pressure Waves

W. Heilig

Fraunhofer Institut für Kurzzeitdynamik

Ernst - Mach - Institut

Freiburg im Breisgau, Germany

## Abstract

The paper deals with a two-dimensional numerical study applying the code SHARC for the reflection of planar blast waves at wedges with angles of  $30^\circ$ ,  $45^\circ$ , and  $60^\circ$ . The initial conditions of SHARC are chosen in such a way that a blast wave in the spatial distribution is located close to the wedge tip. The wave is generated using the built-in 1 kt standard blast data by specifying 5 bar peak overpressure and a positive time duration of 10 msec. The numerical results are presented in the form of isopycnics in time intervals of 5 msec, of the pressure distribution on the wall and of the pressure profiles of the undisturbed wave at these times. It is clearly seen that the front amplitude decays in its strength with distance and that the length of the blast wave increases as it is known for wave attenuation. The isopycnics show wave patterns which are different from those occurring with shock wave reflection at the same obstacles. Especially the reflected wave does no longer turn to the wedge base line but fades out in the afterflow region of the wave. The pressure values along the wedge wall at a fixed time instant are smaller than those with shock wave reflection. But regular and irregular reflections appear as usual meaning that these phenomena are created at the fronts of the blast wave. The SHARC runs are evaluated with respect to the decaying front pressure of the incident wave, to the front pressure of the reflected wave and to the wave length versus distance, resp..

## Introduction

The shadow-schlieren pictures visualizing the wave patterns of regular reflection (RR) and of irregular reflection (IR) in the various forms are well-known. With the aid of the shock-tube technique they are produced by shock waves, i.e. by pressure waves which as incident waves carry a profile of constant flow parameters behind the fronts. When reflecting at an obstacle, say at a wedge, the reflected shock travels into the uniform afterflow region of the incident shock; it gets curved and meets the bottom of the tube

perpendicularly or interacts with the boundary layer there. Incident shock waves of this type are usually created by nuclear events.

A conventional explosion produces a pressure wave the profile of which is different from that of a shock wave. This type of wave is called blast wave and comes into existence by a short-time energy release. At a fixed time instant the pressure signature of a free blast wave in space consists of a sharp rise which indicates its front; it is followed by a pressure decay which can be approximated by the curve of an exponential function. At a certain place the curve runs below the ambient pressure, the distance from this locus to the front is called the wave length. The corresponding holds for the remaining flow parameters.



Fig. 1: An incident plane shock wave of moderate strength produces a single Mach reflection at the 30°-wedge. The reflected shock meets the bottom of the tube. Visualization made in the EMI Shock Tube Lab.

Fig. 1 recalls the reflection pattern in the form of a single Mach reflection which is produced by a shock wave hitting a wedge. Especially note the shape of the reflected shock. One has to become aware that the reflection- and diffraction patterns of blast waves show other features than those produced by shock waves. So the pressure loading of the obstacle which is an important parameter for practical applications deviates from that one caused by a shock wave. The wave length plays an important role especially in the case if it is of the same order of magnitude as a characteristic length (diameter, e.g.) of the body.

In general the visualization of blast waves effects is not so common as it is for shock waves. However, numerical simulation can provide a rather good insight into the processes.

The paper presents some first results for the simple case of the reflection of a planar blast wave at rigid wedges with angles of 30°, 45°, and 60° and at a cylinder as 2-d processes. They are obtained by applying the code SHARC. Fig. 2 schematically shows the



items of this study. The processes can be considered as taking place in a "2-d tube" in which the objects are mounted.

### Blast Wave Reflection at Wedges

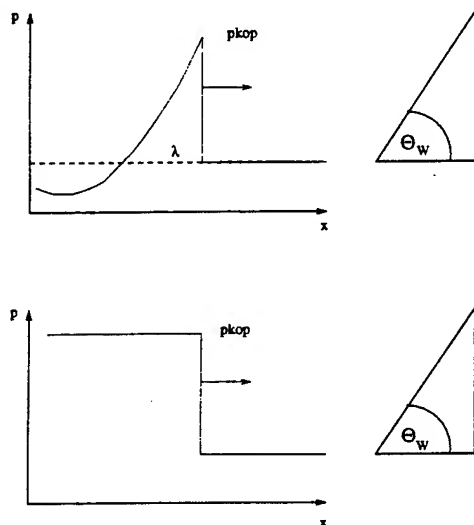


Fig. 2: Definition of terms

#### Incident Wave

pkop = 5 bar  
 $t_+ = 10 \text{ msec}$   
 $\lambda \sim 10 \text{ m}$

pkop: Peak overpressure  
 $t_+$ : Positive pressure time  
duration

$\lambda$ : Length of the blast wave

#### Wedges

$\theta_w = \begin{cases} 30^\circ \\ 45^\circ \\ 60^\circ \end{cases}$

$\theta_w$ : Wedge angle

### Setups for the SHARC Computation

Since some years SHARC is successfully applied at EMI for the computation of processes such as the shock wave propagation in tunnel systems [1], the interaction of shock waves with obstacles for gaining the loading [2], the simulation of detonation events [3], etc.. For this study some initial preparations to the code are necessary. With the aid of the built-in 1 kt standard blast wave data file a wave with 5 bar peak overpressure and with 10 msec positive time duration is specified. Using the firein option of the code this wave is brought into the tube in the spatial distribution, so that the wave front is placed in front of the obstacle at time 0. This initial condition is shown in Fig. 3a. - In Fig. 3b the pressure profile is seen. It does not yet show a definite wave length at this time instant, this will appear later. The SHARC results are presented as isopycnics, as pressure horizontal histograms for the undisturbed wave and along the body surface for successive time instants. All computations in this report are made for this initial condition of the incident blast wave. As the wave attenuation of the blast wave specified becomes noticeable only for larger distances the body dimensions must be chosen in meter scales. According to this the zoning has to be adjusted properly. Viscous attenuation is not taken into account.

## Results and Discussion

The process for the 30°-wedge is presented in Figs. 3a, 3b; Figs. 4a, 4b; ... to Figs. 12a, 12b.

For the time instant 15 msec Figs. 4a, 4b and Fig. 9b show that the reflected shock is not yet strongly influenced by the pressure decay in the blast wave field; its shape is curved towards the tube bottom like it is with the shock wave reflection. The profile of the undisturbed blast wave at the horizontal line  $j = 485$  (Fig. 4b) with the front pressure of 3.8 bar indicates a significant attenuation compared to the front pressure of 5.8 bar at time = 5.845 msec or start cycle = 0 (Fig. 3b). The pressure profile along the wall (Fig. 9b) shows a peak pressure of 6.4 bar which is the strength of the Mach stem at 15 msec. The reflected wave at the bottom is very weak recognizable by the small bump in Fig. 9b.

The results for the time instant 20 msec (Figs 5a, 5b and 10a) indicate that the reflected shock fades out; it does no longer meet the bottom of the tube; the blast wave front is weaker than before, a blast wave length of roughly 10 meters can be read from Fig. 5b.; the Mach shock still has a strength of 5.7 bar compared to that one of 6.4 bar at time 15 msec.

This trend continues for the following time instants 25 msec, 30 msec, 35 msec and gets more and more pronounced (see Figs. 6a, 6b, and Fig. 10b for 25 msec; etc.).

A remarkable fact is the appearance of irregular reflection in the form of a single Mach reflection in the well-known form (see Fig. 8a, e.g.) with an established contact line. This obviously demonstrates that the phenomenon is not influenced by the afterflow of the st wave but it is caused by a flow mechanism acting at the front of the incident wave.

For comparing these findings with a shock wave reflection (front strength 5 bar peak overpressure; shock Mach number  $Mo = 2.3$ ) a SHARC computation is performed (see Figs. 12a, 12b for 20 msec) at the 30°-wedge. The isopycnics show the well-known features, especially note the shape of the reflected shock being continuously curved until it reaches the bottom. However, the pressure trend along the wall  $j = 1$  (Fig. 12b) is different from that for the blast wave interaction (Fig. 10a).

In order to point out these facts the analogous procedure was repeated for two other inclined wedges. The incident blast wave is specified as the same mentioned above. Therefore the pressure profiles of the undisturbed wave are those shown in Figs. 3b to 8b.

For the 45°-wedge the isopycnics and the wall pressures are given in Figs. 13a and 13b for 35 msec. Again the fading out of the reflected shock can be confirmed and the pressure jump across the Mach stem is indicated. A single Mach reflection appears.

For comparison to this the shock wave reflection with the shock strength of 5 bar peak overpressure is computed and the output is seen in Figs. 14a and 14b. Here we find that

instead of a single Mach reflection a double Mach reflection appears. The wall pressure in Fig. 14b is different from that in Fig. 13b holding for the blast wave reflection.

For the 60°-wedge the same procedure yields the results in Figs. 15a and 15b for the blast wave reflection and in Figs. 16a and 16b for the shock wave reflection. They are consistent with the above mentioned ones. As expected regular reflection now appears. The attention is drawn to the shapes of the reflected waves and to the discrepancy in the wall pressures.

As an example for the blast wave reflection at a non-plane obstacle, a cylinder, the isopycnics are shown in Fig. 17 for comparison to the process at the wedges.

### Evaluation of the SHARC Runs

The plot output of the SHARC computations is evaluated concerning the incident blast wave i.e. its front attenuation as well as the increase of the blast wave length - as far as available - (see Fig. 18). It is found that a remarkable amount of attenuation of the front pressure occurs along the distance of approx. 20 m, whereas the length increases only slightly above the value of 10 m roughly.

In the same way the reflected blast wave is considered concerning its front pressure, i.e. the decrease of the strength of the Mach shock for the case of the 30°-wedge. The decay of the data versus the distance is given in Fig. 19. Using the incident front strength at a fixed time instant as computed by SHARC (Fig. 18) and the wedge angle (30°) as input values the von Neumann Three Shock Theory yields a value for the strength of the Mach shock. Such data are also put in Fig. 19 to be compared to the Mach shock strengths resulting from SHARC.

### Conclusions

Blast wave reflection at oblique plane walls (wedges) produces isopycnic-contours which are different from those produced by the reflection of shock waves. Especially the reflected wave is deformed.

The pressure loading of obstacles hit by blast waves is smaller than the corresponding one exerted by shock waves.

The process of blast wave reflection at wedges is not pseudo-steady as it is in the sense of shock wave reflection.

Data of the blast wave reflection at obstacles can apparently be obtained by numerical methods only.

## References

- [1] Bücking P.W., "Camp Stanley 336 kg Comp-B Detonation. Berechnung des Einflusses von Parametervariationen auf den explosionsinduzierten Druckverlauf" (Camp Stanley 336 kg Comp-B Detonation. Computation of the influence of parameter variations on the explosive-induced pressure history) EMI Report E 13/92
- [2] Heilig W., "Measured Parameters of the Airblast Loading of Generic Models from Shock Tube Tests and Comparison with SHARC-Code Calculations" Proceedings: 5. International Symposium on Interaction of the Effects of Munitions with Structures, Mannheim, BRD, 22. - 26. April 1991
- [3] Bücking P.W., "Effects of TNT Detonations at Reiteralpe. Computation of 50, 100, 200, 500, 1000 and 2000 kg Explosions. A detailed Investigation - Comparison with Experiments" EMI-Report E 2/93

## Acknowledgements

The author likes to express his gratitude to the representatives of the German Ministries, to Mr. BDir. M. Kropatscheck (Ministry of Defense, Bonn), to Messrs. Dr. K. A. Köhler and to Mr. BR. K. Neugebauer (Office of Armament and Procurement, Koblenz), for their continuous interest in this work and for the financial support. - In the same way he thanks Mr. J.E. Crepeau, Applied Research Association, Albuquerque, NM, USA, for helpful pieces of advice.

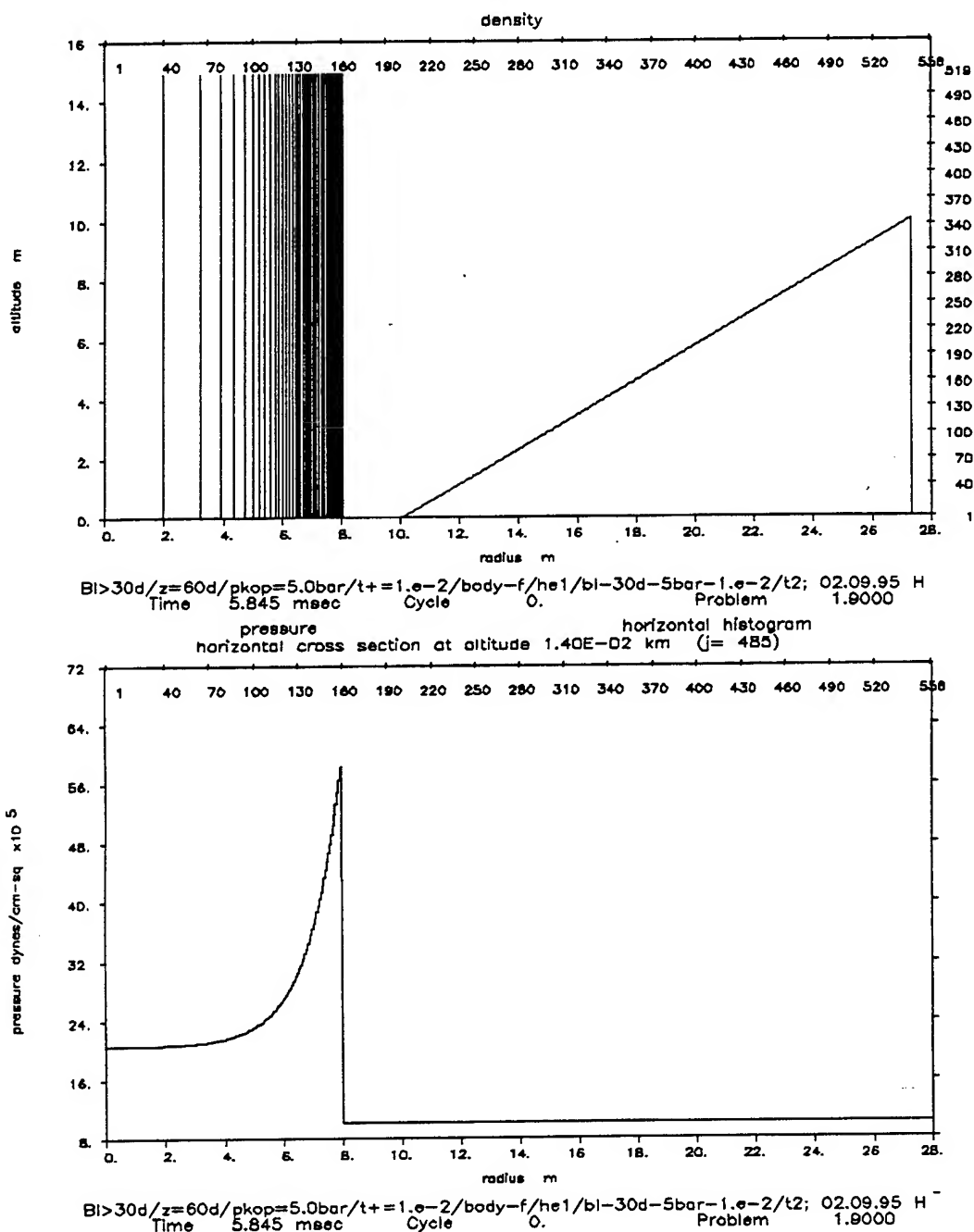


Fig. 3a (above): Initial position of the blast wave in the spatial density distribution at the start of the SHARC computation (start time = 5.845 msec; cycle = 0). Geometry is in meters.

Fig. 3b: Profile of the blast wave as a horizontal pressure histogram at the vertical height of  $j = 485$ .

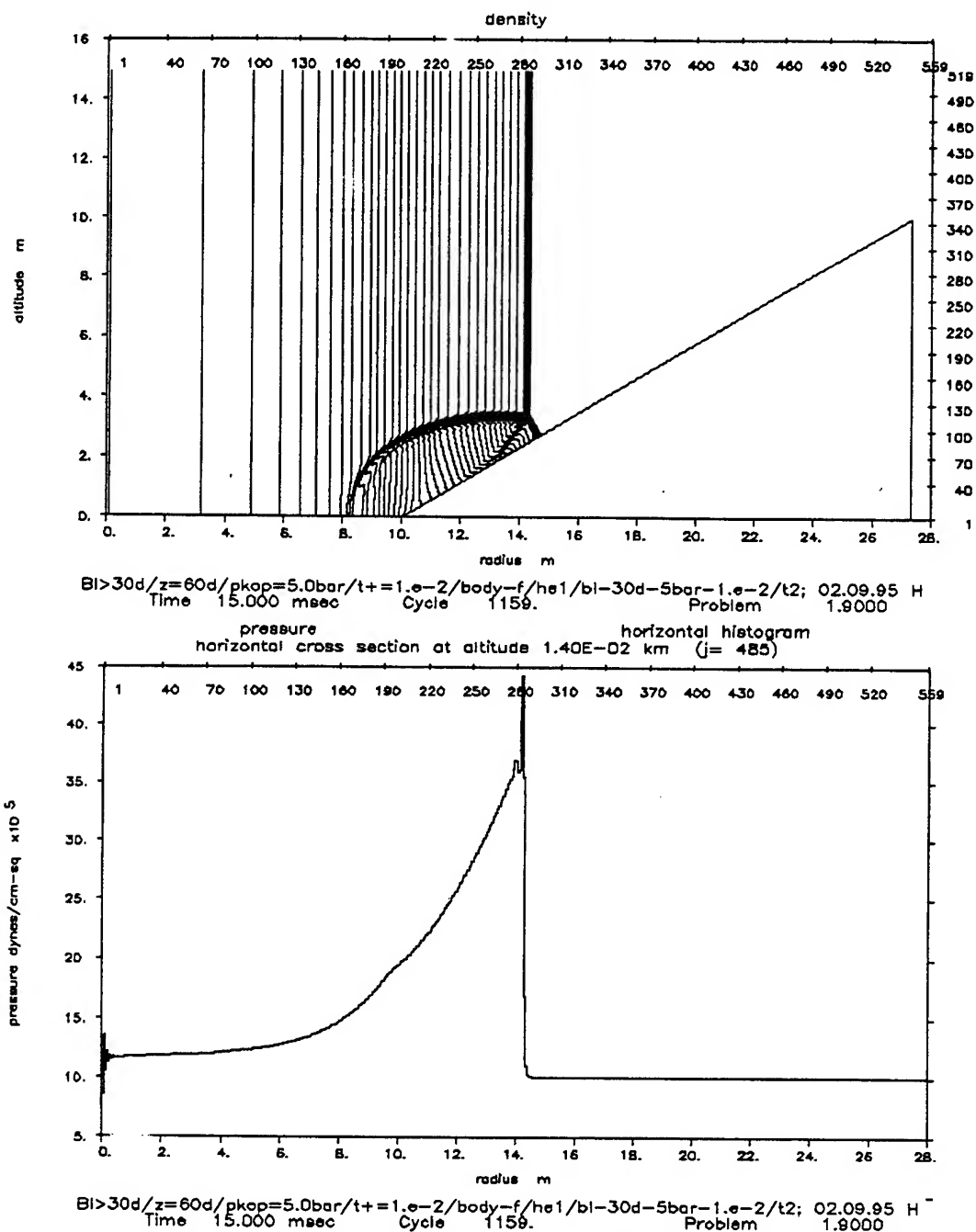
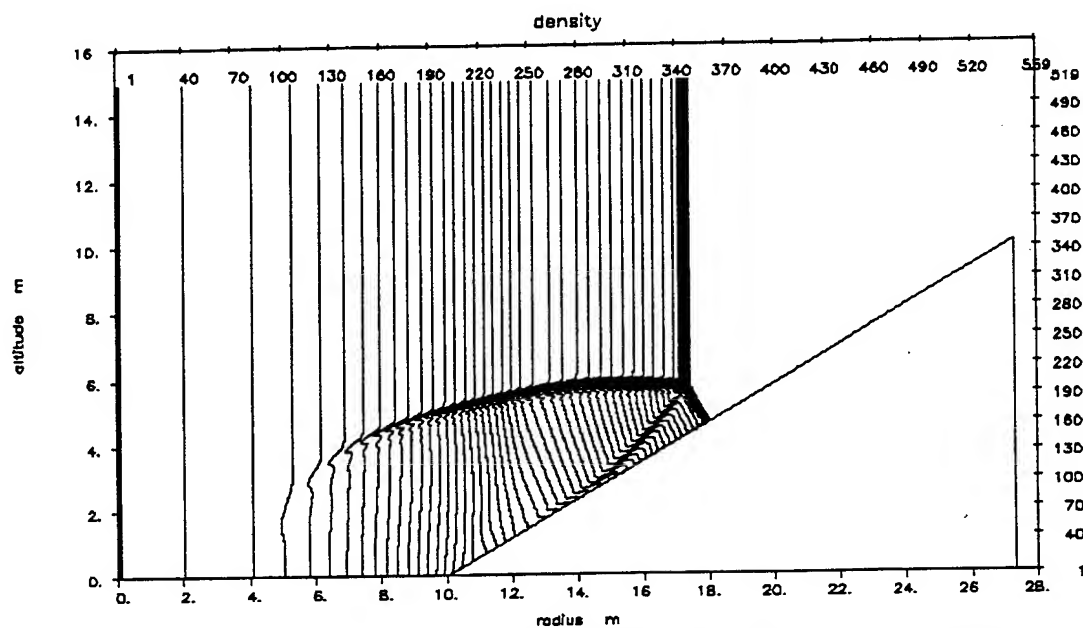
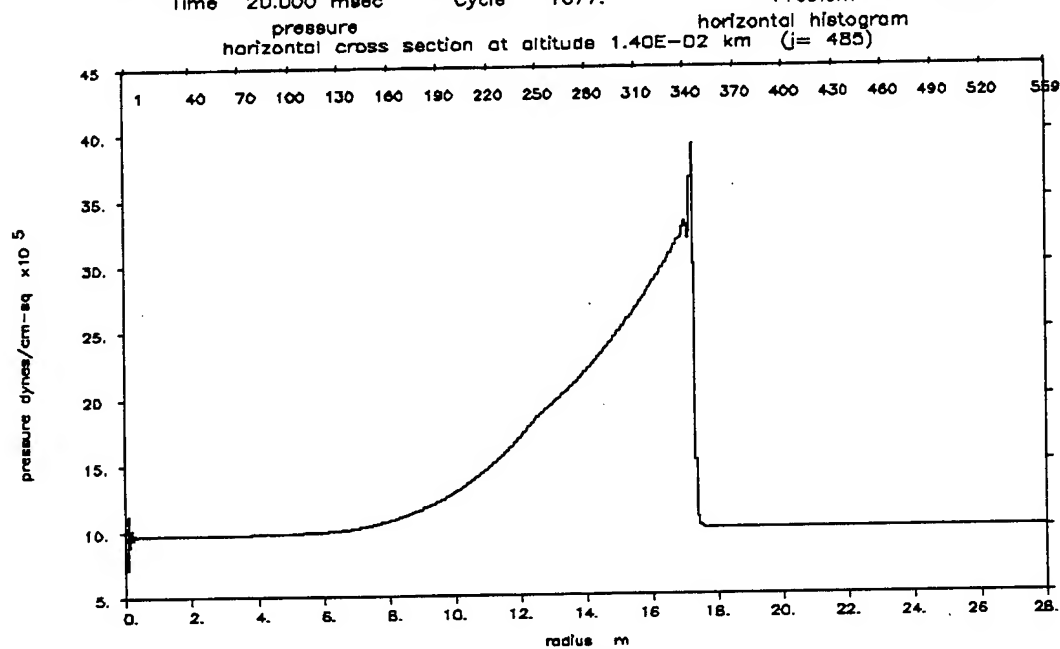


Fig. 4a: Isopycnic presentation of the blast wave reflection at 15 msec. Single Mach reflection appears at the 30°-wedge. The reflected shock meets the bottom almost perpendicularly and is rather weak there.

Fig. 4b: Pressure horizontal histogram of the undisturbed blast wave at the height of  $j = 485$ . Its front strength is smaller than in Fig. 3b by 2.0 bar due to wave attenuation.



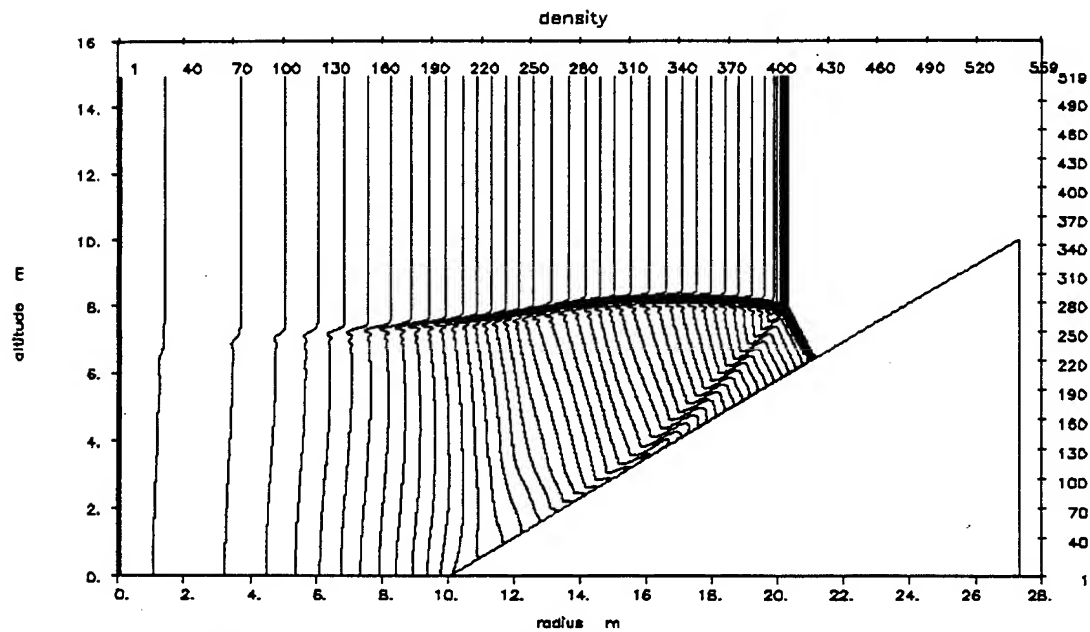
$Bl > 30d/z = 60d/pkop = 5.0bar/t+ = 1.e-2/body-f/he1/bl-30d-5bar-1.e-2/t2$ ; 02.09.95 H  
 Time 20.000 msec Cycle 1677. Problem 1.9000



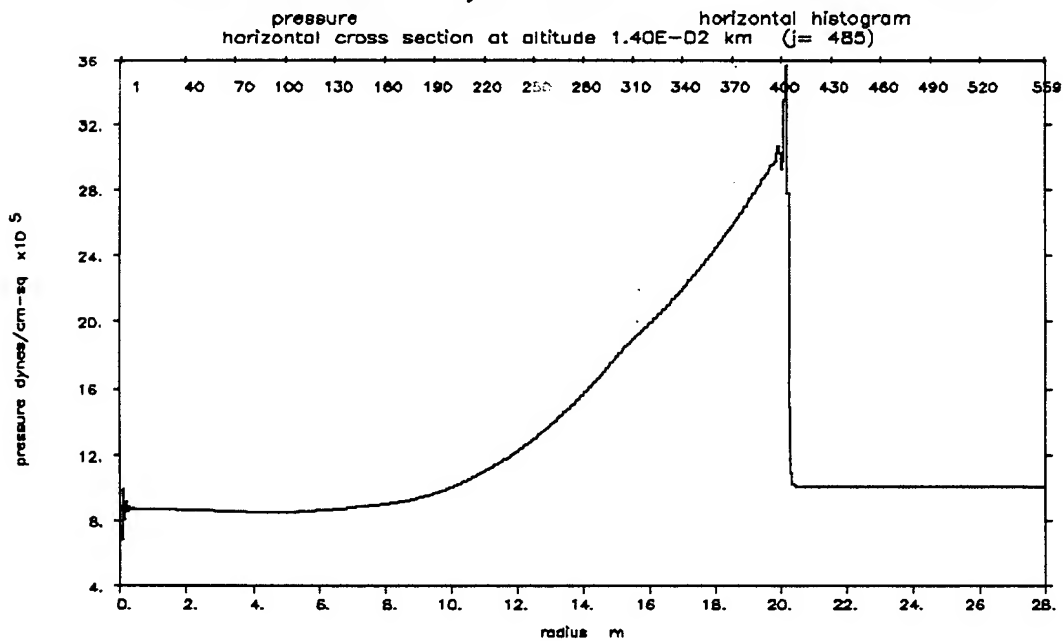
$Bl > 30d/z = 60d/pkop = 5.0bar/t+ = 1.e-2/body-f/he1/bl-30d-5bar-1.e-2/t2$ ; 02.09.95 H  
 Time 20.000 msec Cycle 1677. Problem 1.9000

Fig. 5a: Conditions of the process at 20 msec. The reflected shock starts fading out in the afterflow region of the blast wave.

Fig. 5b: Pressure horizontal histogram of the undisturbed blast wave at the height of  $j = 485$ . The blast wave length amounts to  $\lambda = 10$  m roughly.



BI>30d/z=60d/pkop=5.0bar/t+=1.e-2/body-f/he1/bi-30d-5bar-1.e-2/t2; 02.09.95 H  
Time 25.000 msec Cycle 2109. Problem 1.9000

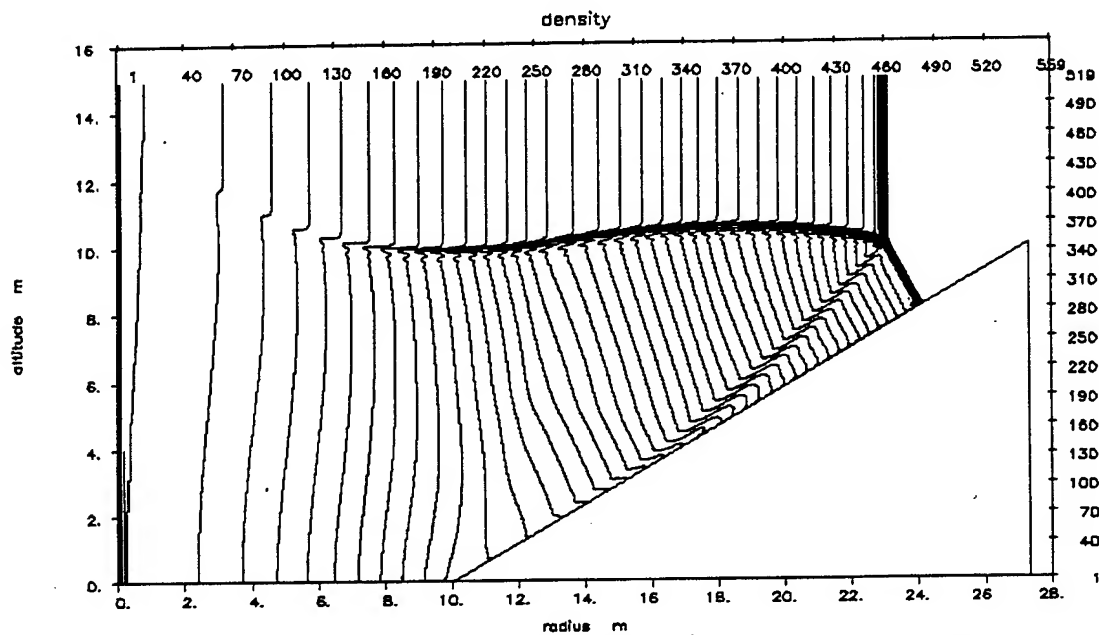


BI>30d/z=60d/pkop=5.0bar/t+=1.e-2/body-f/he1/bi-30d-5bar-1.e-2/t2; 02.09.95 H  
Time 25.000 msec Cycle 2109. Problem 1.9000

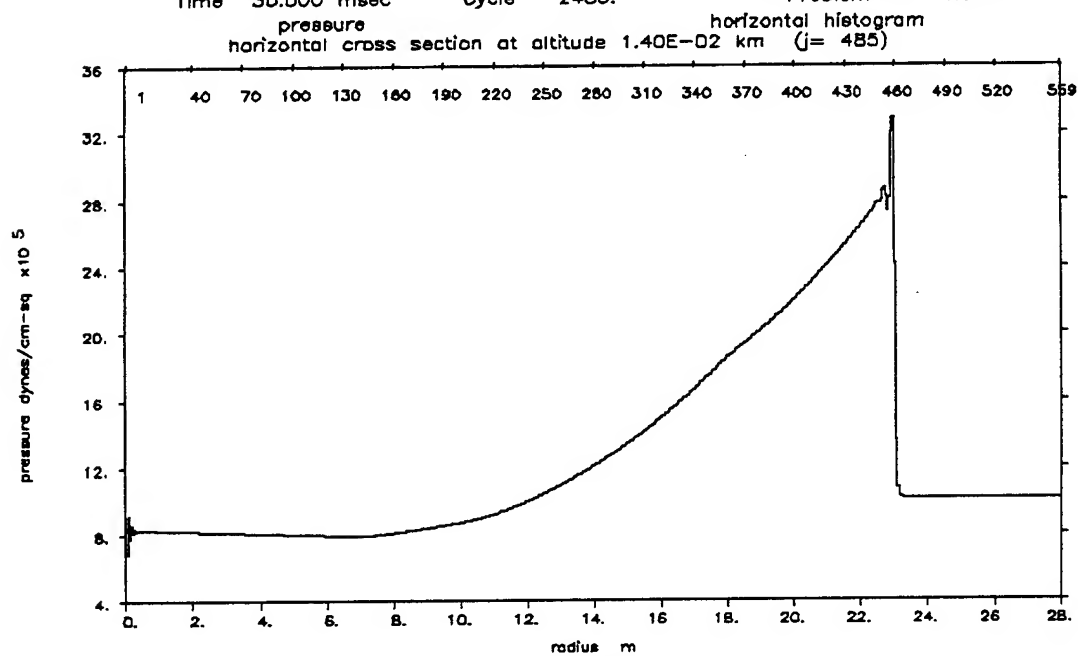
Fig. 6a: Conditions of the process at 25 msec. The reflected shock continues fading out and travels upwards in vertical direction.

Fig. 6b: Compare to Figs: 5b, 4b, 3b and note the decreasing front strength,  $\lambda = 10.5$  m roughly.





$Bl > 30d/z = 60d/pkop = 5.0bar/t + = 1.e-2/body-f/he1/bl-30d-5bar-1.e-2/t2$ ; 02.09.95 H  
 Time 30.000 msec Cycle 2485. Problem 1.9000



pressure horizontal histogram  
 horizontal cross section at altitude  $1.40E-02$  km ( $j = 485$ )  
 $Bl > 30d/z = 60d/pkop = 5.0bar/t + = 1.e-2/body-f/he1/bl-30d-5bar-1.e-2/t2$ ; 02.09.95 H  
 Time 30.000 msec Cycle 2485. Problem 1.9000

Fig. 7a: See legend of Fig. 6a. Time instant = 30 msec.

Fig. 7b: See legend of Figs. 6b, 5b, 4b, 3b;  $\lambda = 11$  m.

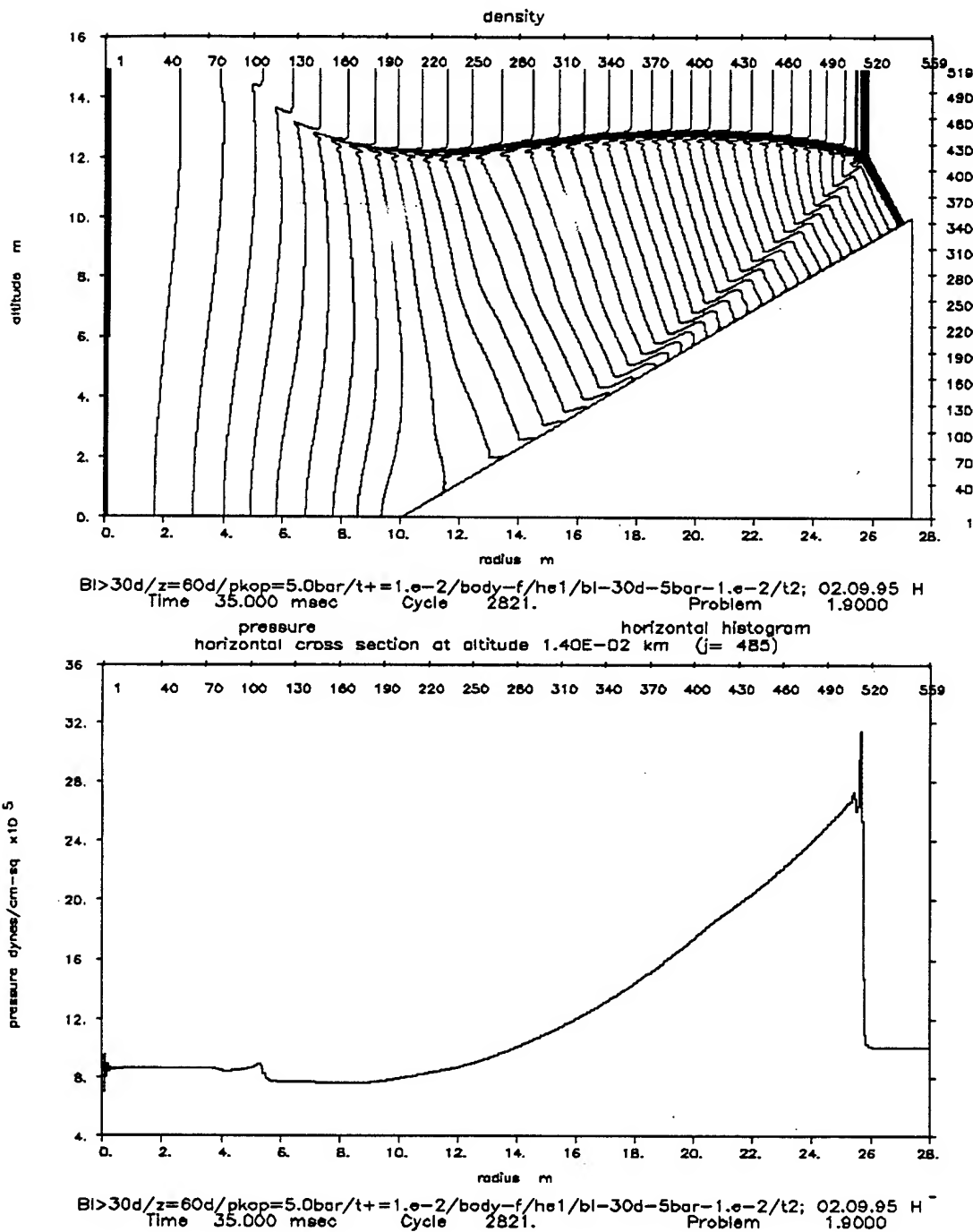
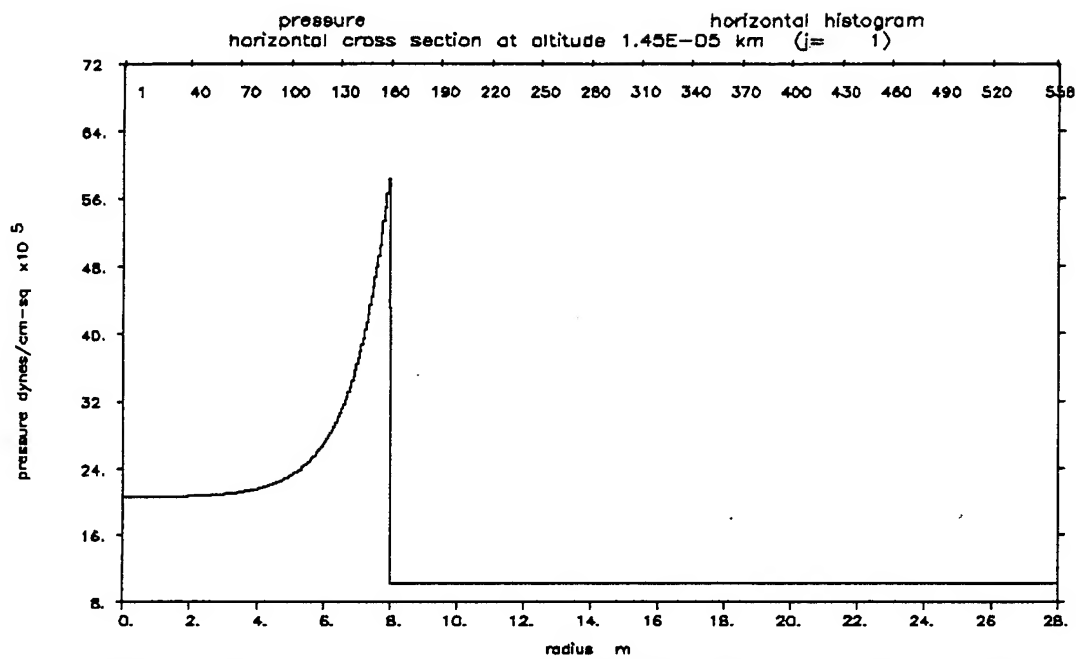
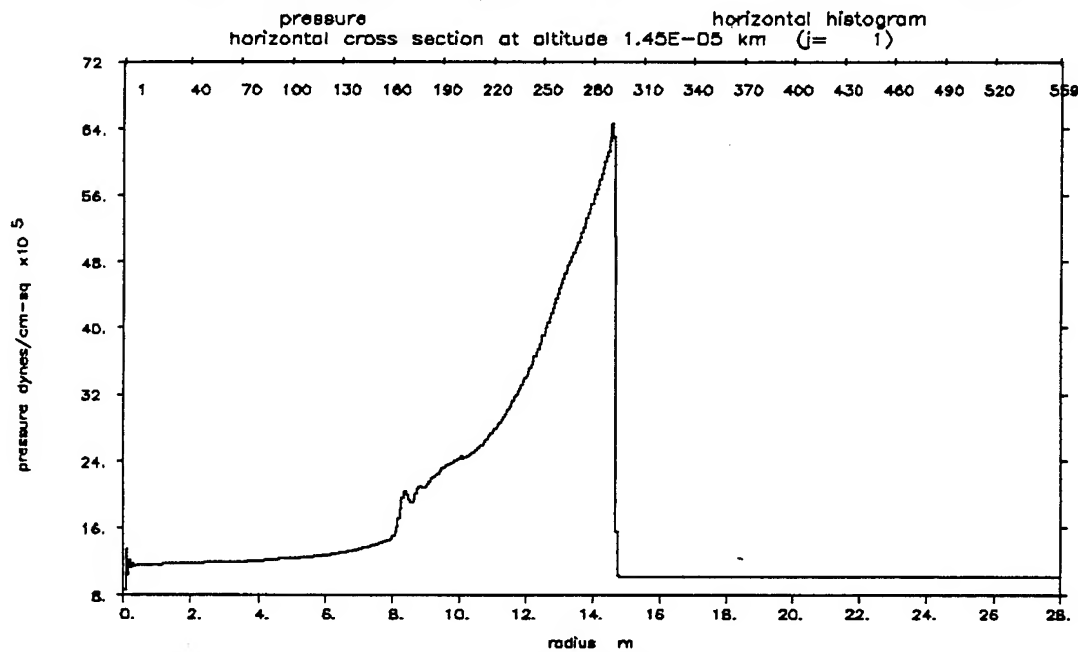


Fig. 8a: Conditions of the process at 35 msec. The reflected shock turns upwards in the vertical direction. The single Mach reflection pattern is well developed at the front of the blast wave together with a pronounced slip line.

Fig. 8b: Compare to legends of Figs. 7b, 6b, ... 3b.  $\lambda = 12$  m

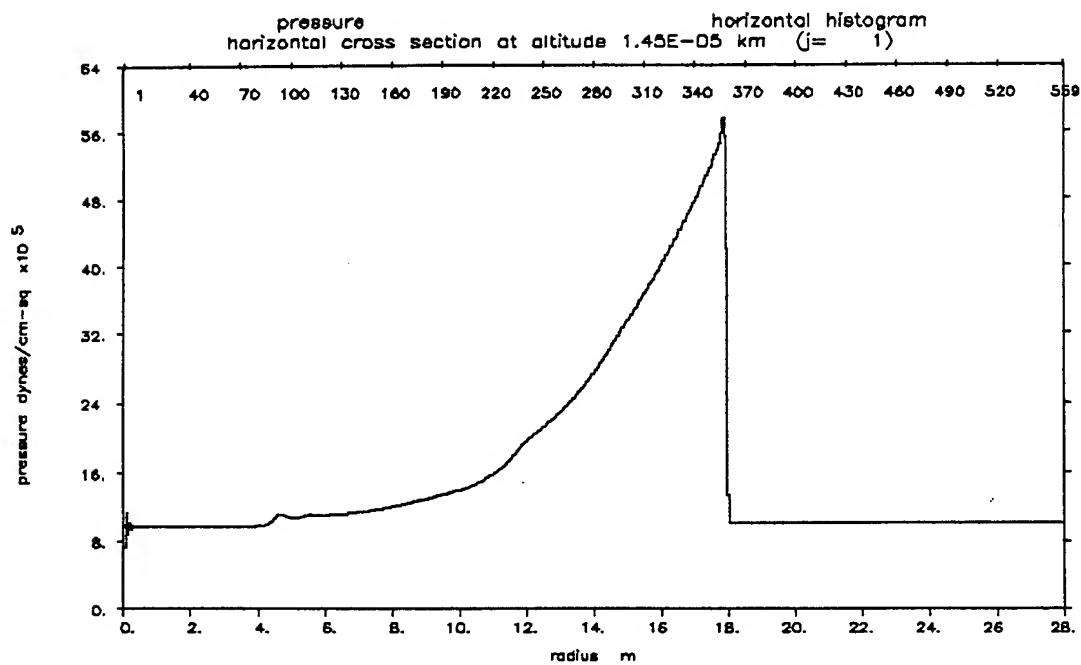


BI>30d/z=60d/pkop=5.0bar/t+=1.e-2/body-f/hel/bl-30d-5bar-1.e-2/t2; 02.09.95 H<sup>-</sup>  
Time 5.845 msec Cycle 0. Problem 1.9000

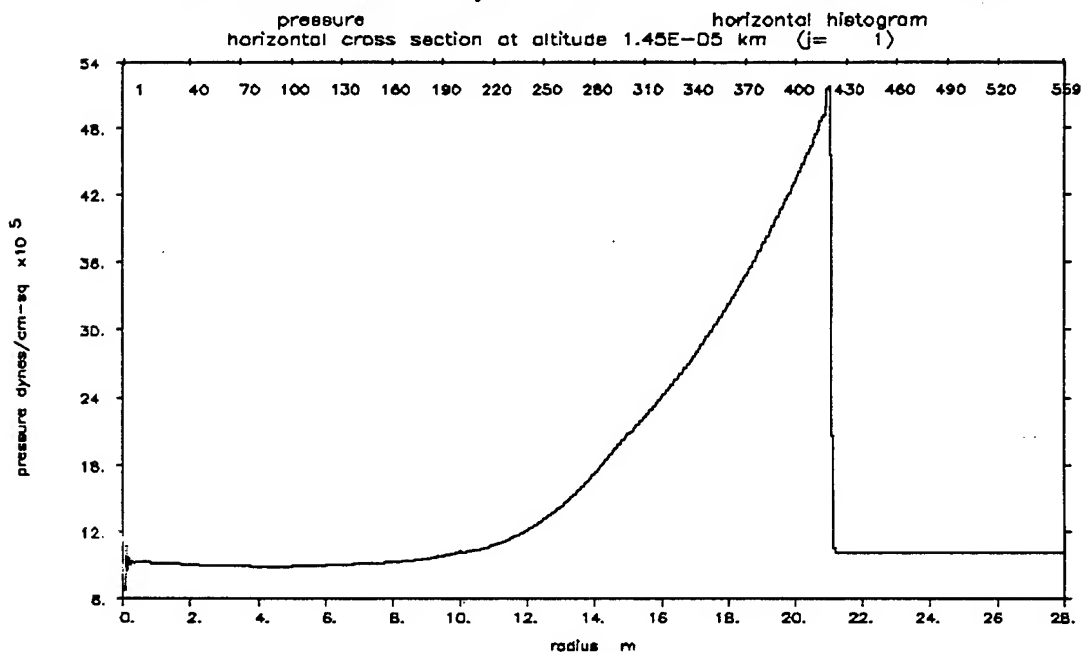


BI>30d/z=60d/pkop=5.0bar/t+=1.e-2/body-f/hel/bl-30d-5bar-1.e-2/t2; 02.09.95 H<sup>-</sup>  
Time 15.000 msec Cycle 1159. Problem 1.9000

Figs. 9a and 9b: Pressure histograms at  $j = 1$  along the wall of the tube and along the wall of the wedge at  $t = 5.845$  msec and  $t = 15$  msec resp.. The front amplitude at  $t = 15$  msec indicates the strength of the Mach shock.

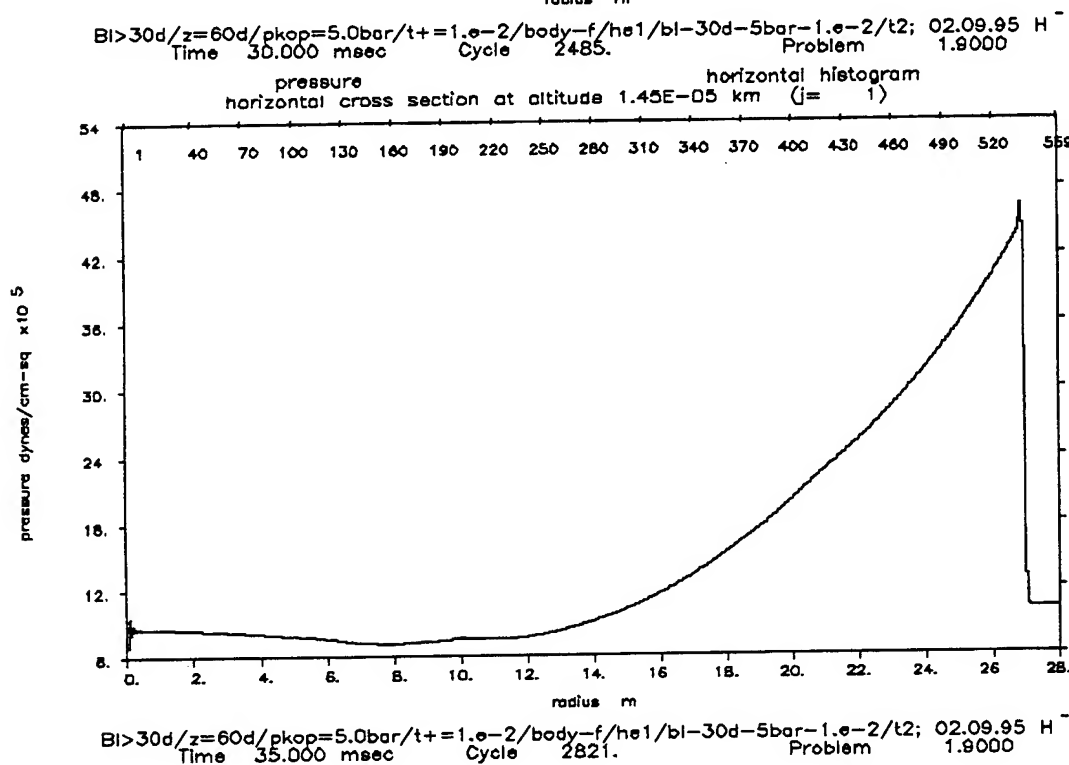
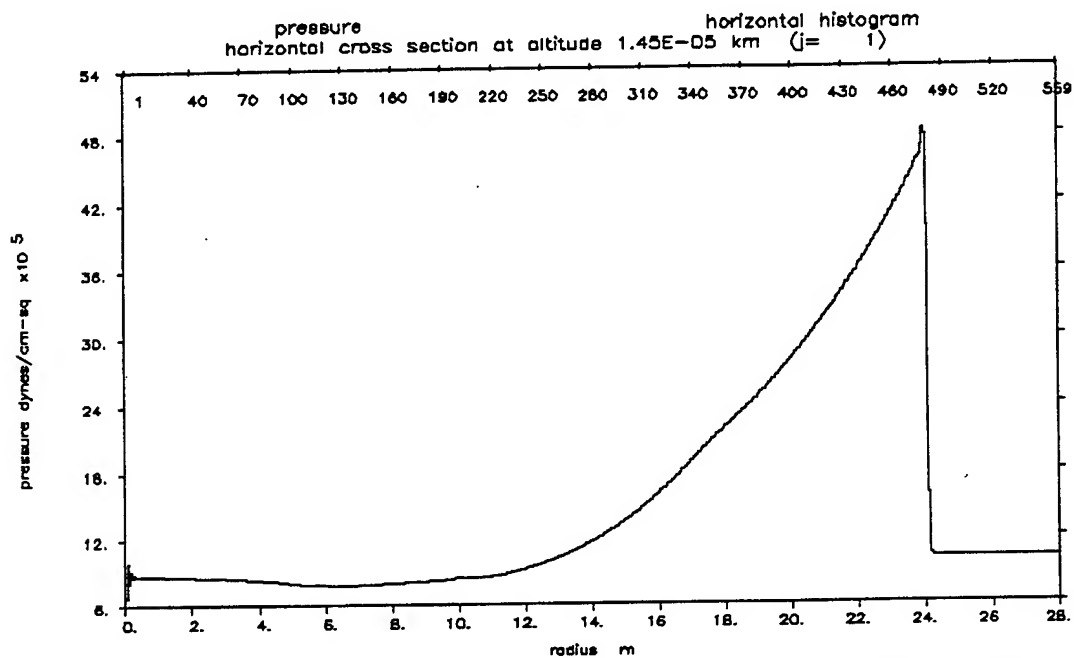


BI>30d/z=60d/pkop=5.0bar/t+=1.e-2/body-f/he1/bl-30d-5bar-1.e-2/t2; 02.09.95 H<sup>-</sup>  
Time 20.000 msec Cycle 1677. Problem 1.8000



BI>30d/z=60d/pkop=5.0bar/t+=1.e-2/body-f/he1/bl-30d-5bar-1.e-2/t2; 02.09.95 H<sup>-</sup>  
Time 25.000 msec Cycle 2109. Problem 1.8000

Figs. 10a and 10b: Pressure histograms at  $j=1$  at the times  $t=20$  msec and  $t=25$  msec. The front pressures are the strengths of the resp. Mach shocks.



Figs. 11a and 11b: See legends of Figs. 10a and 10b, but for time  $t = 30$  msec and  $t = 35$  msec.

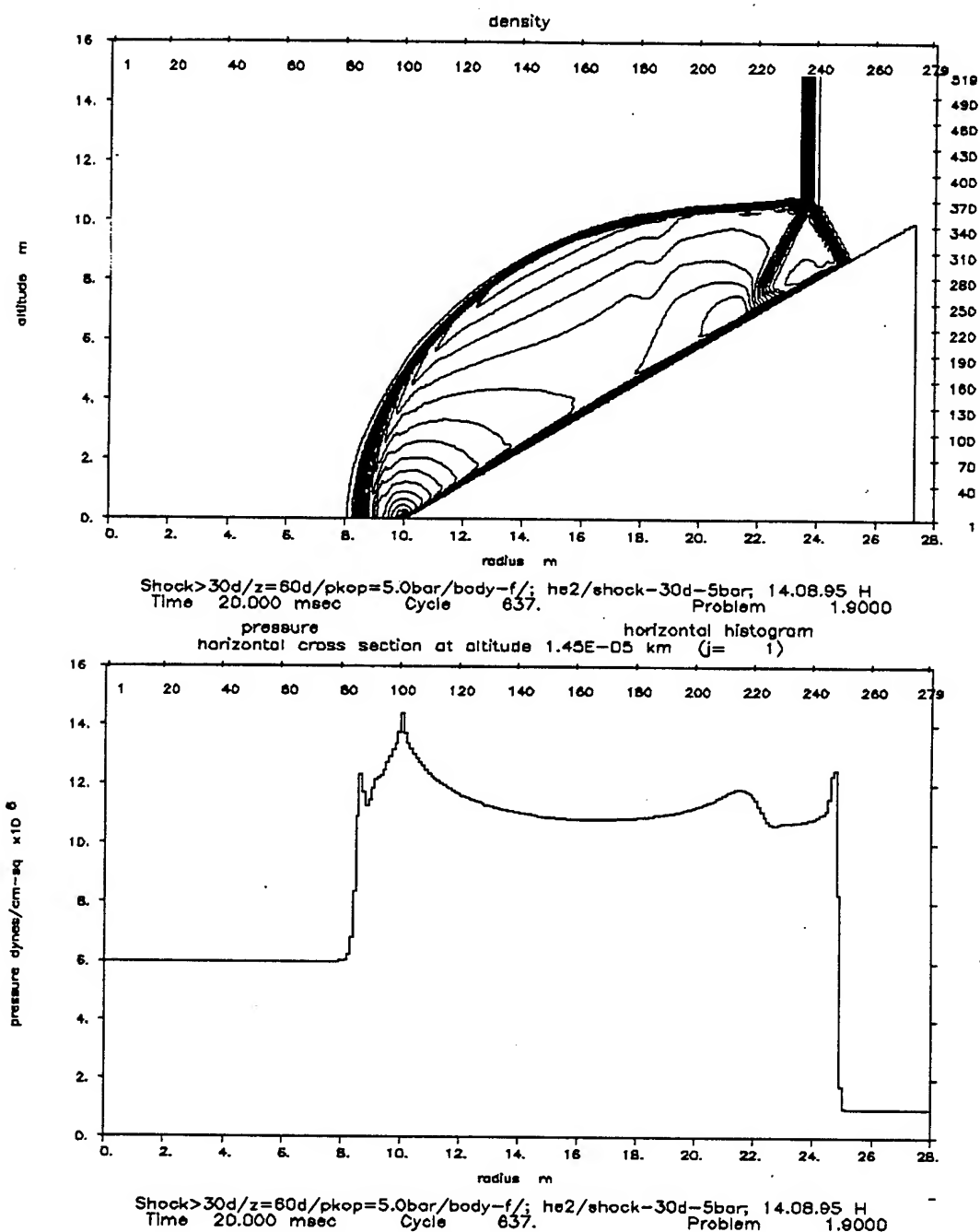


Fig. 12a: Reflection of a shock wave with  $p_{kop} = 5$  bar (amb. pressure 1 bar, i.e. shock Mach number  $Mo = 2.3$  and with uniform flow region behind the front) at the  $30^\circ$ -wedge. Time instant = 20 msec. Typical single Mach reflection appears.

Fig. 12b: Pressure histograms at  $j = 1$  along the bottom and along the wedge wall. Note the different pressure loading of the wall in comparison to Figs. 9b, 10a, ... 11b.

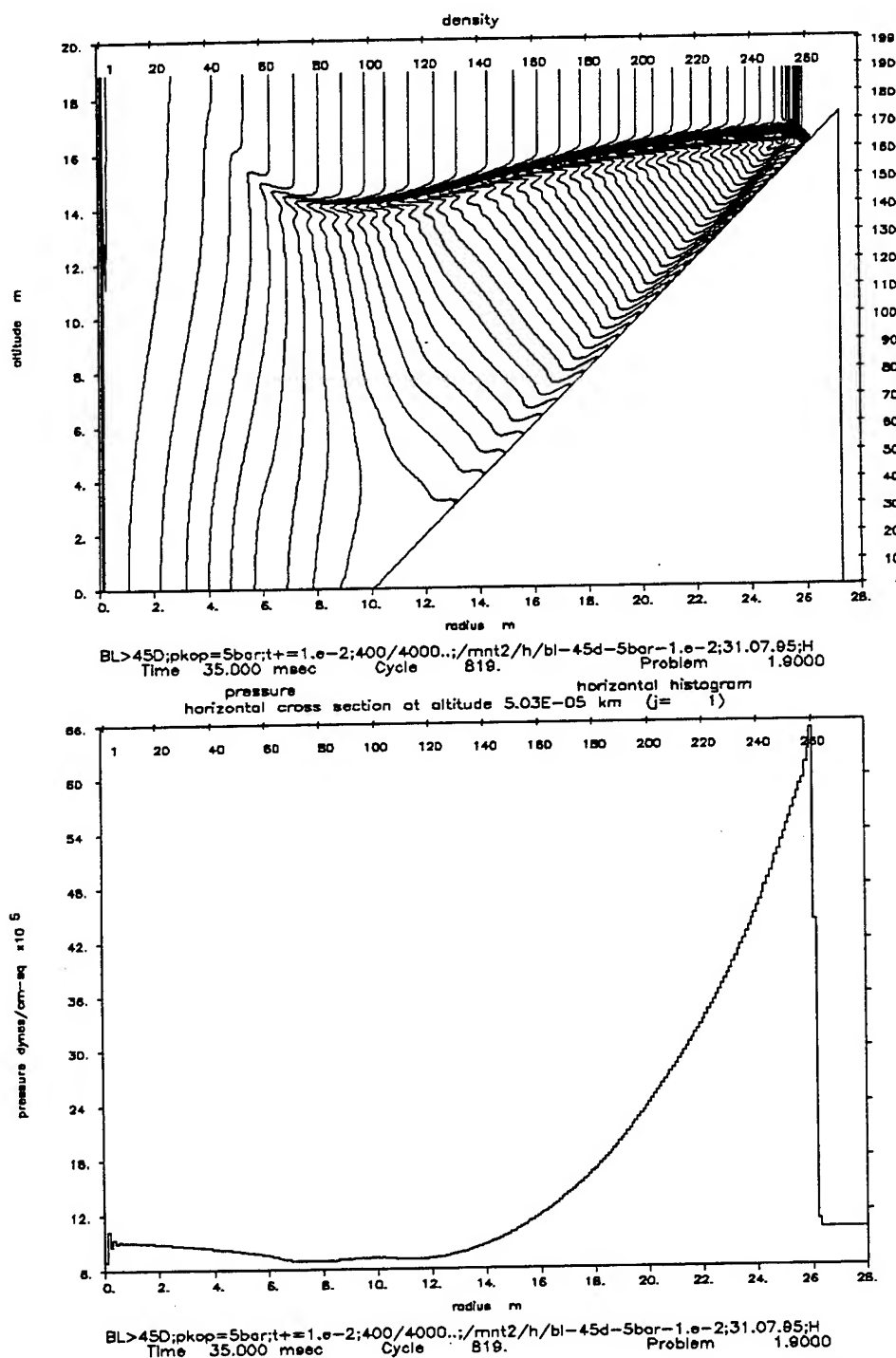


Fig. 13a: Isopycnics of the blast wave reflection at the 45°-wedge. Time instant = 35 msec. Single Mach reflection with faded out reflected shock.

Fig. 13b: Pressure histogram (j = 1) along the bottom and along the wedge wall.

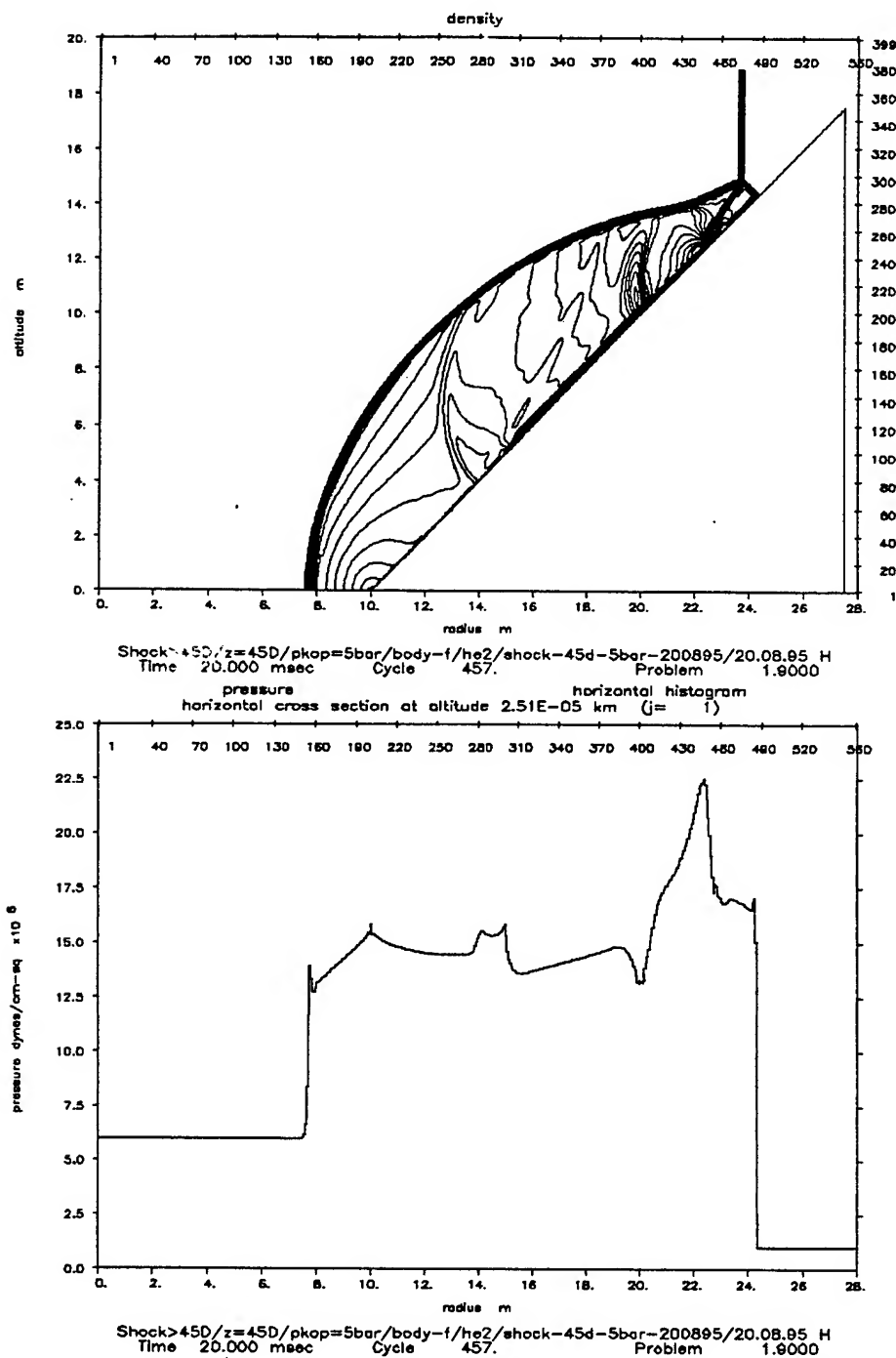


Fig. 14a: Reflection of the shock wave with  $p_{kop} = 5\text{bar}$  (see legend of Fig. 12a) at the  $45^\circ$ -wedge. Time instant = 20 msec.

Fig. 14b: Pressure histogram ( $j = 1$ ) along the bottom and the wedge wall to be compared to Fig. 13b.



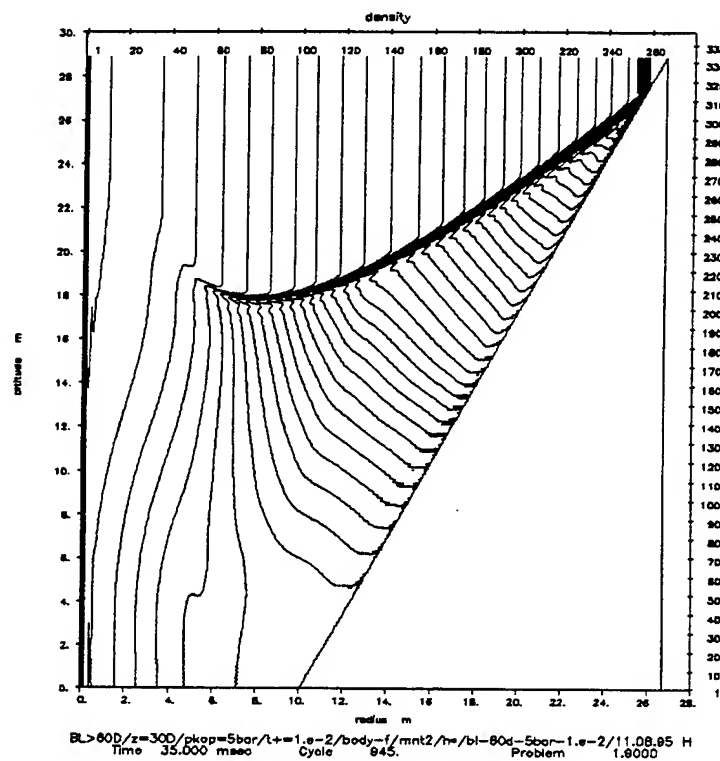


Fig. 15a: Isopycnics of the blast wave reflection at the 60°-wedge. Time instant = 35 msec. Regular reflection with a faded out reflected shock appears.

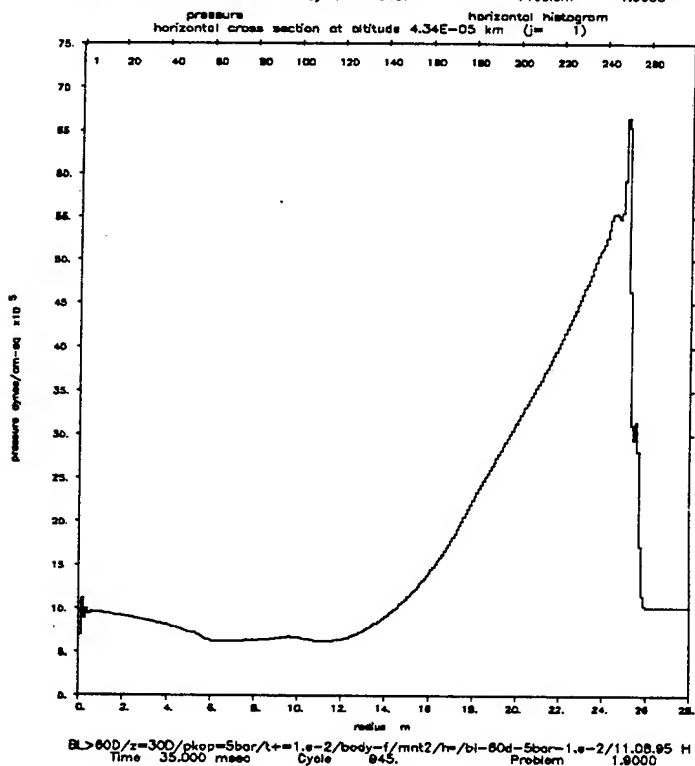


Fig. 15b: Pressure histogram ( $j = 1$ ) along the bottom and along the wedge wall at the same time.

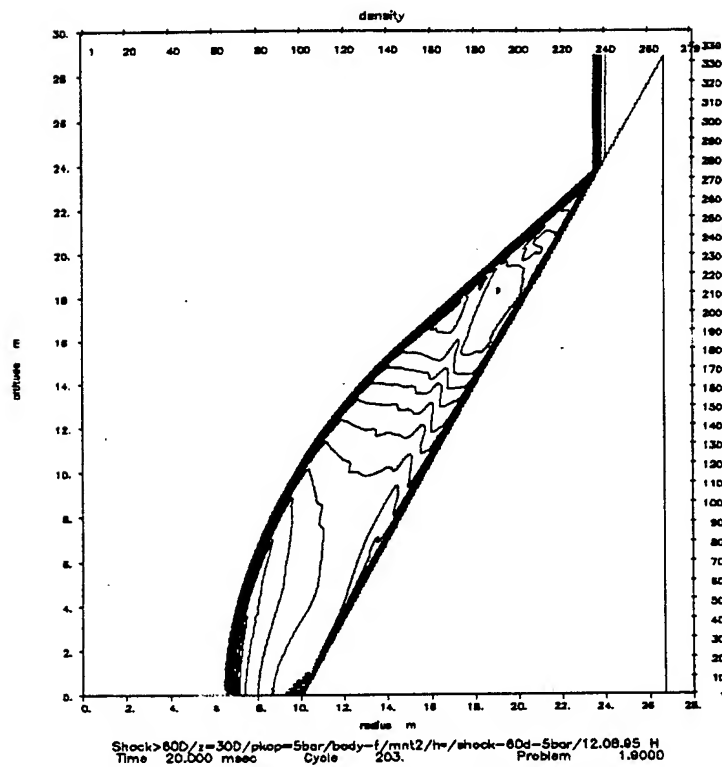


Fig. 16a: Reflection of the shock with  $p_{kop} = 5\text{bar}$  (see legend of Fig. 12a) at the  $60^\circ$ -wedge. Time instant 20 msec.

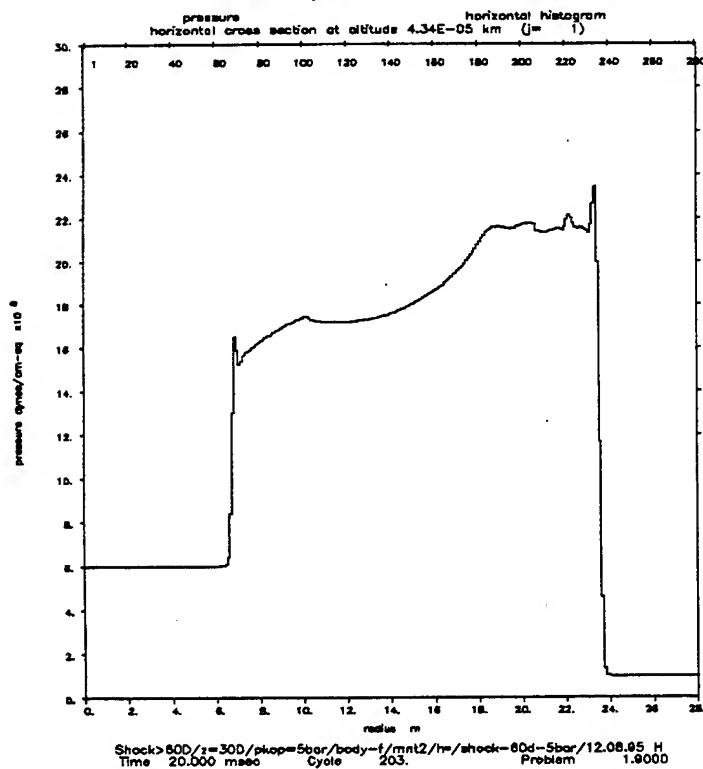


Fig. 16b: Pressure histogram ( $j = 1$ ) along bottom and wedge wall at the same time instant (to be compared to Fig. 15b).

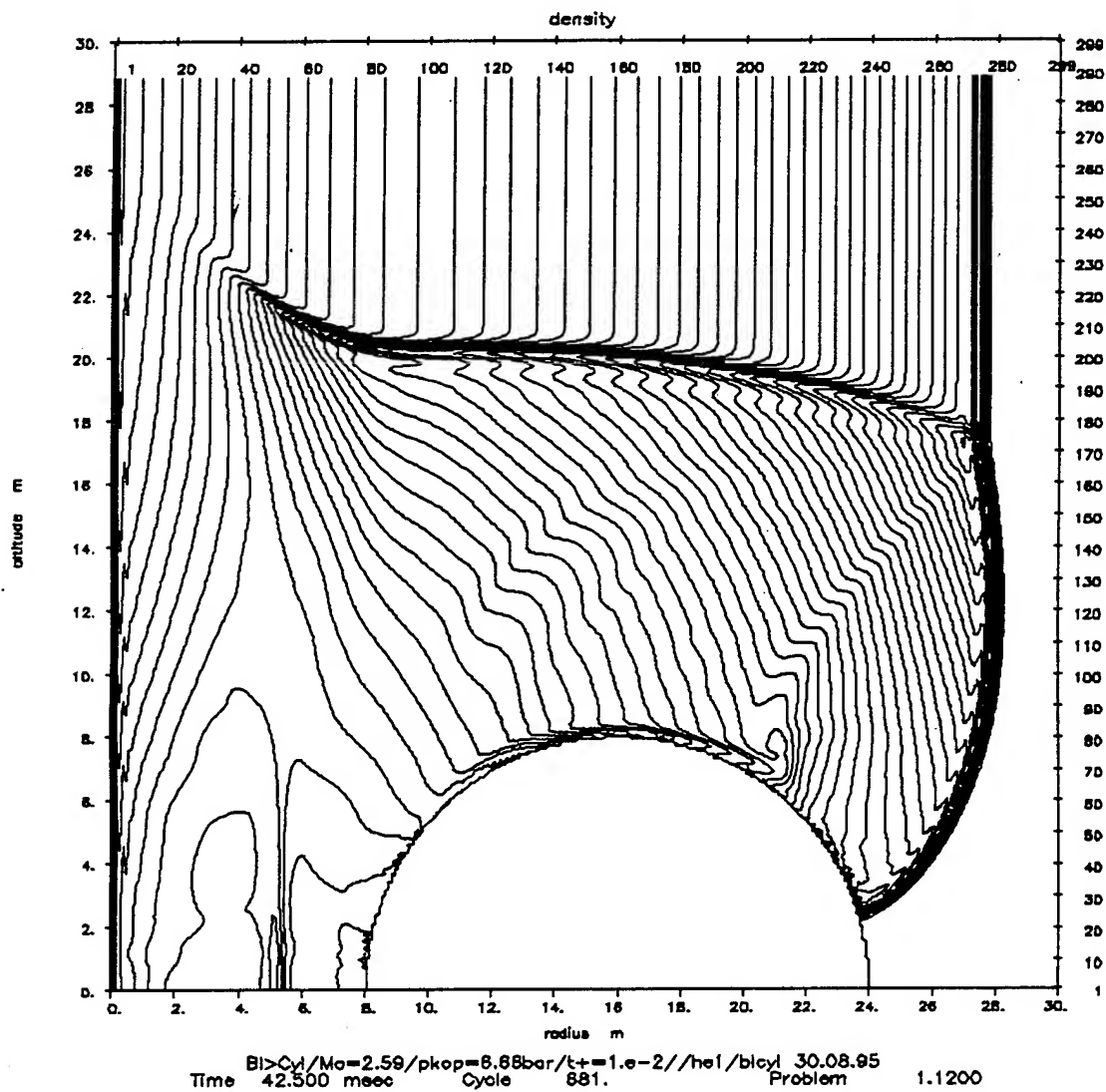


Fig. 17: Isopycnics of the reflection- and diffraction pattern of an incident blast wave with  $p_{kop} = 6.66$  bar and with a positive pressure time duration  $t^+ = 10$  msec at a cylinder (see Fig. 3a).

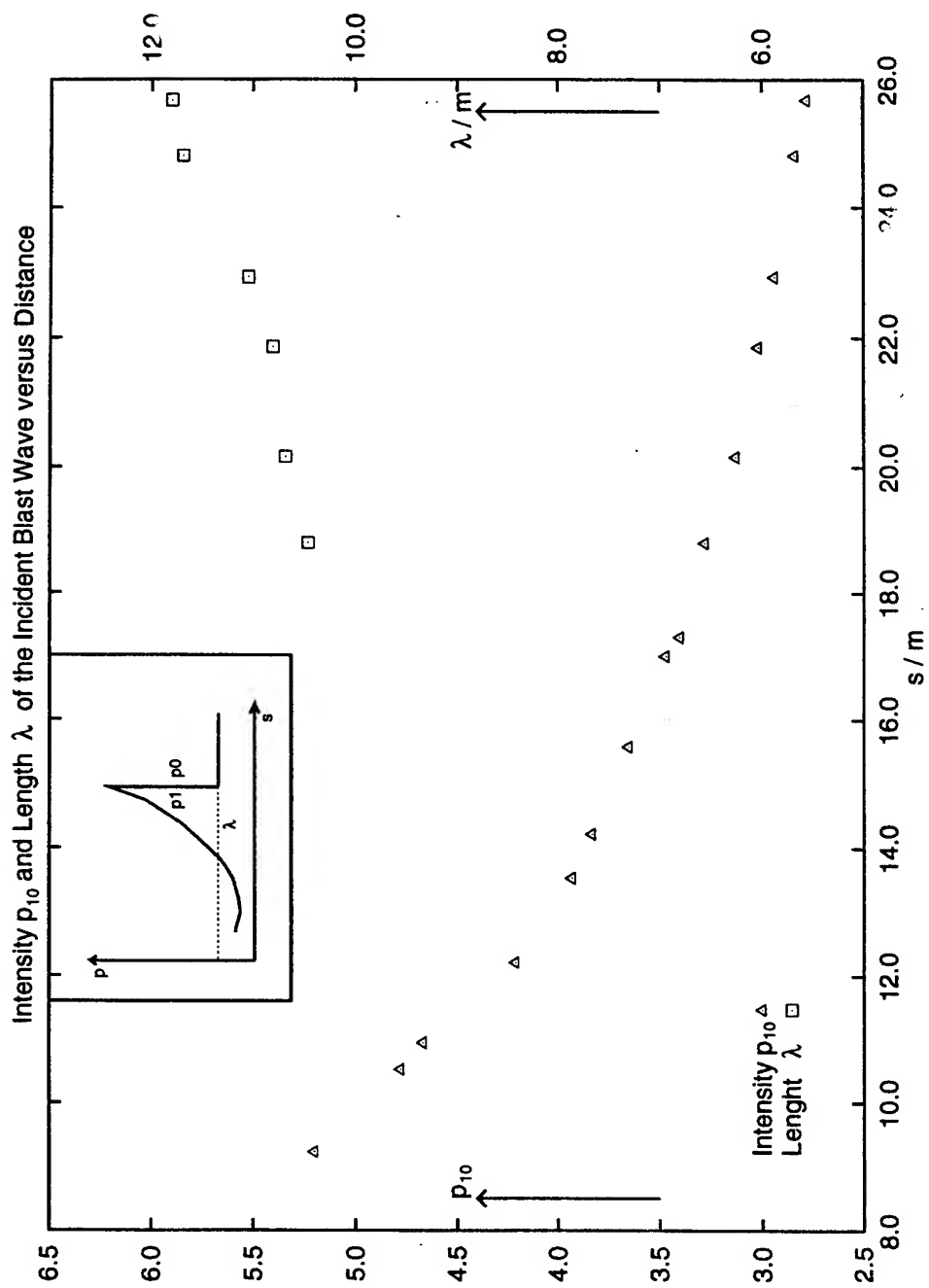


Fig. 18 (above): Attenuation of the front pressure of the blast wave (see Fig. 3a) along a distance of roughly 20 m. It starts at  $s = 8$  m. The wave length increases only slowly.

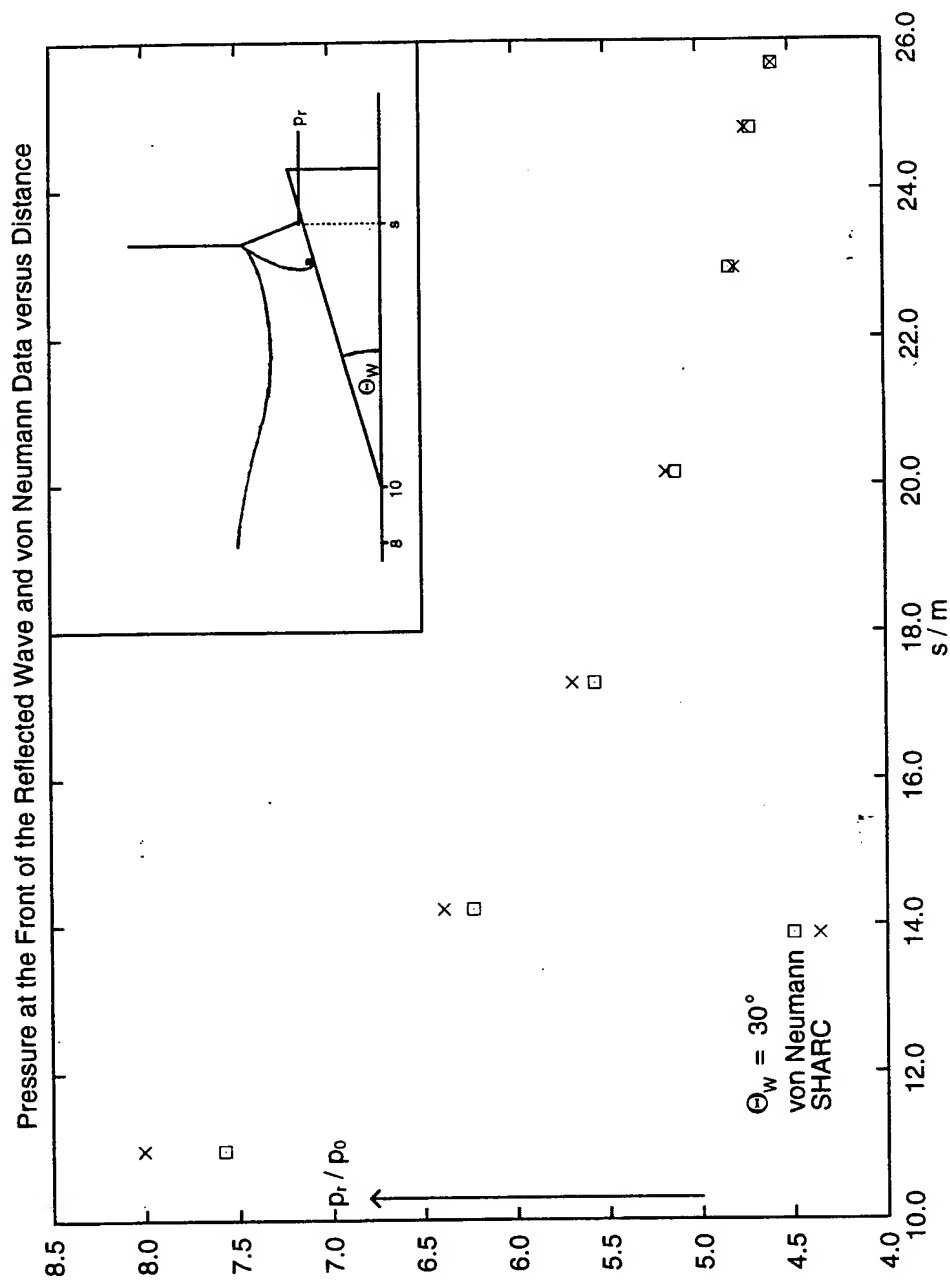


Fig. 19: Decay of the front reflected pressure (strength of the Mach shock) along the same distance for the 30°-wedge to be compared to the von Neumann data

# SOURCE CHARACTERISTICS OF ALUMINIZED EXPLOSIVES

Eric J. Rinehart, PhD  
Field Command, Defense Nuclear Agency  
Kirtland AFB, NM 87117

Susan M. Babcock, PhD  
Titan Research and Technology  
Kirtland AFB, NM 87117

## ABSTRACT

An effort is currently in progress to characterize TNT mixed with 20% aluminum. This paper will compare results from this effort to existing (both recent and older) data, pure TNT characteristic equation of state and free-air curves. This effort is aimed at identifying obvious differences (greater than 20% in total energy) between TNT and TNT with aluminum (tritonol). Differences between this effort and previous experiments will be presented. Four cases will be tested: unconfined spherical charges (TNT and aluminized TNT) at two charge sizes, and charges detonated in steel cylinders (TNT and aluminized TNT). Pressure histories obtained from the experiments will be compared. Early time detonation physics will be quantified by measurements of shock time-of-arrivals (detonation velocities) measured in the explosive. Finally, close-in, free air curves will be presented for both explosives.

## INTRODUCTION

During DNA's weapon effects studies of conventional weapon performance, the source model of a common high explosive filler, tritonol, has come into question. Tritonal is a mixture of trinitrotoluene (TNT) and aluminum power (80% to 20% ratio). It appears to be something other than an ideal explosive and may require a rate dependent or time dependent equation-of-state [1]. When the usual JWL [2] equation-of-state for ideal explosives is used, measured performance differs from calculations. Source data include parameters for aluminized explosives; however, they do not address specific parameters for tritonol. Existing tritonol data comes from [3] and [4] and consists of properties such as [3]:

PROPERTY	TNT	Tritonal
Casting Temperature	177°C	186°C
Impact Testing	unaffected	unaffected
Explosion Temperature	458°C	432°C
Det Vel (2"x2"x6")	22,475 ft/s	21,380 ft/s
Frag Vel (@ 20 ft)	14,370 ft/s	14,560 ft/s
Mechanical Properties	fracture toughness, Youngs modulus, etc.	

Some characterization work in understanding tritonal was undertaken in 1992 by [1], under contract to DNA. This work involved impulse measurement on small samples (a few grams) of tritonal detonated under water. This work provided an initial understanding of rate expansion of tritonal under some confinement and the resulting data was used in developing parameters for use in a modified "time dependent" JWL [1]. The resulting equation-of-state was used as a basis for predictions and analysis of data found in this paper. As a result of the questions surrounding time dependent source parameters, this work was initiated to provide improved data for modeling tritonal. The project was designed to obtain data from spherical, unconfined charges and to obtain data from tritonal and TNT contained in hardened steel cylinders with one open end and one closed end.

To establish a basis, both for explosive and experimental techniques, three 8 lb TNT spheres were fired in a natural atmosphere and one in an inert (nitrogen) atmosphere. Then, one 8 lb and one 500 lb tritonal, spherical charge were cast and fired in a natural atmosphere. Follow-up work will include an 8 lb tritonal charge fired in an inert, nitrogen atmosphere. (Firing the charge in a nitrogen atmosphere eliminates afterburning, thus allows estimation of the aluminum's impact in tritonal.) Following the unconfined charge work, TNT and tritonal were cast into hardened steel cylinders with one open end and one closed end.

Typical data obtained in this effort included detonation velocities, close-in time-of-arrival measurements, reflected pressure measurements and energy considerations (case expansion and fragment velocities). The data lead to development of free-air curves for tritonal and TNT, an understanding of delivered airblast from fragmented thick-walled cylinders and, through calculations, the applicability of the "time dependent" JWL suggested by [1].

First, the typical charges will be discussed. Then, free air curves measured for TNT and tritonal will be presented. The free-air curve for TNT will be compared to existing models. Next, the expansion rates and detonation velocities obtained in the steel cased charges will be shown and finally the airblast impulse from bare charges and cased charges will be presented.

## EXPLOSIVE CHARGES

TNT was melted and cast into molds and directly into the steel cylinders. To help assure that curing shrinkage and air voids were not a problem, pellets of cold TNT were added to the melt which was then allowed to cool. Densities achieved by the TNT were nominal, 1.6 g/cc.

The tritonal was manufactured by Energetic Materials Research and Technology Center at New Mexico Tech, Socorro, NM, in a manner that reduces the chance of introduction of air voids and shrinkage during cooling. This was again done by adding cold TNT pellets to the melt and then adding the aluminum powder. Air Force Document AP8394794A, dated April 1987 was used for the grain size standard. The melt was continuously mixed until the temperature was such that the explosive was "like cream of wheat" (near 78 to 79 degrees C). From X-ray analysis it has been shown that this procedure helps assure that the aluminum powder does not settle-out during final cooling. After final cooling all charges were X-rayed and no voids were noted larger than 2 to 3 mm in diameter. Nominal theoretical densities were achieved in the tritonal (1.7 g/cc).

### FREE AIR CURVE EXPERIMENTS

The free-air curve experiments for TNT were conducted by Applied Research Associates at Kirtland AFB, NM [5,6]. Basically, bare charges were hung under a steel superstructure and time-of-arrivals of the shock wave in air were measured within the charges and near the charges. Additionally, airblast measurements were made on a free surface for the tritonal charges. From the arrival times, shock velocity in air was measured and a known air equation-of-state [7] was used to determine the free air pressures.

The primary arrival times were measured in the free field by two ladders of TOA sensors located on the sides, but beneath the spheres. Since the test bed for the 8 lb charges was so small, care was taken to assure that the TOA gages could resolve time adequately. Corrections were made for the momentum of gage closures. Resultant shock velocities were validated with streak camera measurements.

The four TNT experiments are represented in Figure 1. FACs 1-3 were 8 lb TNT detonations in air and FAC 4 was an 8 lb TNT detonation in nitrogen. A regression polynomial was fit to the shock wave time-of-arrival data and was inverted to provide the shock wave velocity. An eighth degree polynomial fit was necessary to reduce the data error residuals to a minimum. Figure 1 is a comparison of the TNT data in a natural atmosphere and in nitrogen with the Kinney and Graham [8] TNT curve. (Comparisons of the Kinney and Graham curve with other standard curves were made and we felt that this representation of older data was the best to use.) For pressures greater than 3000 psi (20 MPa) and less than 30 psi (0.2 MPa) the resulting free air curves were affected by the fitting procedure and should not be used. For pressures between these limits, the data indicate a 25% to 50% reduction in peak pressures near a range of 2 ft scaled to 8 lb. We believe that this discrepancy is real and would like to better understand the differences.

The detonation velocity data obtained from the 8 lb and 500 lb tritonal, bare charges are shown in Figure 2. Figure 2 contains rate stick time-of-arrival measurements inside the charge. A final detonation velocity of 22,350 ft/s was measured in the tritonal. Both the 8 lb and 500 lb charges showed that this final detonation velocity was not reached until a range of 0.3 ft. The detonation velocity is somewhat higher than that previously measured for tritonal.



Time-of-arrival of the air shock wave from the tritonal charges was analyzed in a manner similar to the TNT charges. The final free air curve for peak pressures is shown in Figure 3. Data from the 8 lb charge compare well with those from the 500 lb charge. A direct comparison (no explosive energy differences accounted for) between the TNT curve and the tritonal data is also shown in Figure 3. Notice that the difference in apparent energy delivered varies as the pressure varies. Equivalency between the two types of explosives is range (pressure) dependent.

Beneath the unconfined 8 lb and 500 lb tritonal charges (HOB: 3.17 ft for the 8 lb and 12.6 ft for the 500 lb), air blast pressure gages (Kulite diaphragm and PCB crystal gages) were installed to measure reflected pressures. Good data were obtained and a comparison between the 8 lb and 500 lb charges is shown for one range in Figure 4. Figure 4 has impulse curves for the 500 lb shot at a test range of 13.2 ft, the 8 lb charge for 3.3 ft (scaled to 500 lb). (No reflected pressures were measured on the TNT tests. TNT has been calibrated and validated so that calculations are appropriate for the comparisons [9].) The arrival times for the 8 lb charge are early; however, the impulse delivered is near that of the 500 lb tritonal charge. The TNT charge has lower impulse.

Finite difference calculations of the tritonal were carried out to better understand the time-dependent JWL proposed by [1]. For the calculations an adaptive grid, second order code, MAZE [10] was used in two dimensions. The numerics of this code have been validated repeatedly and it was the equation-of-state that was investigated. Tritonal can be represented using the normal JWL [2] with the normally constant internal energy being allowed to increase due to aluminum burning. From the usual JWL:

$$p = A \left( 1 - \frac{\omega}{R_1 v} \right) e^{-R_1 v} + B \left( 1 - \frac{\omega}{R_1 v} \right) e^{-R_2 v} + \frac{\omega E}{v}$$

at each time step internal energy is subtracted due to expansive work but added from the combustion of the aluminum powder by

$$\begin{aligned}\Delta\lambda &= a(1-\lambda)^{1/2} p^{1/6} \Delta t \\ \lambda &= \lambda + \Delta\lambda \\ \Delta e &= -p\Delta v + \Delta\lambda Q_0 \\ E &= E + \Delta e\end{aligned}$$

where  $\lambda$  is the mass fraction of the aluminum powder added,  $Q_0$  is the heat of combustion of the aluminum,  $a$  is a material constant empirically derived,  $v$  is the specific volume and  $p$  is the pressure. For the calculation, the constants used were:

A	4.8084
B	0.05748
$R_1$	4.7
$R_2$	1.0

$\omega$	0.32
$\rho_0$	1.72
$E_0$	0.0587 Mbar-cc/cc, (815 cal/g)
$Q_0$	0.0800 Mbar-cc/cc, (1111 cal/g)
$a_0$	0.00325

These constants were developed by [1].

Figure 5 shows three ranges from which reflected pressure data was recorded for the 8 lb and 500 lb tritonal charge with the calculated results. The calculations show good agreement with the data and no further adjustments appear necessary.

This completes the charge characterization data for the bare TNT and bare tritonal experiments. The two types of explosives react differently. The modified JWL has been shown to model tritonal accurately for bare charges.

### CASED CHARGES

To quantify and understand how tritonal reacts when cased, two steel cylinders were manufactured and filled with tritonal. In addition and for comparison, one cylinder was filled and tested with a pure TNT fill.

Detonation and case expansion of the cylinders were measured in a manner similar to that mentioned above for the bare charges. During expansion, the steel cases become fragmented and approximately 60% of the energy produced in the explosion is transferred to mechanical work in the fragments (fracture of the case and momentum of the fragment). An objective of this experiment was to measure the work left as airblast impulse. [11 & 12] contain details of the experiments. Basically, a 8x12 ft, 1 ft thick concrete slab was placed 12 ft beneath the cylinder. The total impulse delivered from the cylinder was measured using the resulting velocity of the slab. This impulse acting on the slab contained both fragment momentum and air blast impulse. Airblast pressure gages were embedded in the slab to measure the pressure histories and airblast impulse from the cylinder. By subtracting the two, the ratio of the two could be determined.

The steel cylinders were manufactured from 4340 steel heat treated to MIL-H-6875, class A specifications. This resulted in a Rockwell hardness of 38 to 44. One tritonal test was half the size of the larger tests. The half scale test had a steel wall thickness of 0.1875 ft and had an outer diameter of 0.604 ft. The two larger scale tests had TNT and tritonal fills. The cylinders were ignited at one end; the other end was sealed.

On the outside of the steel, time-of-arrival crystals were mounted to measure the detonation velocity of the explosive. The TNT cased charge had a detonation velocity of 22,160 ft/sec, near the velocity expected. Figure 6 compares the detonation velocities between the large tritonal and smaller scale tritonal test. The detonation velocity of 22,123 ft/sec was measured for the large test, but only two TOA measurements survived. The smaller charge gave a detonation velocity of 21,809 ft/sec, near that of the full scale. Based upon this data, there does

not appear to be much difference in the detonation velocity between confined TNT and tritonal. This suggests that the aluminum powder does not react at detonation, but later in time as suggested in the model. Note that the steel confinement of the tritonal allowed the explosive to attain maximum detonation velocity before the 0.3 ft observed in the bare charge experiment earlier described.

Both charge types were instrumented to measure steel case expansion for future modeling activities. Figure 7 compares all of the available data from the experiments. The TNT case appeared to expand earlier than that of the tritonal; the final velocity of the case, just at charge break out, was 4,200 ft/sec. The tritonal case ended up with a final expansion velocity of 4,166 ft/sec. This suggests that the aluminum begins reacting at early time in cased charges.

Figure 8 is a plan view of the concrete slab used to differentiate between the air blast impulse and the total impulse. The airblast measured was not of the usual outstanding quality; however, impulses were measured and averaged. Figure 9 compares the impulse delivered from the tritonal and TNT filled steel cylinders. TNT had approximately 70% of the tritonal impulse. Analysis of the experiment indicated that the airblast accounted for approximately 40% of the total delivered impulse.

These experiments should be of help to the source modelers. Expansion rates of tritonal filled steel cylinders were measured. Air blast at a specific range was also measured along with the explosive parameters.

## CONCLUSIONS

1. Experimental data is available for TNT and tritonal bare charges. The data suggest that the established free air curves for TNT might over predict peak pressures in the 800 psi range. Comparison of the free air curves for TNT and tritonal suggest a variable energy equivalence between the two explosives.
2. Data from steel case charges is available for modeling activities. The data suggest that involvement of the tritonal aluminum powder does not begin until after the detonation.
3. The proposed rate dependent equation-of-state developed by [1] can model the bare tritonal charge well.
4. Continued work is being done to calculate the cased charges. In addition, a bare tritonal charge will be fired in a nitrogen atmosphere to account for afterburning effects.

## REFERENCES

1. Guirguis, R. H. and P. J. Miller, (1993). *Time-Dependent Equations of State for Aluminized Underwater Explosions*, in the 10th Detonation Symposium, Boston.
2. *LLNL Handbook of Explosives*, UCRL-52997, (1981).

3. Slape, R. J. and J. A. Crutchner and G. T. West, (1974). *Some Sensitivity and Performance Characteristics of the Explosives H-6 and Tritonal*, AD-B013563, Air Force Armament Laboratory, Eglin AFB, Florida.
4. Costain, T. S. and R. V. Motto, (1973). *The Sensitivity, Performance and Material Properties of Some High Explosive Formulations*, AD915795, Picatinny Arsenal, Dover, New Jersey.
5. Babcock, S. M., (1994). *Free Air Curves Experiments: Instrumentation Validation and Preliminary Tests- FAC#1 through FAC #3*, Applied Research and Associates, Inc, Kirtland AFB, NM.
6. Babcock, S. M., (1994). *Free Air Curves Experiments: TNT in a Nitrogen Atmosphere*, Applied Research and Associates, Inc, Kirtland AFB, NM.
7. Zeldovich, Y. B., P. Raizer and R. Yu, (1966). *Physics of Shock Waves and High Temperature Hydrodynamics Phenomena, Vol I and II*, Ed. W. D. Hayes and R. F. Probstein, Academic Press, NY & London.
8. Kinney G. F. and K. J. Graham, (1985). *Explosive Shocks in Air*, Springer-Verlag, Berlin, Heidelberg, NY and Tokyo.
9. G. Ullrich, (1995). Personnel Communications, Defense Nuclear Agency, Wash. D.C.
10. Schlamp, R. J., (1994). *MAZ Users Manual*, Titan Research and Technology, Chatsworth, CA.
11. Seusy, F. E., (1994). *CWE Blast/Fragmentation Phenomenology Tests*, Letter Report, DNA Test Operations Technology and Test Support Contract No. DNA001-93-C-0147, Kirtland AFB, NM.
12. Babcock, S. M., (1995). Report in Progress, DNA Test Operations Technology and Test Support Contract No. DNA001-93-C-0147, Kirtland AFB, NM.

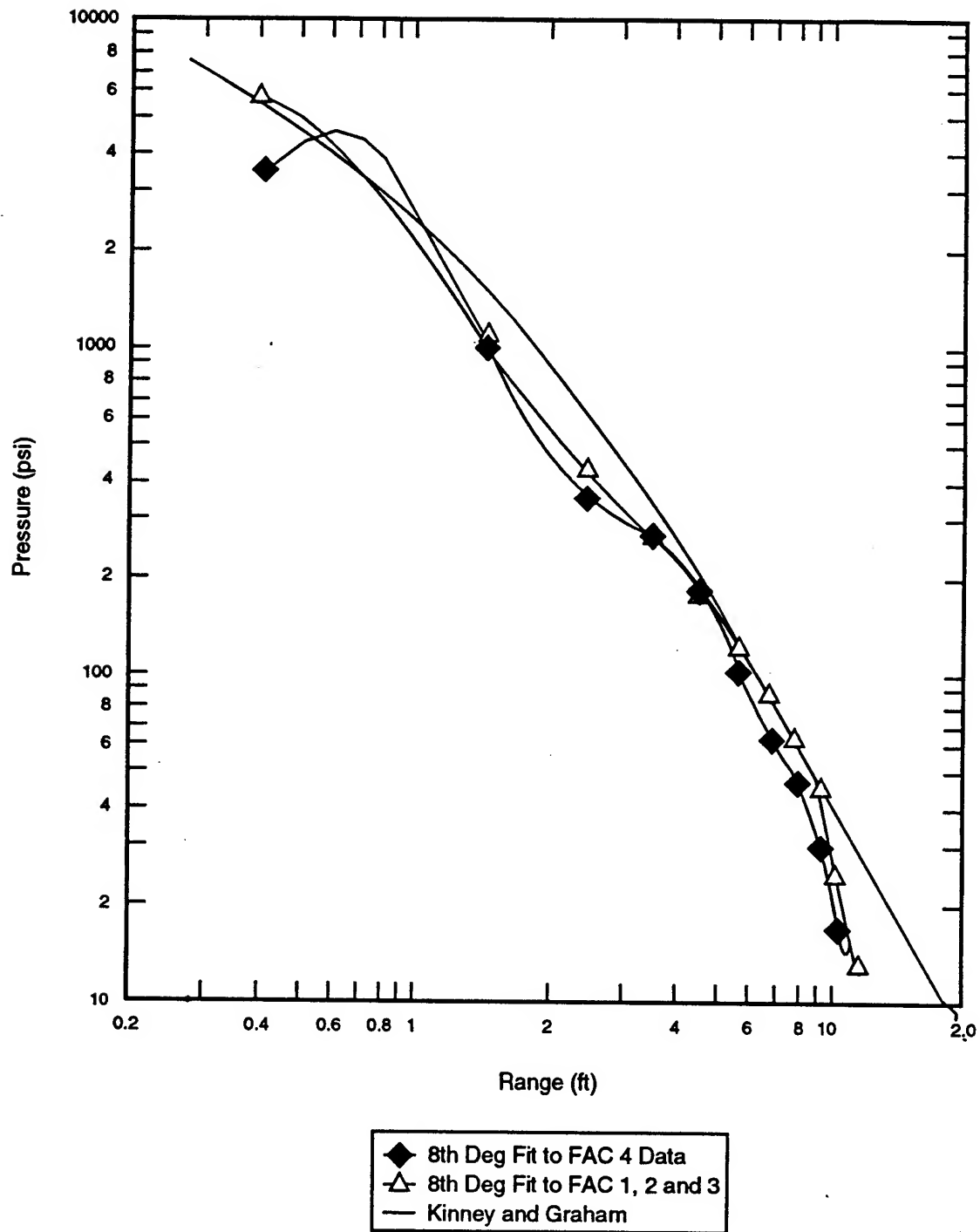


Figure 1. Eighth-degree polynomial Fits for FACs 1 - 4 compared to Kinney and Graham (1985).

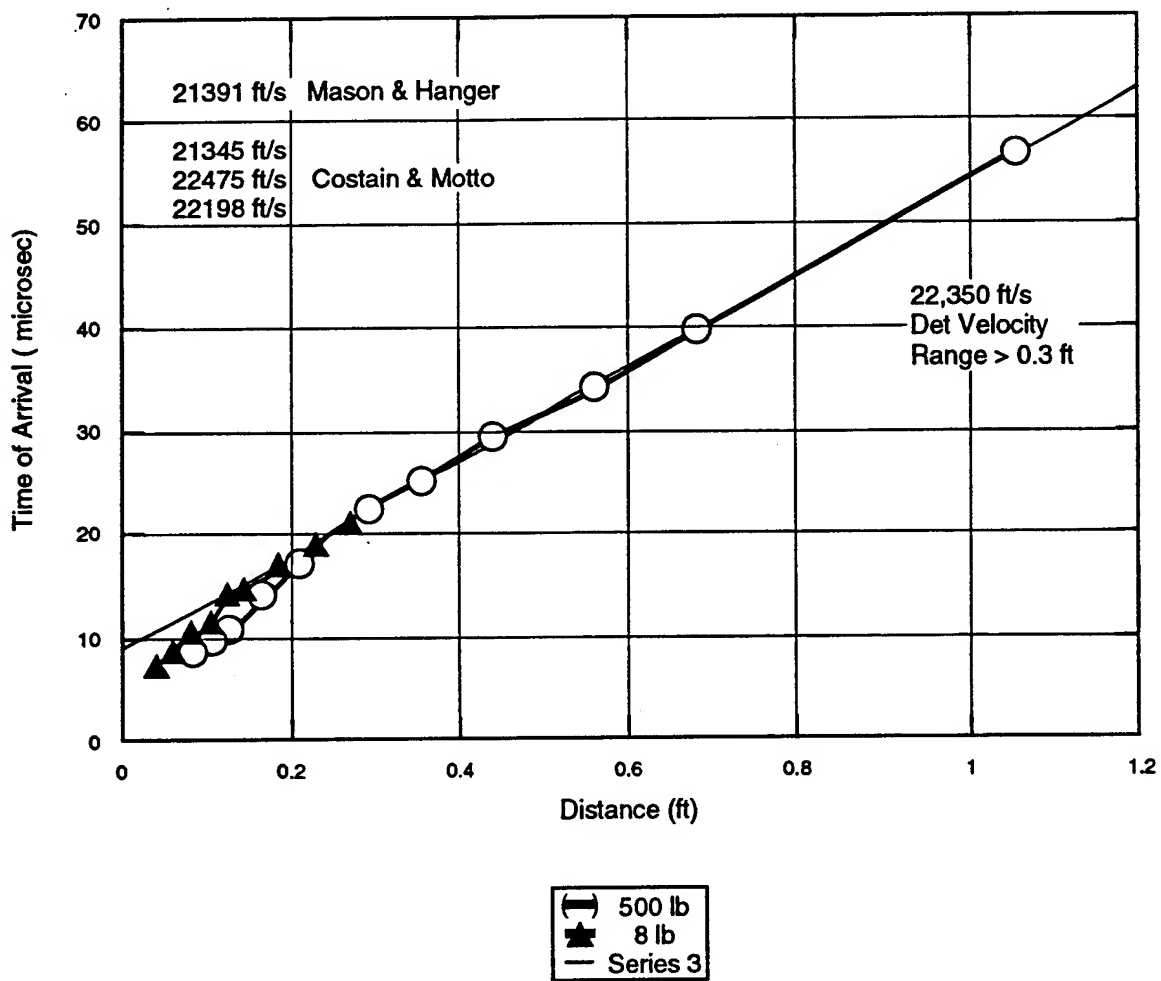


Figure 2. Tritonal detonation velocity, rate stick inside charge.

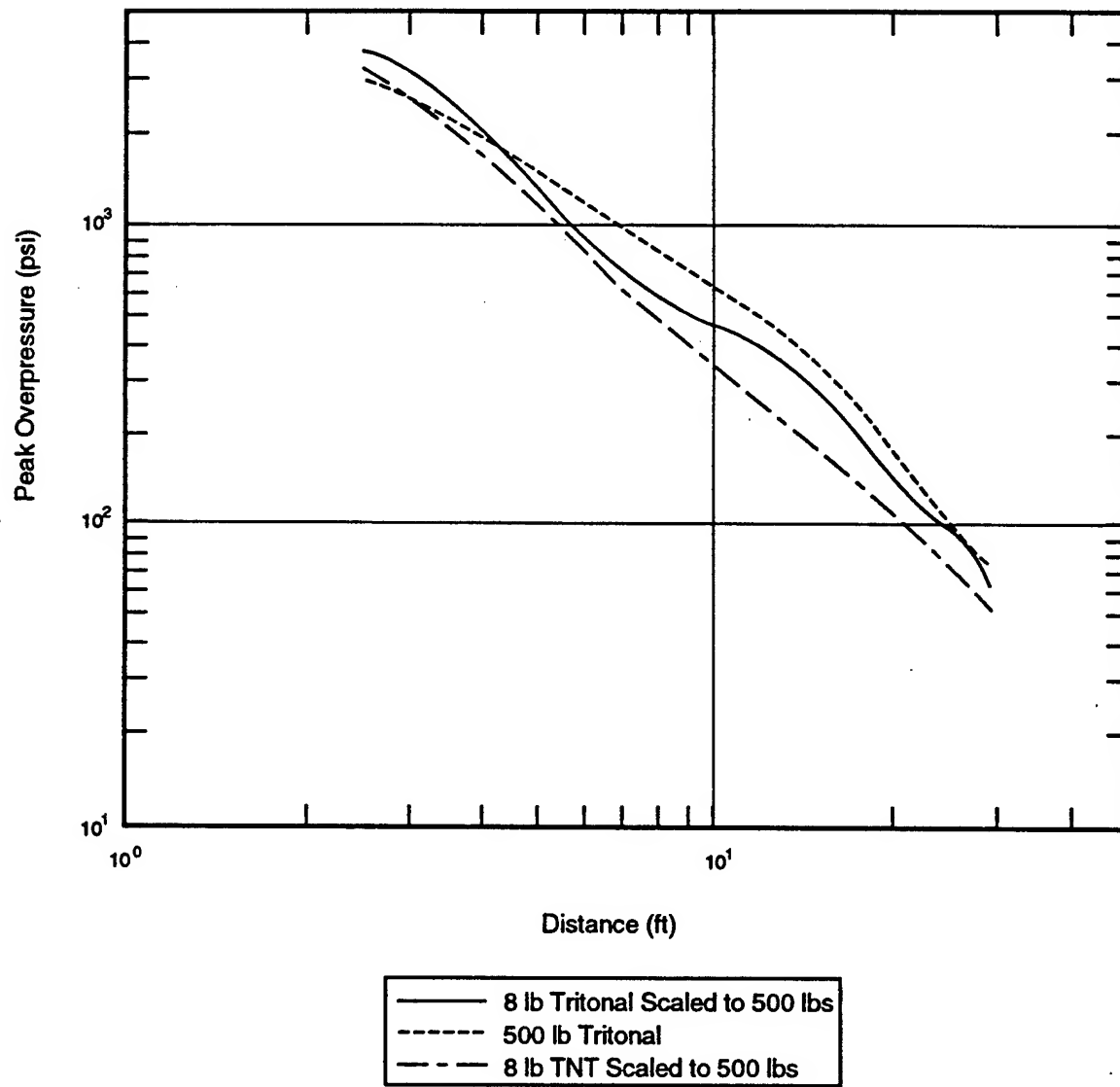


Figure 3. Tritonal and TNT free-air curves.

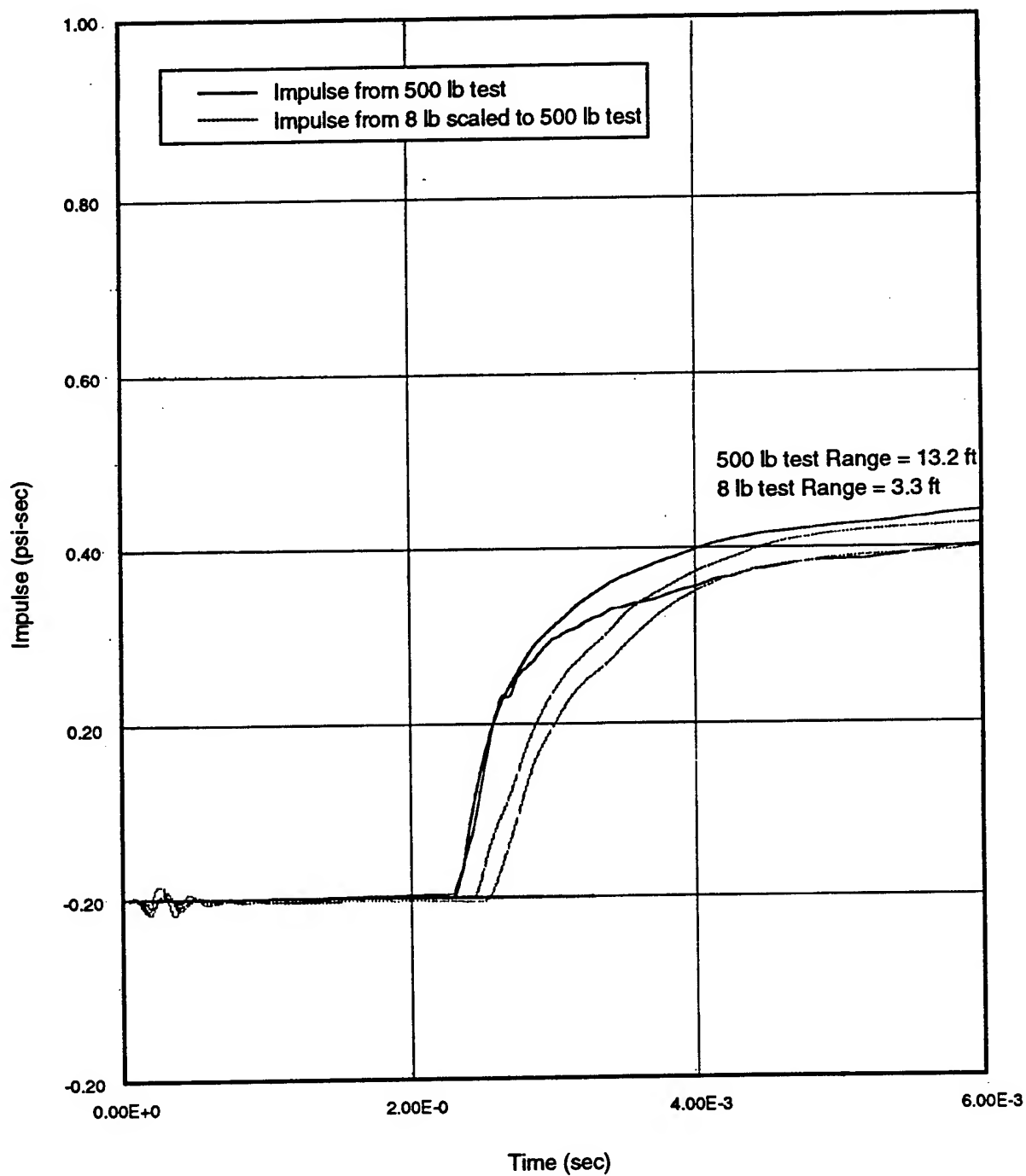


Figure 4. Free-air impulse curves for Tritonal.



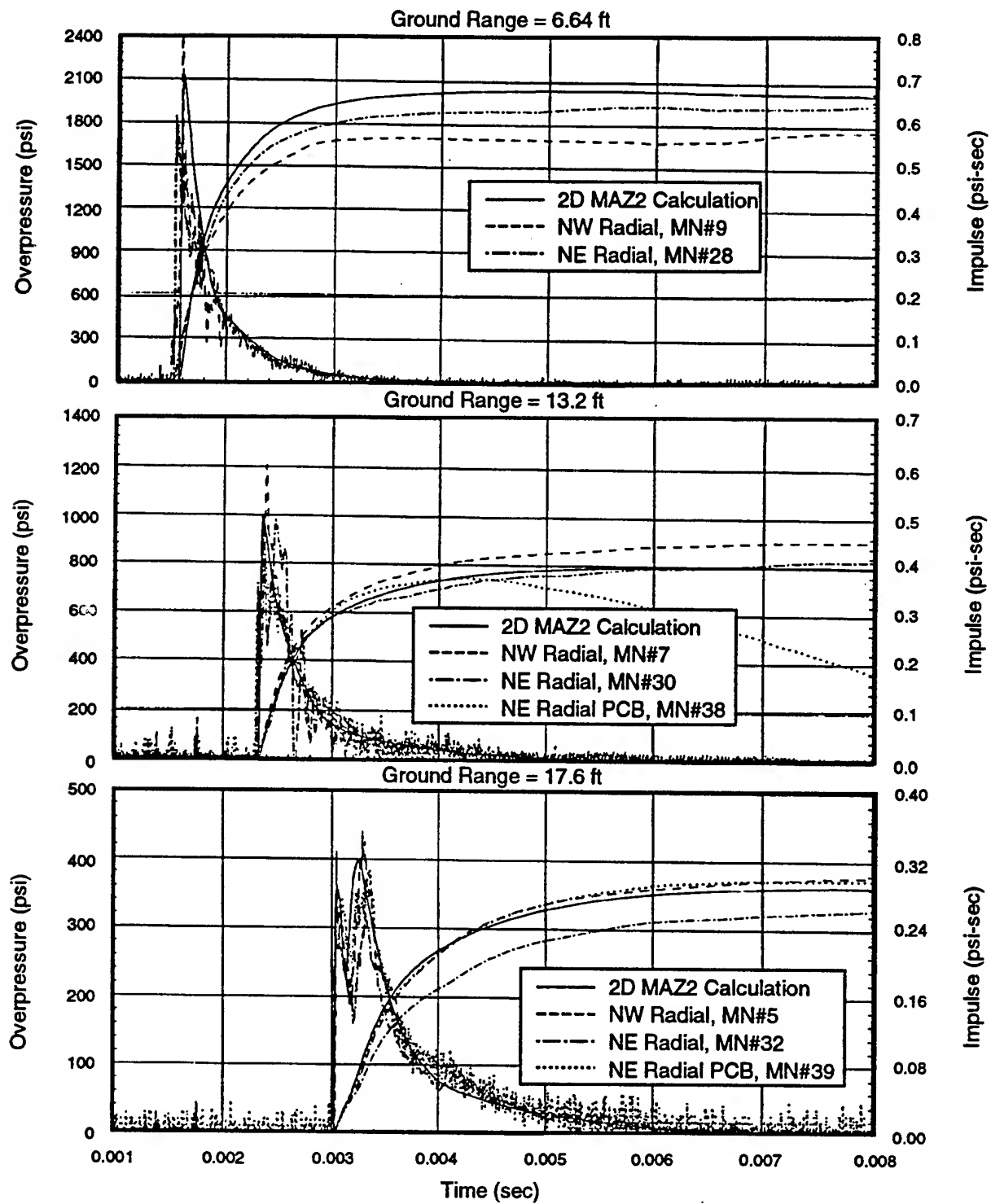


Figure 5. Comparison of calculations with data, Tritonal 500 U bomb

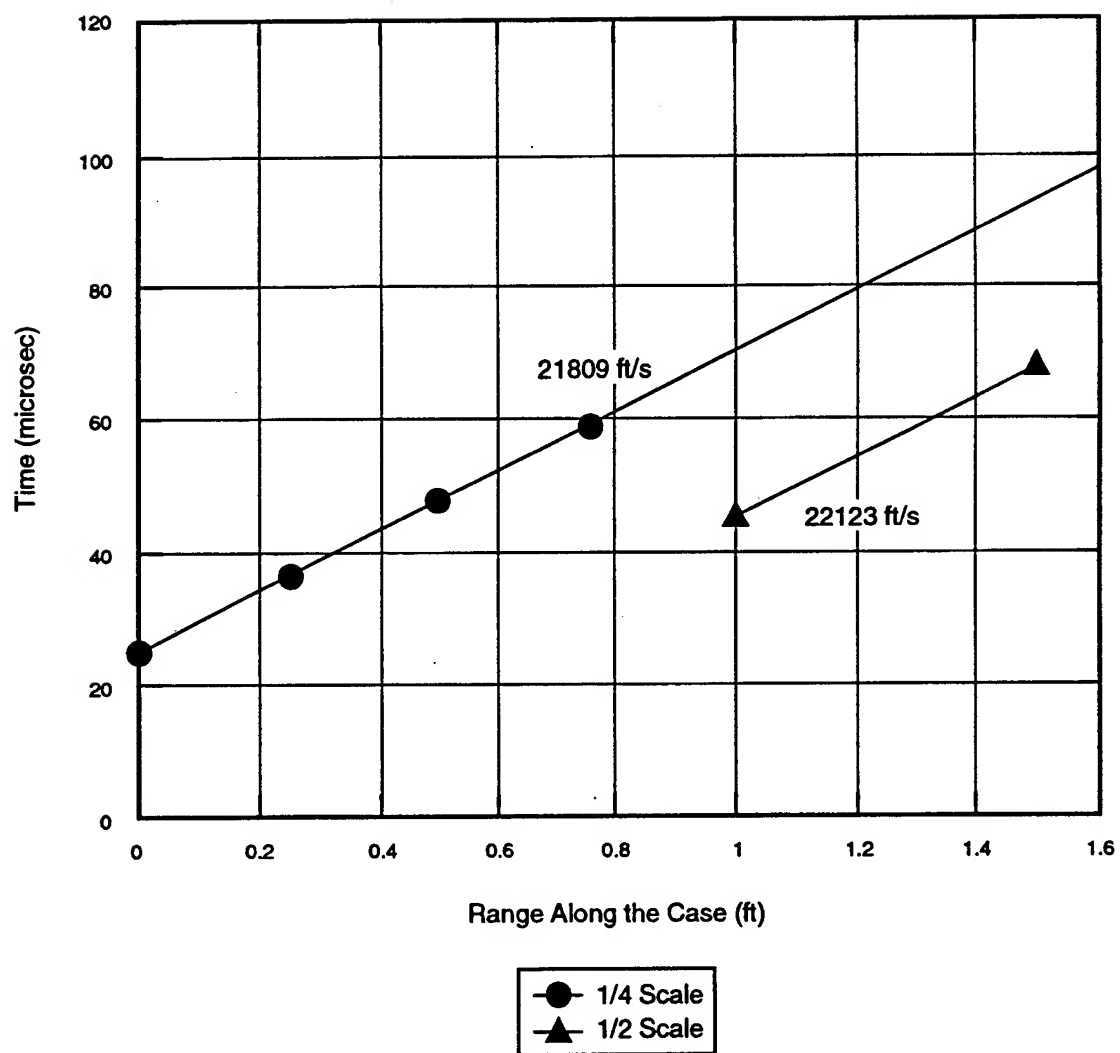


Figure 6. Measured detonation velocity along bomb case.

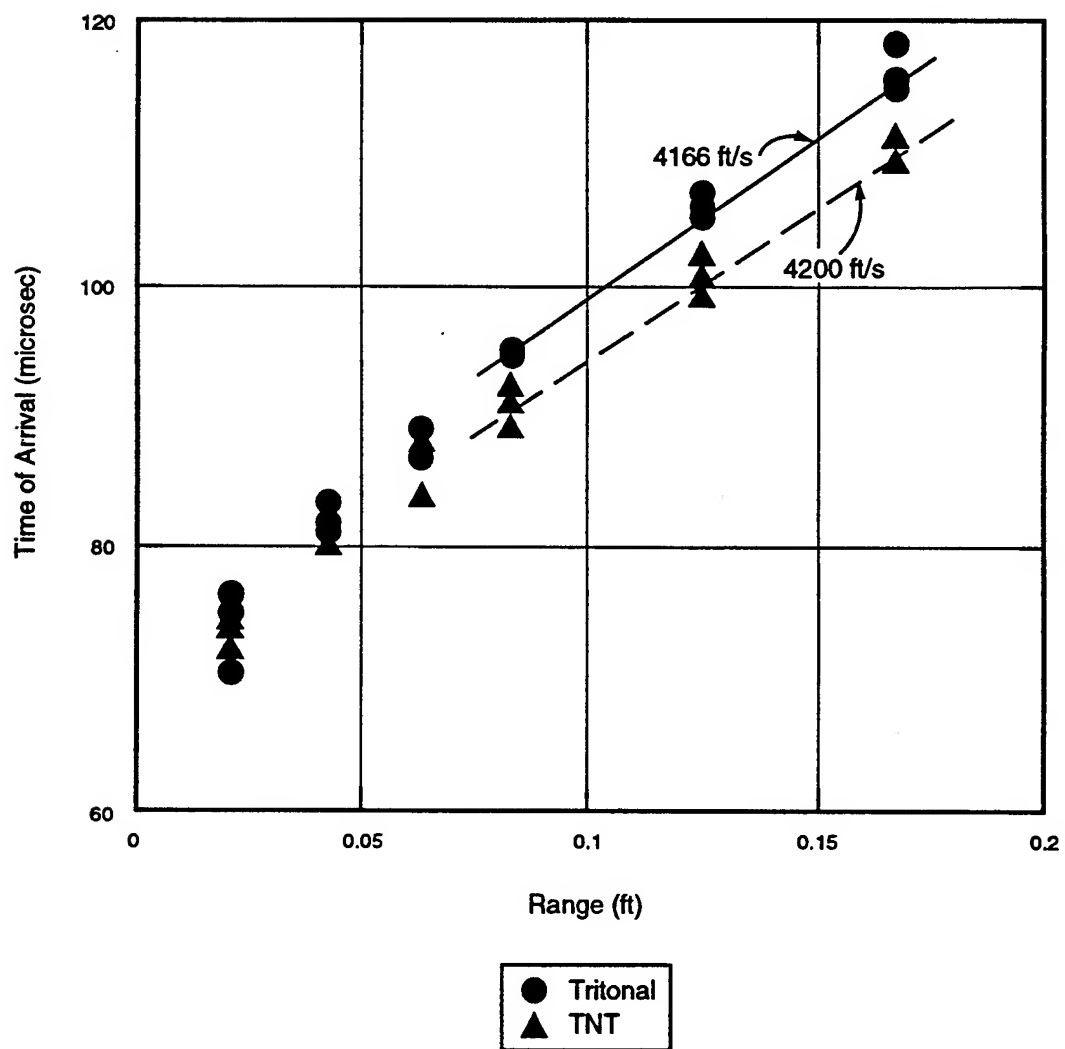
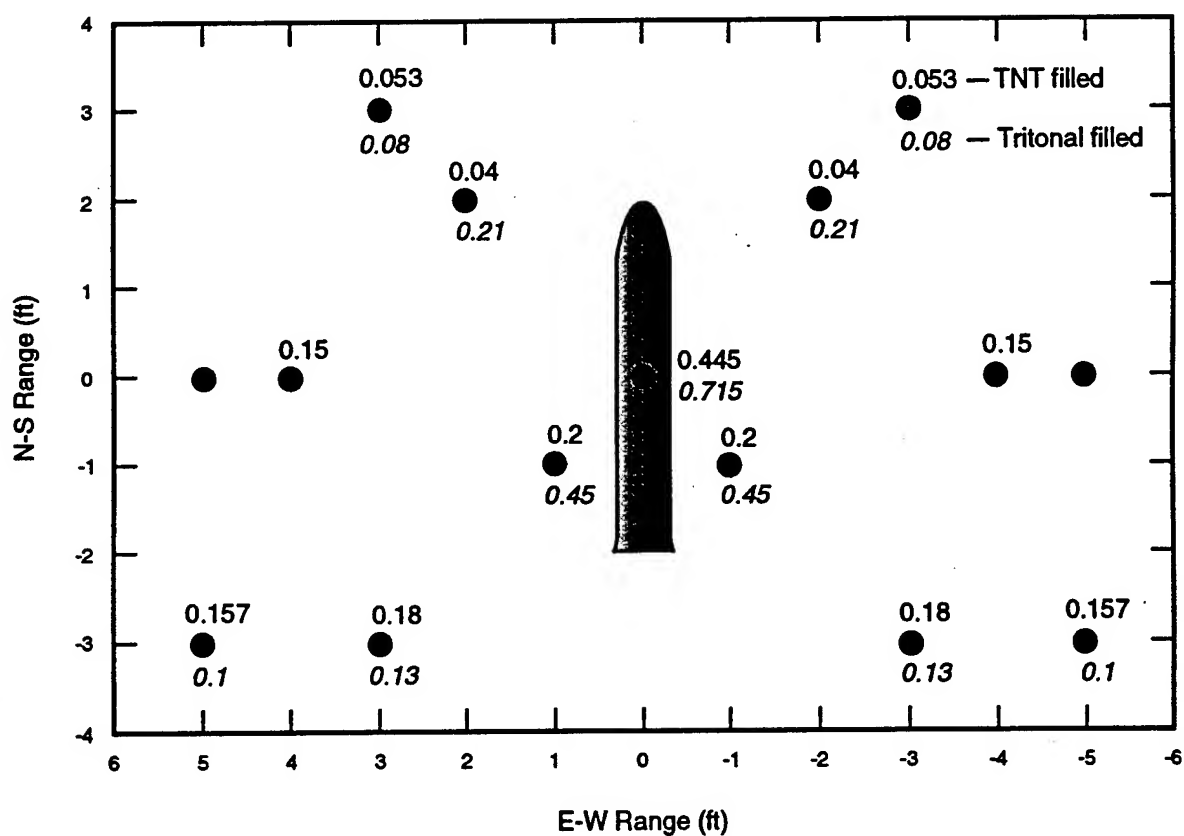


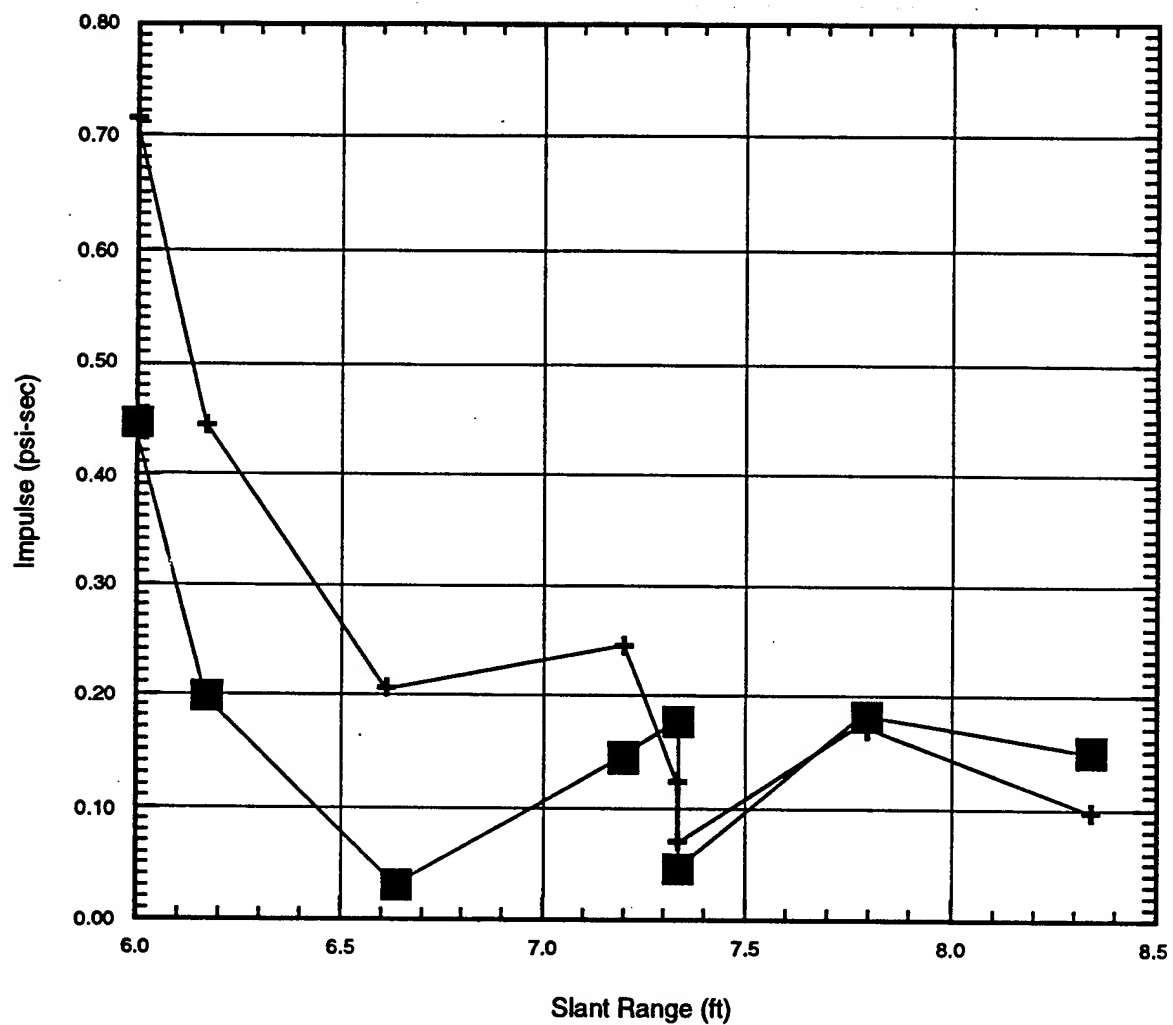
Figure 7. Comparison of bomb case expansion, Tritonal vs TNT.

12 ft x 8 ft x 1 ft Concrete Slab



- Average Impulses at Gage Location
- Average Impulses at Virtual Gage Location (from symmetry)

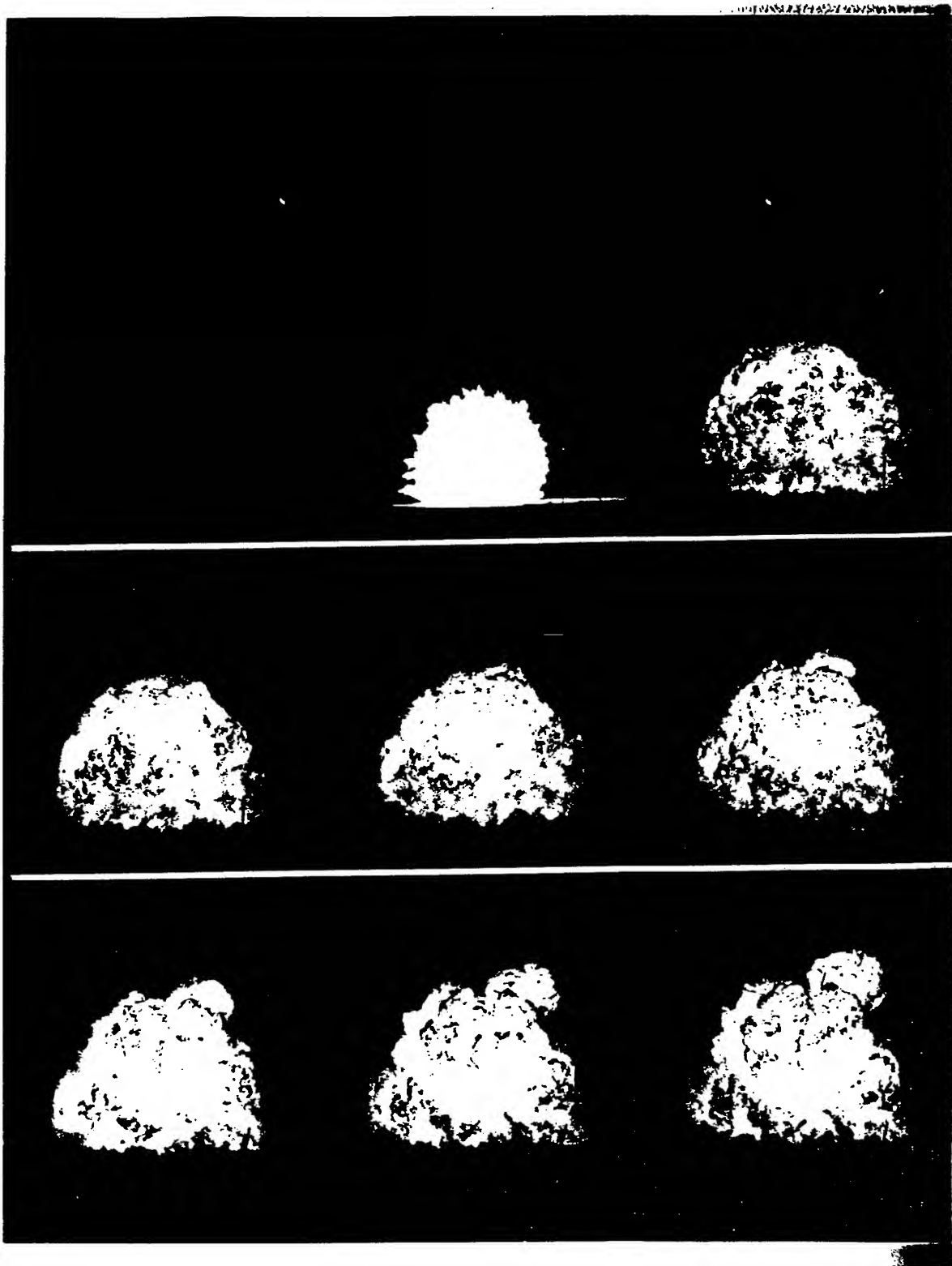
Figure 8. Impulse data vs location, Tritonal and TNT.

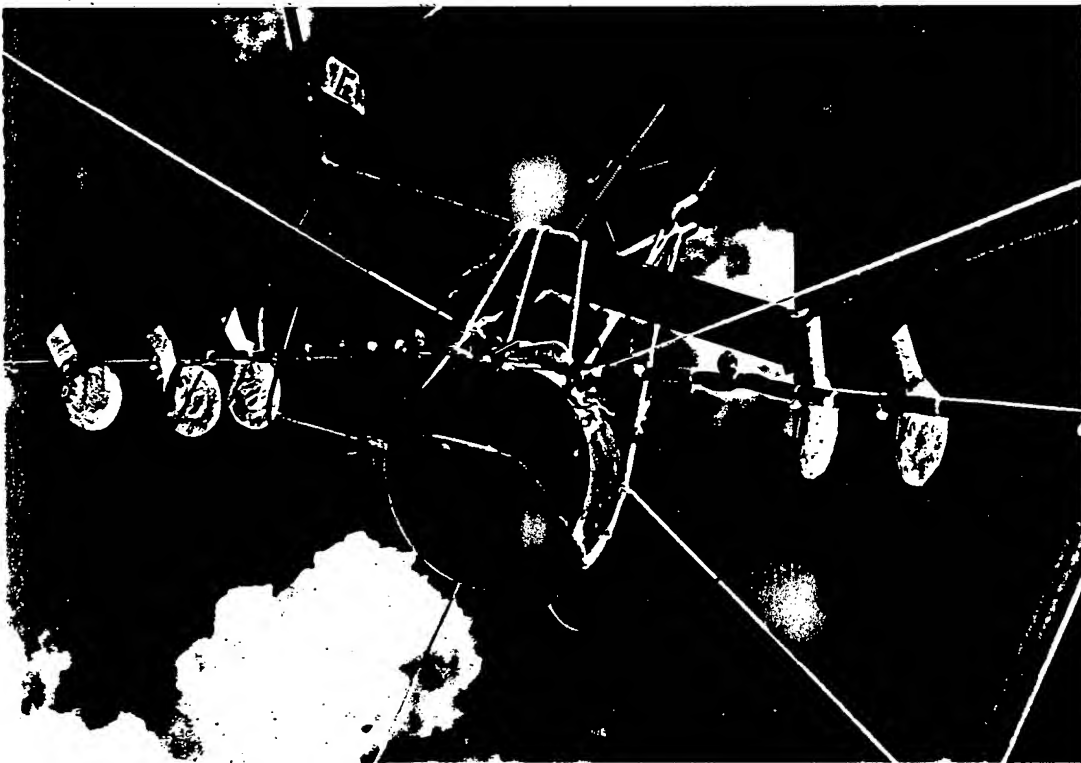
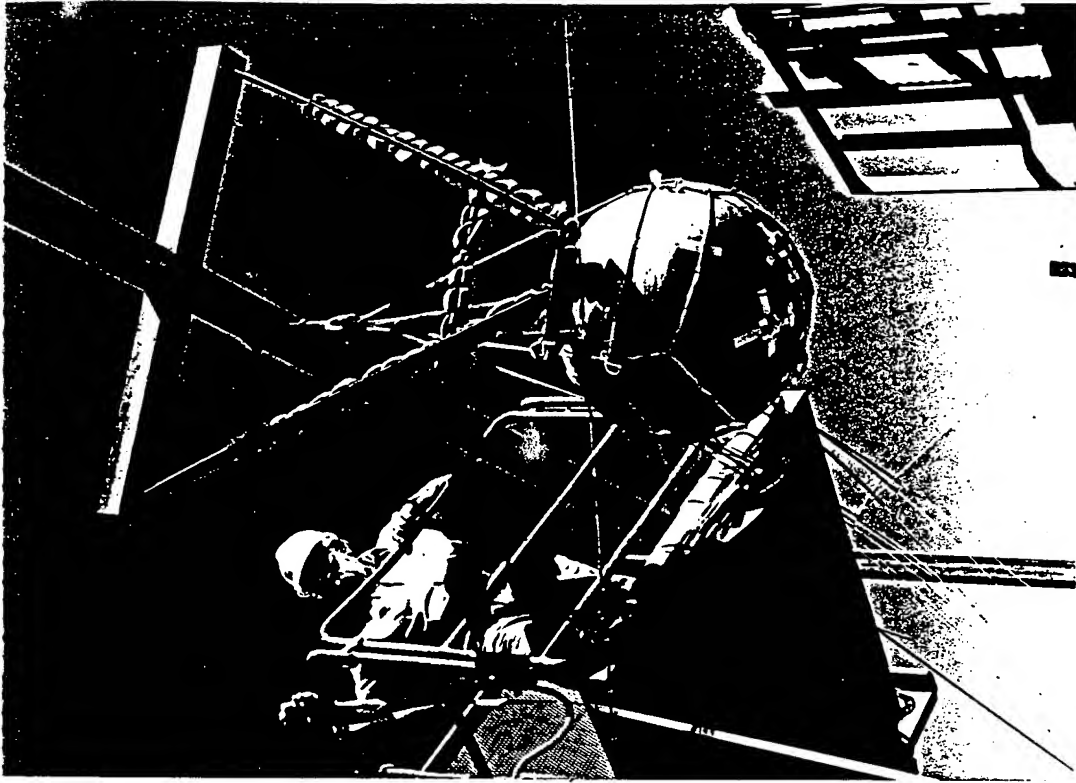


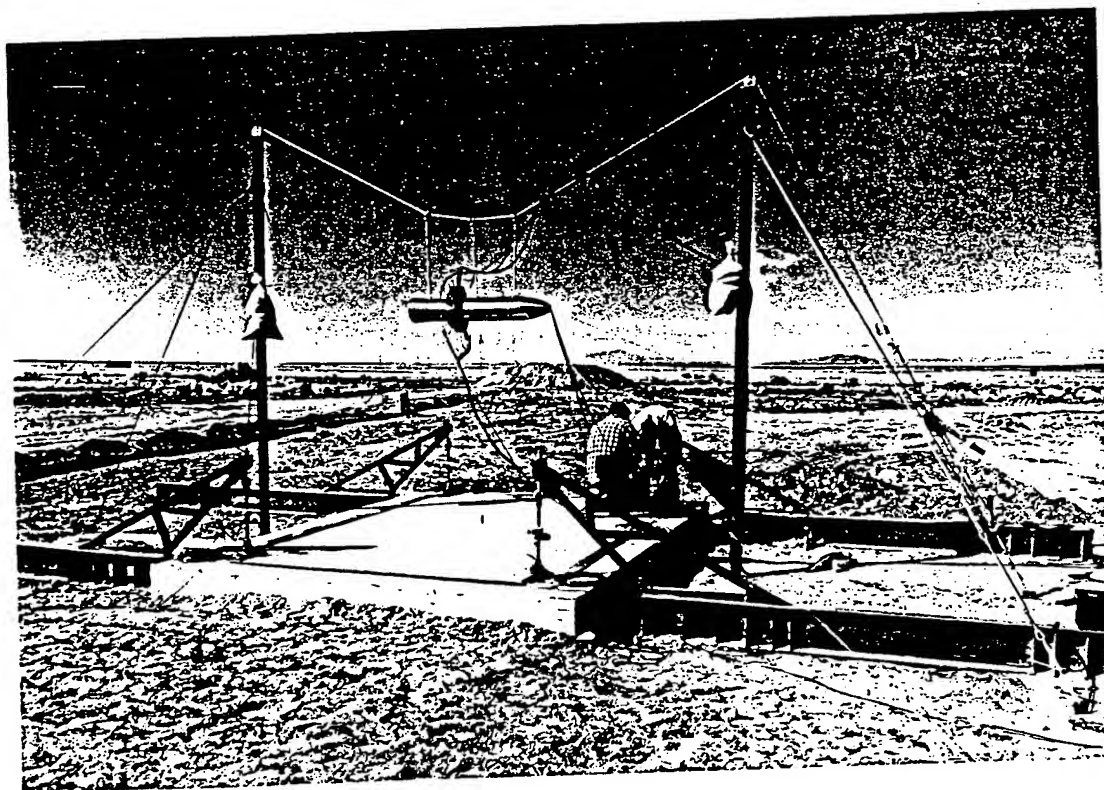
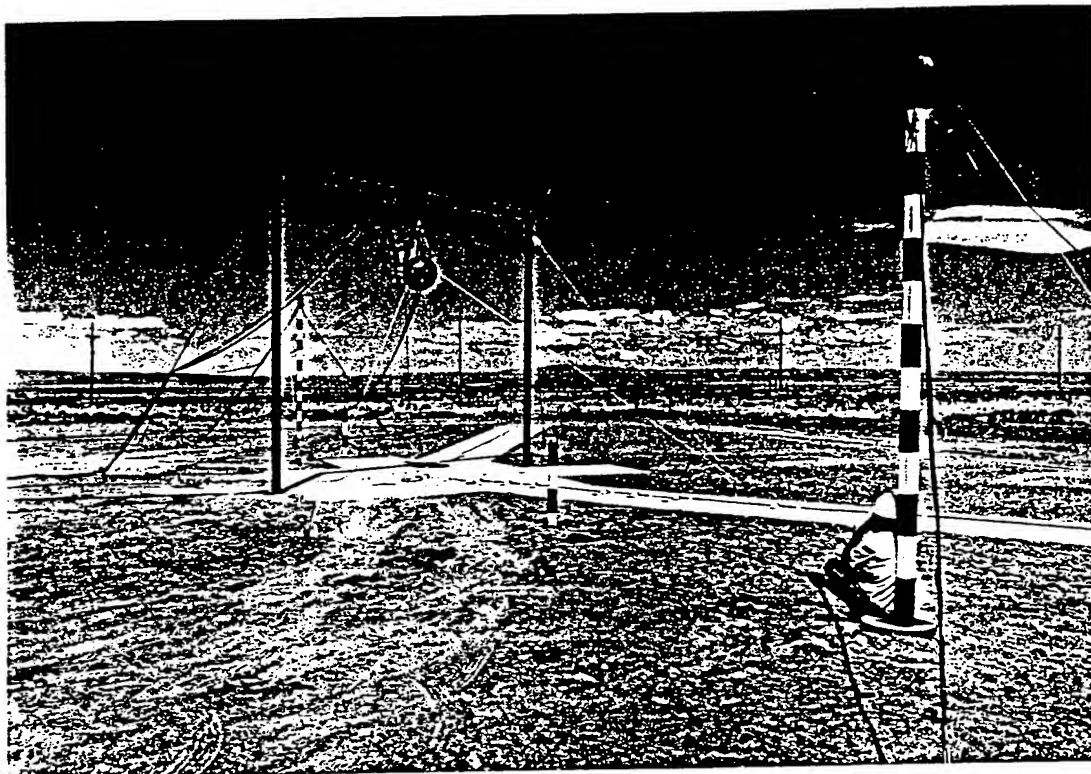
Impulse Comparison for TNT and Tritonal  
Half Scale BLU 109 Bombs

■ TNT Filled Bomb  
+ Tritonal Filled Bomb

Figure 9. Impulse vs range for Tritonal and TNT.









# **AN EXPERIMENTAL STUDY OF DAMAGE TO SCALE MODEL CYLINDERS FROM NEAR FIELD UNDERWATER EXPLOSIONS.**

**J. M. Brett, P. van der Schaaf and M. Barclay**

**Australian Department of Defence  
Defence Science and Technology Organisation  
Aeronautical and Maritime Research Laboratory  
PO Box 4331  
Melbourne  
Victoria  
Australia 3001**

## **Abstract**

An important facet of submarine vulnerability is the study of hull deformation arising from a near field underwater explosion. The mechanisms causing this damage can be broadly characterised as shock wave interaction and hydrodynamic loading due to the expansion of the bubble of detonation products and its possible collapse onto the hull. The total amount of deformation and the contribution made to it by each damage mechanism will depend on charge size, charge stand-off and charge to target orientation. To investigate these aspects of the damage process we have conducted an experimental study with small scale cylinders and explosive charges at our underwater test site. This paper describes the experiment and presents a preliminary analysis of the results. Our analysis of target deformation shows that a considerable fraction must be attributed to bubble damage mechanisms. An analysis of deformation contours indicates that much of this suggests water jet damage.

## **Introduction**

The underwater detonation of a warhead in close proximity to a submerged vessel produces a number of potentially damaging weapon effects. The first of these to affect the vessel is the interaction with the waterborne shock wave generated by the detonation. Following this there is the potential for target damage by a number of mechanisms associated with the dynamics of the bubble of detonation product gases and the surrounding water. These include the bubble pulse shock wave and water jet caused by bubble collapse. For warheads detonated in close proximity to a submerged vessel the contribution that each of these weapon effects makes to the total hull damage is unclear.

Accurately predicting damage to submarine hulls clearly requires an understanding of the major damage mechanisms and the contribution they make to the total damage. Full scale studies of hull damage for underwater explosions is both expensive and difficult. Scale model experiments overcome these problems but introduce the problem of the scalability of small scale results to full scale. Computer prediction using finite element analysis (FEA) codes is an attractive alternative but their capability to model underwater damage processes is not yet convincingly demonstrated. Work currently under way at DSTO is aimed at developing this ability.

The experiments described in this paper had two major objectives;

1. an investigation of underwater damage mechanisms and their contribution to total damage.
2. the provision of a data set for the testing and development of an FEA based damage prediction ability.

FEA analysis of the experiments is currently under way but the results of this will not be available for some time. In this paper we limit ourselves to a presentation of the experimental work and an initial analysis of the results with emphasis on investigating the relative importance of shock wave and bubble damage effects.

## Experimental

To study aspects of damage to submarines we undertook a number of experiments involving scale model cylinders and explosive charges. Because our general approach is to develop an FEA based damage prediction ability it was not necessary to stringently apply scaling rules. However, the experiments were scaled with the target dimensions and charge sizes of a typical submarine hull and torpedo warhead in mind. This scaling was done by application of Hopkinson's scaling rules to the cylinder diameter and wall thickness and to the torpedo warhead weight.

Whereas the damage caused by the primary or detonation shock wave is not affected by charge - target orientation, the bubble mechanisms discussed above are affected by the dynamics and buoyancy of the bubble and as a result they are influenced by this orientation. We attempted to explore the relative importance of shock versus bubble damage by utilising this difference in dependence on orientation.

### Target Cylinders

The target cylinders used in this trial were simple unstiffened cylinders fabricated from 0.2 cm mild steel plate which was rolled to an outside diameter of 27.7 cm and then joined with a single continuous weld running along its length. To avoid end effects the cylinders were made 180 cm long (three times the expected maximum bubble diameter). However, due to constraints on fabrication length the complete cylinders had to be assembled from three shorter sections; a central section 120 cm long and two end sections of length 30 cm. End caps of 0.2 cm steel plate were attached to give a watertight seal.

### Charges

Two charge sizes of 10 and 5 gms (including the detonator) were used in this experiment. Whilst centrally detonated, spherical charges are preferable it is difficult to achieve this with such small charge masses. Thus both were fabricated from plastic explosive PE4 in the shape of a right cylinder formed by pressing the PE4 into a perspex charge and detonator holder. An earlier investigation (Chung and Brett 1995) determined that the detonation of this arrangement produces a satisfactorily spherical shock wave. The charges were end initiated with an electronic bridge wire (EBW) detonator suitably waterproofed for use at our test depth of 4 m.

Table 1. Shot Parameters

Cylinder #	Charge Size (gms)	Stand-off (cm)	Charge Orientation
1	10	15.0	beside
2	10	30.0	beside
3	10	45.0	beside
4	5	15.0	beside
5	5	7.5	beside
6	5	30.0	beside
7	10	30.0	below
8	10	15.0	below
9	10	45.0	below
10	5	7.5	below
11	5	15.0	below
12	5	30.0	below
17	10	30.0	above
18	10	15.0	above
19	5	15.0	above
20	5	7.5	above

### Test Plan

A minimal set of sixteen shots was undertaken to investigate the dependencies of target damage on explosive charge size, stand-off and orientation. Three charge stand-offs ( $S$ ) were selected based on maximum bubble radius ( $R_{\text{bubble}}$ ) of which only the two closest were used for the overhead position. For the 10.0 gm charge, three stand-offs of 15.0, 30.0 and 45.0 cm were chosen corresponding to approximately 0.5, 1.0 and 1.5  $R_{\text{bubble}}$ . For the 5.0 gm charge the three chosen stand-offs of 7.5, 15.0 and 30.0 cm correspond to approximately 0.3, 0.6 and 1.2  $R_{\text{bubble}}$ . The dependence on charge to target orientation was explored by repeating most charge and stand-off combinations with the charge positioned below, beside and above the target. Because of buoyancy effects we expect the contribution to target damage arising from bubble mechanisms to vary with the relative orientation of the charge and target, being greatest when the charge was detonated underneath the target, and least when detonated above.

### The Test Platform

The experiment was conducted from the specially constructed floating platform shown in Figure 1 which was designed to provide flotation to the test rig under all circumstances and to serve as a working platform for the positioning and deployment of the target and charge. The basic structure consists of a connected pair of foam filled pontoons, an overhead A frame equipped with a winch, and an experimental cage containing the target and charge. The cage is suspended from the A frame and is lowered between the pontoons to the selected test depth. The buoyancy of the cage and target was overcome with four equal ballast weights hanging beneath the cage. The experiment cage was designed to allow charge stand-offs of up to 90 cm. Metal work was minimised where it might interfere with the bubble development. Charge to target orientations of below, alongside and above were obtained by rotating the cage through angles of 90 degrees.

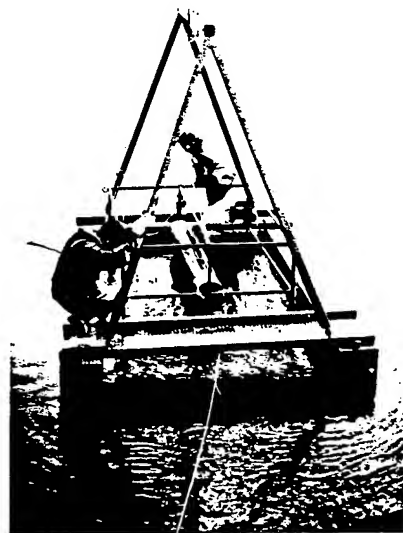


Figure 1. Floating test platform with cylinder being deployed.

### Cylinder Measurement Rig

Measurements of each cylinder's deformed surface profile were recorded by the use of the measurement rig illustrated in Figure 2. The cylinders were mounted on the axis of a lathe with a Linear Variable Displacement Transducer (LVDT) positioned above to measure the radial distance from a fixed reference point to the deformed surface. This device was affixed to a laboratory stand attached to the lathe's tool post which aided in the referencing of z-axis increments and ease of traversal along the cylinder's length. A scale of degrees was attached around the lathe's chuck in order to reference the rotational axis increments. Recordings were taken every 8 degrees around the cylinder's axis at increments of 3 cm along its length. To ensure the maximum cylinder

distortion could be attained, a DC150 30 cm Schlumberger LVDT was selected and a nylon stylus was added to its moving core. The resolution of this device is 335mV/cm which exceeded the required precision of  $\pm 0.05\text{cm}$  and produced a practical DC voltage output.

The measurement process was semi-automated by incorporating a user triggered data-taker to log the output of the LVDT. The data-taker was programmed to accept and convert the DC voltage to displacement in millimetres upon an input trigger pulse. A laptop computer was added to the system to display each measurement against its rotational position and to confirm each reading as it was collected. Another trigger was incorporated to reset the data set rotational position after each complete revolution and to distinguish between sets of data. A hand-held switch unit was used to supply these trigger pulses to the data-taker at each interval while the cylinder was manually rotated. Once the cylinder's profile was complete the information was down-loaded from the data-taker to the laptop and saved to disk. From this data the cylinder surface was reconstructed and used to compute deformation profiles and volumes for quantitative analysis.

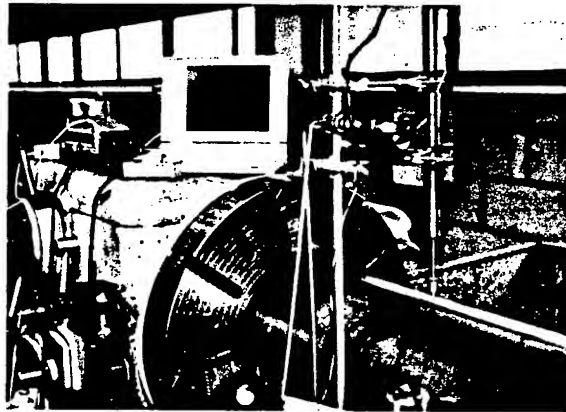


Figure 2. Apparatus for measurement of damaged cylinders.

## Results and Discussion

### Visual Impressions

A qualitative feel of the results can be obtained from inspection of the photographs in Figure 3. These photographs were taken with selected cylinders grouped to illustrate the effect of charge stand-off, charge size and charge-target orientation on the target damage.

Figure 3a shows the variation in target damage caused by a 10 gm charge, positioned beside the target at the three stand-off values corresponding to 0.5, 1.0 and 1.5  $R_{\text{bubble}}$  and as expected the damage decreases with increasing stand-off. The absence of any damage for  $S > 1.0 R_{\text{bubble}}$  hints at the importance of bubble mechanisms in the damage process.

Figure 3b shows the expected effect of charge size at a given distance and orientation on cylinder damage. We note that of all the 4 shots shown in Figure 3b the only one which exhibits no obvious damage is that for which  $S > 1.0 R_{\text{bubble}}$ , so again the visual inspection hints at the importance of bubble damage mechanisms.

Figure 3c shows the dependency of cylinder damage on charge - target orientation for a charge size of 10.0 gms and a stand-off of 30.0 cm ( $1.0 R_{\text{bubble}}$ ). This comparison allows a more direct investigation of the importance of bubble mechanisms because the only damage mechanisms affected by orientation will be those involving the bubble. There is considerable variation in the damage for these three cases which implies that the bubble mechanisms account for a considerable fraction of the total damage. In the following we shall refer to this target damage that is clearly not associated with the primary shock wave as the "bubble damage". As will be discussed below we expect bubble damage to be most effective when the bubble is below the target and least effective when it is above. This dependency is seen in Figure 3c. It should be recognised that in general this experiment does not

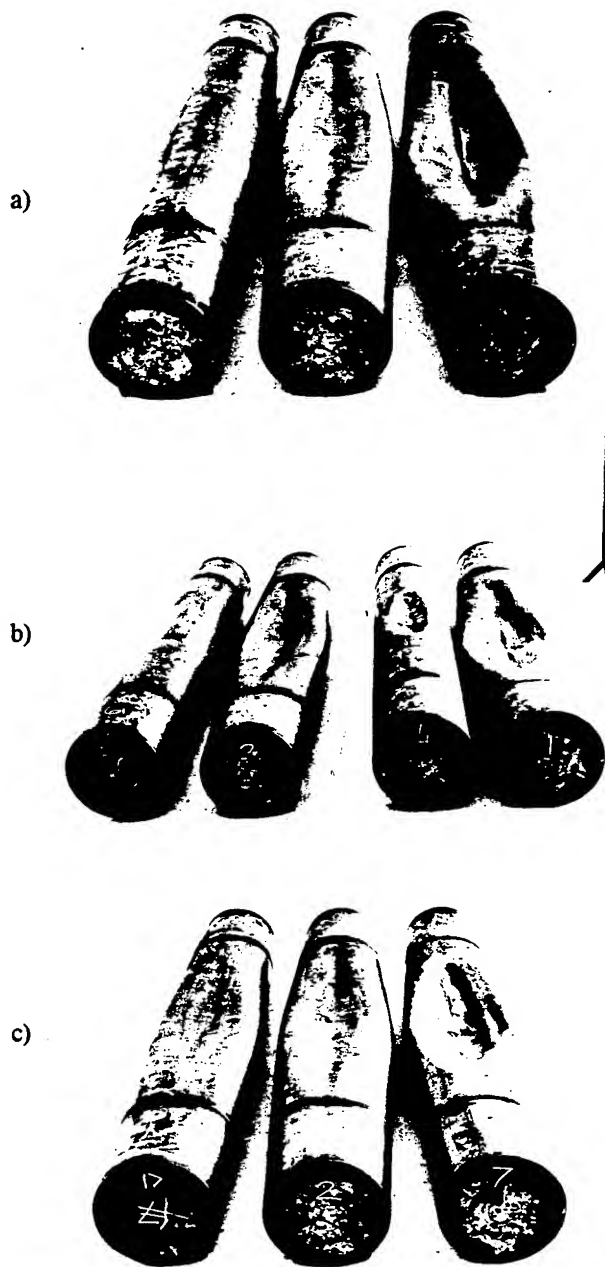


Figure 3. Target cylinders arranged to illustrate dependence of damage on: a) Stand-off; 10 gm charges positioned beside target at stand-offs of 45, 30 and 15 cm (left to right). b) Charge size; all charges positioned beside the target with left pair at 30 cm stand-off, right pair at 15 cm stand-off, 5 gm charge on left and 10 gm on right in both cases c) Orientation; (left to right) 10 gms charge at a stand-off of 30 cm, positioned above, beside and below the cylinder.

record the actual bubble damage but only its variation with orientation because bubble damage may be occurring for all orientations. Thus we can only interpret the variation we see as the minimum contribution from bubble damage.

An initial concern regarding the orientation dependence seen in Figure 3 was that it was associated with the different constraints experienced by the target for each of the three orientations i.e. the target is constrained by the

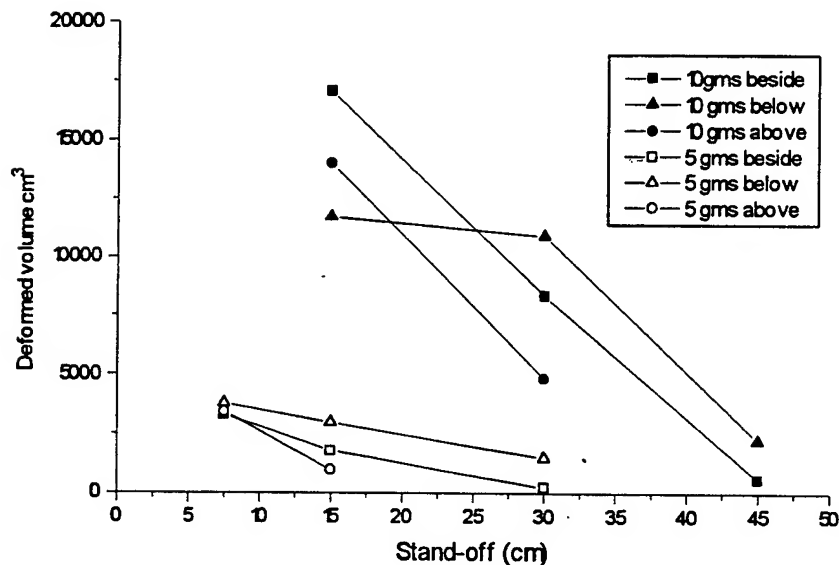


Figure 4. Plot of deformed volume versus stand-off for all target cylinders. Equivalent stand-offs in terms of maximum bubble radii are  $0.5 R_{\text{bubble}}$ ,  $1.0 R_{\text{bubble}}$  and  $1.5 R_{\text{bubble}}$  for 10 gm charges and  $0.3 R_{\text{bubble}}$ ,  $0.6 R_{\text{bubble}}$  and  $1.0 R_{\text{bubble}}$  for 5 gm charges.

ballast weights when pushed upward, by the buoyancy of the platform when pushed downwards and only by the water flow resistance of itself and the cage when pushed sideways. Although it is conceivable that some of the difference between the above and below shots may be connected with this problem we would expect that if constraints on the target are significant, or at least dominant, it should experience least damage when the charge is detonated beside it. That this is not the case is clearly evident in the results.

#### Quantitative Analysis

The target deformation can be quantified in a number of ways but the simplest for our purpose is perhaps the volume of deformation which we calculate as

$$\text{deformed volume} = \text{internal volume of undeformed cylinder} - \text{internal volume of deformed cylinder}.$$

This value is plotted versus stand-off for both charge sizes in Figure 4 which clearly shows the expected qualitative dependency on both stand-off and charge size. The paucity of data points on this graph prevents us from investigating the quantitative dependency of damage on these parameters but the importance of orientation is clearly displayed, in agreement with our visual inspection above. The dependency of deformed volume on orientation is quite strong (e.g. 50% of the maximum value for a 10 gm charge at  $S = 30$  cm) demonstrating that a substantial amount of damage is being done by something other than the primary detonation shock wave.

For  $S > 0.5 R_{\text{bubble}}$  the orientation dependency is as seen in Figure 3c i.e. least damage when the charge is above the target, increased damage when beside and maximum damage when positioned below. This strongly suggests that the additional damage mechanism is connected with the bubble which due to its buoyancy will move closer to the target when formed below it, away from the target when formed above and away to a lesser extent when formed beside. Some idea of the expected movement caused by buoyancy of the bubble during the first bubble cycle can be obtained from equation 8.32 of Cole (1948) which predicts a rise of 18 cm for the bubble formed from a 10 gm charge at the time of the first bubble minimum. Changes of this amount in the stand-off of the bubble from the target can be expected to significantly affect the potential of any bubble damage mechanism.

For smaller stand-offs the orientation dependence changes such that at a stand-off of  $0.3 R_{\text{bubble}}$  our 5 gm results indicate that it essentially disappears. Our 10 gm results at  $S=0.5 R_{\text{bubble}}$  may be evidence of a transition stage. This behaviour can be explained by the phenomena of bubble migration to a rigid surface (the Bjerknes effect). Estimates of the extent of this bubble migration are available from computations of bubble collapse near flat boundaries, e.g. Plesset and Chapman (1971) and Best (1995). These studies indicate that bubble migration will occur for initial stand-offs of less than  $1.5 R_{\text{bubble}}$  which is the maximum studied in our experiment. Unfortunately the predictions of these flat boundary studies can only serve as an upper estimate of the migration expected in our experiment for which the bubble diameter is approximately twice that of the target. However, it seems clear that at some sufficiently small value of initial stand-off the Bjerknes effect will dominate over that of bubble buoyancy so that orientation dependence would disappear or be noticeably modified as we observe in Figure 4.

#### Possible Bubble Damage Mechanisms

We believe that the results summarised in Figure 4 clearly indicate the presence of bubble damage in this experiment. We now proceed to investigate this matter further to determine whether our results can illuminate the mechanisms responsible for this bubble damage.

The bubble of gas formed by the explosion expands to a maximum radius beyond an equilibrium balance of internal and external pressures, and then driven by this imbalance, collapses back to a minimum radius from which a new expansion occurs. At this time of minimum radius the bubble emits a new pressure wave into the water known as the bubble pulse. This process repeats itself but the associated loss of energy incurred makes only the first bubble pulse a likely source of damage. The bubble pulse has a much longer duration but a considerably lower peak pressure than the primary shock wave, so its relative importance as a damage mechanism is unclear. However, if migration towards the target reduces the stand-off of the bubble pulse source compared to that of the primary shock wave, then its relative effectiveness is considerably increased.

Asymmetric collapse of the bubble caused by both the presence of the target (the Bjerknes effect) and the depth dependence of the hydrostatic pressure produces a water jet directed against the target. The damage potential of this jet is likely to be dependent upon its stand-off from the target and the jet speed. Whilst the Bjerknes effect is the same for all orientations, that of hydrostatic pressure is not, acting to enforce the Bjerknes effect when the charge is below the target, to weaken it when above, and acting perpendicular to it when the charge is beside the target. As we have seen above, bubble migration is dominated by the attractive Bjerknes effect for very small stand-offs but outside this the bubble's buoyancy will position the jet closest to the target when the bubble is formed below, furthest away when above and at an intermediate distance when beside. By combination of these two effects we expect the most damaging jet below the target, the least effective above and a jet of intermediate effect beside.

A further possible damage mechanism is the loading produced from the incompressible flow of water associated with the passage of the shock wave and the initial expansion of the bubble to its maximum radius. Of these only the latter could be affected by orientation but it is difficult to imagine that this mechanism would exhibit the pronounced dependence seen in Figure 4 because very little upward movement of the bubble occurs when its expansion is most energetic.

It is not possible to distinguish between the suspected damage mechanisms on the basis of the total damage volume alone. Because of its directional nature the damage caused by the water jet could be expected to be concentrated over a smaller target area than that caused by the bubble pulse pressure wave. Thus an inspection of damage contours might be useful in identifying the major contributor to the bubble damage. In Figure 5 we present selected axial contours for the 5 gm shots taken through the centre of the damaged region. For the smallest stand-off of 7.5 cm ( $0.3 R_{\text{bubble}}$ ) shown in Figure 5a the contours are similar for all orientations indicating that the Bjerknes effect is dominating the bubble migration. For the larger stand-off of 15 cm ( $0.3 R_{\text{bubble}}$ ) shown in Figure 5b the orientation dependence of the damage is once again clearly seen, indicating that the buoyancy of the bubble is also contributing to its movement with respect to the target. An interesting feature of the contours is that they appear to show two different regions of deformation - a region of gentle slope starting at the ends of the cylinder and an inner region in which the slope increases, sometimes dramatically. Because the depth of the inner feature is particularly orientation dependent it seems reasonable to attribute it to the bubble damage mechanism.

A water jet is inherently a localised and directional loading which will locally deform the target area immediately beneath its footprint. Because the target is not supported it is likely to hinge at the outskirts of this footprint and as the depth of the depression is increased we can expect the hinge point to travel outwards, acting to widen the depression as it becomes deeper. Furthermore, models of bubble jet formation (Chapman and Plesset, 1971, Best 1994) predict that the collapse of a bubble further away from a target produces a narrower jet

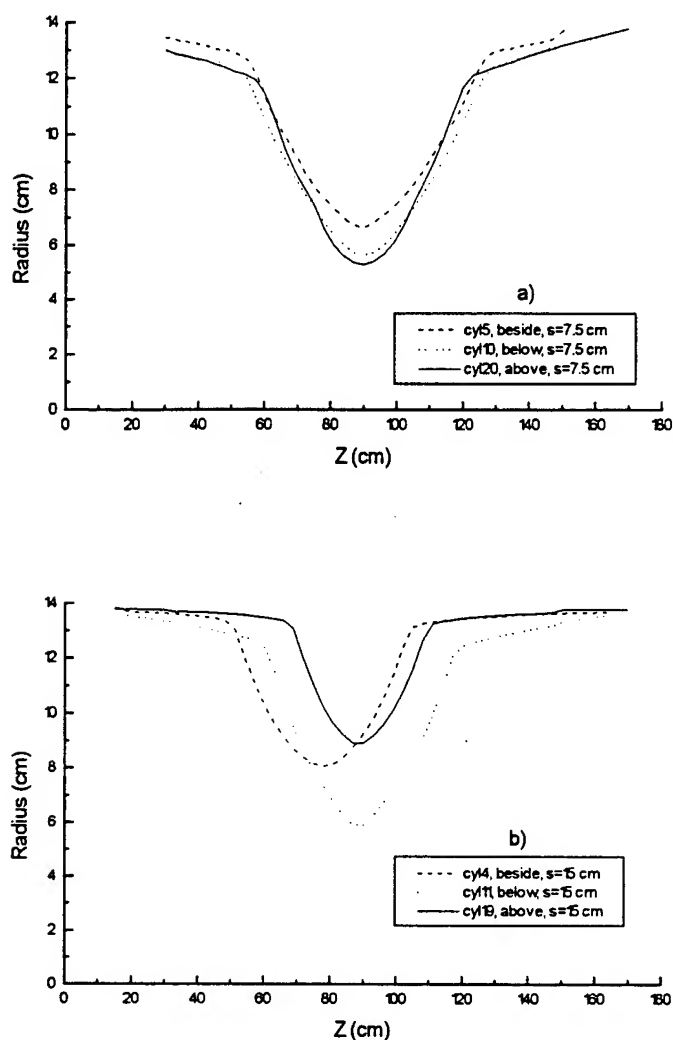


Figure 5. Surface contours along the length of cylinders from selected 5 gm shots, taken through the centre of maximum deformation.

(albeit with higher velocity) than does a bubble collapsing closer in. Provided the potentially more damaging effect of a higher velocity jet is counterbalanced by its smaller dimension and the greater intervening quantity of water we can accordingly expect a shallower depression to be narrower. Thus the contours of the central depression shown in Figure 5 are consistent with the expected features of water jet damage.

Although the contours of Figure 5 are suggestive of having been formed by a directional loading like a water jet the supposition of damage caused by two shock waves emitted at different distances from the target might also be capable of producing the two component profile we observe. If the bubble has moved closer to the target in the time before it collapses, then the bubble pulse pressure wave will produce a more localised target loading than the detonation shock wave. Provided the bubble pulse pressure wave is strong enough, this will produce a central depression. Conversely if its buoyancy has moved the bubble further away from the target then we would not expect the central depression. In principle this permits us to distinguish between the two damage mechanisms but it is not clear whether the buoyancy dominates the bubble migration or only acts to weaken or enhance the constant attraction of the Bjerknes effect in these experiments.



It seems therefore that the existence of the central depression in the deformation contours cannot be used to conclusively distinguish between bubble pulse or water jet damage. Fortunately an analysis of the details of the shape of the central depression and its variation is more helpful and is we believe, more consistent with it being primarily caused by water jet damage. Firstly the transition point between the inner and outer zones of the contours is in many cases quite abrupt. This is more consistent with it being a hinge point arising from a localised central loading than the limit of effect from a spherical pressure wave. The latter would vary smoothly with distance from the bubble collapse centre and the angle of inclination of the pressure wave with the cylinder surface. Secondly, calculations of the free field bubble collapse (Best, 1995) predict typical jet widths of 7 cm and 5 cm for the bubbles produced by 10 and 5 gms charges respectively. In most cases the contours appear to exhibit central flat intervals of a dimension consistent with these predictions. Thirdly from Figure 5b we observe that the width of the central depression decreases as it becomes shallower. This is not what we expect from a bubble pulse pressure wave for which a shallower depression would be caused by a larger stand-off. For a given position on the target a larger stand-off corresponds to a larger angle of incidence and hence a more effective pressure wave interaction. Thus for bubble pulse pressure wave loading we would expect a shallower and broader depression for a pulse emitted further away from the target. For these reasons we believe that on the whole the deformation profiles are best explained by a water jet as the *major* damage mechanism.

## Conclusions

We have conducted a series of small scale experiments in which we investigated the deformation of a submerged cylinder subjected to loading from a nearby underwater explosion. The dependencies of this damage upon charge size, charge stand-off and charge to target orientation were explored. The analysis of the orientation dependence showed clear evidence for the presence and importance of bubble related damage. At a charge stand-off of one bubble radius the *variation* of total deformed volume with orientation amounted to roughly 50% of the total damage. This implies that at that stand-off the bubble damage mechanisms caused at *least half* the total damage. The two most likely bubble mechanisms consistent with these results are the bubble pulse pressure wave and the water jet associated with the first collapse of the bubble. These two mechanisms have different target loading distributions and so in an effort to distinguish between their effects we studied the axial profiles of the damaged targets. This analysis favours the water jet as the dominant cause of damage for our simple targets but we were not able to conclusively discount the bubble pulse pressure wave as an effective damage mechanism. Further studies and computer modelling utilising FEA techniques are under way to illuminate this problem.

## Acknowledgments

It is a pleasure to thank Greg Foreman and the staff of the Army Technology and Engineering Agency, Maribrynong, Melbourne for the provision of equipment and their generous assistance in the measuring of the damaged cylinders. We also thank Norbert Burman for his many helpful comments on this paper.

## References

- Best, J. P. , 1995, DSTO private communication.
- Best, J. P. , 1994, "Underwater Explosion Bubble Collapse Against Marine Targets." *In Proceedings of the Naval Platform Vulnerability/Survivability Technical Workshop*. TTCP WTP-1 and ABCA-7, 21-24 Nov. 1994.
- Chung, M. and Brett, J. M. 1994. "Underwater Blast Effects on Scaled, Submerged Cylindrical Objects." *In Proceedings of the Naval Platform Vulnerability/Survivability Technical Workshop*. TTCP WTP-1 and ABCA-7, 21-24 Nov. 1994.
- Cole, R., 1948, *Underwater Explosions*, Princeton University Press.
- Plesset, M. S. and Chapman, R. B., 1970, *J. Fluid Mech.*, 47, 283.



## Analysis of Blast Loads on Commercial Buildings

Naury K. Birnbaum\*  
Richard A. Clegg †  
Greg E. Fairlie †  
Colin J. Hayhurst †  
Nigel J. Francis †

\*Century Dynamics Incorporated, 7700 Edgewater Drive, Suite 626, Oakland, CA 94621

†Century Dynamics Limited, 12 City Business Centre, Brighton Road, Horsham, West Sussex RH13 5BA, England

**ABSTRACT.** Analytic techniques and computational fluid dynamics (CFD) software programs are currently in use for assessing the blast loads on military structures for a variety of situations. These approaches, of necessity, are now being extended to the calculation of explosion-structure interaction problems where the loadings are not upon hardened military targets but rather on civilian structures. This has become of great importance as high explosive bomb attacks have been increasingly directed against many commercial, financial and civic centers consisting of buildings of conventional, "soft" construction.

One aspect in the protection of such structures is the accurate prediction of the blast loadings on structural components using analytic or advanced numerical tools taking into account the complexity of the building, its geometry and the surrounding environment. Such an understanding of the loads can help define building protection options such as selection of materials, relocation of building services, siting, and construction techniques.

Various different numerical and analytic techniques are discussed and illustrated by example. Applications discussed include:

- Idealized one and two dimensional problems
- Blast propagation over multiple structures in two dimensions
- Blast in a three dimensional urban setting due to a terrorist bomb including multiple interactions with buildings and roads.
- Three dimensional blast study of the Oklahoma City Federal Building

Important effects such as multiple blast wave reflections, rarefactions, and the negative phase of the blast wave can be readily modeled in CFD codes. Simplified analytic and semi-empirical techniques many times ignore such phenomena. Thus, modeling modern

buildings set in congested city centers usually requires the use of sophisticated CFD numerical calculations. The use of both analytic techniques and CFD calculations can provide a cost-efficient and accurate approach to determining blast loads. Such information is critical in any effort to effectively harden commercial structures.

## 1. INTRODUCTION.

Commercial buildings are constructed quite differently than hardened military structures and as such are generally quite vulnerable to blast and ballistic threats. In order to design structures which are able to withstand the effects of explosions it is necessary to assess the effects of explosions on the structure. Using a variety of methods, explosion effects can be quantified for many situations. Such quantification should lead to better and more cost effective design. Typically, it takes a combination of specialist expertise, experimental tests, and analysis tools to properly quantify the effects.

This paper concentrates on various analysis tools available to predict the loads from a high explosive blast on commercial buildings. Different analysis methods are appropriate to different situations. The loading types and structural design requirements are discussed in the context of what the software tools should provide. A number of example analyses are shown.

## 2. SOFTWARE TOOLS

A variety of software tools are available from various sources to quantify the effects of explosives on structures. The table below summarizes those in use by the authors. The table does not purport to encompass the wide variety of software available to the community.

Software Tools

AUTODYN-2D	Numerical	Century Dynamics	Impact/penetration, high explosive and blast simulation
AUTODYN-3D	Numerical	Century Dynamics	Impact/penetration, high explosive and blast simulation
AutoReaGas (3D)	Numerical	Century Dynamics/TNO	Gas explosions and blast simulation
MADER codes	Numerical & Analytical	Charles Mader	Characterization of explosive properties
US Army codes	Analytical	US DOD	Weapons effects calculations
BLAPAN	Analytical	Century Dynamics	Calculation of blast loads on panels
SPLIT-X	Analytical	CONDAT/Century Dynamics	Fragmentation code

### 3. TYPICAL STRUCTURAL RESPONSE TO EXPLOSIVE LOADINGS

The nature of the explosive loading on a structure can be summarized as shown in the table below. Depending on the size of the device and the type of response to be quantified different software tools can be employed.

Typical Responses	Small Devices	Large Devices
Air blast	Component damage / failure Small secondary missiles Local in-structure shock	Component damage/ failure Structural collapse Secondary fragments & damage escalation In-structure shock
Primary fragments	Localized damage	Localized damage
Secondary fragments	Localized damage	Localized damage Tertiary fragments & damage escalation

### 4. STRUCTURAL DESIGNER'S REQUIREMENTS

The structural designer in order to design a new structure or retrofit an existing structure for explosion resistance generally requires certain information as summarized below:

#### Blast Loads:

- Peak pressures
- Impulses
- Load time-histories on structural components

#### Impact Loads:

- Velocities / Trajectories of projectiles
- Size / Shape / Materials

In this paper, impact type loads will be ignored with the focus on blast. However, the software tools summarized above are quite proficient at handling both types of loads.

### 5. ANALYTIC METHODS

The US Army manual TM5-855<sup>1</sup> provides a useful screening tool for assessing blast loads when many combinations of explosive device and location must be considered. Load time histories for buildings and structural members may be calculated according to the method outlined in TM5-855. The principal steps of the method are:

- Divide a surface into sub-sections and calculate a pressure time history and impulse for each small area.
- Summing the impulse for each sub-section then provides the total impulse applied to the surface.
- The total load-time history is then defined to have an exponential form with a peak calculated assuming an average peak pressure applied over all the surfaces.

While this simplified method can supply very useful information it exhibits the following limitations:

- Typical real situations are three-dimensional and the resultant multiple blast reflections and rarefactions are not treated.
- The assumption that the load-time history is applied to the all parts of the surface at the same time with an exponential form is a poor approximation for near field effects.
- The negative phase of the blast pressure is ignored.

Other analytic methods have been developed to overcome some of the above limitations. One of these is codified in the BLAPAN program.<sup>2</sup> In this program the total load on a surface at a particular time is computed by summing the load on each surface at that time. Thus, the calculation then predicts a load time history which has the same impulse as calculated by TM5-855 but with a different time history.

The scope of this paper does not allow for a wide review of analytic methods but it can be stated that generally these various methods, of necessity, neglect some portion of the true physics of the phenomena.

Numerical methods such as 2- and 3-dimensional CFD (Computational Fluids Dynamics) codes can provide a more accurate approach than the analytical methods. The true physics of the problem, including 3D geometries, can be handled with such codes. The detonation of the explosive, rapid expansion and formation of the blast wave, multiple blast reflections, rarefactions and the negative phase of the blast can all be modeled.

## 6. NUMERICAL METHODS

The numerical methods most appropriate to the simulation of the blast problem are typically based upon a finite difference, finite volume, and/or finite element method utilizing explicit time integration. By way of illustration, the AUTODYN<sup>TM</sup><sup>3</sup> and

AutoReaGas™<sup>4</sup> system of programs will be used to illustrate some of the capabilities of these types of codes for predicting the blast loads on structures.

AUTODYN-2D, AUTODYN-3D and AutoReaGas incorporate a number of different widely used numerical techniques. Each of these techniques has certain advantages and disadvantages. No single method can handle all regimes of a typical problem. The challenge is to apply these techniques in the most efficient and accurate fashion for an optimum solution.

The various techniques available are summarized below:

- Lagrange : the numerical mesh moves and distorts with the material motion
- Euler: the numerical mesh is fixed with the material flowing through it. First and second order accurate schemes are available. Also, a high speed second order Euler method for blast simulation can be used.
- ALE: Arbitrary Lagrange Euler. Provides a type of automatic rezoning overcoming some of the limitations of both Euler and Lagrange.
- Structural elements: Formulations for thin shells and other structural members are available.

In addition to the ability to use different numerical methods for a problem, it is also possible within AUTODYN to apply multiple methods within a given simulation. For example, this can be very important for studying the effects of fluid-structure interaction, e.g. blast loads on a deformable structure. In such a case the structure might be modeled with a Lagrange or structural representation while the explosive-air domain would be modeled with an Eulerian approach. The two domains are then dynamically coupled together in space and time.

The following sections review specific applications of the above techniques. Details of each simulation are available in the cited references. Finally, a more detailed case study as applied to the recent Oklahoma City Federal Building bombing is presented.

## 7. COMPARISON OF ANALYTIC AND NUMERICAL RESULTS FOR A VALIDATING CASE

The differing capabilities of the analytic and numerical methods outlined above can be illustrated in a sample case of a explosive device located near an office building as shown in Figure 1. This shows a 100kg TNT device located in a street 15m from an isolated office building. One typical component of this building to be assessed or designed could be a double glazed unit 1.5 m by 2m high with its center 12m above the ground.

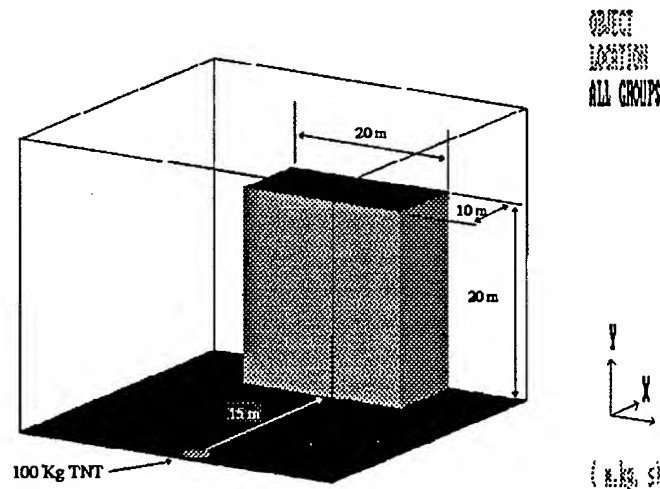


Figure 1. Explosive Device near an office block, analysis geometry

Figure 2 indicates the predicted load-time histories on this panel using TM5-855, BLAPAN, and AUTODYN-2D. The positive phase impulse predicted using TM5-855 and BLAPAN are identical and the AUTODYN-2D impulse is within 3% of this value. The differences are in the time phasing and peak magnitude of the loads. The TM5-855 curve shows a peak load 57% higher than the other two predictions. The exponential form of the load time history is evidenced in all cases. The BLAPAN and AUTODYN results both show similar peak loads and timing to each other. After 40ms a major difference appears when the blast wave enters the negative phase. AUTODYN is able to capture the correct physics while the analytic results do not account for this phenomenon.

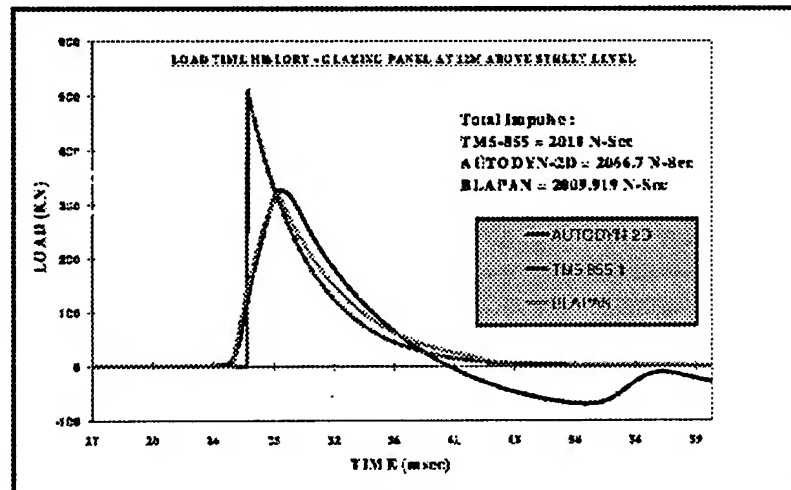


Figure 2. TMS-855, BLAPAN, and AUTODYN-2D panel load time history



## 8. BLAST OVER STRUCTURE (2D EULER)

In this example, the far-field blast loading on two buildings is computed.<sup>5</sup> Figure 3 shows the interaction with two idealized buildings of 10 meters width and 15 meters high at two different times. A plane blast wave of 10 kPa and 0.1 secs impinges on the structures from the left. The blast wave first reflects at the front of the first building. The wave then passes over the first building and diffracts down the back side hitting the ground surface. Gauges monitor the pressure on the various surfaces of the structures. Typical pressure traces are shown in Figure 4. The wave phenomena and interaction with the structures is clearly evidenced. The front of the second building experiences a substantial reduction in loading due to the obstruction of the first building.

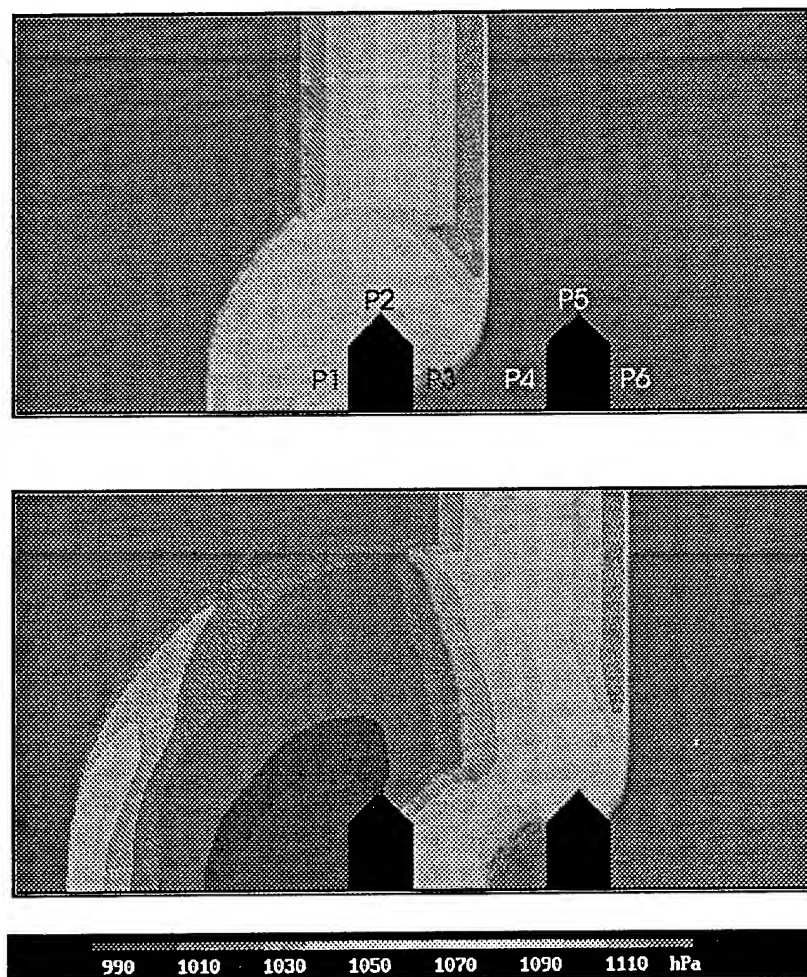


Figure 3. Visualization of Blast Wave Interaction with Two Buildings.

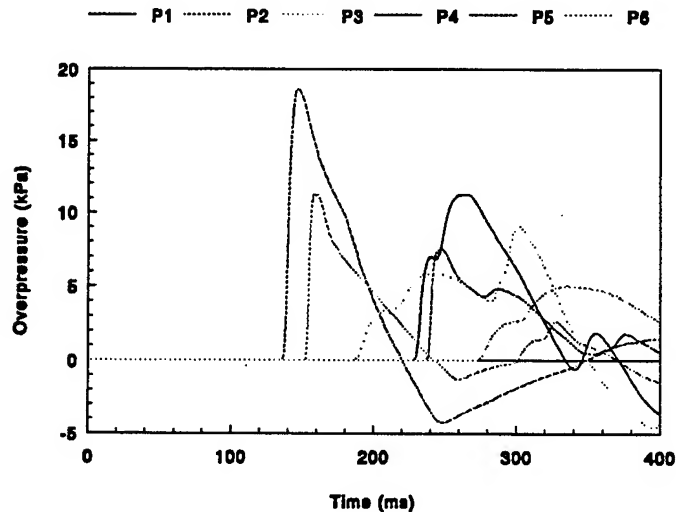


Figure 4. Overpressure-time Traces Recorded at Gauges P1, P2, P3, P4, P5 and P6

TNO has carried a number of numerical simulations and corroborating experiments to validate the method.<sup>6</sup> The correctness of the underlying assumption that the blast loading on objects of large dimension (i.e. buildings) can be modeled as inviscid compressible flow has been verified. Moreover, the numerical technique has been shown to accurately handle steep gradients and shocks with a minimum of artificial diffusion.

#### 9. TERRORIST BOMB IN CITY CENTER STREET (3D EULER).

In order to study the effects of partial confinement of a blast wave in a street, a simulation was made of a 1000kg TNT charge detonating at ground level in the center of a 10m wide street as shown in Figure 5. Because of symmetry only the left half of the geometry was simulated. The size of the numerical mesh is 300,000 cells. The office building is 80m wide by 40m high and is centered directly opposite the street containing the charge. Two buildings are located on either side of the street creating a channel. Building 1 is 20m high and 36m long. Building 2 is 14m high and 40m long. There is an 8m wide and 25m long blind alley between buildings 1 and 2, and a 12m wide street in front of the office building.

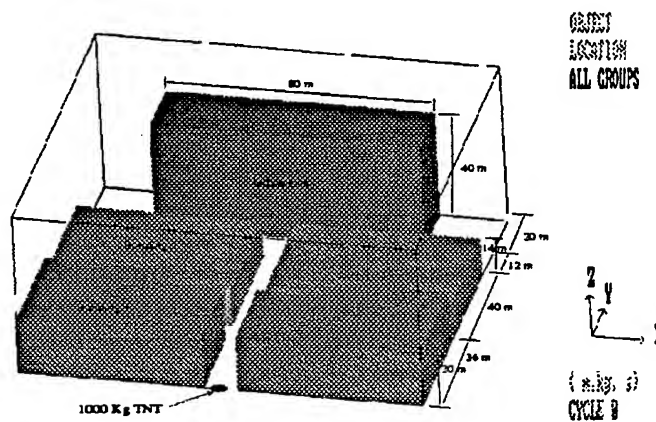


Figure 5. Street channeled blast analysis geometry

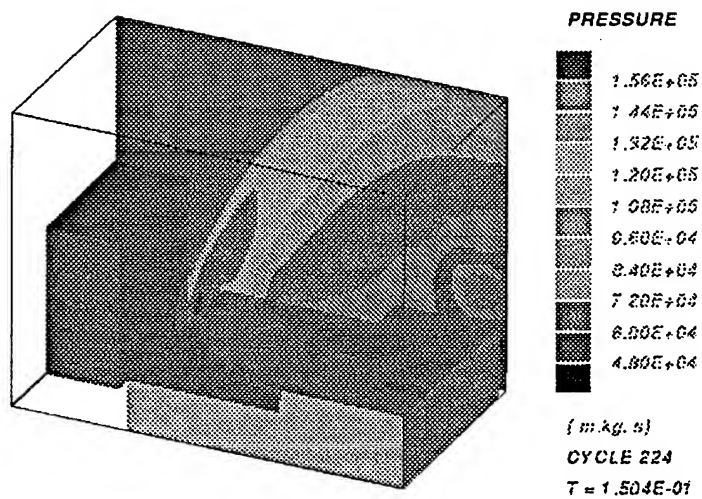


Figure 6. Street channeled blast pressures 0.15 seconds after charge detonation

Figure 6 shows the pressure contour at a time 0.15 secs after charge detonation. At this time the blast wave has expanded spherically over the top of buildings 1 and 2 and is about

to reach the office block. The channeling effect along the street is evidenced by the higher pressure at the end of the street near the ground.

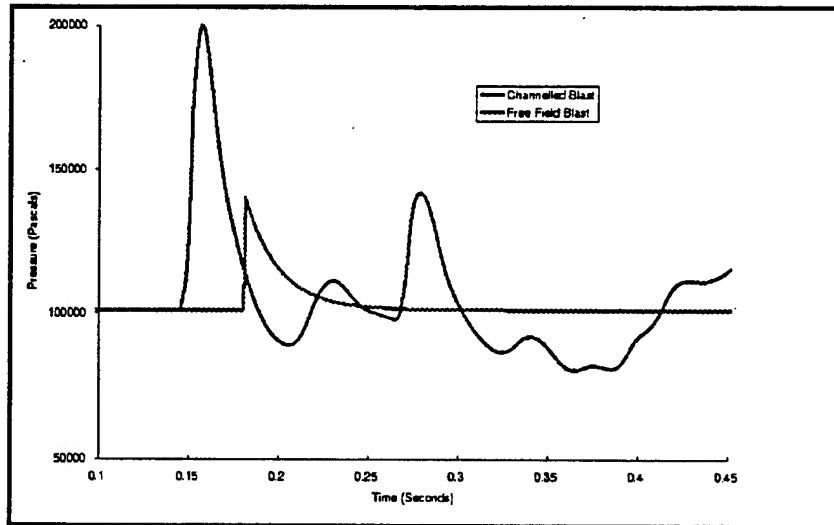


Figure 7. Street channeled blast pressure time history at base of office block

The computed pressure history at the base of the office block directly at the end of the street is shown in Figure 7. The free field blast is also depicted in this figure for comparison. The free field curve assumes that the blast expands hemispherically over a flat surface before reflecting from the office building. The channeling of the blast is shown to increase peak overpressure by 153% and maximum impulse by 340% compared with the simplified analytic result. The distribution of maximum impulse applied to the front surface of the office building is shown in Figure 8 where the high impulse at the end of the street is clearly shown.

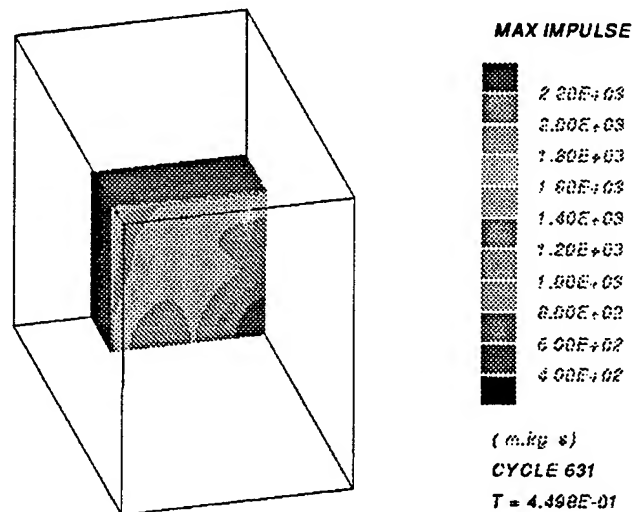


Figure 8. Street channeled blast maximum impulse on the office block

## 10. EXPLOSION AND BLAST WITHIN A 3-D BUILDING (ALE)

The calculation of a confined explosion within a bunker type building is used to illustrate the coupled 3D ALE (Arbitrary Lagrange Euler) technique. The basic geometry of the simulation is shown in Figure 9. A plane of symmetry allows half of the system to be modeled. In the simulation, the internal walls and roof are treated as deformable Lagrangian structures while the air and explosive are computed using an Eulerian/ALE formulation.

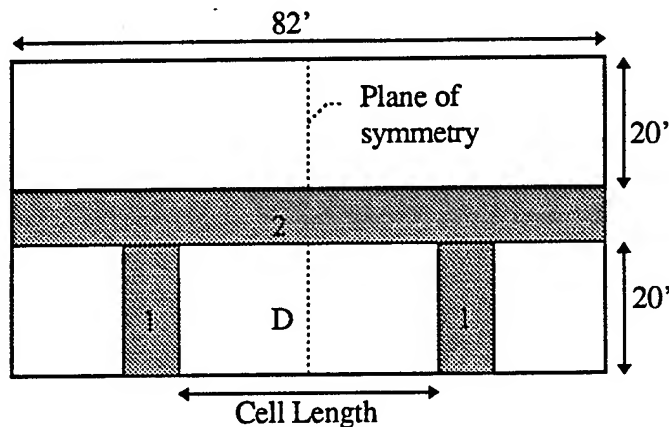


Figure 9. Plan view of 3D building with internal explosion

In the simulation, a total of 30,000 lbs of TNT are detonated at 24 locations within the central cell region 'D'. The outer walls are considered rigid while the inner walls '1' and '2' are deformable structures. The series of plots in Figure 10 shows the numerical mesh, material locations, and the deformed state of the internal walls and roof at 14 msec after detonation of the explosive devices. This ALE simulation uses Euler for the explosive-air regions and Lagrange for the deformable structures. Thus, fluid-structure interaction may be taken into account. Further details are provided in reference <sup>7</sup>.

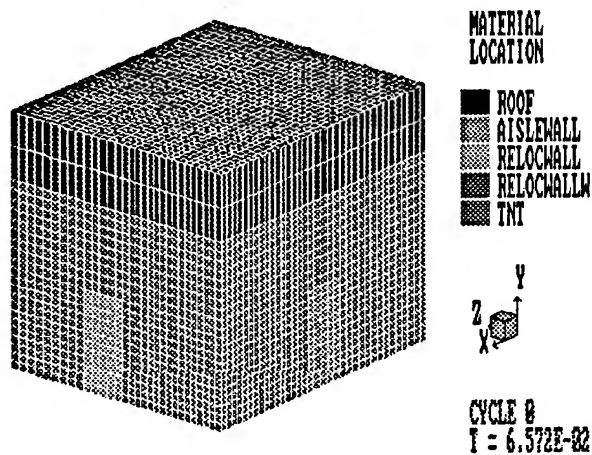


Figure 10a. Explosion inside building, model setup

AUTODYN-3D Version 2.1.00

Century Dynamics Incorporated

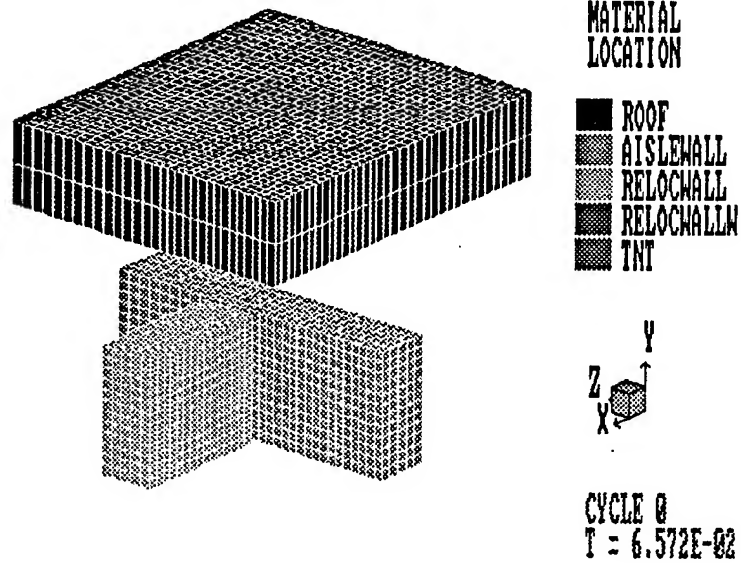


Figure 10b. Location of internal walls and roof at time 0

AUTODYN-3D Version 2.1.00

Century Dynamics Incorporated

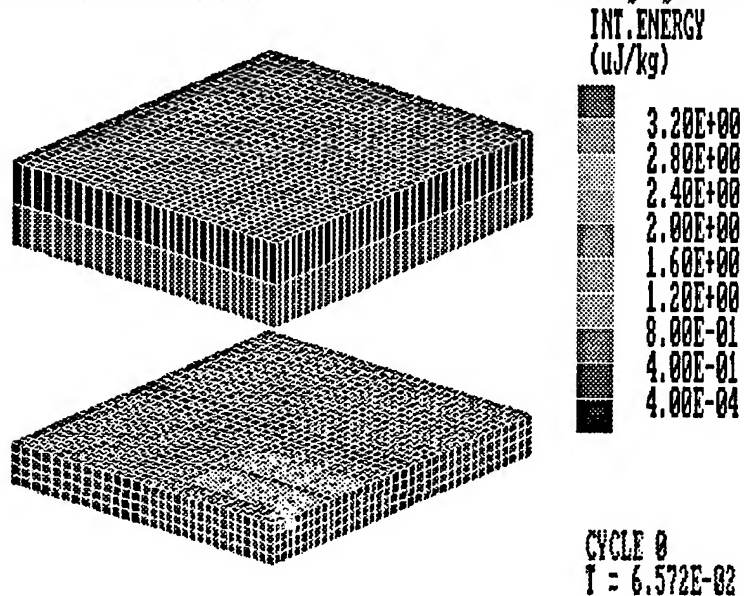


Figure 10c. Location of explosive sites.

AUTODYN-3D Version 2.1.0E

Century Dynamics Incorporated

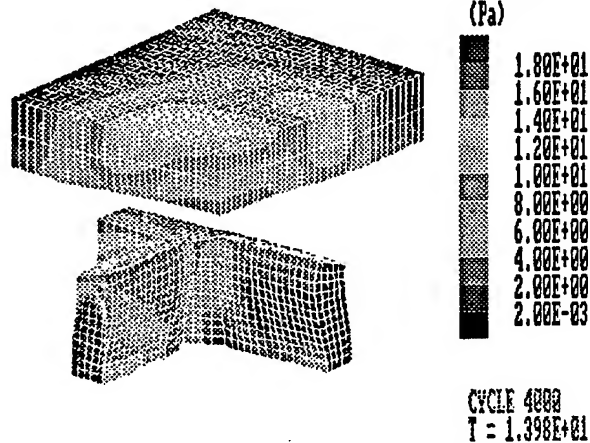


Figure 10d. Deformation of walls and roof (explosive/air not depicted)

## 11. OKLAHOMA CITY FEDERAL BUILDING BOMBING CASE STUDY(2D and 3D EULER)

This is a detailed case study which illustrates the methodology one may employ to effectively quantify the blast loads for a "real" case. The above numerical techniques are employed in one, two, and three-dimensions.

### 11.1 Objectives

On April 19, 1995 a terrorist explosive device was detonated outside the Alfred P Murrah Federal Building in Oklahoma City causing severe damage to 75 buildings. Nearly half of the 200ft x 70ft federal building tower was brought down along with a major loss of life. To gain further information relating to the loads which the explosive device imposed on the building, a numerical analysis of the event using the AUTODYN-2D and AUTODYN-3D analysis software was carried out.

The objectives of this work were to:

- Model the detonation and expansion of a 4800lb ANFO threat.
- Assess the loads that a 4,800lb ANFO explosion would impose on the Murrah Building assuming the facades to be rigid. This approach allows the overall load levels around the building to be established without the added expense and complexity of a coupled analysis with the building structure responding to the blast loading.

- Use only the information available in public domain literature
- Achieve the above objectives using numerical techniques available in the AUTODYN-2D and AUTODYN-3D analysis software using a minimum amount of time and effort

## 11.2 Numerical Analysis

Two analyses were performed: A "Large" model which encompassed the entire building and parking structure and a "Small" model with higher resolution which included only the north facade and east corner of the building.

Each numerical analysis was performed in two steps:

- Modeling of the 1D detonation and initial expansion of the 4,800lb threat before interaction with the building takes place using AUTODYN-2D
- Remap the results of the 1D analysis into a 3D numerical grid and analyze using AUTODYN-3D

The loads on the building can then be assessed from the results of the analysis by means of contour plots of pressure over the surface of the building and recordings of pressure variations with time at designated gauge points in the numerical grid.

### 11.2.1 Detonation/Initial Expansion of device

- The explosive device used at Oklahoma City was estimated to consist of 4,800lbs ANFO + 1 cartridge of TNT as a booster
  1. The explosive performance and in particular the numerical modeling of ANFO are not well understood at this time. Therefore it was assumed to use a TNT equivalency of 0.6lb of TNT per lb of ANFO
  2. Use the well established JWL equation of state data for TNT
  3. Assume device is resting on rigid ground
- Model the detonation/initial expansion of the 2880lb equivalent TNT device using AUTODYN-2D



1. Assume the actual device is a hemisphere. Model the initial charge as a 1D sphere of twice the actual charge weight ( 5760lb )
2. Use the Euler processor of AUTODYN-2D and assume a 1D spherically symmetric expansion of the device.
3. Figure 11 shows the 1D AUTODYN-2D model setup
4. Create a remap file of the analysis results before the blast wave reaches the end of the 1D grid to be subsequently remapped into the 3D program.

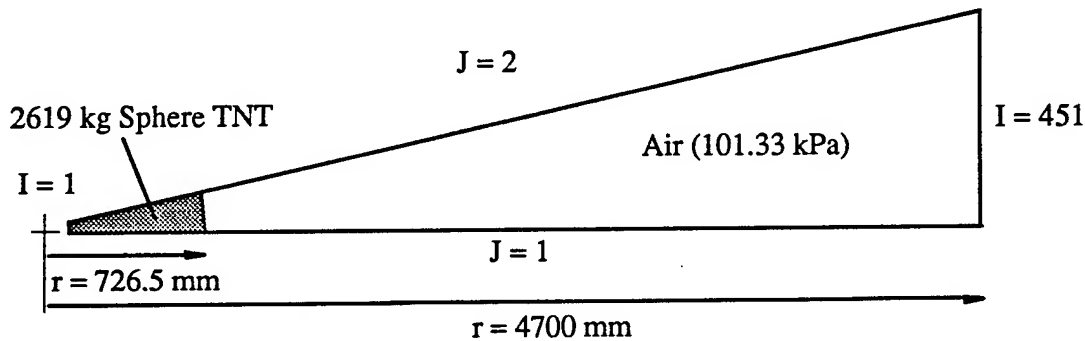


Figure 11. AUTODYN-2D, 1D Spherically Symmetric Model Setup

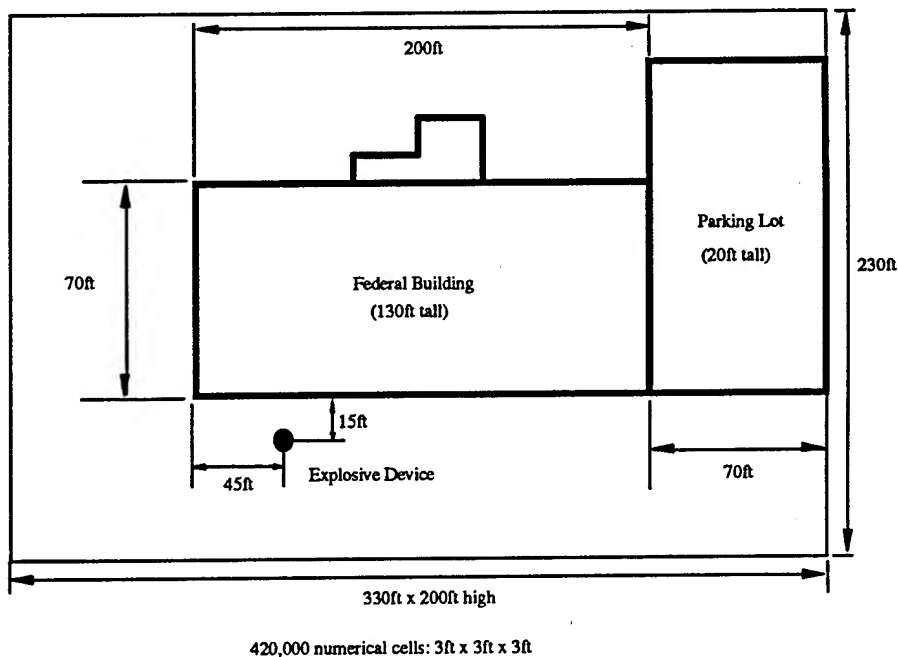


Figure 12. Geometry and Extent of Numerical Model used for Full 3D Numerical Analysis (Large Model)

### **11.2.2 AUTODYN-3D Analysis of Blast Wave Expansion/Interaction with Building (Large Model)**

1. Use the 2nd Order Euler, FCT processor - Computationally efficient allowing the use of relatively large computational domains.
2. Model the main building features using rigid obstacles (Unused cells). The dimensions used are shown in Figure 12.
3. Fill the remaining computational domain with air at ambient atmospheric conditions. Use an Ideal Gas Equation of State.
4. Apply the initial conditions of the blast wave to the numerical grid by importing the remap file(1D expansion) created at the end of the AUTODYN-2D analysis.
5. Specify target points(gauge locations) for recording variable time histories
6. Execute the analysis

### **11.2.3 Large Model Results**

The analysis required 12 hours of CPU time running on a DEC Alpha/3000-400 workstation. The final results are shown in Figures 13 and take the form of:

- Sequence of pressure contour plots - front elevation of building
- Sequence of pressure contour plots - rear elevation of building
- Pressure time history plots at selected gauge points

Note that it is also possible to plot contours, isosurfaces and histories of other variables such as impulse and dynamic pressure. Velocity vectors of the flow field can be also be depicted.

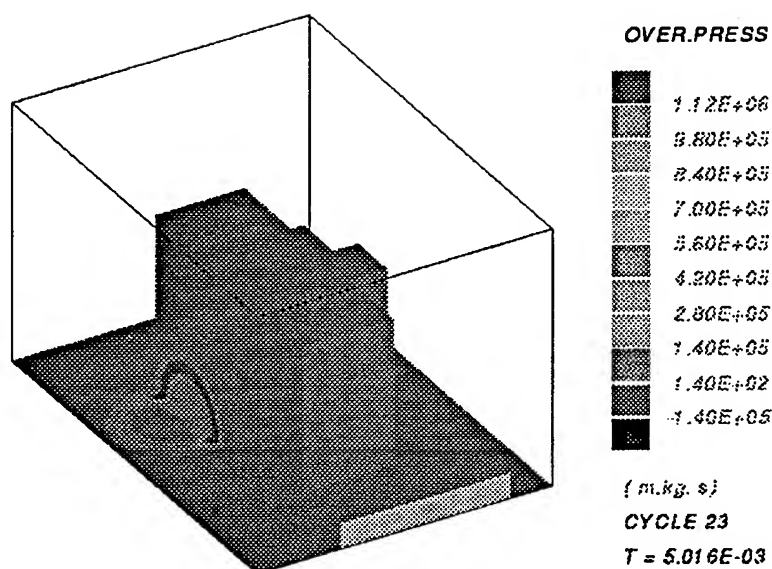
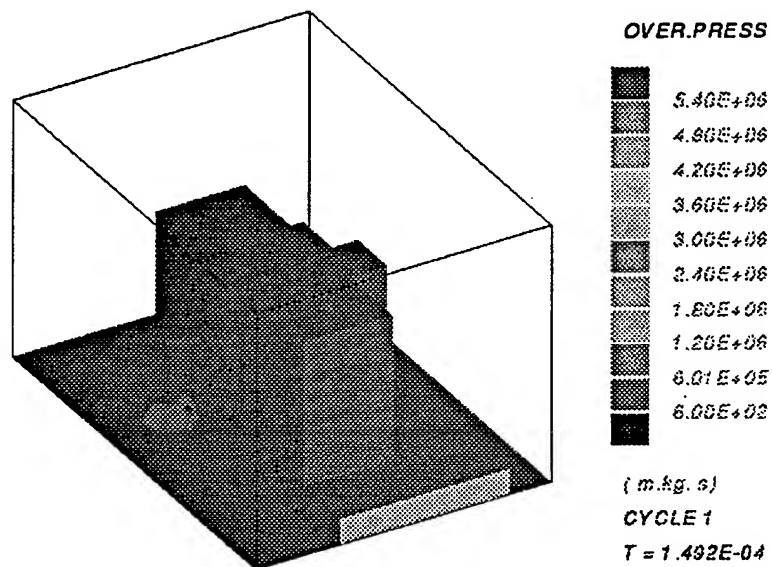


Figure 13. Full building analysis, time sequence of blast overpressure, front elevation

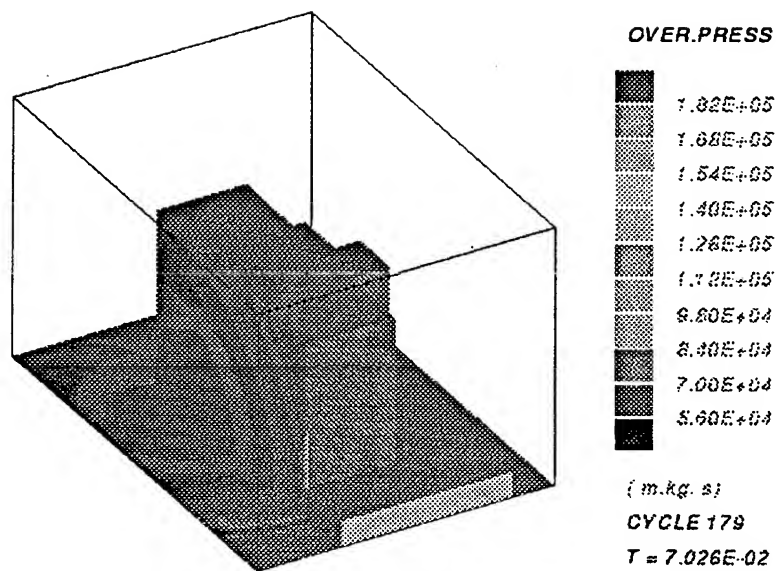
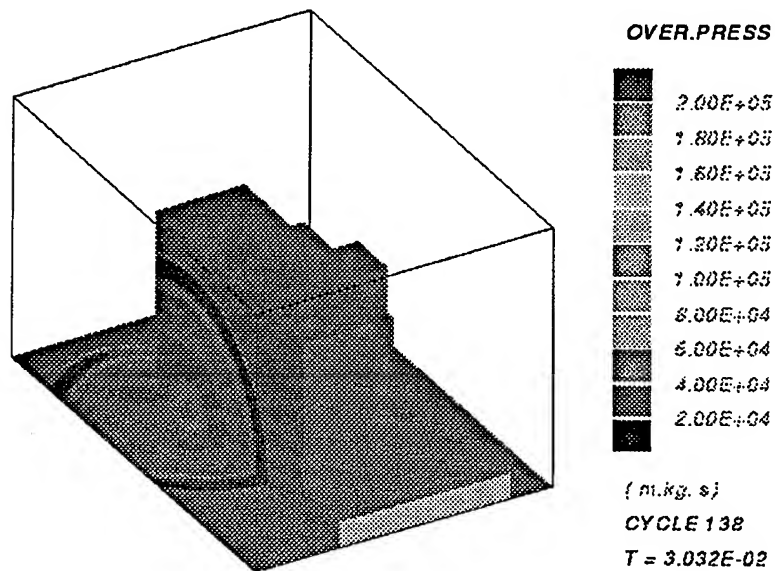


Figure 13. cont'd: Full building analysis, time sequence of blast overpressure, front elevation

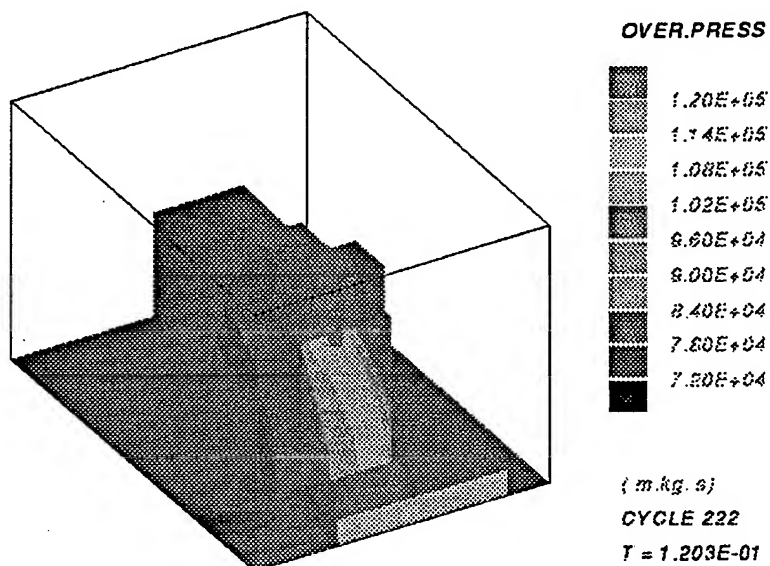


Figure 13 cont'd: Full building analysis, time sequence of blast overpressure, front elevation

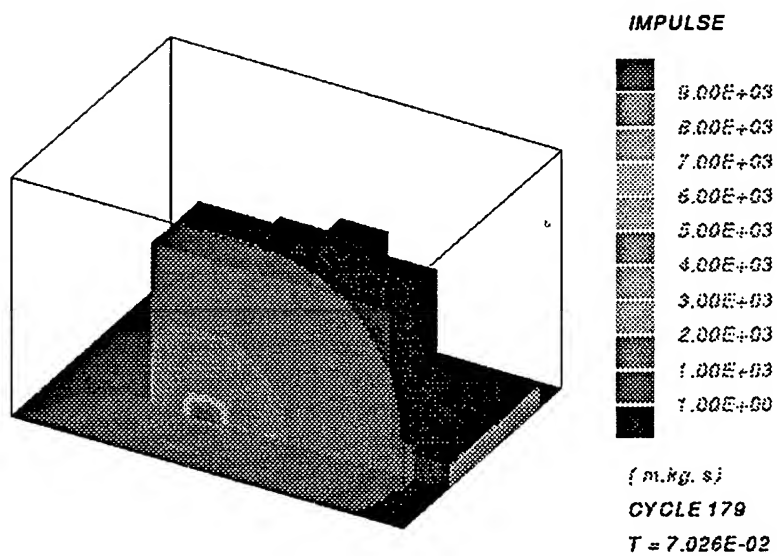


Figure 14: Full building analysis, impulse at 70 msec, front elevation

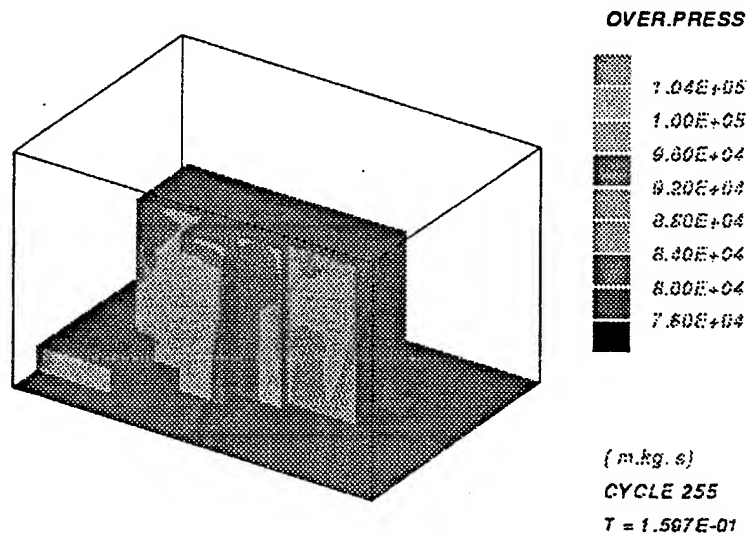


Figure 15. Full Building analysis, at .16 secs, rear elevation

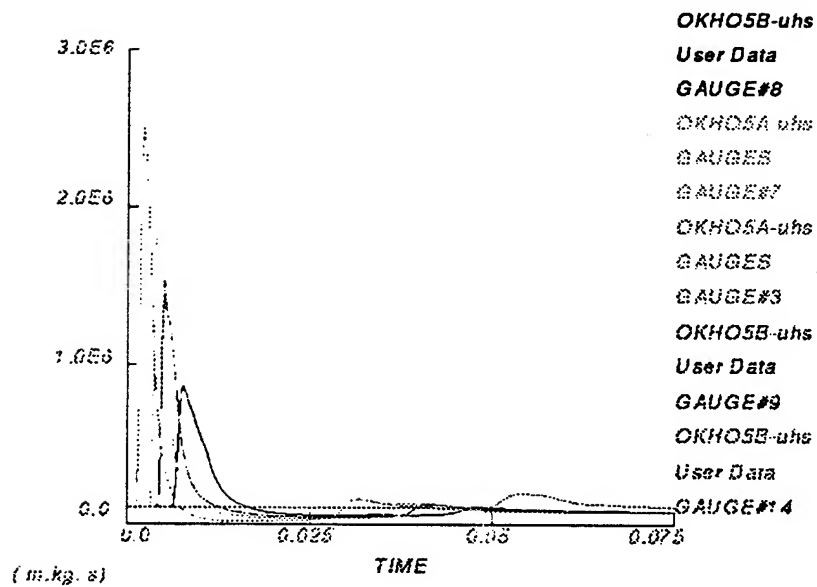


Figure 16. Typical pressure records at various gauge locations

#### 11.2.4 Large Model Conclusions

1. It is not possible to accurately resolve the peak pressures and impulses at all locations of the building using a single analysis because of the large range in scaled distances involved in this particular problem:
  - To accurately resolve the peak pressures at all length scales it is estimated that approximately 250,000,000 cells of size 0.125m x 0.125m x 0.125m are required.
  - Not possible with computing power available at this time.
2. Therefore, for a full investigation into the loading applied to the building, one needs to run several analyses covering different scale ranges:
  - Use the results of the sensitivity study to establish the number and extent of each analysis model to give the required accuracy.
  - For example, it is suggested that the use of at least three analyses to obtain reasonably accurate predictions over all the building facades should be used:
    - i) Entire building (1m x 1m x 1m cells)
    - ii) North facade and East corner of building (0.5m x 0.5m x 0.5m cells)
    - iii) North facade local to device (0.125m x 0.125m x 0.125m cells) - extent depends on particular feature of the building which is of interest

#### 11.2.5 AUTODYN-3D Blast Wave/Interaction with Building (Small Model)

As suggested above, a local analysis of the North facade and East corner of the building (see Figure 17) was also performed using double the spatial resolution relative to the Large Model. The AUTODYN-3D setup and a summary of the Small Model results are shown in Figures 18.

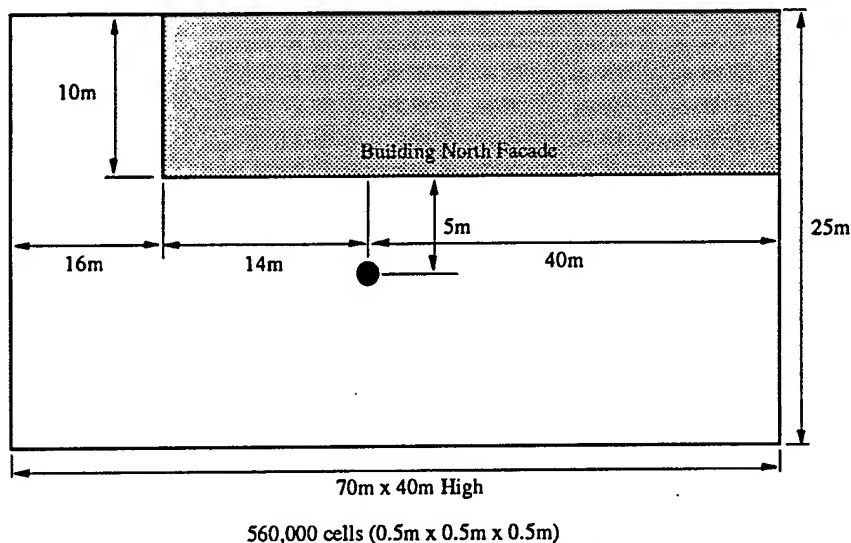


Figure 17. Geometry and Extent for 3D Numerical Analysis of the North Facade and East Corner (Small Model)

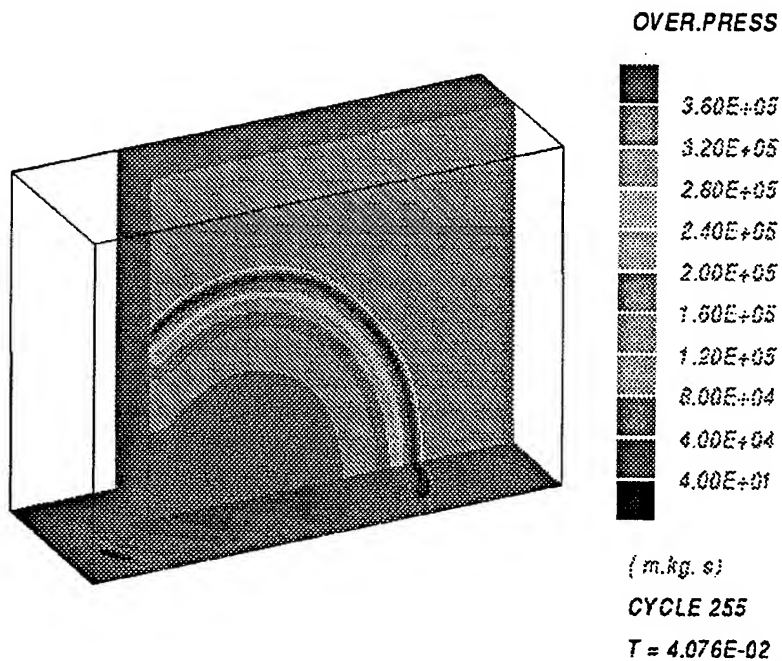
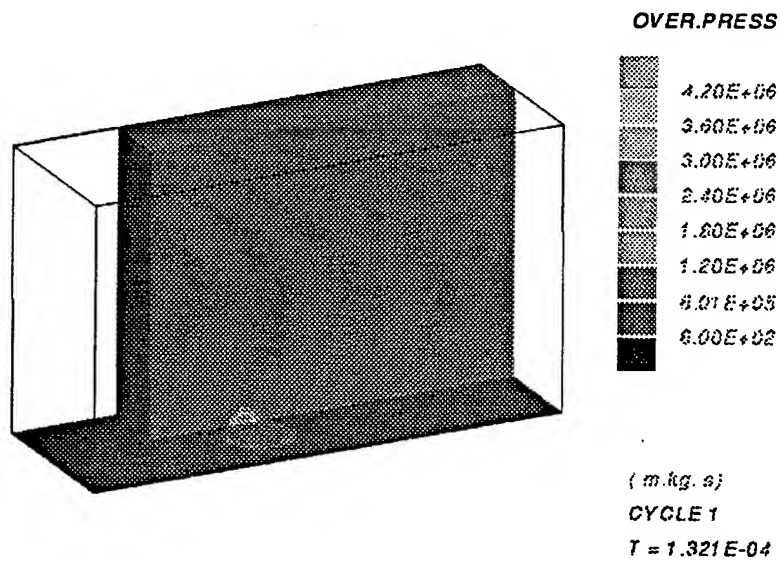


Figure 18. Small model overpressure results



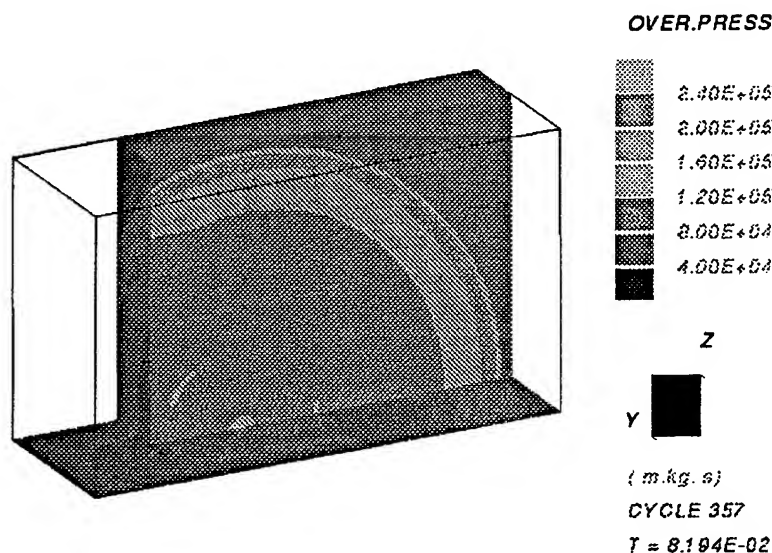


Figure 18 cont'd. Small model overpressure results

### 11.3 Oklahoma City case study conclusions

Several numerical analyses of the bombing of the Alfred P Murrah Federal Building in Oklahoma City were successfully carried out. The main conclusions to be drawn are:

- The AUTODYN-2D software can be used for the analysis of the detonation and initial expansion of HE assuming a spherically symmetric expansion.
- The results of the AUTODYN-2D analysis can be remapped into the AUTODYN-3D numerical grid as initial conditions.
- The AUTODYN-3D FCT Euler processor can be used efficiently to simulate the expansion and interaction of a blast wave against rigid buildings and surfaces. This approach allows the overall load levels around the building to be established without the added expense and complexity of a coupled analysis with the building structure responding to the blast wave.
- It is not possible to accurately resolve the peak pressures and impulses on all building surfaces using a single model of the whole building because of computer memory restrictions. However, a series of localized models can be used to accurately resolve the solution in the areas of concern.

- The loads on the building can be assessed by means of contour plots of pressure/impulse over the building surfaces and via recordings of variable time histories at specified locations in the numerical grid.

## 12. SUMMARY

Currently available analytic and numerical techniques can be used to effectively assess the loadings on commercial buildings from the detonation of high explosive devices. Numerical techniques encompassing Eulerian, Lagrangian, ALE, and structural representations can address different aspects of the loading and response of buildings. Moreover, large numerical models on the order of  $10^6$  cells can now be routinely handled without the requirement of a supercomputer. The applications discussed herein were all calculated on modern PC's and workstations.

Thus, sophisticated and detailed blast load analyses can and should be regularly performed. The accurate prediction of these loads provides the building designer with the necessary information to allow for better protection for the building and its people.

## References:

- 
- <sup>1</sup> TM5-855-1 "Fundamentals of Protective Design for Conventional Weapons", Department of the Army, Technical Manual (1986)
  - <sup>2</sup> Zintilis et al, "Protection of Commercial Buildings against Blast and Ballistic Threats", 7th International Symposium on Interaction of the Effects of Munitions with Structures, Mannheim (1995).
  - <sup>3</sup> AUTODYN<sup>TM</sup> software for non-linear dynamics, proprietary to Century Dynamics (1985-1995).
  - <sup>4</sup> AutoReaGas<sup>TM</sup> software for reactive gas dynamics and blast analysis, proprietary to Century Dynamics / TNO (1994-1995).
  - <sup>5</sup> W.P.M. Mercx et al, "Simulation of Vapour Cloud Explosion and Subsequent Blast Propagation in Built-up Areas", TNO/INERIS and Century Dynamics (1995).
  - <sup>6</sup> "AutoReaGas<sup>TM</sup> Compendium of Papers", AutoReaGas User Documentation, TNO/Century Dynamics (1995).
  - <sup>7</sup> N. Birnbaum et al, "Calculation of Blast Loading in the High Performance Magazine with AUTODYN-3D", 26th Department of Defense Explosive Safety Seminar, Miami (1994).

# **BLAST WAVE ATTENUATION IN TUNNELS AND EXPANSION CHAMBERS CONTAINING DISCRETE ROUGHNESS ELEMENTS**

**PD Smith<sup>\*</sup>, P Vismeg<sup>\*</sup> and L Tingey<sup>\*\*</sup>**

<sup>\*</sup>Civil Engineering Group, School of Mechanical Materials and Civil Engineering,  
Cranfield University, Royal Military College of Science, Shrivenham, Swindon,  
Wiltshire, SN6 8LA, United Kingdom (Tel 01793 785341)

<sup>\*\*</sup>Corps of Royal Engineers.

## **ABSTRACT**

The attenuation of blast waves as they pass along tunnels, ducts and expansion chambers has been the subject of a number of recent studies whose aim has usually been to identify means of providing protection to a sensitive facility. Such studies have generally concentrated on smooth-walled tunnels and chambers or those which have relatively small-scale distributed wall roughness. This paper presents the results of an investigation into the attenuation of blast waves along tunnels and through expansion chambers which have been equipped with relatively large discrete roughness elements.

A small shock tube was used to provide a repeatable simulated blast wave pressure-time history which became the input waveform to a scale model of either a straight tunnel or an expansion chamber. Measurements of overpressure-time histories at the closed far end of the tunnel and expansion chamber were made. Experiments were first carried out with roughness elements absent to establish a basis for comparison. When roughness elements were installed, they effectively reduced the cross-sectional area of the tunnel or chamber. These elements were uniformly-distributed along the tunnel in both symmetrical and staggered arrangements. In the case of the expansion chamber, up to five steel "baffle-plates" could be installed for any one experiment.

In an attempt to correlate the results from experiments that involved a range of different configurations a non-dimensional "attenuation coefficient" based on system geometry was developed. Graphs of non-dimensionalised peak reflected overpressure and reflected overpressure impulse measured at the end of the tunnel and at the back wall of the expansion chamber were produced. From such information the effect of the different discrete roughness elements could be assessed and potential attenuation geometries identified that would provide good protection yet still allow access to the facility.

## Introduction

There has been a considerable interest in recent years in the performance of tunnel systems as a means of providing protection from blast loading. The reason for such interest was highlighted by Ullrich [1] who suggested that current conventional munitions (such as those deployed during the conflict in the Gulf in 1991) would have difficulty in defeating a buried facility or one located at the end of a tunnel-like entranceway. There have been a number of studies into the blast attenuating potential of tunnel systems. Some of the more recent tunnel studies include those by Schecklinski-Glück [2] and Binggeli *et al* [3] while Heilig [4] has reported investigations concerned with expansion chambers. The majority of such studies have been involved with smooth-walled tunnels and chambers. When roughness has been considered it has generally been as uniformly-distributed roughness (formed, for example, from the natural rock through which the tunnel has been driven) as reported by Skeltorp [5]. Recently, however, Smith and Teo [6] presented information about the attenuation in blast resultants produced by discrete roughness elements (sometimes termed "excrescences") uniformly spaced along the walls of a tunnel. Results from this work suggested that optimum attenuation was produced with an excrescence height to spacing ratio of 0.5.

This paper presents the results of studies of the performance of straight, model-scale tunnels located at the end of a small shock-tube facility when excrescences of different dimensions are introduced onto the tunnel wall in a number of different configurations. In addition, the performance of an expansion chamber attached to the shock tube and equipped with a variable number of "baffles" (steel plates with different sized apertures) is discussed.

## Experimental Apparatus

The shock tube used to provide a simulated blast wave at the entrance to the tunnel or expansion chamber is that described by Smith and Pennelegion [7] which, with some modification, was recalibrated by Hunter [8]. Using helium as the driver gas, a typical reflected pressure-time history is shown in Figure 1 where it should be noted that the "useful" duration of the pulse is about 16 milliseconds after which subsequent reflections arrive at the pressure transducer located at the end of the shock tube.

The model tunnel, which was 500mm long, 50mm wide and 50mm deep was constructed from rolled hollow section tubing of wall thickness 3mm by Tingey [9]. Slots were cut at 40mm intervals in the top of the tunnel to allow the introduction of roughness elements. If a particular slot was not equipped with a roughness element a blanking piece was placed in the slot. Roughness and blanking pieces were clamped firmly in place during an experiment.

Figure 2 shows the tunnel and an example of the excrescences used. The pressure measurements reported here were made using a Kistler 603B pressure transducer located flush with the end of the tunnel, data being recorded by a Nicolet transient digital storage oscilloscope and stored on floppy disk for subsequent analysis.

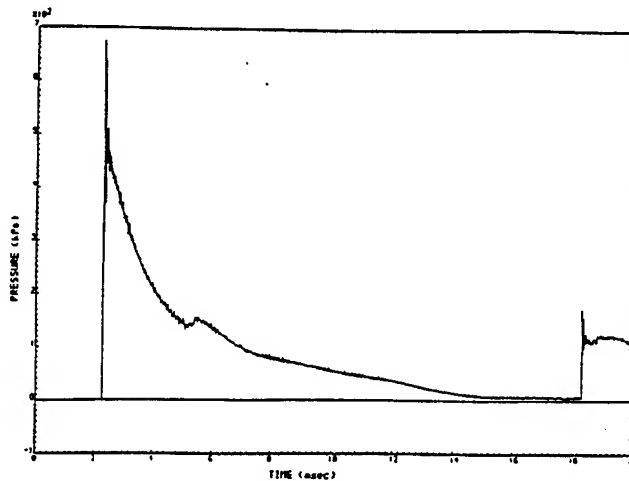


FIGURE 1

The model expansion chamber, which was 250mm long, 141mm wide and 142mm high, was constructed by Vismeg [10] from 6mm thick steel plate welded together.

Using the same technique as for the tunnel, slots were cut in the top of the tunnel to allow the introduction of 6mm thick baffle plates. Pressure measurements were made at the centre of the end wall of the expansion chamber which is shown in Figure 3 together with an example of the baffle plates used.

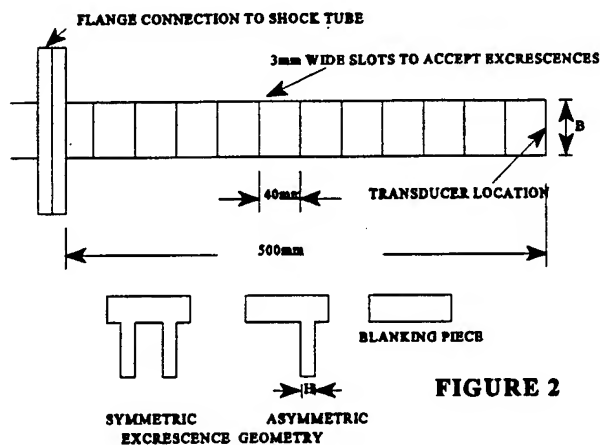


FIGURE 2

### Experimental Programme

The tunnel was equipped with excrescences in the following configurations, examples of which are shown in Figure 4:

- (a) Symmetrical: increasing numbers uniformly spaced
- (b) Asymmetric: increasing numbers uniformly spaced (centred halfway along the tunnel)
- (c) Asymmetric: groups of 3 and 5 elements centred at different locations
- (d) Randomly distributed.

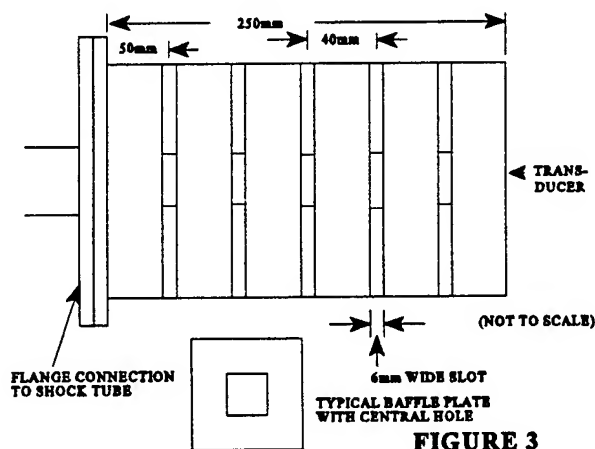


FIGURE 3

The expansion chamber was equipped with baffle plates either singly or with all five in place. When just one was used,

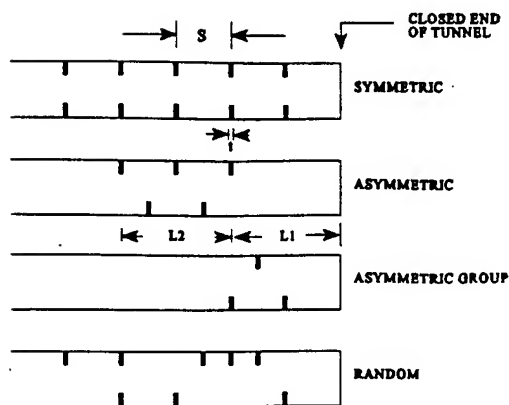


FIGURE 4

experiments were conducted with it in each of the five available positions.

For each experiment the "standard" simulated blast was produced by the shock tube and a pressure-time history was recorded. Between shots the system was purged of the helium driver gas mixture to ensure that each blast wave propagated into an air-filled tunnel or chamber.

## Results

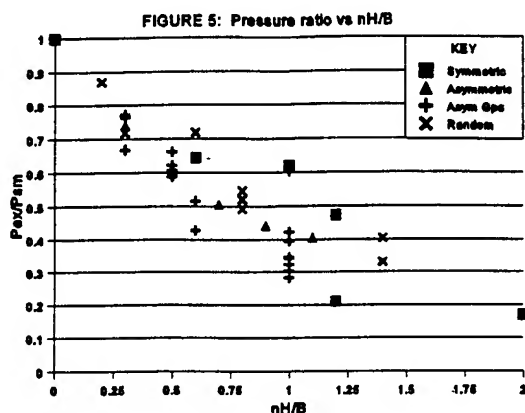
The experimental programme was designed such that a wide range of excrescence geometries and locations could be studied with a view to developing general rules about the requirements for optimum blast wave attenuation by a tunnel or chamber. Factors that were considered to be of possible significance were the number of excrescences present ( $n$ ), the distance they extended across the tunnel ( $H$ ) and their thickness ( $t$ ), the spacing between each roughness element or baffle plate ( $S$ ), the location of the elements relative to the end of the tunnel ( $L_1$ ) (of significance in, for example, categories b, c and d for the tunnel) and the length of tunnel over which the elements extended ( $L_2$ ) (of possible relevance in categories b and c for the tunnel).

### (a) Tunnel

A number of different combinations of these parameters were formed with regard to each's physical significance. For example, the group  $[2HnS]/[L_2(L_1 + L_2)]$  could be considered to represent the ratio of the extra surface area produced by the excrescences to the length of tunnel in which the excrescences are located  $[2Hn/L_2]$  multiplied by the ratio of the volume of the tunnel between the elements to the total volume of tunnel beyond the location of the first element  $[S/(L_1 + L_2)]$ . Alternatively, the group  $[(2H + t)L_2n]/[(L_1 + L_2)L_1]$  could be considered to represent the ratio of the area of the excrescences "intercepting" the blast to the surface area of the smooth tunnel  $[(2H + t)n/(L_1 + L_2)]$  multiplied by a "position" ratio  $[L_2/L_1]$ . There are, of course, a number of other possibilities. Such groups could be thought to account for the size and number of elements and their location in the tunnel relative to the end. When formed for the various tunnel configurations and plotted against either the ratio of the peak reflected overpressure with excrescences present  $P_{EX}$  to the value recorded with a smooth tunnel  $P_{SM}$ , or the associated impulse ratio  $(I_{EX}/I_{SM})$ , these apparently comprehensive geometrical factors correlated disappointingly.

It was concluded that there were factors that had much greater influence on the blast wave than others and the formation of such complex groupings masked the

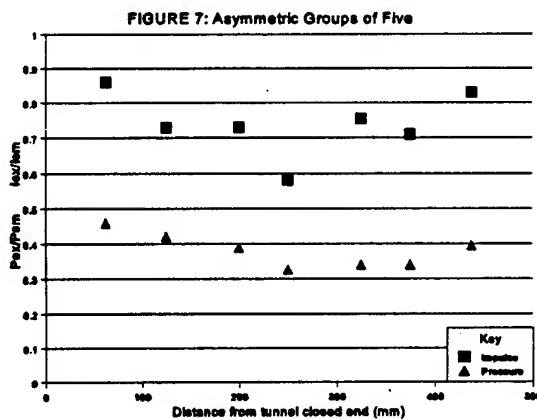
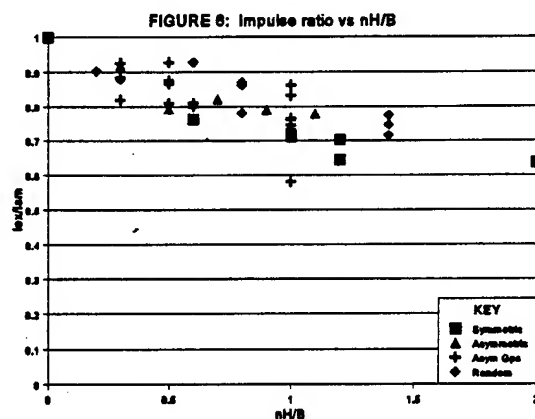
important aspects of the system. Consequently, a much simpler tunnel geometry factor was formed as  $[nH/B]$  representing the number of excrescences available times the ratio of the excrescence height  $H$  to tunnel width  $B$ . In the case of symmetrical dispositions of roughness,  $H$  was set equal to the actual height of the element. For asymmetric configurations,  $H$  was taken as half the physical value. Figures 5 and 6 show the pressure and impulse ratios plotted against this parameter.



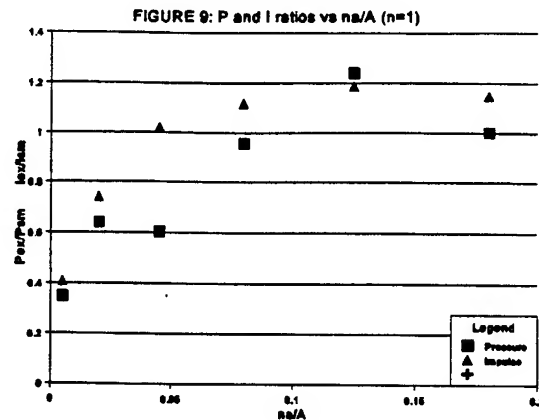
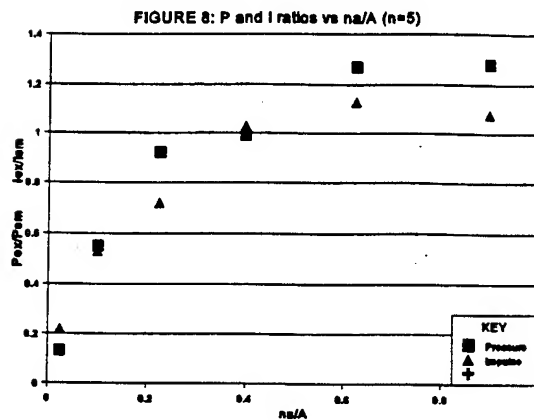
It would appear that there is some dependence on element location within the tunnel as seen from the spread of results for, say,  $nH/B = 1$ . Most of these results were from configuration category (c). For groups of 5 asymmetric excrescences moved to different locations along the tunnel Figure 7 shows that location may affect resulting pressure and impulse but that the influence is possibly of secondary significance: the number and size of excrescences is of paramount importance.

### (b) Chamber

Although it was attractive to view the chamber as a short, fat tunnel, the particular geometry of the baffle plates did not allow the simple definition of an excrescence height. Attempts to form comprehensive groups as those discussed for the tunnel met with similar problems of poor correlation. However,



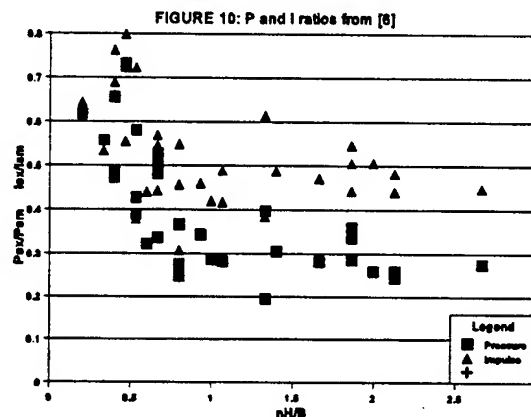
a simple ratio of the area of the hole in the baffle ( $a$ ) to the cross-sectional area of the smooth chamber ( $A$ ) can be formed and modified to account for the number of baffles ( $n$ ): the geometrical factor here is  $[na/A]$ . Just as for the tunnel, pressure and impulse ratios are plotted against the geometry ratio as shown in Figures 8 for five baffles ( $n=5$ ) and in Figure 9 for a single baffle ( $n=1$ ). In this latter case the position of the single baffle in the box did not seem to make a significant difference to the resultant signal at the transducer. As a consequence, the points shown are averages from all five positions in the chamber.



## Conclusions

The interpretation of the results obtained for the tunnel is relatively straightforward. As the number of excrescences increases or as their height increases, the attenuation of the blast wave resultants at the end of the tunnel increases. Other factors such as the location of the excrescences relative to the end of the tunnel and the length of tunnel occupied by them are of smaller significance when compared with these considerations.

Although the experiments were conducted using a different tunnel and with high explosive charges providing the blast wave at the tunnel entrance, the data from [6] when plotted in the manner described above do show a correlation: as  $nH/B$  increases so the pressure and impulse ratios reduce as shown in Figure 10. It should be noted that control of the input blast wave was much less easy than in the work described here and there would undoubtedly have been some variation in the non-





dimensionalising pressure or impulse for each experiment. Here an average from a number of experiments with no excrescences present was used as  $P_{SM}$  and  $I_{SM}$  for each experiment with roughness present. This could be a significant factor in producing the spread of results.

In the case of the expansion chamber, the effect of the baffles is not as clear though it is evident that, as the size of the hole in the baffle reduces, so the attenuation increases. The use of multiple baffles does not appear to lead to a significant change in blast attenuation. More puzzling is the apparent enhancement of pressure and impulse when the baffle has a hole that is relatively large compared to the chamber area, though it should be noted that even the largest baffle hole was only 18% of the chamber cross-section. An explanation for this effect could be that multiple reflections are set up between the baffle nearest the transducer leading to an enhanced overpressure and impulse in some circumstances as the effective duration of the pulse is increased. Figure 11 shows the pressure-time history for a baffle with a 30mm x 30mm hole at the location closest to the entrance to the chamber.

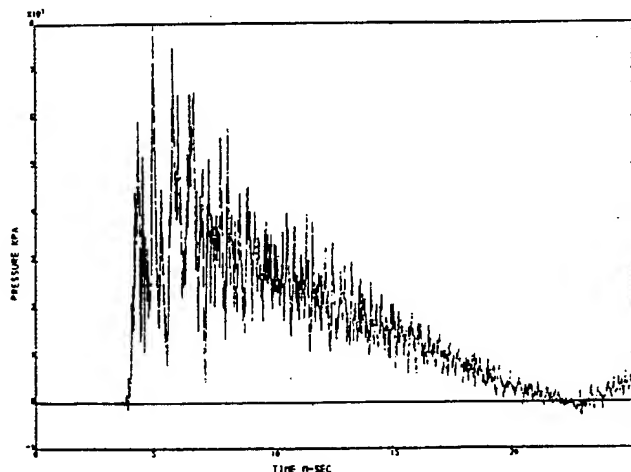


FIGURE 11

The peak reflected overpressure occurs about one millisecond after the arrival of the first peak at the transducer thus indicating the process described. Note should be made of the subsequent complex reverberating shocks within the chamber.

These results suggest that care should be taken in determining baffle hole size: it may be that further investigation with somewhat larger apertures is required to determine at what area ratio attenuation (rather than enhancement) is re-established. Also, it is suggested that further study would be desirable to develop a simple method of categorising the performance of widely-different attenuating systems, possibly based on the groups used in this study.

## References

1. Ullrich GW *Evolution of hardened facilities and threats against them* Keynote Address, 7th International Symposium Interaction of the Effects of Munitions with

Structures, Mannheim, Germany (1995)

2. **Schecklinski-Gluck G** *A Calculation procedure for blast in tunnel branchings developed from experiments and AUTODYN calculations* Proceedings of the 7th International Symposium Interaction of the Effects of Munitions with Structures, Mannheim, Germany (1995)

3. **Binggeli E, Schläpfer D** *Blast wave propagation through tunnel systems* Proceedings of the 13th International Symposium on Military Applications of Blast Simulation, The Hague, Netherlands (1993)

4. **Heilig W** *About the attenuating effects of expansion chambers in channels.* Proceedings of the 13th International Symposium on Military Applications of Blast Simulation, The Hague, Netherlands (1993)

5. **Skeltorp AT** *Airblast propagation through tunnels and the effects of wall roughness* Norwegian Defence Construction Service Note 103/75 (1975)

6. **Smith PD, Teo LC** *Blast wave transmission along rough-walled tunnels* Proceedings of the 13th International Symposium on Military Applications of Blast Simulation, The Hague, Netherlands (1993)

7. **Smith PD, Pennelegion L** *A tailored shock tunnel for the investigation of shock wave propagation in solids and foams* Proceedings of the 6th International Symposium on Military Applications of Blast Simulation, Cahors, France (1979)

8. **Hunter CW** *Study of RMCS shock tube facility* 44 Degree Course Project Report RMCS 1992

9. **Tingey L** *A study of blast wave attenuation in rough-walled tunnels* 46 Degree Course Project Report RMCS 1994

10. **Vismeg P** *The attenuation of shock waves by plate/expansion chamber combinations and a proposed method of passive attenuator classification* No8 MSc Weapons Effects on Structures Research Project Report 1994

**INTERMEDIATE-SCALE UNDERGROUND MAGAZINE TESTS:  
RESULTS OF AIRBLAST STUDIES FROM AN  
IDEALIZED DETONATION EXPERIMENT**

Charles E. Joachim  
Landon K. Davis  
U.S. Army Engineer Waterways Experiment Station  
Vicksburg, Mississippi 39180-6199

**ABSTRACT**

A series of 1/3-scale explosive tests (up to 2,600 kg net explosive weight) were conducted at the Lynchburg Mine, near Magdalena, NM, to provide airblast data from detonations which simulated accidental explosions in underground munitions storage chambers. In addition, computer calculations were performed for selected experiments to validate hydrocode predictive models. The extensive data base developed from these tests provide insights into blast propagation in confined volumes of multi-chamber underground ammunition storage facilities and the relative effect of shock and gas pressures that define the external hazard Quantity-Distance. This paper presents the analyses and discussion of the measured and calculated data.

**INTRODUCTION**

The Joint U.S./Republic of Korea (ROK) R&D Program for New Underground Ammunition Storage Technologies (UAST) is a comprehensive research effort to evaluate design concepts for underground magazines which can significantly reduce the airblast and fragment/debris hazards of an accidental explosion. In conjunction with this program, a series of decoupled detonations were conducted in an intermediate-scale (1/3-scale), multi-chamber, underground facility to measure the airblast hazards and evaluate the accuracy of airblast prediction techniques. An idealized detonation experiment, named the "No Excuses" test was conducted by the U.S. Army Engineer Waterways Experiment Station (WES) to evaluate the accuracy of numerical prediction methods. Measured airblast data are compared to calculations made with SHARC (first principles, hydrodynamic, finite difference, numerical code with second order accuracy) and BLASTX (an empirically based airblast prediction code).

The U.S. portion of the UAST program was funded by the Office, Secretary of Defense and the U.S. Army. The SHARC hydrocode calculations of the "No Excuses test were funded by the KLOTZ Club, which is an ad hoc committee representing the interests of France, Germany, Norway, Sweden, Switzerland, the United Kingdom, and the U.S. in the area of military explosives storage safety.

## OBJECTIVE

The objectives of the "No Excuses" experiment was to evaluate the accuracy and of numerical airblast prediction techniques when applied to an idealized test configuration.

## DESCRIPTION OF EXPERIMENT

The "No Excuses" test involved the detonation of a 2,569.5 kg charge of Composition B explosive, simulating an accidental explosion of ammunition stored inside an underground magazine. The experiment was conducted on 26 May 1994, in a 1/3-scale storage chamber and tunnel system constructed in the Linchburg Mine near Magdalena, NM. The explosive loading density was 37.3 kg/m<sup>3</sup> of chamber volume. The site layout, showing the main mine drift and test Regions A and B, is given in Figure 1. Active measurements included airblast pressure histories in the test chambers and tunnel drifts, and the external "free-field" airblast along the 0, 5, and 10-degree azimuths, measured in a clock-wise direction from the portal.

## TUNNEL AND CHAMBER

The test chambers and their access tunnels were excavated in competent limestone. The experiment was conducted in Chamber No. 4 (Region A). Nominal dimensions of the test chamber were 8.5 m (length), by 4 m (width) by 2 m (height), with a volume of 75.8 m<sup>3</sup> and an average cross-sectional area of 8.92 m<sup>2</sup>. The ceiling of the test chamber was rock bolted and covered with wire mesh and steel mats after excavation to stabilize the chamber for repeated detonations. The "No Excuse" test was the fifth experiment conducted in Chamber No. 4. The previous detonations, which involved smaller loading densities, destroyed most of the wire mesh and some of the steel mat on the rock surfaces of the chamber, leaving rock bolts as the primary support.

The chamber entrance tunnel was 5 m long, 1.35 m wide, and 1.5 m high, with a minimum cross-section of 2.38 m<sup>2</sup>. The average cross-section in the Linchburg Mine drift was 4.3 m<sup>2</sup>. The estimated total volume of the underground space was 3250 m<sup>3</sup>.

## EXPLOSIVE CHARGE

The explosive charge for the "No Excuses" test consisted of 180 blocks of Comp B explosive stacked on a wooden platform with a 203.2 mm layer of 192.2 kg/m<sup>3</sup> rock wool between the explosive and the plywood. The assembled charge was a rectangular parallelepiped 20 blocks long by 3 blocks wide and 3 blocks high. The charge was centered along the long axis of the chamber, with the center of the charge 1.05 m above the floor of the chamber.

A 0.8 m square sheet of C-6 detasheet was attached to the front vertical face (end nearest the chamber entrance) of the charge. Two Nonel initiators with 3.7 m Nonel lines attached

were taped to the detasheet at mid-height, each 0.2 m off the vertical center of the stacked charge. Each Nonel initiator was covered with a 50-mm square of C-6, placing the initiator between two layers of detasheet. The opposite ends of the Nonel lines were connected to 4.6 m length of detonator cord and in turn attached to two Nonel lines (dual priming the charge) which extended from the chamber to a point 10 m outside the portal where the electric bridge wire (EBW) detonators were attached for final arming.

### AIRBLAST INSTRUMENTATION

A total of 67 airblast gages were installed for the "No Excuses" experiment. A shock-mounted self-recording gage package (two transducers) was installed in the chamber rib (side wall mid-height, mid-length) to measure chamber pressure. Two similar packages were installed in the adjacent chambers (Chambers No. 1, 2, and 3) to record airblast pressures (Figure 2). The access drifts to the adjacent chambers (1, 2, and 3, Region A) were instrumented with two sets of co-located, side-on and total pressure transducers. One gage pair was positioned to measure the blast wave entering the access drift and the second pair measured the airblast wave flowing out of that chamber. Additional side-on and total pressure pairs were located in the left access (Region A, Figure 2), right access (region B) and main drifts to evaluate shock and gas flow throughout the underground facility.

Ten pressure transducers were installed outside the portal to measure airblast and flow parameters in the free-field. Side-on and total pressure were installed along the extended tunnel centerline at 5, 10, and 30 m from the portal. Additional side-on pressure gages were positioned along the 10 and 30 m arcs at 5 and 10 degrees (clock-wise) off the extended tunnel centerline.

### NUMERICAL MODELS

Numerical models were developed for the "No Excuses" experiment using SHARC<sup>1</sup> and BLASTX<sup>2</sup> (Britt, 1994). Independent SHARC models were developed by S-Cubed and the Ernst Mach Institut (EMI), Freiburg, Germany. The S-Cubed SHARC calculation used a two-dimensional, plane geometry model with perfect reflecting surfaces to model the detonation and airblast

---

<sup>1</sup> S-Cubed Hydrodynamic Advanced Research Code, developed by the S-Cubed Division of Maxwell Laboratories.

<sup>2</sup> BLASTX version 3, an empirical code for predicting airblast from detonations in multi-room structures and underground ammunition storage magazines.

propagation in Region A (Figure 1). A constant chamber and tunnel height of 1.95 m was assumed for this portion of the calculation. The two-dimensional, plane geometry model was coupled to a two-dimensional, cylindrical geometry model for the propagation of the blast wave (including turbulence) through the long main drift to the portal. The one-dimensional SAP (Spherical Air Puff) code was used to extend the calculation from just outside the portal into the free-field. The charge mass for the calculations was 2784 kg, giving a chamber loading density of 42 kg/m<sup>3</sup>.

The layout of the "No Excuses" experiment was modeled, for the BLASTX calculation, as a fifty-room complex, which was the maximum number of rooms allowed in the executable version of BLASTX. Britt (1994) suggests that BLASTX would efficiently model rooms with an aspect (length-to-width) ratio of 3:1. At greater distances from the source, the aspect ratio may be increased (doubled or tripled) without significantly affecting the airblast pressure prediction. However, fifty rooms was insufficient to model the vast extent of the underground layout of the experiment without significantly exceeding the recommended aspect ratio. Therefore, portions of the main drift and the entire volume of Region B (Figure 1) were modeled as single rooms with a large aspect ratio.

BLASTX models explosive charges as spherical sources. Therefore, the "No Excuses" explosive charge, which was actually a rectangular parallelepiped, was modeled as a single Composition B sphere positioned at the center of the chamber.

#### COMPARISON OF RESULTS

Calculated (hydrocode) and measured arrival time data are plotted versus distance in Figure 3. The calculated shock wave traveled faster than the measured, giving shorter arrival times. Good agreement is seen between the arrival time data calculated by S-Cubed and EMI.

Measured peak side-on overpressure is plotted versus distance in Figure 4. The data scatter is attributed to stagnation of the flow in adjacent chambers. These data have been removed from the plot shown in Figure 4, where the measured peak side-on overpressures are compared with calculated values. As shown in Figure 4, the calculated peak values are a factor of two higher than the measured data in the access drift outside the detonation chamber. This ratio increases to an order of magnitude as the distance from the source increases.

The BLASTX code was used to calculate gas pressures only (shock pressures were ignored) in the Lynchburg underground facility. BLASTX provides a good prediction of the measured peak data close-in to the detonation chamber. The ratio of the BLASTX-calculated values to measured peak data increases to a factor of two or three as the blast wave nears the Lynchburg Mine

drift (Figure 4). As the blast wave progresses through the Linchburg Mine drift towards the portal, this ratio decreases, as shown by the down-turn of the closely spaced triangular symbols, until the final room (Room 48) connecting to the portal is reached. Room 48 of the BLASTX model is long and narrow with an aspect ratio of 48.8. A similar shaped room (Room 49) models the volume of the access drift and chambers of Region B (aspect ratio of 43.8). These large aspect ratio's are necessary to complete the model within the 50-room limitation of the executable version of the BLASTX code. Therefore, the increase in calculated peak overpressure shown in the final interior room and the free-field is attributed to the very large aspect ratio of this room.

Measured peak side-on overpressure-impulse versus distance is plotted Figure 5. The real-time duration of the SHARC calculations was not sufficient to yield impulse data. The measured impulse data indicate a nearly uniform value of approximately 4 MPa-sec throughout Region A. The peak impulse decreased to approximately 0.6 MPa-sec at the portal, and rapidly decreased further as the blast wave enters the free-field.

Measured peak total pressure is plotted versus distance in Figure 6. An upper bound line is provided as a reference. Total pressure gages were placed in the left access drift (Region A), in the access drift to Chambers No. 1, 2, and 3, and in the Linchburg Mine drift. The gages in the chamber access drifts were positioned to measure both the flow into the chamber and the reverse flow back out of the chamber. These gages recorded lower peak pressures than those in the main line flow path (left access drift and Linchburg Mine drift) and are not shown in Figure 6.

A comparison between measured and calculated (by S-Cubed SHARC) peak total pressures in the left drift (Region A) is presented in Figure 6. The calculated values are an order of magnitude lower than the measured data.

### CONCLUSIONS

The "No Excuses" experiment was conducted in a realistic rock chamber in a multi-chamber underground facility of significant volume and extent. Peak pressure in the left access drift (Region A) is dominated close-in by the peak shock pressure. At greater distances (25 to 30 tunnel diameters), the shock pressures diminish and gas pressures dominate. The BLASTX code gives good agreement with measured data in the immediate vicinity of the detonation chamber. At greater distances, the calculated pressures are approximately a factor of two higher than the measured values. The 50-room limitation of the PC executable version of the BLASTX code resulted increased over-prediction of peak pressure at the exit and in the free-field.

The SHARC hydrocode predicted shorter arrival times and over predicted peak side-on overpressure, compared to the measured

data. The degree of over-prediction was a function of distance from the source; a factor of two close-in and increasing to an order of magnitude as the blast wave traversed the left access drift (Region A) and Linchburg Mine drift. Several potential causes for the over-prediction have been suggested and are being investigated. These include: 1) the SHARC modeled the walls of the underground facility as rigid, totally reflective surfaces and did not allow for energy losses through elastic/plastic movement of the storage (detonation) chamber walls; 2) the SHARC model did not account for energy losses through heat transfer to dust particles (video of gas flow out the portal show significant quantities of dust); 3) heat loss through conduction into the rock walls of the chamber; 4) heat loss vaporizing the humid atmosphere underground (Region A); 5) wall roughness (the SHARC model included a turbulence function and surface irregularities but not on the order of roughness found in the Linchburg Mine drift). Initial evaluation of these energy loss mechanisms indicate that heat losses to the walls of the chamber, vaporizing moisture, and tunnel roughness, summed together would account for a reduction in peak pressure of less than twenty percent. The effect of elastic/plastic chamber response and heat loss to dust are undergoing further study.

#### ACKNOWLEDGEMENTS

We appreciate the cooperation of the authorities at the U.S. Army Technical Center for Explosives Safety, the U.S. Army Engineer Waterways Experiment Station, and the Headquarters, U.S. Army Corps of Engineers that permitted us to prepare and present this paper for publication.

#### REFERENCES

1. J. R. Britt, and M. G. Lunsden; "Internal Blast and Thermal Environment from Internal and External Explosions: A User's Guide for the BLASTX Code, Version 3.0," SAIC 405-94-2, May 1994, Science Applications International Corporation, Theoretical Physics Division, San Diego, CA.
2. C. E. Joachim; Prediction of Airblast Pressures from Explosions in Underground Magazines Using BLASTX, Version 3," Twenty-Sixth DOD Explosives Safety Seminar, 16-18 August 1994, Miami, FL.



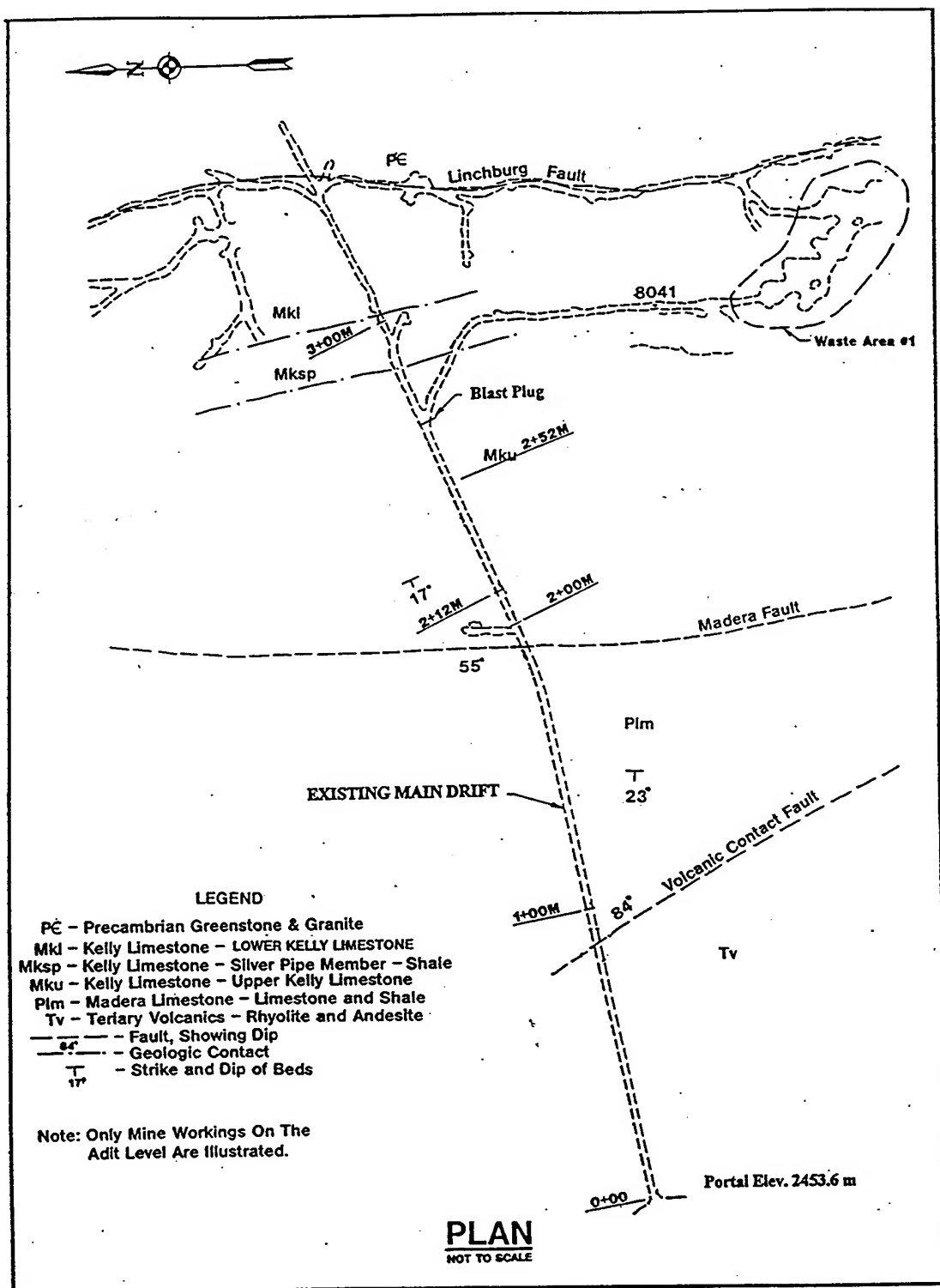


Figure 1. Test area layout and general geologic map of Linchburg Mine.

# REGION A

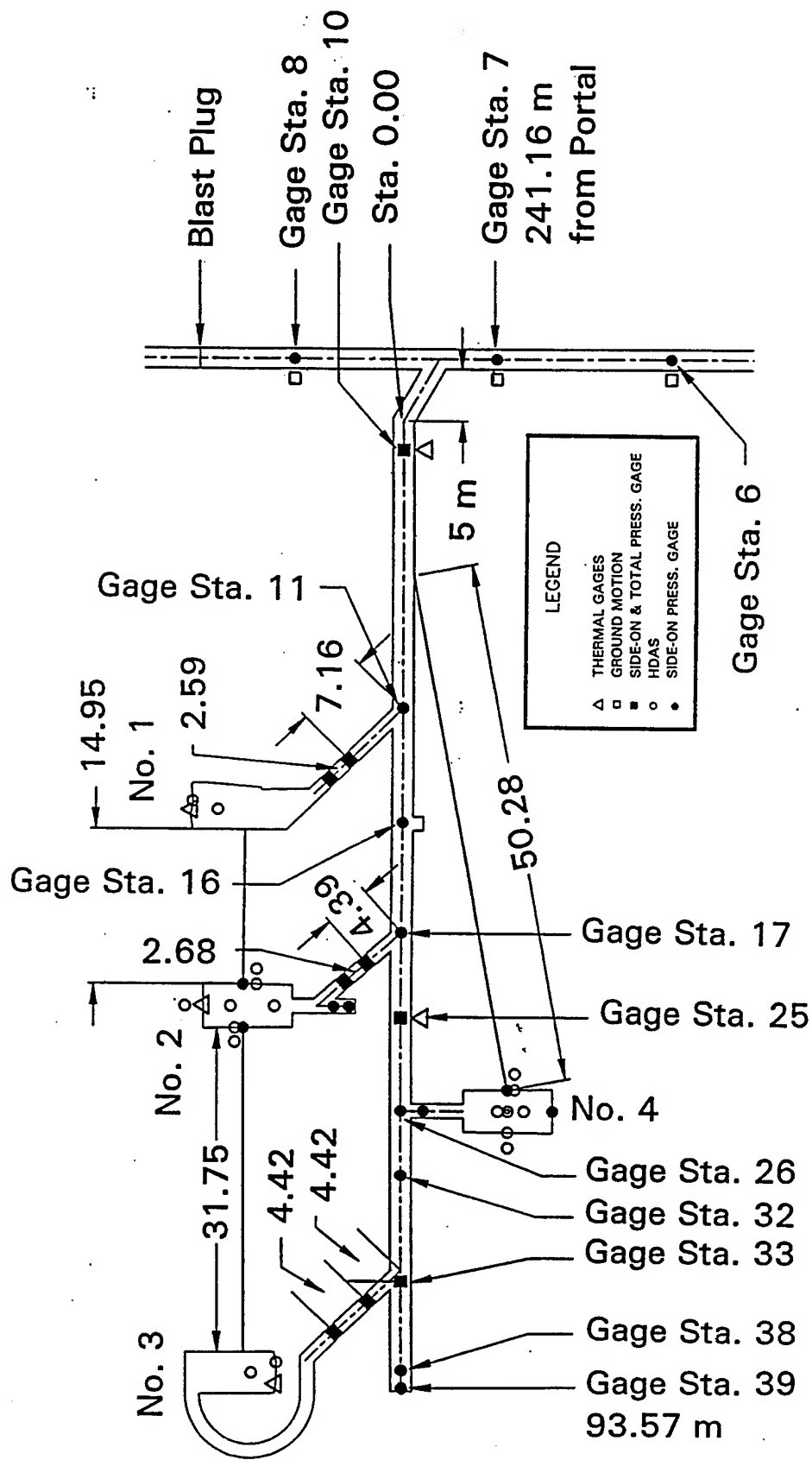


Figure 2. Test drift layout and instrumentation plan for the "No Excuses" experiment.

INTERMEDIATE-SCALE  
 UNDERGROUND MAGAZINE TEST  
 LOADING DENSITY (TNT)  $37.3 \text{ kg/m}^3$   
 TEST NO. 4, CHAMBER NO 4  
 2826.4 kg (NEW) - CAST COMP B

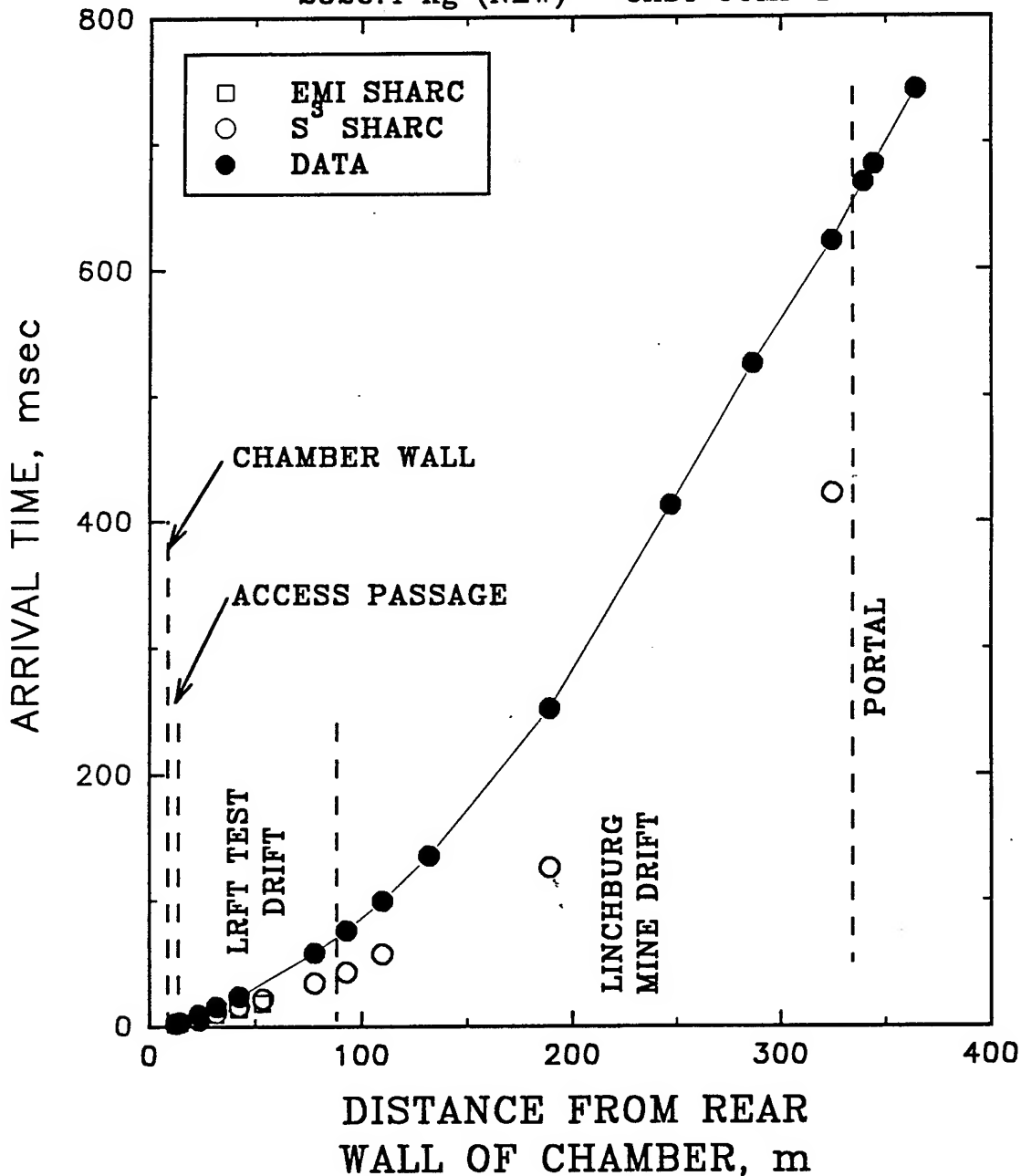


Figure 3. Comparison of calculated (SHARC) and measured arrival times from the "No Excuses" test, plotted versus distance from the rear wall of the detonation chamber (Chamber No. 4).

INTERMEDIATE-SCALE  
UNDERGROUND MAGAZINE TESTS  
LOADING DENSITY (TNT)  $37.3 \text{ kg/m}^3$   
TEST NO. 6, CHAMBER NO. 4  
2826.4 kg (NEW) - CAST COMP B

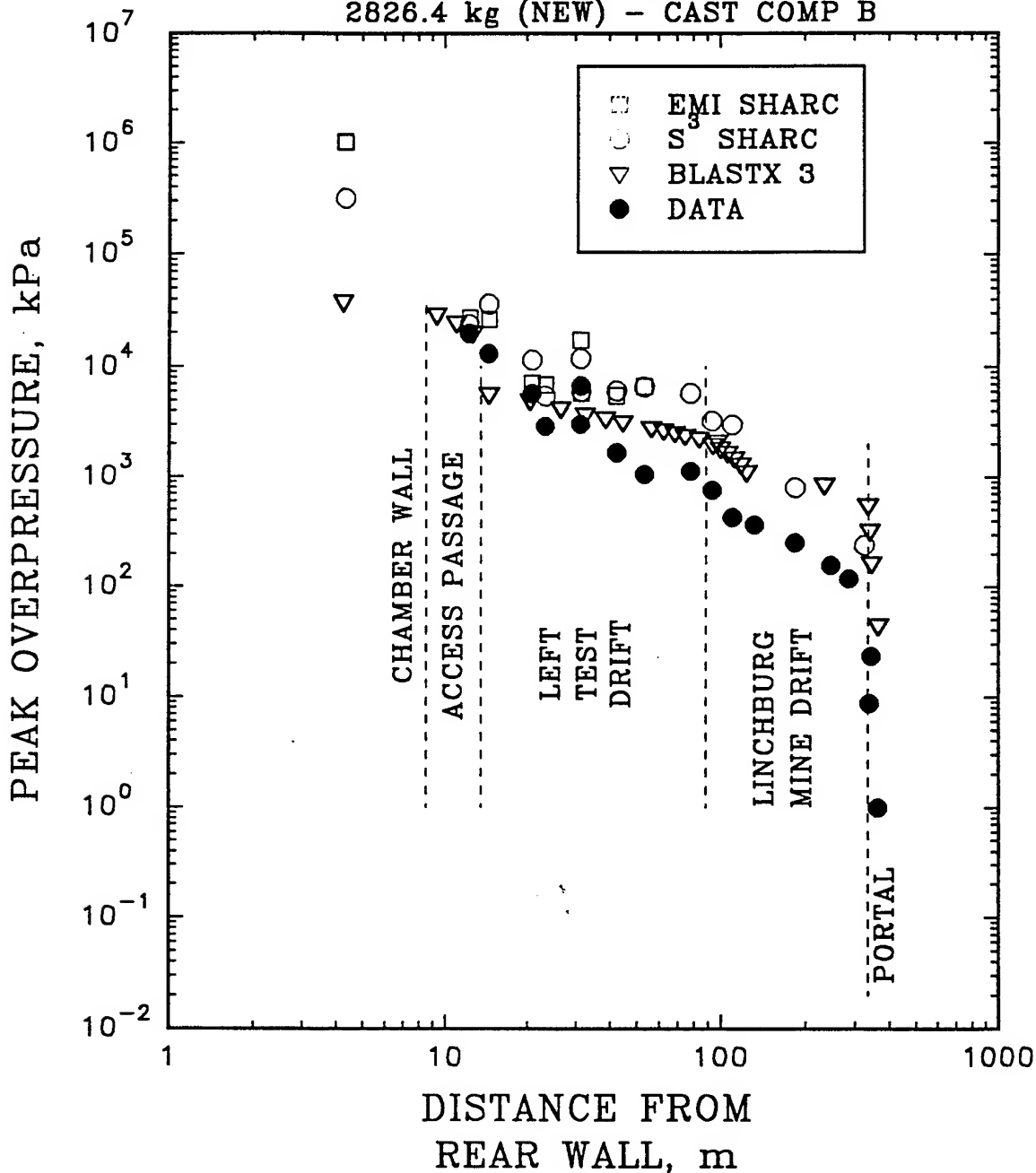


Figure 4. Comparison of calculated (SHARC and BLASTX) and measured peak overpressure versus distance from the rear wall of the detonation chamber (Chamber No. 4) along the airblast flow path from the detonation chamber to the Linchburg Mine portal.

INTERMEDIATE-SCALE  
 UNDERGROUND MAGAZINE TESTS  
 LOADING DENSITY (TNT)  $37.3 \text{ kg/m}^3$   
 TEST NO. 6, CHAMBER NO. 4  
 2826.4 kg (NEW) - CAST COMP B

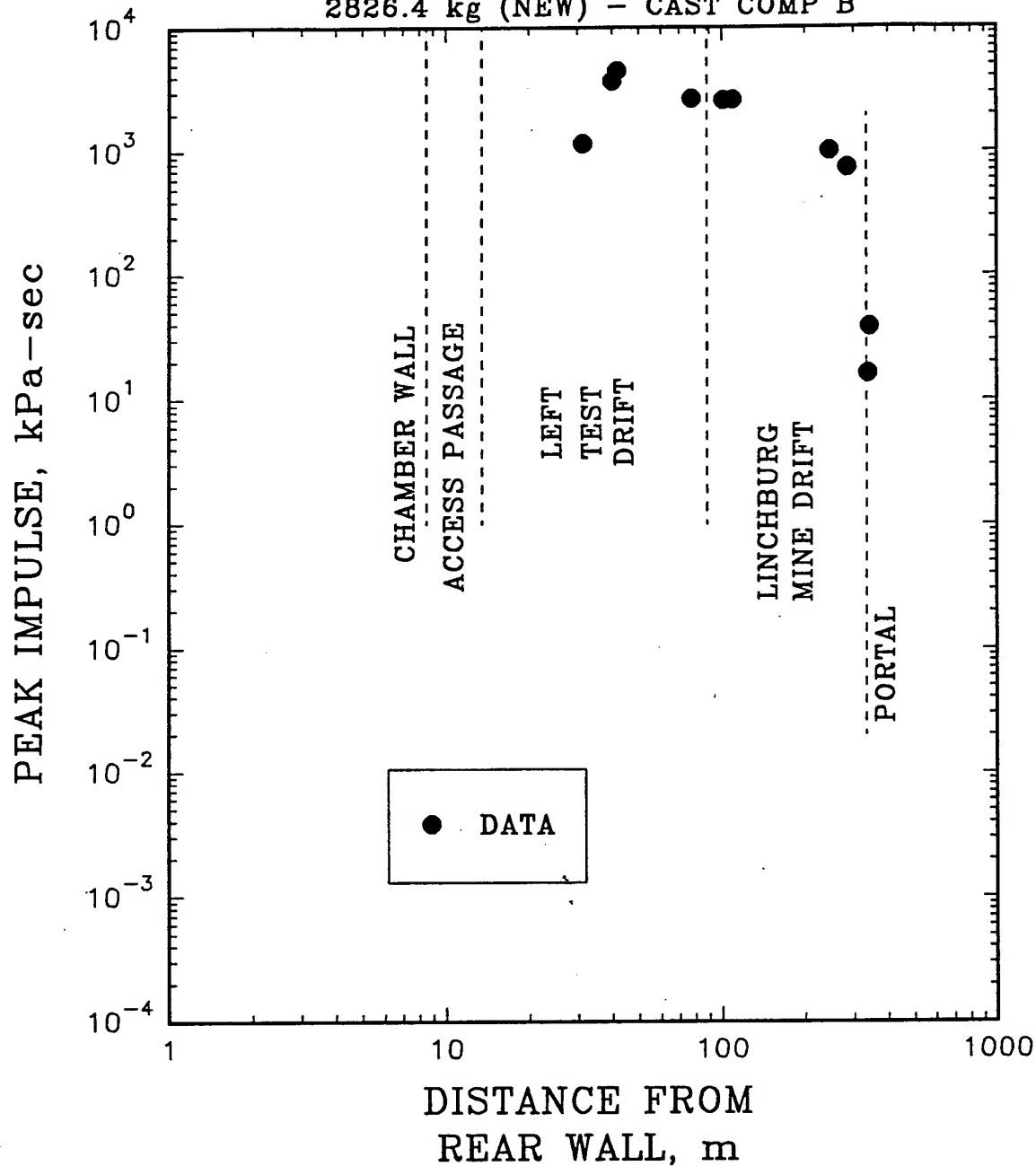


Figure 5. Measured peak overpressure-impulse (all data) versus distance from the rear wall of the detonation chamber (Chamber No. 4).

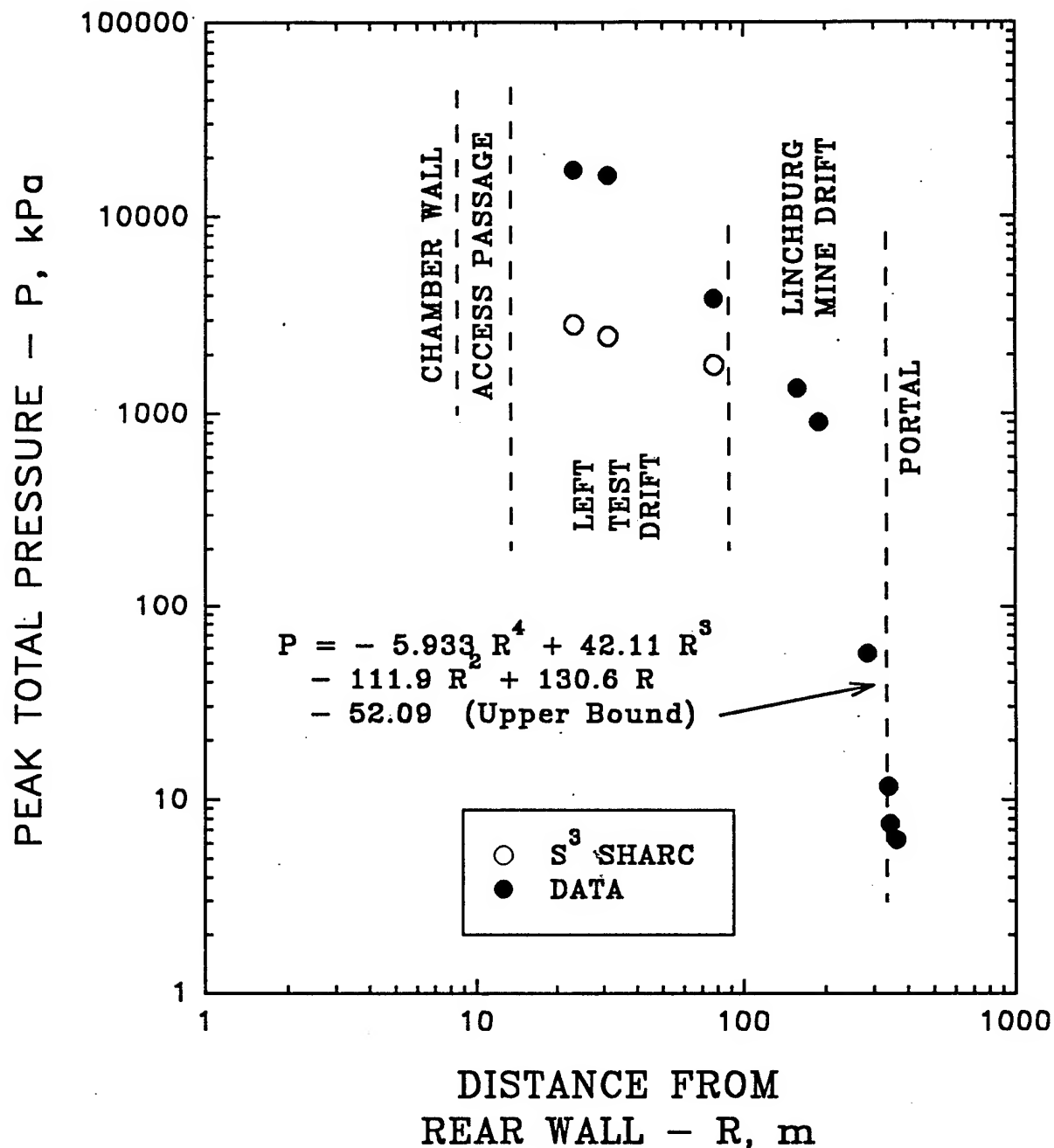


Figure 6. Comparison of calculated (SHARC) and measured peak total pressure versus distance from the rear wall of the detonation chamber (Chamber No. 4) along the airblast flow path from the detonation chamber to the Linchburg Mine portal.

# **MEASUREMENT AND SIMULATION OF AIR BLAST HAZARDS ASSOCIATED WITH DOOR BREACHING OPERATIONS**

P.L. Winter, D.M. Thornton, L.A. Learmonth, D.A. Jones,

G. Kemister and D.V. Ritzel

Defence Science and Technology Organisation  
Aeronautical and Maritime Research Laboratory

Weapons Systems Division  
PO Box 4331, Melbourne, Victoria, 3001  
AUSTRALIA

## **Abstract**

We report experimental results and numerical simulations of overpressure levels from experimental high explosive breaching charges designed to facilitate emergency access into a building. Two types of charge were tested, a "snib charge", and a larger "frame charge". They were functioned on solid core doors positioned either flush or recessed with respect to the adjacent wall. Experimental records for the snib charge showed that peak pressure decreased rapidly with increasing distance from the charge for both flush and recessed door configurations, and peak pressures for the recessed charge were always lower than those for charges on the flush door. Results for the frame charge showed that close to the charge the peak pressures for the recessed door were always lower than those on the flush door, but once the distance exceeded two metres the peak pressures were higher for the charge on the recessed door. We have performed numerical simulations for each of the charge/door configurations using a 3D hydrocode based on the Flux-Corrected Transport algorithm. Simulated pressure-time records are in excellent agreement with experiment. Our simulations show that the higher pressure for the frame charge on the recessed door is caused by pressure enhancement resulting from the coalescence of the weakened primary shock from the distributed frame charge and its ground reflection.

## 1. INTRODUCTION

An AMRL field trial was recently conducted at P&EE Graytown to investigate airblast hazards associated with door breaching operations [1]. Two types of door breaching charges were tested and reported; a "snib charge", which was designed to break the lock and throw the door open on its hinges, and a larger "frame charge", which was designed to breach an access hole through a 38 mm thick solid core door. An array of four stand mounted pressure transducers was used to record the pressure-time records along the wall at selected locations, and the charges were evaluated with the door fixed in two positions within the wall opening; either flush with the wall, or recessed by 15 cm. These charges could be used by emergency access crews to gain rapid entry into a building and hence it is important to characterise their blast effects.

The results for the snib charge were qualitatively as expected; for both the flush door and recessed door configurations the peak pressure decreased rapidly with increasing distance from the charge and the peak pressures for the recessed charge were always lower than those for the charge mounted on a flush door. Similarly, the mean positive phase impulse was always lower for the charge mounted on the recessed door.

The results for the frame charge were more complicated. At locations close to the charge the peak pressures for the charge on the recessed door were always lower than those on the flush door, but once the distance along the wall exceeded approximately two metres the situation reversed and the peak pressures were higher for the charge mounted on the recessed door. Also, in direct contrast with the snib charge, the mean positive phase impulse for the frame charge mounted on the recessed door was always higher than when mounted on the flush door.

A qualitative explanation of these results has been given by D.V. Ritzel in Annex C to reference [1], and a two-dimensional numerical simulation of the frame charge on both a flush door and a recessed door has been used to illustrate the effect of the recess on the flow field. In the case of the flush door the pressure-time record seen at the location of each of the pressure transducers will consist of a shock from the detonation of the explosive on the near side of the frame, followed a short time later by another strong shock from the explosive on the far side of the frame. Each of these shocks will also undergo a ground reflection and at some distance from the frame charge the primary shocks and their respective ground shocks will coalesce and result in an enhanced shock pressure. For the flush door the primary shocks have sufficient strength to ensure that this pressure



enhancement occurs at relatively large distances from the frame charge where the pressures will have fallen below levels of concern. For the recessed door however the ledge produces a weakening of the diffracted primary blast and the pressure enhancement effect occurs much closer to the charge. Close study of the experimental records shows that this effect occurs at a distance of approximately 2 m from the door edge for the recessed charge. Due to the elongated shape and small size of the snib charge it has a very weak ground reflection which will arrive well behind the primary wave for both the flush and recessed geometries, and so no enhancement of peak pressure will be seen for either case at the locations of interest.

The enhanced impulse found for the frame charge on the recessed door is also explained by the diffraction and weakening of the blast from the near side of the charge by the ledge. This allows the shock from the far side of the frame to arrive earlier in the positive phase of the primary shock, and it is the arrival of this shock superimposed on the reduced negative phase of the primary shock which is responsible for the higher impulse in the case of the frame charge. This effect will not occur for the snib charge because the shape of the charge results in only a single primary shock.

In the calculations referred to above the computational grid did not extend to locations comparable to experimental measurements, and the simulations were performed on a two-dimensional cartesian grid. The calculations were therefore unable to simulate the pressure-time records at the experimental gauge positions, but they were successful in showing the basic features and differences of the blast propagation process for recessed and flush door geometries. The aims of this study are therefore to extend these calculations to realistic grid sizes and geometries and to accurately reproduce the pressure-time records measured experimentally, and to quantitatively verify the correctness of the explanation given above.

## 2. EXPERIMENTAL DETAIL

The experimental program comprised 28 instrumented firings conducted at P&EE Graytown in April 92. Two types of door breaching charges were tested; a 'frame charge', designed to breach an access hole through a solid core door and a 'snib charge' designed to break a lock and throw open a door on the hinges. The air blast from the breaching charges was measured with the door fixed in two positions within the wall opening; **recessed** and the assumed worst case of a **flush**

**door.** Pressure measurements were made along the wall containing the door and covered the range typically occupied by rescue teams.

### **2.1 Test Arrangement**

A 3 m high wall containing a door opening (0.9 x 1.8 m) was constructed from concrete Pendine blocks at Explosives Battery, P&EE Graytown. An adjustable steel frame was bolted into the opening to support the target doors, either in the flush position or recessed by 150 mm. A panel of 38 mm thick solid particle board was rigidly attached to the supporting frame by screws for each test and hence were not designed to hinge.

Four stand-mounted pressure transducers were positioned 950 mm above the ground and approximately 300 mm out from the wall. Depending upon the charge type they were positioned at distances between 1 and 3.5 m from the near edge of the door opening. A reference gauge was located flush with the ground at a position 2.5 m normal from the door surface. This gauge would enable the blast output from each charge to be directly compared and would indicate any charge functioning problems.

The stand-mounted transducers were housed in circular aluminium plates designed to minimise the disturbance to the blast wave. Two transducer orientations were used; the gauge face at a slight angle to and facing away from the wall (baffle plate vertical) and the gauge face normal to the ground pointing skyward (baffle plate horizontal). In each case the baffle plates were oriented to primarily measure side-on overpressure values of the incident shock wave. The signature of the ground reflected waves was the principal difference expected between the records obtained using the two plate orientations.

### **2.2 Charge Design and Placement**

Both charge designs were built using strips of the PETN based sheet explosive 'Metabel'. The **frame charge** consisted of a rectangular geometry of narrow Metabel strip attached to a plywood frame. The sheet explosive was initiated using two 5 g 'Detaprime' boosters positioned at diagonally opposite corners. Net explosive quantity (NEQ) of the charge, including the detonating cord links, was approximately 180 g. The frame charge was positioned on the door with its horizontal centre line 950 mm above ground level. The pressure transducers were levelled to this same height.

The **snib charge** consisted of a single short strip of Metabel initiated from one end (NEQ was 15 g). The charge was oriented vertically and centred 1100 mm

from the ground and 80 mm in from the edge of the door. This position corresponds to typical door lock positions.

### **2.3 Air Blast Data Reduction**

The tabulated experimental results reported in the tables below record the **incident pressure wave** and do not include reflections from surfaces other than the ground and the wall returns exposed in the recessed door scenario. The results presented are the average of a number of tests, ranging between three and eight and include measurements from both baffle plate orientations. Consistency of the pressure/time records was excellent with only a small standard deviation associated with the mean values.

The B-duration for each scenario to be used in the military airblast criteria calculations was determined from the simple external breach arrangement and the values given do not include the effect of any adjacent reflecting walls. For the snib charge the B-duration for the simple external breach scenario was estimated at approximately 5 ms for the flush door and 7 ms for the recessed door. The B-duration for the frame charge was estimated to be around 8 ms for both the recessed and the flush door scenario.

### **2.4 Experimental Results**

The mean peak overpressures measured at each of the gauge locations are plotted in Figure 1. As an indication of the level of the likely risk of air blast hazard to nearby personnel, the plot includes the various maximum overpressure levels prescribed by UK, US and Australian military impulse noise criteria relevant to this scenario.

## **3. CODE DETAILS**

Preliminary two-dimensional calculations were performed with a commercial code written by Combustion Dynamics Ltd. [2]. The three dimensional calculations were performed with an in-house AMRL CFD code, BLAST3D. Both codes are based on the Flux-Corrected Transport (FCT) algorithm of Boris and Book [3], which is an explicit, nonlinear finite difference algorithm designed to eliminate nonphysical ripples and numerical dispersion. The method minimises phase and amplitude errors and maintains positivity and conservation. The BLAST3D code is a three-dimensional finite difference computer program, developed at AMRL, which solves the Euler equations for the conservation of mass, momentum and energy of an inviscid, compressible fluid (in this case air). A three-dimensional Cartesian grid with fixed spacing was used as a basis for the

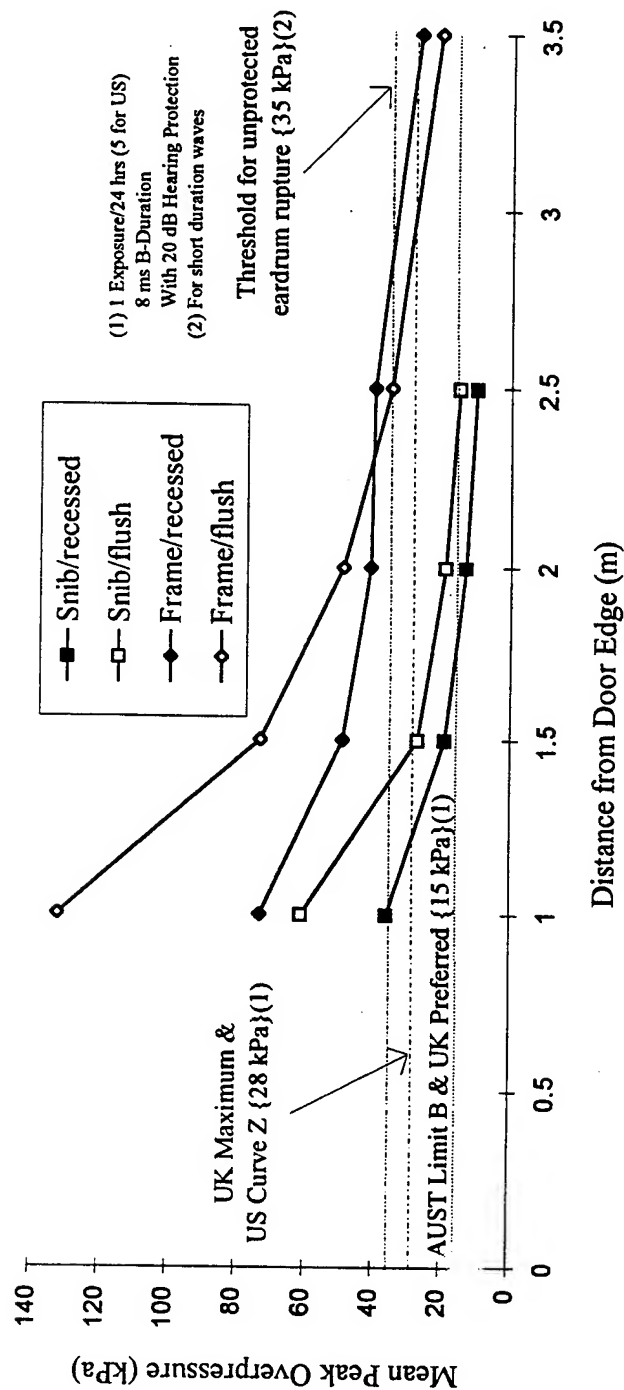


Figure 1. Mean Peak Overpressure vs Distance

calculation. Operator splitting, which reduces the complexity of a three-dimensional calculation down to three one-dimensional calculations at each time-step and grid point, was also used. A one-dimensional FCT algorithm, with fourth order phase accuracy and an overall second order accuracy on uniform grids, was used to solve the one-dimensional calculations [4]. Rigid wall boundary conditions were used for the walls and the ground in the calculations whilst outflow boundary conditions were used at all the other edges of the computational grid.

The program has a 3D Cartesian grid as a basis for its computations. To illustrate the way in which arbitrary geometries are included in three dimensions we will examine the 2D case with dimensions  $ncx$  and  $ncy$ . The method chosen in this approach can be easily shown graphically below where the final geometry is simply built up by a series of overlaying levels which contain a rectangle, either solid to make an obstruction or empty to open up a space as shown in Figure 2.

Since the calculations are split into three 1D calculations this means that for each 1D calculation there can be multiple ranges on which to solve the equations. To do this there must be an extra control variable giving the number of ranges to be done for that particular 1D calculation. This method of including complex rectangular shapes provides a quick and easy way of inputting a complicated scenario into the computational program.

#### **4. SNIB CHARGE**

##### **4.1 Choice of Computational Grid Size**

We began our study of this charge by assuming that the 15g PETN snib charge could be replaced by a point charge having an NEQ of 18 g of TNT and calculating the peak pressure of the primary shock wave at the location of each of the pressure transducers using the semi-empirical CONWEP code [5]. This seemed initially to be a rather gross simplification of the true situation, but the results were surprisingly good. Table 1 shows a comparison between the peak overpressure ( $\Delta P$ ), time of arrival ( $t_a$ ), and positive phase duration ( $\Delta t$ ) obtained experimentally with those obtained from CONWEP for the four stand mounted pressure gauges for the snib charge when detonated on the flush mounted door. The good agreement shown in Table 1 indicated that it may be possible to simulate the snib charge using a simple point source model.

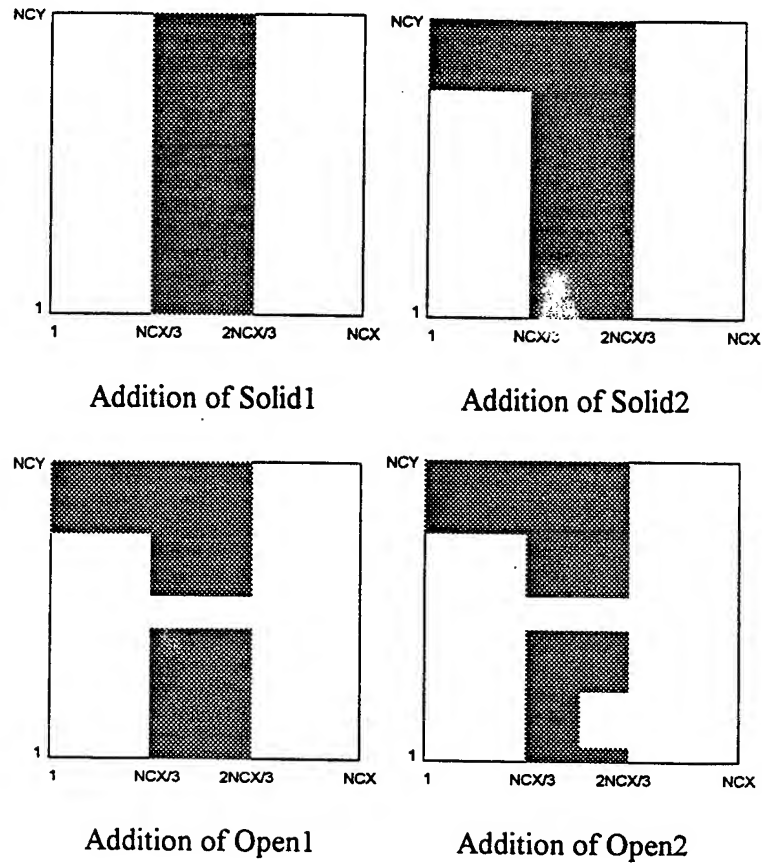


Figure 2. Diagrammatic representation of the addition of solid and open spaces.

**TABLE 1**  
Snib charge on flush door.  
Comparison of experimental results and CONWEP calculation.

Gauge	Distance (m)	EXPERIMENT			CONWEP		
		$\Delta P$ (kPa)	$t_a$ (ms)	$\Delta t$ (ms)	$\Delta P$ (kPa)	$t_a$ (ms)	$\Delta t$ (ms)
P2	1.13	61	1.8	0.5	62.7	1.64	0.95
P3	1.62	27	3.0	0.8	32.3	2.89	1.1
P4	2.11	19	4.3	1.0	21.0	4.21	1.2
P5	2.60	15	5.7	1.0	15.4	5.56	1.29

To check this possibility we used the CFD module of the Combustion Dynamics software to calculate the flow field resulting from the detonation of 18 g of TNT, and compared the numerically calculated pressure-time records at the positions of the pressure transducers with those obtained experimentally. The initial conditions for the simulation were obtained from a pressurised sphere model. A small region of the grid contained gas at an initial pressure of 1000 atmospheres and a temperature of 3000 K, and had a specific heat ratio of 1.4. The volume of the sphere was chosen so that the energy corresponded to the detonation energy of the equivalent weight of TNT. Combustion Dynamics Ltd. have found that this approach considerably simplifies the explosive modelling as it removes the need to follow the detailed detonation processes occurring within the condensed explosive. To attempt to model the detonation process in detail would require a very fine grid and very short time steps, which would then severely limit the extent to which the flow field could be calculated. A disadvantage of the method is that it only provides a good description of the blast decay in the far field limit.

The simulation was run for a total time of 10 ms with a spatial resolution of 1 cm, and the peak pressure, time of arrival, and positive phase duration for the primary shock are shown in Table 2. The results compare well with both experiment, and also with the CONWEP predictions. The peak pressure at the position of the closest gauge (P2) is too low by about 15% when compared with either experiment or the CONWEP result, and this is probably due to the inadequacies of the pressurised sphere model in the near field. The peak pressures at the remaining gauge positions are very accurately reproduced, the arrival times agree quite well with those calculated from CONWEP, and the lengths of the positive phase durations lie between the experimental values and the CONWEP results.

To be able to simulate the differences between the blast on the flush door and the recessed door a fully three-dimensional code has to be used, and to follow the flow out to the position of the furthest gauge using 1 cm cell resolution in a three-dimensional code would be far too time consuming. Table 3 shows that the peak pressures, positive phase duration and arrival times for calculations at grid resolutions of 1 cm and 2 cm. The only significant differences occur in the peak pressures, where the values at the coarse resolution are approximately 20% lower. This is typical of the effect of grid resolution [6], and provided we are only interested in comparisons between the flow on the recessed door and the flush door, then this degree of resolution is suitable for the current calculations.

**TABLE 2**

Snib charge on flush door.

Comparison of experimental results with CDL software simulation using 1 cm pressurised sphere to initiate the calculation.

Gauge	Distance (m)	EXPERIMENT			2D CFD Code		
		$\Delta P$ (kPa)	$t_a$ (ms)	$\Delta t$ (ms)	$\Delta P$ (kPa)	$t_a$ (ms)	$\Delta t$ (ms)
P2	1.13	61	1.8	0.5	52	1.6	0.7
P3	1.62	27	3.0	0.8	27	2.8	0.9
P4	2.11	19	4.3	1.0	18	4.2	1.0
P5	2.60	15	5.7	1.0	14	5.4	1.1
P1	2.76	25	6.3	1.1	28	6.1	1.1

**TABLE 3**

Snib charge on flush door.

Comparison of pressurised sphere model at 1 cm and 2 cm cell resolution

Gauge	Distance (m)	Sphere 1 cm cell size			Sphere 2 cm cell size		
		$\Delta P$ (kPa)	$t_a$ (ms)	$\Delta t$ (ms)	$\Delta P$ (kPa)	$t_a$ (ms)	$\Delta t$ (ms)
P2	1.13	52	1.6	0.7	40	1.63	0.75
P3	1.62	27	2.8	0.9	22	2.8	1.0
P4	2.11	18	4.2	1.0	14	4.15	1.05
P5	2.60	14	5.4	1.1	10	5.5	1.15
P1	2.76	28	6.1	1.1	22	6.1	1.1

We now turn to modelling the experiments using the 3D code which will be needed due to the inherent 3D nature of the recessed door. We begin by using the code to model the flow on the flush mounted door. The 3D code has a Cartesian grid and we used  $\Delta x = \Delta y = \Delta z = 2$  cm and a fixed time step of  $\Delta t = 5.0 \times 10^{-6}$  s. The region simulating the explosive was modelled using the pressurised sphere model with 40 cells arranged in a  $2 \times 2 \times 10$  array.

#### 4.2 Flush Door

Figure 3 shows the simulated and experimental pressure-time records, and Table 4 shows a comparison between the peak pressure, time of arrival, and positive phase duration for the primary shock from the 3D simulation with those obtained



Figure 3a. Snib Charge on Flush Door at 1.0m

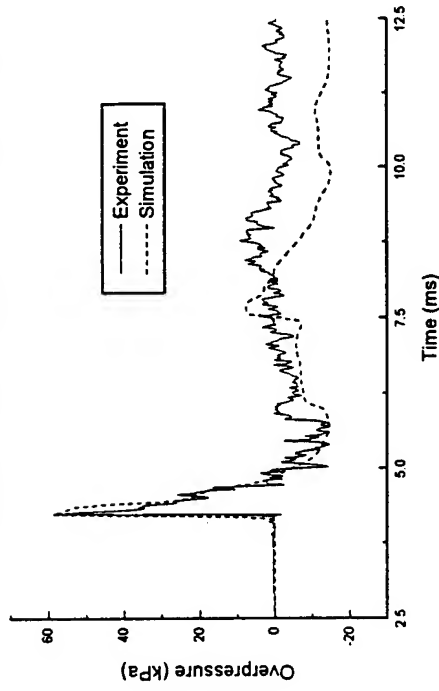


Figure 3b. Snib Charge on Flush Door at 1.5m

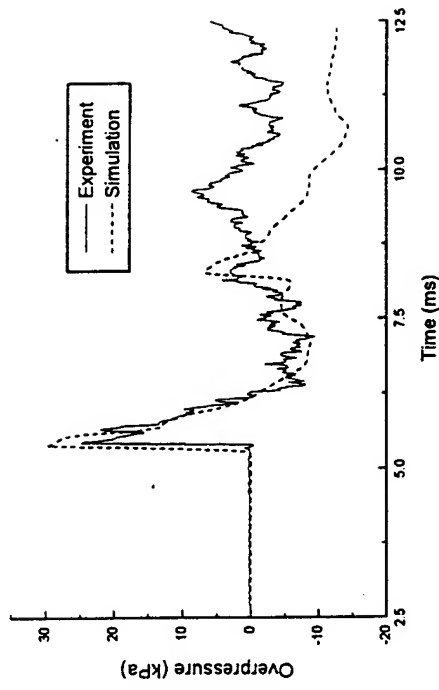


Figure 3c. Snib Charge on Flush Door at 2.0m

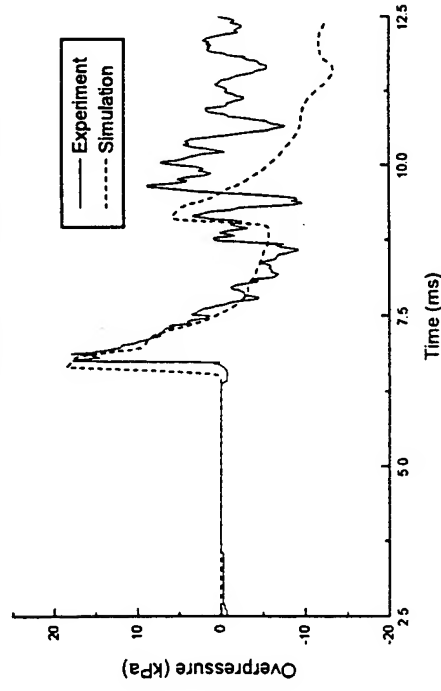


Figure 3d. Snib Charge on Flush Door at 2.5m

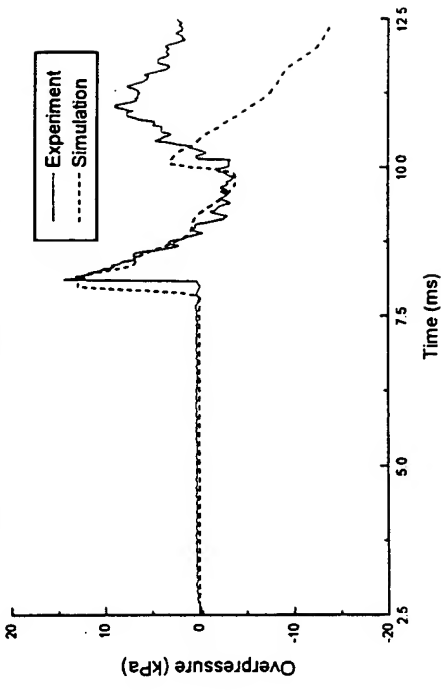


Figure 3. Comparison of experimental and simulated pressure-time traces for the snib charge on the flush door

experimentally. The peak pressures agree well with the experimental values, but the arrival times are consistently too low by approximately 7% to 13%. The likely explanation for the faster arrival times shown in Table 4 for the simulation is the use of the pressurised sphere model. This is being investigated elsewhere in more detail [6].

**TABLE 4**  
Snib charge on flush door.  
Comparison of experimental results with 3D code simulation.

Gauge	Distance (m)	EXPERIMENT			3D CODE		
		$\Delta P$ (kPa)	$t_a$ (ms)	$\Delta t$ (ms)	$\Delta P$ (kPa)	$t_a$ (ms)	$\Delta t$ (ms)
P2	1.13	61	1.8	0.5	59	1.5	0.7
P3	1.62	27	3.0	0.8	30	2.6	0.9
P4	2.11	19	4.3	1.0	18	4.0	0.8
P5	2.60	15	5.7	1.0	13	5.3	1.2

#### 4.3 Recessed Door

We now consider the effect of the ledge created by the recessed door on the above results. The ledge was easily modelled using the technique described by Kemister [7], and because of the finite nature of the computational grid, and the minimum cell size of 2 cm, the depth of the ledge used in the calculations was 16 cm (experimentally the value is 15 cm). Figure 4 shows the simulated and experimental pressure-time records, and Table 5 compares the simulated peak pressures, arrival times and positive phase duration for the primary shock with the experimental results. The simulated pressure at the closest gauge is too low, but the pressures at the remaining gauge locations show excellent agreement between simulation and experiment. Examination of the simulated pressure-time records in Figure 4 shows that diffraction around the ledge has weakened and delayed the primary shock and also prevented the formation of a clean secondary shock. For the flush door Figure 3c shows that the secondary shock and the ground reflection of the primary shock have coalesced by the time the flow has reached the position of gauge P4. This does not happen for the flow on the recessed door however; in this case the weakened secondary shock appears to move up into the positive phase of the primary shock and lead to a slight increase in the positive phase impulse. A further difference between the simulated results for the flush and recessed cases is evident in the time delay between the arrival of the primary shock and its ground reflection at each of the transducer locations.

Figure 4a. Snib Charge on Recess Door at 1.0m

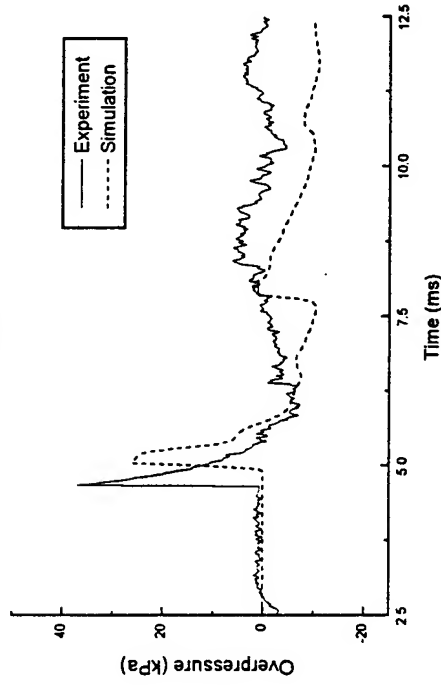


Figure 4b. Snib Charge on Recess Door at 1.5m

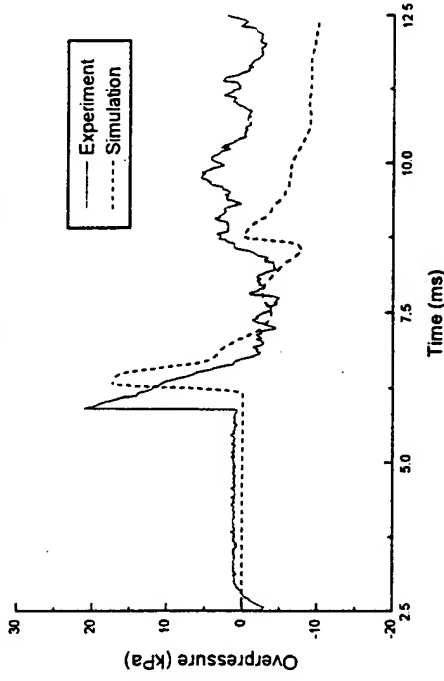


Figure 4c. Snib Charge on Recess Door at 2.0m

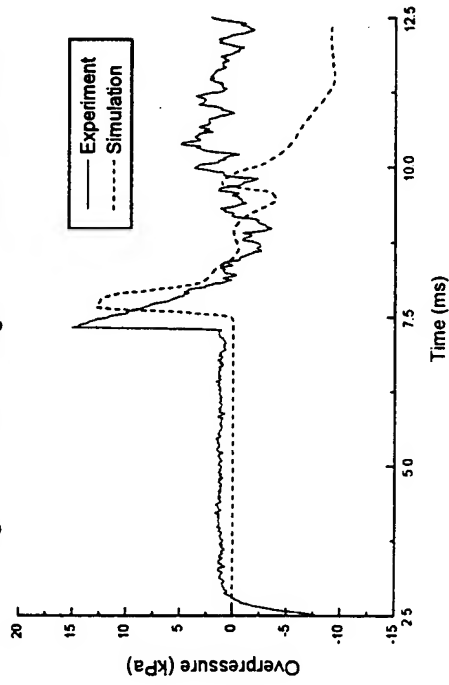


Figure 4d. Snib Charge on Recess Door at 2.5m

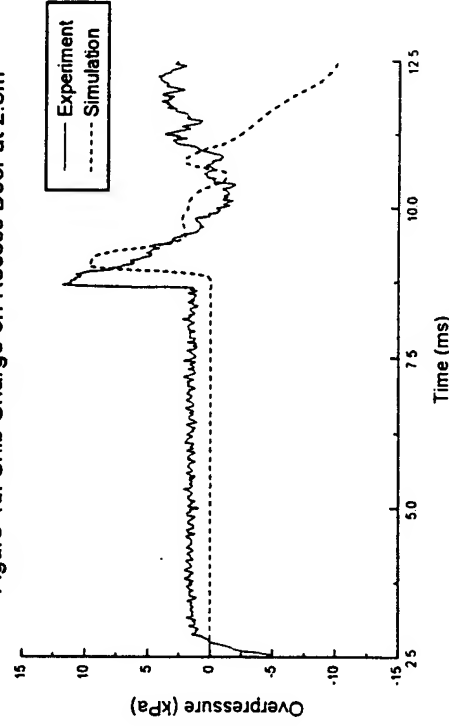


Figure 4. Comparison of experimental and simulated pressure-time traces for the snib charge on the recessed door

Because the primary shock has been weakened by diffraction around the ledge the ground reflected shock is able to catch up with the front sooner and arrives earlier in the signature, hence the time interval between the arrival of the primary shock and the ground reflected shock is smaller for the charge on the recessed door than for the charge on the flush door. This effect also occurs for the frame charge, and will be discussed in more detail in the next section.

**TABLE 5**  
Snib charge on recessed door.  
Comparison of experimental results with 3D code simulation.

Gauge	Distance (m)	EXPERIMENT			3D CODE		
		$\Delta P$ (kPa)	$t_a$ (ms)	$\Delta t$ (ms)	$\Delta P$ (kPa)	$t_a$ (ms)	$\Delta t$ (ms)
P2	1.13	36	2.2	0.7	26	2.4	0.6
P3	1.62	19	3.5	0.8	18	3.6	0.8
P4	2.11	13	4.8	0.8	13	5.0	0.8
P5	2.60	10	6.3	0.9	10	6.4	1.3

The trends in the mean positive phase impulse shown by the experimental records for the snib charge on both the flush and recessed doors are also reproduced by the numerical simulations. Table 6 shows a comparison of the experimental and simulated results. Experimentally the impulse decreases with increasing distance from the charge for both the flush and recessed cases, and the impulse for the recessed door is always lower than the impulse for the flush door at equivalent distances. The simulations also show this trend, although quantitatively the simulated results on the flush door are approximately 25% - 50% higher than the experimental values. Figure 3 explains the reason for the discrepancies. Close comparison of the traces in the vicinity of each of the primary shocks shows that, in each case, the shock has either a higher peak value, or a greater positive phase duration. These differences are undoubtedly due to a combination of the effects of grid resolution, and the effect of the shape of the high pressure region used to initiate the simulation, as discussed earlier.

Agreement between simulation and experiment for the mean positive phase impulse is very much better for the recessed door scenario, as Table 6 shows. However, examination of the simulated and experimental pressure-time records, Figure 4, shows that for this particular set of data the simulated arrival time is

**TABLE 6**  
**Snib charge on both flush and recessed doors.**  
**Comparison of experimental and simulated mean positive phase impulse.**

Distance from door edge (m)	Mean Positive Phase Impulse Experimental (Pa.s)		Mean Positive Phase Impulse Simulation (Pa.s)	
	Flush Door	Recessed Door	Flush Door	Recessed Door
1.0	14	9	18.3	9.6
1.5	10	7	12.4	7.2
2.0	6	5	9.3	5.6
2.5	5	4	7.5	5.6

consistently in error by about 0.25 ms. Because time zero for the experimental results corresponds to the firing of the detonator, whereas for the simulated results it corresponds to the release of a high pressure region of air, a small adjustment has to be made to the simulated results to ensure a correct time zero. For the 3D simulations of the snib charge on the flush and recessed doors described in this section, and also for the frame charge simulations discussed in the next section, we allowed for this time difference by adding a constant value of 2.72 ms to the simulated results. This figure was determined by a comparison between the experimental and simulated pressure-time records. In most cases this resulted in quite good agreement between simulated and experimental arrival time data, as can be seen in Figures 3 and 6. The consistent disagreement in arrival times shown in Figure 4 may possibly be due to either small experimental errors, or an inadequacy in the pressurised cylinder model used to initiate the calculation.

## 5. FRAME CHARGE

### 5.1 Charge Model

We used the 3D code with a uniform grid to model the frame charge on both the flush and recessed door positions. The 180 g of Metabel is equivalent to 216 g of TNT, and was simulated using the pressurised sphere model. Because of the distributed nature of the frame charge and the relative distances of the gauges and the dimensions of the frame it would not have been realistic to model the charge as a point source. Hence the region simulating the explosive was modelled using a total of 640 cells arranged in four groups of  $2 \times 2 \times 40$ , with each group placed at an appropriate position on the grid to represent one of the sides of the frame. This gave an explosive weight approximately 40% too high. However the pressure scales as the cube root of the weight, and so this would produce an error in the peak pressure of no more than about 3.5%.

### 5.2 Flush Door

Figure 5 shows the simulated and experimental pressure-time records for the four stand mounted gauges for the frame charge on the flush mounted door. Comparison of the simulated results with those shown in either Figure 3 or Figure 4 shows that there is a notable difference in the shape of the primary shock profile for the frame charge compared with the snib charge for the closer gauge locations. The double spike profile shown in Figure 5a is due to the distributed nature of the frame charge, the first peak is caused by the blast from the near side of the frame, while the second peak comes from the blast on the far side of the frame. At distances large compared to the dimensions of the frame these shocks merge and the profile is similar to that for the snib charge. Figure 5 shows that this occurs at a distance of approximately 2.5 m from the door edge. Experimentally though these peaks do not appear to be well resolved. The experimental pressure transducer records shown in Figure 5 for each of the stand mounted gauges show that some structure is evident in the main pulse for some of the gauges, but this does not correlate well with the profiles shown in the simulated results. This may be due to the inability of the pressure transducers to resolve the data on such a short time scale, but is more likely to be due to the way we have chosen to model the explosive charge. Possibly a more refined model is required for such near field conditions, and accurate calculations may require the use of a multi-material code and explicit modelling of the initiation and detonation of the explosive charges.

Although there are differences in the fine structure of the primary peak the overall flow structure is well reproduced. Table 7 shows a comparison between the simulated peak pressure, time of arrival, and positive phase duration for the primary shock with those obtained experimentally. The simulated peak pressures agree well with the experimental values, but the arrival times are again slightly too low, and the positive phase durations are consistently higher. The latter feature is undoubtedly due to the pressurised volume model used to start the calculation. One of the problems associated with this method is that the separate peaks from the distributed charge do not coalesce as quickly as the experimental traces indicate. The prolonged double peak structure therefore results in a longer positive phase, and consequently a larger value of the positive phase impulse, which will be discussed shortly.

### 5.3 Recessed Door

We now consider the effect of the ledge created by the recessed door on the frame charge results. Figure 6 shows the simulated and experimental pressure-

Figure 5a. Frame Charge on Flush Door at 1.0m

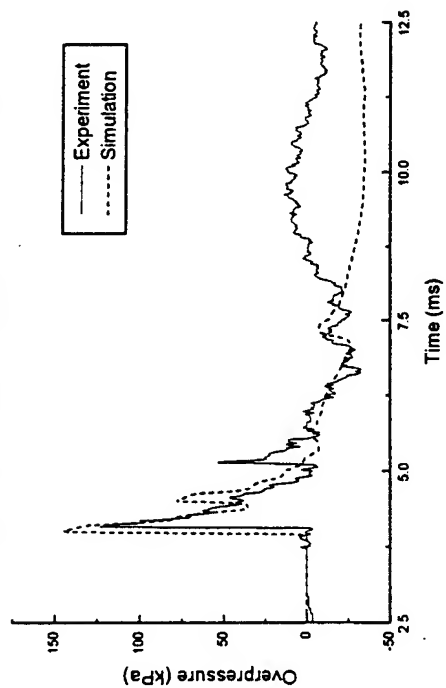


Figure 5b. Frame Charge on Flush Door at 1.5m

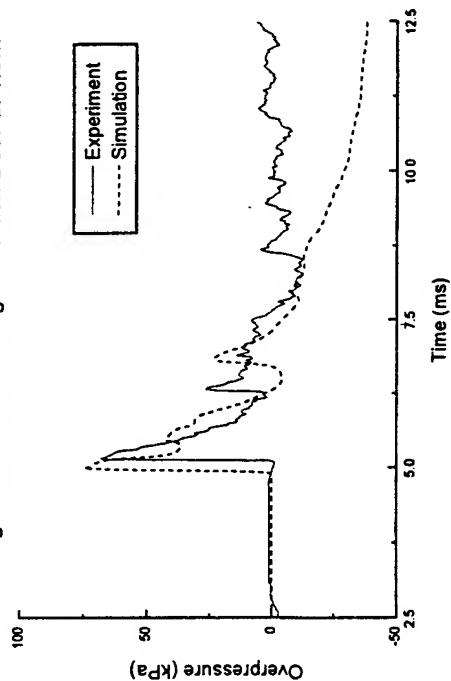


Figure 5c. Frame Charge on Flush Door at 2.0m

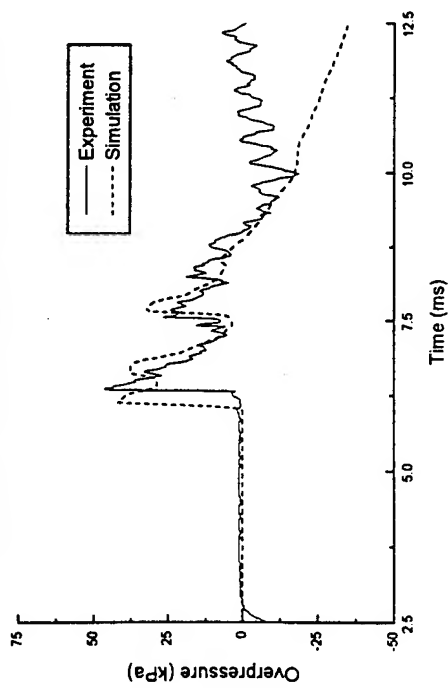


Figure 5d. Frame Charge on Flush Door at 2.5m

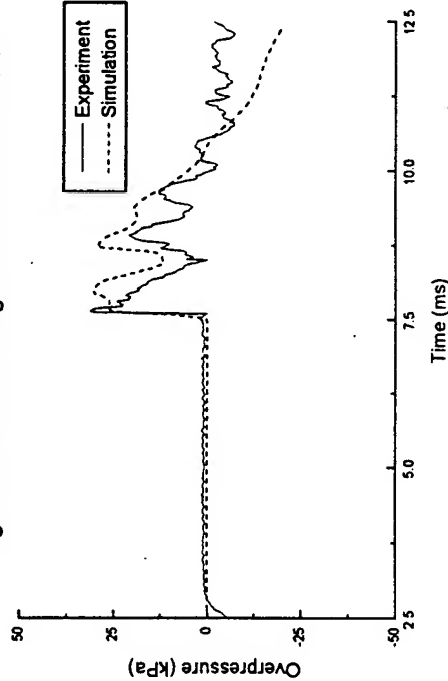


Figure 5. Comparison of experimental and simulated pressure-time traces for the frame charge on the flush door

Figure 6a. Frame Charge on Recess Door at 1.0m

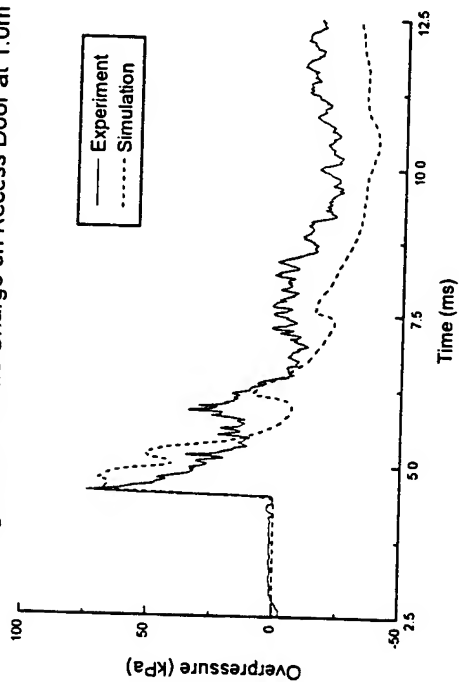


Figure 6c. Frame Charge on Recess Door at 2.0m

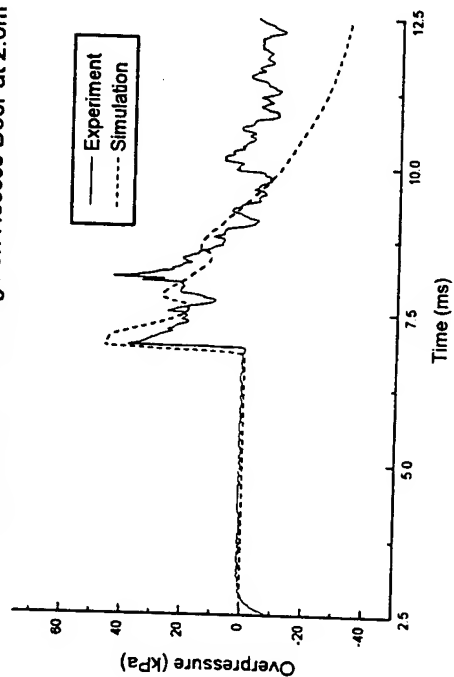


Figure 6b. Frame Charge on Recess Door at 1.5m

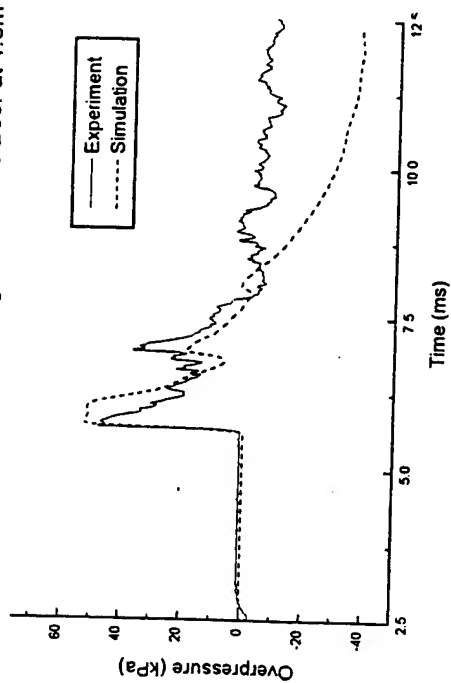


Figure 6d. Frame Charge on Recess Door at 2.5m

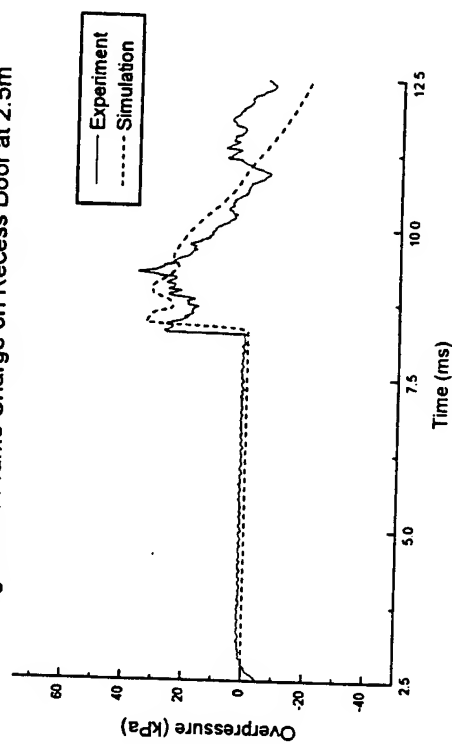


Figure 6. Comparison of experimental and simulated pressure-time traces for the frame charge on the recessed door



**TABLE 7**  
**Frame charge on flush door.**  
Comparison of experimental results with 3D code simulation.

Distance (m)	EXPERIMENT			3D CODE		
	$\Delta P$ (kPa)	$t_a$ (ms)	$\Delta t$ (ms)	$\Delta P$ (kPa)	$t_a$ (ms)	$\Delta t$ (ms)
1.0	132	1.6	0.9	145	1.3	1.3
1.5	73	2.7	1.1	75	2.3	1.3
2.0	49	3.8	1.2	42	3.4	1.6
2.5	35	5.2	-	31	5.0	-
3.5	21	-	-	27	7.3	-

time records, and Table 8 compares the simulated peak pressures, arrival times and positive phase duration for the primary shock with the experimental results. Examination of the results in Table 8 shows excellent agreement between the simulated and experimental peak pressures at the first two gauge locations, and reasonable agreement at the remaining three gauge locations. Comparison of the simulated peak pressure data for both flush and recessed doors shown in Tables 7 and 8 also shows that the calculations have reproduced the crossover effect seen experimentally, ie. the simulated peak pressure at the three furthest gauge locations for the charge on the recessed door is actually higher than the peak pressures at the corresponding locations for the charge on the flush door. Experimentally this is only seen for the gauges located 2.5 and 3.5 m from the door edge, and comparison of the experimental pressure-time records for the flush (Figure 5) and recessed cases (Figure 6) shows that this is caused by the coalescence of the primary shock and its reflected ground shock at the location of these gauges. As explained in the introduction, this occurs earlier for the blast on the recessed door because the diffraction effect of the resulting ledge weakens the primary blast and allows the ground reflected shock to catch up with the primary shock sooner. Figure 7 show that the higher pressure at the 3.5 m gauge for the recessed charge is due to this effect; in Figure 7a the ground reflected shock and the primary shock have just started to merge, whereas in Figure 7b the primary shock and ground shock have fully coalesced.

The simulated higher pressures for the recessed charge at 2.0 and 2.5 m from the door edge have a different explanation however. As noted in the discussion above for the frame charge on the flush door, the simulated pressure-time records for this case have clearly resolved the individual peaks from the distributed nature of

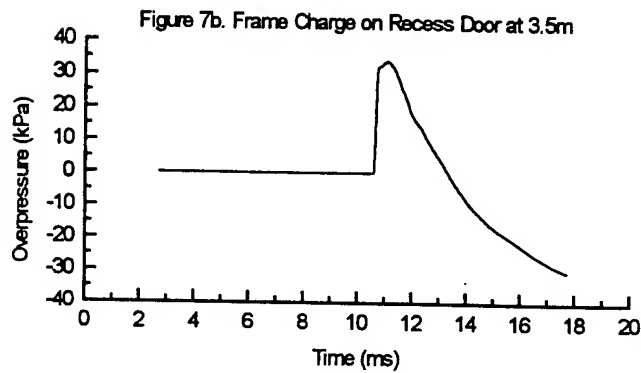
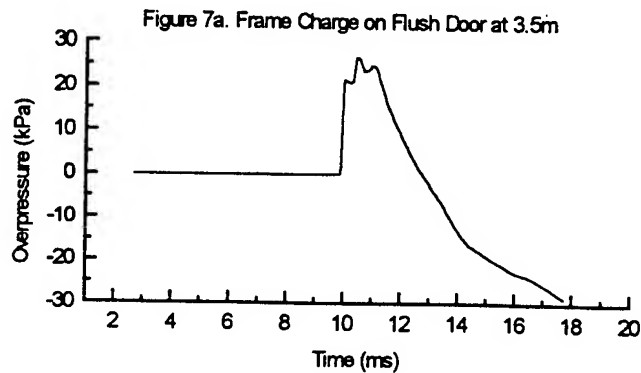


Figure 7. Comparison of simulated pressure-time traces for the frame charge at 3.5m on the flush and recessed doors

the frame charge, and these individual peaks only begin to merge at about 2.5 m from the door edge. On the recessed door the individual peaks from the frame charge are also clearly resolved, as Figure 6a shows. However, the effect of the ledge is to again weaken the leading shock and therefore allow the following shock contributions from the remainder of the frame charge to catch up with the leading shock sooner. Figure 6c shows that on the recessed door all contributions to the primary shock from the distributed charge have coalesced at 2.0 m from the door edge, whereas the simulation in Figure 5c shows two distinct peaks at 2.0 m from the door edge for the flush charge, and Figure 5d shows that these two peaks have yet to fully merge at 2.5 m from the door edge. Hence the enhanced peak pressures at 2.0 and 2.5 m from the door edge seen in the

**TABLE 8**  
 Frame charge on recessed door.  
 Comparison of experimental results with 3D code simulation.

Distance (m)	EXPERIMENT			3D CODE		
	$\Delta P$ (kPa)	$t_a$ (ms)	$\Delta t$ (ms)	$\Delta P$ (kPa)	$t_a$ (ms)	$\Delta t$ (ms)
1.0	73	2.1	1.9	70	1.8	1.2
1.5	49	3.2	2.2	52	3.0	2.0
2.0	41	4.5	2.2	47	4.3	2.4
2.5	40	5.8	2.4	34	5.7	2.7
3.5	27	-	-	34	8.0	2.7

simulation for the recessed door arise because, at these distances, the gauges are experiencing the full charge weight from the frame charge instantaneously, whereas in the flush door scenario the gauges experience two shocks separated by a very small time delay, but each produced by effectively half the total charge weight.

Although this second pressure enhancement mechanism does not appear to have been seen in the experimental pressure-time records shown here, it would appear to be a valid mechanism which could be seen experimentally given the right combination of charge shape, geometry, and gauge location. With regard to the experimental records discussed here though, it would seem to indicate that our model for the frame charge needs to be improved slightly so that the individual contributions from the distributed parts of the charge coalesce during the earlier part of the flow. As mentioned elsewhere, this may require the use of a multi-material code and explicit modelling of the initiation and detonation of the explosive charges.

For the frame charge, the experimental records showed that the mean positive phase impulse was always greater on the recessed door than on the flush door, at equivalent distances. This is shown in Table 9. The simulated results do not show the same qualitative behaviour however. Table 9 shows that in most cases the impulse calculated from the simulated results is higher for the charge mounted on the flush door, although at distances of 1.5 and 2.0 m the calculated values are very similar, and at 2.5 m the impulse on the flush door is lower than the impulse on the recessed door. Also, for the flush door case, the simulated results are consistently higher than the experimental results. The reason for these

discrepancies is related to the pressurised volume model used to initiate the calculations for the frame charge simulations.

**TABLE 9**  
Frame charge on both flush and recessed doors.  
Comparison of experimental and simulated mean positive phase impulse.

Distance from door edge (m)	Mean Positive Phase Impulse Experimental (Pa.s)		Mean Positive Phase Impulse Simulation (Pa.s)	
	Flush Door	Recessed Door	Flush Door	Recessed Door
1.0	40	44	65.0	49.7
1.5	44	50	47.0	46.3
2.0	38	40	51.6	50.1
2.5	32	41	49.3	51.9
3.5	29	31	45.2	50.9

As noted earlier in this section, the pressurised volume model used to initiate the calculation produces a double peaked structure which persists longer in the simulation than in the experimental traces. This broadens the overall width of the primary shock, and results in an enhanced value for both positive phase duration and mean positive phase impulse. This can be clearly seen in Figures 5a to 5d.

Although the simulations have been able to show the effect of the ledge in enhancing the peak pressure at the more distant gauge locations, comparison of the simulated mean positive phase impulse on the flush and recessed doors shows that they have not been able to accurately model the effect of the ledge on the complete pressure history of the flow. The similarity between the simulated mean positive phase impulse values for the flush and recessed doors for distances between 1.5 m and 2.5 m shows that the detailed effects of the recess have been washed out in the following flow. Whether this is due to our method of modelling the initial energy release from the distributed charge, or simply an effect of the discrete nature of the grid, is currently unknown.

## 6. CONCLUSION

We have presented experimental results and 3D numerical simulations of the gas dynamic flow fields produced by the detonation of both snib and frame charges on both flush and recessed doors. Comparison of the numerically simulated peak pressure, arrival times, and positive phase durations show good agreement with those obtained from experimental pressure transducer records, when the

limitations on the accuracy of the calculations imposed by the finite grid size and the method used to simulate the initial detonation of the explosive are taken into account. In addition, the simulated results reproduce one of the more interesting trends in the experimental data, where the peak pressure at the more distant gauge locations for the frame charge is found to be higher for the recessed door, rather than the flush door. Our simulations have clearly shown that this effect is caused by pressure enhancement resulting from the coalescence of the weakened primary shock from the distributed frame charge and its ground reflection.

## 7. ACKNOWLEDGMENTS

We thank G. Yannikopoulos for providing the pressure-time records in a suitable format, and P. Thibault of Combustion Dynamics Ltd. for helpful advice.

## 8. REFERENCES

1. Winter, P.L., Thornton, D.M. and Learmonth, L.A., 1995. "*Air Blast Hazards Associated with Door Breaching Operations*". Interim DSTO Technical Report (Classified).
2. Thibault, P and Sulmistras, A., 1992. "*Fluid Dynamics / Blast Prediction & Structural Response Workstation*",. Proceedings of the TTCP TLG-3 Blast / Thermal Symposium, Melbourne, May 26-28, 1992.
3. Boris, J.P. and Book, D.L., 1973. "*Flux-Corrected Transport 1: SHASTA, A Fluid Transport Algorithm that Works*." J. Comp. Phys. 11, 38.
4. Oran, Elaine S. and Boris, Jay P., "Numerical Simulation of Reactive Flow", Elsevier, New York, 1987.
5. Hyde, D.W., 1988. "*CONWEP - Conventional Weapons Effects*". Computer program based on the conventional weapons effects calculations. contained in TM-5-8855-1.
6. Kemister, G., Borg, R.A.J. and Jones, D.A. "*Accuracy of Airblast Simulations Initiated by a Pressurised Volume Model*". DSTO Technical Report, in preparation.
7. Kemister, G. "*CFD Simulations of The Australian Challenge*". DSTO Technical Report, to be published.

# Nonlinear Analysis of Tunnel-Section Subjected to Explosion Loading

K. Høiseth

SINTEF Structures and Concrete, 7034 Trondheim, Norway \*

P.Nauta

TNO Building and Construction Research, P.O.Box 49, 2600 AA Delft, The Netherlands

## Abstract

The paper contains the first results of a numerical study on the response of a typical tunnel-section in reinforced concrete, being subjected to an idealized internal explosion load. The results of a two-dimensional transient dynamic analysis show that a mechanical system of plastic hinges develops before completion of the load-history, and that the deformations involved exceed the rupture limit of the reinforcement. Due to the quasistatical character of the problem, also nonlinear static analyses were performed. The results indicate that shear failure would occur at an early stage of the load-history, before plastic hinges would develop. The study demonstrate the capabilities of numerical simulations, which account for the main mechanical properties of reinforced concrete, to predict load carrying capacity and associated failure modes. The paper highlights however the importance of a carefull evaluation of numerical results, also when adequate formulations are used.

## Introduction

The increasing amount of vehicles, which transport explosive and combustible cargo, represents particular danger in connection with tunnels. To limit the damage in case of accidental events, the loadcarrying capacity must sustain possible impulsive loadings.

This is the subject for a case study within the field of computational mechanics, which is being carried out at TNO Building and Construction Research, on behalf of the Ministry of Traffic, Public Works and Water Management in the Netherlands.

The purpose of the study is twofold:

- to investigate the mechanical behaviour of a typical tunnel subjected to explosion loading. This is necessary in order to evaluate the degree of safety, and to produce sound renovation proposals.
- to demonstrate the capabilities of nonlinear analysis to predict loadcarrying capacity and associated failure mode. If properly reinforced, concrete structures can absorb a significant amount of energy, when the complete nonlinear material behaviour is accounted for.

The constitutive behaviour of reinforced concrete is however complex, because it is highly dependent on the stress level, the stress path which has been undergone, and hence also

---

\*Presently at TNO Building and Construction Research

the state of stress. Under transient dynamic loading, all material points in the structure are subjected to unproportional loading conditions, to continuously varying states of stress. Unless the main constitutive phenomenaes of reinforced concrete are being properly accounted for, unreliable results are obviously obtained. In the development of DIANA<sup>1</sup>, the main efforts have always been directed towards concrete mechanics, and the package offers material models which should be highly adequate also for the problem at hand.

The project is performed in two phases. The current paper deals with the results obtained in the first phase.

## 1 Problem description and analysis approach

The investigation is being carried out on a typical tunnel-section, being exposed to an idealized explosion loading. The tunnel-section, which consists of two compartments, separated by a double wall, is shown in Fig 1. The figure also illustrates that the idealized internal overpressure, which is due to the explosion, effects one of the compartments. Fig 2 shows the amount and layout of the reinforcement, as well as the material properties of reinforcement and concrete.

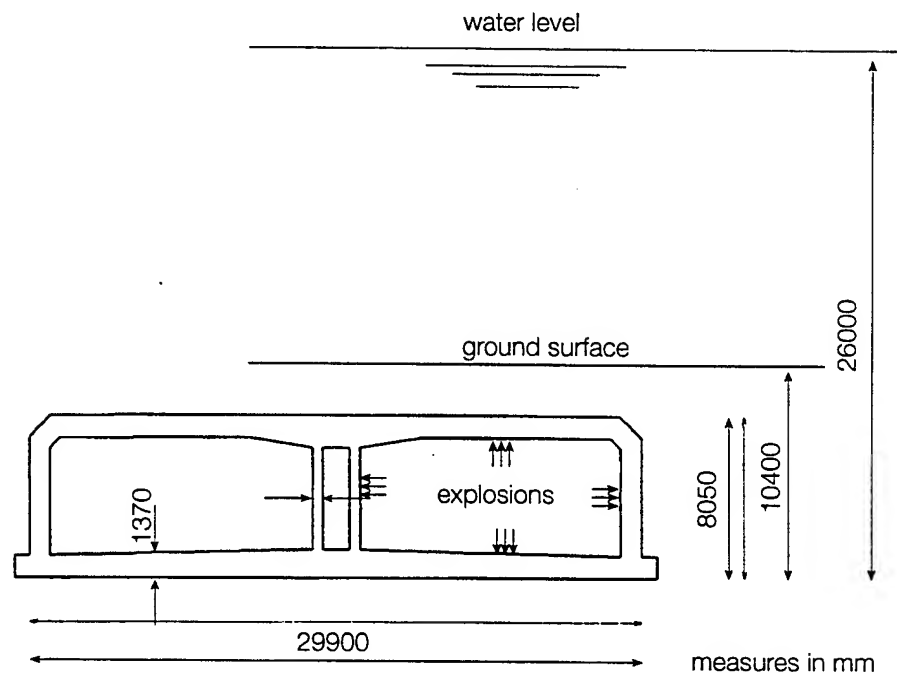


Figure 1: Tunnel cross-section

The tunnel is anticipated to be under ground, surrounded by sandy material, and submerged in water. In the first part of the study, which is covered in the present paper, the external loading is accounted for, while the mass of the surrounding material is neglected.

<sup>1</sup>DIANA is a registered trademark of TNO

The applied pressure-history originates from a model provided by TNO Prins Maurits Laboratory for gas explosions in tunnels, see Fig 3. The model is based on a number of tests performed at Beveren in Belgium, in a tunnel specifically used for explosion testing. The pressure history has an immediate onset of 25 bar, which is reduced by a parabolic curve, to 7 bar after 25 ms. A pressure level of 7 bar is maintained for 100 ms, after which the pressure is reduced linearly to zero at 150 ms.

The immediate onset of pressure generate equivoluminal stress waves, as well as distortional stress waves, in the structure. In concrete, these high frequency vibrations can cause internal cracking, delamination or scabbing<sup>2</sup>. It is however generally anticipated that the rate of loading in connection with gas explosions is too low to cause stress wave induced cracking. In the present study, a precise description of stress-wave propagation is consequently not aimed at. This does however not implicate that the high-frequency vibrations are neglected. In the dynamic analyses, a time-step length of 0.2 ms, was used, which gives a resolution sufficient to trace vibrations with frequencies up to 600 Hz.

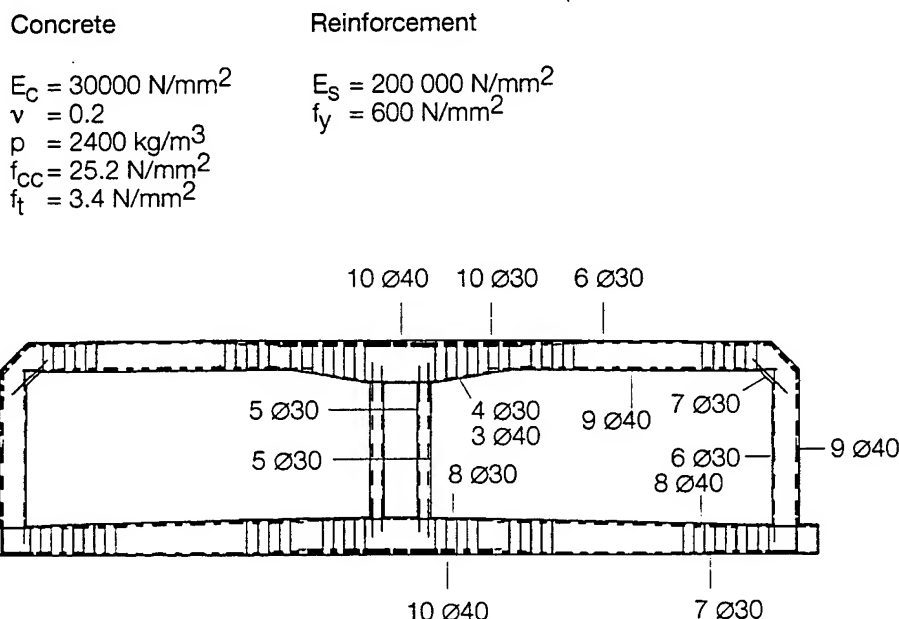


Figure 2: Reinforcement layout (1.5 m wide section) and material properties

The first phase of the study was carried out in the following manner:

**Calculations of characteristic properties.** As a first approach, to get an impression of the mechanics involved, the first modes of vibration, together with the eigenmodes, were calculated. This revealed that the duration of loading was long, compared to the first frequencies, and hence that the inertia forces would amplify the deformations caused by the relatively long duration of constant pressure. This was confirmed by a subsequent linear elastic analysis.

**Two-dimensional nonlinear dynamic analysis.** However the results clearly showed that

<sup>2</sup>When a concrete surface is exposed to a high rate compressive loading, concrete is frequently torn off at the opposite face. This is due to wave reflection, and is commonly termed scabbing.



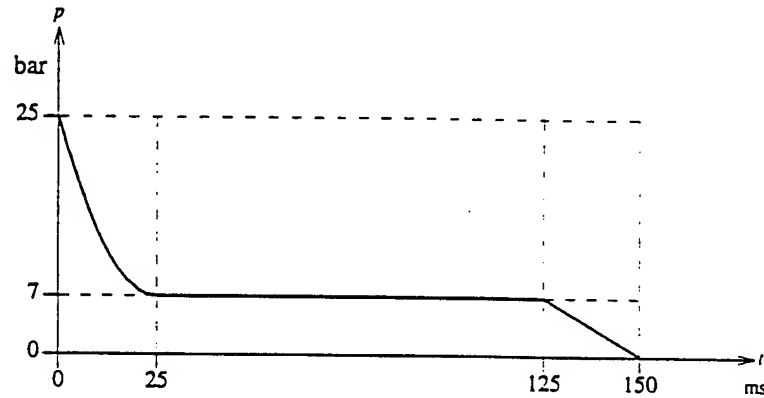


Figure 3: Internal pressure-history due to idealized explosion

the pressure-load would exceed the load carrying capacity of the tunnel-section, a non-linear analysis was performed in order to study possible failure modes.

**Nonlinear Static Analyses.** Due to the quasistatic character of the problem, also nonlinear static analyses were carried out, to improve the understanding of the most likely failure mechanism.

## 2 Calculations of characteristic properties

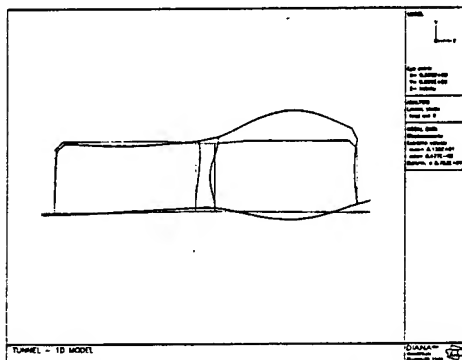
A geometric model, consisting of 3-node Mindlin beam elements [1], was used to study the basic dynamic properties of the problem. The boundary conditions, the internal pressure, the elastic material properties and the density, were identical to those used in the nonlinear analyses, see Section 1 and Section 3

Fig 4 shows the deformed shape of the model, as obtained by a static linear elastic analysis, in addition to the frequencies and the shape of the first five eigenmodes.

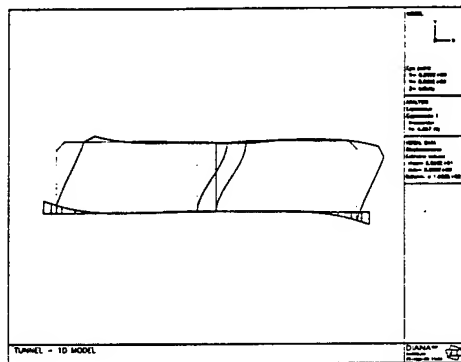
It should be noticed that the deformation due to static loading has a shape almost similar to that belonging to the 5. mode of vibration. A discrepancy concerns the horizontal displacement of the mid-wall. The internal pressure force the mid-wall to bend outwards, which give a shape similar to that of a clamped beam. The 5. mode of vibration also shows a vertical displacement of the outer wall, directed downward, which contradicts the deformed shape of the statically loaded model. What this concerns, the deformed shape of the statically loaded model is more in agreement with the 3. mode of vibration.

The eigenmodes as well as the corresponding periods, which are long compared to the duration of the pressure-history, signify that the lower modes of vibration will be highly activated during the load application. This is clearly illustrated in Fig 5 which shows the vertical displacement of a point P, located in the middle of the roof-span, in the exposed compartment. Due to the immediate onset of pressure load, the inertia forces has a favourable effect on the displacements, when it concerns the initial peak of the pressure history.

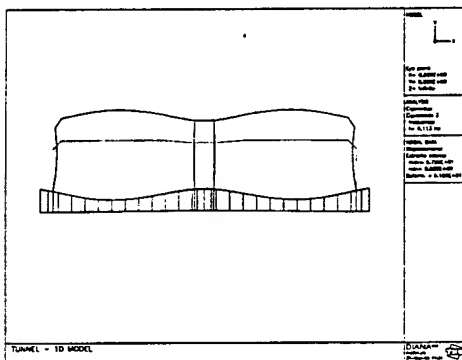
Regarding the relatively long duration of constant pressure, however, the figure shows that the response belongs to the quasistatical domain, which imply that the inertia forces has an unfavourable effect on the maximum deformations, and thus on the loadcarrying capacity.



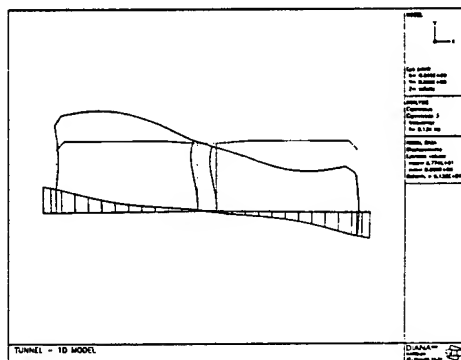
Mode of deformation, static pressure



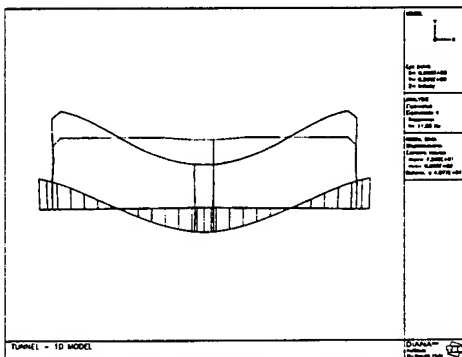
1. Mode of vibration 4.6 Hz



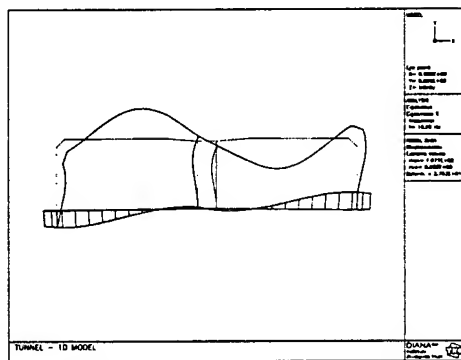
2. Mode of vibration 9.1 Hz



3. Mode of vibration 9.1 Hz



4. Mode of vibration 11.6 Hz



5. Mode of vibration 17.0 Hz

Figure 4: Static shape of deformation due to internal pressure, and the first 5 Eigenmodes

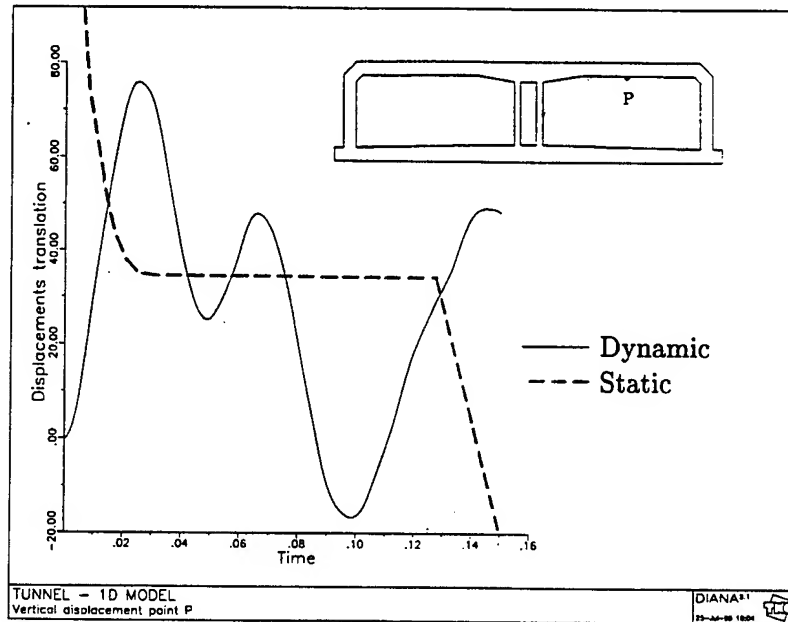


Figure 5: Vertical displacements in the middle of roof span - Dynamic versus static linear elastic analyses

### 3 Two-dimensional nonlinear dynamic analysis

#### Two-dimensional model

The concrete section, which was taken as 300 mm in the longitudinal direction, was modelled by 8-node plane stress elements. In the quadrilaterals, which are termed CQ16M in DIANA [1], the reinforcement was represented by integrated bar elements. The numerical integration was performed by a 2x2 scheme for the quadrilaterals, and a 2 point scheme for the bar elements, see Fig 6.

The interaction between the foundation of the tunnel-section and the ground, was accounted for by two-dimensional interface elements, with 6 nodes (CL12I). The stiffness of the elements in the vertical direction (normal traction) and the horizontal direction (shear traction) was anticipated, see Fig 7. The stiffness modulus in the vertical direction,  $3 \cdot 10^{-2} \text{ N/mm}^3$ , gives an elastic bedding, which imply that a compressive traction of  $30 \text{ N/mm}^2$  between the foundation of the tunnel and the ground yields a deflection of 1.0 m. In tension, the stiffness was almost zero. The negligible value was given in order to omit numerical instability. In the horizontal direction, a friction stiffness of  $1 \cdot 10^{-4} \text{ N/mm}^3$ , was used.

The geometric model of the compartment subjected to explosion loading is shown with dotted lines in Fig 9. The belonging bar elements, which represents the reinforcement, appears in the Figures 12 - 16. The remaining part of the model was symmetric about the mid wall of the subjected compartment.

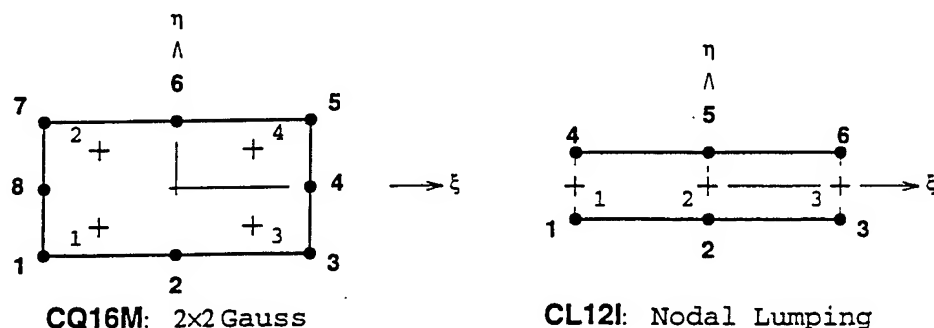


Figure 6: Elements in two-dimensional model

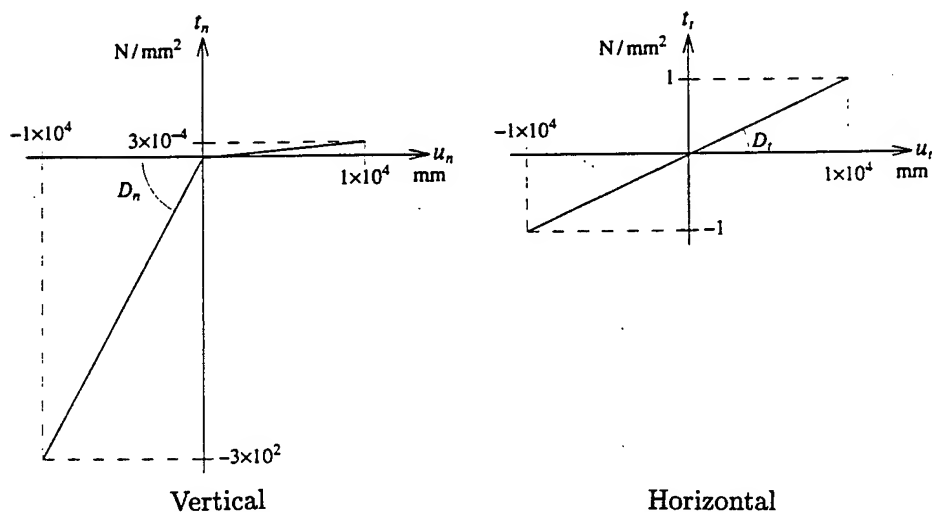


Figure 7: Stiffness properties between foundation and ground

## Material models

A smeared fixed crack model was used for concrete under tensile states of stress. The applied relationship between the normal stress and strain normal to a crack plane is shown in Fig 8.

For concrete sections with a high reinforcement ratio, the ultimate loadcarrying tensile strain  $\epsilon_{us}$  across a crack plane, is frequently taken equal to the yield strain of the reinforcement, according to the so-called tension-stiffening approach. Due to the moderate reinforcement ratio in the tunnel-section, the following assumption was made:

$$\epsilon_{us} = 0.4 \frac{f_y}{E_s} = 0.001 \quad (1)$$

The shear strength in the crack-plane, the aggregate interlock effect, was accounted for by a shear-retention factor  $\beta = 0.01$ . This means that the shear modulus is reduced to 1 % of the elastic value in a crack plane.

The smeared crack model allows multiple cracks to develop in an integration point. In the current model, the threshold angle between consecutive cracks was set equal to  $90^\circ$ .

The smeared crack model was combined with an elastoplastic model for compressive states of stress. The well-known Drucker-Prager yield surface was used, with an associated flow rule. Based on the compressive strength  $f_c$  and an anticipated friction angle  $\phi$  of the concrete, the belonging cohesion reads:

$$f_c = 25.2 \text{ N/mm}^2 \quad (2)$$

$$\phi = 30^\circ \quad (3)$$

$$c = f_c \frac{1 - \sin \phi}{2 \cos \phi} = 7.3 \text{ N/mm}^2 \quad (4)$$

The uniaxial stress/strain relationship for the reinforcement was represented by an elastoplastic model, as shown in fig 8.

The material properties of concrete and reinforcement is given in fig 2

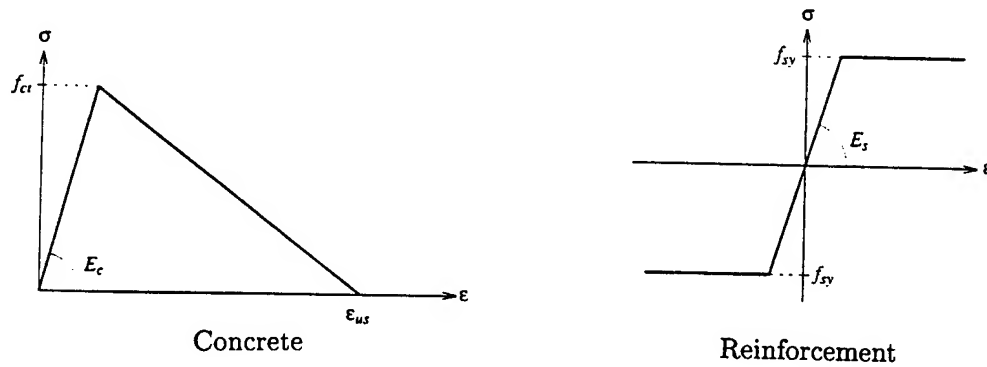


Figure 8: Uniaxial stress/strain relationship for concrete under tension and reinforcement steel.

## Computational procedure

Prior to the dynamic analysis, a static nonlinear analysis was performed, in order to account for the initial conditions. The applied loadings consisted of:

- the deadload of the concrete section,
- the deadload of a surfacelayer on the base of the section

- the surrounding ground - and waterpressure.

The initial deformations, as well as the corresponding stresses and the external loadvector were applied at timestatation  $t_0$  in the dynamic analysis. The internal pressure history, as given in Fig 3 was applied, and the semidiscrete equation of motion was solved at intervals of 0.2 ms between consecutive time stations. The dynamic analysis was carried out until  $t=300$  ms was reached.

The time integration was carried out by the well-known Newmark's Average Acceleration algorithm.

Both the static analysis and the subsequent dynamic analysis was performed with an incremental-iterative solution process, according to the Constant Stiffness approach.

## Numerical results

The deformations and velocities of the subjected compartment at time  $t=100.0$  ms, is shown in Fig 9 and Fig 10.

The deformed compartment has a similar shape as that belonging to the 5. mode of vibration, as shown in Fig 4. A discrepancy concerns the horizontal displacement of the mid-wall. The internal pressure force the mid-wall to bend outwards, which give a shape similar to that of a clamped beam. The results show however that the lower modes of vibrations are highly activated. during the load application. Hence, the response in the quasistatistical domain imply that the inertia forces has an unfavourable effect on the maximum deformations, and thus on the loadcarrying capacity.

The deformations and velocities, with respect to time, is illustrated by means of two points on the internal surface. The location of the points are given in Fig 9. Point P is located almost in the midst of the roof, point Q in the middle of the left wall.

Fig 11 shows the vertical displacement and the velocity of point P. At the end of the analysis, the vertical displacement exceeds 5.0 m, The vertical velocity has at this moment dropped to zero, which means that the maximum displacement is reached.

Fig 12 shows the horizontal displacement and the velocity of point Q. The maximum displacement, which with respect to the span length is approximately equal to the vertical displacement in the midst of the roof, is reached after approximately 150 ms. This is about half the time needed for point P to arrive at its maximum vertical displacement, which can be due to two reasons.

The mass of the roof section is considerably larger than the mass of the mid-wall. Hence the time needed for retardation of the roof is longer than for the mid-wall. This is clearly shown by the velocities in Fig 11 and Fig 12.

The vertical displacement of the roof subjects the mid-wall to a large resultant tensile force, which compensate the horizontal movement of point Q.

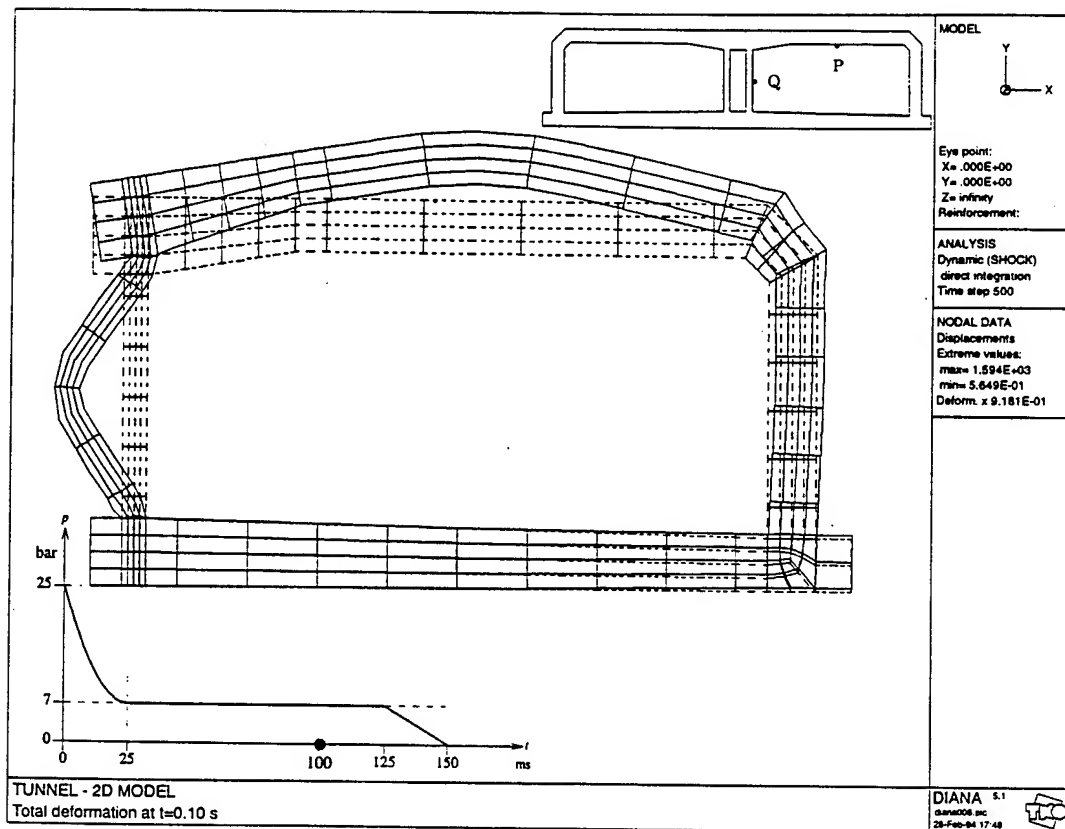


Figure 9: Deformations after 100 ms of pressure loading

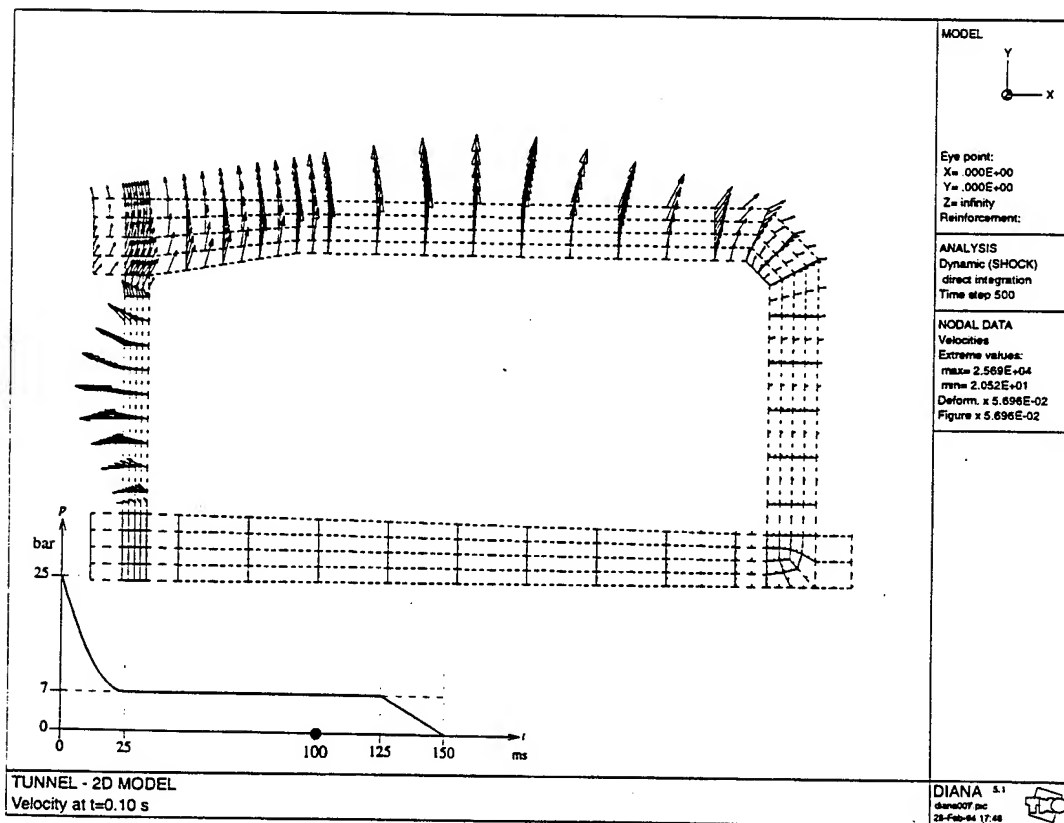


Figure 10: Velocities after 100 ms of pressure loading

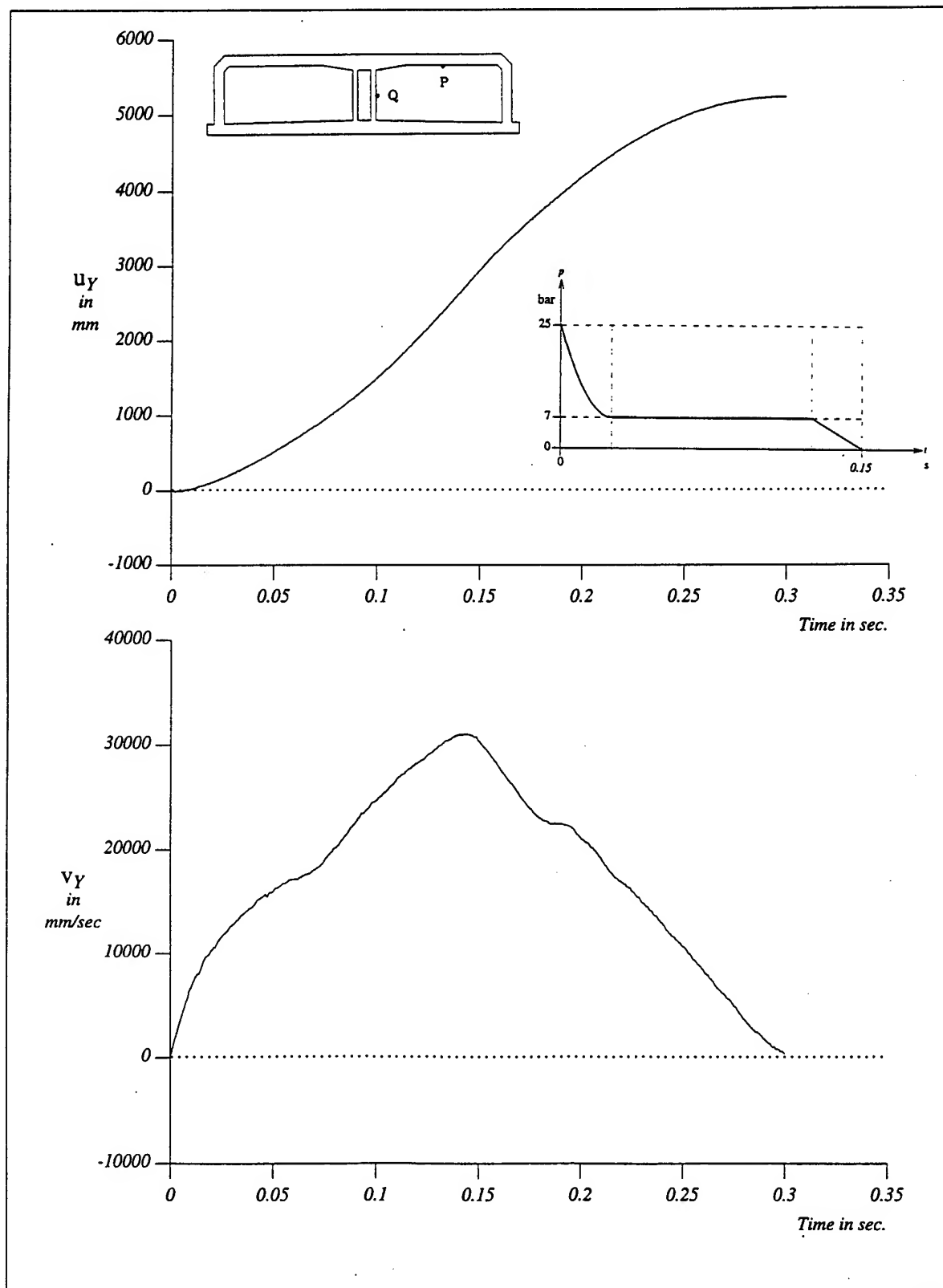


Figure 11: Displacement and velocity of point P (node 411)



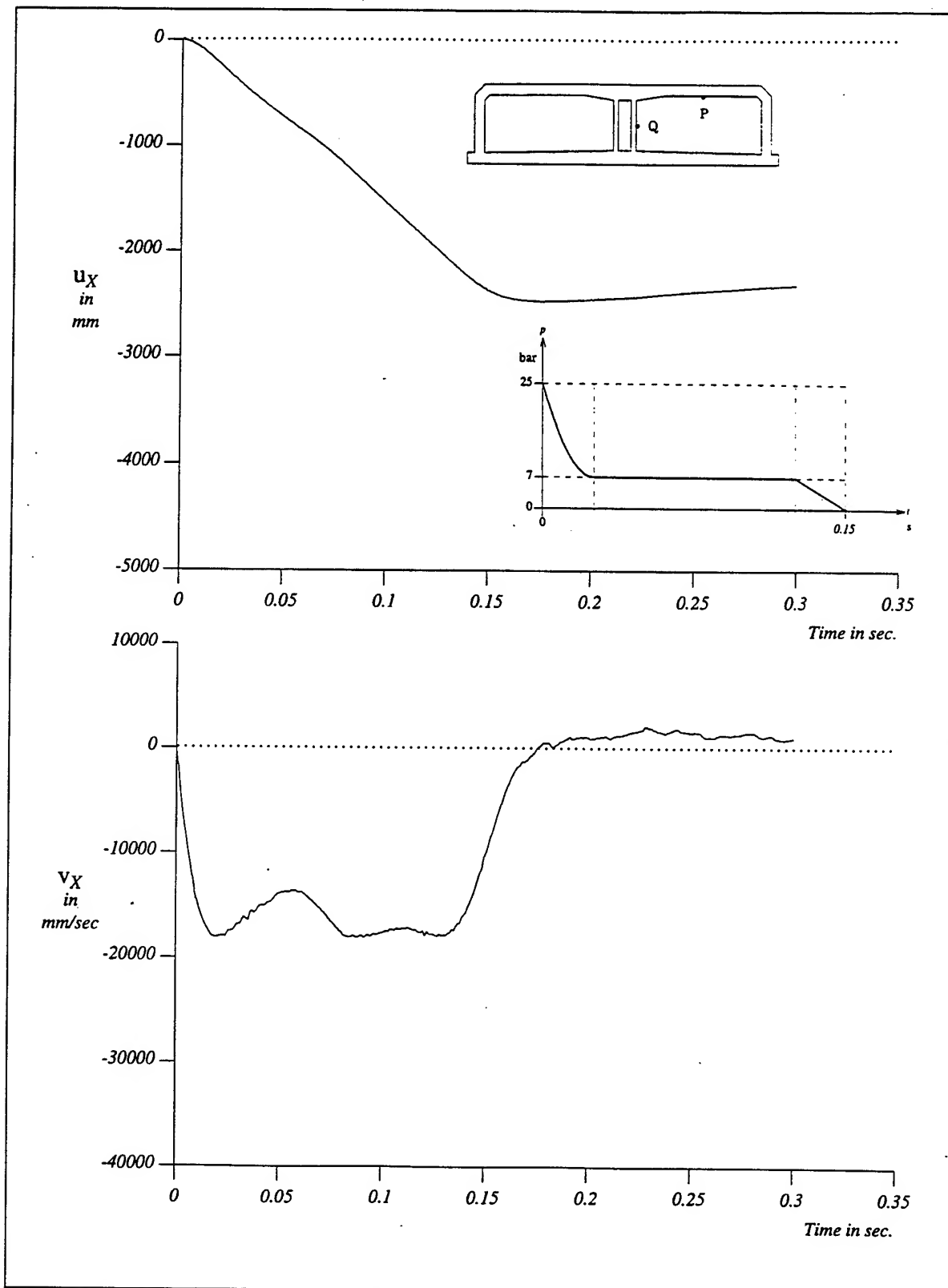


Figure 12: Displacement and velocity of point Q (node 621)

The maximum displacements of the mid-wall and the roof, relative to the span lengths, are much larger than the displacements that can be expected even by ductile failure of reinforced concrete members. Hence, the loadcarrying capacity of the tunnel is exceeded at an early stage of the analysis. This is illustrated by the following Figures, which belong to the time-station 100 ms.

**Fig 13** Shows the stress level in the longitudinal reinforcement in the roof and the foundation. In the roof, plastic hinges have developed in the top right corner, in the middle section, and in the connection with the mid-wall. Due to the large vertical translation of the middle section of the roof, even the uppermost reinforcement in the bottom face is yielding in tension. The compression zone is thus limited to the area under the lowest reinforcement layer, which confirm the large rotations shown in Fig 11. In the reinforcement in the top face, the plastic strains exceeding 17 %, which indicate that rupture would have taken place, and that the loadcarrying capacity is by far exceeded.

**Fig 14** Shows the stress level in the reinforcement bars in the top right corner, and in the outer face of the wall. It clearly shows the plastic hinge which has developed in the connection between the roof and the right wall. Compared to the stress level in this area, the stresses in the outer face of the wall are moderate.

**Fig 15** The plastic hinge between the mid-wall and the roof is clearly illustrated. Also in the mid-wall, a three hinge mechanism has developed.

**Fig 16** Shows the areas in the mid-wall reinforcement, where plastic strain occur. The three-hinge mechanism is clearly demonstrated. In the connection between mid-wall and roof, the plastic strain is more than 70 %, which is far more than the rupture limit. Hence, the mid-wall would have failed in the connection with the roof, and probably also in the connection with the foundation, before the large bending shown in Fig 11 would have time to develop. The lack of stirrups in these regions would produce shear failures.

**Fig 17** Shows the stress level in the stirrups in the exposed compartment. The stirrups in the roof are yielding in the area close to the mid-wall, and in the right corner.

**Fig 18** Shows the fully open cracks. Fully open cracks signify crackstrains larger than the loadcarrying tensile strain  $\epsilon_{us}$ . The crack pattern confirm the large deformations, and the development of plastic hinges. In the mid-wall, cracks are fully open in almost all integration points, which indicate that failure has occurred. The direction of the cracks in the mid-wall, near the connections with the foundation and the roof, are similar to the crack-directions experienced by shear failure under static loading conditions. In the middle of the mid-wall, the crack pattern corresponds with a typical bending mode. Due to the inertia forces, it is reasonable to believe that shear failures would occur before the large bending of the mid-wall is activated.

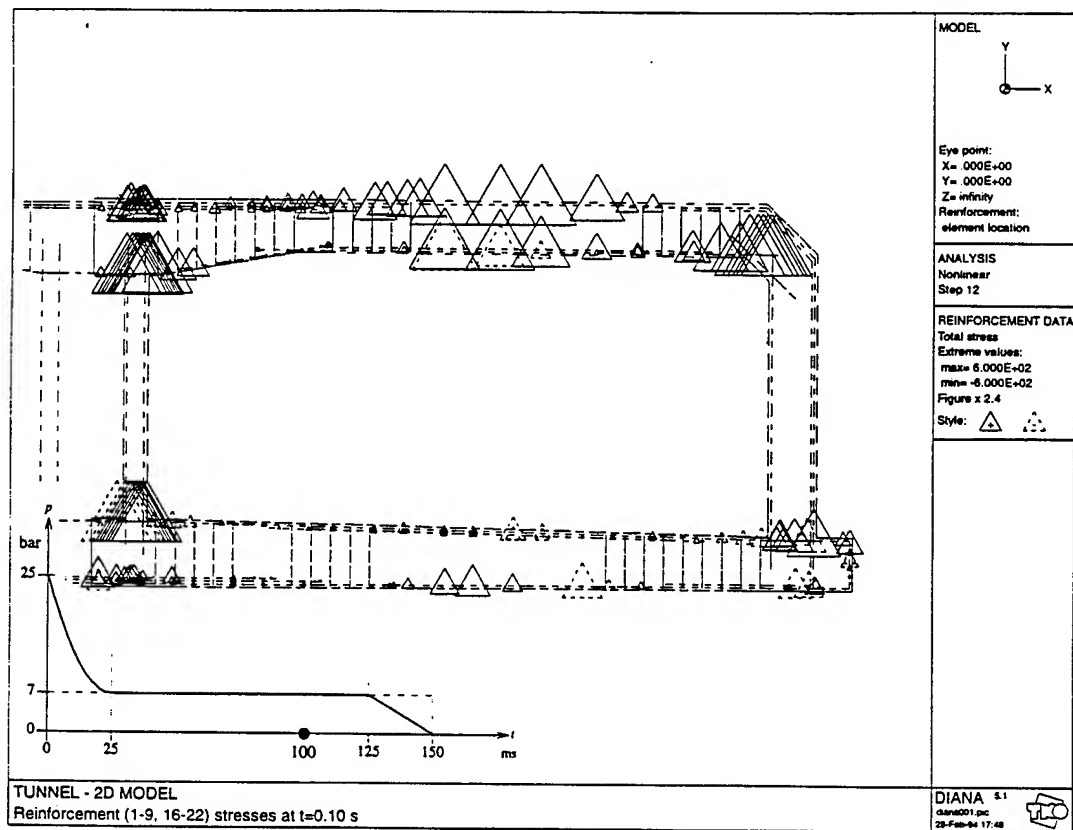


Figure 13: Stresses in longitudinal reinforcement in foundation and roof after 100 ms pressure loading

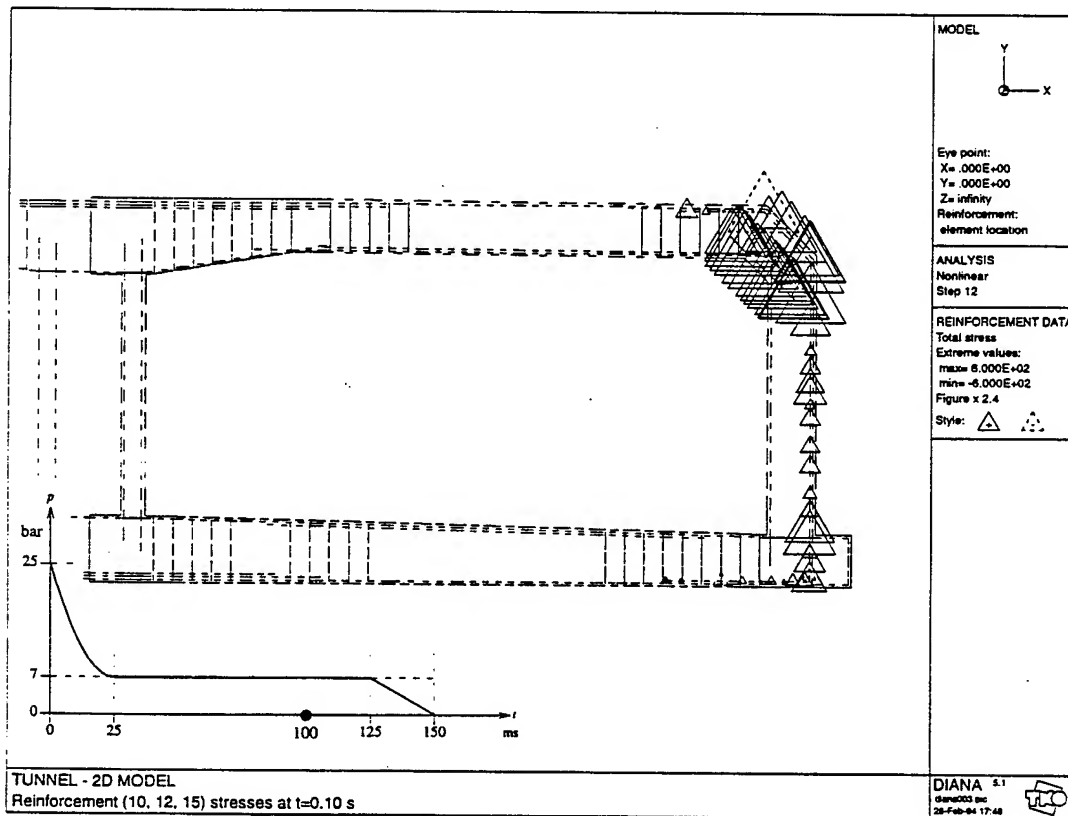


Figure 14: Stresses in longitudinal reinforcement in outer wall (outer face) and top right corner after 100 ms pressure loading

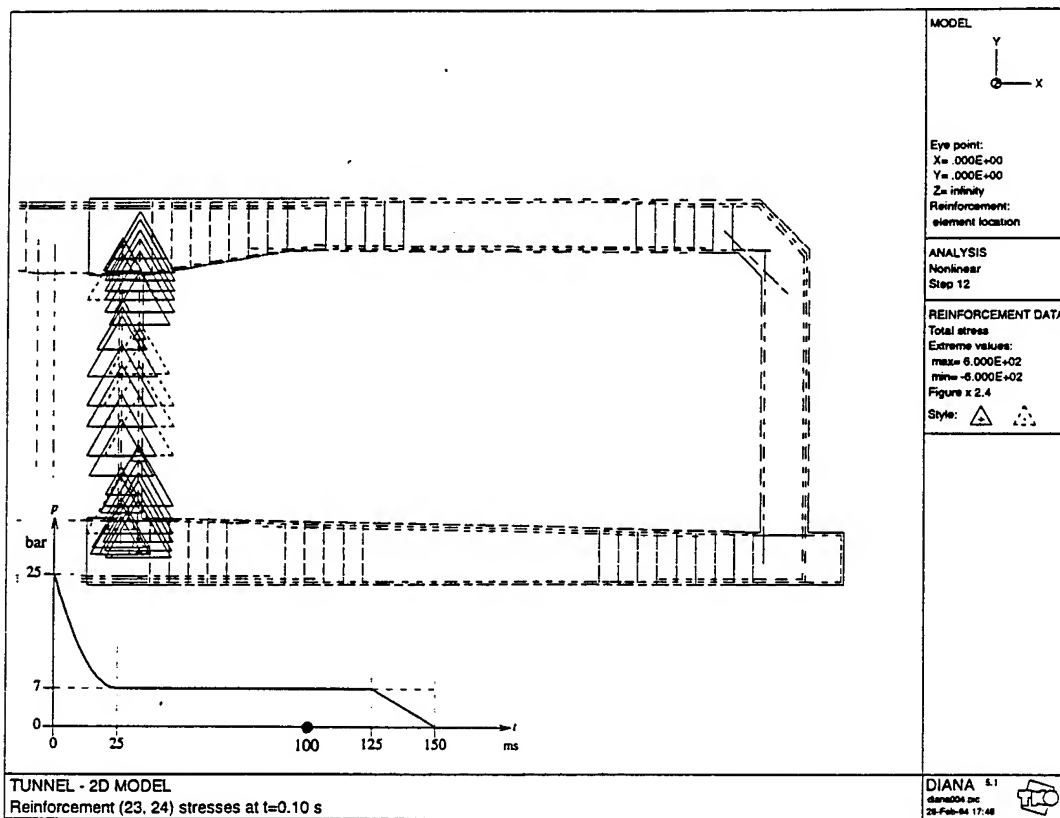


Figure 15: Stresses in longitudinal reinforcement in mid-wall after 100 ms pressure loading

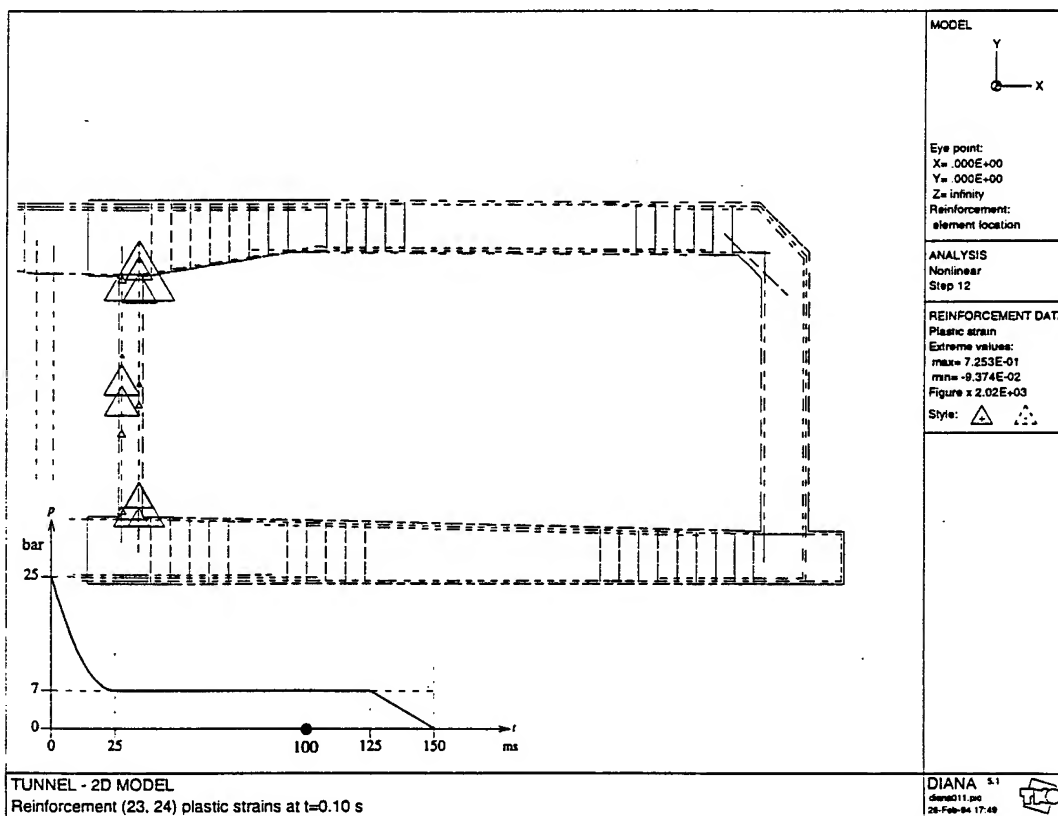


Figure 16: Plastic strains in longitudinal reinforcement in mid-wall after 100 ms pressure loading

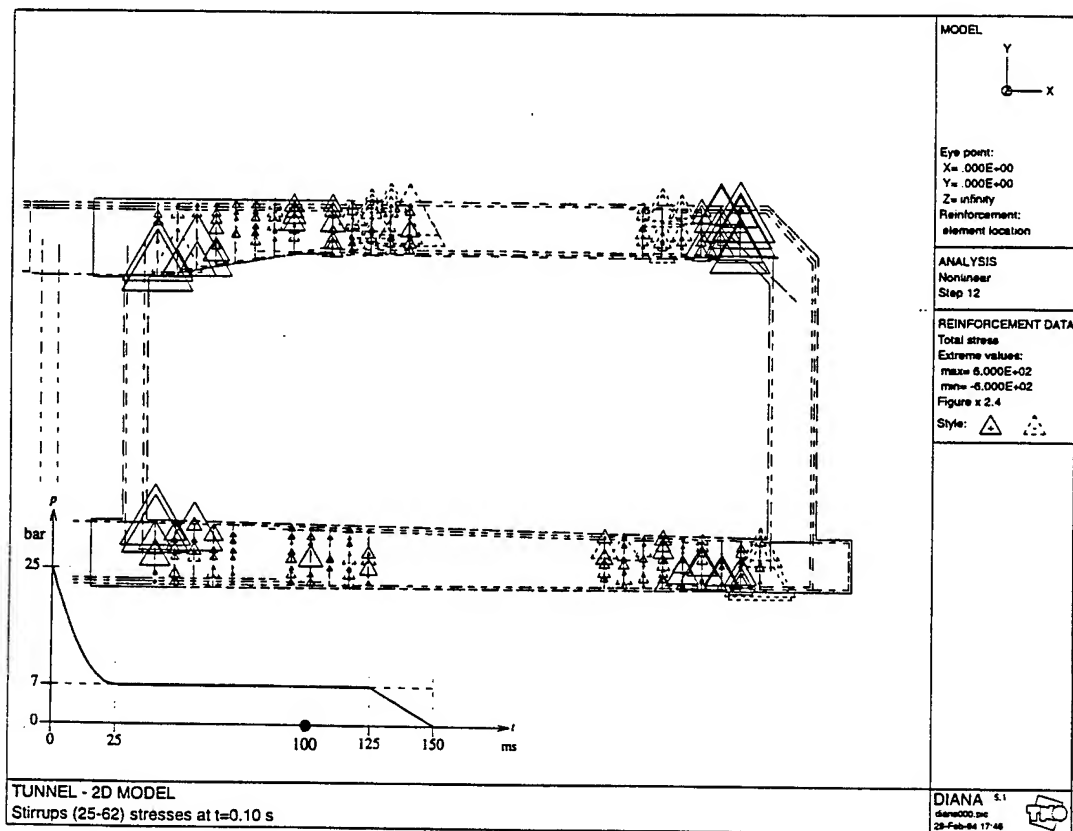


Figure 17: Stresses in stirrups after 100 ms pressure loading

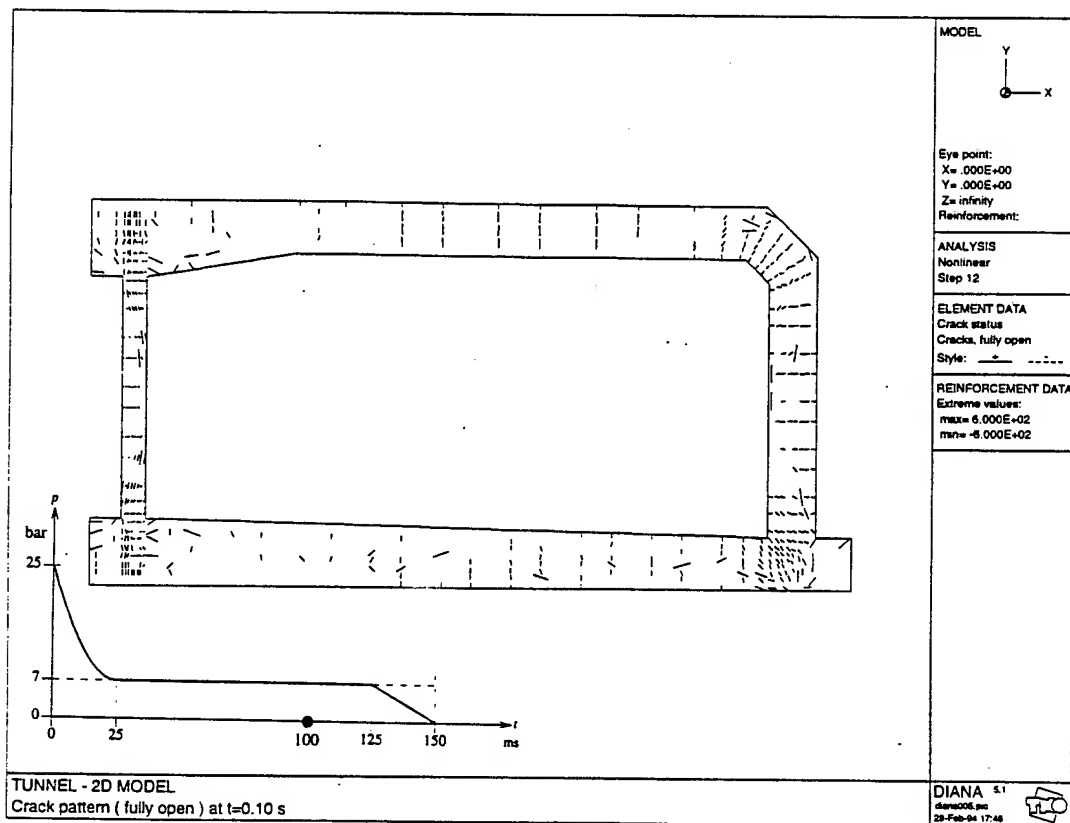


Figure 18: Fully open cracks after 100 ms pressure loading

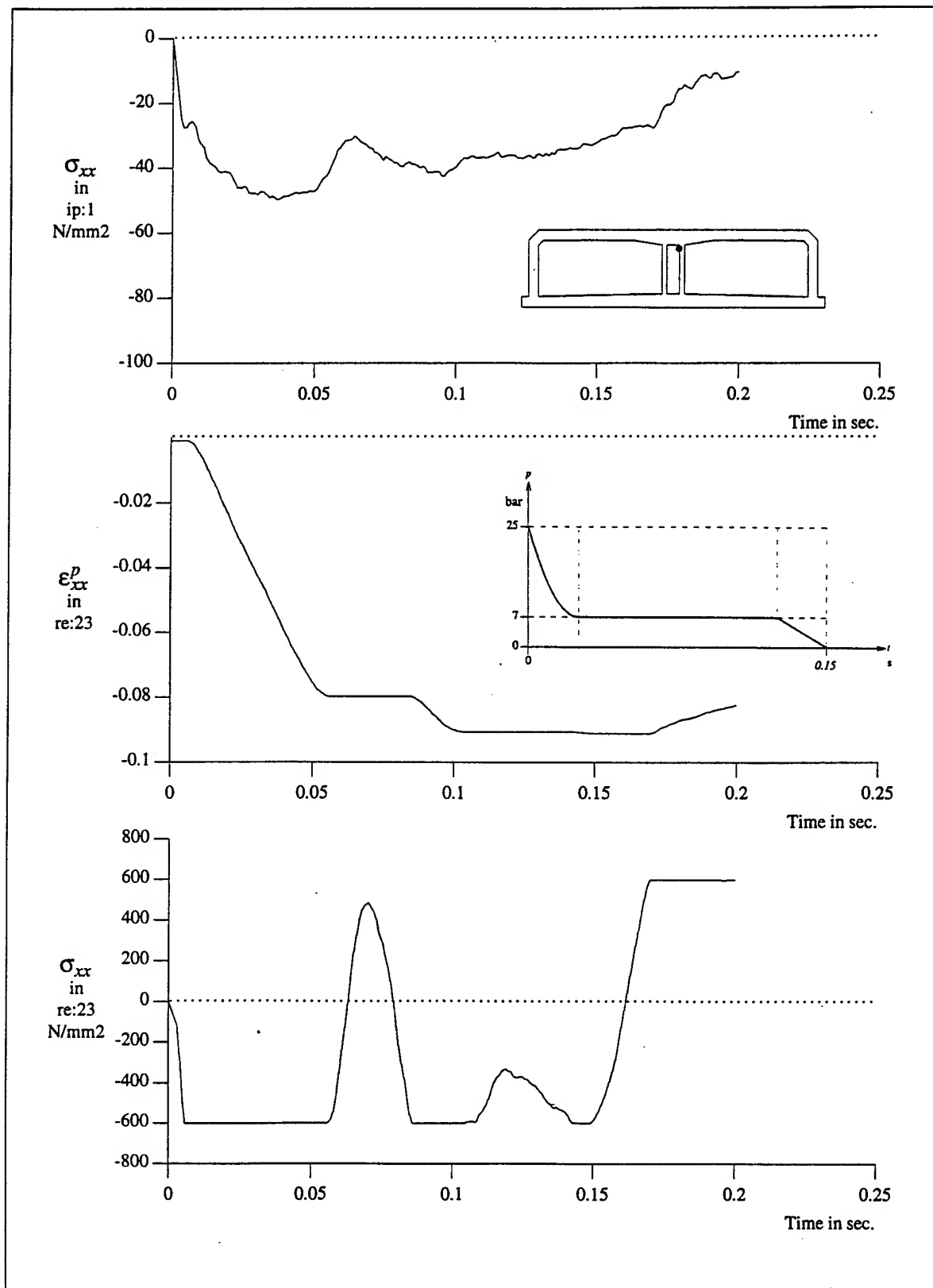


Figure 19: Element normal stress, plastic strain - and stress in reinforcement in mid-wall, at upper left connection with roof

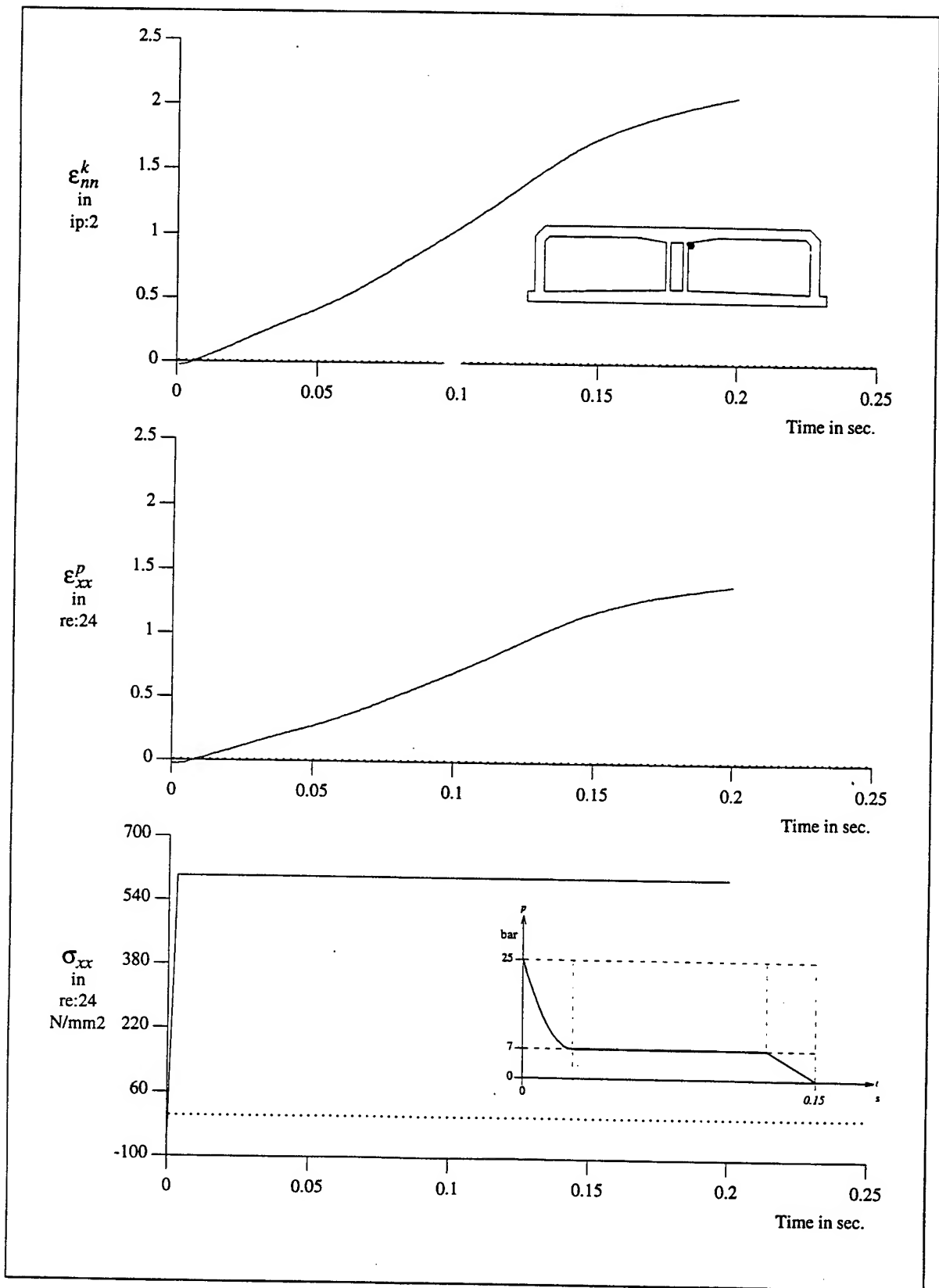


Figure 20: Crack-strain, plastic strain - and stress in reinforcement in mid-wall, at upper right connection with roof

Fig 19 illustrates the stress - and strain conditions in an element located on the left surface of the mid-wall, and connected to the roof. The normal longitudinal stress,  $\sigma_{xx}$ , in the concrete exceeds the compression strength at a very early stage of the pressure history. Because the state of stress is not coherent with the principal direction, the material model permits the concrete to carry a larger normal stress than the uniaxial compressive strength. The relative stiff connection between the roof and the mid-wall allows an arch-mechanism to be activated in the early phase of the pressure history. In the connection with the roof, this give a compressive resultant in the uppermost left area of the mid-wall. The direction of this strut, makes a small angle with the vertical axis of the wall. The direction is indicated by the crack planes in Fig 18.

The compressive resultant is also noticeable in the reinforcement stress. The yield limit is reached almost at the same time as the compressive strength in the concrete, and the plastic strain in the reinforcement  $\epsilon_{xx}^p$  increase at a high and almost constant rate. After approximately 60 ms, the normal compressive stress in the concrete, as well as the reinforcement stress decrease rapidly. This is probably due to one of the lower eigenfrequencies of the system. The duration of the stress decrease and the subsequent increase, is close to the period of the 5.th mode of vibration. The onset of stress decrease is somewhat delayed compared to the decrease in horizontal translation of the middle of the wall, as shown in Fig 12, which may be due to the plastic state in large areas of the wall.

Fig 20 Shows the stress - and strain conditions in an the element located on the opposite side, that is on the right surface of the mid-wall, and connected to the roof. The crack strain in the outermost integration point increases rapidly, at an almost constant rate. The maximum loadcarrying tensile strain,  $\epsilon_{us}$ , is reached almost immediately after the onset of pressure-load, which imply that the tensile stresses must be carried by the longitudinal reinforcement solely. Hence, the yield limit is also reached at an early stage of the pressure-loading. The plastic strain in the reinforcement exceeds the level of rupture between 25 and 50 ms after the onset of pressure load.

The results after 100 ms of pressure-loading show that plastic hinge mechanisms develop in the roof and the mid-wall. Due to the lack of stirrups, the plastic hinges in the mid-wall will likely not develop before shear failures occur.

## 4 Initial shear failure - nonlinear static analyses

### Geometric model

The area of interest, the connection between mid-wall and roof, was represented by a high resolution mesh of 8-node plane stress elements (CQ16M). The remaining parts of the tunnel-section was modelled by 3-node Mindlin beam elements (CL9BE). The interface between foundation and ground was modelled as in the dynamic analysis, with two-dimensional interface elements. The plane stress elements and the beam elements were coupled by linear constraints in the interface. The geometric model is illustrated in Fig 21.

For the beam elements, a 2 point Gauss scheme was used in the longitudinal direction, and a 5 point Simpson over the height. The plane stress elements were integrated by a 3x3 Gauss procedure.



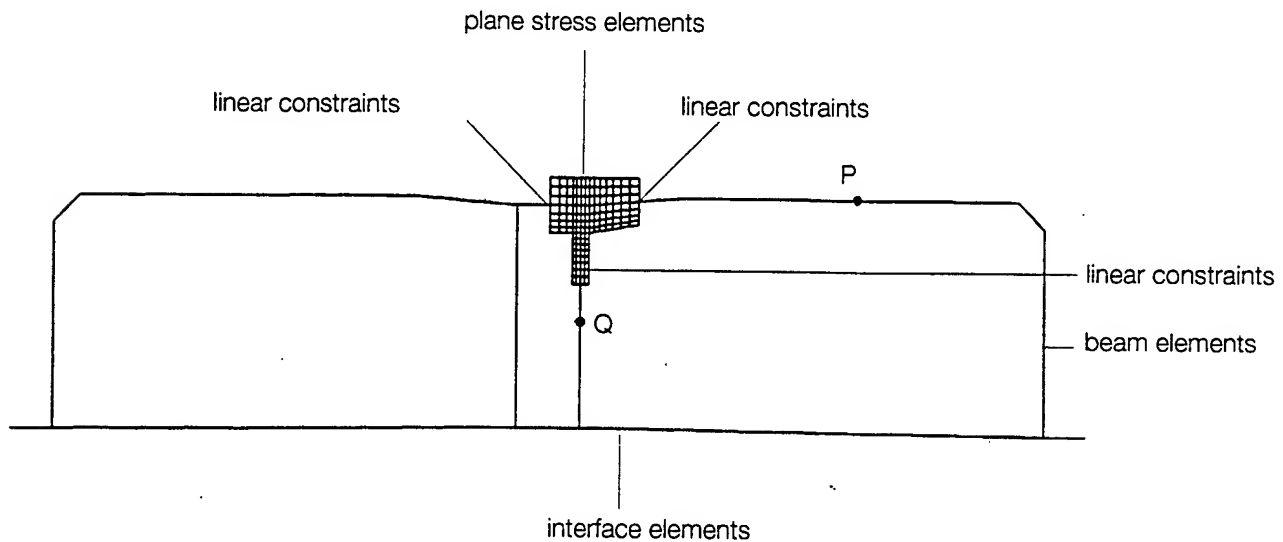


Figure 21: Geometric model

## Material models

The beam elements were intended to provide approximate boundary conditions for the local area of interest, and were therefore taken to be linearly elastic.

In the plane stress elements, the material models for concrete and reinforcement were the same as described in Section 3. However, to examine the tension stiffening effect, and the transfer of shear in cracks, the following variations were made:

The maximum loadcarrying tensile strain  $\epsilon_{us}$ , was in one analysis given the value 0.0015, while in the subsequent analysis half this value was used.

In the first analysis, the value of the shear retention factor was maintained, thus  $\beta = 0.01$ , while in the second analysis  $\beta = 0.05$  was used.

## Computational procedure

To account for the initial conditions, the dead loads given in Section 3, were applied incrementally. The internal pressure was subsequently incremented by 0.5 bar, until 1.5 bar was reached. After that, the internal pressure was incremented by 0.1 bar until failure occurred.

Both analyses were performed according to a modified Newton-Raphson procedure.

## Numerical results

The exposed compartment sustained a maximum internal pressure of:

- 2.55 bar with  $\epsilon_{us} = 0.0015$  and  $\beta = 0.01$
- 2.85 bar with  $\epsilon_{us} = 0.00075$  and  $\beta = 0.05$

At these pressure levels, the solution diverged, and the results clearly illustrated shear failures in the mid-wall, in the connection with the roof.

The following figures belong to the analysis with  $\epsilon_{us} = 0.0015$  and  $\beta = 0.01$ .

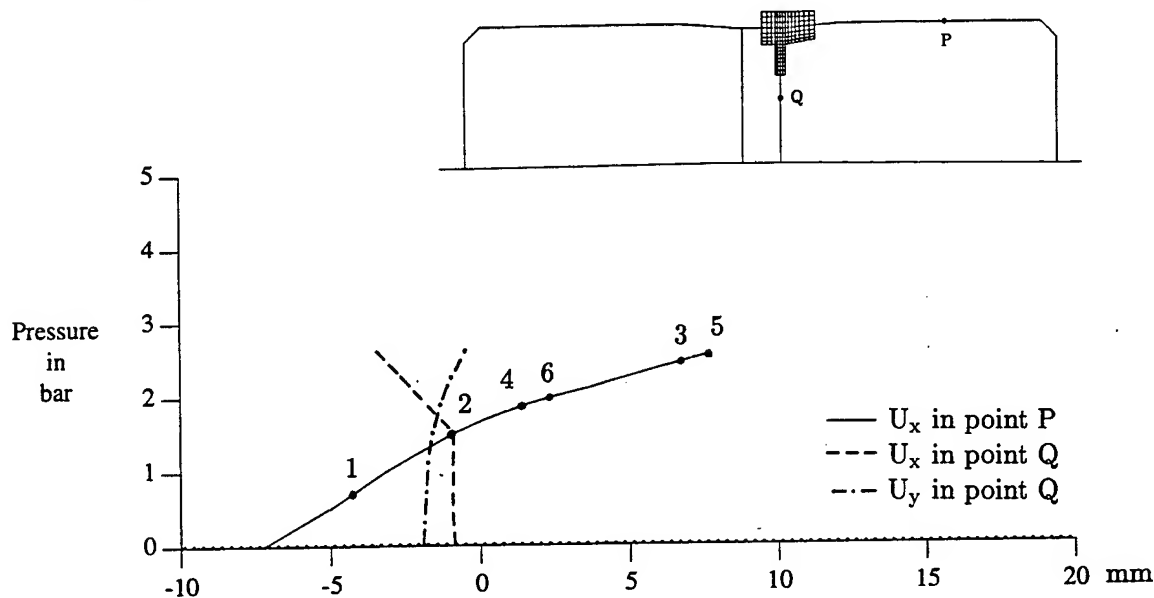
Fig 22 shows the vertical displacement of point P, and the horizontal and vertical displacement of point Q. It should be noticed that the deformations involved are small, compared to the deformations after 100 ms dynamic loading, as shown in Section 3. At an internal pressure of 1.5 bar, the first crack appears in the mid-wall, and the horizontal displacement of the mid-wall show a sudden increase. The vertical displacement of the mid-wall increase in an upwards direction at this point, which is significant, because the beneficial compression from the initial loadings is thus reduced.

Fig 23 and Fig 24 show the crack pattern and the fully open cracks, respectively, at maximum sustained internal pressure. The shear failure mode is clearly demonstrated.

Fig 25 shows the principal compression stress at maximum internal pressure. The compressive strut, which have the same direction as the crack planes, is in agreement with a typical shear failure of reinforced concrete members.

Fig 26 shows the stress in the longitudinal reinforcement. The reinforcement located on the outer face of mid-wall is hardly active, whereas the stress level in the reinforcement in the face subjected to internal pressure increases rapidly when the internal pressure exceeds 1.5 bar. At maximum sustained pressure, the stress level is close to yielding.

The analysis with  $\epsilon_{us} = 0.0075$  and  $\beta = 0.05$ , produced similar evidence of shear failure in the same area of the mid-wall.



- 1: Stress in reinforcement R2 (see Fig 26) changes from compression to tension (0.70 bar)
- 2: First crack in mid-wall
- 3: Stress in reinforcement R1 (see fig 26) changes from compression to tension (2.54 bar)
- 4: Cracking through cross-section mid-wall, except for left-most integration point (1.9 bar)
- 5: Yielding (tension) in reinforcement R2 (see Fig 26) (2.55 bar)
- 6: Stress in reinforcement R3 (see Fig 26) changes from compression to tension (2.03 bar)

Figure 22: Vertical displacement of point P, horizontal and vertical displacement of point Q

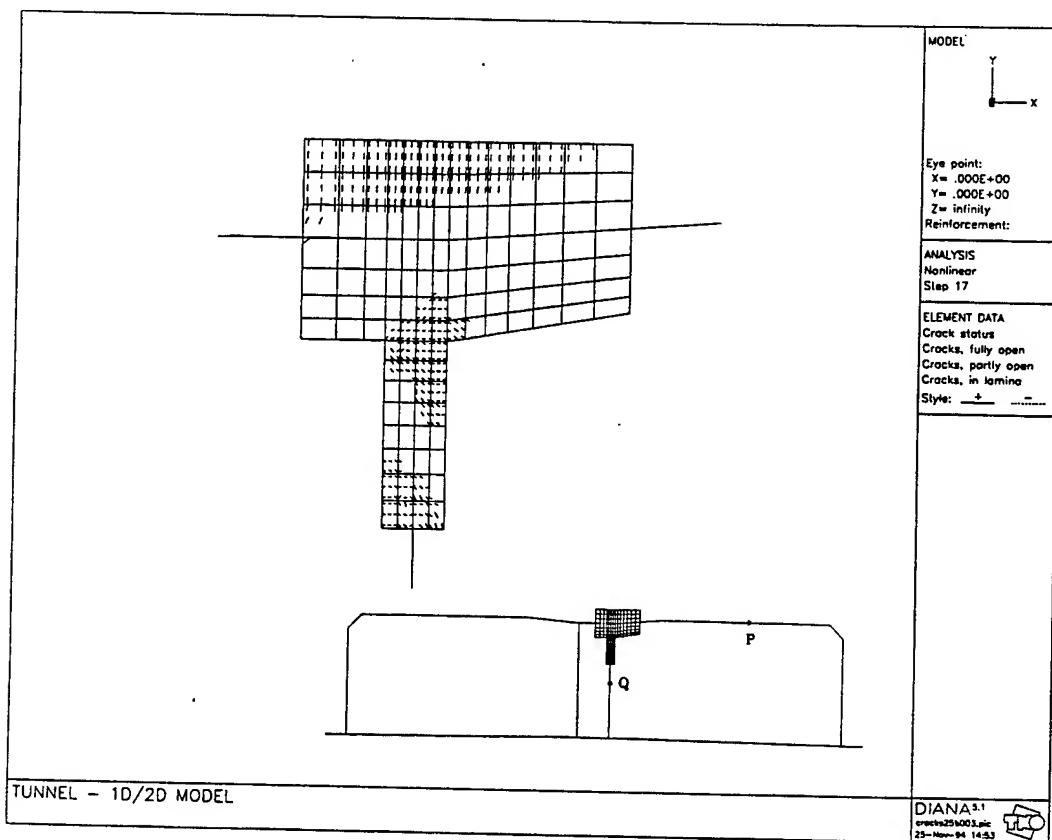


Figure 23: Cracks at maximum sustained internal pressure

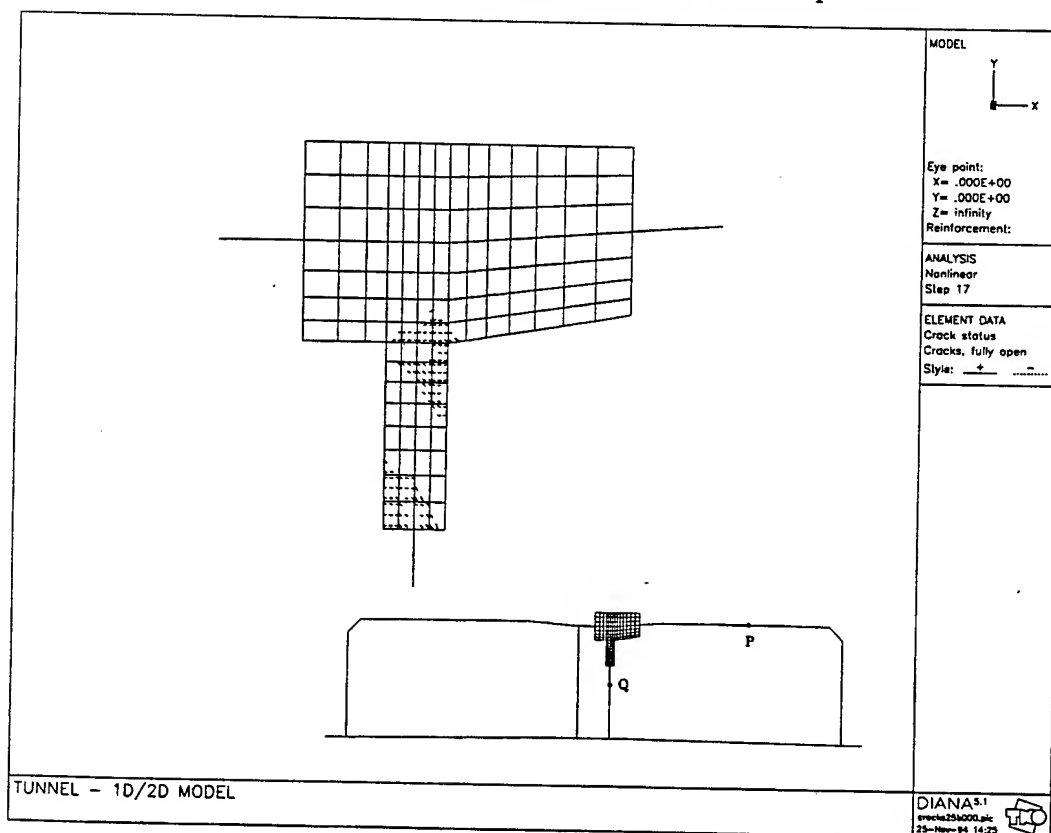


Figure 24: Fully open cracks at maximum sustained internal pressure

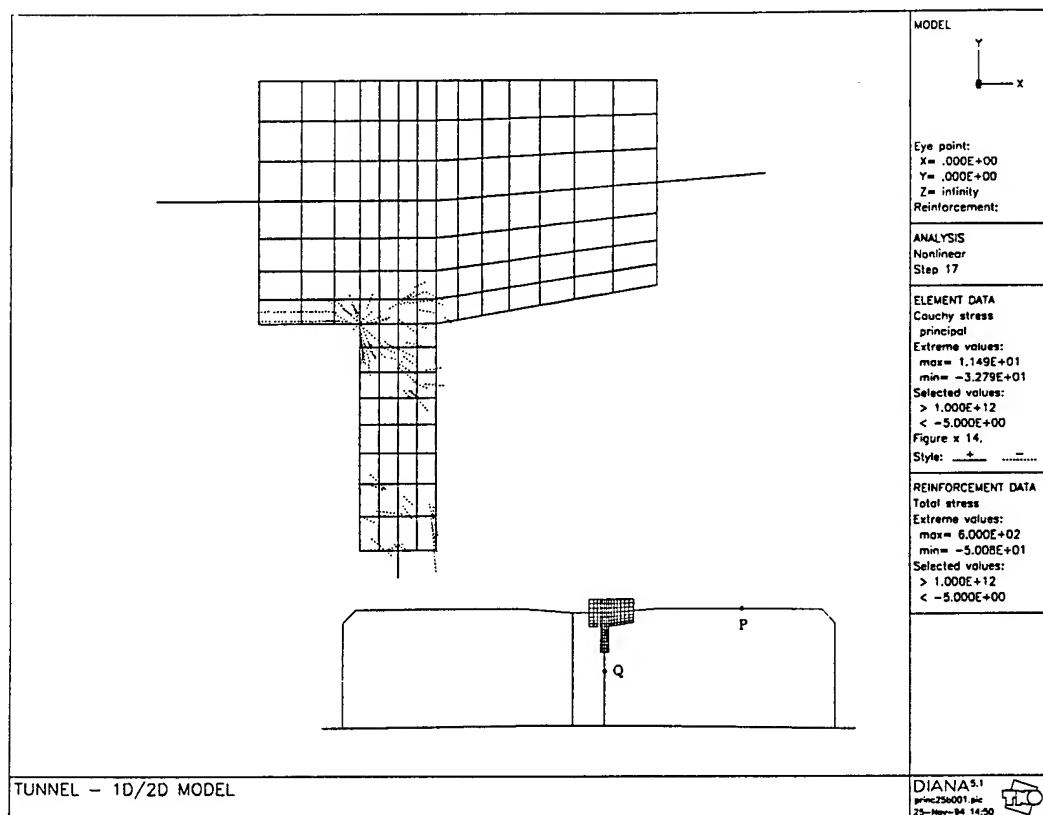


Figure 25: Principal compressive stress at maximum sustained internal pressure

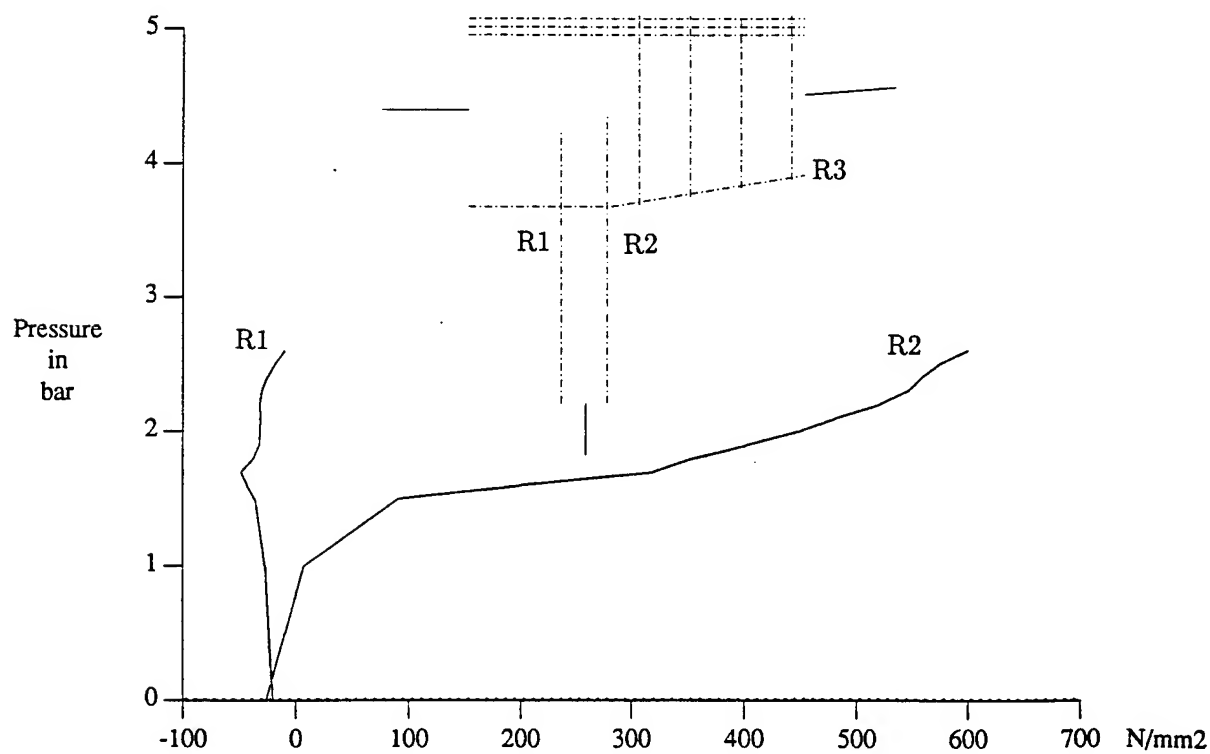


Figure 26: Reinforcement stress

## 5 Conclusions

The first part of the study has demonstrated the capabilities of numerical simulations to produce reliable predictions of structures subjected to transient dynamic loadings.

The results show that a significant amount of energy can be absorbed, when the constitutive models account for the basic mechanical properties of reinforced concrete. In contrast to static analysis, the inertia term in the equation of motion allows the loadcarrying capacity of a structure to be exceeded, without causing divergent solutions. Hence, stable and convergent solutions are found for deformations which are far outside the applied material models range of validation. This demands a careful evaluation of the numerical results.

The results of the dynamic analysis clearly showed that plastic hinge mechanisms developed in the tunnel-section. Before the pressure history was completed, the plastic strains in the hinges exceeded the rupture limit of the reinforcement bars, which suggests that both the mid-wall and the roof of the tunnel section would suffer a ductile bending failure.

The subsequent static analysis, however, showed clear signs of shear failures in the connection between mid-wall and roof. This implies that the mid-wall would be torn off before plastic hinges would have the time to materialize.

Depending on the applied ultimate strain,  $\epsilon_{us}$ , and the shear retention factor  $\beta$ , the shear capacity is between 2.55 and 2.85 bar, in addition to the in-situ dead weight conditions. A close examination of the generalized shear stress across the concrete section, which appeared in the dynamic analysis, showed that this level of stress is reached within 3 ms after the onset of internal pressure.

## Acknowledgements

The contents of this paper form a part in a series of investigations on the mechanical behaviour of an underwater tunnel subjected to a gas explosion. The study is conducted by the Ministry of Transport, Public Works and Water Management (RWS), Civil Engineering Division, in the Netherlands. The advice and discussions with N. Otaredian at RWS are highly appreciated.

## References

- [1] DIANA Users Manual 5.2. TNO Bouw, 1995.
- [2] P. Nauta. Analysis of Tunnel Subjected to Explosion Loading. Technical Report 94-NM-R1341, TNO-Bouw, Rijswijk, 1994.
- [3] K. Hoiseth. Casestudy Softeningmodel for Concrete Applied in Structural Analysis of Tunnelsection. Technical Report 94-NM-R1611, TNO-Bouw, Rijswijk, 1994.
- [4] R. de Borst. The Zero-Normal Stress Condition in Plane-Stress and Shell Elasto-Plasticity. *Communications in Applied Numerical Methods*, 4:245-249, 1976.
- [5] J. G. Rots. *Computational Modeling of Concrete Fracture*. PhD thesis, Delft Univ. of Techn., 1988.

# REDUCTION OF MUZZLE BLAST BY BARRIERS

L.H.J. Absil, H.H. Kodde and J. Weerheijm

TNO Prins Maurits Laboratory  
P.O. Box 45, 2280 AA Rijswijk  
The Netherlands  
Phone +31 15 2842842  
Fax. +31 15 2843958

## ABSTRACT

Noise pollution around military training facilities caused by firing of explosives, artillery or large caliber guns poses a severe problem to neighbouring communities. One possible way to attenuate the blast is the construction of blast walls close to the explosion center. This paper describes a combined experimental and numerical study of the effectiveness of blast walls. An extensive series of blast measurements was performed on scale models (1:10) of a screen and a dike-shaped wall. In addition, blast measurements were performed at an actual howitzer shooting range during the firing of a 155 mm M109 Howitzer. The linear-acoustic model PRISMA was used to calculate the attenuation of the muzzle blast by the barrier.

From the results of the research programme it emerges that blast walls are not effective for blast reduction in the far field. At short distances the geometry of the blast wall has a clear influence on the shielding effect.

From the comparison of the results from the experiments and the acoustic calculations it clearly emerges that the linear acoustic theory should not be used to estimate the reduction of the noise caused by firing of large caliber weapons by blast walls.

## 1 INTRODUCTION

Noise pollution around military training facilities caused by firing of explosives, artillery or large caliber guns poses a severe problem to neighbouring communities. One way to attenuate the blast is the construction of blast walls close to the explosion center. Unfortunately, little information is available about the effectiveness of barriers in attenuating blast waves and there is still a need for experimental data. In the past, much effort has been put into assessing the effectiveness of sound screens in reducing the noise-pollution caused by heavy traffic. The propagation of sound waves can be described by the linear-acoustic theory [Pierce A.D., 1981]. Often the linear-acoustic theory is used to predict the impact of firing-noise on communities surrounding army training facilities. Close to the weapon, however, the front of the blast wave is formed by a shock wave and it is highly questionable whether the acoustic theory is valid.

Some differences between acoustic waves and shock waves can be summarized as:

- Sound waves are pressure waves with pressure variations of small amplitude ( $< 1$  kPa), while the amplitude of pressure variations in shock waves can be considerable.
- Sound waves do not generate a flow in the medium, while shock waves form the front of a flow. Hence, numerical schemes for the simulation of the propagation of shock waves should be based upon the conservation of mass, impulse and energy of the flow field, e.g. as described by the Euler equations.
- Sound waves move at constant speed, i.e. with the speed of sound which is about 340 m/s in air. In nonlinear acoustics the propagation speed depends on the local amplitude of the pressure wave.
- The propagation of sound waves can be described by the linear wave-equation [Pierce, A.D., 1981]. This equation does not hold for pressure waves of large amplitudes. In that case the effects of higher order terms should also be taken into account. A typical non-linear feature is the waveform steepening effect: i.e. waveform portions with higher overpressures move faster than those with lower overpressure resulting in a steepening of the front of the pressure wave.
- In the linear-acoustic theory the influence of viscosity and other dissipative effects is neglected. However, these typical non-linear effects are responsible for the loss of blast energy which lead to a reduction in peak overpressure of the shock waves. Hence, the peak overpressure decay in shock waves is faster than in sound waves, indicating larger decay rates.

In the present paper the validity of the linear-acoustic theory for describing the diffraction of weak shock waves over barriers will be discussed.

On behalf of the Dutch Ministry of Defence, at the TNO Prins Maurits Laboratory (TNO-PML) an extensive research programme is performed aimed at studying the effectiveness of blast walls in reducing the noise from artillery fire. This research programme comprises:

- an experimental study at laboratory scale using a shock tube, aimed at investigating the effect of barrier geometry on the degree of blast attenuation;
- an extensive series of measurements on a 1:10 scale model of an howitzer test site;
- blast measurements at an actual (1:1) howitzer test site.

The major findings of the first phase of this project are reported in Absil et al. (1993). In the present paper the major findings of the 1:10 scale model and the full scale tests will be reported.

## **2 EXPERIMENTAL SET-UP**

### **2.1 The 1:10 scale model tests**

A 1:10 scale model of the howitzer training site was built. Figure 1 shows a schematic diagram of the experimental set-up. Two types of blast walls were investigated: a 0.5 m high screen and a 0.4 m high dike with a 0.1 m high screen on top. The latter

barrier is a model of the one in use at the actual training site. The barriers were made of acoustically-hard 10 thick plywood to minimize acoustic absorption. To minimize terrain effects, the ground on the test site, consisting of concrete tiles, was leveled.

Eight piezo-electric transducers (PCB 137 A11), mounted inside aerodynamically-shaped blast probes, were used to measure the pressure-time signals at different locations on the test-site. The locations of the measurement points are indicated in Figure 1. Transducers P1 to P6 were positioned in the shadow region of the blast wall, while transducers P7 and P8 were placed at the weapon side. Transducers P1 to P4 measure the overpressure decay in a direction perpendicular to the direction of the blast. Transducers P5 and P6 are positioned such as to give an indication of the symmetry of the shock wave propagation over the walls. Transducer P7 measures the free field pressure at a distance of 2 m from the detonator, while transducer P8, which is turned over an angle of  $45^\circ$  towards the wall measures the reflected pressure. Prior to the measurements, the pressure transducers were calibrated against the relatively low measurement range of overpressures of 0.5 to 5 kPa in a blast simulator.

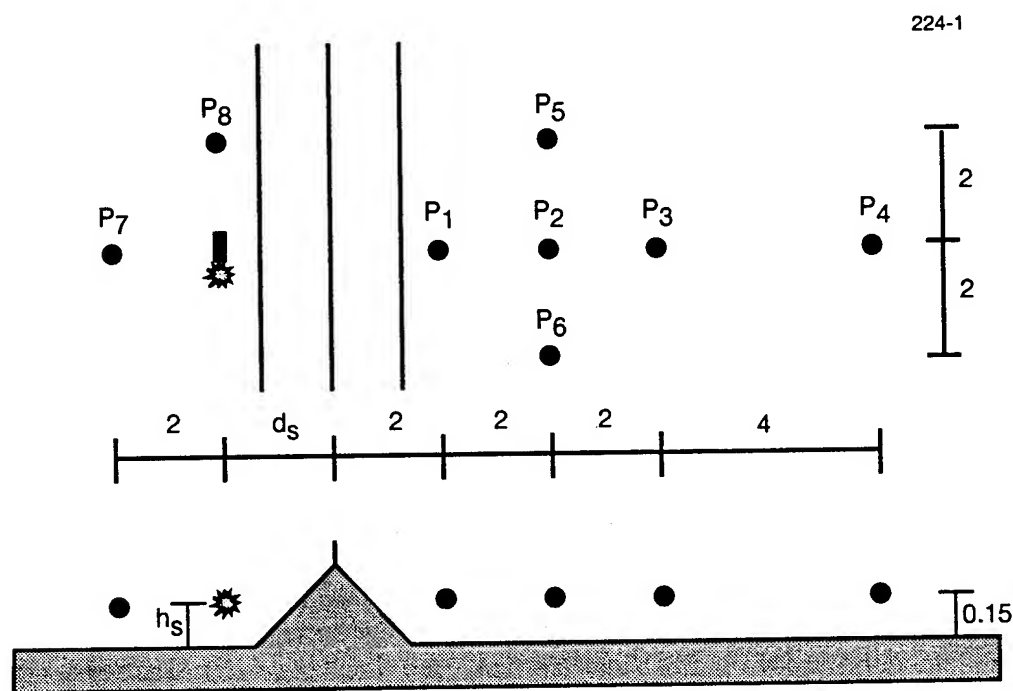


Figure 1: Experimental set-up 1:10 scale model tests. The points labeled P1 to P8 are pressure transducer locations,  $d_s$  and  $h_s$  indicate the location of the detonator. All dimensions are given in meters.

The blast generated by several electronic detonators was evaluated to select the one that simulates the scaled howitzer blast the best. Electric detonator nr.8, with a charge equivalent to 1.4 gr TNT, was selected. To eliminate sideward expansion of the blast, the detonator was mounted inside a 10 cm long metal cylinder ( $\varnothing$  4 cm), leaving some



space to simulate the barrel of the weapon. The overpressure levels in the 155 mm howitzer blast vary from 100 kPa in the vicinity of the weapon to about 4 kPa at 25 m, with a positive phase duration of 6 ms, as will be shown in Section 2.2. According to the Hopkinson scaling law [Baker et al. 1973], the positive phase duration of the blast wave in the scale model experiments should be reduced by the same amount as the length scale (1:10), yielding a duration of 0.6 ms. Figure 2 shows the overpressure signature as measured at a distance of 2.5 m from the detonator. The signal features a peak overpressure of 4.7 kPa and a phase duration of about 0.6 ms, which meets the requirements fairly well. The decay rate of the overpressures of the detonator blast showed to be 1.1 [Absil et al. 1993], which agrees well with the value usually found in the far-field of large caliber-weapons. Because the detonator-firings showed a bad reproducibility, the measurements on each barrier-configuration were repeated 3 times and the overpressures averaged over the three separate firings.

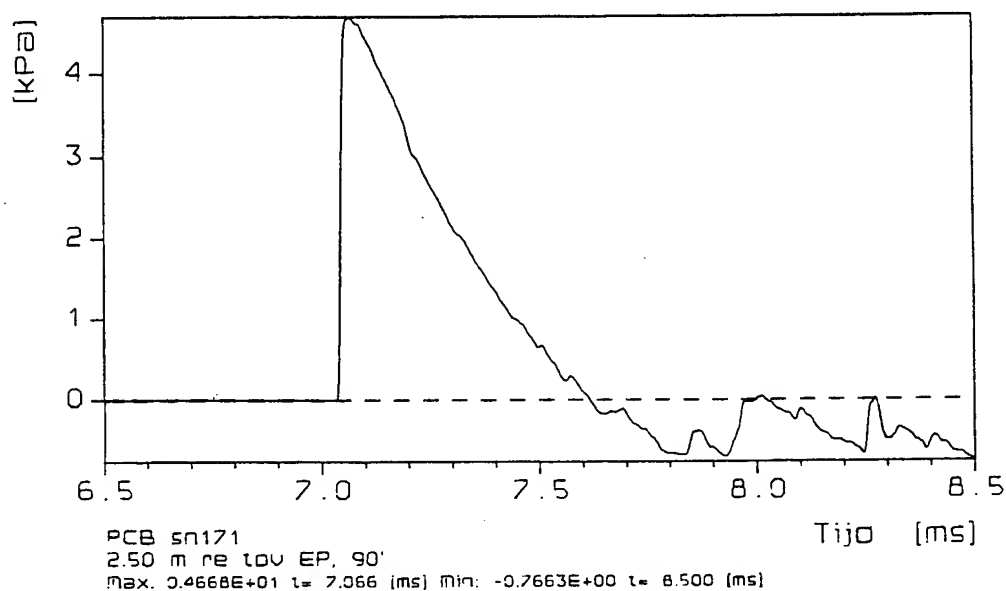


Figure 2: Measured overpressure signature at a distance of 2.5 m from the detonator.

## 2.2 Howitzer training site

The full-scale blast measurements were conducted at the Hojel-firing range at the artillery training site "Oldebroek". Along the firing-range three 4-m high dike-shaped earth walls, provided with a 1-m high wooden top-screen, were constructed. The 70-m long walls were placed in line and 130 m apart. The blast measurements were conducted on a 155 mm M109 howitzer which was placed at a distance of 7.5 m from the centre of the last wall. During the firing the mouth of the barrel was at a height of 2 m. The weapon was placed on the sandy road along the walls. On the shadow-side of the walls, there was a 9-m wide paved road, which adjoined a slightly-sloped sandy area on which the blast pencils were positioned.

The blast measurements were conducted during the firing of 155 mm M107 shells. The High-Explosive bursting charge was removed from the grenades to prevent the

appearance of the detonation blast. The howitzer was provided with a muzzle brake to reduce the recoiling of the barrel of the gun. Two types of propellant charges were used: a small 3M4 and a large 7M4 charge. By using different propellant charges, the effectiveness of the blast wall for blast waves of different overpressure and duration could be studied.

Eight piezo-resistive pressure transducers (Kulite XCQ 117-093 and XCS 093) were used to measure the pressure-time signals at different locations in front of and behind the wall. The blast pencils were positioned at identical locations as was the case for the 1:10 scale model tests, as shown in Figure 1. All distances were proportionally scaled. Consequently, blast pencils P1 to P4 were placed at distances of 20, 40, 60 and 100 m from the wall respectively. All transducers were located at a height of 1.5 m above ground level. The free-field conditions were obtained by placing the howitzer in between the second and third wall.

Figure 3 shows the pressure-time signal as measured at a distance of 27.5 m from the howitzer in the situation without wall, for the 7M4 propellant charge. As can be seen from the signal, the peak overpressure of the muzzle blast is about 4 kPa and the positive phase duration about 6 ms at this distance. With the small 3M4 propellant charge a peak overpressure of 1.2 kPa and a positive phase duration of 5 ms was obtained at this location. Overpressure decay rates of 1.21 and 1.104 were found for the 7M4 and 3M4 charge respectively, which are typical for a large caliber weapon-blast. It should be noted that the overpressure in sound waves typically decays at a rate of 1, i.e. proportional to  $1/R$ . To reduce the influence of experimental scatter, all tests were repeated 5 times after which an averaging procedure was applied. Hence, all overpressures presented in the following are averaged over 5 separate firings.

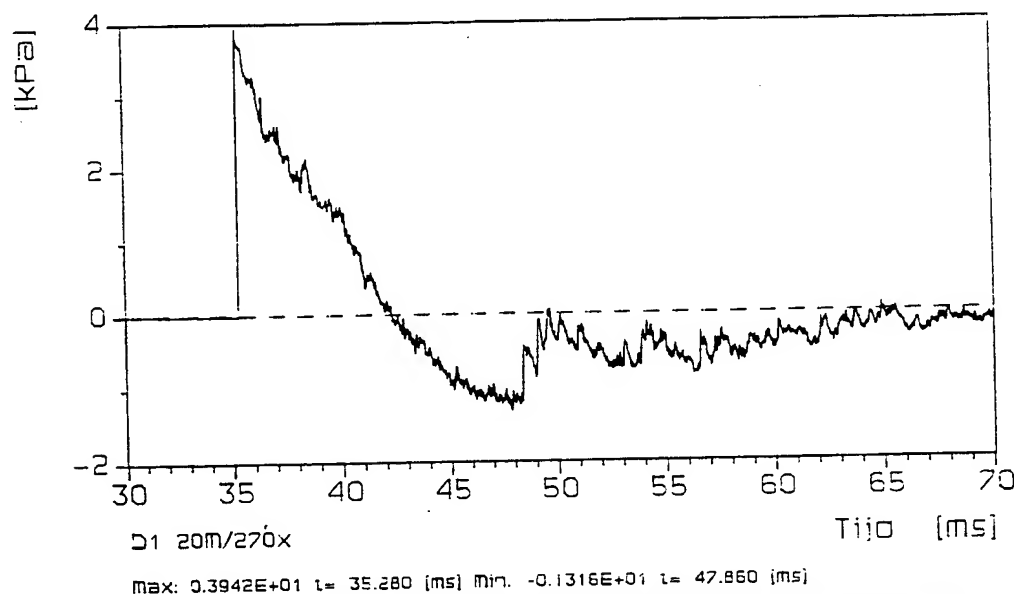


Figure 3: Measured overpressure signature at a distance of 27.5 m from the howitzer for a 7M4 propellant charge.

### 3 RESEARCH PROGRAMME

#### 1:10 scale model tests

Two series of measurements were performed.

- In the first series, the distance between the detonator and the barriers (screen and dike) was varied from 0.5 to 2 m, with the detonator placed at a constant height of 0.2 m.
- In the second series, the height of the source was varied from 0.02 m, i.e. level ground, to 0.4 m, with the detonator placed at a distance of 0.75 m from the wall.

Both series were conducted with and without blast wall. At the beginning of each day of the measurement campaign, the wall was first removed to check the free-field pressure decay by previous results. Meteorological data, like the ambient pressure, temperature, wind speed and humidity, were also recorded. All experiments were conducted on days of similar weather to minimize the effect of meteorological variations.

#### Full scale tests

- 5 firings of the 155-mm M109 howitzer with a 3M4 propellant charge, with the weapon in between the walls (free-field condition).
- 5 firings of the 155-mm M109 howitzer with a 7M4 propellant charge, with the weapon in between the walls (free-field condition).
- 5 firings of the 155-mm M109 howitzer with a 3M4 propellant charge, with the weapon next to the wall.
- 5 firings of the 155-mm M109 howitzer with a 7M4 propellant charge, with the weapon next to the wall.

#### Calculations with linear acoustic theory

The linear-acoustic model PRISMA, which is developed by the Acoustics Group of TNO-TPD, was used to predict the attenuation of the blast by the wall at the howitzer training site. The calculations were performed for an acoustically-soft ground surface.

### 4 RESULTS

#### 4.1 Results 1:10 scale model tests

First the results obtained at the 1:10 scale model tests will be presented.

In the following, the shielding efficiency of the walls will be evaluated on the basis of the reduction of the peak overpressure and the attenuation in dB(lin,peak). A-weighted dB(A)-distributions were also calculated from the measured pressure-time signals but will not be presented in this paper.

In Figure 4 and 5 the decay of the peak overpressure behind the screen and dike-shaped wall are shown for varying distance of the detonator to the wall. The corresponding values measured without the blast wall are also given in the graph.

From these figures it can be seen that, close behind the screen, the peak overpressure is reduced to about 30% of the unshielded overpressure, while further away the attenuation is about 50%. Similar results are found for the dike-shaped wall, except that the attenuation in overpressure immediately behind the dike is less, about 50% in peak overpressure. Furthermore, it is found that even the shielded blast overpressures are of the order of 1 kPa, which is usually considered as an upper limit to the shock strength for the linear acoustic theory to be valid.

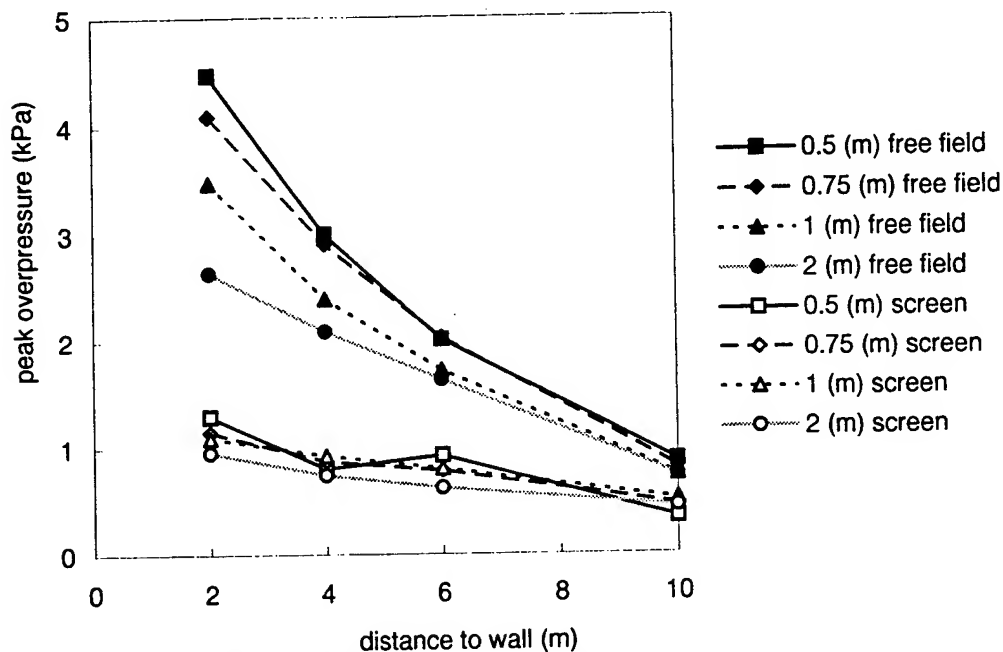


Figure 4: Measured peak overpressures behind the screen for varying distance of the detonator to the wall  $d_s$  ( $h_s = 0.2$  m) and corresponding free-field data.

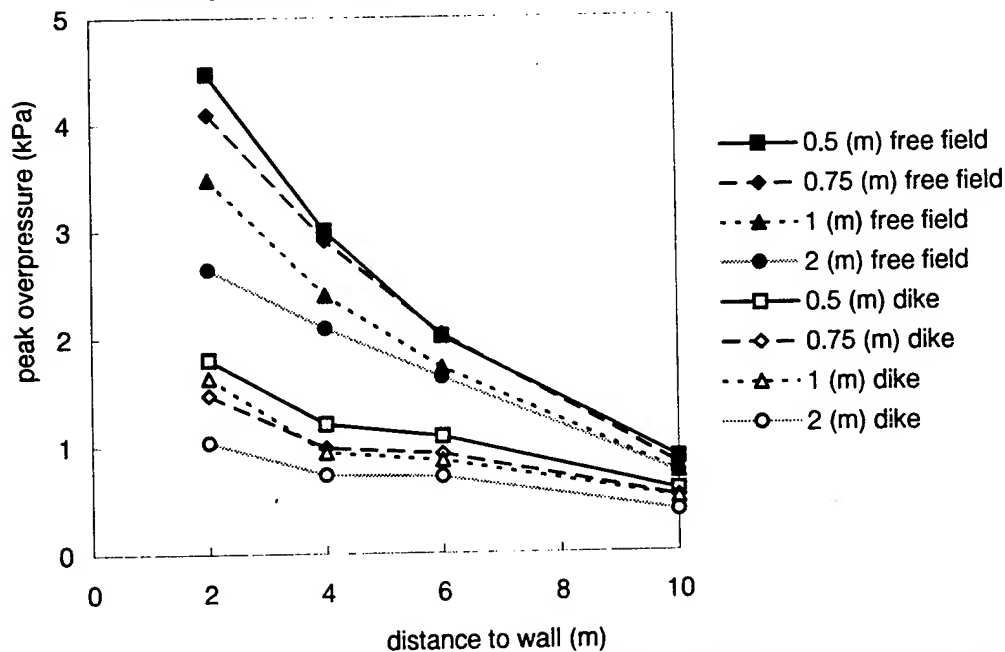


Figure 5: Measured peak overpressures behind the dike for varying distance of the detonator to the wall  $d_s$  ( $h_s = 0.2$  m) and corresponding free-field data.

Figure 6 shows the attenuation by the screen and dike expressed in peak sound-pressure level dB(lin,peak). Close behind the screen a reduction in sound-pressure level of about 10 dB is found, while the dike shows an attenuation of about 8 dB in that region. At 10 m distance, both types of walls show an attenuation of about 5 dB. The lower shielding efficiency found close to the dike is due to the fact that the diffracted wave will also contain a contribution from the upward reflected shock wave from the front of the dike and that there is lesser expansion space at the rear face, as compared to the screen. Further downstream, hardly any difference between the overpressure reduction by the screen or dike can be seen, indicating that the geometry of the wall is not critical with regard to the far-field conditions. The fact that the shielding efficiency of a wall is maximal when it is placed as close to the source as possible [Raspet, 1987] is not clearly confirmed by our data, though this might be obscured by the relatively large experimental scatter of the results.

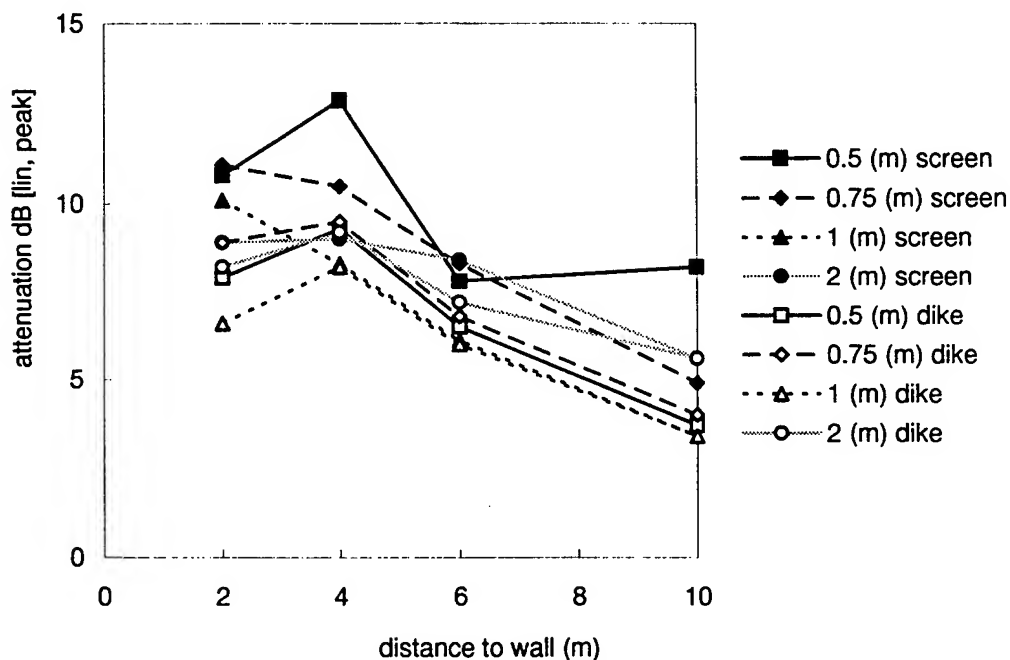


Figure 6: Peak sound pressure insertion loss for varying distances of the detonator to the wall  $d_s$  ( $h_s = 0.2$  m).

In Figure 7 and 8 the effect of the variation in detonator height on the peak overpressure is shown. Figure 9 shows the attenuation by the screen and the dike expressed in dB(lin,peak). Close to the screen, a reduction in peak sound-pressure level of 10 dB is found decreasing to about 4 dB at 10 m distance. Similar trends are found for the dike, though the reduction in sound-pressure level is about 2 dB lower immediately behind the dike as compared to the screen. The effect of the variation in height of the detonator on the shielding efficiency seems to be of the same order as the experimental scatter ( $\pm 1$  dB) such that it is impossible to draw any firm conclusions on the influence of the detonator height on the shielding efficiency. Rather puzzling are the results found for the dike, when the detonator was placed on the ground (0.02 mm height), since it deviates considerably from the other curves in the graph

measured for other heights of the detonator. No clear explanation for this finding could be given.

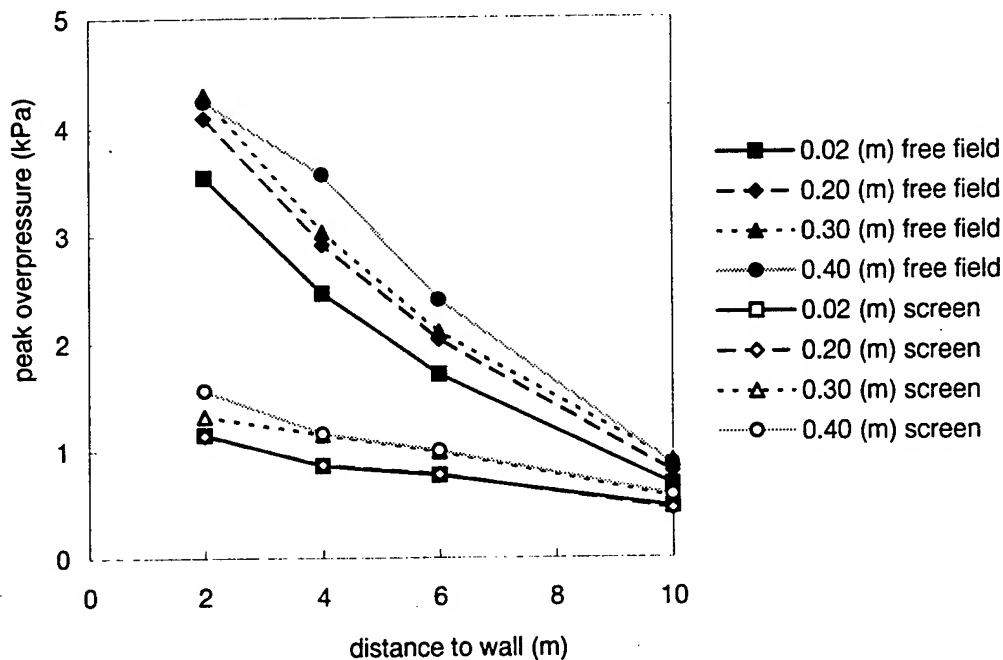


Figure 7: Measured peak overpressures behind the screen for varying heights of the detonator  $h_s$  ( $d_s = 0.75$  m) and corresponding free-field data.

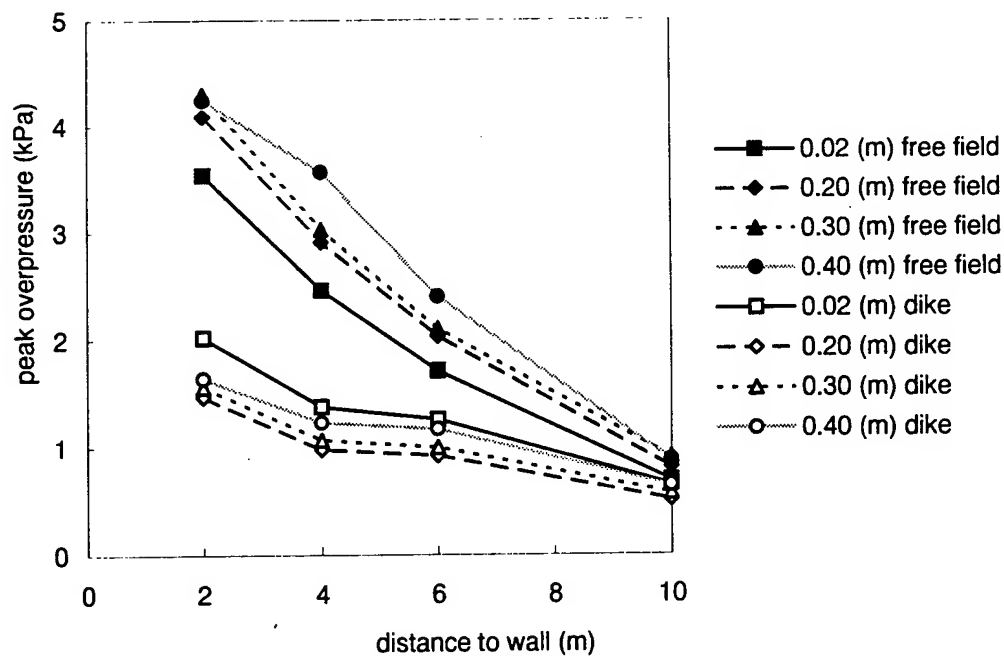


Figure 8: Measured peak overpressures behind the dike for varying heights of the detonator  $h_s$  ( $d_s = 0.75$  m) and corresponding free-field data.

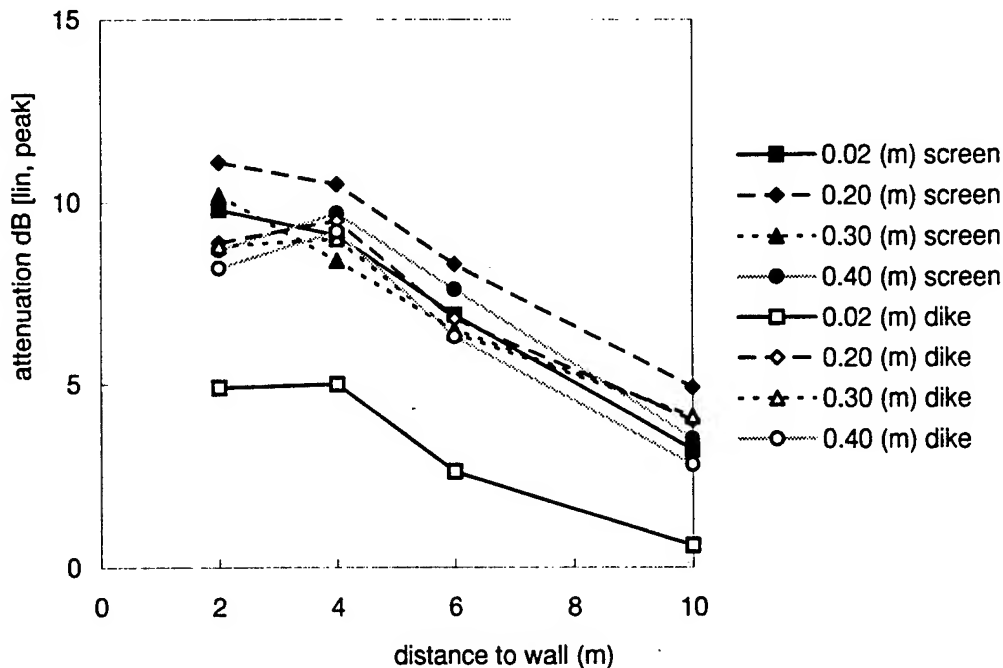


Figure 9: Peak sound pressure insertion loss for varying heights of the detonator  $h_s$  ( $d_s = 0.75$  m).

The good similarity between signals measured with pressure transducers P5 and P6 indicated a nearly symmetric propagation of the shock wave over the walls. The signals measured with pressure transducer P8 did not indicate any additional overpressure increase at the weapon due to the reflection by the wall. The reflected wave reaches transducer P8 after the positive phase of the primary wave has been expired. Hence, the primary and the reflected wave will not interfere and the overpressure the gun crew is exposed to is not increased.

#### 4.2 Results full-scale blast measurements at howitzer training site

Figure 10 shows the decay of the peak overpressure behind the wall as obtained for firings of the 155 mm M109 howitzer using the 3M4 propellant charge. The corresponding free-field data are also plotted in the graph. From this figure it can be seen that the greatest blast reduction is obtained close behind the wall where the peak overpressure is reduced from 1.4 to 0.35 kPa (75% reduction). Further from the wall, the blast attenuation decreases to a value of about 63%.

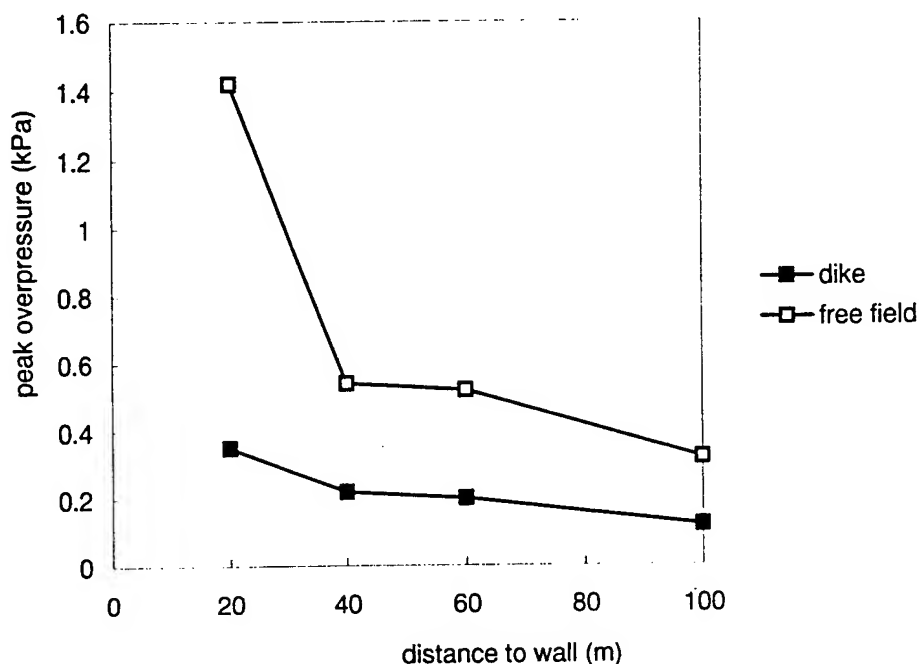


Figure 10: Measured peak overpressures behind the wall for firings of the howitzer with propellant charge 3M4 and corresponding free-field data.

In Figure 11 the decay of the peak overpressure behind the wall as measured for firings of the howitzer using the 7M4 propellant charge are shown. The corresponding values measured without the blast wall are also plotted in the figure. Obviously, the free-field overpressures obtained for the 7M4 charge are about 3 times higher than those obtained with the 3M4 charge. At 20 m distance from the wall, the peak overpressure is reduced from 4.1 to 1.3 kPa, yielding a blast reduction of 68%. Hence, in the vicinity of the blast wall a significant shielding effect is found. At 100 m distance from the wall the blast reduction is about 44%. Hence, the effectiveness of the blast wall reduces at greater distance, as was also found for the 1:10 scale model tests.

Next to the howitzer data, the peak overpressures as obtained at the 1:10 scale model tests at corresponding distances are plotted. In the graph the results as measured with the detonator placed at a height of 0.2 m, at a distance of 0.75 m from the dike-shaped wall are depicted. This set-up corresponds to the distance of the howitzer barrel to the wall of 7.5 m and the height of the barrel-mouth of 2 m. At the measurement station 20 m from the wall (2 m at 1:10 scale), the peak overpressures as measured at the 1:10 scale model tests show good agreement with the full scale measurements. The fact that the free-field pressures show good agreement is not surprising since electric detonator nr. 8 was selected because it yielded an overpressure of about 4 kPa at this distance. But also the shielded overpressures show good agreement at this station. At this station the scale model tests seem to simulate the full scale test quite well. At larger distance from the wall, however, the free-field overpressures as measured at the full scale and the 1:10 scale model tests show a large deviation. At the last



measurement station, at 100 m distance from the wall, the deviation between the full scale and scale model tests is small again.

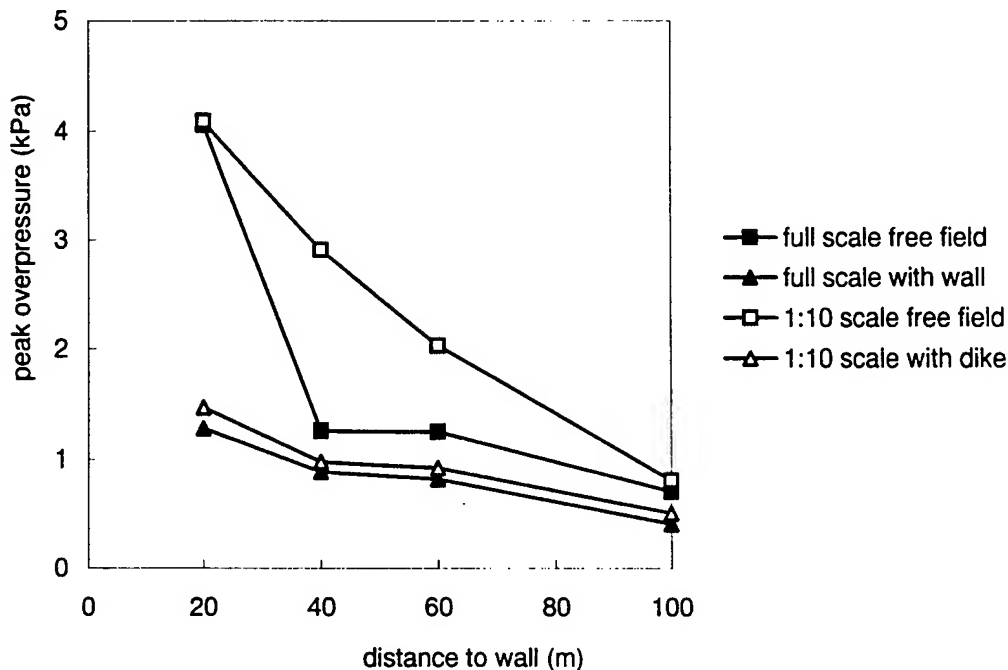


Figure 11: Comparison of peak overpressures as measured at full scale with the 7M4-charge and the 1:10 scale model tests ( $d_s = 0.75$  m,  $h_s = 0.2$  m).

Two possible explanations for the difference in free-field overpressures as obtained for the full scale and the scale model tests are:

- In the scale model tests acoustically-hard concrete tiles were used as ground surface, while in the full scale tests the ground surface was sand, which is an acoustically-soft medium. Now, it is well-known that the waveform is very dependent on the nature of the ground surface over which the blast wave propagates [Ford, 1991].
- The blast generated by the detonator is pointed in the forward direction, while a large portion of the howitzer muzzle blast is directed backwards due to the muzzle brake.

Furthermore, it should be noted that, because of the relatively small distance from the noise-source, the influence of different weather conditions during the full scale tests and the scale model tests on the blast propagation is negligible. Further research is needed to identify the actual cause of the difference found.

In Figure 12 the peak sound pressure insertion loss is depicted for the firings with the 7M4 and the 3M4-charge. For the small 3M4 charge, the insertion loss decreases from 12 dB(lin,peak) at 20 m behind the wall to 8.5 dB(lin,peak) at 100 m. For the heavy 7M4 charge the attenuation is about 10 dB(lin,peak), while at larger distance the insertion loss is only about 3 to 4 dB(lin, peak). Hence, the effectiveness of the blast

wall strongly depends on the propellant charge used and decreases as the blast gets stronger.

In Figure 12 also the insertion loss as measured for the corresponding 1:10 scale model tests are shown. This curve should be compared with the graph obtained for the 7M4-charge. As seen in Figure 11, the scale model tests and the full scale tests show good agreement at 20 and 100 m from the wall. Because of the rapid decrease of the free-field overpressure measured at full scale at 40 and 60 m from the wall, the latter shows a lower shielding efficiency than found for the scale model tests.

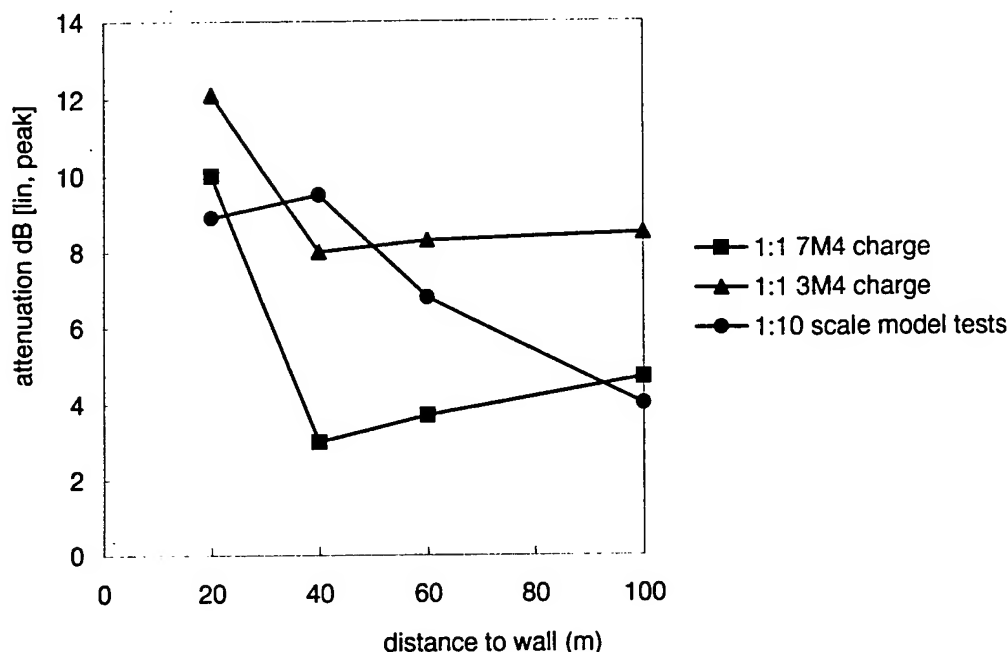


Figure 12: Comparison of peak sound pressure insertion loss as measured at the full scale and the scale model tests

The pressure-time signals as measured at the full scale tests clearly illustrated a shock wave steepening effect, which is a typical non-linear feature. Furthermore, it should be noted that, even at 100 m from the wall, the front of the pressure signal was formed by a shock wave featuring a steep pressure jump.

By evaluating the peak overpressures and the shock wave arrival time at pressure transducers P2, P5 and P6, it could be concluded that a large portion of the muzzle blast is directed backwards. This can probably be attributed to the muzzle brake which reflects most of the muzzle blast backwards. Consequently, close to the weapon, the propagation of the muzzle blast was not symmetric. Note that a symmetric propagation was found at the scale model tests.

By comparing the pressure signals as measured with transducer P8 with and without wall, it could be concluded that the overpressure the gun crew is exposed to is not increased. The reflected wave reaches the gun crew after the positive phase duration

of the primary wave has been expired. Only in the immediate vicinity of the wall a pressure increase can be expected due to the reflection against the wall.

### 4.3 Calculations with linear acoustic model

In this section the full scale measurements will be compared to the results obtained with the linear-acoustic model PRISMA. The calculations were made for an acoustically-soft ground surface.

The frequency-spectrum of the measured pressure signal was used for the comparison. Figure 13 shows the (1/3-octave band) spectrum of the signal as measured for charge 3M4 with pressure transducers P1 and P4, with and without wall. The quantity is expressed as the sound-exposure level  $L_p$  which is defined as,

$$L_p = 10 \log \left( \frac{p_{eff}}{p_{ref}} \right)^2 \quad [1]$$

where  $p_{ref}$  is a reference pressure of 20  $\mu$ Pa and  $p_{eff}^2$  is a measure for the energy in the wave, which is defined as,

$$p_{eff}^2 = 1/T \int p(t)^2 dt \quad [2]$$

with the integration over 1 second. By subtracting the spectra as obtained with and without wall the spectrum of the insertion loss is obtained, which is also included in Figure 13. Obviously, the insertion loss measured, indicated by the solid line, increases with increasing frequency. This trend is also predicted by the acoustic model. The measured spectrum-averaged insertion loss at a distance of 20 m behind the screen is 3.5 dB, while the acoustic model predict an attenuation of 7.3 dB at this distance. At 100 m behind the wall, the spectrum-averaged insertion loss measured is 3.8 dB, while the model predicts a value of 5.6 dB.

224-13

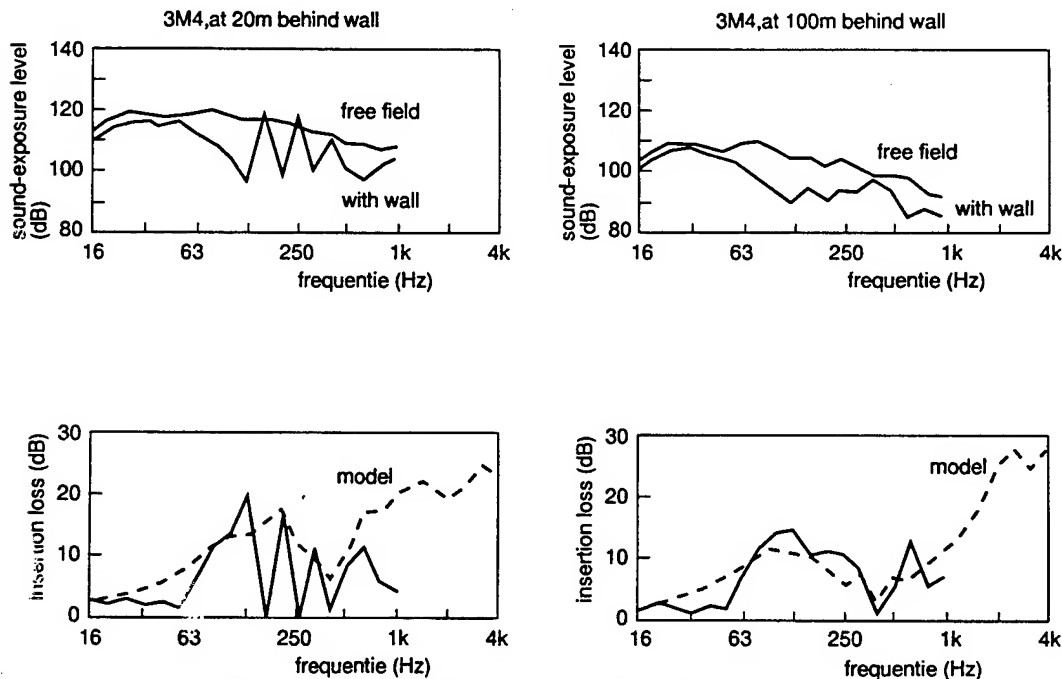


Figure 13: The measured and calculated insertion loss for charge 3M4 at 20 and 100 m behind the wall.

Figure 14 shows similar graphs for the firings with the 7M4 charge. In this case the measured spectrum-averaged insertion loss is 4.8 dB at 20 m behind the wall, while the model predicts 6.8 dB. At 100 m behind the wall, the measured spectrum-averaged insertion loss is 1.7 dB, while the model predicts 5.4 dB. Hence, the linear acoustic model clearly overestimates the shielding efficiency of the wall. The deviation between the measured insertion loss and the predicted value seems to increase with increasing strength of the muzzle blast.

224-14

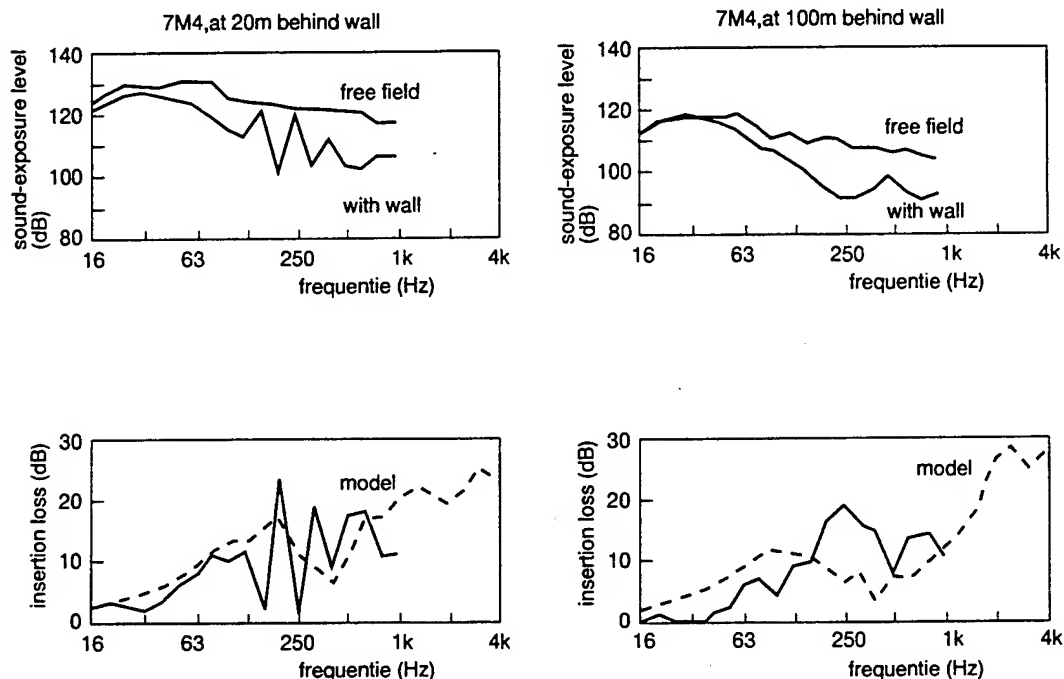


Figure 14: The measured and calculated insertion loss for charge 3M4 at 20 and 100 m behind the wall.

## 5 CONCLUDING REMARKS

In the presented study, the effectiveness of blast walls to reduce the noise pollution due to firing of explosives or artillery was studied at full scale and 1:10 scale.

The main conclusions of this research can be summarized as

- The effectiveness of blast walls to reduce noise pollution, caused by firing of explosives or artillery, is very limited for large distances.

The reduction of the impulse-noise strongly depends on the geometry of the wall and the distance to the wall. At 1:10 scale two geometry's were tested, i.e. a screen and a dike shaped blast wall.

The muzzle blast from a 155 mm M109 Howitzer ( peak pressure at 40 meter in the order of 4 kPa) was simulated.

Close behind the wall a screen is more effective in reducing impulse noise than a dike. A noise-reduction of the order of 10 dB was obtained close behind the screen and of 8 dB for the dike. At larger distances, however, the effect of the wall geometry on the blast attenuation becomes marginal and both walls yield a noise

reduction of the order of 5 dB. Hence, the effectiveness of the blast walls is reduced at greater distances.

- At full scale, the influence of the weight of the propellant charge was examined. It is concluded that the effectiveness of blast walls reduces with increasing source strength.
- Comparing the full scale and small scale results it is concluded that at the reference distance of 27 meter, very good agreement is obtained for free field as well as non-free field conditions. For larger distances significant differences are observed. This is probably caused by the fact that at full scale the muzzle blast propagation is far from spherical, while for the small scale (detonator in steel tube) is almost spherical.

There was also a significant difference in ground surface material; concrete tiles for the small scale tests and loose sandy soil for the full scale.

- The consequences of the simplification for the blast propagation of being an acoustic phenomenon emerge from the comparison of the results of the experiments and the calculations with the linear acoustic model PRISMA.

The linear acoustic model clearly overestimates the shielding efficiency of the blast wall. The differences increase with increasing charge weight.

Therefore, the linear acoustic theory should not be used to estimate the reduction of noise caused by firing of large-caliber weapons by blast walls.

- For the near future another test session is planned to validate the observed phenomena.

In order to obtain reliable predictions for noise pollution in the far field, a numerical tool will be developed. In this model the non-linear blast effects in the near field will be coupled to the linear acoustic blast propagation at larger distances. The tool will be validated against experimental data.

## 6 ACKNOWLEDGEMENTS

The authors are indebted to P. Jonker, M. Dirkse and R. van de Kastele for performing the measurements, to M. Jongen for preparing the paper and to TNO-TPD for performing the calculations with the linear acoustic model.

This study was funded by the Dutch Ministry of Defence.

## 7 REFERENCES

Absil, L.H.J., Kodde, H.H. and Mercx, W.P.M.,  
"The effectiveness of blast walls",  
MABS 13, 1993.

Baker, E., Westine, P. and Dodge, F.,  
"Similarity methods in engineering dynamics",  
Spartan Books, 1973.

Ford, R.D.,  
"Propagation of air blast from small HE charges",  
MABS 12, 1991.

Pierce, A.D.,  
"Acoustics, an introduction to its physical principles and applications",  
Acoustical Society of America, 1981.

Raspet, R.,  
"Development and description of a computer program for predicting impulse noise  
reduction by barriers",  
US Army Corps of Engineers, Research Lab. AD-A179 404, 1987.



From: Mr K B Gorrie DD HQ Sy(S&T)2a  
**MINISTRY OF DEFENCE** Room 3/57  
 Metropole Building, Northumberland Avenue, London WC2N 5BL

Telephone (Direct dial) 0171 218 5496  
 (Switchboard) 0171 218 9000

Mr T J Weeks  
 Security, Bldg F6.1  
 Atomic Weapons Establishment  
 Aldermaston  
 Reading  
 Berks  
 RG7 4PR

**Your reference**  
 AWE 54/7765  
**Our reference**  
 D/PUB C/22/1335/95  
**Date**  
 7 September 1995

**PAPER ENTITLED:**

**TECHNIQUES DEVELOPED FOR ACCURATE SCALE MODELLING OF REINFORCED CONCRETE STRUCTURES AND THE RESULTS FOR A GENERIC MODEL**  
 for "K. B. Gorrie"

**BY:** W. J. Woods (AWE, Foulness)

1. The Department raises no objection to presentation and publication of the above paper forwarded with your application dated 1st September 1995.

**NB.** For publication in other than Learned Society Journals or conference proceedings: permission to reproduce Crown copyright material must be separately sought from DERA: Intellectual Property Department, R69 Building, DRA Farnborough, Hampshire, GU14 6TD. Full details of the material to be reproduced must be supplied as a fee may be payable to the Department.

2. Copyright must be acknowledged in the published full text in the following form:

(c) British Crown Copyright 19\*\* /DERA

Published with the permission of the controller of Her  
 Britannic Majesty's Stationery Office.

**OR**

(c) British Crown Copyright 19\*\* /DERA

Reproduced with the permission of the controller of Her  
 Britannic Majesty's Stationery Office.

)When first  
 )published  
 )outside HMG  
 )

)When first  
 )reproduced  
 )outside HMG  
 )and subsequently

(NOTE 19\*\* = year of first open dissemination)

3. The author/s must ensure that no classified or sensitive information is disclosed during or following the presentation or publication of the paper.

K B Gorrie  
 For Publication Clearance  
 (Scientific & Technical)

# TECHNIQUES DEVELOPED FOR ACCURATE SCALE MODELLING OF REINFORCED CONCRETE STRUCTURES AND THE RESULTS FOR A GENERIC MODEL

W A Seeds

AWE Foulness  
Foulness Island  
Southend-on-Sea  
Essex SS3 9XE  
UK

## Abstract

During the past 40 years, AWE Foulness have developed specialised techniques to study the vulnerability of hardened reinforced concrete structures to nuclear blast using scale modelling and modest amounts of high explosives.

This paper describes the techniques used to scale accurately the parameters involved, and presents the results for a typical generic structure to validate the methodology.

## Modelling Techniques

### General

In order to create an accurate scale model, it is very important to know the properties of all the materials used in the full scale structure, and to recreate these at the model scale as accurately as possible. Our experience has shown that small inaccuracies in the model can have a very profound effect.

The information required about the full scale structure is the type and specification of the reinforcement and concrete used. In ideal circumstances, we prefer to obtain samples of the actual materials used to allow us to carry out our own characterisation tests. Other information about the structure is also of use, such as the type of ground upon which it is built, the type of soil used as cover etc. If all or any of this information is unavailable, we must make assumptions using standard design practice or any other sources of information we can employ, such as knowledge of other structures of a similar type built in a similar way.

### Reinforcement

The details of the reinforcement required are: size, yield strength, ultimate tensile strength, elongation at break and layout within the structure. The availability of directly scaled bar size is dependent upon the scale selected; it is sometimes



necessary to select what appears to be a peculiar scale factor (such as 5.6:1) in order to utilise a readily available bar (or wire) size. If the scale is fixed due to other experimental parameters (such as mode of attack), this will determine whether the reinforcement is scaled on a 'bar-for-bar' manner (where each bar in the full scale structure is modelled on the small scale), or a percentage reinforcement technique is used (where the total percentage of steel in each face is reproduced). If the percentage reinforcement technique is used, particular attention must be paid to corners of the structure and any joints within it.

Once a scale has been selected, samples of wire of the required bar/wire size are obtained from our standard supplier and tensile tested to give the wire's characteristic properties. It is very rare on smaller scales to obtain wire with the required properties direct from the supplier. The standard procedure is to obtain wire that is stronger and less ductile than that required, and to heat treat it to produce the desired qualities. Figure 1 shows the typical results for a sample of 1.6mm diameter wire before and after testing. The oven used at AWE Foulness is two metres long with a maximum temperature rating of 800 °C and three zones of control which give a temperature regulation of  $\pm 3$  °C over the full length.

The technique used for heat treating the wires has been developed over a considerable period of time. The oven is configured at a selected temperature (usually around 500 °C for the first test), the sample of wire straightened and placed within the oven for a chosen time (usually 30 minutes). Once this time is elapsed, the wire is removed from the oven and quenched in an oil bath immediately. Oil is used for quenching because experience has shown that it is a much more even quench than either water or air. Tensile test are then carried out on the sample and the results compared to the required values. Adjustments can then be made to the temperature and time regime of the heat treatment and more samples treated. This process continues in an iterative manner until a close match of values is obtained. In some cases the characteristics of the supplied wire cannot be modified to match the requirement, in which case the wire is discarded and samples obtained from a different supplier.

Once a wire has been found that can be brought to the required parameters, the production process begins. Wires are treated in batches of up to 50 where they are straightened, heat treated and tested. Any samples from a batch that fall outside of the designated range of values cause that batch to be rejected. All acceptable batches are identified and passed on to the mesh production areas. All wires (main steel, distribution steel, shear steel etc) used in a model are treated in a similar way to produce the required strengths.

## Concrete

The information required about the concrete within the structure are the compressive (cube) strength and the type of aggregate. In many cases, we scale the aggregate in the mix by using filter media as used in the water industry which is supplied dried and graded. This allows us to create a scaled grading of aggregate very easily. If a particular type of aggregate is required (for example, limestone) we can obtain crushed rock of the designated size from various quarries in the UK, and dry

the aggregate ourselves. It is important to use dry aggregate because it allows precise control of the water content of the concrete mix. The other constituents of the mix are Ordinary Portland Cement (OPC) and mains water.

The preliminary stages for arriving at a mix for a particular application involves designing a series of mixes with the required aggregate and varying the amounts of water and cement. This results in a span of mixes with varying water/cement and sand/cement ratios but with the same aggregate. Each mix is cast in our laboratory in the way laid down in the relevant British Standard, and control samples are taken. These control samples are in the form of 100mm cubes, 100mm x 100mm x 300mm beams and 150mm x 300mm cylinders. The beams give the compressive strength, the beams the flexural strength and the cylinders the tensile splitting strength. In these cases, the test samples (once demoulded) are stored under water for 28 days when they are tested according to the relevant British Standard. These results are then compared with the required values and a mix selected. If the results do not meet the desired figures, further test mixes will be made. Another characteristic that must be considered is the workability of the mix. If small scale models are to be cast with intricate meshes, a workable mix must be designed to allow easy casting to be carried out.

### Mesh Construction

On larger scales, standard build techniques can be employed during the construction of the meshes, for example, tying the joints and overlaps. On smaller scales this becomes impractical for a number of reasons, and other methods have been arrived at. Single layers of reinforcement are spot welded where they cross. This spot welding is adjusted to give merely a locating effect to hold the bars in position. The weld is designed to not affect the strength of the metal in the mesh, the settings for which are arrived at by carrying out test welds on the metal to be joined. All stirrups and shear steel is placed by hand and crimped to hold the layers of mesh at the desired distance apart. The whole activity is highly labour intensive and requires workers with much manual dexterity and patience.

### Casting

It is important to design the moulds used for the models so that the mix will flow into all areas of the structure. On complex models it is quite often necessary to cast in sections (just like real life) in order to allow simple mould design. Smaller models are vibrated as a whole while the mix is being cast on a vibrating table which allows precise control of the intensity and mode of vibration. It is essential that the amount of vibration given is enough to cause the mix to flow to all areas of the model and to remove any air, but not sufficient to disturb the reinforcement or to cause separation of the mix. Each type of structure requires a different mode of vibration.

Concrete control samples are taken from each mix used to complete a model. Some are stored under water for 28 days to give a reference value for the mix, whilst others are stored with the model at all times until it is fired upon. These samples then

give the figures for the concrete that is within the model, having experienced the same environment as the model itself.

## Model Tests

### Generic Structure

The structure that was modelled at scale and tested was a multi-bay heavily reinforced concrete structure. The design was developed from a structure that WES carried out tests on in the years 1980-84, some tests that the Structures Group at AWE Foulness had undertaken in the same period and from information obtained from design manuals. The structure was fielded in various forms at 1/40th scale on the Rugwood series of trials in the UK between 1985-89 and at the Middle Key trial at WSMR in 1993 at 3/40th scale.

### Model Design

The basic model design was a simple structure of a heavily reinforced flat slab spanning steel (overstrong) walls for ease of manufacture. The reinforcement consisted of 1% main and 0.5% distribution steel in each face, and 0.34% shear steel. On full scale the bays of the structure were 6m wide, 48m long with 1m thick walls and roof. At 3/40th scale this became 0.45m wide, 3.6m long with 0.075m thick walls and roof; at 1/40th scale, 150mm wide, 1200mm long with 25mm thick walls and roof. The structure had an earth cover 1m thick over the roof at full scale (75mm at 3/40th and 25mm at 1/40th).

The reference structure used at 1/40th comprised a model with 7 full length bays and 1m (scaled) earth cover on the roof. Other model type were fielded on the Rugwood series: 2 storey models of 4 bays 750mm long with fully structural walls and floors; simple models with 4 bays 750 mm long; and standard 7-bay models with internal wall dividers to create rooms within the bays. Other parameters modified were the thickness of the roof and the depth of the earth cover.

The models to be shipped for Middle Key were limited in size by freight restrictions, so 4 bay models with bays of 2250mm length were constructed at 3/40th scale.

### Reinforcement Properties

At 1/40th scale 1.6mm  $\phi$  wire was used as the main and distribution steel. This wire had an Ultimate Tensile Strength (UTS) of 472.6 MPa and an elongation at break of 15.0 %. 1.0mm  $\phi$  wire was used as the stirrups (shear steel) which had an UTS of 449.8 MPa and an elongation of 27.9 %. The 3/40th scale models had 4.8mm  $\phi$  bar as main and distribution steel (UTS 471.9 MPa, elongation 19.6 %) and a combination of 1.0mm  $\phi$  wire (UTS 446.8 MPa, elongation 27.3 %) and 2.03mm  $\phi$  wire (UTS 441.6 MPa, elongation 25.3 %) as the stirrups. Figure 2 shows the

layout of the reinforcement on the 1/40th scale model.

### Concrete Properties

The aggregate used on both scales was taken from our supplies of filter media. On 1/40th scale, the maximum aggregate size was 1.6mm, the water/cement ratio was 0.5/1 and the sand/cement ration 2.97/1. This gave a compressive strength for the concrete (taken from cube results) of 31.88 MPa. The 3/40th scale concrete had a maximum aggregate size of 4.8mm, and water/cement ratio of 0.8/1 and a sand/cement ration of 7.2/1. The compressive strength of the concrete was 31.02MPa.

### Scaling Environment

To provide a correctly scaled environment for the Middle Key test, the cube law of scaling explosive was used, taking the Rugwood scale as 1/40th and the Middle Key scale as 3/40th. This gave a direct scaling of the charge size, HOB and overpressure environment. The actual results obtained showed good agreement, the overpressures at scaled ranges were all within 10% of those predicted.

### Rugwood Results

The Rugwood trial series gave much information about the behaviour of the structure when loaded. The generic structure was found to be sensitive to a combination of overpressure and impulse delivered. If the overpressure was below a critical pressure, the model would not be damaged, and the amount of damage once this critical pressure was reached was dependent upon the impulse delivered. For the standard 7 bay model with 1m (scaled) depth of cover, this critical pressure was found to be about 9 MPa (1300 psi). The response of the model was seen to be very much a 'go' - 'no-go' situation, with small changes in overpressure/impulse around the critical pressure resulting in large differences in the amount of damage. Other findings were that changing the depth of cover dramatically changes the quantity of damage: double the cover gave much less than half the amount of damage. The lower floors of the 2 storey models survived intact, even close to ground zero, which indicated that these targets were not particularly vulnerable to the size of weapon being used.

### Middle Key Models

Thirteen models were constructed for the Middle Key trial, and they were as follows. Two 3/40th scale 4-bay models for direct comparison with Rugwood experiments were fielded; one (Large Scale 1 [LS1]) with 1m (scaled) cover at a predicted overpressure range of 10 to 8 MPa (1500 to 1200 psi) to compare with the

'standard' Rugwood models and the other (LS2) with 1.5m (scaled) cover at 12 to 10 MPa (1800 to 1500 psi) to check the effects of deeper cover. Five 1/40th scale two-storey models (Multi-Storey 1 to 5 [MS1-5]) were placed close in to ground zero at pressure ranges of 17 to 14.8 MPa (2500 to 2150 psi) to examine the damage to the internal floors. Three 1/40th scale standard 7-bay models (Standard 1 to 3 [S1-3]) were placed in the field at predicted pressures of 6.6 to 4.8 MPa (960 to 700 psi) to examine the effects of the longer durations found with the larger charge. Three 1/40th scale four bay models with short bays (Small Standard 1 to 3 [SS1-3]) were also fielded at the same predicted pressures to allow a cross-reference of the effect of the shorter bays to the standard structures.

## Middle Key Results

The 3/40th scale model designated LS1 was exposed to measured pressures of 10 to 8.8 MPa (1440 to 1280 psi) and suffered a range of damage from the bay nearest GZ having heavy deflections (117mm max) to light across the other three (80 - 50mm). LS2 experienced pressures of 12.2 to 10.8 MPa (1770 to 1570 psi) and the damage levels were light (22 to 15 mm) across the model. The MS models were exposed to pressures of 15.2 to 12.5 MPa (2200 to 1820 psi) and all roofs and internal floors were destroyed. The standard 7-bay models designated S1 to S3 experienced pressures of 6.1 to 4.6 MPa (890 to 660 psi) and showed heavy (80 mm) damage to the front bays and medium to light (10 to 6 mm) across the others. SS1 to SS3 were exposed to pressure of 6.2 to 4.8 MPa (900 to 700 psi) and had heavy (80 mm) damage to the front bays and medium to light (20 to 4 mm) damage to the others.

## Damage Comparisons

Because of the complex nature of the failure of this generic structure, it is necessary to look at both overpressures and impulses when comparing damage levels. Despite all the models that have been fielded on both the Rugwood and Middle Key trials, there are very few that allow a direct comparison using measured results from gauges.

### 1. Overpressure

LS1 fielded at Middle Key experienced pressures of 10 to 8.8 MPa (1440 to 1280 psi). Two comparable models from the Rugwood series were, from test 3, model 6 bays 3 to 6 which was exposed to 9.9 to 7.9 MPa (1430 to 1140 psi) and, from test 4, model 3 bays 3 to 6 which experienced 9.8 to 6.6 MPa (1420 to 960 psi). Test 3, model 6 showed heavier damage than Middle Key LS1, whilst Test 4, model 3 had very similar amounts of damage.

## 2. Impulse from interface gauges

Looking at the figures from the interface gauges placed on the surface of the model roof to measure the interface pressures between the model and the cover gives an indication of why the damage levels were somewhat different. The interface gauge on bay 2 of LS1 from Middle Key showed a total impulse being delivered of 15.8 MPa.ms (2301 psi.ms). Rugwood Test 3 model 6 bay 4 experienced an impulse of 5.6 MPa.ms (812 psi.ms) which scales to an impulse of 16.8 MPa.ms (2436 psi.ms) for a heavier amount of damage. Test 4 model 3 bay 3 experienced an impulse of 5.2 MPa.ms (760 psi.ms) which scales to 15.7 MPa.ms (2280 psi.ms) and gave a similar amount of damage which was selected as the reference for comparison.

This emphasises the fine dividing line for amount of damage when considering the overpressure and total impulse delivered to this type of target.

## Other Middle Key Results

LS2 as fielded on Middle Key suffered very little damage, thus confirming the effect of increasing the amount of cover on the structure as seen on Rugwood test 2. The destruction of the 2-storey models on Middle Key showed that the longer durations of the larger charge were sufficient to attack the lower floors of a multi-storey structure, although, as all the models were heavily damaged, the details of the critical pressure/impulse for these structures was not determined. The standard and small standard models confirmed the higher amount of damage for similar pressures but longer durations as compared to Rugwood, and the good comparison of damage on the standard and small standard models confirmed that the smaller panels give valid results.

## Conclusions

### Modelling Techniques

It is essential to know as much as possible about the structure to be modelled and the scenario of interest and to reproduce these parameters at scale as accurately as possible

### Model Tests

The model tests at 1/40th and 3/40th scale on Rugwood and Middle Key respectively validated the scaling techniques used. The test series also produced enhanced knowledge of the behaviour of the generic structure.

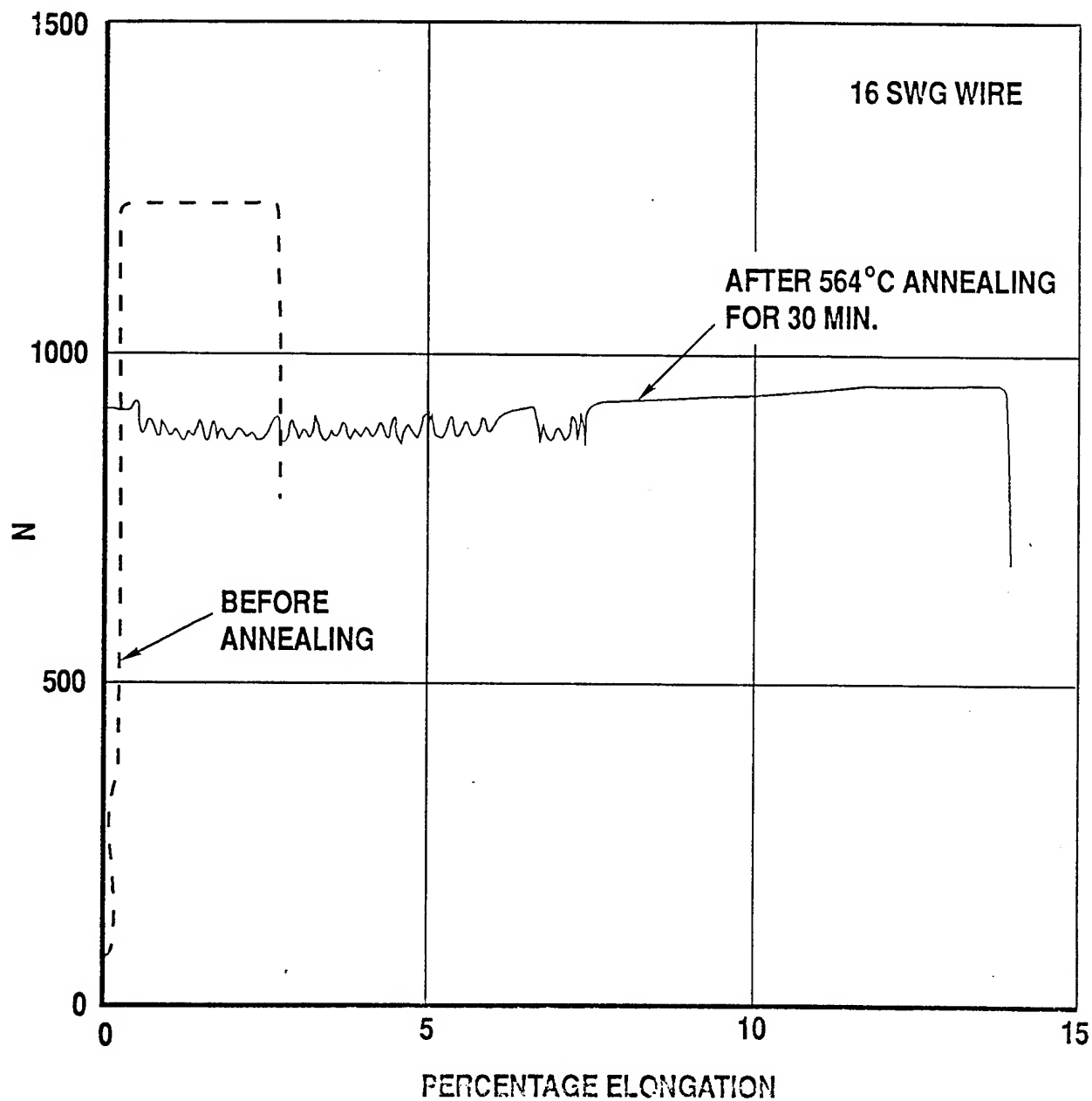
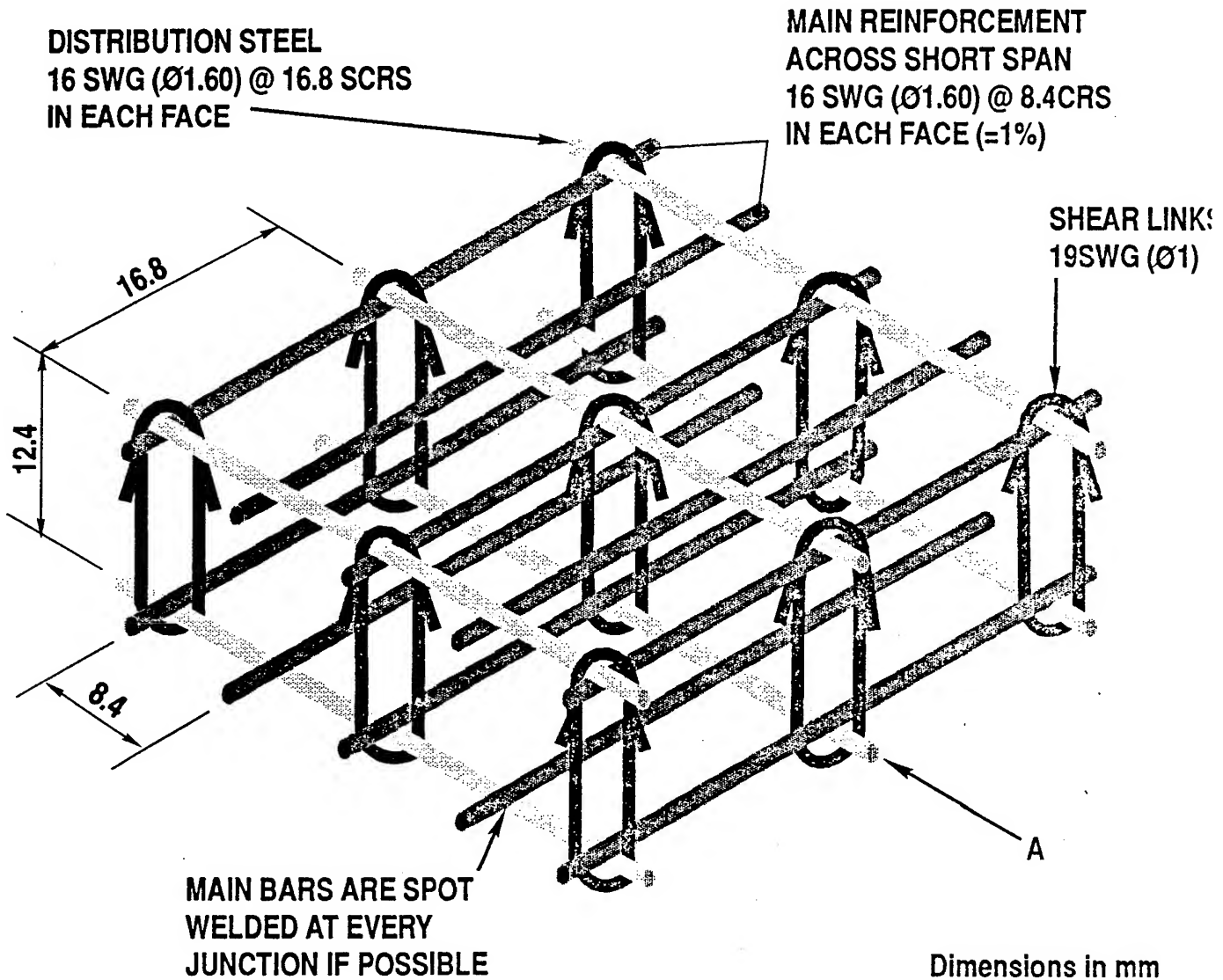


Figure 1. . Comparison of Wire before and after Heat Treatment



### GENERAL VIEW OF REINFORCEMENT

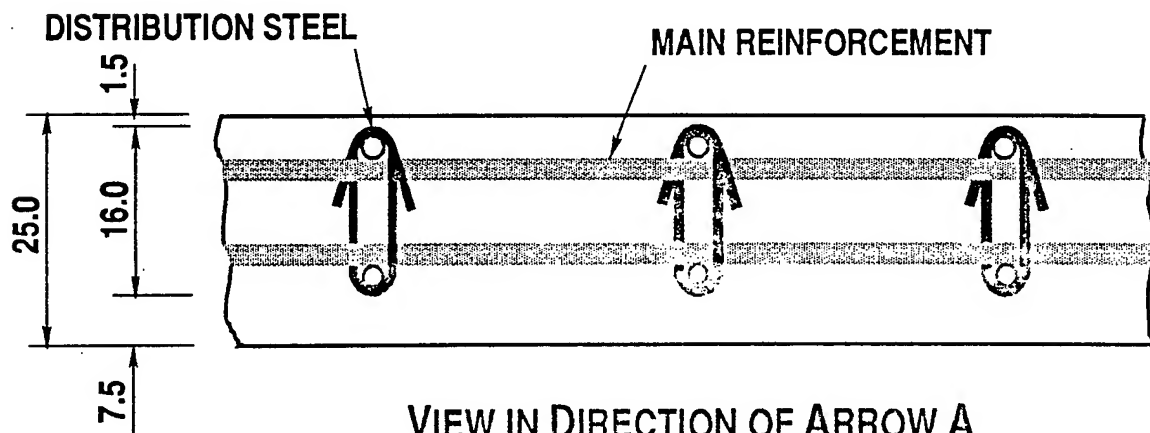


Figure 2. Position of Reinforcement in Concrete Slab



## USE OF CFD/CSD CAPABILITY FOR DESIGN OF BLAST DEFLECTORS FOR A MINE RESISTANT VEHICLE

Isaac Lottati<sup>1</sup>, James Dillon<sup>2</sup>, Sergio Sergi<sup>2</sup>, Kenneth Strittmatter<sup>2</sup>,  
Stephen Sousk<sup>2</sup>, and Shmuel Eidelman<sup>1</sup>

<sup>1</sup>Science Applications International Corporation, McLean, VA 22102, USA

<sup>2</sup>US Army Communications-Electronics Command, Research  
Development & Engineering Center, Ft. Belvoir, VA 22060-5806, USA

### Abstract

Results of a successful effort to significantly improve resistance of the tactical wheeled vehicle to mine detonation are reported. The design methodology is based on a comprehensive use of numerical simulation for blast/structure interaction and structure deformation as a result of blast load. Both Computational Fluid and Structural Dynamic (CFD and CSD) simulations are performed in three dimensions for the most comprehensive representation of the tactical wheeled vehicle geometry. Detailed three dimensional simulations of interaction of the blast waves generated by mine detonations against full configurations of tactical wheeled vehicles were validated by dedicated experiments. Validated numerical capability was used for the analysis of blast structure interaction. Results of this analysis were used to design blast deflectors for placement in key locations to reduce structural damage, and to prevent injuries and loss of life. Three main scenarios for mine detonation were considered: command detonation of a mine under the truck crew cab, detonation of the mine under the front wheel, and detonation under the middle or aft wheel.

CFD simulations were performed with the AUGUST-3D code, using the Second Order Godunov method on adaptive unstructured tetrahedral grids. The BKW equation of state was used for accurate simulation of the initial phases of blast expansion. The DYNA3D code was used for structural dynamic simulations. A comparison between numerical simulations with the AUGUST-3D code and experimental data is given.

Blast deflectors, designed using this comprehensive CFD/CSD methodology, were built and tested for blast loads generated by high explosive detonations. Results of these tests demonstrate a remarkable level of blast protection achieved by low cost deflectors of very simple geometry placed in key locations. The study demonstrates the advantages of including high level CFD/CSD simulations in blast deflectors design.

### 1. Introduction

Land mine detonations are a serious threat in military operations and operations other than war. For military operations, blast simulations have been an effective tool for understanding the performance of countermine systems, as described in previous Military Aspects of Blast Symposium (MABS) meetings.<sup>1,2</sup> Equally important, as covered in this

paper, high fidelity simulations can be invaluable in protecting military truck crews from the devastation of an antitank mine detonation.

Our main objective has been the development of vehicles hardened against antitank land mines. The basic vehicle is the M939 series 5-ton cargo truck. Numerical simulations have been carried out to determine the dynamic loads produced by the mine detonation on the truck crew cab and other structural elements of the truck.

Current emphasis in CFD calls for solutions of applied physical problems for complex realistic geometries.<sup>3-5</sup> In addition to the inherent difficulties in describing the details of the complex three-dimensional geometry, the flow fields usually have an inhomogeneous structure. Regions of rapid change of the flow functions and chemical reactions will be embedded in regions where the flow gradients are relatively small. Accurate simulations of flows in regions with strong gradients are key to the overall accuracy of physical, chemical and biological simulations. For this reason most of the software and hardware computational resources are defined by the accuracy requirements of these flow regions and geometry of the computational domain.

Currently, most numerical simulations employ structured meshes composed of quadrilaterals in two dimensions or hexahedra in three dimensions. However, it has become evident that the hexahedra structured grids cannot satisfy the requirements of large scale numerical simulations over complex geometries in three dimensions. The diversity of computational requirements cannot be satisfied by the quadrilateral structured grids.

Recently proposed alternatives to quadrilateral grids use triangles in two dimensions and tetrahedra in three dimensions. For these grids the mesh will generally lose its structure, allowing a new degree of flexibility in treating complex geometries.<sup>6,7,8</sup> Unstructured grids can relatively easily be adapted to follow flow features, thereby increasing the solution accuracy. The result has been the development of adaptive refinement techniques which have been used with great success for two dimensional simulations on unstructured triangular grids. These methods have resulted in the resolution of details difficult to resolve in the evolving flows over complex configurations.

However, it is not a trivial task to adapt this approach to three-dimensional simulations. One of the problems is the complexity of generating the adaptive grid for unsteady flow. Since the grid is constructed from the volume elements (tetrahedra) the moving shock front is made up of a surface of triangular faces. It should be noted that this moving front can and will change its shape during the computation as time evolves. The adaptive procedure becomes very complex and CPU intensive in three-dimensions.

The A a d a p t i v e U n s t r u c t u r e d G r i d U p w i n d S e c o n d T r i a n g l e s (AUGUST) code was developed by SAIC for two- and three-dimensional simulation. The developed AUGUST-3D code was implemented for calculating flows over complex three-dimensional geometries. Use of unstructured triangular (in two dimensions) or tetrahedral (in three dimensions) grids allows adjustment of the grid resolution to the accuracy requirements in the flow subdomains. The AUGUST-3D applies the Second-Order Godunov method to solve the Euler equations of gasdynamics. The philosophy behind it is to treat the local values of the dependent variables at every point on the grid as initial

conditions for a Riemann problem, and to use the resultant solution of that problem to calculate the fluxes of density, momentum, and energy flows through the interfaces of the cells. Previous implementations of this method were confined to structured meshes.

## 2. Computational Method

The mathematical models used in AUGUST code and details of numerical methods implemented for solution are given in Refs. 6, 7, 8, 9, 13. The codes were validated for a set of benchmark problems. Validation effort is reported in references 7, 8, 10-13.

As stated, an unstructured grid is very well suited to implement boundary conditions on complex geometrical shapes and to refine the grid if necessary. This feature of the unstructured triangular grid is compatible with efficient use of memory resources. The original AUGUST-2D algorithm was modified to enable adaptivity of the grid in the course of the computation. In AUGUST, we implemented an algorithm with multiple criteria for capturing a variety of features that might exist in the physics of the problem to be solved. To identify the location of a moving shock, a total flux of energy density and momentum into triangles are considered.

In Fig. 1, we illustrate how the basic process of grid refinement is accomplished. The original grid is shown in Fig. 1a. Figure 1b illustrates a one-step scheme refinement in which a new vertex is introduced into a triangular cell, forming three new cells. This is followed by reconnection, which modifies the grid as demonstrated in Fig. 1c. The process of refinement and reconnection can be continued until the necessary grid resolution is achieved, as illustrated in Figs. 1d and 1e. This direct approach to the grid refinement provides extreme flexibility in resolving local flow features. A similar simple method is applied to grid coarsening.

AUGUST has proven to have a very robust and efficient algorithm capable of computing transient phenomena, and with the ability to sense the region of physical interest and resolve it by refining and coarsening the grid as needed. Similar methodology is used for 3-D refinement and coarsening. To allow a detailed description of the validation results and blast deflectors design methodology we will omit here discussion of the three-dimensional grid generation. The 3-D domain discretization using tetrahedra is implemented in a number of codes<sup>14,15,16</sup> that can be used to create grids over configurations as complex as a military cargo truck. We should note here, that due to complexity of the truck geometry, the grid generation is very laborious and requires careful implementation regardless what code is used for gridding.

## 3. Equation of State

The truck-mine blast interaction occurs in the near field of the detonation product expansion. Thus, it is very important in numerical simulations to take into account the equation of state of the detonation products. In AUGUST codes we have implemented the Becker-Kistiakowsky-Wilson (BKW) equation of state for both the detonation products and surrounding air. Simulation with the real gas equations of state allow accurate predictions of pressures developed in the near field blast/structure interactions. A

detailed description of our implementation of the BKW equation of state can be found in Reference 17.

#### **4. Simulation Results**

Numerical simulations of the truck/blast interaction were validated by the full scale field experiments. To validate the simulations result without interference of the complex phenomena of tire/blast interaction, the front left tire was removed in both simulations and experiments. Although AUGUST-3D is equipped with an adaptive regridding capability, regridding is not efficacious in the present calculations. There are reflected shocks and vortices over such a large portion of the volume grid that refinement would have to be carried out essentially everywhere or nowhere. Consequently, after the initial blast solution was laid down on the grid, we retained the initial grid without change during the entire calculation.

In Figure 2 simulation results are shown in the form of pressure contour plots over the truck and ground surface. It should be noted that even though we were able to define most of the main components of the truck with its fairly complex geometry, there are obviously still minor differences in geometry between the model and the actual truck. These minor differences can cause discrepancies between the experimental and computed results.

The first computer run was to simulate a small high explosive compound detonation under the right wheel, while the tire was removed. Table 1 compares the computed peak pressure values and the values obtained experimentally. As shown in Table 1, the comparison between the experimental and computed peak pressures is very good. The experimental results obtained by two different test sets can differ considerably (see Table 1) due to the discrepancies in the experimental set up and equipment. The two sets of experiments were conducted by CECOM (U.S. Army Communication Electronic Research Development and Engineering Center) and by WES (U.S. Army Engineer Waterways Experiment Station).

The second computer run was to simulate an increased quantity high explosive under the left wheel while the tire was removed. Figure 3 shows the computed pressure at the truck channel recorded by AUGUST-3D. Figure 4 shows the computed impulse histories for the mentioned station. Table 2 compares the computed peak pressure values to the values obtained experimentally.

Figure 5 shows the experimental pressure history as recorded for the truck frame corresponding to data obtained computationally and presented in Figures 3 and 4. Here it is obvious that the resolution of the experimental data is higher than the resolution we obtained computationally using a relatively coarse grid. Nevertheless, the calculations described above reproduce all the essential features of the measurements, in most cases within the experimental error. Based on these results, we can confidently predict load on the same model truck due to arbitrary explosive charge detonations. The calculations done with AUGUST-3D used only 20,000 - 30,000 grid points. Even though the code is not able to show very narrow shocks due to the resolution of the grid, the overall trend and magnitude of pressure is computed correctly.

Simulation can do more than reproduce the measurements. Specifically, there are at least three areas in which the calculations described here provide a distinct advantage to the design engineer:

1. In order to do studies of failure modes of the structure, predictions of deformation and damage, etc., using a code like NASTRAN, ALGOR, or DYNA3D, it is necessary to input pressure histories at a large number of points ( $\geq 10^3$ ). Whereas using that many pressure gauges would be expensive, time-consuming, and possibly impractical, it is perfectly straightforward with a simulation. With AUGUST-3D we could as easily have generated 20,000 pressure histories (one at every point on the mesh) to provide accurate input for the structural response simulations.
2. Simulations using AUGUST-3D provide more than pressure histories. We can watch shocks propagate through the truck, see which ones reflect where, and in general obtain a much better interpretative picture than is possible with pressure gauges alone. If we want to rerun a calculation with new sensor locations or new diagnostics, we can be sure that nothing else has changed.
3. In order to study the effect of design changes experimentally, it is not only necessary to do another test, but also to build a prototype truck. With its powerful mesh generation capabilities, AUGUST-3D allows us to introduce deflectors, change the sizes of housing, reshape the cab, etc., with very little work. (The major effort is in the specification of the corners in the initial grid generation process.) And we can be sure that except for the modifications thus made, everything else about the truck and explosion is exactly the same.

In short, AUGUST-3D is a tool that can play a valuable role in the design of protective measures for military vehicles from mine damage, and have shown that is flexible, reliable, and cost-effective.

## 5. Parametric Study of the Centerline Wedge Geometries

We were assigned the task to protect the crew of a military cargo truck from a centerline detonation. Initially, we assumed that the truck crew cab could be adequately protected by a wedge-like shield placed under the drive train of the truck to deflect blast waves and prevent components from being driven through the cabin floor. We believed that proper selection of this wedge angle would deflect most of the blast energy to the sides of the truck and at the same time protect the drive train of the truck from the blast impact. To study the blast effect parametrics, six two-dimensional simulations were performed for different wedge angles and geometries. Four V wedge angles between 86 and 140 degrees were examined. For one of these angles, the calculation was also performed with the deflector located ten inches closer to the ground. Also, one calculation was performed for a semicircular deflector.

The numerical simulations were performed with AUGUST-2D using the BKW equation of state for the initial stages of solid explosive detonation. The overall conclusions from the parametric study can be summarized as follows:

- Blast waves reflected from the crew cab floor can interact and focus leading to significant damage and possible penetration of the floor;
- All the deflectors examined produce unacceptable pressure loads on the truck's crew cab;
- The most effective means of reducing the blast load on the crew cab is to deflect the blast wave to the sides as early as possible.

Following our initial study we concluded that the single wedge deflector is not adequate. Understanding of the blast/truck interaction dynamics and consultation with personnel involved in design of the deflector allowed us to arrive at the deflector geometry shown in Fig. 6. We have called this configuration a wedge/wing deflector, since it combines two configurations: a sharp wedge for protection of the drive train, and a flat wedge for reflection of the blast energy to the sides thus preventing exposure of the crew cab to the blast load.

Initially, the pressure on the wedge is comparable with the values we have observed for flatter wedges. For the wedge/wing configuration the maximum reflected pressure on the crew cab corner is 30 atm which is about ten times smaller than pressures observed for a single wedge geometry. After assuring the selected design gives good results from the blast deflection point of view, we performed structural dynamic simulations to design the deflector structure that can withstand a high explosive blast.

## **6. Structural Dynamics Simulations for the Wedge/Wing Design**

We performed structural dynamics simulations of the wedge/wing design using the DYNA2D code. Since the basic geometry of the wedge/wing design has shown to be very efficient in deflecting the blast wave, the main focus of the structural dynamics study was to design the structural elements of the wedge/wing as well as other support structures to be able to withstand the blast.

The sequential (CFD-structural) approach allowed us to consider a number of design options in terms of wedge material properties, thickness of various wedge elements, and optional methods of the wedge assembly using blast load data from a single gasdynamic simulation. The advantage of conducting a 2D analysis whenever possible is, of course, the lower cost and faster turnaround, which allows us to examine a larger number of design options in less time. To validate this assumption we performed full 3D simulations of both the gasdynamics and structural effects of the land mine detonation. Figure 7 shows the DYNA3D simulation results for the key elements of the truck and deflector structure for a sequence of time intervals. The 3D simulations allowed us to introduce elements of the deflector structure into the model that were not represented in the 2D case. The 3D simulation confirmed the primary conclusions of the 2D study.

End-to-end simulations that include mine blast/structure interaction and structural response simulations were demonstrated in the study of the design options for the centerline deflector. In field experiments, the main results of this study were confirmed. After detonation of a high explosive, the crew cab floor was undamaged, the anthropomorphic dummies were located in the crew cab, and the measured overpressure did not exceed 5 psi.

We are also reporting the results of a parametric study of the blast effects produced by a high explosive on the cab of a military cargo truck for off-center detonation. We performed detailed two- and three-dimensional numerical simulations of the interaction between the blast and the truck structure, with subsequent simulations of the structural response of the blast deflector elements to the blast load for different off-center detonation locations. The wedge/wing combination in the design of the blast deflector proved to be a very robust way to protect the vehicle in the event of land mine detonation under the vehicle. To define the worst case scenario for the off-center detonation, a parametric analysis was performed for different blast locations. Based on the results of this analysis, 3-D fluid and structural dynamics simulations were performed for several high explosives detonations. The simulation results were validated by field tests.

## **7. Summary and Conclusions**

We conclude that our approach to blast deflector design can lead to significant improvement in the blast survivability of land vehicles. The design concepts developed here can be applied to a design for comprehensive vehicle protection from land mine detonation, thus assuring survivability of crew and cargo. Therefore, using an optimal set of low cost geometry modification options for the vehicles (including deflectors, diffusers, absorbers and other elements) when implemented, will make the tactical wheeled vehicle much less susceptible to land mine attack. The same methodology can be applied with even greater effect to the design of new vehicles with increased protection against the threat of land mines. Maintaining structured integrity of the crew cab is critical for survivability. In addition, energy absorbing components/seats and proper restraints are required for crew survivability.

## **8. Acknowledgment**

Code development, modeling, and simulation were performed by SAIC while under contract to the U.S. Army. Funding was provided by the U.S. Marine Corps and the Advanced Research Projects Agency. Testing was performed at the U.S. Army Fort A.P. Hill.

## **9. References**

1. S. Sousk, B. Westich, M. Ford, and S. Eidelman, "Enhanced Performance of Conventional Explosive Line Charges," Proceedings MABS-12, Perpignon, France, September 1991.
2. S. Sousk, S. Eidelman, and X. Yang, "Blast Simulations of Dispersed Powered Explosives for Minefield Breaching," Proceedings MABS-13, The Hague, The Netherlands, September 1993.
3. S. Eidelman, I. Lottati, X. Yang, "Development of Mine-Resistant Vehicles," SAIC Report 93/1141, 1993.

4. T. J. Baker and A. Jameson, "A Novel Finite Element Method for the Calculation of Inviscid Flow Over a Complete Aircraft," Sixth International Symposium on Finite Element Methods in Flow Problems, Antibes, France (1986).
5. T. J. Baker, "Developments and Trends in Three-Dimensional Mesh Generations," Transonic Symposium held at NASA Langley Research Center, Virginia (1988).
6. I. Lottati, S. Eidelman, and A. Drobot, "A Fast Unstructured Grid Second Order Godunov Solver (FUGGS)," 28th Aerospace Sciences Meeting, AIA-90-0699, Reno, NV (1990).
7. I. Lottati, S. Eidelman, and A. Drobot, "Solution of Euler's Equations on Adaptive Grids Using a Fast Unstructured Grid Second Order Godunov Solver," Proceeding of the Free Lagrange Conference, Jackson Lake, WY, June 1990.
8. I. Lottati, and S. Eidelman, "Second Order Godunov Solver on Adaptive Unstructured Grids," Proceeding of the 4th International Symposium on Computational Fluid Dynamics, Davis, CA, September 1991.
9. S. Eidelman, P. Collela, and R. P. Shreeve, "Application of the Godunov Method and Its Second Order Extension to Cascade Flow Modeling," AIA J. 22, 10 (1984).
10. I. Lottati and S. Eidelman, "Blast and Structural Simulation/Analysis for Development of a Centerline Blast Deflector for the Cab of an M923A2, 5-Ton Cargo Truck," SAIC Final Technical Report, May 2, 1994.
11. S. Eidelman and I. Lottati, "Blast Simulation and Analysis," SAIC Report, May 30, 1994.
12. I. Lottati and S. Eidelman, "Blast and Structural Simulation/Analysis for Development of an Off-Centerline Blast Deflector for the Cab of an M923A2, 5-Ton Cargo Truck," SAIC Report, May 1, 1995.
13. I. Lottati and S. Eidelman, "A Second-order Godunov Scheme on a Spatial Adapted Triangular Grid,," Applied Numerical Mathematics, 14, pp. 353-365, 1994.
14. M. S. Shephard and M. K. Georges, "Automatic Three-Dimensional Mesh Generation by the Finite OCTREE Technique," International Journal for Numerical Methods on Engineering, 32, pp. 709-749, 1991.
15. J. Peraore, K. Morgan and J. Peuro, "Unstructured Finite Element Mesh Generation and Adaptive Procedures for CFD," AGARD-CP-464, 1990.
16. R. Löhner and P. Parikh, "Generation of Three-Dimensional Unstructured Grids by the Advancing Front Method," International Journal for Numerical Method in Fluid, 8, pp. 1135-1149, 1988.
17. S. Eidelman and X. Yang, "Detonation Wave Propagation in Combustible Mixtures with Variable Particle Density Distributions," AIAA J. 31, 228, 1993.



Table 1

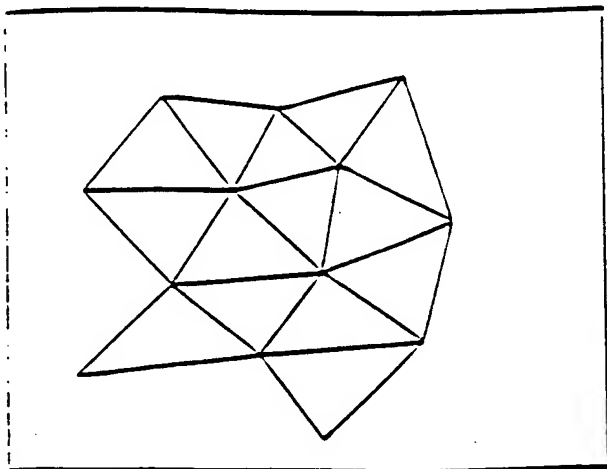
Comparison of experimental and computed results for small quantity of high explosive compound explosive under the right front wheel, tire removed.

<u>Experimental Sensor Location</u>	<u>Duration msec CECOM/WES/SAIC</u>	<u>Peak Pressure psi CECOM/WES/SAIC</u>
C-channel (Truck frame)	1.4/1.6/1.2	440/520/305
Top outside corner of fire wall	3/3/3.2	45/27/120
Door	1.2/1.2/2	77/80/20
Angled fire wall	1.0/1.0/0.7	1100/575/990
Blast side foot (right side foot)	1.2/1/1.1	130/250/175
Blast side seat (right side seat)	2/3.5/3.9	120/65/92
Away side foot (left side foot)	2.6/3/3.	67/60/60
Away side seat (left side seat)	2.6/3/3.	50/88/47

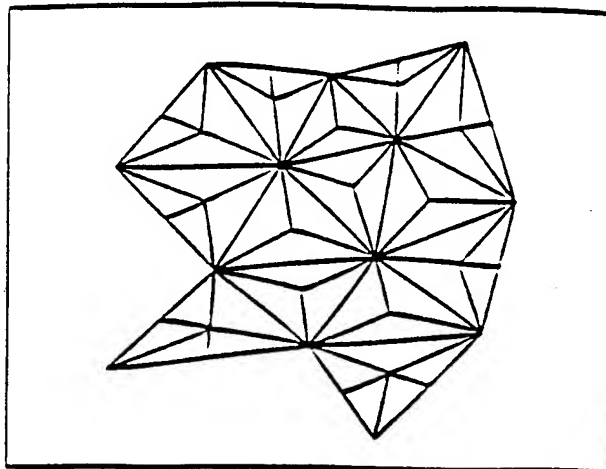
Table 2

Comparison of experimental and computed results for larger quantity of high explosive compound explosive under the left front wheel, tire removed.

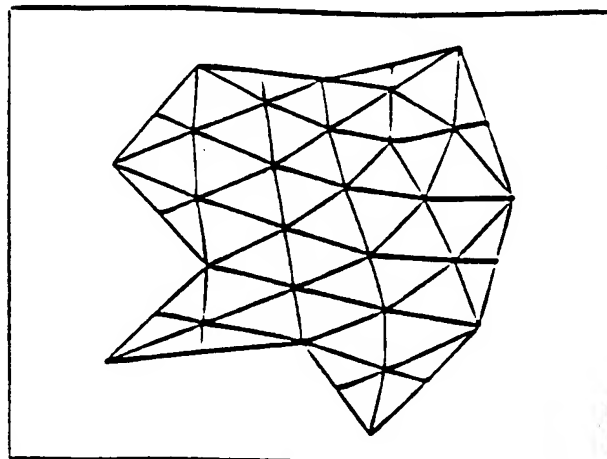
Experimental Sensor <u>Location</u>	Duration msec <u>CECOM/WES/SAIC</u>	Peak Pressure psi <u>CECOM/WES/SAIC</u>
Top outside corner of fire wall	2/1.8/1.8	108/68/180
Door	1.2/1.2/1.	135/180/100
Angled fire wall	1.2/1.5/1.1	1120/950/700
Blast side foot (right side foot)	1.2/1/1	550/1100/700
Blast side seat (right side seat)	0.8/ /0.8	270/ /340
Away side foot (left side foot)	/ /1.9	/ /100
Away side seat (left side seat)	/0.8/2.	/600/90



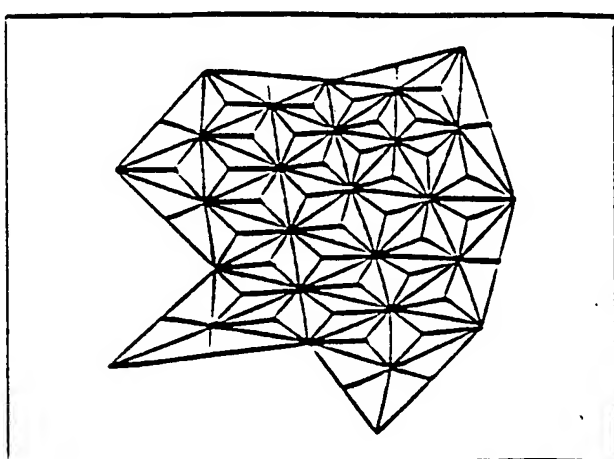
a. Original grid.



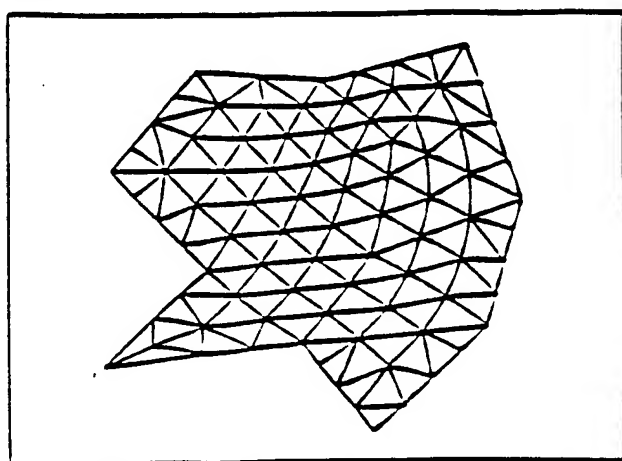
b. Grid after one refinement.



c. Grid after one refinement  
and one reconnection.



d. Second refinement.



e. Second reconnection.

Figure 1. Illustration of the grid refinement process.

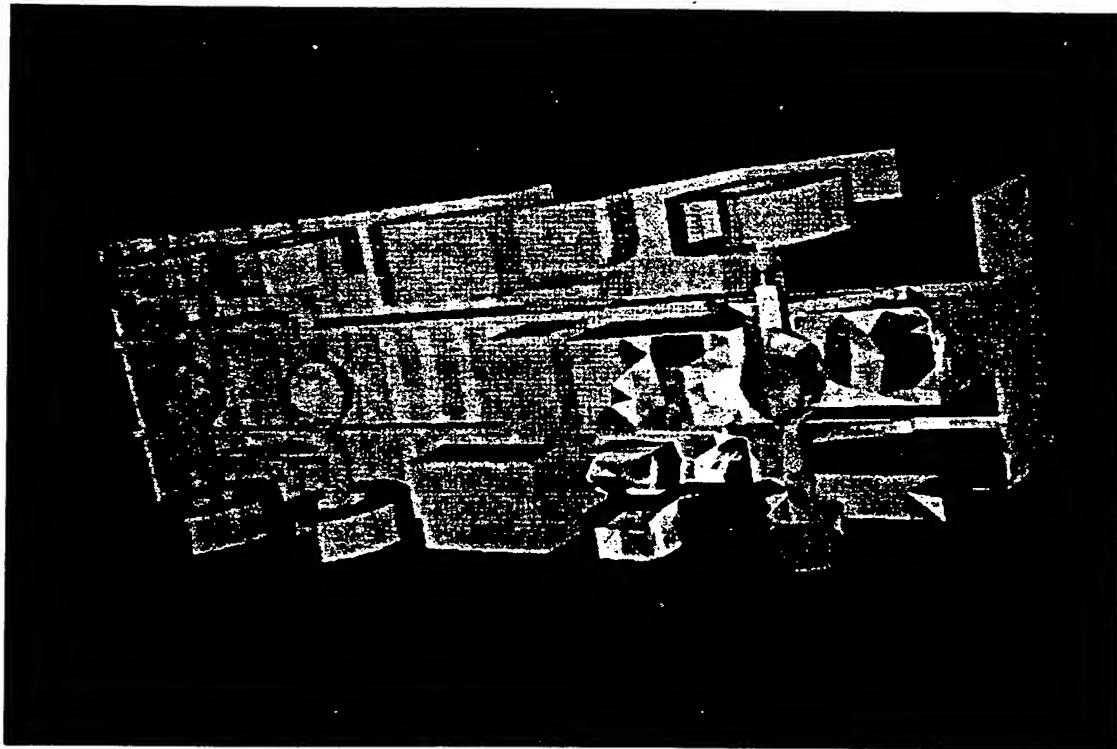
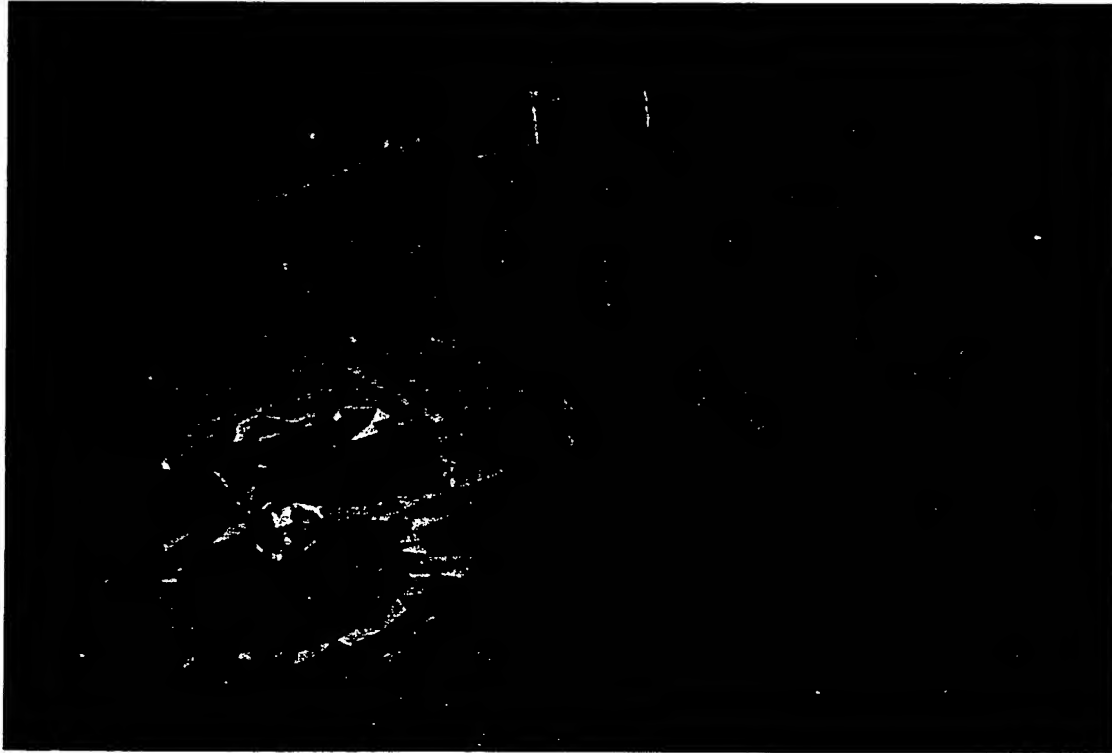


Figure 2. Snapshots of the computed blast pressure values beneath the truck.

M56 TRUCK, MINE 8 lbs High Explosive  
STATION NO. 1

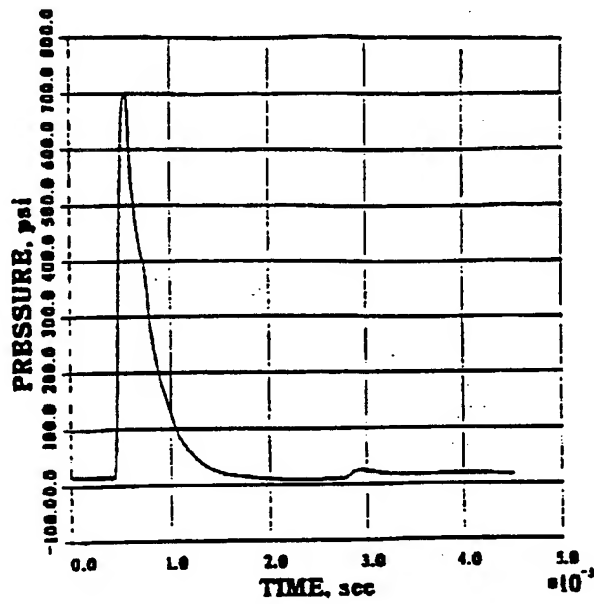


Figure 3. Computed pressure history for 8 lb. case.

M56 TRUCK, MINE 8lbs High Explosive  
STATION NO. 1

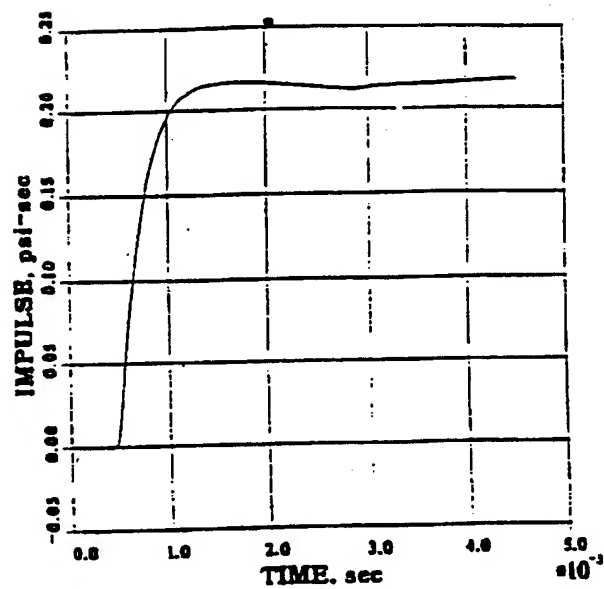


Figure 4. Computed impulse history for 8 lb. case.

Mine Survivable Vehicle Test  
Truck 3 Test 2 930520-01  
HP-2 Angled Firewall  
Hemisphere, Surface  
Left Brake Drum, Front Axle

Digital Gage  
Array Size: 300050  
Cal val 1570.0473  
Deflection -1526

1000 KHZ 06/07/93

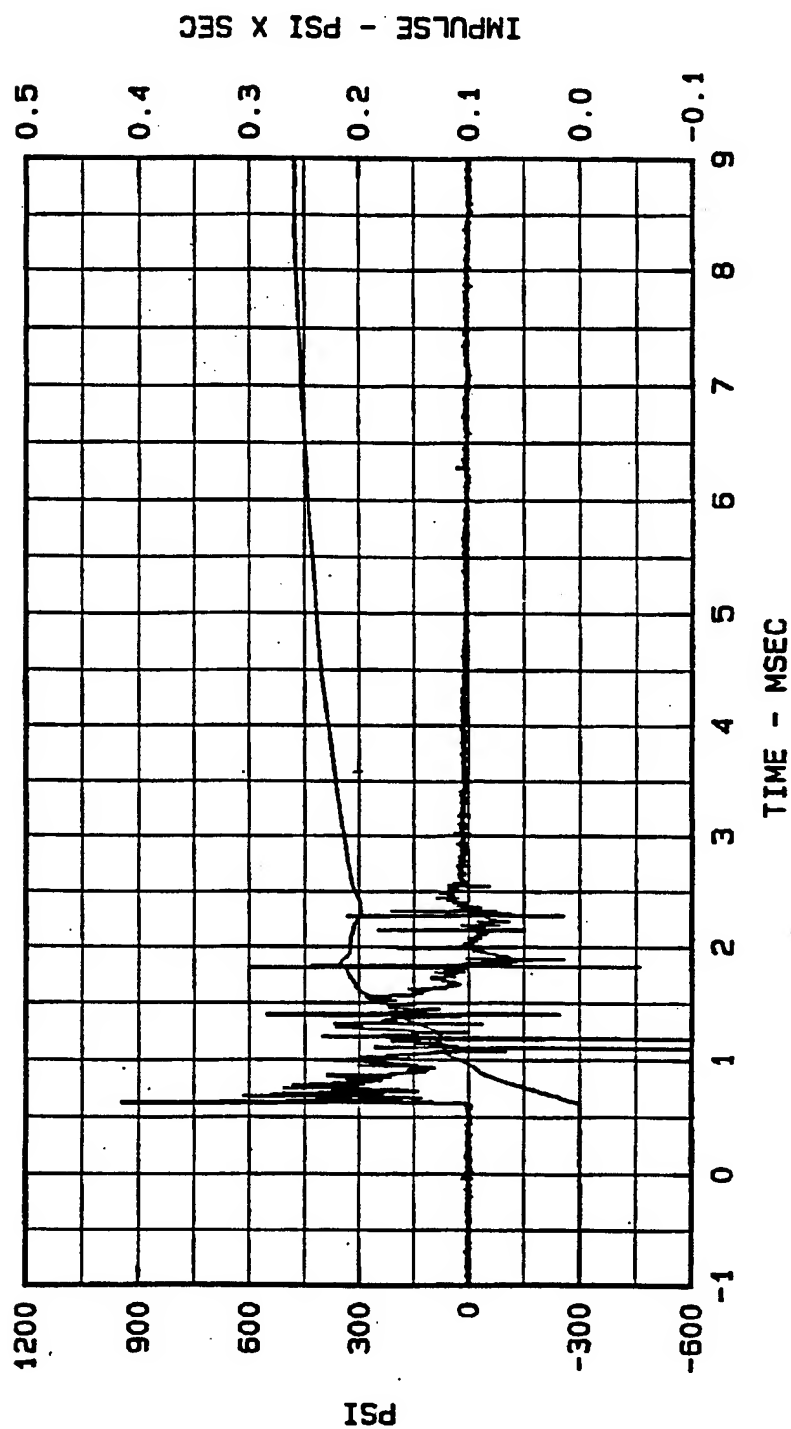


Figure 5. Mine survivable vehicle test.

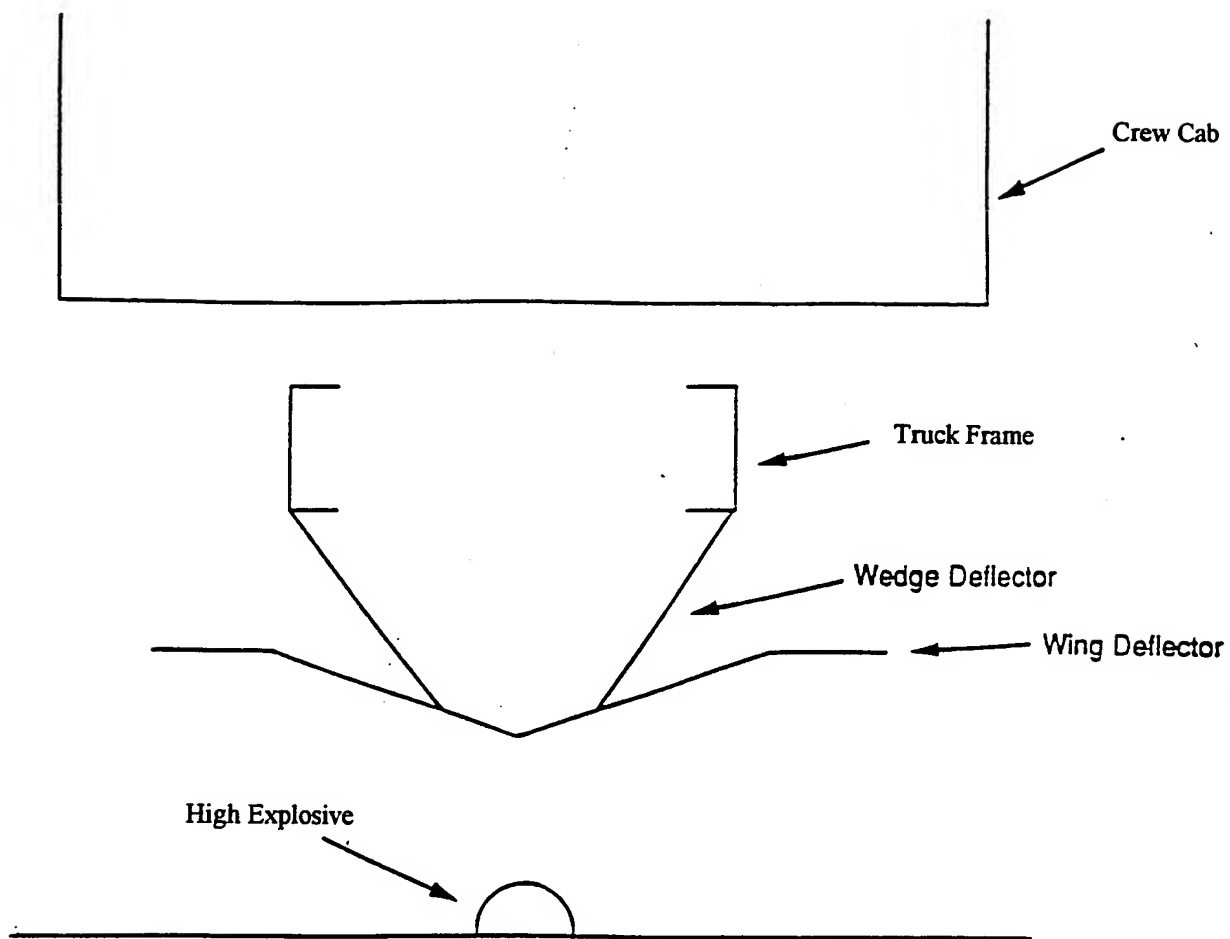


Figure 6. Design of wing/wedge deflector geometry.

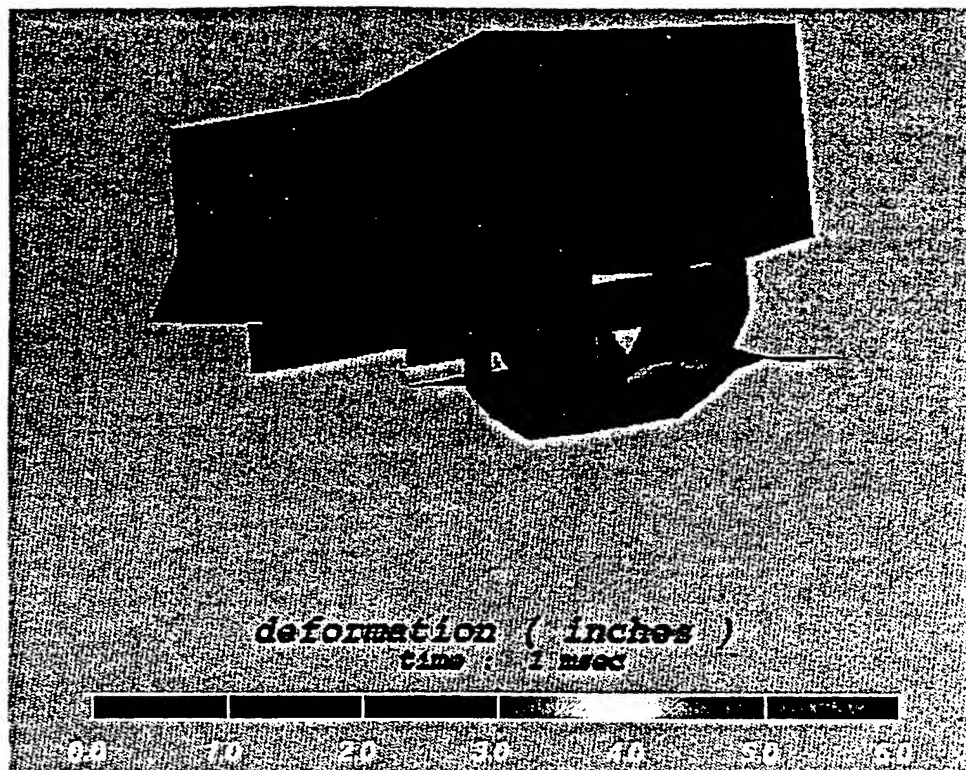


Figure 7a.

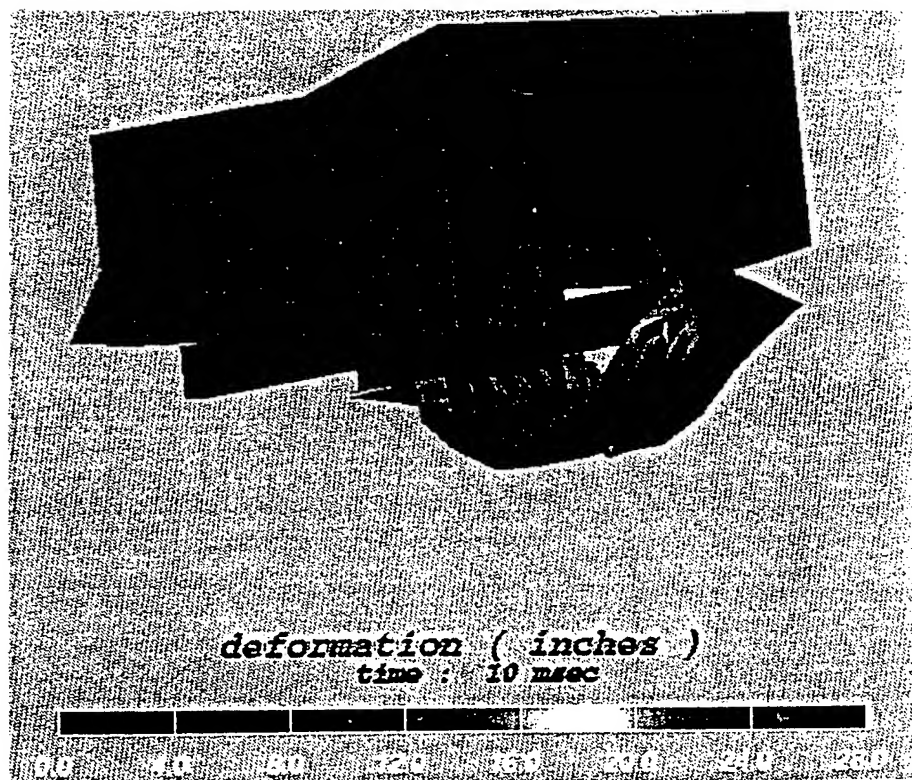


Figure 7b.

Figure 7. Deformation of the double wedge assembly predicted by the DYNA3D simulation..



# Blast Resultants Behind Cantilever Walls: Comparison Between Full-Scale and Model Scale Experiments

F. G. Hulton<sup>†</sup>, P. D. Smith<sup>‡</sup> and T. A. Rose<sup>‡</sup>

<sup>†</sup>Defence Research Agency, LSF3 – Fortifications, Chobham Lane,  
Chertsey, Surrey, KT16 0EE, United Kingdom (Tel: 01344 633058)

<sup>‡</sup>Civil Engineering Group, Cranfield University, Royal Military College of Science,  
Shrivenham, Swindon, Wiltshire, SN6 8LA, United Kingdom (Tel: 01793 785341)

## **Abstract**

Car and other vehicle bombs have proved to be a major terrorist threat in many parts of the world. They can have a devastating effect not only on the occupants of a building but also on the building structure itself. Although a significant degree of hardening may be incorporated into new buildings at relatively low cost, the hardening of an existing building could be an expensive procedure and result in a structure with a very austere appearance. An alternative method of protection is the construction of a perimeter wall around and at some distance from the building. This has the effect of increasing the stand-off distance to the building from any bomb, so reducing the blast resultants (overpressure, impulse and fragment loads) to an more acceptable level.

This paper describes a programme of research in which detailed measurements of the blast environment were made behind protective cantilever walls firstly at model-scale and secondly at full-size. In the first investigation measurements were made behind a 1/10<sup>th</sup> scale vertical blast wall in front of which scaled realistic threats were detonated. A grid for measurement was established out to six wall heights behind the wall and up to three wall heights above the ground and side-on overpressure-time histories were obtained. From these records, contour plots of overpressure and impulse were developed. A similar procedure was adopted for the second set of experiments at full-size in which walls approximately three metres high were subjected to blast loading from a simulated terrorist car bomb. In addition, pressure measurements were made in the model-scale grid with the wall removed.

The paper clearly demonstrates the benefit of providing a blast wall for protecting a building and shows the regions where such benefit is maximised. The paper also presents a comparison between the model-scale and full-size investigations and shows that there is good agreement between the two sets of data emphasising the value of well-designed, model-scale experiments.

## **1 Introduction**

Car and other vehicle bombs have proved to be a major terrorist threat in many parts of the world. They can have devastating effects not only on the occupants of buildings but also on the building structure itself. The hardening of an existing building to minimise the damage sustained from every conceivable form of attack is a very expensive procedure. Furthermore, the resulting appearance of the hardened structure is likely to be extremely austere. An alternative method of protection is to construct a perimeter wall which increases the stand-off between the bomb and building so reducing the blast resultants (overpressure, impulse

and fragments), to an acceptable level from the point of view of the building and its occupants.

Procedures exist to enable solid and composite reinforced concrete walls to be designed to resist these threats provided there is some separation between the wall and the point of detonation of the explosive device. The blast environment behind the wall is less well-understood and as a consequence the designer's task is not so straightforward. The document TM5-1300 [1] provides some design charts to enable the prediction of the blast environment outside three- and four-walled cubicles containing fully- and partially-vented explosions. The document allows calculation of the enhancement of pressure in the front and reduction of pressure to the side and rear of such structures. However, TM5-1300 contains no information about the magnitude of the blast environment adjacent to simple plane cantilever barriers.

In this paper a number of points are made. Firstly, the beneficial effect of a wall in reducing blast resultants is demonstrated. Secondly, the value of presenting this information in the form of design charts is discussed. Finally, and perhaps most importantly, the paper shows that, when compared with full-scale events, results obtained from model-scale experiments demonstrate encouraging correlation.

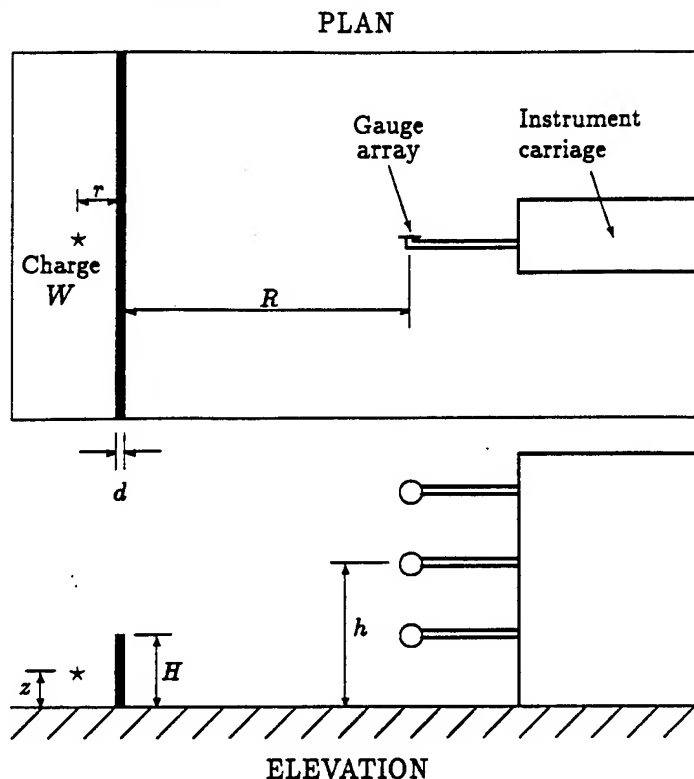
## 2 Experimentals Programme — Model Scale

As reported by Rose et al [2], an investigation was made of the blast environment behind a plane cantilever blast wall at  $1/10^{\text{th}}$  scale in a region extending to approximately six wall heights behind the wall and to three wall heights above the ground. The series of experiments was extended as described in a second document by Rose et al [3] for scales from about  $1/8^{\text{th}}$  to  $1/14^{\text{th}}$  to enhance the data base. In addition, experiments were conducted without a wall in place. The walls had heights as given in Table 1 below and were constructed from 20 mm thick steel plate. Other details about the experimental set-up can be found in Reference [3].

Table 1: Experimental Programme — Model Scale

Scaled wall height $H/W^{1/3}$ (m/kg <sup>1/3</sup> )	Scaled stand-off $r/W^{1/3}$ (m/kg <sup>1/3</sup> )	Actual wall height (m)	Charge weight TNT eqv. (kg)
0.50	0.327	0.211	0.0750
0.60			0.0435
0.71	0.692	0.300	0.0750
	1.058		
	1.423		
0.80	0.327	0.380	0.0527
0.90			0.0750
1.00			0.0549
$z/W^{1/3} = 0.258 \text{ m/kg}^{1/3}$			

In all experiments the horizontal location of the charge relative to the wall is  $r$ , the measuring position measured horizontally behind the wall is  $R$ , the measuring position height above the ground is  $h$ , the height of the wall is  $H$  and the height of the charge from the ground is  $z$  as shown in Figure 1.



- $H$  = Wall height, (m)
- $d$  = Wall thickness, (m)
- $R$  = Distance to point of interest behind wall, (m)
- $h$  = Elevation of point of interest behind wall, (m)
- $W$  = Charge weight (kg TNT equivalent)
- $r$  = Distance of charge to wall, (m)
- $z$  = Elevation of charge above ground, (m)

Figure 1: Nomenclature and model scale experimental layout

In all, nine complete sets of data were obtained for the range of parameters shown in Table 1, where the dimensions are represented as scaled distances  $r/W^{1/3}$ ,  $R/W^{1/3}$ ,  $h/W^{1/3}$ ,  $H/W^{1/3}$  and  $z/W^{1/3}$  respectively and  $W$  is the charge mass in kilogrammes of TNT equivalent. Six sets of data are concerned with the variation of the parameter  $H/W^{1/3}$  and 4 sets with the variation of  $r/W^{1/3}$ . One set is common to both investigations. The scaled wall height  $H/W^{1/3}$  was varied to represent terrorist threats ranging from a typical car bomb at 1 m standoff from the wall to a truck bomb at 2 m standoff.

### 3 Experimental Programme — Full-Scale

In September 1994 the Defence Research Agency carried out a series of trials to investigate the performance of protective walls. The trials were not confined to the study of the behind-wall blast effects, they also covered levels of ballistic protection, the resistance of walls to multiple attacks, and the ultimate resistance of walls.

In planning these trials the results of the model scale tests were used for the initial choice of appropriate pressure gauge settings behind walls. Gauges were set behind walls for a number of different types of investigation:

- To compare the explosive performance of different varieties of cased charges.
- To check the consistency of performance of the devices used to attack walls.
- To provide data to compare with the predictions of the model scale work.

Although a number of different wall types were tested during the trials, the wall most useful for the last investigation was 3.3 m high and 1.4 m thick. This wall was massive enough to resist repeated attacks from charges ranging from 30 kg to 250 kg at stand-offs of 7 m downwards, allowing the set up of a permanent array of pressure gauges in a 12 m long by 4 m high grid of positions normal to the centre of a 21 m long blast wall. At each end the blast wall was extended by a further 3 m by lighter walls of similar height. This arrangement ensured that end effects would be unlikely to be significant. The maximum gauge height was dictated by the risk of fragment damage to any gauge higher than the wall. At 4 m the risk of damage was low, and the difficulties of replacing damaged gauges were not excessive.

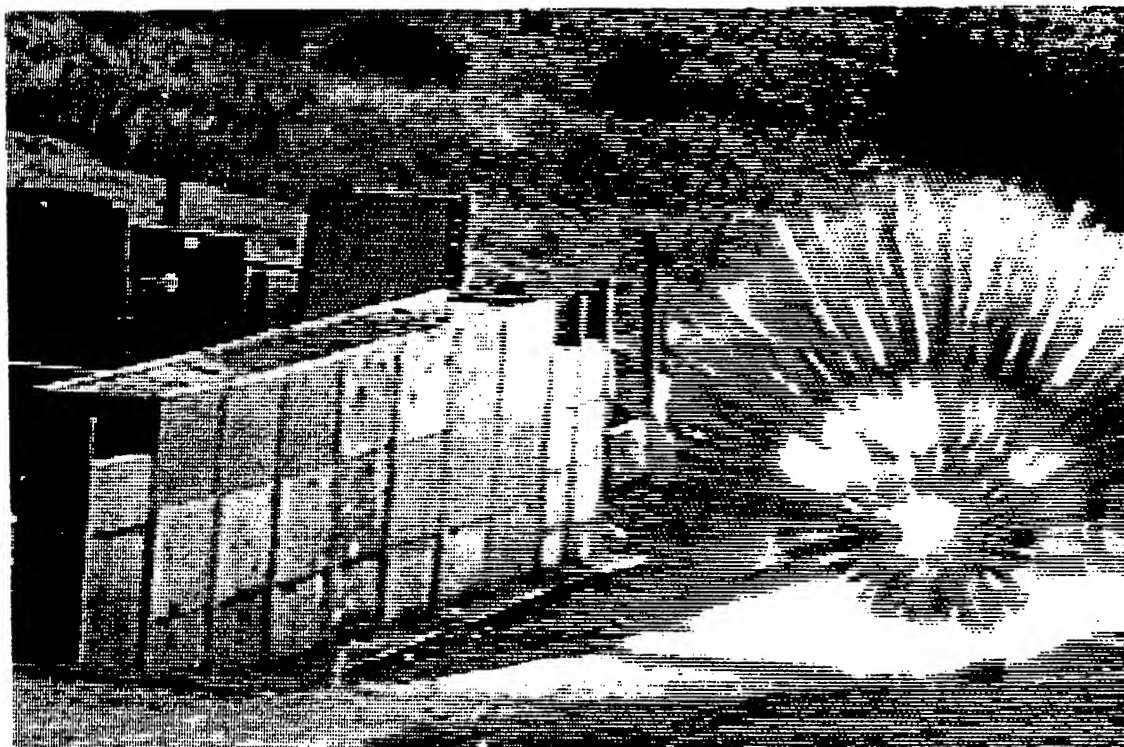


Figure 2: Testing a cased charge against a 3 m high blast wall

Against this wall a series of attacks was made using spherical charges of standard military plastic explosive (PE4). The charges were placed in the positions which were to be used later to test cased charges against the wall. The behind-wall gauge readings would then provide a comparison of explosive outputs against the output of standard charges. Gauges were also positioned in front of some walls, but they had an uncertain life expectancy. Each attack was recorded on film and video.

This arrangement proved successful. There were some gauge casualties from fragments at the 4 m level, but in most cases at least ten good sets of readings were observed.

The trials conditions differed from the model scale experiments in a number of respects, in particular the thickness of the wall and the non-ideal condition of the reflecting surfaces. None the less, the predictions from the model scale work proved useful and appeared to give sufficiently consistent results for design and assessment purposes, given the inevitable non-ideal conditions and uncertainties in real cases.

After the trials, data from the spherical PE4 charges were compared with model scale results.

## 4 Results

### 4.1 Benefit of Providing a Blast Wall

The benefit of a blast wall will be demonstrated by comparing the pressure and impulse data from two sets of model scale experiments, with and without the blast wall.

Figures 3 and 4 are "benefit plots", i.e., they show the pressures and impulses which occur in the region behind the wall in terms of the percentage of the quantity measured when the wall was not present. For example:

$$\text{Pressure benefit} = \frac{P_{\text{wall}}}{P_{\text{no wall}}} \times 100\%$$

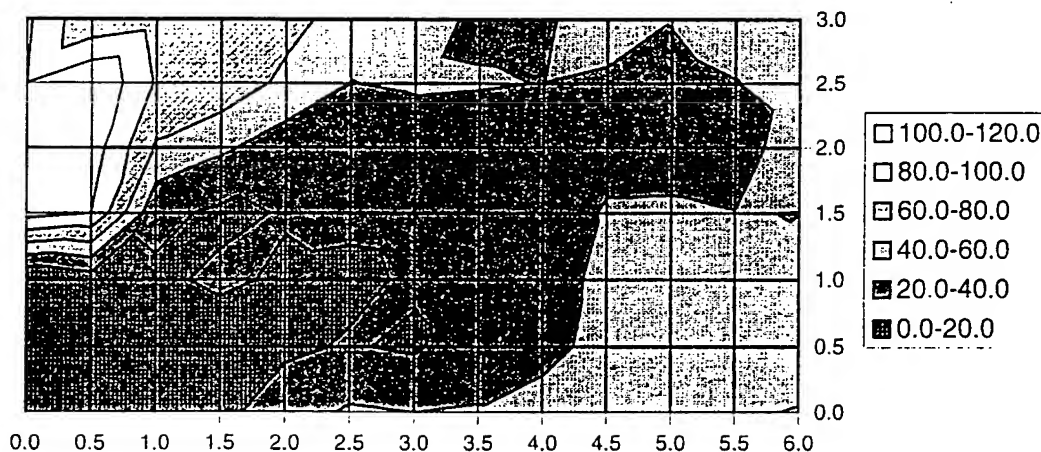


Figure 3: Percentage peak pressure contour plot - wall/no wall

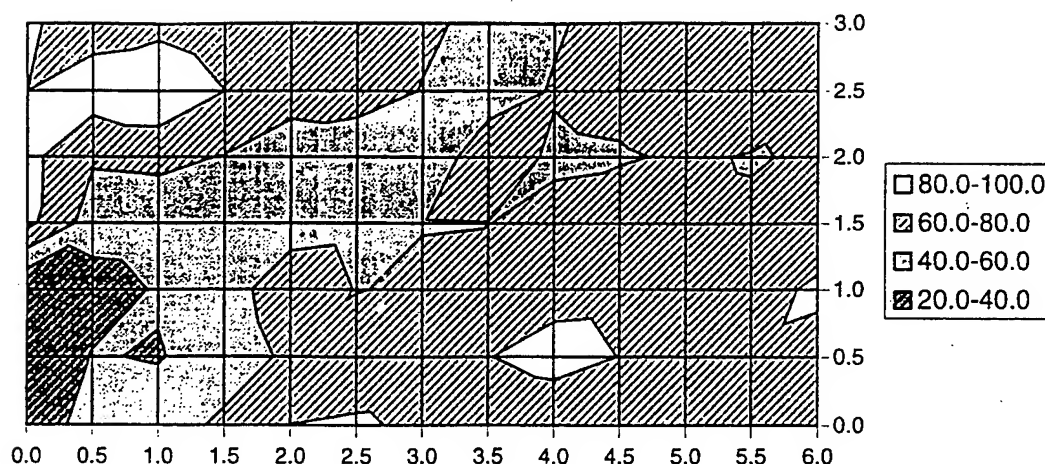


Figure 4: Percentage impulse contour plot – wall/no wall

Intuitively, one might expect to find a region extending a short distance above and beyond the top of the wall where the pressures will be greater than with no wall, because of the “focussing” effect caused by reflected waves travelling up the front face of the wall. However, everywhere else, particularly in the region shadowed by the wall, the blast resultants should be greatly reduced.

Referring to the pressure plot (Figure 3) it can be seen that the area where the pressures are higher than if there was no wall present, extends upwards to over  $3H$  and backwards to  $\approx 0.75H$ . The most benefit is seen directly behind the wall in the “shadow region” where the pressures are less than 10% of those experienced without a wall. From a designer’s point of view the most important generalisations which can be drawn from the plot are that in the area up to a distance of  $3H$  behind the wall the pressures are less than 50% and up to  $4H$  they are 30% – 40% of those without the wall. Beyond  $4H$ , although the pressures are less, the benefit is reduced.

The benefit plot for impulse (Figure 4) shows a very similar pattern, except the reduction is less pronounced than for the pressure. The area above the wall and for a distance of  $H$  behind it shows a small impulse enhancement and the shadow region immediately behind the wall shows a reduction to 40% of the no wall value. Generally, for the area extending beyond  $3H$  the impulses are between 60% and 80% of those measured without the wall. These results for pressure and impulse reduction are in good agreement with the conclusions of Jones et al [4].

## 4.2 Design Charts and Computer Program Derived from Model Scale Experiments

In order to present the data obtained in the model scale investigation in an accessible form for the designer and to generalise it so that comparison with the full-size experimental data was possible, it was necessary to modify the way the peak pressure and scaled impulse information from the model scale experimental records was presented. This necessity arose because the pressure records obtained during the trials that comprised the  $H/W^{1/3}$  study

were captured on a fixed spacial grid but used 4 different charge weights. The result was that the measuring locations in scaled coordinates  $R/W^{1/3}$  and  $h/W^{1/3}$  were not coincident for all sets of data. Similarly, the overall size of the scaled measuring space varied from one data set to another. Another small anomaly arose from the arbitrary selection of  $H/W^{1/3} = 0.71 \text{ m/kg}^{1/3}$  for the first series of experiments. This value was slightly out of step with the other 0.1 increments used for the remainder of the investigation. Clearly, for a set of design curves to be of use, the data must belong to a common set of parameter intervals. This problem was addressed by using interpolation to map the data onto a regular subgrid in scaled space as described by Rose et al [3]. Curve fitting was then used to approximate the data closely over the whole of its range. By this method, the entire pressure and impulse data was represented in polynomial form. These resulting formulae were used to produce a series of design charts and a complementary FORTRAN program called DESIGNP, which performs the data extraction process. The design charts and the program require as input the stand-off of the charge from the wall as well as charge weight and wall height.

In this paper, the output from the DESIGNP program has been used for comparison with the full-size experiments.

## 5 Comparison Between Full-Scale and Model Scale Experiments

### 5.1 Scaled Distance: Limitation of Comparison

Because the program DESIGNP is based on a subset of the data obtained from the small scale trials, restrictions apply to its use. The scaled wall height,  $H/W^{1/3}$ , should be in the range  $0.5 \text{ m/kg}^{1/3}$  to  $1.0 \text{ m/kg}^{1/3}$ . The horizontal scaled distance of the measuring location behind the wall,  $R/W^{1/3}$ , should be between  $0.5 \text{ m/kg}^{1/3}$  and  $4.0 \text{ m/kg}^{1/3}$ . The vertical scaled height of the measuring location above the ground,  $h/W^{1/3}$ , should be in the range  $0.0 \text{ m/kg}^{1/3}$  to  $2.0 \text{ m/kg}^{1/3}$ . The horizontal scaled distance of the charge centre from the wall,  $r/W^{1/3}$ , should be between  $0.327 \text{ m/kg}^{1/3}$  and  $1.423 \text{ m/kg}^{1/3}$ . The vertical scaled height of the charge centre above the ground,  $z/W^{1/3}$ , should be constant at a value of  $0.258 \text{ m/kg}^{1/3}$ . The scaled wall thickness  $d/W^{1/3}$  was not investigated or accounted for in the RMCS trials and there is no wall thickness parameter in the program DESIGNP.

From the series of full-size building trials, there are 8 trials (here designated Attacks 1 to 8) which comply with the requirement for scaled wall height  $H/W^{1/3}$  (Table 2). Of these, 5 comply with the restriction on the horizontal charge location  $r/W^{1/3}$ . The 3 trials for which  $r/W^{1/3}$  is beyond the maximum permissible value are compared with predictions for the maximum permissible value. The outcome of this approach will be addressed in the discussion below.

Strictly, none of the 8 trials comply with the fixed scaled charge height condition  $z/W^{1/3} = 0.258 \text{ m/kg}^{1/3}$ , although the effect of small variations in this parameter should not be significant. Each of the full scale trials employed 12 measuring locations; of these, 9 were within the bounds for  $R/W^{1/3}$  and  $h/W^{1/3}$  described above.

The TNT equivalence of PE4 used in this comparison was 1.32, both for pressure and impulse. This is the same value used for the identical civilian explosive (Demex) used in the small scale trials.

Table 2: Full scale experimental programme

Attack number	1	2	3	4	5	6	7	8
Charge weight PE4 (kg)	30.0	40.0	47.2	40.0	30.0	30.0	40.0	50.0
Charge weight $W$ (kg) TNT eqv.	39.6	52.8	62.3	52.8	39.6	39.6	52.8	66.0
Scaled wall height $H/W^{1/3}$ (m/kg <sup>1/3</sup> )	0.968	0.880	0.832	0.880	0.968	0.968	0.880	0.817
Charge stand-off $r$ (m)	3.0	3.0	5.0	5.0	5.0 <sup>†</sup>	7.0 <sup>†</sup>	7.0 <sup>‡</sup>	5.0
Scaled charge stand-off $r/W^{1/3}$ (m/kg <sup>1/3</sup> )	0.880	0.797	1.261	1.333	1.467	2.054	1.866	1.237
Height of charge $z$ (m)	0.80	0.88	1.00	1.20	1.20	1.50	1.50	1.00
Scaled height of charge $z/W^{1/3}$ (m/kg <sup>1/3</sup> )	0.235	0.235	0.252	0.320	0.352	0.440	0.400	0.247
Wall height $H = 3.3$ m Wall thickness $d = 1.4$ m								

<sup>†</sup> Maximum value of  $r$  used in DESIGNP = 4.850 m.

<sup>‡</sup> Maximum value of  $r$  used in DESIGNP = 5.338 m.

Figures 5 and 6 show the full scale experimental peak pressure and peak scaled impulse points plotted alongside curves calculated from the program DESIGNP. The two examples presented here are for Attack 1, with measurements behind the wall made at heights above the ground of 2.0 m and 4.0 m respectively.

There are number of important factors which affect the comparison of the full scale trials with the predictions of DESIGNP. The photographic record of the full scale trials shows that, although the reflecting surface on the near side of the wall was reasonably smooth, that on the far side was locally more uneven. A particular point that should be noted is that in some cases there were baulks of timber or sandbags directly beneath gauge locations and, as many of the gauge locations were relatively close to the ground (in terms of scaled distance), it should be expected that a degradation of the measured peak pressures would result. Although the initial part of the pressure-time history of the blast wave is affected by the characteristics of the ground near the measuring station, a similar degradation of the impulses would not be expected. Modification to the early shape of the wave will not alter significantly the overall impulse generated.

The program DESIGNP uses data for the minimum value of  $r/W^{1/3}$  to calculate pressures and impulses, and then uses a "modifier" based on an exponential decay to account for values of  $r/W^{1/3}$  greater than the minimum as detailed in [3]. This modifier was developed from a set of data captured at a fixed scaled wall height  $H/W^{1/3} = 0.71$  m. All of the full scale trials employed values of  $H/W^{1/3}$  between 0.82 m/kg<sup>1/3</sup> and 0.97 m/kg<sup>1/3</sup>. Therefore, very close agreement would not be expected at large values of  $r/W^{1/3}$ . The



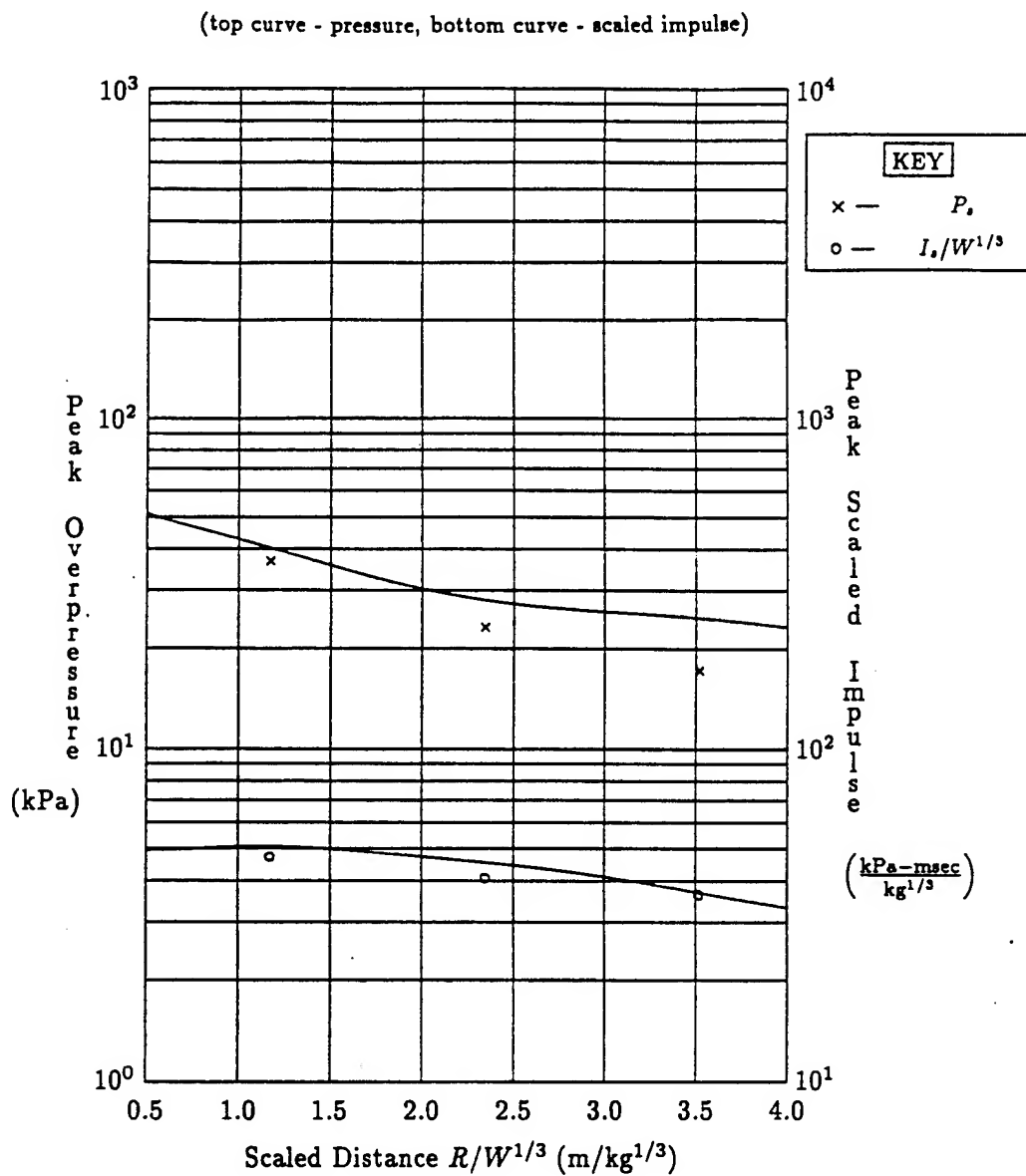


Figure 5:

Attack 1  
 $h = 2.0 \text{ m}$

(top curve - pressure, bottom curve - scaled impulse)

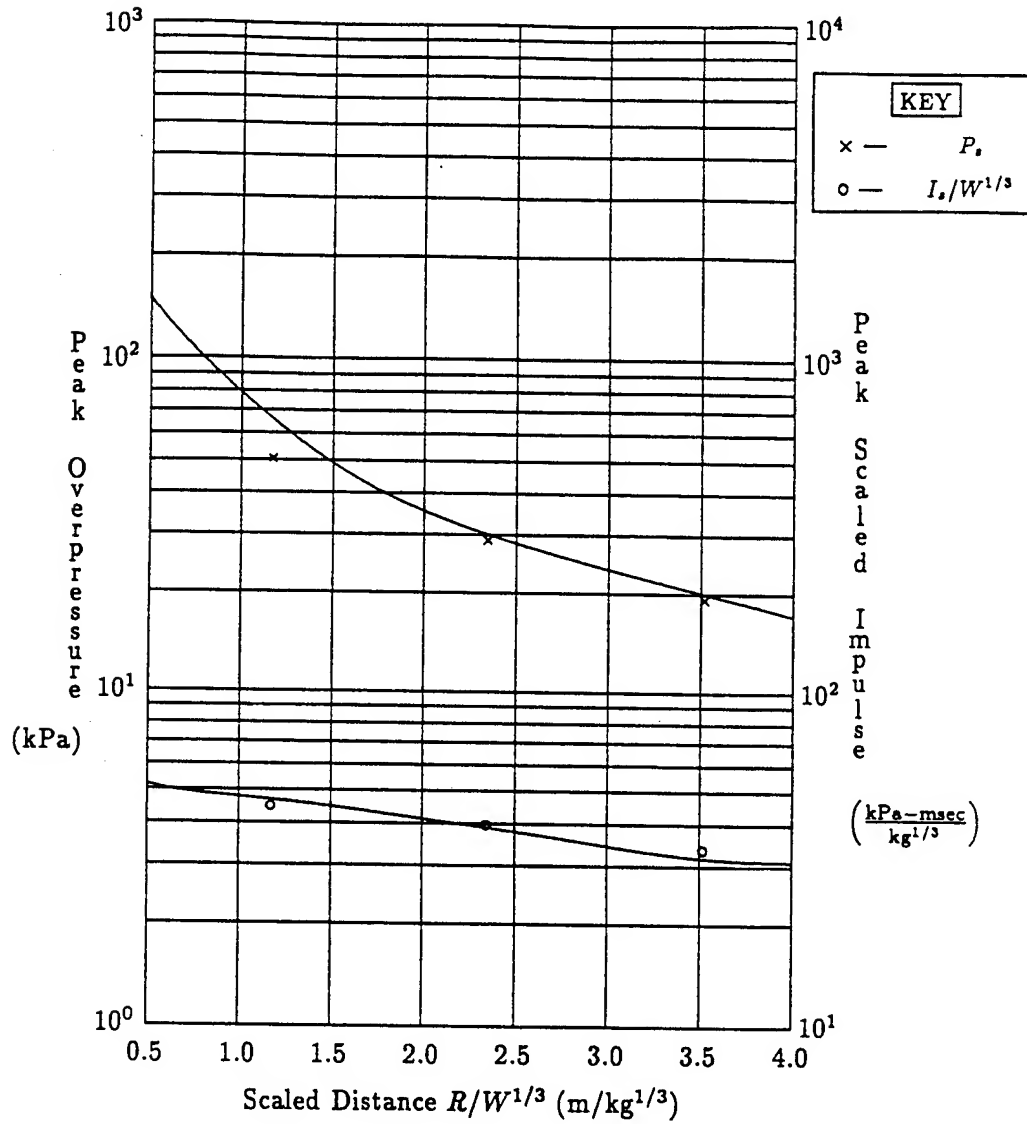


Figure 6:

Attack 1  
 $h = 4.0 \text{ m}$

small scale investigation included information from a space behind the wall which extended 6 wall heights behind the wall and 3 wall heights above the ground. The consequence of this is that the single modifier which resulted is an average taken from the whole of the measuring space and does not reflect the actual change at a particular location. As mentioned above, all the gauge locations in the full scale trials were close to the ground and mostly in the "shadow" of the wall. This might adversely affect the predictions of the program DESIGNP, as the single modifier was calculated to give the best results over the whole of the measuring space for which the program can calculate.

The scaled wall thickness  $d/W^{1/3}$  employed during the full scale trials was significantly greater than that used for the trials on which the program DESIGNP was based. Because the values  $r$  and  $R$  are measured from the front and rear surface of the wall respectively, the actual thickness of the wall and any resulting increase in stand-off is effectively ignored. The comparison presented here has used DESIGNP in this manner. It is suggested that the effect of wall thickness on the magnitude of blast resultants behind the wall should be the subject of future studies.

## 5.2 Quantative Assessment of Comparison

Attacks 1 & 2 employed a parameter set close to that used in the formulation of the program DESIGNP. In this respect, the key parameter was  $r/W^{1/3}$ . In both cases the value of this parameter was significantly closer to the minimum value  $r/W^{1/3} = 0.327 \text{ m/kg}^{1/3}$  used by DESIGNP than in each of the other attacks. Therefore, the amount of modification applied to the calculations for the first two attacks was not great and good agreement would be expected. The peak pressure and impulses measured were 73.8% and 99.1% of the values predicted by DESIGNP. For the reasons discussed above, it would be expected that peak pressures might be reduced compared to DESIGNP values, but impulse values provide a more reliable indicator and the comparison is good.

The three Attacks 3, 4 & 8 are near the bounds of the prediction program in terms of  $r/W^{1/3}$  and so the reduction of the calculated pressures and impulses due to the decay algorithm will be significant. Measured values of peak pressure and peak impulse are 81.6% and 112.7% of the predicted DESIGNP values respectively. It is hard to comment on the accuracy of the DESIGNP predictions for these attacks because only a small portion of the predictive range of the program (in terms to  $R/W^{1/3}$  and  $h/W^{1/3}$ ) was utilised by the gauge locations used in the full scale trials. However, because of the form of the decay algorithm, the program underpredicts impulse by approximately 13% at these specific locations.

Each of the Attacks 5, 6 & 7 was outside the limit of the program for the parameter  $r/W^{1/3}$ . They also used relatively large values of  $z/W^{1/3}$ , which would also make comparison difficult. These trials have been included in the paper for completeness, and although they are not suitable for validation purposes, they are nonetheless interesting. The average measured peak pressure for the three Attacks is 79.1% of the DESIGNP prediction and the average measured peak impulse is 119.4% of the DESIGNP prediction.

Averages of the percentages of peak pressure and peak impulse for all attacks which comply with the stated limits of the program DESIGNP are 78.6% and 107.4% of the DESIGNP prediction respectively.

The agreement between the predicted and measured values of peak pressure are in close agreement for the  $h = 4.0 \text{ m}$  horizontal gauge line. In particular, the two gauge locations at  $h = 4.0 \text{ m}$ ,  $R = 8.0 \text{ m}$  and  $12.0 \text{ m}$ , situated where the effect of wall thickness is thought to be less significant, produced even closer agreement. The average percentage peak pressure

was 96.5% of the DESIGNP value compared to 78.6% for all attacks listed above. This result reinforces the view that the poor reflecting surface is responsible for the reduction in peak pressure at the lower gauge positions.

## 6 Conclusions

It has been shown that the program DESIGNP can predict accurately peak side-on impulses at locations behind a plane undeforming cantilever wall for experiments conducted at full scale when the charge stand-off of the experiment is close to the minimum allowable by the program. Reasonable predictions can be obtained at larger charge stand-offs, but allowance should be made for possible underprediction if the program is used in this manner.

The program DESIGNP consistently overpredicted peak side-on overpressures when compared to the results of the full scale experiments. However, this may be explainable by the non-ideal reflecting surface of the full scale trials, as good agreement was observed at gauge locations where the initial blast wave was not reflected from the ground.

## References

- [1] "TM5-1300: Structures to Resist the Effects of Accidental Explosions, Volume II. Blast, Fragment, and Shock Loads." US Department of the Army Technical Manual, Washington DC. November 1990.
- [2] Mays, G.C.; Smith, P.D.; Rose, T.A. "Leakage Pressures Behind Blast Walls." Proceedings of the 6<sup>th</sup> International Symposium on the Interaction of the Effects of Munitions with Structures. Panama City, Florida, USA. May 1993.
- [3] Rose, T.A.; Smith, P.D.; Mays, G.C. "Design Charts Derived from Blast Wall Leakage Pressure Measurements" Proceedings of the 7<sup>th</sup> International Symposium on the Interaction of the Effects of Munitions with Structures. Mannheim, Germany. April 1995.
- [4] Jones, P.S; Vitaya-Udom, K.P.; Watt, J.M., Jr. "Design of Structures to Resist Terrorist Attack, Report 1, 1/10<sup>th</sup> Scale Model Perimeter Wall Tests", Technical Report SL-87-13. Structures Laboratory, Waterways Experimental Station, U.S. Army Corps of Engineers, Vicksburg, Mississippi, October 1987.

# ANOMALIES IN PRESSURE-TIME RECORDINGS CAUSED BY WATER DROPS ON A PENCIL BLAST PRESSURE PROBE

Andrew Medin, Håkan Axelsson and Börje Selin  
National Defence Research Establishment (FOA)  
Department of Weapons and Protection  
P.O.Box 551, S-14725 TUMBA  
Sweden

## Abstract

In a rainy environment water drops on a blast pressure probe can cause anomalies in the recorded pressure-time history. Limited experiments have been performed with a pencil shaped blast pressure probe outside a small shock tube at 43 kPa side-on overpressure level. The water drops (10, 29, 49 and 79  $\mu\text{l}$ ) were applied close to or on the pressure sensitive diaphragm of the transducer.

One extreme was with the largest drop centred on the diaphragm where the recorded peak overpressure was decreased to 36.6 kPa (-1.4 dB) and the rise time was increased from 12  $\mu\text{s}$  to 31  $\mu\text{s}$ . The other extreme was with that drop in a downstream position and covering a part of the diaphragm where the peak overpressure was increased to 62.6 kPa (+3.3 dB) with a 8  $\mu\text{s}$  rise time.

It is recommended not to make pressure measurements when it is raining because water drops on the pressure transducer can cause anomalies in the pressure-time recordings. One consequence of these anomalies is that a new weapon system can be approved or disapproved.

## 1. Introduction

Blast pressures around firing weapons may be a hazardous risk for the gunner and the loader. In assessing that risk, damage-risk criteria (DRC) are used where the peak overpressure can be a limiting parameter. In one DRC, MILSTD 1474C (1991), the peak overpressure and a characteristic duration (B-dur) in the measured pressure-time history give the maximum number of allowable exposures per day for a given impulse noise limit. One limit is the Z-curve wherein for e.g. 1 ms duration the peak overpressure must not exceed 55 kPa and for 10 ms not 25 kPa. An accurate measurement of the peak overpressure is then required. Besides using the right pressure transducers and recording electronic equipment the transducer must also be aligned to the flow direction of the blast wave and be protected to thermal influences from the afterburning of the propellants.

In a rainy environment water drops on the blast pressure probe can cause anomalies in the recorded pressure-time histories. Limited experiments have been performed with a pencil shaped blast pressure probe outside a small shock tube at 43 kPa overpressure level where water drops were applied close to or on the pressure sensitive diaphragm of the pressure transducer.

## 2. Materials and methods

### 2.1 Shock tube

A small open-ended shock tube, with inner diameter 0.4 m and length 1.54 m was used to generate the blast waves (Jönsson, 1990). Small spherical explosive charges made of a plastic explosive were used to produce the blast waves. The weight of the charges was 2.0 g and together with the electrical blasting caps used the peak overpressure and positive phase duration for the nearly Friedlander type blast wave were 43 kPa and 0.7 ms (Figure 1) at a distance of 0.69 m outside the open end of the indoor operated shock tube. Room temperature was held at 293 K.

### 2.2 Pressure transducer and recording instrumentation

The pencil shaped blast pressure probe, PCB Series 137M30 with serial #1487, is 0.4 m long, has a diameter of 22.4 mm with a conical front end. The pressure sensing element (quartz), with its diaphragm flush with the flat surface of the cylindrical probe, has a diameter of 5.53 mm and is 157 mm from the front tip of the probe. The diaphragm was covered with one layer of black electrical tape and an aluminium foil as a thermal protection. The transducer with its built-in amplifier was connected to a PCB Power Unit 484B, transient recorders KONTRON WW700 and DATALAB DL 2000 and to a computer HP9816S. Other characteristics of the transducer are shown below.

---

#### PCB transducer 137M30 specifications

---

Sensitivity	2.77 mV/kPa
Resonant frequency	>200 kHz
Rise time	4 $\mu$ s
Discharge time	>10 s

---

The probe was placed along the central axis of the shock tube recording the incident or side-on overpressure in the blast wave. The distance from the open end of the shock tube to the probe's diaphragm was 0.69 m.

### 2.3 Water drops

The tap water drops representing a typical rain were applied on the surface of the probe with an automatic pipette (EPPENDORF 4710) operated by the experi-

mentalist's steady hand. The drops attained an almost hemispherical shape with radii according to the table below.

-----  
Dimensions of the  
hemispherical water drops  
-----

Volume ( $\mu$ l)	Radius (mm)
10	1.7
29	2.4
49	2.9
79	3.4

-----  
/Diaphragm radius=2.8 mm/  
-----

In one of the series of experiments the drops were centred on the diaphragm and the volumes were varied. In the other the distance from the diaphragm and the volume were varied (10  $\mu$ l not tested). The distances measured are from the centre of the drop to the centre of the diaphragm. They were 3, 6 and 9 mm both upstream and down-stream to the diaphragm where upstream is defined as from where the pressure wave is approaching.

### 3. Results

#### 3.1 No drop

During the series 8 experiments were made without any drop. The recorded pressure-time history on the probe (Figure 1) is characterized by a 12  $\mu$ s rise time (0-100%) to a peak overpressure of 43.0 kPa with  $\sigma = 0.7$  (Table 1) followed by a smooth exponential decay to atmospheric pressure. The duration of the overpressure phase is close to 0.7 ms with an impulse of 9.4 kPa\*ms. The overpressure phase is followed by some small shocks and underpressures until approximately 1.5 ms when a second strong shock wave arrives with an overpressure of 20.7 kPa. Times greater than 1.6 ms have not been recorded.

Three experiments were also made without the thermal protective cover on the probe. These were in very good agreement with the covered ones. The peak overpressure was 42.9 kPa (Table 1) and the impulse 9.5 kPa\*ms. The rise time was still 12  $\mu$ s.

#### 3.2 Drops centred on the diaphragm

The drop volumes used were 10, 29, 49 and 79  $\mu$ l and the recorded peak overpressures (Table 2) show a decrease for an increasing drop volume. These data are presented in Figure 2 (top diagram) together with "no drop" data from Table 1. For 10  $\mu$ l the peak overpressure is down to 39.9 kPa then slowly decreasing to

Table 1: Peak overpressures with and without thermal protection (one layer electrical tape and an aluminium foil) on the probe's pressure sensitive diaphragm without a water drop.

Thermal Protection	Yes			No
Overpressure (kPa)	43.6	42.9	43.2	43.4
	43.7	43.7	41.6	42.3
	42.5	42.9		43.1
Mean Value	43.0			42.9

Table 2: Peak overpressures for 10, 29, 49, and 79  $\mu\text{l}$  water drops centred on the probe's pressure sensitive diaphragm.

Centred Position	Drop Volume ( $\mu\text{l}$ )					
	10	29		49	79	
Overpressure (kPa)	41.5	37.3	38.3	38.0	36.8	35.9
	39.1	38.9	37.6	37.6	38.0	
	39.1	38.8		37.2	35.5	
Mean Value	39.9	38.2		37.6	36.6	



36.6 kPa for 79  $\mu$ l. The rise time (0-100%) is increasing for increasing drop volume, from 12  $\mu$ s for no drop to a maximum of 31  $\mu$ s for the 79  $\mu$ l drop with the mean values given in the table below and with one experiment exemplified in Figure 3.

Rise time (0-100%) to peak recorded overpressure	
Drop volume ( $\mu$ l)	Rise time ( $\mu$ s)
0	12
10	19
29	27
49	21
79	31

The drops not only effect the first shock front but also the following shocks for example the one at 1.5 ms. Instead of being rounded off there is a sharp rise in pressure followed by pressure oscillations. This is most pronounced for 29 and 49  $\mu$ l drops where the peaks reach levels as high as the first peak overpressure. One example is shown for the 29  $\mu$ l drop in Figure 4 where both peaks are almost the same, 37.6 kPa. The frequency of that oscillation is around 400 kHz. Similar responses are for 10 and 79  $\mu$ l drops but to a more lower magnitude.

### 3.3 Drops along the probe

For each drop size (29, 49 and 79  $\mu$ l) and position on the probe at least three experiments were made in a random manner. With the drop in the upstream position the recorded pressure-time history is very similar to the one without any drop on the diaphragm except for a short duration overshoot pulse in the beginning of the pressure-time history exemplified for the 49  $\mu$ l drop in Figure 5 & 6. This is followed by a small increase in pressure, 1-3 kPa during the first 100-200  $\mu$ s. The peak overpressures are in Table 3 and exceed the "no drop" case with at most 6 kPa. The pulse duration for all three drop volumes is in the order of 10  $\mu$ s at 3 and 6 mm distance and 5  $\mu$ s for 9 mm. The rise times are 10-11  $\mu$ s, slightly shorter than without a drop.

In the downstream position a shock wave is reflected back on the drop. At 3 mm distance, where the drop covers a part of the diaphragm, there is an 8  $\mu$ s rise time up to a peak overpressure of e.g. 62.6 kPa for the 79  $\mu$ l drop (Table 3). That pressure rapidly drops off and after 16, 26 and 21  $\mu$ s for the three drop sizes (Figure 7 & 8) the pressure is back almost to the "no drop" situation. At 6 and 9 mm distance the reflected shock wave arrives after 5-25  $\mu$ s as a 25  $\mu$ s long pressure pulse and at a reduced amplitude. That amplitude can exceed the incident overpressure and thus be the peak overpressure. This is exemplified in Figure 9 & 10 for the 49  $\mu$ l drop and in Figure 2 (bottom diagram) are the peak overpressures for all drops sizes and positions with the centred drops included.

Table 3: Peak overpressures for 29, 49 and 79  $\mu\text{l}$  water drops at 0, 3, 6 and 9 mm up- and downstream positions along the blast pressure probe.

Drop Volume 29  $\mu\text{l}$

Position (mm)	Upstream			Centred	Downstream		
	-9	-6	-3	0	3	6	9
Overpressure (kPa)	43.9	46.0	48.0	37.3	59.3	44.4	43.4
	44.1	45.1	47.8	38.9	56.2	45.9	42.5
	43.6	46.3	47.3	38.8	57.4	45.1	42.4
				38.3			
				37.6			
Mean Value	43.9	45.8	47.7	38.2	57.6	45.1	42.8

Drop Volume 49  $\mu\text{l}$

Position (mm)	Upstream			Centred	Downstream		
	-9	-6	-3	0	3	6	9
Overpressure (kPa)	44.9	50.4	49.6	38.0	63.5	47.2	42.5
	44.7	47.5	48.2	37.6	62.2	47.9	42.5
	44.9	49.4	49.2	37.2	57.7	46.7	43.7
Mean Value	44.8	49.1	49.0	37.6	61.1	47.3	42.9

Drop Volume 79  $\mu\text{l}$

Position (mm)	Upstream			Centred	Downstream		
	-9	-6	-3	0	3	6	9
Overpressure (kPa)	44.7	47.6	45.3	36.8	60.2	52.9	43.4
	45.3	47.1	48.3	38.0	63.7	52.6	43.3
	46.8	48.1	47.1	35.5	63.9	51.2	43.7
				35.9			
Mean Value	45.6	47.6	46.9	36.6	62.6	52.2	43.5

#### 4. Discussion

Our experimental method is well suited for the purpose of studying these anomalies. The shock tube is easy to handle and lot of experiments can be made during a day. The application of the thermal protection, electrical tape and aluminium foil, doesn't change the transducer's sensitivity and will not cause any anomalies in the pressure recording. The application of the drops on the probe with the experimenter's free hand can explain some of the differences in the results for the same drop volume and position. This is especially true for the 3 mm position where the drops cover part of the diaphragm.

The experiments have clearly shown the effects of water drops on the recorded overpressure for an incident overpressure of 43 kPa. The peak overpressure varies both with drop volume (10-79  $\mu\text{l}$ ) and up- and downstream position (0-9 mm) along the pencil shaped blast pressure probe. With the drop centred on the pressure sensitive diaphragm the rise time is increased and the peak overpressure is decreased to as much as 36.6 kPa corresponding to -1.4 dB compared to the no drop case. For an upstream situation the shock diffraction process around the drop results in a peak pressure increase of +1.4 dB at most. Downstream the influence of the drop is very accentuated, due to the reflection of the shock on the drop, resulting in a recorded peak overpressure as high as 62.6 kPa (+3.3 dB) with the 79  $\mu\text{l}$  drop at 3 mm where the drop covers almost half of the diaphragm. The difference between the lowest and highest recorded peak overpressures is then 4.7 dB taken for the mean values. The drops also have an influence on the shocks at later times e.g. at 1.5 ms which is illustrated in Figure 4 where the peak overpressure is almost doubled reaching levels higher than the front peak overpressure.

Our investigation is made only for an incident overpressure of 43 kPa and the PCB 137M30 blast pressure probe but similar anomalies in the recorded pressures are expected even for other incident overpressures and probes. To what extent has to be investigated in other series of experiments.

#### 5. Conclusion

Measuring the blast overpressures in a rainy environment causes anomalies in the recorded pressure-time history due to rain drops on or near the pressure sensitive diaphragm of the pencil blast pressure probe. Depending on the drop's position the recorded peak overpressure can be higher or lower than in the incident blast wave. For the incident overpressure in this series of experiments, 43 kPa, the difference was 4.7 dB between the lowest and highest recorded peak overpressure where the highest overpressure was 3.3 dB over the incident overpressure.

One example of serious consequences of these anomalies is when assessing the hazardous risk for the gunner or loader firing e.g. a new weapon system where recorded anomalies both in pressure and duration can approve or disapprove the system.

It is expected that these anomalies also exist for other pressure levels and pressure probes and it is strongly recommended to avoid water drops on blast pressure probes during blast overpressure tests.

## **6. References**

- |                         |   |
|-------------------------|---|
| Jönsson, Arne<br>(1990) | Pressure Measurements in the External Auditory Canal of a Human Head Model Exposed to Air Shock Waves. Journal of Trauma (China), 6(2) Supplement: 235 - 242; 1990. |
| MIL-STD-1474C<br>(1991) | Military Standard. Noise Limits for Military Materiel (Metric). MIL-STD-1474C, 8 March 1991, Department of Defense.   |

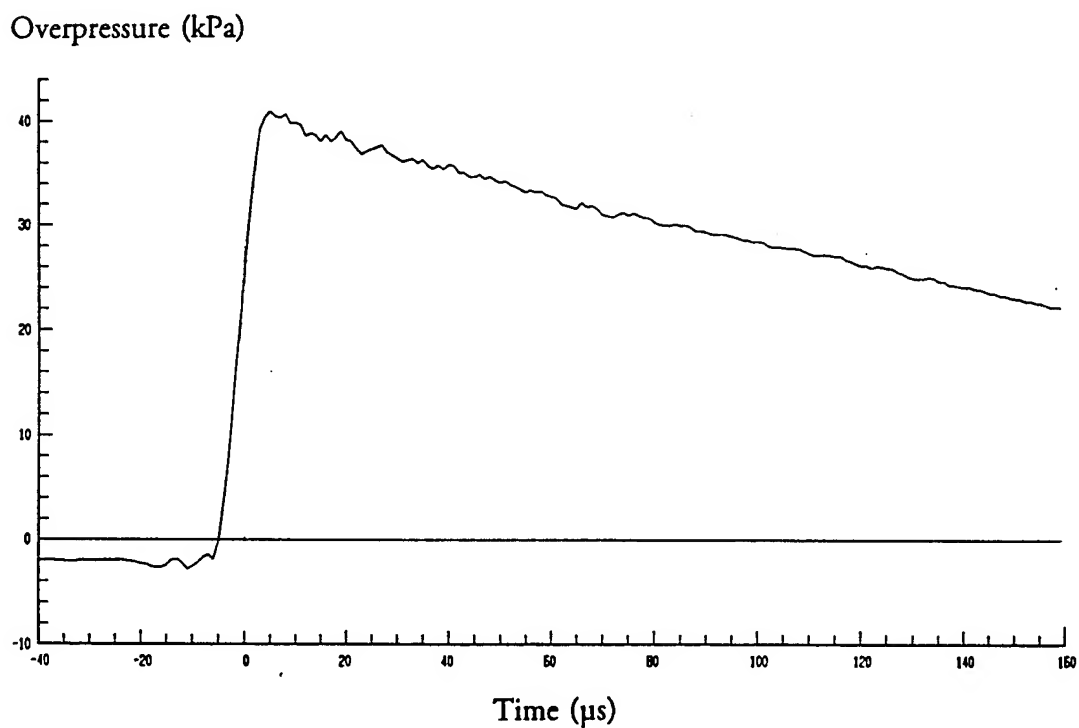
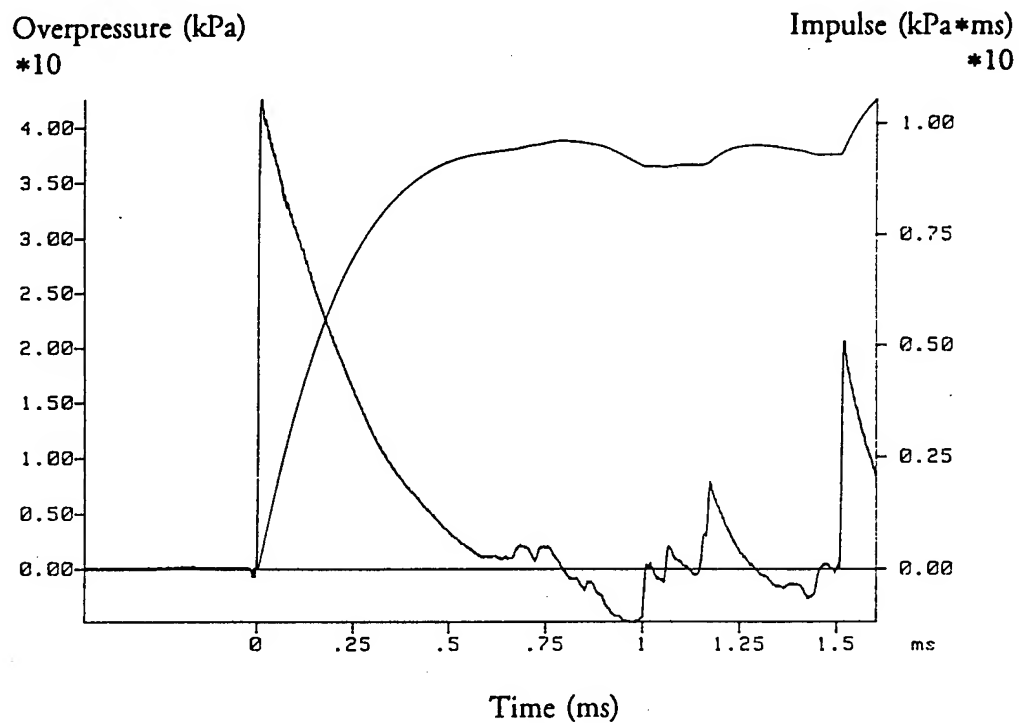


Figure 1: Recorded pressure-time history without a drop on the probe for the first 1.6 ms (top) and the first 160  $\mu$ s (bottom).

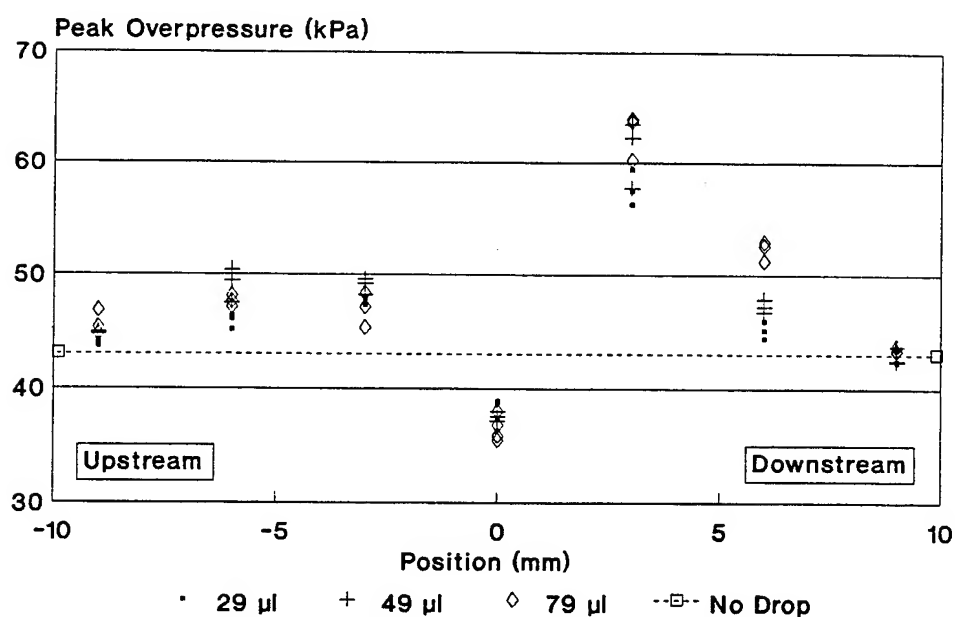
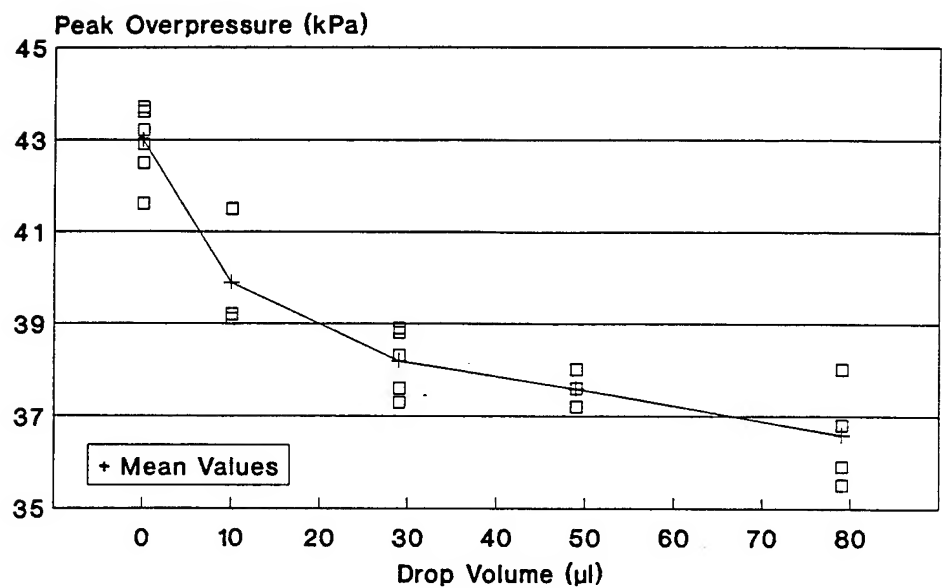


Figure 2: Recorded peak overpressure without a drop and for 10, 29, 49 and 79  $\mu\text{l}$  drops centred on the probe's pressure sensitive diaphragm (top) and for 29, 49 and 79  $\mu\text{l}$  drops at 0, 3, 6 and 9 mm upstream and downstream positions along the probe (bottom).

Overpressure (kPa)

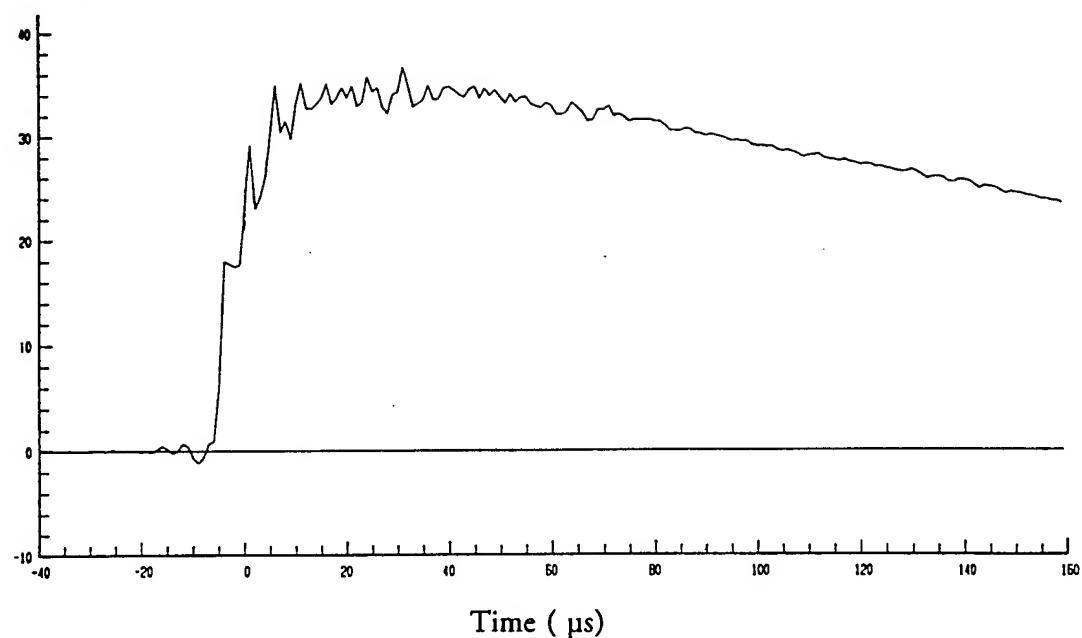


Figure 3: Pressure-time history with a 79  $\mu\text{l}$  drop centred on the diaphragm. Notice the long rise time (37  $\mu\text{s}$ ) to the peak overpressure.

Overpressure (kPa)  
\*10

Impulse (kPa\*ms)  
\*10

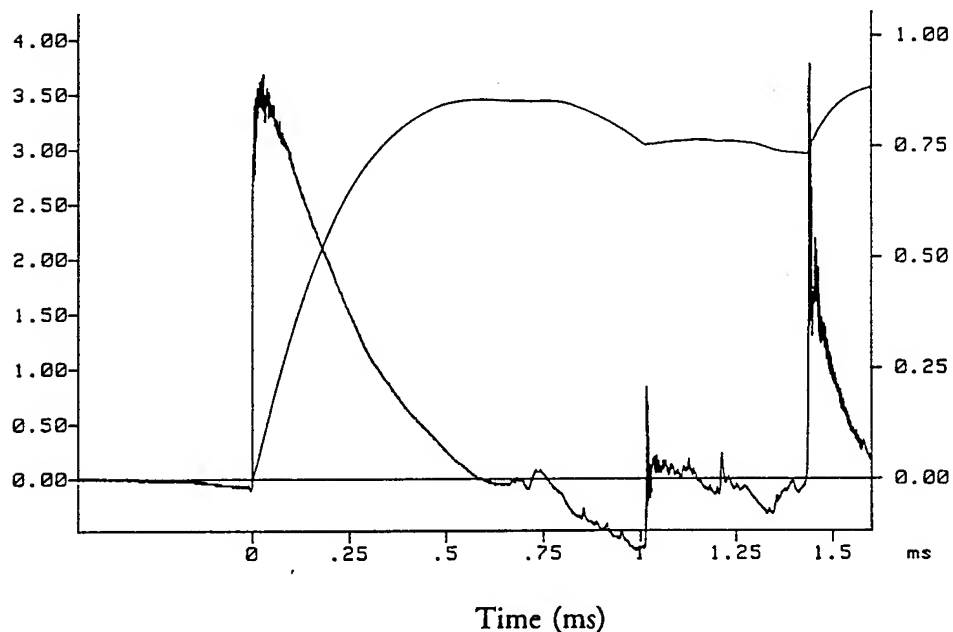
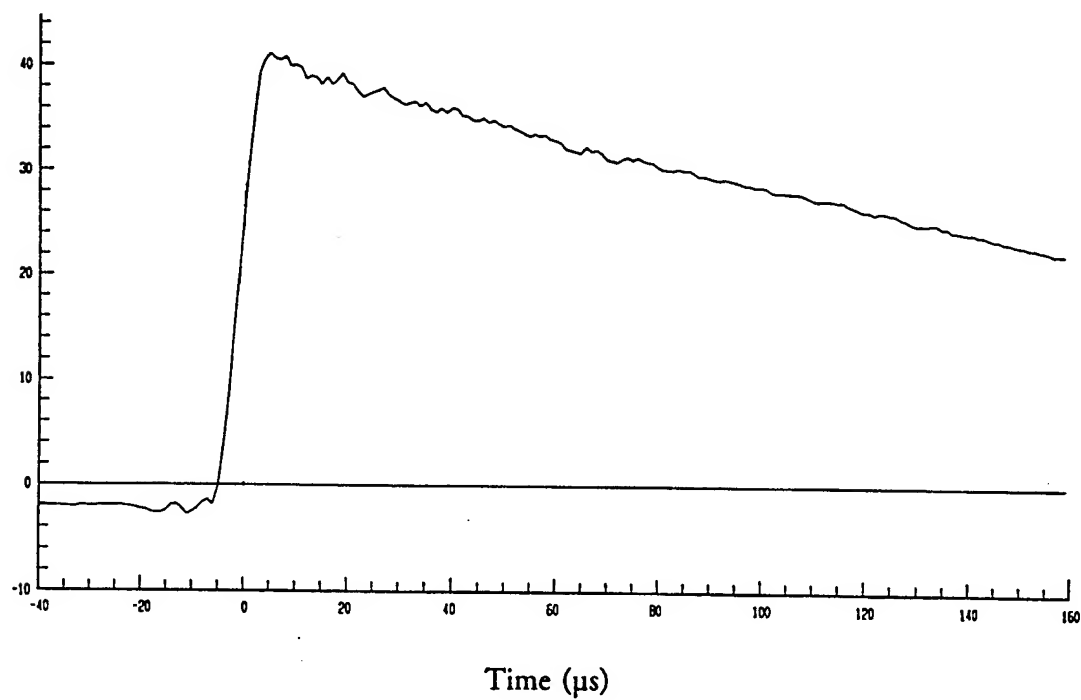


Figure 4: Pressure-time history with a 29  $\mu\text{l}$  drop centred on the diaphragm. Notice the effect on the first shock front but also on the other shocks and especially the one at 1.4 ms.

Overpressure (kPa)



Overpressure (kPa)

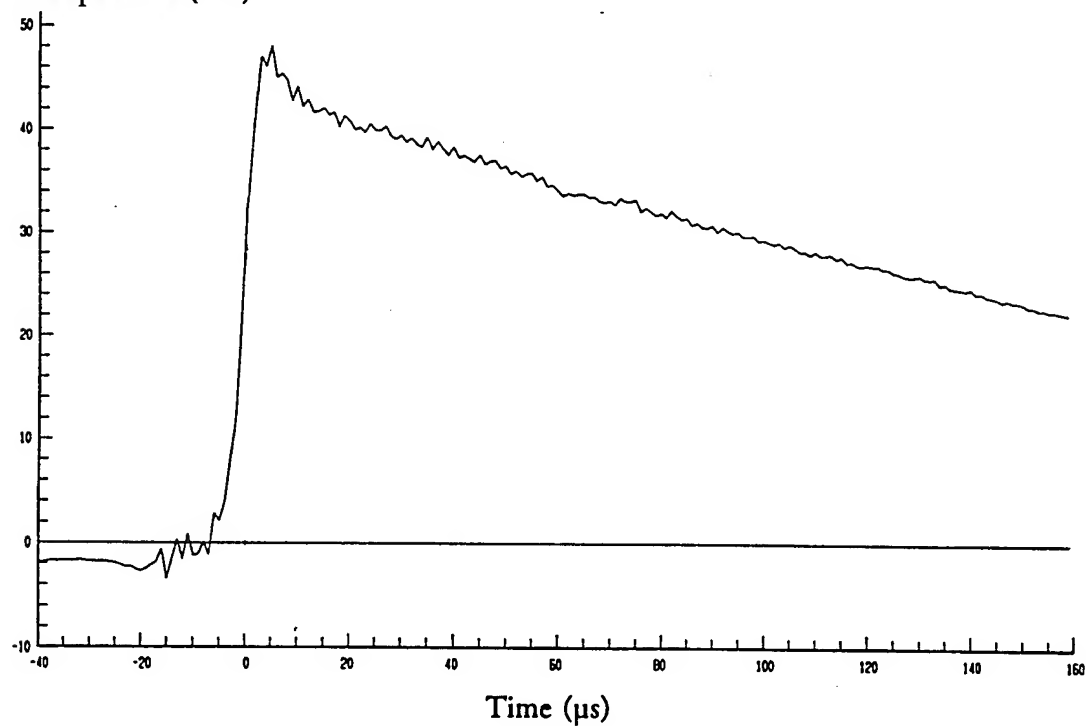


Figure 5: Pressure-time history without a drop (top) and with a 49  $\mu$ l drop positioned 3mm upstream (bottom).



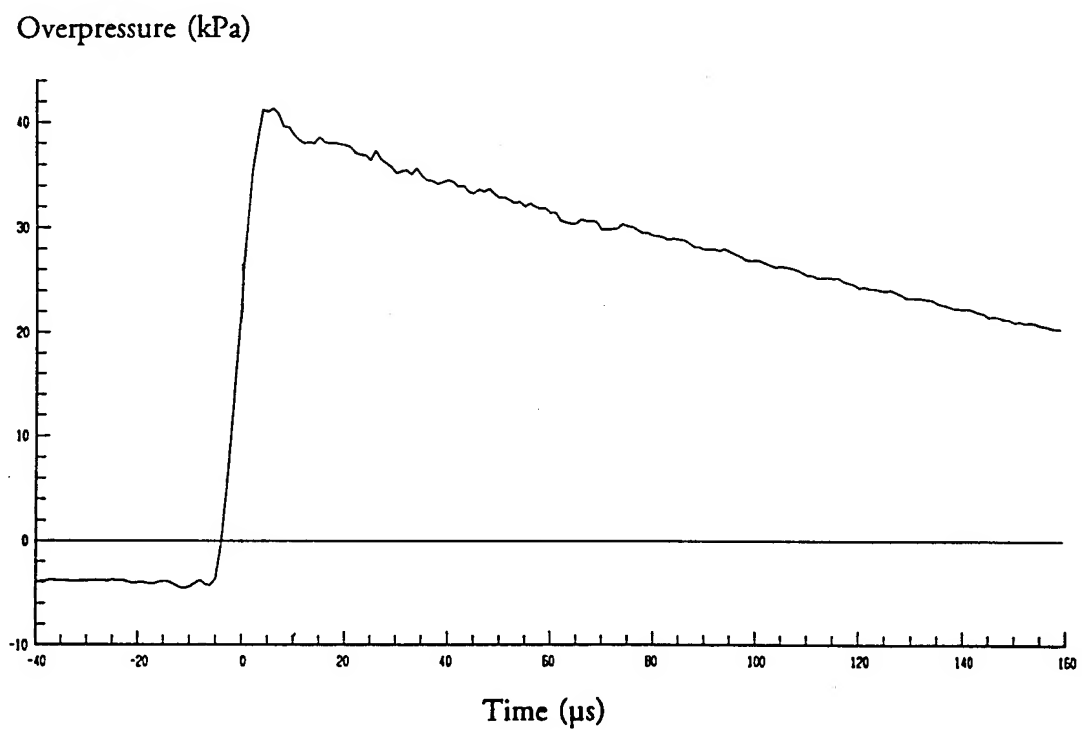
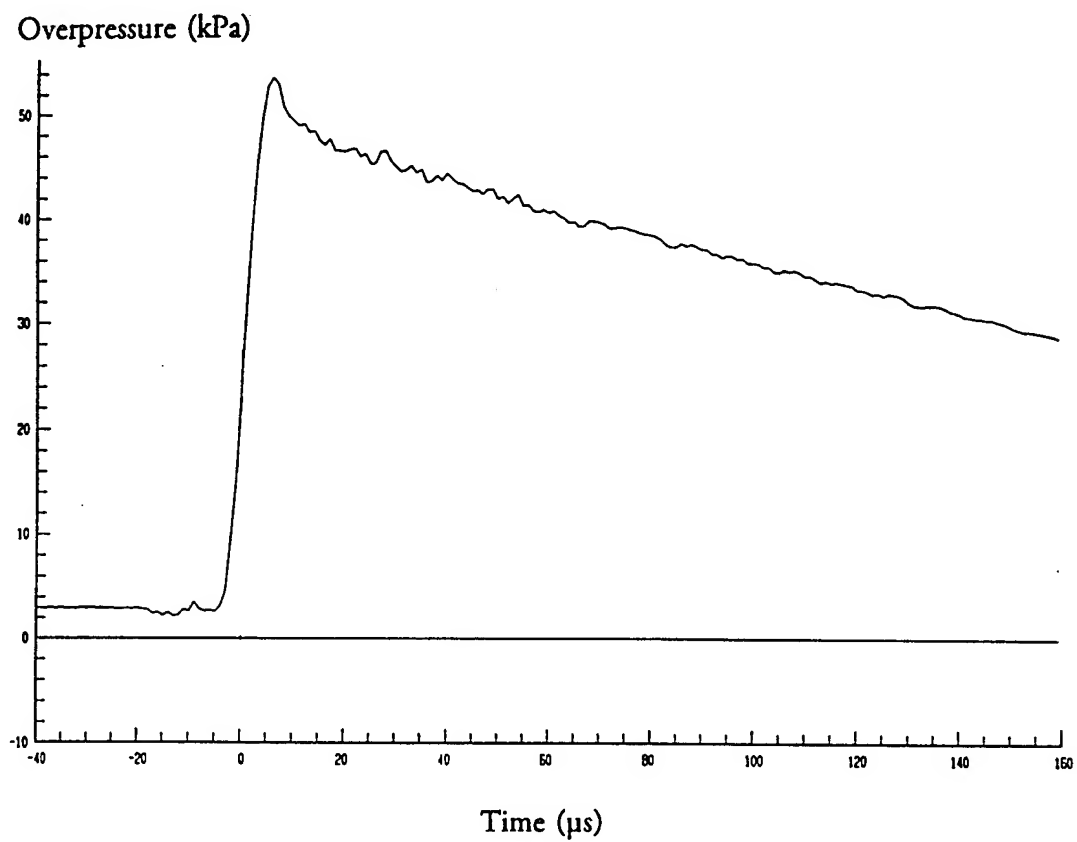
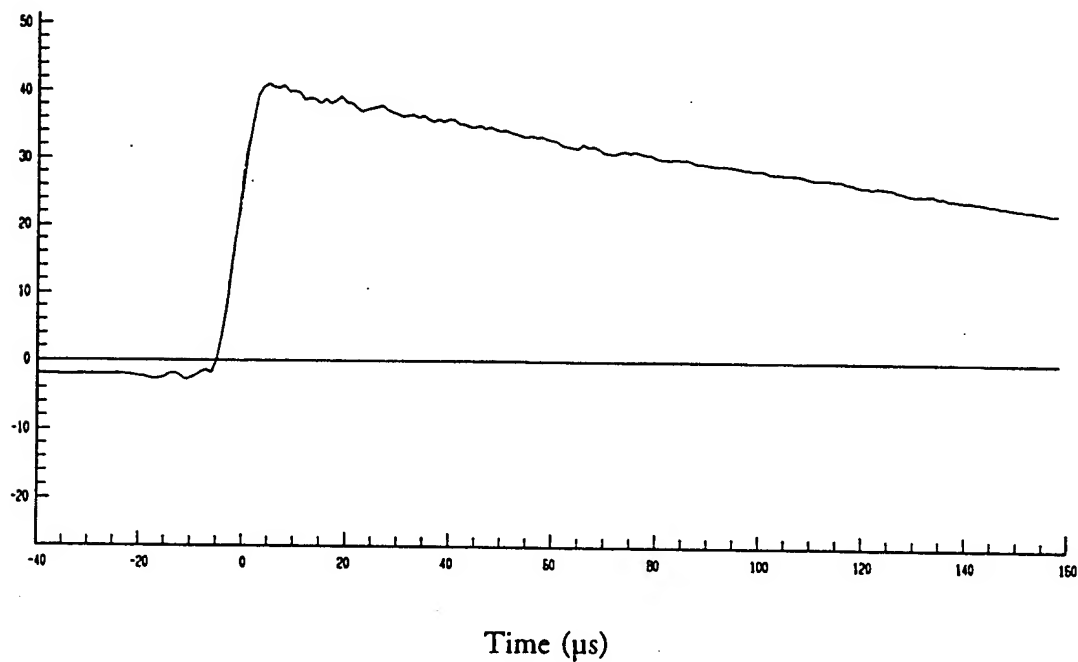


Figure 6: Pressure-time history with a 49  $\mu\text{l}$  drop positioned 6 mm upstream (top) and 9 mm upstream (bottom).

Overpressure (kPa)



Overpressure (kPa)

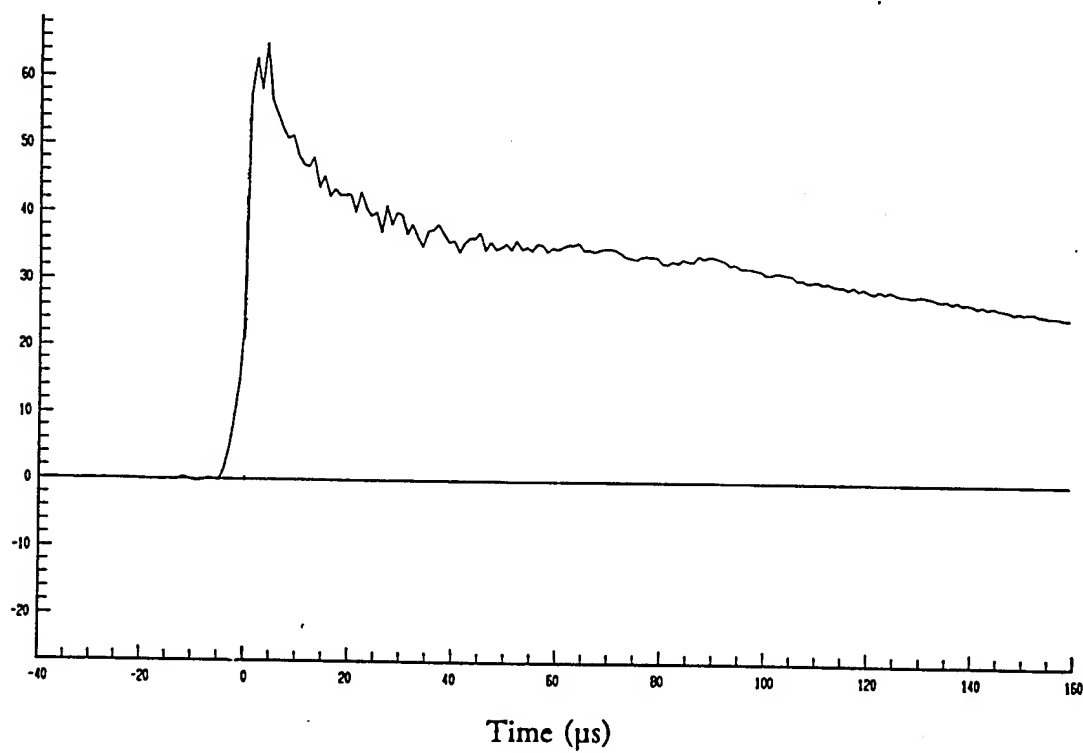
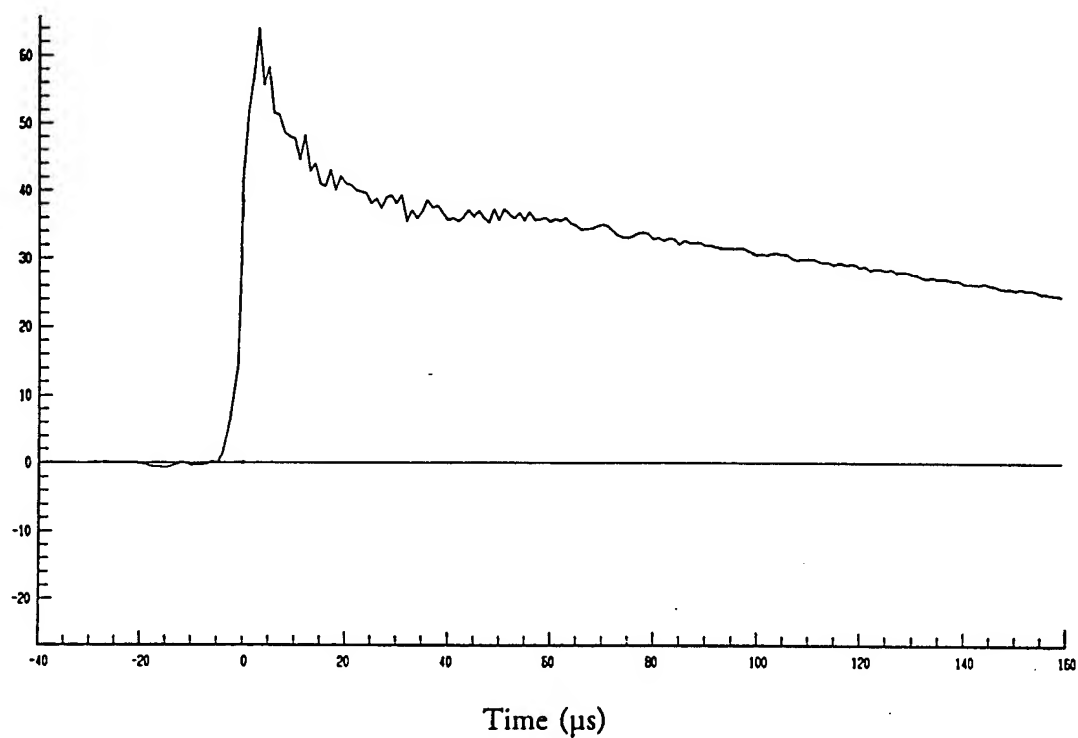


Figure 7: Pressure-time history without a drop (top) and with a 29  $\mu$ l drop positioned 3 mm downstream (bottom).

Overpressure (kPa)



Overpressure (kPa)

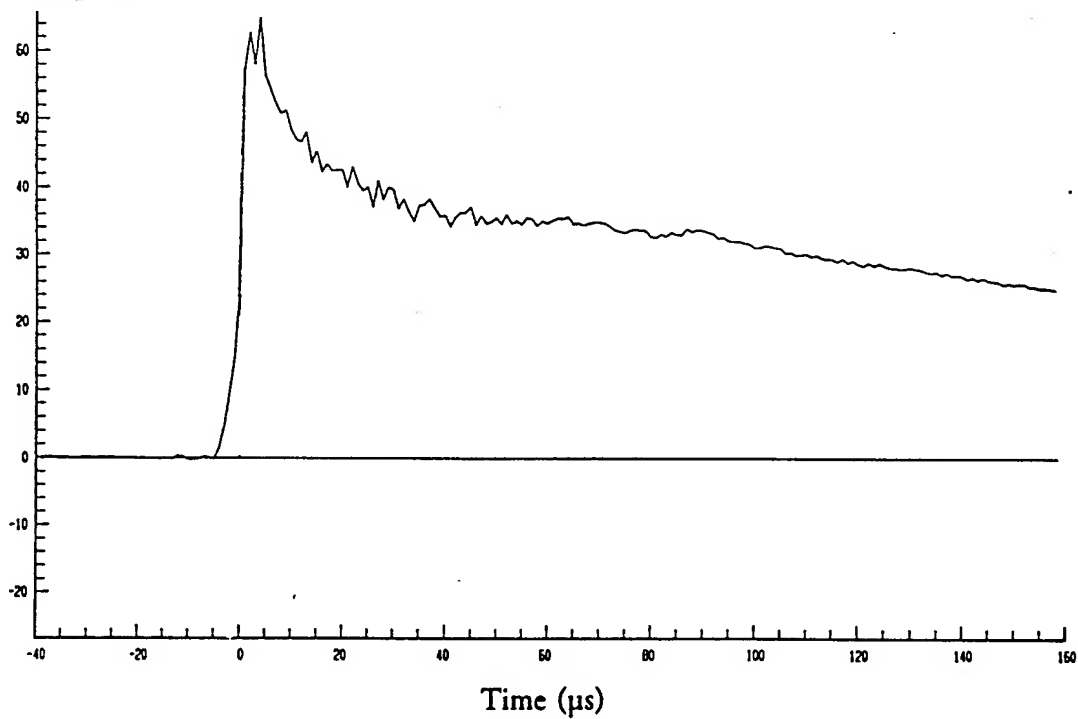


Figure 8: Pressure-time history with a 49  $\mu\text{l}$  drop (top) and a 79  $\mu\text{l}$  drop (bottom) positioned 3 mm downstream.

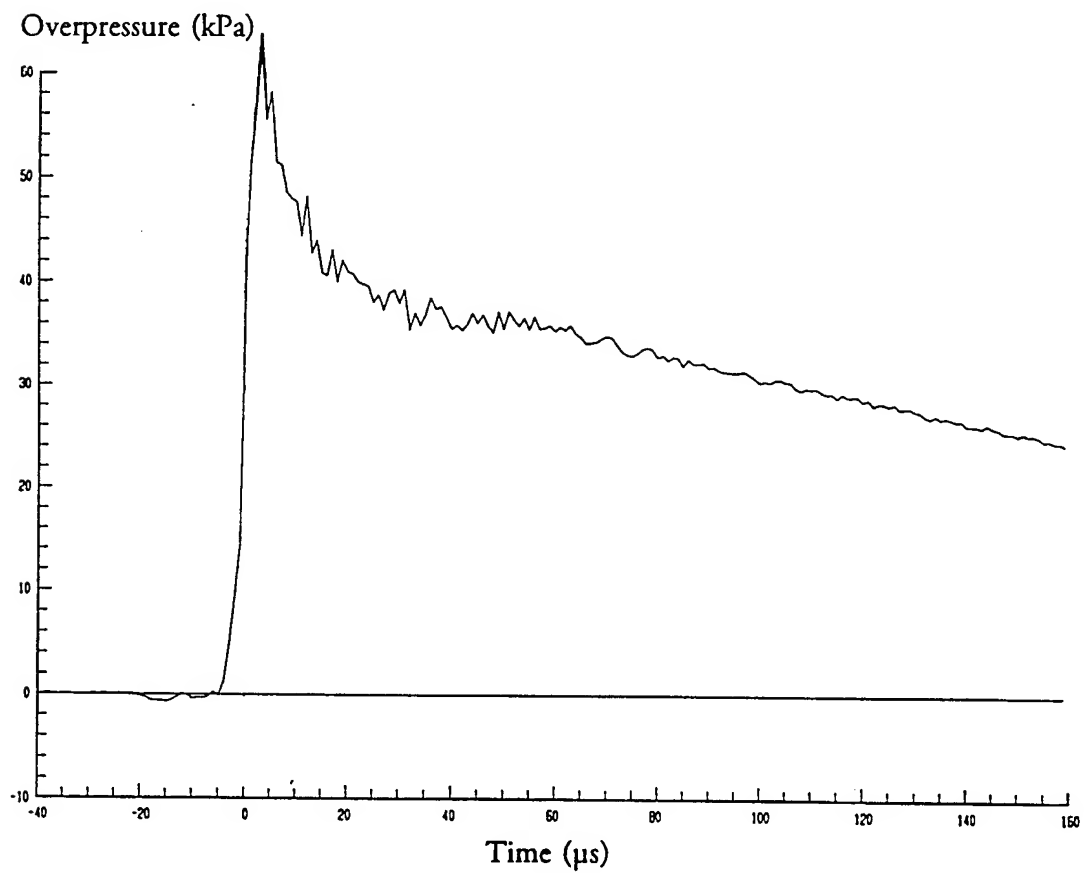
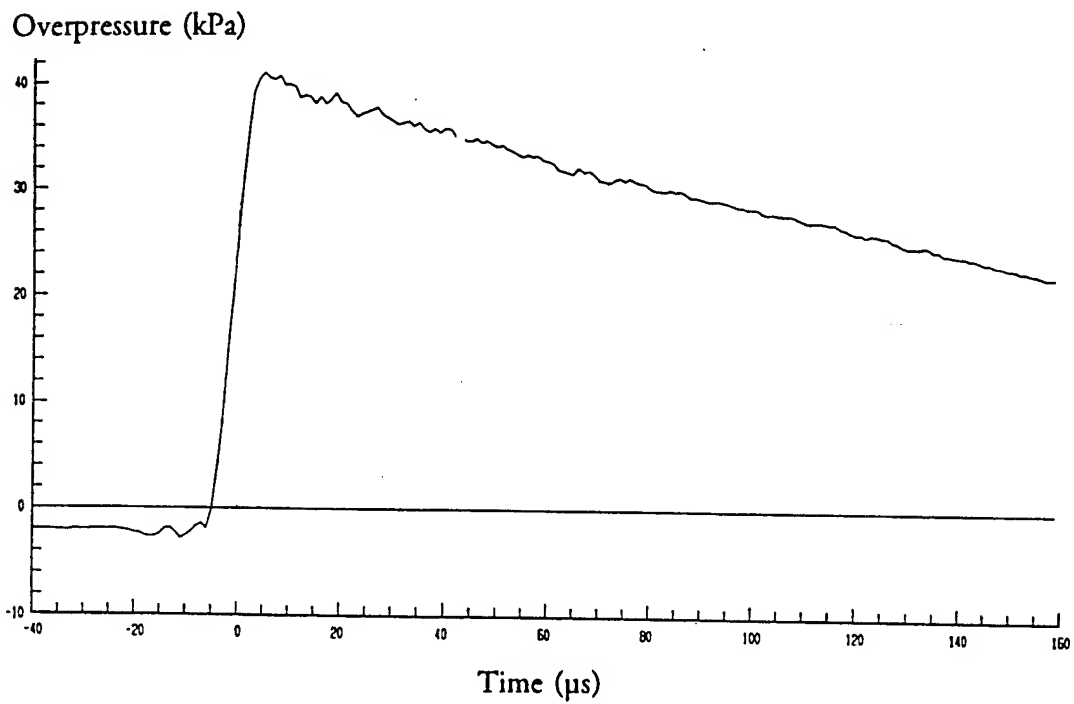


Figure 9: Pressure-time history without a drop (top) and with a 49  $\mu\text{l}$  drop positioned 3 mm downstream (bottom).

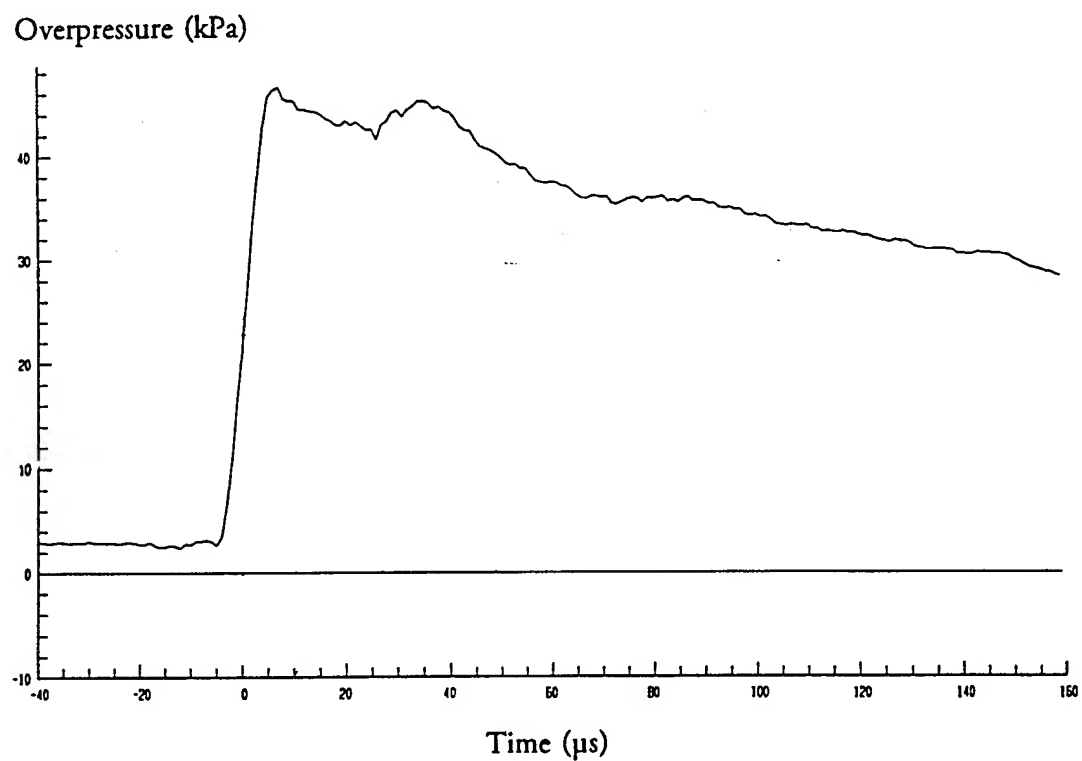
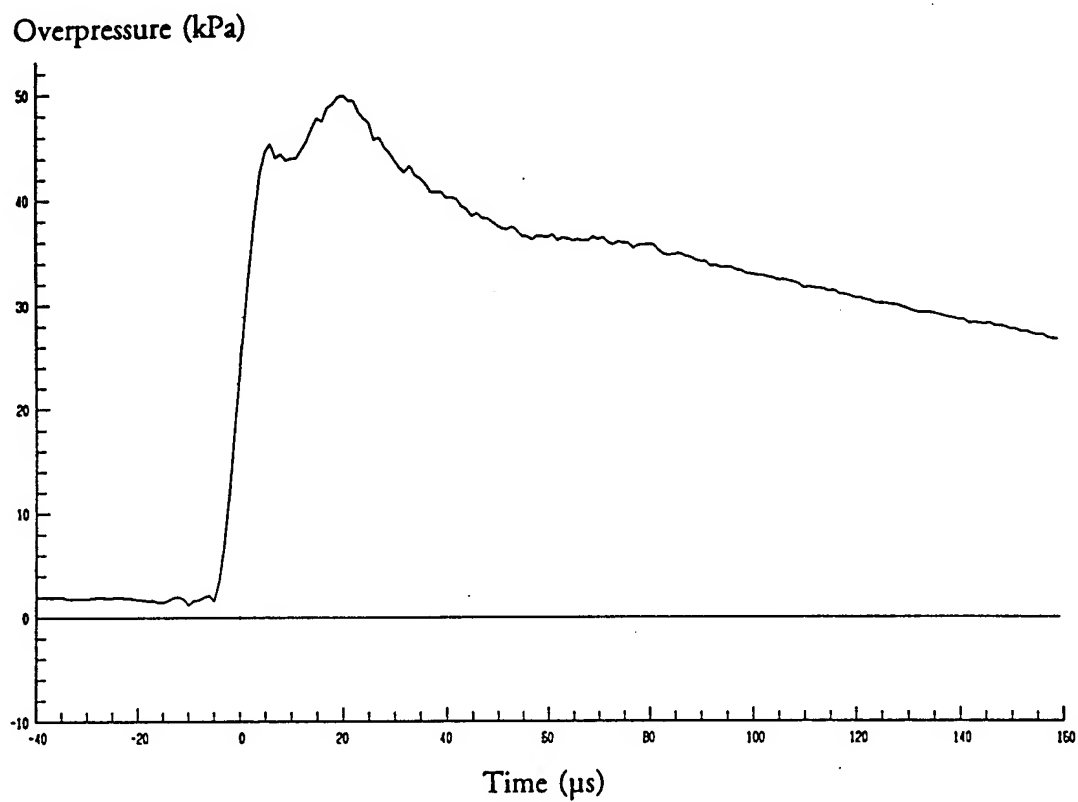


Figure 10: Pressure-time history for a 49  $\mu\text{l}$  drop positioned 6 mm downstream (top) and 9 mm downstream (bottom).

# Development of a Transducer for the Measurement of Temperature of Airblast Flow Fields

Peter C. Muller  
Stephen J. Schraml  
Audrey F. Mihalcin  
Army Research Laboratory

## Abstract

The development of a transducer which can measure the temperature behind a shock wave gives the airblast community an avenue for the determination of such flow parameters as density and particle velocity. This paper covers a study to develop such a transducer using a combination of experimental and computational approaches. The application of temperature measurement to the determination of density and particle velocity as well as contact surface tracking is also covered.

## 1. Introduction

The measurement of the static temperature conditions behind a shockwave, in combination with other measurements, makes the determination of several other parameters possible. In combination with static pressure, the static temperature allows the determination of density. Once the density is known, the use of dynamic pressure makes it possible to calculate particle velocity. Temperature measurements can also be used in shock tube studies to accurately locate the contact surface discontinuity between the driver gas and the expansion tube gas, or in the case of a heated driver, show the quality of the contact surface discontinuity matching.

This paper covers a study to develop the ability to measure directly or indirectly the static temperature behind a shockwave. The device used to measure the temperature is a very fine wire thermocouple of  $25.4\text{ }\mu\text{m}$  (0.001") in diameter. Various probe designs were tested both experimentally in the ARL 0.61 m shock tube and computationally in an attempt to find a survivable design with an adequate response rate from the sensor. The final design measures the temperature in the 0.61 m shock tube with a rise to peak temperature in about 20 ms. This response rate is adequate for use in the large shock tubes used to simulate nuclear blast effects, but additional work was done to improve the response mathematically. Finally, the temperature was successfully used to calculate a value for density and particle velocity which closely matched computational predictions.

## 2. Probe designs

### 2.1. Experimental Procedure

The transducer chosen in this study is a type K thermocouple made from 25.4  $\mu\text{m}$  diameter wire. The manufacturer's specifications for this thermocouple state that the time constant in moving air is about 4 ms. This sensor was placed in various probe configurations in a effort to find a design that is survivable and yet maintains the quick response of the thermocouple.

The probe designs were tested in the ARL 0.61 m shock tube. The reason for using this tube was that it generates a square shock pulse of about 50 ms duration. The conditions in the pulse are easy to calculate using first principles so comparisons can be made to the experimental data. Also, the long duration of the flat top makes the determination of the true response of the sensor possible. Figure 1 is a representative static pressure time history from the shock tube. All of the other flow parameters have a similar time history.

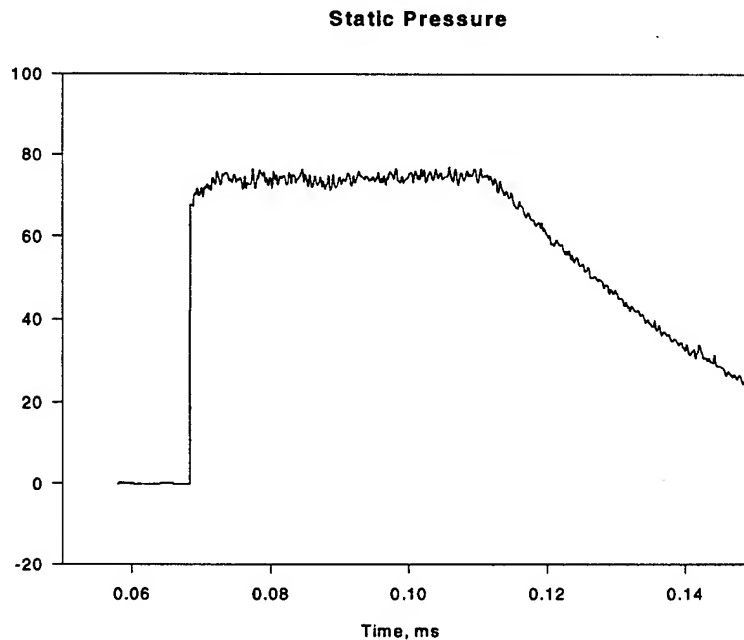
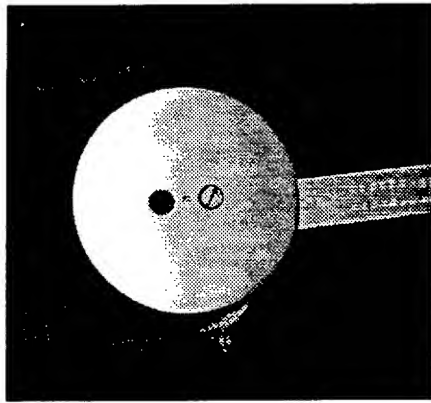


Figure 1. Static pressure record from the 0.61 m shock tube.

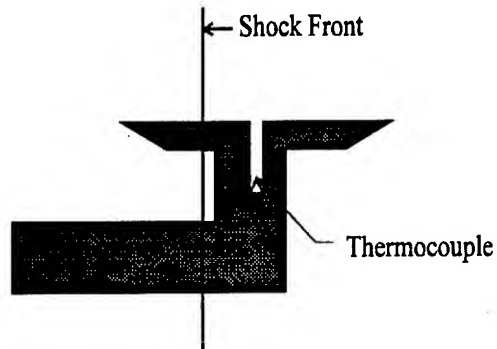
### 2.2. Static Probe

Figure 2a is a picture of the first probe design used to try to measure static temperature conditions. Figure 2b is a cross-section of the probe showing the location of

the thermocouple. The surface of the disk was placed parallel to the flow. This configuration was chosen because it protects the bead from damage by the flow.



(a)



Static Probe Cross-Section

(b)

Figure 2. Static probe design.

After experimental results showed unusual records, a Rockwell USA code run was done to determine the temperature conditions inside of the cavity where the thermocouple was located. Figure 3 is a contour plot generated by the code showing the temperature inside of the cavity is not at static temperature.

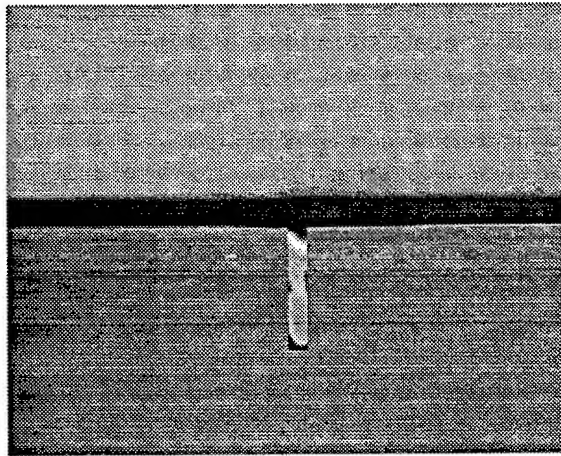


Figure 3. Temperature contours.

### 2.3. Stagnation Probe

Figure 4 is a picture of the second probe design. The thermocouple bead is located in the front cavity. The static probe showed a temperature effect from the heat sink of the probe body. The temperature conditions in a stagnation probe configuration were expected to reach stagnation temperature because of the constant influx of energy



from the flow. If stagnation temperature could be successfully measured, static temperature could be calculated if static and stagnation pressure were also known.

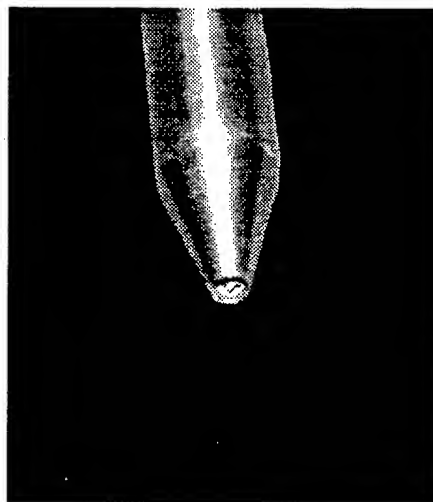


Figure 4. Stagnation temperature probe.

Before the probe was actually built and tested a second Rockwell USA code run was done to verify that stagnation temperature conditions did exist in the cavity. Figure 5 is the temperature contours from this run showing that stagnation temperature conditions were found in the cavity.

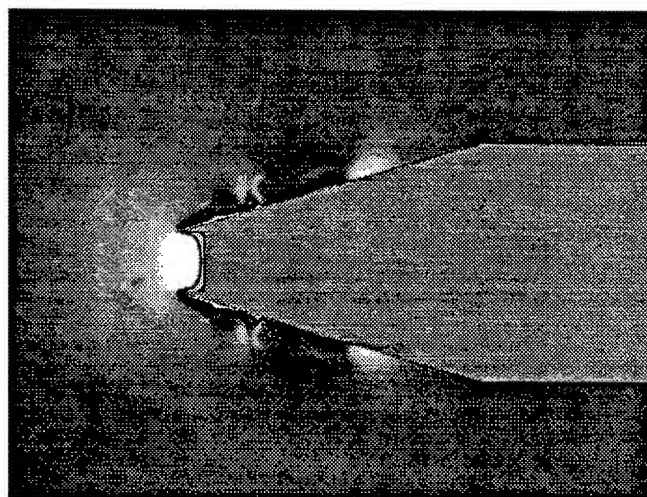


Figure 5. Temperature contours.

Unfortunately, because stagnated flow has no velocity, this reduced the rise time of the temperature record. Figure 6 is a plot of the recorded stagnation temperature showing

a rise time approaching 50 ms. The peak temperature did come very close to the expected stagnation temperature.

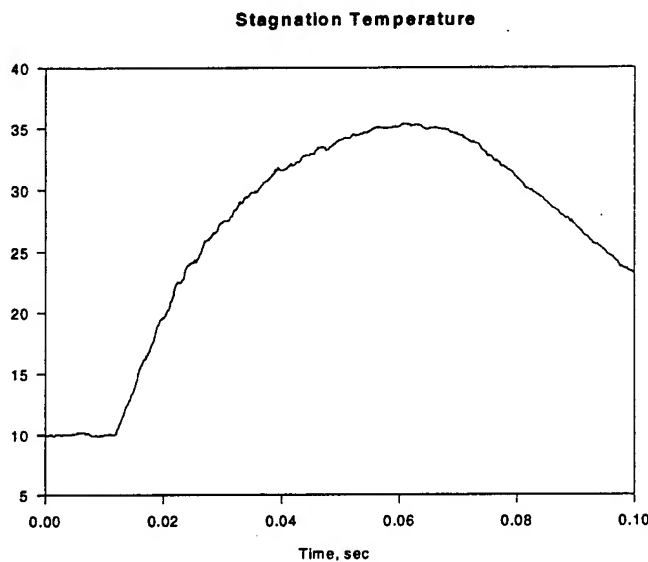


Figure 6. Stagnation temperature record.

#### 2.4. Flow on Bead Probe

To improve the response of the measurement, the decision was made to expose the bead directly to the flow. Figure 7 is a drawing of the new configuration using the static probe mount. The bead was positioned as far out as considered feasible.

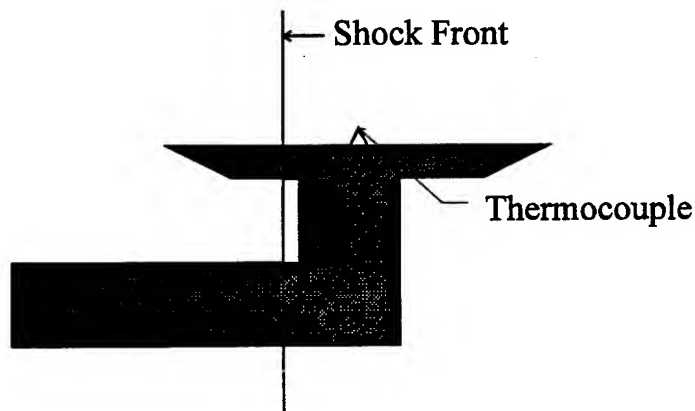


Figure 7. Flow on bead configuration.

Figure 8 is a temperature record compared to a plot of static temperature from a SHARC calculation for the same driver conditions as the experiment. The rise time of the experimental data is much better, but it exceeds the predicted static temperature. This is due to the flow stagnating on the front of the bead and generating stagnation temperature conditions on part of the bead. The bead temperature does not reach stagnation temperature however. There are two possibilities for this: the bead is not exposed to stagnation temperature conditions over the whole surface or the bead may not be fully out in the flow.

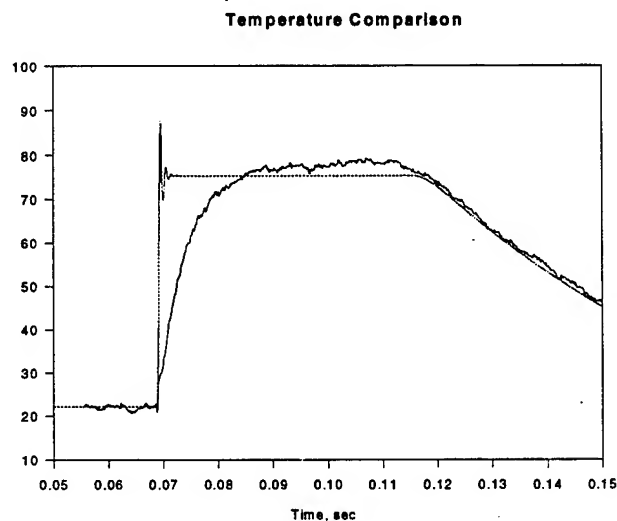
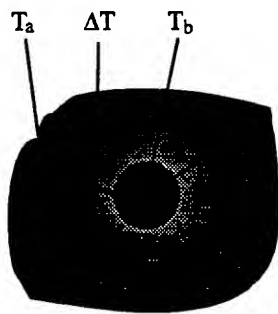


Figure 8. Flow on bead record vs. SHARC.

### 3. Calculations

Because a respectable response rate had been achieved and the error in the temperature measurement was not excessive, the experimenters decided to more completely evaluate this design. To determine the effect of the error in the temperature data, calculations were done to determine density and particle velocity. First, however, a correction needed to be made to either the temperature data or the pressure data to account for the different rise times. The simplest and most conservative approach would be to filter the pressure data to give it the same response at the thermocouple. A more aggressive approach is to correct for the known rise time of the thermocouple. Figure 9 is a representation of a thermocouple bead in air. A lumped heat capacitance is a valid assumption for the bead because of its small size. The derivation shows that the air temperature time history can be determined from the bead temperature record.



$$T_a = \Delta T + T_b$$

$$\Delta T = \frac{q}{hA}$$

$$q = c\rho V \frac{dT_b}{dt}$$

$$T_a = \frac{c\rho V}{hA} \frac{dT_b}{dt} + T_b$$

Where  $T_a$  = Air temperature  
 $T_b$  = Bead temperature  
 $q$  = Heat flux  
 $h$  = Film heat transfer coefficient  
 $A$  = Surface area of the bead  
 $c$  = Heat capacitance of the bead material  
 $\rho$  = Density of the bead material  
 $V$  = Volume of the bead

Figure 9. Temperature correction.

The quantity  $\frac{c\rho V}{hA}$  is equal to the reciprocal of the time constant of the thermocouple (J. P. Holman, 1981). By using a flat-topped shock wave the time constant can be determined and a correction for the temperature can be made. Figure 10 is the corrected temperature. You can see that any noise in the record is magnified by this technique, but that the record does have the correct response.

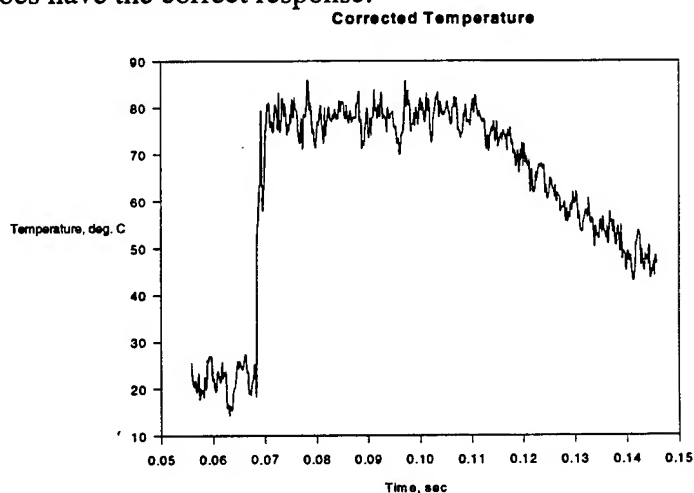


Figure 10. Corrected temperature record.

Figure 11 is a comparison of density calculations to a SHARC prediction showing the effects on the calculation of no correction, filtering the pressure data, and correcting the temperature. In all cases the density is under the prediction because the measured temperature was too high. Density was calculated by the relation  $\rho = \frac{P}{RT}$ .

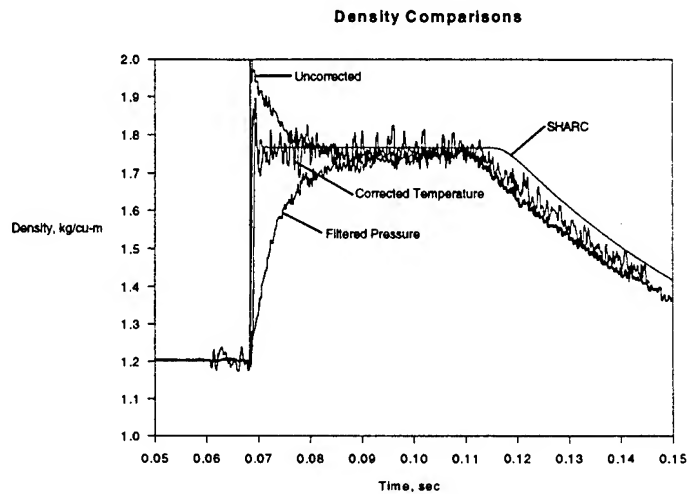


Figure 11. Density calculations.

Finally the density derived using the corrected temperature record was used to calculate particle velocity using the formula  $u = \sqrt{\frac{2P_q}{\rho}}$ . Figure 12 is a plot of this calculation again plotted against a SHARC prediction.

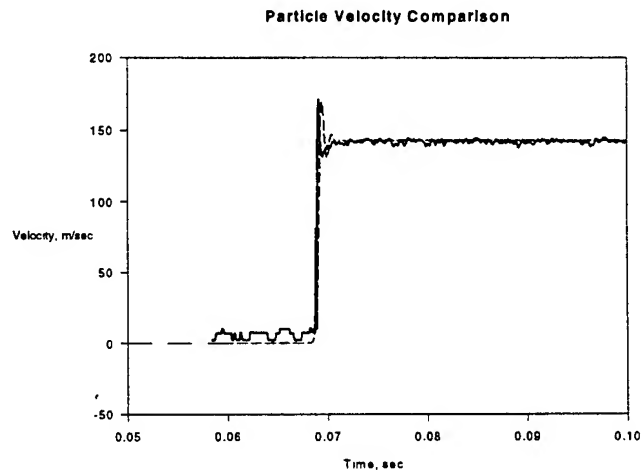


Figure 12. Particle velocity calculations.

Both the noisy baseline, and the accuracy of the experimental calculation indicate that the dominant parameter for calculating particle velocity is dynamic pressure. This leads to the conclusion that with an accurate dynamic pressure measurement the temperature measurement technique presented here can give good particle velocity data.

#### 4. Contact Surface Tracking

Another use for temperature measurement in shock tubes is to track a contact surface discontinuity (the boundary between driver gas and expansion section gas). Figure 13 is various measurable parameters generated by a BRL Q1D calculation for the ARL 2.44 m shock simulator. The dashed line indicates the expected location of the contact surface. By inspecting the plots, one can see that the temperature record is the most sensitive to the contact surface. Static pressure is not affected at all and dynamic pressure shows only a minor variation which would probably be lost in experimental data. Density shows a more pronounced effect but can only be measured by an expensive beta-densitometer or by measuring the temperature.

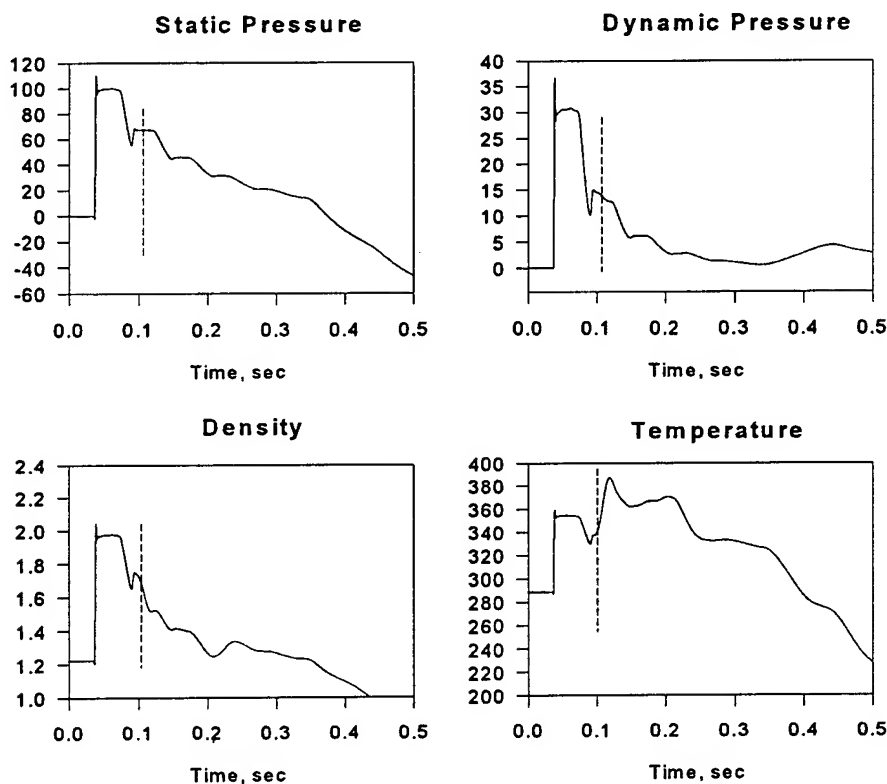


Figure 13. Contact surface effects.

## 5. Conclusions

The temperature measurement technique presented here is a good start towards the development of a measurement set to fully measure all of the flow parameters. In combination with static pressure, density can be calculated with fair accuracy. The density calculation, in combination with an accurate dynamic pressure measurement, gives a value for particle velocity which is surprisingly accurate. Therefore, with the measurement of temperature, static pressure, and stagnation or differential pressure, the flow field can be fully characterized.

## 6. Recommendations

To improve the accuracy and response rate of the temperature measurement, more work needs to be done. The bead should be positioned farther out in the flow, possibly by stretching it across a gap. The use of a smaller bead or a ribbon thermocouple should also be investigated. Protection for the sensor from particle impact is another important consideration.

Finally, once an accurate, faster, and survivable design is perfected, it should be incorporated into a probe which measures temperature, static pressure and either stagnation or differential pressure at essentially the same point.

## 7. References

Holman J. P., 1981, *Heat Transfer*, McGraw Hill, New York, New York

INTERMEDIATE-SCALE UNDERGROUND MAGAZINE TESTS:  
ANALYSIS OF THERMAL INSTRUMENTATION  
AND PREDICTION TECHNIQUES

by

Charles E. Joachim  
U.S. Army Engineer Waterways Experiment Station  
Vicksburg, Mississippi 39180-6199

ABSTRACT

A series of decoupled detonations were conducted to evaluate techniques for the measurement and prediction of thermal effects from simulations of accidental detonations in underground magazines. The 1/3-scale underground magazine tests were instrumented to record thermal effects within the detonation and adjacent chambers, and to indicate mass flow effects within the tunnel system. This paper presents the analyses of the experimental data and a comparison with predictions.

INTRODUCTION

The Joint U.S./Republic of Korea (ROK) R&D Program for New Underground Ammunition Storage Technologies (UAST) is a comprehensive research effort to evaluate design concepts for underground magazines which can significantly reduce the airblast and fragment/debris hazards of an accidental explosion. In conjunction with this program, a series of decoupled detonations were conducted in an intermediate-scale (1/3-scale), multi-chamber, underground facility to measure the airblast and thermal hazards, and evaluate the accuracy of thermal prediction techniques. Four decoupled detonation experiment with chamber loading densities of 1.1, 5.5, 14.6 and 37.3 kg/m<sup>3</sup> were conducted by the U.S. Army Engineer Waterways Experiment Station (WES) to evaluate the accuracy of thermal prediction methods. Measured thermal data are compared to calculations made with the TOPAZ (Transient One-Dimensional Pipe-Flow Analyzer) code as modified by REMTECH (Knox, 1993).

The U.S. portion of the UAST program was funded by the Office, Secretary of Defense and the U.S. Army.

OBJECTIVE

The objectives of the experimental work reported in this paper was to define the thermal environment in the detonation chamber, measure the flow through the test drifts, and to evaluate the accuracy of thermal numerical prediction techniques.

DESCRIPTION OF EXPERIMENT

The thermal experiments involved the detonation of 78, 378, 1037, and 2,569.5 kg net explosive weight (NEW) charges of bare



Composition B explosive, simulating an accidental explosion of ammunition stored inside an underground magazine. The experiments were conducted during the period from 2 to 26 May 1994, in a 1/3-scale storage chamber and tunnel system constructed in the Linchburg Mine near Magdalena, NM. The explosive loading densities for these experiments were 1.1, 5.5, 14.6, and 37.3 kg/m<sup>3</sup> of chamber volume, respectively. The site layout, showing the main mine drift and test Regions A and B, is given in Figure 1. Active measurements included total and radiative heat flux, surface and total temperature, and airblast pressure histories in the test chambers and tunnel drifts.

#### TUNNEL AND CHAMBER

The test chambers and their access tunnels were excavated in competent limestone. The experiments were conducted in Chamber No. 4 (Region A). Nominal dimensions of the test chamber were 8.5 m (length), by 4 m (width) by 2 m (height). Repeated testing with successively larger explosive charges produced some damage to the detonation chamber (ceiling and floor). Thus, the volume of the chamber for Tests 2, 3, 5, and 6 was 68.8, 68.8, 71.2, and 75.8 m<sup>3</sup>, respectively. The ceiling of the test chamber was rock bolted and covered with wire mesh and steel mats after excavation to stabilize the chamber for repeated detonations. The smaller loading densities, destroyed most of the wire mesh and some of the steel mat on the rock surfaces of the chamber, leaving rock bolts as the primary roof support.

The chamber entrance tunnel was 5 m long, 1.35 m wide, and 1.5 m high, with a minimum cross-section of 2.38 m<sup>2</sup>. The average cross-section in the Linchburg Mine drift was 4.3 m<sup>2</sup>. The estimated total volume of the underground space was 1220.37 m<sup>3</sup>.

#### EXPLOSIVE CHARGES

The explosive charges for the thermal evaluation experiments were assembled from 203.2-mm Comp B cubes. The charges consisted of blocks of Comp B explosive stacked on a wooden platform with a 203.2 mm layer of 192.2 kg/m<sup>3</sup> rock wool between the explosive and the plywood. The number of blocks used for successive charges were 5, 24, 66, and 180, respectively. The assembled charges were rectangular parallelepipeds. Charges were centered along the long axis of the chamber, with the center of the charge at the mid-height of the chamber.

A rectangular sheet of C-6 detasheet was attached to the front vertical face (end nearest the chamber entrance) of each charge. Two Nonel initiators with 3.7 m Nonel lines attached were taped to the detasheet at mid-height, each 0.2 m off the vertical center of the stacked charge. Each Nonel initiator was covered with a 50-mm square of C-6, placing the initiator between two layers of detasheet. The opposite ends of the Nonel lines were connected to 4.6 m length of detonator cord and in turn attached to two Nonel lines (dual priming the charge) which

extended from the chamber to a point 10 m outside the portal where the electric bridge wire (EBW) detonators were attached for final arming.

### INSTRUMENTATION

A total of 45 internal airblast gages and 18 thermal transducers were installed for the initial thermal evaluation experiment. The airblast transducers included shock-mounted self-recording gage packages (two transducers) installed in the detonation and adjacent chamber walls, and side-on and probe mounted gages placed in the left test drift (Region A, Figure 2), right test drift (region B) and Lynchburg Mine drift to evaluate shock and gas flow throughout the underground facility.

Thermal transducers were installed adjacent to airblast gages (ten stations) in the chambers and test drifts (Figure 2). Radiative and total heat flux gages were installed in a 177.8-mm diameter by 25.4-mm thick plate, which in turn was bolted to a metal canister attached to rock bolt anchors and grouted into the wall of the chamber or drift. Stainless steel plate (304 stainless), was selected to provide the appropriate thermal conduction environment for analysis of the coaxial surface thermocouple temperature-time history to obtain the incident heat flux and heat-transfer coefficient. Gas total temperature transducers were installed in the detonation chamber, Chamber No. 2, and atop total pressure probes in the test drifts.

### NUMERICAL MODEL

A numerical model was developed for the thermal effects experiments using TOPAZ<sup>1</sup> (Knox, 1993). TOPAZ is a finite differencing computer code for modeling the one-dimensional-transient physics of gas transfer in an arbitrary arrangement of chambers, pipes, valves, and flow branches. REMTECH modified the public domain version of TOPAZ to calculate detonations in confined spaces. Heat transfer models were installed to include conduction and radiation to the flow boundaries and entrance effects on heat transfer and wall friction for short pipes were included.

The layout of the Intermediate-Scale experiments was modeled, for the TOPAZ calculation, 21 chambers, and 24 pipes. Chambers in the computational model included the six simulated munitions storage chambers, the intersections of drifts, and the ends of drifts. Since the accuracy of the results depends fineness of the gridding, the code further subdivides each pipe into smaller units to precision.

---

<sup>1</sup> Transient One-dimensional Pipe Flow Analyzer, developed by the Sandia National Laboratories and adapted for this application by REMTECH, Inc.

The chemical formulation of Comp B were used with the element heats-of-formation as input to the Blake code (Knox 1993) to compute the energy release and maximum temperatures in the detonation process. Using the conservation and thermodynamic equations with these values for the pre-test chamber loading densities (1, 5, 15, and 42 kg/m<sup>3</sup>), the mass and heat generation schedules for each experiment were developed. The time of energy release was 0.1 msec (time to peak value was 0.05 msec) (Knox, 1993).

#### COMPARISON OF RESULTS

Comparisons of measured peak pressure and TOPAZ calculated data at stations along the flow path between the detonation chamber and the mine portal are shown in Figure 3 for loading densities of (a) 1.1 (Test 2), (b) 5.5 (Test 3), (c) 14.6 (Test 5) and (d) 37.3 kg/m<sup>3</sup> (Test 6). As shown, the TOPAZ calculated peak pressures under predict the gas pressures in the detonation chamber for the lower loading densities and over predict pressures near the Lynchburg portal. Knox (1993) suggests that the input parameters in the TOPAZ model which affect venting of the detonation chamber were too restrictive reducing the mass flow rate out of the chamber. In addition, finer gridding of the model and shorter time computational time step were recommended.

A similar comparison of TOPAZ calculated gas temperatures and measured peak temperature data (surface and total) are shown in Figure 4. The mortality of the temperature transducers, especially the total temperature sensors, was high. Thus, there are limited data for comparison. The total temperature data are greater than the TOPAZ predicted values for the lower loading density tests (1.1 and 5.5 kg/m<sup>3</sup>) but give an accurate prediction at 286 m (one data point) for Test 5 (14.6 kg/m<sup>3</sup>).

The effect of loading density on peak (surface) temperature data are shown in Figure 5. Calculated peak data from the TOPAZ model indicate an increase in gas temperature with increased loading density. The limited surface temperature data appears to be relatively constance over this range of loading densities tested (1.1 to 37.3 kg/m<sup>3</sup>).

A measured total temperature-time history is plotted in Figure 6. TOPAZ computed gas pressure data and radiometer inferred gas temperature data (opacity of 0.97 assumed) are shown for comparison. The total temperature sensor was located beside a radiative heat flux gage which recorded the heat transfer rate. If the materials and design of the sensor are known the temperature of the hot gases may be inferred. As shown in Figure the inferred data reasonably approximates the measured waveform but the TOPAZ predicted data are almost a factor of 2 greater. This comparison suggests that the measured data are consistent.

A comparison of radiative heat flux-time histories from Tests 5 (14.6 kg/m<sup>3</sup>) and 6 (37.3 kg/m<sup>3</sup>) are presented in Figures

7 (Chamber No. 1) and 8 (Chamber No. 2). The hot gases flowed from the detonation chamber (Chamber No. 4) through the left test drift and chamber access drift into these adjacent storage chambers. Since Chamber No. 2 is closer than No. 1, we expect the peak gas temperature and heat flux to be higher in this chamber. The peak gas temperatures predicted by TOPAZ and inferred (for opacities of 0.5 and 1.0) from these measured data are tabulated in the figures. The estimated peak gas temperatures (opacity of 1.0) from Test No. 5 ( $14.6 \text{ kg/m}^3$ ) in Chamber No. 1 and No. 2 were 847 and 1121 °K, respectively. Similarly, the estimated temperatures from Test No. 6 ( $37.3 \text{ kg/m}^3$ ) were 1304 and 1389 °K, respectively. The measured peak total (gas) pressure in Chamber No. 2 from Test No. 5 was 899 °K. Thus, the radiometer inferred temperatures (for an opacity of 1.0) in Chambers No. 1 and 2 appear reasonable.

### CONCLUSIONS

Thermal instrumentation was installed to define the thermo/fluid dynamic environment in the underground test facility. Unfortunately, high sensor mortality in the hostile environment of detonation products, debris and dust destroyed a large number of the thermal transducers installed. A few correlations (where possible) made between measurements indicate that the data are consistent.

The TOPAZ code predictions of peak data agree with the test results within a nominal factor of two. Observed differences in temperature are most likely due to dust, with some contributions from real-gas effects in dissociation of the combustion gas elements (Knox, 1993). These effects are not presently modeled in TOPAZ. The code requires that the user estimate form and frictional losses in the fluid dynamic flow process. Thus, a second iteration on these parameters is required to force the computed detonation pressure-time history to match the test data (Knox, 1993).

### ACKNOWLEDGEMENTS

We appreciate the cooperation of the authorities at the U.S. Army Technical Center for Explosives Safety, the U.S. Army Engineer Waterways Experiment Station, and the Headquarters, U.S. Army Corps of Engineers that permitted us to prepare and present this paper for publication.

### REFERENCES

1. E. C. Knox, "Explosion Effects Measurement and Prediction, Comparison of TOPAZ 1-D Code Predictions with Measurements from Explosives Detonation in Confined Areas," RTR 265-01, August 1994, REMTECH, Inc, Huntsville, AL.

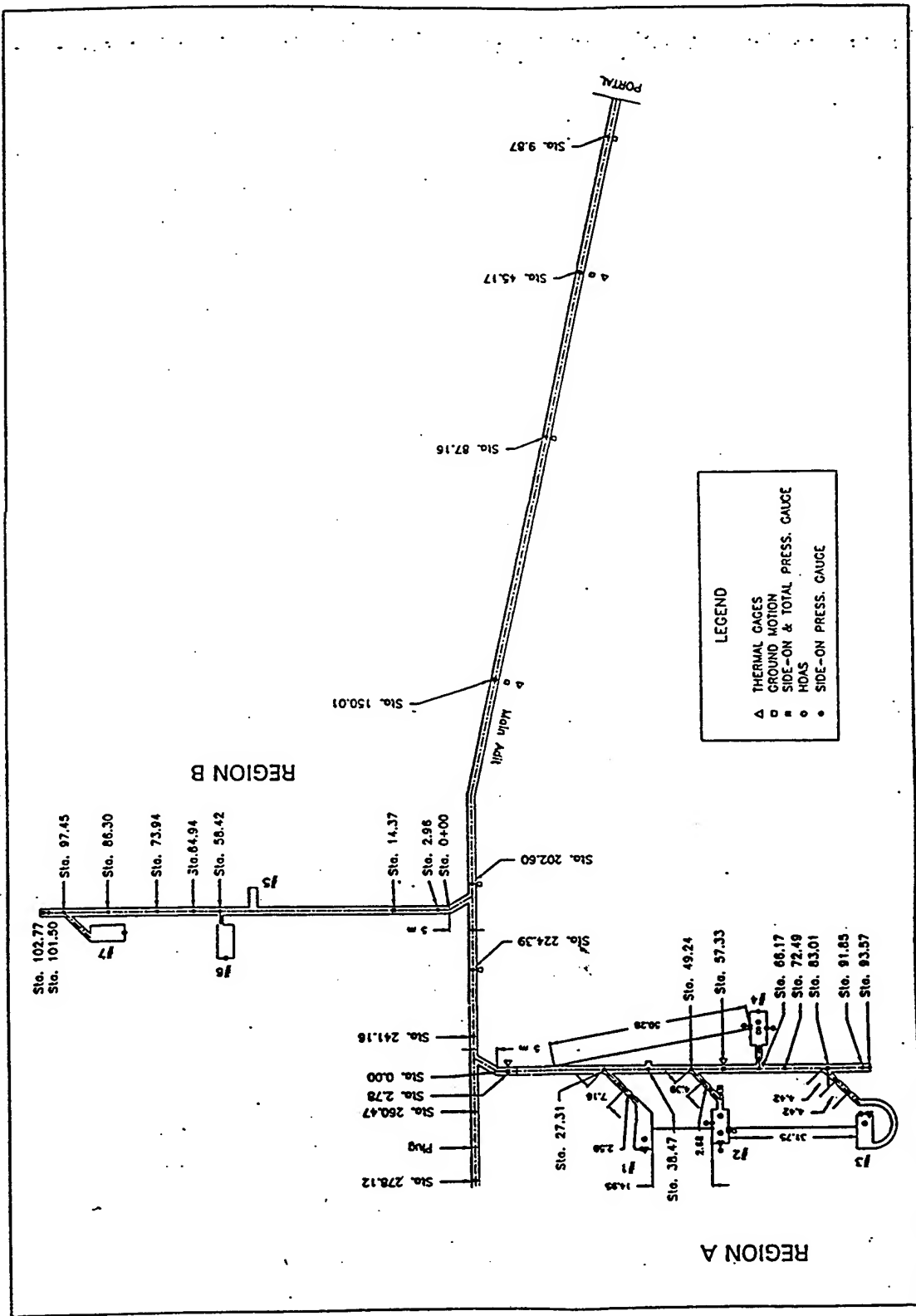


Figure 1. Test layout and instrumentation plan for Intermediate-Scale underground ammunition storage magazine experiments

# REGION A

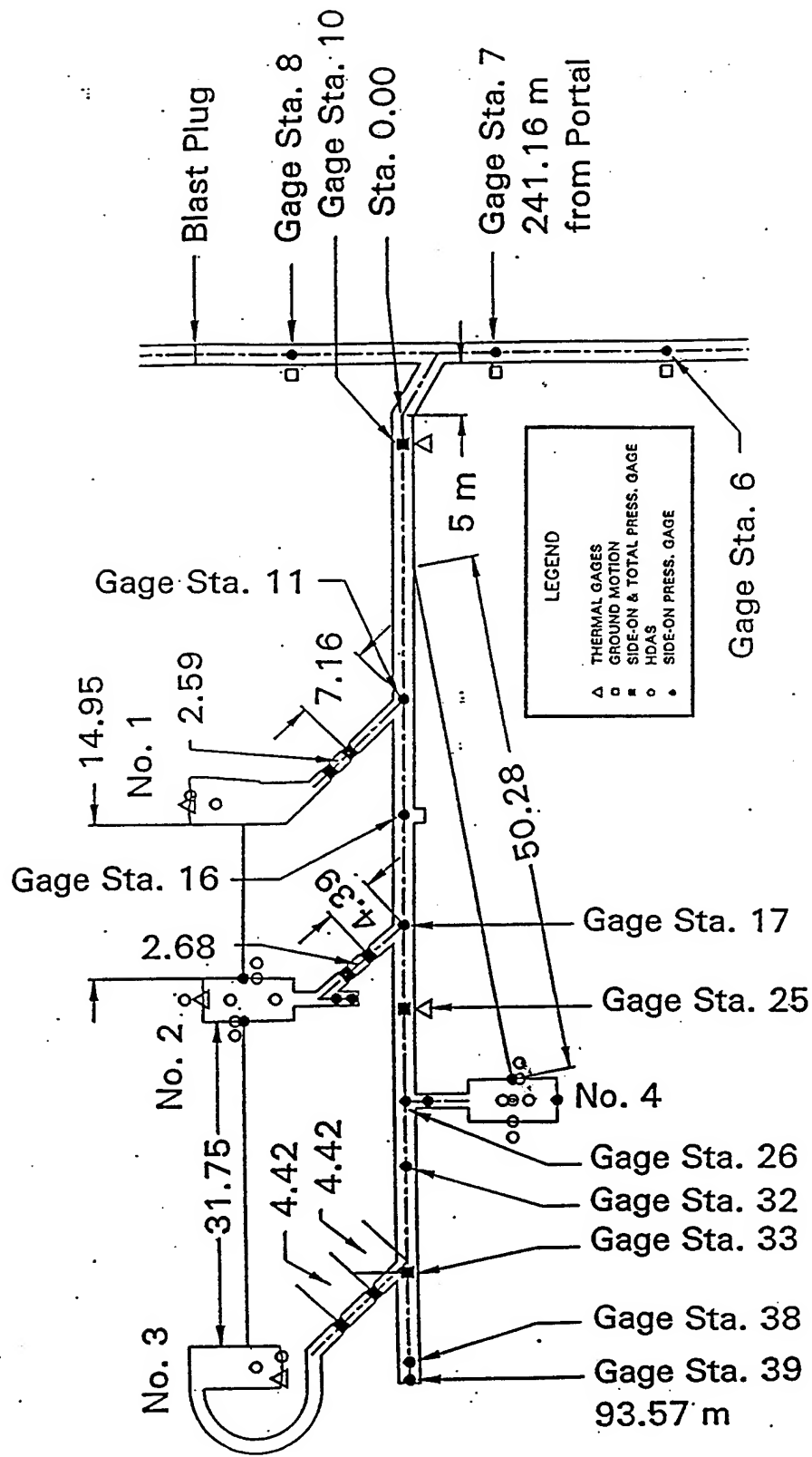
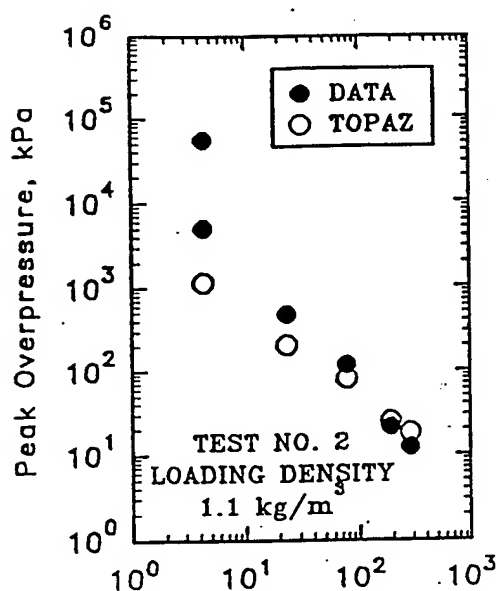
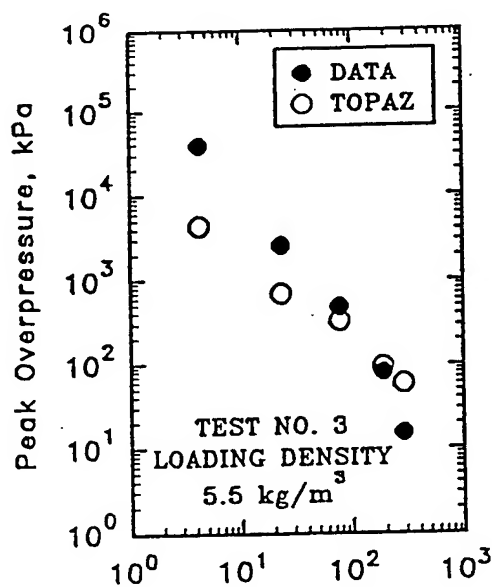


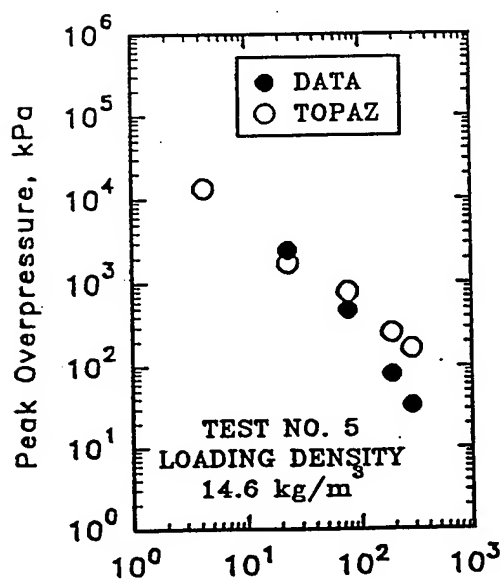
Figure 2. Test drift layout and instrumentation plan for the thermal effects experiments.



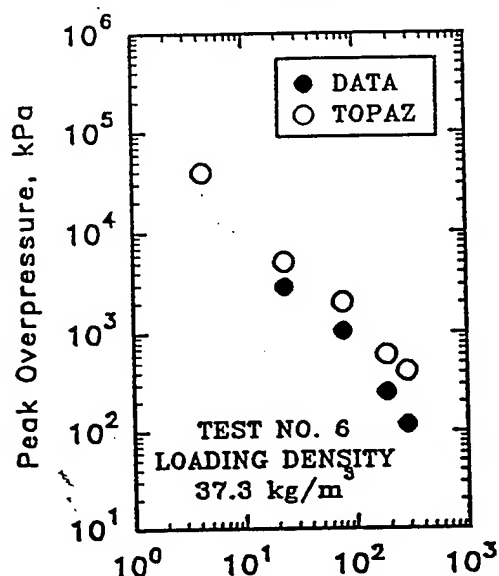
(a) TEST NO. 2  
1.1 kg/m<sup>3</sup>



(b) TEST NO. 3  
5.5 kg/m<sup>3</sup>

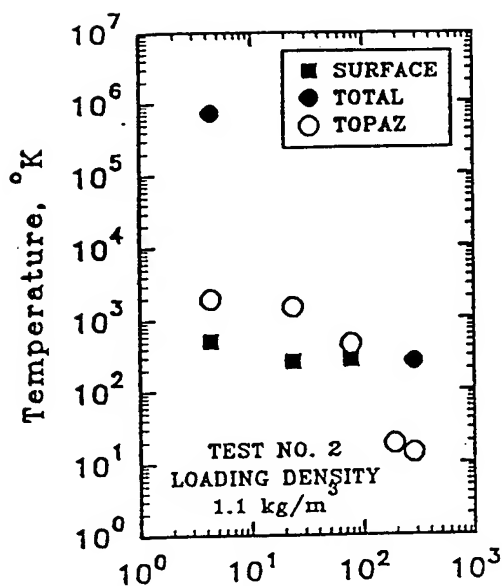


(c) TEST NO. 5  
14.6 kg/m<sup>3</sup>

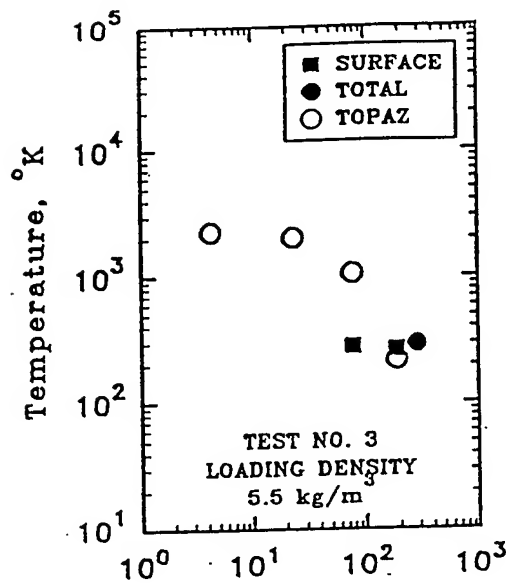


(d) TEST NO. 6  
37.3 kg/m<sup>3</sup>

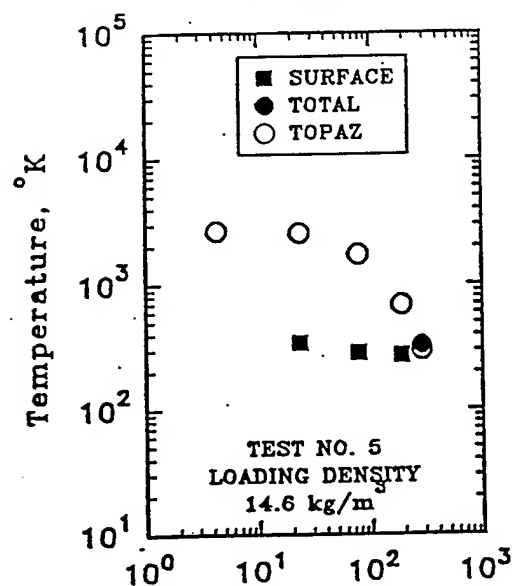
Figure 3. Comparison of calculated gas (TOPAZ) and measured peak overpressure versus distance from the rear wall of the detonation chamber (Chamber No. 4) along the airblast flow path from the detonation chamber to the Lynchburg Mine portal..



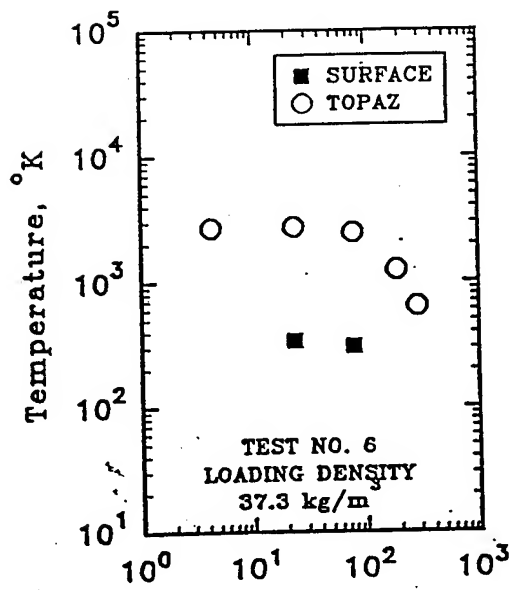
(a) TEST NO. 2  
1.1 kg/m<sup>3</sup>



(b) TEST NO. 3  
5.5 kg/m<sup>3</sup>



(c) TEST NO. 5  
14.6 kg/m<sup>3</sup>



(d) TEST NO. 6  
37.3 kg/m<sup>3</sup>

Figure 4. Comparison of calculated (TOPAZ) gas and measured peak temperatures (surface and total) versus distance from the rear wall of the detonation chamber (Chamber No. 4) along the airblast flow path from the detonation chamber to the Linchburg Mine portal.



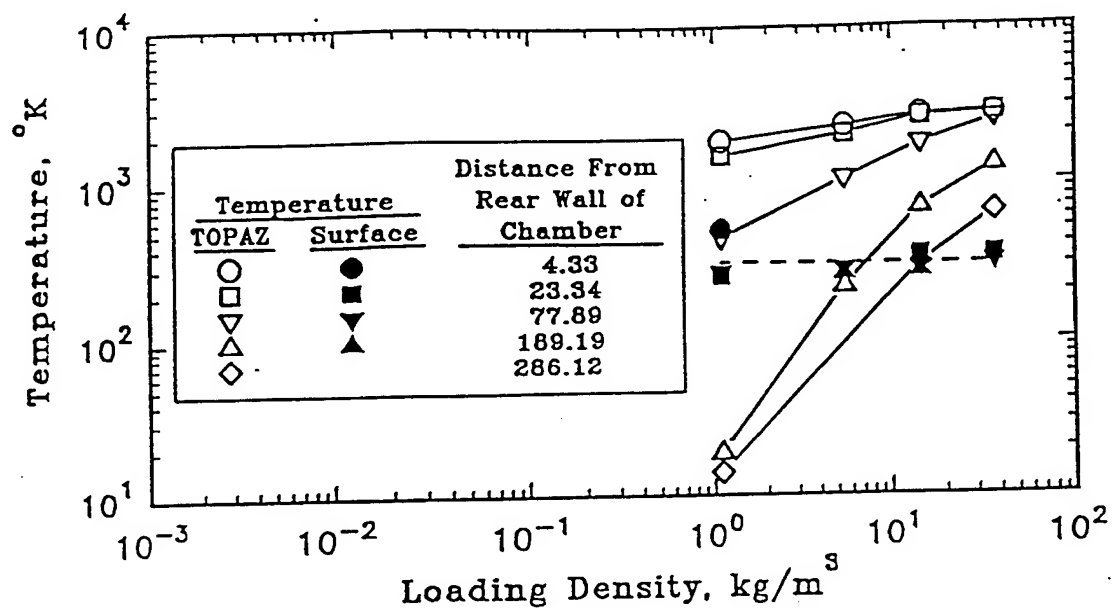


Figure 5. Comparison of calculated (TOPAZ) gas and measured peak surface temperature versus chamber loading density at various distances along the airblast flow path from the detonation chamber to the Lynchburg Mine portal.

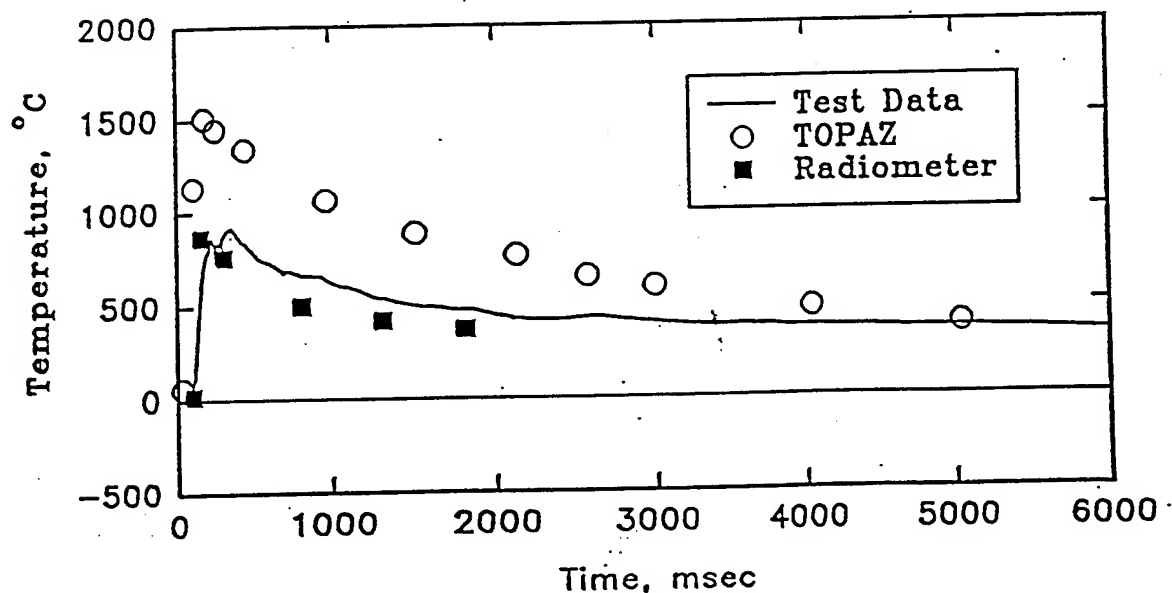


Figure 6. Comparison of calculated (TOPAZ) and radiometer-inferred (assumed opacity of 0.97) gas temperature-time histories at Gage Station 24 (Test No. 5, 14.6 kg/m³) located in Chamber No. 2.

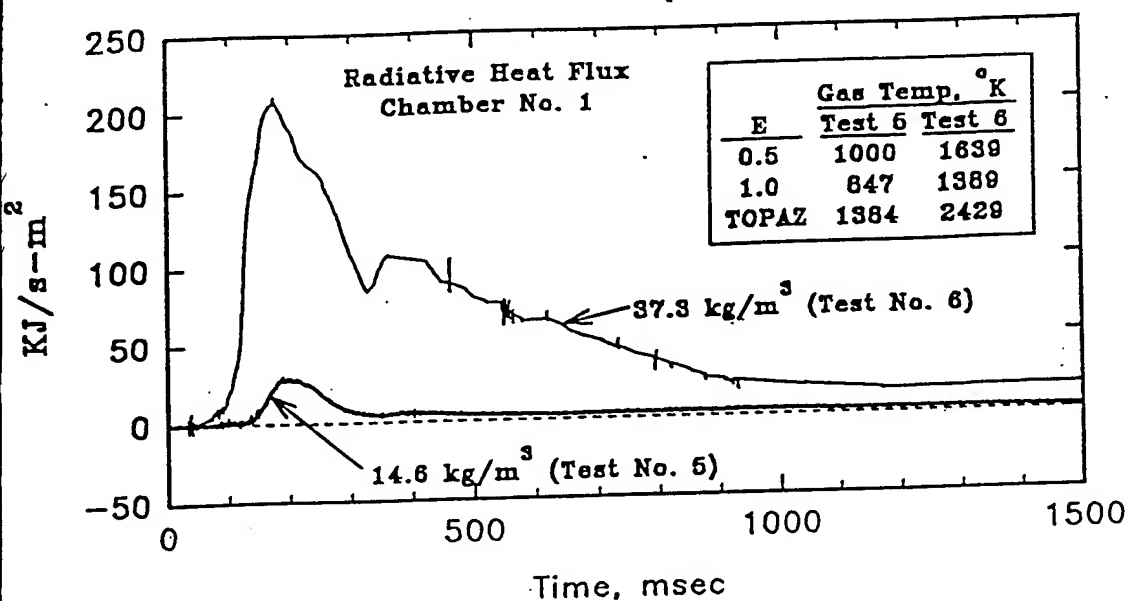


Figure 7. Comparison of measured radiative heat flux-time histories in Chamber No. 1 at Gage No. 15 from Tests 5 (14.6 kg/m<sup>3</sup>) and 6 (37.3 kg/m<sup>3</sup>).

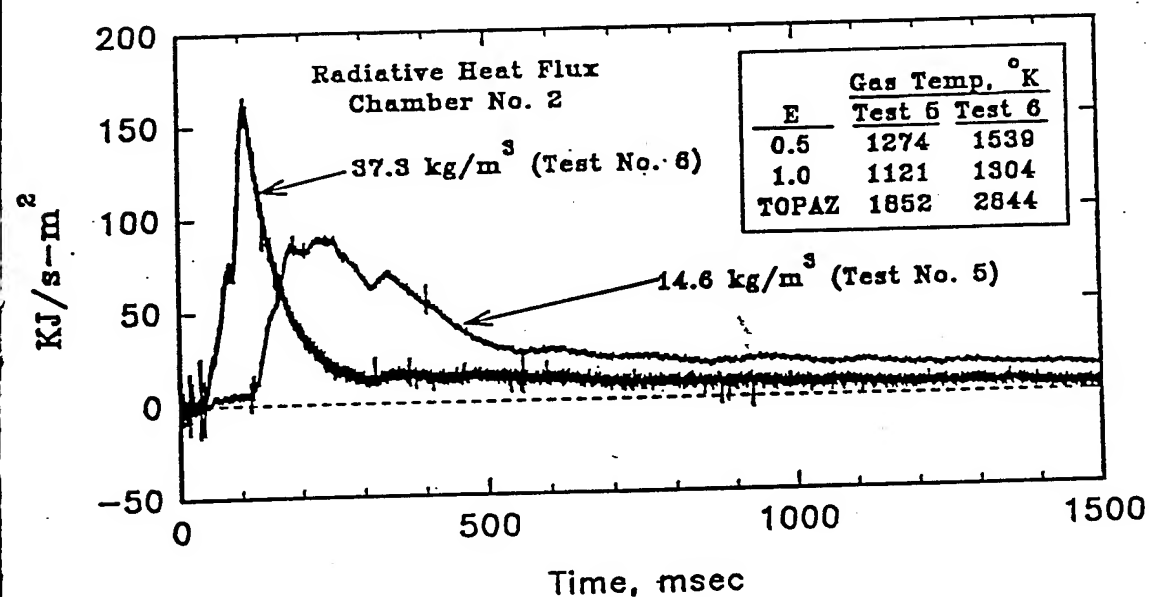


Figure 8. Comparison of measured radiative heat flux-time histories in Chamber No. 2 at Gage No. 24 from Tests 5 (14.6 kg/m<sup>3</sup>) and 6 (37.3 kg/m<sup>3</sup>).

# INTERNAL PRESSURE MEASUREMENTS FROM EXPLOSIVELY LOADED CUBICLES.

**George Yiannakopoulos**  
Defence Science and Technology Organisation  
Aeronautical & Maritime Research Laboratory  
GPO Box 4331 Melbourne  
Victoria 3001 Australia  
61 3 626 8713

## ABSTRACT

A series of experiments was conducted to measure the explosive pressure-time histories on the interior of 1 m<sup>3</sup> cubicles that are used for modelling structural damage from explosive loading. In this experimental configuration each cubicle, consisting of mild steel walls 5 mm thick, was explosively loaded by a centrally positioned pentolite sphere. In such studies it is imperative to obtain reliable measurements of the pressure-time histories. The pressure transducers were subjected to high pressures from the explosive detonation products, as well as thermal flash, convection and high acceleration. The instrumentation used required sufficient bandwidth to record the transient pressure pulses with minimal or no effects from the other explosive by-products. Interpretation of the material's failure mechanisms can be completely erroneous if these issues are not clearly delineated. Therefore, additional post-experimental investigations were undertaken to validate the data and the investigations included repeating measurements from previous tests on identical cubicles. It was the purpose of these investigations to determine the consequences of the unwanted effects on the data. Both piezoelectric and piezoresistive pressure transducers were used and the relative merits of each are discussed for this application.

## 1. INTRODUCTION

An extensive experimental program has been undertaken by the Aeronautical and Maritime Research Laboratory (AMRL) on internal blast damage in ship's compartments from explosive munitions. A parametric study was first conducted on 1 m<sup>3</sup> cubicles [1], followed by experiments on two mock-up ship's compartments [2], culminating in full scale tests on a Royal Australian Navy decommissioned vessel, the Derwent. These experiments have been supported by computational simulations where finite-difference and fine-element codes have been used for studies of structural damage, and semi-empirical blast codes have been used to predict the pressure on wall panels [3]. Measurements in these studies play an important role in helping to understand the structural failure and in confirming and improving computer models. This procedure is iterative, where results from the software enable the refinement of the measurement technique, and measurements can illuminate limitations in the software which can then be modified.

During the parametric cubicle studies the mounting technique for the pressure transducers was developed. These experiments represented extreme environmental conditions for the transducers, which included thermal flash from the explosive, high acceleration on the panels, and convective and conductive heating from the detonation products and surrounding walls. The transducers are not commonly used in this harsh environment. The measurements required additional investigative studies ensuring that the instrumentation recorded pressure only and not other unwanted effects. Two cubicles, identical with those in the previous parametric cubicle studies, enabled the repeat of pressure measurements at the same locations. Additional instrumentation included accelerometers, strain gauges, high speed cinematography and high speed video. The aims were as follows:

- (1) To confirm pressure measurements from the parametric cubicle studies;
- (2) To compare the performance between piezoelectric and piezoresistive types in this environment;
- (3) To determine whether the environmental effects on the pressure transducers due to thermal flash, acceleration, and heating by conduction and convection generate a significant signal;
- (4) To test the inertial effects from the transducer mount using a modified mount of reduced mass and comparing these results with those from the parametric cubicle study;

The above aims represent only one aspect of the post-experimental investigations. Installation techniques were also investigated for accelerometers and strain gauges. Although these measurements are not the subject of this report, results are discussed to confirm the validity of the pressure measurements.

## **2. EXPERIMENTAL**

Five events were conducted using two cubicles in which three events (designated events 1 to 3) consisted of firing detonators and two events (designated events 4 and 5) in which a pentolite sphere was detonated. Firing detonators enabled function-testing of the instrumentation, and the pentolite sphere experiments repeated two experiments from the parametric cubicle studies.

### **2.1 Description of Cubicles**

The two cubicles were constructed from unstiffened mild steel panels of 1 m  $\times$  1 m (outside dimensions), 5 mm thickness. Five panels were joined by high quality through-thickness manual arc welds, welded internally and externally. The final panel was welded using an external through-wall weld. A hole on the top face of the cubicle enabled insertion of the charge (110 mm diameter) and two holes on adjacent sides provided mounting of the pressure transducers (38 mm diameter), Figure 1. The top hole was not

covered after insertion of the charge and allowed slight venting (less than 0.2 % of the total area of the cubicle).

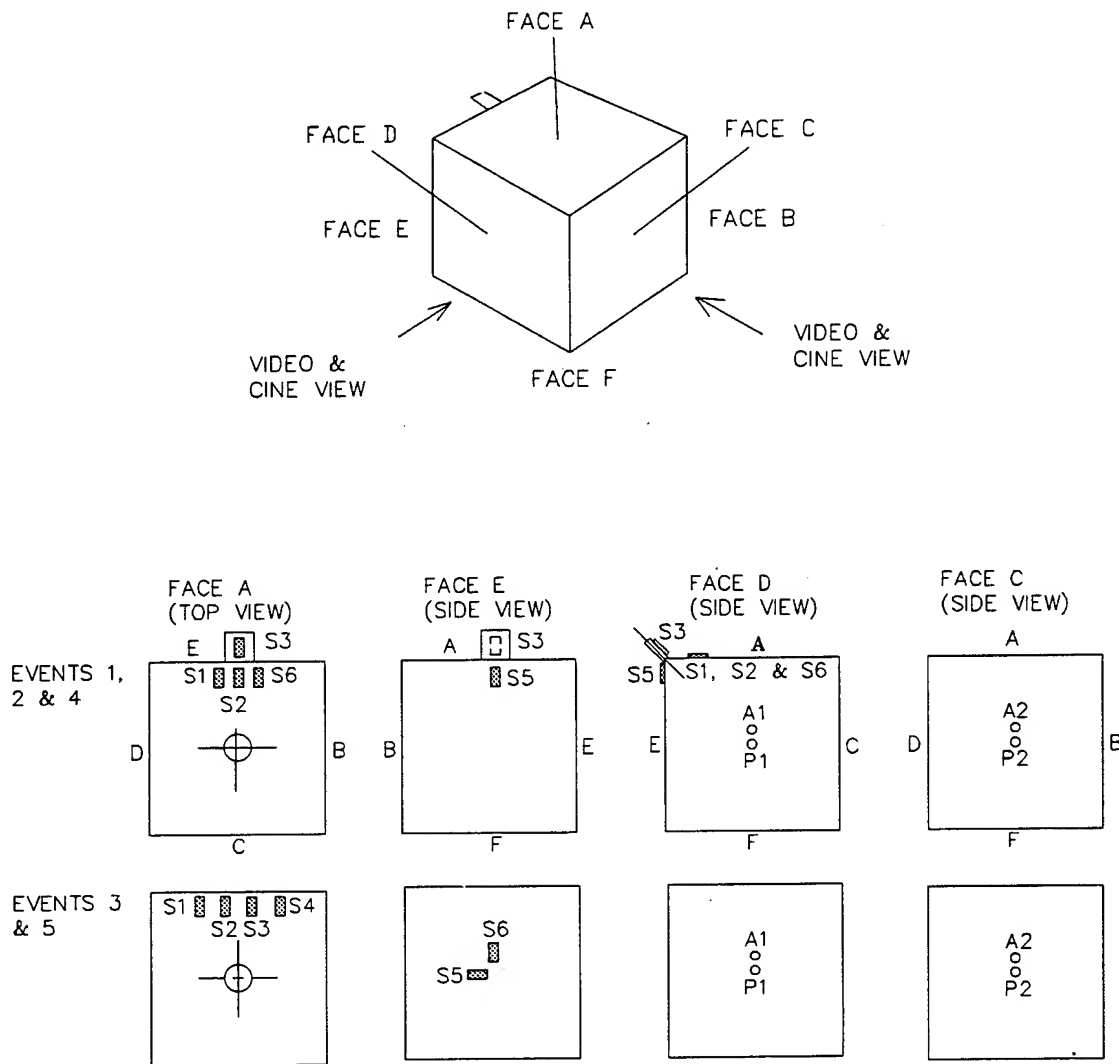


**Figure 1 Schematic of cubicles and location of transducers, where A denotes accelerometers, P pressure transducers, S strain gauges. Single letters denote adjoining cubicle faces.**

## 2.2 Description of the Explosive

The detonators were the Reynolds 501 Electrical Bridge Wire (EBW) type, having a net explosive equivalent less than a gram, which were used for all five events. During events 1 to 3 each detonator was fired in the centre of the cubicle generating a small pressure pulse thus enabling function testing of the recording instrumentation. During events 4 and 5 more explosive was used, consisting of 250 g pentolite in the form of a sphere with a cavity to suit an EBW for central initiation. The pentolite composition consisted of the components of 50% TNT and 50% PETN and this composition was chosen because the

performance of pentolite is considered repeatable compared to other explosive types. In fact it is used at AMRL to calibrate pressure transducers for underwater blast measurements, and considerable knowledge has been obtained in its explosive handling and performance during these measurements.

The pentolite sphere was also placed in the centre of the cubicle and the mass chosen was based on results from the parametric cubicle studies, which indicated that rupture of the panel would not occur. Therefore, by selecting a 250 g mass, the aim was to enable further tests to be conducted on the same cubicle.

## **2.3 Instrumentation**

The instrumentation consisted of a tape recorder, a digital CRO, two pressure transducers, two accelerometers fitted using mechanical filters, up to six strain gauges, a precision resistor and suitable line power units. High speed cine and video were also used.

### **2.3.1 Pressure Transducers**

The pressure transducers were the piezoresistive Endevco 8511A-20k and the piezoelectric PCB 109A which both have applications in blast work. The Endevco 8511A-20k has a range of 140 MPa (20,000 psi). The cable, which is four core-shielded, is directly attached to the transducer. A disadvantage with this configuration is that if the cable is broken at the transducer end, repairs cannot be made and the transducer is rendered unserviceable. Acceleration sensitivity is rated by the manufacturer as 21 Pa/g or 0.003 psi/g.

The PCB 109A, normally used for gun breech measurements, has a range of 550 MPa (80,000 psi). The cable consists of miniature coaxial 50  $\Omega$  cable and is attached to the transducer by a connector. A damaged cable can either be easily repaired or replaced. These transducers are cheaper than the Endevco type, costing about half the amount. The piezoelectric transducers have a discharge constant of 2000 s resulting in 1 % signal loss in 20 s. This feature is only possible by using the DC mode of the signal conditioner. The sensitivity to acceleration is quoted as 28 Pa/g or 0.004 psi/g.

#### **(1) Mounting**

Pressure transducers were mounted in the centre of two panels. Externally threaded nylon inserts secured the transducer in the mounts (Figure 2). The nylon insert electrically insulated the transducer and overcame ground loop problems arising from attaching directly to the metallic mount. It also aimed to attenuate laterally induced acceleration. The transducer mounts, constructed from high strength steel, were reduced in mass from the original mounts used during the parametric cubicle studies by approximately 40 %. The reduction in weight aimed at minimising the inertial effects on the pressure transducers. In this mounting configuration the transducers were located at 0.506 m from the charge, below the accelerometers which were located in the centre of the panels.

## (2) Heat Protection

The detonation generates thermal flash and heat from convection of the combustion by-products. The transducers are sensitive to these effects and it is necessary to screen against them. The Endevco 8511A-20k transducer can be provided by the manufacturer with the M1 silicone grease option and a perforated thin metallic disk, thus offering thermal protection. The PCB 109A, which has an ablative ceramic coating for screening against thermal flash, does not offer protection against thermal conduction. However the manufacturer recommends applying 2 mm thick silicone grease, and two layers of electrical PVC tape, which were applied for the measurements.

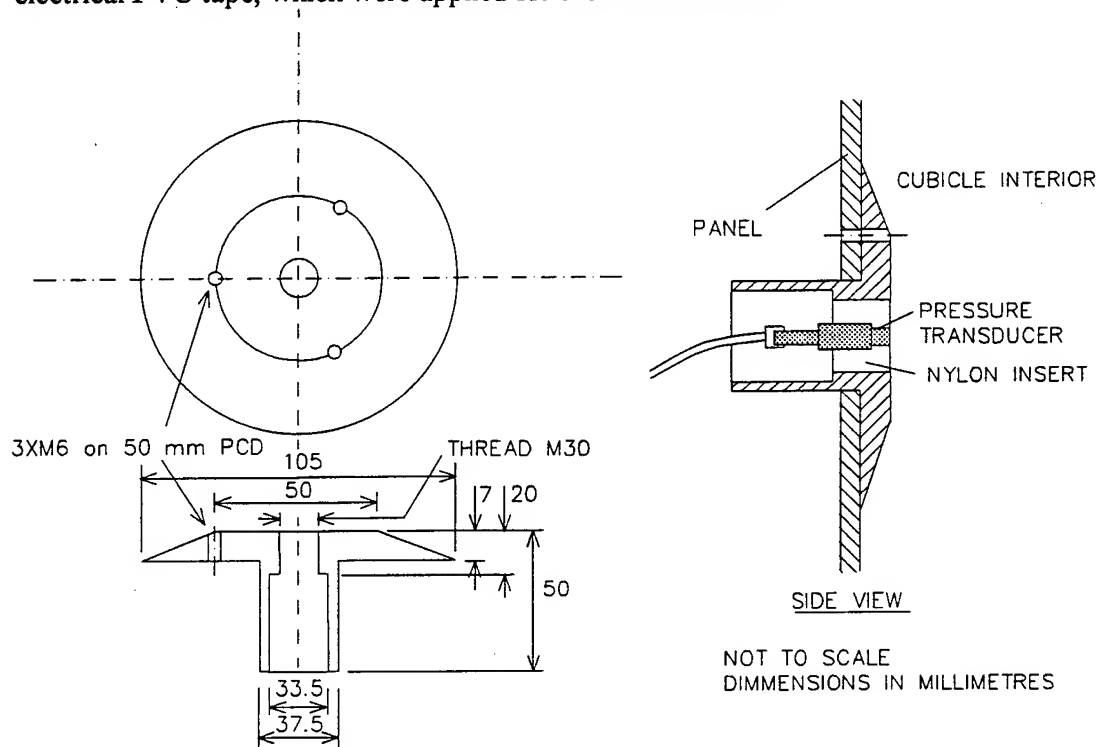


**Figure 2 Schematic of pressure transducer mount and nylon insert.**

### (3) Calibration

The transducers were calibrated before and after the tests using a Budenberg dead weight static press. Calibration after the event is performed to check that the transducer has not been damaged during the measurements. The Budenberg press applies a hydrostatic load on the transducer. The predicted pressure levels for the experiment, using a semi-empirical code, were about 12 MPa. Calibration was performed at 80% of the expected level, that

is, calibration levels up to 10 MPa were used. This was the maximum level available from this calibration instrument.

As a coarse check of the sensitivities obtained from the Budenberg press a comparison was made with results from the PCB 903A aperiodic pulse calibrator, which generates pressure steps with rise times around 6 to 8 ms. These rise times are still very slow but relatively closer to the rise times of the events of interest. The maximum pressure level attained by this device was 620 kPa and for this reason it could not be used to calibrate the transducers. This value represented calibration at 0.125 % of the maximum range of the PCB 109A transducers and about 6 % of the predicted levels for the experiment. However the manufacturer claims that the resolution of the transducer is 14 kPa, or 0.0025 % (ie  $14 \text{ kPa} / 550,000 \text{ kPa} \times 100 \%$ ) of the maximum transducer range. The average sensitivities derived from the two different pressure standards were within 2.5 %.

The situation was similar for the Endevco 8511A-20k transducers in which the pulse represented 0.5% of the maximum range of the transducer. Average sensitivities also were within 2.5%.

### **2.3.2 Accelerometers**

The Endevco 7270A-2k accelerometers, mounted between shock isolating pads and enclosed in an aluminium housing, were attached at the centre of the panels located near each pressure transducer (Figure 1). The aim of this part of the experiment was proof of concept of the accelerometer mounts and to estimate the acceleration levels on the pressure transducers. Previous attempts during the parametric cubicle studies were unsuccessful resulting in failure to the accelerometer and commercial mechanical filter.

Three screws secured the accelerometer housing (Figure 3). The shock isolating materials consisted of either bromobutyl or polysulphide, 2 mm thick. Butyl mechanical filters are available commercially from Bruel & Kaer, model 0550, which was used during the previous unsuccessful attempts. Polysulphide has also been used as a shock isolation material and is commonly used as a sealant in aircraft fuel tanks where it has good heat resistance properties. It is currently used for this purpose by Endevco for a mechanical filter that will be commercially available soon.

### **2.3.3 Strain gauges**

Up to six strain gauges and a precision resistor were attached to the box (Figure 1). Strain gauges were installed in locations where it was considered that rupture would occur and in event 5, at the centre of the panel for comparison with the results from the pressure transducers and accelerometers. The precision resistor was used to study spurious noise arising from inductively coupled noise and cable stretching from whipping caused by the acceleration of the cubicle walls. Strain gauges with comparatively shorter lengths were used to study the strain rise time. However, only the results from the shock transit times are presented and details of the strain gauges will not be discussed in this report.



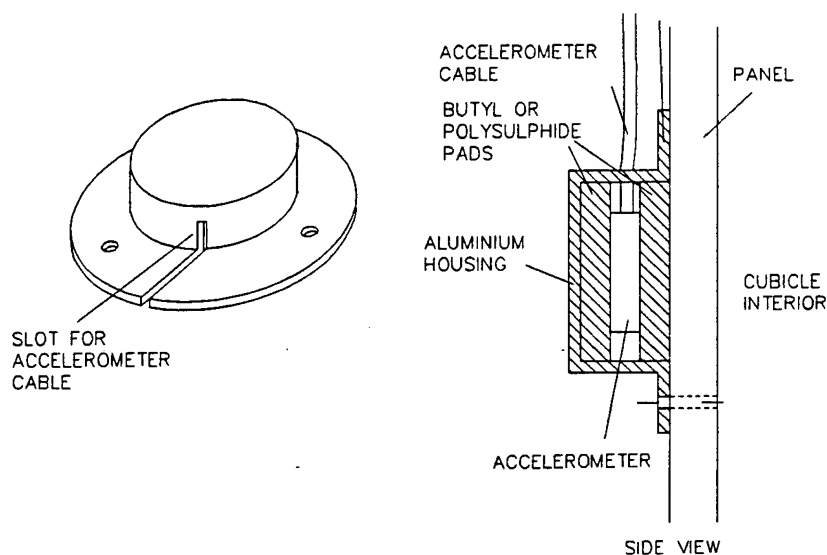


**Figure 3 Schematic of accelerometer mechanical filter.**

### **2.3.4 High Speed Cine**

Streak photography, at a writing speed of 64.24 mm/ms, enabled the derivation of displacement-time profiles of the panels at the accelerometer and pressure transducer locations.

### **2.3.5 High Speed Video**

The Kodak SP2000 in one view, at 2000 frames per second, recorded the overall deformation of the cubicle and in another view, at 6000 frames per second, the pressure transducer and accelerometer trajectories. Two cameras recorded the history of the two panels in which the pressure transducers and accelerometers were mounted, that is face C and D. The aim was to record the expansion and contraction phases of the cubicle, fireball effects and cable whipping.

### **2.3.6 Firing Unit and Reference Time Zero**

Reference time zero was obtained from the firing unit where a signal was recorded on tape which coincided with the high voltage pulse that initiated the EBW. The firing pulse is also inductively coupled to the pressure-time profiles. Tests have shown that this signal can be reliably used as reference time zero.

### **2.3.7 Recording Instrumentation**

#### **(1) Tape Recorder and digital CRO**

The tape recorder consisted of the Ampex PR-2230 with 14 channels, an analogue bandwidth of 80 kHz, or maximum signal rise time of 4.4  $\mu$ s, and a signal to noise ratio of

48 dB. The signal was recorded in FM analogue form and calibration voltage signals were recorded from a voltage standard, accurate to six significant figures prior to the events. A channel was allocated to 1.0 and 0.1 ms time marks, which were recorded during the events.

The analogue signals from the tape recorder were digitised, upon tape play-back, by the IQ 400 digital CRO and down-loaded to a PC. This instrument has 8-bit vertical resolution at 50 MHz maximum sampling frequency. For event 5, the signal from the transducers were successfully recorded in parallel onto the CRO for comparison with the tape results.

## **(2) Signal Conditioner**

The piezoelectric transducer was connected to the PCB model 482A10 line power supply and signal conditioner. This supplies a constant current at 12 mA to the transducer and is therefore suitable for long cable lengths (longer than 150 m). The signal conditioner couples to the transducer in AC mode and has an analogue bandwidth of 200 kHz at unity gain.

The Endveco model 4423 signal conditioner was connected to the piezoresistive transducers and provided the transducer with excitation, bridge balance adjustment and amplification. An 85 mA peak to the bridge permitted long cable lengths, approximately 20 m, which is relatively long by piezoresistive transducer standards.

### **2.3.8 Signal Rise Time**

Measurements have shown that the peak pressures have rise times of about 6  $\mu\text{s}$ . This value is close to the overall rise time of the instrumentation, i.e. 4.4  $\mu\text{s}$ , which is the bandwidth of the tape recorder. Tests were conducted to determine the rise time of each individual component in the instrumentation and therefore to determine the overall instrumentation rise time.

Similar tests to those performed on the tape recorder were conducted to check the manufacturer's bandwidth of the PCB model 482A10 signal conditioners. The first test involved applying a voltage step to the signal conditioner through a PCB transducer simulator. Results indicated a rise-time of 0.3  $\mu\text{s}$ . In the second test a 100 kHz sine wave was applied from a voltage standard. The output signal was attenuated by 1.4 %. These results indicated that at unity gain the analogue bandwidth is better than 200 kHz, closer to 1.0 MHz. Some signal conditioners indicated a bandwidth 2-3 times better than this value.

The tests for the Endevco model 4423 signal conditioner were not as direct and involved using the Hopkinson bar in which strain gauges were connected and results were compared to an amplifier with a 1 MHz bandwidth. Typical rise-times of the signals were 2-5  $\mu\text{s}$  at strain rates  $10^3$ - $10^4 \text{ s}^{-1}$  at a load of 1.2 GPa. The rise times were representative

of those expected from the cubicle tests. Results from both amplifiers were similar and it was concluded that the signals were amplified faithfully at these rise times.

Shock tube tests were performed on the PCB 109A (with heat protection) and the Endevco 8511A transducers. Results confirmed the manufacturer's specifications at 1  $\mu$ s rise time.

### 3. EXPERIMENTAL RESULTS

#### 3.1 Pressure-time profiles

Pressure-time profiles are presented for events 4 and 5 for the piezoresistive transducer, designated P1, and the piezoelectric transducer, P2. Windows at 1.4 ms are shown (Figure 4). There was cable failure for all the transducers, only evident on the traces shown for P1 during event 4. The failure occurred earlier for the piezoresistive transducers, at 0.48 ms and 2.6 ms for events 4 and 5, respectively. Cable failure of the piezoelectric transducer occurred much later, beyond 30 ms, for both events.

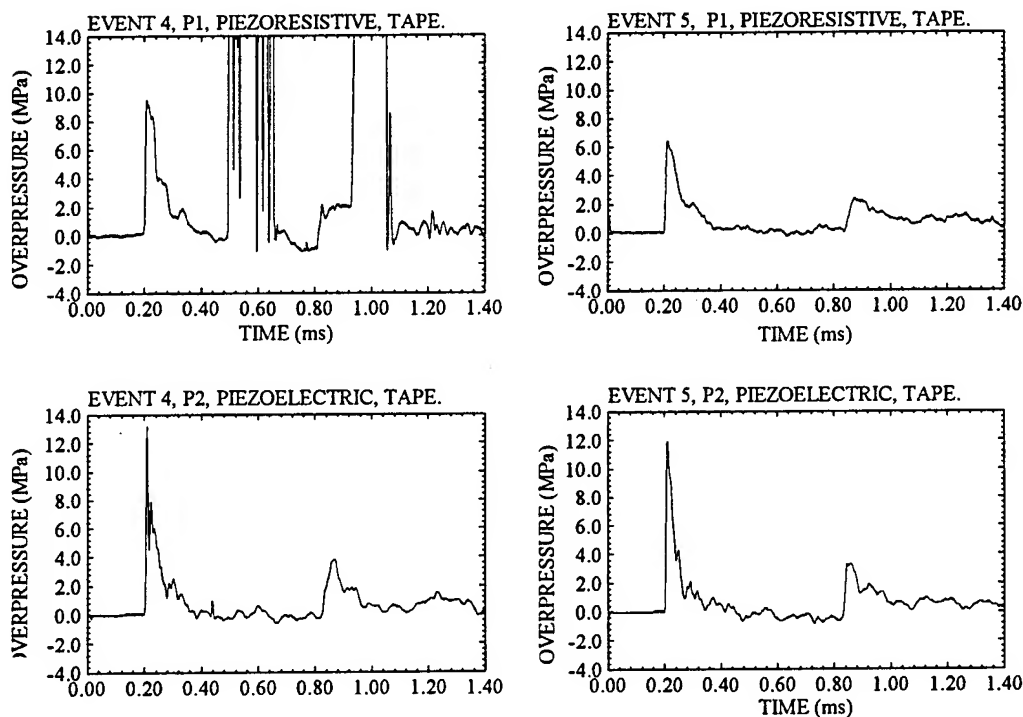


**Figure 4 Pressure-time profiles at locations P1 and P2 for events 4 and 5.**

Peak pressures, time of arrival for the first and second pulses, and impulse are presented in Table 1.

Direct records were only obtained for P1 and P2 during event 5 (Figure 5). These were captured at 10 MHz sample frequency directly on the digital CRO and were recorded in

parallel at greater time resolution enabling more accurate determination of the rise time of the signal compared to that obtained from tape play back. The record for P2, event 5, is clipped due to incorrect setting on the CRO.

**Table 1**  
**Summary of pressure results**

Parameter	From Tape Play Back				Directly from CRO	
	Event 4		Event 5		Event 5	
Distance = 0.506 (m)	P1	P2	P1	P2	P1	P2
1st Peak (MPa)	9.0	13	6.6	12.0	6.9	> 6.1
(psi)	1,300	1880	910	1740	1000	clipped
Rise time of 1st peak ( $\mu$ s)	7.6	6.0	8.4	6.6	6.4	-
2nd Peak (MPa)	2.1	4.8	2.2	3.22	2.5	3.8
(psi)	300	700	320	460	360	560
TOA of first peak ( $\mu$ s)	197	198	198	200	200*	200*
TOA of second peak ( $\mu$ s)	825	869	864	843	868	837
Positive Phase ( $\mu$ s)	238	180	210	140	200	140
Reflected Impulse (Pa.s)	620	490	450	460	430	380

\* Estimated from the inductively coupled pulse on the record.

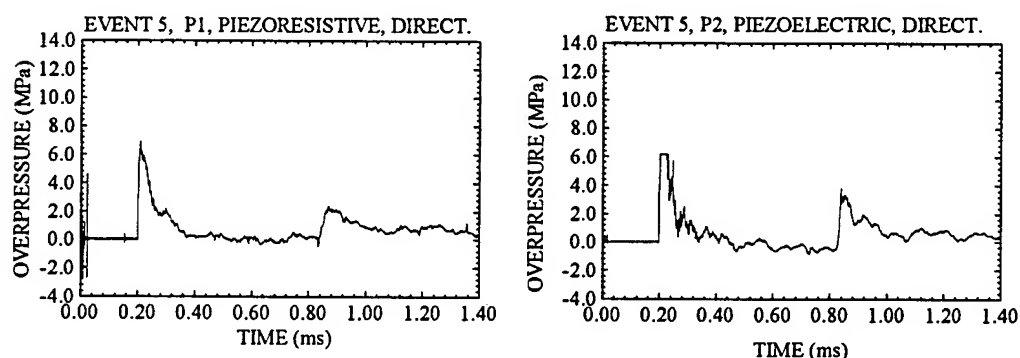


**Figure 5 Results recorded directly on the digital CRO.**

Inspection of the transducer after the event indicated soot on the transducer and mount, resulting from the explosive by-products. The PVC tape was always scorched and was replaced.

### 3.2 Accelerometer and strain results

Time of arrival information from the accelerometers and strain gauges is presented in Table 2 for comparison. An acceleration-time profile, electronically filtered, is shown from A2 event 5 (Figure 6). The analogue signal from the tape was filtered by using the Krohn-Hite model 3550 at 20 kHz. It is a four-pole Butterworth filter with an attenuation slope of 24 dB/octave. This is a preliminary result and should be used as indicative of the levels. Further development work is required for absolute measurements to determine transducer

characteristics such as linearity, resonance frequency and cross-axis sensitivity. Strain profiles are not presented but will be reported in future.

**Table 2**  
**Time of arrival measurements from accelerometers and strain gauges.**

Transducer Type	Event 4		Event 5	
	Distance (m)	TOA ( $\mu$ s)	Distance (m)	TOA ( $\mu$ s)
Accelerometer A1	0.5	204	0.5	205
Accelerometer A2	0.5	203	0.5	206
Strain gauge S1	0.7	no result	0.7	436
Strain gauge S2	0.7	428	0.7	436
Strain gauge S3	0.7	436	0.7	440
Strain gauge S4	not used	not used	0.7	432
Strain gauge S5	Precision Resistor		0.5	440
Strain gauge S6	0.7	432	0.5	440

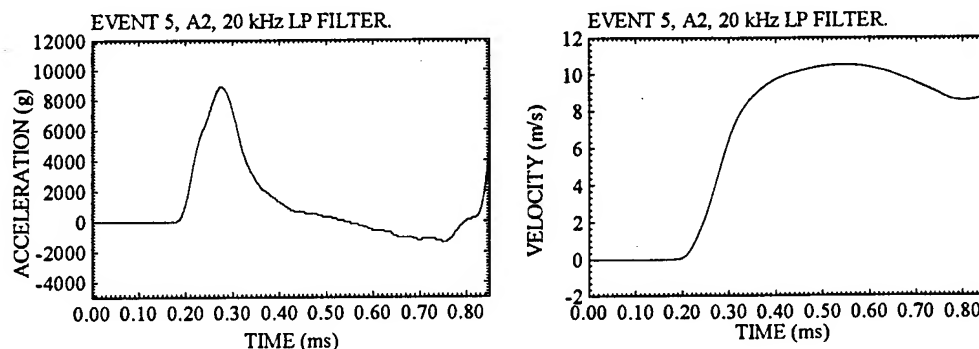


**Figure 6 Accelerometer result for location A2, event 5.**

During the detonator tests acceleration levels of approximately 800 g were measured on the panels. Therefore the results indicated that both pressure transducer types are acceleration sensitive. This can be seen in an envelope of levels equivalent to  $\pm 150$  kPa, that is the acceleration effects would be registered at these levels in the pressure record. This represents 1.25 % of the peak overpressure, that is  $0.15 \text{ MPa} / 12.0 \text{ MPa} \times 100 \%$ , and within the manufacturer's specification.

### 3.3 Streak photography results

Displacement-time profiles were obtained at 28  $\mu$ s sample rates for a 11.2 ms window. Unfortunately greater resolution is both time consuming and results in a profile that is noisy. Displacement and velocity, by differentiation, at the accelerometer location A2 is presented (Figure 7). The qualitative features of the velocity curves obtained from the streak photography and acceleration records were similar but a detailed analysis is required and will be reported in the future.

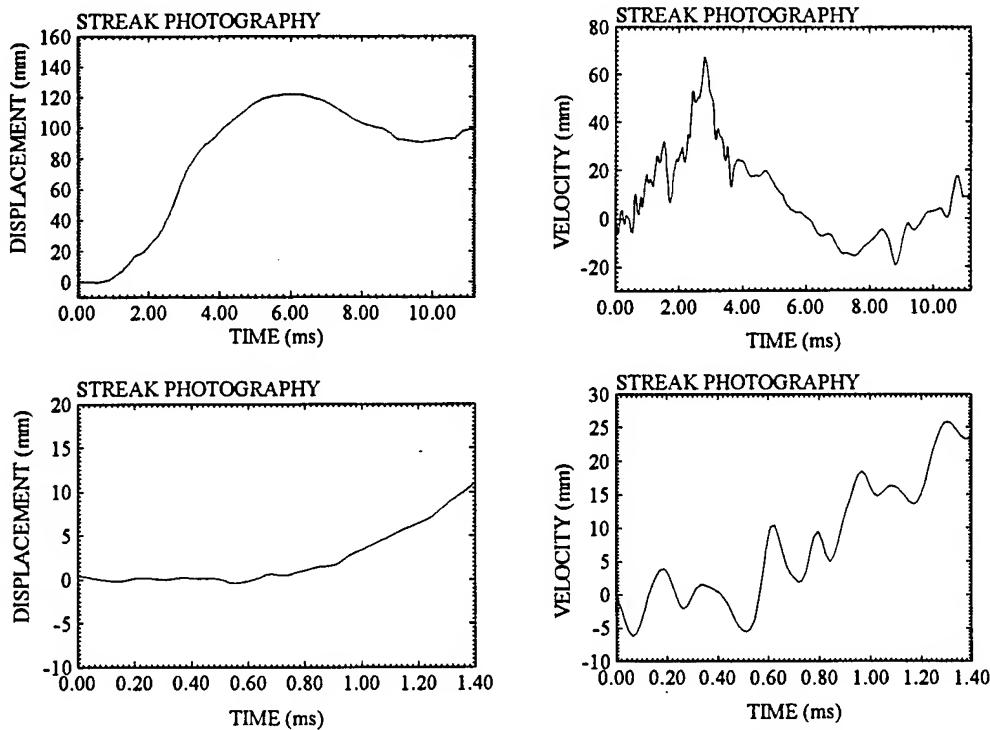


**Figure 7 Streak photography result for location A1, event 4.**

### 3.4 High speed video results

High speed cine from the parametric cubicle studies showed the cubicle undergoes a cycle in the deformation consisting of an expansion and contraction. This contraction phase was not observed for events 4 and 5. The high speed video indicated failure of the cubicle occurred immediately at the single welded panel, eliminating the contraction phase. The cubicle failed at approximately 12-14 frames (that is, 6-8 ms) and the failure resulted at the single weld. This failure did not occur as a rule during the parametric cubicle studies, even with 1.0 kg explosive charges and indicated a problem with weld quality control.

The video indicated the severity on the transducer of the heat from the fireball. This was seen from the 25 mm thick nylon insert in which the transducer was mounted, where an intermittent glow lasted 0.67 ms (4 frames), followed by dimming for 0.17 ms (1 frame) then glowing again, for 0.33 ms (2 frames), hence a total of 1.17 ms. Whipping of the piezoresistive pressure transducer occurred immediately during the expansion phase resulting in detachment of the cable near the end of this phase as the panel expanded to its limit.

## 4. DISCUSSION

### 4.1 Thermal effects and cable whipping

A profile is presented for event 5, transducer P2, to illustrate heat conduction effects on this transducer type (Figure 8). This effect is characterised by a negative baseline drift and is apparent at approximately 4-8 ms into the event. However, at approximately this time, a quasi-static pressure is expected lasting for a comparatively longer duration, depending on venting and rupture. Therefore the piezoelectric transducer, with the current thermal protection technique, is considered unsuitable for quasi-static pressure measurements.

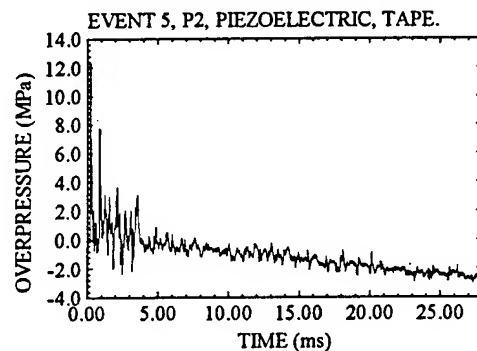


**Figure 8 Heat conduction effects on the piezoelectric pressure transducer P2, event 5.**

On the other hand, the piezoresistive transducers can record static pressure and are more resistant to heat conduction. However, they suffer from a design limitation where the cable is hard wired directly to the transducer. Being four-core shielded it is heavier and more prone to whipping because of its inertia and the high acceleration of the panels. Failure occurs approximately 4-5 ms into the event.

During event 4 for P1, another related failure was observed. It resulted from a connector at about 1 m from the transducer, which was placed to enable a quick break in the connection upon the onset of cable whipping. The aim was to relieve stress on the cable so that it did not break at the transducer end, which experience has shown to be the weakest point. This connector did not withstand the initial pressure, giving rise to intermittent continuity in the circuit, as is evident from the profile, sending the signal high at 0.46 ms. In event 5 this approach was not used. Instead the male and female connectors were removed and the two cables were joined directly by soldering. This resulted in a longer recording history but damage to the transducer.

### 4.2 Acceleration effects

Acceleration measurements within the 0.85 ms window indicate positive levels between 8,000 and 10,000 g. Using the acceleration sensitivity provided by the manufacturer, this results in signal levels up to 300 and 450 kPa for the piezoresistive and piezoelectric transducers, respectively (Section 2.3.1). This is approximately 4 % of the maximum peak

pressure recorded. Therefore acceleration effects, although present, are negligible within the 0.8 ms window.

Beyond the 0.8 ms window the results from the accelerometers clipped, indicating levels up to 20,000 g. At approximately 1 to 2 ms, acceleration levels reach their maximum values. In this interval the pressure-time profiles do not indicate the presence of acceleration where the profiles are smooth. Therefore it is concluded that acceleration from the walls has negligible effect, below 5 %, on the pressure results.

#### 4.3 Comparison with predictive computer models.

Results are provided from a semi-empirical program CONWEP [4] for comparisons with the measured results and to illustrate the sensitivity of the explosive parameters to the charge and transducer separation distance, Table 3. From these results an error in the separation distance of +5 or -5 cm (ie. 1 %) gives rise to an error in the peak reflected pressure of 32 % and 22 % respectively. This error is conceivable in the experimental configuration but time of arrival of the shock wave indicates that the transducers were located close to 0.50 m. Hence differences in the peak pressures between piezoelectric and piezoresistive transducers are not due to the transducer separation distance.

**Table 3**  
**Predictions from CONWEP.**

Explosive Parameter	Charge to transducer separation distance (m)								
	0.400	0.425	0.450	0.475	0.500	0.525	0.550	0.575	0.600
Incident Pressure (MPa)	2.78	2.47	2.20	1.97	1.77	1.60	1.45	1.31	1.20
Normally Reflected (MPa)	20.1	17.3	14.99	13.0	11.38	9.98	8.79	7.77	6.90
Time of Arrival (ms)	0.14	0.155	0.172	0.189	0.208	0.227	0.247	0.268	0.290
Positive Phase (ms)	0.327	0.394	0.479	0.583	0.706	0.840	0.968	1.07	1.12
Incident Impulse (Pa.s)	104	108	112	118	124	130	131	129	126
Reflected Impulse (Pa.s)	759	697	643	597	556	521	489	461	435
Shock Front Velocity (km/s)	1.67	1.58	1.50	1.42	1.35	1.29	1.23	1.18	1.13

A profile from a simulation using the Ray Tracer module on the BLAST software from Combustion Dynamics [5] is also provided (Figure 9). The charge mass, 0.3025 kg TNT equivalent, was assumed spherical and the measurement point was taken at location 0.5 m, 0.5 m and 0.007 m. The simulation was run for 4 ms at 1  $\mu$ s increments calculated to fourth order reflections, with an initial pressure of 101.3 kPa, that is, atmospheric pressure. The output profile was plotted every 50  $\mu$ s.

Both the predictions from CONWEP and the simulation from BLAST are in good agreement with the experimental results, considering that the problem has been oversimplified. For example, these results do not take into consideration the properties of the combustion by-products, which alter the specific heat ratio  $\gamma$ . Other effects not considered are the deformation on the panels and energy transmission through the walls, suggesting that these effects are initially negligible.



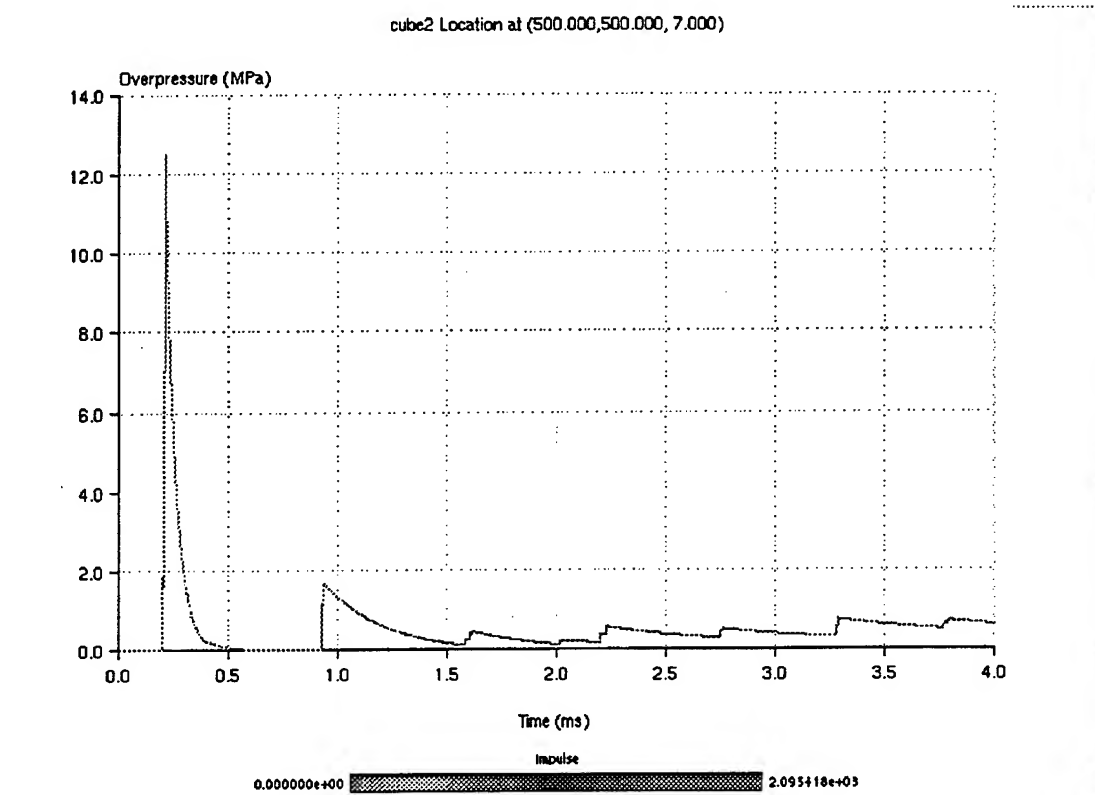


**Figure 9 Simulation from BLAST using Ray Tracer.**

#### **4.4 Repeatability and consistency of the pressure measurements and future developments.**

Overall the results indicate similar profiles with closest correlation in time of arrival. Peak pressures are not in agreement, although impulse measurements are within 400-500 Pa.s, except for event 4, P1. This may have resulted from the connector which may have given rise to an intermittent signal, therefore resulting in a higher level.

The only complete direct record, event 5, P1, indicated that the rise time of the incident pressure is around 6  $\mu$ s (Figure 10). Although it is evident the tape recorder does smooth the signal, which is expected given its 80 kHz bandwidth, peaks are faithfully recorded to within 5 %. Furthermore, time marks with a 5 ns rise time, which were recorded on a separate channel during each event, confirmed that the tape recorder is capable of faithfully recording a 6  $\mu$ s rise time. The time marks rise time on tape were 4.4  $\mu$ s.

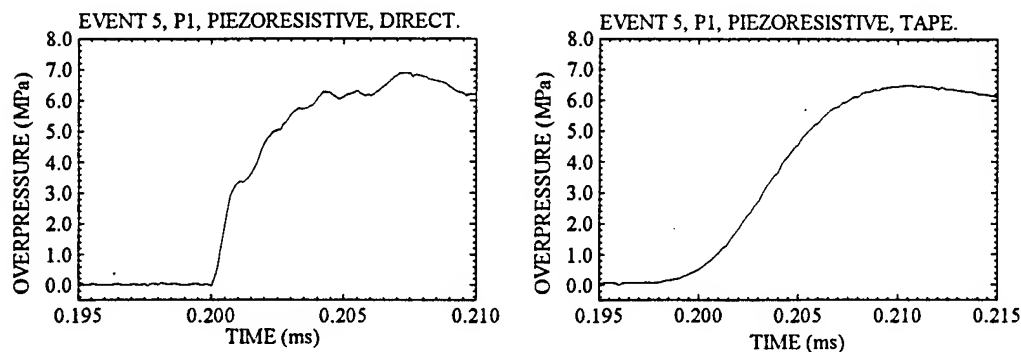


**Figure 10 Comparison of peak pressure rise times between recording directly on the CRO and on tape.**

Results have shown that the measurement and recording technique is adequate for these experiments but the instrumentation needs refining and additional tests are required. The limitation in the analogue bandwidth means that the tape recorder is the weakest link in the system. The next stage is to use digitisers with similar signal to noise ratio but capable of capturing faster signal rise times. AMRL has since procured 12 bit digitisers which satisfy this criterion.

Additional experiments need to check the repeatability of measurements and determine if the detonation is symmetrical, especially close in to the explosive charge. Comparisons between transducers should be made with the transducers on the same panels almost exactly at the same location.

The piezoelectric transducers are better suited in this environment but suffer from thermal effects. Further tests will be conducted to investigate improved thermal protection techniques [6].

## 5. CONCLUSION

This series of experiments has indicated that previous measurements conducted on a parametric cubicle study by using the PCB 109A piezoelectric transducer and an 80 kHz analogue tape recorder are valid to 4-6 ms. Beyond this time, heat conduction effects predominate, resulting in a negative baseline drift. Although piezoresistive transducers are more resistant to heat conduction and therefore record static pressures, they suffer from a design limitation in the cable connection at the transducer end. This limits the application of these transducers for this experimental configuration, where damage occurs to the transducer from cable whipping early in the event.

High speed video has shown that the transducers are exposed to a thermal environment resulting from the explosive fire ball for up to 1.17 ms after detonation of the pentolite charge. Cable whipping of the piezoresistive transducer occurs in the initial expansion phase, where failure arises at about 3.5 ms. Thermal flash does not appear to occur in the pressure records.

Streak photography and acceleration measurements were in good agreement. To obtain peak accelerations further analysis is required and will be the subject of another report. The results indicated that the pressure transducers are insensitive to acceleration in the pressure regime of interest.

The new pressure transducer mounts proved mechanically superior to the previous mounts used during the cubicle parametric studies where they did not suffer deformation. The reduction in mass by 40 % in the mounts had no effect on the peak pressures compared with results from the parametric study, further confirming that acceleration effects on the transducers are negligible.

Further experiments will be conducted to test the repeatability of the results, namely explosive performance and the symmetry of shock propagation. This will include measurements to quantify heat effects and to further develop heat protection and acceleration mounting techniques.

This report has demonstrated the need to carefully assess secondary effects on the transducers from nearby explosive events. The recording instrumentation also needs to be assessed so that it faithfully records the signals. If these effects are not delineated, or the instrumentation limitations not clearly understood, results may be erroneously interpreted.

## 6. ACKNOWLEDGMENTS

The author would like to thank Dr N. Burman for support of this work and Mr D. Ritzel for valuable discussions. Also thanked are Mr D. H. Sanford for strain measurements, Miss G. Halden for recording, Mr M. Buckland for the preparation of the cubicles, and Mr P. G. Kiernan for assistance on the mounting of the pressure transducers. Mr C. Killoh is thanked for the fabrication of the accelerometer housings, Messrs T. E. Symes and R. H. E. Huang for the accelerometer isolation pads, Mr M.G. Wilson for the firings, Mr T. Kinsey for the streak photography and Mr J. O. Nicholls for high speed video. Mr E. Northeast is acknowledged for the pressure-time profile from Ray Tracer (Figure 9).

## 7. REFERENCES

- [1] Burman M N, Saunders D S, Ritzel D V and Buckland M E (1993), "Deformation and Fracture of Compartments Subjected to Internal Blast Loading", 5th Australian Aeronautical Conference, 13-17 September 1993, The Institution of Engineers, Australia, National Conference Publication no, 93/6, Melbourne.
- [2] Burman M N, Buckland M E, Turner T G, Boyd S D and Walsh B E, "Derwent Mockup Compartment Blast/Fragmentation Testing for SSEP", presented at International Naval Platform Vulnerability/Survivability Workshop, HMAS Stirling, Australia, 1994.

[3] Ritzel D V, Burman M N, Saunders D S and Buckland M E (1993), "Internal Blast Damage to Ship Compartments", 13th International Symposium on the Military Application of Blast Simulation, 13-17 September 1993, The Hague, The Netherlands, Proceedings, vol. 1.

[4] CONWEP, U.S. Army Corps of Engineers, Washington, 1990.

[5] Thibault P and Sulmistras A, "Fluid Dynamics/Blast Prediction and Structural Response Workstation", Combustion Dynamics Ltd, Medicine Hat AB, Canada, 1991.

[6] Dumitrescu M P, Labracherie L, Burtschell Y and Houas L (1992), "Protecting Pressure Gauges with Grease in High Temperature Facilities", Shock Waves, 2, pp 269-271.

# THE CHARACTERIZATION OF A NEW EXPLOSIVE USING SMOKE TRAIL PHOTO-DIAGNOSTICS

D.J. McMillin and J.M. Dewey

Dewey McMillin & Associates Ltd  
Suite 100, 1741 Feltham Road, Victoria, BC  
Canada V8N 2A4

## SUMMARY

Smoke trail photo-diagnostics were used to characterize the blast wave produced in the explosion of a 23-ton spherical charge of QM-100/R suspended 57 feet above the ground surface. Shock front and particle trajectories were measured, including the trajectory of the triple point and the trajectories of both the free-air shock front and the Mach stem. Also measured were the reflected shock front above the triple point and the slipstream, or contact surface. From the free-air shock front trajectory it was determined that the energy yield of the charge used was equivalent to 20.9 tons TNT at five atmospheres peak static overpressure. Greater values were determined at other peak overpressure levels and in the Mach stem region. Measured particle trajectories were used to define piston paths, to numerically reconstruct the complete free-air and Mach stem blast waves. The *AirBlast* database and retrieval system was used to compare these reconstructed blast waves with other measurements and the generic reconstructions of other blast waves, those from standard TNT for example.

## 1. INTRODUCTION

The correct evaluation of the results from any experiment, of target response for example, depends on a diagnosis of the airblast environment for that experiment. For such a diagnosis a large number of electronic, point measurements are usually made. However, the best measurement of the airblast environment is obtained using photogrammetric methods.

Photographic measurements of particle motion permit the use of the piston path method and the derivation of a complete set of airblast parameters, thereby providing a relatively accurate, direct measurement of the environment. Such characterizations are not necessarily local; one photographic measurement can be used to characterize the airblast environment over the entire test bed. Photographic measurements also provide a relatively inexpensive backup for the electronic point systems.

The overall objective of this experiment was to provide a measurement of the airblast environment on the entire test bed, thereby characterizing the new explosive

being used. Specific objectives included the construction and fielding of an airblast diagnostic system using smoke trails, to make measurements which later allowed the calculation of all of the physical parameters in the blast waves from a large scale height-of-burst explosion, specifically, static, dynamic and total pressures, particle velocities, densities, temperatures, sound speeds and available energy densities and fluxes. Measurements were to be made allowing the calculation of time histories and wave profiles, as well as peak data values, over a large range of distances measured from the charge centre in the primary, free-air shock region above the triple point and measured as ground ranges in the Mach reflection region. TNT equivalent energy yields of the new explosive being used were to be calculated.

## **2. DESCRIPTION OF THE EXPERIMENT**

### **2.1 Test parameters**

The MIDDLE KEY 4 test involved the detonation of 22.7 tons of a new explosive called QM-100/R suspended in a flexible spherical container the center of which was 57.3 feet above the ground surface. Two pounds of Pentolite were used to initiate the detonation at approximately 11:00 AM local time on 17 September 1993 at the White Sands Missile Range in New Mexico. At the time of the test the ambient air temperature was 75.2 F, the atmospheric pressure was 12.5 psi and the relative humidity was 30.5%. The wind speed varied between 10 ft/s and 20 ft/s. The sound speed, calculated from the ambient temperature and humidity, was 1136 ft/s.

### **2.2 Smoke launchers**

The usual smoke launcher design was altered specifically for this experiment. The smoke launchers usually employed on large HE tests use a 2-foot piece of 2-inch diameter plastic tube as a mortar barrel. One-inch diameter inner tubes are fired into the air just prior to the arrival of the blast wave from the main explosion. The moving tubes leave behind them a trail of smoke, which is a very fine powder being either carbon lamp black or a 20:1 mixture by volume of fumed silica and titanium dioxide. These smoke powders consist of sub-micron sized particles which behave as excellent flow tracers. Smoke launchers and use of smoke tracers on large ANFO tests are described in references 1 through 5.

For this experiment the launchers' inner tubes were capped instead of being left open at each end. The cap used on the upper end of each inner tube was loose fitting while the cap placed on the lower end of each tube was tight fitting. To each of the tight fitting caps was fastened one end of strong nylon fishing line, the other end of which was fastened to the ground beside the smoke launcher. The line was wrapped loosely around an inverted peach bucket in a manner that let the bucket behave as a spool, allowing the line to unwind freely after the inner pipe was

launched. When shot into the air, the inner tube reaches the end of its tether line and is brought to an abrupt halt. The loose fitting cap is shaken off and additional smoke powder is released, at a height roughly equal to the length of the tether line.

The purpose of the tethering described above was to ensure that there would be smoke placed at heights in the region of the free-air blast wave over the triple point trajectory, higher than the normal 40-50 ft reached by the previously used, untethered smoke trails. The lengths of nylon line used and therefore the heights of maximum smoke placement were 60 ft on launchers near the charge to generate smoke trails slightly higher than the charge height of 57.3 ft, and 100 ft on launchers farther from the charge where the triple point trajectory was higher. The pipe cap modification did not prevent smoke from being left in the air at heights lower than the maximum height.

The smoke trails as they were intended to appear in this experiment are shown in figure 1. Two groups of four trails each were to be used, with black and white smoke alternating. The two groups were to be fired independently of each other, both one-half second before the main charge. The triple point trajectory used for planning was taken from the photogrammetric analysis of a 1000-lb TNT explosion at a height of burst equal to that of the present test after cube-root charge weight scaling.

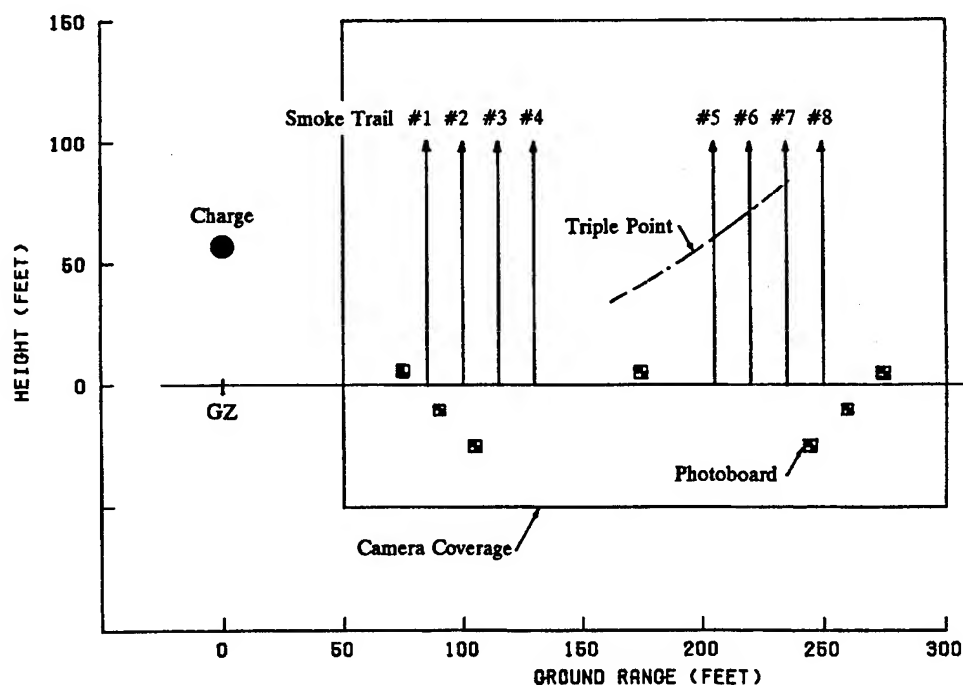


Figure 1. The smoke trail experiment as it was planned, as seen from the camera position. Smoke was needed higher than the charge and the triple point in order to measure the free-air blast wave, and near the ground surface in order to measure the Mach stem blast wave. The triple point trajectory shown here is a prediction which was made by scaling results from a 1000-lb TNT height-of-burst experiment.

### 2.3 Experiment layout

The closest smoke trail was 85 ft from the charge, where the peak static overpressure in the free-air blast wave was expected to be 10 atm (125 psi). The closest trail was hopefully the one which would provide the desired piston path. The other trails in the first group of four trails were backups, in case the first trail failed to define an adequate path. The sought-for path would be used to numerically reconstruct the primary, spherical free-air blast wave, above the triple point. It was also hoped that at least one of the trails in the closest group would provide a second path, one which could be used to reconstruct the Mach stem blast flow under the triple point.

The farthest smoke trail was 250 ft from the charge, at the distance where the triple point trajectory was predicted to be about 100 ft above ground. Smoke trails above the triple point beyond 200 ft ground range were desired for use in adjusting the free-air reconstruction. The reconstructed far-out flow would be compared with measurements and the close-in piston path would be fine-tuned if necessary. The far-out group of trails would also be used in the Mach stem reconstruction, to fine-tune it as described above or to define a piston path should the close-in trails not be able to do so.

A plan view of the experiment is shown in figure 2. Two lines of smoke launchers were installed along two opposing radials, one to the south-east from ground zero, bearing 130 degrees, and the other to the north-west, bearing 327 degrees and 30 minutes. Four cameras were used to photograph the motions of the smoke trails,

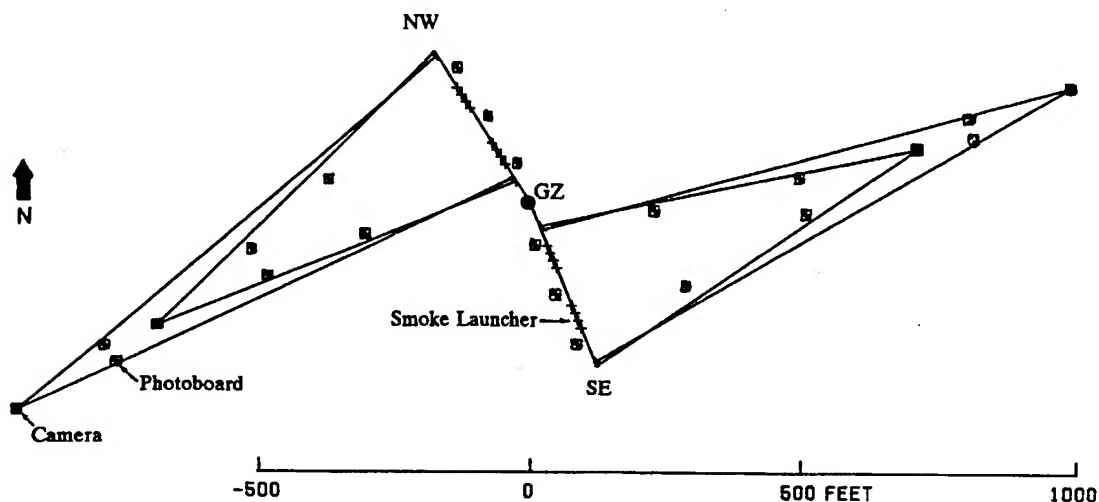


Figure 2. Layout of the smoke launcher experiment. Eight launchers were placed on each of two radial lines passing through GZ, one to the south-east (SE) and the other to the north-west (NW). Two cameras were used per radial line to photograph the motions of the smoke trails. A total of eighteen photoboards were positioned and surveyed for use as reference markers in the later analysis of the smoke trails' motions.



two for each radial line of eight launchers. For each radial, one 70-mm PS10B was positioned to act as the main camera, providing high resolution images, and one 35-mm PS4C was positioned to act as a backup camera. For each of these cameras on both radials, the fields of view were nearly identical. All four cameras were loaded with colour film and were to record IRIG timing signals. The two 70-mm cameras were set to run at a speed of 720 pps and the two 35-mm cameras were set to run at 1000 pps. A total of 18 accurately-surveyed photomarkers were positioned in the cameras' fields of view, for use in the subsequent analysis of the motions of the smoke trails in the blast wave.

### 3. RESULTS

#### 3.1 Operation of the launchers and cameras

All cameras operated as planned. The fields of view were as intended and all of the appropriate photomarkers were clearly visible on the films. Exposure and focus were good. The IRIG timing marks were recorded.

All 16 smoke launchers fired. Fourteen made smoke trails as planned. Two made trails reaching a height of only about 15 ft (trail number 2 on the south-east radial at 100 ft ground radius and trail number 7 on the north-west radial at 235 ft ground radius, both white). All 8 trails in the two groups close to the charge, with one exception, reached heights equal to or exceeding the charge height. None of the far-out trails reached the planned height of 100 ft, but the triple point was lower than predicted and consequently all 8 far-out trails, with one exception, reached heights above the triple point.

The motions of all of the smoke trails were recorded successfully on film with satisfactory contrast and resolution. The black smoke trails were seen more clearly than the whites, as has been the case in all previous smoke trail experiments done in bright sunlight at the WSMR New Mexico test site.

An early photograph of the smoke trails is shown as figure 3a, on the south-east radial approximately 37 ms after charge detonation. The four smoke trails on the left hand side of the photograph have not been hit by the blast wave from the explosion, but all four trails beside the black detonation cloud on the right hand side have been hit and are moving. Refractive images of the shock fronts can be seen against, and just to the left of, the support tower. These are the primary and the reflected shock fronts, and the Mach stem shock front. The point where they all intersect, the triple point, is also seen. The slipstream, or contact surface, can be seen both refractively and as a sharp, step-like discontinuity in two of the close-in smoke trails.

A later photograph of the smoke trails is shown as figure 3b, approximately 117 ms after detonation. All trails have been hit. The slipstream is seen near the top of trail number 5, the first trail in the far-out group (black) and trail number 6 (white).

The lower portions of all the smoke trails in the close-in group are, increasingly,

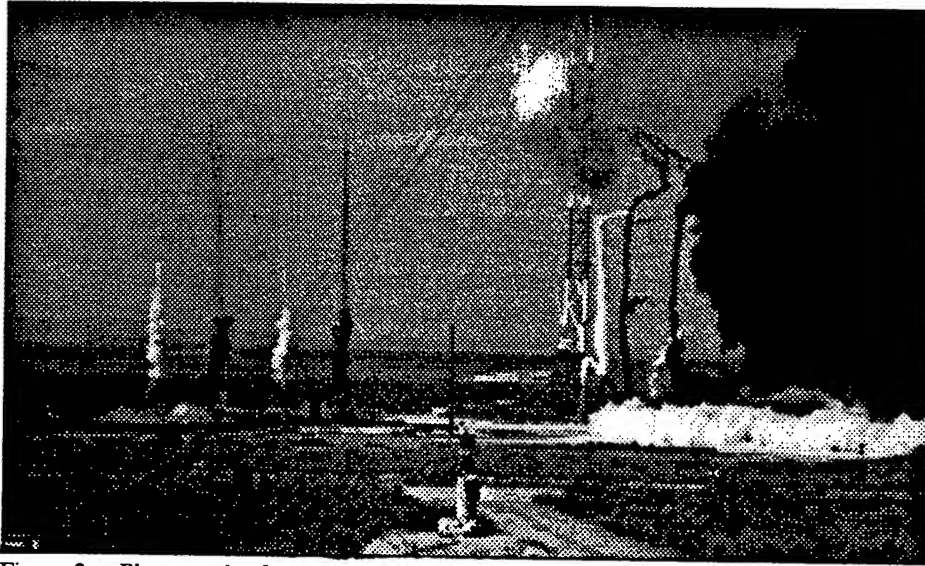


Figure 3a. Photograph of smoke trails on the south-east radial approximately 37 ms after detonation. The four trails on the left hand side have not yet been hit by the blast wave. The four trails on the right have been hit by the shock fronts whose refractive images can be seen near the charge support tower. Trail number 2, the second trail from the right and white, is short because of a launcher failure. The contact surface can be seen as a sharp, step-like discontinuity at the bottom of trails number 3 (black) and 4 (white).

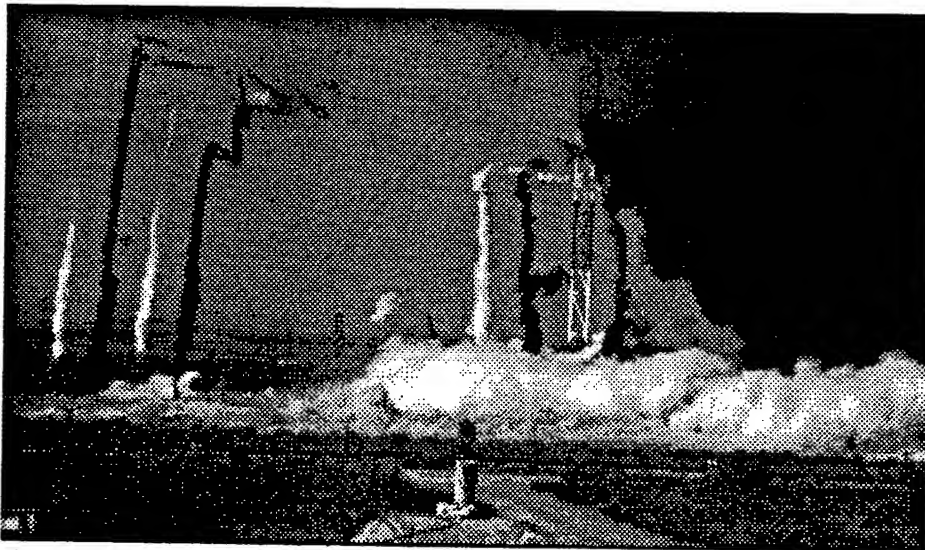


Figure 3b. Photograph of smoke trails on the south-east radial approximately 117 ms after detonation. All trails are now moving. The contact surface is seen near the top of trails number 5 (black) and 6 (white). The shock fronts have left the photo on the left.

obscured by a cloud of white dust and smoke rising from the ground surface. Trail number 2, shorter than intended because of a launcher misfire, is totally obscured.

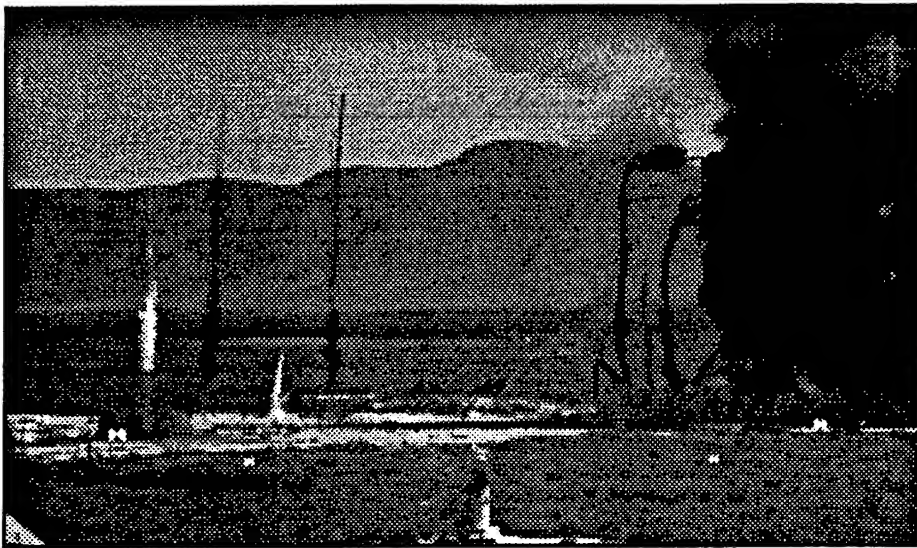


Figure 4a. Photograph of smoke trails on the north-west radial approximately 37 ms after detonation. The four trails on the left have not been hit and the four on the right have been hit by the shock fronts whose refractive images can be seen against the natural background and the charge support cables. The contact surface is seen as a sharp discontinuity at the bottom of smoke trails number 3 (black) and 4 (white). The closer-in white trails appear grey in the shadow of the fireball. Trail number 6 (white) is short because of a launcher failure.

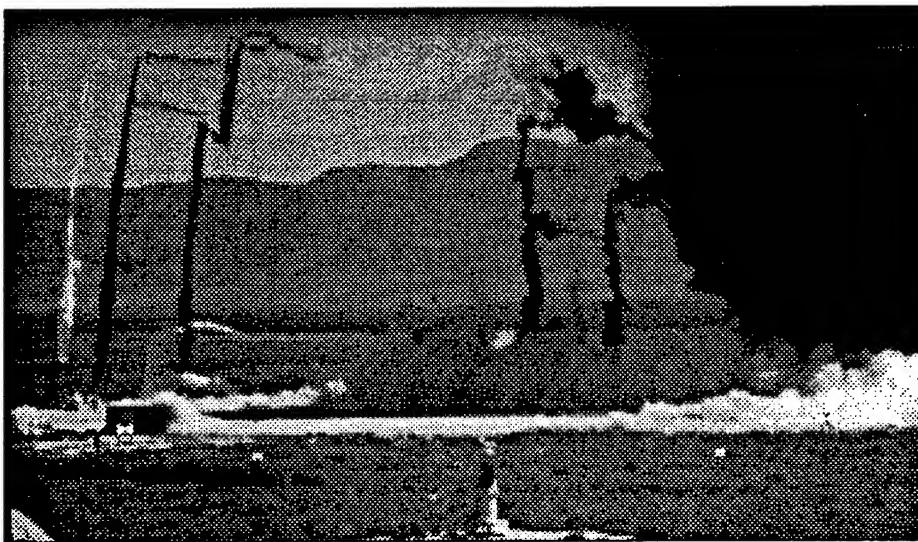


Figure 4b. Photograph of smoke trails on the north-west radial approximately 117 ms after detonation. All the trails are moving. The contact surface is seen near the top of trail number 5 (black). The horizontal branch lines of smoke are created by various launcher artifacts.

The photographs shown in figure 4 correspond in time to those shown in figure 3, but are from the opposing radial (north-west compared to south-east).

Various features such as horizontal lines, smudges and wiggles, can be seen in both figures 3 and 4, but these are familiar artifacts caused by the pipes, caps, blocks and rags, which are shot into the air when the smoke launchers are fired. These artifacts do not interfere with the flow and do not affect the analysis of the smoke trails, and they should be ignored.

To examine the motion of the smoke trails more closely, a photogrammetric analysis was undertaken. This involved the transformation of measurements made on a projector tabletop into a real-world object plane. Vital for the transformation are visible images of accurately surveyed photomarkers and accurate positions of the camera lenses. In this experiment, all the required camera calibration constants were calculated without any problems, indicating that the photomarkers and camera lenses were accurately surveyed.

### 3.2 Shock front trajectory measurements

The visible shock fronts and triple point were digitized relative to the accurately surveyed photomarkers, frame by frame, and transformed into real-world positions using proven algorithms which correct for optical distortion, perspective, *etc.* Time values were assigned to each frame using the timing marks written onto the film at the time of its exposure.

The measured trajectory of the triple point is shown in figure 5. The measured trajectories are only slightly different along the two opposing radials, south-east and north-west, and in both cases the triple point heights are definitely lower than those which were predicted before the test.

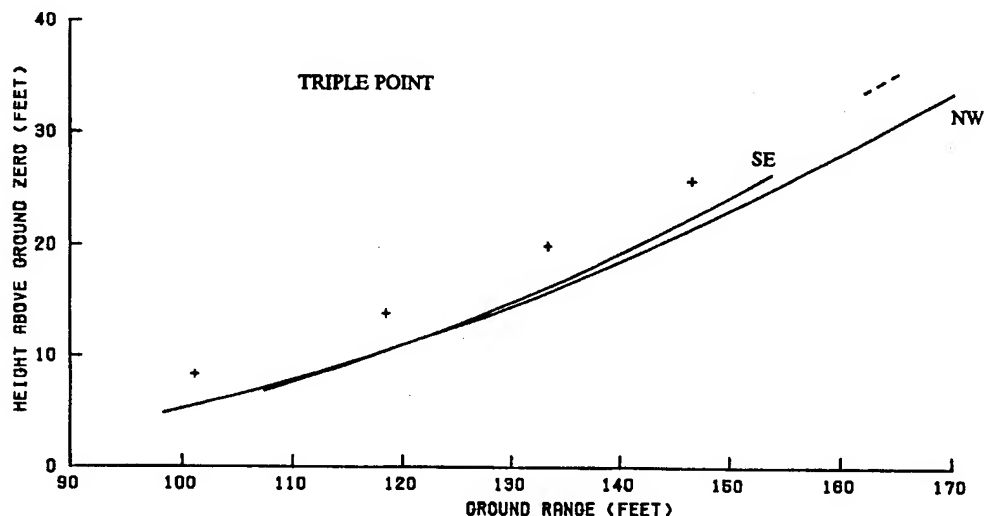


Figure 5. Triple point trajectory. Solid lines are results from the refractive analysis. SE is the south-east radial result and NW the north-west. The broken line is the prediction which was used to plan the experiment, scaled from a 1000-lb TNT experiment, and the points are predicted heights calculated using a 2-dimensional hydrocode (ARA).

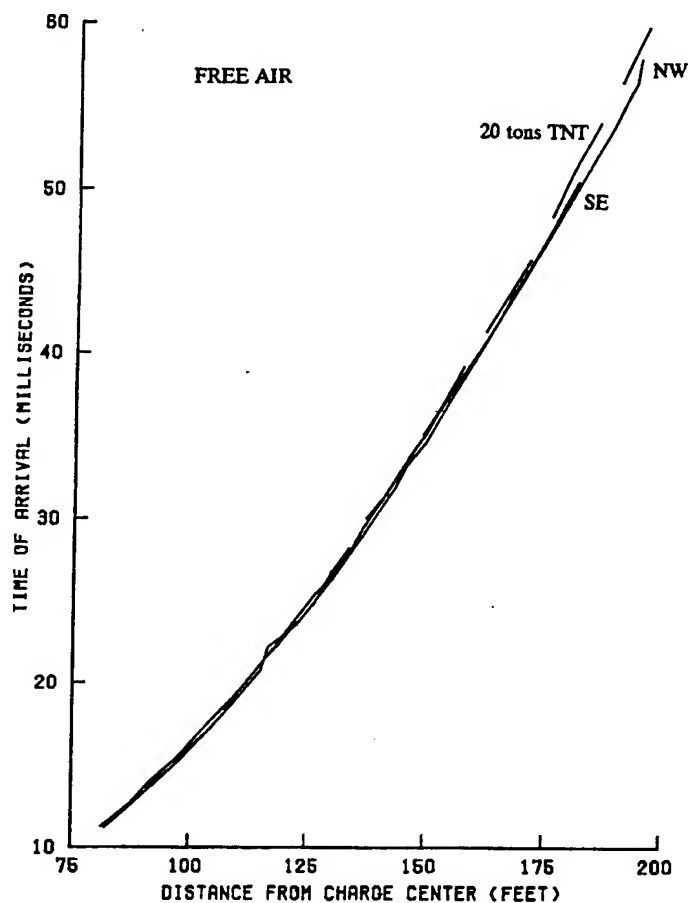


Figure 6. Times of arrival of the primary, free-air shock front. Solid lines are the results from refractive image analysis. SE is the south-east radial and NW the north-west. The broken line is a result for 20 tons of standard TNT in free air under the test conditions, obtained from a database called *AirBlast*.

The measured trajectory of the free-air shock front is shown in figure 6. It was assumed in the analysis that the portions of the shock front seen on film were spherical and centred on the surveyed charge center. The measured results support this assumption, that is, the two trajectories which were measured in the opposing directions, south-east and north-west, are virtually identical.

Peak overpressures behind the free-air shock are shown in figure 7. These were derived from the trajectories shown in the previous figure. The trajectories were smoothed and differentiated to obtain shock speeds and then the Rankine-Hugoniot equations used to compute the peak overpressures. There is no significant difference in the results for the two opposing directions, south-east and north-west.

The measured overpressures were compared to those which would be produced by 20 tons of standard TNT under the same test conditions. Overpressures which

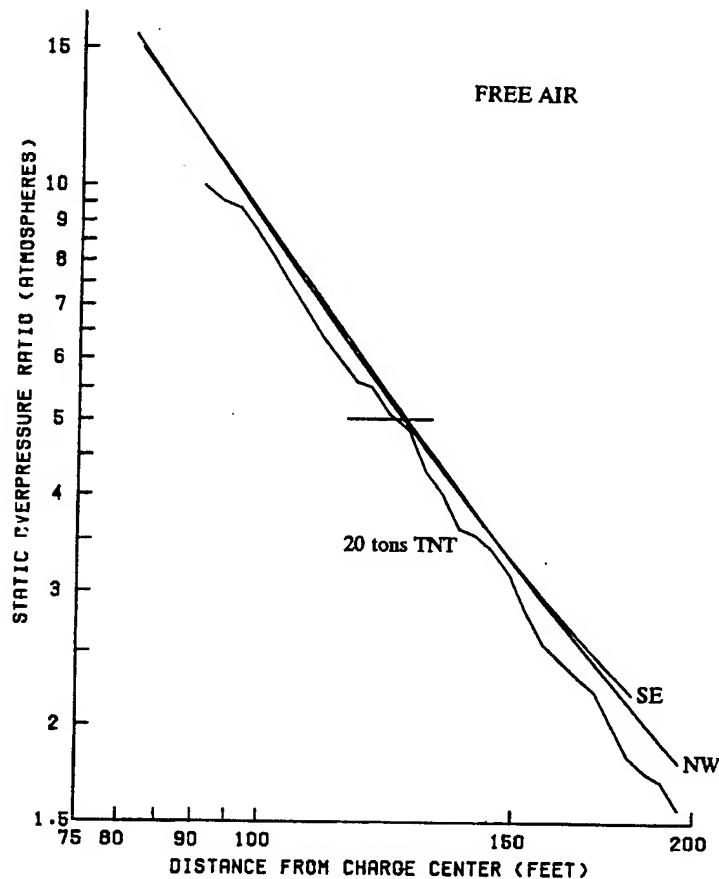


Figure 7. Peak static overpressures behind the free-air shock. Solid lines are the results from refractive image analysis. The broken line is the 20-ton TNT result from the *AirBlast* database. Comparing results at 5 atm overpressure puts the energy yield of the MIDDLE KEY 4 charge at 20.9 tons TNT equivalent.

were measured were found to be everywhere greater than the 20-ton TNT values, with the smallest differences at the 5 atm peak overpressure level, at around 125 ft spherical radius. The cube of the ratio of the distances at which the overpressures were exactly 5 atm was used to estimate the (minimum) relative energy yield.

The measured Mach stem trajectory and overpressures are shown in figures 8 and 9, respectively. Again, both measurements are virtually identical in the two opposing directions, south-east and north-west. If Mach stem overpressures are compared to 20 tons of standard TNT at the same charge height and test conditions, even greater differences are seen, compared to the differences seen in the free-air case.

Electronically-measured results are included in both figures 8 and 9, and are in both cases in good agreement with the results determined photographically. (No electronic gauges were positioned in the free-air region at distances where the blast wave was photographed, and no comparisons were possible in the free-air case.)

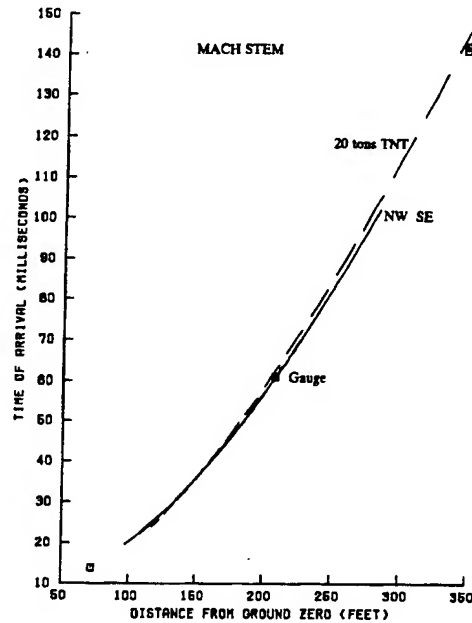


Figure 8. Times of arrival of the Mach stem shock front. Solid lines are the results from refractive image analysis. They are virtually identical on each of the two radials. The broken line is 20-tons of TNT scaled to the same height of burst and test conditions, using the *AirBlast* database and retrieval program. The points are electronically-measured results.

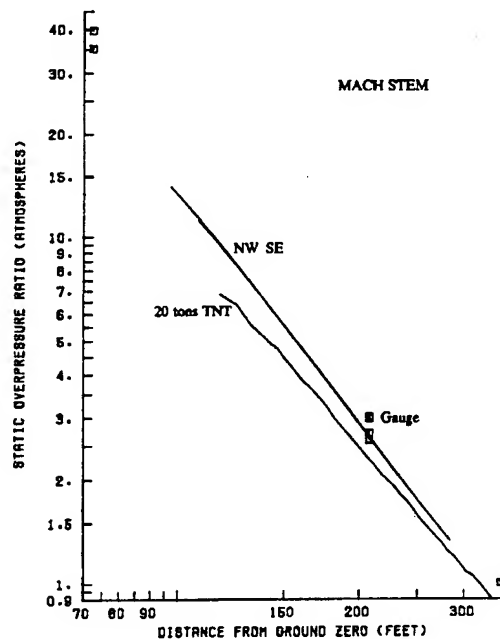
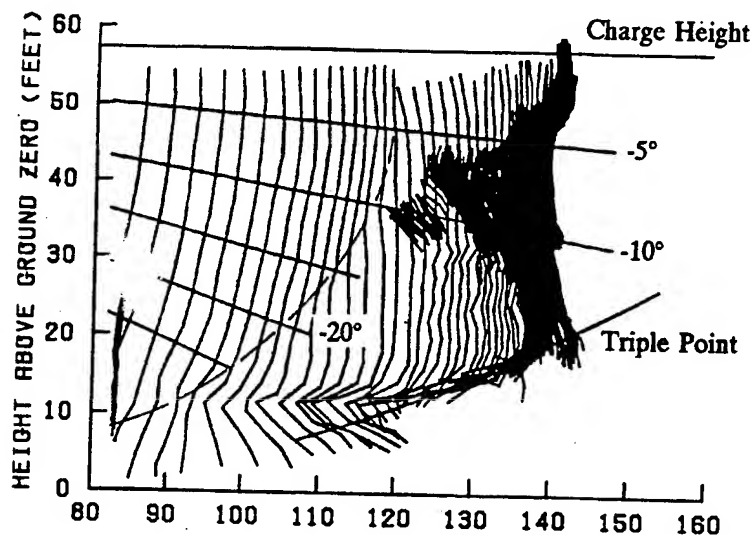


Figure 9. Peak static overpressures behind the Mach stem. The solid lines are results from the refractive image analysis, again virtually identical on the two radials. The broken line is the 20-ton TNT result from *AirBlast*. The points are electronically-measured results.

# TRAIL 1

a) SE



b) NW

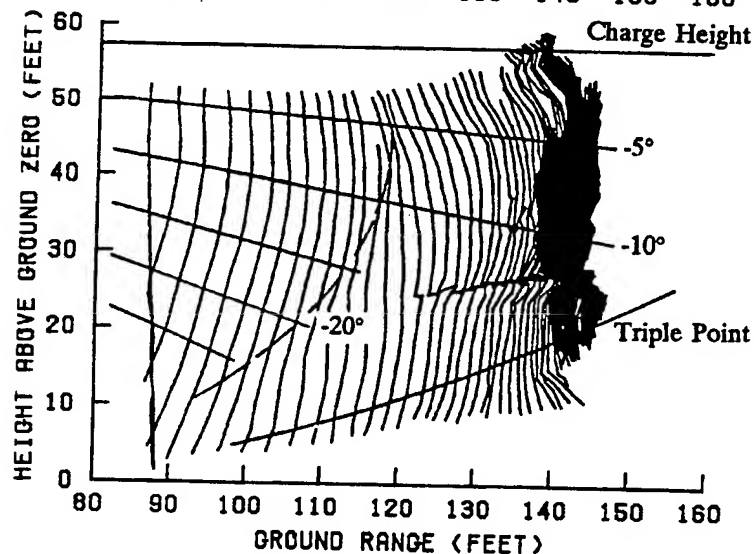


Figure 10. Frame-by-frame positions of smoke trail number 1, as it moves in the blast wave along (a) the south east radial and (b) the north-west radial. The trajectory of the triple point was measured using refractive image analysis. Straight lines passing through the charge centre were used in computing individual particle trajectories. The spherical free-air flow ends when the upward-moving reflected shock front arrives (shown approximately by a broken line). The dark mass on the right hand side is the smoke trail stopping and reversing direction, moving back towards the charge and overwriting its earlier positions. In this and the next two figures the initial position of the smoke trail is on the far left and the direction of motion in the blast wave is opposite to that shown earlier in the photographs (figures 3 and 4).



### 3.3 Particle trajectory measurements

The centerlines of all the smoke trails were digitized as they appeared in projected film frames, relative to the surveyed photomarkers. Each smoke trail's motion was recorded for several frames before the arrival of the blast wave, and then until the frame in which either the trail left the camera's field of view or its motion no longer appeared to represent simple blast wave flow (when the trail was lost to turbulence or when it began to move upwards behind the rising detonation products).

The digitized data were transformed using the calculated camera calibration constants into the object plane which contained the actual smoke trails, the vertical plane on their line through ground zero. It was assumed that the smoke trails were all initially formed in that object plane and that the blast wave was symmetrical about the vertical axis through the charge center, and that therefore the smoke trails did not move out of their original plane.

The complete history of the smoke trail closest to the charge, trail number 1, is shown in figure 10. Shown are the trail's positions in the object plane along both the SE and NW radial lines, for all of the film frames digitized. The largest portion of the trail lies above the triple point trajectory. Dust raised by the blast increasingly obscured the lower ends of all trails, but especially those close in.

Straight lines are drawn in figure 10, all through the charge center including a horizontal line at the charge center height. These straight lines end at a boundary approximated in the figure by a broken curved line. This boundary is where the flow is no longer spherical, but is influenced by the upward-moving reflected shock (the trails are need *not* look circular in the spherical flow, note). Although the reflected shock itself is not shown in figure 10, its effect is seen in the changing shapes of the smoke trails and in the speed at which they move along the straight lines.

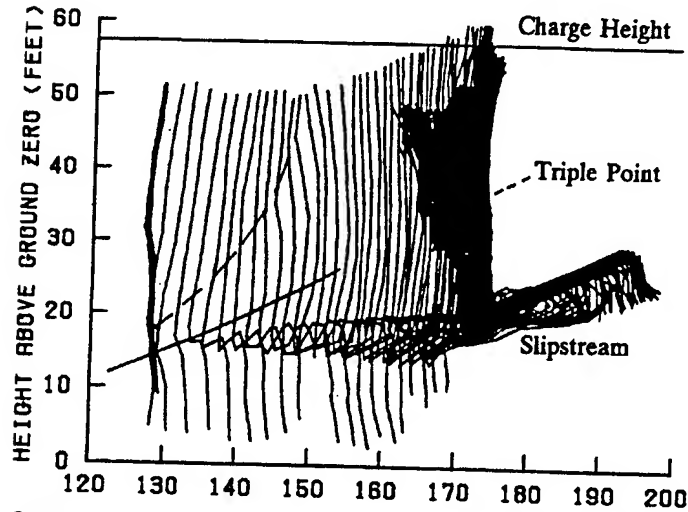
The complete history of trail number 4 is shown in figure 11. At this position the triple point is higher and a sharp, step-like discontinuity in the smoke trails is seen, the length of which increases in time. This discontinuity is the slipstream, or contact surface. Air above the contact surface has been shocked twice, once by the primary shock and again by reflected shock, while air below it has been shocked only once, by the Mach stem shock. At the ground ranges shown in this figure, the heights of the contact surface above the ground run from about 15 ft to about 25 ft.

The history of the first far-out trail, trail number 5, is shown in figure 12. The slipstream discontinuity is seen near the upper end of the trail at heights between about 55 ft and about 70 ft, generally higher than the charge. The trails beyond trail number 5 (trails 6, 7 and 8) did not show the slipstream. They remained more-or-less straight and vertical, moving entirely in the Mach stem flow.

The time-resolved trajectories of intersection points, intersections of the smoke trails and specific straight lines, were measured in order to obtain piston paths for the numerical reconstruction of the free-air blast wave and, independently, the Mach stem blast wave.

# TRAIL 4

a) SE



b) NW

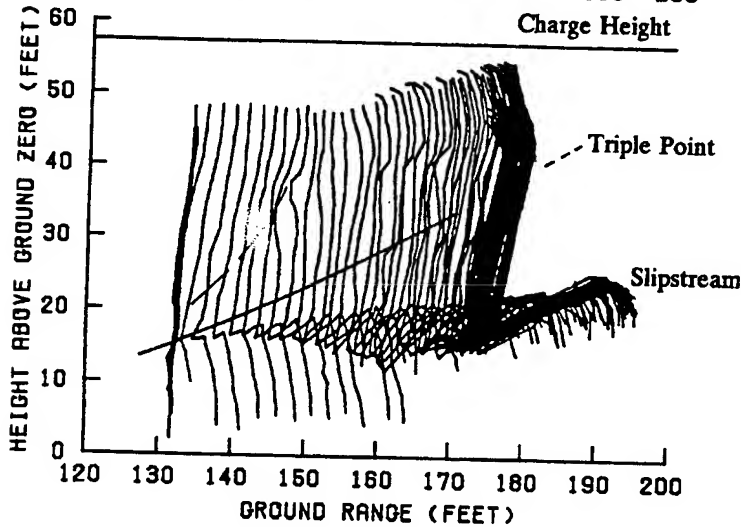
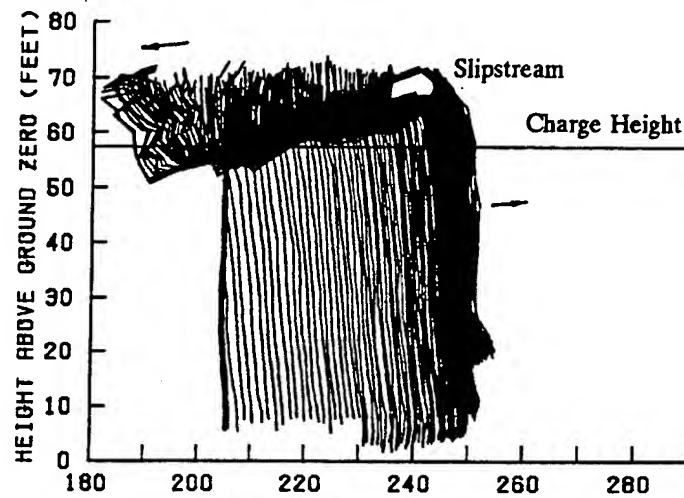


Figure 11. Frame-by-frame positions of smoke trail number 4, as it moves along (a) the south east and (b) north-west radials. Refer to the text and the previous caption for more details.

The motions of trail number 5 are especially interesting when the trail's positions are viewed cinematically, frame-by-frame in time sequence rather than all together as in figure 12. The trail moves in the blast wave away from its starting position and comes slowly to a halt at about 250 ft. Then the portion below the slipstream moves backwards in the negative flow phase, but only for a relatively short time, after which it moves outwards again in the secondary shock flow. It continues to move outwards in the secondary flow for a relatively long time. The upper portion of the smoke trail moves initially like its lower portion, at first outwards in the primary flow and then backwards in the negative flow, but unlike the lower portion the upper portion never

# TRAIL 5

a) SE



b) NW

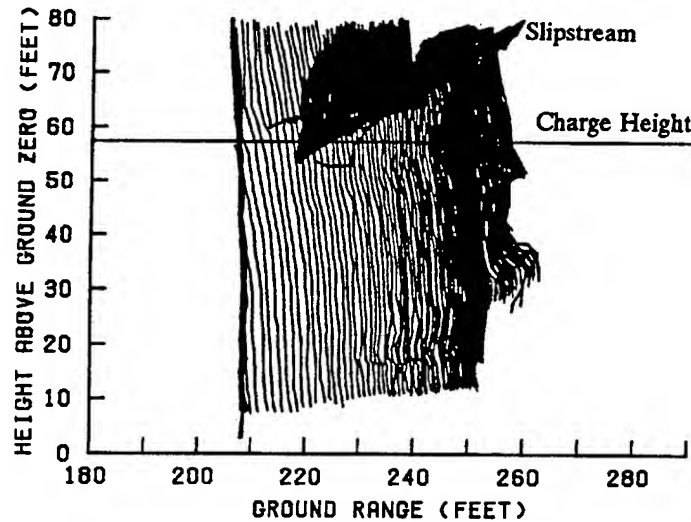


Figure 12. Frame-by-frame positions of smoke trail number 5, along (a) the south east and (b) the north-west radial. Refer to the text and the caption for figure 10 for more details.

moves definitely outwards again. As the lower portion of the trail moves outwards in its strong secondary flow, the upper portion continues to move inwards in its strong (second?) negative phase. Such definite contrary motions on the two sides of a contact surface have not been seen before by these authors.

As far as measurements made on the ground surface are concerned, a single Mach reflection is pseudo-one-dimensional and can be numerically reconstructed using a (hemi)spherical piston (but the flows do *not* copy surface burst flow, note). For a wide range of HOB, it has been shown that Mach stem flows can be modelled on a single position coordinate, radial distance from ground zero (reference 6).

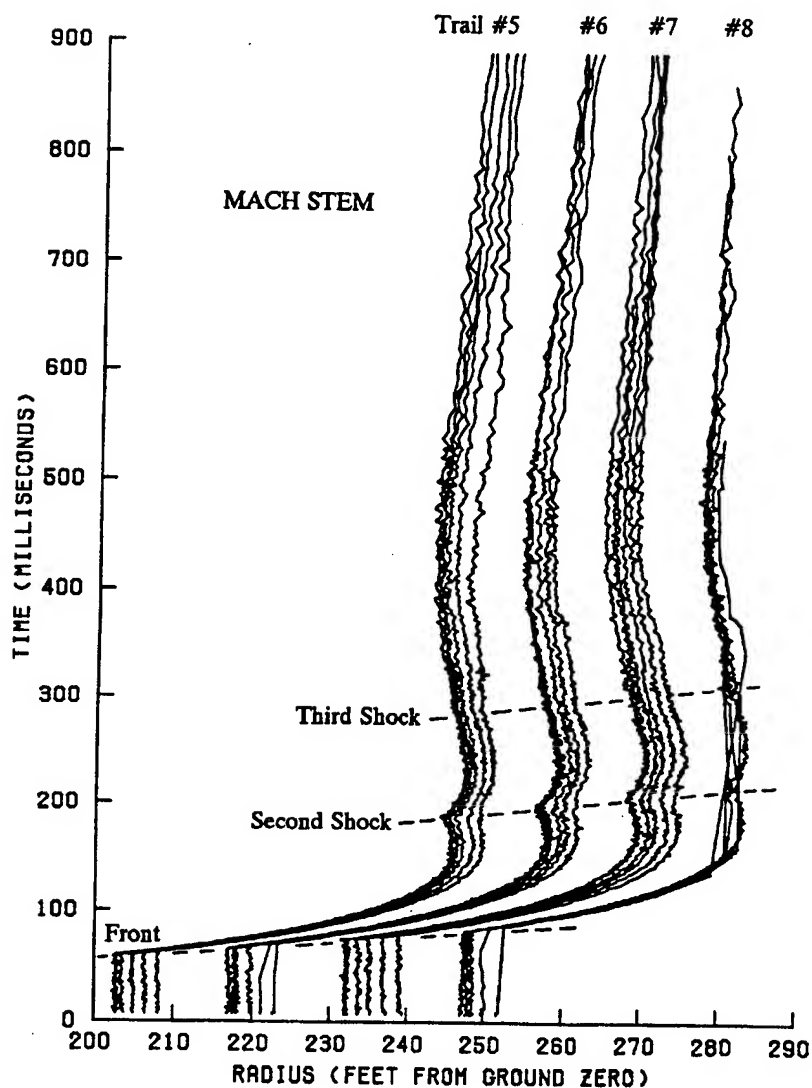


Figure 13. Individual particle trajectories in the Mach stem flow. Any of these trajectories is sufficient to define a piston path which enables the numerical reconstruction of the flow.

Particle trajectories in the Mach stem region are shown in figure 13. These are the motions of individual intersection points along straight lines through ground zero at different elevations in the object plane. They can be used to define piston paths.

The arrival times of the first and second shock fronts can be easily seen in the individual trajectories. The arrival of the third shock front can also be seen (seen more easily if the trajectories are plotted on a magnified scale, however).

The results shown are from the far-out group of SE smoke trails. Similar results were seen on the NW line. Results were not obtained from either close-in group in the Mach stem region because of the low triple point and the dust bench.

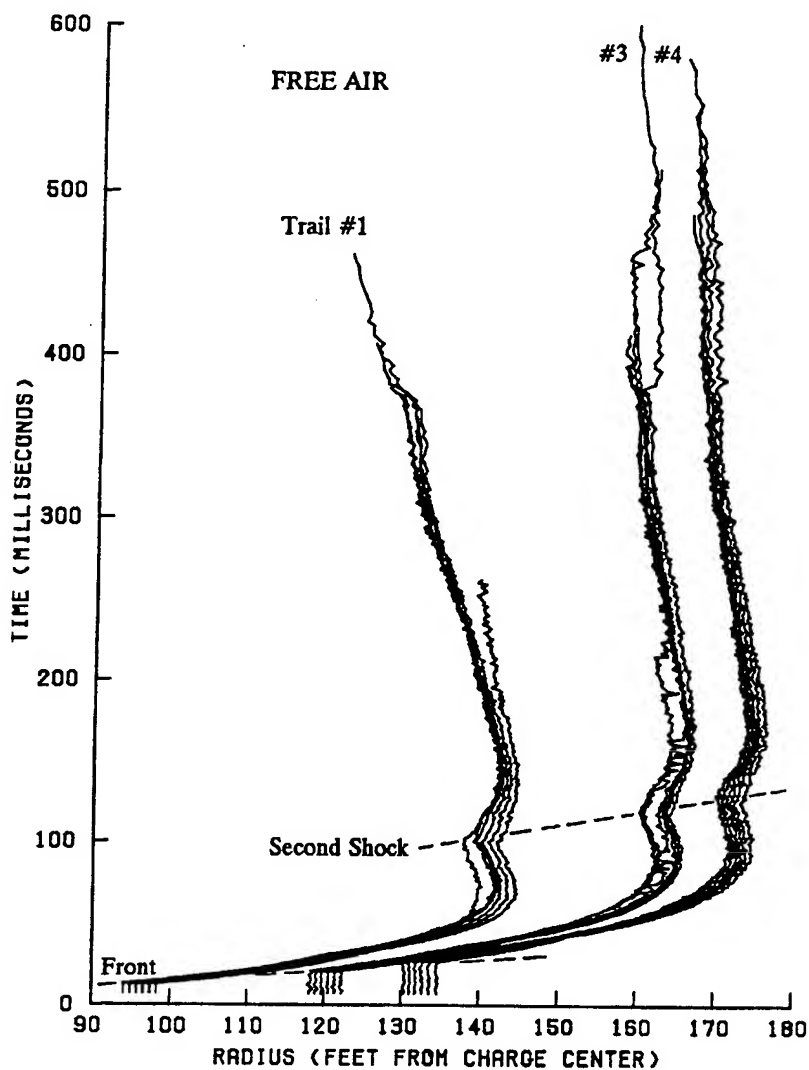


Figure 14. Individual particle trajectories in the free-air flow. Any of these trajectories is sufficient to define a piston path and enable a numerical reconstruction of the free-air flow, up to the time of arrival of the reflected shock front.

Particle trajectories in the free-air region are shown in figure 14. In this region, they are the motions of intersection points along lines through the charge centre. The results shown are all from the close-in group of SE smoke trails. Results were also obtained from the NE and far-out groups.

The arrival of the reflected shock front can be detected in the magnified data in figure 15, and it determines the amount of the free-air data which are available for the definition of a piston path. This is because, behind the reflected shock, the flow is no longer spherical and cannot be reconstructed using a pseudo-one-dimensional,

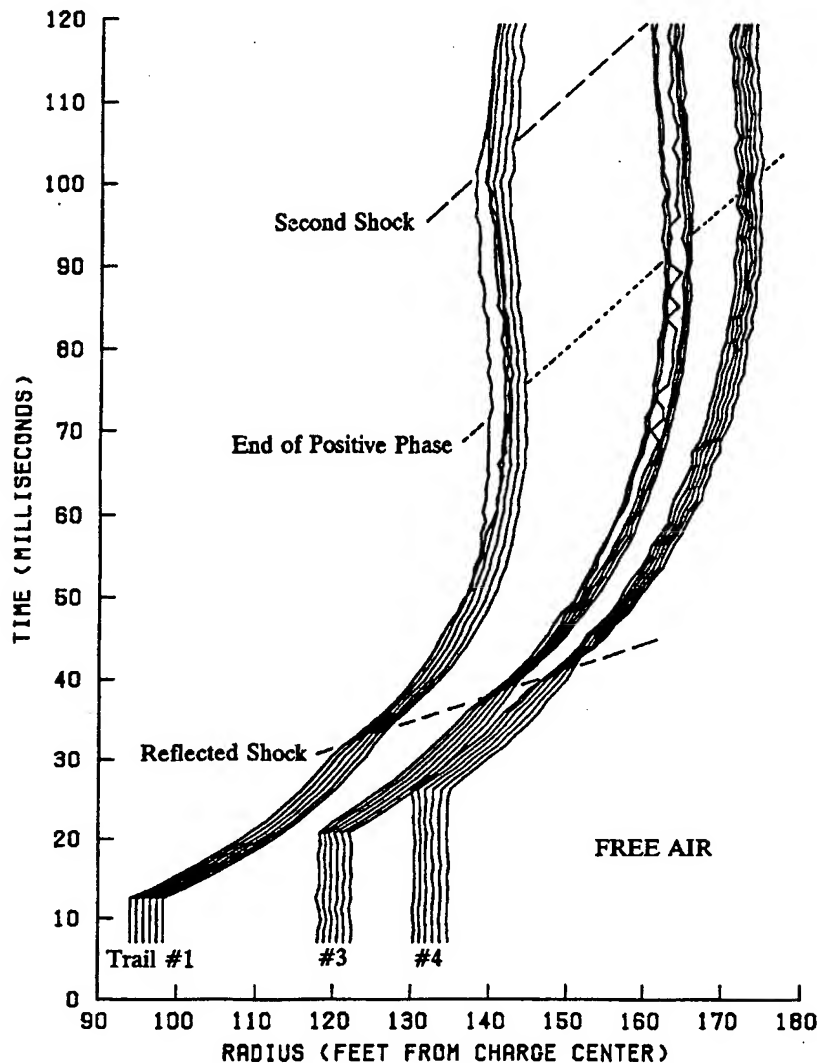


Figure 15. Close-up of the particle trajectories in the free-air flow showing the arrival of the reflected shock front. Spherical reconstruction of the free-air flow must end at the time of arrival of the reflected shock front, which in this case is well before the end of the positive phase of the blast flow.

piston-driven model. The reflected shock front could be 'moved out of the way' by 'removing' the ground surface, that is, raising the charge, or, what is effectively the same, decreasing the charge size. Measurement of the flow field in free-air blast waves is usually done in tests using small charges at relatively large heights.

In the present experiment, however, the reflected shock arrives well before the end of the positive flow phase. Only a relatively small gain would have been made had the smoke trails been longer and the measurements been made at greater heights.

### 3. CONCLUSIONS

Modified smoke launchers were used to successfully determine the overall airblast environment in this experiment. Tethered pipes were fired from the ground surface to create smoke trails 60 ft to 80 ft high, which were photographed as they followed the air flow in the blast wave in the regions above and below the triple point.

The trajectory of the triple point was measured between 98 ft and 170 ft ground radius. Its height above the ground increased from 4.5 ft to 34 ft over that range of distance. The free-air shock trajectory was measured between 80 ft and 195 ft, spherical radius, and its peak static overpressure fell from 15 atm to 1.8 atm over that range (from 190 psi to 22 psi). The Mach stem shock trajectory was also measured, between 98 ft and 285 ft ground range. Its peak static overpressure fell from 12 atm to 0.12 atm over that range (from 150 psi to 15 psi). Good agreement was obtained with results measured electronically (times of arrival and peak overpressures).

The minimum energy equivalence of the charge used in this test was measured to be 20.9 tons TNT at 5 atm peak overpressure in the free-air region. Comparisons at other overpressures and in the Mach stem region both indicated greater energy yields. Non-scalable ground surface effects may have influenced the comparison in the Mach stem case. The average free-air energy yield is about 21.8 tons TNT.

The TNT results used for the comparisons were scaled to the conditions of the test. The results were obtained from, and the scaling done by, the *AirBlast* database and retrieval system. The *AirBlast* database summarizes a large body of experimental measurements made in actual TNT tests, including free-air, surface burst and height-of-burst tests, using various measurement techniques (references 7 and 8).

Smoke trail motions were used to measure particle trajectories in both the free-air and Mach stem flow regions. Position-time data along straight lines through the trails and ground zero were determined and used to define a piston path, used to reconstruct the entire Mach stem flow beyond 203 ft ground range (35 psi).

Position-time data along straight lines through the trails and charge center were also measured, and used to reconstruct the entire free-air flow beyond 93 ft spherical radius (140 psi). The reflected shock ended the free-air reconstruction before the end of the positive phase. Since the HOB was relatively low in this test, it is unlikely that a much longer free-air reconstruction would have resulted had measurements been made at greater heights using longer smoke trails.

The reconstruction of the free-air blast wave can be used to characterize the new explosive in terms of peak physical data and their initial decay rates (pressure-time, density-time, etc.) over the ideal-gas range, below 15 atm. The reconstruction lasts about one-third of the free-air positive phase. The reconstruction of the Mach stem lasts for six times its positive phase, but cannot be used to characterize the explosive until ground surface effects can be accounted for.

The numerical reconstructions of the free-air and Mach stem blast waves are both available in the *AirBlast* database format. Its data retrieval program allows the user to extract time histories and wave profiles, as well as peak profiles, of all physical

parameters: static, dynamic and total pressure, flow velocity, density, temperature, sound speed, energy density and flux, and amount of energy available to do work. Computer software which offers its users options such as time-of-interest, position-of-interest, units system, data format, interpolation and integration, scaling, *etc.*, is more likely to be able to meet users' needs than is any (non-specific) hard-copy report. The official report on this test is not available yet (reference 9).

## ACKNOWLEDGEMENTS

The authors thank the staff of the FCDNA Test Group for their on-site assistance, especially Steve Tharnstrom (photo). They also thank Patricia Parkes for her on-site assistance and Susanna Clemas for her careful reading of the films.

## REFERENCES

- 1 Dewey, J.M., & McMillin, D.J. 1985. Proceedings of the DIRECT COURSE Symposium. FCDNA-TOD, Project Officer's Report POR 7119-9 (14 January 1985), Vol. IX, pp. 139-158. "Analysis of particle trajectories in the Mach stem."
- 2 Dewey, J.M., & McMillin, D.J. 1988. Proceedings of the MISTY PICTURE Symposium. FCDNA-TOD, Project Officer's Report POR 7187-5 (30 November 1988), Vol. V, pp. 14-1 to 14-64. "Forest blowdown, smoke puff diagnostics."
- 3 Dewey, J.M., & McMillin, D.J. 1991. Proceedings of the MISERS GOLD Symposium. FCDNA-TOD, Project Officer's Report POR 7352-2 (May 1991), Vol. II, Chapter 5, pp. 207 to 387. "Smoke puff photo-diagnostics."
- 4 Dewey, J.M., & McMillin, D.J. 1993. Proceedings of the DISTANT IMAGE Symposium. FCDNA-TOD, Project Officer's Report POR 7379-2 (April 1993), Vol. 2, Chapter 5, pp. 5-1 to 5-46. "Smoke puff diagnostics."
- 5 Dewey, J.M., & McMillin, D.J. 1995. MINOR UNCLE Symposium Report, Dr Roy McCrory FCDNA-TOD, Project Officer's Report POR 7453-2. (January 1995), Vol. 2, Chap. 2, pp. 2-1 to 2-48. "Smoke trail photo-diagnostics."
- 6 Dewey, J.M., & McMillin, D.J. 1987. Proc. 10th Intl Symp. Military Applications Blast Simulation. MABS-10, Bad Reichenhall, FR-Germany, 21-25 September 1987. Vol. I, pp. 287-299. "Numerical reconstruction of the flow field in experimentally observed Mach stem blast waves."
- 7 Dewey, J.M., & McMillin, D.J. 1989. Proc. 11th Intl Symp. Military Applications Blast Simulation. MABS-11, Albuquerque, NM, 11-15 September 1989. pp. 554-561. "A computer system for presenting the properties of blast waves."
- 8 Dewey, J.M., & McMillin, D.J. 1991. Proc. 12th Intl Symp. Military Applications Blast Simulation. MABS-12, Perpignan, France, 22-27 September 1991. pp. 287-296. "An integrated HOB blast wave database."
- 9 Proceedings of the MIDDLE KEY 4 Symposium (August 1994). FCDNA-TOD, Project Officer's Report. (September 1995: awaiting publication and release).



# NEW MEASUREMENT TECHNIQUES TO DETERMINE MATERIAL PROPERTIES FOR THE CALCULATION OF TEMPERATURE DISTRIBUTIONS

K. Simon\*, B.K. Bein\*\*, G. Eggers\*, K. Köhler\*\*\*, W. Neurath\*, J. Pelzl\*\*

\*Research Agency for Protective Technology NBC-Defense, PO Box 1142,  
D-29623 Munster, Germany

\*\*Ruhr-Universität Bochum, Fakultät für Physik und Astronomie

\*\*\*Federal Office of Defense Technology and Procurement, Koblenz

## Abstract

Photoacoustic measurement techniques, which are based on the generation, propagation and detection of thermal waves, offer the possibility to determine material properties with the accuracy needed for meaningful calculations of temperature distributions. Due to the ability to perform a thermal-depth-profiling of the surface region, these measurement techniques can be applied to materials with surface properties which may differ from the bulk parameters given in literature or supplied by the manufacturer. In this paper we present the basic physical theory of thermal waves, the experimental set-up and the principles of thermal wave analysis. The information which can be obtained from the target by nondestructive photoacoustic techniques is illustrated by experimental results from different materials.

## 1. Introduction

Equipment which is loaded by the nuclear thermal pulse may temporarily develop large internal stresses or significant changes in those material properties which are relevant for its structural strength. Failure under the load of the following blast wave may then result (synergistic effect). A first step to assess theoretically the survivability of equipment in such an event is the calculation of the temporal and spatial temperature distributions in the loaded material. If the surface temperature or the net heat flux absorbed is known, then the calculation requires the knowledge of mainly two quantities:

- thermal diffusivity, which characterises the speed of heat wave propagation,
- thermal effusivity, which describes the resistance of a boundary to the flux of a heat wave.

This is strictly true for materials absorbing ideally at the surface. In the case of semi-transparent materials, which absorb the thermal radiation inside the volume, additionally the optical absorption length and the heat capacity of the materials have to be considered.

Unfortunately, the material properties are often not known with the accuracy needed for meaningful calculations. Due to mechanical or thermal treatment the surface values may be different from the bulk parameters given in literature or supplied by the manufacturer. The material properties also may change with temperature over the wide temperature range which has to be considered and may vary locally due to impurities. With photoacoustic measurement techniques, which are based on the generation, propagation and detection of thermal waves, the required material properties can be determined and the above mentioned problems are taken into account. Due to the ability to perform a thermal-depth-profiling of the surface region, these nondestructive measurement techniques also can be applied to targets with thin surface layers, which cannot be separated from the bulk material.

## 2. Basic Theory of Thermal Waves

### 2.1 Heat Diffusion Equation and Thermal Wave Solutions

In solid-state materials, heat generation and propagation are governed by the heat diffusion equation

$$\rho c \frac{\partial T(\vec{r}, t)}{\partial t} = -\text{div} \vec{F}(\vec{r}, t) + Q(\vec{r}, t), \quad (1)$$

by the appropriate boundary conditions and by the strength and localization of the heat sources  $Q(\vec{r}, t)$ . The heat flow  $\vec{F}(\vec{r}, t)$  in Eq. (1) is related to the temperature distribution  $T(\vec{r}, t)$  by

$$\vec{F}(\vec{r}, t) = -k \text{grad} T(\vec{r}, t) \quad (2)$$

Here  $\rho$ ,  $c$  and  $k$  are the mass density, specific heat capacity and thermal conductivity of the solid, which in general can vary with the space-coordinates  $\vec{r}$  and the time  $t$ .  $Q(\vec{r}, t)$  represents a time-dependent volume or surface heat source.

If an homogeneous solid of constant thermophysical parameters is considered, Eq. (1) can be simplified in one-dimensional geometry to

$$\frac{\partial T(x, t)}{\partial t} = \alpha \frac{\partial^2 T(x, t)}{\partial x^2} + \frac{Q(x, t)}{\rho c}, \quad (3)$$

where  $\alpha = k/(\rho c)$  is the thermal diffusivity of the solid.

If prompt heating by electromagnetic radiation is assumed, the heat source is given by

$$Q(x, t) = -\eta \frac{dI(x, t)}{dx} = \eta \beta I(x = 0, t) \exp(-\beta x). \quad (4)$$

The intensity of the incident radiation may be described by

$$I(x = 0, t) = \frac{I_0}{2} \operatorname{Re}[1 + \exp(i\omega t)], \quad (5)$$

where  $\omega$  is related to the modulation frequency  $f$  of the intensity by  $\omega = 2\pi f$ . In Eq. (4),  $\beta$  is the optical absorption constant of the solid ( $\beta^{-1}$ : optical absorption length), and  $\eta$  is the ratio of the intensity of the unreflected part of the radiation to the total incident intensity. The optical parameters  $\beta$  and  $\eta$ , in general, are functions of the wave length  $\lambda$  of the incident radiation. For simplification of the following derivations, we only consider radiation of a definite wave length  $\lambda$ . The partial differential equation resulting from the insertion of Eqs. (4) and (5) into Eq. (3) can be solved by an approach

$$T(x, t) = \bar{T}(x) + T'(x, t)$$

which allows a separation of the stationary from the time-dependent problem. The time-dependent complex solution for the solid can be written as

$$T'(x, t) = [A \exp(\sigma x) + B \exp(-\sigma x) + C \exp(-\beta x)] \exp(i\omega t) \quad (6)$$

with

$$\sigma = (1 + i) \sqrt{\frac{\pi f}{\alpha}}, \quad i = \sqrt{-1}, \quad (7)$$

and

$$C = \frac{-\eta I_0}{2k\beta \left(1 - \frac{\sigma^2}{\beta^2}\right)}. \quad (8)$$

For a solid immersed in a gas atmosphere the integration constants  $A$  and  $B$  can be determined from the boundary conditions of negligible temperature variations at the outer boundaries and from the conditions of temperature and heat flow continuity at the solid/gas interface.

For a rather extended gas region and a semi-infinite solid the complex temperature distribution for the solid of a finite optical absorption constant then results as [1]

$$T_s'(x, t) = \frac{\eta I_0 \exp(i\omega t)}{2k\sigma \left(1 - \frac{\sigma^2}{\beta^2}\right)} \left[ \frac{1 + g_{gs} \frac{\sigma}{\beta}}{1 + g_{gs}} \exp(-\sigma x) - \frac{\sigma}{\beta} \exp(-\beta x) \right] \quad (9)$$

In Eq. (9) the quantity  $g_{gs} = \sqrt{(k\rho c)_g} / \sqrt{(k\rho c)_s}$  is the ratio of the effusivity  $\sqrt{k\rho c}$  of the gas and the solid material, respectively. For most gas/solid interfaces the quantity  $g_{gs}$  is relatively small ( $10^{-4} \dots 10^{-2}$ ).

Equation (9) can considerably be simplified if the condition  $g_s \ll 1$  is taken into account and if, additionally, the limit of a surface-heated opaque solid,  $|\sigma|/\beta \ll 1$ , is considered. From the resulting complex solution,

$$T'(x, t) = \frac{\eta I_0}{2k\sigma} \exp(-\sigma x + i\omega t), \quad (10)$$

the real part solution can be easily derived,

$$T'(x, t) = \frac{\eta I_0}{2\sqrt{k\rho c}\sqrt{2\pi f}} \exp\left(-\sqrt{\frac{\pi f}{\alpha}}x\right) \cos\left(2\pi ft - \sqrt{\frac{\pi f}{\alpha}}x - \frac{\pi}{4}\right) \quad (11)$$

which reveals that in a periodically heated solid, space- and time-dependent temperature fluctuations are induced which can be interpreted as thermal waves.

## 2.2 Main Properties of Thermal Waves and the Physical Relevance of the Material Parameters

As can be seen from Eq. (11), the principal features of such thermal waves are:

- From the wave number  $\sqrt{\pi f/\alpha}$  the thermal wave length  $\lambda_{th.w.}$  and the propagation velocity  $v_{th.w.}$  of the temperature maxima or minima can be calculated as

$$\lambda_{th.w.} = \frac{2\pi}{\sqrt{\pi f/\alpha}} = \sqrt{4\pi\alpha/f} \quad (12)$$

$$v_{th.w.} = \lambda_{th.w.} f = \sqrt{4\pi\alpha f} \quad (13)$$

- Between the periodic heating process according to Eq. (5) and the thermal response (11), there is a phase lag

$$\Delta\phi = \sqrt{\frac{\pi f}{\alpha}}x + \frac{\pi}{4}, \quad (14)$$

which increases with the propagation distance of the thermal wave.

- The amplitude of the thermal wave is strongly damped; at a distance

$$x = \mu = \sqrt{\frac{\alpha}{\pi f}} \quad (15)$$

it decays to  $1/e$  [ $\approx 37\%$ ] of its initial value, and at a propagation distance of a wavelength it is damped by a factor of  $\exp(-2\pi)$  [ $\approx 0.2\%$ ], which means that the solution Eq. (11) for the opaque semi-infinite solid can even be applied to geometrically thin samples as long as their thickness is comparable to the thermal wave length.

- Since the attenuation length  $\mu$  of the amplitude, the so-called thermal diffusion length, and the phase shift vary with the modulation frequency of the heating process, a systematic variation of the modulation frequency  $f$  can be used for subsurface depth inspections of solid samples.

Among the parameter which affect the excitation and propagation of thermal waves according to Eqs. (9) or (11), the thermal diffusivity is the relevant parameter for time-dependent diffusion processes within homogeneous isotropic materials. As can be seen from Eq. (13), the thermal diffusivity characterizes the speed of heat wave propagation.

The combined quantity  $\sqrt{k\rho c}$ , the thermal effusivity, might be, at a first glance, a rather abstract quantity. The physical importance of the effusivity can easily be understood if we study time-dependent surface heating processes. If the net heat flux absorbed at the surface of an homogeneous isotropic and opaque semi-infinite solid is given by  $F_s(t)$ , the temperature rise at the surface can be calculated by [2]

$$T_s(t) = \frac{1}{\sqrt{\pi}\sqrt{k\rho c}} \int_0^t F_s(t-t') \frac{dt'}{\sqrt{t'}} \quad (16)$$

Equation (16) shows that the effusivity  $\sqrt{k\rho c}$  is the relevant thermophysical parameter, which determines the surface temperature and characterises the resistance of a boundary to the flux of a heat wave, and not the thermal conductivity, mass density or specific heat separately. At ideal surfaces of compact homogeneous solids the value calculated for the effusivity from the bulk parameters  $k$ ,  $\rho$ , and  $c$  and the value which effectively governs a surface heating process may be identical; under realistic conditions, however, changes of the surface due to machining, heat treatment, roughness and porosity can contribute to a changed effective effusivity at the surface, which can affect cooling or heating processes across surfaces.

If we consider a semi-infinite solid, which does not absorb the thermal radiation ideally at its surface, the optical absorption constant  $\beta$  has to be taken into account according to Eq. (9). In the case of very weak optical absorption, so that the optical absorption length is large compared to the thermal diffusion length, Eq. (9) simplifies to

$$T_s'(x, t) = \frac{\eta\beta I_0 \exp(i\omega t) \exp(-\beta x)}{2k\sigma^2} \sim \frac{\eta\beta I_0}{\rho c \cdot f} \quad (17)$$

showing that the temperature is mainly determined by the product of heat capacity  $\rho c$  and optical absorption length  $\beta^{-1}$ . When you compare thermal wave solutions for opaque solids and materials with very weak optical absorption, Eqs. (11) and (17), you can see that the amplitude of the thermal waves has a different frequency

dependence, offering the possibility to get information about the optical absorption constant  $\beta$ .

### 2.3 Reflection and Scattering of Thermal Waves

Since the amplitude and the phase of thermal waves depend on the effusivity and thermal diffusivity, their propagation (damping and phase retardation) will change when regions of different thermal properties are reached. In the terms of wave propagation, these phenomena can be interpreted as reflection and scattering of thermal waves. Subsequently, the one-dimensional solution for a composite layered solid will be derived to study reflection phenomena which will be used later to analyze photoacoustic measurements.

If we consider a system consisting of a thick substrate (b), a surface layer (s) of thickness  $l$  where optical absorption takes place and a gas region (g) in front of the solid, the complex temperature distribution in the surface layer ( $0 \leq x \leq l$ ) is given by

$$T_s'(x, t) = \frac{\eta I_0 \exp(i\omega t)}{2k\sigma \left(1 - \frac{\sigma^2}{\beta^2}\right)} \left[ \frac{1 + g_{gs} \frac{\sigma}{\beta}}{1 + g_{gs}} \exp(-\sigma x) \frac{1 + R_{sb} \exp[-2\sigma(l-x)]}{1 - R_{sb} \exp(-2\sigma l)} - \frac{\sigma}{\beta} \exp(-\beta x) \right] \quad (18)$$

In the limit of surface heating,  $|\sigma|/\beta \ll 1$ , and if additionally the relation  $g_{gs} \ll 1$  holds, the solution for the composite layered solid simplifies to [1]

$$T_s'(x, t) = \frac{\eta I_0}{2k\sigma} \frac{1 + R_{sb} \exp[-2\sigma(l-x)]}{1 - R_{sb} \exp(-2\sigma l)} \exp(-\sigma x + i\omega t) \quad (19)$$

and can be compared with the surface-heated semi-infinite solid, Eq. (10).

The quantity

$$R_{sb} = -\frac{1 - g_{sb}}{1 + g_{sb}} \quad (20)$$

in Eqs. (18) and (19) can be understood as the thermal reflection coefficient, corresponding to the transition from the surface layer to the substrate. If the surface layer and the substrate have equal effusivities,  $g_{sb} = \sqrt{(k\rho c)_s} / \sqrt{(k\rho c)_b} = 1$ , the thermal reflection coefficient is  $R_{sb} = 0$  and solution (19) will be identical to solution (10) for the homogeneous solid. If the surface layer has a lower effusivity value than the substrate,  $0 < g_{sb} < 1$ , the thermal reflectivity will have negative values,  $-1 < R_{sb} < 0$ . By comparing Eq. (19) with Eq. (10), the temperature of the surface layer will be lower in general. If the substrate has a lower effusivity value than the surface layer,  $g_{sb} > 1$ , the reflectivity will be positive,  $0 < R_{sb} < 1$ . In this latter case,

the temperature within the surface layer will be higher than in the corresponding homogeneous solid.

### **3. Experimental Set-Up**

#### **3.1 Generation and Detection of Thermal Waves, Photoacoustic Effect**

As can be seen from the thermal wave solutions of the heat diffusion equation, thermal waves are induced by intensity-modulated heating processes, which can be generated by the absorption of modulated electromagnetic radiation. Radiation sources suitable for thermal wave studies generally require high luminosities because of the strong, exponential damping of thermal waves. On the other hand the radiation source must offer the possibility, that the electromagnetic radiation can be focused on the target and that the radiation can easily be modulated in intensity. Therefore a cw-laser, operating in the visible range, is the most favourable radiation source. Especially the argon-ion-laser is very often used in thermal wave studies. For a cw-laser an external modulation device has to be inserted into the laser beam, e.g. a mechanical chopper, an electro-optic or acousto-optic modulator. Mechanical choppers offer the advantage of being able to handle high laser powers and radiation of different wavelength, but the modulation frequency range is limited and a change in the modulation frequency takes much more time compared to an electro-optic or acousto-optic modulator. Considering the modulators which are commercially available nowadays, acousto-optic modulators seem to be the best choice.

Normally, the thermal wave response of a target is analyzed using lock-in techniques, thereby probing selectively the amplitude and the phase of the signal. Thermal waves, which are temporally and spatially oscillating temperature distributions, are associated with changes of other physical quantities. Consequently, thermal waves can be detected either directly by a measurement of the local temperatures or indirectly by monitoring other properties. In the photoacoustic sensing technique the periodic thermal response of the sample surface is transferred to the surrounding gas in a gas-tight cell. The pressure fluctuations induced in the gas volume by the heat flux across the solid/gas interface are detected by a microphone mounted inside the cell. Although the photoacoustic effect was discovered by Bell in 1880, photoacoustic measurement techniques are relatively new measurement techniques, because it took nearly a century to get a theoretical understanding of the signal generation process associated with a solid in a photoacoustic cell. The first theoretical interpretation of the signal generation on the basis of thermal waves was given in 1976 by Rosencwaig and Gersho. It was based on the assumption of a one-dimensional thermal boundary-layer expanding and contracting at the solid/gas interface, thereby acting as a piston on the major part of the gas volume, which is governed by the adiabatic gas law. Based on the one-dimensional piston model, the pressure fluctuations are given by [3]

$$\delta p = \gamma \bar{P} \mu_g \frac{T}{l_g \bar{T}} \quad (21)$$

where  $\gamma$  is the adiabatic coefficient,  $\bar{P}$  and  $\bar{T}$  are the steady state pressure and temperature,  $l_g$  the length of the gas cavity, and  $\mu_g$  the thermal diffusion length of the gas. According to Eq. (21) the pressure fluctuations, which can be detected by a microphone, are directly correlated to the thermal waves. In a more general derivation based on the principles of continuum mechanics, it could be shown that this statement holds, independent of special model assumptions [4] .

### 3.2 Principle Experimental Arrangement

The conventional experimental photoacoustic setup consists of a light source (typically a cw-laser), an external modulation device, the photoacoustic cell containing the sample and the microphone, a lock-in amplifier and a personal-computer for data storage. Figure 1 shows a schematic of the arrangement used for photoacoustic reflection measurements, where the thermal waves are detected at the illuminated front side of the sample.

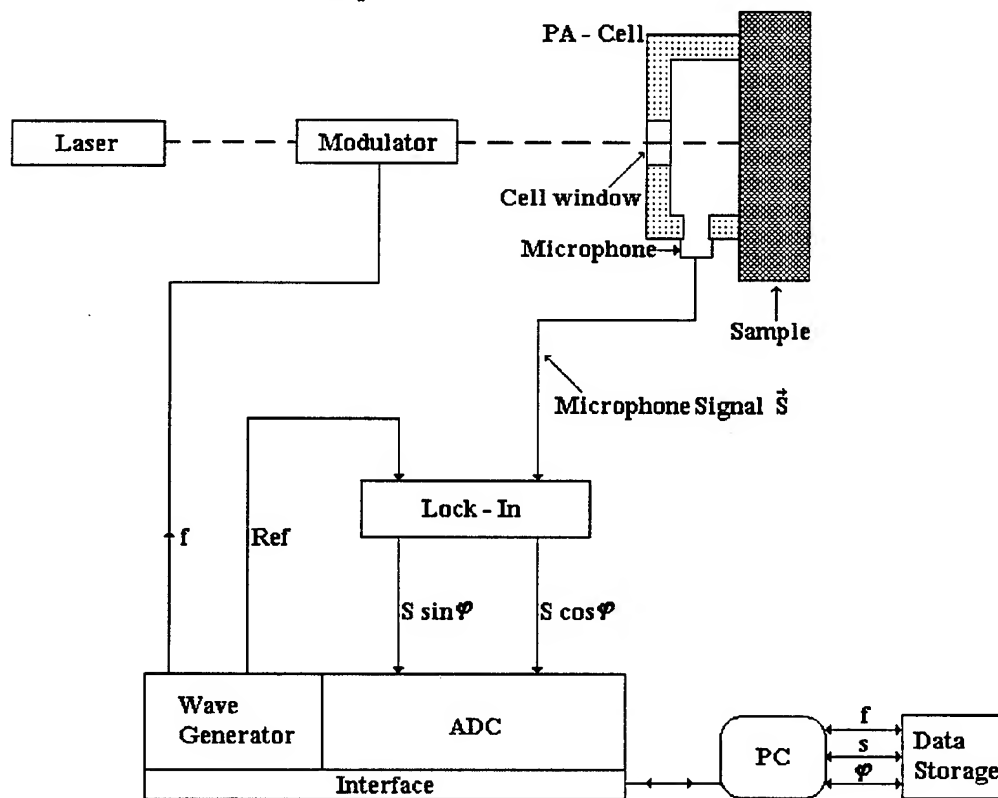


Fig. 1 Schematic of the experimental setup used for photoacoustic reflection measurements.



The same arrangement can be used for photoacoustic transmission measurements, where the thermal waves, which have travelled through the sample, are detected. In this case, only the configuration measurement cell-sample is changed, so that the laser beam directly illuminates the sample. The measurement cell is at the rear side of the sample in this case.

The in-phase and out-of-phase components of the microphone signal with respect to the modulator reference are analyzed with a lock-in amplifier. The amplitude and the phase angle of the photoacoustic signal are recorded and interpreted as a function of the modulation frequency  $f$ . The personal computer used in the experiment is equipped with a special software for automatic data acquisition, remote control of the lock-in amplifier and the wave generator and for theoretical interpretation of the measurement data.

### 3.3 Photoacoustic Measurement Cells

Photoacoustic cells can be built for measurements at room temperature as well as for high temperature measurements. The photoacoustic room temperature measurement cell used at the research establishment in Munster is shown in Fig.2.

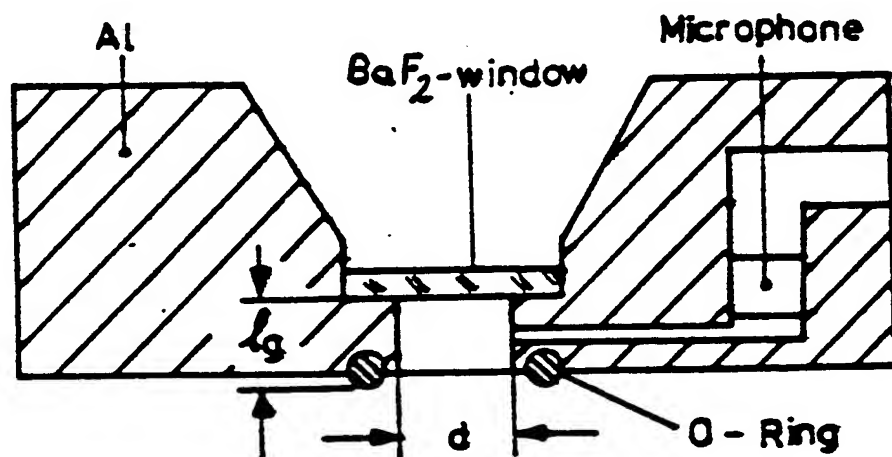


Fig. 2 Cross section of the photoacoustic room temperature measurement cell.

The body of the photoacoustic cell is made of aluminum to minimize the signal contributions from the cell walls. At the top the cylindrical gas cavity is closed by the cell window and at the bottom by the sample itself. As cell window BaF<sub>2</sub> has been used, which is transparent in the visible range as well as in the infrared, so that we can use our argon-ion-laser and our CO<sub>2</sub>-laser for photoacoustic reflection measurements.

A rubber ring between the cell body and the sample is used for acoustic sealing. To prevent the microphone from direct illumination of light, it is separated from the main cavity by a narrow channel. As a consequence of this construction, the acoustic transfer function of the photoacoustic cell shows resonances in the kHz region (see Fig. 3).

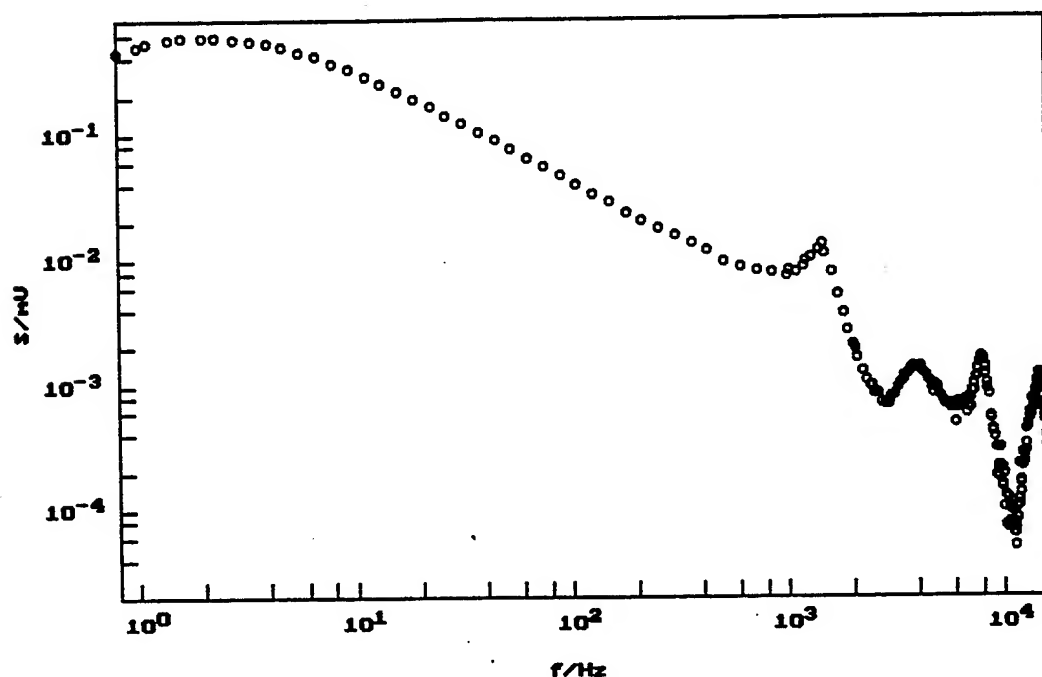


Fig. 3 Resonances of the photoacoustic cell

The increased signal-to-noise ratio of the resonances allows an extension of the measurements to higher frequencies. Another important aspect to get a good sensitivity of the photoacoustic cell is the length  $l_g$  of the gas cavity. According to Eq. (21) the sensitivity can be increased, if the gas volume (considered in the one-dimensional treatment by the gas length  $l_g$ ) can be decreased. This reduction however is limited to sizes larger than the thermal diffusion length in the gas, otherwise the heat losses through the top window would falsify the interpretation. Typical values of  $l_g$  are in the range of 5 to 10 mm.

Fig. 4 shows a high temperature measurement cell. This photoacoustic cell has been used successfully at the University of Bochum in the temperature range from 300 to 1000 K.

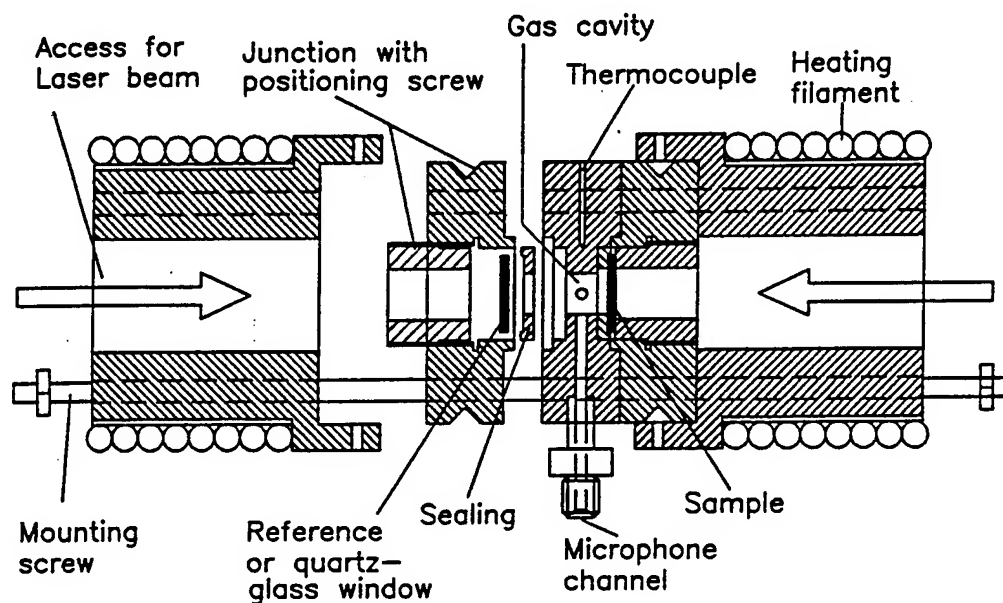


Fig. 4 High temperature photoacoustic cell used at Ruhr-Universität Bochum, Germany.

### 3.4 Reference Samples

Since the amplitude and the phase angle of the microphone signal, which are analyzed by the lock-in amplifier in photoacoustic measurements, are influenced by the acoustic transfer function of the photoacoustic cell, especially at frequencies near the cell resonances, the recorded measurement data are not in agreement with theory. To eliminate the frequency response function of the experimental set-up, the signals of the sample of unknown material properties are compared with the signals of a reference material of known parameters by a "normalization" procedure, consisting of a division of the measured complex signals. If the sample of unknown material properties and the reference sample are measured under equal conditions, the properties of the sample are directly related to the parameters of the reference material such that the normalized signal amplitude and phase shift are only governed by the parameters of the sample and the reference material. For certain applications, and also for a test, that the measurement data of the reference samples are of good quality, it is useful to have several reference samples with different thermophysical properties.

It is also desirable to have samples with different optical absorption properties: opaque solids, which absorb the laser light at its surface and semi-transparent materials with different absorption constants  $\beta$ .

Table 1 gives a survey, which materials have been used successfully as reference samples.

Argon - Ion - Laser	
Reflection:	Neutral Density Glass, PVC, Aluminum, Glassy Carbon (SIGRADUR)
Transmission:	Aluminum, V2A-Steel
CO <sub>2</sub> - Laser	
Reflection:	Glass, Teflon (PTFE), PVC, Glassy Carbon (SIGRADUR)
Transmission:	Aluminum, V2A-Steel

Tab. 1 Reference Samples used successfully for photoacoustic measurements

#### 4. Thermal Wave Analysis

##### 4.1 Photoacoustic Reflection Measurements

###### 4.1.1 Test of the Reference Samples

Before performing the normalization procedure, it is useful to insure that the measurement data of the reference sample are of good quality. Such a test can easily be performed, if two reference samples with different optical absorption properties are used: an opaque surface absorbing reference sample and a semi-transparent material, for which the thermal diffusion length is very small compared to the optical penetration depth

$$\sqrt{\alpha / (\pi f)} \ll \beta^{-1}$$

Then the ratio of the photoacoustic amplitudes is given by

$$S_n = \frac{S_1}{S_2} = \frac{\eta_1 (\kappa \rho c)_2^{1/2}}{\eta_2 (\kappa \rho c)_1^{1/2}} \left[ 1 + \sqrt{4\pi f / (\alpha \beta^2)_2} + 2\pi f / (\alpha \beta^2)_2 \right]^{1/2} \quad (22)$$

Here the index 1 refers to the opaque sample and the index 2 to the semi-transparent material.

In the high frequency range the normalized amplitude  $S_n$  should increase with  $f^{1/2}$ .

If a surface absorbing homogeneous sample and an optical very weak absorbing material are considered, the phase measurements have also simple and experimentally easily detectable limits [5]:

$$f^{1/2}[\cot(\varphi_n) + 1] = \sqrt{\frac{\alpha\beta^2}{\pi}} + 2f^{1/2} \quad (23)$$

$$f^{1/2}[\cot(\varphi_n) - 1] = \sqrt{\frac{\alpha\beta^2}{\pi}} \quad (24)$$

#### 4.1.2 Opaque and Surface absorbing Solids

After a test (described in 4.1.1); that the measurement data of the reference samples are of good quality, the normalized photoacoustic amplitude and phase of the opaque solid of unknown material properties are calculated. For this normalization procedure usually the opaque reference sample is taken. If the sample is a surface heated homogenous solid, the normalized amplitude  $S_n$  and phase  $\varphi_n$  have simple and experimentally easily detectable limits:

$$S_n = \frac{\eta_s}{\eta_{ref}} \frac{\sqrt{(kpc)_{ref}}}{\sqrt{(kps)_s}} \quad (25)$$

$$\varphi_n = 0 \quad (26)$$

The parameters  $\eta_s$  and  $\eta_{ref}$  are determined in an additional optical measurement. Since the effusivity of the sample,  $e_s = \sqrt{(kpc)_s}$ , then is the only unknown quantity in Eq. (25), it can be calculated directly from the normalized amplitude. If  $S_n^{-1}$  is plotted, the inverse normalized amplitude is directly proportional to the effusivity of the sample. If an unhomogenous opaque sample is considered, the normalized amplitude and phase have a frequency dependence. Then the inverse normalized amplitude can be interpreted as a thermal-depth-profile of the surface region. In the high frequency limit  $S_n^{-1}$  gives information about the effusivity at the surface of the solid and with decreasing modulation frequency subsurface regions with increasing penetration depth of the thermal waves are taken into account.

For a quantitative interpretation the photoacoustic evaluation software is used, trying to fit the measurement curves with theoretical curves based on a multi-layered solid with different material properties in the layers. As can be seen from Eqs. (19) and (20), the analysis reveals information about the effusivities and from the frequency dependence of the measurement data information about the thermal thickness

$l/\sqrt{\alpha}$  of the layers are available. If the geometrical thickness  $l$  of a layer can be determined, e.g. under a microscope, then the thermal diffusivity of the layer can be calculated, even if the layer cannot be separated from the surrounding material.

### 4.1.3 Semi-Transparent Solids

In the one-dimensional theoretical description the normalized photoacoustic amplitude for a homogeneous semi-transparent sample and a reference sample of a finite optical absorption constant  $\beta_{\text{ref}}$  is given by [5]

$$S_n = \frac{S_s}{S_{\text{ref}}} = \frac{\eta_s}{\eta_{\text{ref}}} \frac{\sqrt{(k\rho c)_{\text{ref}}}}{\sqrt{(k\rho c)_s}} \left[ \frac{1 + \sqrt{4\pi f / (\alpha\beta^2)_{\text{ref}}} + 2\pi f / (\alpha\beta^2)_{\text{ref}}}{1 + \sqrt{4\pi f / (\alpha\beta^2)_s} + 2\pi f / (\alpha\beta^2)_s} \right]^{1/2} \quad (27)$$

An analytical solution for the normalized photoacoustic phase lag  $\phi_n$  between two different samples is given by

$$\cot(\phi_s - \phi_{\text{ref}}) + 1 = \frac{\sqrt{\frac{(\alpha\beta^2)_s}{\pi f}} + 2\left(1 + \sqrt{\frac{\pi f}{(\alpha\beta^2)_{\text{ref}}}}\right)}{1 - \sqrt{\frac{(\alpha\beta^2)_s}{(\alpha\beta^2)_{\text{ref}}}}} \quad (28)$$

From the frequency-dependence of Eq. (27) or (28) the value  $(\alpha\beta^2)_s$  can be determined (by using the photoacoustic evaluation software). In the case  $\beta_{\text{ref}} \rightarrow \infty$ , corresponding to a surface heated reference sample, Eqs. (27) and (28) simplify to Eqs. (22), (23) and (24) and the calculation becomes easier. If the sample and the reference material have very weak optical absorption, so that in the high frequency limit the conditions

$$(\alpha\beta^2)_s \ll \pi f$$

$$(\alpha\beta^2)_{\text{ref}} \ll \pi f$$

are fulfilled, Eq. (27) simplifies to

$$S_n = \frac{\eta_s (\rho c)_{\text{ref}} \beta_s}{\eta_{\text{ref}} (\rho c)_s \beta_{\text{ref}}} \quad (29)$$

In this case the normalized amplitude offers the possibility to determine the product of heat capacity  $\rho c$  and optical absorption length  $\beta^{-1}$  of the solid, which is the relevant quantity for transient heating of very weak absorbing materials.

If the same sample has been measured with different wavelengths  $\lambda_1$  and  $\lambda_2$ , Eq.(29) simplifies to (assuming identical laser power)

$$S_n = \frac{\eta(\lambda_1)\beta(\lambda_1)}{\eta(\lambda_2)\beta(\lambda_2)} \quad (30)$$

offering the possibility to compare optical absorption properties at different wavelengths, e.g. in the visible range and in the infrared.

### 4.2 Photoacoustic Transmission Measurements

If two opaque and homogenous samples are measured in transmission, the normalized photoacoustic amplitude is given by [6]

$$S_n = \frac{S_s}{S_{ref}} = \frac{\eta_s}{\eta_{ref}} \cdot \frac{\sqrt{(k\rho c)_{ref}}}{\sqrt{(k\rho c)_s}} \left[ \frac{\exp(2a_{ref}) - 2 \cos(2a_{ref}) + \exp(-2a_{ref})}{\exp(2a_s) - 2 \cos(2a_s) + \exp(-2a_s)} \right]^{1/2} \quad (31)$$

with

$$a_{s,ref} = \sqrt{\frac{\pi f}{\alpha_{s,ref}}} l_{s,ref} \quad (32)$$

containing information about the thermal diffusivity, as well as information about the effusivity.

In the limit of low frequencies, which means  $\pi f \ll l^2 / \alpha$ , the normalized amplitude can be approximated by

$$S_n \approx \frac{\eta_s (\rho c)_{ref} l_{ref}}{\eta_{ref} (\rho c)_s l_s} \quad (33)$$

delivering information about the heat capacity. In the high frequency limit the normalized amplitude can be approximated by

$$\ln(S_n) \approx \ln \left[ \frac{\eta_s}{\eta_{ref}} \frac{\sqrt{(k\rho c)_{ref}}}{\sqrt{(k\rho c)_s}} \right] + \sqrt{\pi} \left[ \frac{l_{ref}}{\sqrt{\alpha_{ref}}} - \frac{l_s}{\sqrt{\alpha_s}} \right] \sqrt{f} \quad (34)$$

This is a straight line in logarithmic representation which can be used to determine the effusivity by direct linear extrapolation from the high frequency limit to  $\sqrt{f} = 0$  and to determine the thermal diffusivity.

In the limit  $\sqrt{f} = 0$  the difference between the low frequency solution, Eq. (33), and the high frequency solution, Eq. (34), is given by

$$\Delta \ln(S_n) = \ln \left[ \frac{\sqrt{\alpha_s}}{\sqrt{\alpha_{ref}}} \frac{l_{ref}}{l_s} \right], \quad (35)$$

depending only on the ratio of geometrical thicknesses and thermal diffusivities of the samples.

Since the photoacoustic amplitude reacts very sensitive to impurities at the samples surface, which is orientated towards the measurement cell, it is often preferable to evaluate the normalized phase for a determination of the thermal diffusivity. The normalized phase is given by

$$\tan(\varphi_s - \varphi_{ref}) = \frac{\tanh(a_s) \cot(a_s) - \tanh(a_{ref}) \cot(a_{ref})}{1 + \tanh(a_s) \cot(a_s) \tanh(a_{ref}) \cot(a_{ref})} \quad (36)$$

In the high frequency limit  $\varphi_n$  can be approximated by

$$\varphi_n = \sqrt{\pi} \left[ \frac{l_s}{\sqrt{\alpha_s}} - \frac{l_{ref}}{\sqrt{\alpha_{ref}}} \right] \sqrt{f} \quad [\varphi \text{ in rad}] \quad (37)$$

or by

$$\varphi_n = \frac{180 \text{ degrees}}{\sqrt{\pi}} \left[ \frac{1_s}{\sqrt{\alpha_s}} - \frac{1_{ref}}{\sqrt{\alpha_{ref}}} \right] \sqrt{f} \quad (38)$$

For a quantitative interpretation of the transmission measurements, usually the photoacoustic evaluation software is used, offering also the possibility to analyze measurement data of semi-transparent materials and unhomogenous samples.

## 5. Experimental Results

### 5.1 Test of the Reference Samples

A lot of optical and photoacoustic measurements have been made to find suitable materials, which can be taken as reference samples. The intension of these test-measurements was to determine the material properties of the reference samples and to insure that the reference samples "behave" like homogenous materials. To test ideal surface absorbing properties the measurement data have been plotted according to Eqs. (22), (23) and (24). Results of photoacoustic reflection measurements with the argon-ion-laser are shown in Fig. 5 and Fig. 6. As reference samples a 5mm thick aluminum plate and a 3mm thick PVC plate have been used.

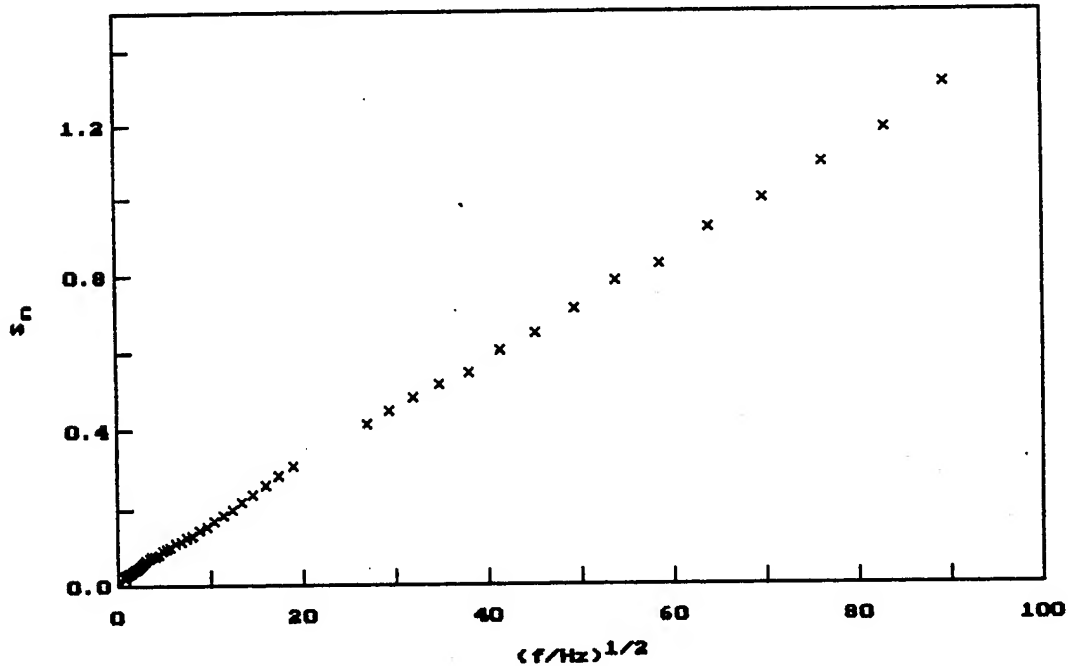


Fig.5 Photoacoustic reflection measurement.

$S_n = S_{Al}/S_{PVC}$  · Test of the measurement amplitudes.



In Fig. 5 the normalized photoacoustic amplitude  $S_n$  increases with  $\sqrt{f}$ , being typical for photoacoustic reflection measurement data of good quality, if two homogenous samples have been used; the first, an ideal surface absorbing material, and the second sample a semi-transparent material with weak optical absorption. To achieve ideal surface absorbing properties of the aluminum plate, the surface had to be cleaned. Fig. 6 shows, that also the phase measurement data are of good quality.

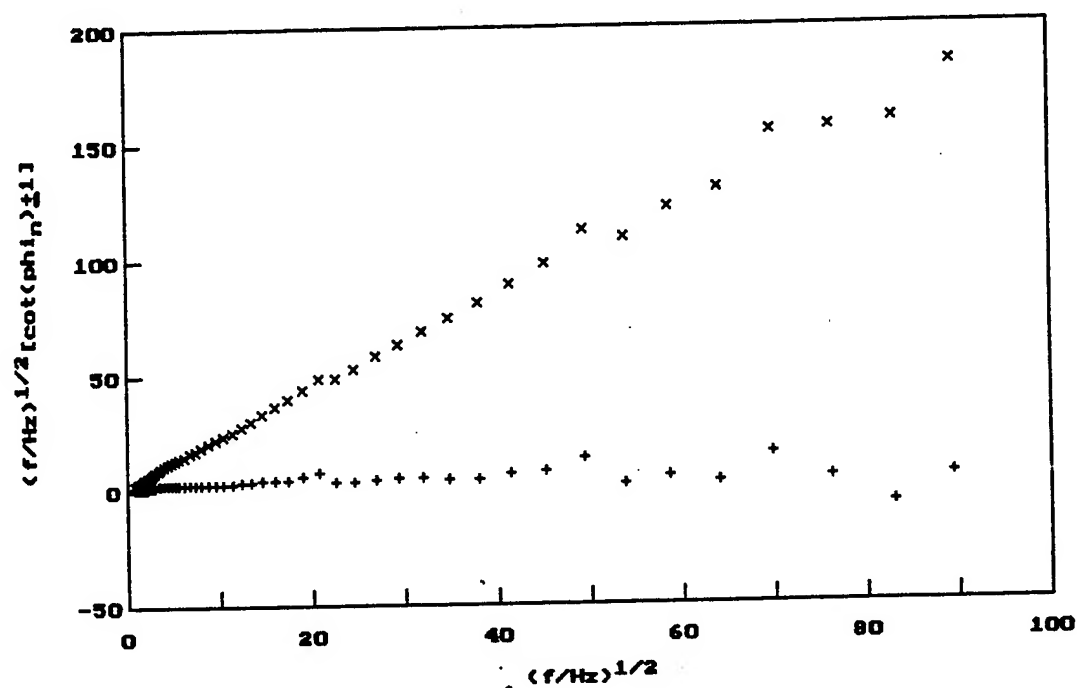


Fig. 6 Photoacoustic reflection measurement.  
Test of the measured phases.

## 5.2 Determination of the Thermal Diffusivity and Heat Capacity

The thermal diffusivity can be determined by analyzing the normalized phase or amplitude of photoacoustic transmission measurements according to Eqs. (34) - (38). Figures 7 and 8 show the normalized phases and amplitudes of the measurement data of a graphit sample (reference is molybdenum), which have been fitted with the photoacoustic evaluation software.

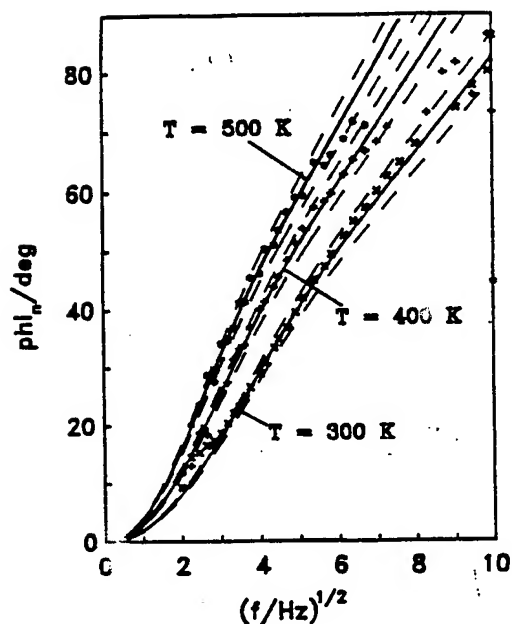


Fig. 7 Normalized phase  
of the graphit sample  
Best fit  $\pm 3\%$  deviation  
of  $\alpha$

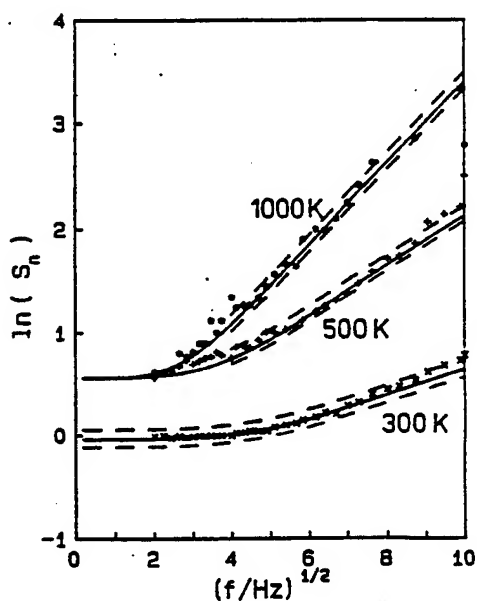


Fig. 8 Normalized amplitude  
of the graphit sample  
Best fit  $\pm 10\%$  deviation  
of  $\alpha$

The measurement data are in good agreement with the theoretical solution (high frequency limit), Eqs. (34) and (38), showing an increase of  $S_n$  and  $\phi_n$  with  $\sqrt{f}$ . For  $T=300\text{K}$  the thermal diffusivity is about  $5.5 \cdot 10^{-5} \text{m}^2 \text{s}^{-1}$ . The temperature dependence of the diffusivity is shown in Fig. 9.

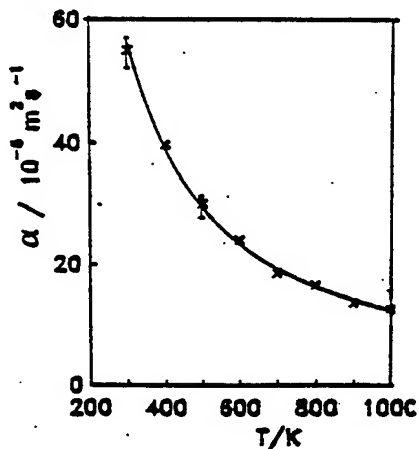


Fig. 9 Temperature dependent diffusivity of the graphit sample obtained from measurements with the high temperature photoacoustic measurement cell.

The heat capacity  $p_c$  can be determined from the normalized photoacoustic amplitude in the limit of low modulation frequencies according to Eq (33). For  $T=300K$  the heat capacity of the graphite sample is  $1.7MJ/(K \cdot m^3)$ .

( $\eta_s=0.87, \eta_{ref}=0.94, p_{c,ref}=2.5MJ/(K \cdot m^3), l_s=1.95mm, l_{ref}=1.38mm$ )

### 5.3 Determination of the Effusivity and Thermal-Depth-Profiling

The thermal effusivity is usually determined from photoacoustic reflection measurements, analyzing the normalized photoacoustic amplitude. In the case of a homogenous sample the effusivity can be evaluated from the normalized amplitude  $S_n$  according to Eq (27), fitting the measurement data with the photoacoustic evaluation software. Fig. 10 shows a photoacoustic reflection measurement of a glassy carbon sample; the reference sample is neutral density glass with an effusivity of  $1460 Ws^{1/2} m^{-2} K^{-1}$ , a thermal diffusivity of  $5.6 \cdot 10^{-7} m^2 s^{-1}$  and an optical absorption constant  $\beta=9100m^{-1}$  at the used argon-ion-laser-wavelength; in an additional optical measurement  $\eta_{NG} = 0.96$  and  $\eta_s = 0.87$  were determined.

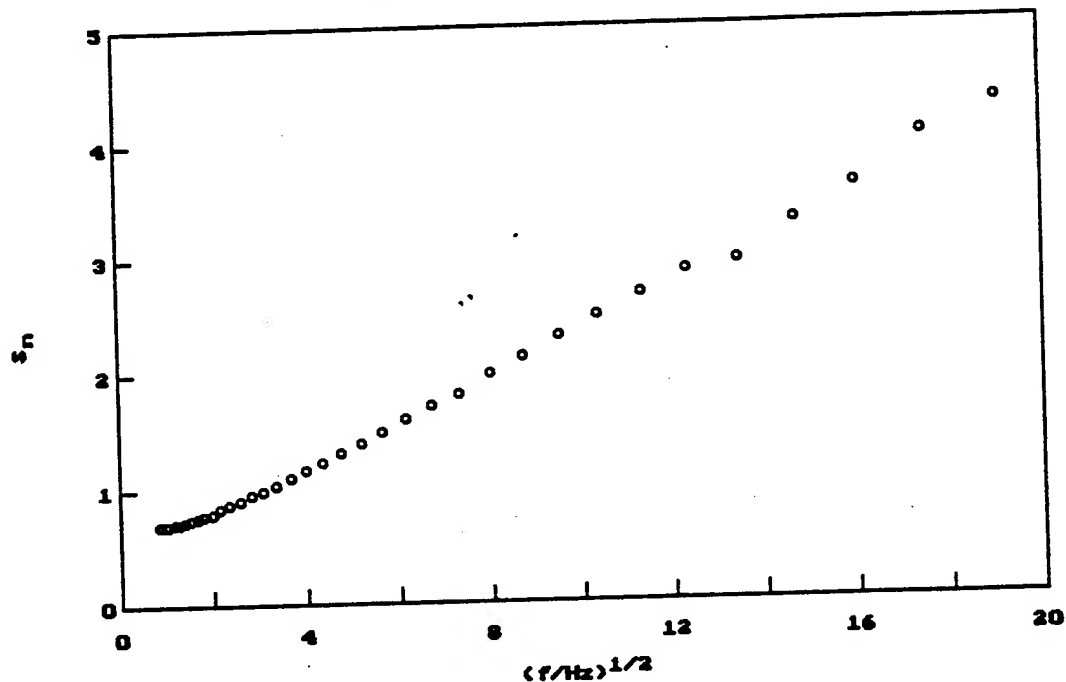


Fig. 10 Photoacoustic reflection measurement; sample is glassy carbon and reference neutral density glass.

Fig. 10 shows, that the glassy carbon sample behaves like a homogenous sample. Evaluating the measurement data with the photoacoustic software leads to an effusivity  $e_s = 2165 Ws^{1/2} m^{-2} K^{-1}$  and reveals, that the sample behaves like an ideal surface absorbing material.

Figure 11 shows the normalized amplitude of different carbon fibre reinforced materials, which do not behave like homogenous materials.

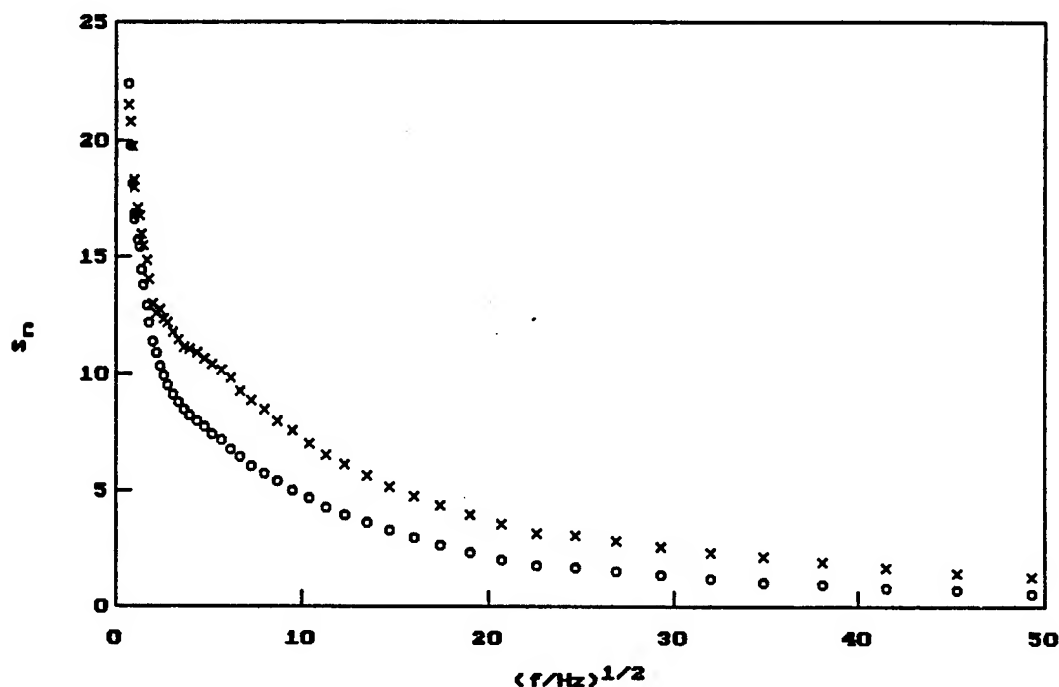


Fig.11 Photoacoustic reflection measurements of carbon fibre reinforced materials.

The samples have surface layers of different thermal thickness. The effusivity in the bulk material is lower than in the surface region.

#### 5.4 Determination of Optical Absorption Properties

Photoacoustic measurements offer the possibility to determine the optical absorption constant  $\beta$ , even if the sample is not transparent. From the frequency-dependence of the normalized amplitude and phase recorded in photoacoustic reflection measurements, Eqs. (27) and (28), the value  $\alpha\beta^2$  of the sample can be determined. If the thermal diffusivity  $\alpha$  is known or has been determined in other measurements, the optical absorption constant  $\beta$  can be calculated. Another and very easy possibility is to determine the absorption constant  $\beta$  directly from the high frequency limit of the normalized amplitude according to Eq. (29). In this case the heat capacity of the sample and the reference material have to be known and both samples have to be very weak absorbing materials. Figure 12 shows the normalized amplitude of two neutral density glass samples with a thermal diffusivity of  $5.6 \cdot 10^{-7} \text{ m}^2 \text{ s}^{-1}$ , but different optical absorption constants  $\beta$ . The neutral density glass taken as reference sample has an absorption constant  $\beta = 9100 \text{ m}^{-1}$ . The absorption constant of the other sample has been calculated to be  $5650 \text{ m}^{-1}$ .

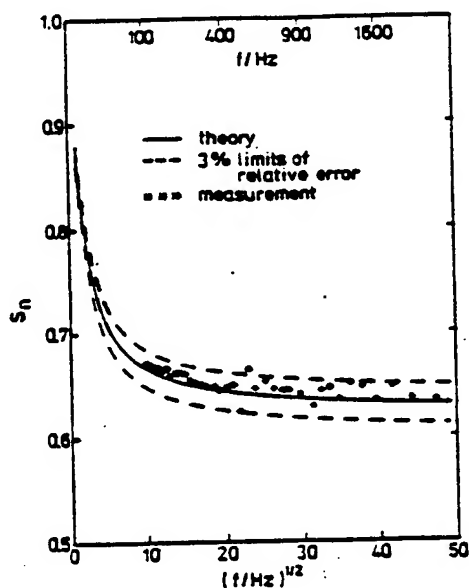


Fig. 12 Ratio of the photoacoustic amplitude of two neutral density glass samples of different absorption constants and equal thermal diffusivity.

Fig. 13 shows the ratio of the amplitudes measured of a carbon fibre reinforced material with a  $\text{CO}_2$ -laser and an argon-ion-laser. From the frequency-dependence of the normalized amplitude we can conclude, that the surface region of the sample is very transparent in the visible and the infrared radiation is absorbed at the surface.

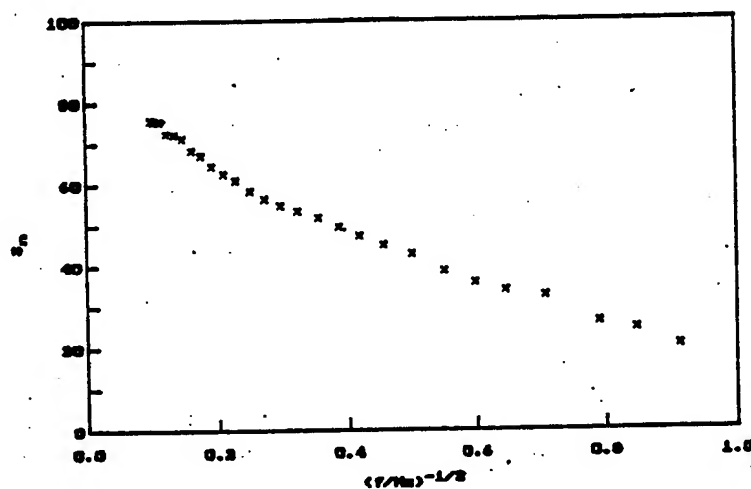


Fig. 13 Ratio of the photoacoustic amplitude of a fibre reinforced material; sample measured with a  $\text{CO}_2$ -laser and an argon-ion-laser.

## 6. Conclusions

Photoacoustic measurement techniques are nondestructive techniques which can be easily handled. Qualitative information about the thermophysical properties of a target can be rapidly obtained, but a thorough theoretical analysis is required to deduce quantitative, reliable information. If the optical reflectivity of the target is known or has been determined in an additional optical measurement, photoacoustic measurements offer the possibility to determine all the material properties needed for the calculation of temperature distributions. Compared to other conventional measurement techniques, photoacoustic measurements have the following advantages:

- direct measurement of the thermal effusivity, which is the relevant material property for the surface-temperature-rise
- thermal depth-profiling of the surface region
- measurement of surface layers, which cannot be separated from the bulk material
- additional information about the optical absorption properties
- low cost experimental set-up

The disadvantages of photoacoustic techniques are as follows:

- photoacoustic measurements fail, if the surface of the target has an extremely high porosity or roughness and does not tighten the measurement cell.
- the target is restricted to certain geometrical dimensions (diameter or length and thickness)
- laser-safety regulations have to be fulfilled.

According to our measurement results and to the above mentioned aspects, we have to draw the conclusion, that the main point of interest for photoacoustic measurements will be the investigation of surfaces and surface regions. Due to the ability to perform a thermal depth-profiling with a very good spatial resolution, which is in the range of a few micrometers, and the possibility to measure the thermal effusivity directly, photoacoustic measurement techniques seem to be one of the most powerful methods in studying heating processes of surfaces.

## 7. References

- [1] B.K. Bein, J. Pelzl: Analysis of Surfaces Exposed to Plasmas by Nondestructive Photoacoustic and Photothermal Techniques, Plasma Diagnostics, Academic Press 1989
- [2] H.S. Carslaw, J.C. Jaeger: Conduction of heat in solids, Oxford Univ. Press, London 1959
- [3] A. Rosencwaig, A. Gersho, J. Appl. Phys. 47, 64 1976
- [4] J. Pelzl, B.K. Bein: The Photoacoustic Effect of Solids: Theoretical Models and Their Limitations, Zeitschrift für Physikalische Chemie, Bd. 135, Oldenbourg Verlag, 1983
- [5] B.K. Bein, S. Krüger, J. Pelzl: Photoacoustic measurement of effective thermal properties of rough and porous limiter graphite, Can. J. Phys., 64, 1208 (1986)
- [6] J. Gibkes, B.K. Bein, D. Krüger, J. Pelzl: Thermophysical Characterization of Fine-Grain Graphites based on Thermal Waves, Carbon 31/5, 1993

# THE DEVELOPMENT OF BLAST WAVE CANTILEVER GAUGES

by

A.A. van Netten and J.M. Dewey

Dewey McMillin & Assoc. Ltd,  
Suite 100, 1741 Feltham Road  
Victoria, B.C. V8N 2A4, Canada

## 1 Abstract

A study has been made of the response of elasto-plastic and brittle cantilevers when subjected to blast wave loading, with a view to using such devices as passive blast wave gauges. In addition, the deformation of cantilever type structures can be used to assess the characteristics of accidental explosions. The study was restricted to cantilevers that were circular in cross-section and made of readily available materials. A cantilever, when loaded by a blast wave, either deforms plasticly, in which case the amount of deformation is the critical parameter, or fractures, in which case the failing or not failing of the cantilever provides the required information.

Two numerical models have been developed to describe the deformation of a dynamically loaded cantilever. Both models assume that the plastic deformation is localized in a region near the fixed end, and that the loading force is a function of the dynamic pressure time history and a variable drag coefficient, which depends on the Reynolds number, Mach number and angle of attack.

The first numerical model assumes a rigid-plastic response of the cantilever. This model accurately describes the response only of cantilevers made of 50/50 lead/tin alloy. It overestimates the deformation of cantilevers made of other materials when exposed to blast waves from high explosives and in a shock tube.

The second model assumes an elastic-plastic response. The algorithm is based on the premise that the elastic curvature of the cantilever is limited by the plastic yielding stress of the material and that as the curvature approaches this limit the cantilever rotates by the amount needed to keep the curvature constant and equal to this maximum. The amount of rotation is determined by fitting a fourth order polynomial with a constrained second derivative based on the maximum allowed curvature. The rotation angle is found from the angle derived from the slope of the fitted function at the origin. A rotation by this angle yields a minimum in curvature in the rotated reference frame. This model improved the predictions for cantilevers constructed of aluminum and steel.

The numerical models have been evaluated by studying the response of cantilevers exposed to shock waves in a shock tube, and to the blast waves from the DISTANT IMAGE and MINOR UNCLE events. The response to the shock tube flows was recorded by high speed photography which showed good agreement between the ob-



served modes of deflection and those predicted by the elastic-plastic model. The models also provided good predictions of the deformation of a wide range of cantilevers exposed to the free field blast waves. These cantilevers were also used to detect any non-radial flows and to study the boundary layers in the blast waves over different surfaces.

It will be demonstrated how the numerical modelling can be used to determine the type of cantilever that might be used as a passive gauge for monitoring the blast wave from an explosion, or for evaluating the deformation of a cantilever exposed to the blast wave from an accidental explosion so as to characterize the explosion.

## 2 Introduction

A need has been expressed for the development of inexpensive instrumentation for the measurement of blast wave properties, especially in experiments where a large number of gauges are required to completely determine the blast field. Such experiments include non-symmetrical blast waves such as the wave from a tunnel entrance or tests where the uniformity of the blast wave is not known. This paper describes the use of cantilevers that are circular in cross-section, and have modes of failure that are either ductile or brittle.

## 3 The loading function

For the response of a cantilever to be theoretically calculated a knowledge of the loading function is required. The loading function depends on the time history of the dynamic pressure in a shock or blast wave, and on the drag coefficient which may itself be a function of the Mach number and/or the Reynolds number of the flow. To describe the loading function on cantilevers placed in a shock tube flow an inviscid one dimensional explicit flux corrected transport(FCT) simulation was written. For the large scale explosions the flow properties were obtained from two programs, *AirBlast* (Dewey and McMillin, 1989) and ANFO.EXE (Needham *et al*, 1991). *AirBlast* is a database of experimentally-measured results, while ANFO.EXE is based on a pure hydrodynamic code.

It was assumed that the loading on the cantilevers considered for this project was directly related to the dynamic pressure in the flow field. It has been shown (van Netten, 1995<sub>a</sub>) that the diffraction of the shock wave around the cantilevers used here does not contribute significantly to the loading and therefore the cantilever can be assumed to be purely drag loaded. The equation relating the dynamic drag force,  $F_d$ , on the cantilever to the dynamic pressure is

$$F_d = C_{d(\alpha, R_e, M)} \frac{1}{2} \rho u^2 A, \quad (1)$$

where  $C_{d(\alpha, R_e, M)}$  is the drag coefficient,  $\rho$  is the air density,  $u$  is the air velocity and  $A$  is the frontal area exposed to the flow. The  $C_d$  of a circular cross-section cantilever

is function of the angle of orientation to the flow( $\alpha$ ), the Reynolds number( $R_e$ ) and the local Mach number( $M$ ) of the flow. The loading of constrained objects subjected to blast loading is a unsteady event and, since both the Reynolds number and Mach numbers are functions of the time varying flow conditions, the drag coefficient is also time varying. In addition, since a cantilever bends elastically throughout its length when subjected to blast loading, each of its elements is inclined at a different angle to the flow and thus experiences a different drag coefficient.

It has been assumed that the drag coefficients for steady flow around cylinders would give a reasonable approximation for the drag coefficients that exist in the unsteady flows around the dynamically loaded cantilever. Figure 1 and 2 show the dependence of the drag coefficients on the Reynolds number and Mach number respectively. The data from these curves was digitized and stored in a file which was subsequently read during the numerical simulation of the blast loaded cantilever. If the Reynolds number is greater than about  $4.0 \times 10^5$  the flow is turbulent and the lower curve in figure 2 is used and if it is laminar the upper curve is used. The drag coefficient is also a function of the angle of inclination of the cantilever. The experimental results obtained from Hoerner (1965) for skewed cylinders in a steady flow show that the drag coefficient can be estimated by the following equation:

$$C_d = C_{d(\alpha=0)} \cos^3(\alpha), \quad (2)$$

where  $C_{d(\alpha=0)}$  is the drag coefficient for zero angle of attack. A value for the drag coefficient was determined using the above criteria at every timestep and for each lengthwise element during the calculation of the response of the blast loaded cantilever.

## 4 Cantilever response

The following sections describe the various mathematical models and the underlying assumptions used to predict the response of the cantilevers in both the shock tube and HE tests. These predictions serve as a basis for deciding which cantilevers will be located at which positions. This is particularly useful for cantilevers made of materials not previously used at HE events. These models can also be used to provide information about the size and position of accidental explosions by reverse engineering the observed damage to cantilever type structures.

### 4.1 Ductile cantilevers: Rigid-plastic

The rigid-plastic model is the most elementary assumed response of a blast loaded cantilever. This response assumes that the cantilever only deforms at the fixed end when the drag force produces a moment about the fixed end which exceeds the maximum resisting moment of the material. When this condition arises a plastic hinge is created and the cantilever rotates about this position as a rigid body until

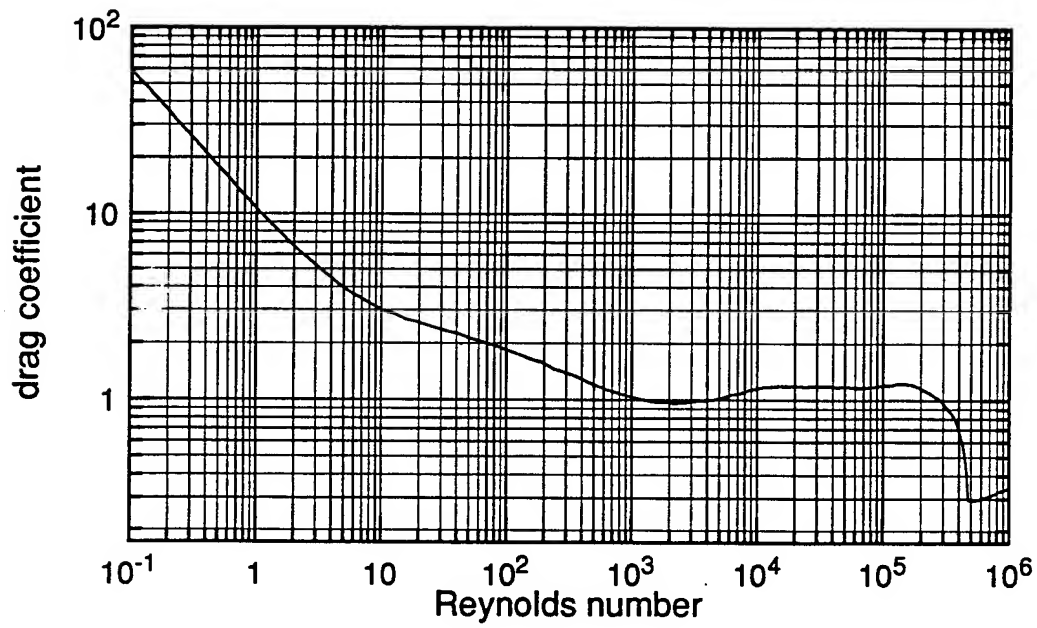


Figure 1: Drag coefficient for a circular cylinder as a function of Reynolds number (Schlichting, 1960).

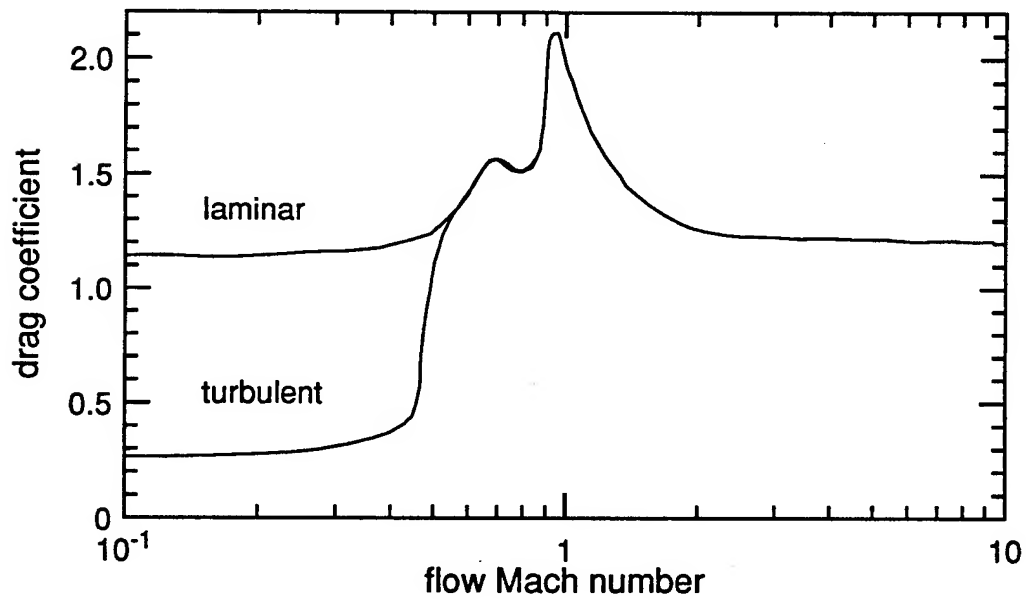


Figure 2: Drag coefficient for a circular cylinder as a function of Mach number (Hoerner, 1965).

all the energy gained in the loading phase is dissipated in plasticity. The equation describing the angular acceleration of the cantilever is shown below:

$$\frac{d^2\alpha}{dt^2} = \frac{1}{I} \left[ \frac{1}{4} \rho_a d L^2 u^2 C_d \cos(\alpha) - \frac{4}{3} \sigma_y (d/2)^3 \right], \quad (3)$$

where  $\alpha$  is the angle through which the cantilever is bent,  $I$  is the moment of inertia of a cylinder rotating about its end ( $\frac{1}{3}mL^3$ ),  $m$  is the mass of the cantilever,  $\rho_a$  is the air density,  $L$  is the length of the cantilever,  $d$  is the diameter of the cantilever,  $\sigma_y$  is the yielding stress of the material,  $u$  is the air velocity, and  $C_d$  is given by equation (2)

A fourth order Runge-Kutta scheme was used in conjunction with the required flow property data and the drag coefficient data to integrate this equation over a large number of timesteps and obtain the final angle of bend. This equation shows that the angular acceleration of the cantilever is produced by the difference between the torque produced by the imposed load and the maximum moment that the material can withstand. If the material is strong enough to withstand the torque no motion will occur, but if the load is larger the cantilever will begin to accelerate and the rate of acceleration is inversely proportional to the moment of inertia of the cantilever. A graphical representation of the solution for a cantilever subjected to a shock tube flow is given in figure 3.

## 4.2 Ductile cantilevers:Elastic-plastic

An elastic-plastic approach is a more realistic description of the response. A cantilever initially responds by deforming elastically until the deformation produces a bending moment within the material which exceeds the maximum allowed by the material. At the position where this maximum occurs the cantilever permanently deforms while still undergoing its elastic deformation elsewhere. For the cantilevers used here this maximum occurred at the base of the cantilever and therefore this is the only position where plasticity was considered in this model.

The algorithm for this model is based on the condition that the elastic curvature cannot exceed a maximum value and this maximum is approximated by the equation below,

$$\frac{d^2y}{dx^2} = \frac{M_b}{EI}, \quad (4)$$

where  $M_b$  is the maximum bending moment allowed within the rod,  $E$  is the Young's modulus,  $I$  is the area moment for the cross section of the rod,  $x$  is the distance measured from the clamped end and  $y$  is the displacement of the rod from the equilibrium position. If the curvature does exceed this value the material will deform in such a way to keep the curvature constant and equal to the value determined by equation (4). The curvature is kept at the maximum allowed curvature by a plastic rotation of the cantilever about the clamped end of the required amount to keep the curvature equal to the maximum. A proof of the apparent reduction of curvature

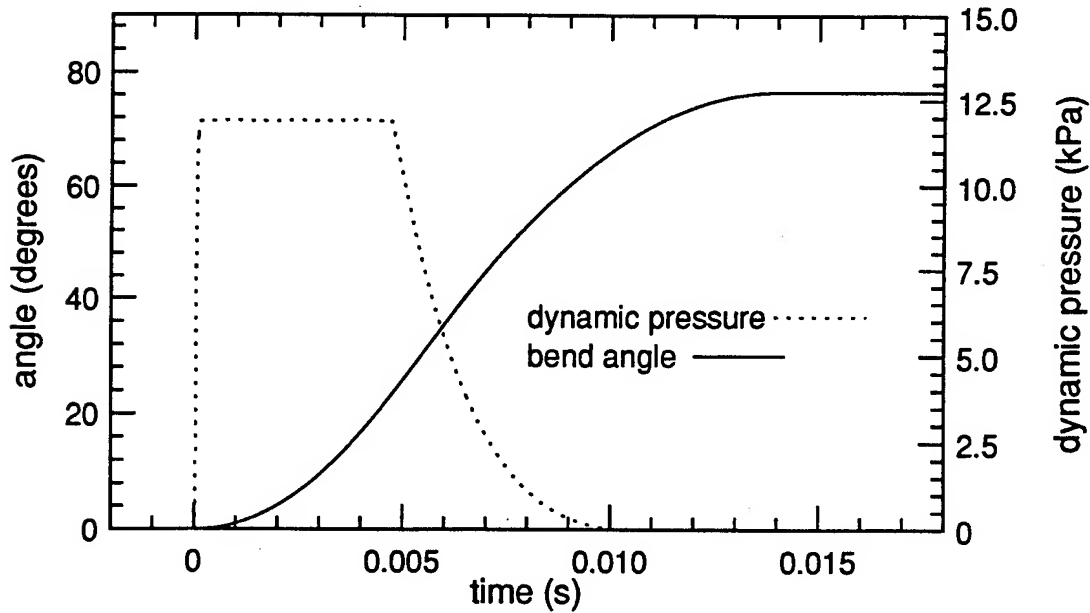


Figure 3: The deformation of a cantilever as a function of time based on equation (3) for a 0.05 cm long solder cantilever subjected to a shock tube flow produced by a  $M=1.23$  incident shock wave.

with a rotation of the cantilever about the clamped end is given in van Netten (1995<sub>a</sub>).

A multi-degree of freedom method was used to simulate the elastic response of the cantilever using an updated stiffness matrix at each timestep. Figure 4 shows the distribution of masses for a cantilever which has been simulated with 5 elements. This program was used to drive the plastic deformation portion of the program by using the criterion that the curvature of the cantilever could not exceed a certain maximum.

Two reference frames were used for the calculation. The first was the elastic reference frame which rotates with the plastic deformation of the hinge and is where the elastic response of the cantilever is calculated. The second reference frame was the laboratory frame. The origins of both reference frames were coincident. A fourth order polynomial of the form

$$y(x) = a_2x^2 + a_3x^3 + a_4x^4 \quad (5)$$

was used to fit the first three nodal positions in the elastic reference frame. The first two coefficients were set to zero because of the boundary conditions at the clamped end of the cantilever, namely  $a_0 = 0$  since the cantilever is hinged at the origin and  $a_1 = 0$  because in this frame the slope at the origin must be zero.

The second derivative with respect to  $x$  of the above function was taken and evaluated at the origin, yielding a value of  $2a_2$ . Substituting this into equation (4)

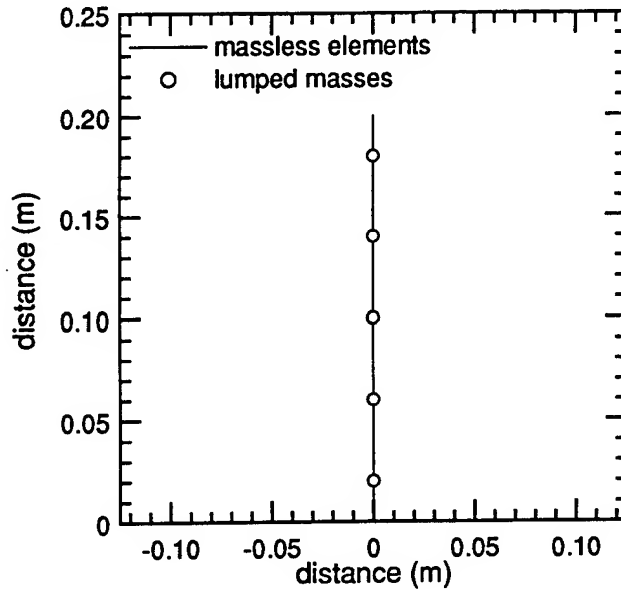


Figure 4: Discretization of a 0.2 m cantilever into five elements.

gives

$$a_2 = \frac{M_b}{2EI} \quad (6)$$

and is the condition for the onset of plastic deformation. The right hand side of (6) sets a maximum to the size of  $a_2$  since the material can only withstand a finite amount of curvature before plastic deformation ensues. At every timestep during the calculation a fit was done to the first three nodal points in the elastic frame to determine the value of  $a_2$ . If the loading is sufficiently large then at some time  $a_2$  will exceed the above limit and a plastic deformation will begin.

To determine the amount of plastic deformation a second fit was done which was of the form

$$y(x) = a_1x + \frac{M_b}{2EI}x^2 + a_3x^3 + a_4x^4. \quad (7)$$

According to van Netten (1995<sub>a</sub>) a minimum in curvature exists at the origin when  $y(x)$  is rotated by an angle of  $-\text{atan}(a_1)$ . The cantilever seeks out this minimum and deforms the required amount since its curvature cannot exceed the maximum value determined by the material. In the numerical solution this angle is the amount of plastic deformation that occurred for the particular timestep. All the nodal points in the elastic reference frame were then rotated back by this same angle to be ready for the next timestep. This algorithm keeps the bending moment at the hinge in the elastic reference frame equal to the maximum bending moment allowed by the material.

Figure 5 shows the deformation time history obtained by using a five element

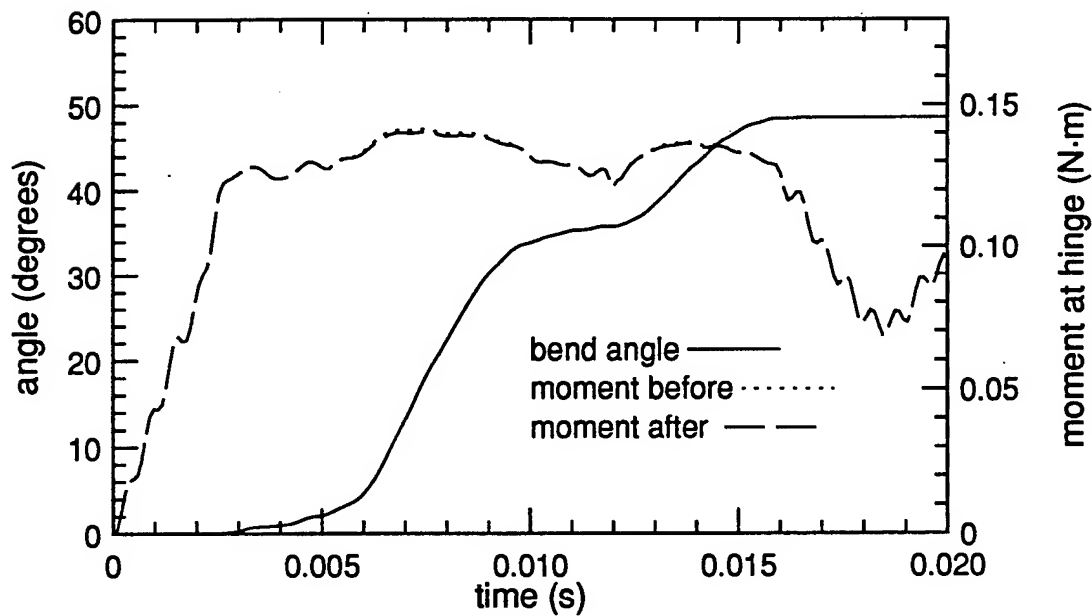


Figure 5: The deformation and hinge-moment time histories of a 0.2 m long, 1.55 mm diameter cantilever made from al4043 subjected to a shock tube flow produced by a  $M=1.23$  shock wave. Two moments are shown, one before rotation of the cantilever and one after rotation.

numerical simulation of a 0.2 m long cantilever made of aluminum 4043 with a diameter of 1.55 mm that has been loaded within the shock tube. Also plotted in this figure are the bending moment at the hinge and the maximum that can exist within the material at that time. The two curves are almost indistinguishable, however the moment after the rotation is slightly less, which is required by the material. The maximum bending moment is not constant, as it would be if no strain hardening effects were included in the solution. The bend angle time history shows various oscillations at periodic intervals which are due to the existence of higher modes within the cantilever. These higher modes create a variation in curvature at the hinge which in turn causes a nonuniform deformation rate.

To test the consistency and stability of the algorithm several runs of the program were performed using the same initial conditions but varying the number of elements and hence timesteps. The results of this test using 3, 5, 20, and 35 elements are given in figure 6 and it is seen that there was a rapid convergence to a stable solution. All of the final deformation angles were within one degree of one another for this particular test. A 35 element run takes approximately 28 min on a 66 MHz 486DX2 computer while a 5 element run takes 9 seconds on the same computer. For most calculations performed for this project either a 5 or 10 element run was used since the small gain in accuracy by using a larger number elements did not justify the increased calculation time.

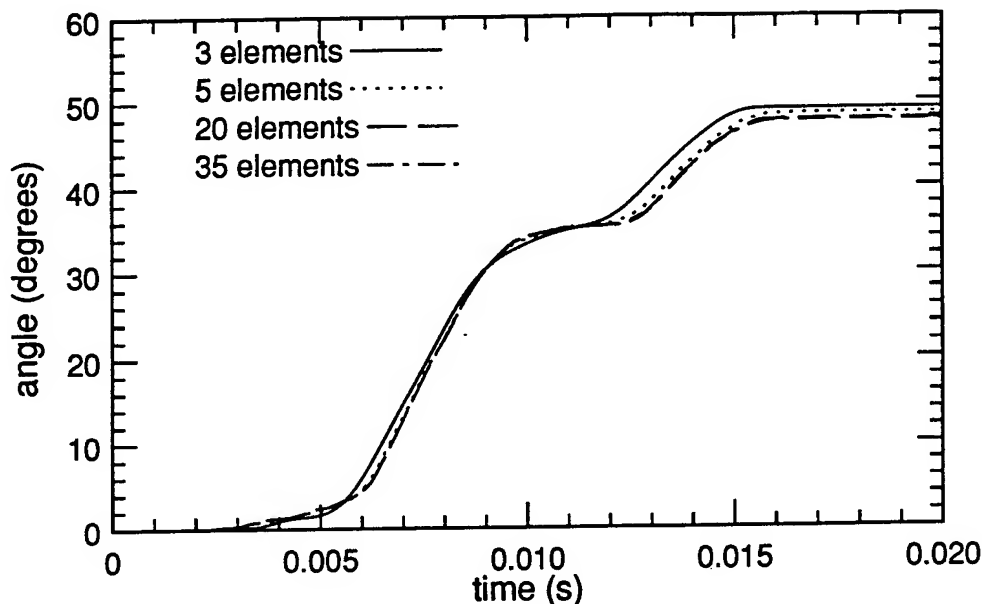


Figure 6: Deformation time histories of a 0.2 m long, 1.55 mm diameter aluminum cantilever using different numbers of elements.

### 4.3 Brittle cantilevers: Rigid-brittle

Some materials such as graphite and glass break rather than bend when rapidly loaded and as a consequence are called brittle. In theory, a brittle cantilever breaks when the imparted load produces a stress in the material which exceeds the maximum yield stress of that material. In the rigid-brittle model it is assumed that, since the response time of the cantilever is significantly smaller than the duration of the positive phase of dynamic pressure, the cantilever will essentially respond to peak dynamic pressure. This model also assumes that the load is instantly transmitted to the base and that the elastic motion is negligible. The force on the rod due to blast loading and the resistance the rod gives before failure are determined in the same way as that for the bending cantilevers. For the cantilever to fail the loading force must be greater than the resisting force. This is shown in the equation

$$C_d P_{kd} L d > \frac{4}{3} \sigma_y \left(\frac{d}{2}\right)^3, \quad (8)$$

where  $C_d$  is the drag coefficient,  $P_{kd}$  the peak dynamic pressure ( $\frac{1}{2} \rho u^2$ ),  $L$  and  $d$  the length and diameter of the rod respectively and  $\sigma_y$  the stress required to break the cantilever. Under this condition the cantilever breaks and gives a lower limit to the peak dynamic pressure. If however, the cantilever does not fail an upper limit is determined. To develop a gauge based on this design one can position a series of rods with different lengths and expose them to a blast wave with the objective of having the longer rods fail and the shorter rods not fail. In this way the peak



dynamic pressure value is bracketed with a resolution depending on the increment in length between rods in the series.

## 5 Experimental results

Two types of experiments were performed to evaluate the performance of the various models. One involved the loading produced by a shock tube and the other was the loading produced by the detonation of two high explosives, DISTANT IMAGE(2.650 kt ANFO, June 20, 1991) and MINOR UNCLE(2.431 kt ANFO, June 10, 1993).

The first set of experiments in the shock tube was performed on cantilevers made from solder wire. The length, diameter and composition of the cantilevers were 5.1 cm (2.0 in), 1.0 mm (.040 in) and 50/50 lead/tin respectively, and were similar to the cantilevers used by Dewey (1962). These cantilevers were exposed in the shock tube to shock waves in the Mach number range from 1.16 to 1.27. The angles of plastic deformation of the cantilevers were measured and are plotted against incident shock Mach number in figure 7. The repeatability of the final angles for nominally identical experiments was approximately  $\pm 5^\circ$ . This variability may have been due to inconsistencies in material properties as well other effects such as diaphragm material striking the cantilever.

A single degree of freedom(SDOF) rigid-plastic model as shown in 4.1 was used to predict the angle of rotation of the cantilevers. These cantilevers were constructed of solder and therefore experienced very little elastic motion before the onset of plastic deformation. It was therefore hypothesized that a SDOF rigid-plastic model might produce a good approximation of the motion of the impulsively loaded cantilevers. The SDOF equation describes the angular deformation of the cantilever as a function of time and it is the most elementary of assumed responses of a blast loaded cantilever. This equation was integrated by using a fourth order Runge-Kutta scheme, and updating all the variables such as air velocity, air density, drag coefficient etc at each time increment. The results are plotted in figure 7 with the experimental results. The agreement is good for the entire range of Mach numbers used, but this may in part be due to canceling of opposing effects. For example, effects such as strain hardening may be taking place but because of the actual drag coefficient being possibly larger than the theoretical values the two errors may cancel. The rigid-plastic model should overestimate the deformation because it assumes that all the strains are concentrated at one point, the plastic hinge at the base, and are not distributed throughout a region near the base, as in the case of the actual cantilever.

Cantilevers made of aluminum 4043 and 5056 with lengths of 99.2 mm (3.9 in) and diameters of 1.55 mm (0.06 in) were also tested in the shock tube. These experiments were to determine if the SDOF rigid-plastic model could be used to predict the final angles of the shock wave loaded cantilevers made of materials which

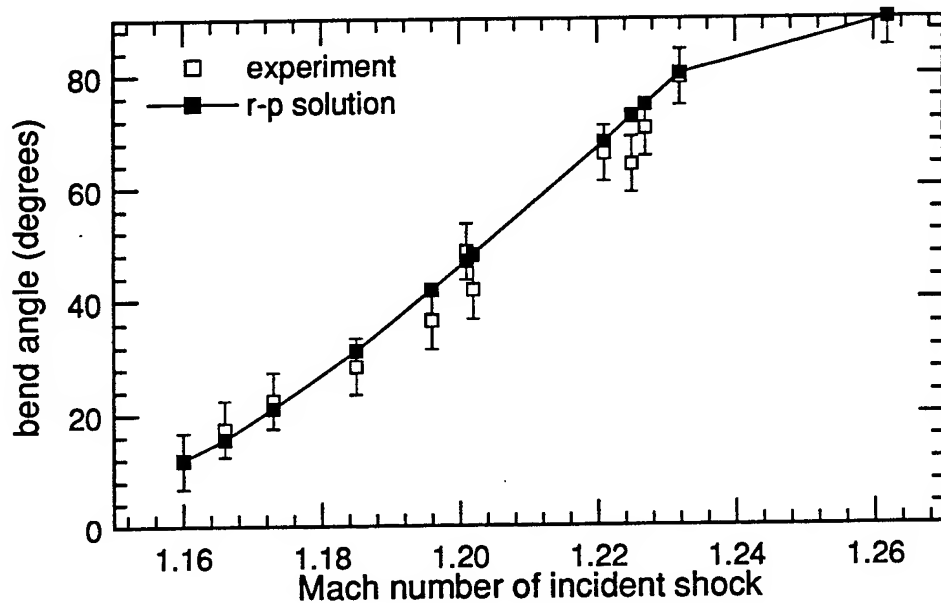


Figure 7: Comparison between the rigid-plastic solution and experimental results for 5.08 cm long, 1 mm diameter solder wires subjected to shock tube flows.

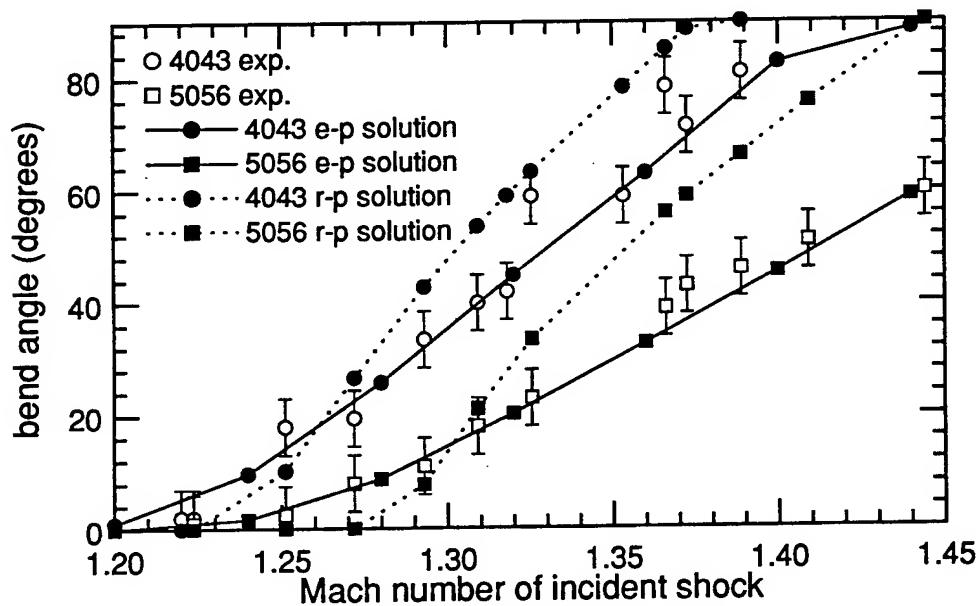


Figure 8: Comparison between the elastic-plastic, rigid-plastic solution and experimental results for aluminum 4043 and 5056 cantilevers 10 cm long, 1.55 mm diameter subjected to a shock tube flow.

have a more extensive elastic response than solder. Figure 8 is a plot of the final angles of rotation for cantilevers made of aluminum 5056 and of 4043 as a function of shock wave Mach number. This figure also shows the theoretical permanent rotation angles obtained by using the rigid-plastic SDOF model. The observed permanent deformations for both types of aluminum were significantly less than the predicted responses obtained from the solution of equation (3).

Although the simplified rigid-plastic model overestimates the amount of deformation that occurs when the aluminum cantilevers are dynamically loaded it does provide a first order approximation to the deformation. This solution may be used when it is necessary to identify if a given cantilever type structure will survive when blast loaded because if the model predicts survival then there is a high probability that it will.

The elastic-plastic approach described in section 4.2 attempts to improve the predictions of the final deflection angle of cantilevers made of metals other than solder by introducing elasticity, strain hardening and strain-rate hardening in the deformation process.

Figure 8 also displays the results of the elastic-plastic model for both types of aluminum. This run of the model discretized the cantilever into 5 elements of equal length, each approximated by a point mass at the center of the element. The model predicted the response of these cantilevers very well. The solution however is sensitive to the strain-rate and strain hardening terms which were based on the values given by Manjoine(1944) and Parkes(1958).

## 5.1 High speed photographic measurements

Further experiments were carried out to provide information about the dynamic deformation of the cantilevers during the shock wave loading process. High speed photography was used to record the motion of cantilevers of four different lengths made from aluminum 4043.

A 1 cm rectangular grid was seen in each frame of the high speed film and provided a scale in the field of view so that the image in each frame could be accurately digitized using an x-y digitizer. It was estimated that the average error in digitizing a specific position in the field of view was approximately 1.0 mm. Figure 9 shows the digitized images of the cantilevers in typical experiment and the shapes predicted by the elastic-plastic model described in 4.2 at the corresponding times. The images have been displayed up to the time when the maximum elastic and plastic displacement had occurred. After that time the cantilever began to reverse its motion and oscillate about the equilibrium plastic deformation angle.

The bending profile displayed in figure 9 show good qualitative agreement between the observed and calculated deformations but the numerical simulation appears to slightly underestimate the elastic displacement even though the final plastic deformed angle agrees well with experiment. This is probably due to the algorithm which updates the stiffness matrix, since this matrix is generated by forcing the dis-

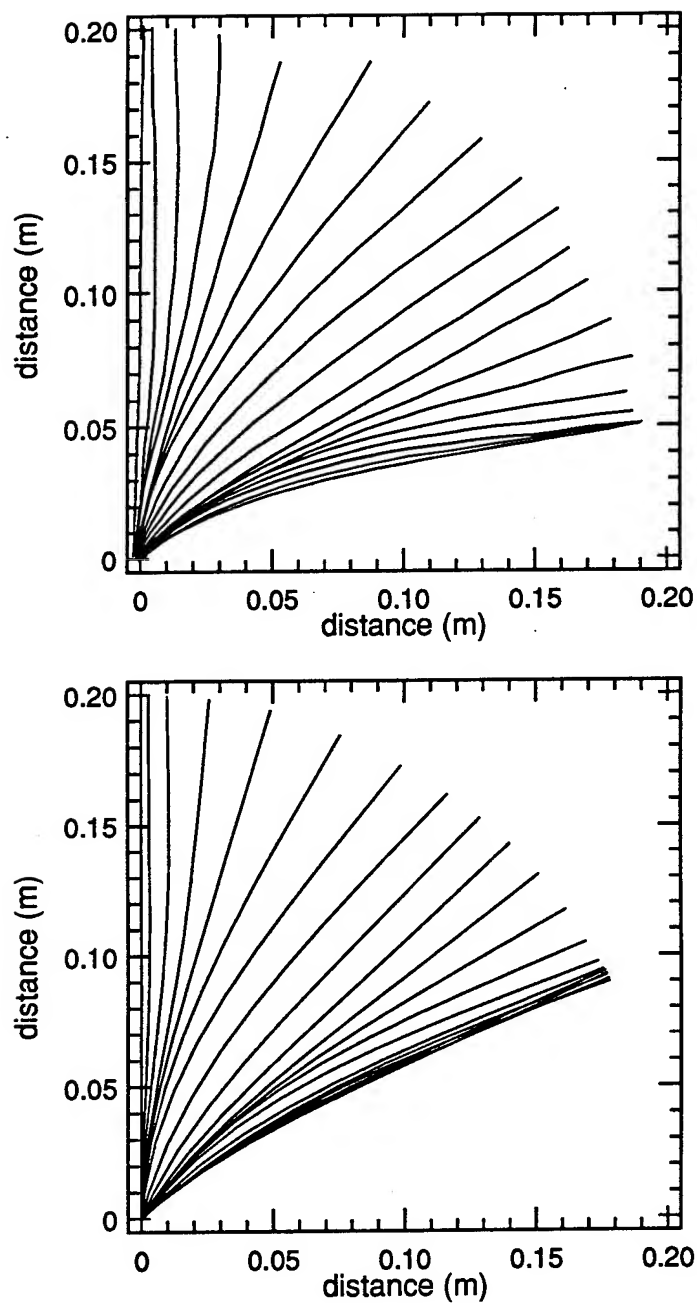


Figure 9: Experimental(top) and theoretical(bottom) deformation of a 0.2 m long, 1.55 mm diameter aluminum cantilever in a shock tube flow induced by a incident shock wave of Mach number 1.23. The theoretical deformation was generated by the elastic-plastic model. The time between adjacent images is approximately 1 ms.

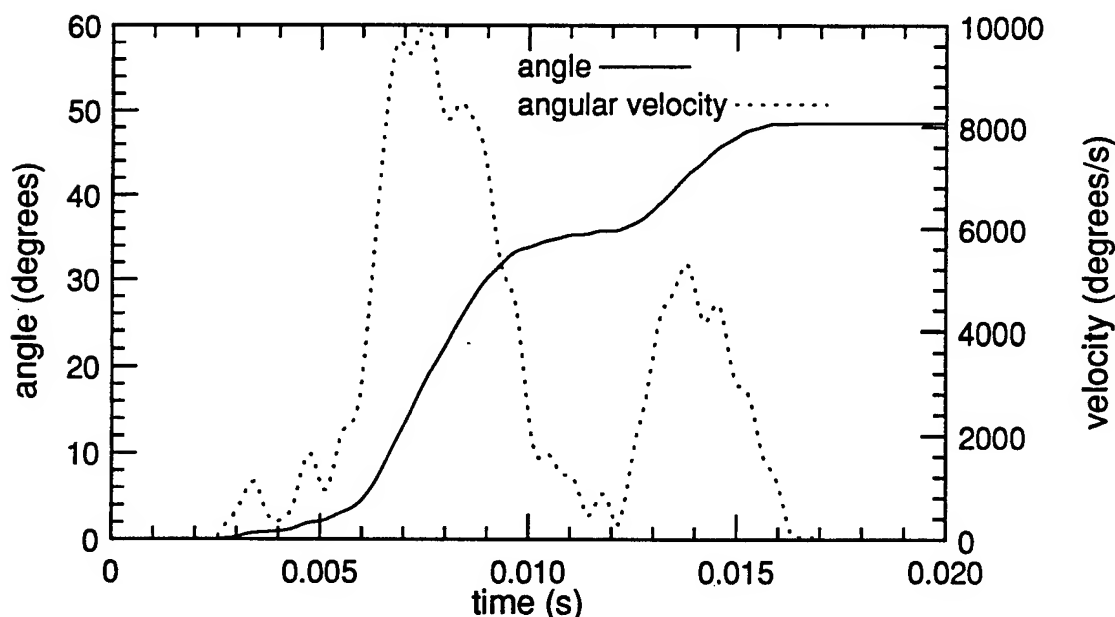


Figure 10: Bending and angular velocity time histories for the 0.2 m long, 1.55 mm diameter aluminum cantilever subjected to the flow shown in figure 9.

tance to each node to remain constant in a non-conservative fashion. This effectively shortens the lever arm as the displacement of each node is increased, causing the cantilever to appear "stiffer". This effect would be significantly reduced if a two-dimensional large-deflection elastic simulation had been used to drive the plastic deformation portion of the simulation.

Figure 10 shows the plastic deformation angle and angular velocity of the same cantilever as functions of time. The numerical model predicts a non-constant deformation rate which oscillates. A similar plot of of angular deformation with time could not be derived from the photographic records of the cantilevers because it was very difficult to determine the plastic deformation angle at the base of the cantilever from the digitized data. Experimental oscillations in the deforming rates can be seen however by viewing the spacing between adjacent profiles. In figure 9 the distance which separates the adjacent cantilever profiles in both the experimental and theoretical plots changes with time, especially near the base. These higher modes are generated by the elastic vibrations induced during the loading of the cantilever. The magnitude of the higher mode elastic vibrations decreases when the cantilever length is reduced. It is clear that the amount of plastic deformation is also a function of the elastic properties of the material and not just of the yield stress.

After being loaded by the shock waves, all the cantilevers in these experiments were straight except in the region close to the base where plastic deformation occurred. The high speed film showed that the cantilever is not straight during the deformation process but is curved due to its elastic nature. In some cases cantilevers

were also observed to have plastic deformations in regions other than the base. This occurred when the length of the cantilever was increased to a length where the induced elastic vibrations were of such magnitude as to produce bending moments larger than the material could withstand. For cantilevers where this effect occurs a model based on a premise that a single plastic hinge exists at the fixed end would be insufficient to describe the response during dynamic loading. The model can be used to predict the length of the cantilever for which this mode of failure is possible, and thus the limiting length for a cantilever with a specific cross-section and material properties.

## 6 High explosive tests

DISTANT IMAGE (van Netten et al, 1992) was the first of two experiments used to evaluate the effectiveness of the numerical models in predicting the response of cantilevers to blast wave loading. 404 cantilevers were used at this event, and 437 cantilevers were used in the second experiment, code named MINOR UNCLE two years later (van Netten et al, 1995<sub>b</sub>). The results obtained from these experiments are given in the following sections.

As shown earlier the rigid-plastic(R-P) model gave a reasonable prediction of the response of solder cantilevers subjected to a shock tube flow. The R-P model was also used to predict the response of the solder cantilevers at both HE events. Figure 11 shows the experimental and predicted final angles of deformation versus range for solder cantilevers 0.07 m long. The agreement between the theoretical response derived from the rigid-plastic model and the experiment is relatively good.

The DISTANT IMAGE explosion was slightly larger than MINOR UNCLE, the ratio of charge weights was 1.09, which corresponds to a scaled difference in distance of about 3 %. The rigid-plastic model predicts a difference in angle, for the solder cantilevers, between DISTANT IMAGE and MINOR UNCLE of about 5° to 10° with this ratio of charge weights. The uncertainty of each measurement is  $\pm 5^\circ$  and is within the expected theoretical difference. It is perhaps unreasonable to expect significantly better agreement than this, taking into consideration local variations in the blast wave, and particularly the effects of such phenomena as dust pickup.

Figure 12 shows the deformation angle versus distance from the MINOR UNCLE explosion for 0.15 m long cantilevers constructed of aluminum 4043. The theoretical deflections predicted by the elastic-plastic(e-p) model are plotted as the solid line and the experimental data are plotted as the squares, and the agreement is good.

### 6.1 Comparison of charge yields

At both DISTANT IMAGE and MINOR UNCLE there were sets of identical cantilevers that were placed at a range of distances from the explosions but not necessarily at the same radial distances in the two experiments. The resulting angles of deformation for one of these sets are plotted vs distance in figure 13. This set

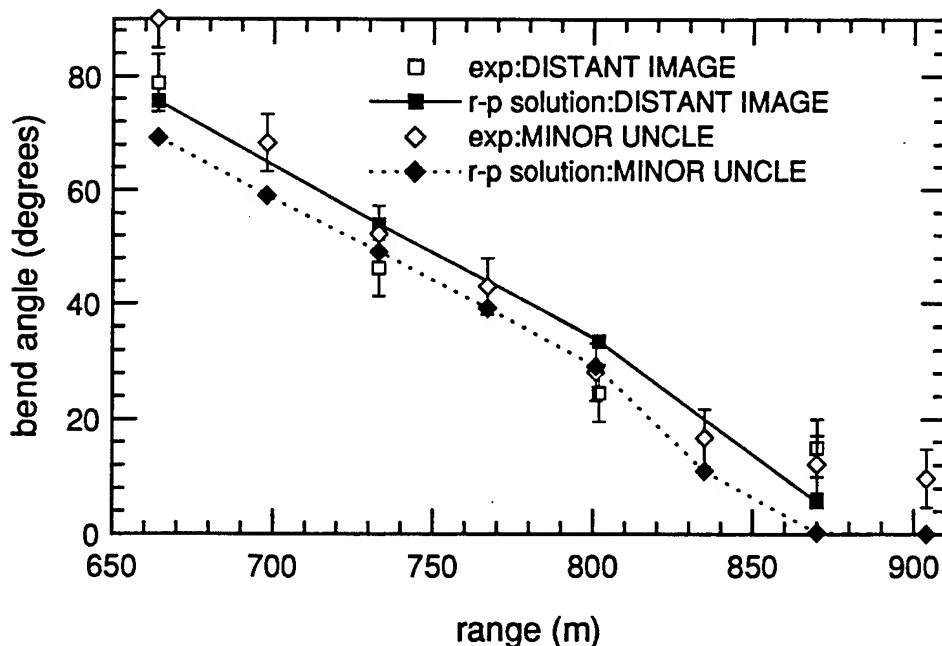


Figure 11: The deformation versus range for 0.07 m long, 1 mm diameter solder cantilevers at DISTANT IMAGE and MINOR UNCLE. The theoretical values were generated by the rigid-plastic model.

of cantilevers were constructed from aluminum 4043 and were 1.55 mm ( 1/16 in) in diameter and 0.15 m (0.5 ft) long. It will be seen that the deflection angles at DISTANT IMAGE were larger than those at MINOR UNCLE, as expected. This particular type of cantilever responds in approximately 15 ms (based on the results from the elastic-plastic model and shown in figure 14), by which time the blast wave has decayed by 5%. The positive phase of the blast wave at the range where the cantilevers were positioned was 446 ms. It is therefore assumed that peak dynamic pressure was the dominant factor in determining the final angle of deformation. The two explosions were very similar in size and hence have similar decay rates. The variation of peak dynamic pressure with distance at DISTANT IMAGE were obtained from *AirBlast* and were used with the data from figure 13 to develop the calibration curve of peak dynamic pressure versus angle of bend. A polynomial fit was made to the data and used to predict the peak dynamic pressure that had occurred at MINOR UNCLE based on the observed deformations. Eight other sets of similar cantilevers, for which this type of analysis could be applied, were used at both tests. The results of peak dynamic pressure versus range obtained for MINOR UNCLE from these cantilevers and the brittle gauges are plotted in figure 15, with the results from the electronic gauges, the MINOR UNCLE version of *AirBlast* and ANFO.EXE. The results based on the analysis of the cantilevers correlate well with those from the other techniques.

The variations of peak dynamic peak pressure as functions of distance, obtained

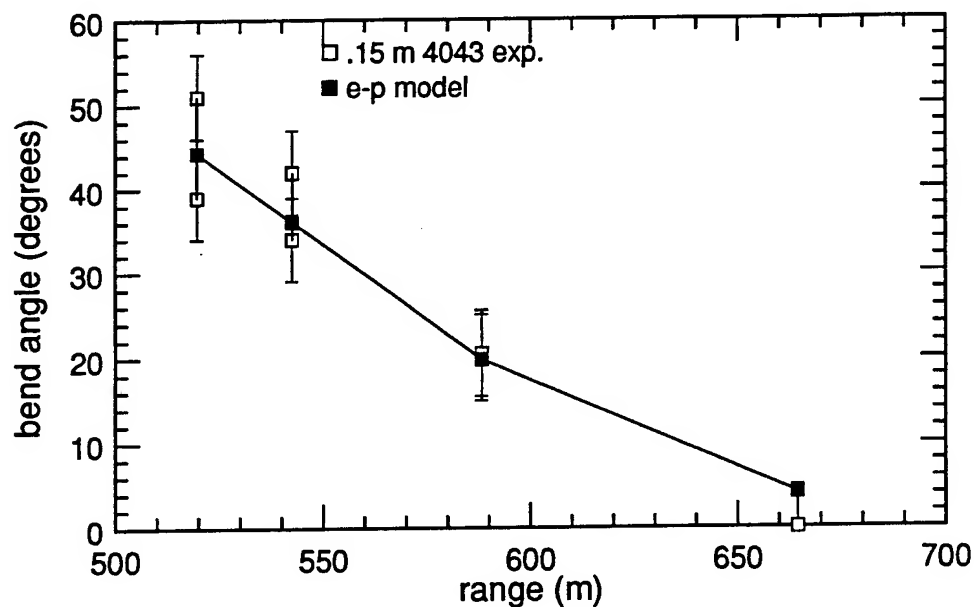


Figure 12: Experimental and theoretical deformation angle versus range for aluminum 4043 cantilevers .15 m long, 1.55 mm diameter at MINOR UNCLE.

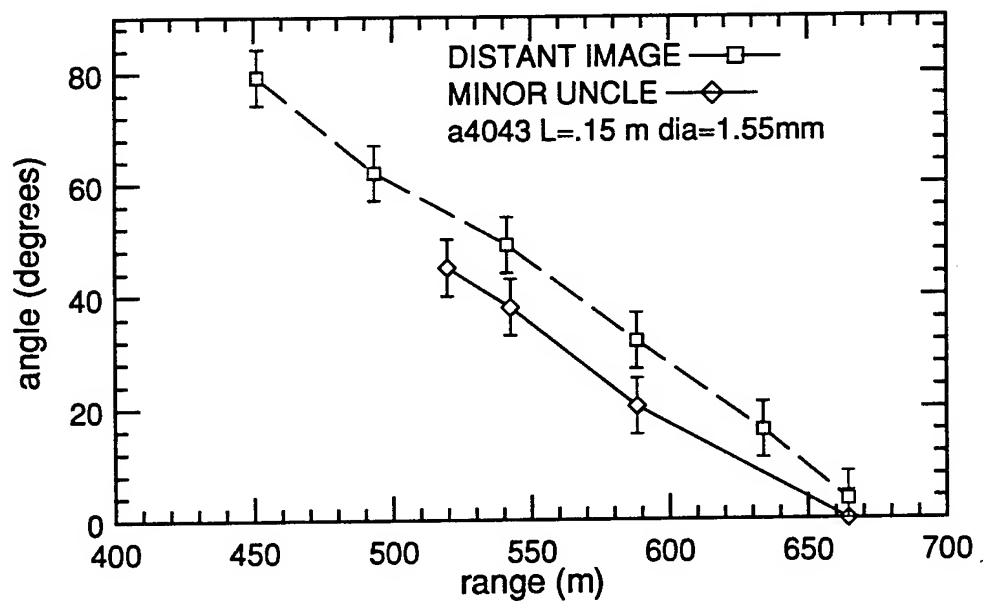


Figure 13: Comparison between deformation angles for 0.15 m long, 1.55 mm diameter aluminum 4043 cantilevers at both DISTANT IMAGE and MINOR UNCLE.



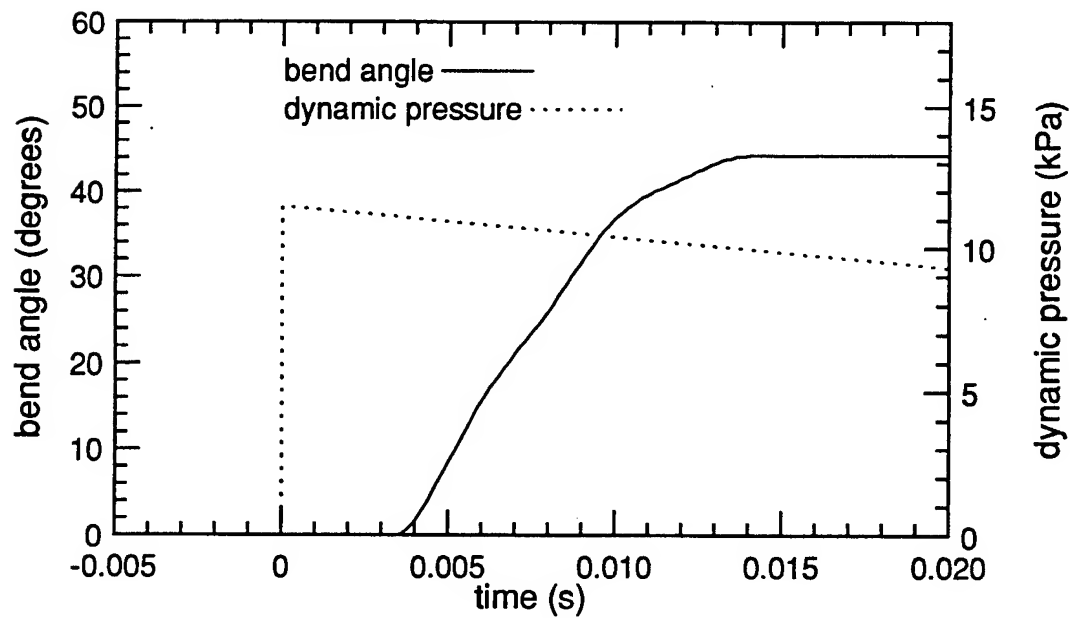


Figure 14: Deformation and dynamic pressure time histories for a 0.15 m long, 1.55 mm diameter aluminum 4043 cantilever 519.0 m from GZ at MINOR UNCLE.

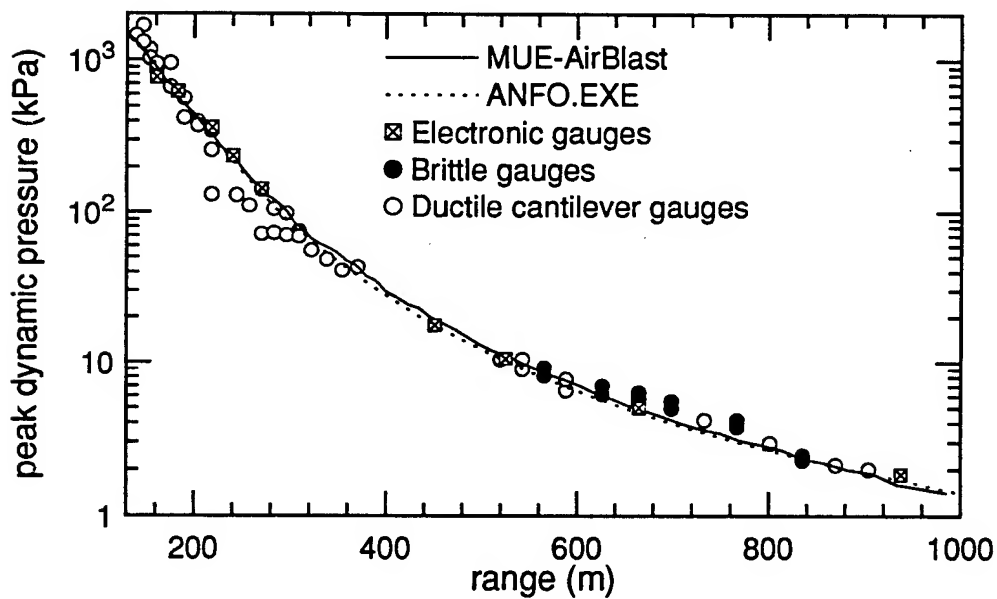


Figure 15: Peak dynamic pressure versus range for MINOR UNCLE obtained from the ductile and brittle cantilevers, electronic gauges *AirBlast* and ANFO.EXE.

from the cantilever measurements on the two experiments, were compared and used with the cube root scaling law to calculate the relative yields of the two explosives. This was done for a range of distances and the average result for all cantilevers is 0.91 while the actual ratio of charge weights is 0.92.

Cantilevers were also used to measure the growth of the boundary layer behind the shock wave at MINOR UNCLE and the results were compared to the theoretical growth obtained by the two dimensional hydrodynamic simulation called the SHARC code (Needham, 1994) with excellent agreement (van Netten, 1995).

## 7 Applications

### 7.1 Evaluation of accidental explosions

In general there will be no electronic measuring devices near an accidental explosion and therefore the only method that can be applied to determine the various blast wave properties of the explosion is one which analyzes the damage to surrounding structures. Examples of simple structures such as cantilevers can be found near most explosions and the deformation of these can be correlated to the strength of the blast wave. The following paragraphs will describe how the peak dynamic pressure and the dynamic pressure impulse can be found from the deformation of a blast loaded cantilever and how this information can provide the TNT equivalent energy yield of the accidental explosion.

Let us assume that a cantilever of length 15.0 cm and diameter 0.15 cm has been found 100 meters from the center of an accidental explosion. The angle of the cantilever was measured to be 45° and it was subsequently removed and the material properties were tested. It was determined that the cantilever was made from aluminum 4043. A pressure-impulse diagram for this particular cantilever is given in figure 16 and was generated by the elastic-plastic numerical model. These curves are based on the hypothetical charges used to provide the blast waves for the theoretical loading imposed on the 15.0 cm aluminum cantilever.

The 45° angle of bend can be produced by very large charges if the cantilever is far from the charge or by very small charges if the cantilever is near to the charge. Figure 16 shows the peak dynamic pressure and impulse combinations for the surface burst TNT charges ranging from about 100 kg to 10<sup>7</sup> kg that produce the 45° bend but it does not directly provide any information about the distance the cantilever was from the center of the explosion. This information is provided by plotting the peak dynamic pressure versus range and the dynamic pressure impulse versus range for the various TNT charges as shown in figures 17 and 18. These curves can all be obtained from a program such as *AirBlast*, or if the variations of peak dynamic pressure and dynamic pressure impulse for a unit charge are obtained from a handbook, the other curves can be derived using cube root scaling.

The peak dynamic pressure and dynamic pressure impulse required to deform the cantilever to 45° can be found in figure 16 by finding the intersections of the various

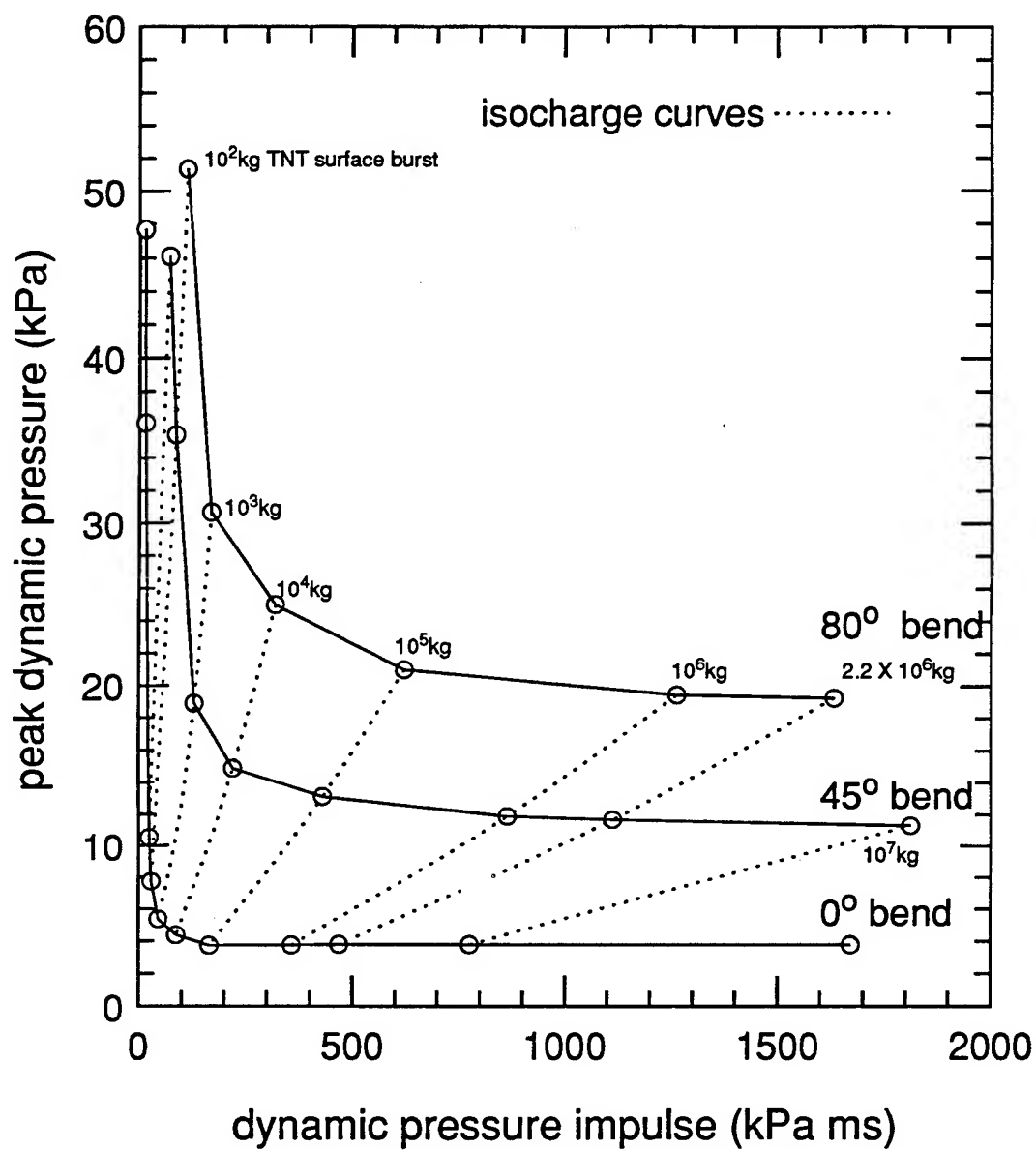


Figure 16: P-I diagram for an aluminum 4043 cantilever 15 cm long and 0.15 cm in diameter. The isodamage curves (0°, 45°, and 80°) were generated by the elastic-plastic model. Also plotted are the isocharge curves which indicate the peak dynamic pressure and dynamic pressure impulse combination required to produce the specified damage.

TNT charges with the 45° deformation curve. These values are plotted in figures 17 and 18 to produce the 45° deformation curves, as shown. The cantilever in question was discovered 100 m from the center of the accidental explosion and therefore the intersection of the 100 m line with the 45° deformation curves as shown in figures 17 and 18 provide the peak dynamic pressure and the dynamic pressure impulse combination that existed at the position of the cantilever during the explosion. The resulting peak dynamic pressure and the dynamic pressure impulse was found to be 14.7 kPa and 253 kPa ms respectively.

The energy yield of the explosion can be found from either value but it is easiest to use the peak dynamic pressure since the value of the peak dynamic pressure does not change as the impulse does through blast wave scaling. The *AirBlast* program was used to determine that the measured peak dynamic pressure of 14.7 kPa exists at a radial distance from a 1 kg TNT surface burst charge of 3.99 m. This value can be used with cube root scaling to determine the effective yield as shown below:

$$W_{eff} = \left[ \frac{100m}{3.99m} \right]^3 1.0kg = 15700kg \quad (9)$$

It can therefore be assumed that the blast wave at 100 m from the accidental explosion is similar to that produced by the detonation of 15,700 kg TNT on the ground surface. The peak dynamic pressure versus range for this charge is also plotted in figure 17.

## 7.2 Identification of potential cantilever gauges

If cantilevers are to be used as blast wave gauges at high explosive tests it will be useful to identify those cantilevers, made from readily available materials, which would provide useful angles of bend for the range of dynamic pressures expected at various locations. This can be determined by using plots similar to those described in section 7.1. For example, if the cantilever as described above was to be used as a blast wave gauge it should be placed at a radial distance from ground zero where a 45° bend would be expected. The distance can be found by observing the intersection points of the 45° curve with the various charge curves in either figure 17 or 18. For a charge thought to be similar to 100 kg TNT surface burst, this cantilever should be placed at about 15 meters from the charge center. If the charge were thought to be equivalent to 10<sup>7</sup> kg of TNT the cantilever should be placed at a distance of about 1000 meters. Plots such as shown in figures 16 to 18 can be made for a wide variety of cantilevers made from easily obtained materials so that at a given explosive event a variety of cantilevers could be placed at different distances to monitor the blast wave.

At most explosions the blast waves produced are far from the ideal blast wave expected for the given charge weight and it is therefore necessary to position cantilevers in such a way as to bracket the optimum 45° bend. This is done to ensure a reasonable measurement at all stations.

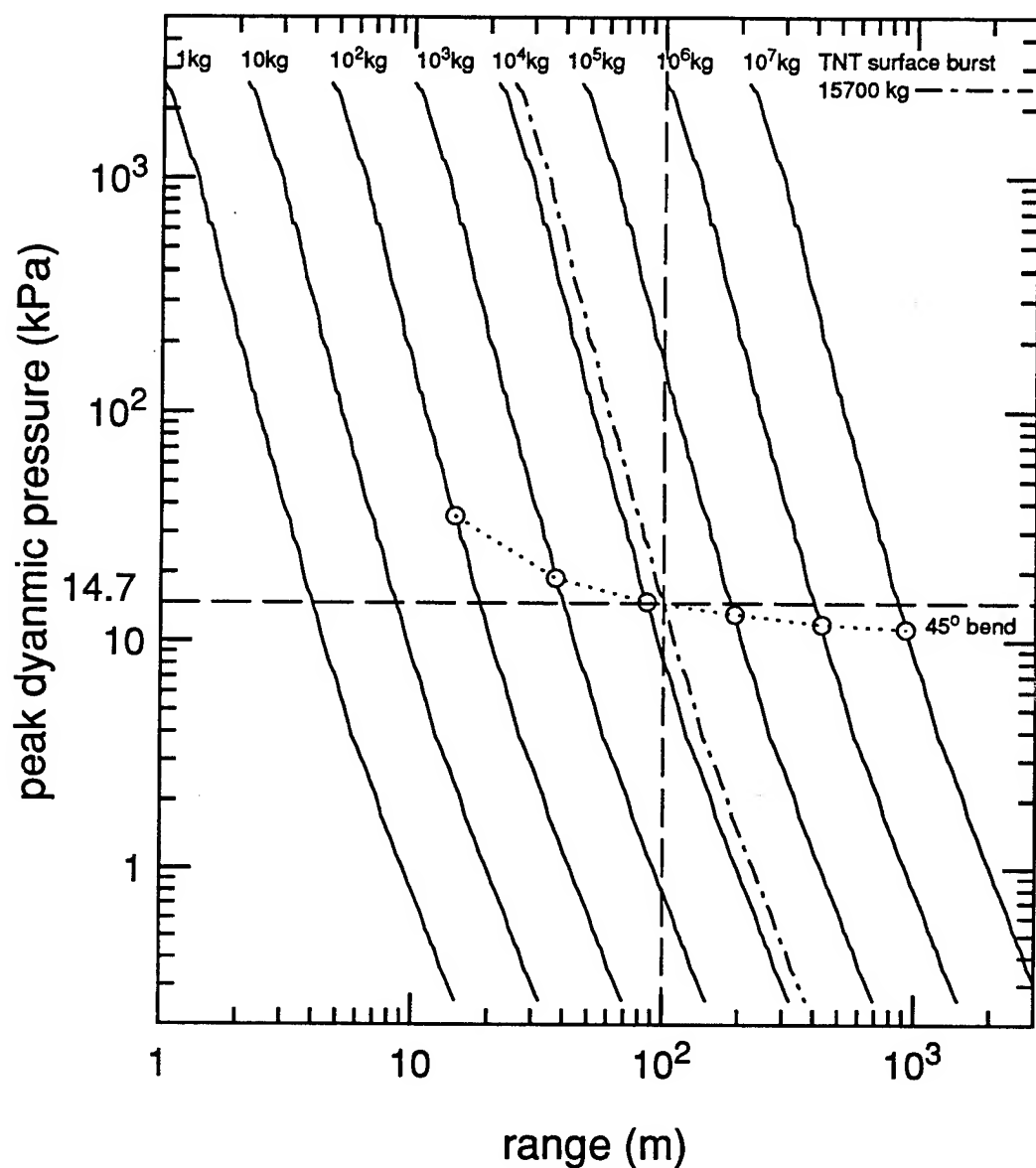


Figure 17: Peak dynamic pressure versus range for various TNT charge weights between 1 kg and 10<sup>7</sup> kg obtained from *AirBlast*. Also plotted is the 45° deformation line for the 15 cm aluminum cantilever. The intersection of this curve with the charge curves gives the peak dynamic pressure and distance from the charge needed to produce a 45° bend for this cantilever. Since the cantilever was assumed to be 100 m from the center of the explosion this identifies the peak dynamic pressure to be 14.7 kPa and the TNT equivalent charge size to be 15,700 kg.

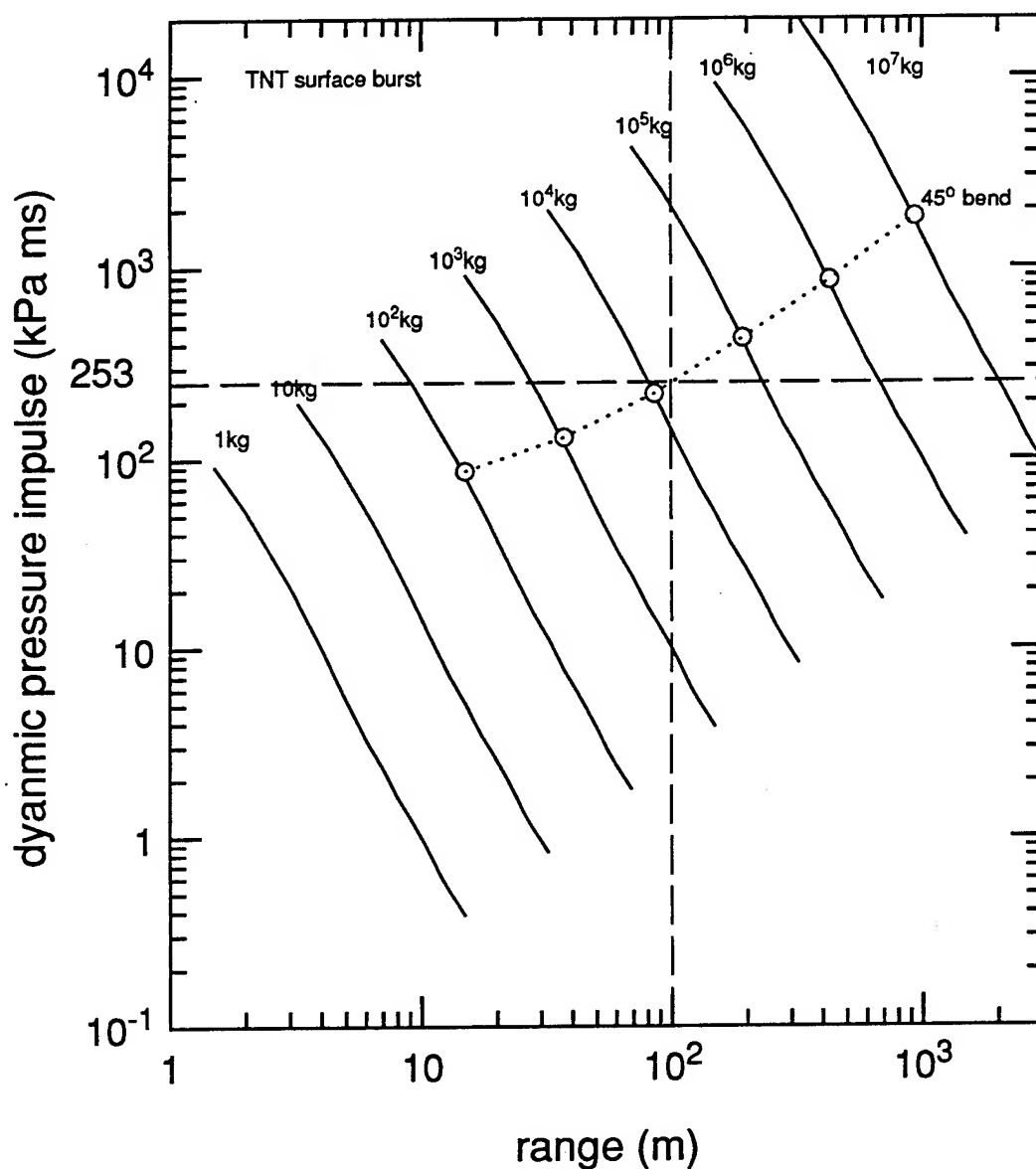


Figure 18: Dynamic pressure impulse versus range for various TNT charge weights between 1 kg and  $10^7$  kg obtained from *AirBlast*. Also plotted is the 45° deformation line for the 15 cm aluminum cantilever. The intersection of this curve with the charge curves gives the dynamic pressure impulse and distance from the charge needed to produce a 45° bend for this cantilever. Since the cantilever was assumed to be 100 m from the center of the explosion this identifies the dynamic pressure impulse to be 253 kPa ms.

It is hoped to use this technique to develop a handbook and/or a software package that will provide experimenters with the information so that appropriate cantilever gauges can be made for expected blast conditions.

## 8 Discussions and conclusions

The main objectives of this project were: to understand the relationships between the physical properties of shock and blast waves and the response of circular cross-section cantilevers exposed to shock and blast waves; to use this understanding to design cantilever gauges that can be used to monitor the physical properties of blast waves, and to illustrate how the deformation of cantilever structures may be used to describe the source of blast waves produced by accidental explosions.

Two models were developed to describe the deformation of the blast loaded ductile cantilevers. These were based on the assumption that the cantilevers would respond to the blast wave either as a rigid-plastic or an elastic-plastic structure. It was found that the rigid-plastic model would accurately describe the deformation of cantilevers made from solid solder but not aluminum or steel. The elastic-plastic model based on the limited curvature concept was developed to improve the predicted response of cantilevers made of other materials. The model predicted the final angle of bend of the cantilevers in most cases to within a few degrees. The dynamic response during the theoretical deformation compared well with that observed via high speed photographic recording.

Gauges based on the above design were used at the DISTANT IMAGE and MINOR UNCLE explosions. These gauges measured a yield for MINOR UNCLE of 0.91 that of DISTANT IMAGE while the actual ratio of charge weights was 0.92. Excellent agreement was also found for the measurement of the growth behind the traveling blast wave.

Using the appropriate model, it has been shown how cantilevers gauges made from easily available materials can be selected to monitor blast waves, whose properties are known approximately. In the case of an accidental explosion it has been shown how the observed bending of a cantilever structure at a known distance from the center of the explosion, can be used to estimate its yield and the physical properties of the blast wave.

**Acknowledgement:** This work is supported by the Norwegian Defence Construction Service, and the help and encouragement of Arnfinn Jenssen is gratefully acknowledged.

## References

- Dewey, J.M., 1962, *Surface Burst of a 100 ton TNT Hemispherical Charge Wire Drag Gauge Measurements*, Suffield Experimental Station, T.N. 80.
- Dewey, J.M., McMillin, D.J., 1989, *A Computer System for Presenting the Properties of Blast Waves*, Proc. 11<sup>th</sup> Int. Symp. on Military Application of Blast Simulation. MABS11, 1, 554-561.
- Hoerner, S.F., 1965, *Fluid Dynamic Drag*, published by author, Midland Park, New Jersey.
- Manjoine M.J., 1944, *Influence of Rate of Strain and Temperature on Yield Stresses in Mild Steel*, J. Appl. Mech. 11, 211.
- Needham, C.E. et al, 1991, *ANFO.EXE: Revised User's Manual*, Defence Nuclear Agency, POR 7375.
- Needham, C.E., 1994, personal communications.
- Parkes, E.W., 1958, *The Permanent Deformation of an Encastre Beam Struck Transversely at Any Point in Its Span*, Proceedings of the Institution of Civil Engineers, 10 277.
- Schlichting, H., 1960, *Boundary Layer Theory*, McGraw-Hill, New York.
- van Netten, A. A., 1995<sub>a</sub>, *The use of Cantilevers as Blast Wave Gauges*, Ph.D. Dissertation, University of Victoria, Canada.
- van Netten, A. A., Dewey, J. M., 1995<sub>b</sub>, *Horizontal Cantilever Gauges and Cantilever Gauges*, MINOR UNCLE symp. rept., Defence Nuclear Agency, POR 7453-5, 5.
- van Netten, A.A., Dewey, J.M., 1992 *Cantilever gauges*, DISTANT IMAGE Symp. Defence Nuclear Agency, POR 7379-5, 5.



# PROPAGATION AND ATTENUATION OF BLAST WAVES IN A LONG MODEL BLAST-SIMULATOR

Hans-Otto Amann

Fraunhofer-Institut für Kurzzeitdynamik  
- ERNST-MACH-INSTITUT -  
Eckerstraße 4  
D-79104 Freiburg, Germany

## Abstract

To study the behavior of blast waves in long blast simulators, in the Ernst-Mach-Institut a model blast simulator with a cross section area of  $432 \text{ cm}^2$  and a length of 19.2 m has been constructed. The simulator is driven by 7 short generators filled with compressed air up to 200 bar, which generate blast overpressures of maximal 1.3 bar. For loading pressures of 50, 100, 150 and 200 bar, pressure-time histories, measured along the blast simulator, for an open, a 47% open (RWE) and a closed simulator exit, give some information about attenuation, decay and reflection of blast waves.

Surprisingly, two attenuation phases can be observed along the simulator. During the first phase, a high attenuation of the blast front occurs, while during the second phase, farther downstream of the simulator, a weaker attenuation is present. Probably there are influences of the generators, because the blowing time of those is in the order of the positive flow duration of the blast wave. However, if the blast wave is produced by 1.47 g explosives - in this case the gas production time is very short - no different attenuation phases can be observed.

The experimental results, both for the open and the 47% open exit, are compared with numerical calculations, using the Q1DEUL-Code. There is a good agreement between experiment and calculation.

## Introduction

There is scarcely any information about the behavior and attenuation of blast waves in long blast simulators with constant cross section areas and  $L/D$ -ratios of 20 and more. The driven sections of the existent large blast simulators of France [1], Germany [2], USA [3] and UK [4] only have  $L/D$  ratios of about 11, 11, 14 and 18. To obtain some more information, a small scale model blast simulator with a cross section area of  $432 \text{ cm}^2$  and a length of 19.2 m ( $L/D = 82$ ) has been constructed in the Ernst-Mach-Institut. It is a model of the large blast simulator of Reiteralpe ( $75 \text{ m}^2/110 \text{ m}$ ), [5], [6], but now with a length corresponding to 800 m Reiteralpe. To produce blast waves, the simulator is driven by 7 short pressure generators filled with compressed air up to 200 bar,

which generate blast overpressures of maximal 1.3 bar just downstream of the generators. Pressure-time histories, measured along the blast simulator give some information about the behavior of blast waves in long tubes.

### Experimental facility

Fig. 1 shows the 19.2 m small scale blast simulator of the EMI. It is driven by 7 generators (Fig. 2) filled with compressed air up to 200 bar. Each is sealed by 2 diaphragms and all are started simultaneously by an intermediate exploding wire. The exit of the simulator can be closed by a solid plate or by a perforated plate simulating a static rarefaction wave eliminator (RWE), (Fig. 3). Pressure-time data were recorded at 32 measuring stations (Fig. 4), using KISTLER 603B gages.

### Experimental results

#### Simulator with an open exit

In Fig. 5 a typical pressure-time history along the simulator is shown. When the blast front leaves the open exit, an upstream traveling rarefaction wave occurs, which causes the decay of the blast wave. The variation of the peak overpressure, impulse and positive flow duration along the simulator for different driver pressures is represented in Figs. 6, 7, 8.

Surprisingly, two attenuation phases can be observed along the simulator (Fig. 6). During the first phase, a high attenuation of the blastfront up to measurement station (300) occurs, while during the second phase, farther downstream, a weaker attenuation occurs. A detailed explanation of this phenomenon does not exist at present. There are probably influences of the drivers, resulting from their blowing times (Fig. 9). Using the same drivers for a short and a long simulator, the blowing time  $t_{\text{tot}}$  of the drivers in the short simulator is much higher than the positive flow duration of the produced blast wave and its running time through the simulator, while for the long simulator the same blowing time is in the order of the positive flow duration and running time as depicted in Fig. 10. (In this figure on each curve the total blowing time  $t_{\text{tot}}$  and the critical blowing time  $t^*$  are marked.  $t^*$  is the time until the critical pressure ratio  $p/p^* = 1.89$  in the drivers is reached). It can be concluded that during the first attenuation phase the blastfront is still influenced by the outflow processes of the drivers and the piston model of the shock tube theory is valid, while the second attenuation phase is more controlled by the attenuation law of free blast waves. However, if the blast wave is produced by 1.47 g explosives (Nitropenta), in this case the gas production time is very short, and no different attenuation phases can be observed (Fig. 6). This phase corresponds to the second attenuation phase.

The question why for all driver pressures the second attenuation phase begins at measurement station (300) is still unclear.

### **Simulator with a 47% open exit (RWE)**

With an only partly closed simulator exit a static rarefaction wave eliminator can be simulated. For the EMI simulator this was realized by a 47% perforated plate (Fig. 3). Instead of a rarefaction wave for the open exit, the pressure-time histories along the simulator show now a weak reflected shock wave traveling upstream (Fig. 11). Depending on the area ratio of the orifice plate a reflectionfree blastwave can be attained (Fig. 12).

### **Numerical results**

The experimental results, both for the open and the 47% open exit, were compared with numerical calculations, using the Q1DEUL-Code. A simplified blast simulator was used for the data input and calculation. So the 7 drivers were combined to a single one with an idealized nozzle (Fig. 13).

### **Simulator with an open exit**

For a driver pressure of 150 bar, as in Figs. 14a, b, the calculated pressure-time histories are compared with the experimental curves.

There is a very good agreement of the arrival times on all output stations. The shape of the pressure curve is also represented satisfactorily, however in contrast to the experiment at the end of the strong pressure decay, a weak compression jump is traveling slowly downstream. This wave probably originates from a numerical disturbance to an early phase of the calculation when a strong upstream-faced secondary shock is formed, as can be seen very clearly in a p-x-diagram (Fig. 15). During the first phase of the starting process this secondary shock fits the region of high supersonic expansion flow just behind the driver exit to the subsonic flow region behind the blast front. During the expansion process this shock decreases and disappears with increasing time. In both figures also the upstream traveling rarefaction wave can be seen which develops when the blast front leaves the simulator exit. At the tail of this wave a shock front occurs which decreases with time.

When comparing the experimental with the numerical results a striking phenomenon is that the intensities of the shocks are calculated about 10 - 15 % too high. For users of the Q1DEUL-Code this is a well known fact [7]. In Fig. 16 this is shown for the blast front intensity along the simulator. Besides, this figure confirms by the numerical calculation that two attenuation phases exist along the blast simulator, as discussed already (Fig. 6).

### **Simulator with a 47% open exit (RWE)**

In Figs. 17a, b and 18 the experimental results of a blast simulator with a 47 % open exit are compared with the numerical calculations. There is the same agreement as discussed for the open exit. Instead of a rarefaction wave now a weak reflected wave travels upstream, when the blast wave hits the exit, closed by a 47% open orifice plate. By a precise adaptation of the open area a reflectionfree blastwave can be attained.

### **Conclusions**

It could be shown that for long blast simulators ( $L/D > 80$ ) two attenuation phases of the blast front exist. During the first phase a high attenuation occurs, while during the second phase a weaker attenuation occurs. It can be assumed that these two phases can be observed when the running time of the blast wave through the simulator is in the order or greater than the blowing time of the drivers.

Though the Q1DEUL-Code has been developed for the numerical calculation of relatively short blast simulators, also the numerical calculation of long blast simulators is entirely sufficient for first estimations of the wave and flow processes. However the shock overpressures are calculated about 10 to 15 % too high.

### **References**

- [1] Cadet, A., Monzac, J.B.G.: Le Simulateur de soufflé à Grand Gabarit du Centre d'Etudes de Gramat: Description et Utilisation operationelle. MABS 7, Medicine Hat, Canada, July 1981, Contr.1.2
- [2] Ackermann, J., Klubert, L.: The New Large Blast Simulator of Reiteralpe Proving Ground. MABS 9, Oxford, England, Sept. 1985, Contr. I.2
- [3] Kennedy, T.E.: Large Blast Thermal Simulator - Status Report. MABS 13, The Hague, The Netherlands, Sept. 1993, Vol. 2, pp. 105-113
- [4] Leys, I.C.: Model Scale Experiments for the Development of an Extension to the AWRE Foulness Nuclear Blast Simulator. MABS 7, Medicine Hat, Canada, July 1981, Contr.1.4
- [5] Amann, H.-O.: First Results with the Model-Blast Simulator of Reiteralpe. MABS 9, Oxford, England, Sept. 1985, Contr. II.6
- [6] Amann, H.-O.: Shaping of a Simulated Blast Wave Signature by a Cone or by Orifice Plates installed in the Drivers of a Blast Simulator. MABS 10, Bad Reichenhall, Germany, Sept. 1987, Proc. I, pp. 81-92
- [7] Opalka, K.-O., ARL, Aberdeen Proving Ground: Private information

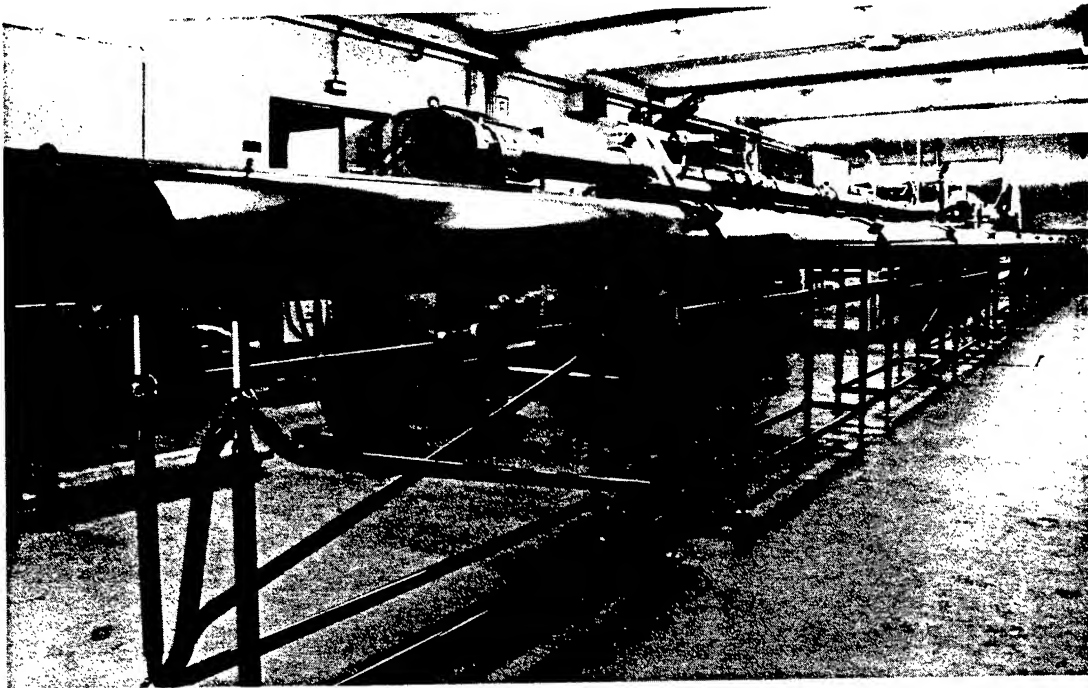


Fig. 1 19.2 m blast simulator of the EMI

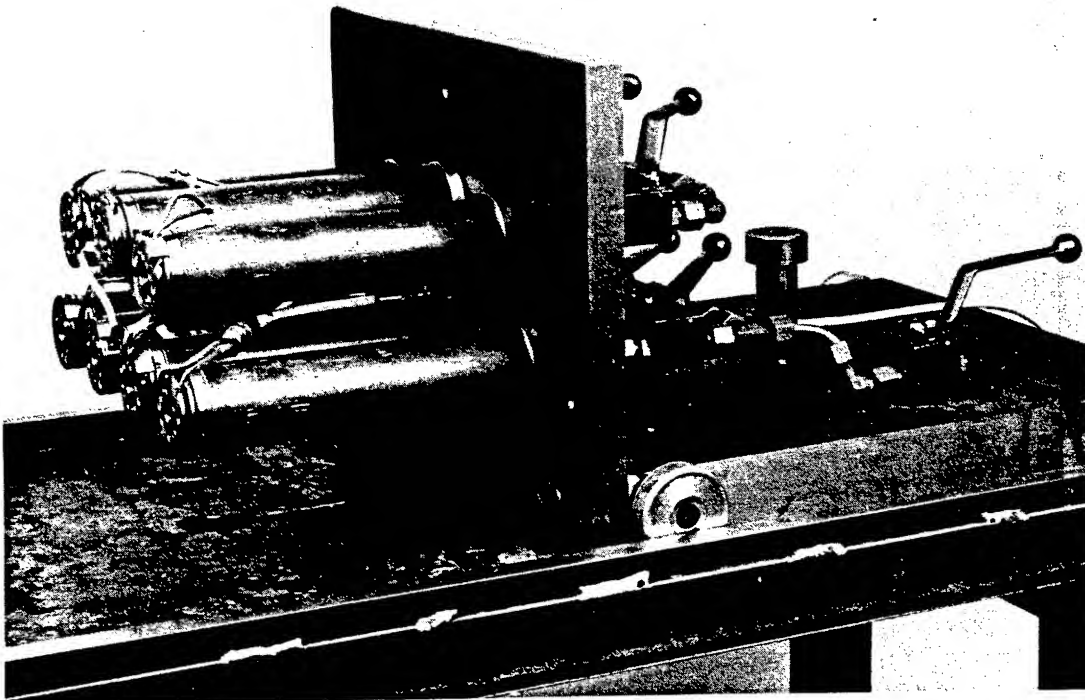


Fig. 2 Drivers for the 19.2 m blast simulator

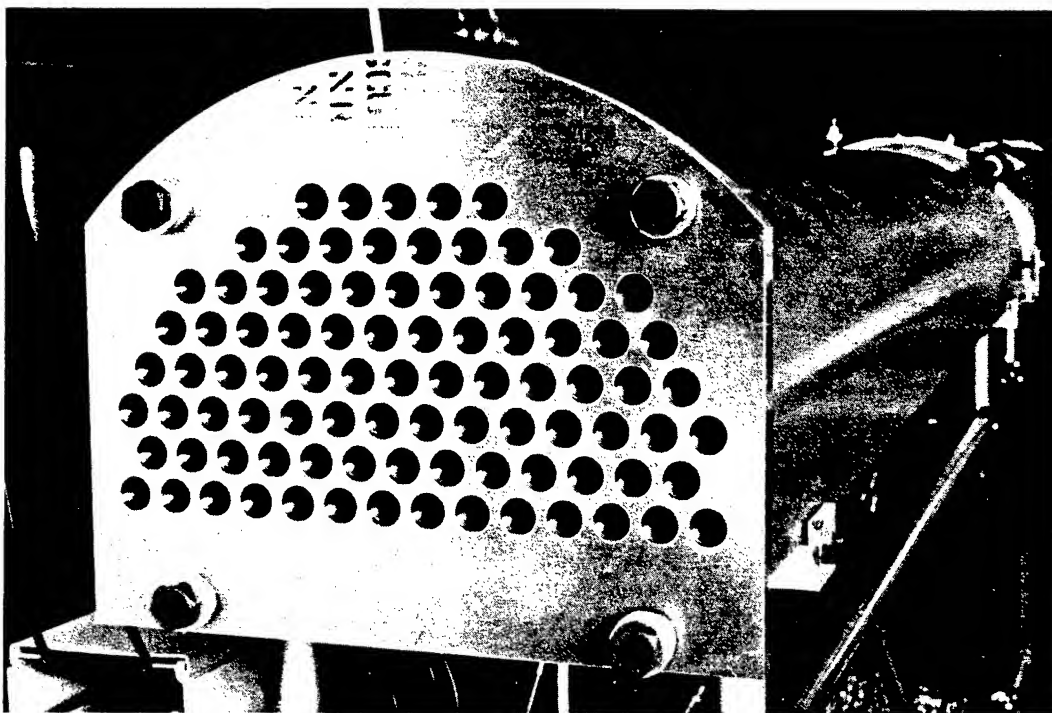


Fig. 3 Perforated plate as static rarefaction wave eliminator (47% open exit)

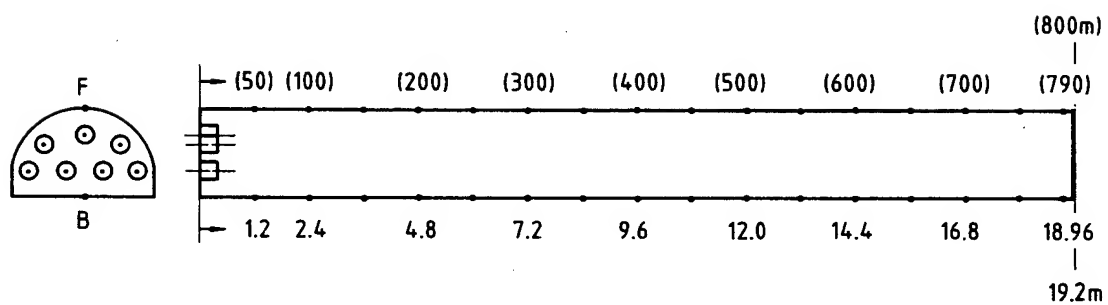


Fig. 4 Measuring stations along the bottom (B) and top (F) of the 19.2 m blast simulator. The measurements in parenthesis correspond to the simulator Reiteralpe

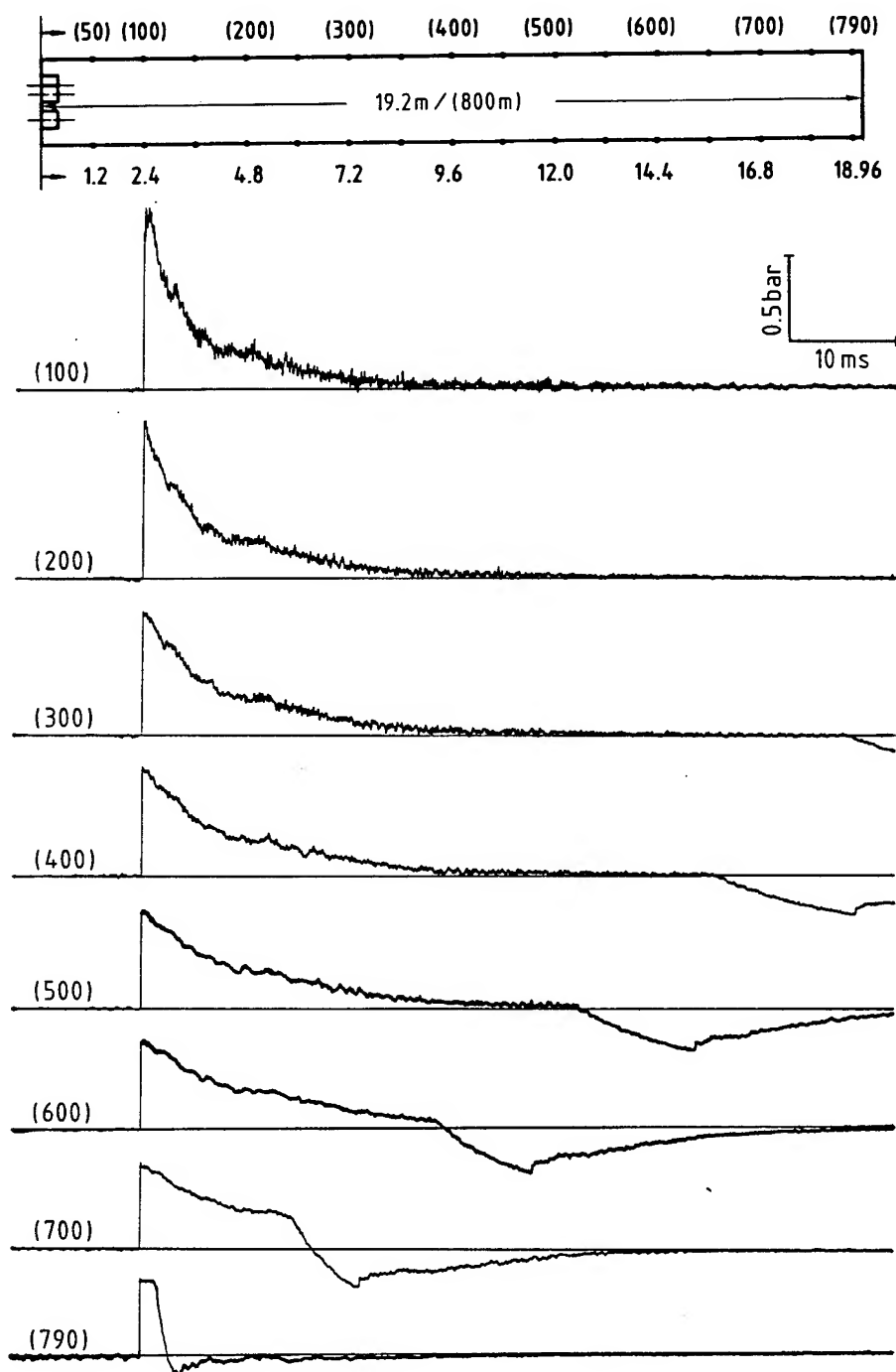


Fig. 5 Typical pressure-time-history along the 19.2 m blast simulator.  
Driver pressure = 150 bar, (# 1669)

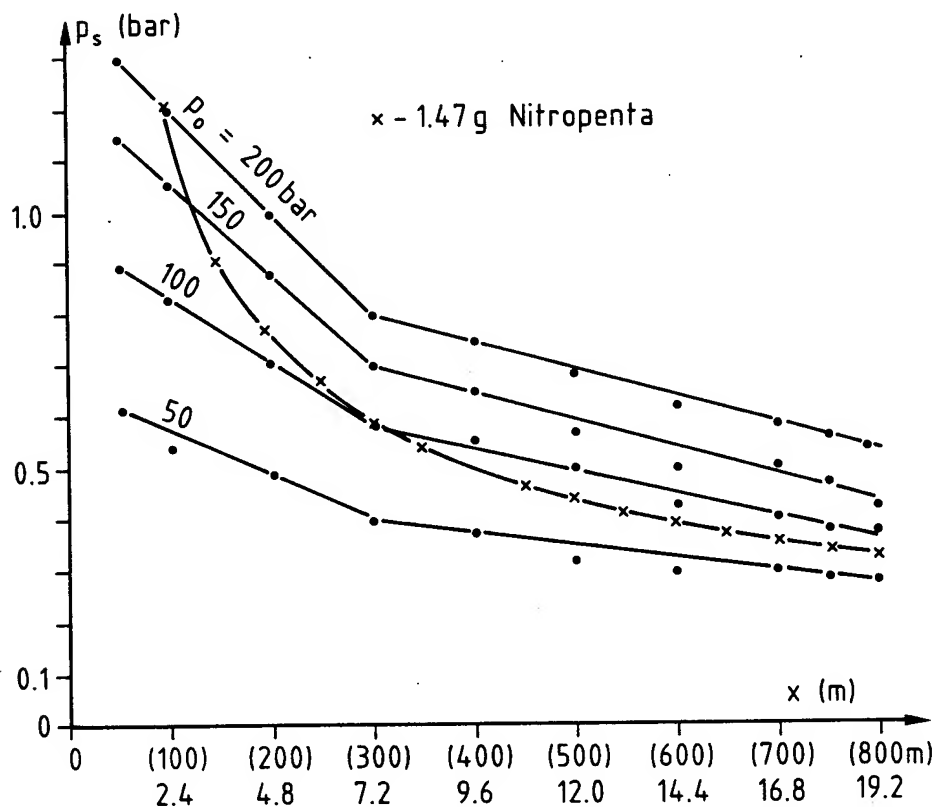


Fig. 6 Peak-overpressures and its attenuation along the 19.2 m blast simulator for different driver pressures  $p_0$  and 1.47 g Nitropenta, (# 1675, 1669, 1670, 1673)

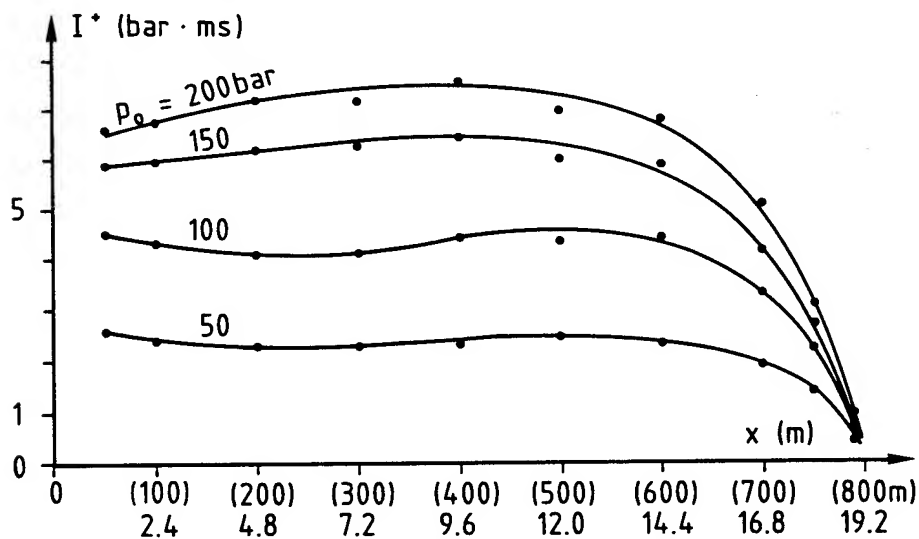


Fig. 7 Positive impulse along the 19.2 m blast simulator for different driver pressures  $p_0$



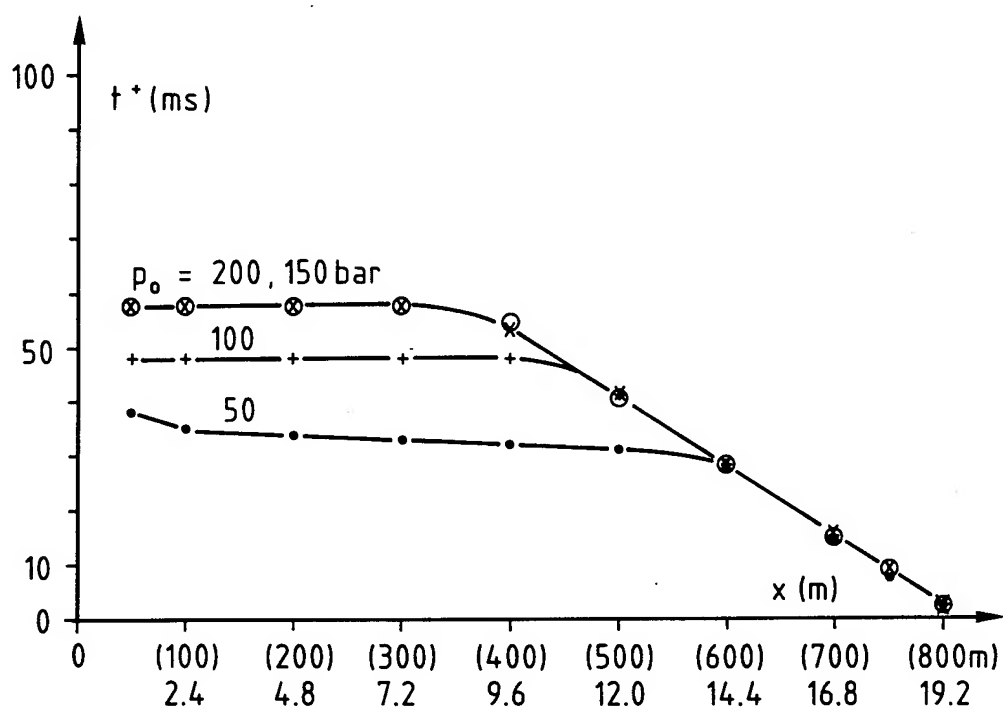


Fig. 8 Positive flow duration along the 19.2 m blast simulator for different driver pressures  $p_0$

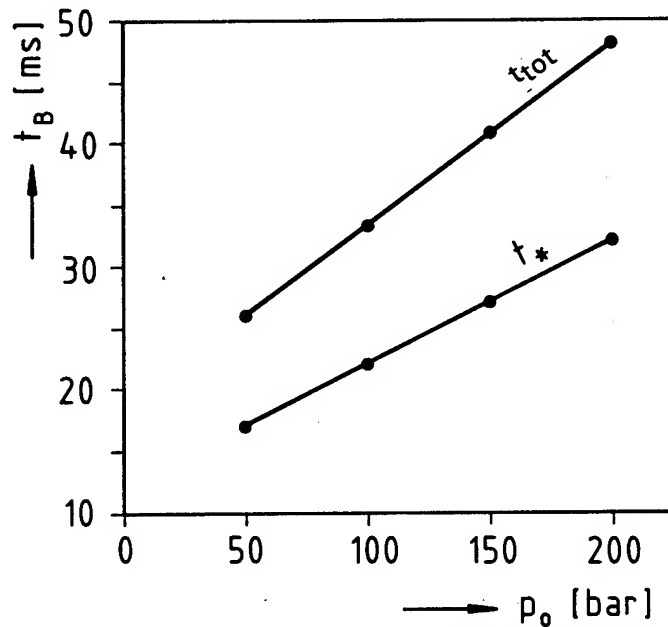


Fig. 9 Experimentally determined driver blowing times  $t_B$  for different driver pressures  $p_0$ .  $t_{tot}$  = total blowing time,  $t^*$  = blowing time up to the critical pressure ratio  $p/p^* = 1.893$  (#1723, 1725, 1728, 1729)

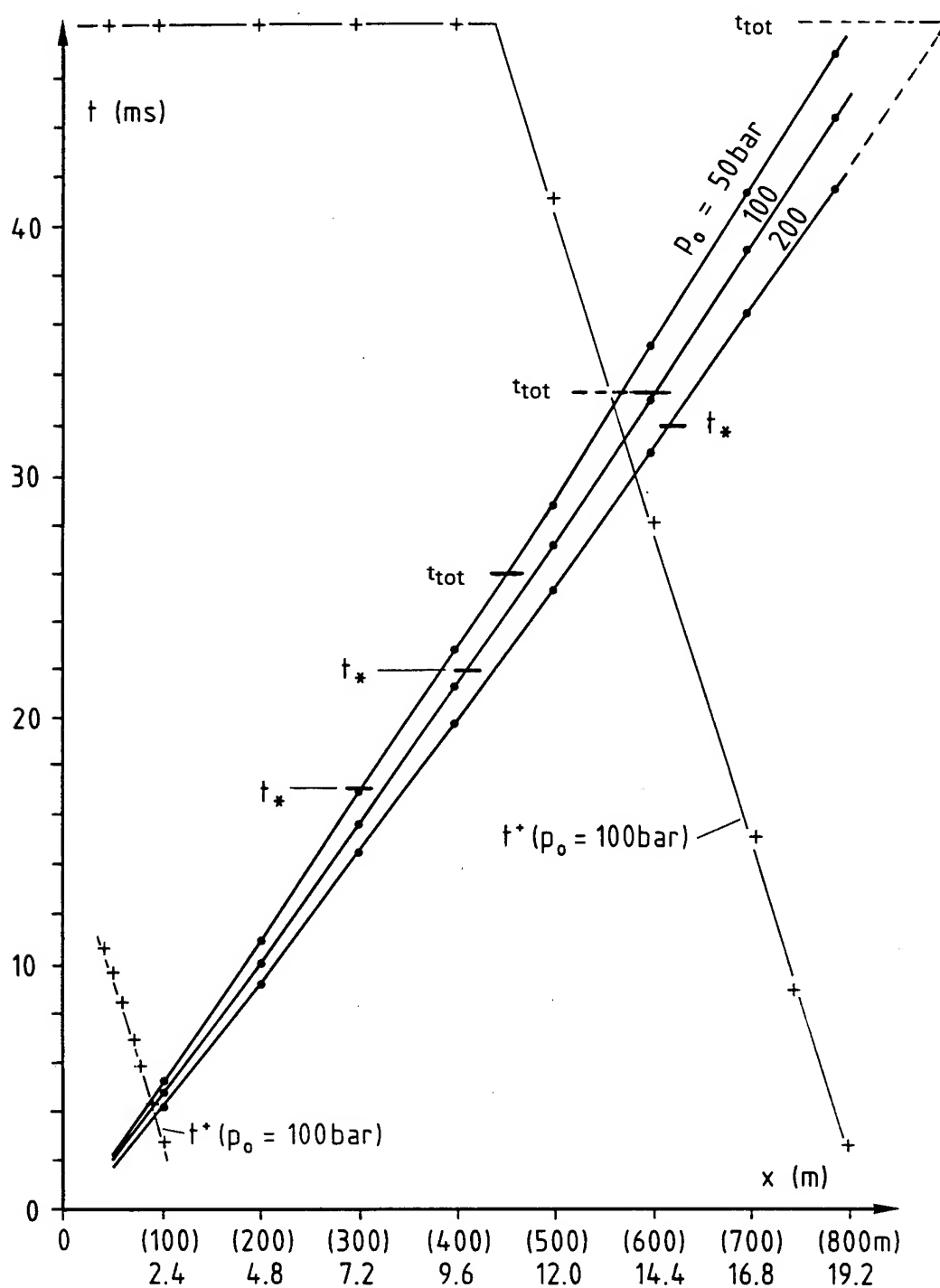


Fig. 10  $x-t$  diagrams of the blast front for different driver pressures  $p_0$  (#1673,1670,1675),  $t_{tot}$  = total blowing time of the drivers  
 $t_*$  = blowing time up to the critical pressure ratio  $p/p_* = 1.893$   
 $t^+$  = positive flow duration in a 2.4 and 19.2 m simulator

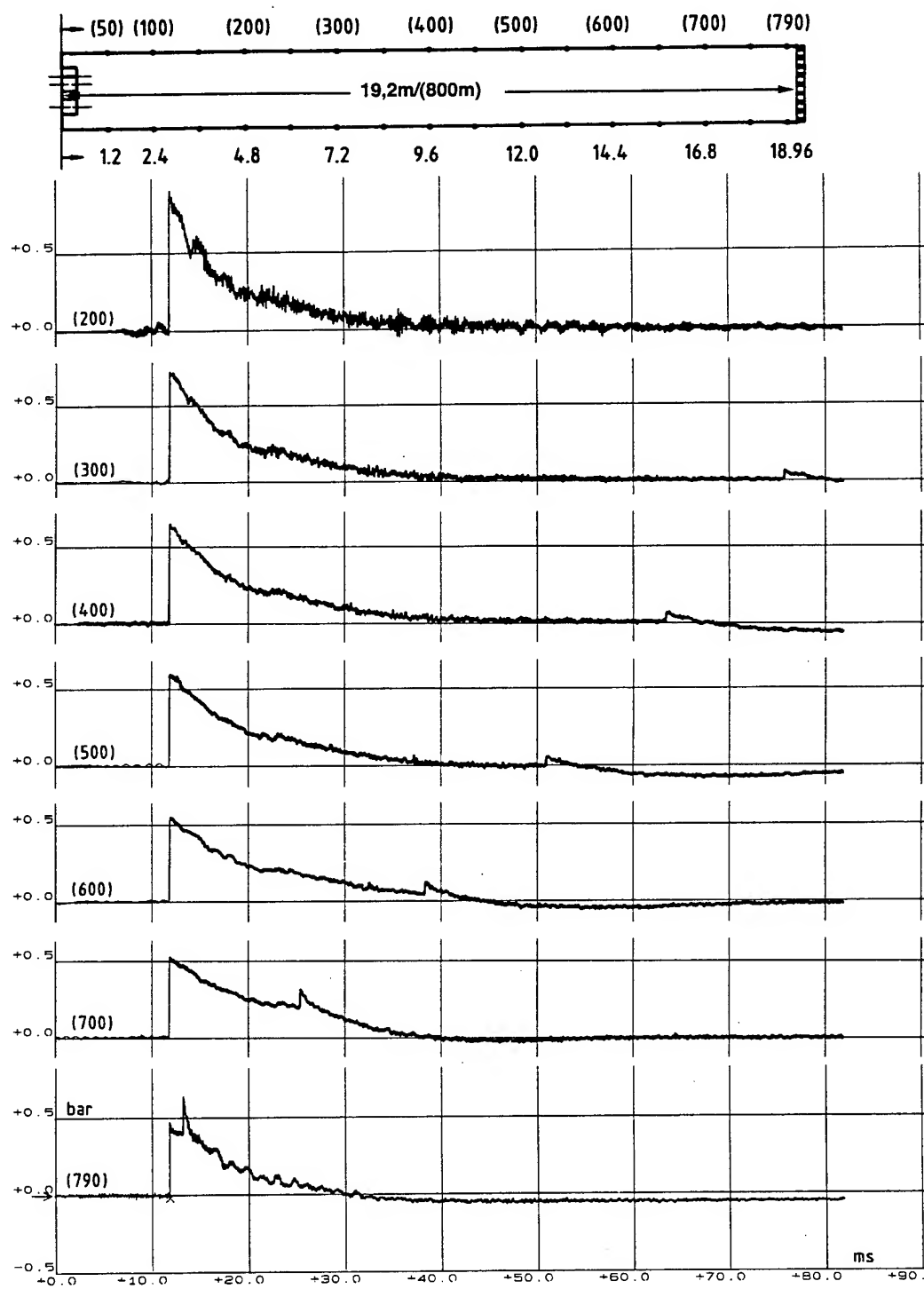


Fig. 11 Pressure-time history along the 19.2 m blast simulator closed with a 47% open orifice plate

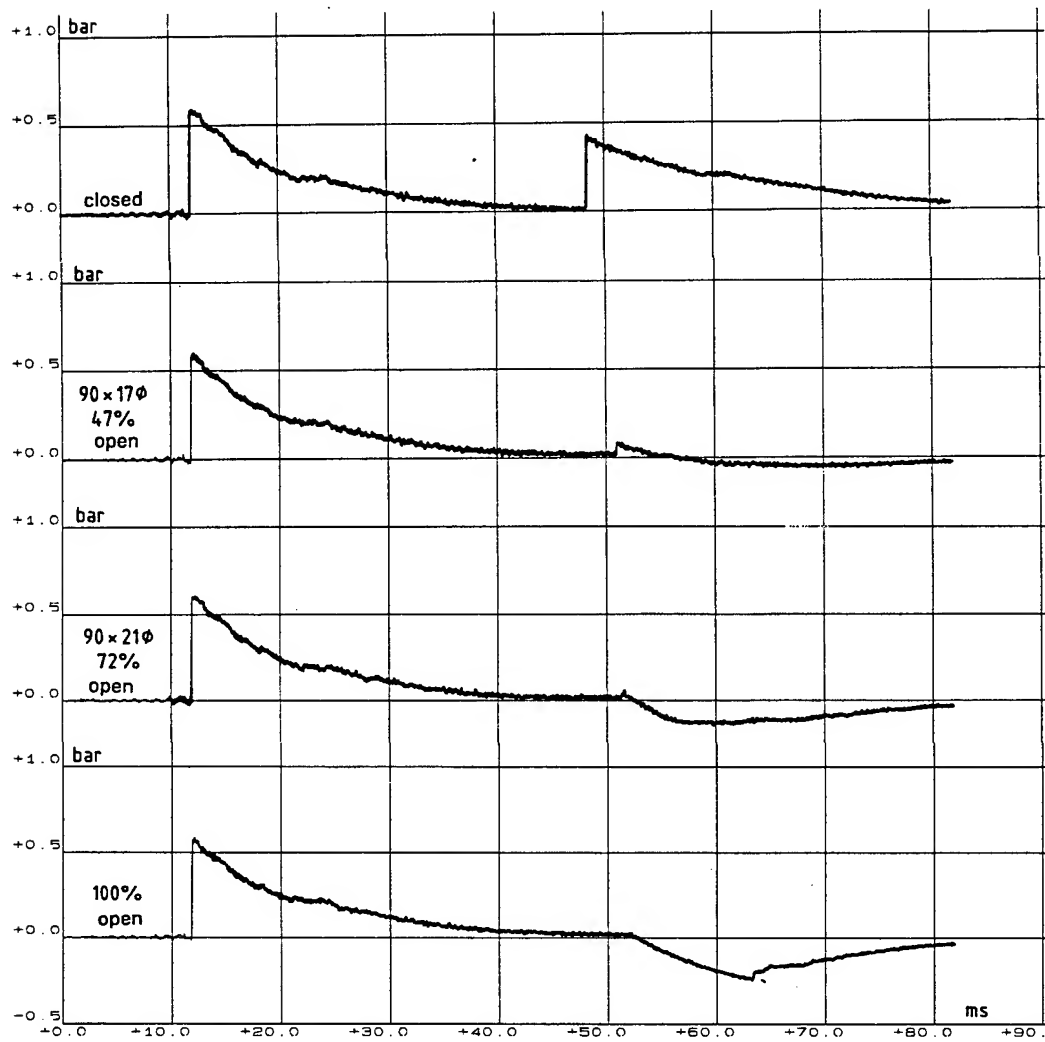


Fig. 12 Influence of the area ratio of the orifice plate on the reflected wave for the measurement station (500). Driver pressure = 150 bar (# 1683, 1698, 1704, 1669)

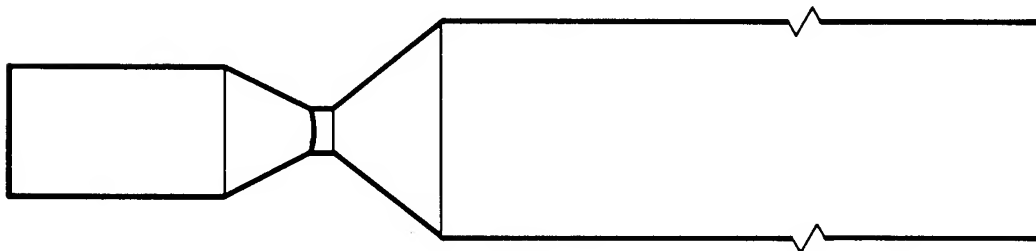


Fig. 13 Idealized blast simulator for the numerical calculation

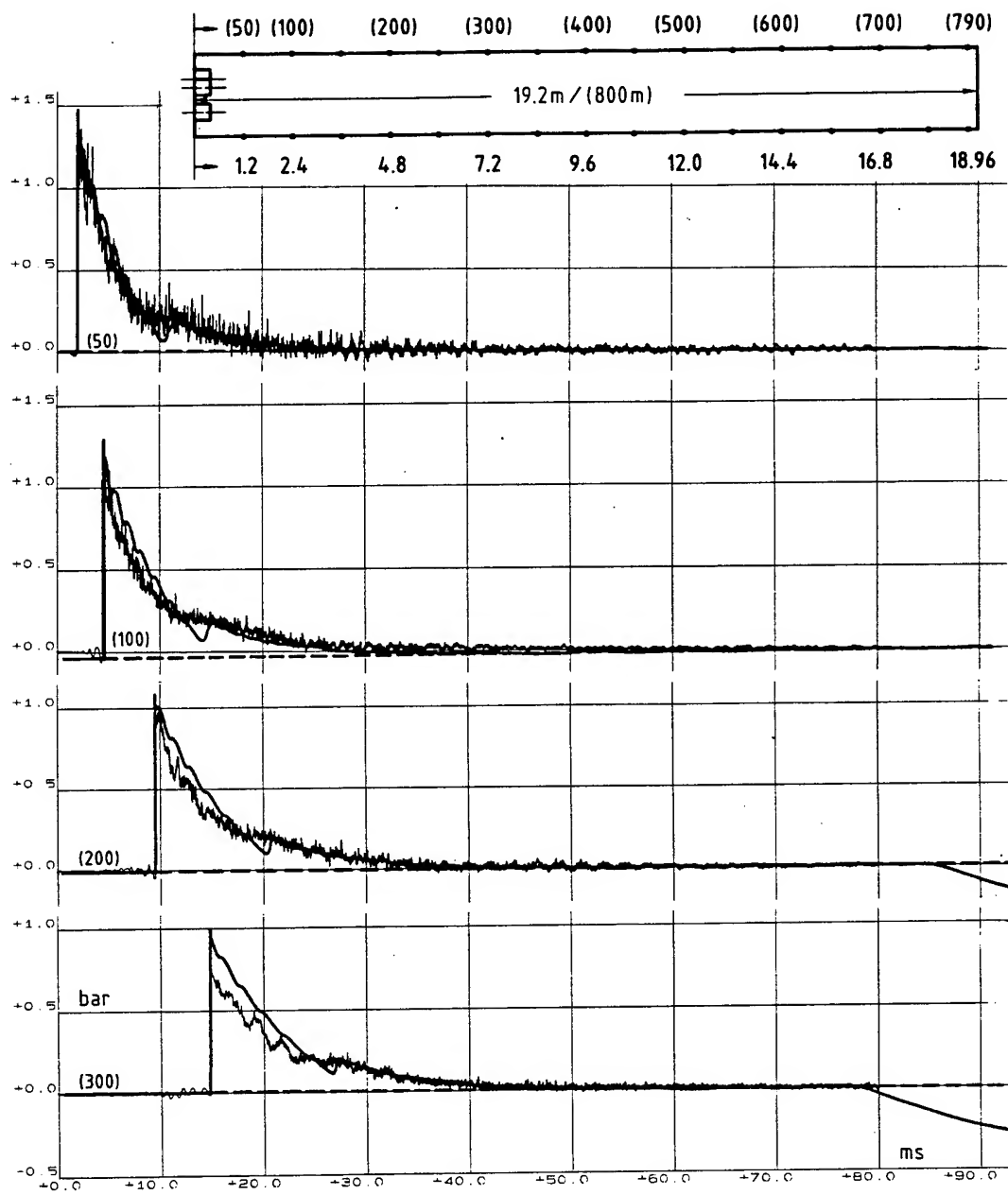


Fig. 14a Pressure-time histories at different points along the 19.2 m blast simulator. Exit: open. Comparison experiment with numerical calculation (Q1DEUL-Code). Driver pressure: 150 bar

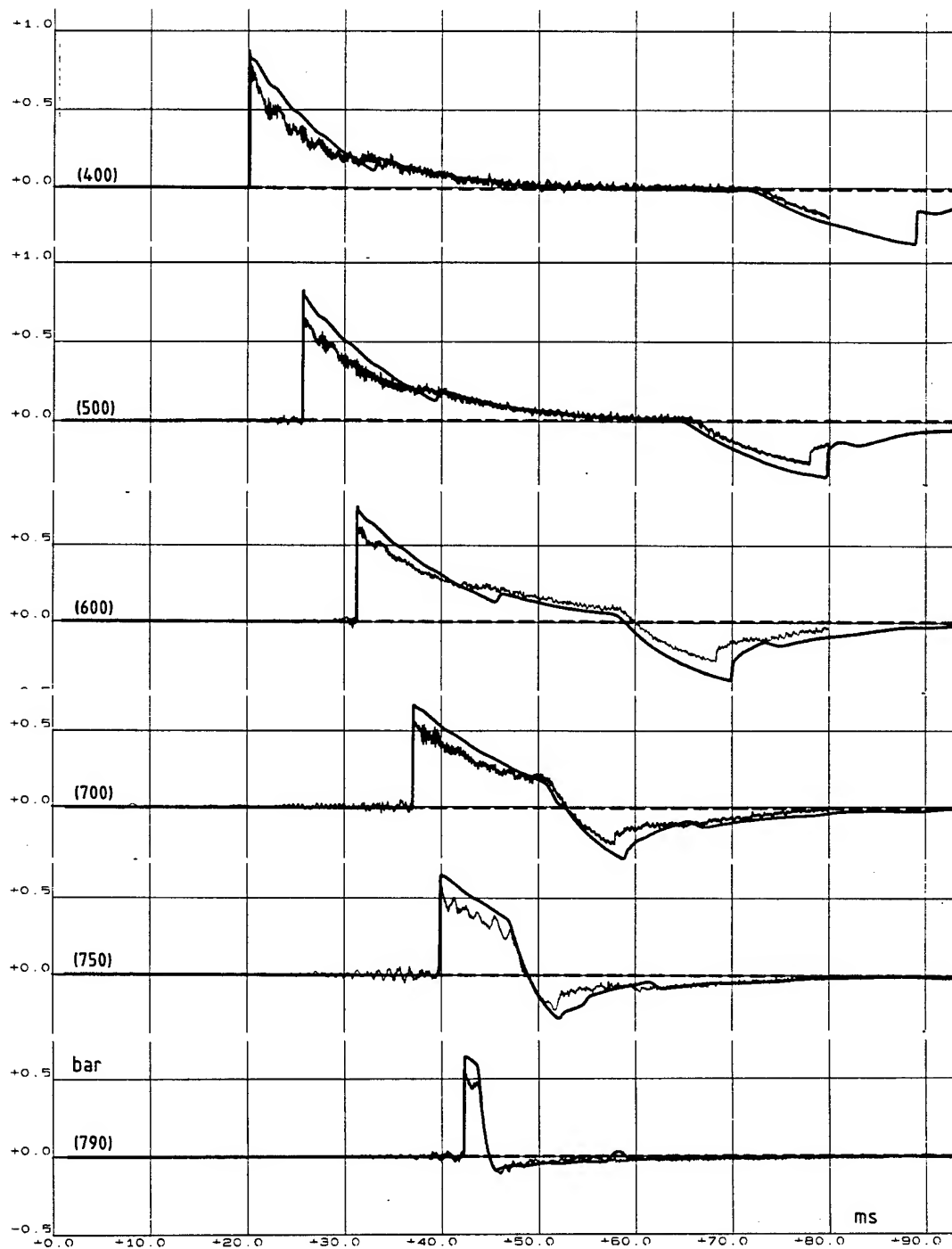


Fig. 14b Continued

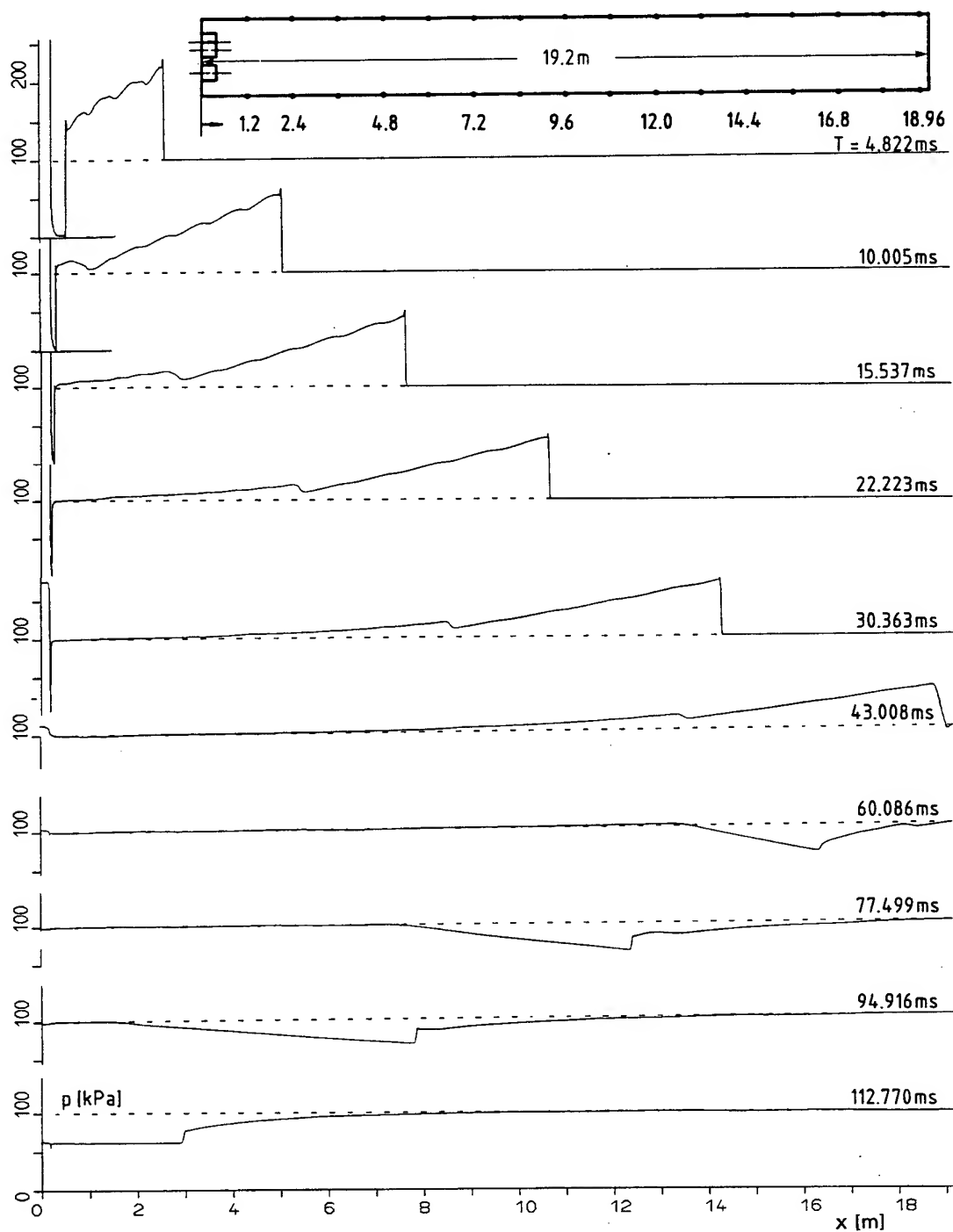


Fig. 15 Numerical calculation (Q1DEUL-Code) of the pressure distribution along the 19.2 m blast simulator at different times. Exit: open, driver pressure: 150 bar

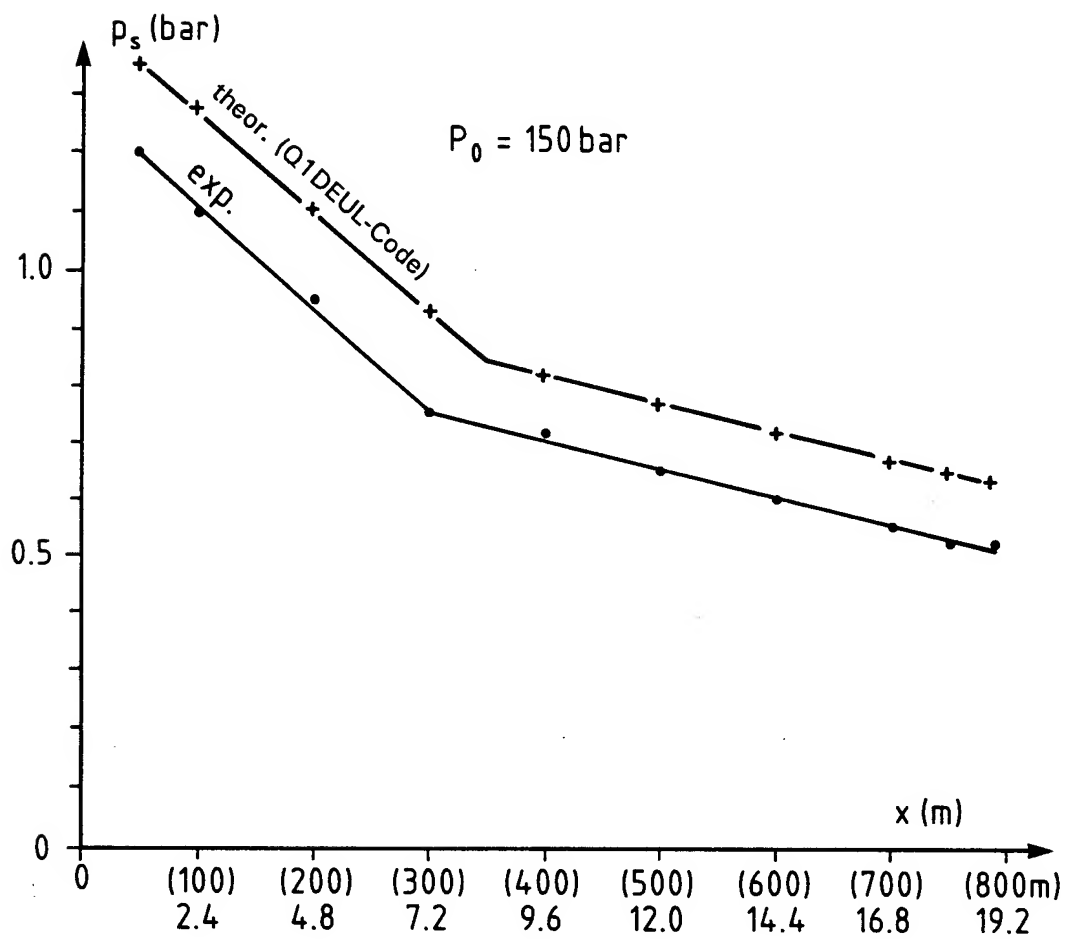


Fig. 16 Peak overpressure along the 19.2 m blast simulator. Comparison experiment with numerical calculation (Q1DEUL-Code). Driver pressure  $p_0$ : 150 bar (# 1744)



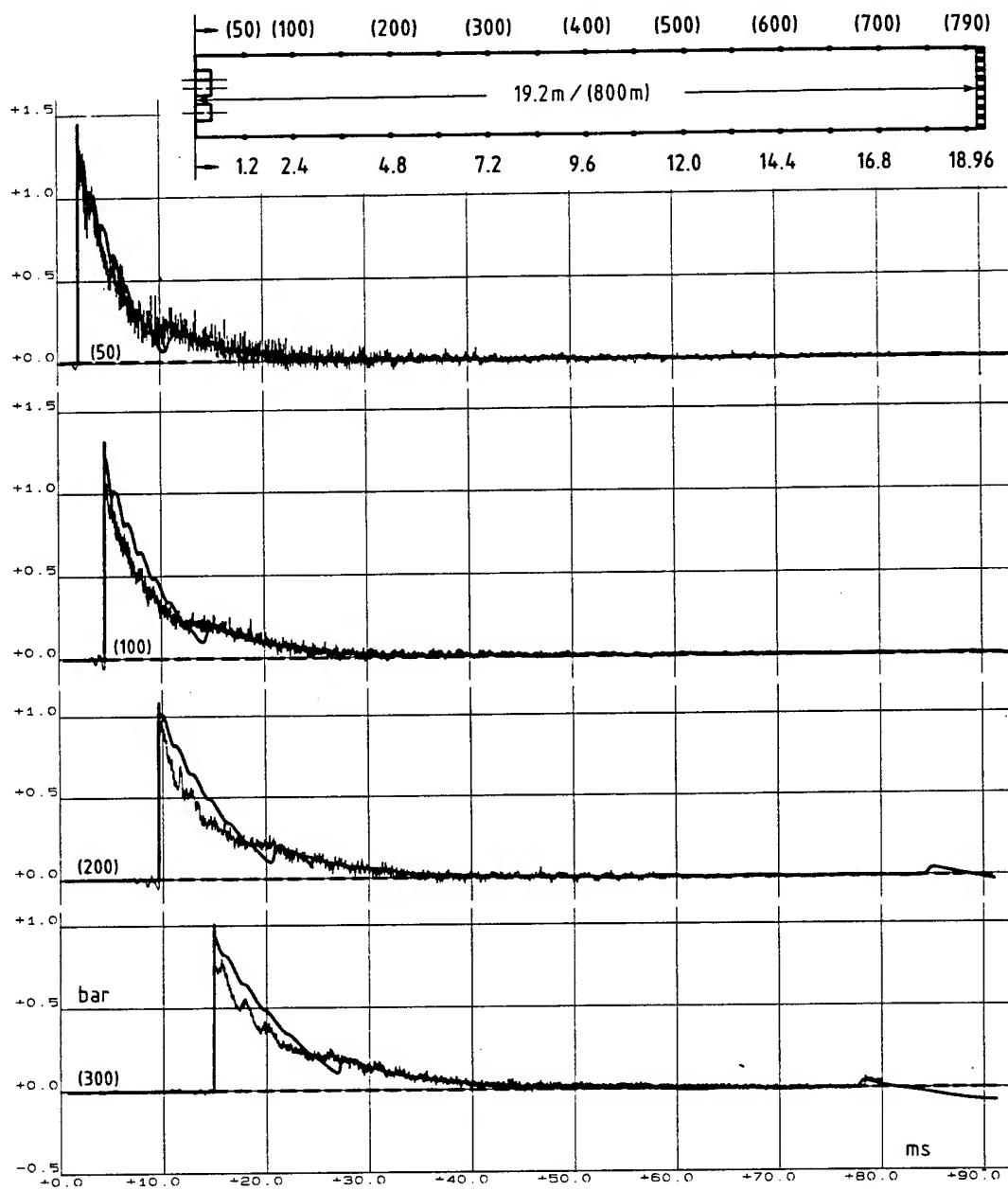


Fig. 17a Pressure-time histories at different points along the 19.2 m blast simulator. Exit: 47% open. Comparison experiment with numerical calculation (Q1DEUL-Code). Driver pressure: 150 bar

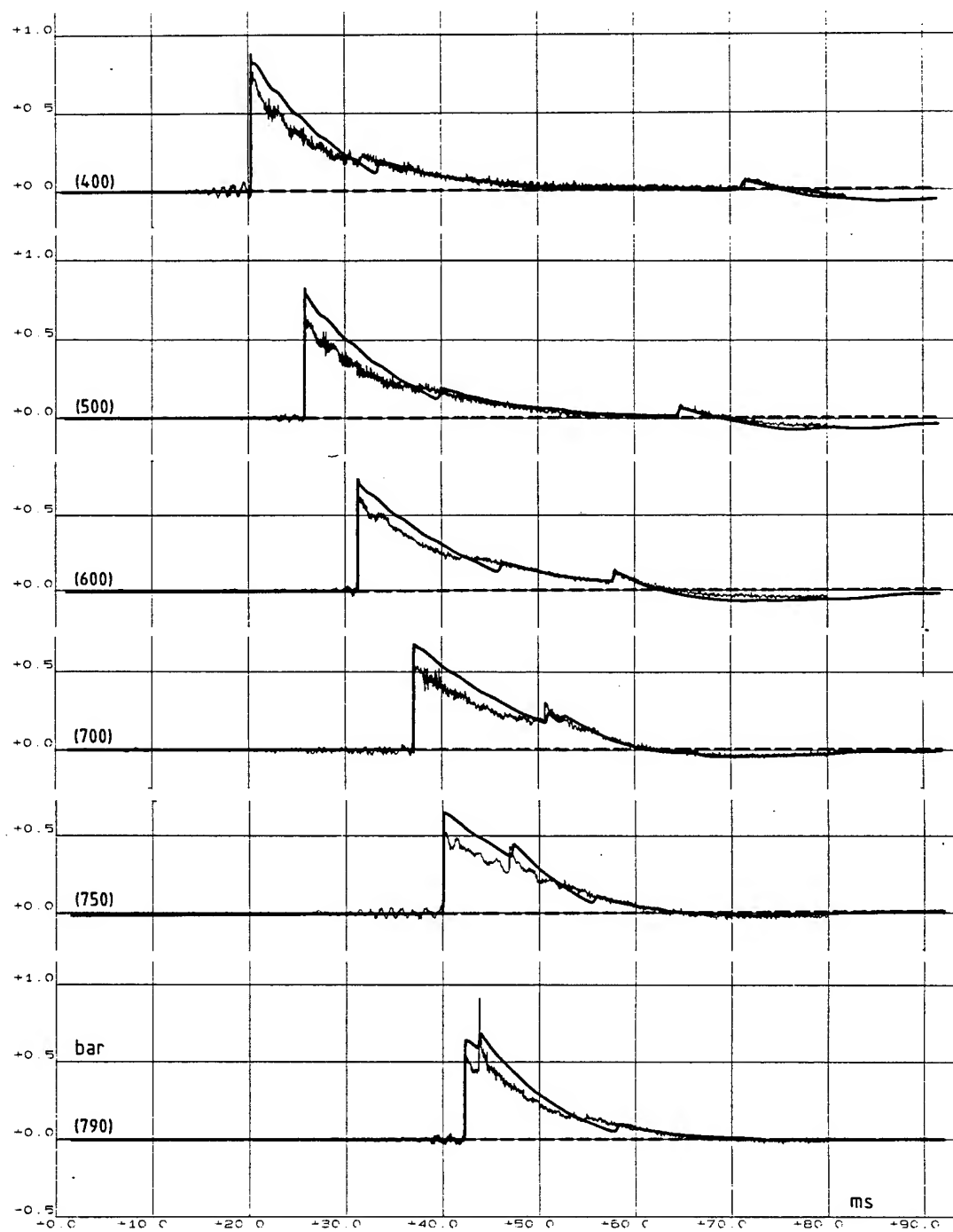


Fig. 17b Continued

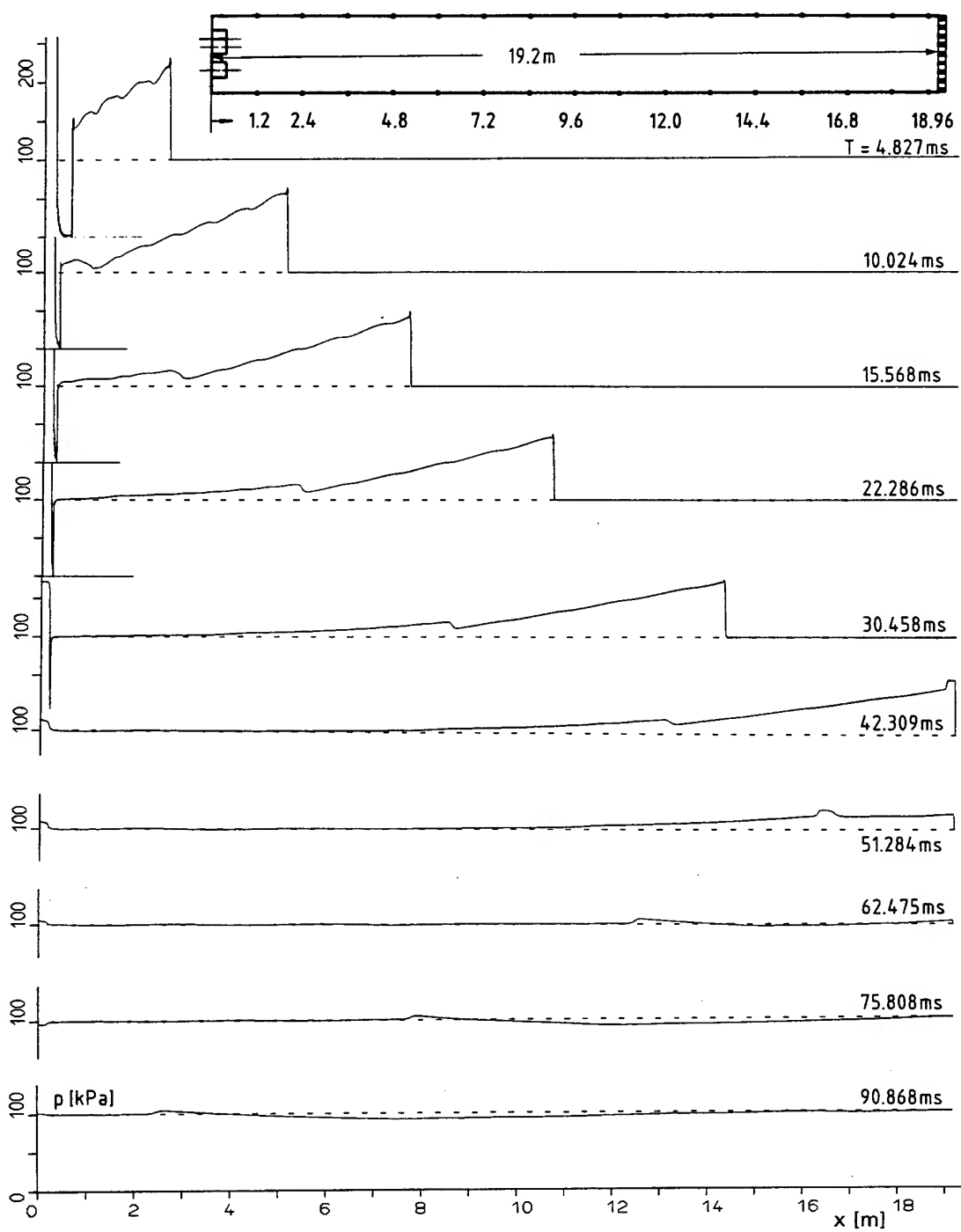


Fig. 18 Numerical calculation (Q1DEUL-Code) of the pressure distribution along the 19.2 m blast simulator at different times. Exit: 47% open, driver pressure: 150 bar

# **LBTS PC PREDICTIVE TOOL**

James M. Sevier

Maxwell Laboratories, S-Cubed Division  
2501 Yale Blvd., SE, Ste. 300  
Albuquerque, NM 87106

Charles E. Needham

Applied Research Associates  
4300 San Mateo Blvd., NE, Ste. A220  
Albuquerque, NM 87110

## **1. Abstract**

The S-Cubed Division of Maxwell Laboratories has produced LBTS PC Predictive Tool as a supporting product for the operation of the Defense Nuclear Agency Large Blast/Thermal Simulator (LBTS) facility. The LBTS PC Predictive Tool is intended to be a culmination of S-Cubed's modeling effort. The modeling effort was undertaken to provide a method for determining the initial driver conditions necessary to produce a desired test condition without having to resort to a hydrocode calculation. The model is based on a set of quasi-empirical fits to characteristic parameters obtained from a series of two-dimensional hydrocode calculations. These calculations were initialized with driver conditions representing a variety of configurations within the LBTS envelope of operation.

The LBTS PC Predictive Tool design includes a Windows-based graphical user interface intended to provide the user access to its capabilities with a minimum of effort necessary to learn its operation. As an analytical tool, it is intended to enable the user to examine a large variety of parameter combinations easily and rapidly. Parameters representing fundamental quantities and derived quantities spawned in the literature of the developing study (*i.e.*, ratios of driver-to-ambient temperature and pressure) are incorporated to specify either an initial driver gas configuration or a desired target test condition.

Anticipated future development includes incorporation of actual test results into the model, and the inclusion of the results of other modeling efforts, modeling of driver evacuation behavior (Blowdown), modeling of the Thermal Radiation Simulators (TRS), and modeling of thermal layer influence, boundary layer influence, and blockage effects.

The results of several LBTS tests are available for validation and the model compares favorably.

## **2. Introduction**

In order to utilize the Large Blast/Thermal Simulator (LBTS) fully, there must be available a fast, simple means to predict the capabilities of the facility. Since it is time consuming and computationally expensive to run full scale hydrocode simulations of the LBTS, the LBTS Predictive Tool was developed to allow definition of the initial conditions needed to obtain a desired waveform at the target location. The target location is defined here to be located 105 meters from the upstream end of the expansion chamber; this is approximately the center of the LBTS test section. Using the information from the LBTS Predictive Tool, a full hydrodynamic calculation can be performed to study details of the flow characteristics, with the confidence that the resulting waveform at the target location will be that which is desired. Without the Predictive Tool, it would be nearly impossible to determine which initial conditions should be used to generate the desired target shock environment.

## **3. Developing the LBTS Predictive Tool**

### **3.1 Hydrocode Calculations**

The first step in modeling the LBTS was to run a series of one-dimensional Cartesian [1] and two-dimensional cylindrical [2] hydrocode calculations. A set of 2-D calculations was chosen to represent LBTS behavior at selected points across the operating envelope of the LBTS. These cases reflect changes in driver gas pressure, driver gas temperature, driver gas volume, and driver exit nozzle baffle plate size. This set of calculations is composed of sixteen with 100% open baffle plates, and five with 40% open baffle plates. The 100% open baffle cases consist of five cases at the minimum volume of driver gas, five cases at an intermediate volume, and six cases at a large volume of driver gas. All five 40% open baffle cases are at the large volume only, since the baffle plates were designed to be used to enhance the pressure impulse for a given peak shock pressure. (Using a smaller volume when the desired result is to maximize impulse is not sensible.) The large volume used was believed at the time the calculations were performed to be near the maximum driver gas volume. Figures 1A and 1B show a synopsis of these characterization cases in both SI and English units. The dimensionless parameters referenced in the table are defined later in this paper (RDAP is a dimensionless pressure ratio and RDAT is a dimensionless temperature ratio).

### **3.2 Fitting a Standard Nuclear Waveform to the Hydrocode Results**

#### **3.2.1 Peak Pressure Determination**

To characterize the waveform at the target location, it was decided to match it to the best-fitting 1-KT standard nuclear waveform [3]. The first step in doing this was to define the peak pressure at shock arrival. Because of the numerical overshoot of the hydrocode at the shock front, the peak pressures were defined to be the geometric mean of the shock front peak pressure and the first minimum after that peak value. This provided peak pressure numbers for both static overpressure and dynamic pressure for each case.

Problem number	Baffle plate (% open)	Driver volume (cubic meters)	RDAP	Driver Pressure (Pa)	RDAT	Driver Temperature (Kelvin)
78.0000	100%	180	9.6	8.15E+05	1.04	300
9472.0200	100%	180	16.7	1.42E+06	1.11	320
9472.0300	100%	180	52.8	4.49E+06	1.43	413
9472.0400	100%	180	102	8.66E+06	1.81	523
9472.0500	100%	180	179	1.52E+07	2.18	629
9473.0100	100%	350	9.6	8.15E+05	1.17	338
9473.0200	100%	350	16.7	1.42E+06	1.311	378
9473.0300	100%	350	52.8	4.49E+06	1.691	488
9473.0400	100%	350	102	8.66E+06	2.128	614
9473.0500	100%	350	179	1.52E+07	2.327	672
9471.0101	100%	498	9.6	8.15E+05	1.17	338
9471.0200	100%	498	16.7	1.42E+06	1.311	378
9471.0250	100%	498	32.8	2.79E+06	1.26	364
9471.0300	100%	498	52.8	4.49E+06	1.691	488
9471.0501	100%	498	102	8.66E+06	1.81	523
9471.0601	100%	498	179	1.52E+07	2.327	672
9474.0100	40%	498	9.6	8.15E+05	1.106	319
9474.0201	40%	498	16.7	1.42E+06	1.202	347
9474.0300	40%	498	52.8	4.49E+06	1.444	417
9474.0400	40%	498	102	8.66E+06	1.665	481
9474.0500	40%	498	179	1.52E+07	1.865	538

FIGURE 1A: LBTS CHARACTERIZATION HYDROCODE CALCULATIONS (S.I. UNITS)

Problem number	Baffle plate (% open)	Driver volume (cubic feet)	RDAP	Driver Pressure (psia)	RDAT	Driver Temperature (Fahrenheit)
78.0000	100%	6357	9.6	118	1.04	81
9472.0200	100%	6357	16.7	206	1.11	117
9472.0300	100%	6357	52.8	650	1.43	283
9472.0400	100%	6357	102	1257	1.81	481
9472.0500	100%	6357	179	2205	2.18	673
9473.0100	100%	12360	9.6	118	1.17	148
9473.0200	100%	12360	16.7	206	1.311	222
9473.0300	100%	12360	52.8	650	1.691	419
9473.0400	100%	12360	102	1257	2.128	646
9473.0500	100%	12360	179	2205	2.327	750
9471.0101	100%	17587	9.6	118	1.17	148
9471.0200	100%	17587	16.7	206	1.311	222
9471.0250	100%	17587	32.8	404	1.26	195
9471.0300	100%	17587	52.8	650	1.691	419
9471.0501	100%	17587	102	1257	1.81	481
9471.0601	100%	17587	179	2205	2.327	750
9474.0100	40%	17587	9.6	118	1.106	115
9474.0201	40%	17587	16.7	206	1.202	165
9474.0300	40%	17587	52.8	650	1.444	291
9474.0400	40%	17587	102	1257	1.665	406
9474.0500	40%	17587	179	2205	1.865	510

FIGURE 1B: LBTS CHARACTERIZATION HYDROCODE CALCULATIONS (ENGLISH UNITS)

### **3.2.2 Impulse Match**

With the peak pressure defined, a 1-KT standard nuclear waveform could then be scaled to provide the best match to the waveform. This best fit was determined to be when the impulses for the complete positive phase were equal. In the cases where the entire positive phase of the hydrocode waveform was not calculated, the calculated waveform was fitted with the corresponding segment of a scaled 1-KT waveform.

This fitting methodology provided a standardized way of characterizing the waveforms. It also provided a reasonable way to extrapolate the waveform to obtain complete positive phase impulse numbers without having to run out the hydrocode calculations further. Figures 2, 3, 4, and 5 show example matchings of scaled 1-KT waveforms to SHARC hydrocode waveforms for one of the characterization cases.

## **3.3 Predicting Performance Across the Operating Envelope**

### **3.3.1 Decision to Use Curve Fits**

With a set of initial characterization cases defined, several methods were considered for predicting the performance of the LBTS across its operating envelope. A method that was abandoned involved using a method of numerical interpolation and extrapolation from the results of the initial characterization hydrocode runs to obtain predicted values for other combinations of initial conditions. Although there were some regions where this method seemed to work acceptably well, there were places where the predicted results were physically unrealistic. Discontinuities in the rate and direction of change of the results existed within the regime being considered as initial condition values were varied past a point where a characterization calculation existed. In addition, it was not possible to obtain good results when specifying the desired final waveform and then working in reverse to determine the desired initial conditions.

This method was abandoned, then, for a method which involved fitting curves to the quasi-empirical waveform data obtained from the characterization hydrocode cases, based upon initial condition parameters. It was hoped, and later found, that these simple, well-behaved curves would simplify the effort to determine which set of initial conditions would produce a desired waveform at the target location.

Because variations in driver gas pressure, temperature, and volume occur across a continuum, parameters based on these variables all appear in the fit formulas. Since baffle plate openings vary in discrete steps, separate fit formulas represent these different cases.

### **3.3.2 Initial Conditions Parameter Definition**

To fit curves to the data, a set of descriptive variables to describe the initial conditions was needed. To describe the pressure of the driver gas, the Ratio of the Driver absolute pressure to Ambient absolute Pressure (RDAP) was chosen. Similarly, driver gas temperature was described as the Ratio of Driver absolute temperature to Ambient absolute Temperature (RDAT). Both RDAP and RDAT are independent of the units used. The third variable used was simply the total volume of driver gas in cubic meters. This volume is varied in the LBTS by the use of movable hydroplugs in the driver tubes.



PROBLEM 9474.0100  
SHARC STATION 60 AT 105 METERS  
DYNAMIC PRESSURE PEAK = 0.18 (PSI)  
YIELD= 10.8 (KT) PEAK IMPULSE= 0.0327 (PSI-S)

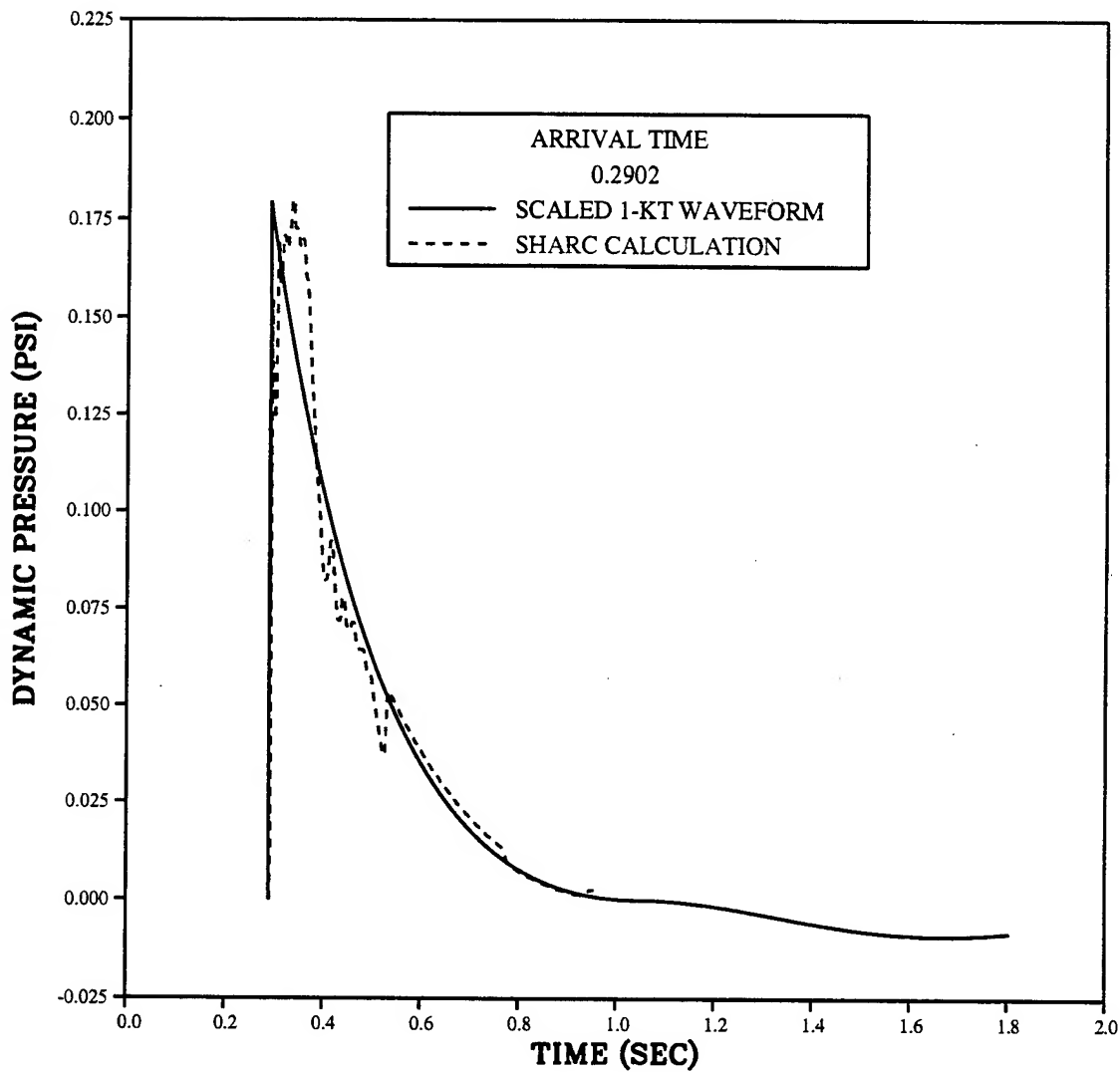


FIGURE 2: DYNAMIC PRESSURE CHARACTERIZATION

PROBLEM 9474.0100  
SHARC STATION 60 AT 105 METERS  
DYNAMIC PRESSURE PEAK = 0.18 (PSI)  
YIELD= 10.8 (KT) PEAK IMPULSE= 0.0327 (PSI-S)

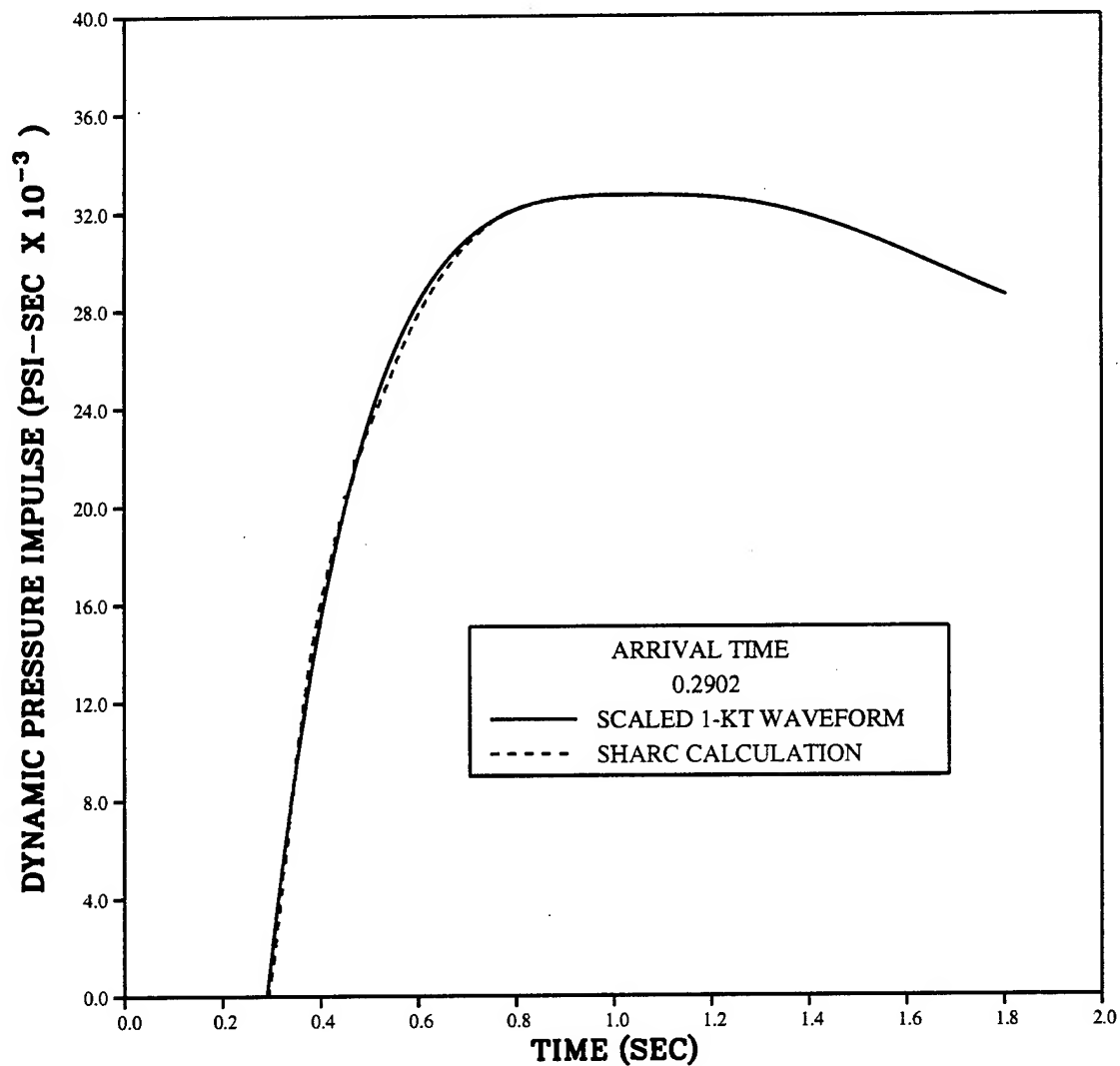


FIGURE 3: DYNAMIC PRESSURE CHARACTERIZATION (IMPULSE)

PROBLEM 9474.0100  
SHARC STATION 60 AT 105 METERS  
OVERPRESSURE PEAK = 2.53 (PSI)  
YIELD= 16.4 (KT) PEAK IMPULSE=0.749 (PSI-S)

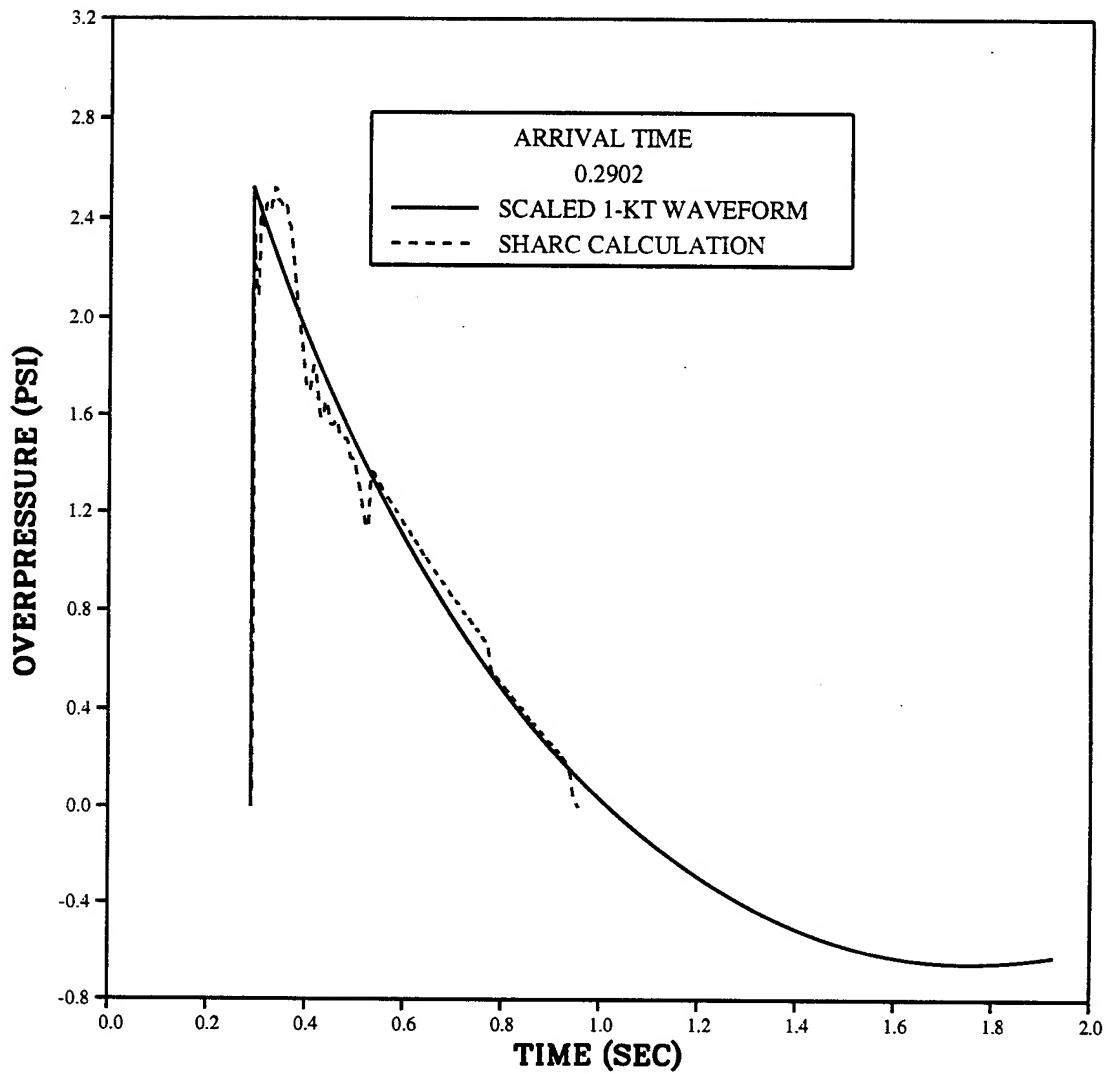


FIGURE 4: OVERPRESSURE CHARACTERIZATION

PROBLEM 9474.0100  
SHARC STATION 60 AT 105 METERS  
OVERPRESSURE PEAK = 2.53 (PSI)  
YIELD= 16.4 (KT) PEAK IMPULSE=0.749 (PSI-S)

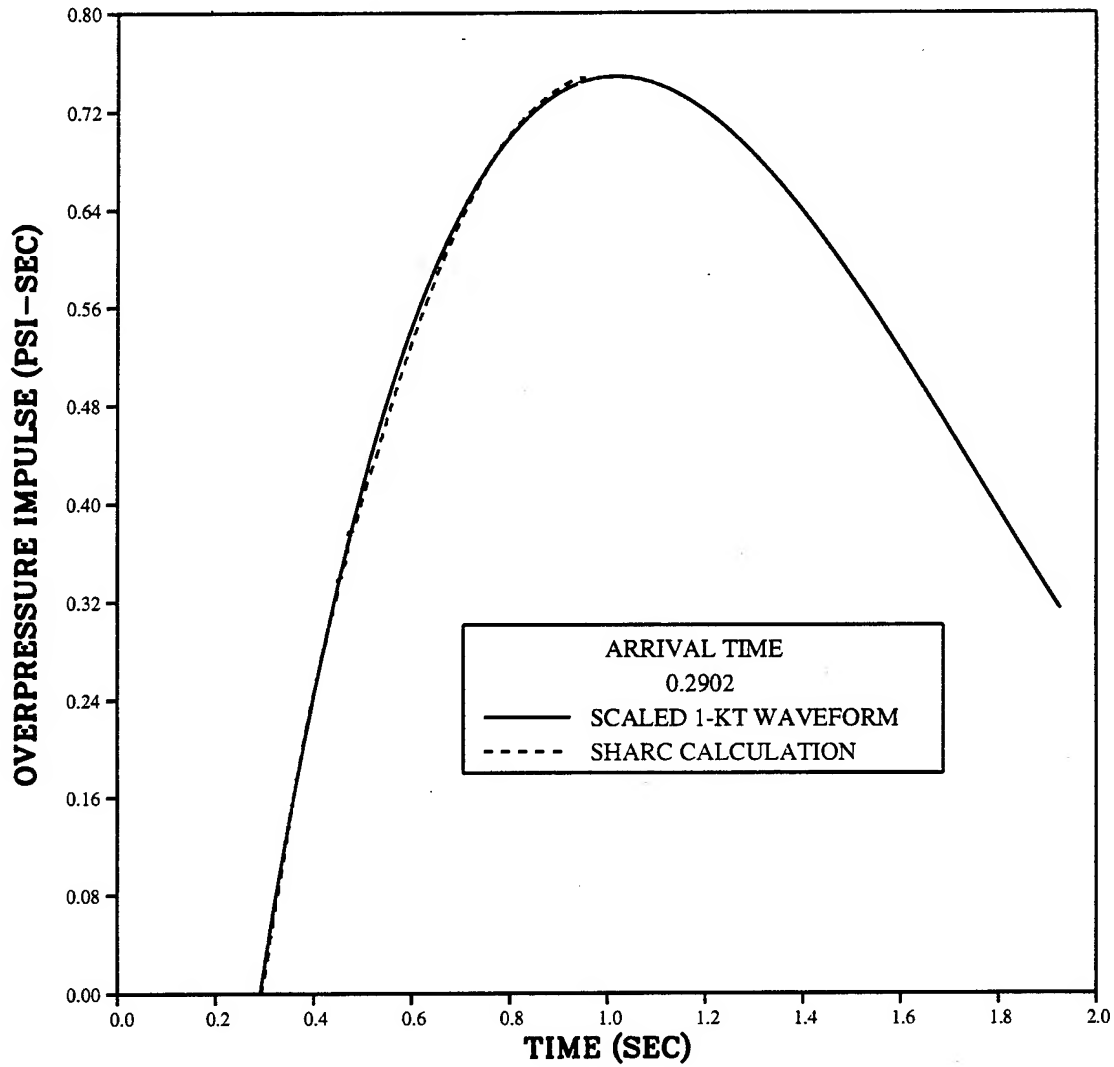


FIGURE 5: OVERPRESSURE CHARACTERIZATION (IMPULSE)

With these descriptive variables, parameters were defined and univariate multiple linear regression based upon these parameters was performed. This resulted in a fit linear in the chosen parameters, but not necessarily linear in the basic variables.

### 3.3.3 Goodness of Fit

When comparing the results of various fit curves, a standard and consistent means of quantifying the closeness to the hydrocode data was needed. The chosen method to evaluate the goodness of various fits was the average percent error for each curve. This value was defined as

$$\text{error} = 1/n \sum ( |y_{\text{data}} - y_{\text{fit}}| / (y_{\text{data}}) )$$

where n is the number of data points being fitted,  $y_{\text{data}}$  is the value of a data point, and  $y_{\text{fit}}$  is the corresponding value of the fit curve. This method gives more importance to missing a small-valued data point by a certain amount than missing a larger-valued data point by the same amount.

### 3.3.4 Peak Pressures

In fitting the peak pressures, both static overpressure and dynamic pressure, it was observed that these peaks were independent of the volume of driver gas used, within the limits of LBTS operation. So, the initial curve fitting efforts centered on describing the peak pressures as a function of parameters based upon RDAP and RDAT only. After investigating many different parameter combinations, the simplest fit that provided the best results was a function that was quadratic in the product of RDAT and RDAP, of the form

$$\text{peak pressure} = A + B (\text{RDAT})(\text{RDAP}) + C ( (\text{RDAT})(\text{RDAP}) )^2$$

where A, B, and C are constants. Investigation was made to see whether other similar combinations of variables produced better results, such as RDAT raised to the one-half power multiplied by RDAP, but no other combination was found that produced better results. The results predicted by all combinations of the initial condition parameters are physically reasonable within the LBTS operating envelope.

Since the Rankine-Hugoniot relationship couples the peak overpressure and peak dynamic pressure at the shock front, it was only necessary to fit one of these peak pressures; the other peak pressure is obtained by applying this relationship to the results obtained from the fit. For the LBTS model, the peak dynamic pressure is obtained from a fit formula and the peak overpressure is determined from the Rankine-Hugoniot relationship.

### 3.3.5 Arrival Times

Since the propagation speed of the shock front is related to the shock strength, and since the decay of the peak pressure of the shock as it propagates down the tube is similar for various waveforms, it was decided to predict shock arrival time based upon peak

overpressure at the target location. Indeed, it was found that good results were obtained from a fit that was quadratic in peak overpressure.

Because there was interest in determining arrival time at locations other than the target location, such as at gauge locations, the propagation of the shock front along the expansion chamber was studied. It was found that once the shock had formed and was planar across the expansion chamber, the propagation speed was essentially constant all the way to the end of the tunnel. Therefore, a fit to the arrival time at 40 meters was performed and a linear combination of the arrival time fits for 40 meters and 105 meters provided arrival time predictions from 40 meters to the end of the expansion chamber.

### 3.3.6 Impulses

To describe the total waveform, one other attribute of the waveform had to be characterized. It could be equivalent nuclear yield, positive phase duration, or positive phase impulse. Because there are many different ways to describe equivalent nuclear yield (e.g. free-air burst at sea level, free-air burst at altitude, surface burst at sea level, surface burst at altitude, etc.) it was decided to describe a physical characteristic of the waveform rather than an interpreted one. The impulse of the complete positive phase was selected as the characteristic to be fitted.

The impulse of the waveform varies whenever any of the three initial condition variables is altered. This means that the fit had to be some combination of RDAP, RDAT, and Volume. Because the data set of hydrocode calculations was very sparse, there was considerable difficulty in defining exactly how the impulse changed with changes in these variables.

It became evident during the fitting process that better results were being attained when the impulse was fitted with parameters based upon driver gas volume and the peak pressure corresponding to the impulse being calculated (i.e. using the peak dynamic pressure when calculating the dynamic pressure impulse). Since the hydrocode calculations had been run at only three different volumes for the 100% open baffle cases, it was decided to investigate the relationship between peak pressure and impulse at each of these discrete volumes, and then to study the relationship between the fit curves at these specific volumes. The variation with volume of the impulses for a given peak pressure level was very nearly linear, so the fits that govern the entirety of the operating envelope reflect that fact. Our decision to extrapolate linearly our results to the maximum operating driver gas volume of the LBTS, which is 17% more than the largest-volume characterization calculation performed, are based upon the fact that the variation is nearly linear. Because we expect the 40% open baffle cases to behave similarly to the 100% open baffle cases, these impulse fits are also scaled linearly based upon changes in driver gas volume, even though hydrocode calculations were only performed at one volume.

The combined volume and peak pressure fit that is used for each impulse calculation is well-behaved over the entirety of the LBTS operating envelope and provides physically reasonable results for all combinations of initial conditions.

### **3.3.7 Agreement Between Fit Curves and Hydrocode Calculations**

The results obtained with the LBTS Predictive Tool agree with the hydrocode calculations performed to within a few percent in each case. Further refinements to the fits are awaiting experimental data, since these numbers are the most important ones to match. As more experimental data become available, the fits will be adjusted as needed to correct any improper trends in prediction that may become evident. Figures 6, 7, 8, 9, 10, and 11 show graphically the agreement between the fits and the hydrocode calculations.

## **3.4 Predictive Tool**

### **3.4.1 General Concept**

Once these fit formulas were obtained, it was decided that there should be a user-friendly way to use them. The product decided upon was a Windows-based graphical user interface (GUI) that allowed the user to point-and-click using a mouse connected to a 486 or better computer to investigate the capabilities of the LBTS.

### **3.4.2 Operational Modes**

It was evident that the system should allow the user to specify a set of initial driver conditions and determine the target location shock environment. Also, it was obvious that the ability to define the desired shock environment and determine what initial conditions would produce that environment would be even more useful.

When the initial driver conditions are specified, the solution of the target shock environment is direct: The fit formulas are applied using the supplied conditions in the fit parameters and the results are calculated directly.

When a desired waveform is specified, there are infinitely many initial configurations that will produce that waveform; it is therefore necessary for the user to constrain the problem partially to obtain a solution. Once the peak pressure and impulse or duration are specified, the driver gas volume needed to reach that point is uniquely determined: From here, the user must specify either the driver gas pressure or temperature to obtain a unique solution.

The methodology that the program uses to reach a solution for this "inverse" method is iterative: For the given peak pressure, the volume is iteratively varied until the impulse matches the specified impulse within a threshold amount. Then, since either the pressure or temperature of the driver gas has been specified, the other can be determined by using a similar iterative method to converge on the desired value.

Once the waveform and initial conditions are all defined, the program displays numerical values for the shock conditions at the target location. These numbers include overpressure peak, impulse, and positive phase duration; dynamic pressure peak, impulse, and positive phase duration; shock arrival time; driver gas pressure, temperature, and volume; RDAP; RDAT; and equivalent free-air overpressure and dynamic pressure nuclear yields based on impulse values. In addition, a graphical display of the overpressure, dynamic pressure, density, velocity, overpressure impulse, or dynamic pressure impulse waveforms is displayed.

PEAK DYNAMIC PRESSURE  
105 METERS  
100% OPEN BAFFLE

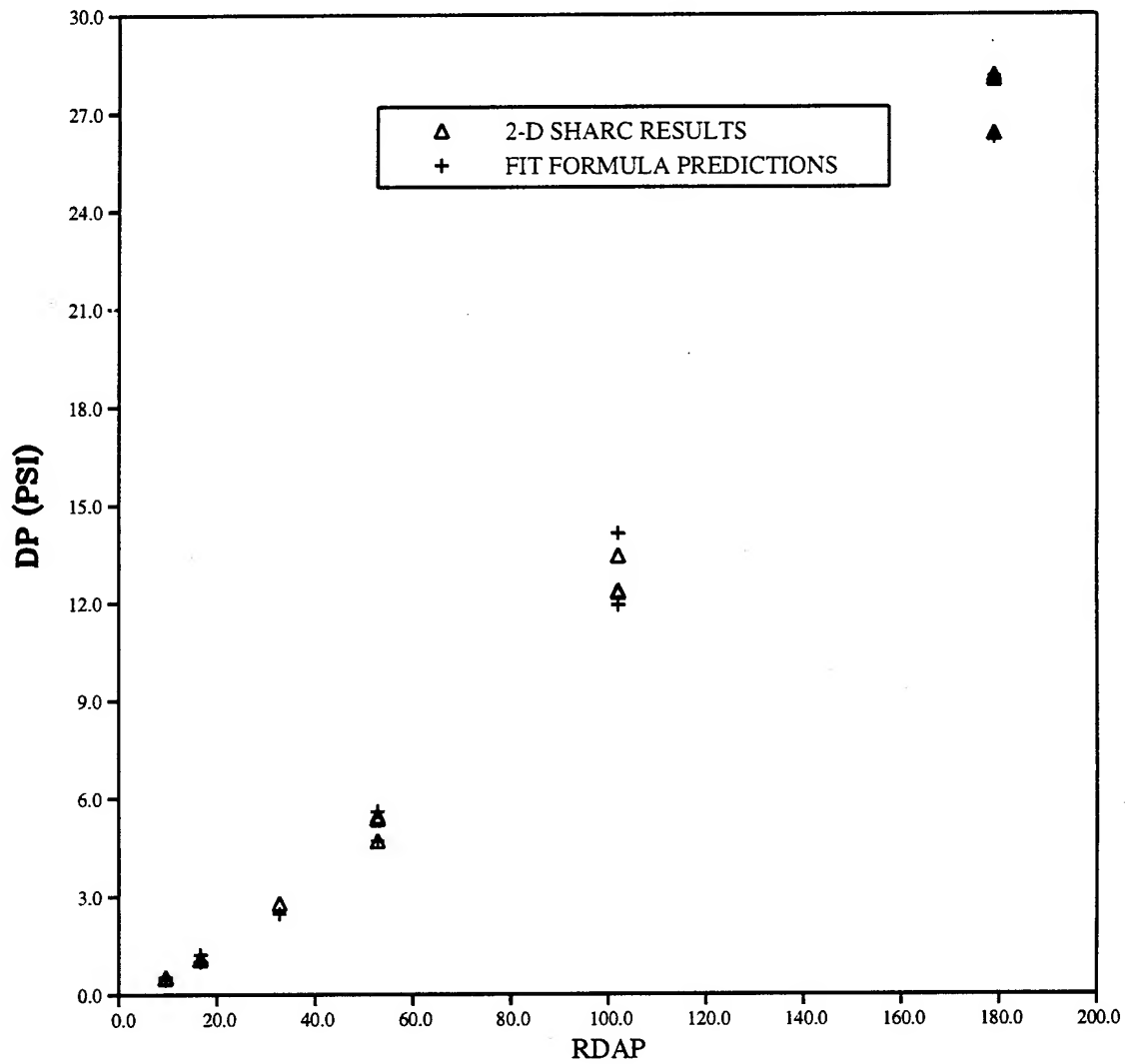


FIGURE 6: DYNAMIC PRESSURE PEAK FITS (100% OPEN BAFFLE)



PEAK OVERPRESSURE  
105 METERS  
100% OPEN BAFFLE

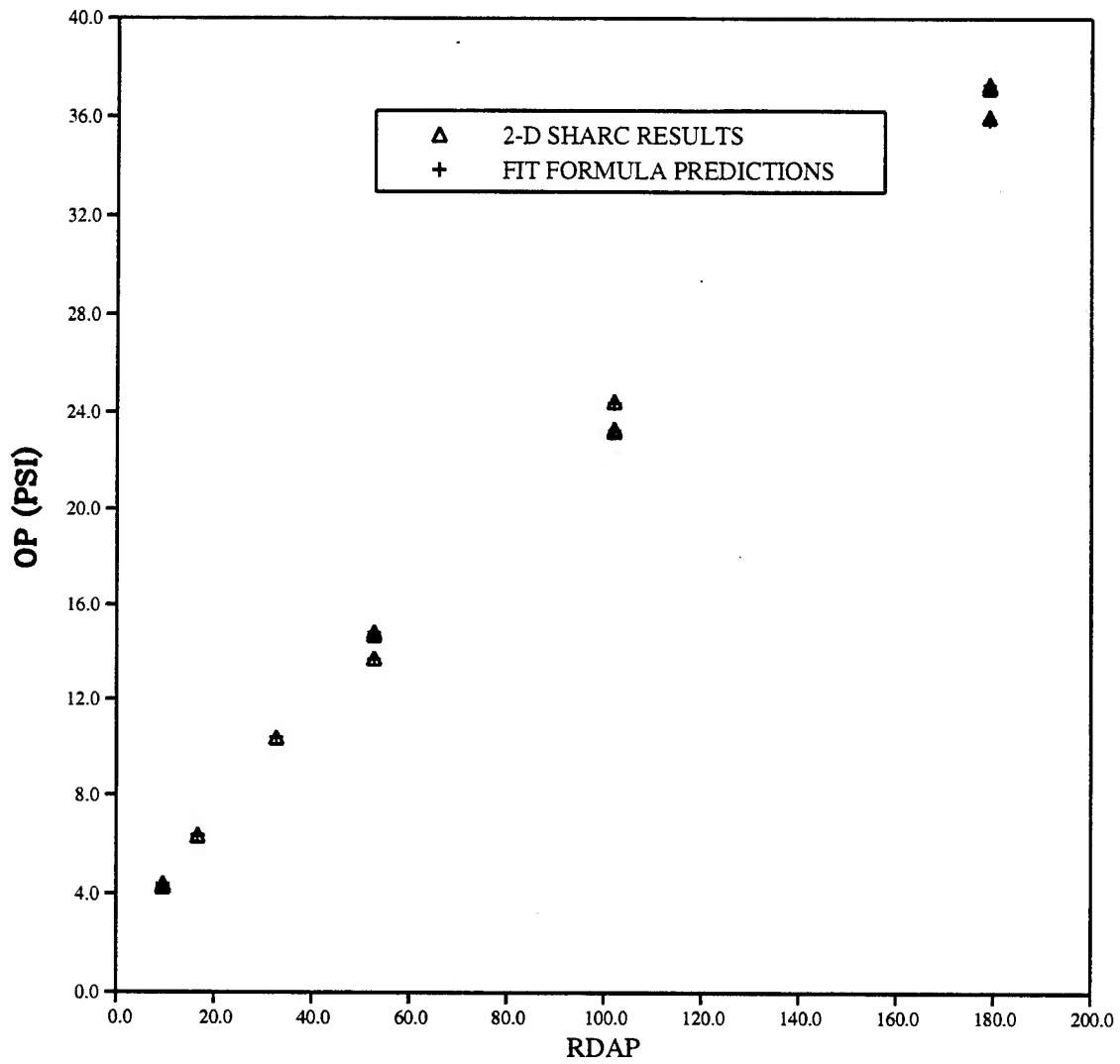


FIGURE 7: OVERPRESSURE PEAK FITS (100% OPEN BAFFLE)

SHOCK ARRIVAL TIME  
105 METERS  
100% OPEN BAFFLE

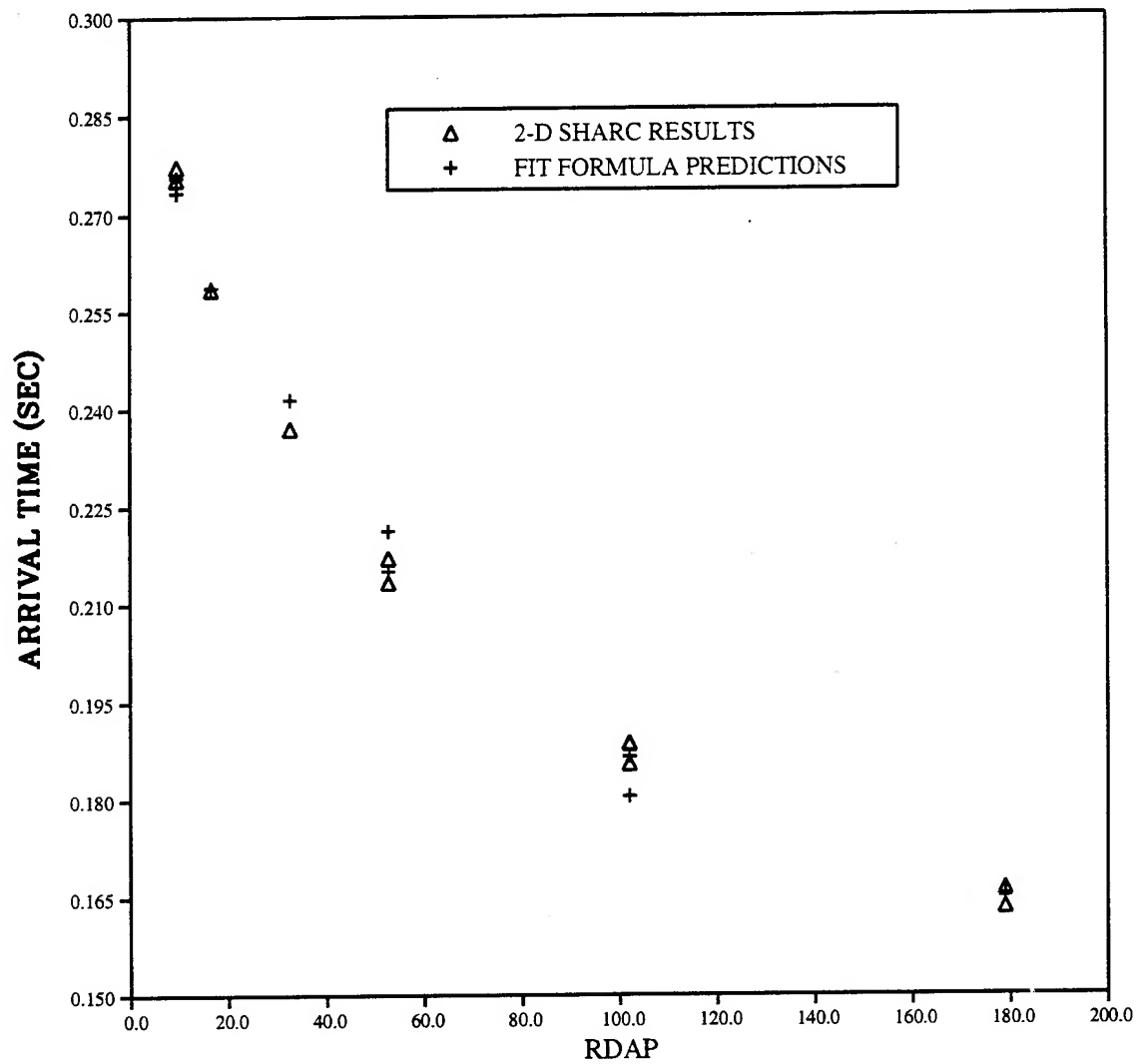


FIGURE 8: ARRIVAL TIME FITS (100% OPEN BAFFLE)

PEAK DYNAMIC PRESSURE  
105 METERS  
40% OPEN BAFFLE

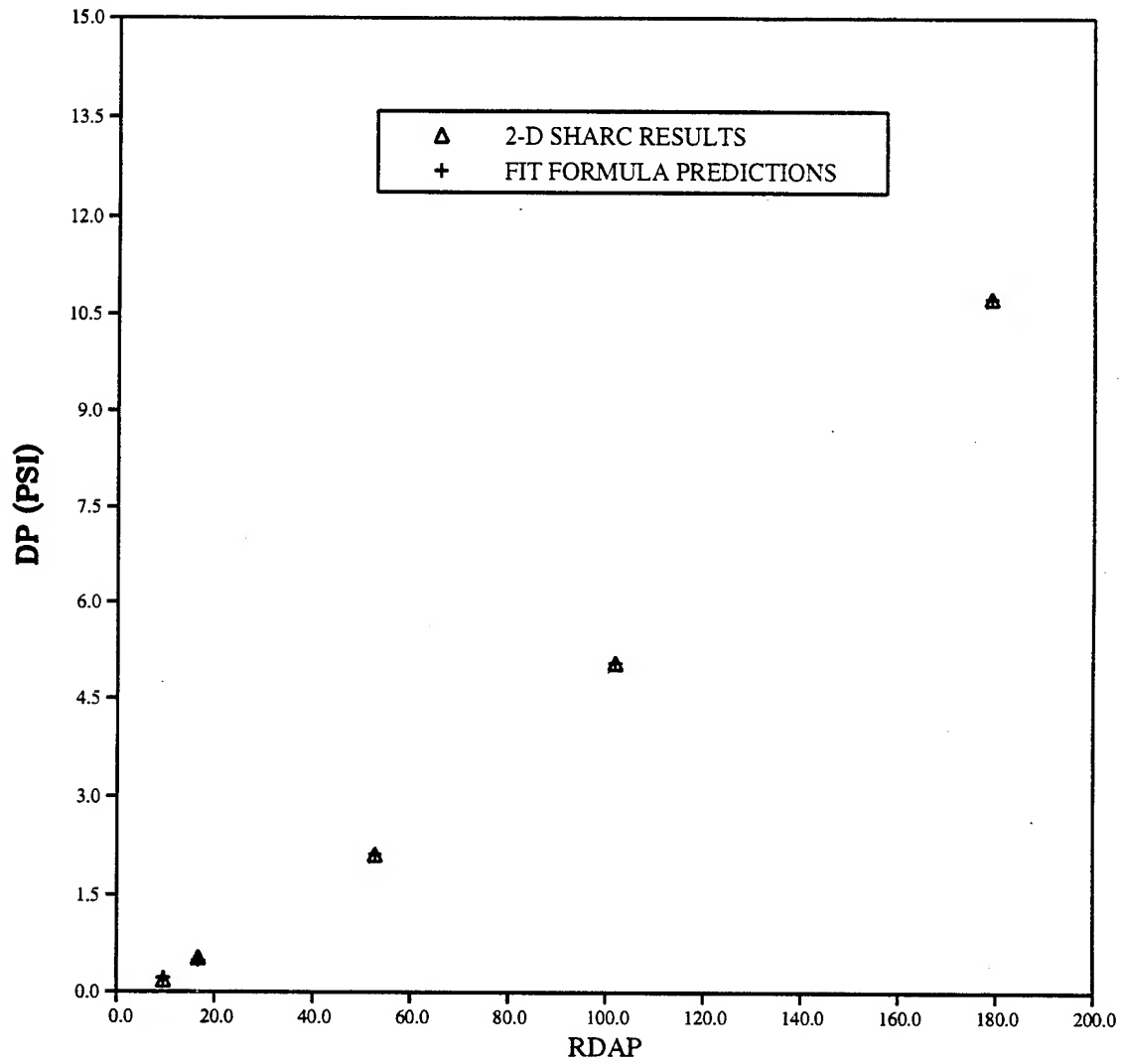


FIGURE 9: DYNAMIC PRESSURE PEAK FITS (40% OPEN BAFFLE)

PEAK OVERPRESSURE  
105 METERS  
40% OPEN BAFFLE

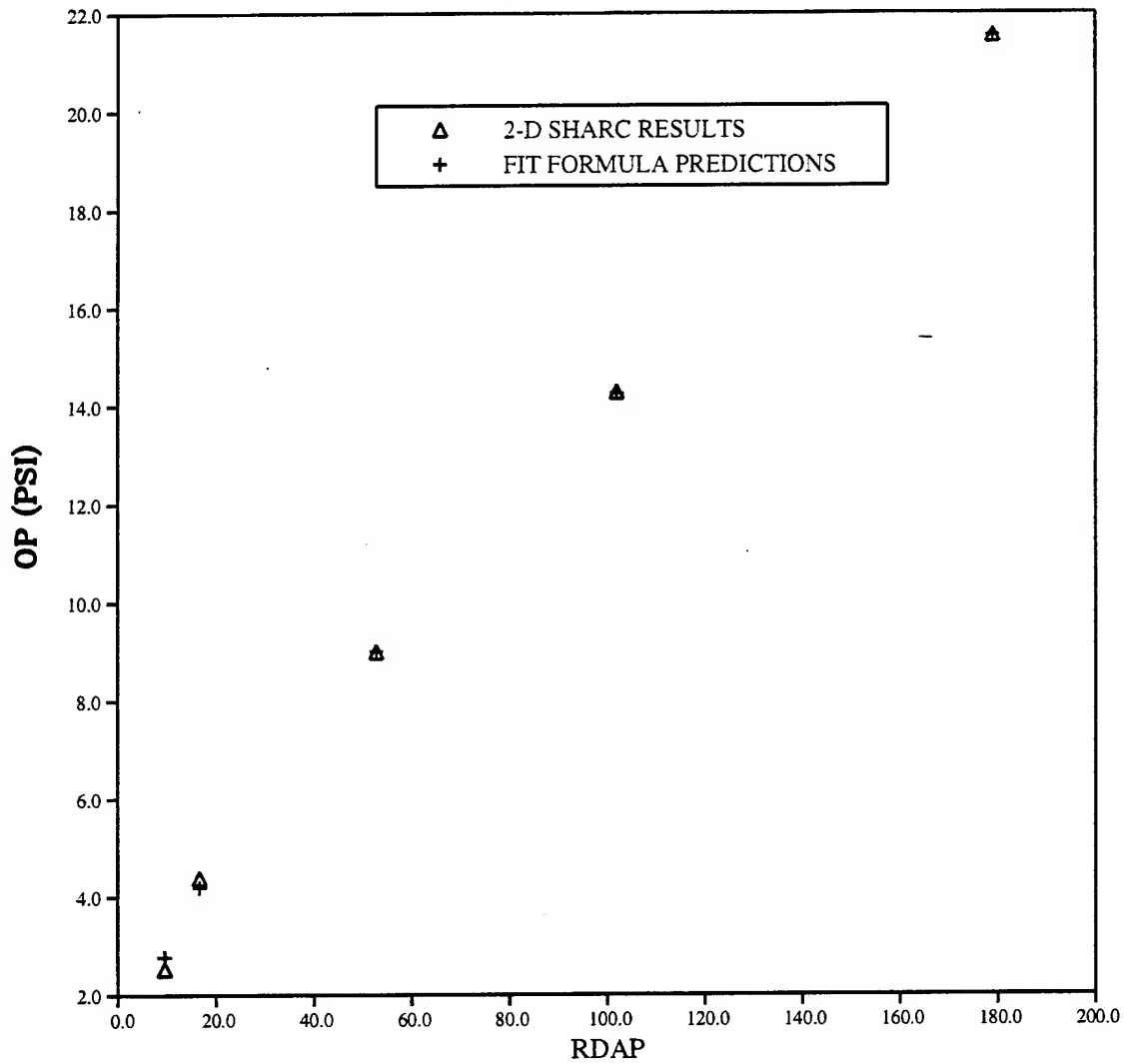


FIGURE 10: OVERPRESSURE PEAK FITS (40% OPEN BAFFLE)

SHOCK ARRIVAL TIME  
105 METERS  
40% OPEN BAFFLE

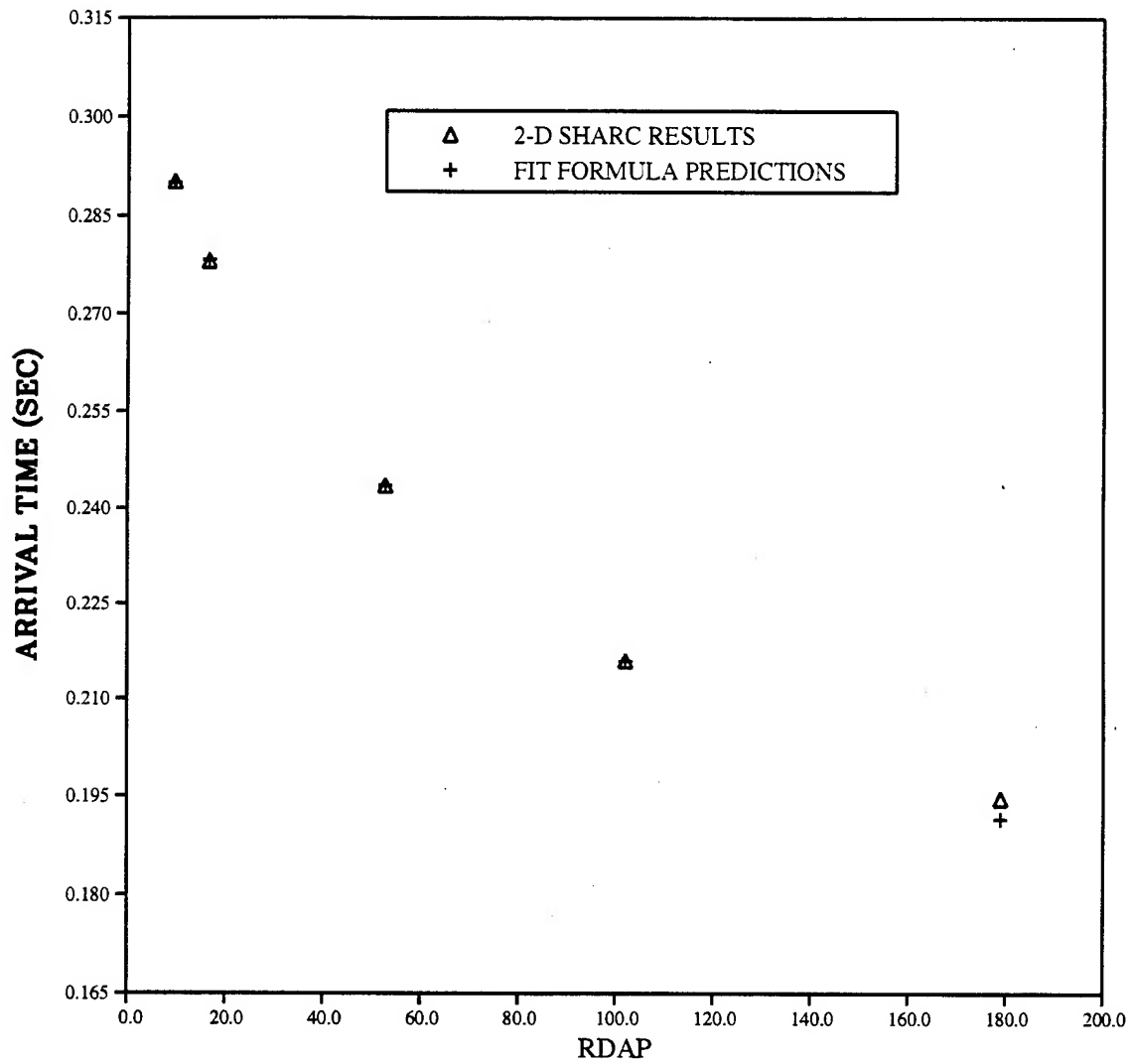


FIGURE 11: ARRIVAL TIME FITS (40% OPEN BAFFLE)

The program also can write an output file containing all the numeric data displayed on the screen to the user, as well as a series of data that describe the waveform characteristics at user-specified time step intervals for the complete positive phase. These data correspond to data points for each of the previously-mentioned graphs that can be displayed on the user screen.

### **3.5 Validity of the Model**

The previously-referenced figures 6 through 11 show the agreement between the model and hydrocode calculations. The only actual shots performed at LBTS that correspond to the model's predictive capabilities are those with 100% open baffle plates. With these shots, the model shows very good agreement. Figures 12, 13, 14, and 15 show experimental data from an actual LBTS shot overlaid with the Predictive Tool waveform. The model predicts good numbers generally, but fit refinements will undoubtedly be needed after more experimental data becomes available.

The use of the product of RDAP and RDAT as a parameter to predict peak pressures has worked very well and we are confident that this aspect of the curve fitting is one that will remain.

The validity of the predictions for the 40% open baffle plate cases has not yet been experimentally determined.

## **4. Future Development**

Other features may be incorporated into the LBTS Predictive Tool in the future. These features include a chamber flow model that provides a nine-tube model of the blowdown of the LBTS driver tubes where each tube can have its own, individually-defined initial pressure, temperature, and volume. This model can be used not only to study the driver blowdown characteristics, but also to provide a boundary condition feed-in for a three-dimensional hydrocode calculation so that only the expansion chamber need be modeled; the driver bottles do not have to be modeled in the calculation. Additional models include one that predicts radiant heat flux from the Thermal Radiation Simulator (TRS) units installed in the LBTS, as well as models to incorporate thermal layer influence, boundary layer influence, and blockage effects into the existing model.

PC MODEL VS. LBTS TEST DATA  
558.9 M3 500 PSI 286 F  
DYNAMIC PRESSURE

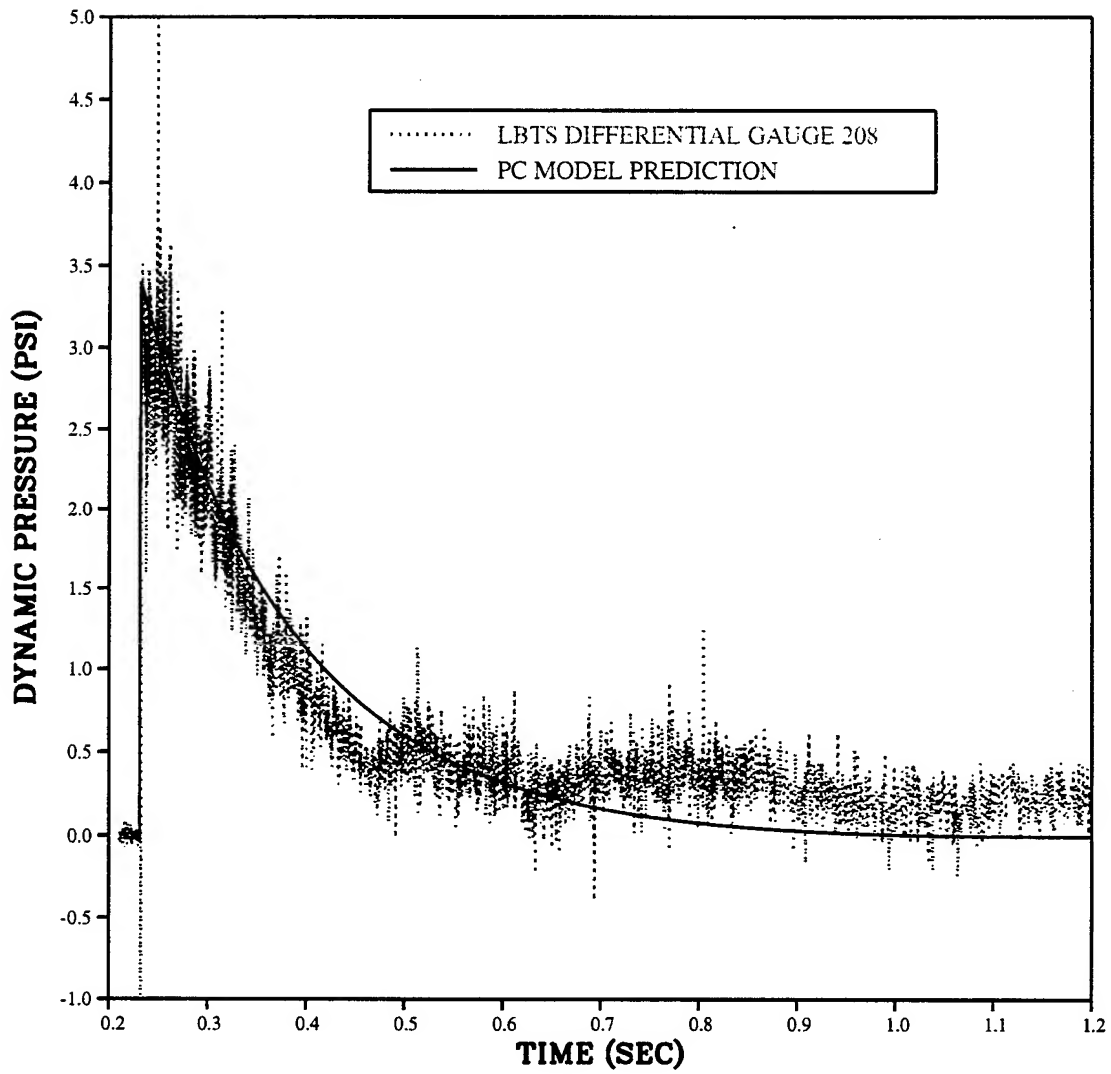


FIGURE 12: PC MODEL DYNAMIC PRESSURE VS TEST DATA

PC MODEL VS. TEST DATA  
558.9 M3 500 PSI 286 F  
DYNAMIC PRESSURE IMPULSE

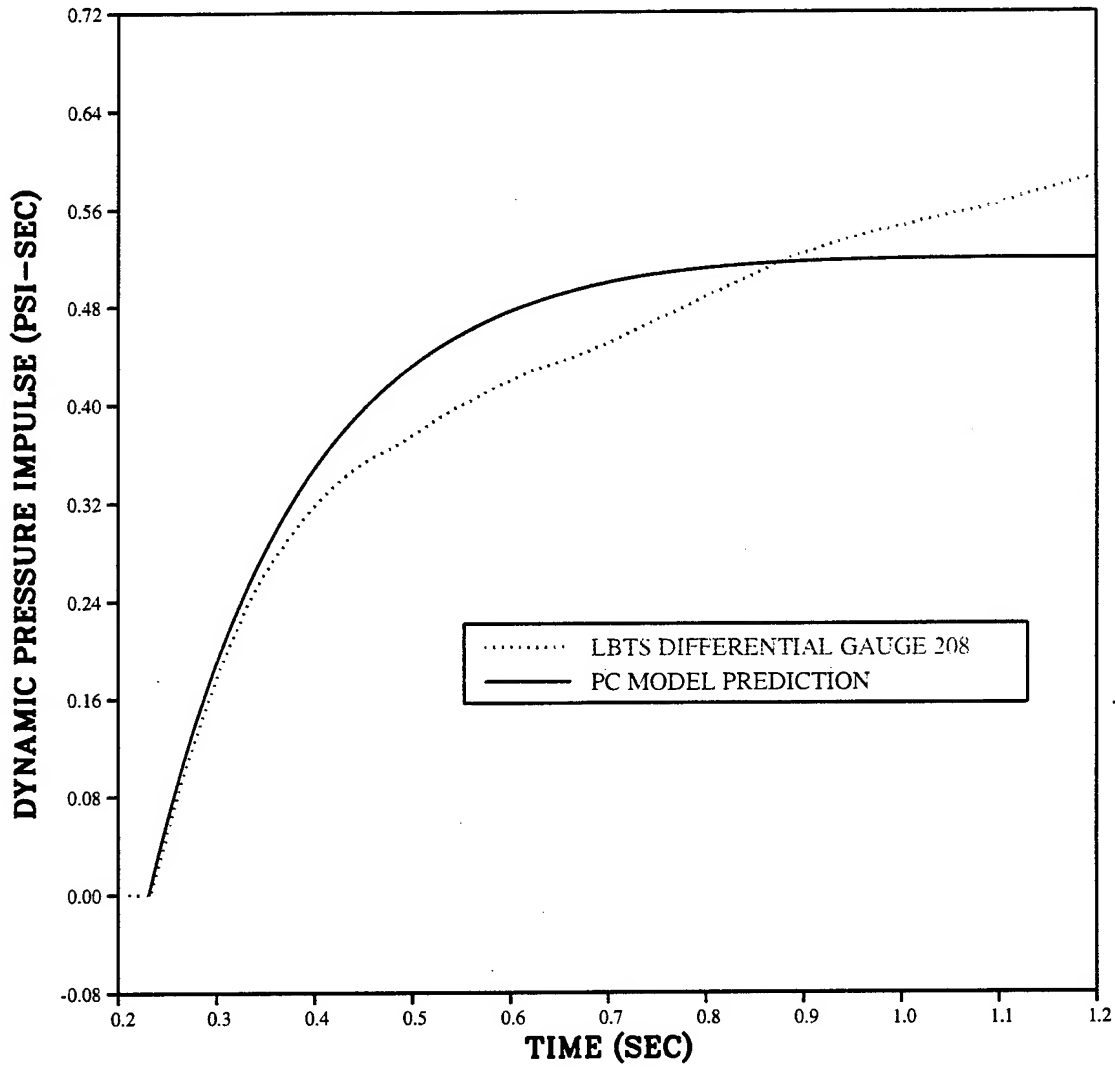


FIGURE 13: PC MODEL DYNAMIC PRESSURE IMPULSE VS TEST DATA



PC MODEL VS. TEST DATA  
558.9 M3 500 PSI 286 F  
OVERPRESSURE

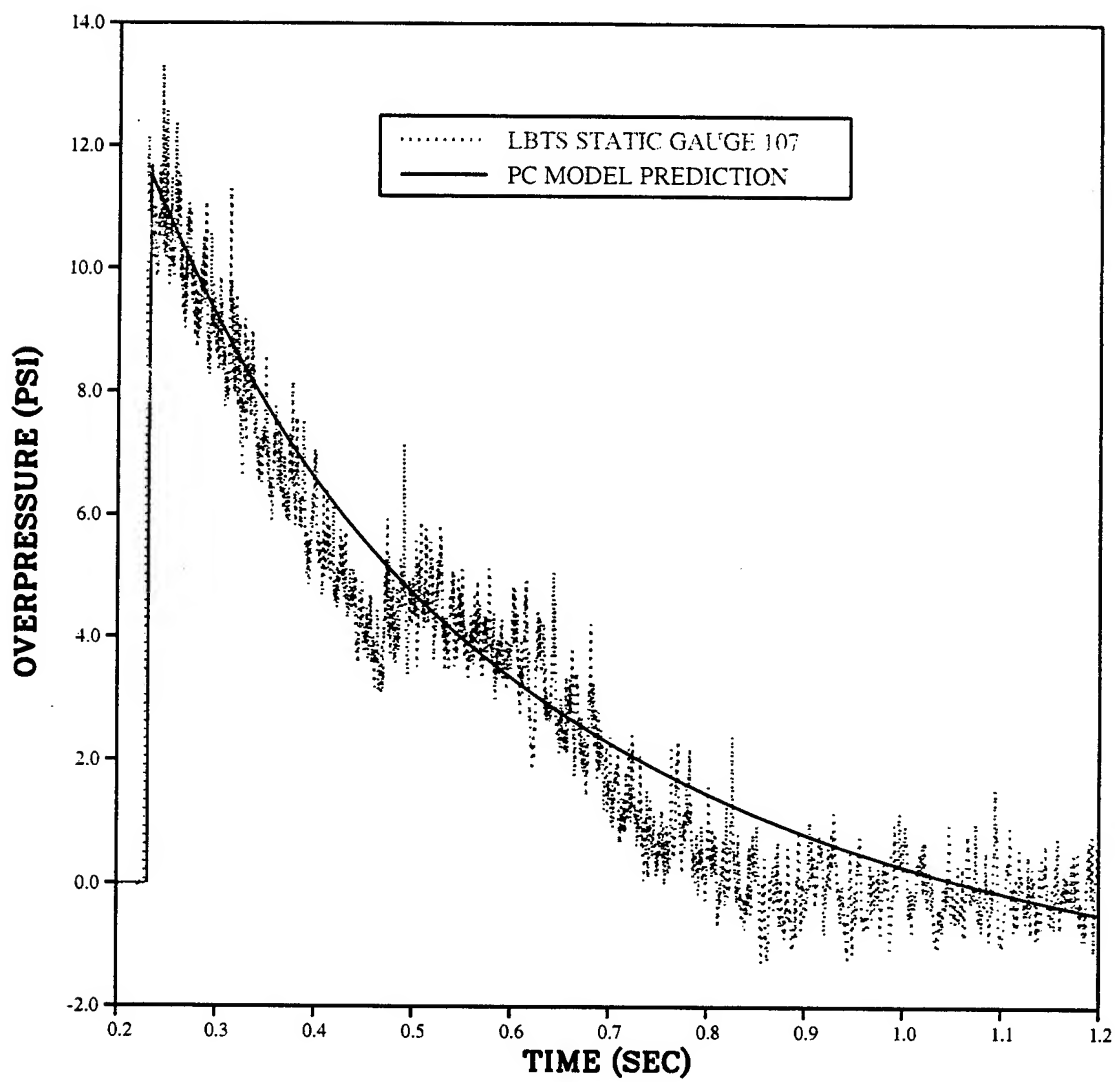


FIGURE 14: PC MODEL OVERPRESSURE VS TEST DATA

PC MODEL VS. TEST DATA  
558.9 M3 500 PSI 286 F  
OVERPRESSURE IMPULSE

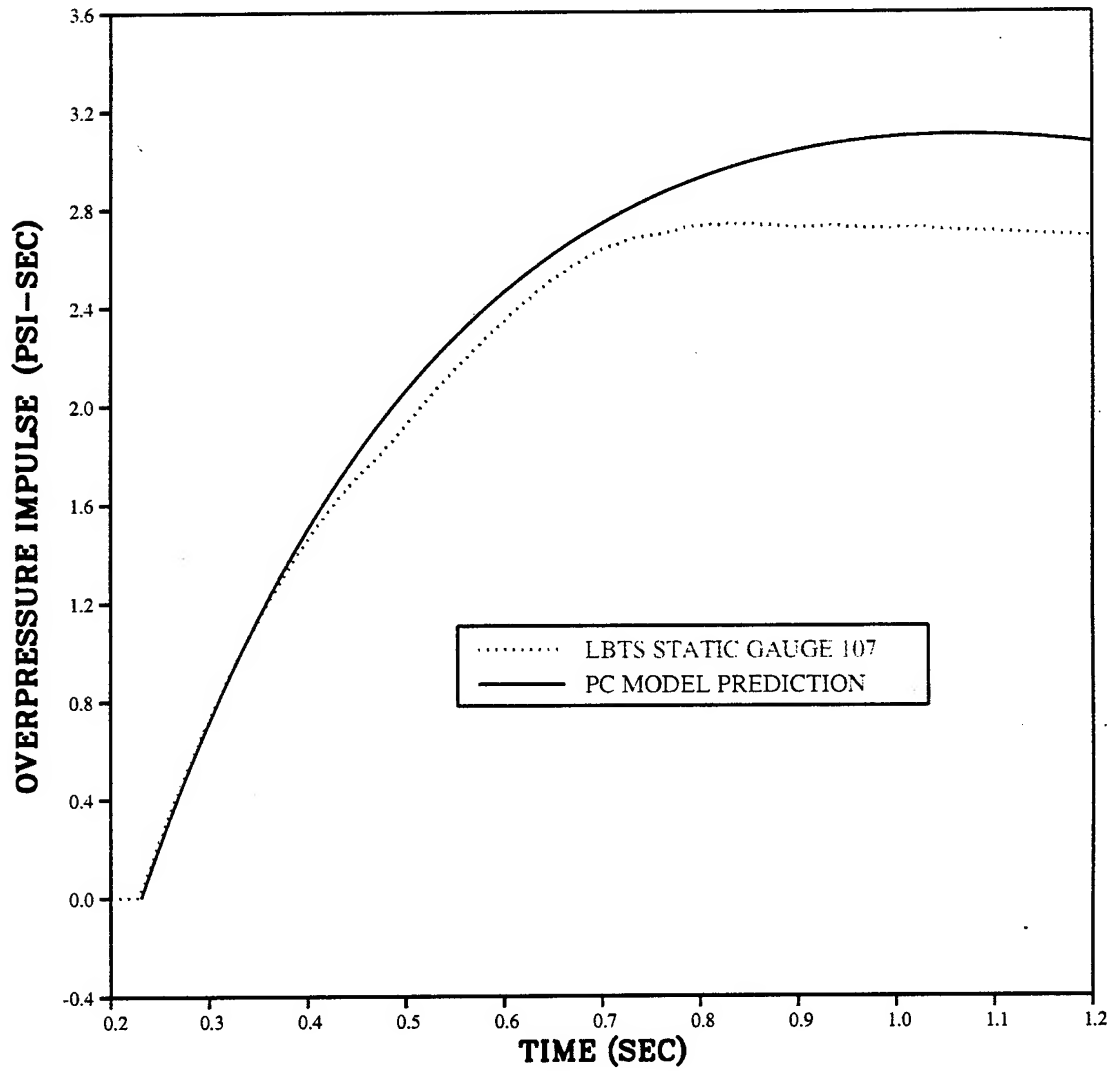


FIGURE 15: PC MODEL OVERPRESSURE IMPULSE VS TEST DATA

## 5. References

1. Ekler, R.G., et al, "Large Blast/Thermal Simulator (LBTS) One-Dimensional Cartesian Calculations," S-Cubed Report SSS-DTR-94-14735, August 1994.
2. Needham, C.E., et al, "Two-Dimensional Calculations to Support the LB/TS Driver Characterization Tests," S-Cubed Report SSS-DTR-94-14860, November 1994.
3. Needham, C.E., and J. E. Crepeau, "The DNA Nuclear Blast Standard (1KT)," Defense Nuclear Agency Report 5648T, January 1981.

## MABS 14

### Simulation of Non-Ideal Blast with a Shock Tube Exit Jet

Richard B. Loucks  
Peter C. Muller  
Richard L. Thane  
Timothy C. Cline  
Larry G. Ferguson  
Christopher Mermagen  
Aberdeen Proving Ground,

#### Abstract

The phenomenon of high dynamic pressure loading at tactical blast overpressure levels induced by the heated precursor region of the nuclear blast has become of great interest due to the increasing proliferation of nuclear arms, and the possibility of those weapons being employed in environments conducive to the production of non-ideal nuclear blast. The U.S. Army Research Laboratory (ARL) has been investigating the feasibility of simulating this non-ideal blast effect by placing a target at a distance beyond the exit of the 1.68-m shock tube. It had been demonstrated in an experiment using a full-scale armored personnel carrier (APC) that the shock tube produced sufficient dynamic pressure impulse to displace the APC more than 50 m. Further investigations have revealed the exit jet can be modified by attaching a device to spread the exit jet more uniformly over a greater area. The jet spreader, developed on scaled versions of the 1.68-m shock tube, was capable of distributing the dynamic pressure impulse over an area four times as great as the unmodified exit jet. Jeep displacement data obtained from several nuclear tests can be compared to jeep displacement experiments conducted at the exit for comparisons of loading and response.

#### 1. INTRODUCTION

Non-ideal blast is a phenomenon produced when the shock wave generated by a nuclear explosion interacts with the layer of heated air created at the ground surface by the nuclear weapon's thermal pulse. The shock wave travels faster in the thermal layer due to the elevated air temperature, producing a precursor at the shock front. The particle velocity difference between the precursor region, and the region above the precursor triple-point generates a rotational field behind the precursor, pulling in and accelerating cooler, denser air from above the precursor, as well as dust particles from the ground. This high velocity, denser air/dust combination increases the dynamic pressure above normal ideal blast levels. This enhancement of dynamic pressure increases the threshold ground range in which drag sensitive equipment is rendered combat ineffective, relative to the same nuclear weapon yield producing a classic, ideal blast (Glasstone and Dolan 1977). The level of enhancement is dependent on the terrain, and the height of burst of the weapon. Above ground testing in the 1940's and 1950's revealed no significant effect over water, while desert tests generated pronounced non-ideal blast effects. Computations have supported that there will be little to no effect over snow and water, but that desert and especially grassland environments will significantly enhance the dynamic properties of the blast (Ekler, Needham and Kennedy, 1995).

Non-ideal blast effects are a significant threat to Army class II and class IV vehicles. Such targets include tactical shelters, light armored vehicles, and several wheeled support vehicles. A nuclear attack which generates non-ideal blast effects will destroy targets at ground ranges which are survivable in ideal blast conditions. Terrain conditions favorable for the production of non-ideal blast are found in about 70% of the Army's expected deployment areas (Keefer and Ethridge, 1994).

In past tests at the open end of shock tubes, other experimenters realized that the exit jet also had a very strong dynamic pressure component that possibly could be used to simulate non-ideal blast. This increase in dynamic pressure is caused by a combination of the increase in particle velocity generated by the rarefaction wave, the arrival of the cold, denser driver gas and the three dimensional expansion of the static overpressure into the open air. In an effort to see if the exit jet could simulate non-ideal effects, the character of the jet of the ARL 1.68-m shock tube was measured and several vehicles were tested. These tests proved that there was sufficient energy in the jet, but they also revealed that the jet was too narrow to uniformly load full scale military targets.

To quickly and inexpensively explore the properties of the exit jet and to determine what it would take to spread it, a 1/16.5 scale model (10.2 cm) of the 1.68-m shock tube was constructed. The exit jet profile was mapped at 5, 10, and 15 diameters from the open end of the shock tube and compared to that of the 1.68-m shock tube. Several designs for jet spreaders were then manufactured and the jet profiles that were generated by the spreaders were mapped. The best jet spreader design in terms of performance and cost to build was chosen. An intermediate scale exit jet spreader based on the best performing candidate was constructed and tested on the 0.56-m shock tube. These experiments verified that scaling of the dynamic pressure impulse maps could be applied to the 1.68-m shock tube. Once verified, design and construction of the 1.68-m shock tube exit jet spreader commenced.

## 2. NON-IDEAL BLAST ENVIRONMENT

Non-ideal blast, defined in this context, is the effect on an ideal blast by a temperature gradient in the ambient air at the ground plane. Others (Heggie 1994, Heilig, 1994, and Landeg, 1994) have defined it as the modification of an ideal blast over several large obstacles on the surface, such as buildings in cities. As will be explained the air temperature gradient causes the dynamic component of the blast-target interaction to increase. The non-ideal effect due to large object interactions tends to attenuate the ideal blast diffraction and dynamic parameters by some degree.

Non-ideal blast is produced when a blast wave travels through a region where the ambient air possesses a large temperature gradient. An example is the height-of-burst detonation of a nuclear weapon. The thermal radiation from the nuclear fireball heats the surrounding area. The heated ground immediately begins to transfer the heat to the local air by free convection. The buoyant air rises, creating a vertical temperature gradient near the surface. Eventually, the blast wave from the nuclear detonation encounters the non-uniform temperature air. The shock front of the blast accelerates through the warmer, higher sound speed region, creating the precursor, as seen in Figure 1. Cooler, denser air within the blast is accelerated down behind the precursor. The higher density air adds to the dynamic pressure (a kinetic energy term). An additional blast parameter, called impulse, takes into account the duration of the positive phase, and variation of overpressure over time. Dynamic pressure impulse is defined as the area under the curve of the dynamic pressure profile (Glastone and Dolan 1977), and is represented as

$$I_Q = \int_0^t Q dt$$

where  $Q$  = dynamic pressure  
 $I_Q$  = dynamic pressure impulse,  
 $t$  = time.

The air in the precursor region is highly turbulent. The vertical turbulent momentum flux significantly increases dust entrainment, adding even further to the dynamic pressure by increasing the average density in the flowfield. The dynamic pressure increases with the increase in density. As a result, a small increase in density, integrated over the positive phase of the blast, can result in significant magnification of the dynamic pressure impulse.

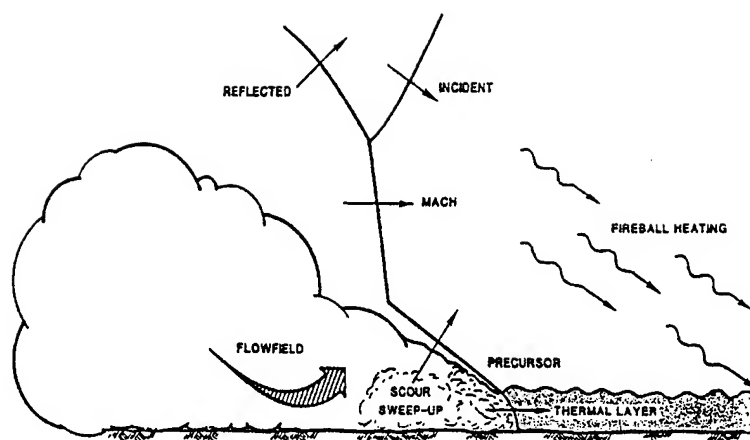


Figure 1. Schematic of typical modification of blast over heated surface.

### 3. SHOCK TUBE SIMULATION

Open-ended shock tubes are commonly used at ARL to produce stepped or decaying shock waves for studying flow over generic structures inside the tubes. The shape and duration of the blast load delivered to a model inside a shock tube can be chosen by positioning the target either closer to or farther away from the open end of the tube.

The 1.68-m shock tube has a total length of 185.9 m and is divided into two sections by an air tight steel diaphragm. As seen in Figure 5a, one part is the compression (driver) section and is 106.7 m long; the other is an expansion (driven) section and is 79.2 m long. Air is pumped into the driver until a predetermined pressure is reached. The maximum driver gauge pressure used is 827.4 kPa. To fire the tube, the diaphragm is ruptured with explosive strip charges, releasing the compressed gas into the expansion section, as seen in Figure 5b. The driver gas, expanding adiabatically, forms a step shock as it travels down the expansion section. Targets are placed in the test area in the expansion section to test their responses to air blast.

#### 3.1 Shock tube interior

Classical shock wave research is conducted in the fore and aft of the shock front. The driver gas behind the contact surface (3) in Figure 2, is the "piston" that drives the shock (Liepmann & Roshko, 1956). It marks the boundary between the gases that were initially on each side of the diaphragm. Blast wave studies in contrast include the effects of the driver gas (3) on structures. Figure 2 shows a typical blast wave in the expansion section of the 1.68-m shock tube. On either side of the contact surface, the pressure and the gas velocity are the same, although temperatures and densities may be different. The temperature of the expanded driver gas can be much lower than ambient and its density is much higher than ambient. Once the shock wave reaches the exit of the shock tube, a rarefaction wave is formed and travels back up the tube from the open end and further accelerates the flow. This combination of cold, dense driver air with enhanced velocity resulting from the rarefaction wave produces a high dynamic pressure that is predominant in the exit jet.

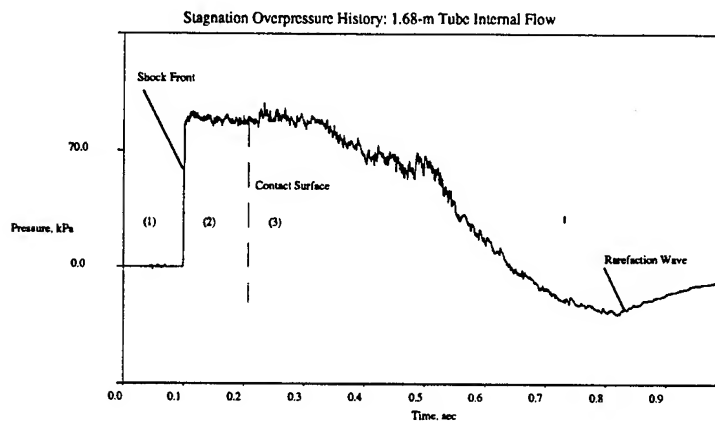


Figure 2. Inside the Shock Tube.

### 3.2 Shock tube exit jet

The shock front is greatly modified as it exits the expansion section of the shock tube. Once outside the tube, the shock front spreads spherically, dissipating its strength at a rate proportional to the cube of the distance traveled. Stagnation and static overpressure behind the shock front in regions 2 and 3, which existed inside the shock tube, decays very rapidly toward ambient atmospheric pressure. The flow is accelerated as it exits the shock tube. This is due to a combination of the rarefaction wave effects and the expanding, dense driver gas. A highly dynamic pressure jet exits the shock tube and remains relatively unaltered well beyond the open end of the shock tube.

The exit jet of the 1.68-m shock tube can deliver a dynamic pressure of up to 240 kPa which equates to a maximum wind speed exceeding 1127 kilometers per hour with a duration of about 800 ms. The power of this wind force became evident when an armored personnel carrier with a mass of approximately 9,000 kg, was tumbled over a distance of 40 m by the shock tube exit jet.

### 3.3 Comparison between Nuclear Data and Shock Tube Exit Jet Data

In the past, the exit jet of the 1.68-m shock tube has been used to test the performance of a mobile electric power outrigger system. During these tests, it was noted that the dynamic pressure records were similar to the class of non-ideal nuclear waveform from nuclear test. Figure 3a shows a differential pressure record from the exit jet of the 1.68-m shock tube and Figure 3b is a dynamic pressure record from the nuclear shot PRISCILLA (Ethridge and Keefer, 1995). It should be pointed out that there is a slight difference between differential and dynamic pressure, but the differences are small, and direct comparisons give fairly accurate matching. As the figures show, there is a good correlation between the two records. The 1.68-m shock tube record has the same general shape as the PRISCILLA record, but it has a longer duration. This indicates that the shock tube simulates a larger yield weapon. On the other hand, the static pressure records shown in Figure 4a and Figure 4b demonstrate that the static pressure from the shock tube is much lower than that from PRISCILLA. Fortunately for the purpose of simulation, the damage mechanism that destroys most military vehicles in a non-ideal environment is the dynamic pressure and not static overpressure.

Many experiments have been conducted at the end of the 1.68-m shock tube, including experiments on W.W.II era jeeps and an armored personal carrier, as well as mapping the profile of the exit jet. From these tests, it has become clear that there is more than enough dynamic pressure impulse in the jet to simulate non-ideal blast effects, but that the jet is too columniated to uniformly load full size military targets. Consequently, it was necessary to find a way to spread the jet.

#### 4. SHOCK TUBE EXIT JET SPREADER

The exit jet maintains a wind distribution that affects a small target area several diameters downstream of the exit (Schetz, 1984). The entrainment region about the potential core diverges little after several decades of diameters downstream. This results in concentrated wind loads on a target, as can be seen from actual data in Figure 5. A device to distribute the wind loading over a wider downstream area was needed to uniformly load full-scale military equipment with the 1.68-m shock tube exit jet. Such a device would allow experimentation on larger structures with a high degree of fidelity in the simulation. The 1.68-m shock tube with a jet spreader should be adequate for evaluating the non-ideal blast induced structural response of full scale military equipment, as well as large scaled models of structures.

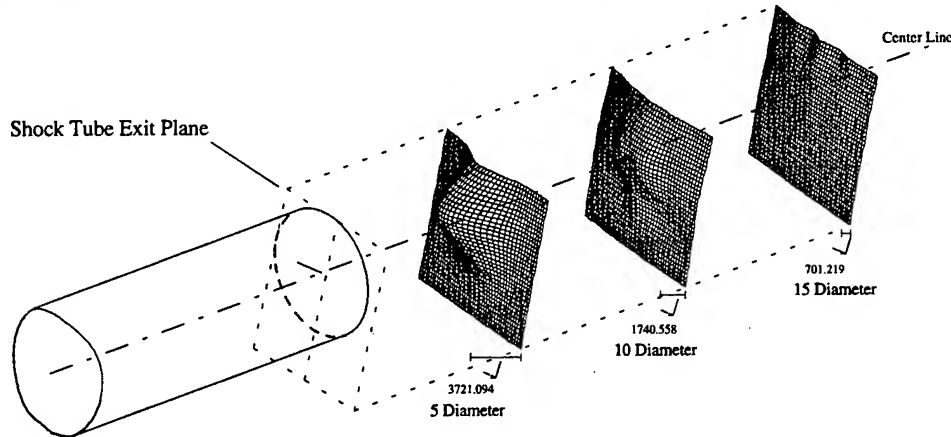


Figure 5. Dynamic pressure impulse maps of the 10.2-cm shock tube exit jet.

##### 4.1 Initial Investigation

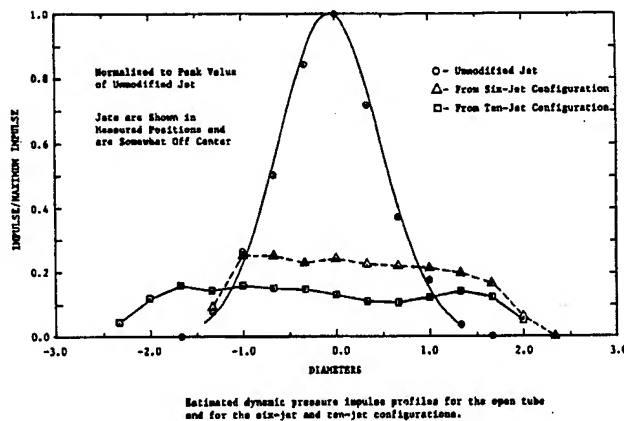


Figure 6. Estimated dynamic pressure impulse profile for an unspread exit jet, six and ten jet spreader configurations.

Experiments were conducted to investigate the feasibility of designing and fabricating a shock tube exit jet spreader. A low velocity wind source, a leaf blower (Ethridge 1991), was used to initially examine the feasibility of jet spreading. Two types of spreader configurations were tried. One



configuration consisted of a fixed attachment to the exit evolving into six separations. The second configuration consisted of ten separations. Figure 6 shows the data of the dynamic pressure impulse profile of the exit jet before spreading, and the results of the two configurations of exit jet spreaders. The ten-jet configuration spreader resulted in a more uniform spread of the dynamic pressure. These results led to the scaled simulation of the 1.68-m shock tube using a 10.2-cm shock tube.

## 4.2 Small-Scale Experiment Facility

To investigate the dynamics of spreading the exit jet of the 1.68-m shock tube, many experiments would have to be performed. Since the turn-around time of the 1.68-m shock tube is 2 days and full size spreaders would need to be constructed, a faster, more cost effective solution was required. A small shock tube scaled in both length and diameter could be fired many times a day and scaled spreaders could be more easily fabricated.

### 4.2.1 Construction of the 10.2-cm shock tube facility

The driver section of the shock tube consisted of an available section of 10.2 cm (4 in) thick walled steel pipe. The size of the pipe section, and its availability defined the scaling of 1/16.5 for the experiment. The expansion section of the tube was constructed from schedule 40 (0.602 cm wall thickness), 4 in (10.2 cm inside diameter) polyvinylchloride (PVC) pipe. The diaphragm section was an aluminum flanged pipe that slid over the expansion tube to open. Figure 7a is an illustration of the 10.2-cm shock tube. Figure 7b is a photograph of the experiment facility

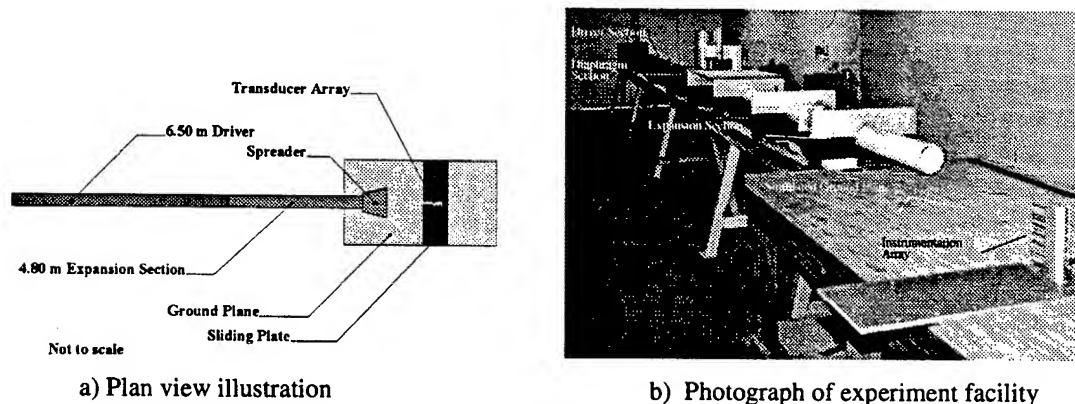


Figure 7. 10.2-cm shock tube experiment facility.

The shock tube was entirely housed in a climate controlled structure. The ground plane was constructed of finish grade plywood, and set at the same proportional distance from the shock tube centerline as the 1.68-m shock tube distance to the ground. The surface was flat and smooth, without any kind of surface treatment. The plywood was sufficiently thick (2.54 cm) such that no deformations could be perceived during the experiments. The entire ground plane was anchored with heavy weights.

### 4.2.2 Instrumentation.

The data in the jet were measured by a vertical array of seven differential pressure gages (Kulite model XCW-8WN-200-25D). The transducers were spaced in 1/4 radius steps from the top of the shock tube down to the ground plane. This array was slid from side to side to map the profile of the exit jet. Figure 8 is a picture of this array. In addition, a static and stagnation gage (Kulite model XT-190) were

placed in the expansion section of the shock tube in a location that would scale to a similar location in the 1.68-m shock tube.

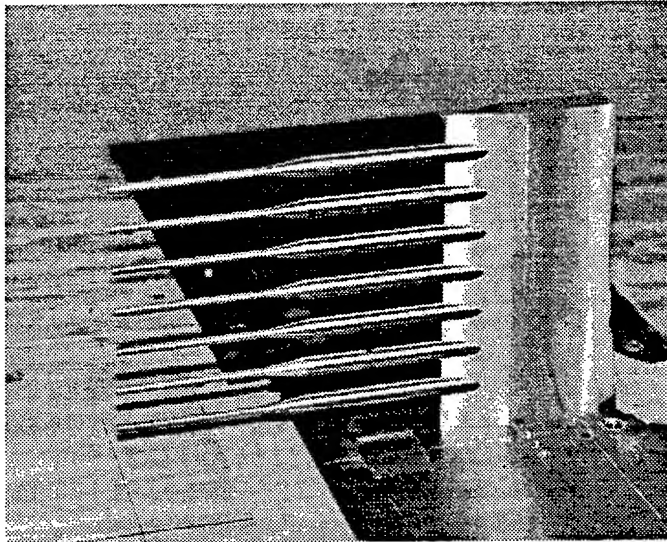


Figure 8. Instrumentation Array.

The signal conditioner/amplifiers used were Pacific model 9255's and the transient data recorders were Pacific model 9830's. The data collected were downloaded after each shot to an IBM compatible computer.

#### 4.2.3 Diaphragms.

Initially, cellophane was used as the diaphragm material. Two crossed heat wires were attached to the diaphragm. The driver section was pumped with nitrogen to a specified driver pressure. The diaphragm was ruptured by heating the crossed wires and melting an opening in the diaphragm. This method proved impractical after a fashion. The cellophane tended to shatter into small flakes. The cellophane flakes would eventually strike the differential gages, and render the gage useless for further data acquisition.

An alternative method of rupturing the diaphragm was implemented. The diaphragms were constructed of different thickness' of aluminum foil, 0.0762, 0.1016, 0.127, and 0.1524 mm (3, 4, 5, and 6 mils, respectively) thick. The foil was folded two ways to form a cross impression with the intersection of the folds coincident with the shock tube axis. With the diaphragm placed, the driver section was pumped. Pumping the driver section continued until the diaphragm material failed, and the diaphragm ruptured. The additional nitrogen pumped into the driver after the diaphragm rupture was negligible when considering the volumetric flow out of the shock tube. Use of the aluminum diaphragms proved very reliable and eliminated the problem of the flaking cellophane. Table 1 lists the diaphragms and their average burst pressures. The maximum deviation is the largest pressure difference to burst the diaphragm from the mean bursting pressure, presented as a percentage of the mean burst pressure. As expected, the thicker diaphragms had a more consistent burst pressure. This is due to decreasing influence of surface irregularities (scratches, folds, etc.) on the thinner diaphragms.

Table 1. Diaphragm Thickness and Average Burst Pressures

Diaphragm Thickness, mm	Burst Pressure, kPa	Maximum Pressure Deviation, %
0.0762	152	5.2
0.1016	228	4.8
0.127	297	4.1
0.1524	414	3.9

#### 4.3 Mapping of the Unspread Jet.

To reduce the number of shots required to map the jet, preliminary experiments were performed to verify the symmetry of the jet in the horizontal direction. The array was moved horizontally in 1/4 diameter increments, and shots were repeated until measurements were taken from one diameter left of the center line to one diameter right of the center line. As expected, the jet was symmetrical, therefore all subsequent tests mapped 1/2 of the jet and assumed symmetry.

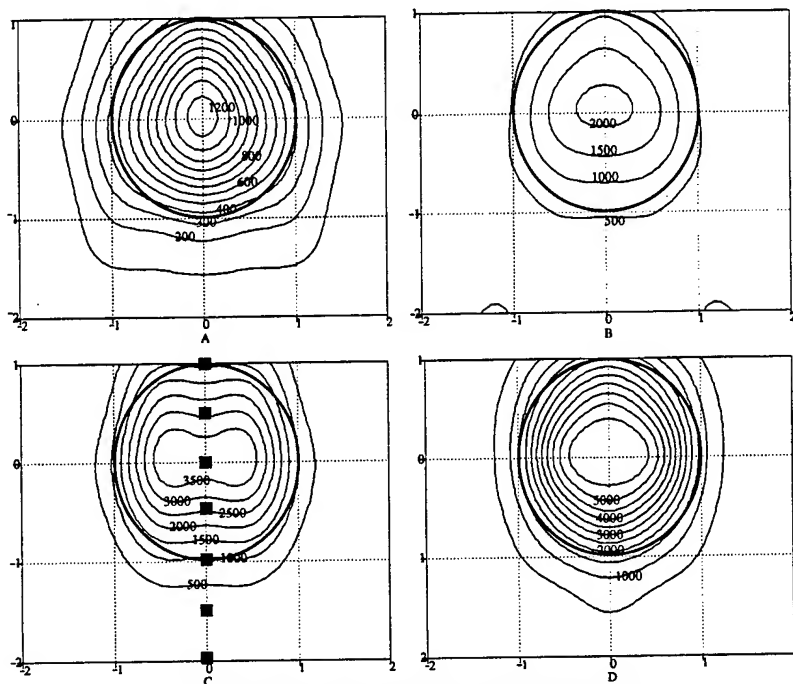
Since the diaphragms did not have a perfectly consistent burst pressure, it was necessary to apply a correction to each shot. The final parameter of interest in the jet was **differential** pressure impulse,  $I_d$ , (as opposed to dynamic) so for each series, the  $I_d$  in the jet were adjusted by the static overpressure impulse in the expansion section of the tube.

The final output format was a 3 dimensional contour plot of the  $I_d$  versus position in a plane at 5, 10, and 15 shock tube diameters from the exit of the shock tube.

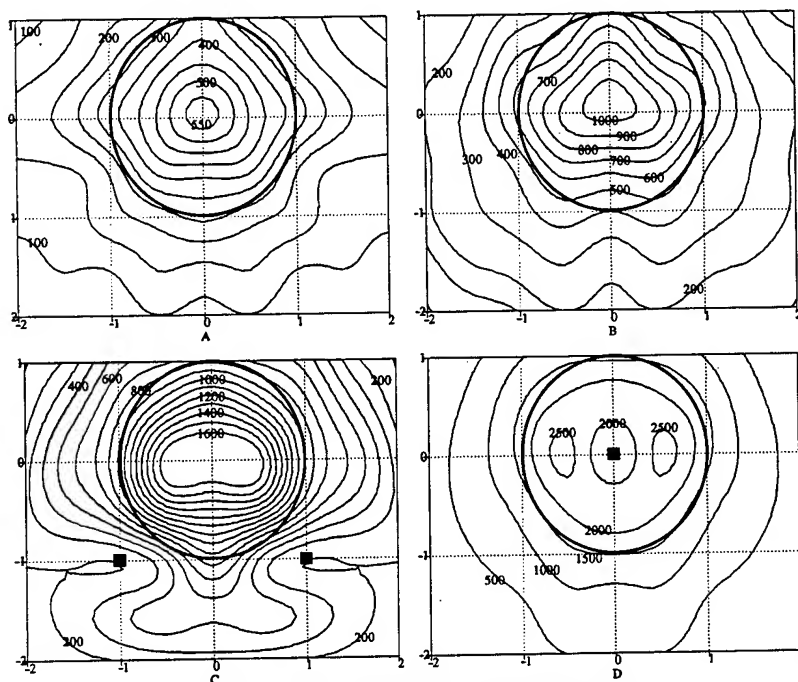
#### 4.4 Unspread exit jet

##### 4.4.1 The shape of the jet

Figure 9 is a series of representative contour plots taken at 5, 10, and 15 diameters using each thickness of diaphragm. Each diaphragm thickness used is represented by a letter: 0.0762, 0.1016, 0.127, and 0.1524 mm as A, B, C, and D, respectively. Points where the pressure data was in question, or not obtained are indicated with a O. The resulting  $I_d$  is still used when constructing the contour plot, but the reader must be aware that these were points where the pressure gage functioned improperly, or not at all. The contours are displayed in units of Pa-s as assembled from several shots. The shock tube inside diameter is superimposed on each contour plot to indicate the relative position of the tube against the profile of the jet. As is evident by the plots, the  $I_d$  exhibits a steep drop that ends at about the shock tube radius.



a) Five diameters downstream from exit plane



b) 10 diameters downstream from exit plane

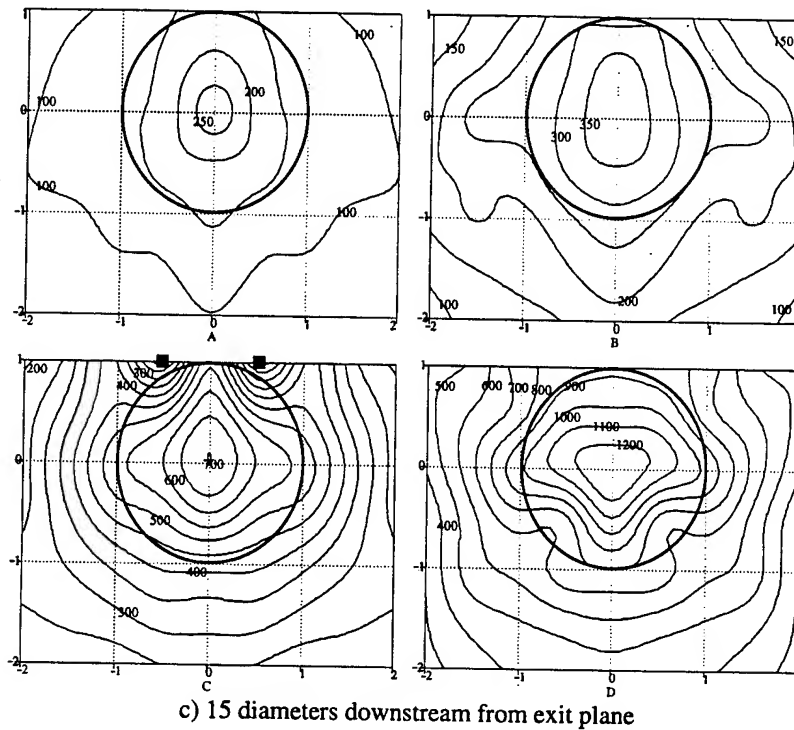


Figure 9. Differential pressure impulse maps of 10.2-cm unspread exit jet.

These plots consisted of one shot at each horizontal station. A 6 point cubic interpolation was performed between each measured point to smooth the contours. In each case, data was obtained from the stations at -2 through 0 radii, and the assumption of symmetry applied in generating data for stations 0.5 to 2 radii.

The surface integral over the map area,  $S$ , of the differential pressure impulse distribution is called the total differential pressure impulse,  $T_d$ , or

$$T_d = \int_S I_d dS.$$

This parameter provides a measure of the total momentum flux through the target area taking into consideration strength and duration of the air flow. The significance  $T_d$  is later exploited when making comparisons between exit jet spreader configurations. Table 3 list the total differential pressure impulse values and area for the plots obtained in Figure 9. In each case, the area  $S$  was 4 by 3 radii.

Table 3. Total Differential Pressure Impulse Values (N-s)

Diaphragm Thickness	Downstream Distance, Diameters		
	5	10	15
0.0762 mm	286.363	214.169	120.626
0.1016 mm	475.689	405.531	221.438
0.127 mm	895.699	612.463	375.045
0.1524 mm	1,299.505	1,363.942	664.291

As is expected, the value of  $T_d$  drops with increasing longitudinal distance from the shock tube exit. The value of  $T_d$  at 15 diameters with a 0.1524 mm diaphragm is about the same as the  $T_d$  at 10 diameters with a 0.127 mm diaphragm. Referring to Figure 9, one can see that although the  $T_d$  is about the same, the distribution of  $I_d$  is more uniform over the 15 diameter, 0.1524 mm diaphragm shot.

The distribution of  $I_d$  is highly concentrated towards the center of the unspreed exit jet flow. Flow velocity beyond one radius from the shock tube axis is very small with respect to the centerline flow. As seen in Figure 9b, there is an interaction of the flow with the ground plane. The normal circular pattern expected for a free-field jet is altered at  $-0.5$  radii in the vertical direction. It appears the vertical component of flow into the ground plane results in an accumulation of mass near the ground plane. As the mass increases, the density increases and contributes to the  $I_d$  in the lower region of the map.

This phenomenon was very consistent throughout all the experiments. A secondary effort to determine the effect of altering the height of the ground plane with respect to the shock tube centerline resulted in little effect

#### 4.4.2 Decay of the jet over distance

The jet decays fairly quickly with distance from the shock tube. Figure 10 shows jet profiles for 5, 10, and 15 shock tube diameters with the profiles normalized to the peak  $I_d$  of the 5 diameter station. The contours are in 10% increments, showing a decline in peak  $I_d$  of more than 50% every 5 diameters from the exit of the tube.

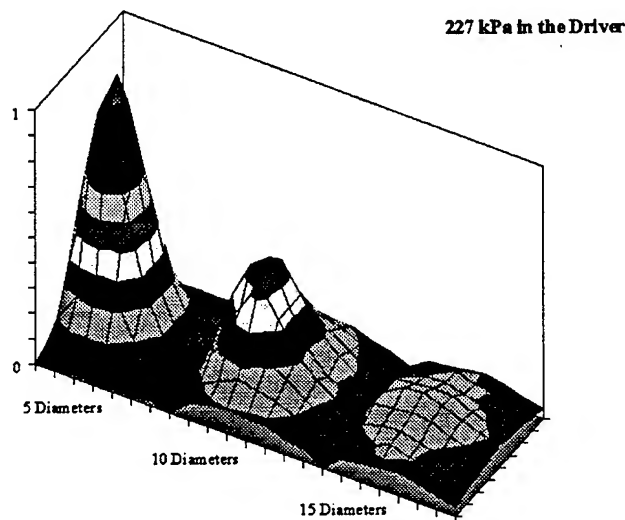


Figure 10. Surface plot of differential pressure impulse at 5, 10, and 15 diameters.

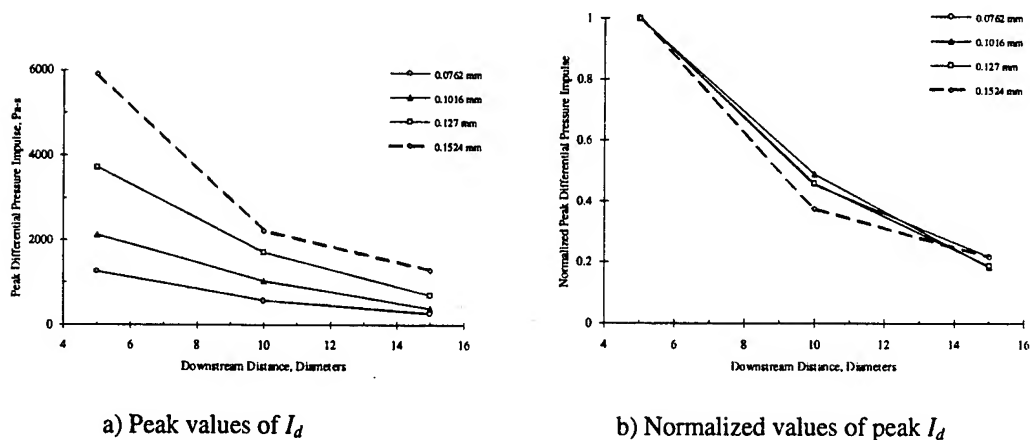


Figure 11. Peak differential pressure impulse decay with distance.

Figure 11a shows the variation of the peak value of  $I_d$  with longitudinal distance from the shock tube exit for each diaphragm thickness. The dashed line used with the 0.1524-mm diaphragm is slightly lower at the 10 diameter station than the others. Recall Figure 11b, plot D, the center gage data was destroyed by debris, and the data were lost. The next highest value was substituted to complete the curve. Figure 9b displays the self-similarity of the decay as the other peak values of  $I_d$  are normalized by the peak value at 5 diameters.

#### 4.4.3 Ground Plane Study

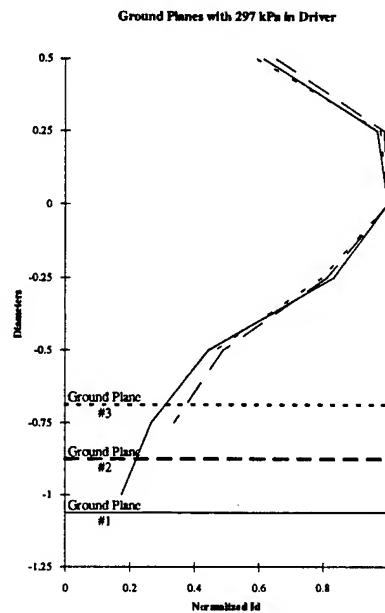


Figure 12. Plots of center position impulse with three ground plane elevations.

A study was performed to investigate the interaction of the ground plane elevation with respect to the shock tube centerline. Sections of 2.54-cm thick plywood were placed on top of the ground plane/table. The probe rake remained at the same elevation so that  $I_d$  comparisons could be made with different ground plane elevations. The results, as are evident in the plots shown in Figure 12, demonstrate that for the unspread exit jet, there was little influence on the exit jet by the ground plane.

#### 4.4.4 Comparisons to 1.68-m shock tube data

To check the scaling of the 10.2-cm shock tube up to the 1.68-m shock tube, shots were fired in the 1.68-m shock tube with driver pressures as in the 10.2-cm shock tube. All measurements were taken by a vertical rake on the centerline at 10 diameters downstream from the exit plane. Figure 13 shows the centerline data from both tubes for a variety of driver pressures with the 10.2 cm data scaled up to the 1.68-m shock tube. Scaled comparisons are made by multiplying the its differential pressure impulse time duration of the 10.2-cm shock tube pressure time history by 16.5. The graph demonstrates that qualitatively the two shock tubes generate exit jets with similar differential pressure impulse profiles, but there is more relative energy in the 1.68-m shock tube exit jet than in the scaled up 10.2-cm shock tube exit jet.

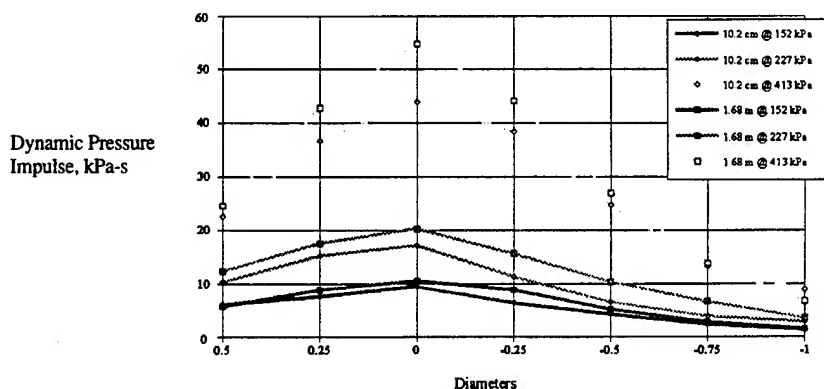


Figure 13. 1.68-m and 10.2-cm shock tube centerline differential pressure impulse comparison.

#### 4.4.5 Exit Jet Spreader Concepts

Three types of spreaders were anchored at the end of a the 10.2-cm shock tube to evaluate uniformity and degree of spreading with jet velocities that simulate non-ideal blast. The first spreader concept (type 1) consisted of an assembly of rigid tubes, as seen in Figure 14a. The tubes were concentrated at the upstream end, and spacers distributed the downstream direction of the tubes into a broad area. The idea was to discretely change the direction of the exit jet flow. The second concept (type 2), also shown in Figure 14b, passed the exit jet through a grid of angled vanes. A combined action of mechanical deflection of the flow by the vanes and the generation of vortex sheets along their edges broke up the flow in the core of the jet. The turbulence intensity was increased, and the wakes forming off the vanes induced a lateral momentum flux with the increased spanwise velocity component. The turbulence flux growth is controlled by the spreaders housing. This concept has proved to be quite effective. The third concept (type 3), had an angled concentric ring set just inside the shock tube exit. The idea was the ring would be redirected some flow into the center of the jet. The change in flow direction would destabilize the potential core's directional momentum, allowing the entrainment region to grow at a faster rate.



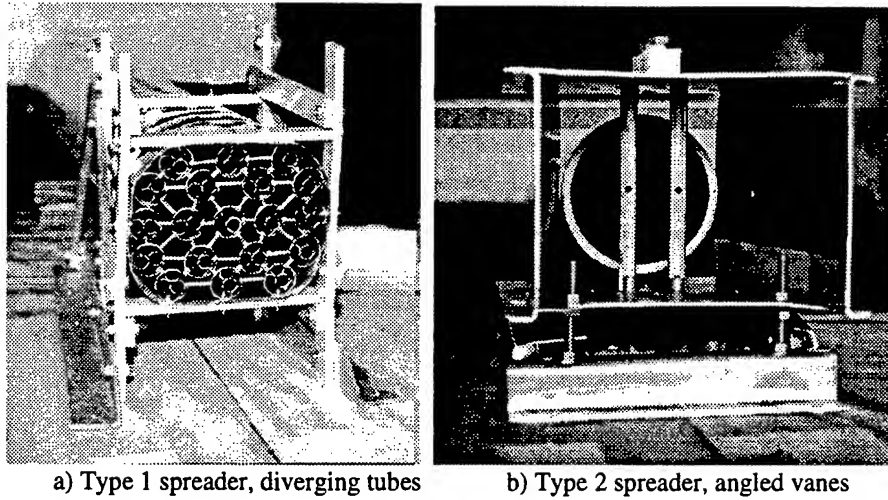


Figure 14. Concept exit jet spreader models.

The contour plots showing the  $I_d$  values helped to qualitatively determine the spreaders performance. To quantitatively determine the spreaders performance, a normalized variance was calculated over the map surface. The variance was calculated using the following equation,

$$V_d = \frac{\sum_{i=1}^I \sum_{j=1}^J \left( \frac{I_{d\,i,j}}{I_{d\,mean}} - 1 \right)^2}{IJ},$$

where

$I$  = total number of vertical positions (9)

$J$  = total number of horizontal positions (7)

$I_{d\,i,j}$  = differential pressure impulse at gage position  $i,j$

$I_{d\,mean}$  = mean differential pressure impulse over the map surface

$V_d$  = normalized variance of the differential pressure impulse

The jet spreaders produce significant interference with the flow. A spreader would be considered impractical if the flow velocities lacked sufficient energy to conduct practical experiments, even if  $I_d$  were spread over the target area evenly. Integrating  $I_d$  over the target area, and comparing against the unspread exit jet  $T_d$  results in a quantified measure of the total strength of the exit jet.  $T_d$  is discretely calculated using the following,

$$T_d = \left\{ 4 \sum_{i=2}^{I-2} \sum_{j=2}^{J-2} I_{d\,i,j} + 2 \left[ \sum_{i=2}^{I-2} (I_{d\,i,1} + I_{d\,i,J}) + \sum_{j=2}^{J-2} (I_{d\,1,j} + I_{d\,I,j}) \right] + I_{d\,1,1} + I_{d\,I,1} + I_{d\,1,J} + I_{d\,I,J} \right\} \frac{r^2}{4},$$

where  $r$  is the inside radius of the shock tube.

Figure 15 exhibits the resulting contour plot of the type 1 exit jet spreader. Here it is displayed with the values normalized with the peak value of  $I_d$ . The spreader was attached to the ground by a structural frame, evident in Figure 14a. The axis centerline was pointed with a slight downward slope of approximately 1:20 ratio. As a result, the center of the  $I_d$  distribution is along the horizontal centerline, but 0.5 diameters below the vertical centerline. Redirection of the centerline flow is advantageous, as the

center of the projected area of a military target will change with each target. Since the ground plane is fixed, slight adjustments of the spreader can align the spread jet center with the target area center. Once again, the shock tube inside diameter is superimposed on the plot to indicate a relative scale.

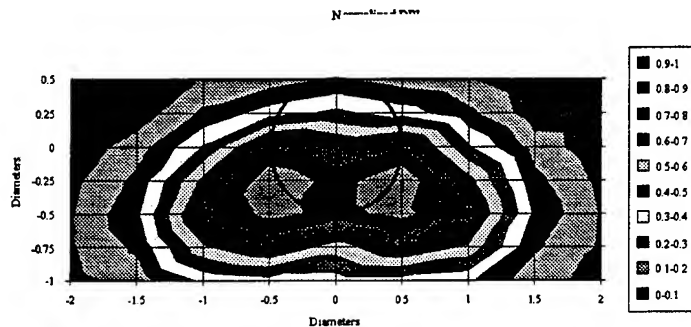
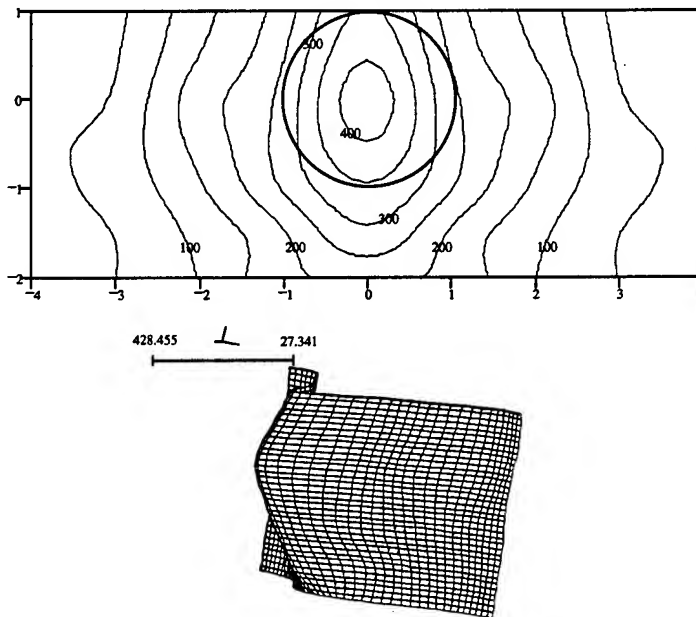
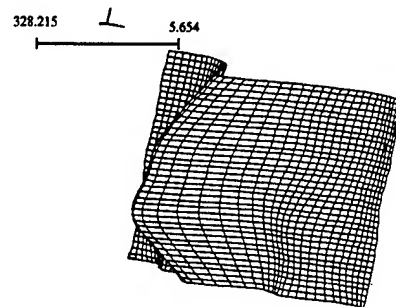
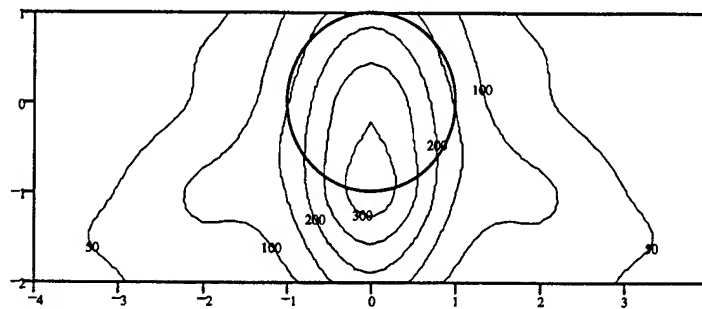


Figure 15. Type 1 exit jet spreader at 10 diameters.

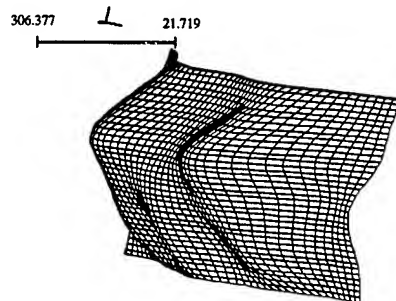
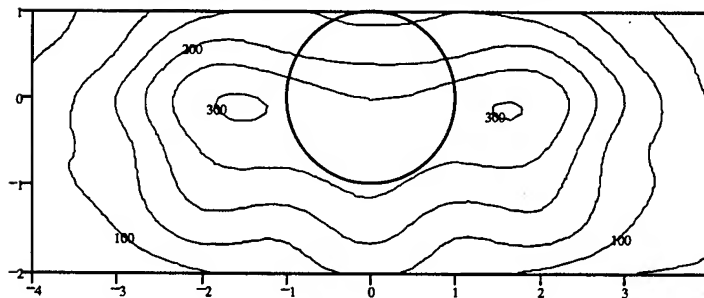
Figure 16 shows the results of three configurations of the type 2 exit jet spreader using two vertical vanes. Figure 16b was the result of having the two vertical vanes with a large separation in the flow path. The shock tube inside diameter is projected onto the map, and is shown as the thick, solid lined circle. Table 4 list the configurations and their respective  $T_d$  and  $V_d$ .



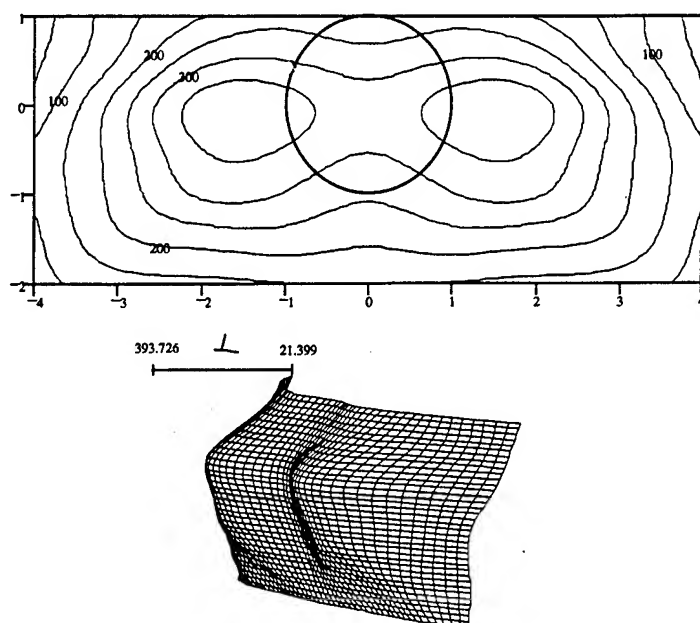
a) One vertical vane



b) Two vertical vanes with large separation



c) Two vertical vanes with medium separation.



d) Two vertical vanes with small separation

Figure 16. 10.2-cm shock tube differential pressure impulse distribution.

Table 4. Type 2 Configurational Specifications

Configuration	$I_{d\text{ mean}}, \text{Pa-s}$	$T_d, \text{Pa-s-r}^2$	$V_d$
Single Vane	141.78	1237.66	0.58
Large Separation	98.291	834.958	0.6763
Medium Separation	149.775	1,967.756	0.2694
Small Separation	204.011	1,444.89	0.2293

The peak impulse is slightly below the shock tube axis, which could be an effect of the spreader's orientation when it was used. On this small scale, subtle errors in direction can be difficult to control. Experiments with the type 3 spreader showed that it did not work. Only two shots were performed with this device before the inner ring detached. The data obtained showed little to no spread, but a definite trend to indicate a significant reduction in  $T_d$ . The type 1 spreader performed satisfactorily. The type 1 spreader was considered impractical when one considered fabrication of such as device for the 1.68-m shock tube. The type 2 exit jet spreader demonstrated the greatest potential for spreading  $I_d$  over the target area.

The maximum  $I_d$  available in the center of the jet of the 1.68-m shock tube is greater than necessary for simulating the desired non-ideal blast. This excess of energy works in favor of the exit jet spreader concept since a 20% degradation of performance can be expected. This excess can be given up to a spreader without the impulse dropping to an unacceptable level. An impulse in excess of 124 kPa-s has been measured in the center of the jet. This value could be reduced by fifty percent or more and still be adequate for overturning many types of wheeled and tracked vehicles.

#### 4.5 Intermediate-Scale Experiment Facility

To test the applicability of scaling from the 10.2-cm shock tube to the 1.68-m shock tube, an intermediate exit jet spreader was designed for the ARL 0.56-m shock tube. The unspread and spread exit jets were compared to the results from the 10.2-cm shock tube experiments. To scale the experiment, an artificial ground plane was introduced since the 0.56-cm shock tube stood much higher off the ground. A ground plane was made up of a several 10 cm thick plates of steel. An instrumentation rake with seven differential pressure gages was placed 10 diameters downstream of the shock tube exit. The gages were placed on the rake at 0.5 radius intervals in the vertical direction. This set up matched the set-up used in the 10.2-cm shock tube experiments and the 1.68-m shock tube experiments. Figure 17 is a photograph of the intermediate set-up, with a type 2 exit jet spreader attached.

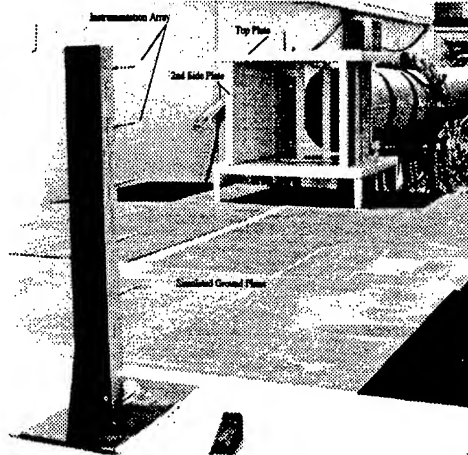
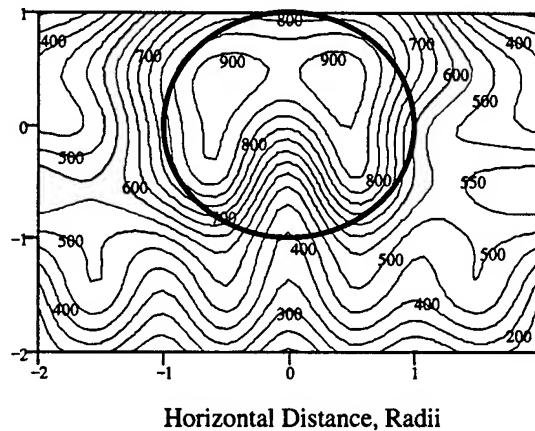


Figure 17. Photograph of 0.56-m shock tube exit jet spreader.

##### 4.5.1 Unspread exit jet

The exit jet from the 0.56-m shock tube was mapped for comparison against the unspread exit-jet from the 10.2-cm shock tube. As can be seen in Figure 18, the results did not match the 10.2-cm shock tube map profile shown in Figure 9.



Note: Contours in 50 Pa-s intervals.

Figure 18. Differential pressure impulse map from 0.56-m shock tube.

The data at the centerline was consistently lower than the half radius data. The cause of the deficit is unclear. Some theories are presented to attempt and explain this phenomenon. A possible explanation suggests there is a slight misalignment between the shock tube axis and the projected center on the map plane (0,0). The results of a careful survey of the shock tube elevation and the instrumentation rake is shown in Figure 19. The exit center is taken to be at the origin. The measurements indicate the shock tube is pointed down in the downstream direction, but the extension added on (from -2.908 m to 0 m) is pointed upward, and in line with the instrumentation rake at 5.588 m.

The conclusion based on the elevation data is that the magnitude of misalignment is within a negligible margin. If the flow did follow the shock tube axis with little to no momentum change due to the slight redirecting of the extension, the strength of the differential pressure impulse mapping would fall below the rake center. If the extension completely re-directed the flow, the peak differential pressure impulse would fall exactly on the rake center. The conclusion is that the peak differential pressure impulse should lie somewhere in between 0 to 3 cm below the center.

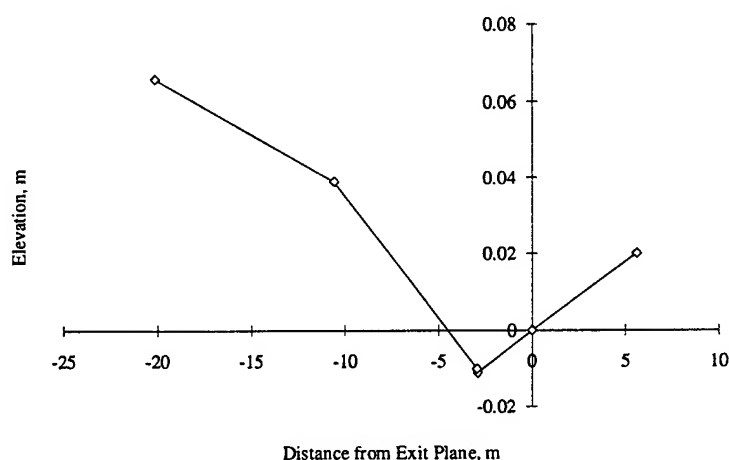


Figure 19. 0.56-m shock tube axis elevation.

Another possibility is the temperature gradient that sometimes exist in the shock tube. The 0.56-m shock tube is partially housed in a climate controlled shelter. The last 20 m and exit plane are outside the shelter. If there is a significant temperature difference between the interior and exterior of the shelter, a thermal gradient exists in the air within the expansion section of the shock tube, especially after an experiment. With the introduction of air of a different temperature from the building exterior after a shot, the denser, cooler gas would tend to settle to the bottom of the shock tube prior to the next firing. A thermal gradient in the exit jet would be the cause if the turbulence in the exit jet were not substantially diffusive to uniformly re-distribute the thermal energy in the flow. A uncertainty in this theory is with respect to the resulting dynamic pressure and Impulse.  $I_Q$  is comprised of the particle velocity squared, and the density. A first look would indicate that the higher temperature gas, which results in a higher particle velocity, would contribute more to  $I_Q$  than the increased density in the cooler region, since the velocity term is squared. For an ideal gas, the velocity increase from a change in temperature is directly proportional to the square root of the temperature increase, as is shown in a Rankine-Hugoniot equation (Glass, 1958),

$$u_2 = \sqrt{\frac{(\rho_2 - \rho_1)(p_2 - p_1)}{\rho_1 \rho_2}},$$

where

$u_2$  = particle velocity behind the shock,

$P_n$  = pressure, state 1 is downstream of the shock, state 2 is upstream,

$\rho_n$  = density, same states as for pressure.

The increase in density is linearly related to the temperature at constant pressure by the Ideal Gas Law. A temperature difference in the expansion section would result in a uniform differential pressure impulse distribution since the increase in velocity would be balanced with the decrease in density.

Possibly the strongest explanation is a combination of these effects. A temperature gradient exist, and must contribute in some fashion. The relative small length of the driver section dictates that some coherent structure development in the expansion section will remain unaffected when exiting the shock tube. There is a slight misalignment with the shock tube centerline.

#### 4.5.2 Spread exit jet

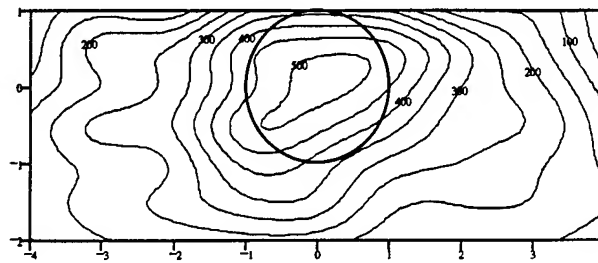
After extensive experimentation with the 10.2-cm shock tube, an intermediate exit-jet spreader was designed and attached to the 0.56-m shock tube. The type 2 spreader dimensions were directly scaled on a 6:1 ratio. With the increase in scale, an exit-jet spreader had to be designed to withstand the loading from the exit-jet, and still be manipulated by personnel without the assistance of weight handling equipment. The process was iterative, using a finite element analysis software called ALGOR to eventually design the spreader components. The spreader was built with six separate plates. The top and bottom plate were assembled to four side plates. The Side plates were adjustable such that the angle of divergence could be varied. The second side plate provided a redirection of the flow back into the jet, the intention being to limit the spread to a certain point.

The different configurations were driven by the results of the previous configuration. The first configuration of exit jet spreader consisted of the first side plates spreading at 8.5°. There were two equidistant vertical vanes. The vanes consisted of a steel angle with each side 5 cm in length. Placed at 45° rotation to the flow, the vane face is at 50 cm downstream of the shock tube exit plane. Table 5 list the various configuration tested.

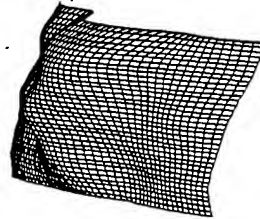
Table 5 Exit Jet Configuration Details

Configuration	Vanes	Size, cm	Spread	% Blockage
A	2	5	8.5°	17.778
B	2	5	14.1°	15.913

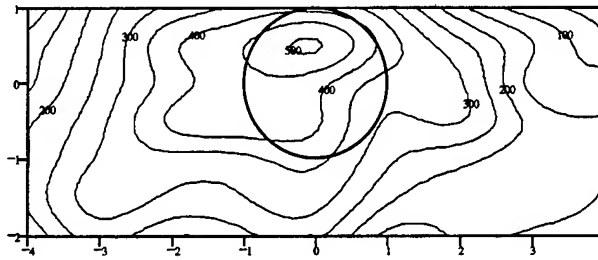
The exit jet was mapped in the same fashion as the unspread exit jet with one exception. The instrumentation placement was from far left to far right. The assumption of symmetry was not made. Two different configurations were tested. The only difference between configuration was the angle of divergence in the side plates. Figure 20 shows the results of the mapping. Contour intervals are at every 500 Pa-s. The abscissa and ordinate are in radii. The inside diameter of the 0.56-m shock tube is outlined on each plot by the thick solid circle.



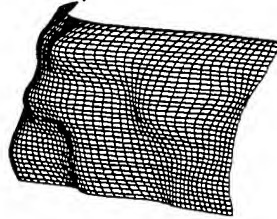
519.483 4.254



a) Configuration A spread exit jet



507.618 27.097



b) Configuration B spread exit jet

Figure 20. Differential pressure impulse map comparison.

Table 6. Exit Jet Configurational Specifications

Configuration	$I_{d\text{ mean}}, \text{ Pa-s}$	$T_d, \text{ Pa-s-r}^2$	$V_d$
A	243.201	1,891.55	0.2364
B	250.964	1,917.29	0.19122

Table 6 gives the results of the exit jet configurational specifications. The resulting maps are similar to the maps in Figure 16. The differences in the unsread exit jet contours along the vertical centerline are eliminated. The resulting spread exit jet differential pressure impulse maps are very similar in profile.  $I_d$  distribution is centered close to the shock tube axis. This indicates that the spreader is either



re-directing the flow towards the center, or the concentration of  $I_d$  found in the unspread exit jet may be an existing thermal gradient effect or an unstable coherent flow. The exit jet spreader vanes would serve to breakup any existing flow structure within the shock tube exit jet.

$T_d$  for Configuration A was higher than that of the equivalent configuration used on the 10.2-cm shock tube (two vertical vanes, large separation). This indicates that the larger scale spreader has lower loss in impulse from the spreader. This can be a result of the higher Reynolds number associated with the larger structure. The components are six times as large as the 10.2-cm components, thus the inertial forces are greater, while the fluid properties and flow characteristics remain essentially unchanged.

A sample of the shape of the differential pressure records are shown in Figure 21. Each gage record is shown in its relative position on the vertical rake, as indicated on the left near the beginning of each data set. The  $I_d$  is indicated at the end of the data set. This particular shot was the second one performed at the center horizontal position. The similarity of these differential pressure profiles to the PRISCILLA dynamic pressure from Figure 7b is quite improved from the unspread exit jet.

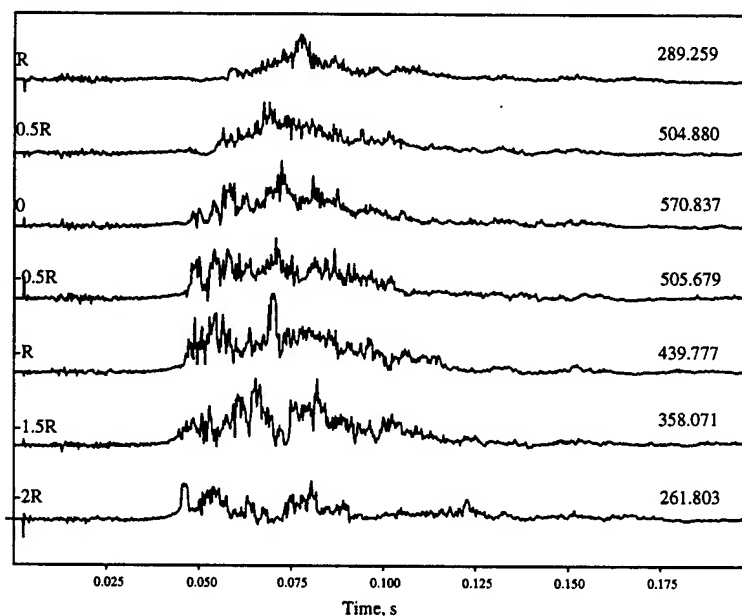


Figure 21. Differential pressure records from A configuration centerline.

## 5. CONCLUSIONS

It is possible to conclude from the results of these experiments that spreading the shock tube exit jet is feasible. Further studies must be conducted to determine to what extent an exit jet spreader configuration can be optimized. The goal is to provide U.S. ground forces with a high fidelity simulator that can perform full scale non-ideal blast experiments. These experiments have established the basis of this work. The results of the experiments can be directly applied to the design and fabrication of the full scale exit jet spreader for the 1.68-m shock tube.

The 1.68-m shock tube has the potential to deliver enough dynamic pressure impulse to overturn almost any ground force vehicle, wheeled and tracked, foreign and domestic. Unfortunately, the exit jet is highly calumniated, concentrating the dynamic pressure into an area slightly larger than the shock tube diameter, and along the shock tube axis. That centerline is slightly over 2 m above the ground plane. Targets with small projected areas, such as jeeps, flatbed trucks without cargo, or shelters placed on the

ground, would be subjected to non-uniform, eccentric loading. Spreading the dynamic pressure impulse, and re-aligning the exit jet center to coincide with the majority of ground forces equipment projected area center is necessary.

Small scale shock tube experiments have demonstrated the feasibility of spreading the exit jet. Due to the small scale, it was difficult to obtain precise data with regards to optimization of the spreader design. The experiments with the intermediate shock tube were crucial in determining if the flow characteristics of the small scale shock tube would scale to the full scale shock tube. It also provided a more precise test bed to vary the vane and spread configurations to determine optimization of the spreading effect.

The type 2 exit jet spreader was selected as the best candidate spreader for full-scale design. It is fair to say the type 1 exit jet spreader performed very well. The additional feature of re-orienting the flow direction of the exit spreader to the projected center of area of a military target had many advantages. Unfortunately the design was far too complex, especially at the necessary scale. The simplicity of the type 2 spreader has many advantages. Foremost are design and construction costs, not to mention ease in future modifications. To eliminate the problem of the exit jet center being higher than the projected area center of military targets, the ground plane will be raised in front of the 1.68-m shock tube.

Enough experimentation has been performed that initial design and preparatory construction can begin to fit the 1.68-m shock tube with an exit jet spreader. This can be done with a minimum of down time for shock tube operation. It would be premature to declare that enough experimentation has been performed to finalize the design and construction of the full-scale exit jet spreader. More studies with a variety of configurations to more uniformly distribute the differential pressure impulse of a target area need to be performed. These can be done with the small and intermediate scale facilities. Once the full scale reaction pier, steel frame work and housing is in place, experiments can begin to verify the experiments of the smaller scaled facilities.

The characterization of the exit jet can occur along two lines. One can make direct comparisons of dynamic pressure measurements from the exit jet, to the dynamic pressure profiles from above ground nuclear test data, such as PRISCILLA. As mentioned before, the profiles of Figure 3b and Figure 21 have distinct similarities. If the duration and overpressure were to match the nuclear non-ideal blast data of a particular yield and ground range, one could confidently conclude that the exit jet produces a high fidelity simulation of non-ideal blast. Another method of comparing the strength of the exit jet with nuclear test results would be to compare the effects on vehicles.

Previous studies have shown that there is a direct relationship between total displacement of objects that are free to tumble when loaded by air blast, and the magnitude of the dynamic pressure impulse experienced by the target. This can be directly correlated with the horizontal dynamic pressure impulse. The tumbling and displacement of wheeled vehicles, especially jeeps, was investigated during many previous nuclear and high explosive tests. Data has shown that total displacement of a vehicle can be used to determine dynamic pressure impulse and vice versa. Figure 22 shows jeep displacement versus dynamic pressure impulse (Allen & Bryant 81). The data is associated with the testing of older vintage (World War II type) jeeps. These older jeeps, M38s for example, differ from more modern versions in that the older models have solid axles rather than independent suspensions. Several M38s have been obtained and will be used for testing in the exit jet of the 1.68-m shock tube. Horizontal dynamic pressure impulse loading produced by the jet will be correlated with horizontal dynamic pressure impulse loading produced by nuclear non-ideal blast.

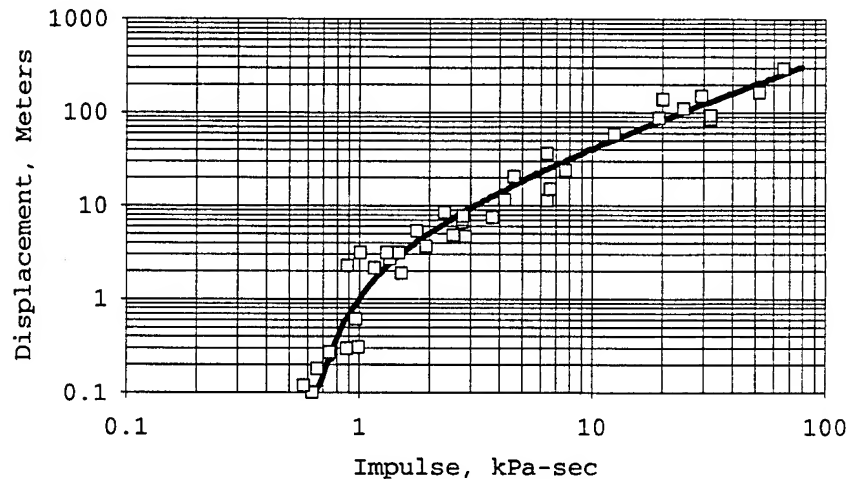


Figure 22. Jeep displacement vs. dynamic pressure impulse.

#### REFERENCES

Allen, F., and E. Bryant, "Dynamic Pressure Impulse and Damage Derived from Vehicle Displacement for Ideal and Near Ideal Blast Waves," (U) - CONFIDENTIAL, General Electric Company - TEMPO Contract Report ARBRL-CR-00443, January 1981

Ekler, R. G., C. E. Needham, and L. W. Kennedy, "Extended Grassland Calculation Results with Comparisons to PRISCILLA Experimental Data and a Near-Ideal Calculation". ARL-CR-236, Contract Number DAAL01-94-P-2257, July 1995

Ethridge, N. H., "Proposed Modification of the Jet Flow from the BRL 1.68 Meter Shock Tube." BRL-CR-664, US Army Ballistic Research Laboratory, APG, MD, May 1991

Ethridge, N. H., and J. H. Keefer, private communication regarding non-ideal blast effects with a given terrain, December 1994

Ethridge, N. H., and J. H. Keefer, "Real (Non-Ideal) Surface Effects on Nuclear Explosion Airblast from PRISCILLA-Type Events, Part I: Comparison and Evaluation of Ideal and Non-Ideal airblast from PRISCILLA Computations." Draft Report, Aberdeen, MD, August 1995

Glass, I. I., Shock Tubes Part I: Theory and Performance of Simple Shock Tubes. Review No. 12, Institute of Aerophysics, University of Toronto, Canada, May 1958

Glasstone, S., and P. J. Dolan. The Effects of Nuclear Weapons. Department of the Army Pamphlet No. 50-3, Headquarters, Department of the Army, Washington, DC, March 1977.

Heggie, D., "Scaled non-ideal air blast experiments conducted at AWE." Presentation at the Fifth Quadri-Partite Meeting, Atomic Weapons Establishment, Foulness, England, May 1994

Heilig, W., "Blast wave reflection at obstacles with non-ideal reflecting surfaces." Presentation at the Fifth Quadri-Partite Meeting, Atomic Weapons Establishment, Foulness, England, May 1994

Keefer, J., Private conversation about the evolution of non-ideal blast, Aberdeen Proving Ground, MD, March 1995

Landeg, D., "Non-Ideal air blast over cities," Presentation at the Fifth Quadri-Partite Meeting, Atomic Weapons Establishment, Foulness, England, May 1994

Liepman, H. W., Roshko, A., 1963, *Elements of Gasdynamics*, GALCIT Aeronautical Series, John Wiley & Sons, Inc., New York, New York, ppg.79-83

Schetz, J.A., 1984, *Foundations of Boundary Layer Theory for Momentum. Heat and Mass Transfer*, Prentice-Hall, Inc. Englewood Cliffs, NJ

# PRECURSOR SIMULATION USING A FLOW SIMULATOR

Michael H. Klaus  
Ralf Duckerschein

Wehrtechnische Dienststelle für  
Sprengmittel und Sondertechnik  
Oberjettenberg  
D - 83458 Schneizlreuth  
Germany

## Abstract

The recent interest in the simulation of the precursor effect motivated us to explore the possibilities of using our simulator for aerodynamic effects (SAE) for this purpose. The reasoning is the well known fact, that the effect of a precursed blast on military targets is predominantly due to the dynamic pressures.

Thus we evaluated in a first step the temporal and spatial behaviour of the flow field in the measuring crosssection. We discovered shortcomings in the homogeneity of the flow. In order to solve this problem we investigated in a second step the influence of varying driver pressures, having high pressures in the outer tubes and lowering the pressure in several steps towards the inner tubes.

Experimental results will be presented, as well as theoretical background. Future projects involve increased packing density of the driver tubes and larger driver crosssections, as well as time delayed diaphragm opening for pulse shaping.

## Introduction and background

We've been operating a simulator for aerodynamic effects (SAE) at our lab since more than 15 years. The facility is mainly used for the testing of pilot equipment during an emergency exit (*Fig. 1*).

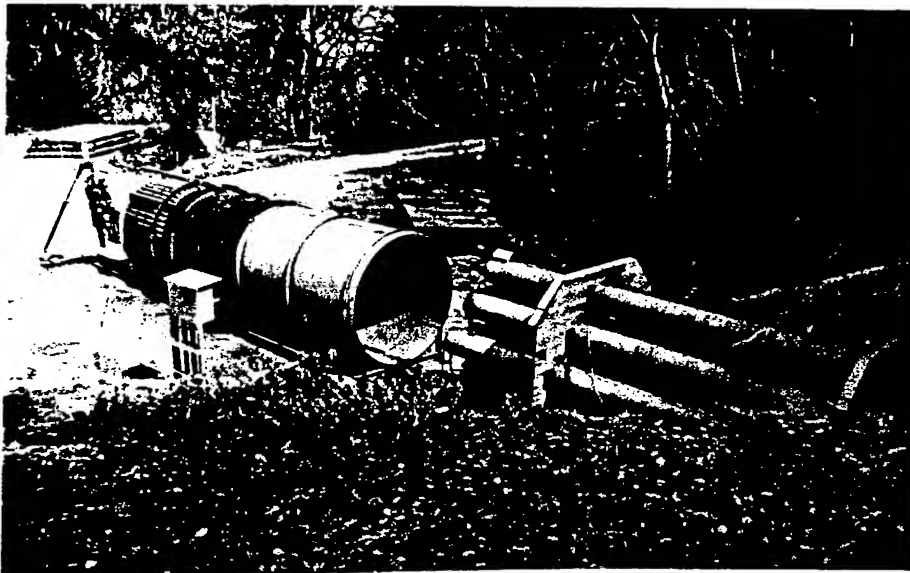


*Fig. 1: Simulator for aerodynamic effects (SAE)*

The increasing interest in the effects of non ideal blast waves motivated us to investigate the possibilities to convert the SAE into a "precursor simulator". It is well known that a precursor (Fig. 2) features a complex fluid mechanical pattern: Behind the curved shock front develops a vortex and a strong jet. The dynamic pressure is increased by factors as compared to an ideal blast. The time pressure history yields two distinct peaks and the whole phenomenon is strongly dependent on the distance from ground zero.

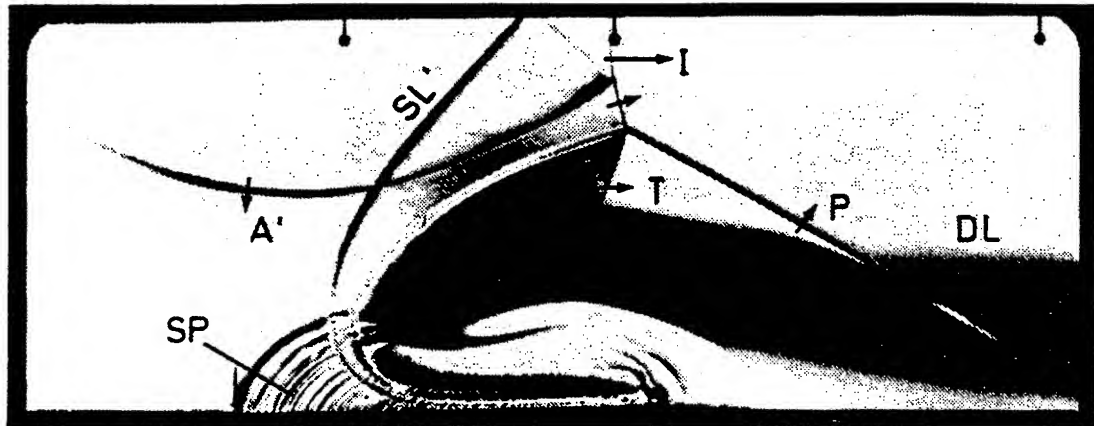


Fig. 2: Shadow Schlieren photograph of a precursor [1]

With our simple flow simulator it is of course not possible to simulate all the above mentioned features, on the other hand it is not necessary to model all the details if care is taken in choosing a target, where the dynamic pressure effects prevail over the static pressure effects.

That's precisely the aim of our investigation: to provide a tool, where it is possible to simulate the dynamic pressure effects of non ideal blast waves. This should be possible using the high dynamic pressures that the driver gas generates in moderate distances of the diaphragms.

## Evaluation of the existing facility

### Test set up

The base for the further discussion is the knowledge about the existing SAE facility. Fig. 3 shows the three main parts:

- first a *driver* which is made up of 13 steel tubes with a volume of  $0.4 \text{ m}^3$  each, filled with compressed air up to 20 MPa and closed by steel diaphragms,
- secondly a *flow guidance* which consists of a steel tube with a diameter of 1.8 m and a tube bundle with the same diameter,
- thirdly the *test section*, where normally a dummy with pilot equipment is located. Fig. 3 shows the test set up with the gage array instead the dummy.

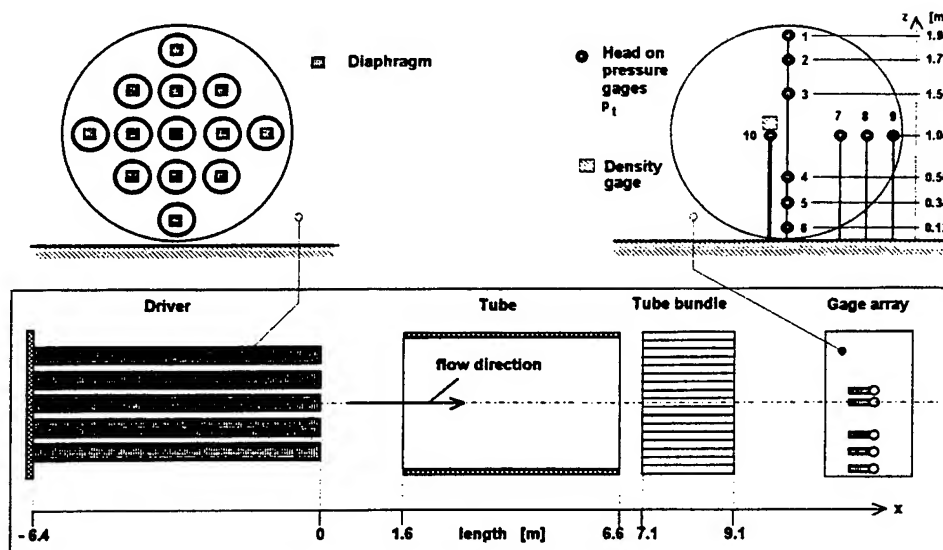


Fig. 3: SAE (test set up)

For the measurements we had 9 total pressure gages and one density gage which is described in [2].

### Flow parameters in the center

By detonating the diaphragms a flow develops which features a rise time of 30 ms in the test crosssection 11 m away from the diaphragms and an exponential decay back to ambient within 3 s. As an example this behaviour is depicted in Fig. 4 for the center of the flow and a driver pressure of 10 MPa.

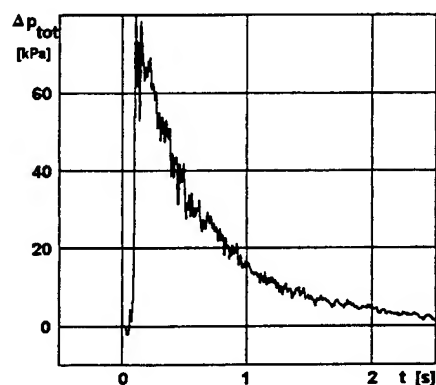


Fig. 4: Total pressure time history in the center of the flow

The first step to a conversion is to investigate the features of the existing facility in detail. Thus we measured the total overpressure  $\Delta p_{tot}$  in the core of the flow in the test crosssection related to the filling pressure in the tubes. These measurements are summarized in Fig. 5, where the dynamic pressure  $q$ , the according impulse  $I_q$  and the flow Mach number  $M$  is plotted as a function of the driver pressure.

The achieved peak dynamic pressures are totally sufficient to simulate the dynamic pressures of precursors.

Just to give two examples: In order to generate a peak dynamic pressure of 70 kPa with an ideal blast wave a static peak overpressure of 155 kPa is necessary. The highest dynamic impulse, that we can generate in our LBS is just 5 kPas.

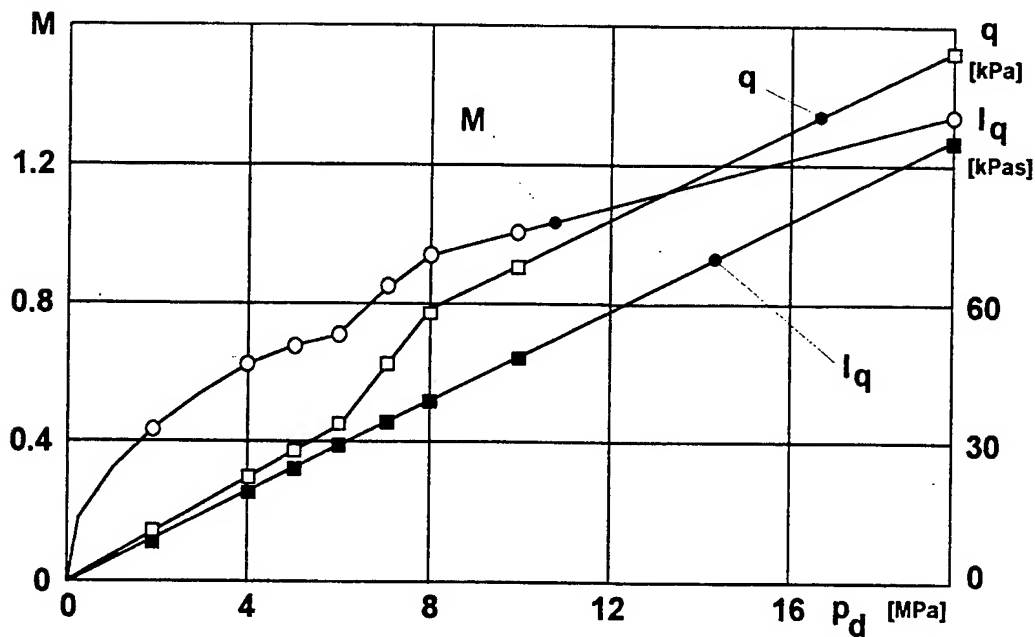


Fig. 5: Core flow parameters in the test crosssection related to the driver pressure

The flow parameters in Fig. 5 can be evaluated from the measured pressure  $\Delta p_{tot}$  using the terms of Fig. 6 as follows:

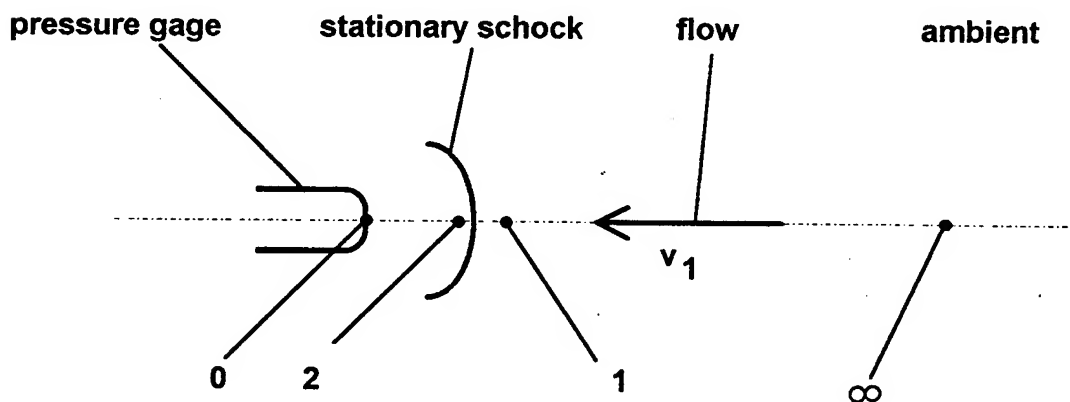


Fig.6 : Definition of the indices of the flow parameters

Assuming that the adiabatic constant  $\kappa = 1.4$  we have:

$$M_1 = v_1/a_1 \quad \text{where : } v_1 = \text{flow velocity} \quad (1)$$

$$\text{and : } a_1 = \text{velocity of sound}$$

$$v_1 = (2 \cdot q_1 / \rho_1)^{1/2} \quad \text{where : } q_1 = \text{dynamic pressure} \quad (2)$$

At this point we have to distinguish three cases:

$$1) M_1 = 0: \quad q_1 = \Delta p_0 \text{ (incompressible limit)} \quad (2a)$$



$$2) M_1 < 1: q_1 = (0.7 \cdot \Delta p_0 \cdot M_1^2) / [(1 + 0.2 \cdot M_1^2)^{3.5} - 1] \quad (2b)$$

$$3) M_1 > 1: q_1 = (0.7 \cdot \Delta p_0 \cdot M_1^2) / \{1.893 \cdot M_1^7 \cdot [2.4 / (2.8 \cdot M_1^2 - 0.4)]^{2.5} - 1\} \quad (2c)$$

where  $\Delta p_0 = p_0 - p_\infty$  = total overpressure, which is the measured variable  $\Delta p_{tot}$ . The equations (2b) and (2c) tell us, that  $\Delta p_{tot}$  is always higher (due to the compressibility), than the dynamic pressure of the flow. For example for  $M = 1$  the difference between  $\Delta p_{tot}$  and  $q$  is about 28%.

The relation for the velocity of sound in the flow is:

$$a_1 = (1.4 \cdot p_1 / \rho_1)^{1/2} \quad \text{where : } p_1 = p_\infty = \text{ambient pressure} \quad (3)$$

Inserting (2) and (3) in (1) yields:

$$M_1 = 1.195 \cdot (q_1 / p_\infty)^{1/2} \quad (4)$$

(4) can only be solved iteratively, because the determination of  $q_1$  using (2b) and (2c) contains  $M_1$  as well.

The requirement for the above described development is, that the static pressure in the flow is identical with the ambient pressure. If this is not the case the jet would have to expand or to choke.

Using (4) and (2b) for the transition between sub- and supersonic flow in a distance of 11 m from the diaphragms with an ambient pressure of 95 kPa yields  $q_1 = 66$  kPa, respectively  $\Delta p_{tot} = 85$  kPa. In order to achieve this measured pressure we need to fill the driver tubes with a pressure of 10 MPa, as can be seen from Fig. 5.

### ***Spatial distribution of the flow parameters***

Not only the core, the whole flow field of the SAE was examined using the test rig shown in Fig. 3. The following main objectives were achieved by these tests:

- examination of the axial distribution of the flow field by setting the test rig in various distances  $x/d$
- investigation of the flow field as a function of the driver pressure
- evaluation of the radial distribution of the flow field

The findings are the necessary data for the modification of the SAE to a precursor simulator.

In order to avoid measurement errors we did not use the peak of the pressure time history, but the average over 100 ms starting with the first peak value for the analysis.

Using these mean peak values, the dynamic pressure and the Mach number were evaluated according equations (2b), (2c) and (4).

The results of measurement and calculation are displayed in Fig. 7 to 9.

Fig. 7 presents the axial distribution of the flow field. The dynamic pressure decreased with increasing distance from the driver as expected.

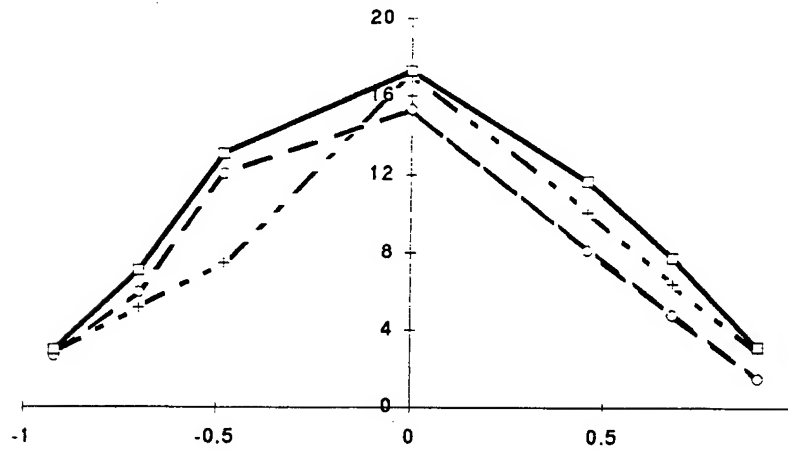


Fig. 7: Dynamic pressure [kPa] on the z-axis at  $x/d=1,0$  ( $\square$ ),  $1,5$  ( $+$ ),  $2,0$  ( $\circ$ ) and a driver pressure of 30 bar

A similar behaviour is found if the driver pressure is decreased (Fig. 8,9).

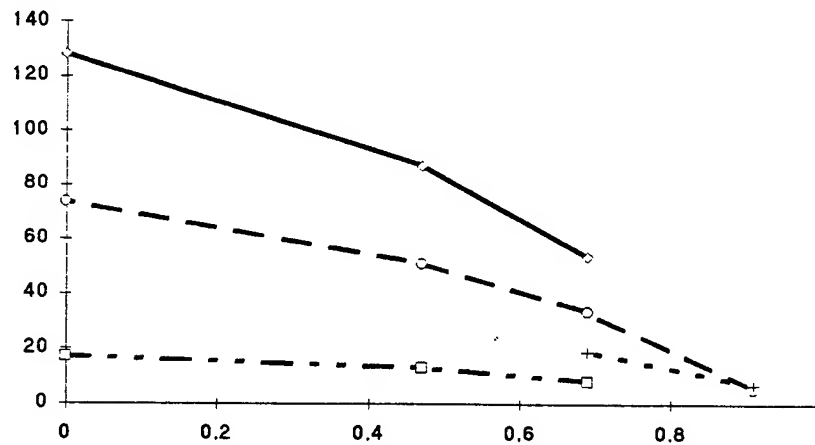


Fig. 8: Dynamic Pressure [kPa] on the y-axis at  $x/d=1,0$  and driver pressures of 30 ( $\square$ ), 60 ( $+$ ), 100 ( $\circ$ ) and 200 ( $\diamond$ ) bar

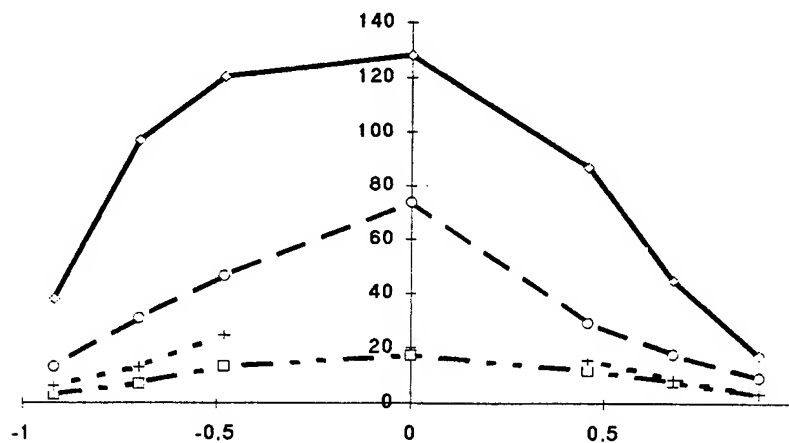


Fig. 9: Dynamic pressure [kPa] on the z-axis at  $x/d=1,0$  and driver pressures of 30 ( $\square$ ), 60 ( $+$ ), 100 ( $\circ$ ), 200 ( $\diamond$ ) bar

The radial distribution reveals a curved – not a linear – decrease of the dynamic pressure.

We could not detect the expected pressure decrease due to a ground effect. In the contrary: the lower gages often measured higher pressures compared to the corresponding upper gages. A theoretical explanation for this phenomenon has not been found yet.

The results of the investigation also showed, that the area with homogenous dynamic pressure is insufficient for further test use.

To improve this behaviour we planned to vary the driver pressure, having high pressures in the outer tubes and lowering the pressure in 3 steps towards the center tube.

Needing a first estimate for the different pressures we searched for a theoretical description of the flow field, which was found in the theory of free jets.

### Theory of free jets

One possible formula describing the radial distribution of free jets is given in [3]:

$$u(r) = \frac{u_c}{10^{\frac{1}{3.3} \cdot \left(\frac{r}{r_{0,5}}\right)^2}} \quad (5)$$

where:  $u_c$  is the velocity in the center of the jet  
 $r_{0,5}$  is the radius where the velocity is reduced to 50% of  $u_c$

Assuming that each pressurized tube is the starting point of one free jet, the flow field can be described as a superposition of 13 jets.

The velocity distribution on the y-axis then is:

$$u(y)_{z=0} = u_c \cdot \left( \begin{aligned} &\frac{1}{10^{\frac{1}{3.3 \cdot r_{0,5}^2} \cdot \frac{y^2}{2}}} + \frac{1}{10^{\frac{1}{3.3 \cdot r_{0,5}^2} \cdot \frac{(y+0,34)^2}{2}}} + \frac{1}{10^{\frac{1}{3.3 \cdot r_{0,5}^2} \cdot \frac{(y+0,68)^2}{2}}} + \frac{1}{10^{\frac{1}{3.3 \cdot r_{0,5}^2} \cdot \frac{(y-0,34)^2}{2}}} + \frac{1}{10^{\frac{1}{3.3 \cdot r_{0,5}^2} \cdot \frac{(y-0,68)^2}{2}}} + \\ &+ \frac{2}{10^{\frac{1}{3.3 \cdot r_{0,5}^2} \cdot \frac{y^2 + 0,38^2}{2}}} + \frac{2}{10^{\frac{1}{3.3 \cdot r_{0,5}^2} \cdot \frac{(y-0,34)^2 + 0,38^2}{2}}} + \frac{2}{10^{\frac{1}{3.3 \cdot r_{0,5}^2} \cdot \frac{(y+0,34)^2 + 0,38^2}{2}}} + \\ &+ \frac{2}{10^{\frac{1}{3.3 \cdot r_{0,5}^2} \cdot \frac{y^2 + 0,76^2}{2}}} \end{aligned} \right) \quad (6)$$

For a first comparison the 2 unknown variables  $u_c$  and  $r_{0,5}$  were treated as follows:

- $u_c$  was eliminated by normalizing the velocity with the maximum appearing velocity.
  - $r_{0,5}$  was found by adapting the calculated curve to the measured points.
- Although this formula originates from air condition engineering without any consideration of compressible effects or the fact that the air flow is guided in tubes, the comparison between calculation and measured data shows a very good agreement (Fig. 10).

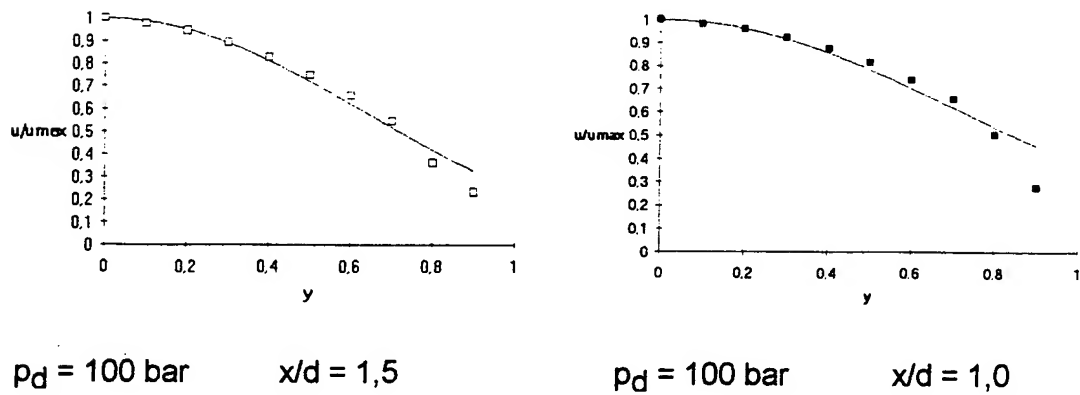


Fig. 10: Measured and calculated velocity profile on the y-axis

### Single tube tests

To validate these results additional tests were made where the flow field of a single driver tube was investigated. As a result we were able to determine the variables  $u_C$  and  $r_{0,5}$  quantitatively.

To achieve a higher resolution a new test rig was used (Fig. 11) on which the pressure gages were mounted in a shorter distance. During the tests only 9 positions out of the 12 held pressure gages.

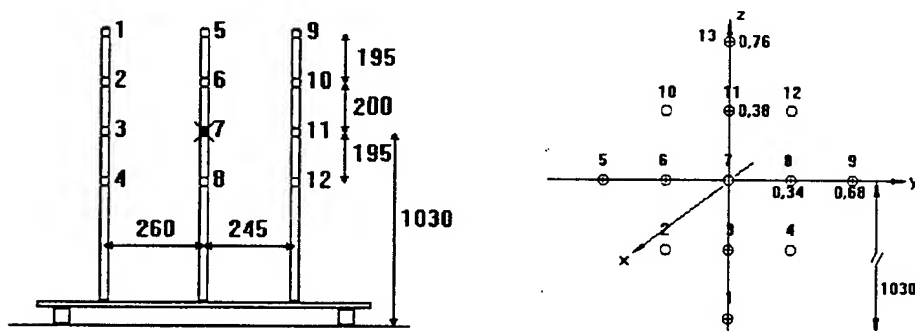


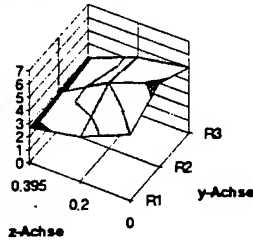
Fig. 11: Test rig and driver definition for single tube tests

As before, the investigations were made for different distances  $x/d$  and different driver pressures.

Typical velocity profiles are shown in Fig. 12.

Taking two calculated velocities and the corresponding distances from the center axis allows the determination of the missing variables  $u_C$  and  $r_{0,5}$ . To minimise the calculation error the mean value was used for further calculation. In the experiments where the driver tube was lined up with a pressure gage, we were able to determine  $u_C$  directly by measuring the total pressure.

Experiment 9: Tube 7, 100 bar,  $x/d=1.5$



Experiment 14: Tube 7, 100 bar,  $x/d=1.0$

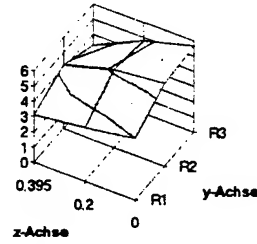


Fig. 12: Total pressure of the flow field

The results of the experiment are summarised in Fig. 13 and 14.

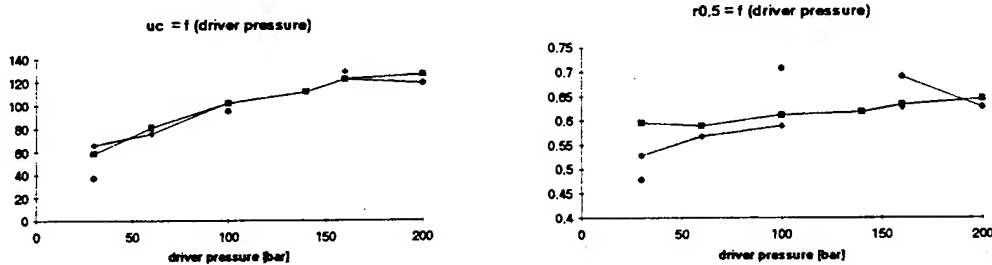


Fig. 13: Center velocity  $u_c$  and radius  $r_{0,5}$  as a function of the driver pressure

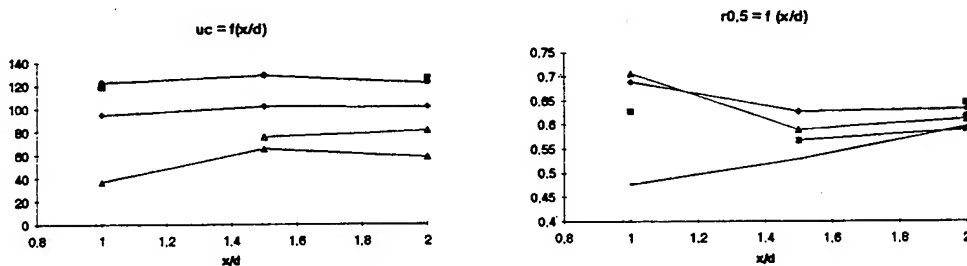


Fig. 14: Center velocity  $u_c$  and radius  $r_{0,5}$  as a function of the distance  $x/d$

Influence of the driver pressure:

The rise of the center velocity  $u_c$  with increasing driver pressure is as expected. This behaviour is due to the increasing pressure ratio driver / ambient which results in a stronger expansion and thus higher air velocities.

The increase of the radius  $r_{0,5}$  can be explained analogically. The increasing strength of the expansion generates a larger turbulence which will enlarge the mixing zone represented by  $r_{0,5}$ .

Influence of the distance  $x/d$ :

According to the free jet theory the center velocity  $u_c$  should drop with increasing distance to the driver tube. This is due to the impulse transfer to the mixed air. Our results just show few changes, in some occasions even an increase of velocity at greater values of  $x/d$ . Since the changes are small,

the measurement error of the pressure gages could be the reason. A reason for the minor changes of velocity could be the large distance between driver and pressure gage. While other experiments are limited to  $x/D$  ratios up to 100 ( $D$  = diameter of the driver nozzle), our pressure gages were positioned in a distance of  $x/D = 190$  to 230.

With respect to  $r_{0,5}$  all the tests (except of 2) show the expected increase of the radius. But again the changes are not very significant.

### Superposition method

Using the results of the above described experiments, the calculations of the superpositioned velocity profile according equation (6) show excessive velocities. The main reason for this behaviour is the compressibility which makes a linear superposition impossible. That the curvature of the graphs still fits quite well can be proved by normalizing the flow velocities with the maximum appearing velocity (see Fig. 15).

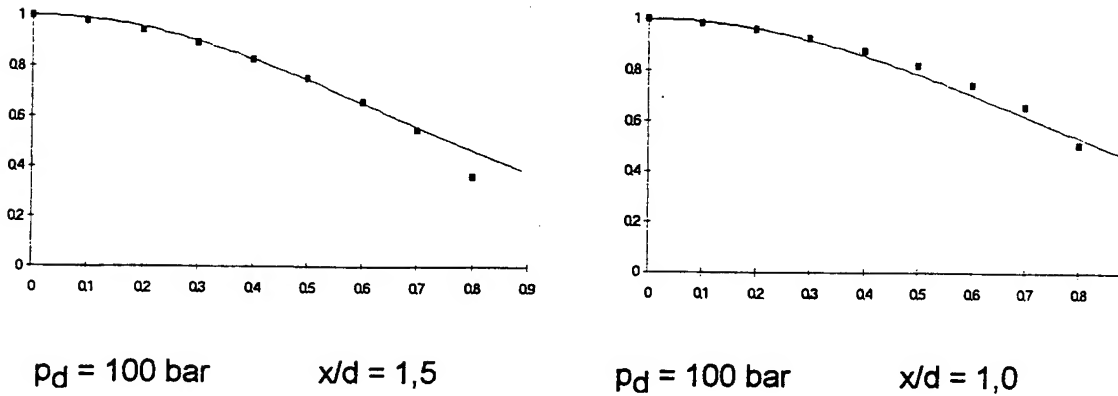


Fig. 15: Superposition of 13 free jets versus measured velocity on the y-axis

Since our main objective was to improve the dynamic pressure distribution and the velocity distribution accordingly the superposition still yields a good approximation if equation (6) is rewritten as follows:

$$u(y)_{z=0} = \left( \begin{aligned} & \frac{u_c(0)}{10 \frac{y^2}{3,3 \cdot r_{0,5}(0)^2}} + \\ & + \frac{u_c(1)}{10 \frac{(y+0,34)^2}{3,3 \cdot r_{0,5}(1)^2}} + \frac{u_c(1)}{10 \frac{(y-0,34)^2}{3,3 \cdot r_{0,5}(1)^2}} + \frac{2 \cdot u_c(1)}{10 \frac{y^2 + 0,38^2}{3,3 \cdot r_{0,5}(1)^2}} + \\ & + \frac{2 \cdot u_c(2)}{10 \frac{(y-0,34)^2 + 0,38^2}{3,3 \cdot r_{0,5}(2)^2}} + \frac{2 \cdot u_c(2)}{10 \frac{(y+0,34)^2 + 0,38^2}{3,3 \cdot r_{0,5}(2)^2}} + \\ & + \frac{u_c(3)}{10 \frac{(y-0,68)^2}{3,3 \cdot r_{0,5}(3)^2}} + \frac{u_c(3)}{10 \frac{(y+0,68)^2}{3,3 \cdot r_{0,5}(3)^2}} + \frac{2 \cdot u_c(3)}{10 \frac{y^2 + 0,76^2}{3,3 \cdot r_{0,5}(3)^2}} \end{aligned} \right) \quad (7)$$

where  $u_c(0), r_{0,5}(0)$  are the quantities of the center  
 $u_c(1), r_{0,5}(1)$  first circle  
 $u_c(2), r_{0,5}(2)$  second circle  
 $u_c(3), r_{0,5}(3)$  third circle

as indicated in Fig. 16.

Thus equation (7) can handle different pressures in the different circles.

For the new tests we used the same measurement rig as in the first experiments but added 3 more pressure gages close to the flow axis (Fig. 16).

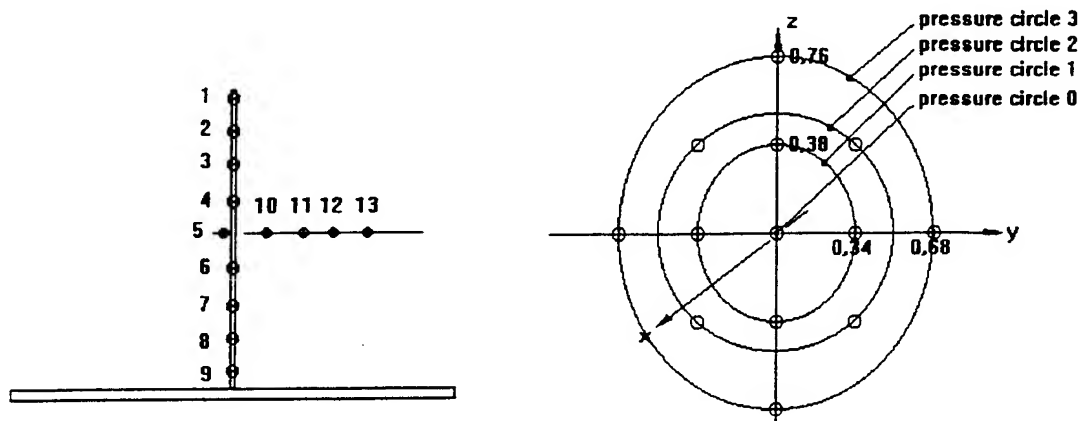


Fig. 16: Test rig and driver definition for the superposition tests

### Variable driver pressures

In a first experiment using variable pressures we filled the pressure circle 3 with 200 bar and left all other tubes empty. As distance for the measurement we choose  $x/d=1,0$ .

According to the single tube tests we expected a superposition of 4 jets having

$$u_c(3) = 140,5 \frac{\text{m}}{\text{s}}, \quad u_c(0) = u_c(1) = u_c(2) = 0 \frac{\text{m}}{\text{s}},$$

$$\text{and } r_{0,5}(3) = 0,63 \text{ m}.$$

A comparison with the result of the experiment is shown in Fig. 17.

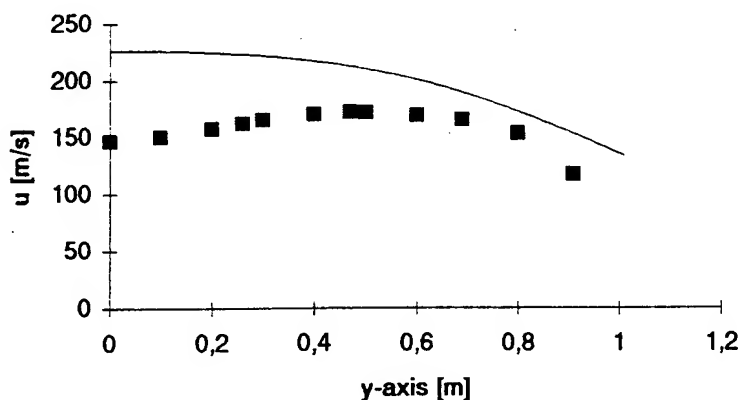


Fig. 17: Comparison of measurement and superposition method with 200 bar in pressure circle 3

The similarity of both curves is not satisfactory. But changing the radius  $r_{0,5(3)}$  from 0.63 m to 0,52 m we almost found 100% conformity as is shown in Fig. 18.

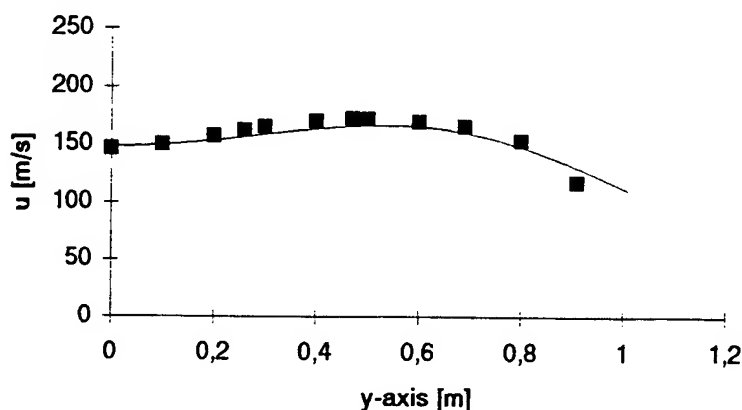


Fig. 18: Comparison of measurement and superposition method with 200 bar in pressure circle 3 with changed  $r_{0,5(3)}$

Since we found low air speeds even the linear superposition of the velocities is now possible.

The necessary reduction of  $r_{0,5(3)}$  can be explained by the interaction of the 4 free jets. Since the air mass which is mixed to the jets cannot be increased due to the geometry in the flow field, each added jet mixes less surrounding air compared to the single jet and therefore has a reduced value for  $r_{0,5}$ .

Concerning the theoretical tools developed the following statements are possible:

- A theoretical description of the total flow field according to the free jet theory is possible.
- A linear superposition of several free jets using the results of single tube experiments do not always fit the reality due to
  - compressible effects when reaching higher velocities,
  - interaction of the jets.

For the modification of the simulator further experiments, trying to avoid the velocity reduction in the centre of the flow field, will be carried out. In these tests the circles 0,1 and/or 2 will be pressurised too.

### Summary and Conclusions

- The performance of the **existing SAE facility** in terms of achievable peak dynamic pressures and impulses (Fig. 5) and homogeneity of the flow (Fig. 7 to 9) has been examined. The dynamic characteristics of the SAE are sufficient. Shortcomings exist concerning the flow homogeneity.
- The **free jet theory** provides data for the computation of the distribution of the flow parameters (Equation (5) ).
- **Single tube tests** provided the necessary data (Fig. 13 and 14) to use the free jet theory.



- A **superposition method** (Equation (6) and (7)) based on the results of the single tube tests and the free jet theory has been developed. This method is used to predict the effect on the flow field when different improvements are tested (*Fig. 10, 15, 17 and 18*).
- The influence of **variable driver pressures** on the homogeneity of the flow field has been examined. On the one hand the improvements of the homogeneity are remarkable but the peak dynamic pressure decreases by factors. (The cure is a higher packing density of the driver tubes.)
- Another measure to generate a flat profile is using a **grid** with variable spacing (dense in the center and wide at the border). This measure has been predicted using the measured data of the existing facility, but it has to be proved in a test (future activity).
- Pulse shaping in order to generate a similar total pressure time history than for a precursor can be achieved by opening the diaphragms with a **time delay**. This has to be tested yet.
- A second method for pulse shaping and an increase of the static pressure component will be to **confine the jet** (like in a shock tube). This will be examined by tests and computations.
- Another future activity is to increase the **packing density** of the driver tubes in order to compensate for the decrease in dynamic pressure when using grids or variable driver pressures.

Using all the results and changing the simulator accordingly, the SAE seems to be a useful tool for examining the dynamic effects of precursors on military equipment.

## References

- [1] H. Reichenbach, A.L. Kuhl  
"Techniques for creating precursors in shock tubes"  
Shock tubes and waves 16, Aachen, 1987
- [2] M.H. Klaus, U. Schwarz, G. Eggers  
"Evaluation of the properties of air in a shock wave using a  $\beta$ -densitometer and numerical methods"  
MABS 12, Perpignan (F), September 1991
- [3] Rietschel, Reiß  
"Heiz- und Klimatechnik"  
Springer Verlag, Hamburg, 1968
- [4] E. Truckenbrodt  
"Strömungsmechanik"  
Springer Verlag, Berlin, 1968

# **SIMULATION OF NON-IDEAL BLAST WAVES PRODUCED BY THE THERMAL PRECURSOR IN NUCLEAR EXPLOSIONS**

DANIEL MERGNAT, DIDIER TOURNEMINE, SOLANGE GRATIAS  
DGA, DRET, CENTRE D'ETUDES DE GRAMAT  
46500 GRAMAT, FRANCE

## **ABSTRACT**

It has been shown that the non-ideal blast waves generated by the thermal precursor can propagate on desert soil or on very low-level landcover over long distances from the point of explosion. CEG therefore decided to study the possibility of simulating this phenomenon, so as to assess its effect on the vulnerability of military equipment. After having defined the significant characteristic parameters of this non-ideal phenomenon, CEG adapted the capabilities of its large blast simulator (SSGG) so as to simulate the effects of non-ideal waves. Initial experiments performed on an armoured vehicle gave highly interesting results.

## **1. INTRODUCTION**

For the last 15 years, France has been using a large blast simulator (SSGG) located at the Centre d'Études de Gramat. This testing facility provides a faithful simulation of the effects of ideal blast waves from 1 kT to 1 MT yield nuclear weapons (Fig.1).

In order to study the effect of the non-ideal waves generated by the thermal precursor, CEG decided to adapt the capabilities of this testing facility, so as to simulate this phenomenon and perform appropriate tests on military equipment.

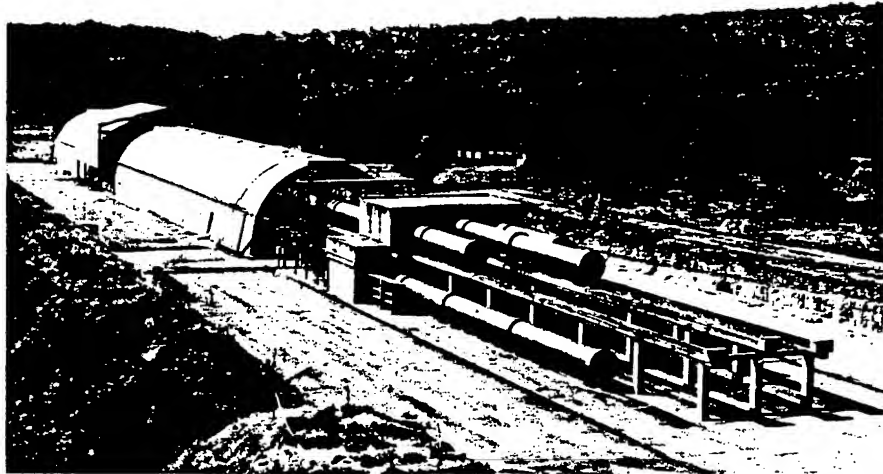


**Fig 1:** View of the SSGG test facility

## **2. NON-IDEAL BLAST WAVES**

### **2.1 Description of the phenomenon**

In the event of an endoatmospheric nuclear explosion, the thermal radiation generated by the fireball is followed by a shock and blast wave, within a time-delay which is dependent upon the yield of the nuclear weapon and the distance from the point of explosion.

With low-altitude explosions, the thermal radiation can have a considerable heating effect on the ground surface. And over desert soil or very low-level landcover, a layer of hot air called thermal layer, often comprising smoke and particles from near-ground bursts, is formed by convection near the surface (Fig.2).

During its propagation through the thermal layer, the shock wave (Mach Front) splits in two. A secondary wave then moves in front of the main shock. This is the "thermal precursor", so-called because it precedes the main wave.

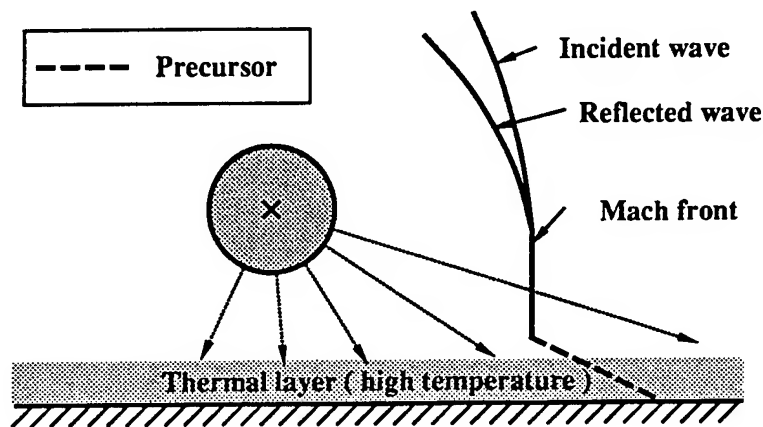


**Fig.2:** Development of the thermal precursor

## 2.2 Characteristics

The characteristics of non-ideal blast waves can be very different from those of the ideal waves usually considered when studying the mechanical effects of nuclear explosions. The chronological profiles of static overpressure and dynamic pressure change during the formation and development of the thermal precursor. Nevertheless, in this study, we took as reference the chronological profiles illustrated at Fig.3, which, qualitatively, seem most representative of an on-going precursor phenomenon. These profiles are compared with the profiles of an equivalent ideal wave, if there was no thermal layer.

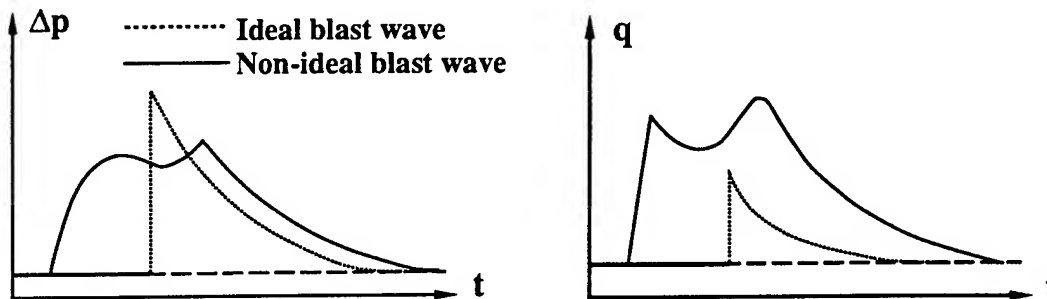


**Fig.3:** Chronological profiles used as reference for non-ideal waves

### 2.3 Significant parameters

To simulate the non-ideal phenomenon, it is necessary to know the influence of characteristic parameters ( $\Delta p_{\max}$ ,  $q_{\max}$ ,  $I_q$ ) on the behaviour of targets under test.

For this purpose, we studied the overturn of an armoured vehicle using the TRUCK computational code. After having validated the vehicle model in the case of an ideal wave, we performed a number of calculations in which schematic non-ideal pressure profiles were considered and characteristic parameters varied.

- The effect of static overpressure on the vehicle overturn can be ignored.
- The effect of the dynamic pressure impulse is illustrated at Fig.4. For a given peak value  $q_{\max}$ , a variation of + or - 15% of the impulse  $I_q$  leads to a very different vehicle behaviour, represented by the ratio curve (angle of roll/critical angle of overturn).
- The effect of the peak dynamic pressure value is illustrated at Fig.5. For a given impulse  $I_q$ , a variation of + or - 15% of the peak value  $q_{\max}$  leads to a very different vehicle behaviour, represented by the ratio curve.

The study shows that the peak value ( $q_{\max}$ ) and impulse ( $I_q$ ) of dynamic pressure have a considerable impact on the dynamic behaviour of a target. Both parameters are therefore considered as significant for the simulation of non-ideal waves. Moreover, it is necessary, in spite of the fact that static overpressure has no significant influence on the dynamic behaviour of targets, to simulate this phenomenon in order to assess the structural resistance of the vehicle. The interesting parameter in this case is the peak static overpressure value  $\Delta p_{\max}$ .

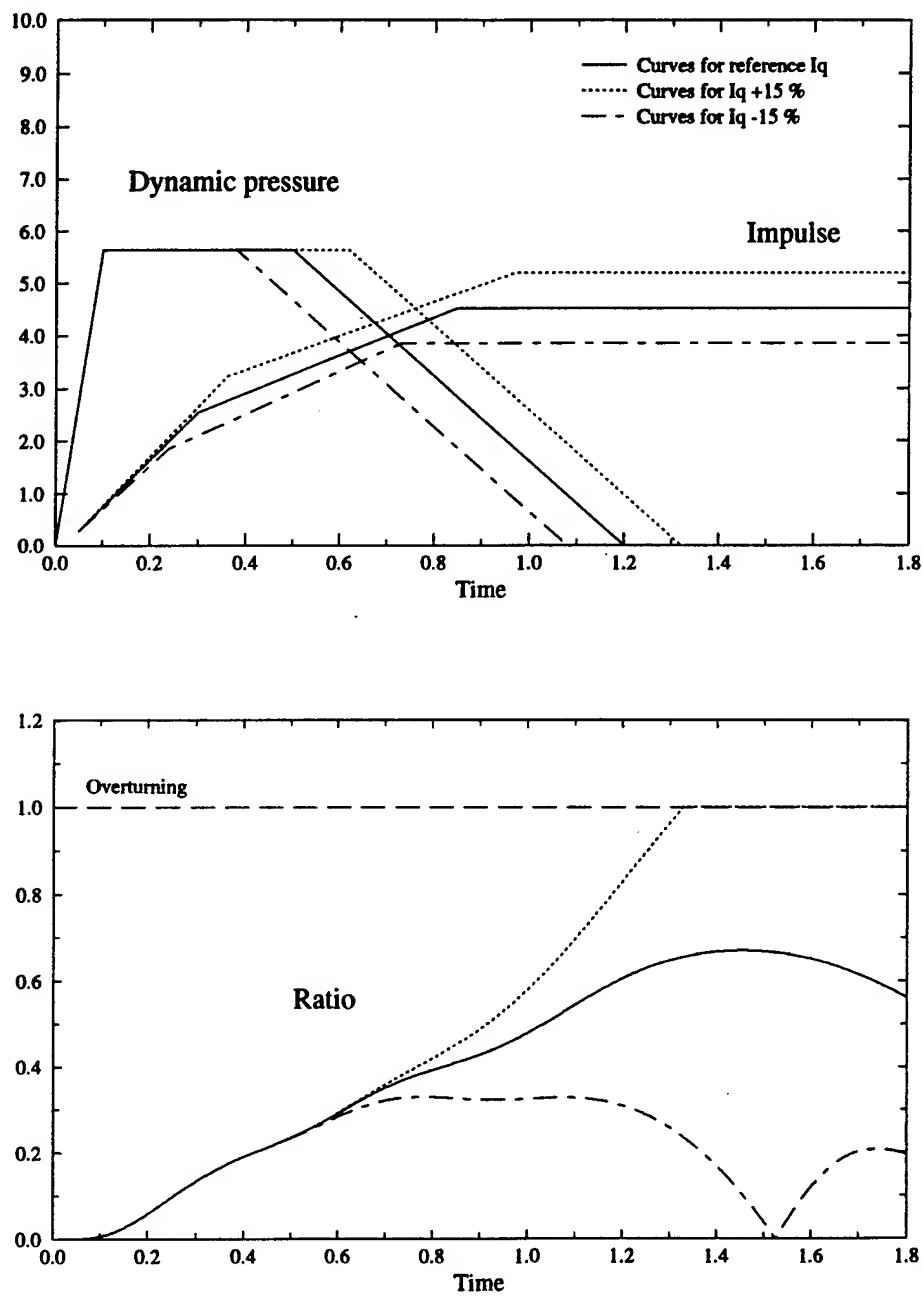


**Fig.4:** Results of calculations on the overturn of an armoured vehicle - Effect of the dynamic pressure impulse  $I_q$  (constant  $q_{\max}$ )

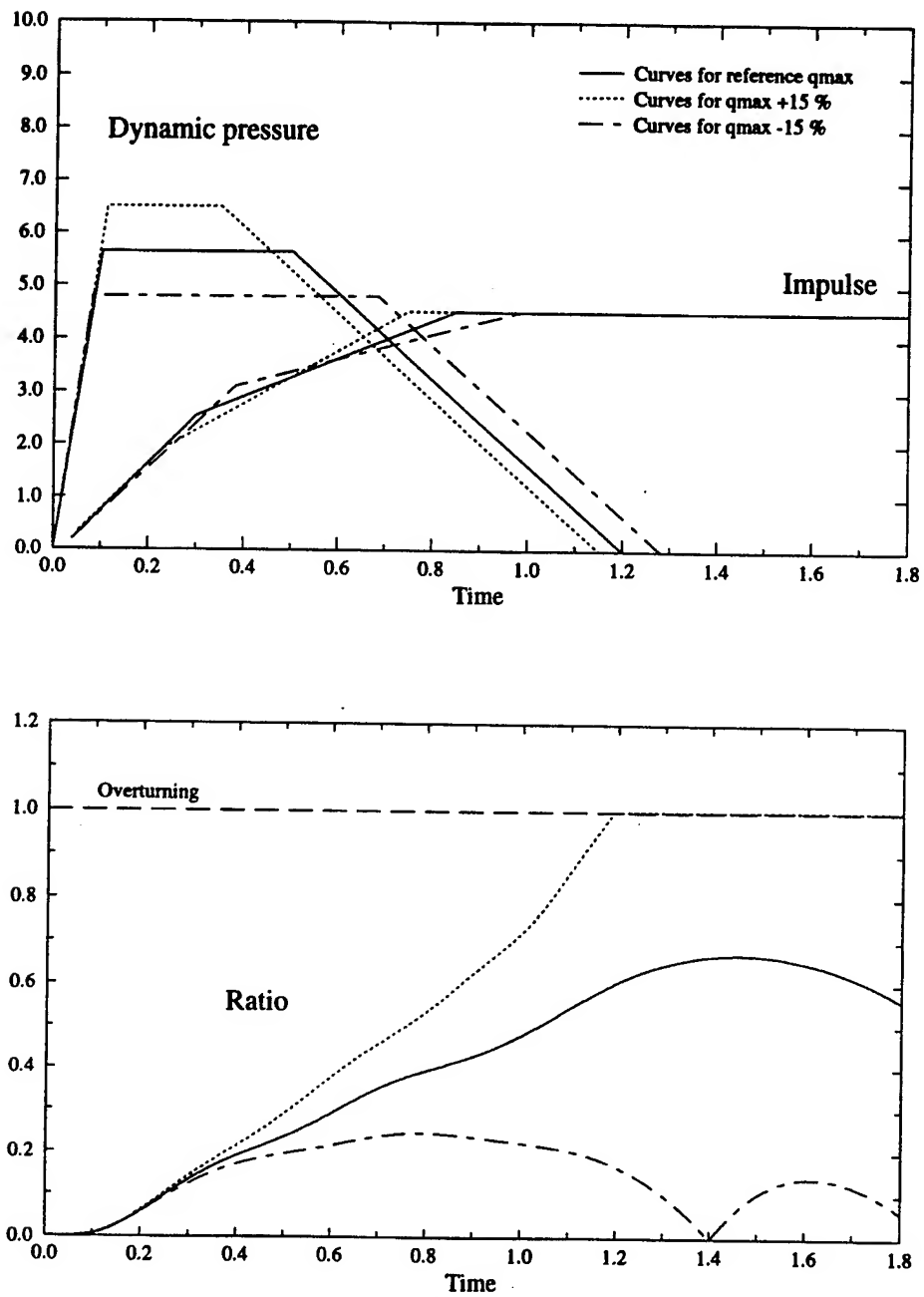


**Fig.5:** Results of calculations on the overturn of an armoured vehicle - Effect of the dynamic pressure peak value  $q_{max}$  (constant  $I_q$ )

### **3. THE LARGE BLAST SIMULATOR (SSGG)**

#### **3.1 Description**

The SSGG was designed and developed by CEG in order to simulate the effects of ideal blast waves from nuclear explosions, so as to assess the behaviour of large-sized military equipment. Fig. 6 presents a block diagram of the facility showing the main dimensions.

In this facility, the shock wave is induced by the sudden discharge of compressed air contained in seven pressurized vessels (drivers) into the expansion tunnel. The history of the pressure signals recorded in the test section containing items to be tested is related to the specific geometry of the facility.

The expansion tunnel, which includes the test section, is of semi-circular shape. Its section area represents  $70\text{m}^2$ . At the mouth of the expansion tunnel, a mechanical device (rarefaction wave eliminator) prevents rarefaction waves from disturbing the flow.

The range of static overpressure simulated within the SSGG is usually between 14 KPa and 140 KPa. The static overpressure and dynamic pressure profiles show decay which is typical of the ideal nuclear phenomenon: the duration of the positive phase is close to 1 second.

#### **3.2 Capabilities**

This simulator, whilst designed to simulate the effects of ideal waves from nuclear explosions, offers a remarkable adaptability:

- The test section was designed to study the behaviour of targets sensitive to the effects of dynamic pressure. For this purpose, a target displacement area was set up to accommodate target motions of up to 30 m. In the same way, instrumentation facilities accommodate wide target displacements. Moreover, the wooden floor for the support of equipment in the test section also covers most of the target displacement area.

- The pressure wave generating system is made of seven pressure vessels (drivers) of varying capacity, which can be controlled independently for pressure levels and opening times. This modularity provides the possibility of generating several waves of the required amplitude, successively and with the desired chronology.



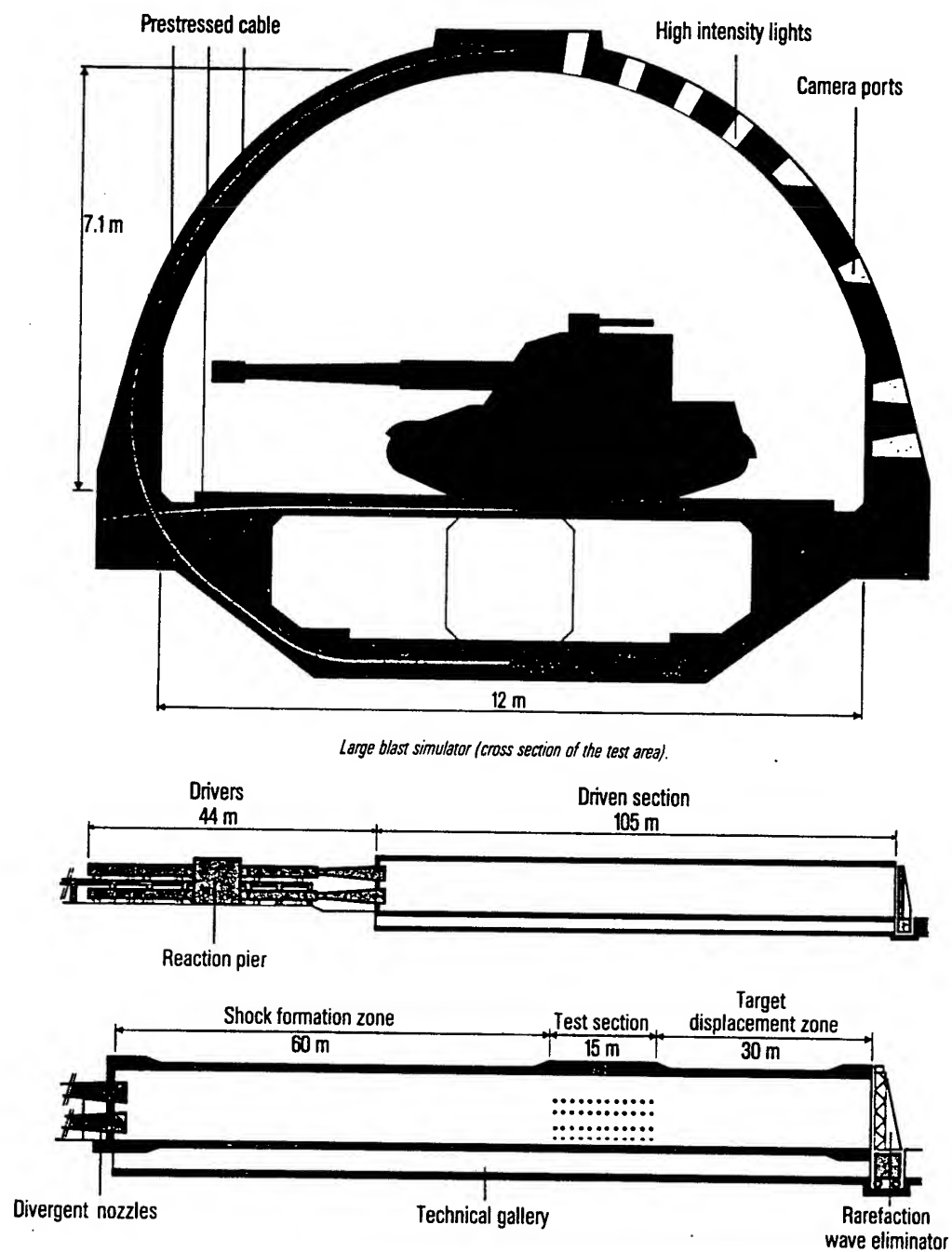


**Fig.6:** Block diagram of the SSGG testing facility

- The active rarefaction wave eliminator located at the downstream end of the expansion tunnel is driven by a computerized servo-control unit. This high-performance facility is able to adapt the expansion phenomena generated within the SSGG test section, and thus act on the dynamic pressure characteristics.

In view of such capabilities, we naturally thought of trying to simulate the effects of non-ideal waves in the expansion tunnel, with targets set up in the test section.

### **3.3 Non-ideal wave simulation concept**

A theoretical study showed that it was possible to greatly increase the amplitude and impulse of the dynamic pressure generated within the simulator, without any significant degradation of the static overpressure profile. This simulation concept is based on two phenomena:

- the rarefaction waves generated when the shock wave reaches the downstream end of the expansion tunnel turns the flow back towards the test section and produce a marked increase in dynamic pressure, through a local increase of the flow rate and a reduction of air temperature. Inversely, and simultaneously, the static overpressure decreases;

- a second shock wave, generated after the first one with an appropriate delay, should reinforce the dynamic pressure increase due to the above mentioned rarefaction waves. The sudden rise in static pressure induced by this wave will partly compensate the static overpressure decrease due to the rarefaction waves.

The diagrams at Fig.7 show the expected static overpressure and dynamic pressure profiles. The first pressure wave is produced by opening a limited number of drivers, and by the effect of the rarefaction waves at the end of the tunnel. A second wave is achieved by opening the remaining drivers at the appropriate moment for this wave to meet the tunnel-end rarefaction wave in the test section.

In order to achieve the required simulation characteristics, a number of calibration tests are necessary to define the testing facility operating parameters (selection of drivers, pressure levels used, opening times, function law for the rarefaction wave eliminator).

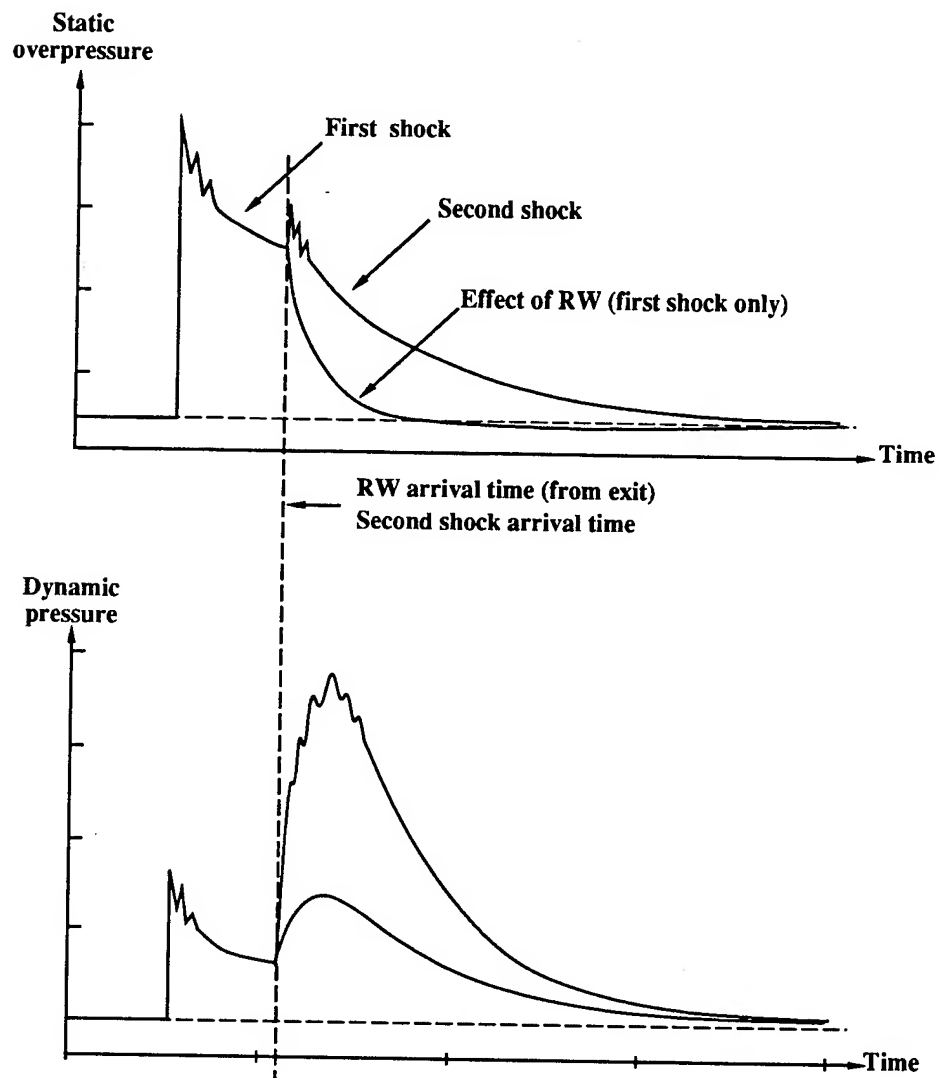


**Fig.7:** Typical static overpressure and dynamic pressure profiles expected at the SSGG for the simulation of non-ideal waves.

## 4. SIMULATION OF NON-IDEAL WAVES

### 4.1 Simulation characteristics

In order to highlight the damaging effects of non-ideal waves on the behaviour of a heavy armoured vehicle, the conditions for simulation in the SSGG were determined as follows:

- Simulation of ideal waves for  $\Delta p = 80$  KPa, which corresponds to a given yield-distance (W-D) couple;
- Simulation of the non-ideal waves related to this W-D couple.

For this purpose, we used the TEAPOT 12 test data, which were extrapolated using the  $W^{1/3}$  law of equivalence in order to determine the characteristics of the simulation to be performed.

The following table shows these characteristic values.

	Ideal case	Non-ideal case
$\Delta p_{\max}$ (KPa)	80	50
$q_{\max}$ (KPa)	21	30
$I_q$ (KPa.s)	8	16,5

### 4.2 Calibration of the SSGG

Fig.8 shows in superimposition, the pressure profiles related to the ideal waves usually achieved in the SSGG simulator and the pressure profiles related to the non-ideal waves achieved after a number of calibration tests. The simulation characteristic values are very close to the required values.

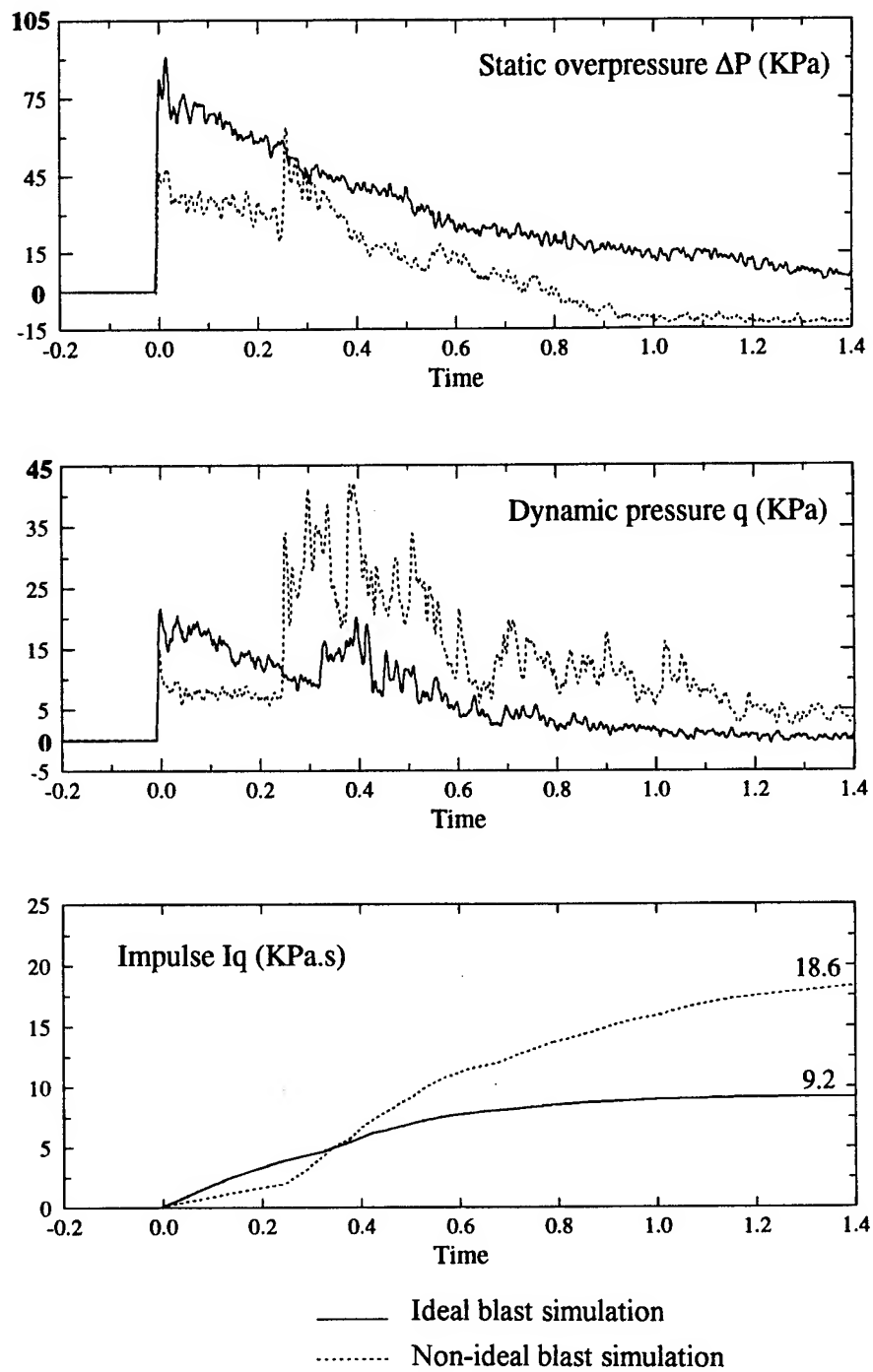


**Fig.8:** Pressure profiles achieved in the SSGG

#### 4.3 Test on a heavy armoured vehicle

In the SSGG testing facility, a tank was successively submitted to the effects of ideal blast waves, then of non-ideal waves as defined above.

Ideal waves : The tank was pushed over a distance of 1.5 m, but did not suffer any functional damage.

Non-ideal waves : Under the dynamic pressure, the tank was violently dragged over 15 m and overturned. Major structural and functional damage was incurred. The tank is unserviceable (Fig.9).

This test, filmed in video, clearly shows the spectacular increase in the damage level caused to equipment by the dynamic phenomenon of the non-ideal wave considered.

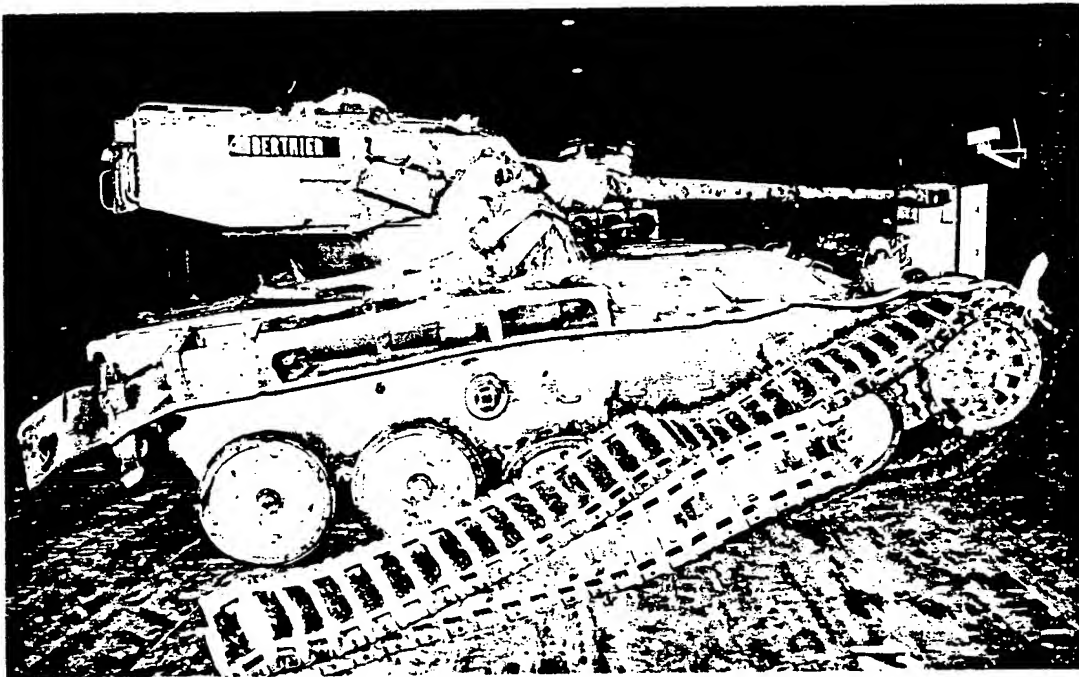


**Fig.9:** View of the tank after testing to the effects of non-ideal waves (overturn, track off sprocket, structural damage)

## **5. CONCLUSION**

Due to the modularity of the driving system and the high adaptability of the active rarefaction wave eliminator, CEG was able, within the SSGG test section, to reproduce dynamic effects representative of the non-ideal waves generated by the thermal precursor in nuclear explosions.

Tests performed on a heavy armoured vehicle initially exposed to an ideal blast wave and then to a corresponding non-ideal blast wave, showed the usefulness of studying the behaviour of items exposed to the effects of non-ideal blast waves.

Initial experiments in the CEG blast simulator demonstrate the efficiency of this facility to simulate such effects, and to perform experiments on military items and equipment in any battlefield environment.

## **REFERENCES**

- Shock and blast simulation. Concept and definition of a Large Blast Simulator
  - Technical paper T74-27f (in French)
  - Technical paper T74-27a (in English)
  - Technical paper T77-13f (in French)
  - Technical paper T77-13a (in English)
- Brochure "Simulateur de Souffle à Grand Gabarit"  
Centre d'Études de Gramat
- D. TOURNEMINE 1987  
Simulation de choc et de souffle - précurseur  
Bibliographical study
- S. GRATIAS , J.B.G. MONZAC  
Le Simulateur de Souffle à Grand Gabarit du Centre d'Études de Gramat -  
Conception, études, performances - MABS 7 .
- A. CADET , J.B.G. MONZAC  
Le Simulateur de Souffle à Grand Gabarit du Centre d'Études de Gramat -  
Description et utilisation opérationnelle - MABS 7 .

# MABS 14

## Thermal Radiation Transmission Through Composite Material

Richard B. Loucks  
Aberdeen Proving Ground, Maryland

### Abstract

On 10 June 1993, the Defense Nuclear Agency (DNA) Field Command at White Sands Missile Range conducted a Thermal Radiation Simulator (TRS) test for the Naval Surface Warfare Center (NSWC) during project MINOR UNCLE. The NSWC was interested in measuring the radiant thermal energy absorbed by a fiberglass panel during a simulated nuclear weapon event. The resultant thermocouple data showed an unusual initial high temperature rise and fall, followed by the expected conductive heating. The initial transient was theorized to be the result of thermal radiation transmitted through the panel. To investigate this theory NSWC prepared several more panels of different thicknesses, pre-instrumented with thermocouples and strain gages for testing with an ARL TRS. ARL also provided additional instrumentation to measure thermal radiation on the front surface as well as behind the panel. The results showed that there was direct heating of the rear of the composite panel by thermal radiation. The quantity of heat transmission through the panel was determined as was the point of ignition of the front surface of the panel. Smoke and charring of the front surface protected the panel from further heating and possible destruction.

### 1. INTRODUCTION

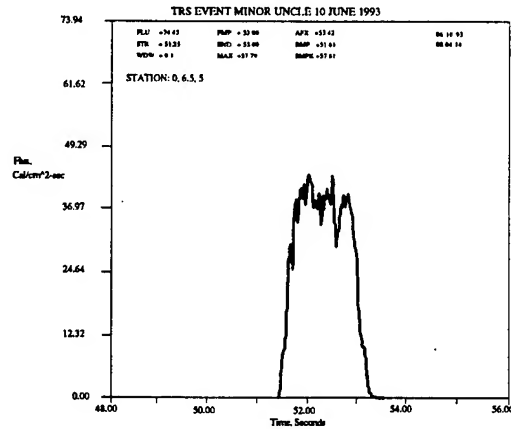
In June 1993, during project MINOR UNCLE at White Sands Missile Range (WSMR), the Naval Surface Warfare Center (NSWC), White Oak Detachment, fielded an experiment with a composite material radome. Part of the testing was to evaluate the resistance of the composite material to thermal radiation. The Defense Nuclear Agency (DNA), Field Command, provided an aluminum powder and liquid oxygen (LOX) Thermal Radiation Source (TRS) for the test. The radome was instrumented with thermocouples and strain gages on the inside and calorimeters on the opposite side of the TRS. The thermocouples were used to measure the temperature vs. time profile of the inside surface during and after the deposition of radiant energy. The calorimeters were used to ensure that the TRS replicated a previous thermal environment of interest. The data shown in Figure 1a are thermal radiation data measured during the test. The resulting radome thermocouple data, shown in Figure 1b, indicate a fast temperature rise and fall, followed by the expected exponential temperature rise due to heat conduction. Strain gages were also placed on the inside surface of the radome to measure deformation of the composite due to thermal effects. The strain gage data demonstrated a similar initial transient followed by the expected deformation attributed to heat conduction through the material. The initial transients were not consistent with theoretical calculations and needed to be explained.

After analysis by U.S. Army Research Laboratory (ARL) engineers, it was determined that the initial temperature and strain transients might be attributed to thermal radiation transmitting through the composite and directly heating the thermocouples and strain gages. The sensors were mounted on the panel backside and covered with a black tape. The tape was used to protect the sensors from environmental effects, such as dust, prior to the test.

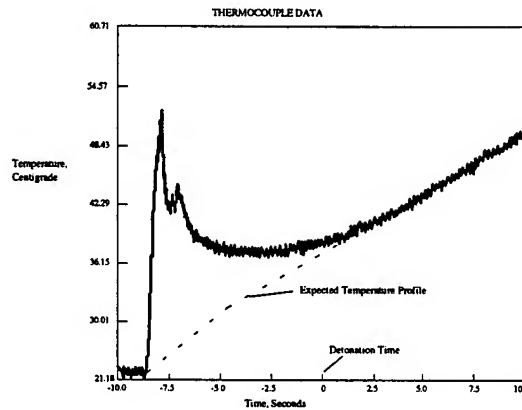
It is thought that the black tape acted as a thin blackbody. Relative to the sensor, the large surface area of the tape absorbed nearly all of the transmitted thermal radiation. Since the backing was very thin, the total energy in the tape was quickly dissipated by conduction to the sensor and composite



material and by natural convection on the exposed side of the tape. The degree of convection on the backside of the tape was small, and the composite acted as an adiabatic surface when compared to the highly conductive sensor material. As a result, the sensors were heated by the backing. When the TRS pulse ceased, excess heat in the tape dissipated quickly since there was very little heat capacitance, the temperature coming to equilibrium with the panel. As the panel backside started to increase in temperature, the thermocouple responded as predicted.



a) TRS Data.



b) Thermocouple Data.

Figure 1. NSWC composite radome data.

In an effort to further investigate this hypothesis, NSWC and ARL conducted a series of experiments at the ARL TRS facility. The objectives of the experiments were to prove the theory about the tape backing affecting the temperature readings, to assess different methods of mounting thermocouples on thin composite panels for future testing, and to measure the amount of thermal radiation transmitted through the panel. Four rectangular composite panels were made with four thermocouples and two strain gages each, with various backings on each sensor. These panels were mounted on an aluminum box filled with insulation, creating an adiabatic surface on the backside of the panel. The aluminum box served to shield the sensors from direct thermal radiation, and to hold the panel in place during the experiments.

Each panel was used in separate TRS experiments. One panel was tested twice. The resulting data showed a repeat of the high transient thermal effects obtained during MINOR UNCLE, as expected.

The data were analyzed to find any relationship between the TRS data and sensor data. The initial effects were compared between sensors to evaluate the effect of the type mounting/backing used. The amount of transmitted thermal radiation was measured. In evaluating the transmitted thermal radiation, the degree of protection afforded by the combustion of paint on the front surface of the panel was also determined.

## 2. COMPOSITE PANEL EXPERIMENT

The objective of the experiment was to prove that thermal radiation transmission through the composite radome accounted for temperature and strain transients in the initial part of the MINOR UNCLE data. It was desired to repeat the experiment. The TRS at ARL provided the same type of aluminum/oxygen TRS used by DNA. NSWC was able to obtain four composite panels of the same material and cover coating, with two different thicknesses. The panels were instrumented with the same type of sensors used at MINOR UNCLE. In addition, the ARL data acquisition system provided longer data recording on a digital system.

### 2.1 Thermal Radiation Simulator

The TRS at ARL uses aluminum powder combusting with LOX to produce thermal radiation on a target. The TRS is situated at Range 11 at the ARL Thermal Radiation Experimental Facility. The aluminum powder is blown by nitrogen from a storage vessel to the combustion chamber. Just prior to entry in to the combustion chamber, LOX is injected into the traveling powder. The mixture is ignited by pilot flames as it exits the nozzle. Momentum and combustion pressure causes the combustion mixture to rise several meters above the combustion chamber. The result is a large, highly luminous flame. The flame acts as a large blackbody panel with the hottest point radiating at about 3,000 K. Radiation from the flame is not uniform. It can be characterized by a specified **flux**, or rate of energy irradiating the target surface, and **fluence**, total irradiated energy on the target surface. Targets as large as 2 m<sup>2</sup> can be irradiated. Figure 2 shows the TRS as a free field source.



Figure 2. TRS unit as a free field source.

For the NSWC experiments, the primary nuclear weapon thermal parameter to be simulated was fluence. Flux was adjusted by placing the target nearer or farther from the flame. Since the TRS at ARL emits a rectangular shaped thermal pulse, as seen in Figure 3, the fluence was adjusted by setting the length of time of aluminum burn. The rectangular shaped pulse is excellent for controlling fluence.

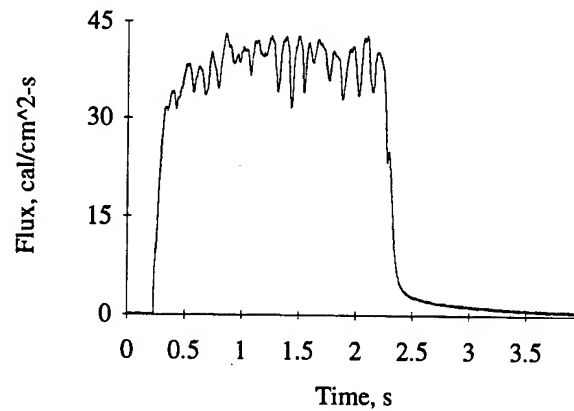


Figure 3. ARL TRS thermal simulation profile.

### 2.1.1 TRS Compared to Nuclear Weapon Thermal Radiation

The drawback of this type of simulator is the lack of fidelity with regard to a nuclear weapon when relating pulse shape, shape factor, and spectral color temperature. A true nuclear weapon thermal pulse is described by the dynamics affecting the resultant fireball. The nuclear weapon fireball emits about 40% of the total weapon energy in thermal radiation (Glasstone and Dolan 1977). Figure 4 shows a typical flux/time profile. As the fireball grows in size and rises above the ground, flux increases rapidly, and as the fireball expands beyond a certain radius, the radiant heat decays as the surface of the fireball cools.

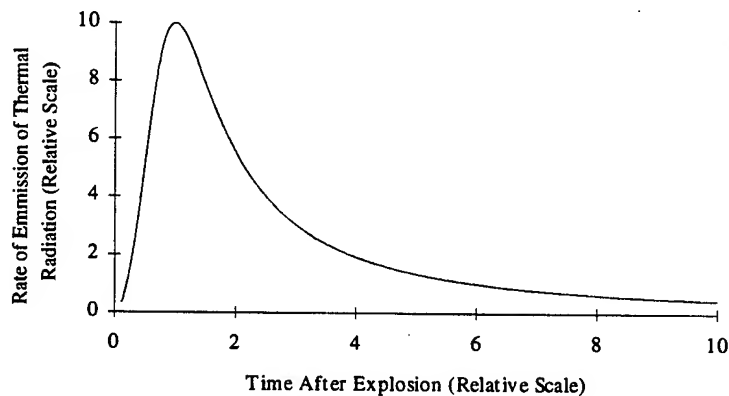


Figure 4. Nuclear thermal pulse profile, relative scale.

For a target that is expected to survive this type of environment, the pulse shape factor is fairly well determined as a radiant heat source that is very small and at a large distance from the target. The

TRS is typically about 1 m from the target. During a TRS experiment, the back and sides of the target can have undesired exposure to thermal radiation. Care must be taken to prevent this in some experiments. The aluminum boxes used to mount the NSWC composite panels served to shield the back of the panels and attached sensors from direct thermal radiation.

The blackbody temperature of a typical nuclear fireball is about 6,000 K, which can be compared to the blackbody temperature of a TRS which is about 3,000 K. Almost 87% of the TRS radiant heat energy is in the infrared region (0.78  $\mu\text{m}$  to 1,000  $\mu\text{m}$ ), the remainder in the visible light region (0.39  $\mu\text{m}$  to 0.78  $\mu\text{m}$ ). A typical nuclear weapon has about 41% of its radiant energy in the infrared region, as much as 46% in the visible light region, and about 13% in the ultraviolet region ( $5 \times 10^{-3}$   $\mu\text{m}$  to 0.39  $\mu\text{m}$ ). Targets will be affected differently, but to what extent is difficult to surmise. This is quickly demonstrated by using the *Stefan-Boltzman law*:

$$E_b = \sigma T^4,$$

where  $\sigma$  is the Stefan-Boltzman constant ( $5.670 \times 10^{-8} \text{ W/m}^2\text{-K}^4$ ), and  $E_b$  is the emissive power of a blackbody at temperature T. *Planck's law* is given as

$$E_{b\lambda}(\lambda, T) = \frac{C_1}{\lambda^5 (e^{C_2/\lambda T} - 1)},$$

where the constants values are generally accepted as

$$\begin{aligned} C_1 &= 3.7413 \times 10^8 \text{ W-}\mu\text{m}^4/\text{m}^2, \\ \text{and} \quad C_2 &= 1.4388 \times 10^4 \mu\text{m-K}, \end{aligned}$$

and the wavelength term,  $\lambda$ , is expressed in micrometers.

The blackbody emissive power shows a peak value. *Wien's law* can be deduced from Planck's and states that the maximum value of  $E_{b\lambda}$  occurs at the wavelength given by

$$\begin{aligned} \lambda_{\max} T &= C_3, \\ &= 2897.8 \mu\text{m-K}. \end{aligned}$$

The fraction of the total emission can be evaluated for specific values of wavelength. This is done by integrating the emissive power equation over the range of wavelength, which can be shown as

$$\begin{aligned} F_{0-\lambda}(T) &= \frac{\int_0^\lambda E_{b\lambda} d\lambda}{\sigma T^4}, \\ &= \int_0^{\lambda T} \frac{C_1 d(\lambda T)}{\sigma (\lambda T)^5 (e^{C_2/\lambda T} - 1)}. \end{aligned}$$

The fraction of energy emitted between two wavelengths,  $\lambda_1$  and  $\lambda_2$ , by a blackbody of temperature T is given as (Chapman 1984)

$$F_{\lambda_1-\lambda_2}(T) = F_{0-\lambda_2}(T) - F_{0-\lambda_1}(T).$$

Table 1 shows the effect of the different temperatures on the blackbody emission from the TRS at 3,000 K, and a nuclear weapon at 6,000 K.

Table 1. Effect of Temperature on Blackbody Emission.

Surface Temperature, K	3,000	6,000
Wavelength of maximum emission, $\mu\text{m}$	0.966	0.483
Total Emissive Power:		
W/m <sup>2</sup>	$4.59 \times 10^6$	$73.48 \times 10^6$
cal/cm <sup>2</sup> -s	108.9	1755.04
Spectral Fraction of Emission :		
Infrared (0.78 $\mu\text{m}$ to 1000 $\mu\text{m}$ )	0.8719	0.4092
Visible Light (0.39 $\mu\text{m}$ to 0.78 $\mu\text{m}$ )	0.1264	0.4626
Ultraviolet ( $5 \times 10^{-3}$ $\mu\text{m}$ to 0.39 $\mu\text{m}$ )	0.0017	0.1212

Spectral color temperature effects on targets can be profound due to protection by coating or surface response. Objects shielded by the target (i.e., housings, covers) may transmit thermal energy differently. For instance, oil-based white paint will reflect up to 80% of visible light, but is essentially a blackbody absorber in the infrared. During a typical TRS experiment, a target coated with white oil-based paint would burn and char to a high degree. A total of 87% of the TRS energy in the infrared would be absorbed by the target. Of the remainder in the visible light, 70% would be absorbed. About 91% of the total thermal radiant energy would be absorbed by the target. In the nuclear environment with the same thermal radiation load, the same target would be significantly less damaged. The white paint would reflect about 37% of the visible light and absorb the remaining 41% of the infrared, thus loading the target with only 78% of the thermal radiant energy. Transmissive material properties are also subject to the same effects.

### 2.1.2 TRS Simulation Profile

The TRS at ARL is the product of several years of improvement to enhance the flux and fluence repeatability between experiments (Loucks, Muller, and Thane 1994). It has served as a prototype for integration with the ARL 2.44-m probative shock tube and as a test-bed for state-of-the-art TRS performance improvements. When a TRS is incorporated into the 2.44-m tube, it will provide an excellent test-bed facility for simulated nuclear thermal and blast synergistic loading experiments. However, it has been determined that, despite improved simulation performance, the TRS is incompatible with the desired integration. The TRS continues, however, to serve as an excellent simulator for experiments requiring high radiant heat for about 500 ms. At the present time, the TRS remains in the 2.44-m tube section as depicted in Figure 5.

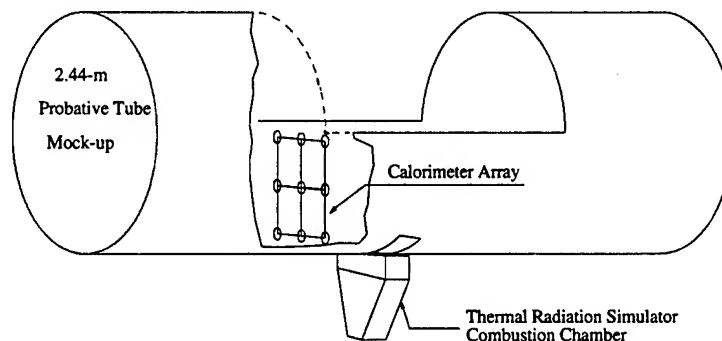


Figure 5. 2.44-m probative tube and TRS showing calorimeter array.

Data collected for several years from the ARL TRS have resulted in a thermal database. Each contour line represents fluence for a given experiment. Data between various calorimeters used during

The isoradiance contours seen in Figure 6 are linearly derived from the fluence data of the nine calorimeters during a given test. The desired thermal loading was determined to be in the middle of the upper right hand quadrant. This was selected because of ease of mounting the target to the calorimeter frame. The average flux is derived using a Fourier Averaging Method (Loucks 1990).

## 2.2 Experiment Setup

The NSWC tested a full scale radome during the MINOR UNCLE experiment. To investigate the effect of infrared (IR) transmission, NSWC used four rectangular panels made of the same material as the radome. This was done to reduce the cost of the IR experiment since the material would be destroyed with each experiment. The panels were readily available. A radome would have taken a great deal of time to fabricate and deliver. Another advantage of using the panels was that extra panels could be tested to verify reproducibility of the TRS and experimental procedure. Several methods of mounting the thermal and strain sensors could be tried and evaluated, and the thermal loading could be varied for each experiment.

Each test panel was made from a fiberglass/epoxy composite. The panels were of two different thicknesses, 3.17 mm and 6.35 mm. Each panel was 20.32 cm by 30.48 cm in size except the last panel. It measured 6.35 mm in thickness and was 30.48 mm by 30.48 mm. All panels were coated with a glossy white polyurethane paint. The edges and back were bare. The thermocouples and strain gages were mounted on the back, as shown in Figure 7.

### 2.2.1 Instrumentation

The TRS facility at ARL is set up primarily to perform research concerning the simulation of nuclear thermal radiation. Much of the thermal radiation simulator assessment is done by direct measurement of the TRS output and its effect on experimental targets. The data acquisition system at the ARL TRS facility is a MEGADAC 2200C, manufactured by OPTIM Electronics. A personal computer (PC) controls the TRS and the MEGADAC. The MEGADAC operates sequentially, sampling data from each channel in a stacked fashion. The data are stored digitally in the MEGADAC and retrieved with the PC when desired (Loucks, Muller, and Thane 1994).

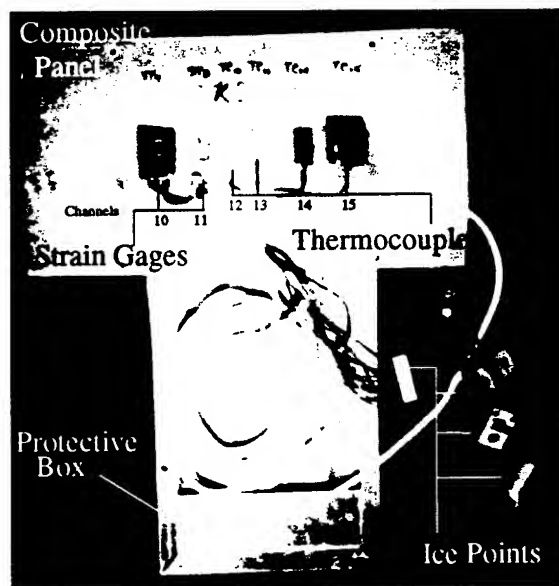


Figure 7. Composite panel with sensors mounted on back.

The Gardon-type gage is the primary transducer used to measure thermal flux. The gage is basically a constantan diaphragm welded to a copper wire and body. This particular construction generates two thermocouple junctions. The diaphragm acts as the heat transfer sensor while the main copper body acts as a heat sink.

### 2.2.2 Experiment Setup and Process

During the NSWC test, the TRS, instrumentation array, and composite panels were set in a mocked-up section of the 2.44-m probative tube, which was depicted earlier in Figure 5. The photograph in Figure 8 is an NSWC composite panel mounted on the test frame. The custom-made frame was fabricated for a similar, previous test of a larger panel.

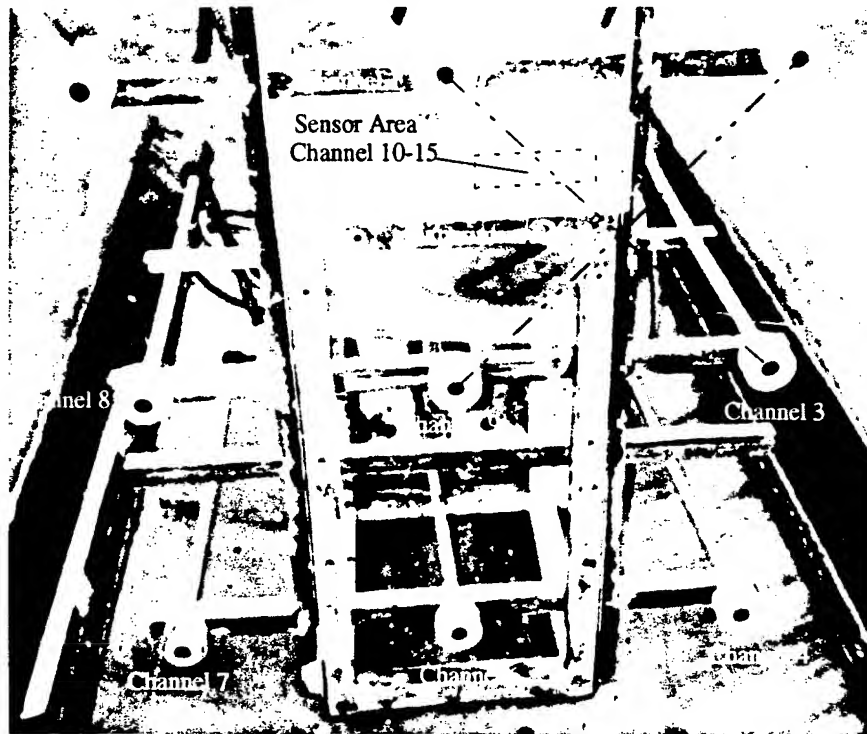


Figure 8. Composite panel on calorimeter array frame.

All NSWC composite panels were mounted in the upper right quadrant of the calorimeter array. This location was chosen after reviewing the data shown in Figure 6. Instrumentation cables were run out the end of the 2.44-m tube through a metal flexible conduit. The conduit was used specifically to protect the cables from thermal effects. All junctions were connected in a junction box with terminal strips. Cables from the junction box traveled underground in a PVC conduit to the instrumentation control bunker. In the bunker, the cables were terminated on junction cards made specifically for the MEGADAC 2200C.

Output voltages from all calorimeters and thermocouples were connected directly into the MEGADAC 2200C as described. Strain gages passed from the junction box to a portable two channel Wheatstone bridge network located in the bunker. Output from the bridge network was connected to the MEGADAC through the junction cards.

Transducers were examined and tested for continuity and channel assignment before each test. Calorimeters were visually examined and tested by briefly applying a flame from a hand-held propane torch to the calorimeter in question and observing the response on the computer screen. The thermocouples and strain gages were visually checked for secure mounting and condition, and were electrically examined for continuity, but they were not tested for functionality as were the calorimeters.

The TRS was operated at least once before each experiment to ensure the system was functioning properly. Once the TRS was determined to be performing as expected, and the instrumentation was verified as operating as expected, the experiment proceeded. The panel was secured to the mount, the instrumentation was monitored, and the experiment countdown was initiated.

Each component of the TRS system requires a finite amount of time to function. An example is preflowing of LOX to the nozzle to precool and condition the LOX delivery system. This is done to ensure that there is adequate oxygen for stoichiometric combustion. The line that supplies the LOX is cooled for about 10 s by flowing LOX while diverting the LOX away prior to the mixing point in the nozzle. As the LOX pipe cools, the LOX evaporation rate inside the line is decreased. The result is that nearly all of the oxygen that enters the mixing chamber is in liquid form. This supplies enough oxygen mass flow to provide stoichiometric combustion with the aluminum powder. The aluminum powder must also be preflowed to establish a steady mass flow rate to the nozzle. The stoichiometric mixture flows past the pilot flames, ignites, and produces high-intensity thermal radiation on the target panel, as can be seen in the photograph in Figure 9.

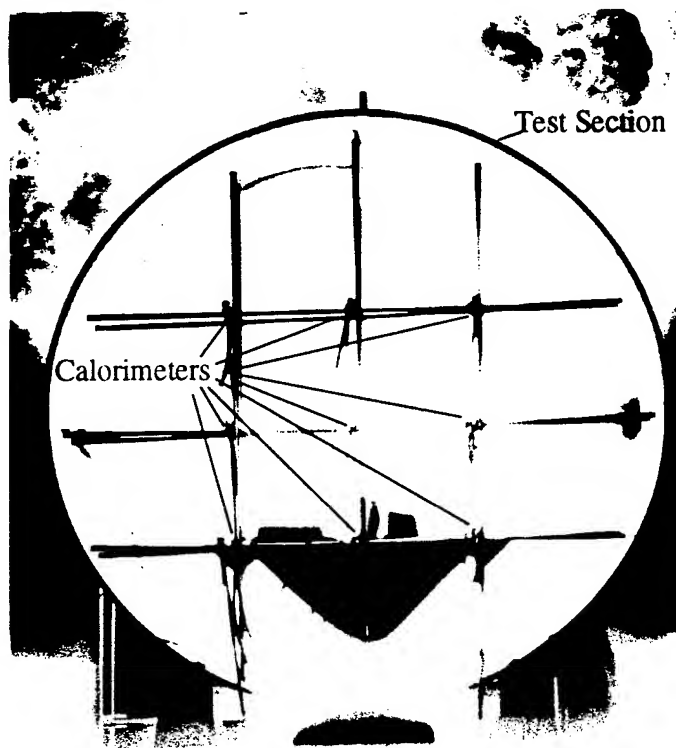


Figure 9. TRS in test section.



experiments were interpolated with a second-order curve fit and, in the same manner, extrapolated to the area outside the calorimeter region. A smooth curve was used to connect the resultant decade flux levels.

It is evident from the contour plot that thermal irradiance from the TRS is not symmetric about the vertical axis. This peculiarity persists, even in different wind conditions. A theory of why this occurs is related to the method in which the aluminum powder is transported to the combustion chamber. The aluminum powder is stored in a pressurized vessel about 15 m from the combustion chamber. A 5-cm-diameter copper tube spans the distance. The aluminum powder is transported through the pipe by means of nitrogen gas blowing through the pipe. Just before it reaches the combustion chamber, the aluminum must turn 90° in a special copper tube. The tube is constructed such that the cross section is circular during the turn. The turn is a gradual curve, as opposed to an elbow fitting, with a radius of curvature at about 75 cm. This was done to minimize flow restriction. The 90° bend may be the cause of the asymmetry in the thermal map. Aluminum powder may concentrate on one side of the tube running in the vertical direction. When the LOX is injected into the powder, the rotational momentum must turn the concentration to the opposite side. When the mixture enters the combustion chamber, a higher concentration may be on one side, resulting in the asymmetric thermal mapping. This is not particularly detrimental to TRS performance, but it does limit the size target that can be tested with uniform irradiance. Asymmetrical irradiance also limits application of the TRS to the probative shock tube. Target placement is normally in the center of the tube cross section. Due to the asymmetry, the maximum radiation would be shifted to one side of the tube.

For small targets, approximately 30 cm by 30 cm, this is not a problem, and the ARL TRS performs well. NSW personnel wanted to repeat the MINOR UNCLE experiment, but with small flat panels as opposed to a full-scale radome. This was primarily due to cost constraints, flat panel specimens being much less expensive to test than a full-scale radome. The procedure for the NSW experiments at ARL would be simple; perform about three TRS experiments to locate the area of desired flux and fluence, then test each panel individually. The desired loading levels were **50 cal/cm<sup>2</sup>-s** flux and **75 cal/cm<sup>2</sup>** fluence. The pretest firings were done with 10 calorimeters, 9 of which were spaced 45 cm apart in an even rectangular array in 3 rows of 3 calorimeters. The remaining calorimeter was placed on the opposite side of the TRS to help evaluate consistency of the TRS with prior experiments. The results of these experiments resulted in contour plots of an average flux and fluence presented in Figure 6.

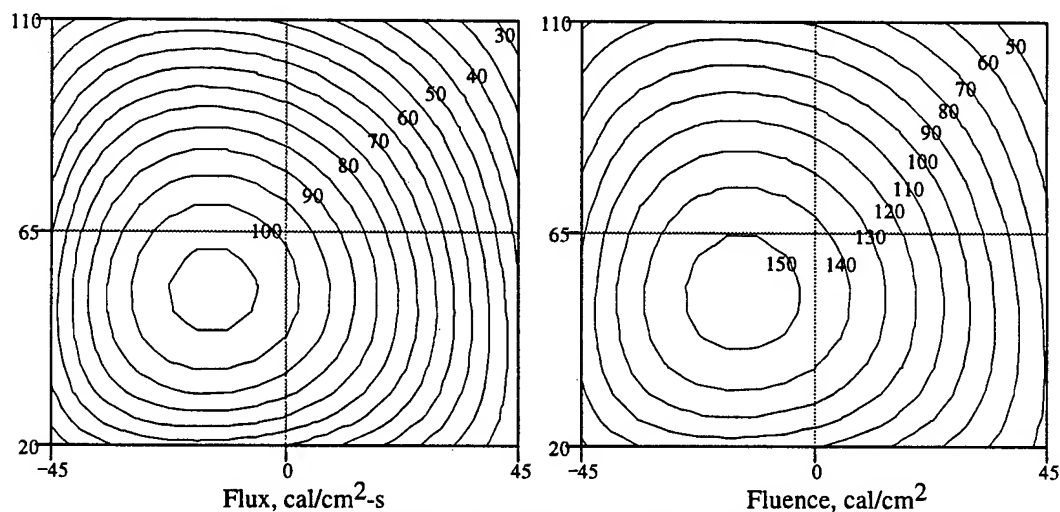


Figure 6. Pre-experiment contour plots at 60 cm.

## 2.3 Post Experiment Process

After each experiment, collected data were transferred from the MEGADAC to a personal computer via an IEEE interface. An ASCII file was created for each data channel and saved on two hard drives and a floppy disk. The beginning of each file had a header section that contained information about that particular channel in the following format: experiment title, experiment number, transducer station, abscissa label, abscissa units, ordinate label, ordinate units, time of arrival and time between samples, in milliseconds, and the number of data points. The data point values immediately followed. This was done so that the data were easily transported to another system for analysis by other researchers.

A quick look at the data immediately revealed that the effect experienced at WSMR was being repeated. The sensors were generating a highly transient signal before the thermal conductive effects could be applied.

## 3. DATA ANALYSIS

There were five TRS experiments. The last panel was tested twice. The data were successfully captured by the MEGADAC 2200C and transferred for analysis on a personal computer. A software product called DADiSP 3.0 was used to analyze the data. DADiSP was limited in only being able to create Fast Fourier Transforms of the data sets. Full Fourier Transforms of the data were performed with a utility written for that purpose (Loucks 1988). Extraction of the forcing mechanism was used to verify that the TRS energy was directly affecting the sensors on the panel backside.

Both the thermocouple and strain gage data repeated the initial high transient phenomenon found in the MINOR UNCLE data. The initial temperature increase is theorized as being a result of the thermal radiation from the TRS directly irradiating the sensor and the material used to mount the sensor. Typically, metals have a very low thermal radiation absorptivity coefficient,  $\alpha'_n$ , across all ranges of thermal radiation (typically  $\alpha'_n = 0.5 - 0.18$  for a highly polished surface, and  $\alpha'_n = 0.75$  for a heavily oxidized surface). The thermocouples used in these experiments were highly polished due to the thermocouple junction being joined by soldering and the solder cooling with a smooth, highly reflective surface, resulting in  $\alpha'_n \approx 0.07$ . The strain gages were observed to also have a highly polished surface. This indicates that the majority of the radiation incident to the sensor would be reflected back into the composite material. This thermal energy would eventually be conducted back to the sensor. Any material used to mount the sensor is obviously in contact with a large portion of the sensor surface. The thermal radiation incident to a large absorptive foil, such as black vinyl tape, used to secure a sensor to the panel may have absorptive coefficients ranging from  $\alpha'_n = 0.20$  for aluminum tape to  $\alpha'_n = 0.88$  for black tape. The relatively large area of the backing would act as a thermal collector, and the heat would conduct to the sensor and the area of composite in contact with the backing. In general, the area thermal state would increase in proportion to the amount of thermal energy irradiating in the components.

In order to prove this, sensor data would have to be directly related to TRS data. Two techniques were explored. The Fourier Transforms of the TRS data and the sensor data were compared for common frequencies. An additional technique actually used sensor data to reveal the TRS data by filtering out the expected material response and isolating the transient effects. A method of extracting the influencing function was compared to the TRS data to see if the forcing function matched the influencing function.

### 3.1 TRS Data

All TRS data were captured. Unexpected flames from the panel on the last experiment caused the level of one channel, channel 1, to go so high that the output voltage exceeded the upper band-edge of the recording device, thus the true peak level of the data for that channel on the last test is unknown. Recorder sample rate was 200 Hz. Flux levels were expected to range from  $30 \text{ cal/cm}^2\text{-s}$  to  $120 \text{ cal/cm}^2\text{-s}$ .

for brief periods. Desired fluence levels for the experiment dictated that the TRS burn for 1.5 s. Figure 10 shows the data captured from channel 9, the low center calorimeter, for all five experiments. TRS titles correspond to the experiment. TRS-7-94 was the first experiment, TRS-8-94 was the second, etc. Table 2 lists important parameters from each experiment.

Table 2. Group Parameters

TRS Station	TRS-7-94		TRS-8-94		TRS-9-94	
	Flux	Fluence	Flux	Fluence	Flux	Fluence
-60/-45/110	42.49	46.39	34.55	47.64	44.44	46.60
-60/0/110	46.56	51.16	34.64	48.37	49.28	53.09
-60/45/110	21.76	25.77	17.00	24.99	29.41	29.35
-60/-45/65	68.83	75.04	63.48	87.74	73.91	76.97
-60/0/65	88.97	101.12	83.50	116.27	99.22	105.81
-60/45/65	35.33	39.73	30.73	43.49	43.31	42.11
-60/-45/20	68.41	72.63	66.96	93.08	69.98	73.77
-60/0/20	72.46	79.87	73.78	103.94	76.39	81.59
-60/45/20	43.26	49.16	41.56	58.00	39.72	43.78

TRS Station	TRS-10-94		TRS-11-94	
	Flux	Fluence	Flux	Fluence
-60/-45/110	35.46	15.31	40.67	143.029
-60/0/110	52.00	20.63	60.00	222.00
-60/45/110	23.90	9.43	21.41	80.41
-60/-45/65	48.42	19.67	70.726	250.47
-60/0/65	84.86	33.05	89.45	334.16
-60/45/65	30.37	12.44	41.73	151.92
-60/-45/20	48.92	18.66	64.74	234.84
-60/0/20	66.72	25.23	74.47	273.34
-60/45/20	27.64	11.46	44.32	164.57

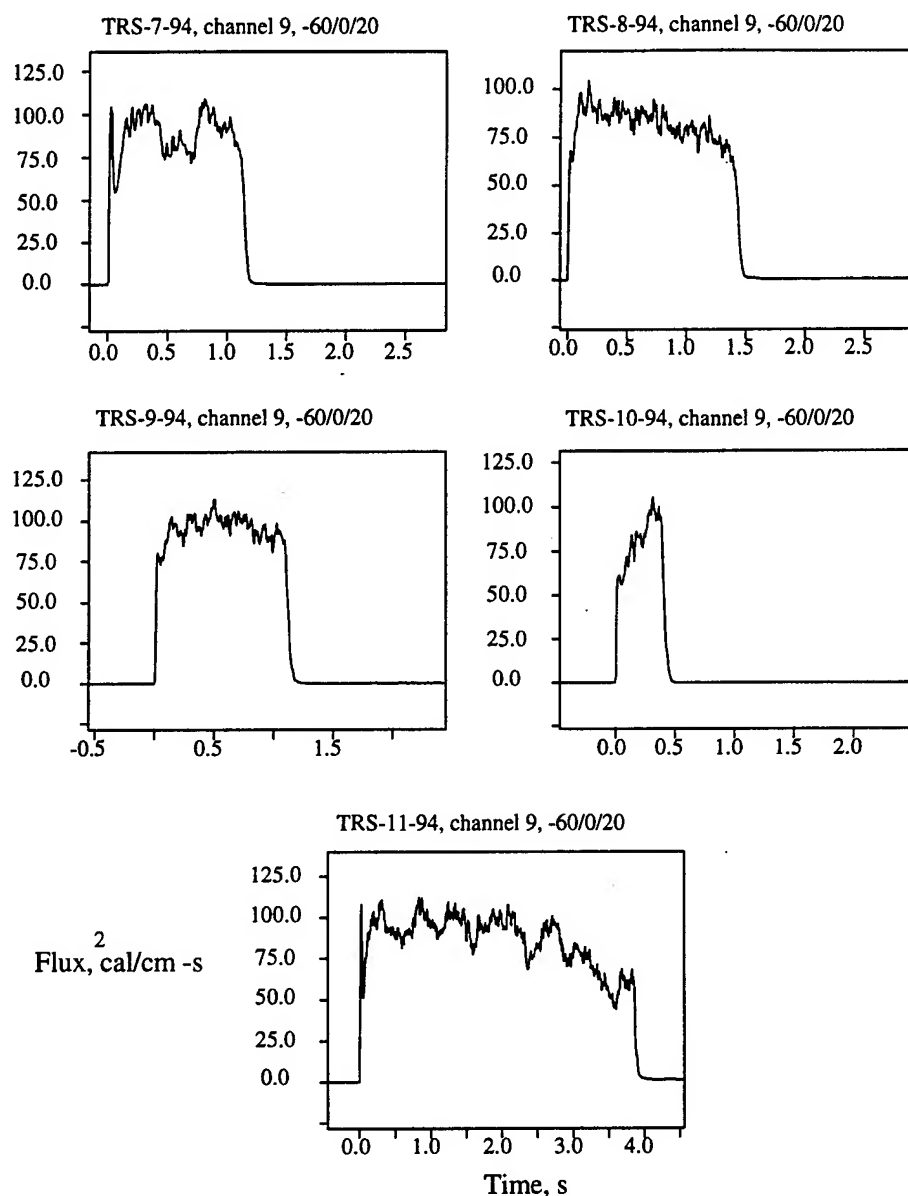


Figure 10. Thermal radiation data for each experiment at channel 9.

### 3.2 Thermocouple and Strain Gage Data

Thermocouple and strain gage data were collected during each test for a period of 60 s. This time interval permitted collection of early transients as well as the longer term response. In all cases, the thermocouple data were good. The strain gages were more delicate, and some channels of strain data were lost during the experiments. The data were captured using the same data acquisition system as the TRS data. The sample rate was 200 Hz. The thermocouples were connected to commercial ice points, then the signal sent directly into the MEGADAC. The strain gages were conditioned through a two-channel Wheatstone bridge/amplifier, and the resultant signal sent to the MEGADAC.

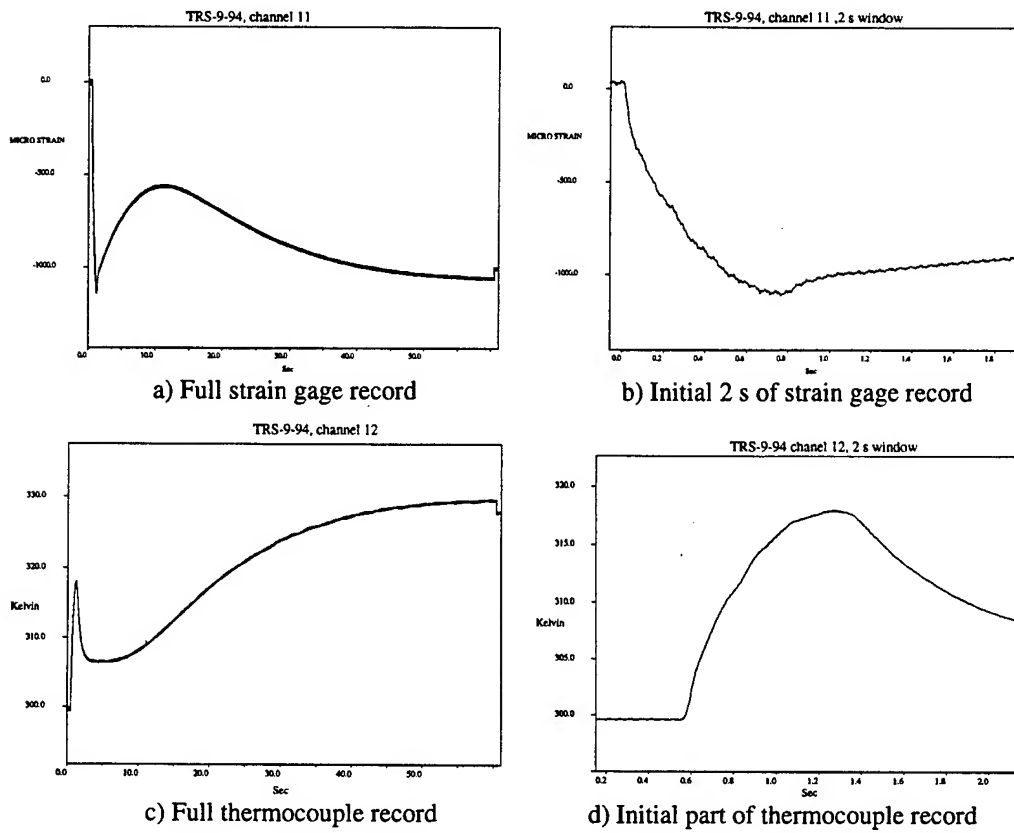


Figure 11. Sensor data from channel 12 and 13, TRS-7-94.

Data from the thermocouples exhibited the same transient phenomenon found in the data from the MINOR UNCLE test. Figure 11 shows the channel 12 thermocouple from TRS-10-94, the only experiment with a complete data set. The distinct initial transient is evident. Figure 12 shows the calorimeter data from the closest calorimeter to the panel.

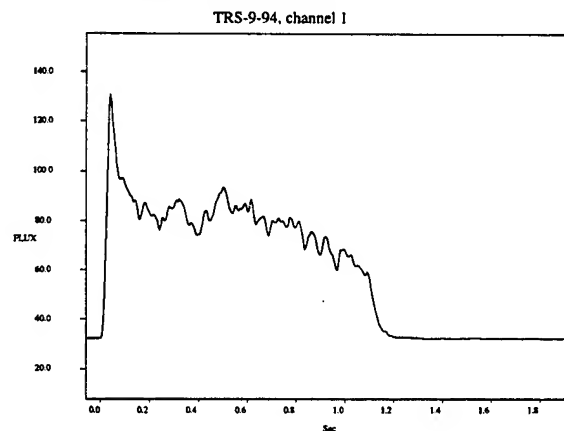


Figure 12. TRS-9-94, calorimeter closest to composite panel.

### 3.2.1 Fourier Transform Analysis.

To identify the source of the transient, it was suggested that a Fourier Transform of the data out to 20 Hz might show a relation between the TRS data and the thermocouple data. A numerical program (Loucks 1988) was used to take the direct Fourier Transform of the data. The results of that transform is shown in Figure 13. The Fourier Transform being defined as

$$G(f) = \int_{-\infty}^{\infty} F(t)e^{-i2\pi ft} dt,$$

where

$f$  is frequency,

$t$  is time,

$G(f)$  is the transformed function in the frequency domain, and

$F(t)$  is the function in the time domain.

The Fourier transform can be used to identify features in the frequency domain that are masked in the temporal domain. The result of such a transformation results in real values and imaginary values. The magnitude of the Fourier transform is the square root of the sum of the squares of the imaginary and real components. The transform was not taken out any further than 20 Hz. The magnitude of the signal beyond this frequency is well within the noise band of the instrumentation.

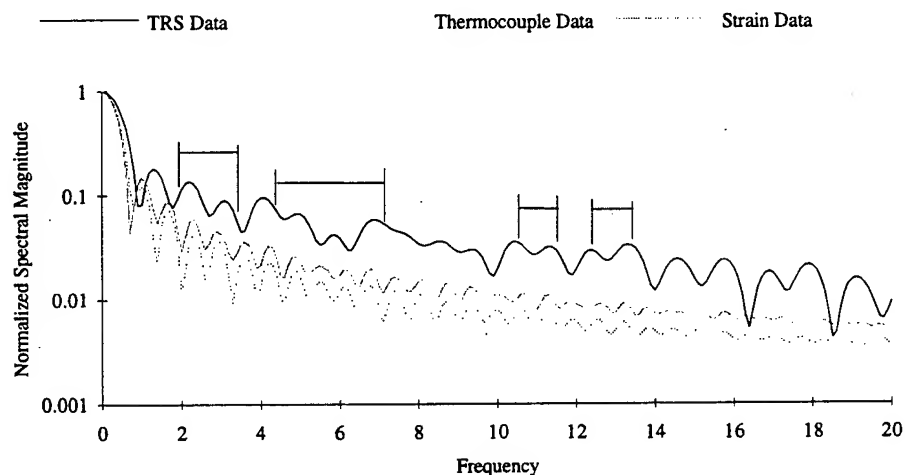


**Figure 13. Magnitude of Fourier transform of thermocouple data and TRS data.**

Few relational features between the TRS data and the sensor data are outstanding in the Fourier Transforms. There is a strong comparison at intervals in the record. These are pointed out by the brackets in Figure 13. If one were to express the transforms in terms of the coefficients of a Fourier series, the thermocouple and strain gage data coefficients would match very well. One could conclude that the phenomenon influencing the thermocouple is the same phenomenon influencing the strain gage. The TRS data coefficients are different. There are points of similarity, such as at 3, 6, 11, and 13 Hz. This indicates the influence of thermal radiation transmission from the TRS. The relation between the sensor response and the transmitted thermal energy is circumstantial, and far from conclusive.

### 3.2.2 Forcing Influence Extraction From the Data

A method of extracting the forcing influence from the response data was derived to demonstrate direct thermal radiation energy influence on the gages. The method involved several steps which are outlined in this section. An example is shown using thermocouple data described in the previous section.

The first step was to determine the signal that was likely to occur without any initial transients. This can be done in one of two ways. The first way, which is much more difficult, would be actually to calculate the target response without transmission effects. An analytical method and a numerical simulation using finite differencing (Loucks 1990) are two possible ways to obtain the response. The second and easier method was to make a simple curve fit of the data without the initial transient. By eliminating a short period of the initial data, a least-squares fit of the slower response was made. Figure 14 graphically illustrates a fifth-order polynomial least-squares fit of the thermocouple data with the first 12.5 s of data removed.

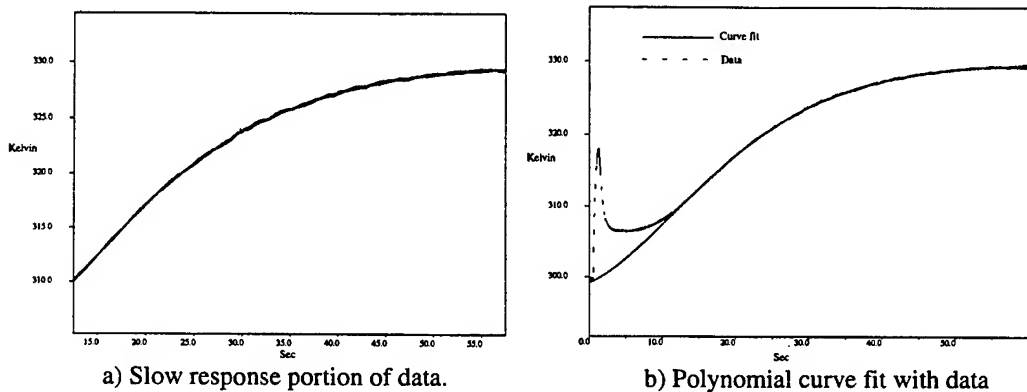


Figure 14. Obtaining a curve from data.

The polynomial used in this curve fit was

$$T(t) = 298.4926 + 0.82904t + 0.10505t^2 - 4.5249 \times 10^{-3}t^3 - 6.976 \times 10^{-5}t^4 - 3.9 \times 10^{-7}t^5,$$

where  $T(t)$  is the temperature in degrees Kelvin, and  $t$  is time in seconds.

The second step was to subtract the curve fit from the data to isolate the initial transient. Figure 15 demonstrates this step.

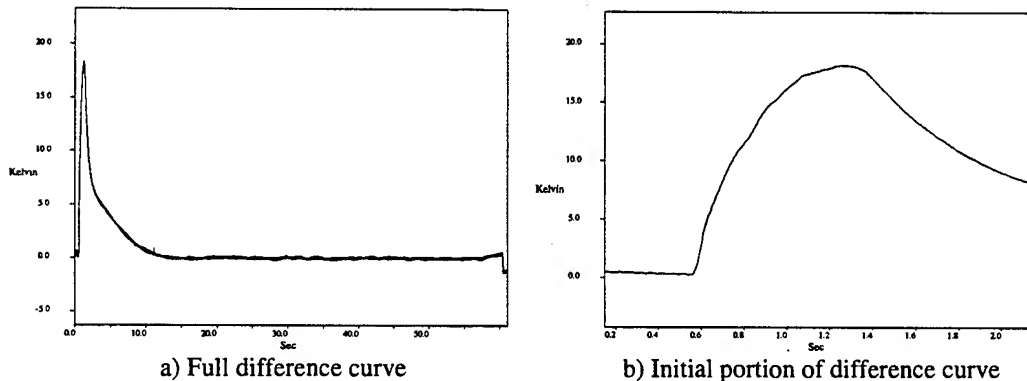


Figure 15. Initial transient isolated from conduction data set.

The curve in Figure 15b appears exponential in form. A thermocouple has an associated, first-order response time. One could conclude that the influencing phenomenon which caused the thermocouple to gain heat is masked by thermocouple response time. If the thermocouple acted as an ideal transducer, the curve of Figure 15 would appear quite different. In fact, it would show the influence in great detail. Using a method to compensate transducer output to that of an ideal, rapid rise time transducer (Loucks, Muller, and Thane 1994), the influencing phenomenon is revealed in Figure 16. The method is to take the signal and add to it its first derivative multiplied by a constant,

$$T_i = T_m + \frac{1}{C_t} \frac{dT_m}{dt},$$

where  $T_i$  is the actual temperature if the influencing phenomenon,  $T_m$  is the thermocouple output,  $C_t$  is the rise time constant, and  $t$  is time.

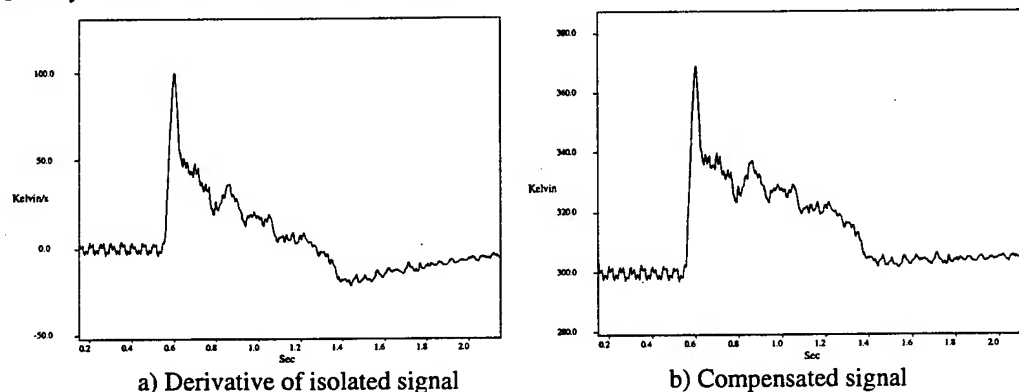


Figure 16. Compensated transducer signal.

The final step was to compare the compensated signal with the nearby calorimeter signal. If the signals are similar, then the TRS output can be directly linked to the initial transient signal. Figure 17 compares the TRS output that was shown in Figure 12 and the compensated signal results from Figure 16b. The traces have been normalized (divided by the maximum positive value in the data set) for comparison.

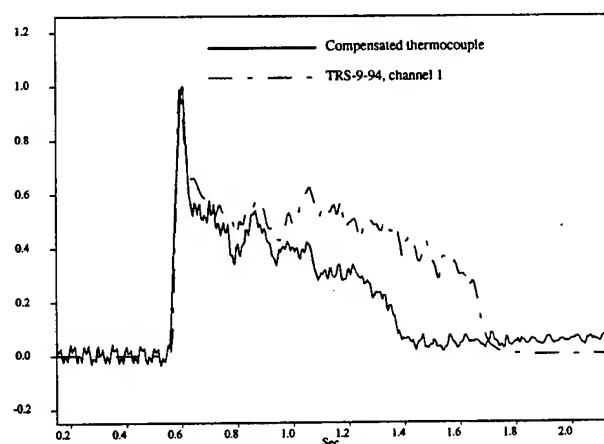


Figure 17. Comparison of normalized signal.



This result demonstrates a clear relation between the initial influence and the TRS output. The signals are identical in the initial 0.1 s. Eventually the thermocouple signal diverges away from the TRS signal with time. This can be attributed to the composite material or the coating on the front face undergoing a property change. At about 0.8 s into the event, the transient thermocouple signal dropped, even though the TRS was still burning. It was later discovered that this was when the painted surface started to emit smoke, protecting the composite material from further direct thermal radiation damage.

## 4. RESULTS

### 4.1 Thermal Effects Due to Different Mounting Methods

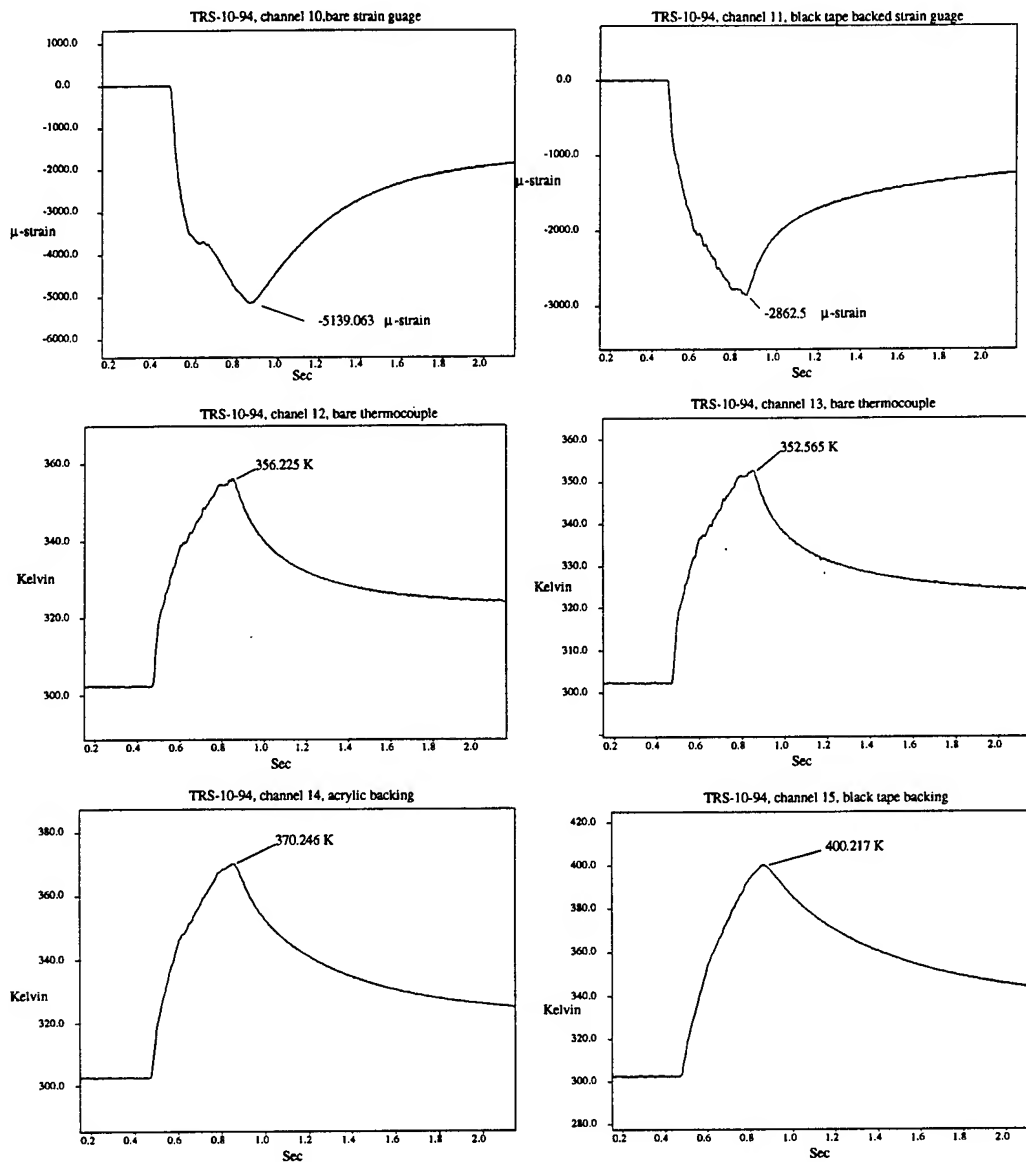
The different mounting used to secure the sensors to the rear face of the panel resulted in a difference in how each sensor responded. The heating effect by thermal radiation transmission is increased when using a backing that is a good thermal radiation absorber. The bare sensors reached a higher peak value when a backing was used. The higher the absorptivity of the backing, the higher the peak value measured. Figure 18 demonstrates this from TRS-10-94. Table 3 lists the temperature and strain values reached for each experiment.

Table 3. Peak Values From Thermal Radiation Transmission Effect

Channel	TRS-7-94	TRS-8-94	TRS-9-94	TRS-10-94	TRS-11-94
10: Bare Strain Gage	NA	-1703 $\mu\epsilon$	NA	-5139 $\mu\epsilon$	-6446 $\mu\epsilon$
11: Black Backed Strain Gage	NA	-726.9 $\mu\epsilon$	-1137 $\mu\epsilon$	-2862 $\mu\epsilon$	-4011 $\mu\epsilon$
12: Bare Thermocouple	384.6 K	NA	317.8 K	356.2 K	379.1 K
13: Bare Thermocouple	383.2 K	NA	314.6 K	352.6 K	375.8 K
14: Acrylic Backed Thermocouple	406.8 K	324.7 K	314.1 K	370.3 K	402.7 K
15: Black Backed Thermocouple	395.4 K	NA	321.4 K	400.2 K	455.7 K

Table 4. Peak Values From Thermal Conduction Effect

Channel	TRS-7-94	TRS-8-94	TRS-9-94	TRS-10-94	TRS-11-94
10: Bare Strain Gage	NA	-1250 $\mu\epsilon$	NA	-1965 $\mu\epsilon$	-5318 $\mu\epsilon$
11: Black Backed Strain Gage	NA	-969.9 $\mu\epsilon$	-1059 $\mu\epsilon$	-1453 $\mu\epsilon$	-5126 $\mu\epsilon$
12: Bare Thermocouple	399 K	NA	329.4 K	344.5 K	466.94 K
13: Bare Thermocouple	399.6 K	NA	330.1 K	342.6 K	464.7 K
14: Acrylic Backed Thermocouple	406.2 K	NA	330.3 K	341.6 K	NA
15: Black Backed Thermocouple	414.7 K	NA	330.5 K	344.2 K	NA



**Figure 18. Comparison of thermal radiation effect on each sensor.**

As seen in Table 4, the longer term conductive effects on strain show a much smaller deviation between mounting types. There is no recognizable difference in the thermocouple measurements. The difference in the strain could be attributed to the location of the strain gage on the panel. The bare strain gage was placed closer to the panel's edge, and possibly there was a combination of strain relief from the edge, as well as conductive cooling from the plate mount. The difference is consistent for each experiment.

## 4.2 Thermal Radiation Transmission

The final two experiments included a highly sensitive calorimeter which was also a Gardon-type gage. The calorimeter was placed behind the panel with 1 cm space between the calorimeter face and the back of the panel. This calorimeter was able to measure the amount of thermal radiation transmitting through the composite panel. The first experiment with this calorimeter, TRS-10-94, is shown in Figure 19.

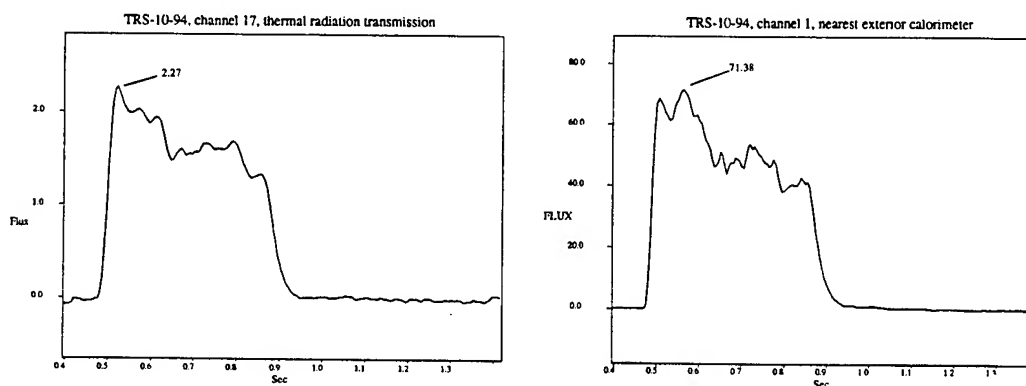


Figure 19. Thermal radiation transmission, TRS-10-94.

The peak thermal flux was  $2.27 \text{ cal/cm}^2\text{-s}$ , and the total fluence was  $0.663 \text{ cal/cm}^2$ . When compared to the data from channel 1, the panel allowed an average 3.09% of the radiant thermal energy to be transmitted.

## 4.3 Smoke Generation and Protection

The second transmission experiment, TRS-11-94, was conducted with the same composite panel used in TRS-10-94. A secondary objective was to determine the point at which smoke may be generated from the panel, and the degree to which it afforded protection from thermal radiation. Figure 20 shows the thermal radiation data of that experiment.

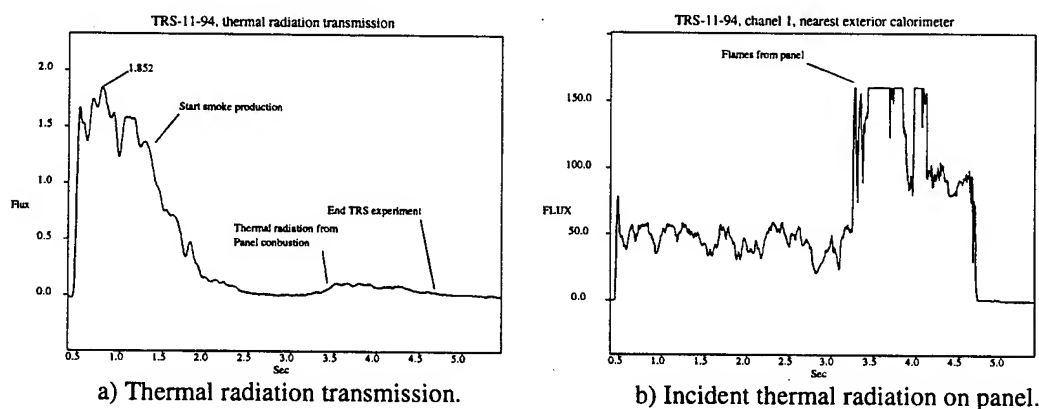


Figure 20. Thermal Radiation transmission, TRS-11-94.

The fluence measured by the calorimeter behind the panel was  $1.88 \text{ cal/cm}^2$ . The peak flux was  $1.852 \text{ cal/cm}^2\text{-s}$ . One can deduce from the data shown that smoke generation can fully protect a target from thermal radiation transmission. As seen in Figure 20a, in a little less than 1 s into the experiment,

smoke from the panel began to obscure the transmission. During this time, the panel was allowing 3.87% of the thermal radiant energy through. About 0.5 s later, the level of thermal transmission had disappeared. At about 2.75 s into the experiment, the panel ignited and began to burn. Some of the energy produced by the combustion radiated through the panel, and amounted to about 0.2 cal/cm<sup>2</sup>-s. Smoke continued to obscure the TRS energy until the end of the experiment.

The panel was completely destroyed after the experiment. It had ignited and burned. The flat profile at 150 cal/cm<sup>2</sup>-s was due to the signal exceeding the band edge of the data recorder. The high levels were due to the panel combustion and the hot combustion products enveloping the calorimeter. No other calorimeter demonstrated this behavior, which eliminated the possibility of a TRS flare.

## 5. CONCLUSIONS

A simple problem in the instrumentation of composite materials has opened a question with regard to protection from thermal radiation effects. Obviously, thermal radiation can be transmitted through composite materials. The question is, to what degree is the equipment that the composite material is designed to protect affected? In the series of experiments discussed, the amount of energy being transmitted was relatively low. Some simple things could be done to reduce the amount of thermal radiation transmission, such as using thicker composite, injecting an opaque dye into the composite matrix material, or using surface coatings that produce heavy smoke when irradiated.

The answer to eliminating the thermal radiation transmission effect from sensors used to measure material response is left unknown. The effort of this experiment was to determine the cause of an unusual behavior in the early part of the data. This was done without any doubt, the cause being thermal radiation transmission through the composite which directly affected the sensor. How does one eliminate this from future work? This could be done by recognizing what the effect is and eliminating it from the data. This could prove to be extremely difficult in some cases and does not make for a sound experimental technique. Another method of eliminating this effect needs to be developed. Perhaps some form of radiation shielding that is similar to that used with thermocouples measuring air temperature in a room, where the walls are at a different temperature than the air, could be used. The shielding could be baked into the composite material with the thermocouple. This would also present certain disadvantages, such as being a potential point for delamination of the material when it is under stress.

Further research in this area is necessary to develop better methods of radiation compensation in semitransparent materials. A supply of composite materials and the use of the TRS facility at ARL would present a unique opportunity to conduct this type of investigation to determine and design effective techniques of taking thermal radiation measurements of nonopaque materials.

## 6. REFERENCES

Chapman, A. J. Heat Transfer. 4th Edition, New York: McMillan Publishing Company, 1984.

Glasstone, S., and P. J. Dolan. The Effects of Nuclear Weapons. Department of the Army Pamphlet No. 50-3, Headquarters, Department of the Army, Washington, DC, March 1977.

Loucks, R. B. "TRSFT.BAS." A basic program to perform a Fourier transform of a function in time described by an ASCII table. U.S. Army Ballistic Research Laboratory, Aberdeen Proving Ground, MD, September 1988.

Loucks, R. B. "Thermal Radiation Simulator Characterization Methods for the Rectangular Pulse." BRL-TR-3148, U.S. Army Ballistic Research Laboratory, Aberdeen Proving Ground, MD, September 1990.

Loucks, R. B., P. C. Muller, and R. Thane. "Rebuilding and Modeling of a Thermal Radiation Source." ARL-TR-501, U.S. Army Research Laboratory, Aberdeen Proving Ground, MD, August 1994.

# Turbulent Boundary Layers in Airblast Precursors

A.L. Kuhl and J.B. Bell

*Lawrence Livermore National Laboratory, Livermore, CA*

R.E. Ferguson, K.-Y. Chien and J.P. Collins

*Naval Surface Warfare Center, Silver Spring, MD*

## Abstract

Explosions always contain turbulent mixing regions such as boundary layers, shear layers, wall jets and unstable interfaces. The inherent unsteadiness of turbulent mixing in explosions and the lack of sufficient data, pose extraordinary difficulties for traditional turbulence modeling of such flows. Proposed here is a large eddy simulation approach—where the three-dimensional (3-D) conservation laws are integrated via a high-order Godunov method. Adaptive Mesh Refinement (AMR) is used to capture the convective-mixing processes on the computational grid. Then, azimuthal-averaging is applied to the 3-D solution in order to extract the instantaneous mean and fluctuating components of the turbulent field. As an illustration, this methodology is applied to the numerical simulation of the turbulent wall jet and dusty boundary layer flow induced by a point explosion above a ground surface. Principal results include the evolution of the turbulent velocity field near the surface. During the wall-jet phase, the mean profiles resemble previous two-dimensional calculations, while the velocity fluctuation profiles and Reynolds stress profiles are qualitatively similar to measurements of self-preserving wall jets. During the boundary-layer phase, mean velocity profiles evolved with time, for example: initially they agreed with measurements of a dusty boundary layer behind a shock; at intermediate times they resembled the dusty boundary layer profiles measured in a wind tunnel; while at late times, they approached a  $1/7$  power-law profile. Velocity-fluctuation profiles were qualitatively similar to those measured for a turbulent boundary layer on a flat plate. This diagnostic procedure can be used to analyze the evolution of other turbulent fields arising from symmetric initial and boundary data such as dust clouds, axi-symmetric jets, fireball instabilities, and dusty boundary layers in shock-tube and wind-tunnel flows.

## 1. Introduction

Explosions always contain embedded turbulent mixing regions such as boundary layers, shear layers, wall jets, and unstable interfaces. There are two approaches that can be used for numerical calculations of such turbulent flows, namely, turbulence modeling or direct numerical simulation. Let us first contrast the strengths and weaknesses of each approach.

Traditional turbulence models all begin by averaging the conservation laws. In physics this is known as the mean-field approximation, which works well if fluctuations are always small compared to mean values. However, density fluctuations are not small in explosions, for example, densities can vary by five orders of magnitude between the hot fireball gases and the dense fluidized bed in the dusty boundary layer along the surface. In addition, as pointed out by Chorin (1975), the equations of fluid dynamics are nonlinear, so the integration of the averaged equations does not equal the average of the integrated equations. This implies that turbulence model equations are not predictive, i.e., they cannot accurately forecast turbulent flows which lack a significant data base. Thus, the traditional turbulence models (e.g.,  $k$ - $\epsilon$ , Reynolds-stress,

etc.) require an extensive data to tune the modeling coefficients. The inherent unsteadiness of turbulent mixing in explosions poses a particularly difficult challenge in this regard (e.g., it is impractical to measure ensemble-averaged flow properties such as Reynolds stresses in explosions). Hence, for this class of flow, one must resort to other approaches that are not tied to the limitations of integrating the averaged equations.

Due to recent advances in computational power and improvements in numerical algorithms (e.g., nonlinear monotone schemes and adaptive mesh refinement), it is now feasible to perform detailed simulations of three-dimensional (3-D) turbulent flows. Recent studies by Bell and Marcus (1992), and Oran and Boris (1993) have shown that numerical solutions of the 3-D conservation laws that are based on monotone upwind schemes exhibit all the properties associated with turbulent flows—including a power spectrum with a slope of  $-5/3$  in the inertial range—if enough grid resolution is used. The problem then becomes: how can one extract order from this turbulent 3-D solution? For example, in engineering applications one is primarily interested in the mean flow. Clearly, the way to construct the mean of nonsteady flows is by ensemble averaging, but it is impractical to perform hundreds of 3-D calculations.

To solve such dilemmas, this paper presents a methodology for evaluating averages of turbulent fields in axi-symmetric explosions from a single direct numerical simulation. As an illustration, this methodology is applied to a 3-D simulation of the dusty boundary layer induced by an explosion above a ground surface.

## 2. Averaging Methodology

We begin with a turbulent flow field  $\phi(x, y, z, t)$  derived from a direct integration of the 3-D conservation laws. The explosion is assumed to be spherical (i.e., no jetting). Then it is reasonable to expect that the laminar flow field outside the turbulent mixing region is azimuthally symmetric. Furthermore, one expects that the mean flow is also axisymmetric. We then take advantage of this underlying symmetry and sample the solution at fixed azimuths  $\theta_k = 2\pi k/K$  in a cylindrical coordinate system:  $\phi(x, y, z, t) \rightarrow \phi(r, z, \theta_k, t)$ . This forms a set  $E\{\phi(\theta_1), \phi(\theta_2), \dots, \phi(\theta_K)\}$ , where the dependence on other variables has temporarily been suppressed for clarity. One can view this set as  $K$  realizations of the turbulent flow, in other words, an ensemble. If this ensemble is statistically representative, then one can think of constructing averages of the turbulent flow. In particular, divide the flow field  $\phi$  into a mean component  $\bar{\phi}$  and a fluctuating component  $\phi'$ :

$$\phi = \bar{\phi} + \phi' \quad (1)$$

such that  $\overline{\phi'} = 0$ . Then, azimuthal averaging of  $\phi$  extracts the mean component of the flow:

$$\bar{\phi}(r, z, t) = \frac{1}{K} \sum_{k=1}^K \phi(r, z, \theta_k, t) \quad (2)$$

while averaging  $(\phi')^n$  extracts the  $n$ -th moments of the flow:

$$\overline{(\phi')^n} = \frac{1}{K} \sum_{k=1}^K [\phi(r, z, \theta_k, t) - \bar{\phi}(r, z, t)]^n \quad (3)$$

and the root-mean-squared (r.m.s.) fluctuations:

$$\phi'(r, z, t) = \sqrt{\overline{(\phi')^2}} \quad (4)$$

The above relations may be used for scalars. In order to calculate the Reynolds stress tensor  $\tau_{ij}$ , one must consider the velocity field  $u_i(r, z, \theta_k, t)$ . Then, averaging  $u'_i u'_j$  extracts the turbulent Reynolds stress:

$$\tau_{ij}(r, z, t) = \overline{u'_i u'_j} \quad (5)$$

$$= \frac{1}{K} \sum_{k=1}^K [u_i(r, z, \theta_k, t) - \bar{u}_i(r, z, t)] [u_j(r, z, \theta_k, t) - \bar{u}_j(r, z, t)] \quad (6)$$

while the r.m.s. velocity fluctuations are related to the diagonal components of the Reynolds stress by:

$$u'_i(r, z, t) = \sqrt{\tau_{ii}} \quad (7)$$

Thus, by storing the complete flow field at a few times  $t^n$ , this methodology allows one to visualize the evolution of the azimuthally-averaged flow. For example, one can make two-dimensional (2-D) contour plots of the mean flow  $\bar{\phi}(r, z, t^n)$  and r.m.s. fluctuations  $\phi'(r, z, t^n)$  at various times. In addition, by selecting fixed ground ranges  $r_l$ , one can display the evolution of the boundary layer profiles:  $\bar{u}_i(r_l, z, t^n)$ ,  $u'_i(r_l, z, t^n)$  and  $\tau_{ij}(r_l, z, t^n)$ . Examples of these will be presented in subsequent sections.

### 3. The Problem

The problem considered here is the turbulent boundary layer flow induced by a 37-KT point explosion detonated 203 meters above a ground surface that had an initial loose dust layer (see Figure 1). While much is known about blast wave reflections from ideal surfaces (e.g., through gas dynamic calculations of Colella et al., [1986] and laboratory experiments of Reichenbach et al., [1992]), much less is known about the details of the boundary layer flow from explosions over real surfaces. One of the reasons is that the flow is considerably more complex, as shown in Figure 1 (and color Plate 1).

For a point explosion over a ground surface, thermal radiation from the fireball heats the air near the surface, creating a thermal layer TL ahead of the shock front. The blast wave propagates faster in the high-sound-speed layer, thus generating an outrunning precursor shock P. Gas from the main blast wave fills in the flow behind the precursor, thus forming a turbulent wall jet (Figure 2 and color Plate 2). At the same time, vorticity is generated by baroclinic effects (i.e., pressure gradients interacting with oblique density gradients). For example, shock interactions with the dust bed create a boundary layer along the surface, while shock interactions with the thermal layer create a vortex sheet that passes up and over the top of the wall jet. These shear layers roll-up and interact, forming the turbulent wall-jet flow seen in Figure 2. Dust scouring occurs because the vortex tubes entrain mass from the fluidized bed and mix it throughout the boundary layer.

The details of modeling the dusty flow have been published elsewhere (Kuhl et al., 1993). The primary assumption was that the dust and air are in thermal and mechanical equilibrium (however, non-equilibrium models may also be used; see Collins et al., 1994). This allows us to model the mixture by the 3-D conservation laws of gas dynamics. These are augmented an advection equation for the dust mass concentration. The conservation laws are integrated numerically with a second-order Godunov algorithm (Colella and Glaz, 1985). Adaptive Mesh Refinement or AMR (Berger and Colella, 1989; Bell et al., 1994) was used to calculate the convective-mixing processes on the computational grid. Three levels of mesh refinements were used: grid 1 defined the computational domain of 2000 m<sup>3</sup> ( $\Delta_l = 24$ -m); grid 2 was used to capture the shock waves ( $\Delta_2 = 6$ -m); while grid 3 followed the dusty wall-jet flow ( $\Delta_3 = 1.5$ -m). The problem was run to a time of 2 seconds; this took about 60 CPU hours on the Cray Y-MP.

A 3-D visualization of the turbulent wall-jet and dusty boundary-layer flow is depicted in Figure 3 (and color Plate 3). Three-dimensional effects are quite evident, for example: streamwise vortex structures (Görtler vortices) in the boundary layer region (view a) and hairpin



structures in the wall jet flow (view b). The question is: does this chaotic mixing layer possess smooth mean profiles that are similar to other well-documented turbulent flows? This question is explored in the next two sections.

#### 4. Wall Jet Profiles

Azimuthal averaging was applied to  $u_r$  in order to determine the mean streamwise velocity  $\bar{u}_r(r, z, t)$ . The time evolution of the resulting mean radial velocity profiles are depicted in Figure 4 for two fixed ranges ( $r = 600$  and  $700$  meters). The profiles exhibit the characteristic wall jet shape: velocities are zero in the fluidized bed ( $z < 17$ -m); they reach a maximum value in the middle of the jet ( $z \approx 40$ -m); and then decay to the freestream flow as one moves away from the surface. For the first time, we can actually visualize the *temporal evolution of the mean profiles*. For example, at 600 meters the wall jet grows in strength to reach a maximum velocity of about 800 m/s at  $t = 0.60$ -s; later it relaxes to a boundary-layer flow ( $u_r < 200$  m/s) after the wall jet has passed over this station. Similar trends are seen at 700 meters, but the peak values are somewhat smaller ( $\sim 600$  m/s) due to blast wave decay with range; maximum velocities in the boundary layer are less than 50 m/s at late times ( $t = 1.45$  s).

In order to compare the present results with other wall-jet flows, the velocities were non-dimensionalized by the instantaneous maximum mean velocity  $u_m(r, t)$ , and then the profiles

$$\bar{u}_r / u_m = F_i(r, \eta_j, t) \quad (8)$$

were scaled with the wall-jet similarity variable  $\eta_j$  (Bajura and Catalano, 1975):

$$\eta_j = (z - z_o) / (z_* - z_o) \quad (9)$$

where

$z_o(r, t)$  = height of the fluidized bed (i.e., where  $\bar{c} = 2/3$ ; see Appendix),  
 $z_*(r, t)$  = height of free shear layer (i.e., where  $\bar{u} = u_* \equiv (u_m + u_\infty) / 2$ ).

The fiducial  $z_o$  removes the flow in the fluidized bed from further consideration. Thus the fluidized bed was an artifice that was used in the present calculations to allow dust entrainment into the flow in a natural way (i.e., without imposing an artificial dust injection model) that mimics the actual fluid-mechanic entrainment process, but is not considered as part of the boundary layer flow per se. The wall jet then scales with the height of the free shear layer,  $\delta_{FSL}$ :

$$\delta_{FSL}(r, t) = z_*(r, t) - z_o(r, t). \quad (10)$$

The mean velocity profiles in the precursor wall jet are depicted in Figure 5 for the same two ground ranges. The azimuthal-averaging procedure gives smooth, well-behaved profiles. The scaling technique seems to collapse the radial velocity profiles (Figures 5a and 5d) into a shape that is characteristic of other wall-jet flows (Launder and Rodi, 1981; Wygnanski et al., 1992). Nevertheless, the profile shape changes somewhat over time, indicating that the wall jet is not truly self-similar. Of course, there is no reason to expect that the profile shape would be independent of time for decaying blast waves.

The mean vertical velocities (Figures 5b and 5e) oscillate about zero ( $-0.1 < \bar{u}_z / u_m < 0.1$ ) in response to the rotational structures in the wall jet. At later times (corresponding to symbol  $x$ ) the flow direction is toward the surface as gas from the main blast wave rushes in to support the wall jet flow. Mean azimuthal velocities (Figures 5c and 5f) are small—typically a few percent of  $u_m$ .

Previously, we had performed detailed two-dimensional (2-D) calculations of this same precursor wall-jet flow (Kuhl et al., 1993). In that case we *time-averaged* the solution in wall-jet coordinates (Equation 9) to evaluate the mean-flow profiles. Note that with that technique, one produces a single profile that is characteristic of the mean flow at that ground range. For comparison purposes, the 2-D results have been plotted in Figure 5 as the solid curves labeled 2-D. Clearly, the 2-D mean profiles are qualitatively similar to the present 3-D results; however, only the 3-D calculation allows one to properly evaluate the temporal evolution of the profiles.

Evolution of the corresponding turbulent velocity fluctuation profiles

$$u'_i / u_m = F'_i(r, \eta_j, t) \quad (11)$$

is depicted in Figure 6 for the same two ground ranges. For comparison, measured profiles for a 2-D, self-preserving, clean wall jet (Launder and Rodi, 1981) are included as dashed-line curves. Profiles of the radial (or streamwise) component of the velocity fluctuations are shown in Figures 6a and 6d. They exhibit a bi-modal distribution, qualitatively similar to the experimental profiles: velocity fluctuations peak in the boundary layer ( $\eta_j \approx 0.2$ ) and then again in the free-shear-layer ( $\eta_j \approx 1$ ) portion of the jet. Values range from 20 to 30 percent of  $u_m$ . The second peak (near  $\eta_j = 1$ ) disappears at late times (time symbol  $x$ ) as the flow relaxes to a boundary-layer flow after the wall jet has passed the considered ground range.

Development of the vertical component of the turbulent velocity fluctuations is depicted in Figures 6b and 6e. The profiles exhibit a single-hump shape, qualitatively similar to the experimental profiles. Values range from 10 to 20 percent of  $u_m$ .

Changes in the azimuthal component of the turbulent velocity fluctuation profiles are depicted in Figures 6c and 6f. They also exhibit a bi-modal shape—with a peak in the boundary layer ( $\eta_j \approx 0.2$ ) and a second peak in the free shear layer ( $\eta_j \approx 1$ )—that is qualitatively similar to the experimental profiles. Values range from 10 to 20 percent of  $u_m$ . The second peak disappears at late times (time symbol  $x$ ) as the flow relaxes to a boundary-layer flow after the wall jet has passed the considered ground range.

For comparison purposes, results from previous 2-D simulations of this problem are presented in Figure 6 as the solid curves labeled 2-D. The 2-D profiles are qualitatively similar to the present 3-D results, but the peak values are too large—typically by a factor of 1.5 to 2. This is a result of the 2-D flow approximation where the turbulent fluctuations are shared among two degrees of freedom versus the three degrees of freedom found in actual turbulent flows.

Evolution of the corresponding turbulent Reynolds stress profiles is depicted in Figure 7. The radial-vertical component  $u'_i u'_j$  (Figure 7a and 7d) has a negative peak in the boundary layer ( $\eta_j \approx 0.2$ ) and a positive peak in the free shear layers ( $\eta_j \approx 0.8$ )—as is typical of measured wall jet profiles. Profiles of other components of the calculated turbulent Reynolds stress are more erratic. Unfortunately there are no experimental measurements to guide further assessment.

In summary, the preceding figures suggest that this blast-wave wall jet is not self-similar (or self-preserving). Instead the profiles evolve over time, and finally relax to a boundary-layer flow, whose properties will be examined in the next section.

## 5. Boundary Layer Profiles

In order to compare the present results with other boundary-layer flows, the mean velocity profiles:

$$\bar{u}_i / u_m = f_i(r, \eta_{BL}, t) \quad (12)$$

were re-scaled with the boundary-layer similarity variable,  $\eta_{BL}$  (see Appendix):

$$\eta_{BL} = (z - z_o) / (z_{BL} - z_o) \quad (13)$$

where  $z_{BL}(r, t)$  denotes the boundary-layer height (i.e., where  $\bar{u}_r = 0.99 u_m$ ). This assumes that the profiles scale with the boundary-layer velocity thickness,  $\delta_{BL}$ :

$$\delta_{BL}(r, t) = z_{BL}(r, t) - z_o(r, t). \quad (14)$$

Again, the fiducial  $z_o$  removes the fluidized bed from the boundary layer analysis.

The evolution of the mean velocity profiles is depicted in Figure 8 for the same two ground ranges. For comparison purposes, various experimental profiles are included as dashed lines: curves labeled NS and WT represent the dusty boundary layer profiles measured behind a normal shock (Batt et al., 1988) and in a steady-flow wind tunnel (Batt et al., 1993), respectively, while curves labeled FP denote the clean turbulent layer on a flat plate (Klebanoff, 1955). Clearly, the mean radial-velocity profile changes with time (Figures 8a and 8d). During the wall-jet phase (symbols q, m,  $\Delta$ , and +), the profiles resemble a dusty boundary layer behind a shock; at intermediate times, the profiles are similar to dusty boundary layers in steady-flow wind tunnels; while at late times, the profiles approach the clean flat-plate case. In effect what happens is that the vortex tubes in the boundary layer entrain dusty mass from the fluidized bed—thereby continuously decreasing its mean density (see Appendix A for more details). The corresponding mean densities in the bottom of the boundary layer also decrease with time—which allows the mean velocities in the bottom of the boundary layer to creep up toward clean flat plate values.

The mean vertical velocity profiles are presented in Figures 8b and 8e. Vertical velocities are essentially zero during the wall-jet phase, but then expand upward during the boundary layer phase as a result of the divergence of the blast-wave flow. Mean azimuthal velocities remain near zero at all times.

Development of the corresponding turbulent velocity-fluctuation profiles:

$$u'_i / u_m = f'_i(r, \eta_{BL}, t) \quad (15)$$

are presented in Figure 9. The azimuthal-averaging procedure gives smooth, well-behaved profiles. The radial velocity fluctuations grow with time, and reach a peak value of 30 percent of  $u_m$  during the wall-jet phase. Then they relax to a profile that is relatively independent of time, with a peak value at the bottom of the boundary layer of about 20 percent of  $u_m$ . This profile is about a factor of two greater than the clean flat plate case.

Similar trends are found in the vertical and azimuthal velocity-fluctuation profiles. At late times, they relax to a time-independent profile. Near  $\eta_{BL} = 0$ , azimuthal fluctuations are fifty percent larger than vertical fluctuations ( $0.12 u_m$  versus  $0.08 u_m$ , respectively). This is the same trend that was observed for turbulent boundary layers on flat plates (see dashed curves) where  $(u'_\theta)_{\max} \simeq 1.5(u'_z)_{\max}$ .

The turbulent Reynolds stress profiles are depicted in Figure 10, using boundary layer scaling. As in Figure 7, the profiles are somewhat erratic. The boundary layer becomes quite thin after the wall jet passes; apparently one needs more resolution (and samples) in the vertical direction to get smooth Reynolds stress profiles.

## 6. Boundary Layer Histories

We begin by considering the boundary layer growth; an example is offered in Figure 11 for one ground range. During the wall-jet phase, the heights of the boundary layer  $\delta_{BL}$  and free shear layer  $\delta_{FSL}$  increase rapidly, attaining peak values of 15 and 20 meters, respectively. The external blast-wave flow that supports the wall jet depresses the boundary layer thickness ( $t = 0.75$  s); then the boundary layer grows as a power-law function of time:

$$\delta_{BL}(m) = 6.7t^{1.35} \quad (\text{at } r = 600 \text{ m and } 0.75 < t(s) < 2). \quad (16)$$

The preceding solution may be used to construct time histories of the mean flow in the boundary layer at fixed ranges  $r$  and heights  $z$ , for example:

$$\bar{u}_i(r, z, t) = u_\infty(r, t) \cdot f_i(r, \eta, t) \quad (17)$$

$$u'_i(r, z, t) = u_\infty(r, t) \cdot f'_i(r, \eta, t) \quad (18)$$

where

$$\eta(r, z, t) = z / \delta_{BL}(r, t). \quad (19)$$

Here  $f_i$  and  $f'_i$  are the boundary-layer profile functions depicted in Figures 8 and 9, while  $u_\infty$  denotes the freestream velocity—obtained for example, by a blast-wave calculation. In that sense, Figure 8 and 9 can be considered the boundary-layer solution for this problem, albeit in graphical form. To illustrate this technique, Figures 12 and 13 present mean and r.m.s. wave forms of velocity, kinetic energy, and static pressure at 1-m, 2-m, and 3-m heights in the boundary layer.

## 7. Discussion

Next we shall explore the adequacy of the azimuthal-averaging methodology. The key issue is whether the azimuthal samples are statistically independent. The maximum number of azimuths  $K$  depends on the width  $Y$  of the fine grid region, and the mesh spacing  $\Delta y$ ; for the present calculation  $K = Y/\Delta y = 240 \text{ m}/1.5 \text{ m} = 160$  samples. At a range  $x = 600$  m, this corresponds to an angular separation of  $\Delta\theta = \{\text{Arctan}(Y/x)\}/K = 0.136$  degrees between azimuths. One can use every azimuth to construct the ensemble  $E_1: \{\phi_1, \phi_2, \phi_3 \dots \phi_k \dots \phi_{160}\}$ . Alternatively, one can use every second azimuth to construct ensemble  $E_2: \{\phi_1, \phi_3, \phi_5 \dots \phi_{159}\}$  with 80 samples; or every third azimuth to construct ensemble  $E_3: \{\phi_1, \phi_4, \phi_7 \dots \phi_{159}\}$  with 56 samples; or every fourth azimuth to construct ensemble  $E_4: \{\phi_1, \phi_5, \phi_9 \dots \phi_{157}\}$  with 40 samples. Each of these ensembles was averaged to evaluate the profiles. The resulting boundary layer profiles were similar—indicating that the profiles are insensitive to the sampling procedure. This can be rationalized by a careful examination of the vorticity cross-section (Figure 2c). Three-dimensional stretching of vortex tubes leads to vorticity concentrations that approach the mesh size (i.e., vorticity islands as small as  $\Delta_3$ ). Thus, the finest-scale structures are essentially independent. The larger-scale structures are four or five cells in diameter; apparently 40 such samples (ensemble  $E_4$ ) are enough to give converged mean profiles.

As a final check on the solution, we have calculated the power spectrum of the turbulent fluctuations. For nonsteady fields such as explosions, it is most appropriate to consider the fluctuating kinetic energy,  $K'$ :

$$K'(r, z, \theta, t) = [(u'_r)^2 + (u'_t)^2 + (u'_\theta)^2] / 2 \quad (20)$$

which removes the time dependence of the mean blast wave flow from subsequent temporal analysis. (Note that the above relation represents a point-valued function, i.e., a non-averaged value.) Figure 14 depicts an example of a fluctuating kinetic energy history in the boundary layer at 4 meters above the fluidized bed; this is characteristic of the turbulent flow during the wall-jet phase. The power spectrum,  $P$ , was calculated by taking a Fourier transform of  $K'(t)$ :

$$P(K'; \omega) = \int_0^{\infty} K'(t) e^{-i\omega t} dt / 2\pi \quad (21)$$

The resulting spectra for the fluctuating kinetic energy are presented in Figure 15 for two characteristic heights:  $z - z_0 = 9$ -m which is in the middle of the boundary layer, and  $z - z_0 = 21$ -m which is in the center of the free shear layer. Of course, most of the energy is in the low frequency range corresponding to the large-scale structures. The spectrum decays steeply at intermediate frequencies, and then flattens off at high frequencies. In the latter range, the spectrum is well approximated by the dashed line whose slope is  $k^{-5/3}$ . This suggests that the calculation has enough grid resolution to cover a portion of the inertial range, and that the spectrum in that range has the proper Kolmogorov slope of  $-5/3$ . In that sense, the present solution is qualitatively similar to other turbulent flows—even through molecular-dissipation scales are not included.

## 8. Conclusions

The evolution of large-scale turbulent structures is problem dependent (Chorin, 1994), and therefore must be calculated—not modeled. This is especially true for non-steady fields like explosions. Kolmogorov scales are however universal (Zakharov et al., 1992); monotonicity constraints and finite grid resolution simulate their dissipative effects in the present calculations. Thus it is not necessary to resolve all length scales of the turbulent flow (e.g., including viscous scales). Instead one needs to resolve enough of the spectrum to reach the inertial range. The present calculations are able to achieve that goal (also see Oran and Boris, 1993).

Azimuthal averaging was used to extract the instantaneous mean from the evolving 3-D turbulent field. Although from symmetry considerations the mean flow is axi-symmetric, turbulent velocity fluctuations are inherently a 3-D phenomenon. Consequently, during the wall-jet phase the mean profiles resemble our previous 2-D calculations, while velocity-fluctuation profiles and Reynolds-stress profiles are qualitatively similar to measurements of self-preserving wall jets. The boundary layer was not self-similar; instead the mean velocity profile evolved with time. Initially it agreed with measurements of a dusty boundary layer behind a shock. At intermediate times it resembled the dusty boundary layer profiles measured in a wind tunnel, while at late times it approached a  $1/7$  power-law profile. Velocity fluctuation profiles were found to be qualitatively similar to those measured for turbulent boundary layers on clean flat plates. The boundary layer height grew according to  $\delta_{BL}(m) = 6.7t^{1.35}$  at 600 meters.

Azimuthal averaging can be used to analyze the evolution of other symmetric turbulent fields such as dust clouds, axi-symmetric jets, fireball instabilities, and dusty boundary layers in shock-tube and wind-tunnel flows.

## Acknowledgments

This work was performed under the auspices of the U.S. Department of Energy by the Lawrence Livermore National Laboratory under Contract Number W-7405-ENG-48. It was also sponsored by the Defense Nuclear Agency under DNA IACRO numbers 94-830 and 94-831, and DNA MIPR number 94-563.

## 9. References

- Bajura, R.A. and Catalano, M.R., (1975) "Transition in a two-dimensional plane wall jet," *J. Fluid Mech.*, **70**, pp. 773-799.
- Batt, R.G., Kulkarny, V.A., Behrens, H.W. and Rungaldier, H. (1988) "Shock induced boundary layer dust lofting", *Shock Tubes and Waves*, H Gronig ed., VCH, Weinheim, Germany, pp. 209-215.
- Batt, R.G., Petach, M.B., Peabody, S.A. and Batt, R.R. (1992) "Experimental investigation of dust and vegetation sweep-up", TRW Report (in press).
- Bell, J.B. and Marcus, D.L. (1992) "Vorticity intensification and transition to turbulence in the 3-D Euler equations," *Comm. Math. Phys.*, **147**, pp. 374-394.
- Bell, J.B., Berger, M., Saltzman, J. and Welcome, M. (1994) "Three-dimensional Adaptive Mesh Refinement for hyperbolic conservation laws", *SAIM J. Stat. Comp.*, **15**(1), pp. 127-138. Also LLNL Report UCRL-JC-108794, Livermore, CA.
- Berger, M.J. and Colella, P. (1989) "Local Adaptive Mesh Refinement for shock hydrodynamics," *J. Comput. Phys.*, **82**, pp. 64-84.
- Chien, K.Y., Ferguson, R.E., Collins, J.P., Kuhl, A.L. and Batt, R.G. (1994) "Turbulent boundary layer over a dust bed", *19th Int. Shock Wave Symp.*, R. Brun ed., Springer-Verlag, Heidelberg, Germany (in press).
- Chorin, A.J., (1975) *Lectures on Turbulence Theory*, Publish or Perish, Inc., Boston (vid. esp. Chapter I-3, "An example of the perils of dishonesty," pp. 21- 23).
- Chorin, A.J., (1994) *Vorticity and Turbulence*, Springer-Verlag, Heidelberg, Germany (in press).
- Colella, P. and Glaz, H.M. (1985) "Efficient solution algorithms for the Riemann problem for real gases," *J. Comput. Phys.*, **59**, pp. 264-289.
- Collins, J.P. et al. (1994) "Simulation of shock-induced dusty gas flows using various models", *25th AIAA Fluid Dynamics Conference*, paper AIAA-94-2309, American Institute of Aeronautics and Astronautics, New York City, NY (in press).
- Launder, B.E. and Rodi, W. (1981) "Turbulent wall jet", *The 1980-81 AFOSR-HTTM Stanford Conference on Complex Turbulent Flows: Comparison of Computation and Experiment*, Vol. I, Mech. Engin. Dept., Stanford University, Stanford, CA, pp. 434-451.
- Klebanoff, P.S. (1955) "Characteristics of turbulence in a boundary layer with zero pressure gradient," *NACA Report 1247*.
- Kuhl, A.L. et al., (1993) "Turbulent wall jet in a blast wave precursor," *Japanese National Symposium on Shock Wave Phenomena*, edited by K. Takayama, Tohoku Print, Sendai, Japan (in press). Also LLNL Report UCRL-JC-112713, Livermore, CA.
- Kuhl, A.L., et al. (1990) "Simulation of a turbulent dusty boundary layer behind a shock", *Current Topics in Shock Waves*, Y.W. Kim ed., AIP Conference Proceedings **208**, American Institute of Physics, New York, N.Y., pp. 762-769.

Oran, E.S. and Boris, J.P. (1993) "Computing turbulent shear flows—a convenient conspiracy", *Computer in Physics*, 7(6), pp. 523-533.

Reichenbach, H., Scheklin-Gluck, G. and Kuhl, A.L. (1992) *Comparison of HOB curves for 0.5-g charges with field test data and calculations*, DNA-TR--90-223, Defense Nuclear Agency, Alexandria, VA.

Wynanski, I., Katz, Y. and Horex, E., (1992) "Applicability of scaling laws to the turbulent wall jet," *J. Fluid Mech.*, 234, pp. 669-690.

Zakharov, V.E., L'vov, V.S., and Falkovich, G. (1992) *Kolmogorov Spectra of Turbulence I: Wave Turbulence*, Springer-Verlag, Heidelberg, Germany.

## Appendix : Scaling of Dusty Boundary Layers

For steady flows over loose dust surfaces, mean dust-density profiles converge to a single profile near the surface. In shock-tube experiments, density profiles converge at a value of  $\rho/\rho_0 = 10$  (Batt et al., 1988), while in wind-tunnel experiments, they converge at a value of  $\rho/\rho_0 = 2.5$  (Batt et al., 1992). This convergence point  $z_0$  can be identified as the effective interface between the dusty boundary layer flow (which is dependent on time after shock passage, or on distance from the leading edge of the dust bed) and the dense two-phase flow in the fluidized bed near the surface (which is independent of time or distance from the leading edge). This observation suggests the following scaling for dusty boundary layers:

$$\eta_{BL} = (z - z_0) / \delta_{BL} \quad (A-1)$$

$$\delta_{BL} = z_{BL} - z_0 \quad (A-2)$$

Thus,  $z_0$  scales the inner region of the boundary layer and  $z_{BL}$  scales the outer region. By applying this fluid-mechanic scaling, Batt and co-workers found that the experimental data collapsed onto similarity curves of a power-law form that were independent of time (for the shock-wave case) or distance (for the wind-tunnel case). We found similar trends in our numerical simulations of those pseudo-steady experiments (Kuhl et al., 1990; Chien et al., 1994).

For blast-wave boundary layers, one should expect the density in the fluidized bed to decay with time; hence, density is not the appropriate variable for identifying the convergence point. We chose instead the dust mass concentration. As shown in Figure A1, the mean dust concentration profiles converge to a single profile near the surface; the convergence point is identified as  $c=2/3$ , and defines the effective fluidized-bed height  $z_0$  used to scale the results. As is evident from Figure A2, this scaling allows the density near the bottom of the boundary layer to evolve over time.

For completeness, Figures A3 and A4 present the mean and r.m.s. profiles of density, static pressure and dynamic pressure during the wall-jet phase. The 2-D and 3-D density profiles are quite similar; however, the pressure fluctuations are unrealistically large in the 2-D case.

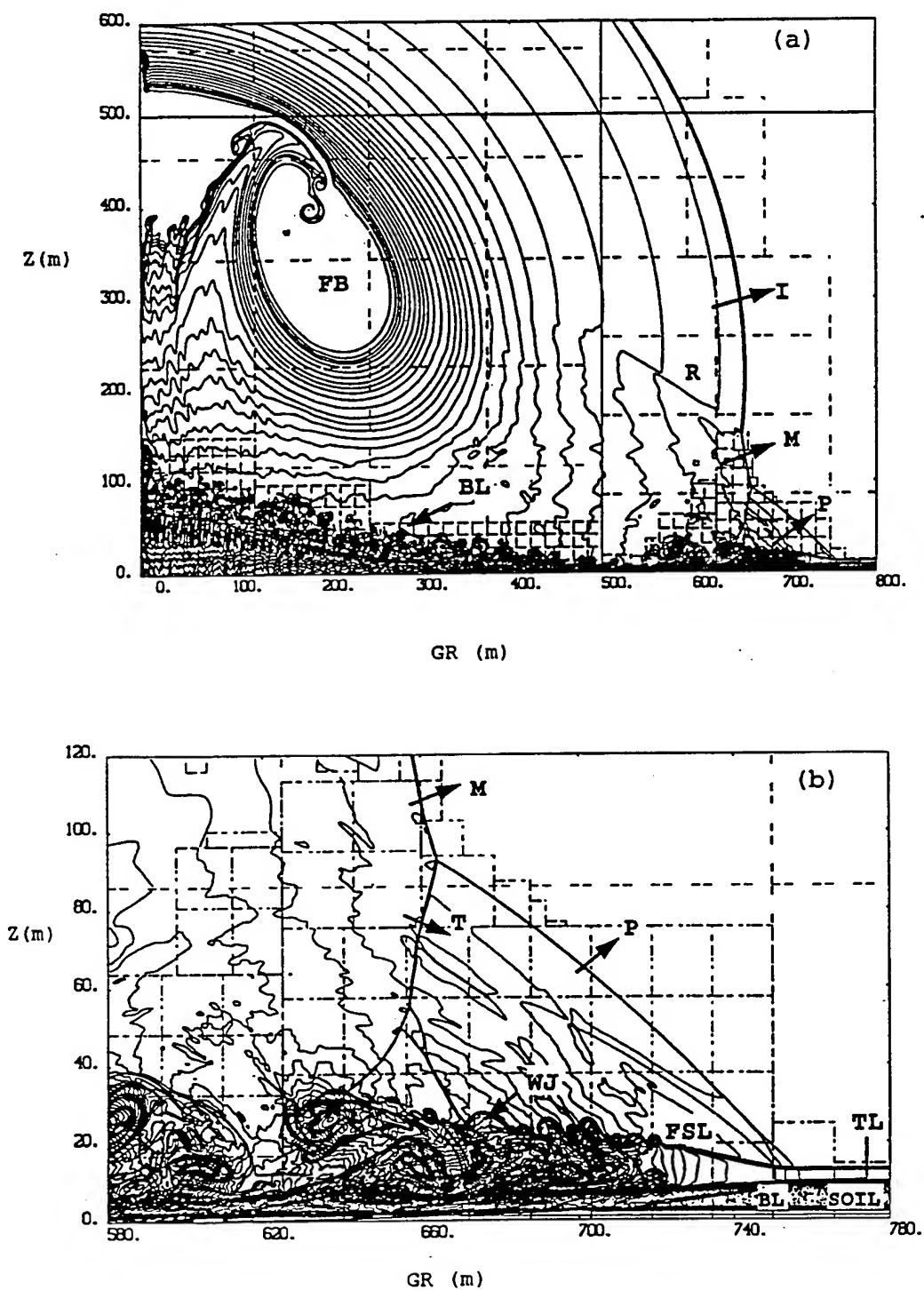


Figure 1. Point explosion over a dusty surface at  $t=0.73s$  : (a) overall view; (b) blowup of the wall jet region (2-D simulation,  $\Delta_3=22cm$ ).



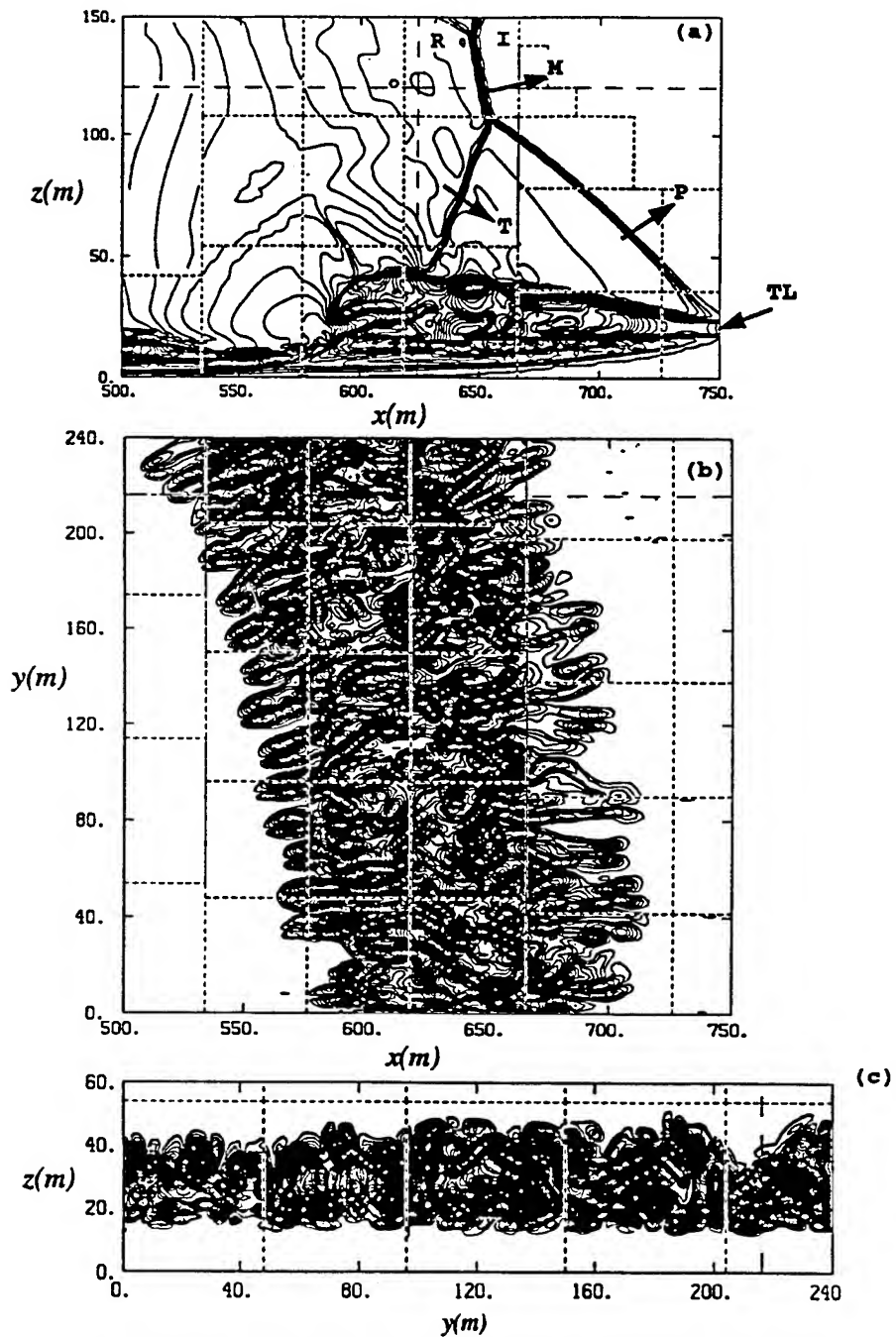
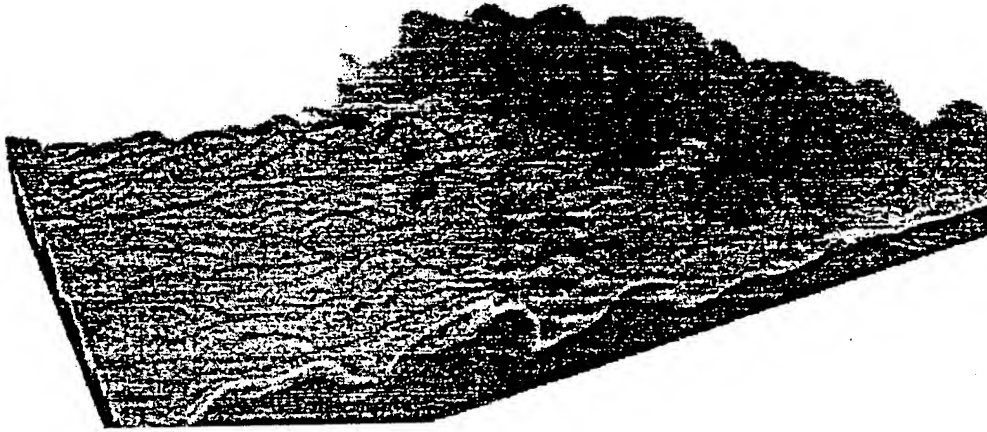


Figure 2. Visualization of the turbulent flow at  $t=0.71s$ : (a) contours of  $\log(p_{air})$  shown in elevation cross-section ( $y=0$ ); (b) platform view of the vorticity contours ( $z=17m$ ); (c) end view cross-section of vorticity contours ( $x=600m$ ).

(a)



(b)

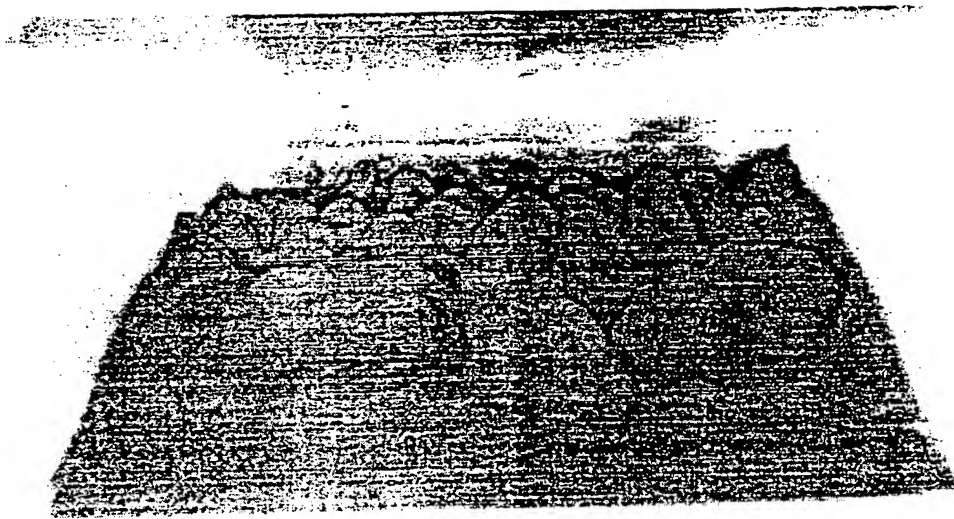


Figure 3. Three-dimensional visualization of the turbulent wall jet and dusty boundary layer flow at 1.38 s: (a) oblique view of the dust concentration; (b) vorticity magnitude, viewed looking toward ground zero.

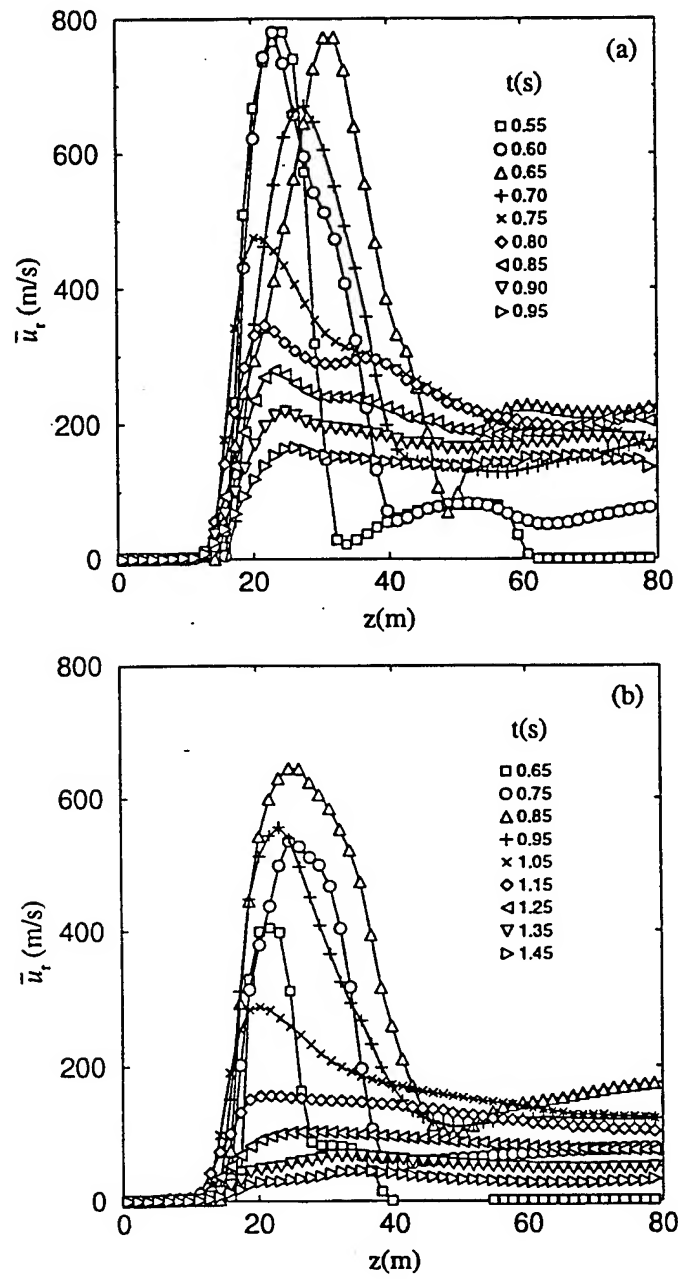


Figure 4. Evolution of the mean radial velocity profile versus time: (a) 600m; (b) 700m.

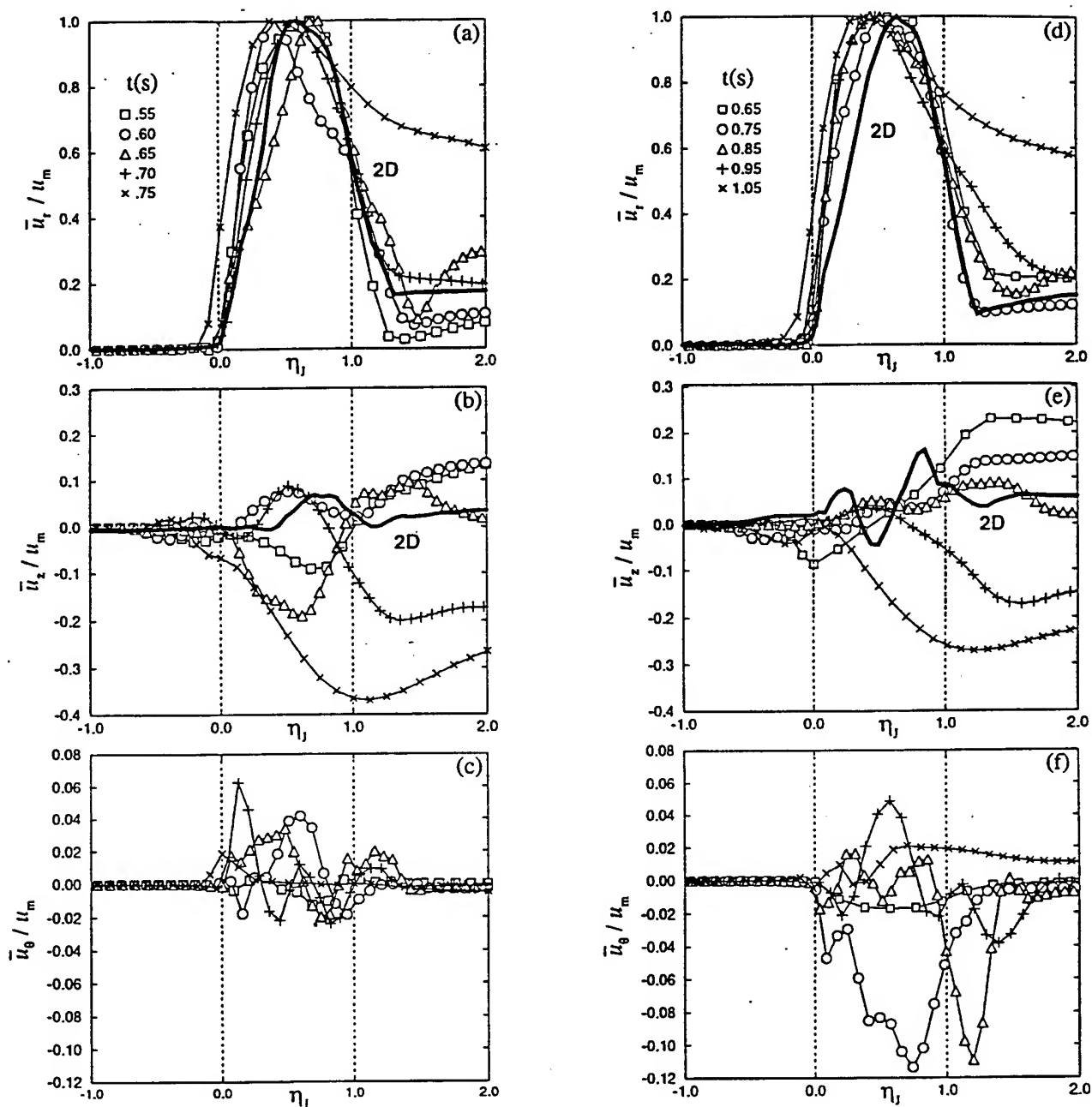


Figure 5. Mean velocity profiles in a precursor wall jet at 600m (a-radial, b-vertical, c-azimuthal) and 700m (d, e, f). Solid line denotes previous 2-D calculation (Kuhl et al., 1993).

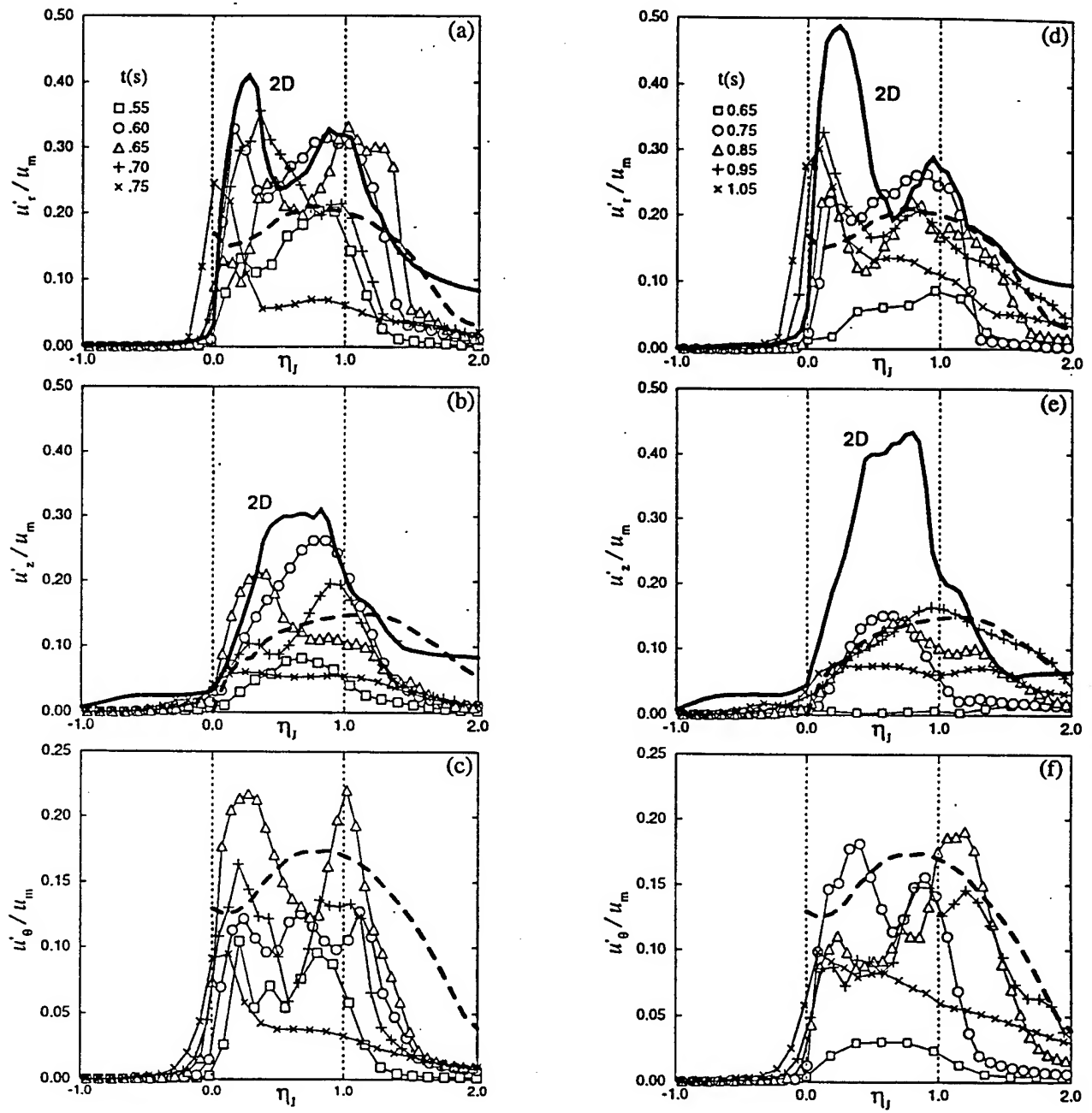


Figure 6. Velocity fluctuation profiles in a precursor wall jet at 600m (a-radial, b-vertical, c-azimuthal) and 700m (d, e, f). Solid line denotes previous 2-D calculation (Kuhl et al., 1993). Dashed lines denote measurements of a self-preserving 2-D clean wall jet (Launder and Rodi, 1981).

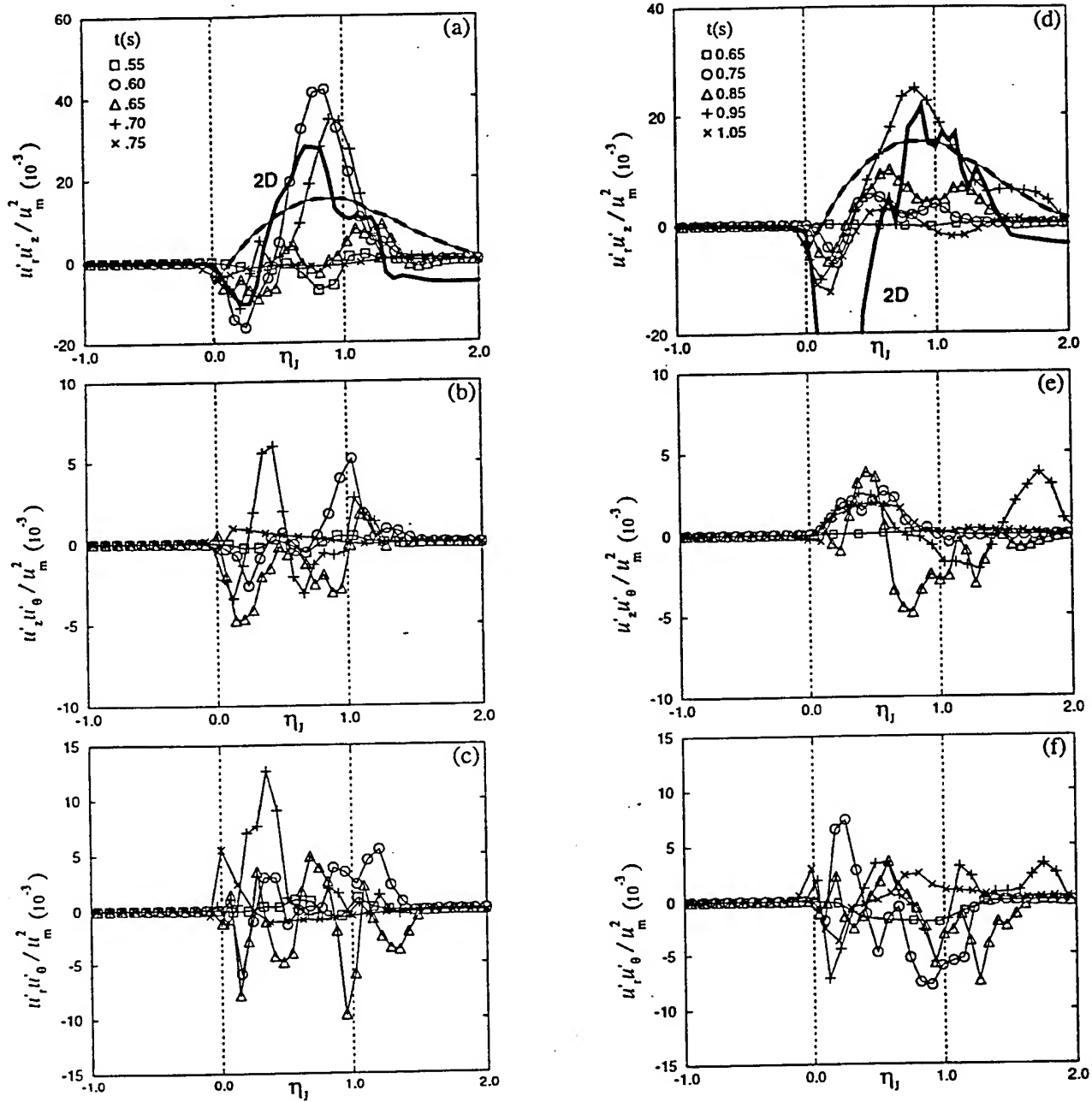


Figure 7. Reynolds stress profiles in a precursor wall jet at 600m (a, b, c) and 700m (d, e, f). Solid line represents previous 2-D calculation (Kuhl et al., 1993). Dashed lines denote measurements of a self-preserving 2-D clean wall jet (Launder and Rodi, 1981).

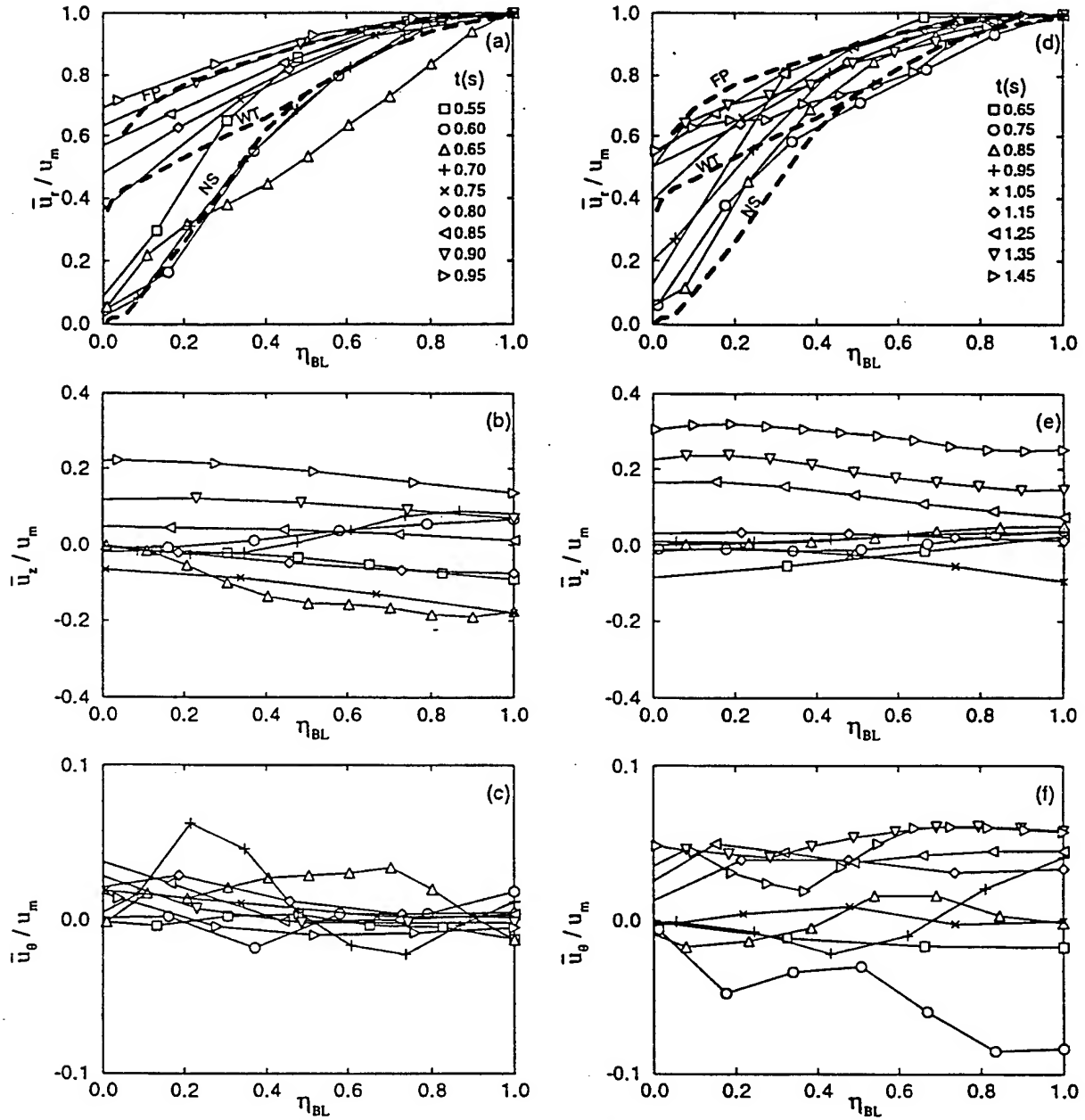


Figure 8. Mean velocity profiles in the boundary layer at 600 m (a - radial, b - vertical, c - azimuthal) and 700 m (d, e, f). Curves labeled NS and WT represent the dusty boundary layer profiles measured behind a normal shock (Batt et al., 1988) and in a wind tunnel (Batt et al., 1993), respectively, while curves labeled FP represent the turbulent boundary layer on a clean flat plate.

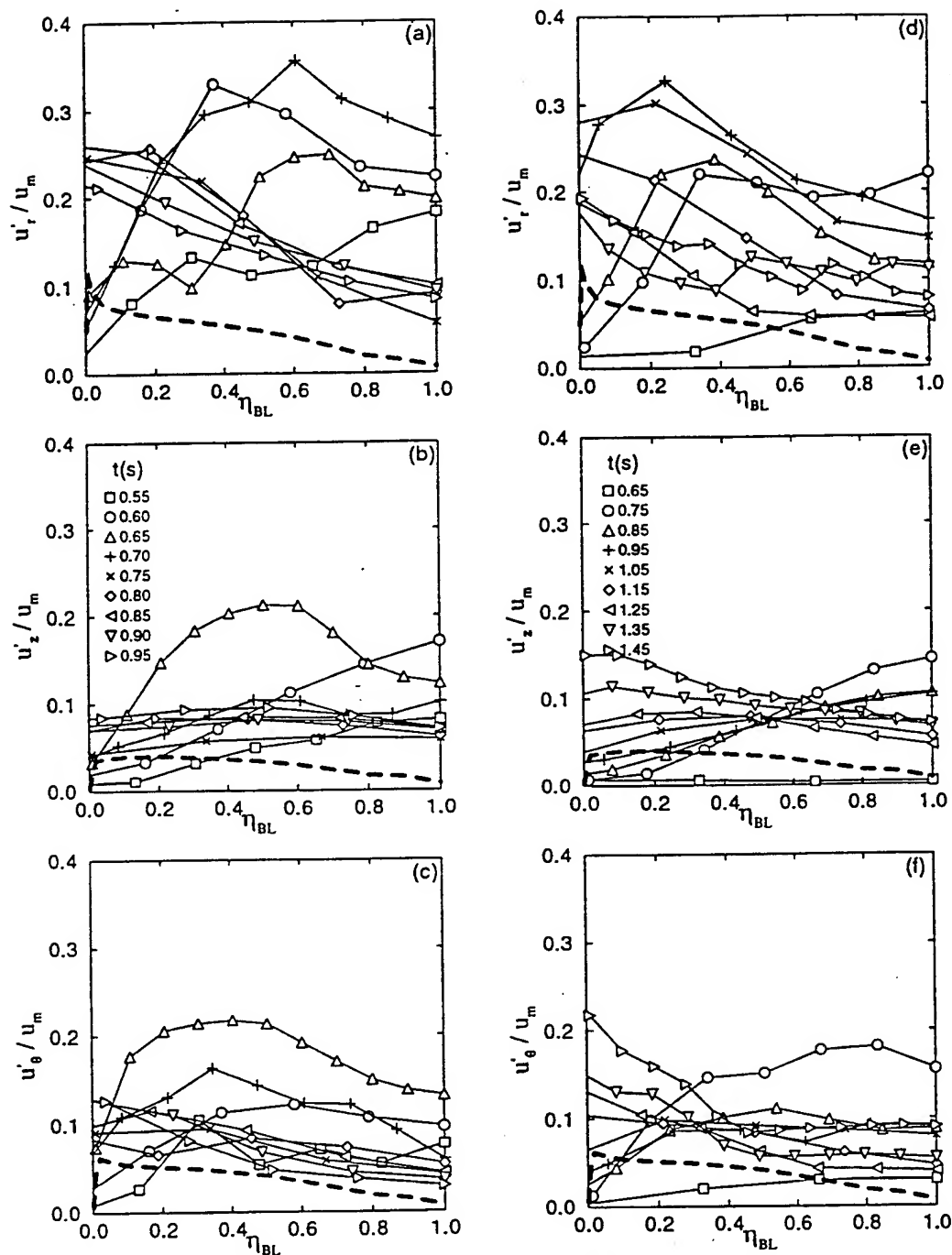


Figure 9. Velocity fluctuation profiles in the boundary layer at 600 m (a - radial, b - vertical, c - azimuthal) and 700 m (d, e, f). Dashed line represents measurements of a turbulent boundary layer on a clean flat plate (Klebanoff, 1955).



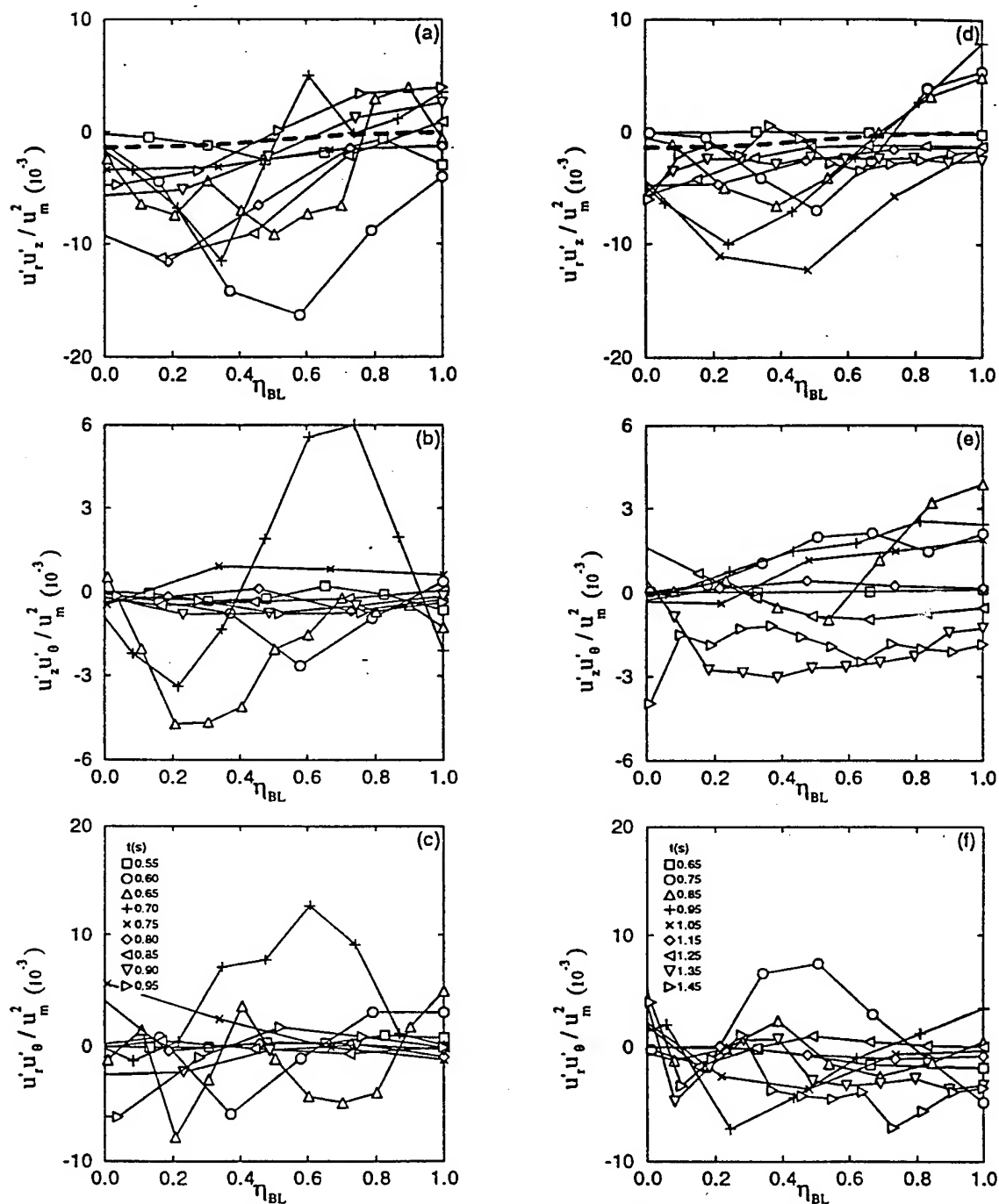


Figure 10. Reynolds stress profiles in the boundary layer at 600 m (a - radial, b - vertical, c - azimuthal) and 700 m (d, e, f). Dashed line represents measurements of a turbulent boundary layer on a clean flat plate (Klebanoff, 1955).

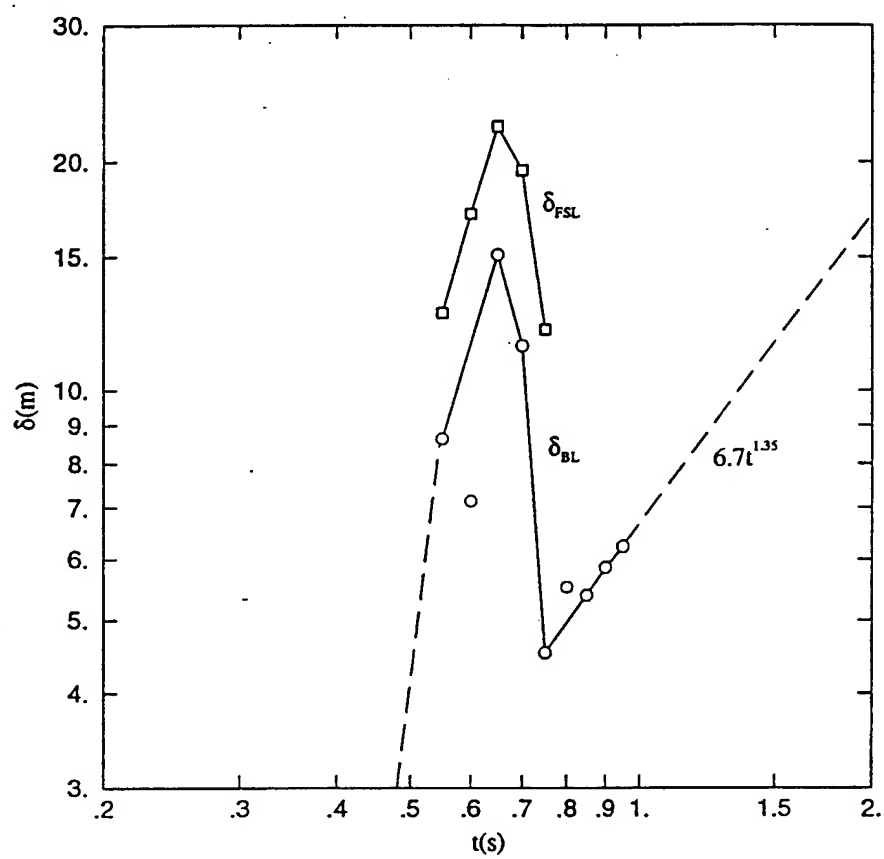


Figure 11. Boundary layer growth at  $r=600\text{m}$ .

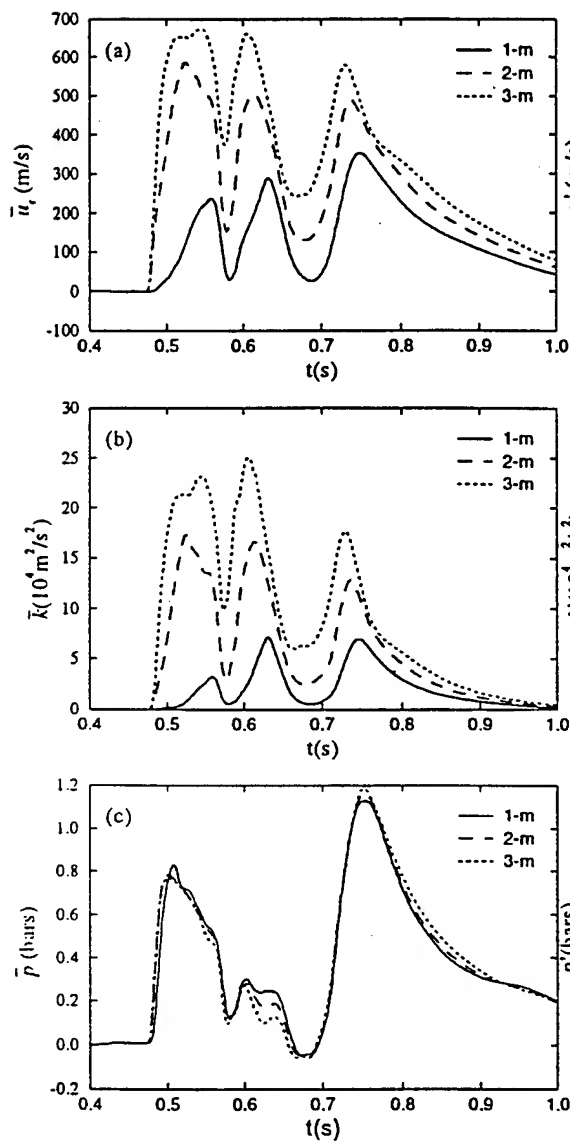


Figure 12. Mean flow histories at 1,2 and 3-m heights in the boundary layer (r=600m); (a) radial velocity; (b) kinetic energy; (c) static overpressure.

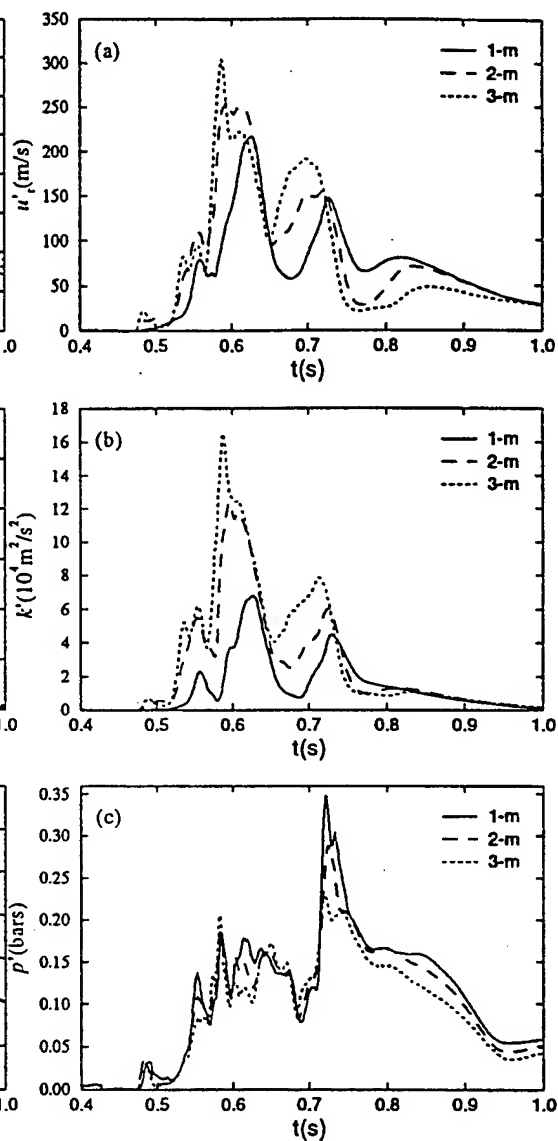


Figure 13. Fluctuation histories at 1,2 and 3-m heights in the boundary layer (r=600m); (a) radial velocity; (b) kinetic energy; (c) static overpressure.

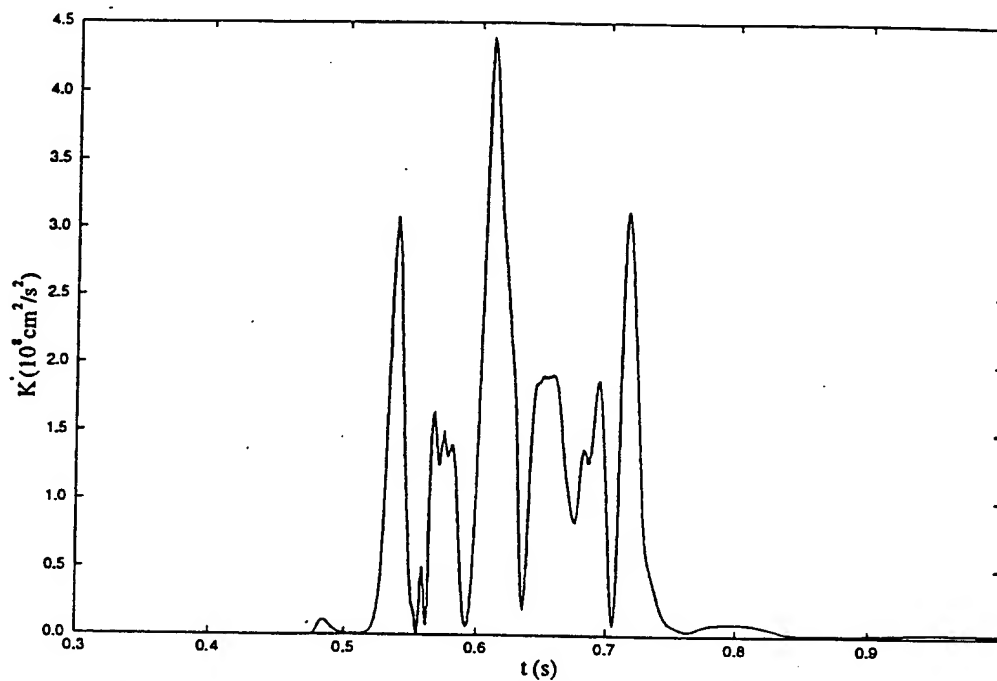


Figure 14. Fluctuating kinetic energy  $K'$  versus time at  $z-z_0 = 4\text{m}$  ( $x=600\text{m}, y=0$ ).

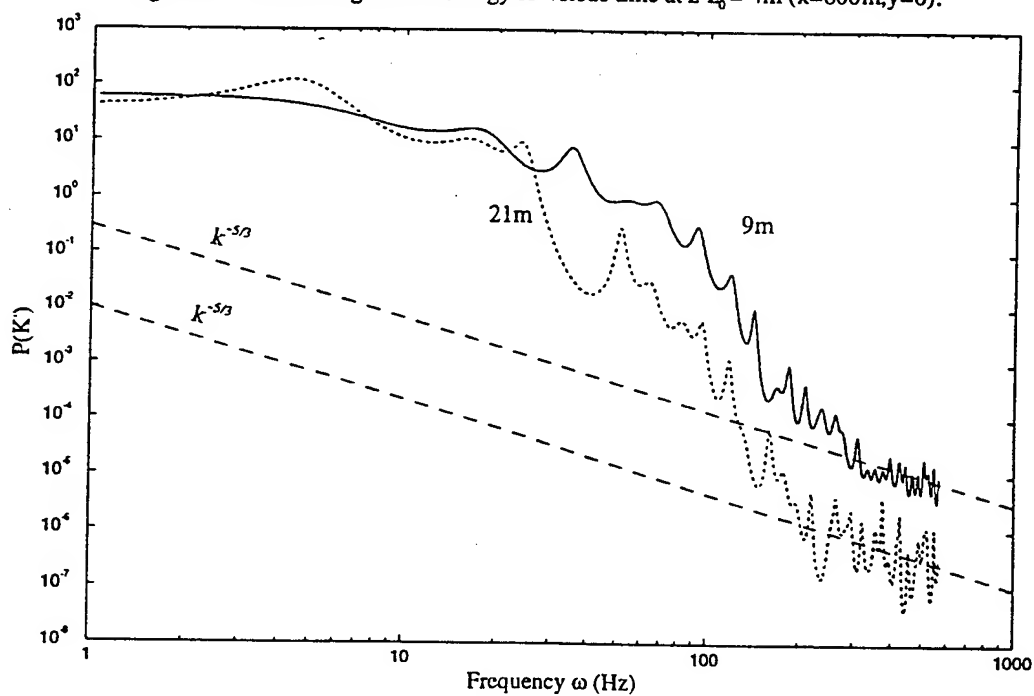


Figure 15. Power spectra of the fluctuating kinetic energy  $K'$  at  $z-z_0=9\text{m}$  and  $21\text{m}$  ( $x=600\text{m}, y=0$ ).

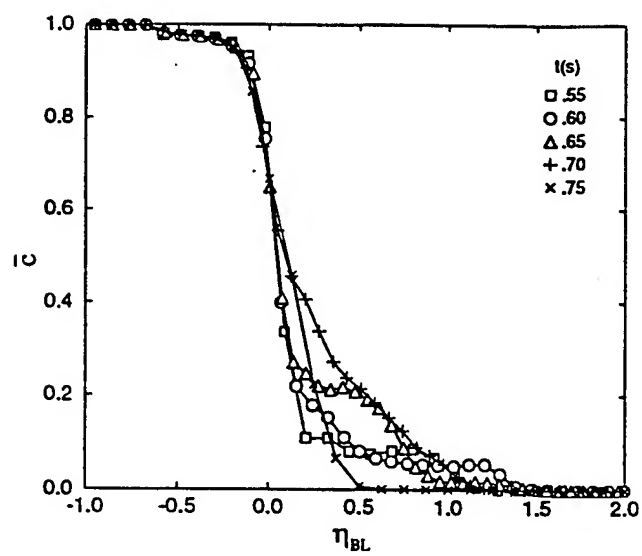


Figure A1. Mean dust concentration profile ( $r = 600m$ ).

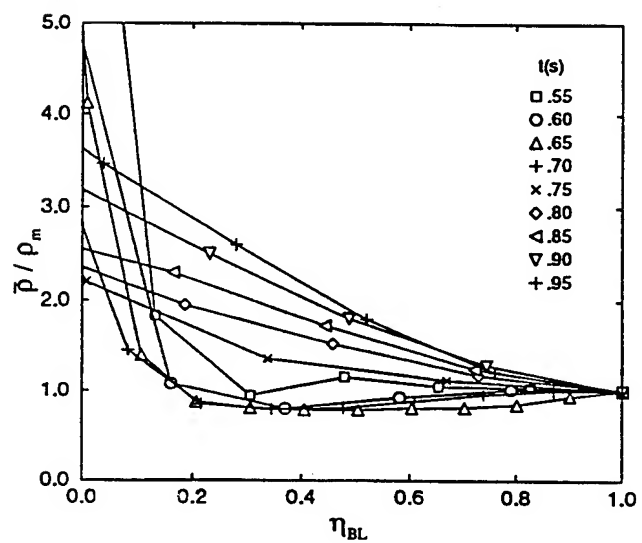


Figure A2. Mean density profile ( $r = 600m$ ).

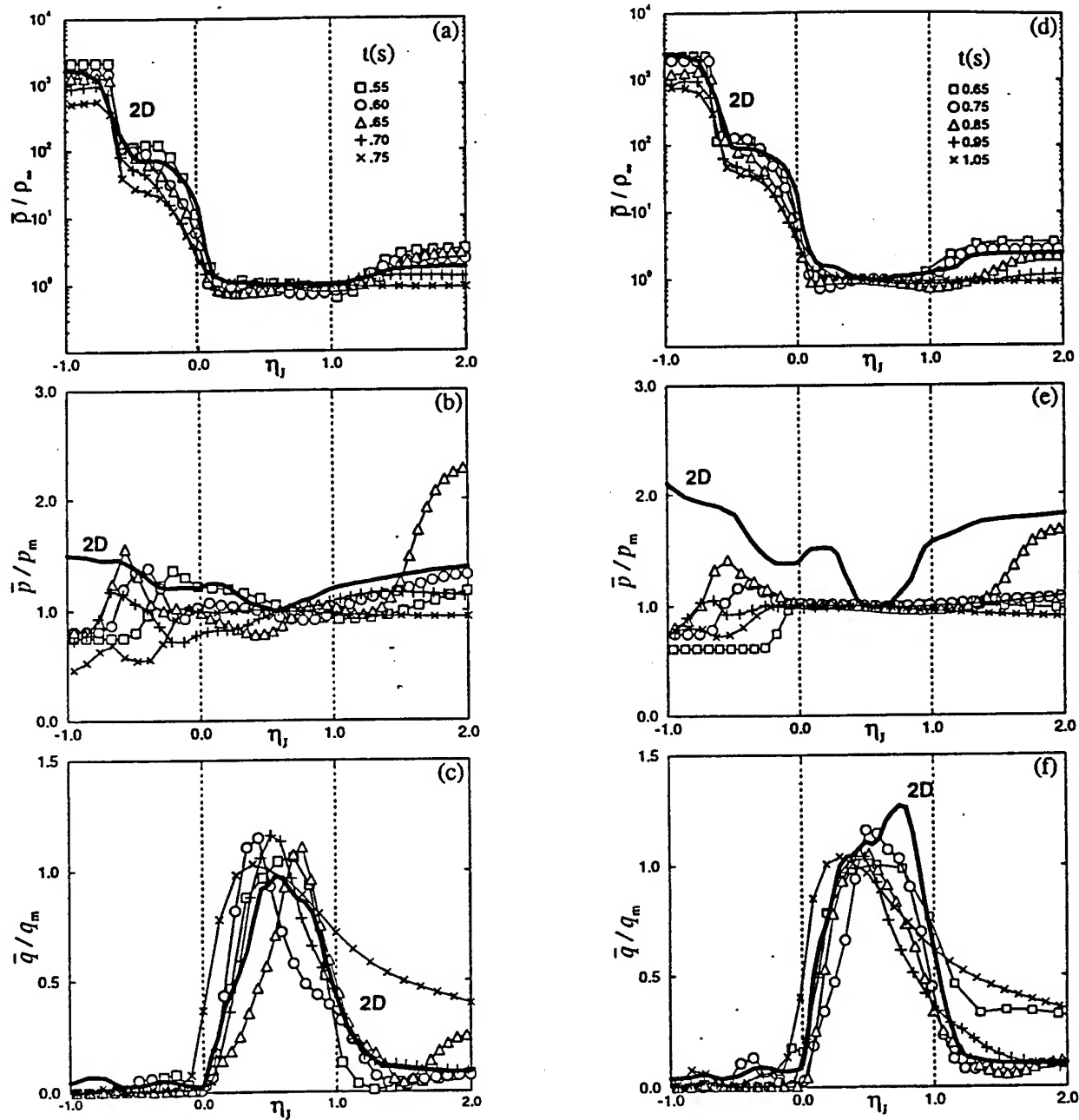


Figure A3. Mean flow profiles in a precursor wall jet at 600m (a-density, b-pressure, c-dynamic pressure) and 700m (d, e, f). Solid line denotes previous 2-D calculation (Kuhl et al., 1993).

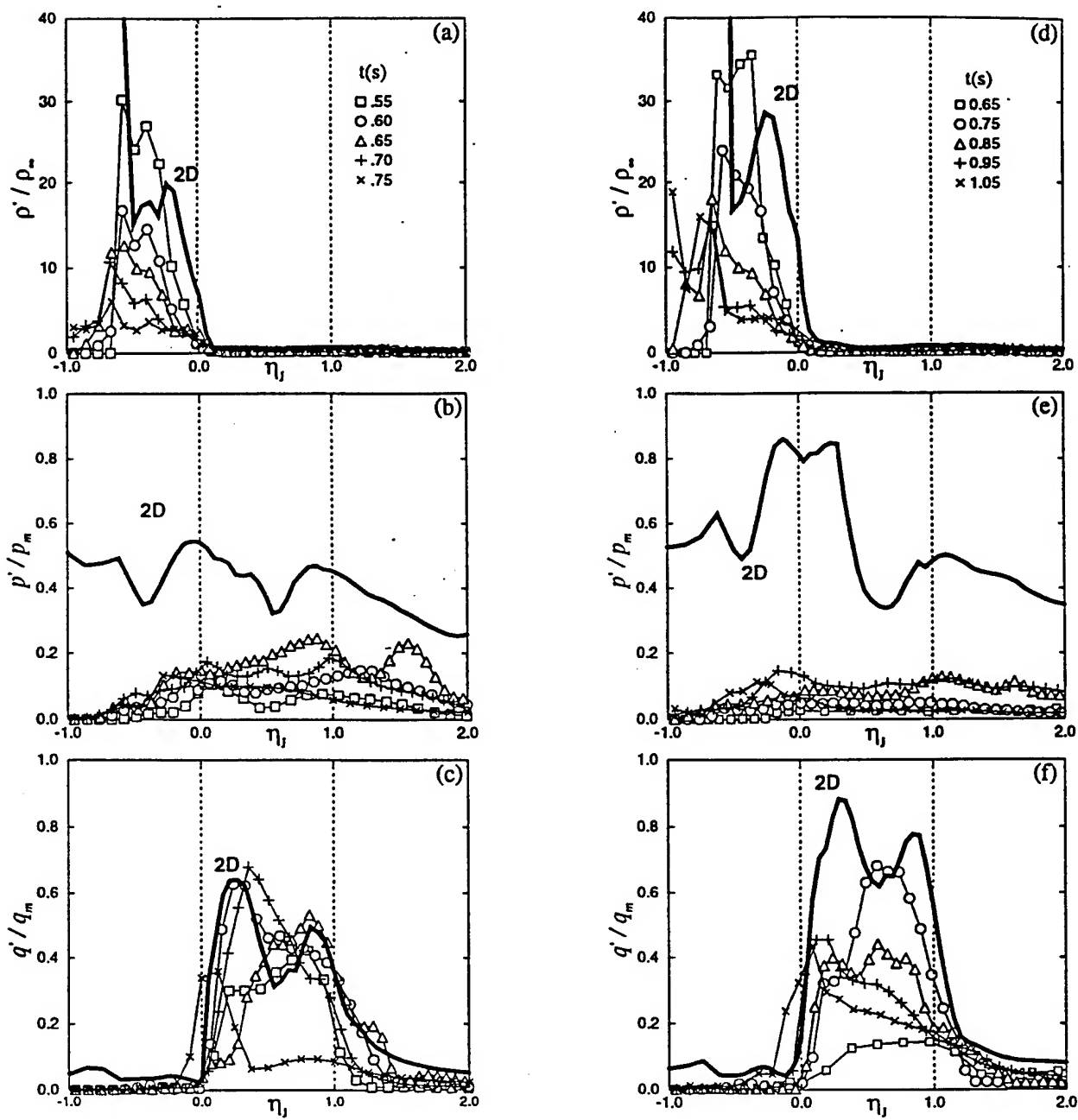


Figure A4. Fluctuation profiles in a precursor wall jet at 600m (a-density, b-pressure, c-dynamic pressure) and 700m (d, e, f). Solid line denotes previous 2-D calculation (Kuhl et al., 1993).

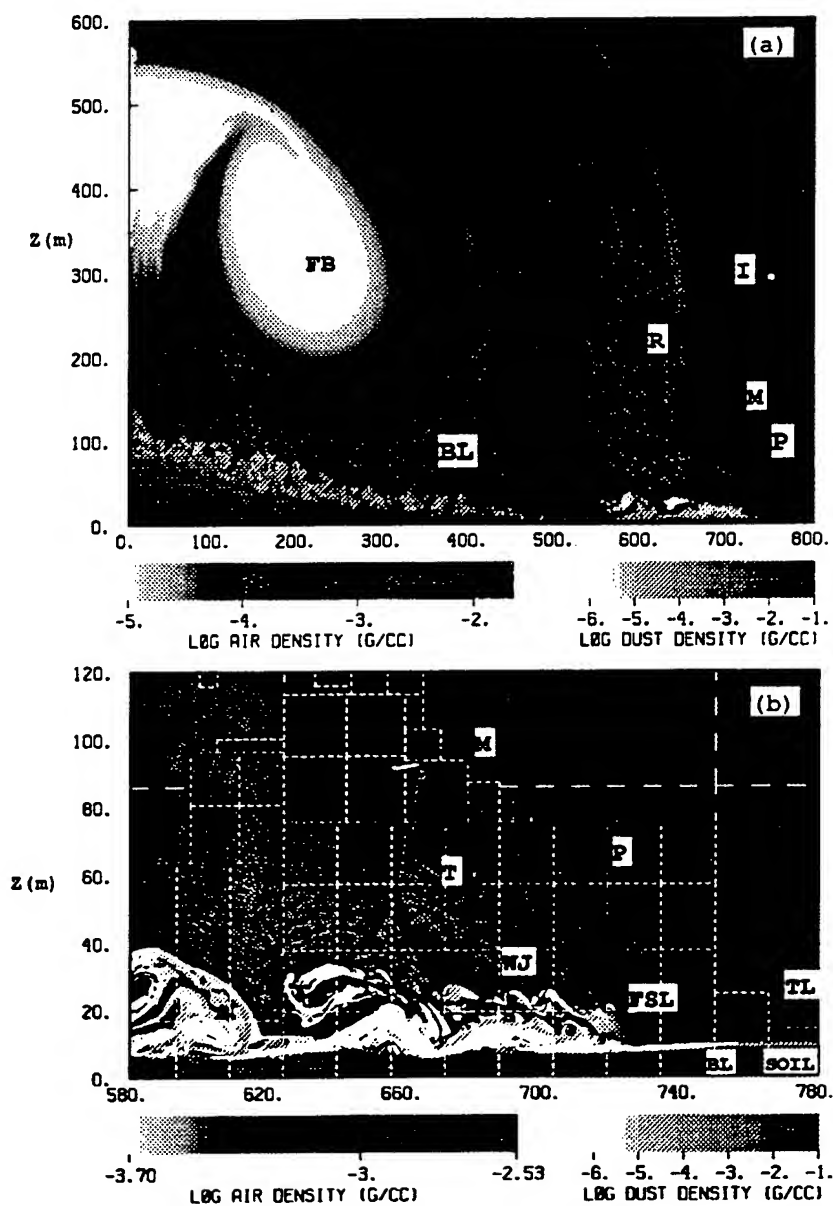


Plate 1. Color visualization of Figure 1. Color bar represents  $\log(\rho_{\text{air}})$ , while dust densities are shown in a grey scale. Black lines in (a) denote pressure contours. In (b), red and white lines represent positive and negative vorticity contours, while black lines represent dilatation contours.



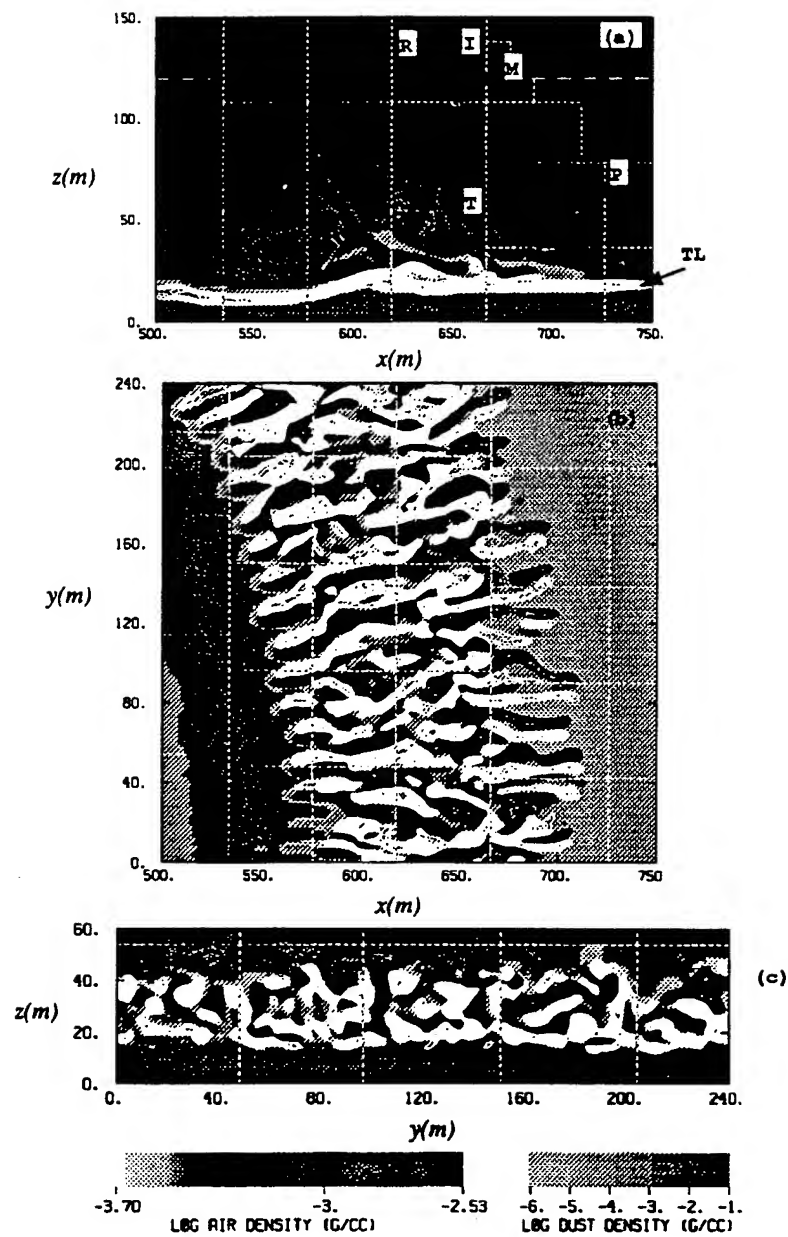
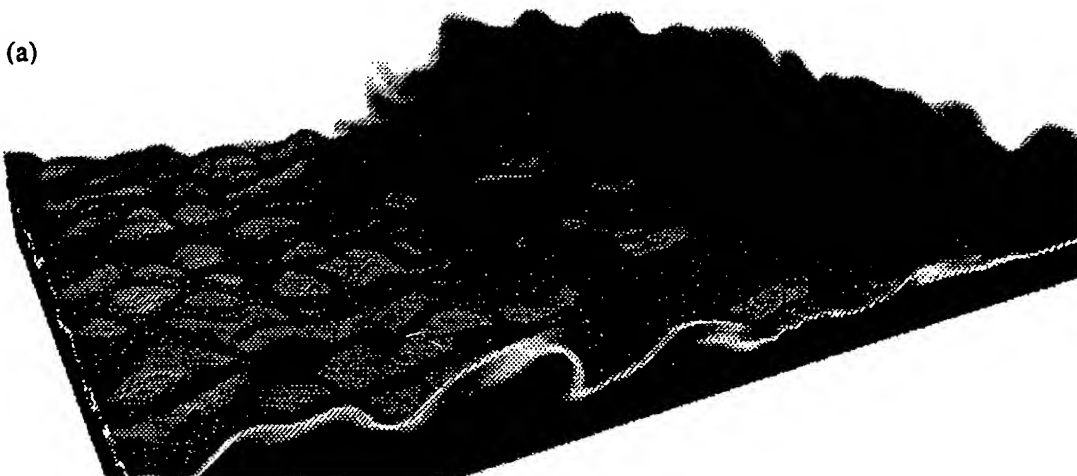


Plate 2. Color visualization of Figure 2. Color scales are the same as in Plate 1(b).

(a)



(b)



Plate 3. Color visualization of Figure 3.

**BIOLOGICAL EFFECTS OF BLAST ON SHEEP:  
COMPARISON OF SHOCK TUBE EXPOSURE TO FREE FIELD EXPOSURE.**

VASSOUT P.,\* MAYORGA M.A.,\*\* ARGYROS,\*\* G., TOPPER, M\*\*\*

\* Group PHYSIOLOGY French-German Institute of Research  
5 rue du Gal CASSAGNOU F-68301 SAINT LOUIS France

\*\* Department of Respiratory Research, Division of Medicine, Walter Reed Army  
Institute of Research, Washington D.C. 20307-5100 USA

\*\*\*Department of Comparative Pathology, Division of Pathology, Walter Reed Army  
Institute of Research, Washington D.C. 20307-5100 USA

**ABSTRACT**

Exposure to Free Field Blast Over Pressure (FFBOP) induces generalized injuries confined primarily to the gas-containing structures of the body: respiratory tract, middle ear, gastrointestinal tract. Free Field Blast Overpressure studies are realistic but require the outdoor detonation of explosives which can be affected by adverse weather conditions. Shock Tube Blast Over Pressure (STBOP) focalizes injury to only the exposed organs. Depending on the size of the shock tube and the animal exposed, the STBOP-induced injuries may vary from those seen in FFBOP exposures. The advantage of STBOP studies is the ability to conduct Shock Tube studies indoors using sophisticated physiological and biochemical measuring equipment. However, we first must understand the differences in resultant FFBOP-versus STBOP-induced injury. The purpose of this study was to compare the level and distribution of injury in sheep exposed to FFBOP versus STBOP. The STBOP study defining "No injury", "Trace", "Slight", "Moderate" and "Severe" Injury levels for sheep was previously completed by Dodd *et al.* This study defines the same levels in FFBOP-exposed sheep. Groups of 2-4 animals were exposed to 0, 100, 200, 300, 350 and 400 kPa BOP with an approximate 2 ms A-duration. Necropsy was performed at time of spontaneous death or at 24 h post exposure. Organs were scored according to the WRAIR BOP Gross Pathology Scoring Methodology. Additionally, lung and gastrointestinal sections were taken for histology examination. The five levels of injury were identified for FFBOP exposure in sheep. The magnitude of peak pressure required to produce the same level of injury in FFBOP appeared to be higher than that required in STBOP exposure. At "Moderate" injury levels slight gastrointestinal and bladder hemorrhages were noted. This study provides for the comparison of levels of injury produced by FFBOP and STBOP exposures. It will serve as a basis for a more comprehensive invasive cardiopulmonary study which will compare the physiological responses of FFBOP-and STBOP-exposed sheep.

**This work was done with a French grant : DRET 92156**

## **INTRODUCTION:**

Primary blast injury, induced by exposure to high level impulse noise is primarily confined to gas-containing structures of the body: the upper respiratory tract (URT), the lungs and the gastrointestinal tract (GI). The entire pressure-time history of the shock wave determines the severity of injury in these susceptible organs<sup>1</sup>. For a single Free Field Blast Overpressure Exposure (FFBOP), rise time, A and B-durations, and positive and negative peak pressure are injury determining features of the pressure-time history (fig.1a). In Shock Tube Exposure (STBOP), the shock wave is localized to a particular organ(s) or may strike the whole body. In this instance, the important parameters are the diameter of the shock tube; body size of the animal; and peak and any reflected pressures as measured by gauges which most accurately represent the pressure applied to the body (Fig.1b).

The injury incurred by FFBOP and STBOP are similar. Previous swine and ovine free-field and shock tube studies have shown that the ensuing lung lesions range from surface petechia to tissue disruption and hemorrhage. These pulmonary injuries resolve in 14-30 days<sup>2,3,4</sup>. However, these results were based solely on gross pathological observation and/or partial measurement of respiratory physiological parameters. Dodd *et al*<sup>4,5</sup> were the first to evaluate the biochemical, blood gas and cardiopulmonary effects of pulmonary contusion and to define the STBOP exposure levels that result in "no injury", "slight", "moderate" and "severe" injury levels with STBOP. These injury levels make up the Walter Reed Blast Overpressure (BOP) Scoring Methodology for Gross Pathology (Fig. 3).

The objective of this study was to determine the level and distribution of injury in sheep exposed to FFBOP and compare the results to Dodd *et al* previous STBOP exposure studies<sup>5,6</sup>. This study will serve as a basis for more comprehensive invasive cardiopulmonary study which will compare the physiological responses of FFBOP and STBOP exposed sheep.

## **MATERIALS AND METHODS:**

Twenty one healthy, parasite free female sheep weighing 28-35 kg were sheared and divided into five exposure groups: control (n=3), 100 kPa, (n=3), 200 kPa (n=4), 300 kPa (n=6), 350 kPa (n=2) and 400 kPa (n=5) (Table 1). The A-duration was kept constant at approximately 2 ms for each exposure group. Accelerometers (BK 4393) were surgically fixed to ribs on the exposed side on two sheep exposed to 200 kPa and on three animals exposed to 300 kPa. Another type of accelerometer (Entran: EGAS-FT-5000) was fixed to two sheep exposed to 300 kPa. Three animals with accelerometers, one exposed to 200 kPa and two exposed to 300 kPa were covered with foam similar to those used for acoustic ear plugs (E.A.R.<sup>®</sup>) (Table 1). One of the animals exposed to 200 kPa was covered with 2 layers of foam (1 layer of yellow foam and 1 layer of blue foam, E.A.R.<sup>®</sup>)

the other 2 animals were covered with 1 layer of yellow foam. The two colors of foam differed in density, the yellow foam having a lesser density than the blue.

On the day of the test, the animals were anaesthetized with Tiletamine/Zolazepam 100 (500 mg IM), placed in a fish net harness and suspended with their left side perpendicular to the direction of the shock wave propagation. All sheep were given additional doses of Tiletamine/Zolazepam, 500 mg for pain relief 0.5 and 6 hr post-exposure. At 24 hours post-exposure, animals were euthanized with an overdose of Tiletamine/Zolazepam anaesthetic and exsanguination by severing of the great vessels, then necropsied. Organs were scored according to the Walter Reed BOP Gross Pathology Scoring Methodology (Table 2). Lung and gastrointestinal sections were taken for histological examination and are not described in this report. The calculation of the lung weight/body weight ratio (LWR) gives an appreciation of the fluid (blood and/or edema) content of the lung. We compare LWR of animals exposed to the blast to LWR of control animals (unexposed). The calculation is expressed as  $Q_i = \text{LWR blasted animals} / \text{LWR control}$  (Jonsson A. 1979) <sup>7</sup>.

## **RESULTS:**

### *Gross Pathology and $Q_i$*

The necropsy of FFBOP controls (unexposed animals but anesthetized) showed small cardiac intraventricular hemorrhages in two animals. The results of the other injury groups are shown in Table 3. These results are comparable to previous FFBOP swine studies conducted at the French-German Institute of Research where animals exposed to 200 and 300 kPa demonstrated slight to moderate and severe lung injury, respectively. The results from STBOP ovine studies demonstrate a lower peak pressure required to produce the same level of injury as in FFBOP (Table 4).

### *Chest Wall Motion and Foam Studies*

Two sheep had an Entran accelerometer fixed to left 8th rib. Because of high output voltage, an adequate recording could not be measured and a BK 4393 accelerometer was substituted in five sheep. In conjunction with these studies, a group of animals were exposed to FFBOP with either one or two layers of blue or yellow foam. The level of FFBOP, chest wall accelerations, gross pathology are described in Table 5. An equivocal effect was seen in the two sheep exposed to 1 layer of yellow foam, however, in one sheep there was a suggestion that an enhancement of injury occurred with two layers of foam (Table 6).

## **CONCLUSIONS:**

This pilot study approximates the levels of injury for 0, 100, 200, 300, 350 and 400 kPa in sheep exposed to FFBOP. Injury is less compared to that induced by the same level of STBOP. The sample size was too small to ascertain whether 1 layer of foam reduces the level of injury, however, there was a suggestion that 2 layers may exacerbate injury.  $Q_i$

may serve as another reliable indicator of injury in addition to gross pathological scoring. Acceleration measurements were equivocal given the small sample size, although there is a suggestion that acceleration increases with increasing peak pressure and level of injury. These results will serve as a basis to perform further FFBOP exposures to increase the number of animals per group and simultaneously measure cardio-pulmonary physiological and biochemical changes after free field exposure. These studies will also be compared to those obtained after STBOP tube exposure inducing the same level of pulmonary injury.

## **DISCUSSION:**

In the FFBOP exposure experiments, the pressure-time history is characterized by a rapid increase of pressure above ambient level, followed by an exponential decay to below ambient level and return to baseline (Figure 1a). In the STBOP exposure experiments, the blast signature is mainly characterized by a slower rise to peak pressure, a plateau, and a secondary positive deflection from a reflective surface placed behind the animal so as to minimize displacement (Figure 1b). In FFBOP studies, the whole animal is exposed to the blast wave, whereas in STBOP, contusion may be localized to an area of the body. In comparing results from different BOP exposure models, it is important to know the method of blast overpressure production (explosives, compressed air, etc.), experimental design, and animal and gauge placement. Since not all shock tubes are the same, it is also helpful to perform computational fluid dynamic modeling of the shock tube environment. Further chest wall acceleration studies are needed to confirm the accelerations for the various pressure-time histories and injury lung levels. A relationship between chest wall velocity and lung injury has been described by Cooper, *et al*<sup>4</sup> and Axelsson, *et al*<sup>5</sup>. However, reproducible and reliable measurements of chest wall acceleration, which occurs when the blast wave interfaces with the thorax, has been difficult. Variables such as type of accelerometers, level of anesthesia and type of animal restraints affect chest wall acceleration measurements. Consideration of these variables are important in comparing studies. Understanding the type and levels of injury, and the biomechanical, physiological and biochemical mechanisms of injury will lead to improved preventative and treatment regimens for BOP and similiar blunt trauma injury.

## REFERENCES

1. Richmond, D.R., Damon E.G., Bowen I.G., Flether, E.R., White, C.S. The relationship between selected blast wave parameters and response of mammals exposed to airblast. *Ann. N.Y. Acad. Scien.* 152:103-121, 1968.
2. White, C.S., Jones R.K., Damon, E.G., Fletcher, E.R., Richmond, D.R., The biodynamics of airblast. Report DNA 2738 T, 1971.
3. Vassout P., Parmentier G., Dancer, A. The relationship between number of blast exposure and lung injury on swine. French-German Research Institute (ISL) Report S-R 904/81, 1981.
4. Cooper, G.J., Townend, D.J., Cater, S.R., Pearce, B.P. The role of stress waves in thoracic visceral injury from blast loading: Modification of stress transmission by foams and high-density materials. Proceedings of the International Research Council on the Biomechanics of Impacts, 13-15 Sept 1989.
5. Vassout, P., Dodd K.T., Laguchik M., Jenkins E., Innskeep W. Chronic (28 days) cardiopulmonary effects of blast overpressure. 12th Military Applications of Blast Simulations 22-27, Sept. 1991.
6. Dodd, K. T., Mundie, T.G., Lagutchik, M.S., Sharpnack, D.D., Ripple, G.R. The effects of pulmonary contusion on cardiopulmonary function in sheep, Federation of American Societies for Experimental Biology Journal, Abstracts Part I, A537, April 1991.
7. Jonsson, A. Experimental investigations on the mechanism of lung injury in blast and impact exposure. Linkoping University Medical Dissertation No 80, 1979.
8. Axelsson, H. and Yelverton, J.T., Chest wall velocity as a predictor of non-auditory blast injury in a complex wave environment. FOA Reprints of the 7th International (5th International Symposium on Wound Ballistics and Weapon Traumatology, St. Petersburg, Russia, FOA-B-95-00066-2.3,5.4-SE, July 1995.

**TABLE 2 Walter Reed Blast Overpressure Gross Pathology Scoring Methodology**

Level of Injury	Description
No injury	No injury attributable to Blast Overpressure
Trace	Petechial hemorrhages involving less than 10% of the lung surface
Slight	Superficial petechial or ecchymotic hemorrhages involving greater than 10% of the lung surface.
Moderate	Subpleural ecchymotic hemorrhage with superficial involvement of 11-30% of the lung surface.
Severe	Diffuse ecchymotic hemorrhage extending into parenchyma involving 31-60% of the lung.
Extensive	Confluent transparenchymal hemorrhage involving 60-100% of the lung.



**TABLE 3 Gross Pathology Changes after Free Field Blast Overpressure Exposure of Sheep**

Injury Level	#	Peak Pressure (kPa)	A-Dur. (msec)	Qi	Description of Pathology
control	3	0	—	—	Two animals had interventricular cardiac petechiae
No injury	3	100	1.7	<1	No gross pathological changes
Trace	A intermediate group between 100-200 kPa was not studied				
Slight to moderate slight	1	200	1.75	1.2	Petechia or ecchymosis of pleura involving less than 10% of lung
mod.	2	200	1.75	1.4	Ecchymosis of pleura and sub-pleura involving 10-30% of the lung in two animals; slight intestinal and bladder hemorrhages, and superficial interventricular cardiac hemorrhages in one animal.
Moderate to Severe severe	4	300	1.8	1.5	Parenchymal ecchymosis involving 30-60% of the lung, small gastrointestinal, tracheal and ventricular cardiac ecchymosis noted in two animals.
mod.	2	350	1.7	1.3	Ecchymosis of pleura and sub-pleura involving 10-30% of the lung; tracheal and intraventricular cardiac ecchymosis.
severe	3	400	1.9	1.8	Transparenchymal ecchymosis involving 30-60% of the lung; tracheal and small gastrointestinal hemorrhages.

**TABLE 4 Comparison of Shock Tube and Free Field Blast Overpressure Peak Levels Producing the Same Degree of Lung Injury in Sheep**

	Shock Tube (kPa)	Free Field (kPa)
No Injury	—	100
Trace	99.3±18.62	—
Slight	122.7±10.34	200
Moderate	134.5±13.79	200-350
Severe	147.6±7.58	300-400

**TABLE 5 Chest Wall Acceleration During Free Field Blast Overpressure Exposure of Sheep**

Foam	Peak Pressure		Acceleration	Level of Injury
	(kPa)	(m/s/s)		
Without foam	200	18,000		Moderate
With 1 layer of foam <sup>a</sup>		18,750		Severe
<hr/>				
Without foam	300	20,000		Severe
		36,000		Severe
With 1 layer of foam <sup>a</sup>		—		Moderate
With 2 layers of foam <sup>b</sup>		100,000		Extensive

<sup>a</sup> one layer of yellow foam applied.

<sup>b</sup> one layer of yellow foam and one layer of blue foam applied.

**TABLE 6 Effect of Foam on Level of Free Field Blast Overpressure-Induced Injury in Sheep**

Pressure (kPa)	No Foam	1 Layer of Foam <sup>a</sup>	2 Layers of Foam <sup>b</sup>
100	No injury (n=3)	_____	_____
200	Slight (n=1) Mod. (n=1)	Severe (n=1)	_____
300	Severe (n=4)	Mod. (n=1)	Extensive (n=1)
350	Mod. (n=2)	_____	_____
400	Severe (n=3)	_____	_____

<sup>a</sup> one layer of yellow foam applied (E.A.R.<sup>®</sup>).

<sup>b</sup> one layer of yellow foam and one layer of blue foam applied (E.A.R.<sup>®</sup>).

### Free Field Blast Overpressure

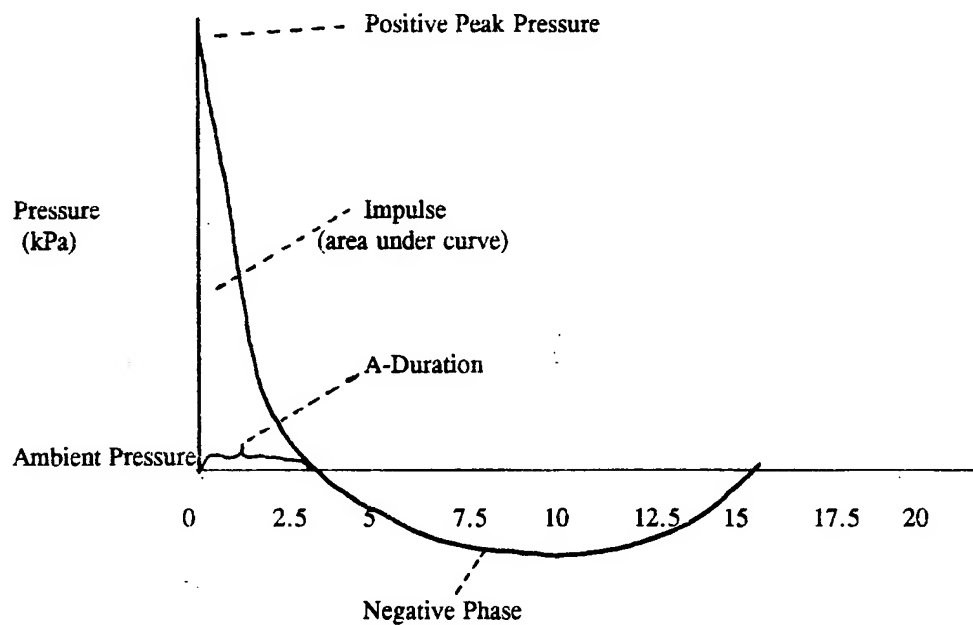


Figure 1a

### Shock Tube Blast Overpressure

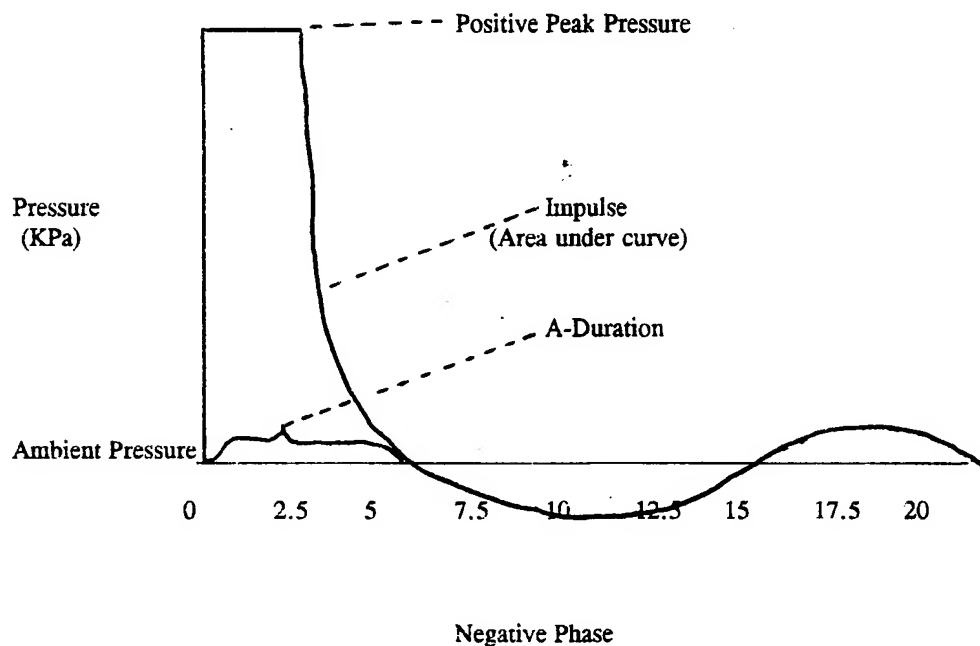


Figure 1b

# AUDITORY AND NONAUDITORY DAMAGE-RISK ASSESSMENT FOR SIMULATED WEAPONS FIRED FROM AN ENCLOSURE

Daniel L. Johnson, John T. Yelverton,  
William Hicks, and Roy Doyal

EG&G MSI  
2450 Alamo SE  
P. O. Box 9100  
Albuquerque, NM 87119-9100

**ABSTRACT.** A test apparatus was fabricated to simulate the blast environment to establish the damage risk from the reverberant wave produced during the firing of an antitank weapon from an enclosure. The simulation was accomplished by detonating C-4 explosive charges outside a 18.2 m<sup>3</sup> all-steel chamber. The blast wave was introduced into the chamber through a 20-cm I.D. tube and was reflected off the back wall and subsequently throughout the chamber. The resulting waveform at the target locations closely approximated that generated by a Carl Gustav antitank weapon fired from a room of about the same volume. The nonauditory threshold was first estimated by exposing anesthetized sheep to various intensities of this reverberant wave environment. A series of 1-shot, 3-shot and 12-shot (2.5 minute intervals) exposures were done. The results indicated that multiple shots have a strong additive effect, decreasing the threshold levels. The threshold for a single exposure was estimated to be near a maximum peak pressure of 65 kPa and near a maximum peak of 46 kPa for three exposures. The threshold for 12 exposures was not found. Forty anesthetized sheep were used statistically to establish 48 kPa for one shot and 44 kPa for three shots as subthreshold levels in which no injury occurs. The auditory limit for the one- and three-shot exposures was then investigated. Using at least 60 human volunteers, a temporary change in hearing level was used as the primary measure of blast effect. Other parameters measured were performance assessment, stool guaiacs, tympanometry, physical well being, and otacoustic emissions. Each subject wore an RACAL® muff, modified so it simulated leaks typical of a poorly fitted muff. The exposures were started at levels of approximately 1/64 of the energy of the final condition. The final conditions were set at the nonauditory threshold limits. Providing no effects occurred, the exposure energy was doubled for the next exposure, i.e., the second exposure was 1/32 of the energy of the final condition, until the nonauditory subthreshold level was reached. No auditory effects occurred. Thus, nonauditory considerations set the safe limit for firing a Carl Gustav-type weapon from an enclosed bunker.

## INTRODUCTION

This report describes the studies undertaken to establish the nonauditory and auditory thresholds for injury in a reverberant wave environment like that produced from firing an antitank weapon from a room.

In the first set of experiments, anesthetized sheep were used throughout the study to determine the extent of the effects from various intensities and repetitions of a simulated weapon blast. After the nonauditory thresholds were established, auditory thresholds were established using human volunteers.<sup>1</sup> The studies were conducted by EG&G MSI at the Blast Overpressure Test Site (BOPTS), Kirtland Air Force Base, NM, for the U.S. Army Medical Research and Materiel Command, Fort Detrick, MD. Previous studies have shown that the complex blast waves generated by detonating various weights of bare, spherical C-4 explosive charges in three different enclosure volumes produced varying degrees of nonauditory injury.<sup>2,3,4</sup> The extent of the injury depended upon the size of the charge detonated and the location of the animal with respect to the charge and position in the chamber. Injury levels increased with increasing charge weight as in the free field. However, they also varied as a function of the location of the subject in the enclosure and not necessarily as a function of range from the explosion as in the free field. Animals in the corners sustained more severe injuries in the form of solid intra-abdominal organ damage than those located away from the multiple reflecting surfaces and at shorter distances from the explosion. This was particularly true at the higher blast levels. At the higher levels, the reflected waves tend to focus, producing incident reflected waves 3 to 10 times higher than those generated in the free field at the same ranges and explosive weights.

It was also shown that the quasi-static pressure did not influence the lung, upper respiratory tract, or GI tract injury to any appreciable degree. Nonetheless, the reverberant nature of the complex wave was altered by changing the quasi-static pressure that did appear to have a slight effect on solid intra-abdominal organ response. There was a higher incidence of solid intra-abdominal organ injury and more severe solid intra-abdominal injury in the subjects exposed in the chamber with the door locked and vent doors closed.

An injury prediction curve using a severity of injury index (SI) and smoothed-peak pressure (Psm) as correlates appeared to be an adequate model for the information collected (Fig. 1). The smoothing function was a moving time window of 175 msec. The Psm was roughly one-half of the maximum peak pressure (Pmax). The severity index data predicted a no-injury window for a Psm extending from 0 to 57 kPa (0 to 123.3 Pmax). The 57 kPa (123.3 Pmax) was adjusted upward from the 40 kPa (82.3 Pmax) zero crossing of the curve to compensate for the control injury level of 0.05. Trace to slight injuries were

estimated for pressures extending from 57.1 to 130 kPa. For Psm values ranging from 130.1 to 221 kPa, slight to extensive injuries were predicted. Moderate to lethal levels of injury were expected over a Psm span of 221 to 428 kPa. At pressures above 428.1 kPa lethality was predicted to exceed 50 percent. It was also found that, intra-abdominal injury aside, by converting Psm to Pmax, there was a good correlation between the injury prediction curve and the "Bowen's free stream survival curves"<sup>5</sup> for 2- to 3-ms duration waves.

This implies that the pulse with the highest peak and longest duration of the individual pressure pulses in the complex wave is primarily responsible for injury production, with limited additive effects from the multiple shocks associated with the reverberant wave. The extent to which this relationship holds true for other classes of waveforms needed to be clarified. The class of waveform selected was the waveform resulting from an antitank weapon fired from an enclosure.

Using this waveform, auditory studies using human volunteers were then carried out to see if adequate hearing protection was available that would protect the ear at the nonauditory limits. The protector used was the RACAL® muff, the same protector shown to provide adequate protection at the free field nonauditory limits.

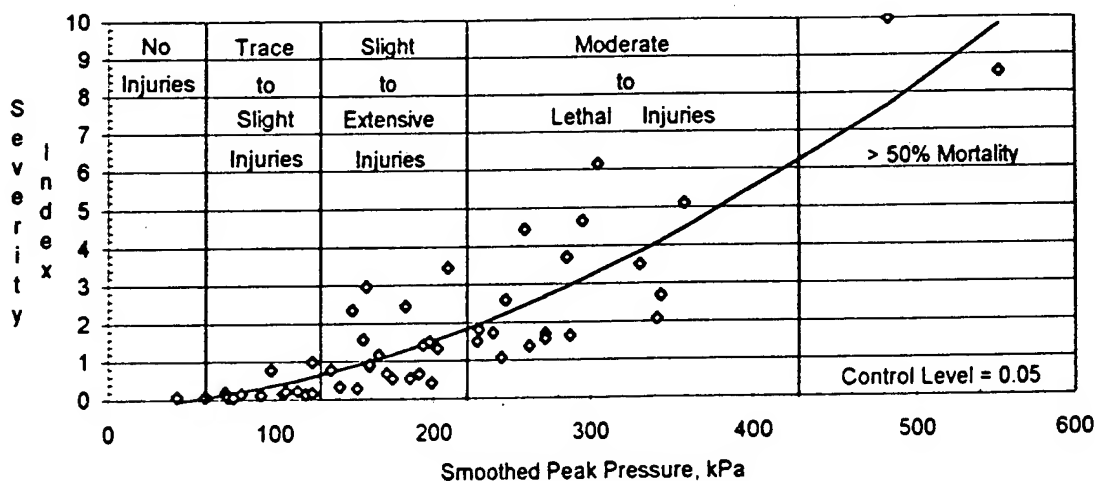


Figure 1. Smoothed peak pressure injury prediction curve for complex blast waves generated by detonating explosive charges in 11.3x18.2x36.3-m<sup>3</sup> enclosures.



## **I. NONAUDITORY DAMAGE-RISK ASSESSMENT**

### **OBJECTIVES**

The basic objective, using anesthetized sheep, was to determine the nonauditory threshold level from 1, 3, and 12 exposures to a complex wave environment similar to that produced from firing an antitank weapon from an enclosure. A secondary objective was to provide data for the validation of the Jaycor injury prediction model by the Walter Reed Army Institute of Research (WRAIR).

### **METHODS**

An instrumentation cylinder was used to map the pressure-time environment at various locations within the blast simulator to develop a waveform similar to that generated by the Carl-Gustav antitank weapon. Once the location in the chamber for the best waveform simulation was established, anesthetized sheep were exposed to various intensities and repetitions of the simulated wave (Figures 2 and 3). Two anesthetized sheep at a time were fitted with cotton webbing or fish net harnesses and suspended from the ceiling of the enclosure at a height of 1.2 m from the floor as measured to the xiphisternum. One sheep was placed in the location the instrument cylinder was in during waveform and calibration curve development and the other sheep was placed on the opposite side of the gun barrel in a mirror image location facing the other sheep.

#### **Waveform Development**

The pressure-time environment was recorded at various locations in the chamber (Figs. 2 and 3) to establish the exposure positions for the test subjects and to provide input parameters to the WRAIR to model the pressure-time environment throughout the room. Most of the pressure-time measurements were taken around the barrel of the simulator at a height of 1.2 m off the floor using the free field gauges and the instrumentation cylinder used in previous experiments. The pressure-time patterns selected by the Walter Reed Army Institute of Research (WRAIR) and the U. S. Army Aeromedical Research Laboratory (USAARL) to simulate the Carl-Gustav antitank weapon blast wave were recorded using the instrumentation cylinder (Figure 4). Pressure-time recordings from 454-, 907-, 1361-, and 1814-g C-4 charge detonations were used

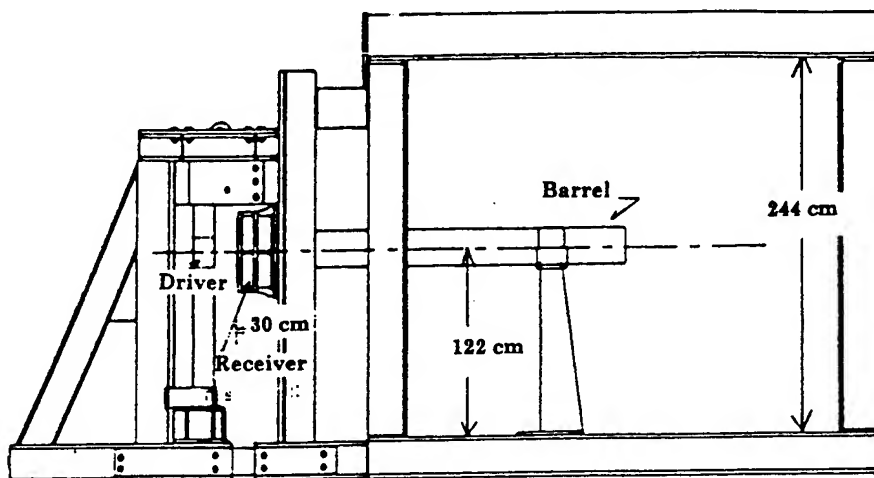


Figure 2. Side view of the 3.05x2.44x2.44-m configuration of the EG&G test enclosure redesigned as a Carl-Gustav antitank weapon blast simulator.

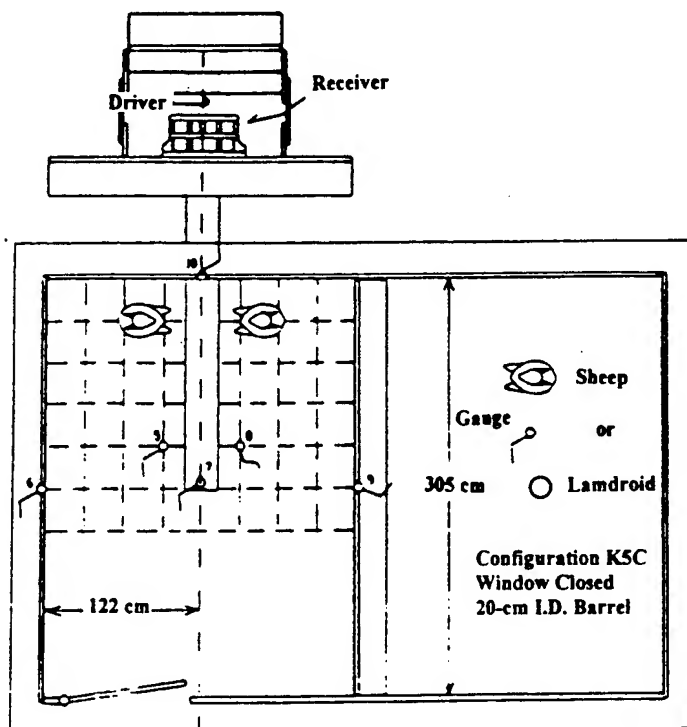


Figure 3. Gauge layout and animal locations for the Carl-Gustav simulation tests in the 3.05x2.44x2.44-m enclosure.

to develop the initial calibration curves for the Psm and the Pmax. Because Psm was less variable than Pmax, Psm was used as the basis of various data analysis. The relation between Psm and Pmax was:

$$P_{\max} = 8.42 + 1.447 P_{\text{sm}} + .00997 P_{\text{sm}}^2$$

Where Pmax was estimated by this formula, the symbol Pmax\* was used. Where Pmax was measured, Pmax was used.

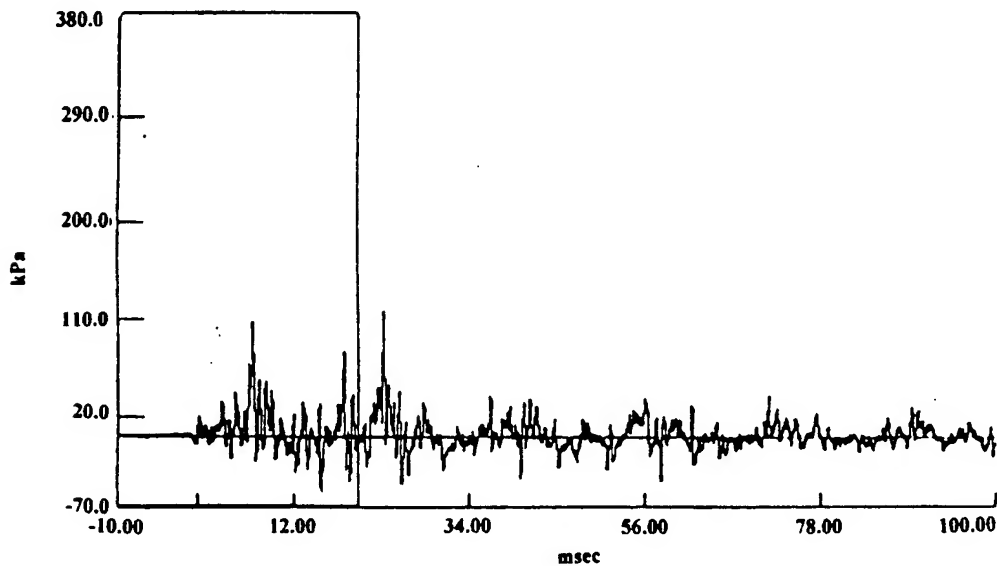


Figure 4. Pressure-time pattern from a 454-g charge detonation in the 3.05x2.44x2.44 m Carl-Gustav antitank weapon blast simulator.

### Experimental Design

The design for the study is presented in Table 1. Varying numbers of anesthetized sheep were subjected to first 12, then 1, and finally, 3 blasts. The initial exposure doses and the corresponding charge weights were derived from the calibration curves mentioned above. There were three experiments based upon the number of exposures the animals received. Pairs of controls were used at intervals throughout the study to compensate for any lesions induced by iatrogenic factors or disease. All animals were treated the same and mounted in position for 28 minutes whether or not they were exposed. This allowed the controls to be compared interchangeably between groups. There were 110 sheep in the single-exposure tests, 82 in the three-exposure tests, and 29 in the 12-

**Table 1. Experimental Design for the Carl-Gustav simulation tests in the 3.05x2.44x2.44-m configuration of the EG&G Test Enclosure.**

Exposure Levels				Groups		
Delta, dB	Pmax, kPa	Psm, kPa	Charge Weight, g	No. of Animals/ No. of Exposures		
				X1	X3	X12
0.0	224.4	84.6	1361	2		5
3.0	134.2	59.8	816	8		4
4.5	108.9	50.3	565	4		
6.0	89.8	42.2	533	30		4
9.0	63.2	29.9	359	12		4
10.5	54.6	25.6	302		20	
12.0	46.1	21.1	245	40	10	4
13.5	39.9	17.7	203		40	
Subtotals				96	70	21
Controls				14	12	8
Totals				110	82	29
<p align="center"><u>Equations from Preliminary Calibration Curves</u></p> <p align="center"><math>P_{max} = 10.31854 + 0.14370x + 0.00001x^2</math> where <math>x</math> = charge weight</p> <p align="center"><math>P_{sm} = 0.49383 + 0.08898x - 0.0002x^2</math> where <math>x</math> = charge weight</p>						

exposure tests. The interval between shots was approximately 2.5 minutes. The exposures used were as follows:

**Twelve-Exposure Experiments:** Five different pressure levels were used starting at a Psm of 84.6 kPa (Pmax of 202.2) and going down in 3-dB step increments to 21.1 kPa (48 Pmax) to establish the approximate severity of injury and injury thresholds for the various organs. At 21.1 kPa (48 Pmax), further exposures were stopped because the injury threshold had not been reached. Emphasis then shifted in doing the three-exposure experiments.

**Single-Exposure Experiments:** For the single-exposure experiments, there were 96 animals in six groups with varying numbers of animals per group, depending upon the pressure level, and 14 controls (Table 1). Initially, two animals each were exposed in 3-dB increments to Psm levels of 84.6, 59.8, 42.2, 29.9 and 21.1 kPa (Pmax\* of 202.2, 130.6, 87.2, 60.6, and 48 kPa) to estimate the threshold and subthreshold levels based on severity of injury scores. The various groups were filled in with additional animals to establish statistically significant threshold and subthreshold levels for injury. One 1.5-dB step down from Psm levels of 59.8 to 50.3 kPa (Pmax levels of 130.6 to 83.89 kPa) was done in addition to the 3-dB steps to estimate the threshold for injury level.

**Three-Exposure Experiments:** Because the threshold for 12 exposures was not found at a level above what the Carl Gustav can currently produce, the protocol was amended to establish the subthreshold for injury level for three exposures. It was felt that no one would fire a weapon 12 times and that the three-exposure scenario better reflected the actual use of the weapon during training. Groups of 20, 10, and 40 subjects each were exposed to respective Psm levels of 25.6, 21.1, and 17.7 kPa (Pmax levels of 52, 48, and 44 Pmax). A total of 12 controls was used during this test series.

## **Test Enclosure**

The all-steel enclosure that was built for the tests that resulted in Figure 1 was converted to a "firing from within an enclosure simulator." The partition was adjusted to the 18.2 m<sup>3</sup> volume (Figs. 2 & 3). A hole was cut in the wall directly opposite the door to allow the introduction of a 249-cm long 'gun barrel' constructed from a seamless high-pressure steel tube, 20 cm I.D. and 2.54 cm thick. This tube extended 152 cm into the chamber. The tube was horizontally mounted with its centerline 122 cm from the floor and supported inside the chamber by a 2.54-cm thick stand that consisted of a 46- x 33-cm base plate, a vertical member that decreased in width from 30 to 19 cm, and a barrel mount. The mount included a 30- x 16- x 2.54-cm support plate and a 15-cm wide by 1.27-cm support plate and a 15-cm wide by 1.27-cm thick band that surrounded the tube. The barrel extended 3 cm beyond the barrier wall and was surrounded by a 'receiver' constructed from a 30-cm length of 2.54-cm-thick wall high-

pressure tubing. The receiver tapered from 42- to 41-cm I.D. It was surrounded by two radial and eight longitudinal gussets fabricated from a 2.54-cm plate to increase its hoop strength. A movable 1521- x 122-cm 'driver' section fabricated from two 15-cm thick plates of salvaged battleship armor was installed 15 cm downstream from the leading edge of the receiver. There was a 20-cm diameter hole cut in the slab or armor next to the receiver and was in line with the centerline of the gun barrel.

The simulator was operated by detonating a spherical charge of C-4 explosive in the mouth of the opening in the driver section to approximate the back blast from a weapon firing. The blast wave traveled down the barrel into the enclosure and was reflected off the back wall. The wave shape varied as a function of location in the room. The wave intensity was changed by changing the charge weight. The simulator was operated with the enclosure inertia vent doors open to minimize a quasi-static pressure rise and to eliminate explosive decomposition products.

## Instrumentation

Piezotronics (PCB) Model 102M152 or Model 102M165 piezoelectric pressure transducers and the instrumentation cylinder, provided by the WRAIR, were used during the study. The instrumentation cylinder was fitted with four ablative coated PCB Model 102M125 gauges at 90-degree intervals around its circumference and at the midpoint of its long axis. The 102M152's and 102M165's were used as side-on free air gauges mounted vertically with their sensing elements pointing face-up or mounted face-on in three of the enclosure walls. A 102M165 with ablative coating was at the end of the barrel during the animal experiments. A 1- to 2-mm-thick layer of temperature resistant, high-vacuum grease impregnated with charcoal was coated on the sensing element of each of the free air gauges before each shot to mitigate any possible thermal or flash effects. Signals from the transducers were passed out of PCB in line voltage mode followers into power conditioners through Tektronix Model AM502 differential unfiltered amplifiers. Unfiltered signals were simultaneously recorded on an Ampex Model PR2230 dc to 80 kHz FM tape recorder and digitized over 13 of 15 segments of 8k data points each at a 4- $\mu$ sec sample interval with a Pacific Instruments data acquisition system operating in conjunction with a personal computer. The first 2 of the 15 segments were used to establish the baseline for the data array. The digitized data were stored on 20 and 44 Mbyte Bernoulli disk cartridges for analysis using the blast data acquisition and analysis software. The data stored on the 44 Mbyte disks were also sent to the WRAIR for further analysis.

## Animal Care

A total of 221 female Columbia-Rambouillet cross sheep having body weights of approximately 41 to 50 kg was used during the study.

The animals were maintained in one of four outdoor pens. One to two weeks before testing, the subjects were sheared in groups of six to 10, given a second application of tick spray, and moved to an indoor holding facility. They were kept in groups of four to six in pens with wood shavings on the floor. Food pellets were provided at a rate of 1 kg/head/day. Water was available *ad libitum*. Each test animal was fasted a minimum of 18 hours before a test.

On the morning of a test, the animals were harnessed, weighed and given an otoscopic examination to remove any obstruction from the ear canals before transport to the test site. The ear or ears that were to be protected were blocked with a selected earplug. Each sheep received a preanesthetic intramuscular (IM) injection of atropine sulfate (0.44 mg/kg) and xylazine (0.22 mg/kg) and was placed in its test position approximately 15 minutes before blast exposure. At 5 minutes before the test, each sheep was anesthetized with an IM injection of ketamine hydrochloride (11 mg/kg) then exposed to blast.<sup>6,7</sup>

## Pathology Scoring

The subjects were not allowed to recover from anesthesia. Starting at approximately one hour after blast exposure, one sheep at a time was given an IM injection of ketamine hydrochloride (22 mg/kg), exsanguinated by severing the jugular veins and carotid arteries, and necropsied. Each animal was assessed for injuries using the alphanumeric scoring system described in the Task Order 2 final report.<sup>4</sup> Trauma to the pharynx/larynx, trachea, lungs, heart, hollow abdominal organs, and solid abdominal organs were assigned individual numerical scores based on the severity of the lesion. The various lesions were also graded as trace, slight, moderate, or extensive depending upon their severity.

The alphanumeric pathology scoring system for the most commonly injured nonauditory organs is listed as follows:

Pathology Scoring System					
Severity	Lung	Pharynx/ Larynx	Trachea	GI Tract	Intra- abdomina l
Negative	0	0	0	0	0
Trace	1-4	1-4	1-4	1-4	1-4
Slight	5-21	5-16	5-18	5-18	5-18
Moderate	22-36	17-22	19-28	19-28	19-28
Extensive	37+	23+	29+	29+	29+
Maximum Possible	64	60	55	48	44

The ears were evaluated based upon the percentage of eardrum ruptured. An additional numerical score was given for each ear for the amount of eardrum damaged and ossicular chain involvement.

Each individual injury score was divided by its preassigned maximum possible score to arrive at a severity of injury ratio for that organ or system. The maximum possible score varied as a function of the number of components the organs were divided into and the possible levels of severity assigned to them. The presence or absence and the extent of a pneumothorax, hemothorax, hemoperitoneum, coronary air or cerebral air were summed and added to the sum of the ratios. The resulting value was the adjusted severity of injury index arrived at by excluding the ear damage values from the sum of the ratios.

### Nonauditory Injury Levels

Mean severity of injury index (SI) values from the pathology assessments versus the Pmax and Psm blast levels are presented in Table 2. The severity indices were grouped in terms of number of exposures and descending order of blast intensity. For the convenience of discussion the results are presented both in terms of Psm and Pmax.



Table 2. Mean severity of injury indices (SI) versus instrument cylinder maximum (Pmax) and smoothed (Psm) peak pressures and charge weights.

Exposure Levels			Exposure Groups		
Pmax, kPa	Psm, kPa	Charge Weight, lb	Mean SI per Group and Level		
			x1	x3	x12
215.4	89.7	1361	0.29		2.18
129.5	60.6	816	0.18		1.61
105.8	50.8	656	0.09		
88.2	42.8	533	0.05		0.29
64.0	31.0	359	0.03		0.29
56.2	26.9	302		0.10	
48.6	22.8	245	0.01	0.09	0.22
43.0	19.7	203		0.01	
Controls			0.03		
<p align="center"><u>Equations from Final Calibration Curves</u></p> <p align="center"><math>P_{max} = 16.7225883 + 0.1264033x + 0.0000144x^2</math> where <math>x</math> = charge weight</p> <p align="center"><math>P_{sm} = 4.2147674 + 0.0786800x - 0.0000117x^2</math> where <math>x</math> = charge weight</p>					

For the 12-exposure group illustrated in Figure 7, the SI ranged from 2.18 for a Psm of 89.7 (Pmax of 215.4 kPa) to 0.22 for a Psm of 22.8 (Pmax of 48 kPa). The number of animals per point was included. The control level SI crossing point occurred at approximately 21.8. However, this approach ignored the strong effect at the low peak values (the SI is still at 0.22) and was clearly not a proper approach for obtaining the nonauditory limit. Even now, we cannot really be sure where the limit is for 12 shots. Since it was determined that the 12-shot threshold series was not likely to be a datum point of use to the Army, the effort to find the 12-shot threshold was terminated and replaced by the 3-shot series.

The SI and Psm values generated by 533-g charge detonations and below were generally equivalent to the SI versus mean instrumentation cylinder Psm pressures for the same range of charge weights listed in Table 2.

Dose response curves for the groups were created using second order polynomial fits of the data relating SI means to Psm.

The single-exposure curve with the number of animals per point is shown in Figure 5. The severity of injury indices (SI) for single exposure group animals ranged from 0.29 for a Psm of 89.7 (Pmax of 215.4 kPa) to 0.01 for a Psm of 22.8 kPa (Pmax of 48 kPa). The control level crossing point occurred at a Psm of 31.0 kPa (Pmax\* of ~65 kPa).

The SI for the three-exposure group animals ranged from 0.10 at a Psm of 26.9 kPa (Pmax\* of 54.6 kPa) to 0.01 at a Psm of 19.7 (Pmax\* of 56.2 kPa). Figure 6 illustrates the response curve and the number of animals per point. For this group the control level crossing point was approximately a Psm of 20.5 kPa (Pmax of 44.1 kPa).

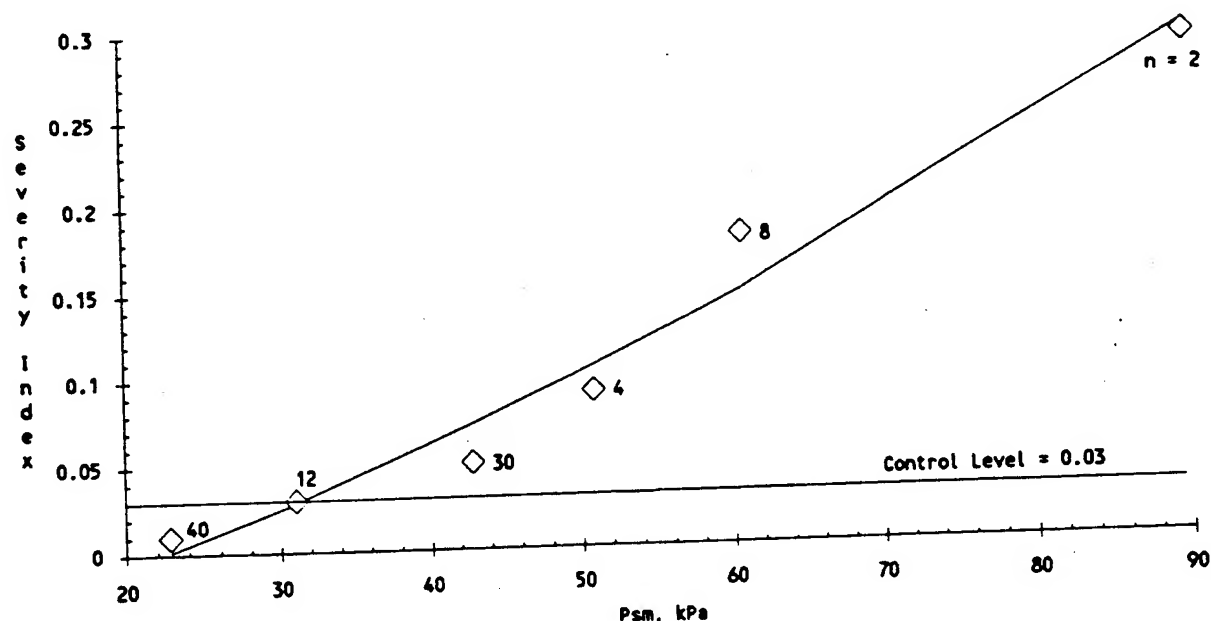


Figure 5. Mean severity of injury indices as a function of the instrumentation cylinder smoothed peak pressure (Psm) for single exposures to a simulated Carl-Gustav blast wave in the 3.05x2.44x2.44-m enclosure.

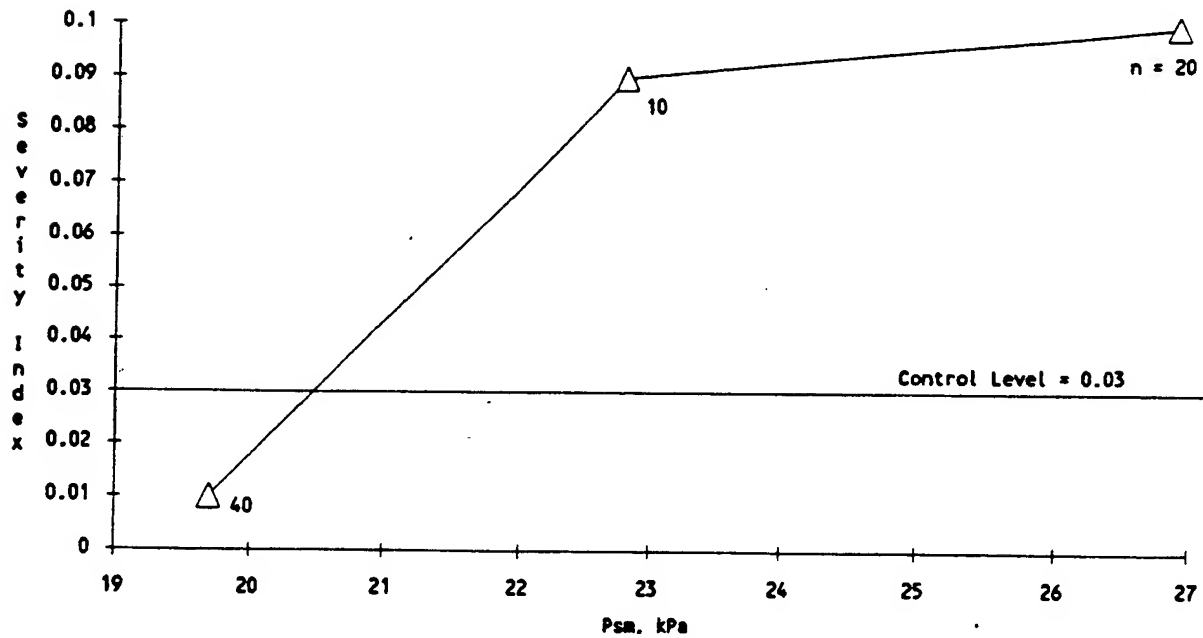


Figure 6. Mean severity of injury indices as a function of the instrumentation cylinder smoothed-peak pressure (Psm) for three exposure to a simulated Carl-Gustav blast wave in the 3.05x2.44x2.44-m enclosure.

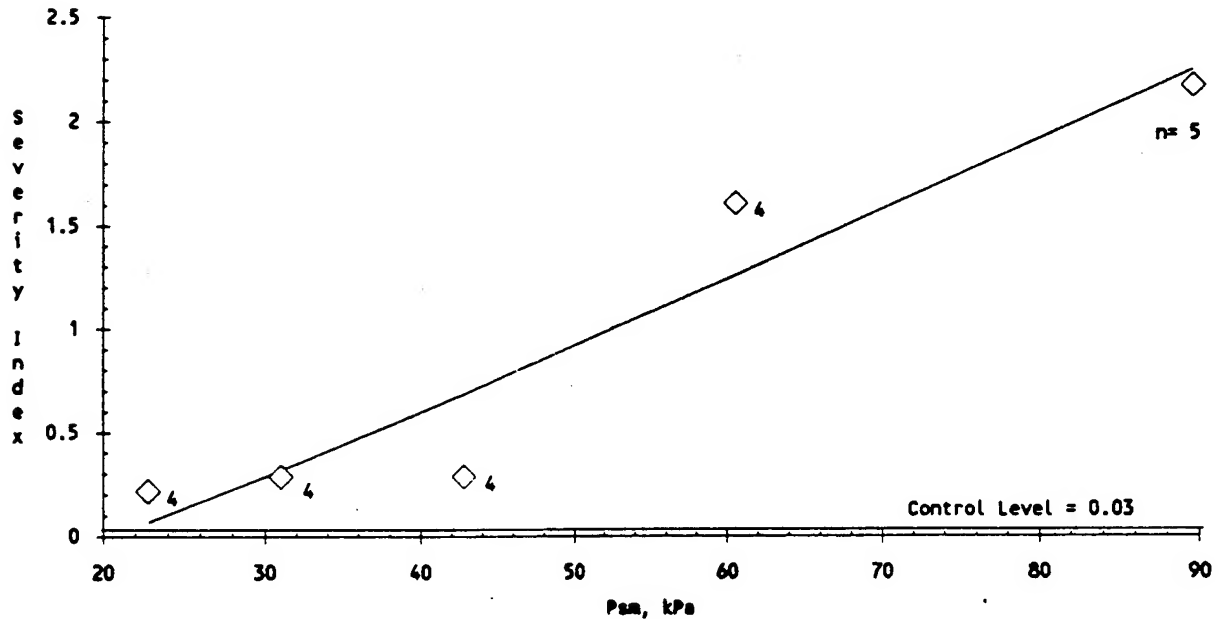


Figure 7. Mean severity of injury indices as a function of the instrumentation cylinder smoothed-peak pressure (Psm) for twelve-exposures to a simulated Carl-Gustav blast wave in the 3.05x2.44x2.44-m enclosure.

## DISCUSSION

The single-shot injury prediction curve developed using charges inside the bunker is illustrated in Figure 1. This curve predicts trace to slight levels of injuries with SI values ranging from 0.05 to 0.66 for a Psm value range of 57.1 to 130 kPa (Pmax\* of 123.6 to 365.0). For a single exposure, the predicted SI from a Psm of 89.7 kPa (Pmax\*, 218.4 kPa) would be 0.28.

The average SI of the Carl-Gustav simulation from 12 exposures to a Psm of 89.7 kPa (Pmax of 218.4 kPa) was 2.18. When compared with a single-blast exposure, these results appear to indicate that once threshold levels of injury are reached, additional exposures have almost an additive effect, increasing the severity of injury with each additional blast. The most heavily injured animal at the Psm of 89.7 kPa level had a SI of 4.28 that included a ruptured liver and an extensive hemoperitoneum with more than 200 cc of free blood in the abdomen. The trace to slight border line single exposure of a Psm of 130 kPa (Pmax\* of 365.0 kPa) injury prediction of 0.66 was not reached until the blast dose was lowered to a Psm of 42.8 kPa (Pmax\* of 88.6 kPa).

The single-exposure group SI data for the animals exposed to a Psm of 89.7 kPa (Pmax of 218.4) are listed in Table 2 compare favorably to the earlier single-shot injury prediction curve in Figure 1. The equation for this curve predicts a SI of 0.28 for a single blast Psm of 89.7 as compared with the mean SI of 0.29 with a range of 0.27 to 0.30 for the two animals actually exposed to this pressure. However, threshold predictions are not as close. Assuming a control level SI of 0.03, the single-exposure threshold prediction curve shown in Figure 5 estimates threshold levels to be below 31.0 kPa (Pmax\*, 62.9 kPa). The actual measurement of this level turned out to be a Pmax of 65 kPa. The subthreshold level in which "no-injury" was verified by 40 animals was a Psm of 22.8 kPa or a Pmax of 48 kPa.

The one-shot injury prediction curve shown in Figure 1 is not as conservative and predicts subthreshold levels below a Psm of 57.0 kPa (Pmax\*, 123.3 kPa) instead of the Psm of 31 kPa (based on a control SI of 0.05). Thus, the longer reverberation times of the Carl-Gustav simulation have effectively lowered the and thus the subthreshold levels that we verified to be safe.

The three-exposure group data listed in Table 2 also show the additive effects of multiple blasts. As illustrated in Figures 5 and 6, the subthreshold limit of a Psm = 31 kPa for a single shot decreases to 20.5 kPa for three exposures. Because of the fewer points used to obtain a subthreshold, a more conservative approach was chosen and a Psm of 19.7 kPa (Pmax, 44 kPa) was used as the no-injury point. This point is clearly below the control SI of 0.03 and was verified using 40 animals.

## II. AUDITORY STUDIES

### OBJECTIVE

To determine the auditory exposure limits of human volunteers while wearing a degraded RACAL® muff.

### INTRODUCTION

Using the established nonauditory subthresholds (or proven no-injury levels) of 48 kPa mean maximum peak (Pmax) for one shot and a Pmax of 44 kPa for three shots, a walkup study using 64 human volunteers was begun. This study was a continuation of previous human "walk-up" studies for various freefield waveforms<sup>8-12</sup>. By "walkup," it is meant that the subjects started their exposures at a level considerably lower than the nonauditory threshold. The exposure conditions were gradually increased until the nonauditory threshold was reached or an auditory problem occurred. The effect of blast on the auditory system was determined by the occurrence of small reversible changes in the hearing level of the subjects. These changes, called temporary threshold shifts (TTS) were determined by audiometric testing. A matrix of exposure conditions that started at 168 dB (5.2 kPa) is shown as Figure 8. If a subject passed an exposure condition (showed less than 15 dB TTS at any frequency), the next day he was eligible to be exposed to the next most energetic condition. If no conditional auditory change (more than 15 dB TTS) or full auditory failure (more than 25 dB TTS) occurred, the typical subject would start at the lowest condition (168 dB, one shot) and work his way up to the 185 dB, one-shot condition. The 185dB (34 kPa) at the ear corresponded to the Pmax of 48 kPa at the chest as measured by the instrumentation cylinder. This was the established nonauditory subthreshold limit. Then, he would be exposed to the 183 dB at the ear two-shot condition, and finally, to the 183 dB, three-shot condition (the three-shot nonauditory no-injury limit). If audiometric failures had occurred, a particular subject would have been exposed to different conditions on the matrix to define his particular boundary of unacceptable TTS. However, since none of the subjects who completed the study had a full audiometric failure, all subjects followed the typical pathway through the matrix.

Level	Number		
	1	2	3
48 kPa 185 dB ⑦	59 pass		
44 kPa 183 dB ⑥	59 pass 1 elect. 1 admin.	59 pass	58 pass 1 cond. pass
180 dB ⑤	61 pass		
177 dB ④	61 pass 1 elect. 1 admin.		
174 dB ③	63 pass		
171 dB ②	63 pass 1 elect.		
168 dB ①	64 pass		

Figure 8.

Number of subjects passed and number of subjects showing an effect on hearing at the firing from an enclosure simulation. The decibel levels are measured at the ear, the kPa levels are measured at the chest. "Elective" refers to a subject's stopping by his own decision. "Admin." refers to a subject being dropped for some cause such as chronic ulcers.

## METHODS

### Audiometry

The audiometric procedure, modified Bekesy tracking, was set up to test up to six volunteers simultaneously. The system was patterned after the system used in previous studies.<sup>8,11,12</sup> A 486 computer controls a separate HP programmable function generator and programmable attenuator for each volunteer. The volunteers track their thresholds by a hand switch that controls the direction of change in the programmable attenuator. The earphones were TDH-49 elements mounted in a David Clark 9AN/2 ear muff for added noise isolation. The calibration of the earphones was accomplished using a Bruel and Kjaer (B&K) artificial ear with a flat plate coupler. The audiometric tests are conducted with the volunteers isolated in one-person, double-walled, double-floored audiometric rooms manufactured by IAC.

This system can measure thresholds as low as 20 dB below the audiometric zero established for the median of a young population.

A baseline of at least eight audiograms was used to establish the hearing threshold level of each subject. Before a daily exposure, two preexposure audiograms were taken to ensure the subject was within his baseline. Exposure to one of the conditions given by the matrix of Figure 8 then occurred. Post exposure audiograms were taken starting at 2 min, 20 mi, and 1 hr. Audiograms were continued past 1 hr in the event a TTS of more than 15 dB occurred.

## **Performance Assessment Battery Tests**

A computer-based performance task, based on the Walter Reed Army Performance Assessment Battery (PAB)<sup>13</sup> was given before each daily exposure and between the 20-min. and 1-hr audiogram. A baseline of eight tests was also established before the first exposure.

## **Medical Evaluations**

Medical evaluations by a physician assistant, under the guidance of the medical monitor, were accomplished each day of the study. Any abnormal results were referred to the medical monitor from Lovelace Medical Center. Spirograms to check lung function were also done daily. Full medical examinations and fiber optic laryngoscopy was also done before the first exposure condition and after the last exposure condition.

Laryngoscopy was also done after condition 7/1 (one shot at Level 7) for the first subjects. Intestinal blood was also checked by hemoguaiac testing. While an effort was made to obtain the tests every other day, subjects were allowed to go several days between tests dependent on the individual's bowel movement patterns.

## **Instrumentation**

The same measurement instrumentation as described in the nonauditory research was used in the human exposures. The east wall gauge was used to estimate the Psm and Pmax of the instrumentation cylinders.

## **RESULTS AND DISCUSSION**

Since the subjects may elect to stop these exposures anytime for any reason, not all subjects finished the study. Of the 64 subjects who started the study, three elected to stop for personal reasons. In addition, one subject was discovered to have a chronic ulcer and was dropped. Another subject reported a dizzy spell during the evening after he had been exposed to Level 2 during the day. He was found to have a history of such spells and was dropped. The medical monitor did not consider the dizzy spell to be blast related. This left 59 subjects who completed the study.

## Auditory

As mentioned earlier, no auditory failures occurred. One subject had a conditional failure after three shots at 183 dB. He had a TTS of 18 dB at 2 minutes after the exposure at 125 Hz and 250 Hz. This TTS recovered completely at 5 hr. Because this conditional failure occurred at the last exposure condition, this failure had no consequence.

A linear regression analysis was also accomplished with respect to level to evaluate any trends of increasing TTS with level. A summary of the results for each frequency is shown in Table 3. Note that the slopes for all but 6 kHz are negative, implying better hearing with increasing exposure level. This is probably the result of a small learning effect. Certainly, no TTS is occurring. The linear regression for 6000 Hz is shown in Figure 9. Note the normal audiometric variability that occurs. This is best shown for one of the conditions in Figure 10. This variability is why a TTS of 25 dB value is used as the point of an audiometric failure.

Table 3. Slope of a linear regression vs intensity level at various audiometric frequencies for firing from an enclosure simulator (right ear).

Configuration	Ear	Frequency, kHz					
		1	2	3	4	6	8
5-meter "B"	Right	-.10	-.05	-.11	-.03	-.06	-.03
	Left	-.17	-.03	-.07	.05	-.08	.01
5-meter "M"	Right	.01	.01	.12	.04	.17	.05
	Left	-.18	.01	.04	.03	.06	-.12
1-meter "D"	Right	.02	.09	.08	.11	.17	.04
	Left	.08	-.12	.05	-.06	-.02	-.02
3-meter "C"	Right	-.25	.09	.12	.39	.38	.48
	Left	-.06	.04	-.06	.02	.08	.02
3-meter P	Right	-.14	.62	.56	.05	.69	.94
	Left	.06	.26	-.07	.06	.31	.25
Firing from Enclosure	Right	- 0.07	- 0.14	- 0.02	- 0.08	0.0	- 0.05



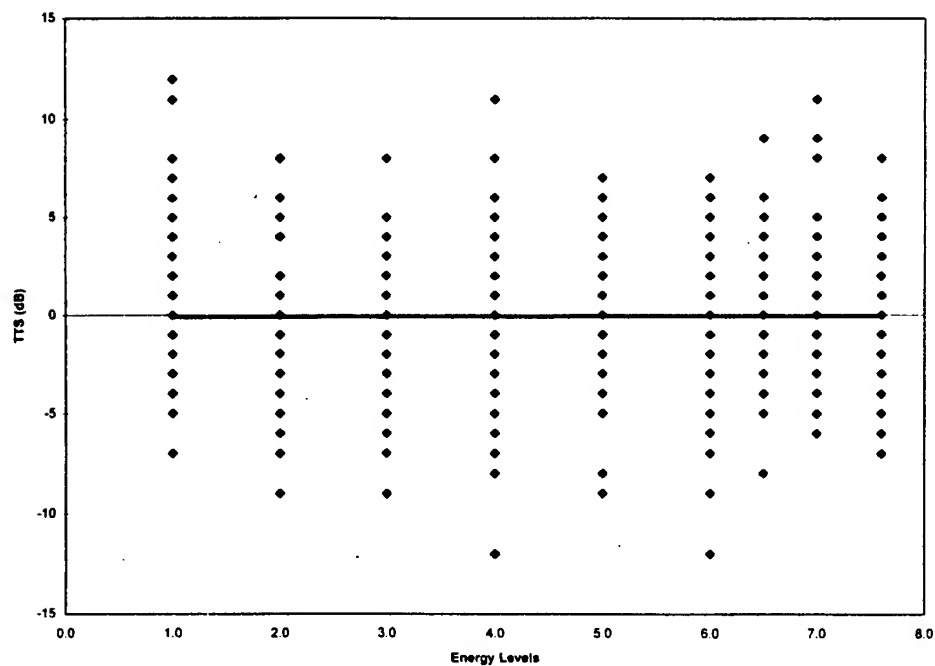


Figure 9. Temporary change in hearing (TTS) 2-minutes post exposure vs energy levels. Each step is a doubling of level.

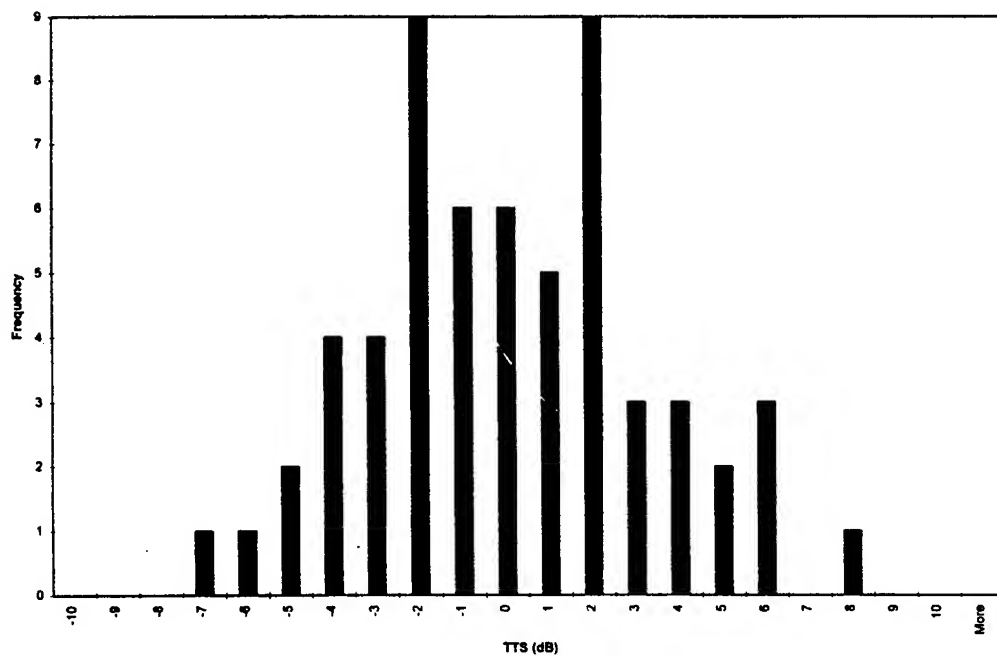


Figure 10. Histogram of post-exposure hearing changes from established baseline, 6000 Hz, right ear.

One final approach to looking at the effect of the total set of testing on the subject's auditory system is to compare the entry hearing threshold levels, accomplished when they first arrived at the BOPTS, with the subject's last hearing threshold levels, accomplished during their exit physicals and just before leaving for their next duty cycle. Figures 11 and 12 show the results. Note the slight improvement in hearing. Again, this improvement is most likely due to the subjects increased proficiency in taking audiograms.

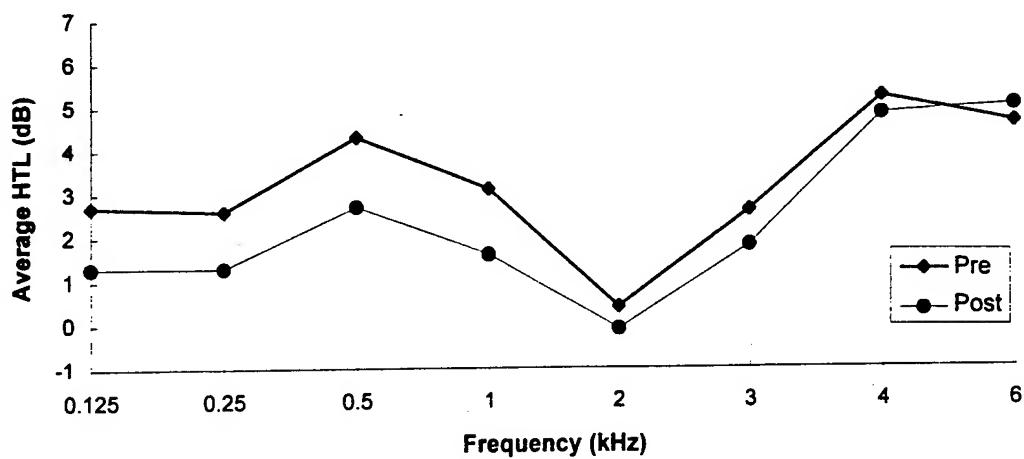


Figure 11. Mean prestudy hearing levels vs final post study hearing levels, nontest (left) ear, 59 subjects.

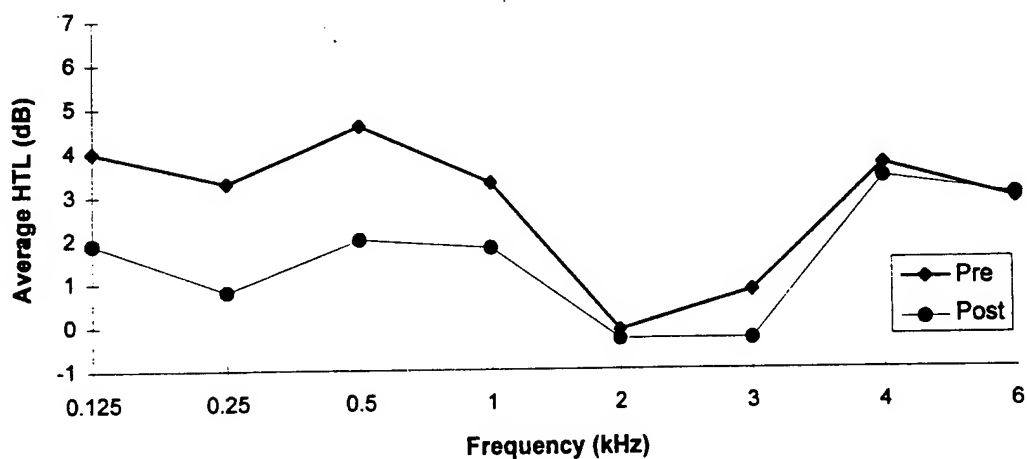


Figure 12. Mean prestudy hearing levels vs final post study hearing levels, test (right) ear, 59 subjects.

## Performance Decrement Assessment

The Performance Assessment Battery tests, as developed by Walter Reed, were given before and after exposure. The tests consisted of various tasks presented by a computer. Post tests were given approximately 35-45 min. after the exposure. No clear difference between pre- and post scores was found.

## Medical

**General.** No general medical problems with the blast exposures were found.

**Laryngoscopy.** All examinations showed negative results, i.e., no petechiae on the larynx were found.

**Hemoguaiac Testing.** Because of minor G.I. tract injury in the sheep occurring above the threshold level, special attention was given to this testing. Figure 13 shows the number of positive results (blood indicated) of the tests

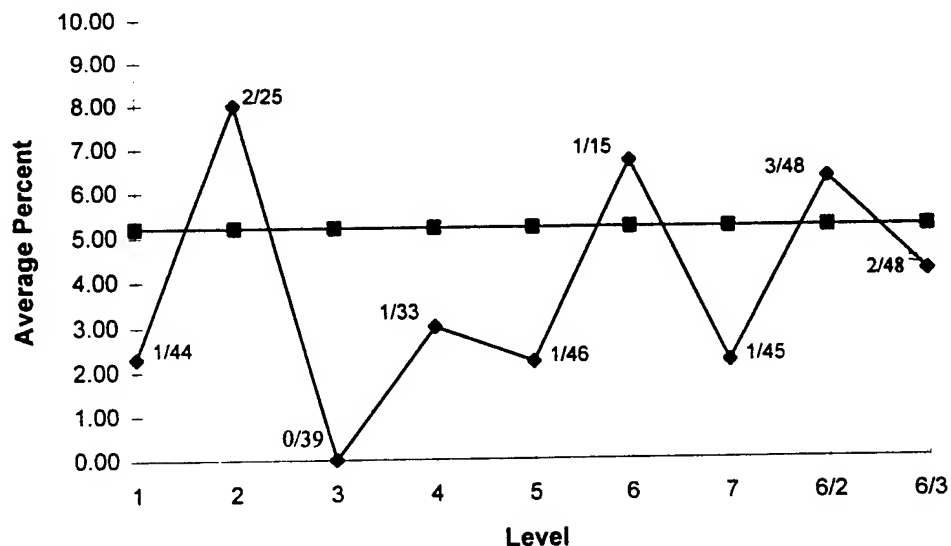


Figure 13. Percent guaiacs that were positive out of total taken. Control level of 5% was the percent positive of the samples taken by all the subjects prior to the first exposure.

results compared with the total tests taken. Since a diet of raw fruits and red meat also can give positive results, we expected a positive preexposure incidence rate of ~10%. The measured preexposure rate was 5%. The positive rate during

the study was below 5% that expected for Level 2, 6, and 6/2. However, no clear trend occurred and the mean rate during the study was only 3.5%. Therefore, we do not believe that any G.I. tract injury was occurring in the subjects.

### Subjective Assessment

As part of the series of questions, the subjects were asked to rate for each exposure condition of the matrix whether or not they would consider a similar exposure during training to be acceptable. For the one-shot limit, more than 78% of the subjects thought the exposure acceptable. For the three-shot limit, more than 70% indicated acceptability. These same questions had to be asked for the free field nonauditory limits for six shots. While there may be some difference due to the number of shots, it is clear that exposure at the nonauditory limit of the firing from enclosure simulation was as acceptable and probably more acceptable than exposure at the various nonauditory limits of the free field conditions, Figure 14. We consider this an important finding. Not only should an exposure be safe, but it should be such that the exposed individual is willing to be exposed without undue reservation.

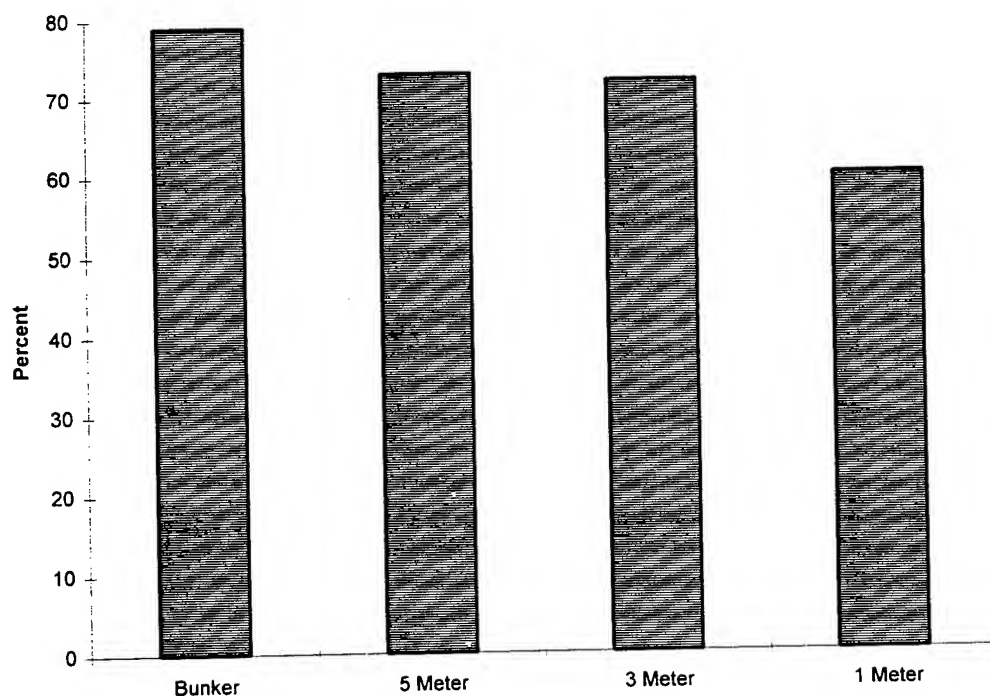


Figure 14. Percent that thought a training exposure would be acceptable. At the 6-shot nonauditory limit (1 shot for firing from bunker distance).

## CONCLUSIONS

The one-shot and three-shot nonauditory subthreshold levels (or no-injury levels) were established by showing that the 40 sheep tested were unaffected. Using these established levels as the maximum exposure levels, 59 human volunteers established that the auditory system can be adequately protected by a muff type protector if it is well fitted and even if it is not so well fitted. Performance assessment battery tests also showed a lack of effect. No medical problems occurred. In addition, the majority of the human volunteers thought the exposures were quite tolerable. Thus, nonauditory considerations set the upper limit of safe exposure of this type of reverberant waveform.

---

This work was supported by the U. S. Army Medical Research and Materiel Command under contract DAMD-17-88-C-8141.

Opinions, interpretations, conclusions, and recommendations are those of the author(s) and are not necessarily endorsed by the U. S. Army.

In conducting research using animals, investigator(s) adhered to the "Guide for the Care and Use of Laboratory Animals," prepared by the Committee on Care and Use of Laboratory Animals of the Institute of Laboratory Animal Resources, National Research Council (NIH Publication No. 86-23, Revised 1985).

In the conduct of research where humans are the subjects, the investigator(s) adhered to the policies regarding the protection of human subjects as prescribed by 45 CFR 46 (Protection of Human Subjects).

## REFERENCES

1. Johnson, D. L., "Blast Overpressure Studies with Animals and Men: A Walk-Up Study," Final Report, USAARL Report No. CR-94-2, U. S. Army Aeromedical Research Laboratory, Fort Rucker, AL 36362-0577, September 1994.
2. Yelverton, J. T. and D. L. Johnson, "Interim Report: Biological Response to Complex Blast Waves in a 17.3 m<sup>3</sup> Enclosure," Contract No. DAMD-17-88-C-8141, U. S. Army Medical Research and Development Command, March 1991.
3. Yelverton, J. T. and D. L. Johnson, "Interim Report: Biological Response to Complex Waves in Various Enclosure Volumes," Contract No. DAMD-17-88-C-8141, December 1994, Table 1— Experimental design for the Carl-Gustav simulation tests in the 3.05 x 2.44 x 2.44- m configuration of the EG&G Test Enclosure.
4. Yelverton, J. T., D. L. Johnson, W. Hicks and R. Doyal, "Final Report: Blast Overpressure Studies with Animals and Man. Subtitle: Nonauditory Effects of Complex Blast on Sheep in Three Different Enclosures," Contract No. DAMD-17-88-C-8141, U. S. Army Medical Research and Development Command, October 1993.

- Enclosures," Contract No. DAMD-17-88-C-8141, U. S. Army Medical Research and Development Command, October 1993.
5. Bowen, I. G., E. R. Fletcher and D. R. Richmond, "Estimate of Man's Tolerance to the Direct Effects of Air Blast," Technical Progress Report No. DASA-2113, Department of Defense, Defense Atomic Support Agency, Washington, D.C., 1968.
  6. Thurmon, J. C., A. Kumar and R. P. Link, "Evaluation of Ketamine Hydrochloride as an Anesthetic in Sheep," J.A.V.M.A. 162(4): 293-297, 1973.
  7. Kumar, A. et al., "Response of Goats to Ketamine Hydrochloride With and Without Premedication of Atropine, Acetylpromazine, Diazepam, or Xylazine," VM/SAC: 955-960, June 1983.
  8. Johnson, D.L., and J.H. Patterson, Jr. Rating of hearing protector performance for impulse noise. Proceedings 1992 Hearing Conservation Conference, Lexington, KY: Office of Engineering Services, College of Engineering, University of Kentucky, 1992.
  9. Patterson, J.H., Jr. and D.L. Johnson. Actual effectiveness of hearing protection in high-impulse noise. J. of Acoust. Soc. of Amer.: 93(4) Part 2: April 1993.
  10. Patterson, J.H., Jr. and D.L. Johnson. Effects of high-intensity impulse noise on the hearing of humans wearing hearing protection. J. of Acoust. Soc. of Amer.: 93(4) Part 2: April 1993.
  11. Patterson, J.H., Jr. and B.T. Mozo, and D.L. Johnson. Actual effectiveness of hearing protection in high level impulse noise. In Noise as a Public Health Problem. Vol. 3, pp. 122-127, M. Valet (ed), Inrets, France, 1993.
  12. Patterson, J.H., Jr., and D.L. Johnson. Limits of exposure to high-intensity impulse noise with a 1.5 millisecond A-duration. In Proceedings Acoust. Soc. of Amer. Semi-Annual Meeting, Cambridge, MA, 6-10 June 1994.
  13. Thorne, D.R., S.G. Genser, H.C. Sing, and F. W. Hegge. The Walter Reed Performance Assessment Battery. Neurobehav. Toxicol. Teratol 7(4): 415-518, 1985.

# A Projected History of Sensing Technology for Earth Kinetics

By  
James K. Ingram  
J. K. Ingram Consulting (I-Con) - Vicksburg, Mississippi  
and  
Christian Madshus  
Norwegian Geotechnical Institute (NGI) - Oslo, Norway

## INTRODUCTION

Man has always been concerned with dynamic and transient motions of the earth surface, those generated naturally that gave him the rumbling warning of destructive earthquakes, volcanic eruptions, approaching tidal waves or stampeding animal herds, and later those that he himself was able to generate. Gradually, he became aware of the shortcomings of his own sensing and observation abilities and realized the need to quantify the motions he sensed or those he witnessed the consequences of. As with the invention and application of other tools in his inventory, beginning with the spear, arrow and wheel, so did man approach the task of developing tools to help him detect, measure and understand the recurring, violent earth motions.

Kinetics began with the "Big Bang" about 4.5 billion years ago (Figure 1). The turbulent, evolving earth was stressed by gravitational forces and impacted by cometary debris. More recently (as viewed from a geologic perspective), the earth dynamism stabilized, and is only rarely affected by other than its own internal mechanics. Recently, man developed the tools of nuclear energy that enable him to produce earth-shaking forces that can equal or, perhaps, even exceed those of nature. It is not improbable that if he so chose to precisely use all of the current nuclear devices available to him, he would greatly exceed any natural earth force, and could possibly even disassociate the very mantle of the earth. The evolution of earth kinetic sources is outlined in Figure 2.

The need for sensing, recording and interpreting earth kinetic phenomena exists in both civil and military applications. There is much commonality in the requirements, and many of the instruments and techniques are similar. The obvious difference is in the time, frequency and amplitude range of interest. Areas of civil and military interest include:

Civil	Military
<ul style="list-style-type: none"><li>- Earthquakes</li><li>- Remote sensing of nuclear blasts</li><li>- Seismic investigations and prospecting</li><li>- Blast excavations, tunneling and mining</li><li>- Vibrations from traffic, industry and other "culturally" related sources.</li></ul>	<ul style="list-style-type: none"><li>- Explosive demolition, excavation barrier formation, ordnance disposal</li><li>- Corollary effects from accidental explosions</li><li>- Explosive weapons effects diagnostics</li><li>- Protective structure design and dynamic response analysis</li><li>- Nuclear detonation detection and assessment</li></ul>

This monograph briefly reviews the history, evolution and future perspective of the methods and devices man has used to sense, record and quantify dynamic earth motions. The intent of this paper is to provide a brief history and correlation of ground shock and motion measurement technology, and a reasonable projection of near-term and future needs and possibilities.

## HISTORICAL PERSPECTIVE

Mankind has been exposed to earthquake effects since his earliest awareness of their presence, and he has been forced to reckon with them by wit and intellect alone (during the millinea when no "technological" devices were available to assist his sensing). Prior to the "technological revolution" in the 17th century, man possessed neither tools sufficiently powerful to generate competitive kinetic energy nor devices to enable detection and quantification of such energies. The development of "modern" sensing technology began with the introduction of electrical methods of measurement.

The desire to understand earthquakes certainly challenged the creative nature of man to build tools to measure something about them. This thirst for understanding lead to crude mechanical devices capable of "*recording*" earth motions and providing some information on the relative magnitude of an event, and perhaps give some "*reasonable*" indication of the direction or location of the source. The first recorded description of a technological device for this purpose dates back to circa 132 AD , when the Chinese scholar Ch'ang Heng, noted astronomer of the Han court, developed the *seismoscope*, which could give the direction of the principal pulse of the earthquake. Chinese officials were worried about earthquakes, which were taken as signs from heaven threatening the government. A possible reconstruction of the device is shown in Figure 3. It consisted of a heavy sphere of carved rock resting on a massive cubical rock base. Carved, open-mouthed, frog figurines were attached around the circumference at the base. A circumferential cord was attached just above the major diameter of the sphere, to which were loosely attached metal weights. Seismic motions would dislodge one or several of the weights from one or more of eight oriented dragons which would fall into the gaping mouths of the frogs below. From the number of weights displaced, an estimate could be made of the relative magnitude of the ground motion, and from the location of the displaced weights, the vector toward the source of the seismic disturbance could be inferred.

Although the principle of the single degree of freedom system response was discovered in the 1600's, the first mechanical seismometer was not developed until about 1850, when a visible recording of an earthquake motion was accomplished for the first time.

The technique of using observations of surface ripples in a vessel of water to detect ground vibrations, appears again in a historical documentation from 1683. That year the Turks besieged Vienna under their Grand Vizier, Kara Mustafa. They intended to conquer the city by digging tunnels under its walls. The military authorities of Vienna located the tunnels by detecting the ground vibrations caused by the digging. They used vessels of



water placed on the ground, as suggested by Palladio 100 years earlier. The Austrians were able to block off the tunnels, and overcame the Turks' assault that year. Whether that success was due to the Austrian's ability to sense ground vibrations or not, still remains to be answered. Using the ripples on a liquid surface to detect earth kinetics appears again in the pioneering work on seismic investigations by Mallet in 1851. In his field experiments, Mallet used vessels of mercury to detect the ground wave arrivals.

Historically, certain animal behavior has been linked to precursor earth tremors. Recent research strongly suggests their ability to detect minute ground motion. The Sand Scorpion from the Mojave Desert is an intriguing example. It uses vibrations in the sand to detect and locate its prey (Figure 4). Using extremely sensitive detectors on its legs, the scorpion is able to precisely locate any prey, like a small moth, at 30 cm distance. The sensors are specialized hairs that can detect and discriminate between compressional and Rayleigh waves. The direction to the prey is determined from the time difference in the compressional wave arrival at the various legs. Distance is determined from the difference in arrival time between the fast compressional wave and the slower Rayleigh wave (Figure 4.c.). An understanding of this response may well lead to integration of this, as yet untapped, resource with more accepted scientific methods to provide enhanced detection.

Prior to the "technological revolution" in the 17th century, man possessed neither tools sufficiently powerful to generate competitive kinetic energy nor devices to enable detection and quantification of such energies.

Major improvements were made to the mechanical, single-degree-of-freedom, seismograph during the period between 1850 and 1900, but the development of "modern" sensing technology truly began with the introduction of electrical methods. The real leap in sensing technology occurred in the late 1930-1940's. Prior to World War II, interest was primarily centered in preventing corollary civilian damage caused by blasting for construction, quarrying and mining operations. Precision application of large high-explosive bombs and weapons detonated at or beneath the ground surface to destroy targets during World War II drove the requirement to understand the cause and effect relationship between detonation phenomenology and target response. This, in turn, required a concentrated effort within the scientific and commercial communities to develop sensors capable of reliably and accurately measuring a broad spectrum of ground motions (and related shock phenomena), as well as the technology for installing these systems and interpreting the results.

## **THE MECHANISMS OF SENSING TECHNOLOGY EVOLUTION**

The methods and devices used for sensing earth kinetics within the various areas have followed the general technological development. As new technologies became available they were adapted, sometimes quite rapidly, by the various disciplines to meet their sensing needs. The ability to implement new technologies for specific use has varied between the disciplines. In this century military research has frequently been the

forerunner in adapting and even developing new technologies.

Wide fluctuations in the funding and supporting resources have historically been the trend in earth kinetic research and development. Most support came from the civil sector during the early period of evolution. Military requirements and funds provided the main support base beginning in the 1940's and continuing until recently. Support now seems to balance between the two disciplines, and is trending once again back to the civil sector. In periods and areas where civil research readily adapted emerging technologies as they became available, they, in turn, were adopted by military research, and vice versa. There has been a significant and continual interchange of knowledge and equipment between the research and development within the various disciplines, both civil and military. Part of the motivation for this paper is to stress the importance of this cooperation and to encourage increased interdisciplinary exchange in the future.

Over the years there has been a progressive demand for higher capability measurement systems. New technologies have evolved in parallel with the demand and have made it feasible to meet most of the requirements. This interaction has led to increased complexity in the systems and a corresponding dramatic increase in the level of effort needed to develop, evaluate and associate the emerging sensing systems. This has shifted the old order of making systems and instruments specific for each earth kinetic area towards providing complete systems or components more universally applicable within several of the earth kinetic areas. This provides corollary benefit to both civil and military sectors.

Commonality of systems has increased the compatibility between the data bases and has increased communication and interchange between disciplines. Most of the technologies, and many of the devices used for earth kinetic sensing were first developed in other areas or for other applications. Those "external" areas that have particularly contributed to the technological development of sensing systems are physics, mechanical engineering, electrical engineering and, lately, consumer electronics.

***Basic Knowledge/Response to Ground Motion*** -- Most vibration sensors are based on a single-degree-of-freedom mechanical system. Vibrations can be sensed in two basically different ways, leading to the two main types of sensors: a) by measuring the relative motion between the instrument mount or canister and the mass, and b) by measuring the force needed to balance the inertia of the mass.

Two different solutions for the response of the single-degree-of-freedom (*1DOF*) system are therefore needed; one that gives the relation between the imposed vibration motion and the relative displacement, and one that relates the imposed motion to the inertia force on the mass. Generally, a *1DOF*-based motion transducer will properly record a wide vibration frequency range, with the lowest frequency content at least three times higher than the natural frequency of the sensor system. If only the amplitude content is to be recorded, and the shape of the wave is not essential, the sensor may be appropriately used down to about its natural frequency, providing the sensor has about 70% damping.

## SENSING TECHNOLOGY EVOLUTION

**The Early Systems** -- Knowledge of geology, materials, mechanical systems and application of practical electricity burgeoned world-wide in the nineteenth century. The development of embryonic theories to explain shock-induced earth motions were rapidly developing and evolving, and produced a corollary requirement for their verification by direct physical measurement. Most of the instruments and recorders used during this period were purely mechanical systems. Activation of the mechanical sensor by some external force typically would be mechanically amplified and the received energy transferred to a metal stylus. Movement of the stylus would inscribe a signature on a blackened glass plate or a sheet of soft lead foil (Figure 5). The displacement and repetitiveness of the scribed signature indicated both motion amplitude and frequencies (within the limits of the mechanical system). Later modification to include addition of a clockwork-driven, rotating cylinder of scribeable material allowed reasonable resolution of relative time of occurrence of an earth moving event. A major shortcoming of this type of measurement was the lack of precise time correlation, between different instruments placed at scattered positions. Most of the early systems (seismographs) were fastened to massive pedestals anchored to bedrock or a stable subsurface soil to isolate them from surface motions. Adaptation of these early systems to explosive event monitoring usually restricted them to placement at locations that were easily accessible, since they had to be recovered to retrieve the recorded data.

A major step forward came when the knowledge gained about electricity in the early 1900's was applied by the introduction of electrical measurement systems. For the first time this opened the possibility to spatially divert the sensing, the signal amplification and the recording.

**Sensors - History, and Working Principles** -- Historically, three general types of sensors have been used: *mechanical*, *electromechanical* and *piezoelectric* (charge generating). Modern sensors mostly fall under the electromechanical classification. This classification can be further subdivided into *inductive*, *capacitive*, or *resistive* (referring to the specific electrical transduction method used). The historical categorization must now be broadened to include emerging technologies such as *electro-optical*, *optoelectric*, *photonic*, *acoustic emission*, *multispectral* and *millimetre wave*, plus a number of others. Photographic techniques have been an important adjunct from the very beginning, and will continue to play a vital role far into the future. Table 1. presents a brief history of sensing technology from the first seismoscope in 123 AD to the present. Table 2 provides an overview of mechanical, electromechanical and electronic sensor chronology from the beginnings in the 1920's to the present.

The first electromechanical sensors were adapted from the simple electrical galvanometer (Figure 6). This self-inductance sensor consisted of a moving coil suspended in a magnetic field provided by permanent magnets. If either the armature or pole magnet were moved by an earth motion, a shift in position of the magnetic field would result, thus inducing an electrical current in the coil. This induced current is proportional to the rotation of the armature relative to the magnetic field, which is proportional to the applied

force (motion).

Commercially available sensors and recorder systems were initially used for ground motion measurement diagnostics. Measurement system capability significantly lagged the scientific need and required major modification and improvement of the commercial systems, or in many instances, dictated development of novel instrumentation by the scientists and technicians directly involved in earthquakes and explosion effects sensing. Specialized instrumentation system development frequently was carried out exclusively by the government, private government contractors and university groups. In many instances, however, joint efforts between government researchers and the commercial sector were undertaken with a high degree of success.

A significant increase in both theoretical and technological development derived from military ordnance effectiveness requirements during World War II. A wide variety of physical examples from bomb cratering, target/structure response, etc., were available for study, analysis and comparison with emerging theories. Direct, empirical measurement of the dynamic phenomena associated with explosive detonations was necessary to validate the operating theories and to understand the mechanics of the energy partitioning from the weapon to, and through, the earth.

The major impetus for the most concentrated development of ground motion, shock (and related parameters) measurement technology was a basic requirement for understanding the effects encountered in the nuclear testing and associated High-Explosive simulation programs, beginning in the mid-1940's. The vast majority of the sensors used during this era were mechanical peak recording gages. Use of this type sensor continued well into the late 1960's, but in dwindling numbers. A few types have survived to the present time for use in special applications. These tests ushered in the early use of electrical sensors, primarily *Piezoelectric (Crystal)* gages and some *Potentiometer* and *Inductance (Reluctance)* gages. During the 1950's a significant shift was made toward the use of electrical sensors in broad application, including resistance strain gage sensors.

Developments in silicon semiconductor technology led to availability of *Piezoresistive* sensors in the 1960's. Transducers based on this material rapidly overtook the role of earlier instruments and today constitute the predominant sensor type in general use.

The military requirement for motion and shock measurement has progressively increased from the relatively low-levels of the early days of testing to measurement in the very high stress region near to the source of the explosion. As motion and shock level measurement threshold level requirements increased, increasingly stringent requirements were placed on sensors, signal conditioning electronics and recording systems. Remarkable progress was made, but in many cases delays were caused by lack of both adequate technology and materials. Current technology now allows credible measurements to be made within a few centimetres of the skin of a detonating explosive.

***Mechanical Sensors*** -- The earliest "modern" mechanical sensor was the pendulum seismometer (late 1700's). It consisted of a mass attached to the earth by a spring and

damping mechanism (Figure 7). The displacement response of the pendulum relative to the point of attachment to the earth provided a measure of dynamic earth motion. The recorded motion is approximately equal to the ground displacement when the earth vibration frequencies are above the natural frequency of the system. This is one of the most sensitive instruments in use. The horizontal sensing version suffers a serious limitation from its difficulty in distinguishing between horizontal motion and gravity effects due to instrument tilt from both vertical and horizontal signals.

The strong motion seismograph (1920's) was an adaptation of much more sensitive pendulum seismometer and measures the strong earth motion directly as acceleration. The main difference is in the much higher natural frequency required for this instrument. To record acceleration faithfully, the instrument must have a natural frequency significantly higher than the highest frequency contained in the signal to be measured. Instrument damping is required to be about 70% critical to optimize amplitude response and to minimize phase shift errors.

One of the earliest concepts for a mechanical sensor used in a wide variety of explosion effects applications was the Ball-Crusher gage (1940's). This gage operated on the deformation of a softer metal in contact with a harder metal by application of an external force. In practice, a "soft" metal sphere was placed in contact with a "hard" metal piston (Figure 8). External force (acceleration) exerted on the piston caused deformation of the sphere (or ball). The degree of deformation could be related to the applied acceleration. Dynamic forces on the order of 10 to 20 kg's could be estimated with this crude sensor. A pressure sensor used to measure explosive water shock could record pressures on the order of 500 MPa.

A later adaptation of this technique used a "soft" metal loading plate in contact with an array of small, geometrically arranged, "hard" spheres ("BB's"). Depending on the physical parameter to be measured, dynamic load was transferred from the plate to the spheres, resulting in formation of dimples in the softer plate. Measurement of the depth and diameter of the dimples gave results proportional to the force applied to the plate. Several sensor configurations of this principle were used. Figure 9 is an illustration of a recent version of the *Ball-Crusher* called the *Brinell Sandwich* gage (1970's). Two advantages were achieved with this technique: sensitivity (or operational range) could be varied by adjusting the number and array of the "BB's", and significantly better average sampling of the sensing area increased the accuracy of the measurement.

The *Drag Gage* is another example of a once popular, but limited capability mechanical sensor (1940's). It was used to measure relative earth displacement and shear near the crater region where plastic flow conditions predominated. One version was constructed of a series of vertical metal rods which were fixed to a rigid pedestal base. The rods varied in stiffness and would bend to various degrees by the movement of the earth. The degree of bend, as functions of rod stiffness and surface area, could be related to the magnitude of the load. The pattern and direction of the bends provided late-time displacement (final displacement) and vector information. *Drag Gages* are still in limited use today for special applications.

Earth and target structure responses were initially measured with a relatively sophisticated mechanical system called the *Reed* gage. This system consisted of a series of mechanical "*reeds*", or thin metal resonators, akin in response to a tuning fork. Each reed was machined to respond to a specific frequency. The reed array was mounted on a rigid base, placed in a protective vault, and mounted in the ground or on a target structure. A stylus was attached to the top of each reed, and contacted a smoked glass (or soft metal) backing plate. Vibration of any of the reeds excited by the blast load would cause the reed to scribe a signature on the backing plate. The approximate frequency spectrum of the transmitted load was determined by which of the reeds were excited, and the relative energy level by the amount of displacement scribed on the backing plate. The *Reed* gage is illustrated in Figure 10.

A major shortcoming of mechanical, peak recording sensors was their inability to provide any precise time reference of the dynamic load application. This was a significant hindrance to serious dynamic analysis of the phenomena or of structural response. Most analyses of the dynamic domain were based on theoretical calculations which could not be adequately validated by empirical data due to the lack of appropriate sensor technology. Modification of the *Reed* gage by substitution of a clockwork-driven cylinder covered with gridded paper and addition of ink-tipped styli allowed relative time resolution (Figure 10.b.).

***Vibrating wire sensors*** -- The *vibrating wire* electrical sensor is an example of an early dynamic motion sensor (Figure 11). It operated on the principle of a stretched wire pulsed with an *a.c.* current which caused it to vibrate at a specific frequency. Motion applied to the sensor displaced the wire, causing an effective change in its length, thus, a proportional change in its resonance frequency. This change in frequency could be related to the magnitude of the applied motion.

***The Electrodynamic Principle - Velocity Transducers*** -- One of the earliest electromechanical sensors was a self-generating velocity transducer, introduced in the 1920's. In principle the device is simply a miniature electrical generator configured such that the voltage output is proportional to the motion imparted to the instrument. Transducers using modern versions of this basic principle are found in widespread use today for seismic detection. Figure 12 is a schematic drawing of a commercial electrodynamic transducer.

The electrodynamic velocity transducer is based on the mechanical single-degree-of-freedom system, and works in the frequency range above its natural frequency. An electrical coil, also working as the seismic mass, is spring-supported in the sensor housing. A permanent magnet is rigidly attached within the housing and maintains a magnetic field cut by the windings of the coil. When the sensor is subjected to vibrations at frequencies above its natural frequency, the coil will remain at rest and the vibrations will appear as relative motions between the coil and the magnetic field. According to the principle of induction, a current proportional to the velocity of the motion will appear in the coil, making this device a velocity transducer.

To obtain an optimum flat amplitude response down to the natural frequency, a damping of about 70% is desirable. This is partly obtained in most designs by eddy currents in the coil and/or by fluid damping. These sensors have about 90° phase distortion at the natural frequency, which reduces to virtually zero at 10 times this frequency.

The basic design of these sensors has changed little since they were first introduced. Most development has been in improving the spring support system and reducing the size. Vertical units have pre-tensioned springs and can not be used horizontally, and *vice versa*. However, modern high frequency types can operate in all directions. Units are available with natural frequencies from about 1 to 100 Hz. While theoretically there should be no upper frequency limit, secondary (transverse) resonances set a practical limit. With modern spring designs, the upper frequency limit is typically 30 to 50 times the natural frequency.

Major benefits of electrodynamic velocity transducers are low cost, rugged design and no need for external voltage supply. High signal output and low impedance make them insensitive to electrical noise. Size and weight impose a problem for some applications. Even though modern high-frequency units may weigh less than 20 g and be less than 2 cm in size, low frequency units are still large and heavy and need careful handling and leveling to operate properly.

The technology of electrodynamic velocity transducers can be considered as mature. No revolutionary new developments are expected.

**Variable Reluctance Sensors** -- Some of the earliest active sensors used moving, magnetically-permeable, metal armatures within a magnetic field (commonly referred to as *variable reluctance* or *variable inductance*). This improvement was a modification of the much older galvanometer sensor and moveable transformer designs. The basic sensor consists of a movable core of some permeable material, such as Ferrite, within a cylindrical transformer. Movement of the core changes the inductance between the primary and secondary coils, thus, regulating the voltage output in direct proportion to its core's linear position. Conversely, voltage applied to the coil will cause the core to move a distance linearly proportional to the voltage change (*solenoid effect*). This principle used an a.c.-coupled, carrier current amplifier which restricted d.c. measurement and limited high frequency response

Improvements resulted in a stable, highly accurate sensor, called an *LVDT (linear variable differential transformer)*, Figure 13. It is effective for linear displacement measurement, but is restricted to short-span measurement at low frequency.

*Variable reluctance* sensors did not require any internal mechanical coupling, which resulted in a long-lived, robust device. Significant output signal and low impedance allowed transmission of relatively noise-free signals over long cable runs to the recorders. Miniature pendulum sensors adapted this principle. The moving pendulum pivoted within the self-inductance of a single coil or, within the mutual-inductance of a coil set (*mutual inductance sensor*). These were in common use during the 1960's and 1970's. The



pendulums normally were pivot supported, were fluid-damped and could measure motions up to about 10 m/sec. The *DX velocity* gage (Figure 14) is a classic example of this sensor and was the principal motion sensor for explosion effects tests for many years. The mechanical pivots were a limiting factor, reaching their failure point at acceleration levels approaching 2,000 g's.

Pendulum sensors have a limited linear response range of only about  $\pm 5^\circ$  rotation either side of the pendulum's null point (center-of-swing-position). This constraint requires precise alignment when they are emplaced. The gages can be used to measure either horizontal or vertical motion. To measure horizontal motion, the unit is mounted such that the pendulum hangs down in the normal vertical position. Vertical sensing units are placed with the pendulum aligned horizontally. A top-mounted spring is required to compensate for gravity effects and, thus, maintain the pendulum in the null position.

A new approach was required to satisfy the requirement for measuring high level velocities near the source of an explosion. A variation of the inductance principle developed in the 1970's resulted in a novel velocity sensor known as the *Mutual Inductance Particle Velocimeter (MIPV)*. This sensor consists of two slightly separated, parallel rectangular coils that are encapsulated in a flat protective plate. One coil is used as the driver, the other as the receiver. The power supply can be either high current *a.c.* or pulsed *d.c.* The most successful field sensor uses a *d.c.* capacitive-discharge system providing an essentially constant current on the order of hundreds of microseconds (but well within the duration of the shock field within the measurement regime). High currents (on the order of 10-100 amperes) are required due to the low sensitivity of this gage. Pulse-power is desirable since neither the sensing elements nor the cable can withstand a continuous high-current load. The gage is placed in the soil or rock medium such that the shock front loads the coils along their long axis. As the engulfing shock wave distorts the coil geometry (Figure 15), a proportional change occurs in the voltage induced in the receiver coil, which can be measured. This transducer is useful only for high motion (up to 1,000 m/sec), very short duration shock measurement. A variation of this concept, also developed in the 1970's, uses very large driver/receiver inductive coil arrays placed in the earth to measure large area motions, as in the Kratz and Cushing gages. Major disadvantages of high-current gages are the large current and voltage fields induced into the ground. These fields induce sufficient voltage and current to completely swamp signals or even destroy sensor elements in nearby low-signal-current gages.

***Servo and Force Balance Sensors*** -- The *force-balance* sensor principle is mainly applied to accelerometers; termed *servo* accelerometers. *Servo* sensors were developed to measure linear motion or rotation. Two common types of *servo* sensors are in use. Both are force-balance systems where the force of a small seismic mass is restrained by an internally provided electromagnetic field. The current required to maintain physical equilibrium is measured as the output signal and is proportional to the external force acting on the sensor.

The first type servo sensor is used for linear motion and is represented by the *Linear Servo* accelerometer. Figure 16 shows a typical sensor layout. The second type of



*servo* is the *rate-gyro* (gyroscope). This is essentially a miniature, very high-speed (typically >20,000 RPM), electrically-driven, gyroscope. Any rotation of the instrument from its initial power-up position results in a change in magnetic flux that induces a current in a sensor coil proportional to the angle of rotation.

*Servo* accelerometers can be made very sensitive, with a threshold sensitivity in the order of a few micro-g's. They have excellent amplitude linearity and phase stability. Typical frequency response is from 0 to 500 Hz, and acceleration resolution ranges from a fraction of a g, for the most sensitive units, to an upper limit of about 40g's.

Early versions often used stone-pivoted hinge for the seismic mass. These types were extremely vulnerable to damage during transportation, handling and mounting. More recent versions have flexing joints, "*Q-flex*" which are more rugged, but still fragile. The first *servo* accelerometers, useful for earth kinetic work, became available late in the 1960's.

These sensors are available in single or multi-axis sensing versions. Determination of true force/motion vectors require use of a composite orthogonal sensor. *Servo* sensors require significantly higher operating power, but compensate for this by their very high-level signal output (as much as 5 volts). Signal output level for a number of applications is sufficient to record directly without resorting to intermediate amplification.

**Capacitive Sensors** -- In principle, the *capacitive* sensor uses opposing metal plates (or diaphragms) which act as the force accumulators. Any change in the spacing of the plates changes the circuit capacitance which causes a proportional change in the circuit output voltage. High frequency *a.c.* carrier currents are normally used with this sensor type. Because of the high frequencies of the system, cable loss is significant, and severely limits the distance the transducer can be placed away from the power supply and amplifier. Although capacitive sensors lack true *d.c.* response, since they must be *a.c.*-powered to function, they are adequate for many types of dynamic measurement. This type of sensor is not commonly used for earth kinetic measurements.

**Piezoelectric Sensors** -- Another early electrical sensor for measuring blast effects was a charge generating device; the *piezoelectric* or *crystal* gage. The first *piezoelectric* sensors used quartz or tourmaline crystals, both naturally occurring materials easily applied to gage applications. Quartz replaced the use of tourmaline and is used in a wide variety of dynamic sensors today. Thin sections of a natural, flaw-free quartz crystal, cut in the X-direction or cast or extruded structures of synthetic piezoelectric materials are fabricated with thin electrodes bonded to opposing surfaces. Any change in the dimension of the piezoelectric material drives electrons from the crystal matrix to one or the other surface of the sensor, thus producing an electrical charge. This in turn can be measured with an appropriate electrical circuit connected to the material. Low-loss coaxial, electrical signal cable is required with this family of sensors.

Since this sensor is self-generating, amplifiers were not required for very short signal cable runs if connected to a very high impedance recording device, such as a vacuum tube oscilloscope. However, for moderate to long cable runs, signal conditioning was required in the form of a cathode-follower (for vacuum tube amplifiers) or emitter-follower (for transistor amplifiers) amplifier to compensate for the extremely rapid decay of the output signal and serious cut-off of high frequency response by the capacitance of the cable. Limitations of the *crystal* sensors included lack of d.c. response, non-linear output and limited time resolution. The crystal can respond only to a change of dimension brought on by application of force from some external source. In a perfect system (perfect insulation resistance), the charge generated by the force (either static or dynamic) should remain constant for some reasonable period of time. This is not actually achievable in the real world, and the net effect is that the charge decays exponentially, much like a capacitor discharge. Accurate time resolution is limited by the time it takes for a shock wave to traverse from the loaded face of the crystal to the rear face. At this time a reflection discontinuity occurs, masking and degrading any further measurement. Yet, these sensors can provide quality data for initial rise time and peak force.

Large-scale use of early *piezoelectric* sensors were primarily for underwater nuclear explosion effects measurement. They performed quite well in this environment since the dynamic pulse in the water was generally a high-amplitude, very short duration phenomenon. Attempts to adapt this mode to measurement of soil stress were never successful, although successful total soil pressures were measured using these crystal sensors suspended in a rubber membrane filled with oil or silicone fluid. Somewhat later, quartz crystals were readily adapted to sense acceleration. A typical *crystal* accelerometer consists of a stiff metal baseplate, a stack of quartz crystals and a top-loading seismic mass, all encased in a small, protective metal case. The applied force accelerates the seismic mass (or the case relative to the seismic mass) which loads the quartz, producing an electrical charge proportional to the compression of the quartz. This in turn, is proportional to the applied force. Figure 17 shows examples of two versions of modern *crystal* accelerometers.

***Resistivity strain gage sensors*** -- The *Wheatstone bridge* circuit for resistance elements (Figure 18) was invented in the late 1800's and was first applied to sensors at the introduction of *resistance strain elements* in the 1940's. This simple, highly linear transduction method was rapidly applied to sensor development and is still the predominant method in use today.

Strain gage sensors are normally configured with precision resistor elements that change their resistances linearly with dimensional change. The earliest strain elements were thin resistance wires. Modern elements are normally thin metal foil grids that are attached to a deflecting or deforming member, such as a diaphragm, load column (Figure 19) or cantilevered beam (Figure 20). Foil strain gages are available as single element, half-bridge or full-bridge rosettes. The elements are connected in a *Wheatstone bridge* electrical circuit. Either a constant current or constant voltage can be used to power the bridge. Change in resistance of the active element(s) causes a proportional change in the electrical output of the circuit. Full-bridge rosettes have all the required elements for

a full-bridge circuit, requiring only the addition of span and temperature compensation, when these are required. An advantage of strain gage sensors is that they can be powered with either *d.c.* or *a.c.* sources. They have true *d.c.* response and can measure both dynamic and static forces. Conventional foil gages have generally been replaced by discrete semiconductor elements or *integrated chip (IC)* sensor elements.

Resistance bridge accelerometers are constructed of a metal seismic mass that loads a strain-gaged column, cantilevered beam or an anvil with a slot machined across its middle. For the anvil-type accelerometer, a single foil strain gage or a half-bridge rosette is bonded across the central slot. The strain gages are configured as a balanced bridge electrical circuit. The base of the seismic column consists of a short pedestal attached to a thick, unyielding base plate (designed to minimize or eliminate any base strain). Acceleration forces acting on the seismic mass induce strains sensed by the strain gage elements. The change in resistance of the strain gage causes a change in the electrical bridge circuit proportional to the acceleration. A number of variations of this concept were manufactured and widely used. They have been largely replaced by semiconductor (*piezoresistive*) elements in modern gages.

***Silicon Technology-Based Sensors*** -- The low sensitivity of conventional strain gages limited the dynamic response of accelerometers using them as sensing elements. A seismic sensor mass sufficiently rigid to have the desired high natural frequency could not respond to produce strain levels adequate to be detected by the strain gages. Silicon-based semiconductor strain gages and microchip technology have overcome these limitations. Accelerometers using these new techniques have completely replaced the older methods. Figure 20 illustrates the basic sensing element in a modern *piezoresistive* accelerometer.

*Piezoresistive* semiconductor strain elements operate on the same principle, and are electrically configured similar to standard foil strain gage networks, but have up to two orders of magnitude higher output. Modern commercial, diaphragm-type gages use a single wafer of silicon semiconductor material as the sensing diaphragm. In essence, this device is an integrated circuit (*IC*), since both the strain elements and electrical compensation networks are fabricated within the same chip. Use of advanced silicon *IC* technology allows fabrication of very small, robust, extremely high frequency response transducers.

Significant advantages are realized with silicon technology. Extremely small, very high-frequency, sensors can be fabricated. These units are ideal for use in many applications impossible for the more bulky strain gage counterparts, due to their small physical size and low mass. Low mass/high-frequency sensors are required for accurate resolution of high intensity, short duration dynamic events, such as near-source explosion effects. *Piezoresistive* accelerometers are now commercially available in ranges from a few g's to 200 kg's.

*Piezoresistive* accelerometers are now commonly used for acceleration and velocity, and, to an extent, displacement. Acceleration is the only "*measured*" parameter. Velocity and

displacement are derived by integration of the acceleration time-history. Attempts have been made to develop a reliable high-shock velocity sensor for many decades, with at best limited results. No acceptable fast-response displacement sensor for use in the free-field has yet been developed. Improvements in accelerometer design in the 1970's, coupled with specialized digital filtration, baseline correction and numerical signal integration algorithms, have allowed derivation of highly accurate velocity data from the acceleration time-history. Double integration allows limited resolution of displacement (this parameter is considerably degraded with increasing time due to the accumulative integration errors from slight acceleration baseline drift and noise offsets that are difficult to eliminate).

One successful version of a "*velocity*" transducer is fabricated by mounting an accelerometer on a specially designed shock-isolation support. This is, in effect, a mechanical filter and allows use of a much lower range accelerometer (for maximum sensitivity). The mechanical filter limits coupling of high-frequency, high-amplitude acceleration to the sensor (these are well above the shock spectra profile of the energy within the velocity domain). Because much higher sensitivity (equivalent higher output) sensors can be used, the signal-to-noise ratio is usually high enough that minimal errors are introduced in the digital integration procedure used to extract velocity data from the acceleration signal. Figure 21 illustrates a typical *Shock-Isolated* accelerometer (SIA) "*velocity*" transducer. These devices are not yet commercially available and are hand-built within the government research laboratories.

More recently (1990's) *hard-mount*, high-range accelerometers have been used in special base strain-isolated canisters. These *High-Fidelity "velocity"* (HFV) gages allow measurement to considerably higher velocity levels than the older SIA "*velocity*" gages and provide a greater level of measurement accuracy.

*Soil stress* gages have been successfully developed using silicon technology sensing elements. The standard gage is the *SE* stress gage developed in the early 1960's (Figure 22). It consists of a thin wafer-shaped housing with stiff diaphragms in both the top and bottom surfaces. This sensor is usable to dynamic stress loads up to about 69 MPa. A more recent, high-range version, the *CBS (Column-Based Stress)* gage, uses a short, stiff column instrumented with silicon strain sensors. It is usable in dynamic stress fields up to 340 MPa (Figure 23). The *Flat Pack* stress gage is a unique adaptation of the piezoresistive effect. It consists of an element of manganin, ytterbium or carbon incased inside two long ribbons of metal. The ribbon is used to protect the signal cable long enough to retrieve early time stress data before failure. It can measure stresses in the 700 MPa to 100 GPa range.

**Sensors with Integrated Circuits** -- One of the first uses of *integrated circuits* (but not a "true" IC in the sense of using silicon-based, micromachine technology) coupled to the sensor was in *HE* and *nuclear* test data acquisition. Unacceptable signal level loss was encountered using the extremely long cable runs required for large detonations. Front-end signal conditioner/amplifiers were installed near the sensors to boost the output

signal and to lower the output impedance to compensate for the significant cable losses encountered. These initial attempts met with mixed success until the advent of semiconductor technology.

Piezoelectric sensors were fitted with emitter-follower type transistor circuits fitted inside the transducer housing to convert the high-impedance gage output to low impedance. This adaptation allowed the output signal to be transmitted over standard twisted pair cable (rather than the much more expensive and more vulnerable coaxial cable) and significantly extended the sensor time constant (charge bleed-off time).

In the most recent devices the entire mechanical system is fabricated from a single silicon chip. micromachining technology allow production of extremely small, extremely rugged precision sensors (Figure 24). Deflection or distortion of the micromachined force elements produce an output electrical signal proportional to the acting force. Modern accelerometers using this technology weigh only a few grams and have natural frequencies in the MHz range.

## RECORDING SYSTEMS

**History** -- Recording systems began with first-hand observations passed down through the ages by oral memory. This progressed to written notes of observations and finally to etchings produced directly by crude mechanical sensors. The explosion of technology in the twentieth century included recording technology

The earliest recorders were truly mechanical. Physical stimuli were sensed by a mechanical system, amplified when required (or when the ability to do so was acquired) and the resulting motion recorded by using a scribe to mark on a "recorder" plate. Somewhat later, a hard stylus was substituted for the needle and scribed its movements onto a smoked glass plate or soft metal foil to form a "permanent" record of the measurement.

Evolution of electrical technology allowed adaptation of a laboratory generator/current detection device to motion recording. Dual galvanometers were used; one for sensing and the other for recording. The mechanical stimuli acting on the "sensor" galvanometer was converted to a proportional electrical current; when this current output was directed to the "recording" galvanometer, the electrical signal was converted back to a proportional mechanical movement, indicated by a pointer. The magnitude of the motion was indicated by the amount of deflection of the pointer. Even minute motions of the earth could provide enough force to activate this sensitive device when properly configured.

The galvanometer remained the primary electromechanical recording method for many decades until it was replaced by analog magnetic tape recorders. Analog tape is still used for back-up systems, but has been largely replaced by digital recording technologies such as digital tape, disk and microchip storage. Digital magneto-optical and optical storage methods are now available and are expected to become a standard for the next

generation of explosion effects and other earth kinetic data recording because of their very high storage density, compact size and near-archival storage life.

A number of novel recording methodologies are maturing and may find their way into standard use. These include non-volatile, multi-layer or three-dimensional optical crystal memory, non-volatile amorphous memory, fast-response bubble memory, and the developing field of organic-photonics molecular memory.

**Amplifiers** -- The oldest, low-signal output, electromechanical sensors were inefficient, could be used to obtain only relative peak magnitudes, and had to be "*human observed*" by watching a moving pointer span across an analog scale. For even "*slow*" dynamic measurement, a keen eye was required, which limited the observation to only "*best estimates*" of the amplitude and duration of an event. Electrical signal conditioning, amplification and recording systems followed, but evolved slowly until maturation of the vacuum tube. Vacuum tube signal conditioning and amplification systems were bulky (essentially laboratory size), power-hungry, created excessive heat and were subject to unpredictable failure, although they could produce enormous amplification (a quantum leap in technology). Vacuum tube amplifiers in the 1920's led to perfection of seismic reflection prospecting.

With perhaps exception of electrical potentiometric sensors (which could be operated in either a *d.c.* or *a.c.* mode), most early signal conditioner/amplifiers were *a.c.*-coupled, carrier current devices, with severely restricted frequency response, dynamic range and lacked true *d.c.* response. One of the most commonly used commercial carrier amplifier systems was the *Consolidated Electrodynamics Corporation (CEC) System-D*, 3-kHz carrier system. Since the more advanced vacuum tube amplifiers used large transformers in their circuits, *a.c.*-coupling was used.

Vacuum tube-driven carrier-amplifiers severely limited both upper frequency response of the measurement system and the length of signal cable that could be used between the sensor and the amplifier. A 3-kHz carrier frequency was the standard and limited frequency response to about 600 Hz, and signal cable length to a few hundred metres. Higher frequency carrier systems were available that allowed improved high frequency response (up to 50 kHz), but restricted signal cable runs to only a few metres (around 10 m). These higher frequency systems were typically used in laboratory environments. Large-scale explosive tests normally relied on the 3-kHz systems. Subsequent development of cable line-matching transformer circuitry allowed use of cable runs of several thousands of metres length.

*D.C.*-coupled transistor amplifiers made rapid headway in the late 1950's, but were not in significant use until the mid-1960's. *D.C.* coupling allowed true *d.c.* frequency response and was ideal for use with resistance strain gage transducers. These amplifiers were small in size, relatively stable, required minimal power and produced little heat, compared with their vacuum tube predecessors, qualities that allowed for the first time construction of mobile data recording vans that could efficiently power, amplify and record signals from many hundreds of separate sensors.

Modern amplifier systems are usually only a subcomponent of a complete signal conditioning/ amplifier/ digital recorder module.

**Galvanometers** -- The earliest (late 1700's), purely mechanical galvanometer used a moving indicator needle that arced across a calibrated dial to indicate the magnitude of phenomena being measured. The second-generation device (1800's) used a metal stylus attached to the tip of the indicator needle that scratched a signature on a smoked glass or soft metal foil plate. The third-generation galvanometer (late 1800 to early 1900's) used amplification of the minute electrical signal to levels that could actuate an ink-filled stylus that "wrote" a signature of the sensed force on a fixed sheet of paper on which was printed a reference grid. Somewhat later (early 1900's), the fixed paper was replaced with a roll of paper, transported at a precise rate(s) by a small electrical motor and gear system (Figure 25). This modification provided the addition of a time base reference and, thus, recording of a true "wave form."

Additional evolution (1930's) led to addition of a small mirror to the rotating galvanometer armature (Figure 26) to replace the mechanical stylus. This development allowed a dynamic event to be recorded on photographic film by optically deflecting a light source across the film by rotation of the mirror. In the 1940's the optical galvanometer was miniaturized into a modular element. Later modification (1950's) allowed a large number of these galvanometers to be installed side-by-side in an electrical connector bus inside a stand-alone housing. As many as sixteen galvanometers could simultaneously record data from individual sensors on the same recording medium. The galvanometers could be installed and removed by simply plugging or unplugging. The individual galvanometer units were available in several sensitivities, greatly adding to the design's usefulness.

Although analog magnetic tape recorders replaced the galvanometers as primary event recorders in the early 1960's, UV galvanometers were still used as the hard-copy "printer" for the tape-recorded data. Even after magnetic tape and later recording techniques had surpassed the high frequency limitations of the galvanometer, it remained (in various evolutionary versions) as the device of choice for recording data for a number of decades, and occasionally is used today for special applications.

**Photographic Recorders** -- Photographic recording proceeded along two distinct, but parallel paths. The initial path was that of recording an event with a standard or modified camera. Still cameras were first used, and were later augmented by movie cameras. These were primarily for overall documentation purposes. High-speed versions of both camera types were developed to allow capture of certain dynamic phenomena at high resolution. The second path was direct photographic recording of transducer signals. Perhaps the first practical development coupled an electromechanical galvanometer, with mirror attached to the moving armature, to a focused light beam. Movement of the indicator arm deflected the light beam and directed it across a photographic plate. When processed, the photographic plate provided a permanent record of the movement of the galvanometer, which allowed significantly higher resolution of dynamic phenomena. Addition of high-speed, motor-driven photosensitive paper cassettes allowed significant



high-frequency resolution, a relatively long time base (exclusively dependent on the length of recording paper that could be packaged inside the cassette), and provided a permanent record that was available for analysis within only a few minutes after recording the dynamic signals.

One method used to obtain records of very fast signals was to couple a camera directly to the face of the oscilloscope. Another method coupled the oscilloscope to a high-speed photosensitive roll paper cassette, similar to that used with galvanometer oscillographs. Resolution of the shortest duration phenomena was attained by attaching a rapidly rotating drum camera to a high-speed oscilloscope.

The third generation recording oscillograph used miniature, fast-response optical galvanometers and photosensitive paper transport cassettes. A significant advantage of this modification was that the galvanometers were available in a wide range of sensitivities and could be switched-out in only a few seconds. Thus, considerable flexibility and operating speed and ease were achieved. Additionally, a significant reduction in equipment volume and weight were realized. Even more flexibility was achieved with the introduction of color photorecording paper, and the addition of changeable color filters for the optical galvanometers. Recording density was increased about ten-fold, since data traces could be allowed to overwrite each other and still be clearly distinguished by the color differences of each trace.

***Cathode Ray Tube/Oscilloscope (Analog)*** -- The cathode ray tube is essentially a specialized vacuum tube. An electron emitter at one end of the tube fires a repeating beam of electrons down the length of the tube to a phosphor coated face at the opposite end. Impact of the electron beam excites the screen phosphors to fluoresce, emitting light in the visible spectrum. Electromagnetic fields control the path of the electron beam. This device can display sensor data as visual display, when coupled to appropriate electronic control systems.

The analog oscilloscope was a direct outgrowth of the cathode ray tube. All that was required was the addition of a magnetic and/or electrostatic lens to focus and control the path of the electron beam, a horizontal sweep circuit to "write" the beam across the face of the tube, and a repeat (or refresh) circuit to keep the screen reference line illuminated (provide a baseline or null voltage reference); Figure 27. Application of an external electrical signal (such as from a sensor) to a vertical deflection circuit caused the horizontal sweep to be deflected upward or downward (depending on polarity of the signal) in an amount proportional to the signal strength. Development of high-frequency vacuum tube oscilloscopes opened the way for resolution of even faster dynamic data recording.

Analog oscilloscopes, coupled with photographic plate or film cassette recorders, dramatically improved data capture for short duration, high-frequency phenomena. In this system, the camera was physically attached to the face of the oscilloscope. A subsequent, major improvement was the adaptation of the oscilloscope to the "recording



*oscillograph*". This modification used a cassette loaded with a long roll of photosensitive paper, motor-driven at transport speeds up to 2,000 cm/sec. For several decades, this type recorder provided an intermediate solution to high-speed data acquisition, rapid access to the recorded data and multi-channel recording, and a reasonably "*permanent record*". True "*high-speed*" recording during this period was made using rapidly rotating drum cameras attached to high-frequency oscilloscopes. Single oscilloscopes could accommodate only one or two channels of data. For large channel-count recording, a large, cumbersome console containing as many as sixteen two-channel oscilloscopes was required. The Miller-Unit was one of the most commonly used multi-channel oscilloscope recorders during the mid-1940's to early 1960's.

**Storage Oscilloscopes (Analog)** -- The analog storage oscilloscope uses basically the same phosphorous screen as the ordinary oscilloscopes, but has the possibility of making a permanent (slowly fading), erasable trace on the screen. When made first available around 1970, they represented a substantial advantage in easy capturing of transients, compared to the previous photo techniques.

When armed, the screen of an analog storage oscilloscope is charged by a high voltage. When triggered, the electron beam discharges a trace on the screen, which stays nearly permanent until the scope is again armed. Digital instruments have essentially displaced their analog counterparts.

**Pen Recorder** -- Pen recorders use electrical signals generated by a variety of sensors. The amplified and conditioned impulses are directed to servo actuators to which pen styli are attached. A motor-driven roll of gridded paper is transported beneath the styli. The speed to the paper provides a moving time base, while excursions of the pens across the paper provide the measure of phenomena amplitudes. Pen recorders when used now are almost exclusively limited to static and slow dynamic stimuli, such as earthquake detection/monitoring.

**UV Recorder** -- The basic UV recorder is a modification of the galvanometer oscillograph. The main difference is that the light source is in the ultraviolet spectrum, and it excites a special "*direct-write*" photographic paper. The paper "*develops*" in seconds when exposed to ordinary visible light. It has the advantages of rapid visualization and requires no cumbersome chemical processing. On the other hand, the paper continues to "*develop*" when exposed to moderate levels of UV, and even ambient room lighting, for a prolonged period. Eventually, the image is unusable. No permanent record is available with this recorder. It has been virtually replaced by high-speed digital printer/plotters coupled to small computers.

**Analog tape recorders** -- The first successful sound recording on magnetic tape was done by BASF in Germany in 1936. The first multi-channel instrumentation recorders became available early in the 1950s, made by AMPEX in the USA. These 4-channel,

direct-record units covered the frequency range from 200 Hz to 80 kHz, with a signal to noise ratio of 40dB at a tape speed of 60 ips. Direct recording was a major shortcoming of the older recorders, since their upper frequency was limited to about 20 kHz and they could not record down to d.c. Frequency modulation (FM) recording was introduced in 1953. 32-track record/playback head units that had both FM and direct record options became the standard recording system during the early 1960's through the mid-1980's.

**Digital techniques** -- Digital oscilloscopes and magnetic tape recorders became available in the early 1980's and have virtually taken over the role of the older analog systems. Modern digital systems are microprocessor controlled and offer significant advantages, such as immediate access to the stored data and direct processing and analysis by sophisticated software. Digital oscilloscopes are a standard for laboratory use and for recording extremely fast dynamic events.

*Digital transient data recorders (TDR's)* represent the current standard for dynamic explosive test data acquisition. Significant advantages are afforded by these innovative systems. *TDR's* use the latest microchip-based technology, are compact, generate little heat, and require minimal power. Most *TDR's* in widespread use are not wholly digital, since most of the available dynamic sensors are still analog signal devices. A typical *TDR* consists of an analog section and a digital section. The analog section is comprised of a transducer power supply, signal conditioning, calibration and amplification electronics. The digital section includes the analog-to-digital converter (ADC), antialiasing and bandpass filters, data block management logic, solid-state memory, and command recognition logic and digital output buffers. These systems allow a trigger delay, one calibration memory segment, and at least one data memory segment. More sophisticated *TDR's* allow for as many as 20 memory segments to maximize data capture resolution and flexibility. For example, high-frequency sampling is desired for the initial signal arrival, initial risetime and decay. Sequentially later times in the phenomena being recorded require increasingly lower frequency resolution as the signal approaches steady-state or quiescent condition. For a dynamic signal where very late-time response is of interest (such as earth velocity or displacement), several fast-sampling (high-frequency) segments can be assigned to the front-end signal for high resolution, and the remainder of the memory assigned to slow-sampling (low-frequency) to allow sufficient recording time to capture the data to the desired point in time. There are some still unresolved problems with sectioned sampling rate recorders. The primary concern is with subtle zero shifts that occur at the point of sample rate change. This is not serious for the mesurand, but becomes critical when performing integrations to derive secondary parameters (e.g., velocity and displacement from measured acceleration).

Some *TDR's* can be run in loop-mode, continuously over-recording previous data. Pre-programmed logic can tell the *TDR* to stop recording at a determined point and to conserve a designated length of pre-trigger data. The input "trigger" can be from a shock sensitive switch or from signal amplitude excursing above an established threshold. This is an attractive mode in which to operate the recorder when it is placed in severe motion and shock environments where it is difficult or impossible to run a zero (or, event initiation) time signal cable.

Pioneering work on a remote digital data system was done by DEVELCO in the 1970's when they demonstrated a system that could be deeply buried in the ground and transmit the recorded data through the earth. The low frequency required long data transmission times.

An occasional drawback of present day *TDR*'s is their rather limited on-board memory capacity (normally between 0.256 to 1 MB), particularly when used at high digital sampling rates (presently, between 1 to 10 MHz (or million samples per second)). Very high-density memory chips are now becoming available and will eliminate this deficiency.

A new, multi-channel, portable *TDR* system has recently been developed and field-tested by WES. This new system is housed in a rugged package and contains 16-channels of signal conditioning, amplifiers and batteries. The case dimensions are approximately 0.6 m long x 0.4 m wide x 0.4 m high. The complete system weighs less than 18 kg. The system can be rapidly air-transported to the designated site and can be set-up within an hour or so. The high-capacity batteries allow for long stand-by times, and, ideally, the system can be auto-triggered by event sensors attached to the instrument packages. The precision quartz oscillator can be adjusted from 1 MHz down to only a few Hz to allow data sampling from  $10^6$  samples/second to 1 or 2 samples/second. The extremely low power consumption allows the system to run as a sealed system without any ancilliary cooling, even in desert temperatures approaching 49° C.

**Computer Technology** -- Computer control of integrated sensor/recording systems is becoming the new standard and is required for most digital recording systems such as *TDR*'s. Some developmental sensors and most modern recorders include at least a basic microprocessor chip. Programming and control of the system through a notebook pc allows rapid set-up of the system and near-real time to real time access to, and processing of, the acquired data.

**Present Status** -- Present day high-explosive ground motion measurement technology relies almost exclusively on analog electromechanical and electronic sensors. Only scant, if any, truly revolutionary development in sensor technology have occurred in last two decades, although some major improvements have been made in the "standard" technology, especially in the applications area. The same basic principles (i.e., *electrodynamic*, *piezoelectric*, *piezoresistive* and *servo*) still dominate the commercial market and are the broadest used sensors in both civil and military activities.

The most widely applied data acquisition systems are comprised of remote positioned, miniature transducers connected with long runs of metallic or fiber optic signal cable to the recording electronics. A few limited, state-of-the-art systems are shock and environmentally hardened, and self-recording. But these systems are essentially in the late development/early application stage, and are not in widespread use outside a few government and private research laboratories. Recording technology presently uses a mix of analog and digital magnetic tape recorders, *TDR*'s with microchip memory, and small pc's with large magnetic hard disk storage. Computer technology has essentially

overtaken other modes of recording and will soon dominate the field with very high density optical disk memories. Emerging "smart," digital sensors can be fully controlled by software commands.

One of the newest and highly promising concepts is that of a self-contained, super shock-hardened data acquisition that can be used to measure in the extreme blast environments in both the near-field and source regions. One such field test validated system is the WES-developed *HDAS* (*HDAS* stands for *Hardened Digital (data) Acquisition System*) recorder module (Figure 28). The sensor, signal conditioner/recorder and power supply are all contained in an extremely hardened protective metal canister. Essentially no extraneous noise is introduced into the system, since the entire measurement system is fully shielded. This significantly increases the effective dynamic range and signal-to-noise ratio, and results in extremely high quality data acquisition. The recorder may be initiated by means of an expendable trigger wire connected to the detonation timing signal pulse or it can be actuated by an internal, range-selectable, shock-sensitive switch (g-switch) closed by the explosion shock. When used in the autonomous mode, the module is placed in record-mode up to one-half hour (or more) before the detonation. The internal recorder records in a continuous loop mode with a predetermined calibration memory segment and pre-trigger memory segment programmed to the system. When the shock switch is activated, the recorder overwrites the older data and stops at the predetermined pre-trigger data delay segment, thus protecting the data segment within the designated time frame. The major shortcoming of the initial systems when used on very large HE tests is the difficulty of locating the modules after the detonation event. Experience has shown that 91 kg canisters will be thrown out to distances of up to 3 or 4 km, when placed near the Source Region (very near to the explosive material). Development of built-in tracking transmitters should significantly alleviate this sometimes serious shortcoming.

Hybrid measurement systems are now coming of age. These consist of conventional electromechanical sensors coupled to high-data transfer rate fiber optical cable (electro-optical systems), electromechanical sensors with built-in digitizers, truly digital sensors, optoelectric and pure optical systems and miniaturized, super-hardened, self-contained data acquisition modules.

## **FUTURE POSSIBILITIES**

New sensing principles appear to be at hand and the trend of development is to make smaller, cheaper and more integrated sensors (i.e. with built-in amplifiers, signal conditioners, filters, etc.). Low cost and small dimensions, generally allow the use of more sensors in a measurement application or placement in locations not easily accessible or in places where the larger units would introduce too much disturbance.

Use of bulky electrodynamic sensors is on the way out. Small, micro-machined servo accelerometers are becoming cheaper, but few, if any, off-the-shelf products based on this improved technology are commercially available.

Most new commercial sensors coming to the market are based on conventional sensing principles, but implemented by micro-machining.

Kinetic sensors based on optical and photonic principles are now emerging. A few such sensors are already on the market and a significant increase in both number and diversification is anticipated in the near future. Fiber optic sensing technology is used in some acceleration sensors. Most of these are based on the principle of interferometric measurement of a small gap at the end of the optical fiber. These sensors can be made extremely small to access, for instance, internal locations in machines. The sensors that are available are tailored to specific applications. Few off-the-shelf products based on this principle are readily available for earth shock measurement.

One new sensing technology using a non-linear spring oscillator is being implemented in some specially designed earthquake sensors. This is based on an oscillator with non-linear spring elements. A shift occurs in the natural frequency of the oscillator when the quasi-static inertia load of the seismic mass is subjected to the frequency components of the ground acceleration being measured. The singular advantage of this technique is that all components are integrated into a single unit. Since the sensor is always active (by its internal oscillator), it has a quasi-inherent self-test feature.

The piezoelectric polymer films, like *Poly Vinylidene Di Fluoride (PVDF)*, have, to some extent, been successfully used in pressure transducers. They may also have a potential use in ultra small accelerometers.

The principle of magnetostriction has, until recently, only been applied in limited seismic exciters, but these are not at present used as kinetic sensors. The technology is perhaps not yet mature. The development of room temperature superconductivity can be combined with magnetostrictive materials on micro-machined chips, and may yield a new generation of sensors that provide a quantum leap in size, high sensitivity, low noise and ruggedness.

Near-term advancements (the next decade or so) for explosion-generated ground motions will likely concentrate on miniature, super-shock hardened, self-recording electronic modules. High efficiency, digital seismic stations (such as the *IRDAT 1000P*) are currently under development and will provide highly flexible, microprocessor controlled, data acquisition and real- or delayed-time recovery of the data via digital radio telemetry links for direct processing at a central location. Non-invasive remote sensing concepts will initially augment, and may eventually supplant, other systems because of their potential accuracy, efficiency and cost effectiveness. Such systems likely will include millimeter wave reflectometry, laser interferometry, three-dimensional digital radar (advanced Doppler radar), acoustic tomography, local magnetic field distortion, microionization potential, microparticle flow, multispectral phase response, photonic emission spectra, and combination technology using advanced holographic techniques.

Improvement and adaptation of miniature, high-resolution ring laser gyroscopes, developed for precision missile guidance, will, for the first time, allow realistic, direct

dynamic displacement measurement. In fact, adaptation of this concept will be allow direct measurement of the three most commonly required motions (displacement, velocity and acceleration) all within the same sensor, and more importantly, at precisely the same locus.

Emerging technology will soon allow commercial production of a new generation of sensors that have true digital output. Microminiaturization using ultra-high density application-specific integrated circuits (ASIC), combined with new, multilayered semiconductor materials and enhanced micromachining capabilities, will permit complete data acquisition entirely within the physical volume now occupied by the sensor housing alone. Advanced remote sensor stations could be solar or microwave powered and have the ability to download their data through satellite links, repeater transponders or high-density laser com-links. Data transmission could be either or both real-time and selectable delay, depending on the requirement urgency. Precise positioning of the sensor location and time synchronization could be determined by an on-board GPS (*Global Positioning System*) microchip.

## CONCLUSIONS

Measurement of earth motions has been briefly traced from its earliest recorded beginnings to the present time. The first concern was to understand natural ground shocks and tremors, such as those produced by earthquakes and volcanic eruptions, and later to the effects and damage from explosive mining, excavation/demolition and tunneling operations. Technology developed in the civil sector was rapidly adopted by military engineers and scientists and was used to measure phenomena produced by military explosive devices. The greatest impetus to modern earth motion and shock measurement technology was born from military explosives development technology requirements, and not from a small amount due to the large sums of money historically available for military preparedness research programs, funds usually not available within the civil arena. With advent of the nuclear age, extremely large nuclear and high-explosive nuclear-simulation tests were able to produce "*manquakes*," imparting motions to the earth equivalent to or exceeding those from natural earthquakes.

Current measurement technology is a hybrid of analog/digital methods. Most modern sensors are still analog devices whose outputs are real-time converted to digital format. This allows extremely rapid computer processing using sophisticated "*smart*" software. A number of true digital sensors are already available, but fast-response digital sensors for explosion-induced motions and shock are only now being developed. These new instruments will soon be available and will quickly be assimilated into the data acquisition inventory.

Development of miniature, super-shock hardened, autonomous digital data acquisition modules now allow measurements to be made within a few centimetres of the skin of a detonating explosive and *survive!*

Development and validation of emerging technologies will allow a greatly expanded capability and higher resolution of ground motion and shock phenomena. Fast response, high resolution photonic sensors and non-invasive sensor technology (such as, doppler radar, wide-aperture millimetre radar, acoustic tomography, holography and multi-spectral sensors, etc.) and autonomous sensor/recorder packages are expected to dominate the next generation of data acquisition methodologies.

### **ACKNOWLEDGEMENTS**

We gratefully acknowledge the support of the Norwegian Defence Construction Service and the U.S. Defense Nuclear Agency for providing both the encouragement and the funding for this joint effort. Particularly, our thanks are due to Mr. Arnfinn Jenssen (NDCS/Norway) who suggested the topic of this paper and seriously supported and encouraged it to its completion, and to Mr. Tom Kennedy (DNA/US) for his technical support and encouragement

Particularly we want to acknowledge our co-authors Farrokh Nadim, Sigurd Lunestad, Harald Westerdahl and Amir Kaynia from the Norwegian Geotechnical Institute (NGI) and Svein Mykkeltveit from NORSAR, and J. Kyle Ingram, Jr. of Ingram Research, Inc. (IRI).

Acknowledgement is also made to the U.S. Office, Chief of Engineers (OCE) and, specifically, Dr. Jimmy P. Balsara, Mr. A. E. Jackson, Jr. and Mrs. Ruth C. Little of the U.S. Army Engineer Waterways Experiment Station (WES), who provided technical reference material, editorial review and contract management for the U.S. portion of this paper.

TABLE 1. HISTORY OF GROUND MOTION SENSING TECHNOLOGY

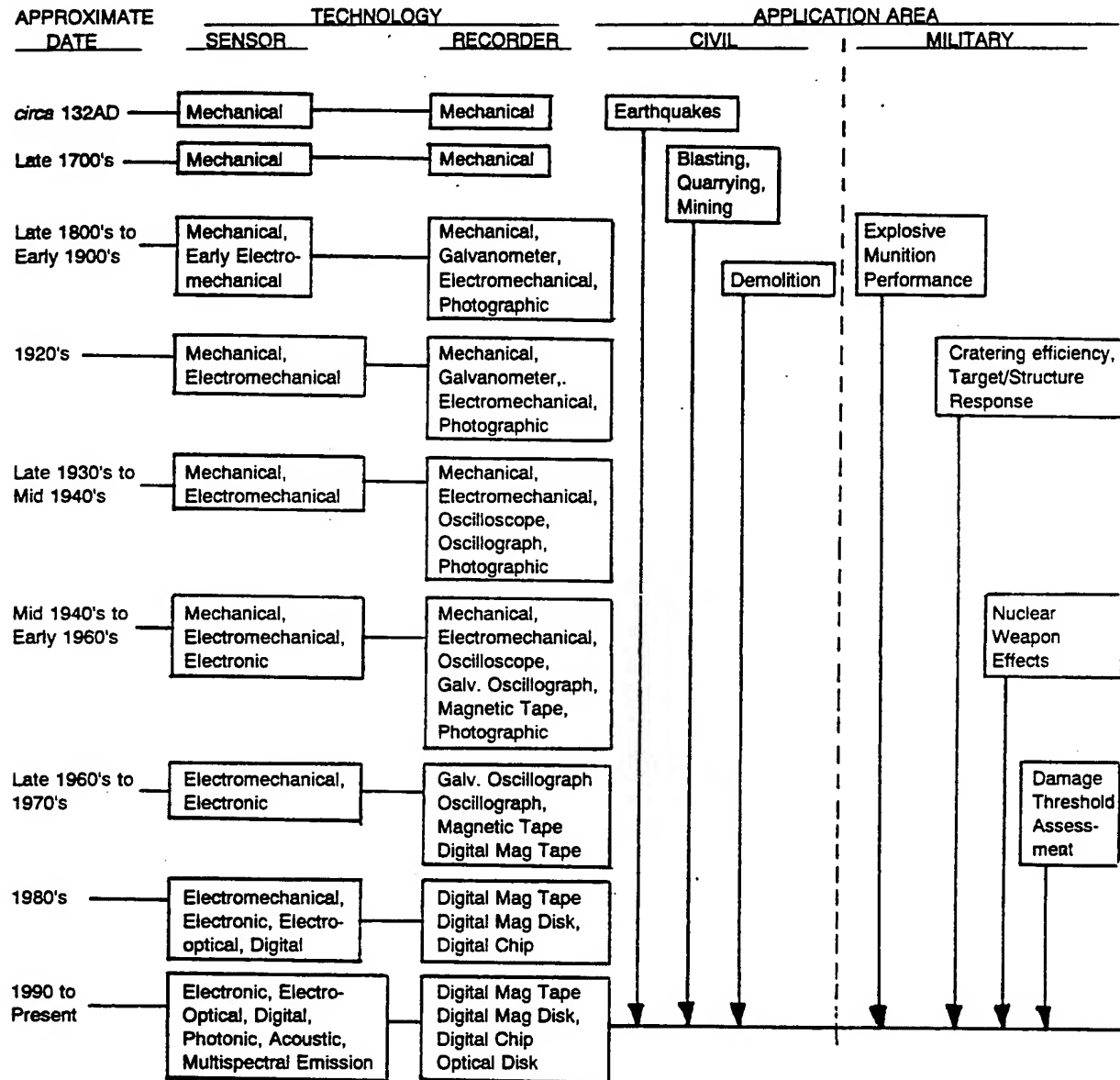




**TABLE 2. SENSOR CHRONOLOGY-EARTHQUAKE MOTION AND EXPLOSIVE GROUND SHOCK MEASUREMENT**

<u>DATE</u>	<u>SENSOR</u>	<u>COMMON NAME</u>	<u>MODE</u>	<u>PRINCIPLE</u>	<u>RANGE</u>	<u>FREQUENCY</u>
1920's	Velocity	Velocimeter	Voltage-Generating	Dynamo	0.1 m/sec	0.01 kHz
1930's	Velocity	Velocimeter	Resistance	Potentiometer	2 m/sec	0.05 kHz
1940's	Stress, Acceleration	Ball Crusher	Mechanical	Brinelling	70 MPa	Passive
1940's	Stress, Impulse	Vane Drag	Mechanical	Bending	4 MPa	Passive
1940's	Stress	Earth Stress	Resistance	Strain Gaged Diaphragm	0.3 MPa	0.5 kHz
1940's	Acceleration	VW Accelerometer	Vibrating Wire	Seismic Beam	50 g	0.6 kHz
1950's	Displacement	LVDT	Inductance	Coil w/ Moving Slug	6 cm	0.5 kHz
1950's	Stress	Pancake	Strain Gage	Diaphragm, Fluid Damped	4 MPa	0.1 kHz
1950's	Acceleration	Quartz Accelerometer	Quartz (Charge generating)	Element Compression	100 kg	100 kHz
1960's	Stress	SE Stress	Semiconductor Strain Gage	Diaphragm. Dual	70 MPa	50 kHz
1960's	Velocity	DX Velocity	E-Coil	Reluctance	10 m/sec	0.6 kHz
1960's	Acceleration	Resistance Accelerometer	Strain Gage	Seismic Mass (Load Column)	2 kg	75 kHz
1960's	Displacement Strain Gage	Long Span Strain	Strain Gage	Element Strain	6 cm	10 kHz
1960's	Velocity		Capacitive	Deflecting Diaphragm	5 m/sec	500 kHz
1960's	Displacement		Capacitive	Moving Plate	2 cm	500 kHz
1960's	Displacement	Bison Coil	Inductive	Moving Coils	10 cm	4 kHz
1970's	Acceleration	Semiconductor Accelerometer	Semiconductor Strain Gage	Seismic Mass (Split Anvil)	100 kg	750 kHz
1970's	Stress	HR Crystal Stress Gage	Quartz	Element Compression	4,000 MPa	1 MHz
1970's	Stress	Brinell Sandwich	Mechanical	Plate-Sphere Brinelling	400 MPa	Passive
1980's	Acceleration	IC Accelerometer	Integrated Chip (IC)	Seismic Mass (Micromachine)	200 kg	2 MHz

Table 2. Continued

<u>DATE</u>	<u>SENSOR</u>	<u>COMMON NAME</u>	<u>MODE</u>	<u>PRINCIPLE</u>	<u>RANGE</u>	<u>FREQUENCY</u>
1980's	Stress	CBS Stress	Semiconductor Strain Gage	Load Column	0-340 Mpa	10 kHz
1980's	Stress	Flat Pack Stress	Piezoresistive	Element Compression	700 MPa-100 GPa	up to 60 kHz
1980's	Velocity	MIPV	Mutual Inductance Coils	Inductive Field	1,000 m/sec	50 MHz
1980's	Pressure- Impulse	Bar-Impulse	Semiconductor Bridge	Very Long Hopkinson Bar	485 MPa	30 kHz
1980's	Velocity	SIA	Accelerometer	Mechanically Filtered Accel.	100 m/sec	4 kHz
1990's	Velocity	HFV	Accelerometer	Base-Isolated Acceleromeater	30 m/sec	100 kHz
1990's	Stress	HFS	CBS	Improved Load Column	340 MPa	100 kHz

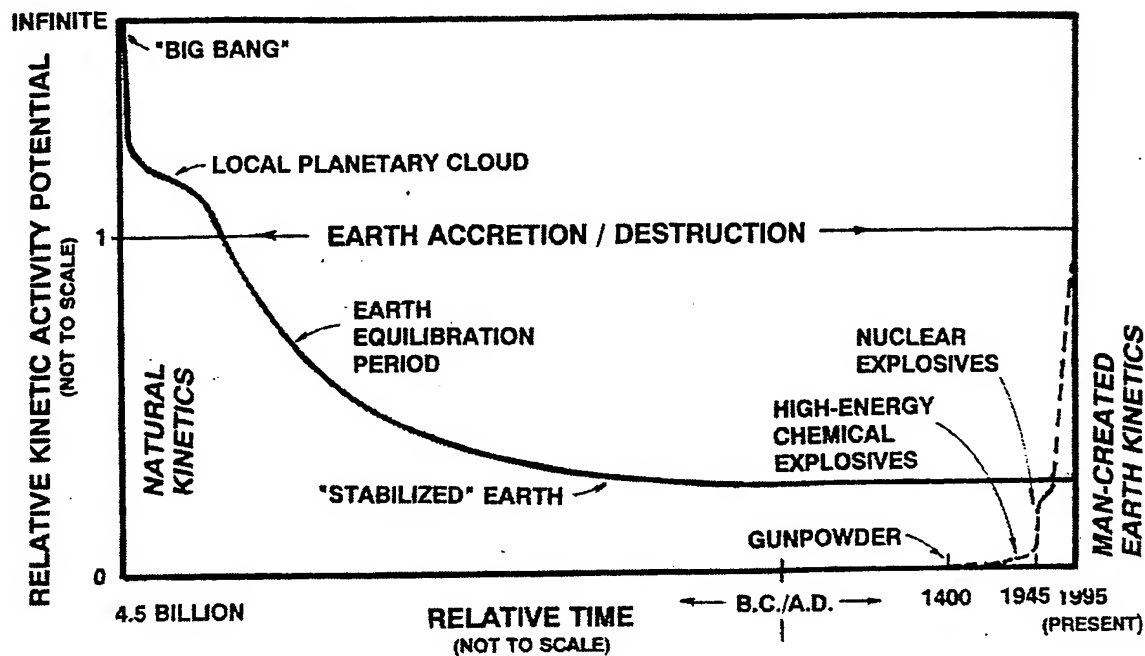


Figure 1. The relationship between natural and man-capable kinetic effects.

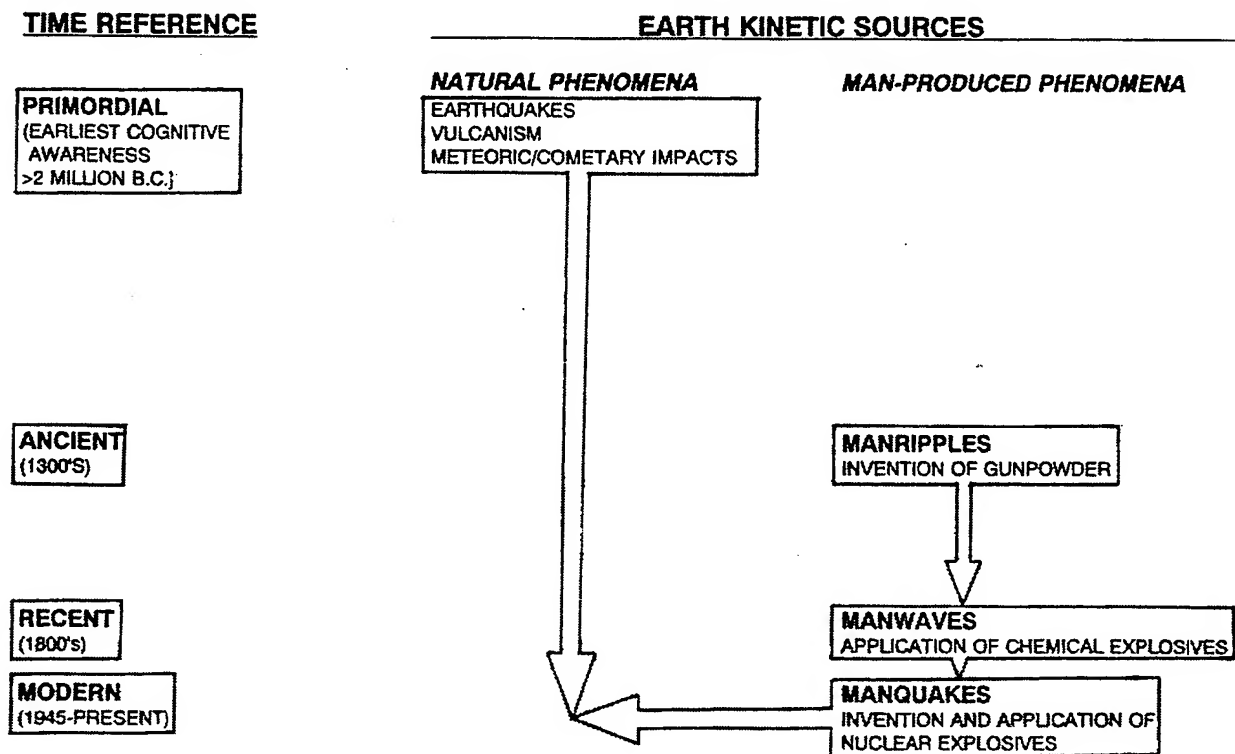


Figure 2. Earth kinetics source evolution.

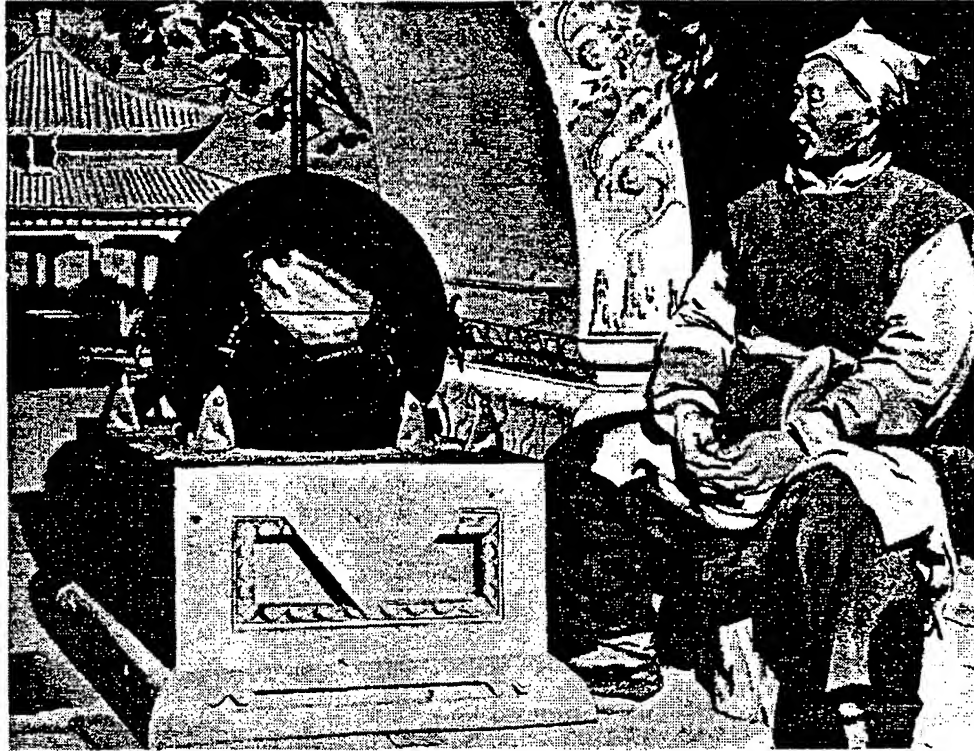
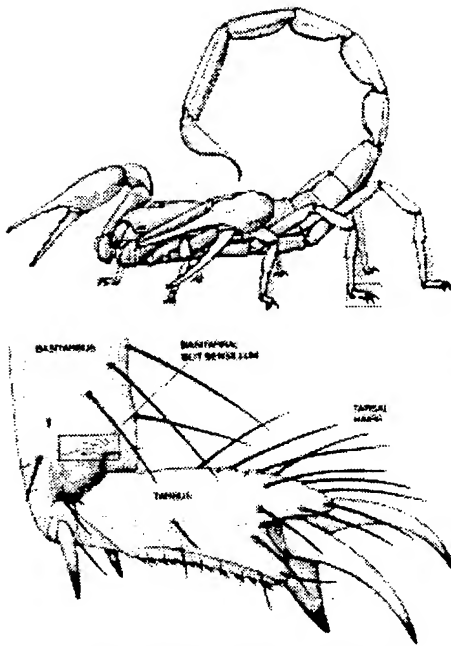
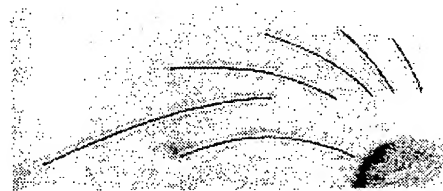


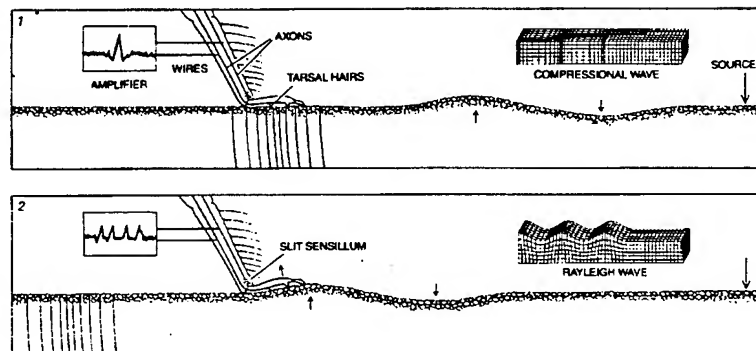
Figure 3. Ch'ang Heng seismoscope (circa 132 AD) - earliest known earth kinetic sensor.



a. Scorpion; leg sensors.



b. Close-up of leg hair sensors.



c. Prey-distance detection from p- and R-waves.

Figure 4. Mojave Desert scorpion: vibration sensing system.

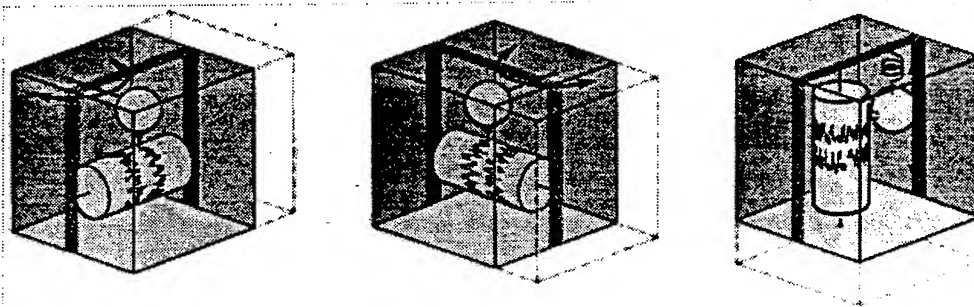


Figure 5. Mechanical seismograph; general principle.

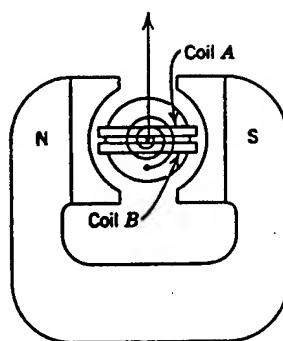


Figure 6. Early permanent coil instrument (galvanometer principle).

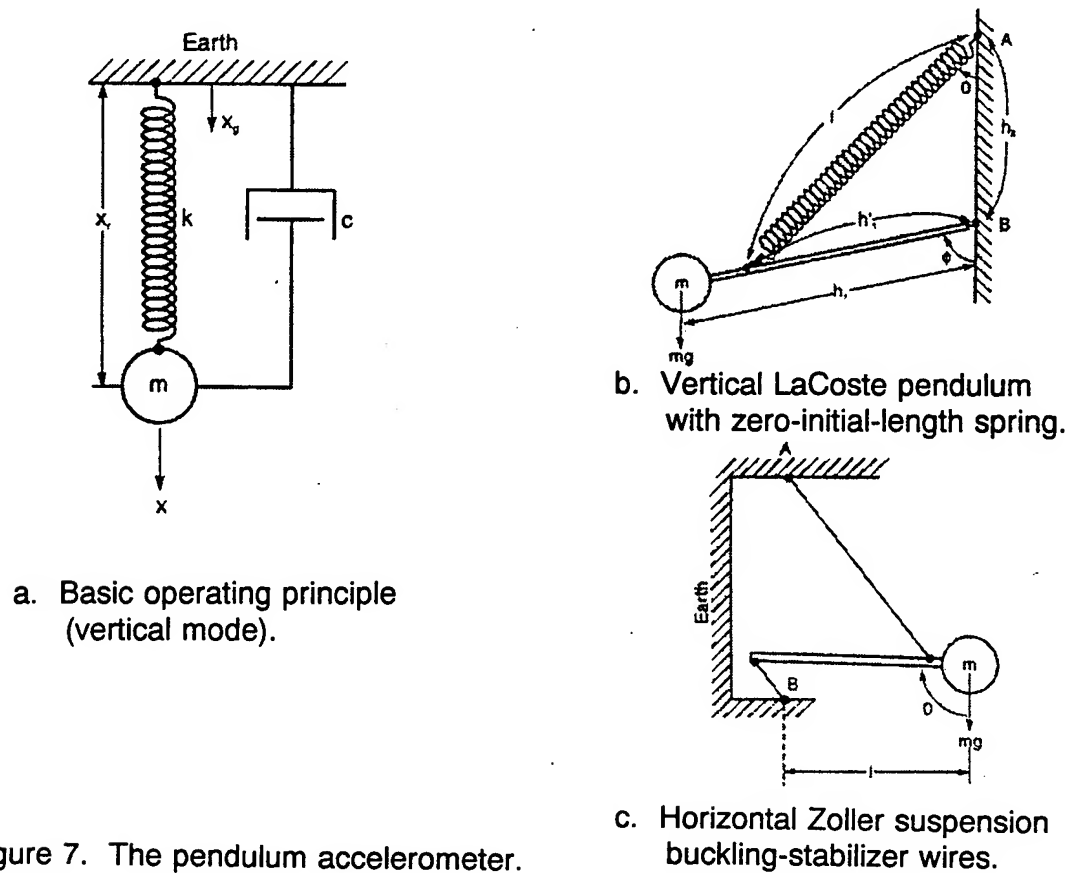


Figure 7. The pendulum accelerometer.

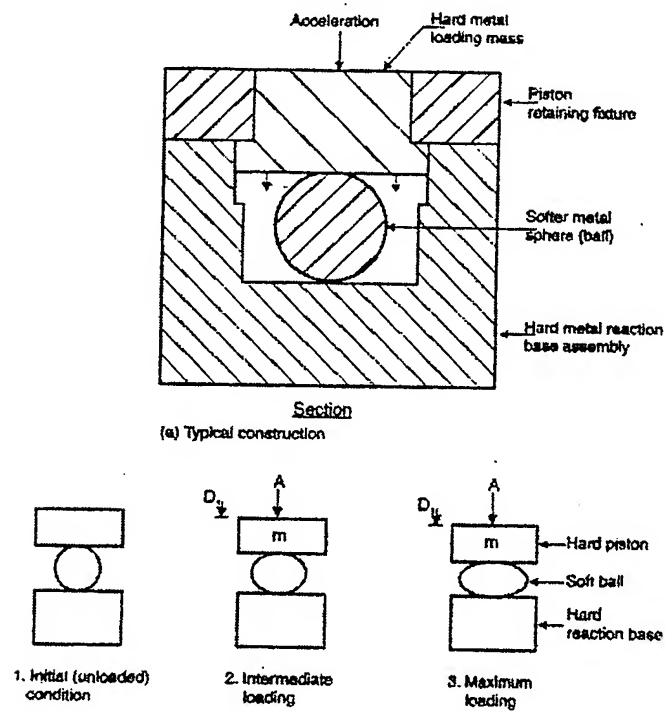
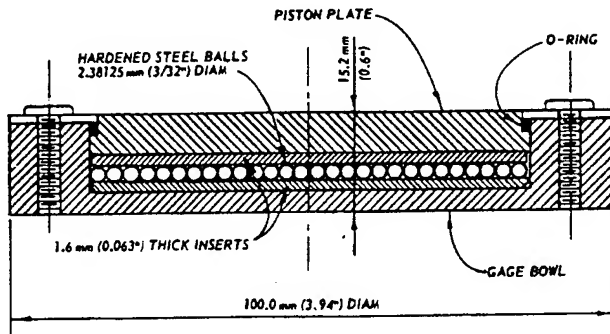
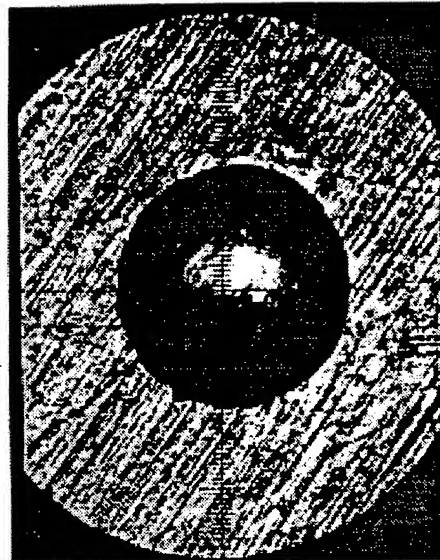


Figure 8. Early mechanical ball-crusher gage.

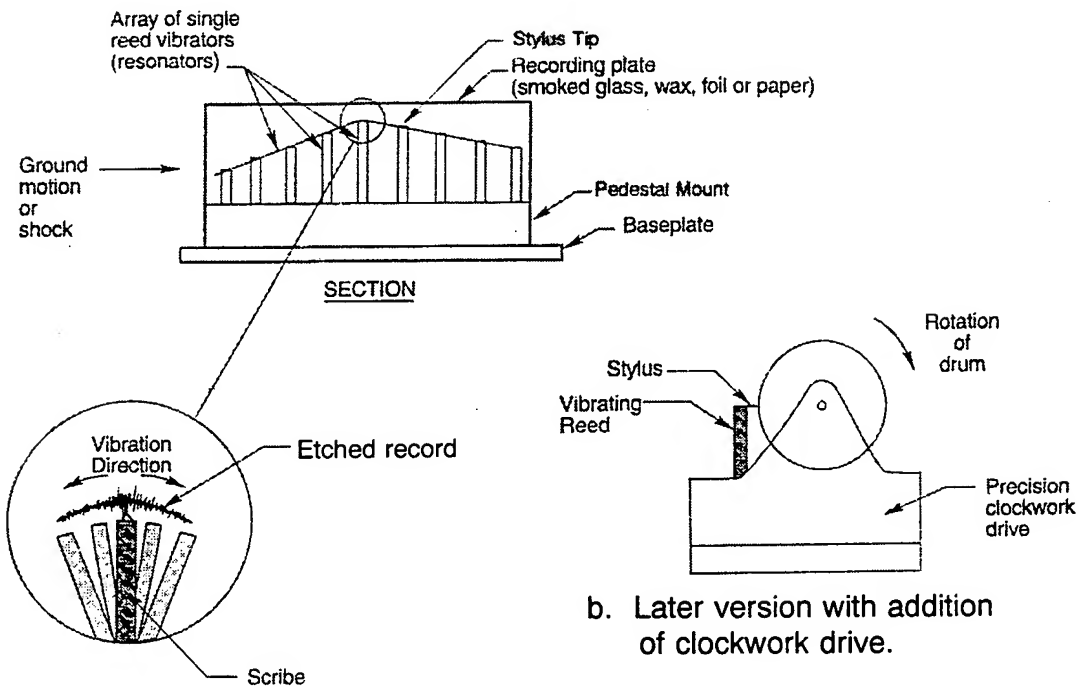


a. Section drawing.



b. Photomicrograph of Brinell pattern.

Figure 9. The Brinell Sandwich stress gage; a modern Ball Crusher gage.



a. Early version of Reed gage.

b. Later version with addition of clockwork drive.

Figure 10. Mechanical Reed gage operating principle.

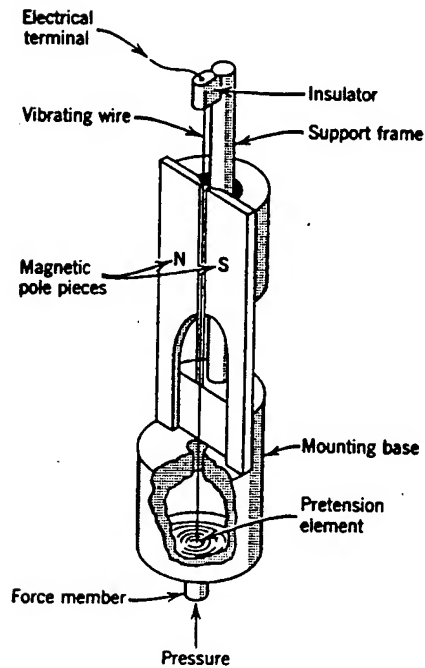


Figure 11. Basic vibrating wire sensor construction details.

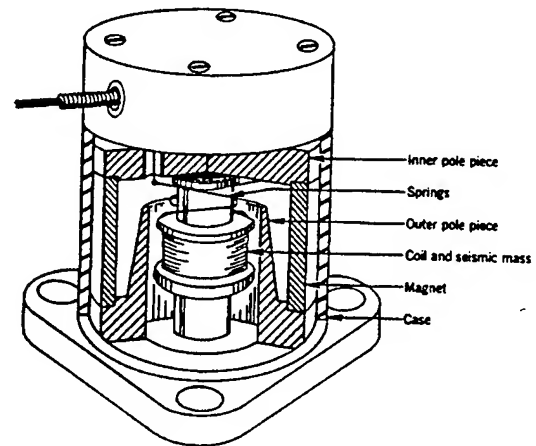


Figure 12. Moving coil electrodynamic velocity gage.

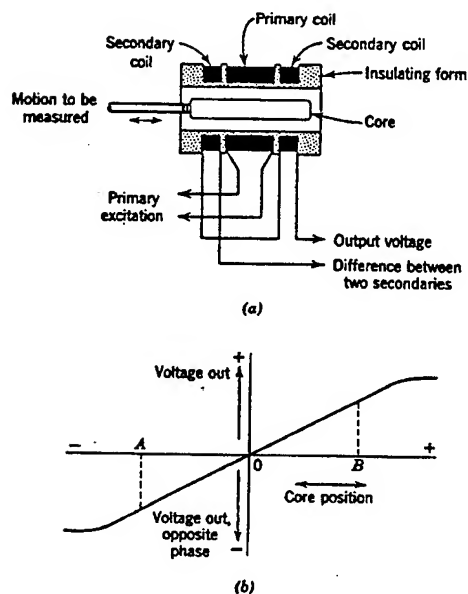


Figure 13. Typical inductance sensor; linear variable differential transformer (LVDT)

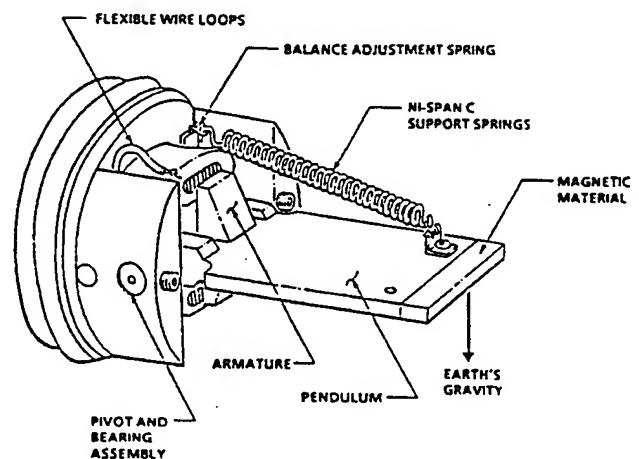


Figure 14. DX vertical velocity gage.



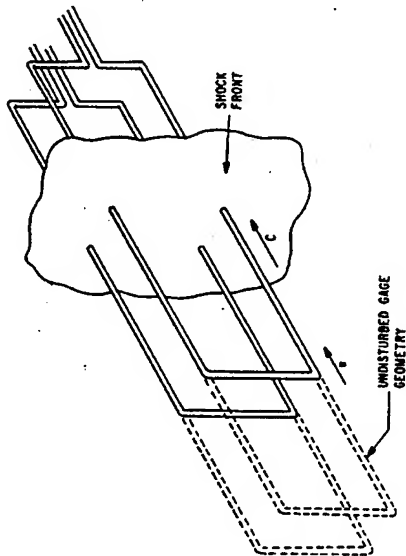


Figure 15. MIPV velocity gage under dynamic loading.

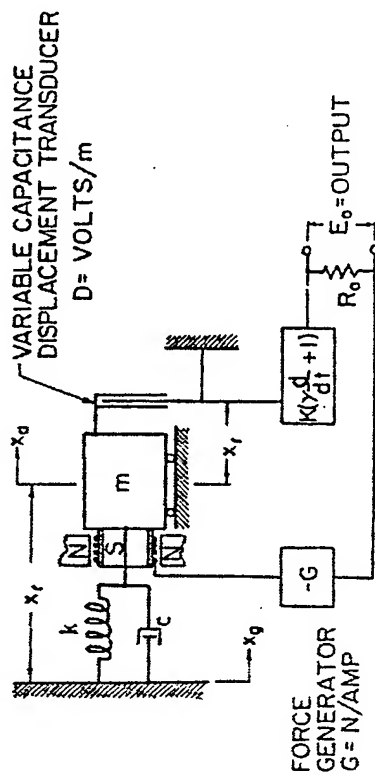
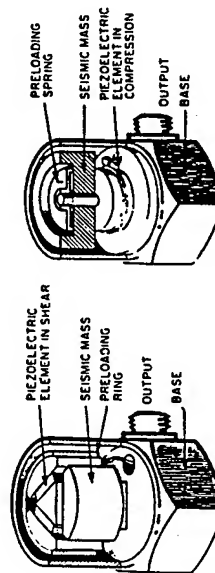


Figure 16. Force-balance (servo) motion sensor operation.



a. Delta Shear      b. Compression

Figure 17. Piezoelectric (crystal) accelerometers.

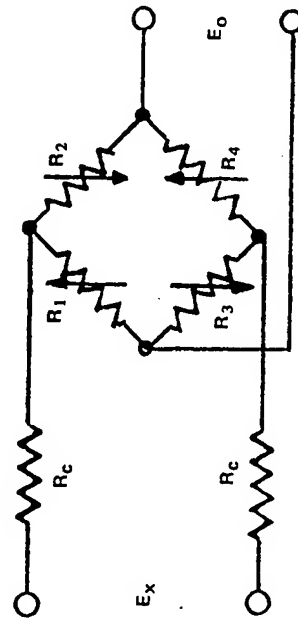


Figure 18. Wheatstone bridge circuit; full-active arm.

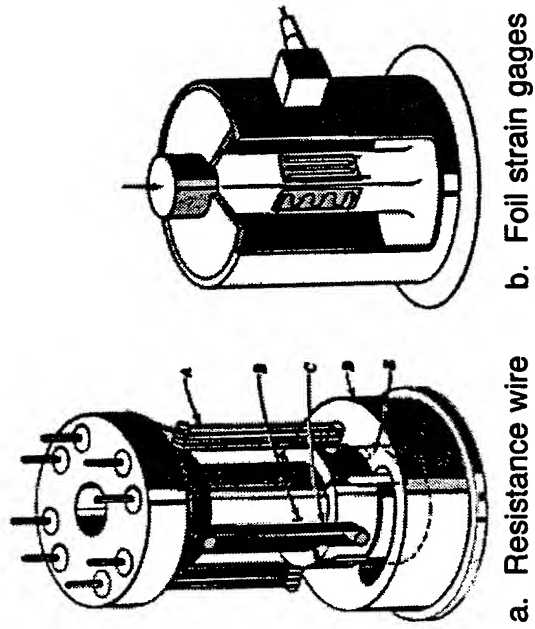


Figure 19. Early column strain gage force transducers.

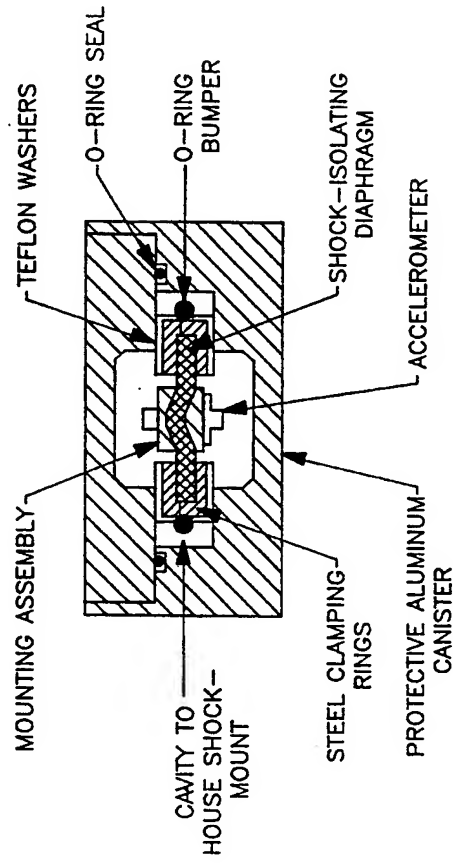


Figure 21. Shock-isolated accelerometer based "velocity" gage (SIA).

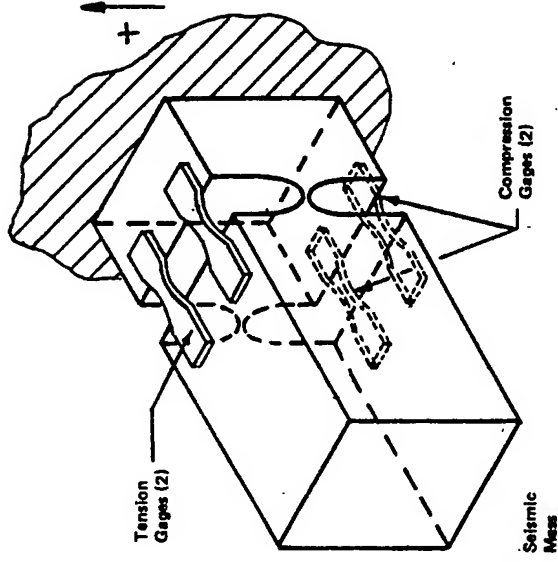


Figure 20. Typical piezoresistive accelerometer.

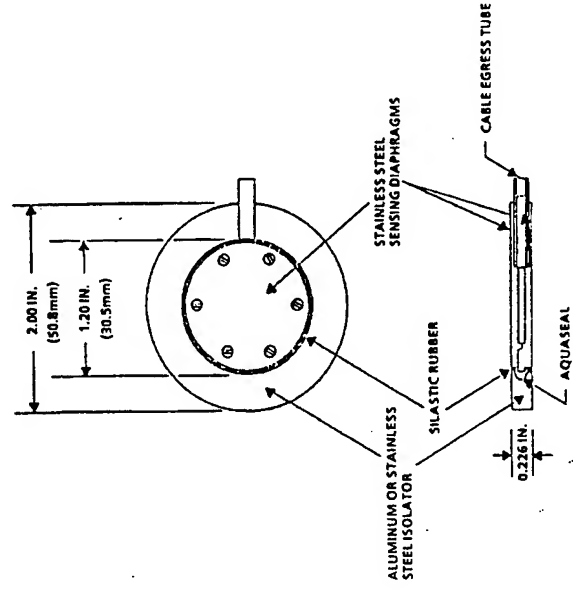


Figure 22. SE diaphragm soil stress gage.

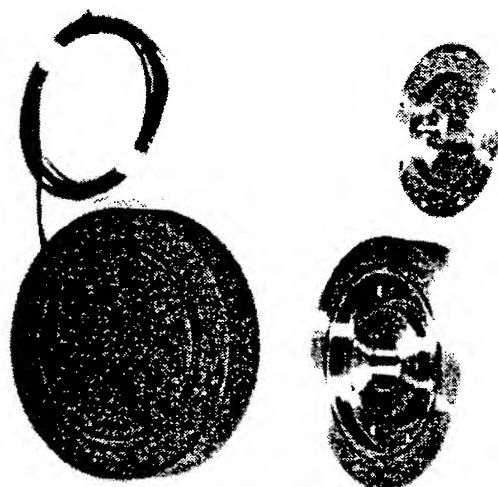


Figure 23. Column-based stress gage (CBS).

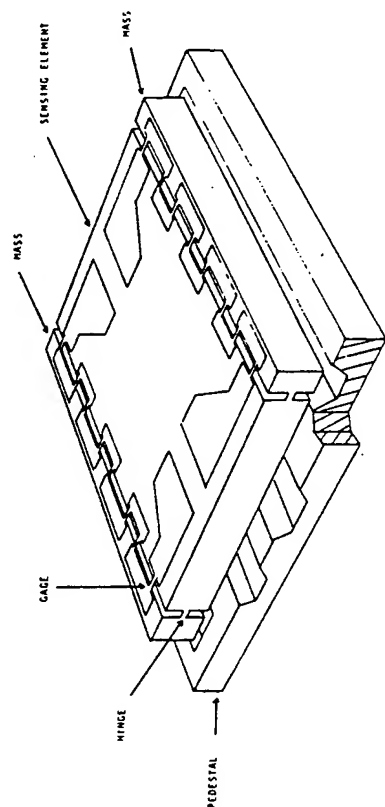


Figure 24. Micromachined IC acceleration sensor element.

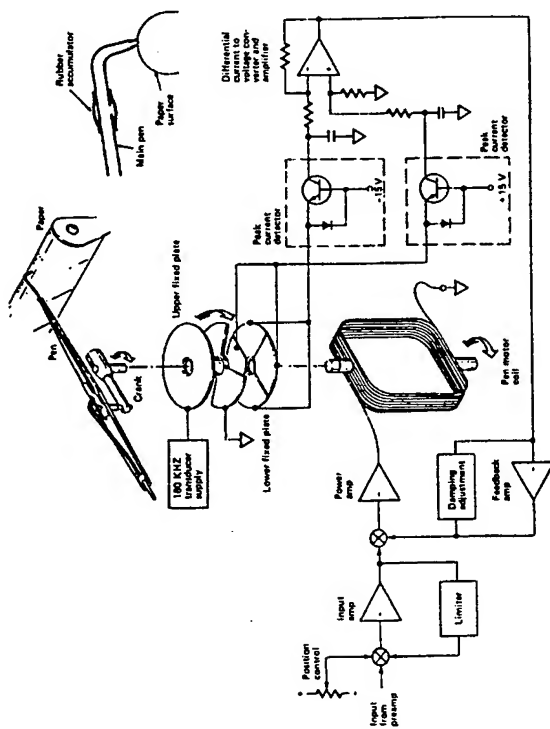


Figure 25. Ink recording oscillograph.

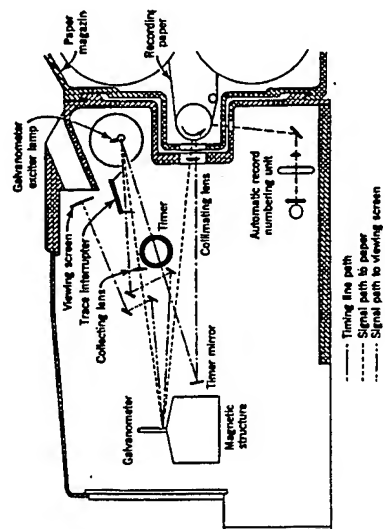


Figure 26. Optical galvanometer paper recorder.

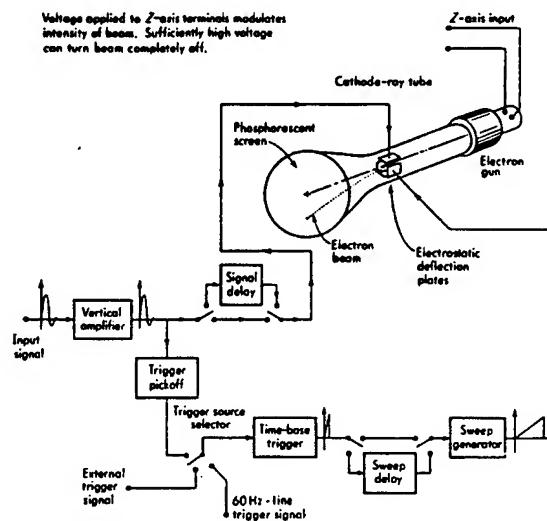
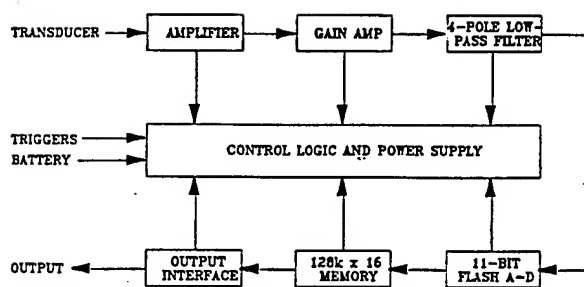
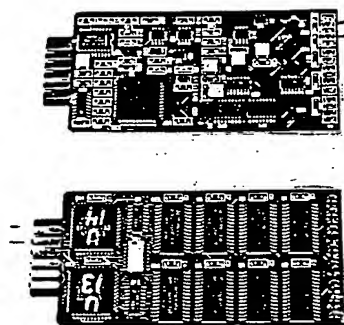


Figure 27. Oscilloscope.



a. HDAS operational schematic



Side 1. Signal conditioner/amplifier.



Side 2. Control logic/digital memory.

b. HDAS circuit board

Figure 28. Next generation autonomous data acquisition modules.

## BIBLIOGRAPHY

- Brownell, P.H., "Prey Detection by the Sand Scorpion"; *Scientific American*, December 1984, pp94-105.
- Bungum, H., E.S. Husebye and F. Ringdal, "The NORSAR Array and Preliminary Results of Data Analysis"; 1971, *Geophysics Journal of the Royal Astronomics Society*, Vol 25, pp 115-126.
- Cerni, R.H.; Foster, L. E., *Instrumentation for Engineering Measurement*, Third Edition, December 1966, John Wiley & Sons, Inc., New York.
- Coleman, P.L., et al, "Review and Development of Ground Motion and Airblast Instrumentation," DNA 4036F, 30 June 1976, Systems, Science and Software Contract Report, Defense Nuclear Agency, Washington, DC.
- de Vries, Leonardo and van Amstel, Ilonkal, "Victorian Inventions"; 1971, John Murray, Fifty Albemarle Street, London.
- Dewey, J., Byerly, P., "The History of Seismometry to 1900"; *Earthquake Information Bulletin*, Vol. 11, No. 2, pp. 64-70, 1979, USA.
- Doebelin, Ernest, *Measurement Systems Application and Design*, Fourth Edition, 1990, McGraw-Hill Publishing Company, New York.
- Farrell, W.E., "A Gyroscopic Seismometer: Measurement During the Borrego Earthquake"; 1969, *Bulletin of the Seismological Society of America*, Vol. 59, pp 1239-1246.
- Farrell, W. E., "Sensors, System and Arrays; Seismic Instrumentation Under VELA-UNIFORM"; *The VELA-UNIFORM Program; A Twenty-Five Year Review of Basic Research*, pp. 465-505, 1985, Science Applications International Corporation, San Diego, CA.
- Finnistone, Sir Monly, Williams, Treavor and Bissel, Christopherl, "Oxford Illustrated Encyclopedia of Inventions and Technology"; Oxford University Press, 1992
- Flanders, P. L.; "NUCLEAR GEOPLOSICS, A Sourcebook of Underground Phenomena and Effects of Nuclear Explosions, Part Three-Test Sites and Instrumentation" DASA-1285 (III), May 1964, The Defense Atomic Support Agency, Washington, D.C.
- Franco, Raphael A., Jr. and Ingram, James K., "A Self-Contained, Multi-Channel, Shock-Hardened Data Acquisition System," *Proceedings of the 1993 Instrumentation for Nuclear Weapons Effects Testing Conference (INWET'93) and 7th Photonics Workshop*, 2-5 November 1993, Menlo Park, CA.
- Galbraith, Frank W., "Shock Spectrum Measurements," 10513-6002-R000, 9 February 1970, TRW Systems Group, Redondo Beach, CA.
- Gould, K. E., "High-Explosive Field Testing (1945-1987)," DASIAC-TN-87-3, 1 December 1987, Kaman Tempo Contract Report, Defense Nuclear Agency, Washington, DC.
- Harpun, Patric, "The Timetable of Technology. A Record of our Century's Achievements"; Michal Joseph, London 1982

Hudson, D.E., "Advances in Earthquake Engineering.", June 16-20, 1980, *Continuing Education in Engineering*, University of California, Earthquake Engineering Research Center, Berkeley, CA .

Hudson, D. E., "History of Accelerograph Development"; *March 30-31, 1983, Proceedings of the Golden Anniversary Workshop on Strong Motion Seismometry*, pp. 29-56, University of Southern California, Los Angeles, CA.

Hudson, D.E., "Ground Motion Measurements In Earthquake Engineering"; 1990; Prentice-Hall Inc., Englewood Cliffs, NJ.

Ingram, J. K., "Development of a Free-Field Soil Stress Gage for Static and Dynamic Measurement," *Instruments and Apparatus for Soil and Rock Mechanics*, pp. 20-36, ASTM Special Technical Publication 392, June 1965, American Society for Testing and Materials, Philadelphia, PA.

Ingram, J. K., "Transducers for High-Shock Environments," Memorandum Report, October 1985, U.S. Army Engineer Waterways Experiment Station, CE, Vicksburg, MS.

Ingram, J. K., "Blast and Shock Instrumentation for Explosives Testing, Enclosure (18)," pp. 247-290, *Proceedings of the Second Tri-Service Symposium on Explosives Testing*, 16-18 May 1989, 14 August 1989, Department of Defense Explosives Safety Board, Washington, DC.

Ingram, J. K., Armstrong, B. J. and Brogan, J. T., "Mobile In-Field Blast Effects Data Processing Facility," pp. 159-169, *Proceedings of the 36th International Instrumentation Symposium*, 6-10 May 1990, Denver, CO, Instrument Society of America, Research Triangle Park, NC.

Ingram, James K. and Dinan, Robert J., "Severe Blast Effects Measurement Using Shock-Hardened, Self-Recording Instrumentation Modules," pp. 91-101, *Proceedings of the 13th International Symposium on the Military Application of Blast Simulation*, 13-17 September 1993, The Hague, The Netherlands.

Mallet, R., "Great Neopolitan Earthquake of 1857; The First Principles of Observational Seismology."; 1862, Chapman and Hall, London.

*Mc Graw-Hill Encyclopedia of Science and Technology*; 1992, 7th edition, Mc Graw-Hill Inc., New York, NY.

McNeal, Ian, *An Encyclopedia of the History of the Technology*; 1990, Routledge, London & NY.

Melton, B. S., "Earthquake Seismograph Development; A Modern History; Part 2"; 1981, *Transactions, American Geophysical Union*, Vol. 62, No. 25, pp. 545-548.

Oliveira, C.S., "Seismic Instrumentation and Monitoring of Geotechnical Structures In Soil Dynamics and Geotechnical Earthquake Engineering"; 1993, A.A. Balkema, Rotterdam/Brookfield, pp 435-475.

Papastamatiou, D., "Contributions of Early Instrumental Seismic Recordings to Engineering Analysis"; *Instrumentation for Ground Vibration and Earthquakes*, pp. 119-124, July 4-5, 1977, The Institute of Civil Engineering, Keel, UK.

Peekna, Andreas, "Development of the Brinell Sandwich Passive Soil Stress Gage," DNA 4608F, 31 December 1977, U.S. Army Engineer Waterways Experiment Station Contract Report, Defense Nuclear Agency, Washington, DC.

Renick, Joseph D., Baum, Neal P., "The Mutual Inductance Particle Velocimeter (MIPV)," AFWL-TR-82-108, January 1983, Air Force Weapons Laboratory, Kirtland AFB, NM.

Singer, Charles , Holmyard, E.J. , Hall , A.R. and Williams,Trevor I., "A History of Technology"; Volume IV, Industrial Revolution 1750-1850, Oxford at the Clarendon Press, 1958

Skipp, B.O., "Ground Vibration Instrumentation - A General Review"; Paper 2, 4-5 July 1977, *Proceedings of the Conference, The Society for Earth and Civil Engineering. Dynamics*, Institute of Civil Engineering, London.

Troitzsch, Ulrich und Weber, Wolfhard, "Die Technik, von den Anfängen bis zur Gegenwart"; Westerman 1982

Welch, C. R., White, H. G., "Shock-Isolated Accelerometer Systems for Measuring Velocities in High-G Environments, " *The Shock and Vibration Bulletin*, January 1987, The Shock and Vibration Information Center, Naval Research Laboratory, Washington, DC.

White, Howard G., "Development of a High-Range Particle Velocity Gage," Technical Report SL-89-3, January 1989, U.S. Army Engineer Waterways Experiment Station, Vicksburg, MS.

Williams, Trevor I., "Science: Invension and Discovery in the 20th Century"; 1990, Harrap, London.

Winiarz, Marek and Raymond, D. W.; "Defense Nuclear Agency Permanent High-Explosive Test Site (PHETS) Instrumentation Source Book," UF775 D46t, 1988, Defense Nuclear Agency, Washington, D.C.

# **BLAST WAVE MEASUREMENTS TECHNIQUES, STRUCTURAL RESPONSE AND CALIBRATION**

Ralph E. Reisler  
John H. Keefer  
Noel H. Ethridge

Applied Research Associates, Inc.  
P.O. Box 548  
30 Centennial Lane  
Aberdeen, Maryland 21001

## **ABSTRACT**

Instrumentation and methods for measuring the response of structures to air blast which have been used in testing over the past fifty years are summarized. Sensor systems in the nuclear days were confronted with the deleterious effects of the detonation itself so systems found to be successful in the free-field testing were adapted for structural measurements. Measurement devices took the form of both passive and active systems similar in principle to those used in free-field work. Self-recording devices were developed and deployed as primary and secondary measurement systems. Typical systems used to measure acceleration, displacement, earth pressure, and time of measurement are presented. Calibration techniques used with the gages are described.

## **INTRODUCTION**

In the midst of preparing the monograph for the free-field air blast instrumentation for the nuclear era, the thought occurred to us that a similar report should be prepared covering the devices used in studying the response of structures to blast. The MABS Executive Committee concurred in this, and Mr. Arnfinn Jenssen of the Norwegian Defence Construction Service joined with the Defense Nuclear Agency (DNA) to sponsor the effort.

With the introduction of nuclear weapons in the 40s, it was soon apparent that experiments would need to be conducted in order to understand and appraise the true potential of the blast forces. The first laboratory for extensive experiments was the Bikini Atoll in the South Pacific in 1946. The primary objective at that time was to determine the effects of the A-bomb on Naval vessels. It would, to quote scientists of that era, "provide answers to such questions as 'What effect would an atomic bomb have on a fleet of Navy vessels,' 'Is an airburst more lethal than an underwater burst?'" It would not, however, answer so directly the questions, "To what extent should accepted principles of ship design be altered in future construction, or how does one build a blast-resistant structure." To obtain answers to the latter would require many experiments. Information would have to be developed on the behavior of the blast wave and the pattern it displays when it interacts with a structure. An understanding of the behavior of materials under dynamic



loads would be necessary. Gaining such information was needed because it was fundamental to a host of problems that were born with the nuclear era.

From the very first experiments it was learned that the loading and target response information sought would come very slowly. Making measurements in an environment electrified by an electromagnetic pulse and bathed in nuclear and thermal radiation was to be a challenge in itself. Finding rugged, reliable gages that would meet these harsh field requirements was not easy. It was stated in those days that since the ships in the Bikini target fleet could not have crews, it was a requirement that the instruments leave some type of permanent record of their responses: ink records writing on a slow-rotating disk drum, scratch-records with a needle scratching its record on a wax-coated disk or drum, magnetic tape records, optical recorders, telemetry recording systems, or permanent deformation gages.

There was an axiom in the nuclear weapons testing business which said: "The first time you do an experiment do everything possible to make it successful. If successful there will be many subsequent opportunities to refine the results. First-time failures have no future."

Numerous structures programs were conducted with nuclear weapons before the moratorium on atmospheric testing went into effect. Structural testing, however, continued with the introduction in the early 60s of high-explosives as a suitable simulation of nuclear airblast. The testing continued through the intervening years until the last large-scale test called MINOR UNCLE was conducted just two years ago, in 1993. From the very beginning, the HE test effort was tripartite in nature; scientists from Britain, Canada and the U.S. participated. Later, in the 70s, testing took the flavor of a multi-national force involving most of the MABS members.

Measurements of the response of structures included at first blast pressure, acceleration, displacement strain, and time-of-collapse of structural elements. Experience gained was continually applied to subsequent tests. Measurements were soon expanded to include the response of soils/pressure, strain, and particle velocity, and angular velocity. Both passive and active sensing devices were developed and deployed in the field; both oscillographs and magnetic tape recorders were used to record electronic data. Magnetic tape recorders soon became the recorder of choice until they were replaced by digital recorders in the late 80s.

## **ACCELERATION**

Early acceleration measurements were made using a gage manufactured by the Wiancko Engineering Company. It used the "E" coil principle so successfully utilized for pressure measurements because of its inherent resistance to radiation effects. The "E" coil in the gage consisted of two windings on coils of a two-arm reluctance bridge wound on the extreme legs of an "E"-shaped magnetic core. As the armature is rotated, the reluctance is changed causing an imbalance of the bridge. Adaptation of this principle was made for acceleration measurements as shown in Figure 1. The sensing element consisted of an armature bonded at its center to the vertex of a "V"-shaped spring member and held in

close proximity to the coil. A weight, the size of which depends upon the range of the accelerometer, is attached to one end of the armature so that an acceleration in a direction normal to the armature causes it to rotate about the vertex of the spring. The rotation of the armature causes an imbalance in a full impedance bridge of which the windings of the coil are a part. The bridge imbalance is proportional to the acceleration.

Modern-day electronic acceleration measurements are made with strain or piezoelectric sensors of commercial manufacture by such companies as Kulite, Endevco, PCB and others.

Non-electronic acceleration devices included self-recording instruments and peak-only gages. One such gage in the 50s was the Engineering Research Associates (ERA) accelerometer. The gage, shown in Figure 2, uses a spring-mass system where a small magnet will erase a pre-recorded signal on a moving magnetic tape in response to acceleration. Damping of the seismic elements is controlled by placing a silicone grease between the magnet and a stationary platform just below.

The French Chocmart from the 50s is a peak device installed on structures to measure the acceleration which it may experience. The unit shown in Figure 3 is made up of five metal tubes mounted on a metal plate with the opposite end of the tube open. When in use the mounting plate is bolted to the section of structure of interest. Each tube in the assembly is inclined at angles of 10 to 50 degrees from the perpendicular to the surface of the mounting plate. A steel ball is inserted in each tube, and each ball is numbered to match the number on the tube. Each steel ball in response to the acceleration experienced by the structure may be ejected from the tube according to the intensity of the pulse. The ball is captured at the end of its travel by a layer of asphalt spread on the floor of the structure. The trajectory of the ball after it leaves the tube is dependent upon the magnitude of the acceleration forces striking the structure. The distance the ball has traveled, together with the angle of inclination of the tube and the mass of the ball enables the magnitude of the acceleration experienced by the structure to be calculated.

## **EARTH PRESSURE**

The "E" coil principle was also incorporated into an earth pressure gage in the 50s. This gage was a combination of the Carlson static stress meter and the Wiancko differential-inductor pickup. The sensing mechanism shown in Figure 4 was formed by two flexible circular plates separated by a spring seal around their edges. One of the plates is bored concentrically, and the hole is covered by a flexible diaphragm flush with the outside surface of the plate. Thus, two adjoining chambers are created; one formed by the volume between the two circular plates and a smaller one formed by the volume of the drilled hole. The chambers are filled with fluid so that when pressure is applied by squeezing the two plates together, the flexible diaphragm is bulged outward. This motion is coupled to an armature and causes it to move the "E" coil. The bored plate is the base of the gage and is placed against the structure.

A typical earth pressure record from a nuclear event is shown in Figure 5.

## DISPLACEMENT

One of the earliest displacement gages was the Sandia Corporation gage which could be used in either a self-recording or electronic recording mode. The gage shown in Figure 6 consists essentially of a paper-supply roller, a take-up roller, and a recording stylus which for most measurements is directly attached by a seamless steel tube to the structural member being displaced. The rollers, driven by a DC motor, accommodate waxed paper 12 inches wide upon which the record is made. A centrifugal governor controls the speed up to  $\pm 1$  percent. Recording is initiated by relay. The device permits a measurement of  $\pm 6$  inches if the stylus is set at one end of the shaft. For electronic recording, a ten-turn Helipot potentiometer is driven by a shaft through a rack and pinion gear. This Helipot is part of a bridge circuit and control of its resistance value permits the sensitivity of the electronic signal to be adjusted to the magnitude of the expected displacement. A field installation of these gages is shown in Figure 7.

Another displacement gage was designed by the Ballistic Research Laboratory (BRL) to measure displacement of  $\pm 0.75$  to  $\pm 5.75$  inches. It consists of a helically-wound spring made of spring steel as illustrated in Figure 8. The spring was 15 feet long, 3 inches wide and 0.028 inch thick, and is attached to a shaft and wound until the assembly fits into the 4-1/2 in. diameter gage case. The shaft of a 500 ohm potentiometer with 360 degrees continuous rotation is connected to the spring shaft. The potentiometer is incorporated in a resistive bridge circuit. For ease of calibration, a dial is attached to the potentiometer shaft. A grooved pulley with a diameter of either 3.66 inches or 2.5 inches, depending upon the expected displacement, is attached to the spring shaft on the opposite end of the potentiometer. The spring shaft is turned until the spring produces a torque of approximately 100 inch-pounds. A ratchet mounted on the spring shaft prevents the spring from unwinding. High-tensile-strength piano wire is clamped and wound several times on the grooved pulley. The free end of the piano wire is attached to the point of measurement. Tension is placed on the wire by releasing the ratchet. Any displacement will turn the shaft, unbalancing the bridge and producing an output proportional to the displacement. Rise times of 14.5 msec and 5.0 msec were achieved with the two pulleys.

Figure 9 shows a field installation of the gages.

For small displacements, 0.001 to 0.75 inches, a linear variable differential transformer (LVDT) was used in conjunction with the BRL gage as shown in Figure 10. The hollow cylindrical armature of the LVDT is threaded over the gage wire and clamped in place. The solenoid winding of the transformer inside which the armature moves axially is held to the gage case by a rigid frame. Thus, the transducer senses directly the linear motion of displacement; the BRL gage serves only to provide tension on the wire. The LVDT was manufactured by the Shaevitz Engineering Company.

A typical record from this device is shown in Figure 11.

Many simple displacement devices were devised to measure peaks only. The following figures show some of these devices.

Figure 12 shows a peak beam deflection gage deployed to measure the maximum and the permanent deflections of shelter roofs and of a blast door.

Figure 13 shows a spring-mounted scratch gage deployed by the Defence Research Establishment - Suffield, Alberta, Canada (DRES) to record the deflection of the membrane in a support kit overhead-protection trench cover. It was spring-mounted to record the upward and downward deflection of the membrane at the center of the cover.

Figure 14 shows a differential motion scratch gage designed to measure the relative displacement of the foundation of a hardened antenna structure and the soil media. The gage incorporated a spring-loaded pointer installed in the structure's foundation and a scratch plate which was designed to move with the soil.

Figure 15 shows arrays of contact registration gages. They were made of thin strips of balsa wood of lengths differing by 0.5 inches. The strips were glued alternately to each side of a length of wood with a cross section of 1/2 inch by 3/4 inch. In case a strip should bend and not break when struck by a panel, each strip was tipped by a red marking material (lipstick) configured to indicate if contact occurred and to mark the contacting surface.

Figure 16 shows a rod scratch gage which consists of a 3/4-inch diameter aluminum rod printed with machinists' bluing and attached to the point of measurement by a pin coupling. The rod passes through a guide hole in a small aluminum bar attached to the reference frame. Double-toothed spring metal scribes ride on opposite sides of the rod and mark maximum inward and outward movements of the rod through the guide hole.

Figure 17 shows a peak recording shock spectra gage. The gage has a number of cantilever springs or rods mounted on a rigid base and a mass on the other end. The masses and spring constants of the reeds are such that their natural frequencies cover the range 2 to 300 Hertz. The masses have scribes which are in contact with a polished record plate coated with lamp black. When the gage base is subjected to shock, the displacement of the reed is recorded. Following the test, the measurements are converted to mass displacement by use of calibration factors.

## **TIME OF MEASUREMENT**

A panel-time-of-break was developed by Sandia Corporation to obtain information regarding the order in which parts of a building fail. Strip conductors were mounted on structural panels as illustrated in Figure 18. When a given panel breaks, severing the conductor mounted on it, the closed relay in the circuitry opens and unbalances the circuit by an amount depending upon which of a number of panel resistors are open circuited. Successive breaking of panels causes changes in the magnitude of the unbalanced signal

which can be related to a particular resistor. The relay had a response time of 0.10 msec, giving the system a comparable time.

A time system designed to measure shock front position was the SLIFER (Shorted Location Indicator by Frequency of Electrical Resonance) cable. The cable is an electrical transmission line which is embedded in the earth so that the stress wave will move along the length of the cable. It is physically weak in comparison with the stress produced by the shock front and will thus be shorted at the shock front by crushing. The short will move with the local shock velocity in the medium. The transmission cable constitutes an inductive bridge in a timed circuit of a Colpitts Oscillator, its inductance being related to the cable length. As the shock continuously shortens the buried cable, the frequency of the oscillator is increased in direct relation to the shock front position along the line. In HE field tests it is common to position the cable three to six months in advance of the test to allow for natural settling and compaction of the soil.

## **CALIBRATION**

In the American Society of Mechanical Engineers' "A Guide for the Dynamic Calibration of Pressure Transducers," calibration is defined as a test during which known values of measurand are applied to a transducer and corresponding output readings are recorded. Others would simply say that calibration is a process of comparison of the output of an instrument to the output of a validated transfer standard.

A static and dynamic calibration are a very necessary and desirable part of any testing procedure. The dynamic calibration is needed for the selection of blast wave transducers intended for use in large-scale field tests. The transducer's natural frequency, rise time, possible deviations from static calibration, and other such characteristics may be observed during the dynamic calibration of the transducer.

Calibration devices take many forms; each is designed to calibrate gages over a specified range of the measurand, to determine frequency response, and to determine response to temperature and acceleration.

Blast measurements are always measurements of rapid pulses. In many applications, the pressure pulse is accompanied by a dynamic temperature pulse, electromagnetic pulse, detonation products, and powerful mechanical shocks and vibrations. To physically protect the gage from these processes, various means such as screens, grease, or some other material or method is employed.

Because the process being measured is a major strain on the gage, users frequently calibrate the gage not only before the test but after the test as well to detect any drastic performance changes which may have taken place during the measurement process.

Blast gages can exhibit hysteresis, nonlinearity, nonrepeatability, zero shift, resonances, and sudden, catastrophic failure. Their output is affected by strain on the cables, thermal transients and shocks, mechanical vibrations, electrical effects (ground loops, lead

resistances, etc.), ambient conditions, photo flash, and warm-up time. Many of these deleterious effects, if they exist, will be determined through calibration; those which cannot be minimized through mounting and installation procedures.

Calibration systems have been divided into three groups: static systems, pressure-pulse systems, and dynamic systems.

The simplest system for conducting a static calibration of pressure gages is a portable one which can be taken to the installed site of the gage. It is very important to conduct an in-place calibration of a gage, for in so doing all the components of a data acquisition system which can influence the accuracy of the data are included. These components are the cabling system, the signal conditioning equipment, the amplifier, and the recorder. A calibration system used in the 50s which incorporated dial pressure gages as secondary standards is shown in Figure 19. A calibration record of this era is shown in Figure 20. It will be observed that calibration steps of 25 percent were used to cover non-linearity effects generally common to the systems of the day. Improvements in transducers and recording systems were soon made and non-linearity problems were essentially eliminated.

The pressure-pulse system generates a pressure pulse with a known rise time. An air pulse system is illustrated in Figure 21. Basically, the calibrator consists of a reservoir, a manual or solenoid valve, and a dial monitor or digital pressure gage to set an accurate static reference pressure. The air reservoir tank volume is very large (20,000:1) compared to the interior of the solenoid valve or manual valve so the control pressure gage may be read and assumed to give the magnitude of the pressure pulse applied to the transducer. The fast-opening device is illustrated in Figure 22. A two-way solenoid valve was modified with a manual release valve. A Teflon o-ring seal was substituted after a standard rubber o-ring did not release properly. The system produces a rise time of 5 msec.

Dynamic calibration systems may be characterized as those which provide a history of the time variation of the calibration pulse. The systems described earlier are both simple and accurate but are somewhat limited by the rise time. This is a disadvantage in that a gage may function during a slow rise air-pulse calibration but may have a different output or fail during the air shock loading. A transducer when shock loaded may be stimulated to vibrate or ring at its natural frequency and may break. To check this possibility, shock tube calibrations are used in a calibration program.

There are several shock tubes of varying sizes used in calibration. A 2-inch shock tube is small and simple to operate. It operates from a cold-gas driver and is of constant area throughout. Instead of air, compressed bottled helium or nitrogen is used as the driver gas. The pressurized gas causes pre-selected diaphragms to break and create the shock waves. Close repeatability of shock pressure is obtained without scoring of the diaphragm. A tube is shown in schematic form in Figure 23. A photograph of a 2-inch tube is shown in Figure 24.

The majority of the structural measurement devices were calibrated using a static forcing function. For example, the earth pressure gage was placed in a circular steel framework with transfer disks as shown in Figure 25 so a force can be applied by a hydraulic jack. A load cell placed in the framework was used to record the pressure applied.

Displacement gages, in particular the low-range LVDT gage, were calibrated using a vernier and a dial gage to record the displacement applied. This is shown in Figure 26. High-range gages had a dial attached to the recording potentiometer shaft which was used to turn the shaft.

Accelerometers, on the other hand, were calibrated using a spin table, a shake table, and/or a drop table. Typical is the spin table shown in Figure 27, which has a control gage to compare with the test gage.

## **CONCLUSION**

Instrumentation of structures and military equipment exposed to nuclear explosions began on a large scale soon after the successful detonation of the A-bomb. In those days large numbers of all conceivable types of electronic and non-electronic devices that gave any evidence of successfully yielding information were deployed. Although the establishment of the moratorium on atmospheric nuclear testing brought an intensive period of testing to an end, the need for continued work was met by large-scale high-explosive testing begun in 1964. Programs of this nature continued on a periodic basis over the past decades through 1993.

Over the years advances in instrumentation to measure the parameters of interests were commonplace; gages became smaller in physical size with an increase in frequency response though many times more sophisticated. Extensive use of commercially available gages was made. Further progress can be expected as new technologies are applied in the field of blast instrumentation.

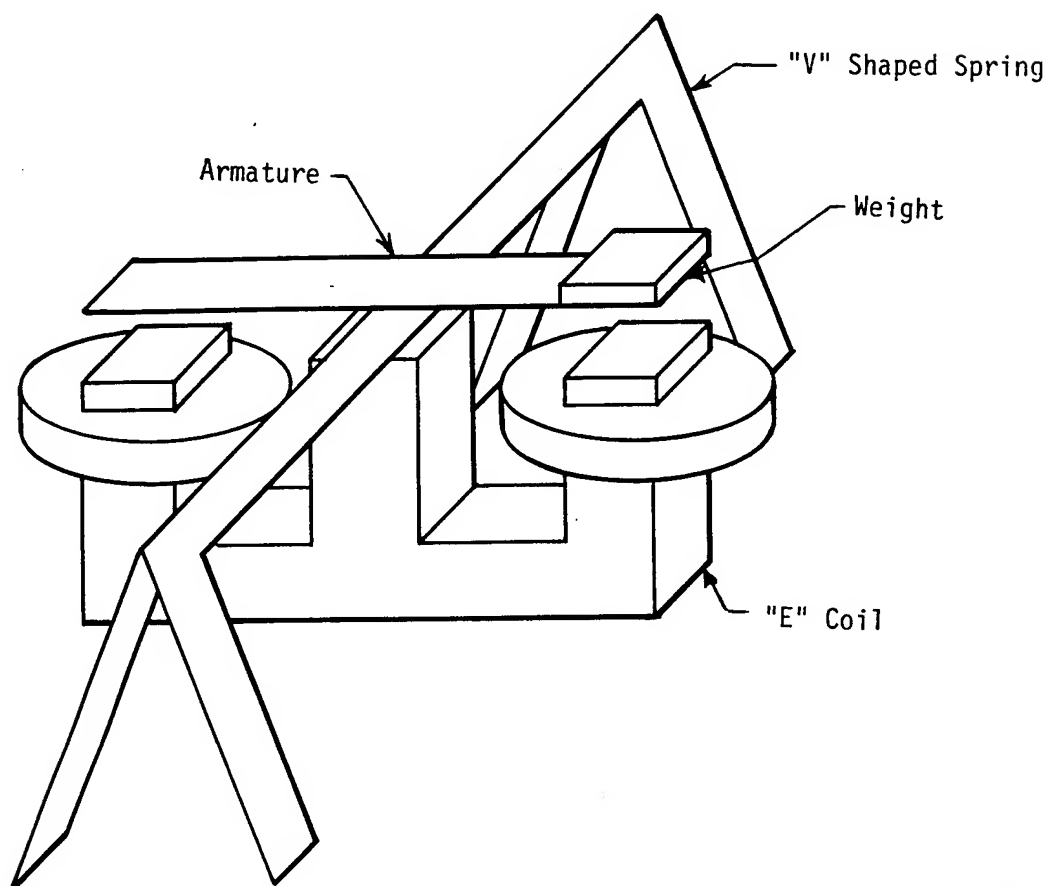


Figure 1. Schematic drawing of accelerometer spring mechanism.



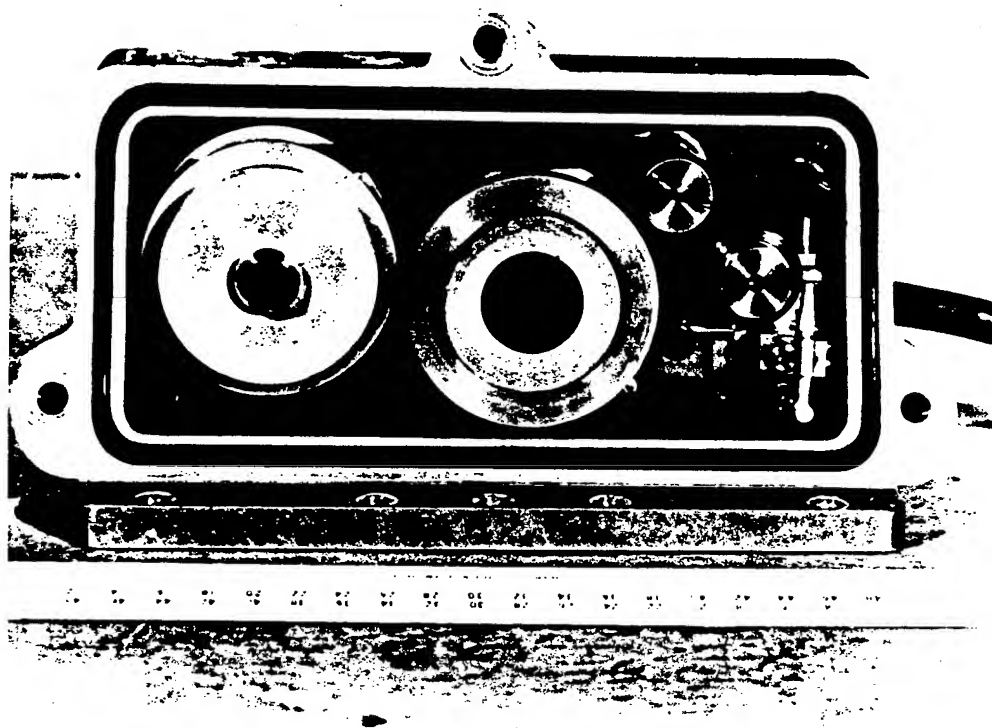


Figure 2. ERA self-recording accelerometer.

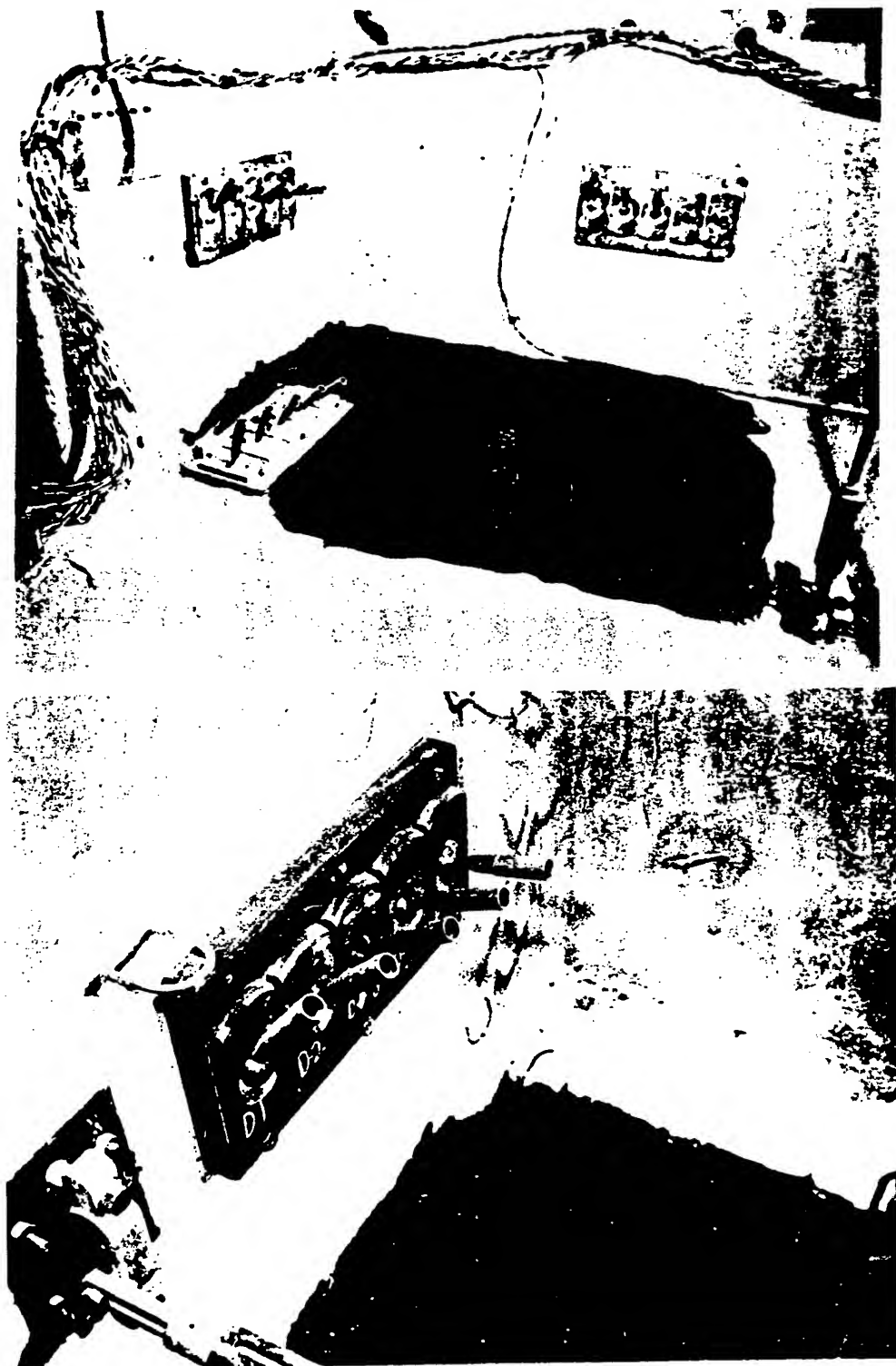


Figure 3. Chocmart gages with asphalt layer.

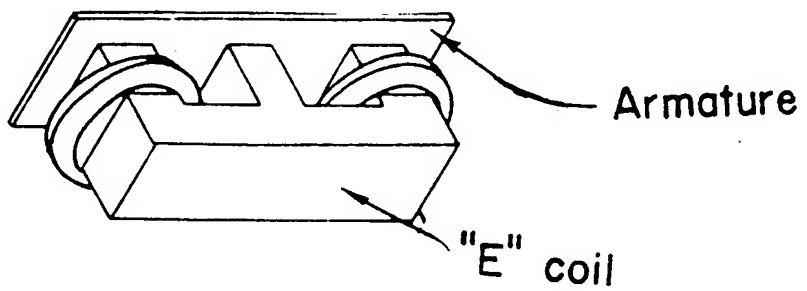
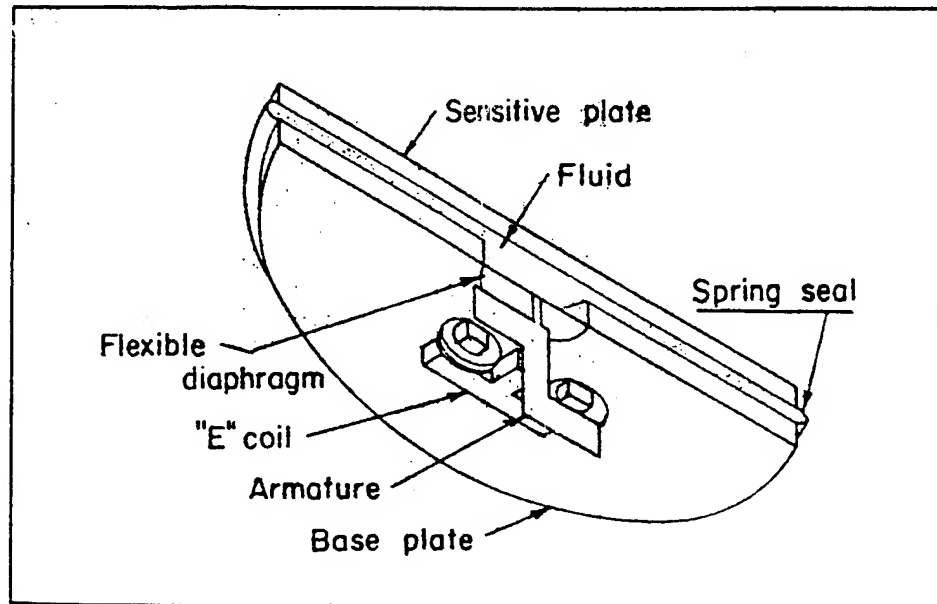


Figure 4. Earth-pressure gage sensing mechanism.

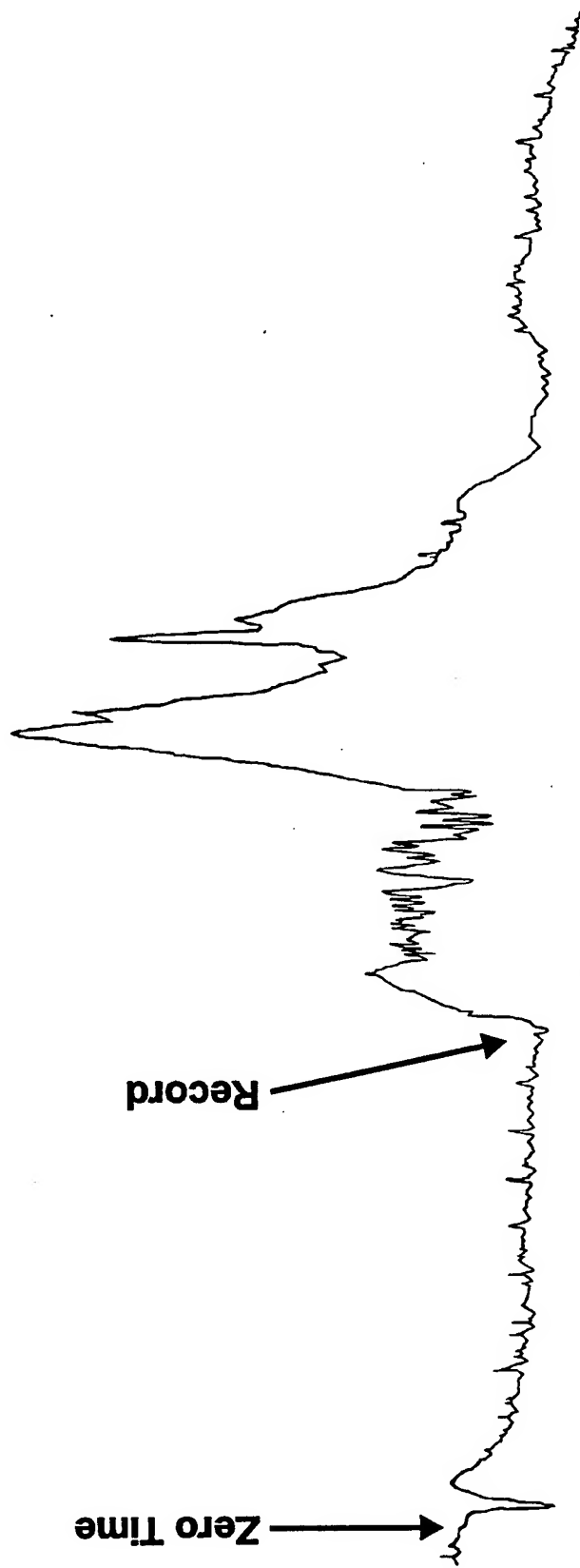


Figure 5. Earth pressure versus time on roof of buried structure.

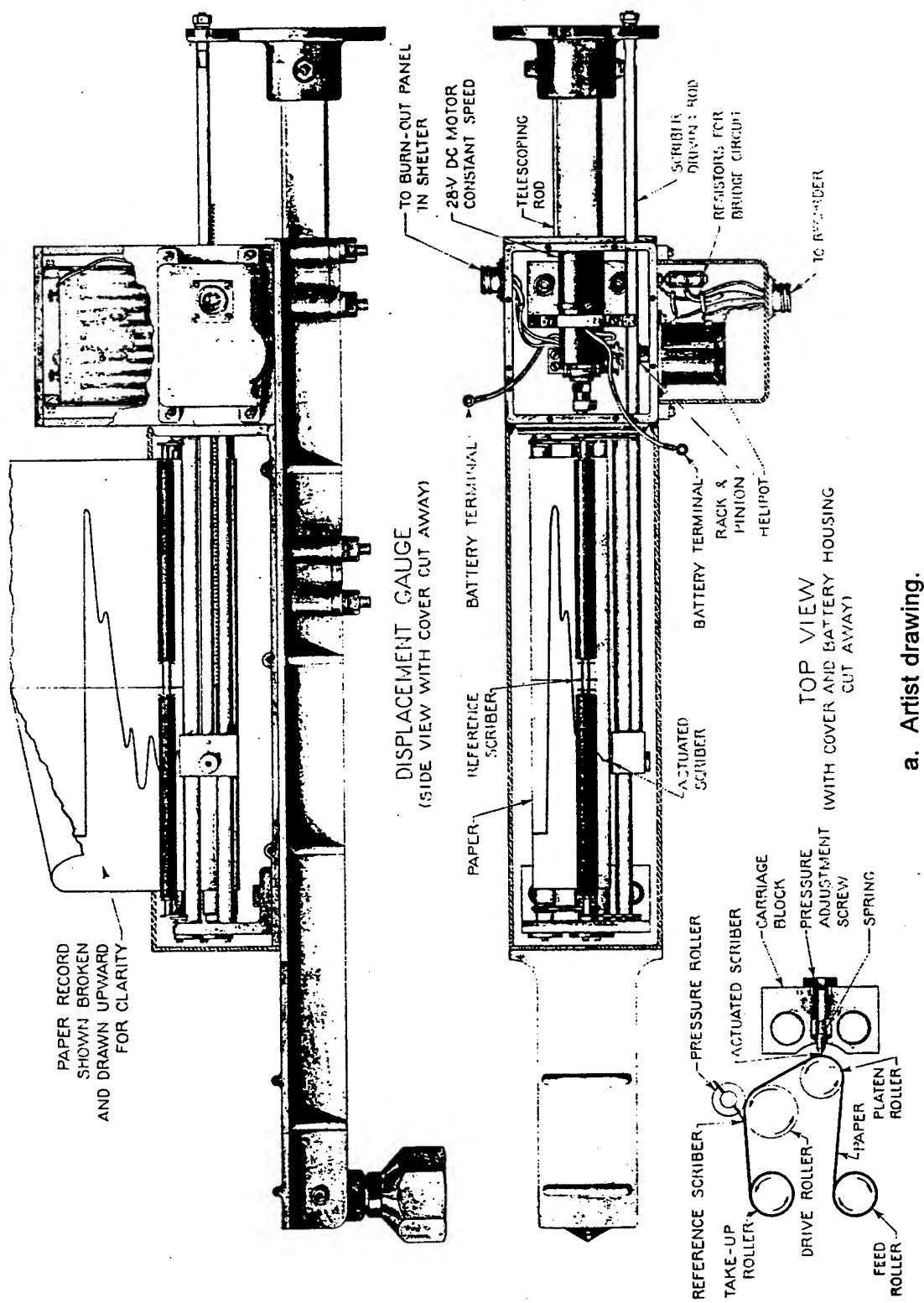


Figure 6. Sandia 12-inch displacement gage.



Figure 7. Pre-shot view showing displacement gages mounted in the interior of a test structure.

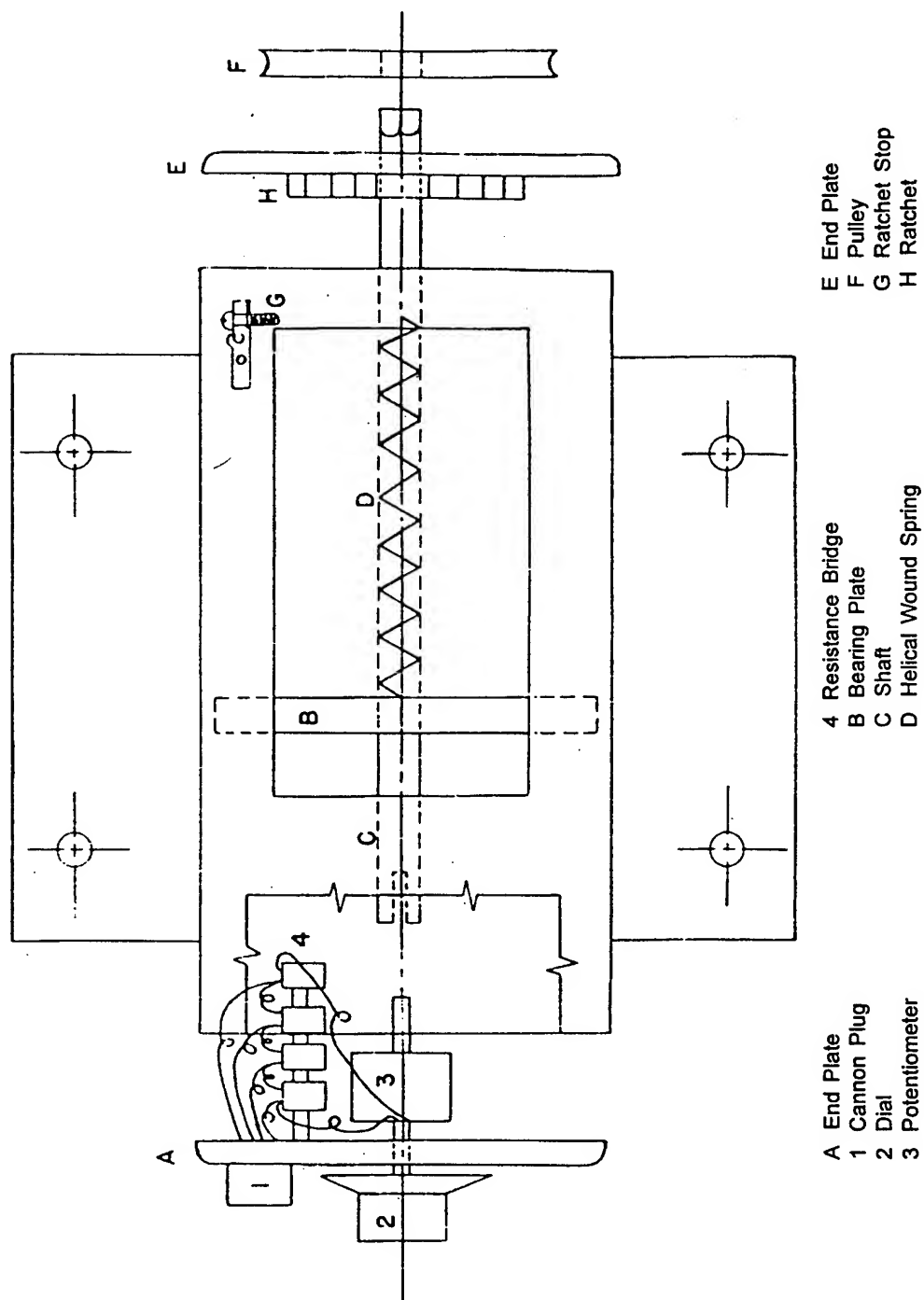


Figure 8. Mechanical drawing of BRL displacement gage.

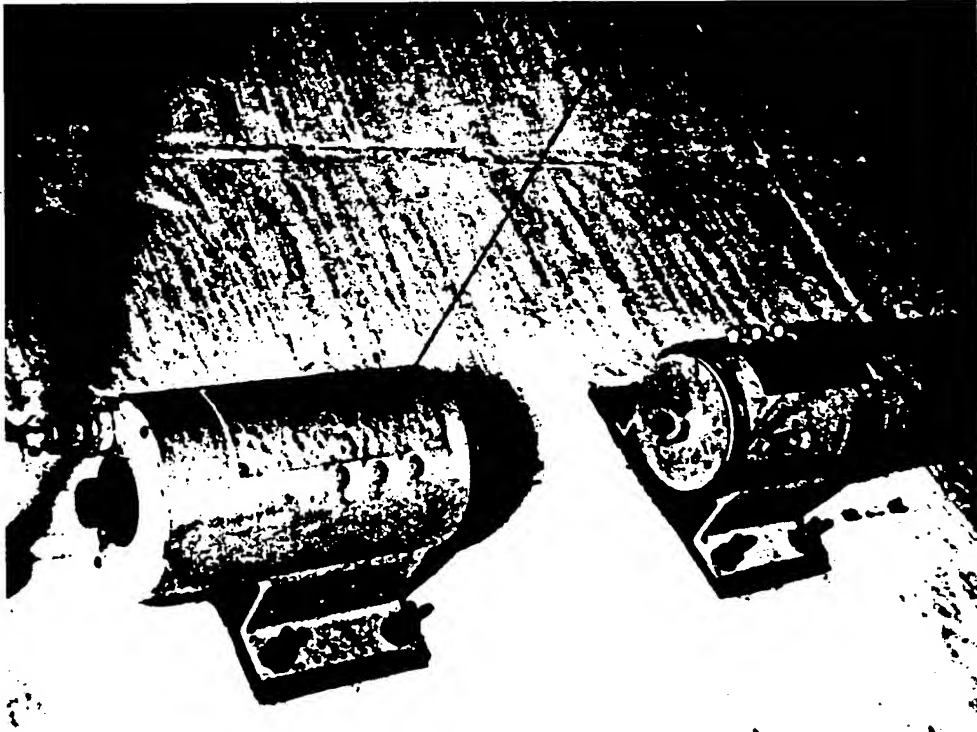


Figure 9. Electronic large-displacement gage (right) mounted on inner shell of cylindrical concrete structure.



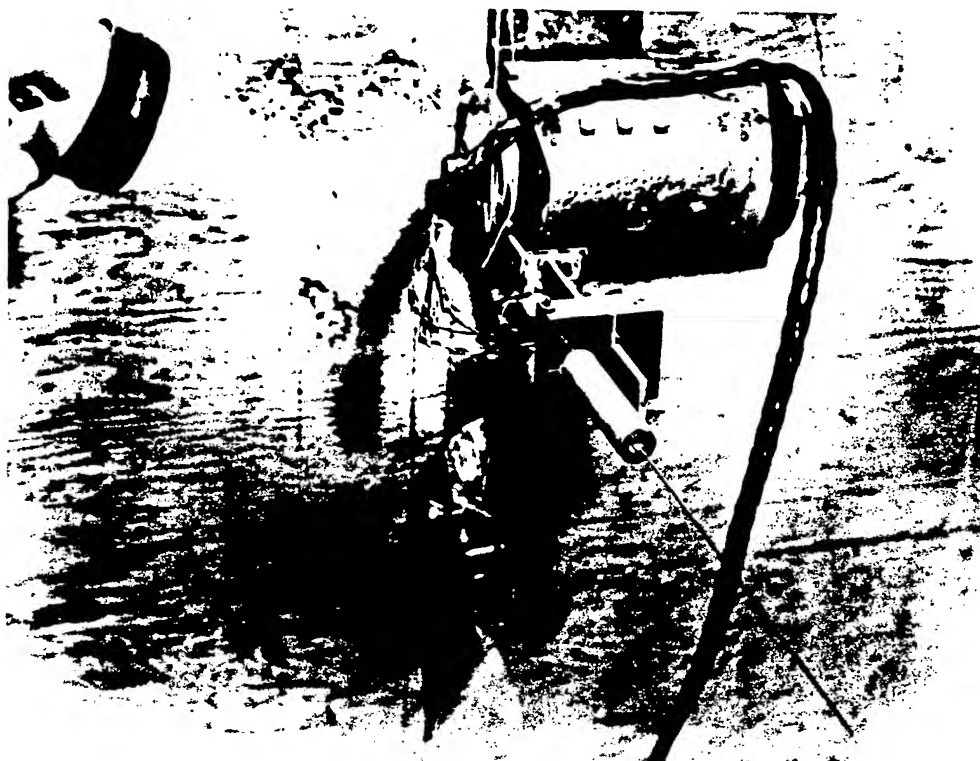


Figure 10. Electronic small-displacement gage mounted on wall of concrete structure.

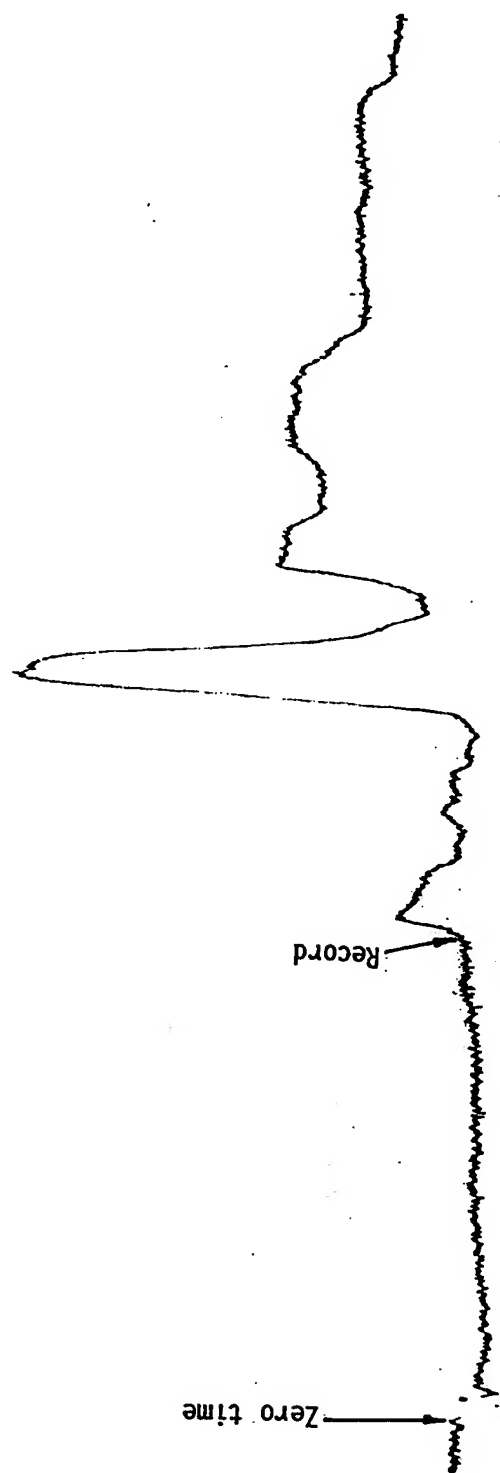


Figure 11. Deflection versus time between roof and column base - LVDT gage.

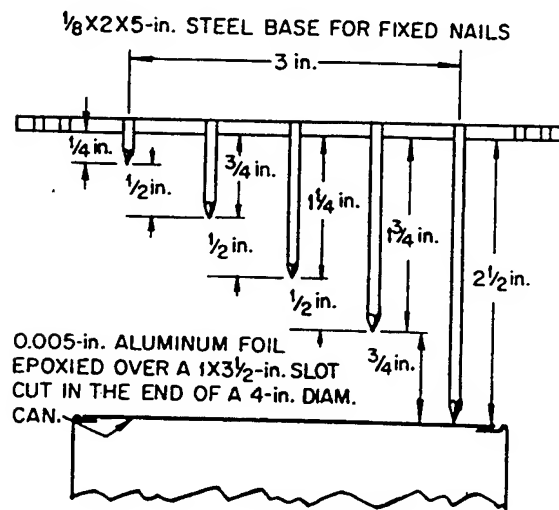


Figure 12. Improvised beam-deflection gage.

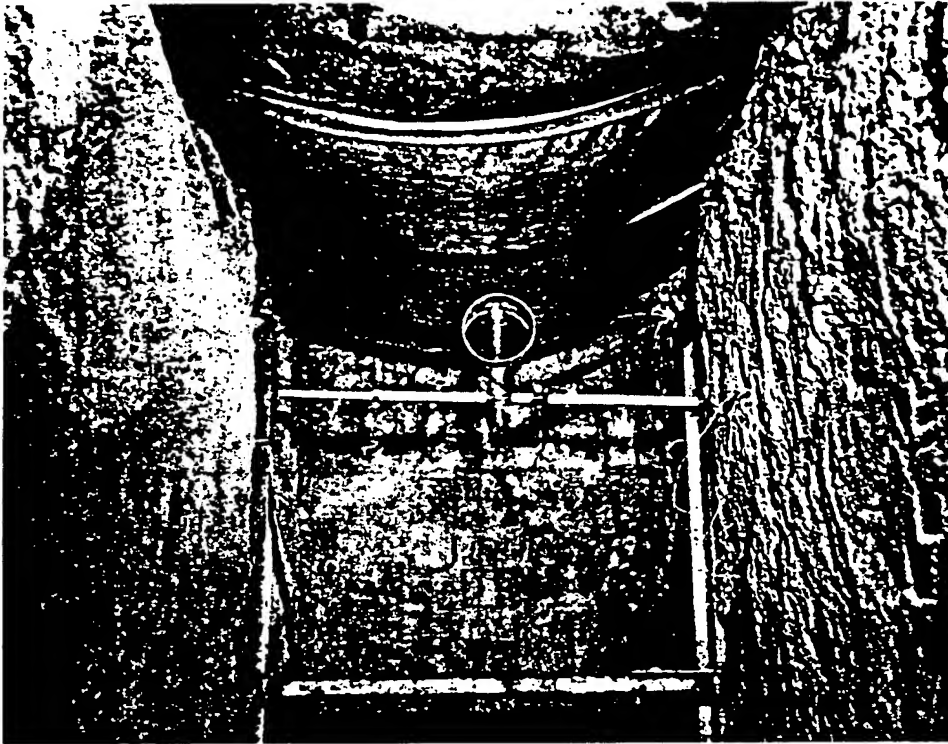


Figure 13. Scratch gage deflection system.

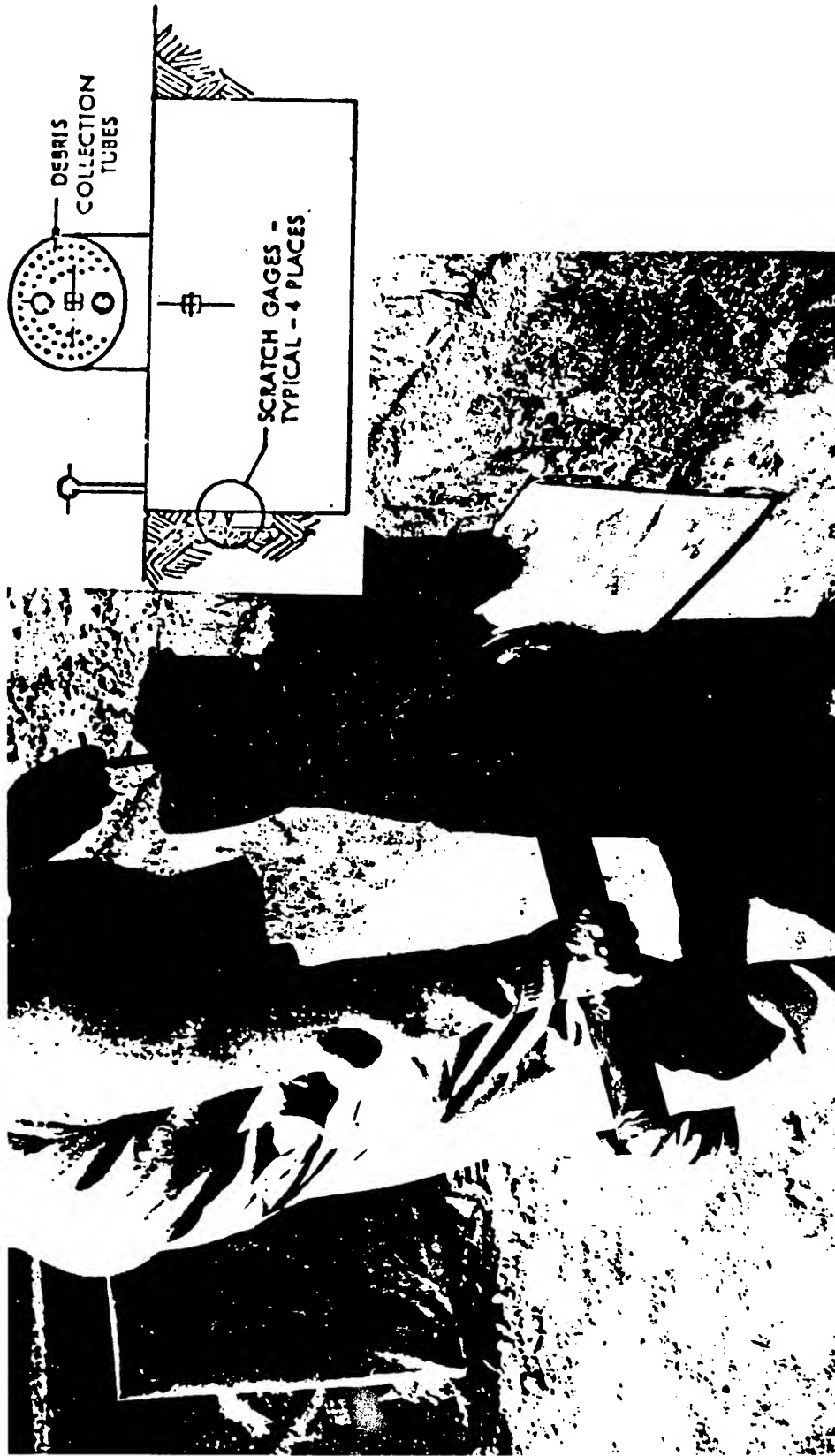


Figure 14. Differential motion scratch gage prior to installation in structure.

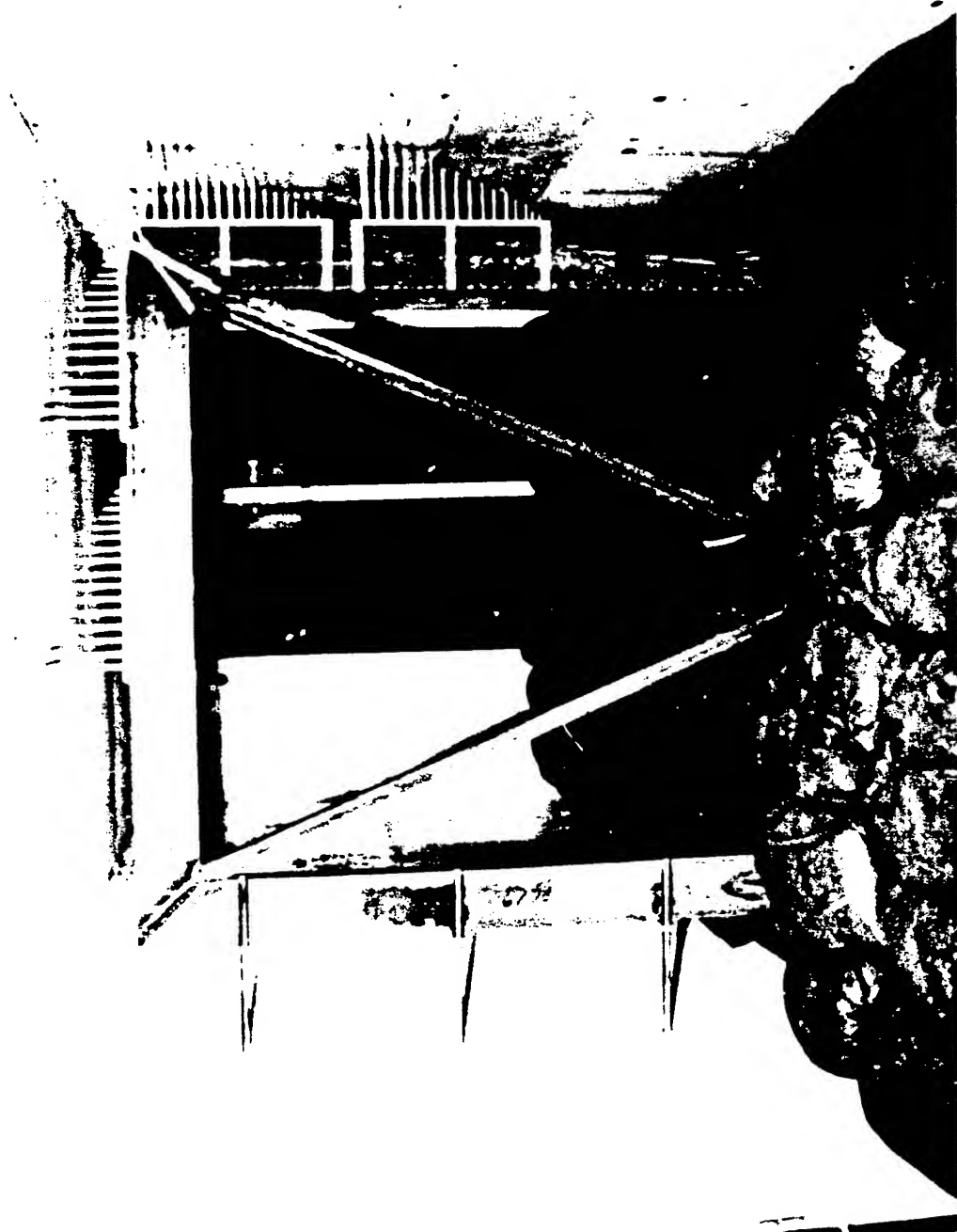


Figure 15. Contact registration displacement gages.

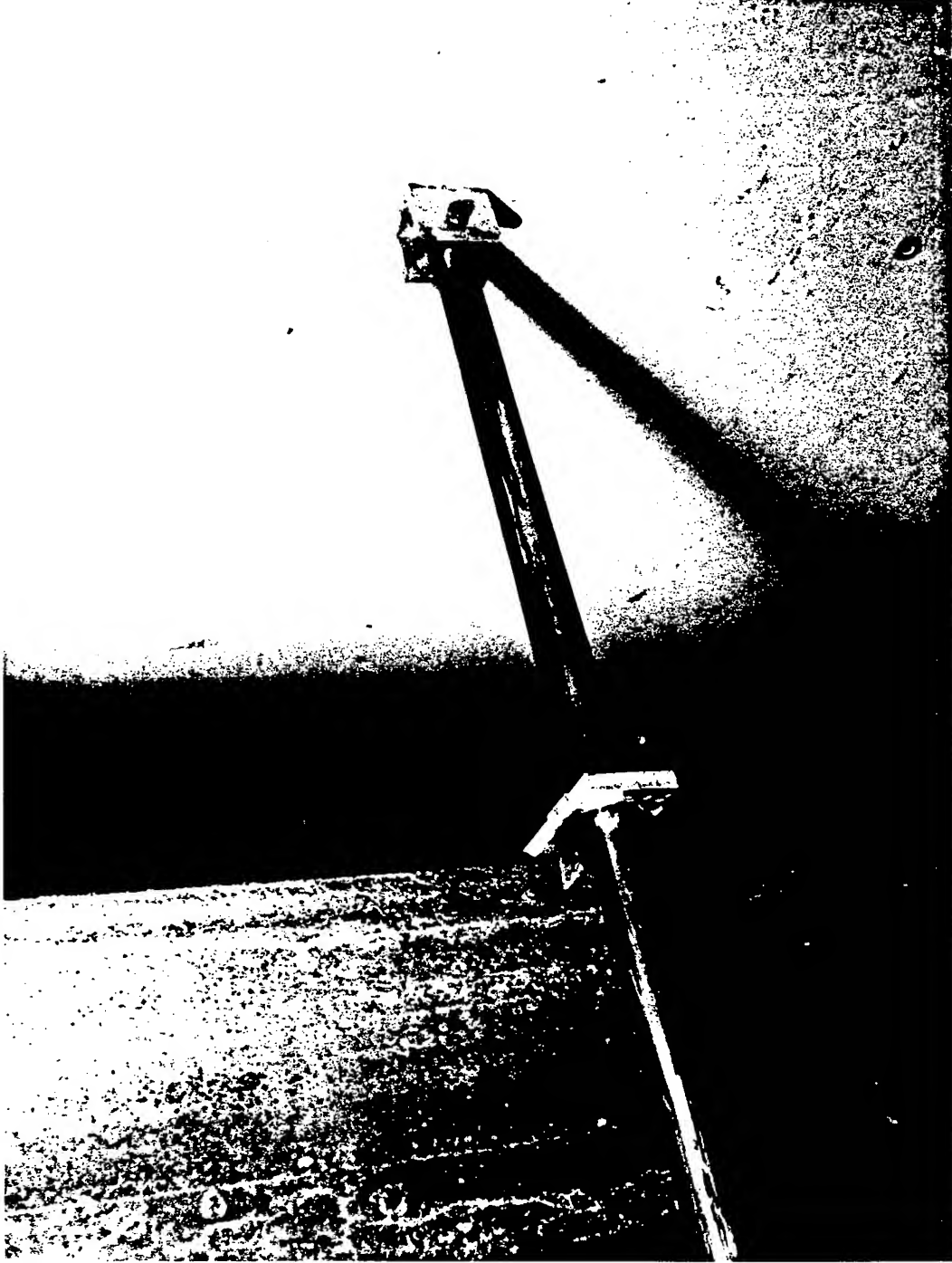


Figure 16. Rod scratch recording peak displacement gage.

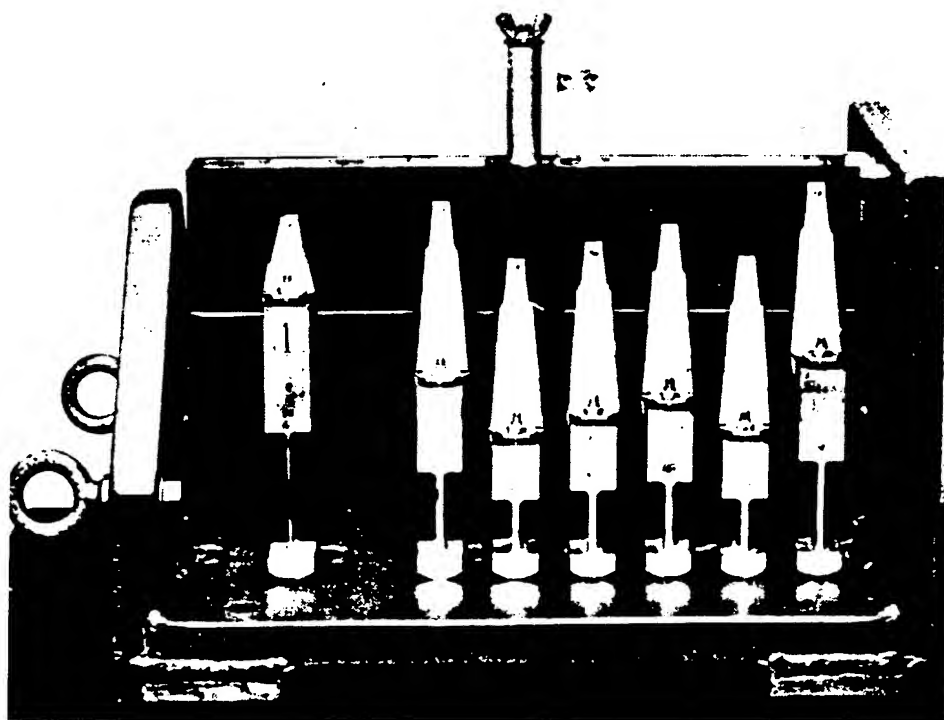


Figure 17. TRW reed gage.



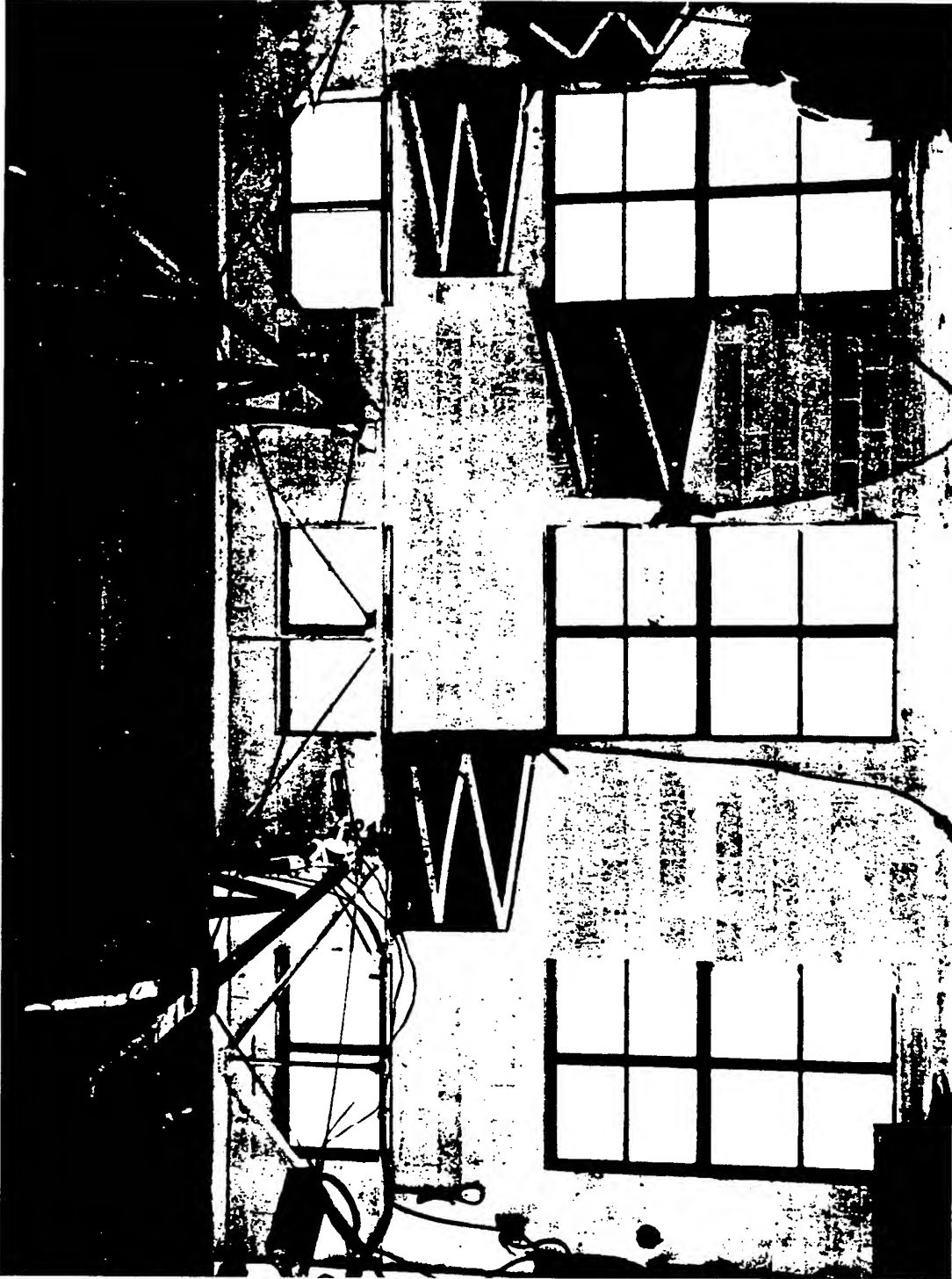


Figure 18. Group of four panel-time-of-break circuits installed on a structure.

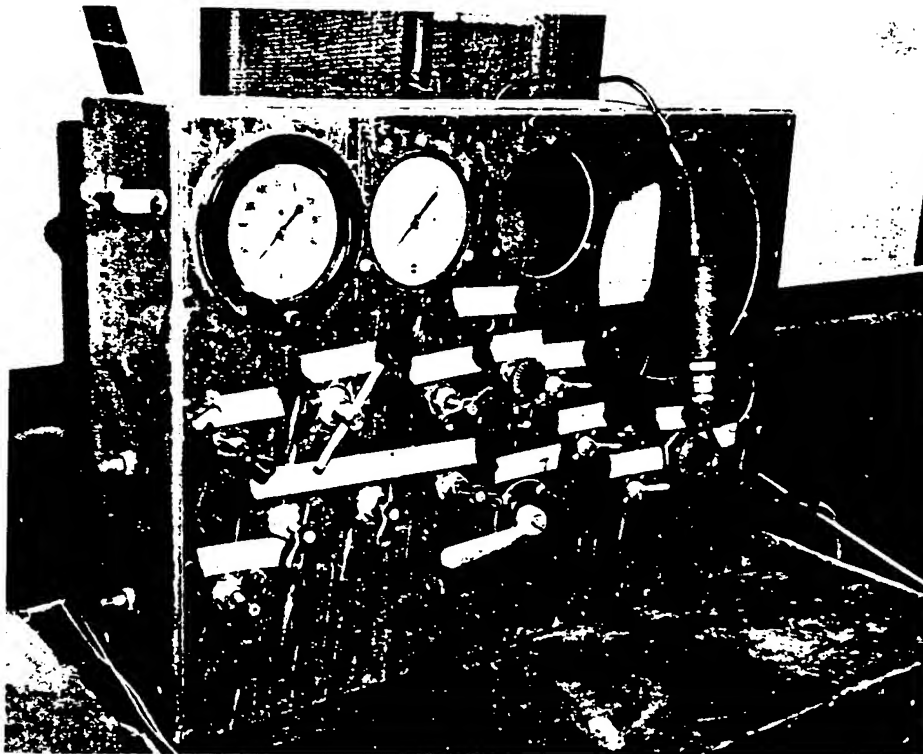


Figure 19. Typical calibration of Wiancko pressure gages.

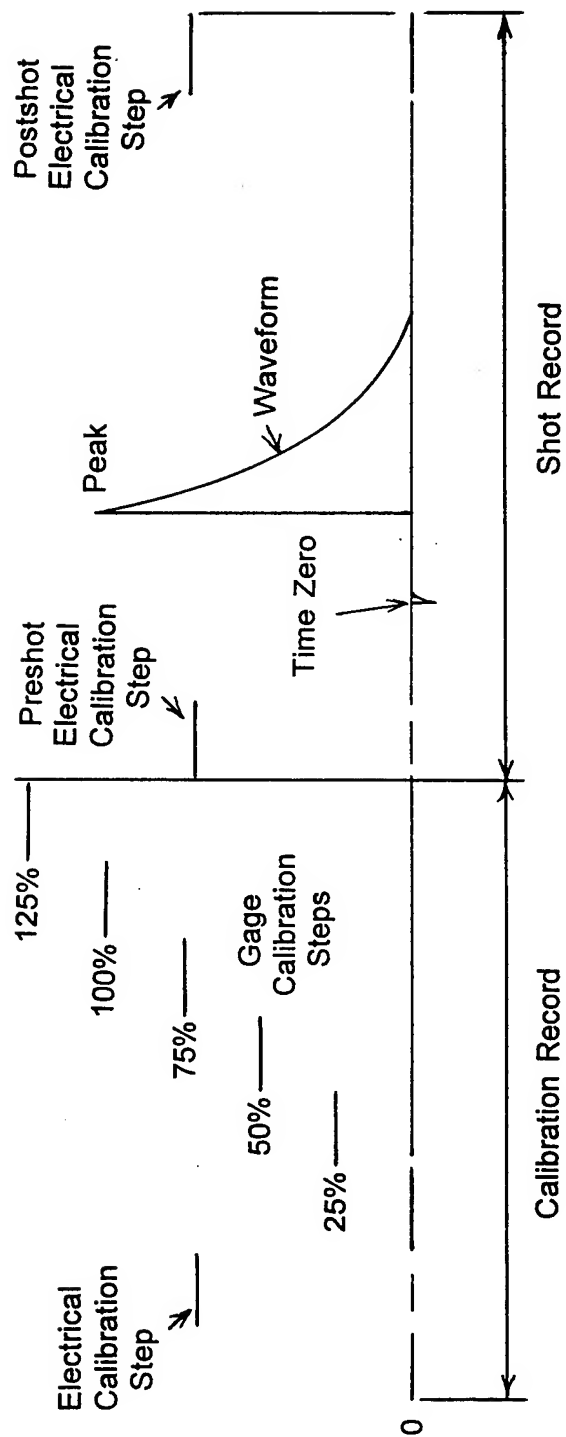
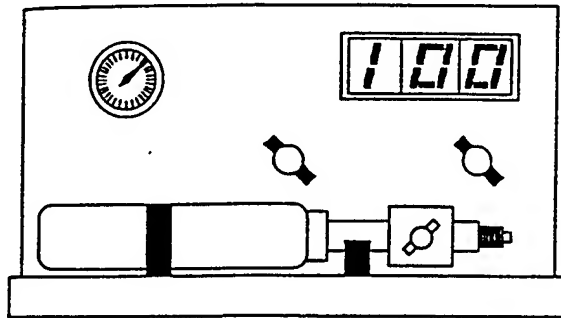
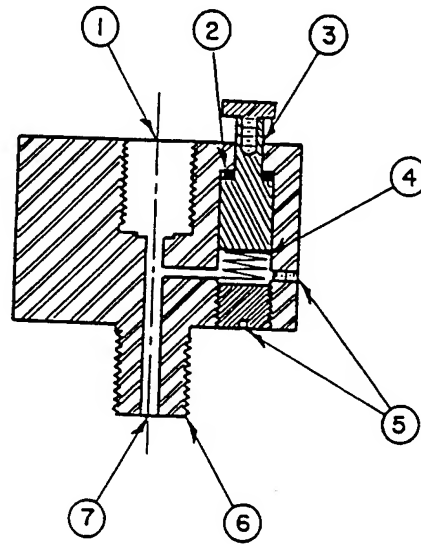
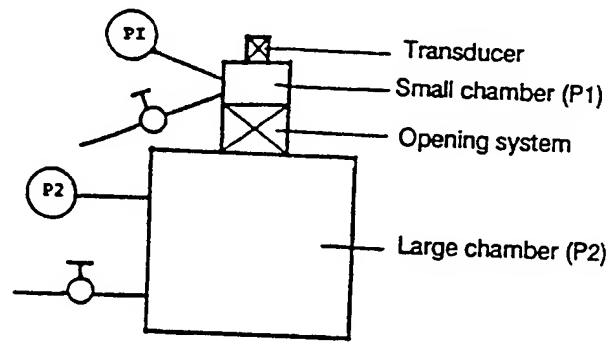


Figure 20. Calibration record from the 50s.



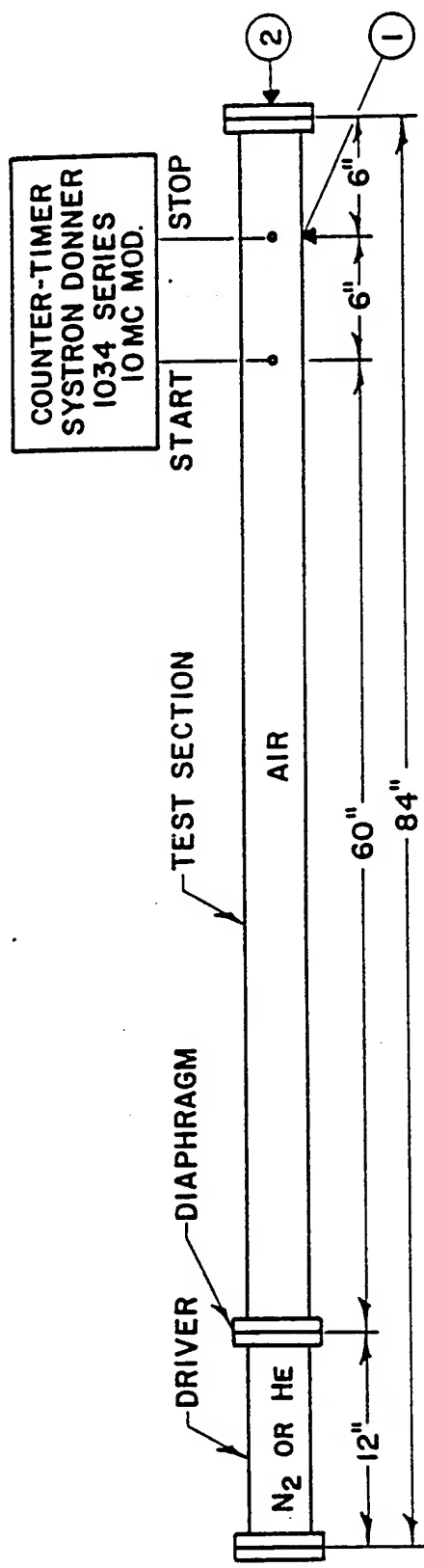
**Pneumatic Pulse Calibrator**  
**PCB Model 903A**

Figure 21. Air pulse calibrator.



- ① TRANSDUCER PORT - 1/2-20 NF
- ② TEFLON O-RING
- ③ RELEASE VALVE
- ④ SPRING
- ⑤ PLUGS
- ⑥ 1/4 - 18 PIPE THREAD
- ⑦ AIR INLET FROM TWO-WAY SOLENOID VALVE

Figure 22. Fast opening device.



- ① SIDE-ON PRESSURE TRANSDUCER
- ② REFLECTED PRESSURE TRANSDUCER

Figure 23. Schematic of a two-inch calibration shock tube.



Figure 24. Photograph of a two-inch calibration shock tube.

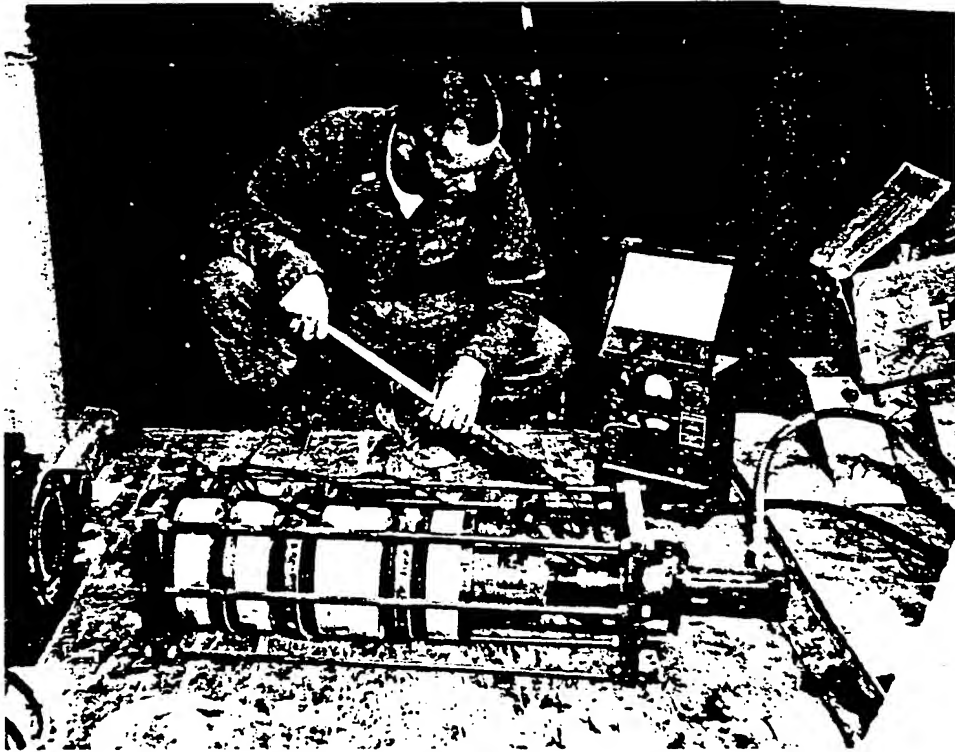


Figure 25. Calibration hardware for an earth pressure gage.



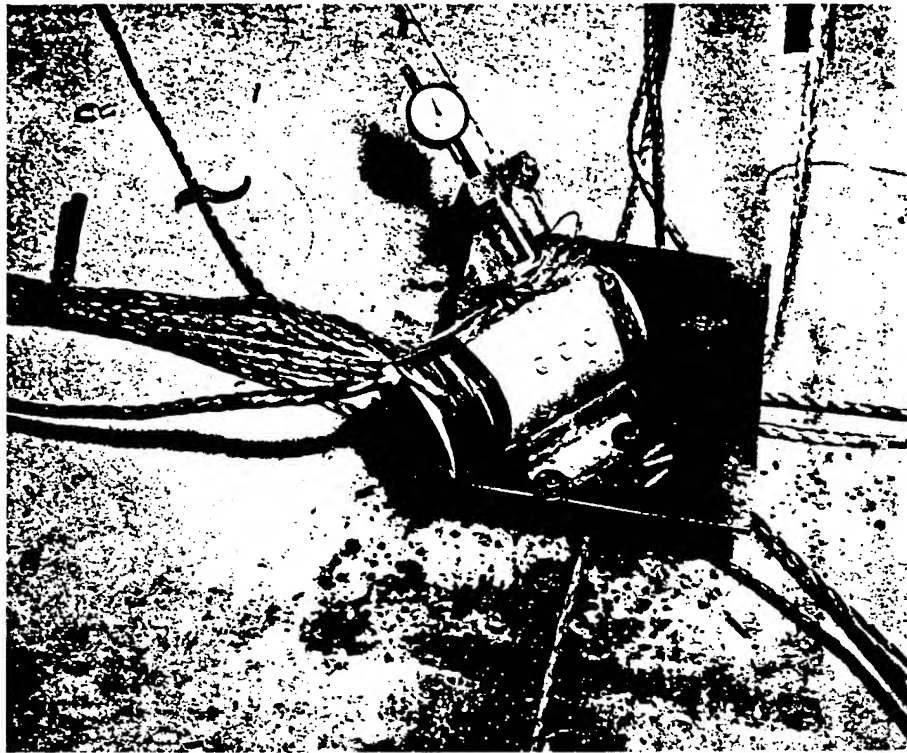


Figure 26. Calibration system for small displacement gages.

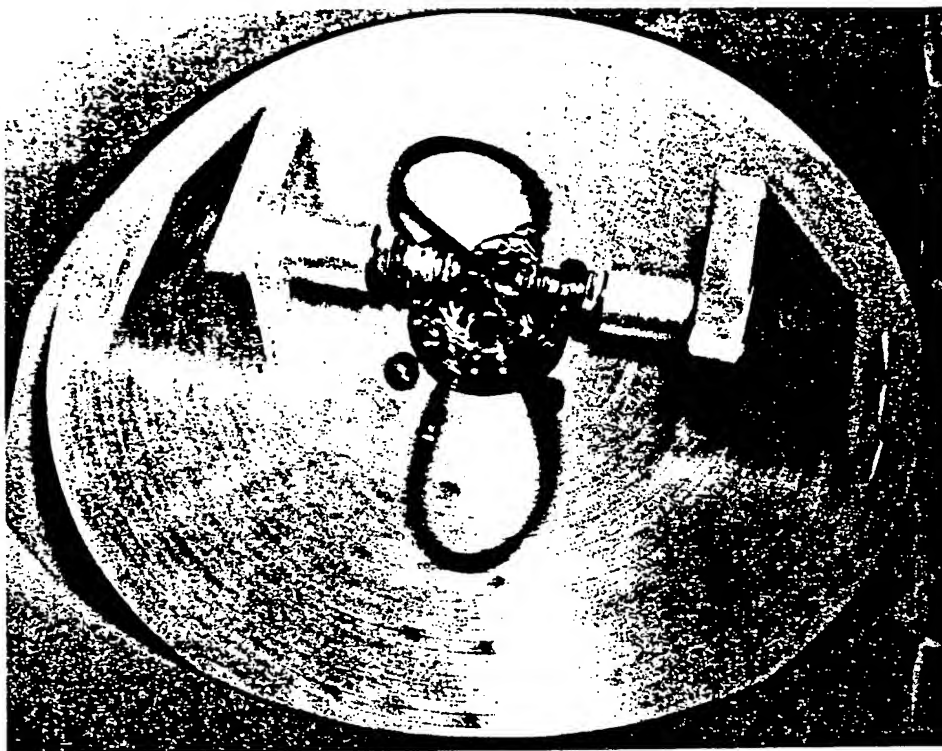


Figure 27. Spin table calibrator for accelerometer gages.



# EXPERIMENTAL AND NUMERICAL STUDY OF FLOW IN MULTI-DRIVER LARGE BLAST SIMULATORS

S. Schraml

U.S. Army Research Laboratory  
AMSRL-WT-NC

Aberdeen Proving Ground, MD 21005-5066 USA

D. Mergnat & S. Gralias

DGA, DRET, Centre d'Etudes de Gramat  
46500 Gramat, France

## ABSTRACT

The U.S. Army Research Laboratory and the Centre d'Etudes de Gramat executed a cooperative study in which the time-dependent flow fields in the SSGG large blast simulator were examined. The flow characteristics of static and stagnation overpressure were measured at two longitudinal positions in the expansion tunnel of the simulator. Instrumentation rakes were designed and fabricated to support a total of 19 pairs of static and stagnation pressure transducers that were distributed across the expansion tunnel cross section at each of the longitudinal positions. Flow measurements were recorded for eight shots with peak static overpressure levels between 20 *kPa*, and 120 *kPa*. The measured data were used to assess the flow uniformity and distribution at each of the longitudinal measurement positions in the simulator. The SHARC inviscid flow solver and the USA-RG3 viscous flow solver were employed in a set of detailed, three-dimensional fluid dynamics calculations that were performed to match the test conditions. The 3-D computational results are compared to the experimental data to further examine the time-dependent flow characteristics and also to validate the fluid dynamics codes for future blast studies.

## 1. INTRODUCTION

The U.S. Army Research Laboratory (ARL) and its predecessor organization, the U.S. Army Ballistic Research Laboratory, have played a significant role in the technology development of the Large Blast/Thermal Simulator (LB/TS), a Defense Nuclear Agency (DNA) testing facility located at the White Sands Missile Range, New Mexico. During the concept and early design phases, the operational characteristics and the primary dimensions of the facility were determined through a combination of small-scale experiments<sup>1</sup>, computational fluid dynamics (CFD) simulations<sup>2</sup>, and a transfer of technology employed at the Centre d'Etudes de Gramat (CEG).<sup>3</sup> To develop the required simulation technology in a timely and cost-effective manner, the experimental work was primarily performed in

small, cylindrical shock tubes. The accompanying numerical simulations were performed in a quasi-one-dimensional, or two-dimensional (2-D), axisymmetric representation.

With the knowledge that three-dimensional (3-D) numerical simulations would be required for the LB/TS characterization and development of advanced testing methodologies, it became necessary to validate some candidate 3-D CFD codes to model the facility in full geometric detail. In order to accomplish this task, CEG and ARL formed a cooperative research agreement in which the flow characteristics of the SSGG<sup>4, 5</sup> large blast simulator at CEG would be mapped experimentally and the data used to validate candidate CFD codes.

While several multiple driver, large blast simulators like the SSGG exist in the world, experimental data providing detailed characteristics of flow throughout the expansion tunnel were sparse or completely unavailable. Because the LB/TS concept is primarily based on the design and operational characteristics of the SSGG, it is the optimum vehicle for providing these data.<sup>6</sup>

It is possible to build and operate a small-scale, multiple driver model of this type of facility<sup>7</sup>, but this approach presents several challenging obstacles. Because this type of blast simulator is very large, a laboratory shock tube model must be constructed on a scale factor of 20 or greater for convenience of operation and manipulation. When scaled down, the throat section of one driver tube may have a diameter as small as two to three centimeters. The fluid boundary layer in a throat section of this size can be a significant fraction of the throat diameter, resulting in driver emptying times that are not representative of the full-scale facility. Simultaneous firing of several drivers is difficult in a small-scale blast simulator because the time scale is identical to the length scale. As a result, a small difference in diaphragm rupture times in the model will be equivalent to a significant delay between driver firings on full-scale.

To overcome these difficulties in performing small-scale tests of multiple driver shock tube flow, the shock tube geometry is sometimes simplified in the development of the model. Small-scale, cylindrical shock tube models are developed using the approach of combining an available set of flow areas at a common longitudinal position into a single cross-section of the equivalent area. Combining the areas at all points along the length of the shock tube results in a simplified model with properly scaled areas, volumes, lengths, masses and energies. The primary experimental advantage of this approach is simplicity in fabrication and operation. A "lumped area" shock tube will typically combine multiple driver tubes into a single, cylindrical driver. The need to change a single diaphragm between tests and eliminating the need for simultaneous firing of several drivers significantly simplifies the testing process.

Computational models of blast simulators are often developed using this same lumped area approach. The advantages of employing this approach for numerical simulation lie primarily in the reduction of the computational domain from three dimensions to two. This simplification alone can decrease model size and required computational resources by one or more orders of magnitude.

Simplifications of the shock tube geometry make it impossible to experimentally or computationally study some of the multi-dimensional characteristics of the time-dependent flow produced by the simulator. Of particular interest are the interactions between driver flow fields during the time when the shortest drivers are nearly empty, while the longest driver are still flowing mass into the expansion tunnel at a high rate. The tendency of the flow to diffuse and uniformly fill the expansion tunnel is essential for a high fidelity simulation of an ideal nuclear blast in such a facility. Understanding these aspects of time-dependent flow in multiple driver blast simulators forms the basis of this study.

By combining the resources of CEG and ARL, it was possible to perform this comprehensive experimental and computational study in a very efficient manner. The use of the SSGG simulator at CEG provided experimental data from a full-scale, multiple driver, shock tube facility. The flow uniformity analysis provides insight to the types of flow fields that are likely to be encountered in the LB/TS. The validated 3-D CFD codes used in this study will be applicable to other blast studies involving complex geometries and flow fields.

This paper is presented in three parts. Part I provides a detailed discussion of the SSGG facility, the configuration of the instrumentation, and the experiments that were performed. Part II describes the flow uniformity analysis, and Part III presents the development of the 3-D numerical models, and comparison of the numerical simulations to the experimental data.



# EXPERIMENTAL AND NUMERICAL STUDY OF FLOW IN MULTI-DRIVER LARGE BLAST SIMULATORS

## PART 1 - SSGG EXPERIMENTS

D. Mergnat - S. Gralias  
DGA , DRET , Centre d'Etudes de Gramat  
46500 Gramat , France

### 1 DESCRIPTION OF THE LARGE BLAST SIMULATEUR (SSGG)

The Large Blast Simulator (SSGG) located at the Centre d'Etudes de Gramat, in France, was commissioned in 1979.

Basically, the SSGG operates as follows: compressed air is suddenly discharged from pressure vessels and the resulting blast wave is channelled into an expansion tunnel where items to be tested are set . Figure 1 shows an external view of the SSGG.

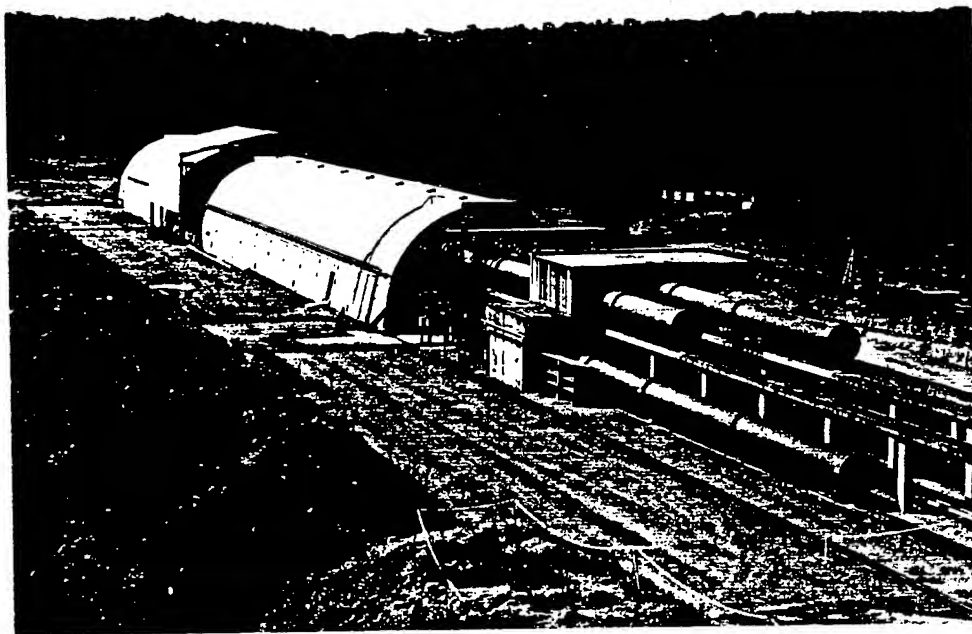


**Figure 1:** View of the SSGG simulator

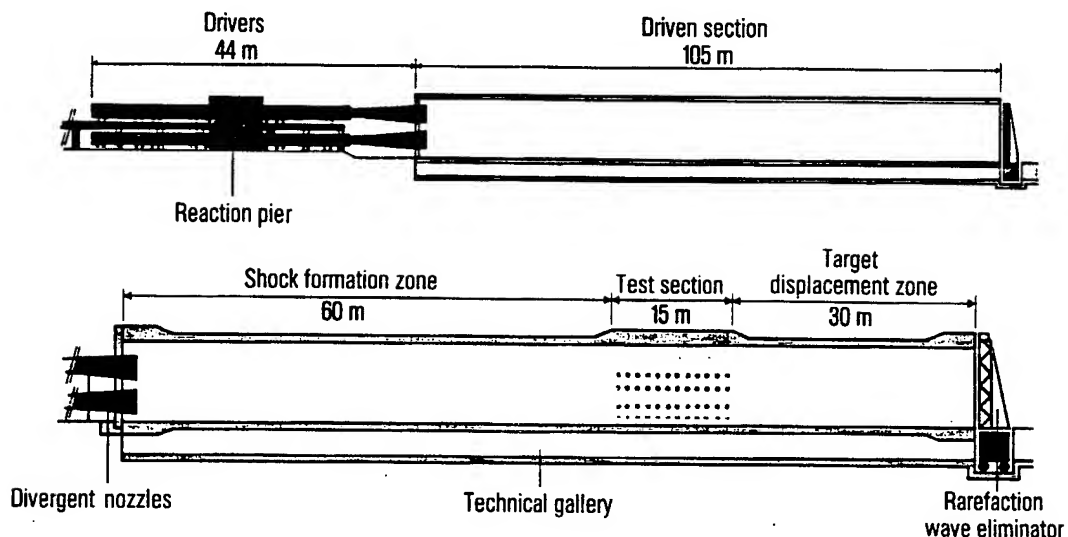


Figure 2 is a block diagram of the testing facility, which is in three parts:

**Driving system:** this comprises seven compressed air vessels (drivers) whose total volume is 300 m<sup>3</sup>, in which the maximum operating pressure is 80 bars. In order to generate the required flow, the vessels have different lengths and are terminated downstream by a converging-diverging system fitted with an obturation mechanism in the throttle area. The obturation mechanism is a steel diaphragm which is ruptured by an explosive device.

**Expansion tunnel:** this is of semi-cylindrical shape, 105 m long, 12 m wide and 7.1 m high. The tunnel is made of prestressed concrete. The test section, at a distance of 60 m from the drivers, is fitted to accommodate materials to be tested. The floor can equally be made of metal, concrete or wood. A powerful lighting system provides appropriate conditions to film target behaviour at a speed of up to 500 frames per second. Instrumentation facilities may accommodate up to 60 measuring channels. A 30 m long downstream target displacement area provides for major target motions during experiments.

**Active rarefaction wave eliminator:** this original device cancels out disturbances generated in the test section of short-length expansion tunnel simulators. The principle consists to create an aerodynamic blockage of the airflow at the downstream end of the expansion tunnel, so as to prevent rarefaction waves from back-flowing. This capability is provided by a system of position-actuated tilting shutters which are governed by a law of motion corresponding to the characteristics of the test to be performed. Figure 3 shows a view of this facility.



**Figure 2:** Cross-section of the SSG

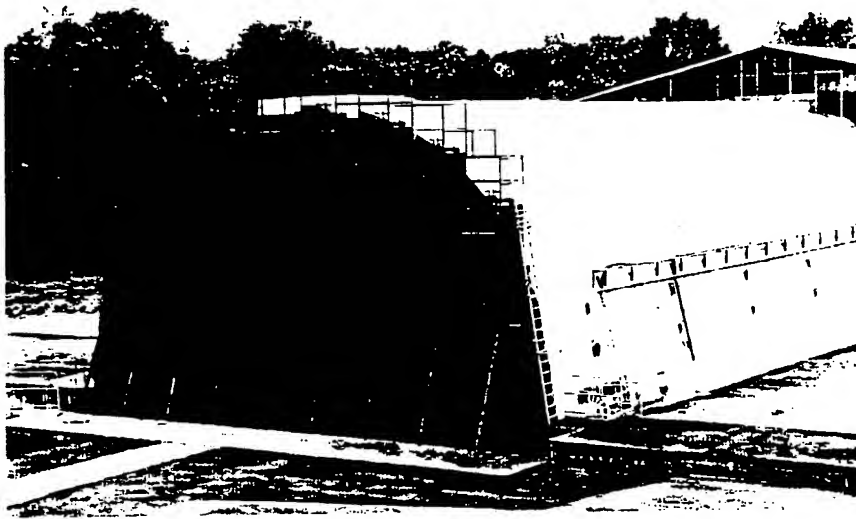


**Figure 3:** View of the rarefaction wave eliminator

The SSGG testing facility was designed to simulate the effects of shock and blast waves from nuclear explosions, in order to test and assess the behaviour of military items and materials. This facility offers the following performance:

Peak static overpressure	$\Delta p$ :	15 KPa	to	140 KPa
Burst duration	$t_+$ :	1 sec	to	1,5 sec
Simulated yields	:	5KT	to	1 MT
Test section area	:	70m <sup>2</sup>		

Figure 4 shows an example of flow profiles recorded in the test section, on which theoretical profiles for the weapon considered were superimposed. This shows the satisfactory match of the static overpressure and dynamic pressure phenomena induced in the SSGG.

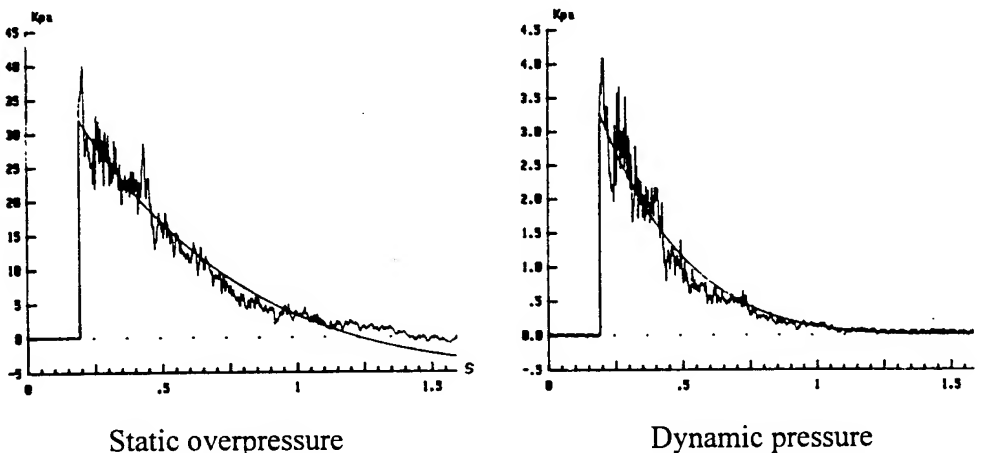


**Figure 4:** Examples of pressure profiles recorded in the SSGG test section

## 2 DESCRIPTION OF THE EXPERIMENTS

These experiments, performed under an USA/F cooperative research agreement, was designed to provide the US Army Research Laboratory (ARL) with flow measurements recorded in the test section of the French SSGG blast simulator, in order to validate computational codes. Static and stagnation overpressures were measured. Whereas the method used at CEG is to directly record differential pressure (regarded as dynamic pressure) using appropriate sensors, the ARL deduces dynamic pressure from static and stagnation overpressure measurements.

Nineteen measurement positions (static and stagnation gauge pairs) were distributed across the expansion tunnel cross section, on a plane perpendicular to the flow as shown in Figure 5. The driver output cross-section is indicated on the diagram in order to show the special sensor positions:

- sensors in positions 1 to 7 between the flow path of the drivers,
- sensors in positions 8 to 10 across the flow path of a 35m length driver,
- sensors in positions 11 to 13 across the flow path of a 19m length driver,
- sensors in positions 14 to 16 across the flow path of a 26m length driver,
- sensors in positions 15 to 19 across the flow path of a 44m length driver.

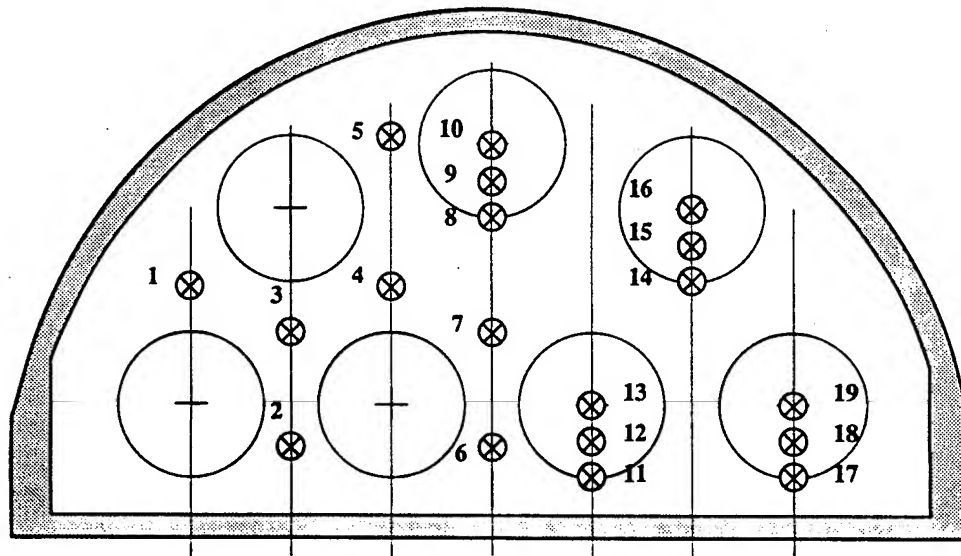


**Figure 5:** Location of sensors in the expansion tunnel

This measurement assembly was successively set up at two different longitudinal positions in the expansion tunnel (see Figure 6):

- Position 1 : SSGG simulator test section
- Position 2 : upstream area, close to the driver/expansion tunnel connection

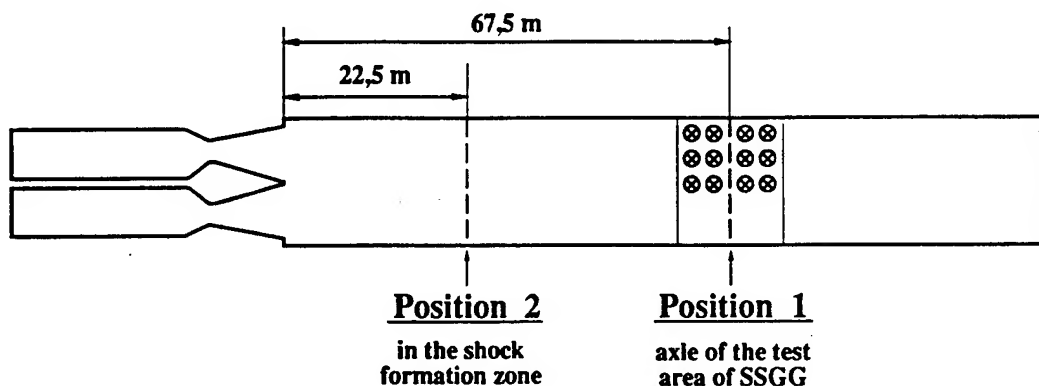


**Figure 6:** Location of measurement assemblies in the expansion tunnel

Several levels of peak static overpressure were simulated for each of the two measurement assembly positions :  $\Delta p = 20$  KPa to  $\Delta p = 120$  KPa.

Under the USA/F cooperative research agreement, CEG was asked to perform these experiments, which required:

- designing and fabricating the instrumentation support structure;
- performing and recording flow measurements;
- performing tests.

### **3 SUPPORT STRUCTURE AND INSTRUMENTATION**

To support the thirty eight sensors distributed within the expansion tunnel, a specific support structure had to be designed, which would withstand the characteristics of the generated flow (windspeed  $> 700$  km/h) and would not interfere with measurements.

We chose a pattern of seven steel masts, arranged as shown in Figure 7. These were fixed to the ground and braced using kevlar fiber cables in order to reduce the vibration induced during tests. Each mast was independently braced in the longitudinal plane. But crosswise, masts were tied to eachother and to the walls of the expansion tunnel.

Figure 8 shows the cross-section of a mast, and the location of static and stagnation pressure sensors. Measurement cables were laid inside the masts so as to avoid possible wrenching or disconnection.

Static overpressure measurements were performed using ENDEVCO 8510B 50PSI sensors, fitted in a bracket flush with the lateral face of the mast (Figure 9). Stagnation overpressure measurements were performed using ENDEVCO 8510C 100PSI sensors fitted at the end of tapered probes (Figure 10).

Preliminary tests enabled us to optimize sensor locations and to ensure that the structure would not disturb the characteristics of the measured flow.

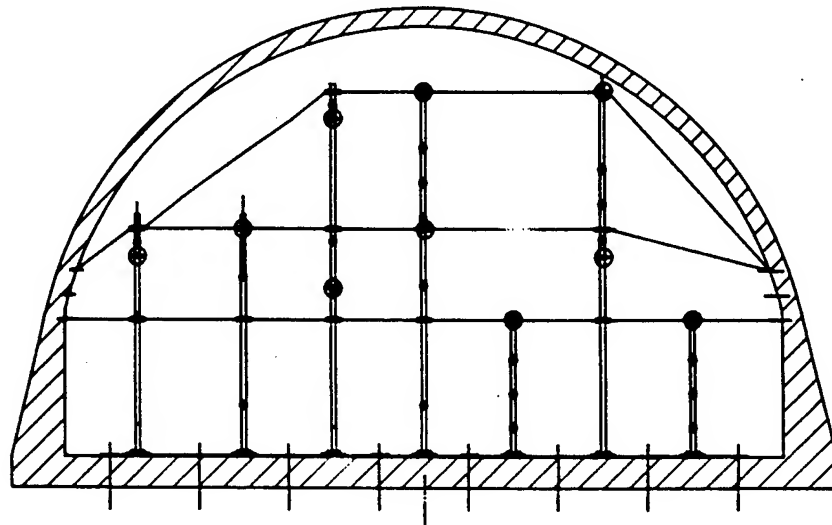


**Figure 7:** Arrangement of the seven masts in the tunnel, and transversal bracing

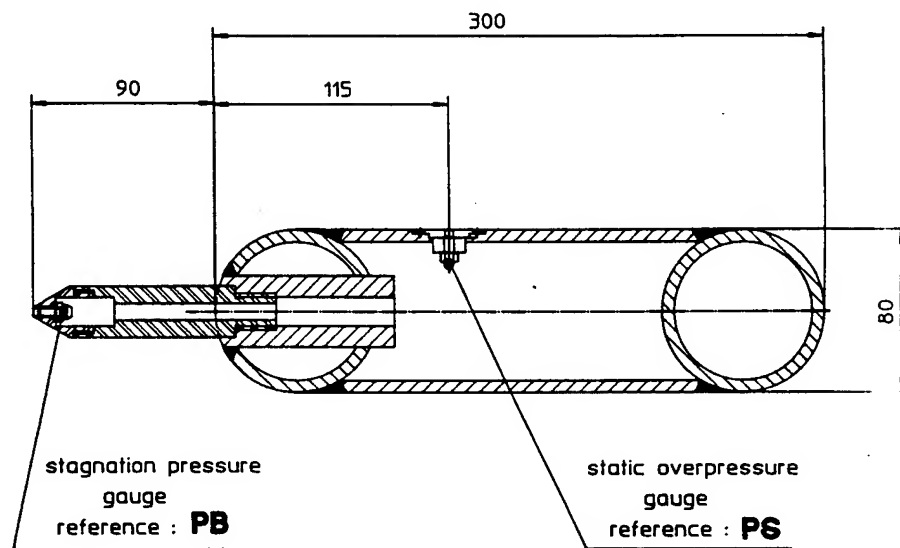


**Figure 8:** Cross-section of mast with sensor location (length unit: mm)

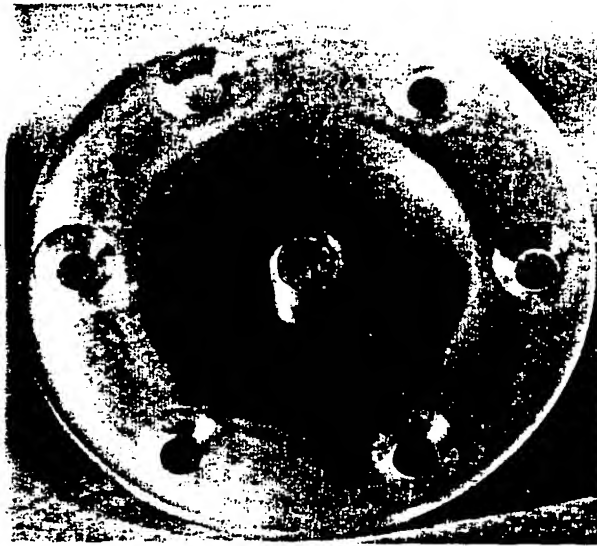


**Figure 9:** View of the static pressure probe

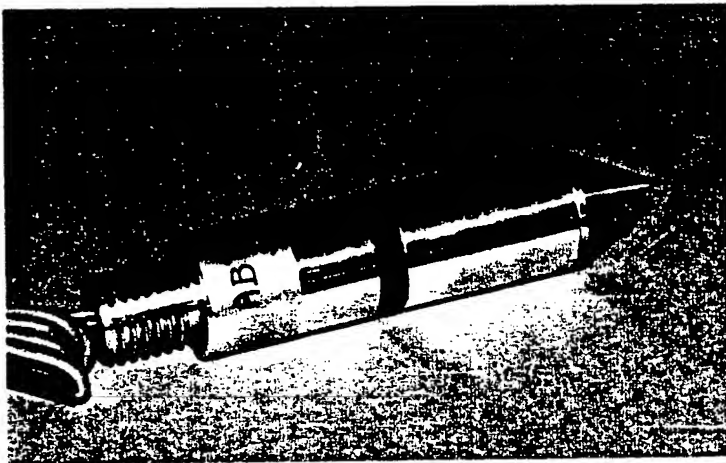


**Figure 10:** View of the stagnation pressure probe

Signals were recorded on an analog data acquisition system. The measurement channel passband was 100 KHz.

Each measurement was marked with specific letters - PS for static overpressure or PB for stagnation overpressure - followed by a number -1 to 19- indicating the location of the sensor (see Figure 5).

#### 4 TEST CONDITIONS

Figure 11 shows a view of the support structure, as installed within the simulator test section (position 1).

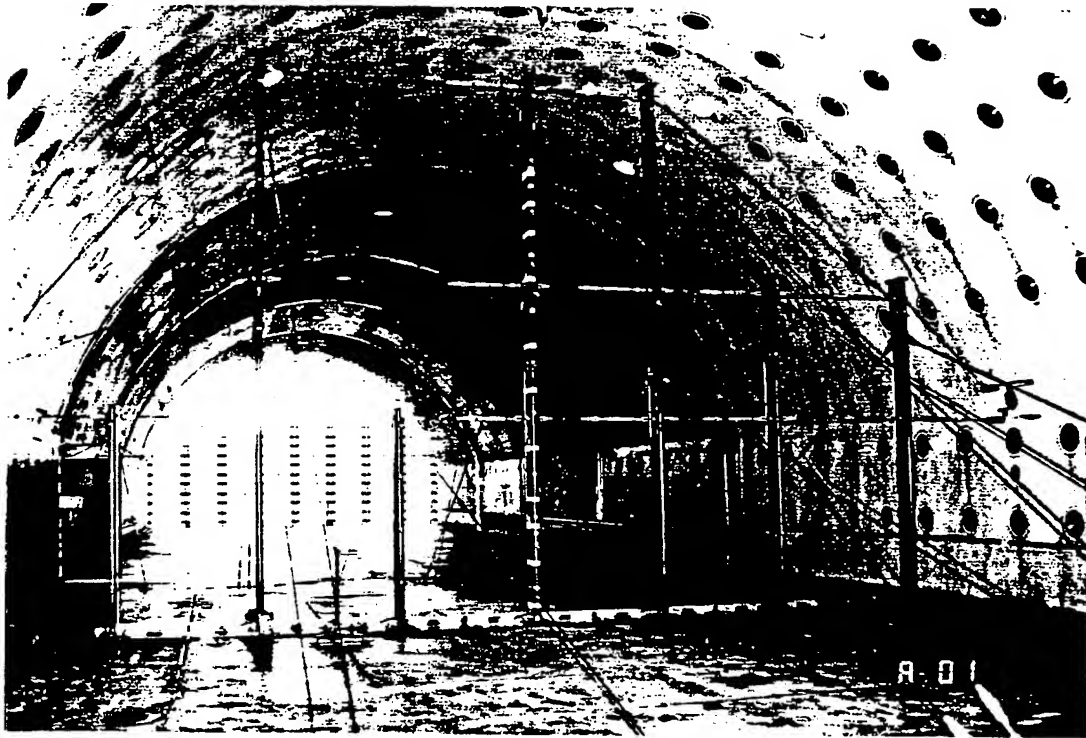


**Figure 11:** View of the support structure at position 1

Tests were initially performed at position 1 (test section) for peak static overpressure levels  $\Delta p = 20$  KPa, 80 KPa and 120 KPa; then at position 2 (close to drivers) for peak static overpressure levels  $\Delta p = 20$  KPa, 50 KPa and 80 KPa.

Some problems arose during high level tests, concerning the resistance of the support structure lateral bracing. Therefore test levels were limited to  $\Delta p = 80$  KPa at position 2.

The following table shows the conditions and theoretical characteristics (in the test section) of tests performed which are representative of this experiment. For each test performed, all the facility and atmospheric actual parameters were precisely recorded.

Measurement plan	Test n°	Driver overpressure (bar)	Static overpressure $\Delta p$ (KPa)	Dynamic pressure q(KPa)	Windspeed (km/h)
Position 1 (test section)	1 (GS 618)	7	20	1,5	145
	2 (GS619)	36,5	80	22	535
	4 (GS 621)	61	120	46	740
Position 2	6 (GS 623)	7	20	1,5	145
	7 (GS 624)	20	50	8	365
	8 (GS 625)	36,5	80	22	535

## 5 TEST RESULTS

Figures 12 to 19 show characteristic examples of the pressure profiles recorded.

In the simulator test section (position 1), some disturbances were observed in the recorded profile of a few stagnation overpressure measurements at  $\Delta p = 120$  KPa (Figure 15). This phenomenon is more pronounced for measurements recorded close to the drivers (position 2), starting with the test at  $\Delta p = 50$  KPa.

Initial signal analysis showed that only stagnation pressure measurements are affected in this way. Moreover, this phenomenon appears for overpressure levels which are lower, the closer sensors are to the drivers. This problem may be due to icing on the sensor grid (Figure 20) caused by the sudden discharge of driver gas. Iced particles would then be projected through the grid against the sensitive part of the sensor. The sensor would react suddenly (positively or negatively), and would later recover its full functional capabilities after projections stopped, if undamaged.

To verify this assumption, a sensor grid was removed for the last test ( $\Delta p = 80$  KPa, position 2), and an additional sensor with larger grid holes was used. The two sensors gave satisfactory results.

Until then, this phenomenon had never been observed at CEG due to the fact that we use differential pressure probes, in which the sensor is located at the bottom of a PITOT tube, and not stagnation pressure probes where the sensor is flush.



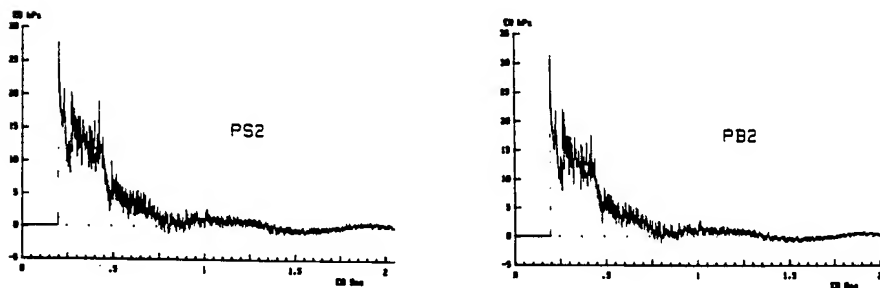


**Figure 12:** Example of pressure profiles - Test n°1 -  $\Delta p = 20$  KPa - Position 1

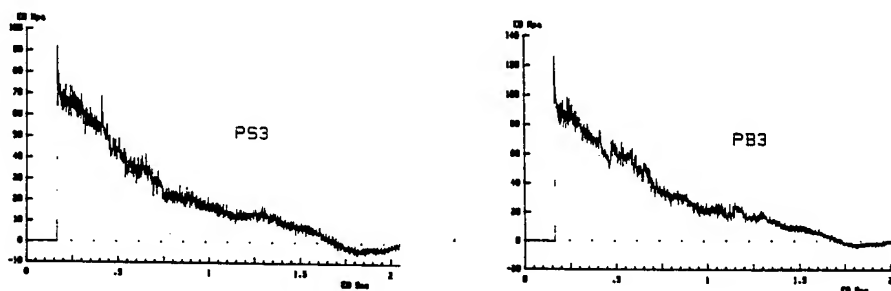


**Figure 13:** Example of pressure profiles - Test n°2 -  $\Delta p = 80$  KPa - Position 1

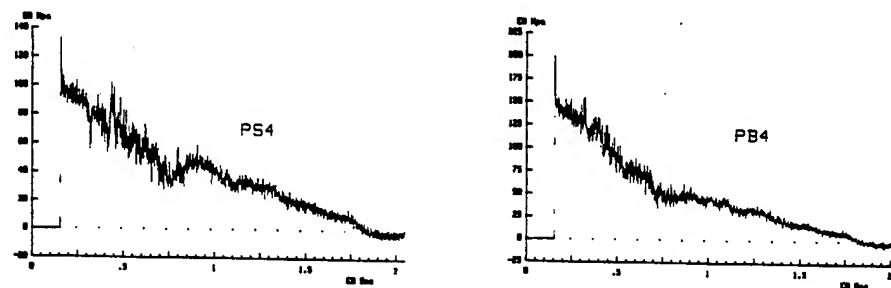


**Figure 14:** Example of pressure profiles - Test n°4 -  $\Delta p = 120$  KPa - Position 1

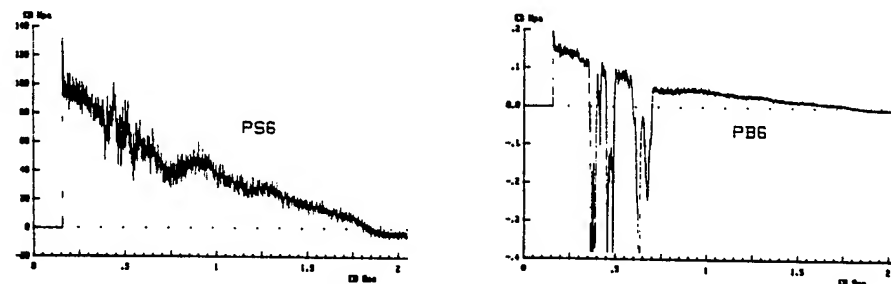


**Figure 15:** Example of pressure profiles - Test n°4 -  $\Delta p = 120$  KPa - Position 1

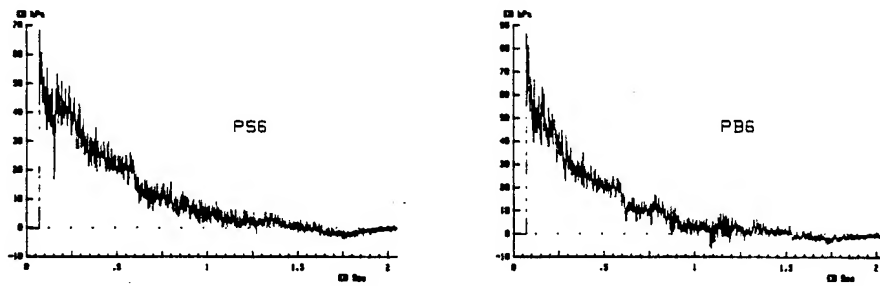


**Figure 16:** Example of pressure profiles - Test n°7 -  $\Delta p = 50$  KPa - Position 2

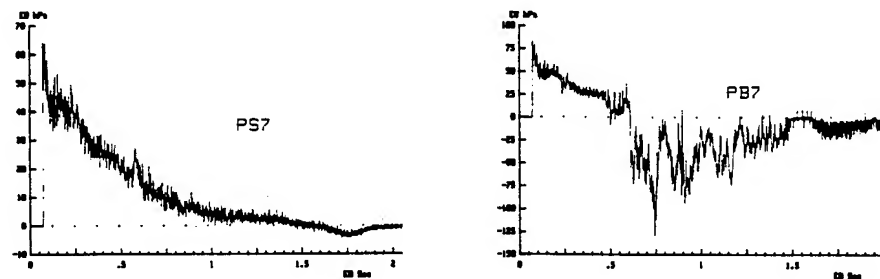


**Figure 17:** Example of pressure profiles - Test n°7 -  $\Delta p = 50$  KPa - Position 2

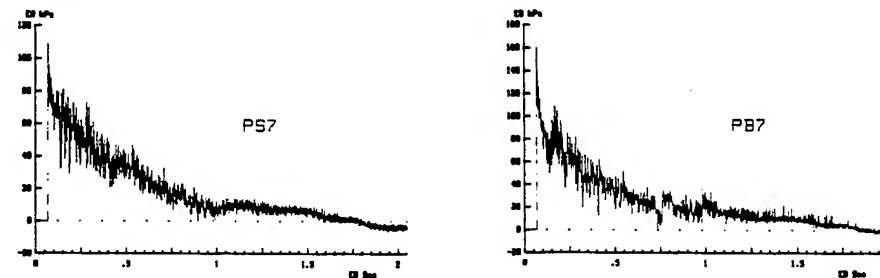


**Figure 18:** Example of pressure profiles - Test n°8 -  $\Delta p = 80$  KPa - Position 2

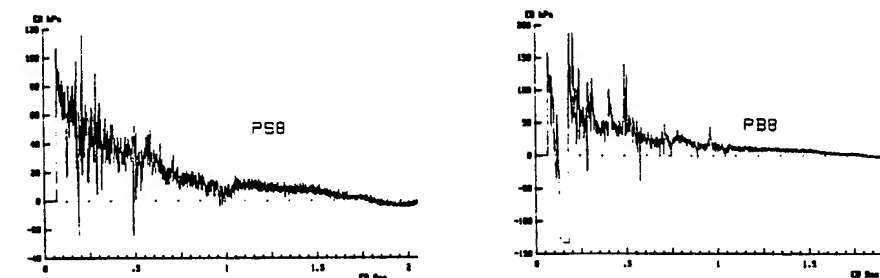


**Figure 19:** Example of pressure profiles - Test n°8 -  $\Delta p = 80$  KPa - Position 2

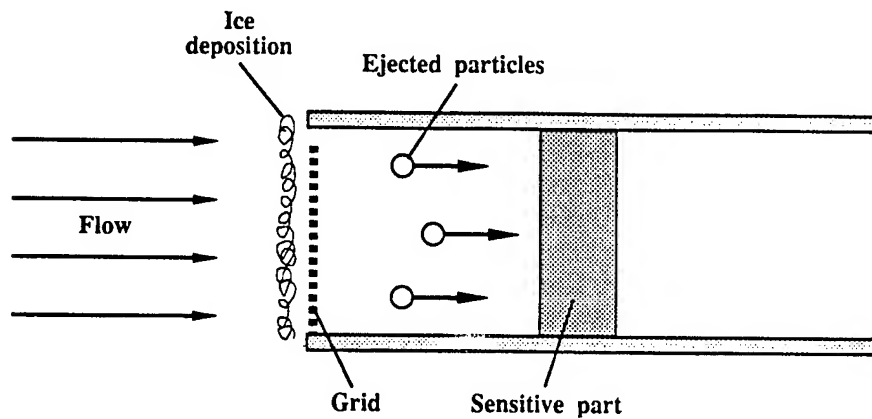


**Figure 20** Stagnation pressure sensor disturbance pattern

## 6 DATA ANALYSIS

A summary analysis of measurements recorded at position 1 shows good shock wave planarity and homogeneous flow in the SSGG blast simulator test section where items under test are set up. This can be seen when a number of pressure profiles recorded during the same test are superimposed. Figure 21 shows this over a 40 ms period.

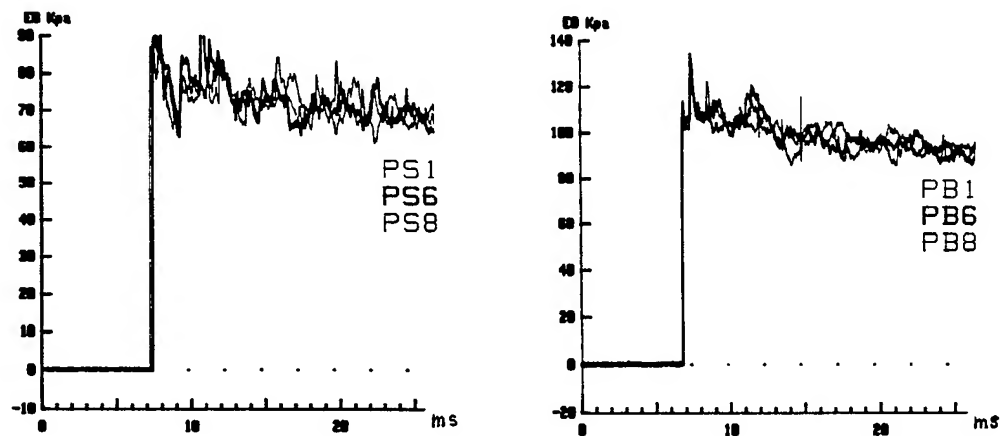


**Figure 21:** Superimposition of pressure profiles recorded during test n°2  
 $\Delta p = 80 \text{ KPa}$  - Position 1

## **7 SUMMARY**

A series of eight tests was performed in the french large blast simulator SSGG with peak static overpressure levels between 20 kpa and 120 kpa. Nineteen static and stagnation pressure gauge pairs were distributed in the tunnel cross section. Flow measurements were recorded successively in two longitudinal positions into the expansion tunnel.

The actual test conditions and the flow measurements recorded during this experiment were provided to the ARL for analysis of the flow uniformity and comparison with the results of numerical calculations.

# EXPERIMENTAL AND NUMERICAL STUDY OF FLOW IN MULTI-DRIVER LARGE BLAST SIMULATORS

## PART II: Flow Uniformity Analysis

S. Schraml  
U.S. Army Research Laboratory  
AMSRL-WT-NC  
Aberdeen Proving Ground, MD 21005-5066 USA

### 1. DATA ANALYSIS METHOD

Before performing an analysis of the test data, it was necessary to develop a method of accessing and displaying those results. Consistent usage of a rigorous analytical method would guarantee an unbiased evaluation of all experimental data. Because the primary goal of the project was to study the uniformity of flow at two different axial positions in the expansion tunnel of the SSGG blast simulator, a data analysis methodology was developed in which the flow histories from various points in the expansion tunnel cross section were compared to determine the variation in the flow field at that longitudinal position.

Figure 1 illustrates the positions of the test instrumentation in the expansion tunnel that was used for all the tests. For the first four shots in the test series, the instrumentation array was positioned at the test section a distance of 67.5 *m* downstream from the beginning of the expansion section. For the last four tests, the array was placed 22.5 *m* from the upstream end. The figure shows the locations of the 19 pairs of static and stagnations pressure gauges that were used. It also shows the projection of the exit diameter of the diverging nozzles onto the instrumentation rakes in the expansion tunnel. The SSGG facility has seven drivers which are distributed symmetrically about the vertical center plane of the expansion tunnel, with one driver split by the center plane. Each of the drivers that feeds into a symmetric half of the expansion tunnel has a unique length. Static and stagnation pressure gauge pairs were positioned in the expansion tunnel such that three sets of gauges were distributed across the flow path of each unique length driver. For each unique driver length gauge pairs were positioned on the driver centerline, on the projected outer radius of that driver's diverging nozzle, and half the distance between the centerline and the outer radius of the diverging nozzle. The remaining seven gauge pairs were positioned between the projected flow paths of the drivers. The information presented in Figure 1 illustrates which gauge pairs fell within the projected flow path of individual drivers, and which gauge pairs fell between drivers. Throughout this paper, the **PS** nomenclature denotes a static pressure gauge while a **PB** denotes a stagnation pressure gauge.

The analysis method for determining flow uniformity employs four different type of pressure-time history comparison:

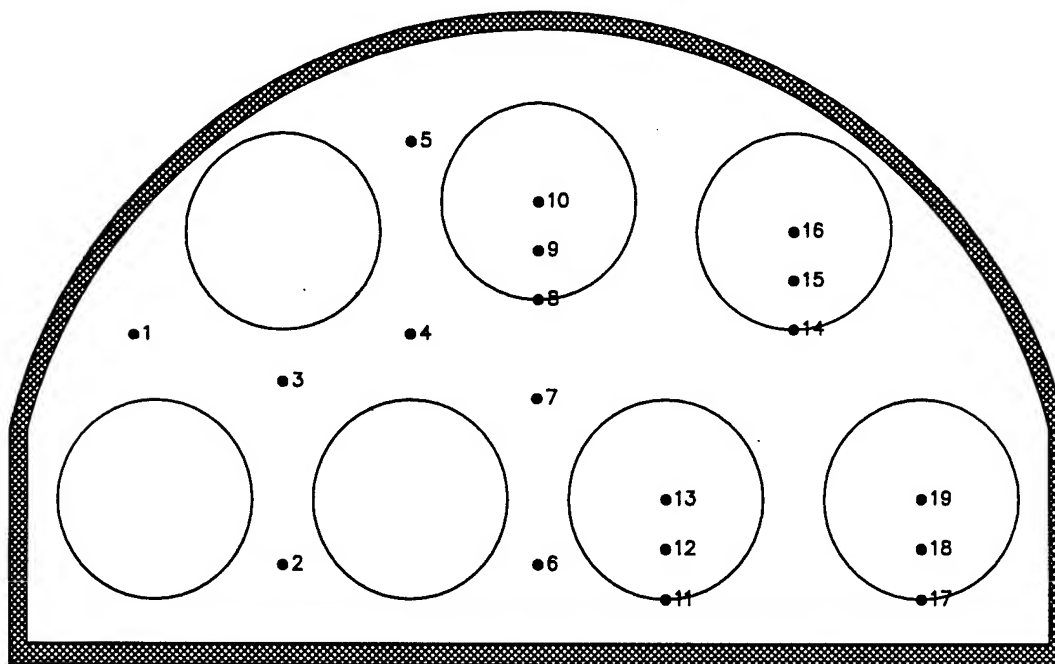


Figure 1. Instrumentation Locations in Expansion Tunnel

1. Pressure histories from gauges located in the flow path of drivers of different lengths were compared to each other to determine the effects of driver length on the flow in that local region. For instance, referring to Figure 1, the static overpressures recorded in the paths of the driver centerlines could be studied by comparing the data from gauges PS10, PS13, PS16, and PS19. The same could be done for gauges on the outer radius of the diverging nozzle (PS8, PS11, PS14, and PS17), or those between the centerline and outer radius (PS9, PS12, PS15, and PS18).
2. Pressure histories from the seven pairs of gauges located between drivers could be compared to each other to determine whether or not the expansion tunnel walls have a significant influence on the flow characteristics. Stagnation overpressure measurements from gauges PB1 and PB2 may be compared to those from PB4 and PB7 for this purpose.
3. Data obtained from gauges distributed across the radius of a particular driver can be compared to each other to determine the presence of jet flow which may originate from the drivers.
4. Flow histories from gauges within the projected flow paths of drivers could be compared to histories obtained from gauges between drivers to assess the diffusion of the individual driver jets into a single, uniform flow field. Stagnation overpressure data from PB19 and PB10 may be compared to that from PB3 and PB7 for this purpose.

Another method of analyzing the uniformity of the flow fields is to select one flow parameter from each of the 19 gauge locations and view the variation of the parameter in the cross section of the expansion section of the blast simulator. This is performed by making

a contour plot of the parameter which is imposed on the shape of the expansion tunnel. This method of analysis can be used to determine the uniformity of such flow parameters as peak static overpressure or stagnation overpressure impulse, as two examples.

Of the eight shots that were performed in the test series, four provided a logical set on which to base the flow uniformity analysis. These were tests at two different pressure levels in which the driver initial conditions for shots with the instrumentation array positioned at 22.5 *m* were nearly the same as the initial conditions of the shots where the array was at the 67.5 *m* location. A summary of the conditions of these four tests is provided in Table 1. By selecting an appropriate pair of tests with nearly identical initial conditions, it is possible to perform an analysis as if the test data were derived from one shot with one instrumentation array at 22.5 *m* and another at 67.5 *m*.

**Table 1.** Summary of Tests Used in Flow Mapping Analysis

Test Number	Rake Position ( <i>m</i> )	Nominal Shock Overpressure ( <i>kPa</i> )	Average Driver Overpressure ( <i>bar</i> )	Ambient Pressure ( <i>mbar</i> )	Ambient Temperature ( <i>°C</i> )	Relative Humidity (%)
1	67.5	20	7.09	968	11	60
6	22.5	20	7.06	964	2	40
2	67.5	80	36.46	965	7	55
8	22.5	80	36.66	982	7	48

In this table, the average driver overpressure refers to the fact that the seven drivers of the SSGG are manifolded together to equilibrate the pressure between the driver tubes. The actual pressures for the tests were recorded independently for each driver tube, and differed slightly from one driver to the next. The values listed in Table 1 is the mean overpressure of all seven drivers for each test.

The nominal shock overpressure refers to the approximate incident static overpressure produced in the expansion tunnel by the blast. The actual peak static overpressure may not be exactly 20 *kPa* and may even vary from one location to the next in the expansion tunnel. The nominal shock overpressure is used here as a means of identifying the tests by a significant flow characteristic, rather than a test number.

This table illustrates that the results of Tests 1 and 6 can be combined to analyze the flow associated with a shot having a peak static overpressure of 20 *kPa*. Similarly, the results of Tests 2 and 8 can be used for the analysis of an 80 *kPa* shot.

## 2. ANALYSIS OF 20 *kPa* TESTS

The flow uniformity analysis was performed by beginning with the lowest overpressure tests and finishing with the high overpressure tests. For each of the two overpressure levels presented here, the data collected at the 67.5 *m* position is addressed first, followed by that

of the 22.5 m position. For the 20 kPa tests, Test 1 had the instrumentation array located at the 67.5 m position while the data from Test 6 was collected at the 22.5 m location.

The results of the tests are presented in a manner which is consistent with the analysis method discussed above. If any non-uniformity exists in the flow field, it is expected to be caused by persistent jets of driver gas traveling downstream. One would expect the strongest area of such flow to exist at the center of the jet. It is with this understanding that the flow uniformity analysis begins by comparing the measured flow histories from gauges located in the flow path of driver centerlines.

Figure 2 compares the early time static overpressure waveforms from Test 1 for gauges located in the flow path of the centerlines of the 26 m driver, the 35 m driver and the 44 m driver: gauges PS16, PS10, and PS19 respectively from Figure 1. This figure shows that, of these three waveforms, PS19 has the greatest peak static overpressure at 23.45 kPa. The lowest of the three peak static overpressures occurred at gauge PS10, in the centerline of the 35 m driver as was 21.96 kPa. The variation between these two peaks is 1.49 kPa or 6.6%. Figure 3 shows the full positive phase duration of the static overpressure of these same three gauges. This figure shows that the static overpressure of the flow in the path of the driver centerlines is uniform.

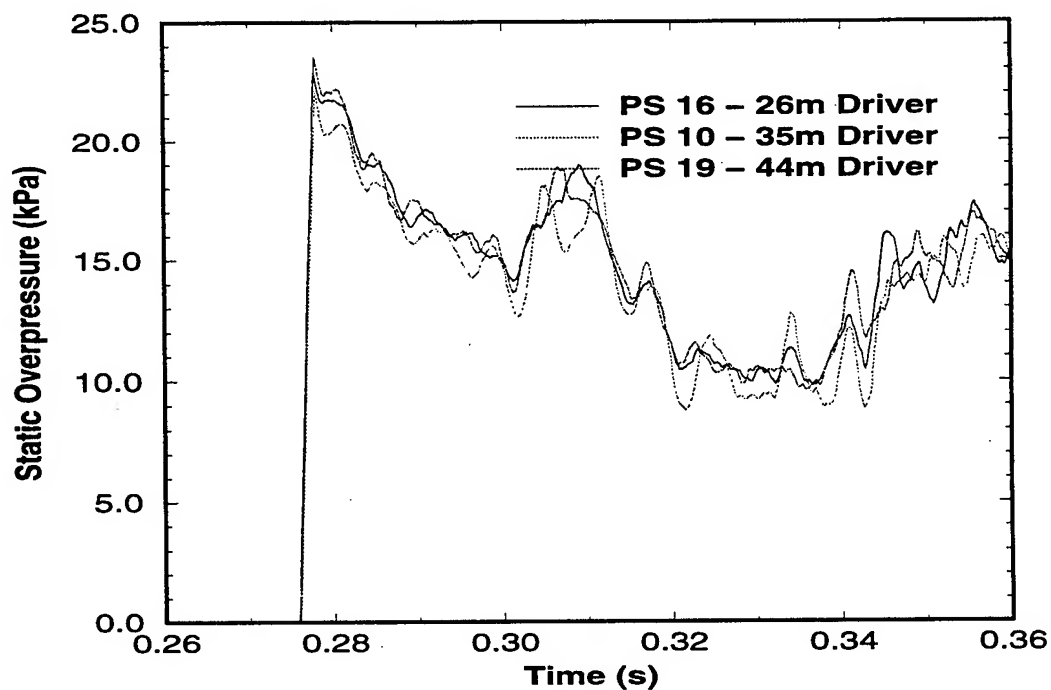


**Figure 2.** Test 1 Static Overpressure from Gauges in Flow Path of Driver Centerlines (Early Time History)

Figures 4 and 5 provide an illustration of Test 1 data from the same driver centerlines as Figures 2 and 3 except that in these figures, stagnation overpressure is plotted instead of static overpressure. Figure 4 shows an early time history in which the peak stagnation overpressure occurred in the centerline of the 35 m driver (gauge PB10) and was 27.90 kPa.



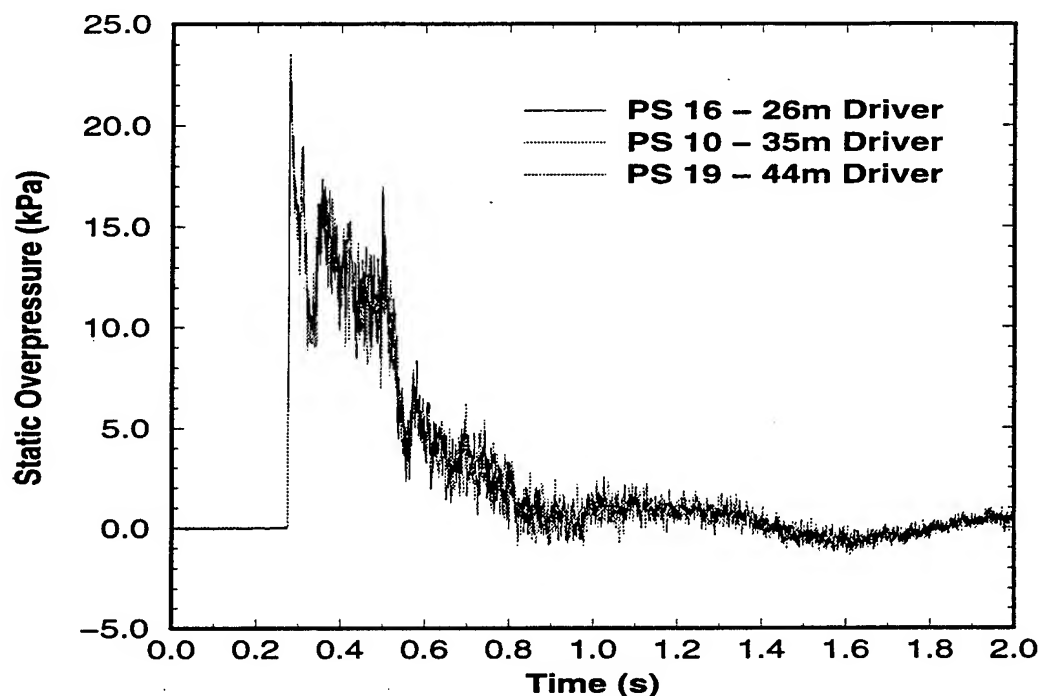


Figure 3. Test 1 Static Overpressure from Gauges in Flow Path of Driver Centerlines

The smallest of the three stagnation overpressure peaks occurred in the centerline of the 26 m driver (gauge PB16) and was 24.63 kPa. The difference between this local maximum and minimum is 3.27 kPa or 12.4%. Figure 5 provides the same full positive phase duration of these three centerline gauges and proves that, like that static overpressure, the stagnation overpressures are nearly identical.

If the driver gas flow were to produce persistent jets which travel downstream in the expansion section, then a shear surface would be produced at the interface between the driver jet and the tunnel gas. Jet flow from shock tubes has been observed to maintain the shape of the exit plane in testing at ARL.<sup>8</sup> In the case of the SSGG large blast simulator, jet flow exiting one of the drivers would be expected to take the size and shape of the exit planes of the diverging nozzles which empty into the expansion section. Thus, it may be possible to determine the presence or absence of driver jet flow at a given longitudinal position by comparing the static and stagnation overpressures of gauges positioned in the path of the outer radius of the diverging nozzles. Test 1 had the instrumentation array located at the 67.5 m position in the expansion tunnel. Test 1 static overpressure data from gauges positioned in the path of the outer radius of the diverging nozzles are presented in Figure 6. The records represented in this figure are from gauges PS14, PS8, and PS17 which lie on the nozzle exit radius of the 26 m driver, 35 m driver, and 44 m driver respectively. These results show that, like the flow in the driver centerline paths, the static overpressure is uniform at these gauges. Figure 7 is a plot of the stagnation overpressure histories from these same three gauges in the path of the nozzle exit radius. Again, these results show no significant difference between the recordings of the subject gauges. These results clearly

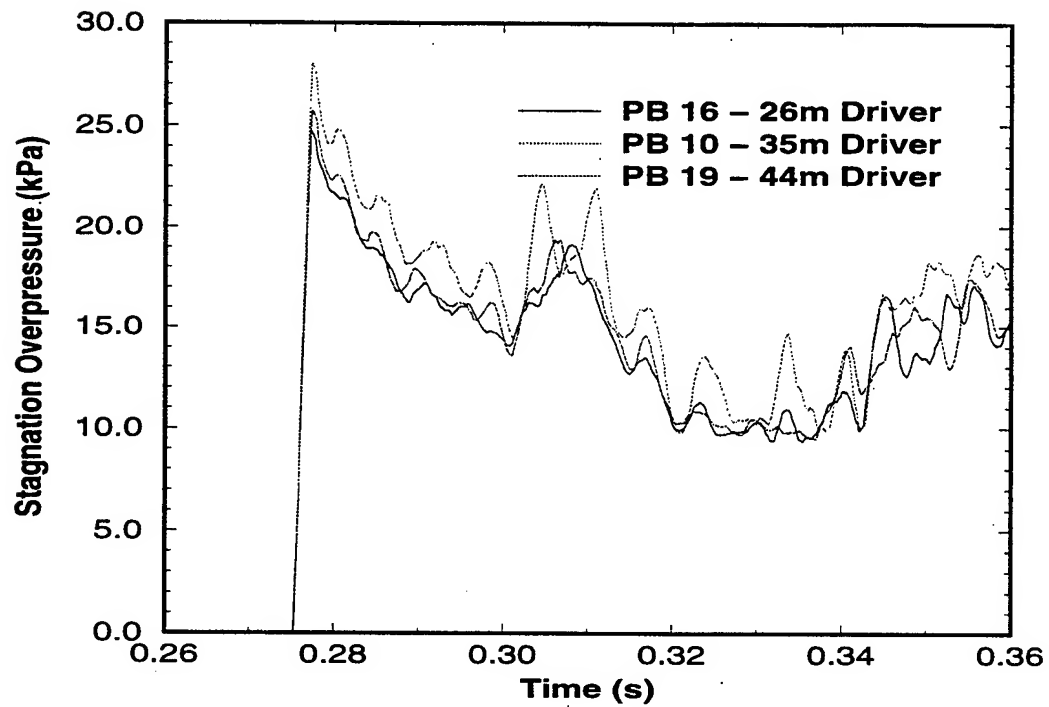


Figure 4. Test 1 Stagnation Overpressure from Gauges in Flow Path of Driver Centerlines (Early Time History)

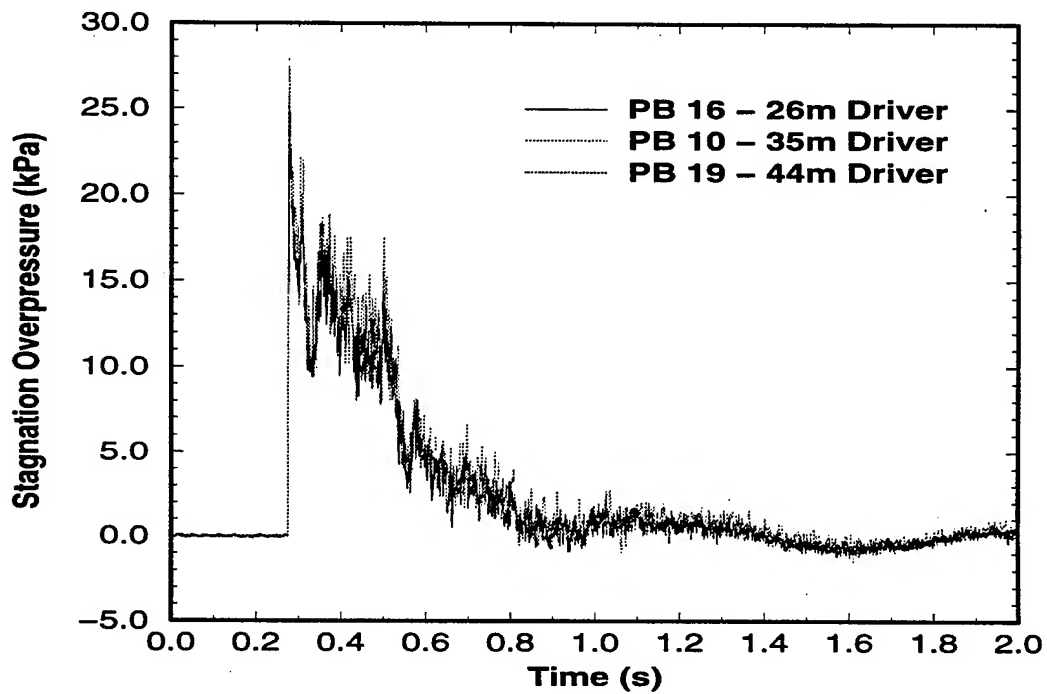


Figure 5. Test 1 Stagnation Overpressure from Gauges in Flow Path of Driver Centerlines

demonstrate that there is no evidence of driver jet flow at the 67.5 *m* test section for tests at the 20 *kPa* overpressure level.

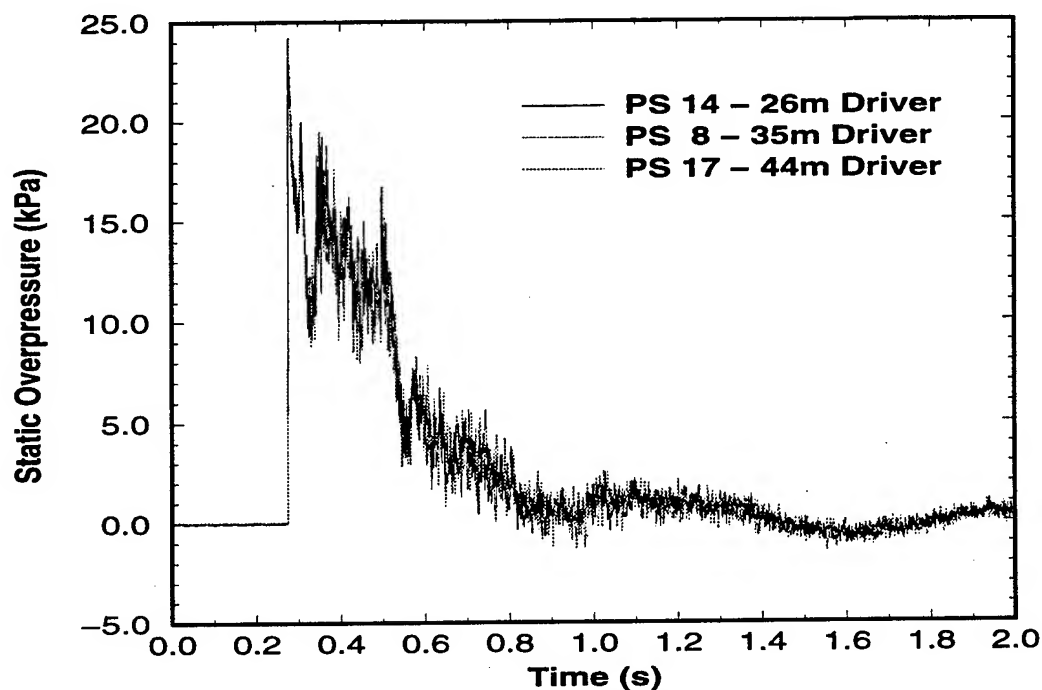


Figure 6. Test 1 Static Overpressure from Gauges in Flow Path of Outer Radius of Driver Diverging Nozzles

It has been shown that the flow in the paths of the drivers is uniform across different driver lengths. The next step in the analysis is to examine the flow recorded at gauges located between the flow paths of the drivers. This analysis will determine the ability of the driver gas to uniformly fill the entire cross-sectional area of the expansion section. Figure 8 provides an early time history of the static overpressure waveforms from gauges PS1, PS2, PS5, and PS6 of Test 1. The illustration of Figure 1 shows that each of these gauges falls between the flow paths of different length drivers and are in gauges which are close to the walls of the expansion tunnel. The peak static overpressures in Figure 8 are bracketed by the gauges PS6 and PS1. Gauge PS6 has the greatest static overpressure of the four at 23.74 *kPa* and PS1 has the lowest at 23.01 *kPa*, a difference of 0.73 *kPa* or 3.1%. While not shown in the figure, the full positive phase static overpressure waveforms of these four gauges are once again nearly identical. The stagnation overpressure from these same gauge locations are plotted in Figure 9 which also shows no significant difference between the four records. These two figures indicate that, at the 20 *kPa* overpressure level, the flow from the drivers is able to sufficiently diffuse to uniformly fill the expansion tunnel at the 67.5 *m* test section.

From these many comparisons, one can confidently conclude that the flow at the 67.5 *m* position, the test section in the SSGG, is highly uniform at the 20 *kPa* overpressure level. Consequently, it can be expected that targets will be uniformly loaded in both shock diffrac-

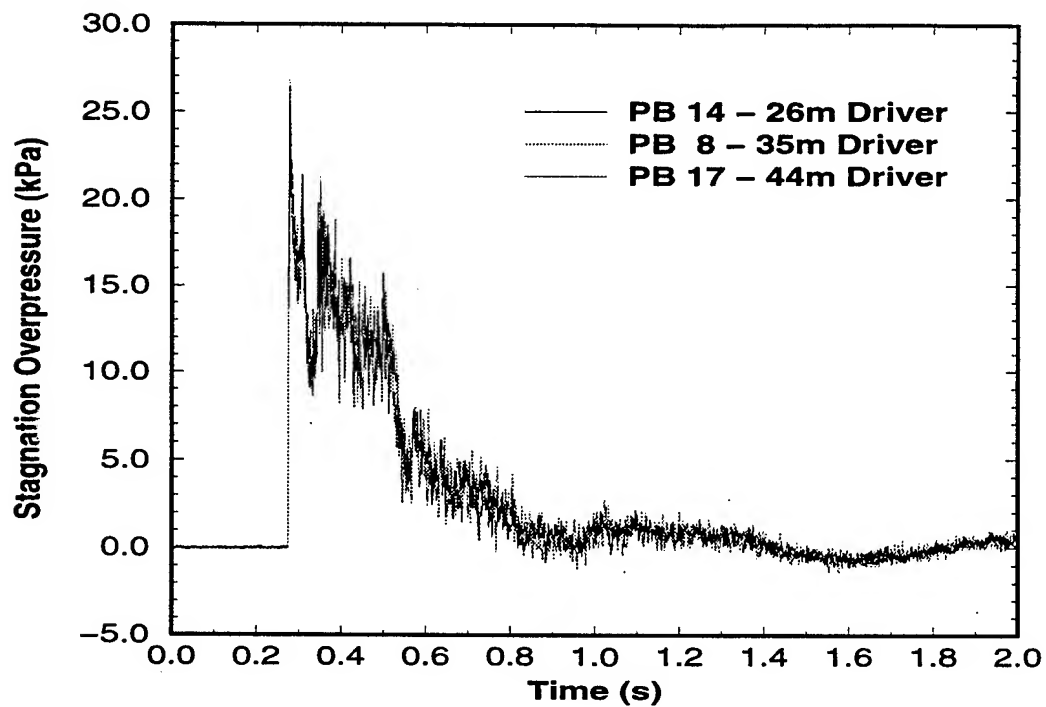


Figure 7. Test 1 Stagnation Overpressure from Gauges in Flow Path of Outer Radius of Driver Diverging Nozzles

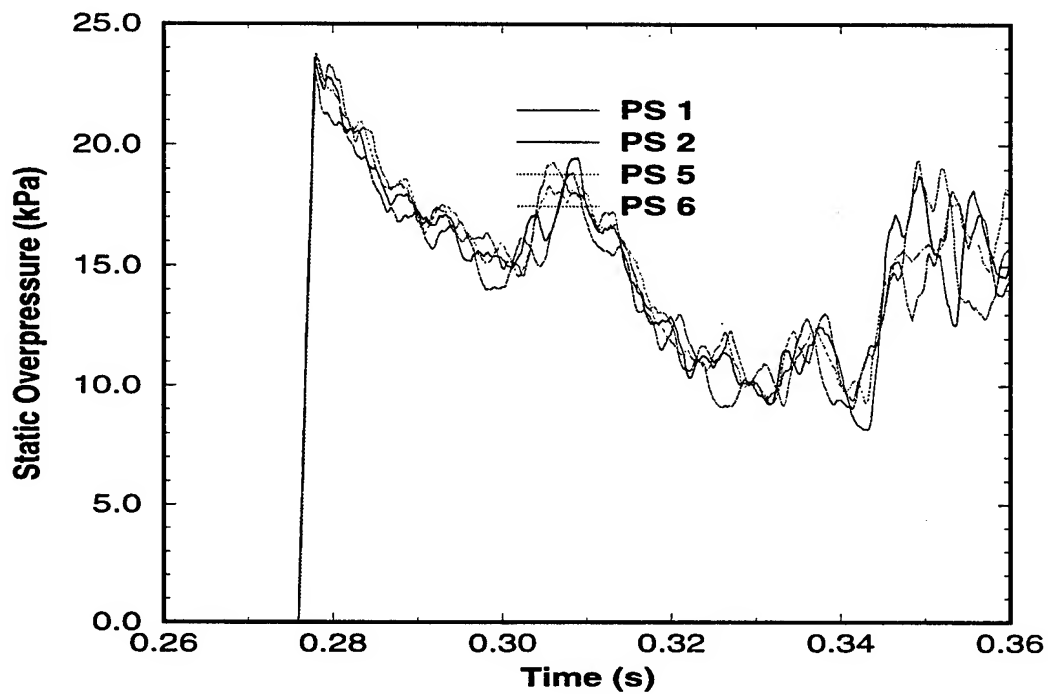


Figure 8. Test 1 Static Overpressure from Gauges Between Drivers

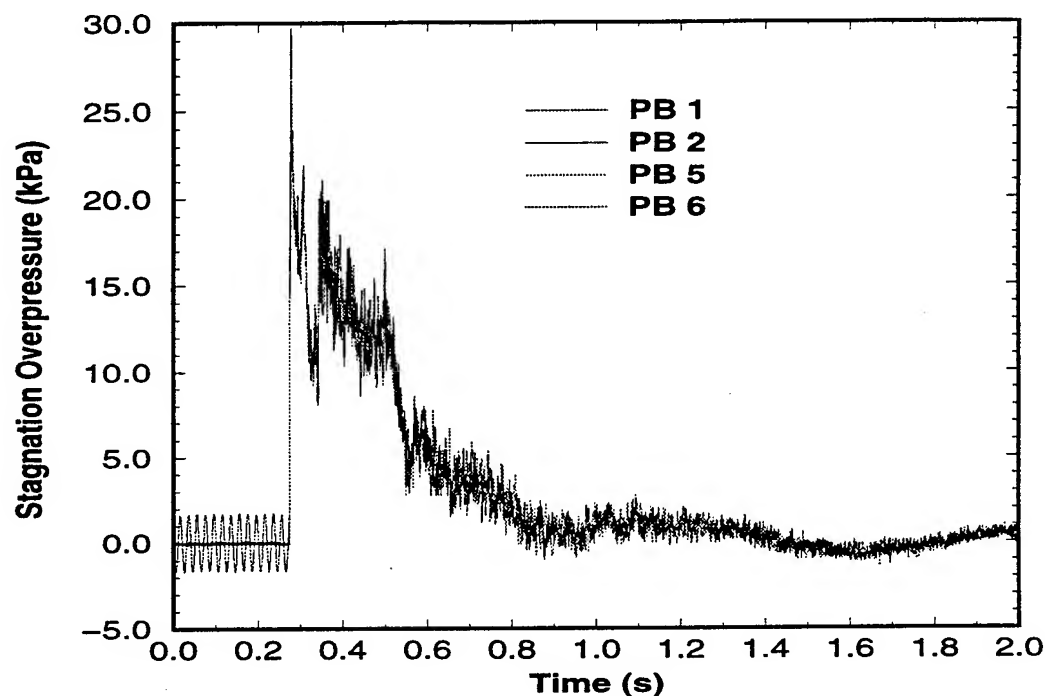


Figure 9. Test 1 Stagnation Overpressure from Gauges in Between Drivers

tion and drag loading when placed in the test section of the SSGG for a test at this overpressure level.

Test 6 was the 20 *kPa* overpressure test in which the instrumentation array was located 22.5 *m* downstream from the beginning of the expansion section. To provide a self-consistent set of results of these shots, the Test 6 data is presented in nearly the same format as Test 1. Figure 10 shows an early time history of the static overpressure records taken from the gauges in the path of the driver centerlines (PS13, PS16, PS10, and PS19). In this figure, the gauge PS13 has the largest peak static overpressure at 28.13 *kPa* while gauge PS10 had the lowest of the four at 26.61 *kPa*, a difference of 1.52 *kPa* or 5.6%. For the remainder of the positive phase (not shown in the figure) the four records are nearly coincident. Figure 11 shows the stagnation overpressure from the same four gauge locations. This figure provides the first indication of any non-uniformity of the flow in the expansion tunnel. The four stagnation overpressure records follow the same pattern until about 530 *ms* where the PB19 record suddenly increases and remains at an elevated level of approximately 10 *kPa* for the remainder of the positive phase. The gauge PB19 is in the path of the centerline of the 44 *m* driver, the longest driver in the SSGG facility. This result is an initial indication that the gas exiting this driver may be forming a jet flow in the expansion tunnel.

To further investigate the possible driver jet flow phenomenon illustrated in Figure 11, the records from the gauges positioned in the path of the outer radius of the diverging nozzles are examined. Figure 12 illustrates the static overpressure records from gauges PS11, PS14, PS8, and PS17 which are aligned with the nozzle exit radii. This figure shows that the static overpressure is again uniform across the different drivers. Figure 13, however, shows

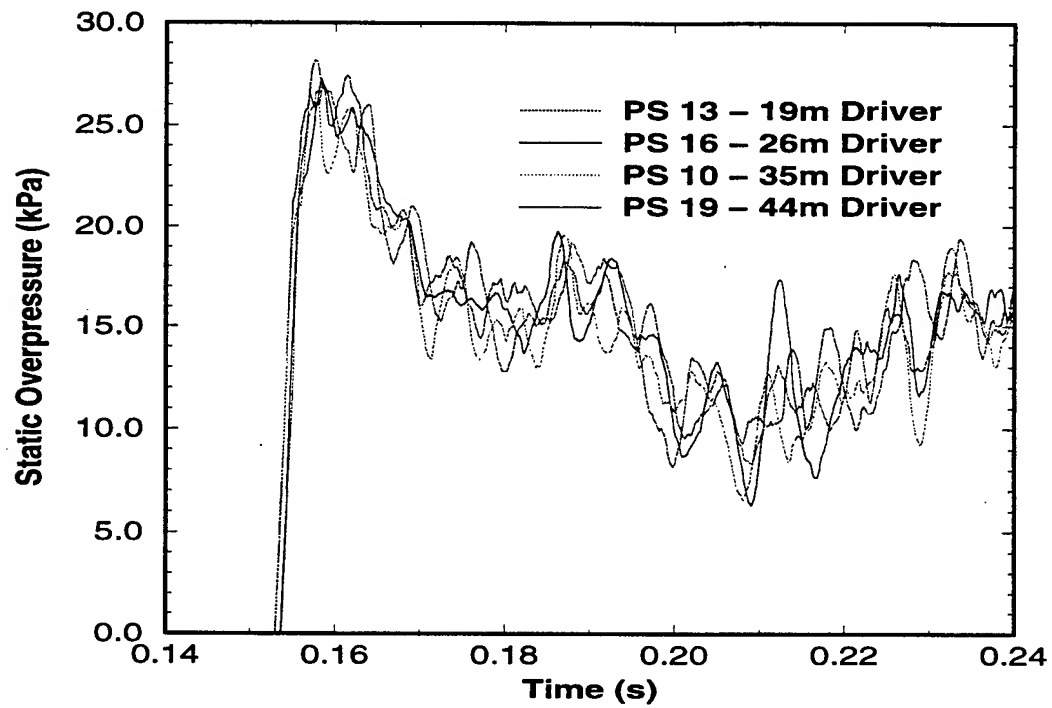


Figure 10. Test 6 Static Overpressure from Gauges in Flow Path of Driver Centerlines

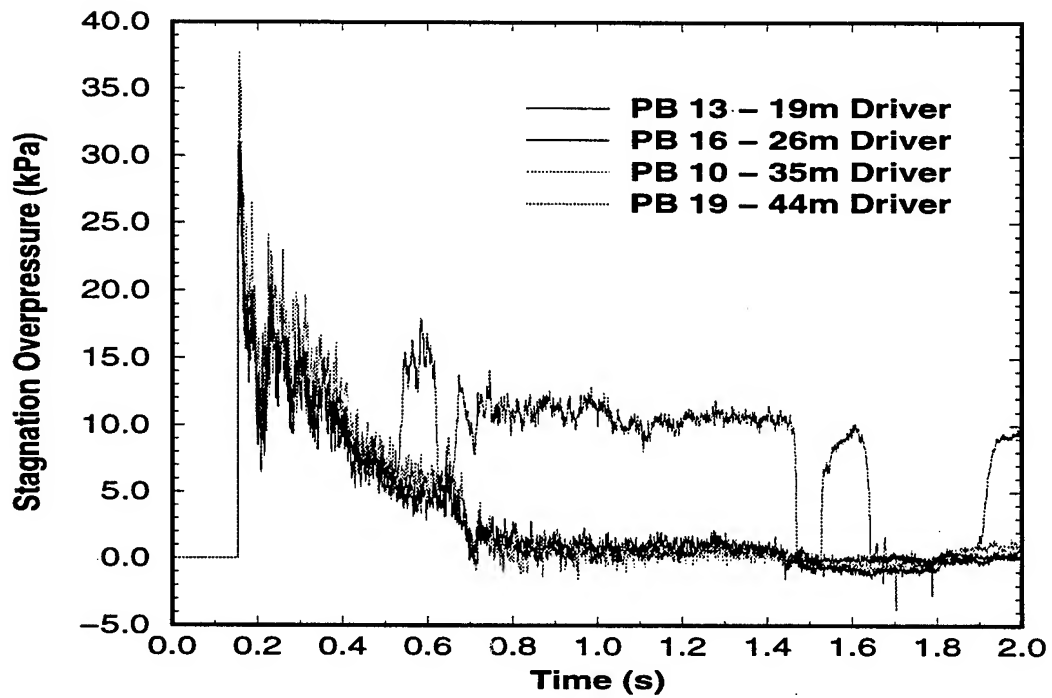
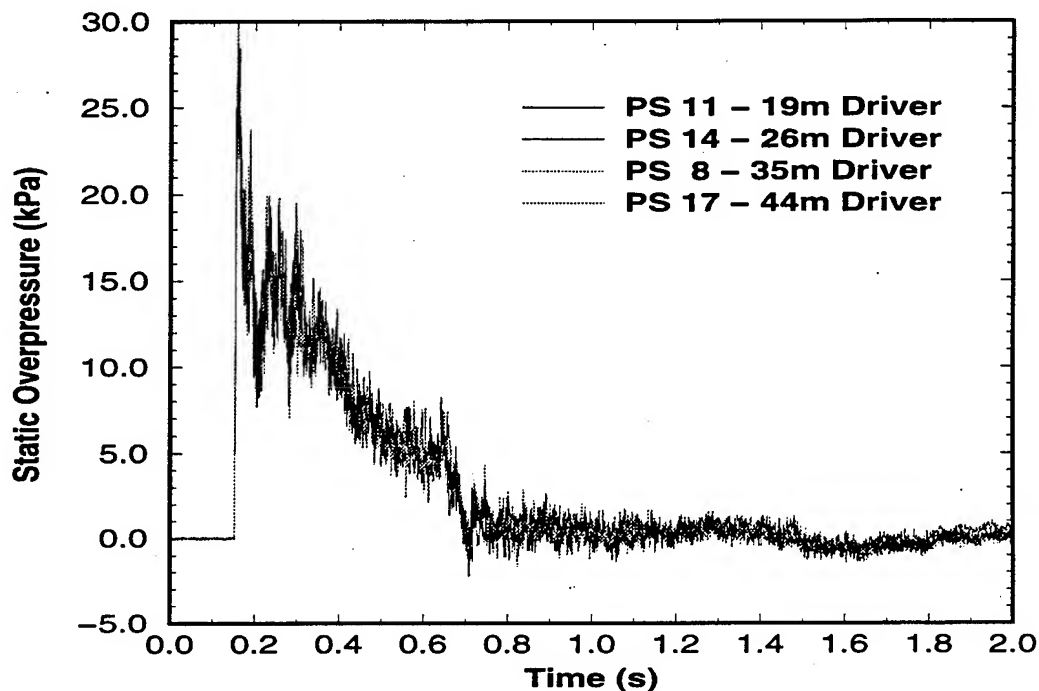


Figure 11. Test 6 Stagnation Overpressure from Gauges in Flow Path of Driver Centerlines

the stagnation overpressure from these gauge positions is uniform for only three of the four. The PB17 record, aligned with the 44 *m* driver, has a much lower value than the rest from 180 *ms* until 650 *ms*.



**Figure 12.** Test 6 Static Overpressure from Gauges in Flow Path of Outer Radius of Driver Diverging Nozzles

To gain a better understanding of the flow from the 44 *m* driver, records from the gauges distributed across the radius of that driver were compared. Figure 14 provides the comparison of the stagnation overpressures measured in the path of the driver centerline (PB17), the nozzle exit radius (PB19), and half the distance between these two points at the nozzle half-radius (PB18). This figure clearly shows the formation of jet flow from the 44 *m* driver. The jet appears to be concentrated in an area which is smaller than the radius of the nozzle exit. This is evidenced by the very high stagnation overpressure in the path of the driver centerline, and a very low stagnation overpressure for much of the PB17 record which is aligned with the nozzle exit radius. The PB18 record on the nozzle half-radius initially follows the centerline record of PB19, then diverges from it at about 540 *ms* to eventually coincide with the PB17 record at about 710 *ms*. These results are evidence that flow separation is occurring as the gas transitions from the throat section to the diverging nozzle. This separated flow then forms the jet which retains its shape for some distance as it travels downstream and passes the 22.5 *m* instrumentation array.

This type of jet flow is consistent in character to that observed on testing of the ARL 10.2 *cm* shock tube.<sup>8</sup> This device was constructed to perform research in the use of shock tube exit jets for the simulation of thermally precursed, non-ideal blast produced by tactical nuclear weapons.<sup>9, 10</sup> A photograph of the 10.2 *cm* shock tube is provided in Figure 15.

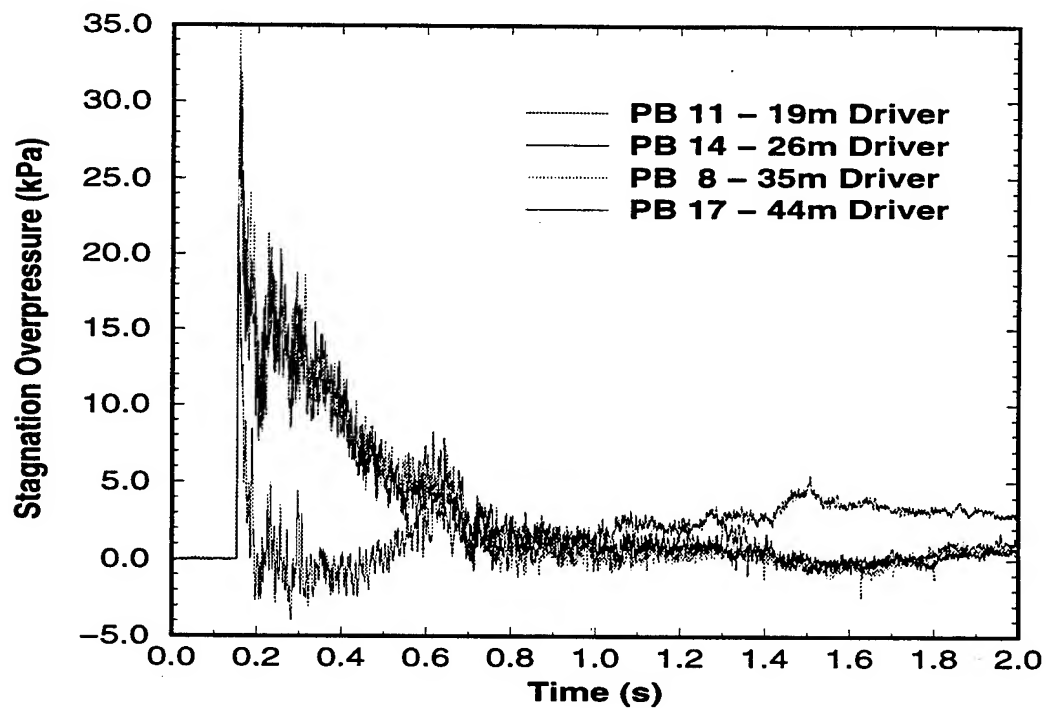


Figure 13. Test 6 Stagnation Overpressure from Gauges in Flow Path of Outer Radius of Driver Diverging Nozzles

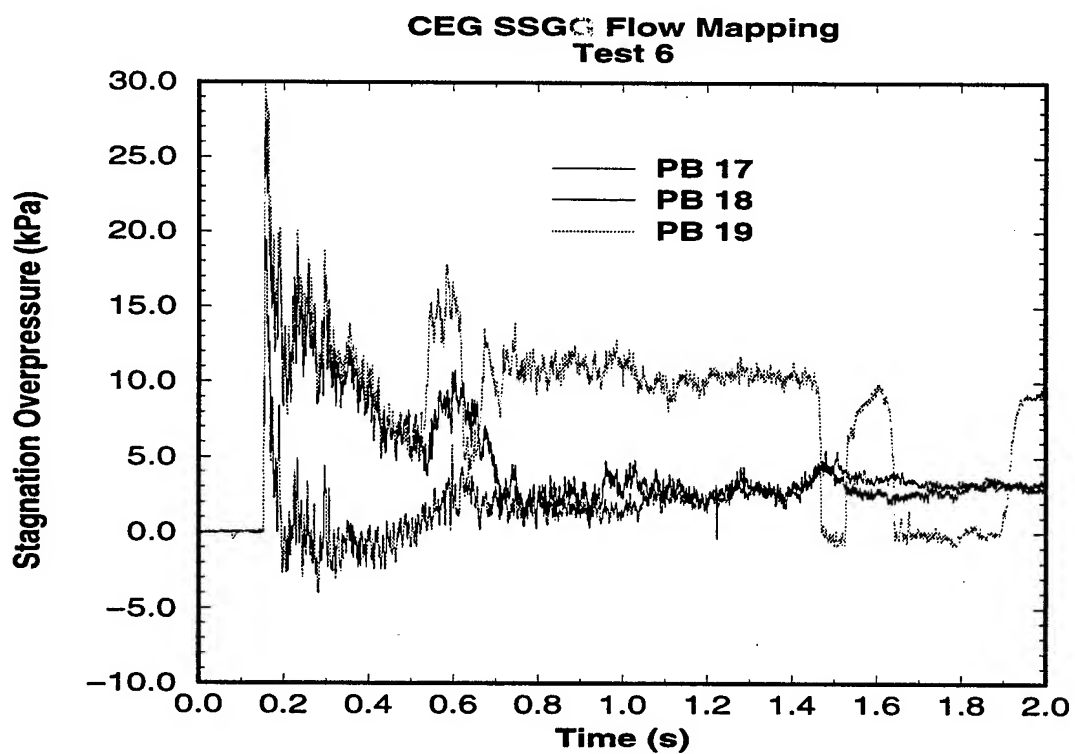


Figure 14. Test 6 Stagnation Overpressure from Gauges Across Radius of 44 m Driver



This photograph was taken from the downstream end of the expansion section and shows the exit plane of the shock tube. Downstream from the shock tube exit plane there is an instrumentation rake which contains a vertical set of differential pressure gauges<sup>11</sup> which are used to measure the characteristics of the flow exiting the tube. In the test configuration of the 10.2 cm shock tube, differential pressure measurements were made in the path of the shock tube centerline, on the exit plane outer radius, and at the half-radius point, in addition to several other vertical locations. Differential pressure time histories from a test of this facility<sup>12</sup> are provided in Figure 16. This figure shows flow which has similar characteristics to those measured in the path of the SSGG 44 m driver. The data from the gauge aligned with the shock tube centerline are at all times greater than those recorded elsewhere. The differential pressure on the exit radius is always the smallest, and the half-radius data falls in between the other two.

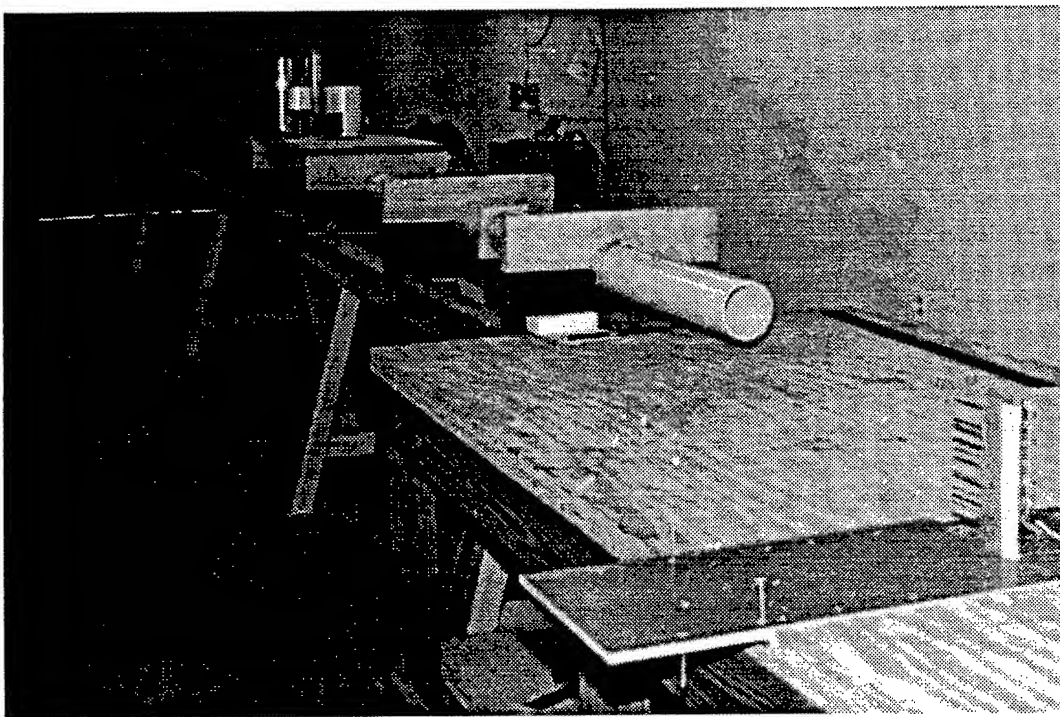


Figure 15. ARL 10.2 cm Shock Tube

These results are clear evidence that driver jet flow does exist in the upstream end of the SSGG expansion tunnel at the 20 kPa overpressure level. However, this phenomenon was only found in the path of the longest driver. The other shorter drivers produced no noticeable jet flow at this shock overpressure level. It is also important to reiterate that, even though some shear flow was found at the 22.5 m position, the flow at the 67.5 m vehicle test station was completely uniform in static and stagnation overpressure. The flow travel distance in the expansion tunnel from the 22.5 m position to the 67.5 m position is sufficient for any driver jet flow produced at this overpressure level to diffuse and form a flow field which is essentially one-dimensional at the test section.

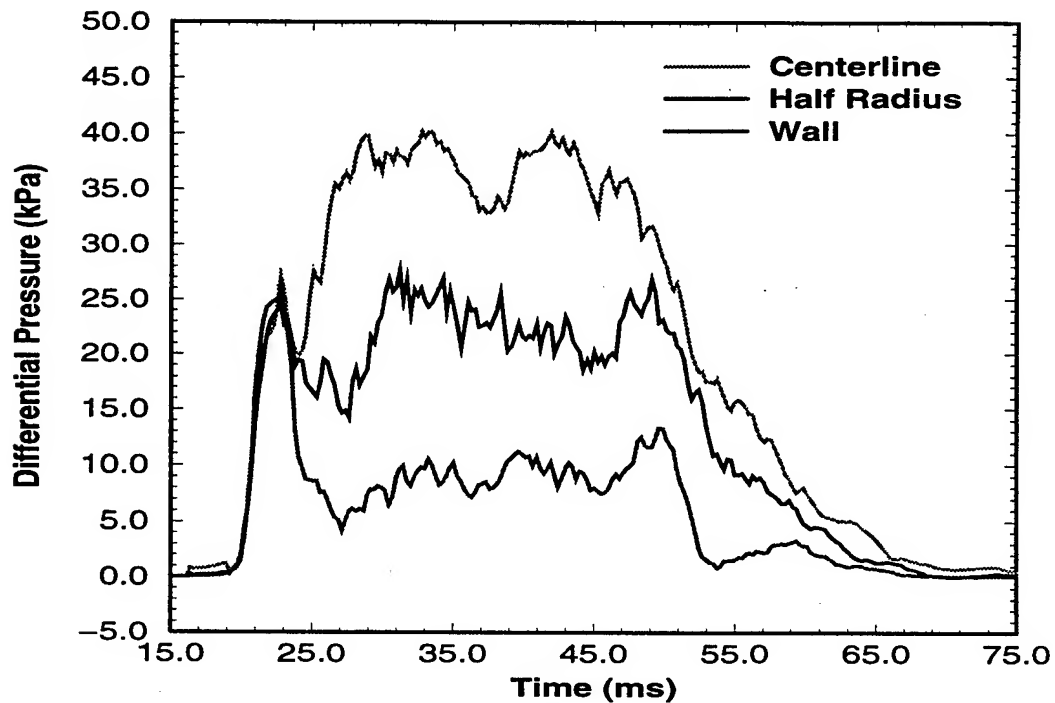
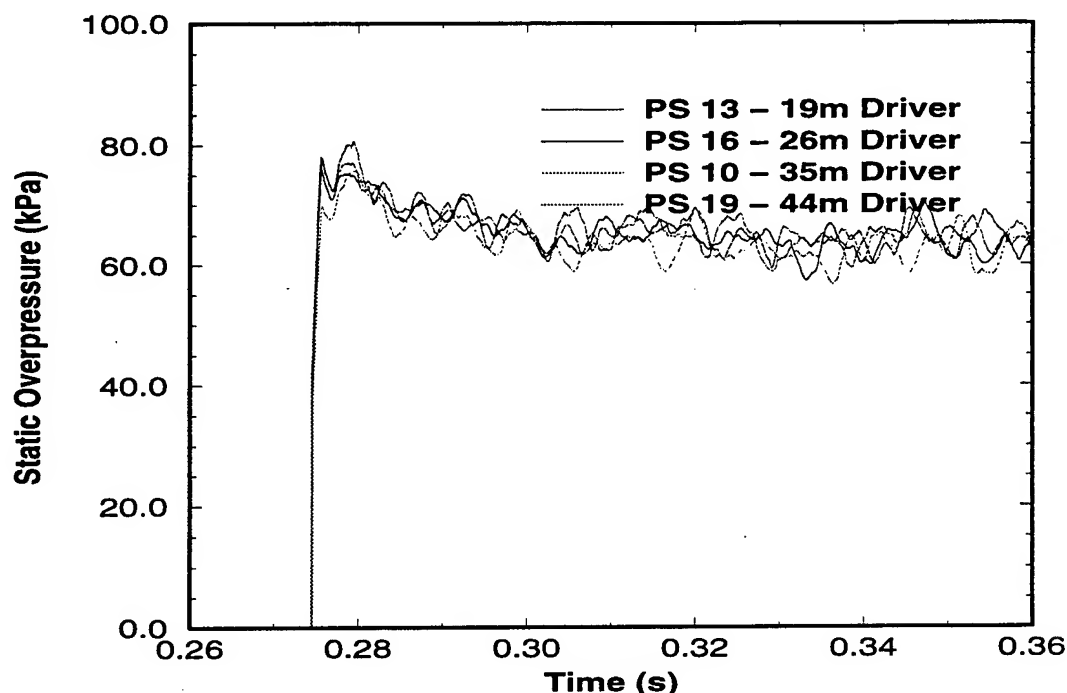


Figure 16. Differential Pressure Histories Across Radius of ARL 10.2 cm Shock Tube

### 3. ANALYSIS OF 80 kPa TESTS

Tests 2 and 8 were shots in which a nominal peak static overpressure of 80 *kPa* was produced in the expansion section. Test 2 had the instrumentation array positioned at the 67.5 *m* location. The early time history of the static overpressure recorded on the gauges in the path of the driver centerlines is presented in Figure 17. The greatest of these four static overpressures was measured on gauges PS13 and PS19 at 77.9 *kPa*, while the lowest of the four peaks occurred on gauge PS10 at 73.9 *kPa*. The difference between these peak static overpressures is 8.00 *kPa* or 10.8%. For the remainder of the positive phase, the static overpressures of the four records are in close agreement. Based on this agreement and that of the prior discussion, it is possible at this point in the analysis to declare the static overpressure to be uniform across a particular cross-section in the expansion tunnel at any point in time during the blast event. Using this conclusion, the remainder of the flow uniformity will concentrate on variations which may exist in the stagnation overpressure records.

The Test 2 stagnation overpressure records from the gauges in the paths of the driver centerlines are presented in Figure 18. The most significant characteristic of these records is the dropout of the PB16 record at 1.0 *s*. At this point in time, the data from that gauge dropped out of the range of physically realistic values and did not recover during the remainder of the positive phase. Also important in this figure is the dropout of the data from gauge PB19 at about 1.1 *s*, which soon returns and again follows the remainder of the traces.



**Figure 17.** Test 2 Static Overpressure from Gauges in Flow Path of Driver Centerlines (Early Time History)

A possible explanation of the reason for these dropouts in these records lies in the configuration of the SSGG blast simulator. The seven drivers and their associated converging/diverging systems are evenly distributed across the diameter of the expansion section of the facility. The reaction pier and other structural supports hold the driver system in place. The transition region between the diverging nozzles and the expansion tunnel is not sealed off. As a result, the shock wave propagation down the expansion tunnel can create a low pressure region at the upstream end of the tunnel which will cause ambient air to be entrained in the flow field. Table 1 shows that when these tests were performed, the ambient air was cold and damp. The driver gas is atmospheric air which is run through compressors to pressurize the drivers. At the time the flow is initiated, the driver air is at the same temperature as the surrounding atmosphere. When flow is initiated, the driver gas expands through the diverging nozzles and cools. It is believed that the expanded driver gas cooled the entrained ambient air and caused small ice particles to be formed in the flow. These ice particles are believed to have clogged the stagnation pressure gauges and caused the dropouts observed in Figure 18.

The stagnation overpressure records in Figure 18 show that there are slight variations between the different records at several points in time during the positive phase. For instance, at 450 ms gauge PB16 recorded a stagnation overpressure of about 61 kPa, while at the same time gauge PB10 recorded a level of about 78 kPa. To better quantify these variations, these traces were numerically integrated to produce stagnation overpressure impulse histories. Figure 19 is a plot of these four impulse histories from Test 2. In this figure, one can see the

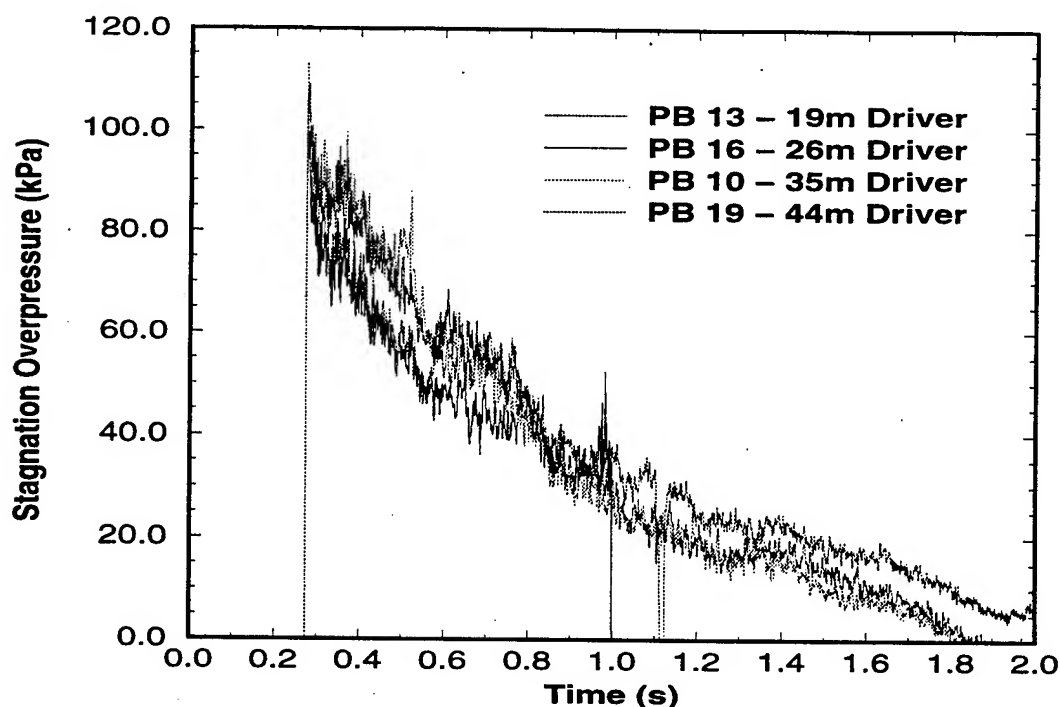


Figure 18. Test 2 Stagnation Overpressure from Gauges in Flow Path of Driver Centerlines

point at which gauge PB16 completely dropped out and also the step in the PB19 record denoting the brief dropout that it experienced. Despite these dropouts, one can see that the stagnation overpressure impulse histories of these four gauges closely followed each other. The integrated impulse values at 2.0 s range from 51.1  $kPa \cdot s$  for PB19 to 53.4  $kPa \cdot s$  for gauge PB10, a spread of 7.4%. The Test 2 stagnation overpressure histories from gauges between drivers are presented in Figure 20. This figure again illustrates nearly coincident records produced by gauges in these positions. The average stagnation overpressure impulse at 2 s from these four gauges was 52.2  $kPa \cdot s$ . The consistency of the recorded stagnation overpressure impulses for these gauges distributed about the cross section of the expansion tunnel along with the nearly coincident static overpressure histories is a clear indication of a uniform flow field being produced at the 67.5 m test section for the 80  $kPa$  overpressure level.

Finally, Test 8 was the 80  $kPa$  overpressure shot in which the instrumentation array was located at the 22.5 m longitudinal position in the expansion section. This was the highest overpressure test performed with the instrumentation placed at this position. This test provides a very informative view at the driver gas flow at this high overpressure level. Figure 21 compares the stagnation overpressures from the gauges located in the path of the driver centerlines. This figure shows that the four records follow nearly the same path from the time of shock arrival at 175 ms until about 220 ms, at which time large oscillations in all four records exist. This period of disturbance lasts until about 800 ms, after which the four histories follow approximately the same pattern. The large oscillations in the flow occur on the arrival of the driver gas at the measurement position. The shear stress produced by the

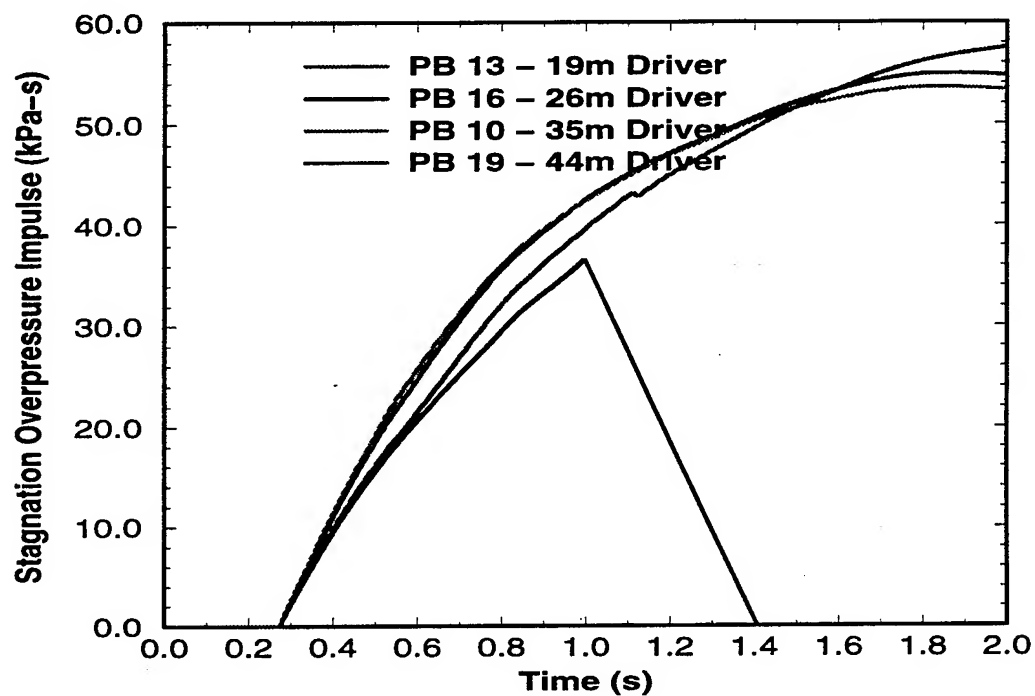


Figure 19. Test 2 Stagnation Overpressure Impulse from Gauges in Flow Path of Driver Centerlines

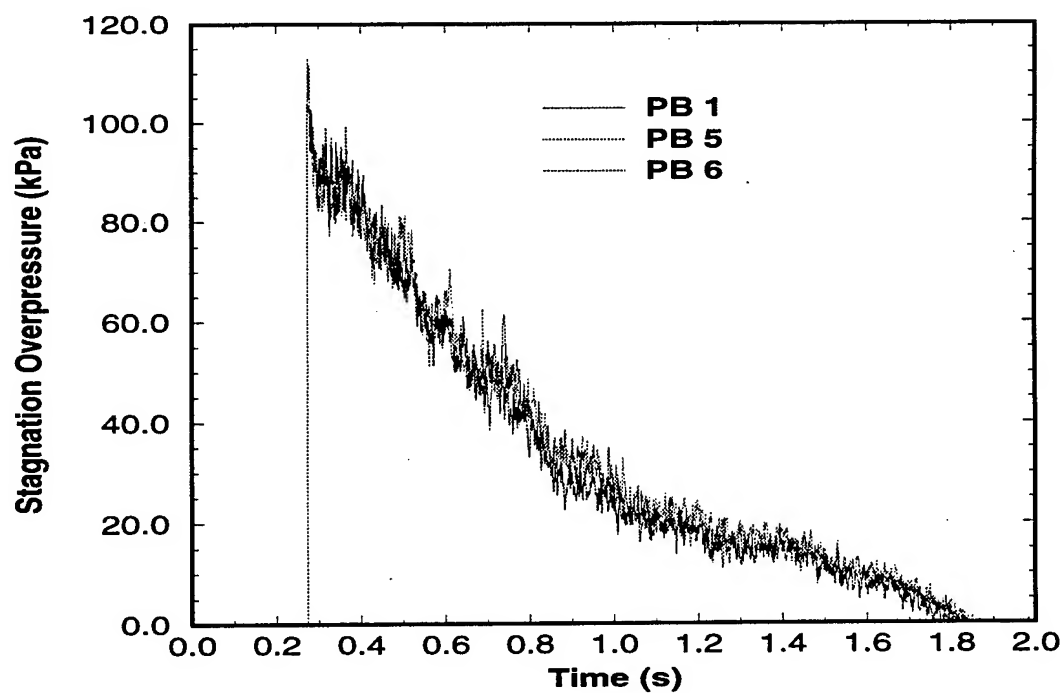
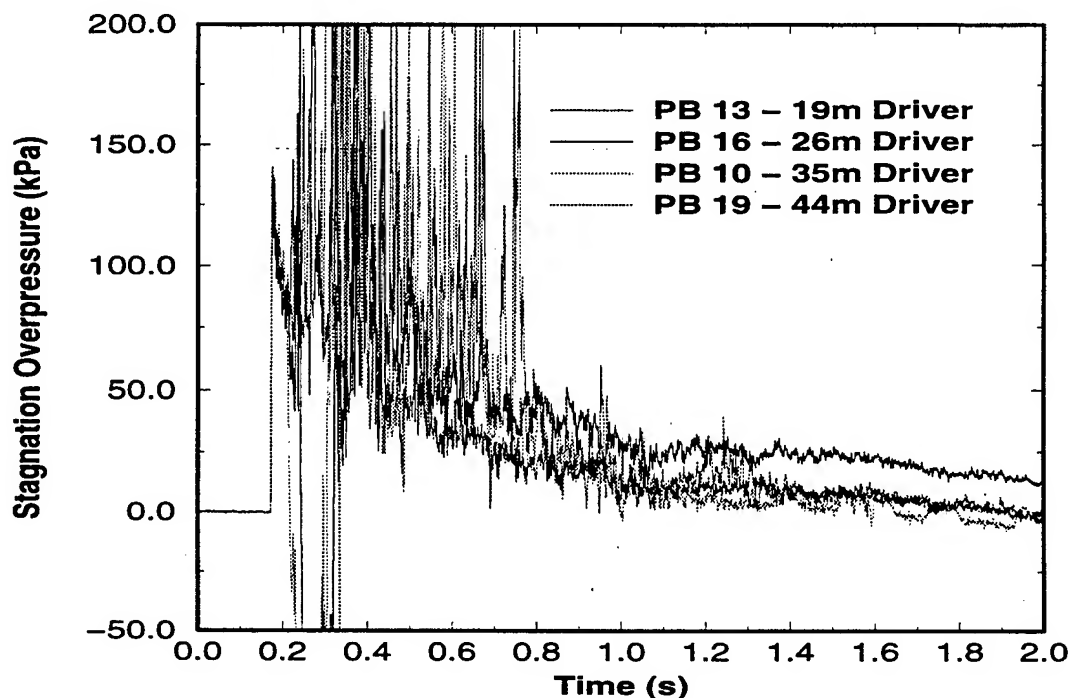


Figure 20. Test 2 Stagnation Overpressure from Gauges Between Drivers

interaction of the driver gas jet with the tunnel air generates a highly turbulent flow field. The turbulent mixing of the driver gas with the tunnel air diffuses the jet and produces the flow disturbances illustrated in Figure 21.



**Figure 21.** Test 8 Stagnation Overpressure from Gauges in Flow Path of Driver Centerlines

Also evident in Figure 21 are dropouts of the records of gauges PB16 and PB10. To better illustrate this phenomenon, the stagnation overpressure histories from these two gauges are plotted together in Figure 22. In this figure, both records experience the dropout at about 230 *ms* and recover at about 330 *ms*. Again, this effect is considered to be caused by ice formation on the stagnation probe. It is interesting to note that these dropouts do not occur on gauges PB13 and PB19 which are plotted together in Figure 23. Referring again to Figure 1, one can see that the gauges which experienced the dropouts are positioned in the paths of the 26 *m* and 35 *m* drivers which are located near the top of the expansion section. The dropouts are not apparent in the records of the gauges located in the paths of the drivers which are near the floor of the expansion section.

To further investigate this phenomenon, Figure 24 was produced to compare the stagnation overpressure histories of gauges in the path of the diverging nozzle exit radius for the 26 *m* and 35 *m* drivers. This figure shows that, on the same test, these gauges experienced the icing effect at the same point in time. In fact, the data show that all six gauges located in the paths of these two drivers experienced the icing effect on Test 8. Conversely, Figure 25 shows the stagnation overpressure records from the gauges in the path of the diverging nozzle exit radii of the 19 *m* and 44 *m* drivers. This figure is consistent with Figure 23 in that it shows no evidence of probe icing for those in the flow path of the drivers near the floor of the expansion section.

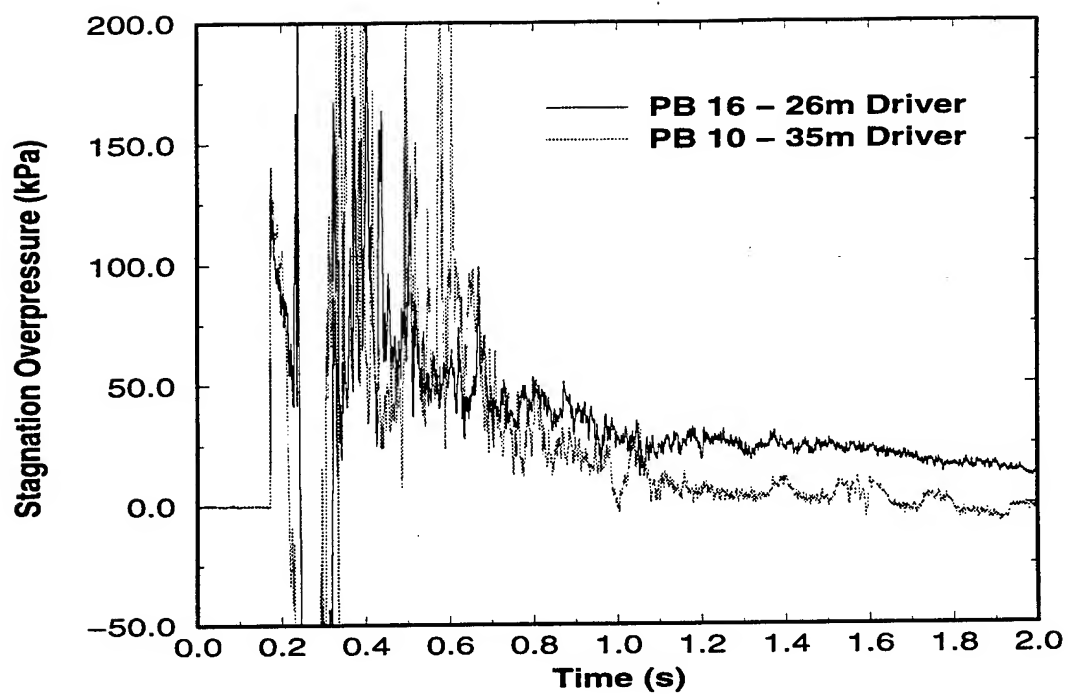


Figure 22. Test 8 Stagnation Overpressure from Gauges PB16 and PB10

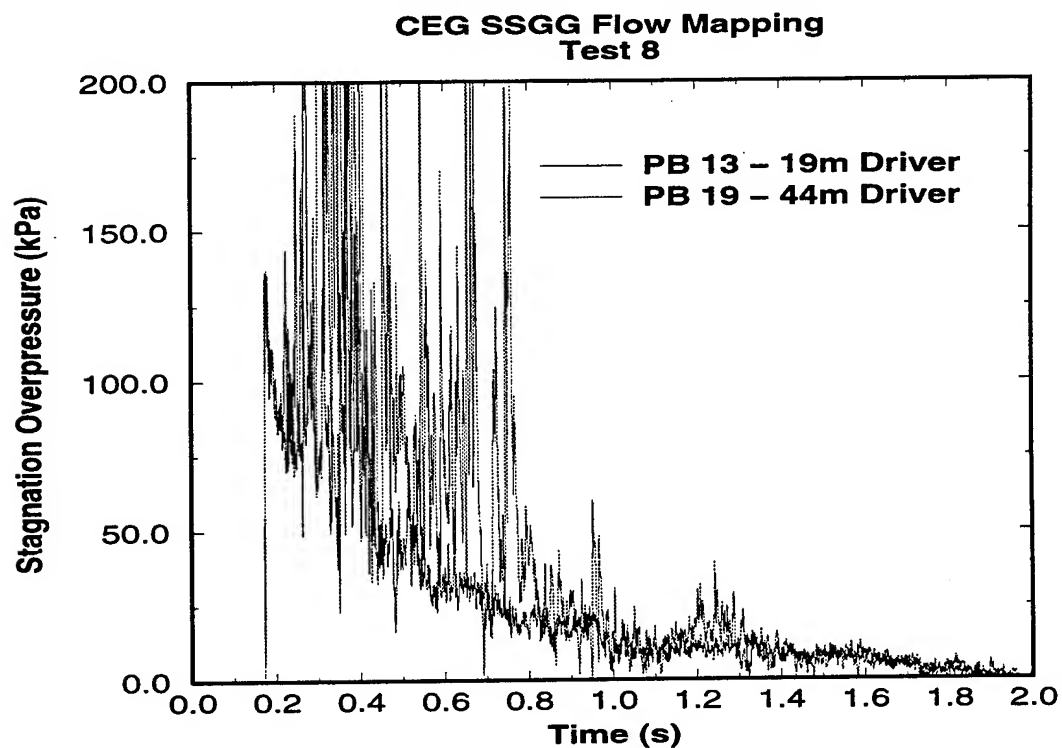


Figure 23. Test 8 Stagnation Overpressure from Gauges PB13 and PB19

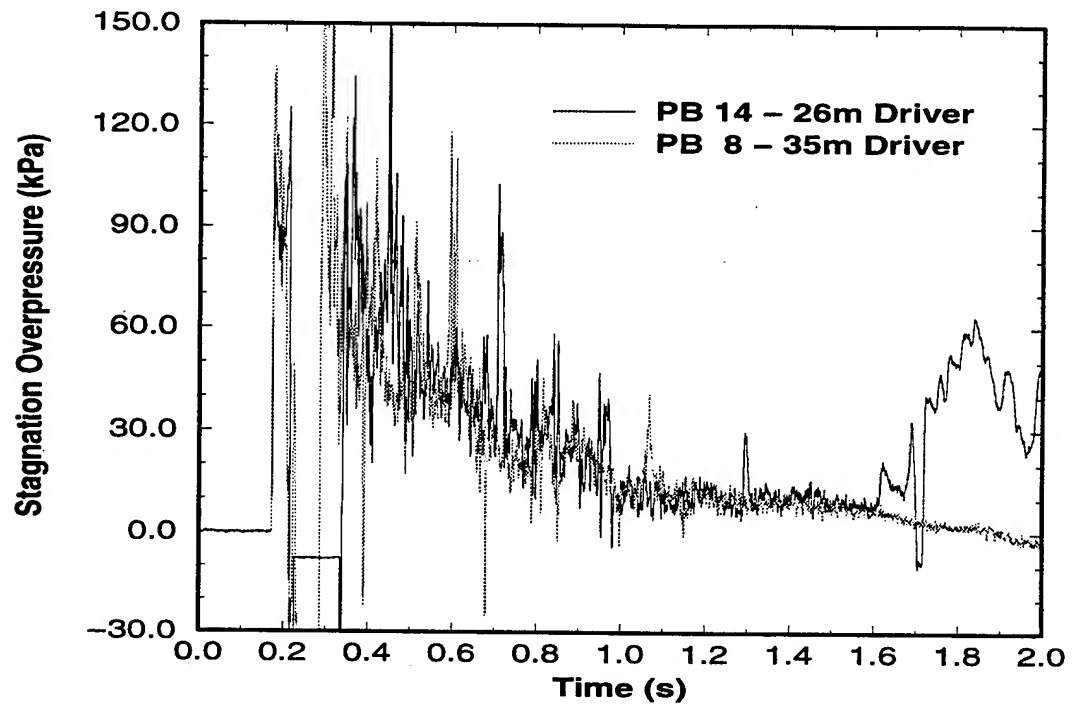


Figure 24. Test 8 Stagnation Overpressure from Gauges PB14 and PB8

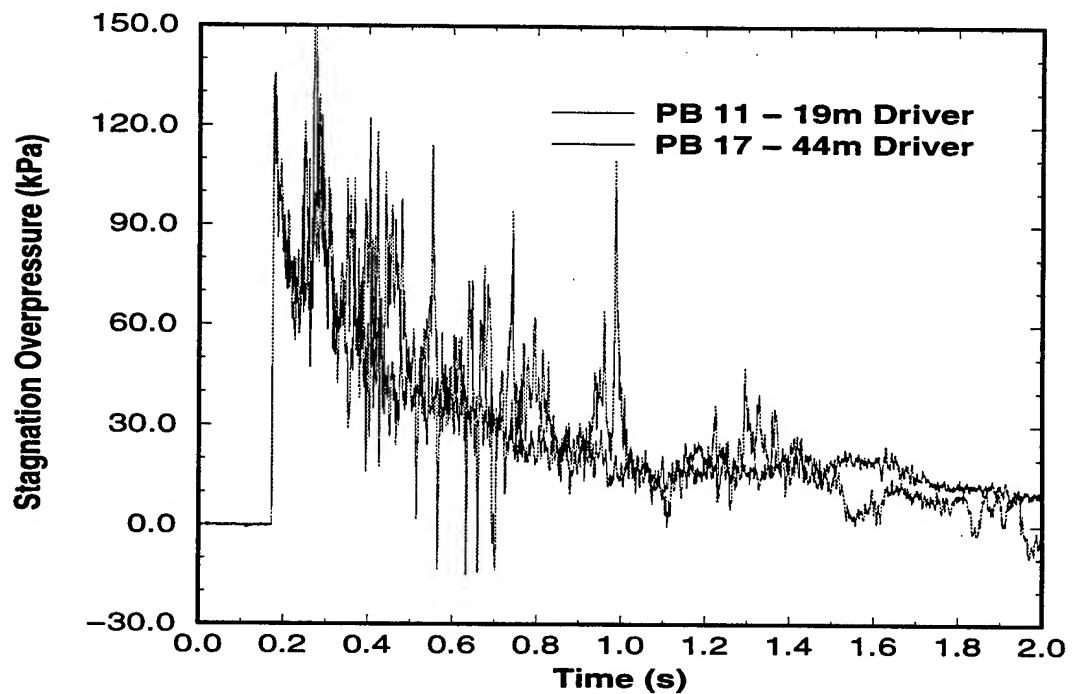


Figure 25. Test 8 Stagnation Overpressure from Gauges PB11 and PB17



A possible explanation for this occurrence of the dropout effect on the high gauges is the available area for entrainment of ambient air into the expansion section. The structure which supports the drivers and nozzles consists of a network of steel beams and a concrete reaction mass, all of which tie into the ground. Even though the upstream end of the SSGG expansion section is open to the surrounding atmosphere, this structure restricts the available area in which air can be entrained around the 19 m and 44 m drivers near the floor. On the other hand, far less support structure exists near the top of the expansion section which allows ambient air to be more readily entrained into the expansion section. The mixing of moist, entrained air, with the cool, expanded driver gas is believed to cause the formation of small ice crystals in the flow.

Lastly, the Test 8 stagnation overpressures from gauges located between the flow paths of the drivers are presented in Figure 26. Here, the flow histories from the different locations in the expansion tunnel are consistent with one another. The average stagnation overpressure impulse from these three gauges at a time of 2 s is 31.03 kPa·s.

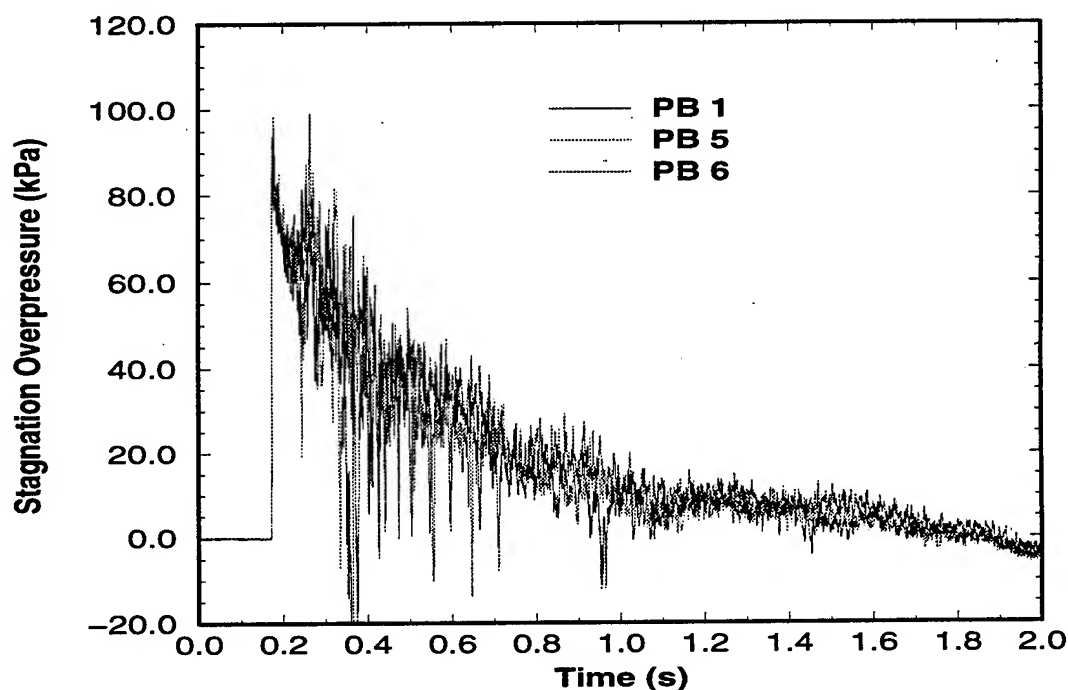


Figure 26. Test 8 Stagnation Overpressure from Gauges Between Drivers

#### 4. SUMMARY

A series of eight tests was performed to map the flow in the expansion tunnel of the SSGG large blast simulator. Four of the eight tests provided a set in which data were gathered at two longitudinal positions in the expansion tunnel, each at the same two overpressure levels. Analysis of these tests was performed by comparing flow characteristics from different gauge locations for a given test.

The static overpressure histories were found to be uniform across the entire cross sectional area of the tunnel for all of the tests. The data from the static and stagnation overpressure histories at the 67.5 *m* test section reveal a highly uniform environment for equipment testing throughout the range of overpressure levels.

Some evidence of jet flow was found from stagnation overpressure histories measured at the 22.5 *m* measurement position. This pattern occurred in the flow path of the 44 *m* driver on 20 *kPa* overpressure test. Additional evidence of driver jet flow at the 22.5 *m* measurement position was found in the paths of each of the drivers on 80 *kPa* test. At both pressure levels, this shear flow diffuses resulting in the aforementioned uniform flow field at the test section.

This experimental effort provides a valuable set of three-dimensional, time dependent, turbulent flow field data which can be used for validation of CFD codes. The data should be of assistance in the evaluation of the characterization tests of the U.S. LB/TS.

# EXPERIMENTAL AND NUMERICAL STUDY OF FLOW IN MULTI-DRIVER LARGE BLAST SIMULATORS

## PART III: 3-D Numerical Simulations

S. Schraml  
U.S. Army Research Laboratory  
AMSRL-WT-NC  
Aberdeen Proving Ground, MD 21005-5066 USA

### 1. BACKGROUND

Computational Fluid Dynamics (CFD) techniques are routinely employed to solve a wide variety of problems in the field of nuclear and conventional blast. Such modeling efforts typically fall under one of two categories, the simulation of blast flow interaction with specific types of targets, and the numerical simulation of time-dependent flow in shock tubes and blast simulators. Many examples of these types of modeling efforts have been presented at previous gatherings of MABS. One common thread that links the vast majority of these studies is that most of them employed an approach which was a one-dimensional (1-D) or two-dimensional (2-D) approximation of a more complex system.

This simplifying approach has practical benefits in both experimental and computational studies. From an experimental standpoint, reduction of one of the spatial dimensions can significantly reduce the cost of fabrication of test articles and instrumentation requirements. The simplified geometry often leads to an improved understanding of the blast phenomena at hand. In some cases, as described in Part I of this paper, experimental configurations are geometrically simplified for the purpose of making direct comparisons to 2-D computational predictions.

This geometric simplification offers several obvious advantages to the world of numerical simulation. A 2-D computational domain is a discrete collection of points which fall onto the curves that define the model. In 3-D these curves project into complex surfaces whose shape may require a great deal of data to sufficiently describe. In fact, much of the time spent in generating a 2-D model lies in the abstraction of a true three-dimensional (3-D) geometry into a 2-D computational domain. Like the advantage offered to the experimenter, model simplification may reduce the complexity of the phenomena under consideration and therefore ease interpretation of the results. But easily the most significant reason behind the use of geometrically simplified numerical models is the extraordinary cost associated with detailed 3-D computation.

These approximations, however, reduce the accuracy and reliability of numerical simulation. The work described in this paper focuses on the recognition that 3-D numerical simulation will play an increasingly large role in assessing the survivability of military equip-

ment in blast environments. Presently, large numbers of 1-D and 2-D simulations are used to carry out studies of time-dependent fluid flow in the free field, either over military equipment or within blast simulators. The results of these many calculations are employed to develop empirical relationships between the governing parameters of the problems. The relationships can then be used to quickly determine the behavior of one parameter with the variation of another. Currently, 3-D CFD simulations of blast phenomena are used as a final, confirming check on the study, if used at all.

The reason for this lies in the cost of 3-D numerical simulation. A model with sufficient resolution to capture the driving flow phenomena in all three spatial dimensions can have millions of grid points. Solution of time-dependent flow such as blast requires a converged solution to be computed for every time step. In other words, the fluid state at each of the millions of grid points must be computed for each time step. Typical tactical nuclear blast waveforms have a positive phase duration as long as two seconds. Tens of thousands of time steps may be required to march this solution through the time period of interest. Consequently, a 3-D numerical simulation of a time-dependent flow may require the calculation of  $10^9$  to  $10^{11}$  grid point fluid states. Such computations take hundreds of hours to complete on today's most powerful supercomputers.

Despite these obstacles which inhibit the present utility of 3-D CFD simulations for blast modeling, it is advantageous to continue to pursue the process of validating CFD algorithms for future use. Recent advances in scalable, parallel computer technology offer the possibility of 3-D numerical modeling of blast effects in a production environment. Research performed at ARL<sup>13, 14</sup> has demonstrated significant performance enhancements of CFD algorithms on massively parallel computers. By validating the predictive capability of candidate 3-D flow solvers for blast modeling, future efforts can be concentrated on modifying and optimizing these codes for execution on scalable, parallel computers. This part of the paper documents the validation of two different 3-D CFD codes for blast modeling through the simulation of time-dependent flow in the SSGG.

## 2. DESCRIPTION OF FLOW SOLVERS

The two fluid dynamics codes selected for validation were the second order, hydrodynamic, advanced research code (SHARC) and the universal solution algorithms, real gas (USA-RG) code. Two-dimensional versions of both of these codes have been used to solve a wide variety of blast problems.<sup>15, 16</sup>

SHARC is an explicit Euler<sup>17</sup> solver<sup>18</sup> which was derived from the HULL code which was originally developed at the U.S. Air Force Weapons Laboratory for the purpose of modeling nuclear blast loading on missile silos.<sup>19</sup> The underlying algorithm of SHARC is a finite difference scheme that employs a rectangular discretized mesh to model the computational domain. The algorithm is a discretization of the Euler equations, a subset of the Navier-Stokes<sup>17</sup> equations, which contain no viscous terms. The SHARC solution algorithm is second order accurate in space and time and also offers a  $k-\epsilon$  turbulence model, which improves the capability of the code in cases that involve shear flow.<sup>20</sup> The code supports

2-D axisymmetric, 2-D cartesian and 3-D cartesian geometries. Variable spacing of grid points along each coordinate axis is allowed. Complex shapes are modeled by placing a perfectly rigid, perfectly reflective material, known as "island" material, in the rectangular (2-D) or box shaped (3-D) computational cells. The degree to which computational results match experimental results is affected by the grid resolution used. In general, higher grid resolutions lead to better agreement. Increasing grid resolution, however, can quickly lead to unreasonably long run times.

Like all explicit, time marching codes, the time step in SHARC is a function of the cell size, particle velocity and sound speed. For every iteration through time, a characteristic time scale for each cell in the grid is determined by the ratio of the cell size, divided by the sum of the particle velocity and fluid sound speed in that cell. The smallest characteristic time of all the cells determines the time step of the entire computational domain. As a result, increasing the grid resolution will cause a drop in the time step, as well an increase in the number of cell in the domain. For example, doubling the grid resolution of the 3-D SHARC computation will increase the run time by a factor of 16, due to the factor of two drop in the time step and the doubling of the number of grid points in each coordinate direction. Thus, the grid resolution selected for a computational study involves a trade off between the accuracy of the result and the time required to obtain a solution.

The USA-RG code discretizes the Navier-Stokes equations using a finite volume, Roe's Riemann solver, total variation diminishing (TVD), implicit algorithm.<sup>21</sup> The implicit scheme produces an algorithm that is well suited for blast wave calculations because upwind flux difference splitting with TVD achieves second order accuracy without introducing spurious oscillations near discontinuities. Strong gradients and complex flow fields are resolved accurately. TVD schemes are often referred to as modern shock capturing methods because the numerical dissipation terms are nonlinear. That is, the amount of dissipation is controlled by automatic feedback mechanisms that can vary from one grid point to another. Also, the dissipation is scaled to the underlying eigensystem of the hyperbolic Euler equations. In classical shock capturing methods, the numerical dissipation terms are either linear so that the same amount of numerical dissipation is added at all grid points or the numerical dissipation is controlled by parameters that must be optimized. Classical shock capturing methods typically result in oscillatory solutions at strong discontinuities.

The conservative nature of the scheme captures shocks and other discontinuities automatically. The finite volume philosophy ensures energy and mass conservation at interior grid points. The implicit version of the scheme requires more computations per integration step than the explicit version but permits larger time steps which, for mathematically stiff (viscous) problems, reduces computational expense. The code has the capability to handle multi-zone grids and has several turbulence models available. The turbulence models available are a modified Baldwin-Lomax<sup>22</sup> (0 equation),  $k-L$ <sup>23</sup> (1 equation), and  $k-\epsilon$ <sup>24</sup> (2 equation) models.

The USA-RG code and other computational fluid dynamics codes like it employ gridding techniques that are quite different from those of SHARC. In particular, the coordinate axes are not required to be straight lines. Rather, the coordinate axes can be defined in practically

any form necessary to define the complex shape of the system being modeled. This type of grid is referred to as "body conformal" because the grid can be wrapped around the body of interest, thus modeling it with a high level of accuracy. An additional level of flexibility is available to the USA-RG code in that it supports multi-zone grids. This basically means that numerous independent body conformal grids can be combined in one computational model to represent the system with a high degree of fidelity without placing a large number of grid points in regions of uniform steady flows.

### 3. 3-D SHARC MODELS

The SHARC code representation of the SSGG facility was developed to model as closely as possible the driver systems and expansion section of the blast simulator. The model takes advantage of the symmetry of the facility about the vertical center plane. The expansion section of the SSGG is 105 m long, with an active rarefaction wave eliminator (RWE) located at the downstream end. The purpose of the RWE is to suppress the generation of a rarefaction wave which forms when the shock front exits the downstream end of the expansion section.<sup>1</sup> Such disturbances in the flow field can destroy the fidelity of the simulated blast environment. An RWE modifies the exit flow from the expansion tunnel in such a way that it makes the tunnel appear infinitely long. In order to avoid the computational complexity of modeling the dynamics of the flow through the RWE, the expansion section in the 3-D SHARC model was made sufficiently long so that no disturbance to the flow field would be observed at the measurement locations during the time of interest.

Two different 3-D SHARC models of the SSGG were developed, the first of which is illustrated in Figure 1. This figure shows the half of the facility which was represented by the model. The vertical center plane was represented as a reflective plane to account for the geometric symmetry of the problem. This figure shows the four unique lengths of driver, each connected to a cylindrical throat section which empty into the diverging nozzles. This figure also demonstrates the means by which the model is shaped by placement of "island" cells in the grid. The actual diverging nozzles are conical shaped, but the figure shows the diameter change in a series of steps. Each step corresponds to a transition of the island material from one grid plane to the next. This characteristic is also evident in the shape of the cylindrical driver tubes.

As discussed in Part II of this paper, the upstream end of the expansion section of the SSGG is open to the surrounding atmosphere. The propagation of the shock down the expansion tunnel causes the ambient air to be entrained into the expansion section and can influence the flow histories there. The initial model SHARC was not developed with the capability to simulate this effect. In Figure 1 one can see the solid wall at the upstream end of the expansion section which connects the diverging nozzles to the walls of the tunnel. Because the entrainment of ambient air is considered to be an important characteristic of the time-dependent flow, a second 3-D SHARC model was developed to provide ambient air surrounding the facility. Figure 2 shows this later model. In this figure, the driver tubes have been eliminated to make the spacing between the diverging nozzles more noticeable.

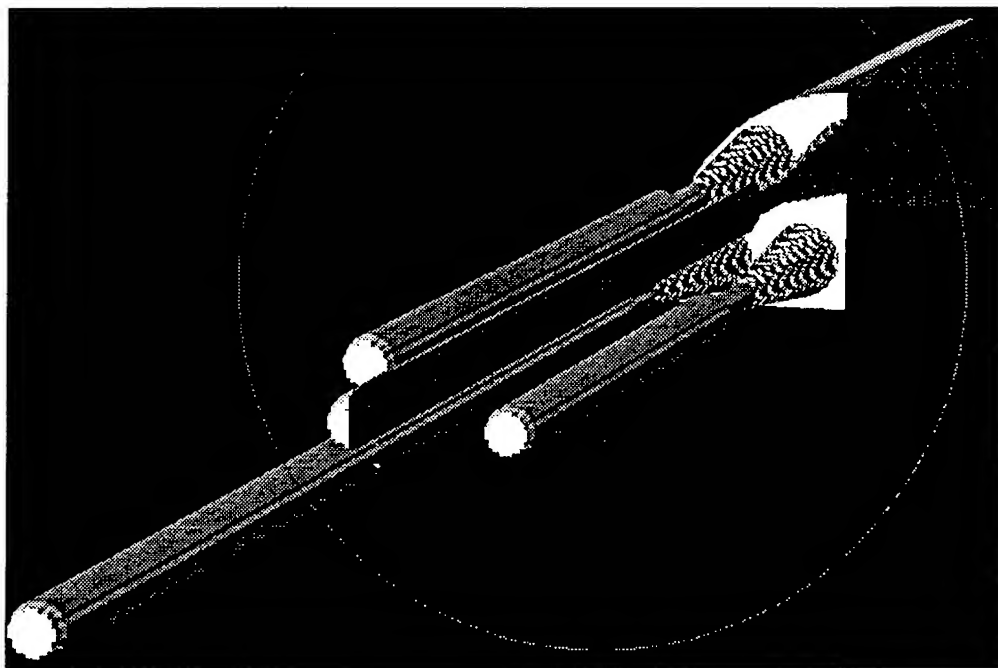


Figure 1. Initial SHARC Model of SSGG



Figure 2. SHARC Model of SSGG for Ambient Air Entrainment

The figure also shows the model reflected about the plane of symmetry to provide a more realistic view of the facility. Figure 2 illustrates that the structural elements which support the driver tubes are not present in the model. As a result, this model has a greater available area for flow to be entrained into the expansion section than the actual blast simulator.

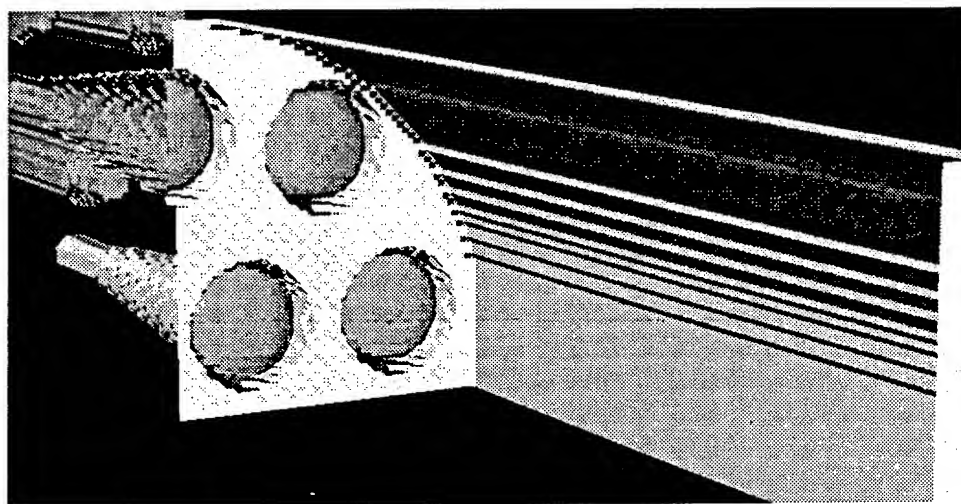
### 3.1. Preliminary SHARC Calculations

The models presented above were developed and tested before the execution of the SSGG experiments described in Parts I and II. These test computations were simulations of experiments which had been performed in the SSGG in 1987 to determine the effects of expansion tunnel blockage on blast flow histories. Figure 3 is from a SHARC calculation which simulates one of the tests in that series in which a shock overpressure of nominally  $75\text{ kPa}$  was produced in the expansion section. The presence of the solid wall at the upstream end of the expansion section shows that this calculation was performed using the model which did not provide ambient air entrainment into the tunnel. The figure shows the formation of the primary shock at  $16\text{ ms}$ ,  $20\text{ ms}$  and  $28\text{ ms}$ . Here a time of zero corresponds to the initiation of flow at the diaphragm position. In Figure 3a, four individual shock fronts produced in the different drivers are evident. At this point in time, the primary shocks have not yet entered the expansion section. At  $20\text{ ms}$ , Figure 3b shows the individual shocks expanding into the expansion section and beginning to coalesce to the wall, floor and interfaces between shocks. Finally, Figure 3c presents a nearly planar shock front at  $28\text{ ms}$  after flow initiation. This series of figures presents that, according to the computation, the shock front is uniform near the upstream end of the expansion section.

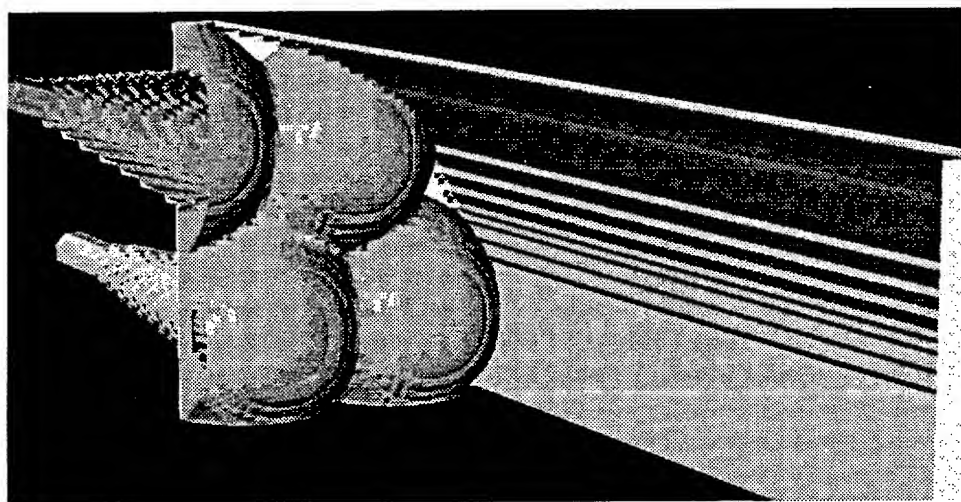
To assess the influence of ambient air entrainment into the SSGG expansion tunnel, a calculation was performed using the second 3-D SHARC model. This calculation used the same initial conditions as the first test calculation. The results of the two calculations are presented in Figure 4 and show stagnation overpressure histories recorded in the expansion section at a distance of  $52.5\text{ m}$  from the upstream end of the expansion section. This figure shows two significant influences of the inflow on the recorded histories in the tunnel. First, the calculation without the entrainment capability produced a significant increase in the stagnation overpressure between  $115\text{ ms}$  and  $180\text{ ms}$  after shock arrival at the measurement position. This increase is caused by the arrival of the driver gas at the measurement position. As described in Part II, the driver tubes in the SSGG are pressurized with air by compressors. At the time of flow initiation, the temperature of the compressed driver air is about the same as the surrounding atmosphere. When the flow is initiated, the driver gas expands into the tunnel which causes the driver gas to cool. This results in an increase in the density of the driver gas and is the cause of the increase in the stagnation overpressure history of Figure 4. In the same figure, the curve generated by the inflow model has a much smaller increase at this same point in time, so small in fact that it would be difficult to differentiate it from the other oscillations if not for the result of the calculation with no inflow. The increase in stagnation overpressure resulting from the arrival of the driver gas is smaller for the inflow case because the entrained, ambient air is at a higher temperature than the expanded driver gas and mixes with the driver gas before arriving at the measurement position. The mixing



a.



b.



c.

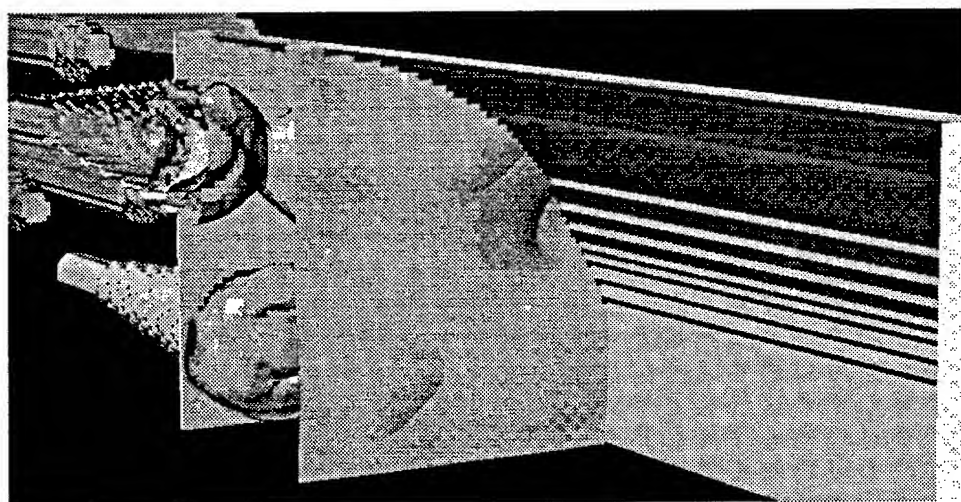


Figure 3. SHARC Simulation of Shock Formation at a.) 16 *ms*, b.) 20 *ms*, and c.) 28 *ms*

of the driver gas with the entrained air increases the temperature of the expanded driver gas, thereby decreasing its density.

The other effect of ambient air entrainment which is noticeable in Figure 4 is the elevated level of the record from the inflow model in late time. This elevated pressure level results from the increased mass flow through the expansion tunnel created by the addition of the entrained ambient air. The elevated pressure level increases the impulse delivery to a test article, and thus the simulated weapon yield is increased. By comparison, the stagnation overpressure impulse of the model without the inflow is  $37.83 \text{ kPa}\cdot\text{s}$ , while that of the inflow model is  $42.57 \text{ kPa}\cdot\text{s}$  at  $870 \text{ ms}$  after shock arrival. At this point in time, the positive phase is not yet complete. It is logical to assume that by the end of the positive phase, the difference in stagnation overpressure impulse between these two records would be even greater.

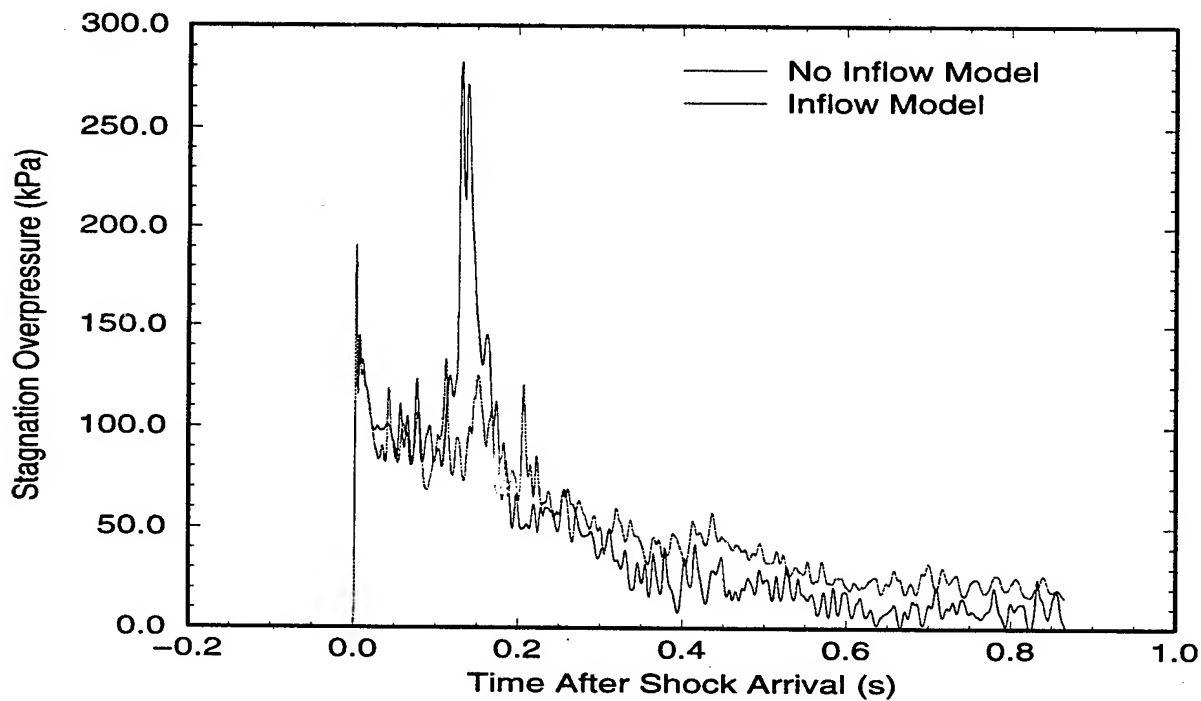


Figure 4. Comparison of SHARC Models with and without Ambient Air Entrainment

#### 4. SHARC CALCULATIONS MATCHING FLOW UNIFORMITY TESTS

After the preliminary test calculations were complete and the SSGG flow mapping tests were done, a series of 3-D SHARC calculations was performed to match the  $20 \text{ kPa}$  and  $80 \text{ kPa}$  tests from the experimental study. Based on the influence of the ambient air entrainment observed in the preliminary calculations, it was decided that the inflow model would be used for the remainder of the numerical study. This model employed a grid with 85 cells in the horizontal direction, distributed along lines normal to the plane of symmetry, 91 cells in the vertical direction normal to the ground plane, and 478 cells

in the longitudinal direction. The size of the cells varied throughout the grid, with the highest concentration of grid points in the area of the converging/diverging nozzles and the upstream end of the expansion section. In this region, a nominal cell size of 7 cm was used. This level of grid resolution placed ten computational cells across the diameter of each throat section, which is considered the minimum amount of cells required to capture the dominant flow characteristics. Additional grid resolution would lead to better definition of the flow structure, but would have made the calculations impossible to complete, even on the most powerful vector supercomputers.

A total of four SHARC calculations were performed with this model: two calculations without the turbulence model, and two using the  $k-\epsilon$  model. A summary of these calculations is provided in Table 1. At regular intervals during the execution of a calculation, the solution is saved in the form of a restart file. The restart file primarily contains the hydrodynamic variables at each grid point. For the cases in which the turbulence model was not used, a single restart file contained five hydrodynamic variables at each of the nearly 3.7 million cells in the grid. The resulting binary restart file for a non-turbulent SHARC calculation was 148MB in size. The turbulent SHARC calculation stores seven variables at each computational cell and the resulting restart file for the inflow model is 207MB.

**Table 1.** Summary of 3-D SHARC Calculations

Calculation	Nominal Shock Overpressure (kPa)	Solution Method	Computed Cycles	Flow Time (ms)	CPU Time (hours)
1	20	Euler	6058	800	45 (C-90)
2	20	Euler + $k-\epsilon$	4485	450	93 (C-90)
3	80	Euler	7516	1000	100 (X-MP)
4	80	Euler + $k-\epsilon$	13741	645	288 (C-90)

Table 1 clearly demonstrates the cost of this type of numerical simulation. For each of the cases, many thousands of computational cycles are required to step the solution through the time of interest. The additional cost of using the  $k-\epsilon$  turbulence model can be determined by comparing a non-turbulent calculation to its otherwise identical turbulent case. For each of the two overpressure levels, the turbulent calculation required more than double the computer time to march the solution through a shorter period of time. This is caused by the combined effect of an increased number of floating point computations to solve the two additional partial differential equations of the turbulence model, and the decrease in the time step which is caused by the numerical formulation of the turbulence model.

#### 4.1. SHARC Calculations of 20 kPa Tests

The first two SHARC calculations to match the flow mapping tests simulated the conditions of the 20 kPa overpressure shots of the test series, Tests 1 and 6. To assess the accuracy

of the calculations in simulating the flow in the expansion tunnel, the time history data generated by the calculations is compared to the data gathered from the experiments. To best assess the code's ability to model the basic flow parameters of pressure, density and velocity, the stagnation overpressure records from the experiments are used as the benchmark. In each of the comparisons, the turbulent and non-turbulent SHARC calculation results are plotted together with the appropriate experimental record to illustrate the differences of the solution methods and the accuracy of the simulations as compared to the experiments.

Figure 5 shows the Test 1 recording from gauge PB19 compared to the SHARC results. This gauge location is at the 67.5 *m* longitudinal position, in the path of the centerline of the longest driver. This figure shows several interesting characteristics of the SHARC predictions. The overall shape of the calculated histories closely follows the experimental data. The non-turbulent solution captures many of the features observed in the experimental data, but has a greater stagnation overpressure than the experiment 250 *ms* after shock arrival. The turbulent solution has a lower stagnation overpressure than the non-turbulent solution and lacks much of the secondary flow structure which is evident in the experiment and the non-turbulent case.

Figure 6 compares the stagnation overpressure from Test 1, gauge PB4, to the equivalent SHARC results. This gauge was positioned between the paths of two drivers. The figure shows a very similar result to the previous comparison. This is to be expected because, as discussed in Part II of this paper, the flow at the test section was found to be highly uniform at the 20 *kPa* and 80 *kPa* overpressure levels. In fact, the flow histories predicted by the turbulent and non-turbulent SHARC solutions are extremely uniform at this 67.5 *m* position. When many are plotted together from different point in the cross section, the curves almost exactly follow one another.

The SHARC results are compared to the Test 6 experimental data in Figures 7 and 8. Again the stagnation overpressure histories from gauges PB19 and PB4 were used. In Test 6, the instrumentation array was located at the 22.5 *m* position. The PB19 experimental result from this test showed signs of the production of jet flow from the 44 *m* driver. This is evident by the increase in stagnation overpressure beginning at about 400 *ms* after shock arrival and continuing for the remainder of the record. The SHARC non-turbulent prediction closely follows the experimental result up to the point where the experimental data increases. The stagnation overpressure of the SHARC turbulent result again was slightly lower than the experimental result.

The comparisons in Figure 8 show the same characteristics in comparison to gauge PB4 from Test 6. The non-turbulent prediction of stagnation overpressure very closely follows the experimental data, while the turbulent solution predicts a lower stagnation overpressure. The advantage of the turbulent solution is evident at about 50 *ms* after shock arrival when the experimental record decreases to approximately 10 *kPa*, then quickly recovers to about 17 *kPa*. The turbulent solution accurately predicts the minimum value and timing of the drop, but does not increase to as high a value as the experiment. The non-turbulent solution overpredicts the drop in stagnation overpressure, reaching a value of about 5 *kPa* and quickly

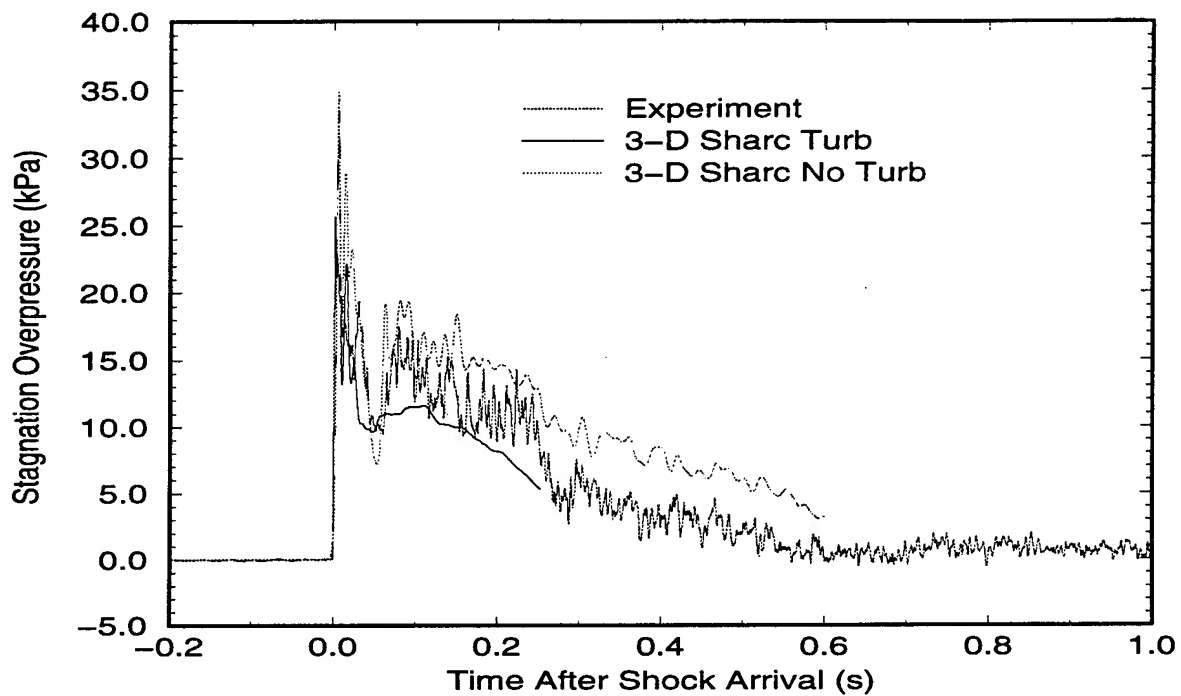


Figure 5. SHARC Simulations of Test 1, Gauge PB19

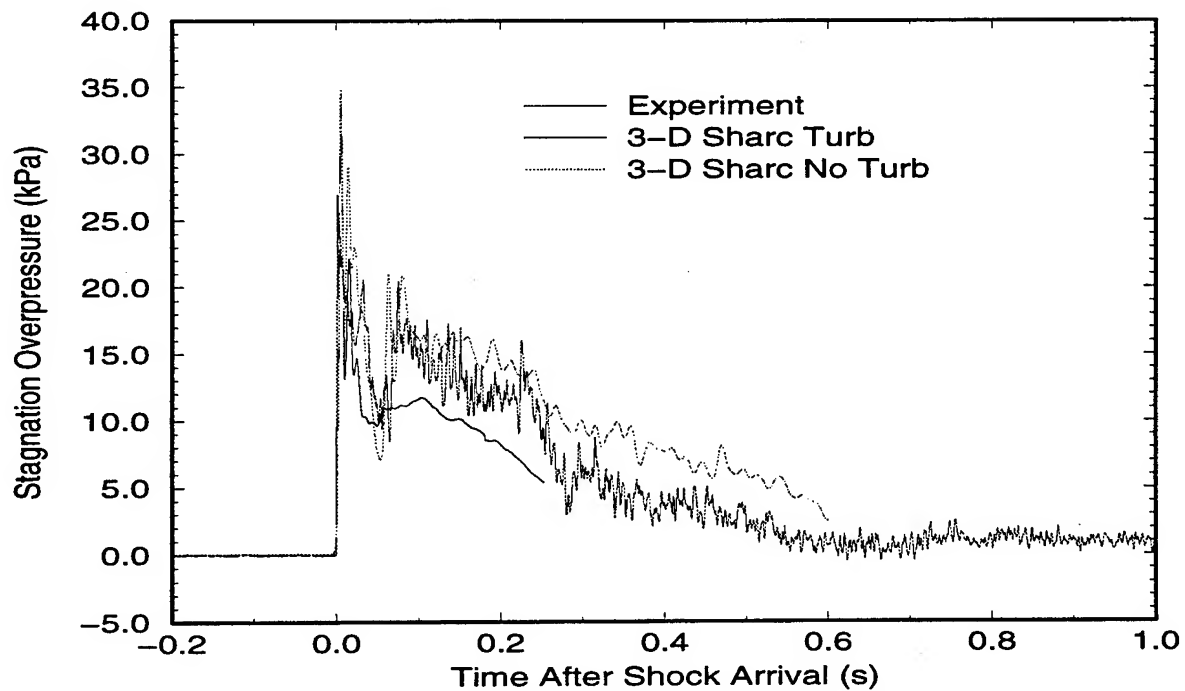


Figure 6. SHARC Simulations of Test 1, Gauge PB4

overcompensating by increasing to a value of 25  $kPa$ , after which it resumes following the experimental data.

The results of Figures 5 through 8 indicate that the  $k-\epsilon$  turbulence model is providing too much dissipation of the flow, thereby eliminating some of the significant flow features and secondary flow structure. This is believed to be the result of the low grid resolution used in the model. Two-dimensional computational studies with SHARC have demonstrated improved performance of the turbulence model with increasing grid resolution. Unfortunately, increasing the grid resolution of this model is not a viable option for the current class of vector supercomputers.

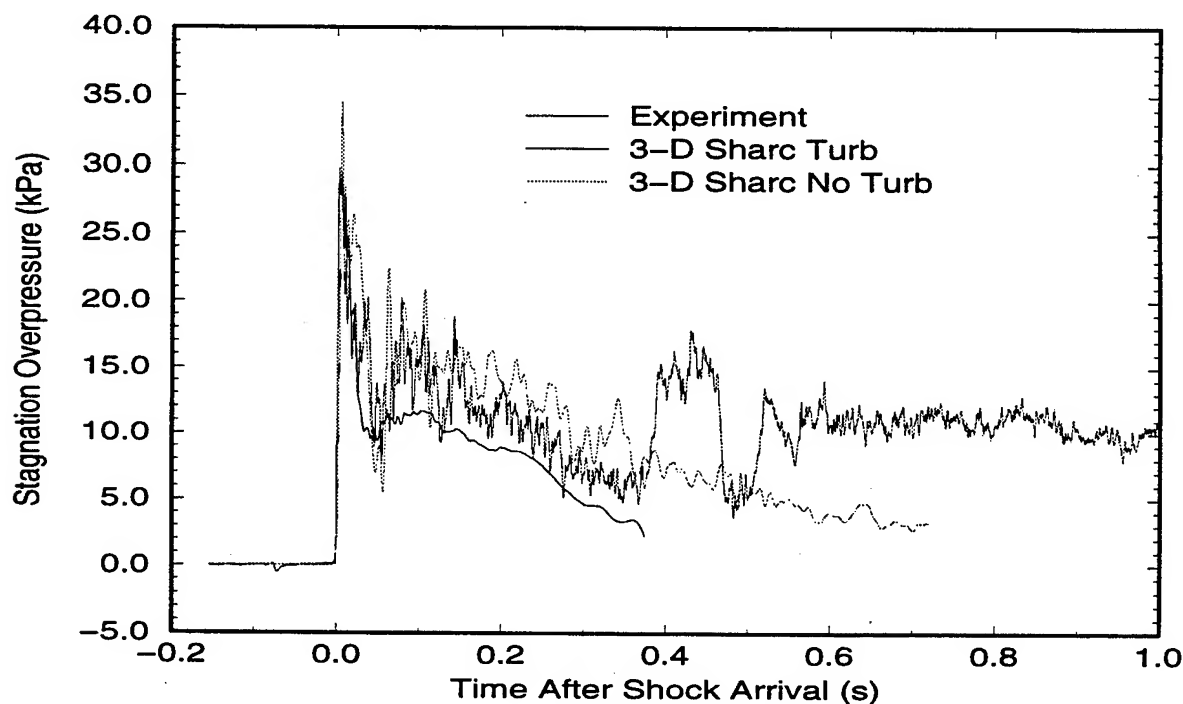


Figure 7. SHARC Simulations of Test 6, Gauge PB19

#### 4.2. SHARC Calculations of 80 $kPa$ Tests

The low grid resolution makes the non-turbulent simulation of the 20  $kPa$  tests appear to be a better prediction than the turbulent solution. However, it should be noted that these comparisons apply to a flow with relatively weak shocks and small gradients. The more challenging test of both solution methods lies in the simulation of the 80  $kPa$  tests. The results of these calculations are presented in Figures 9 through 12, in which the turbulent and non-turbulent predictions are again compared to the PB19 and PB4 stagnation overpressure records. The first two of these figures plot the records from Test 2 which were recorded at the 67.5  $m$  position. In Figure 9 the two SHARC solutions follow similar patterns which are initially greater than the stagnation overpressure of the experiment, then follow more closely after 250  $ms$ . Like the 20  $kPa$  calculations, the turbulent solution lacks some of the

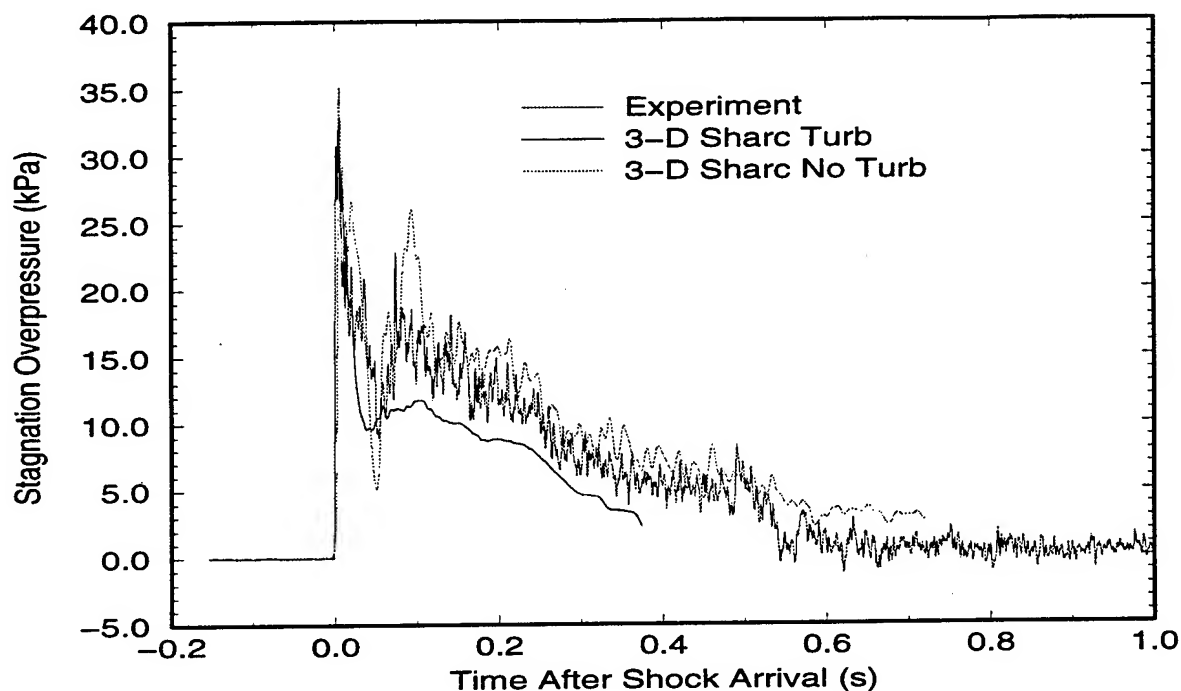


Figure 8. SHARC Simulations of Test 6, Gauge PB4

secondary flow structure of the non-turbulent solution and the experiment, an indication that the use of the  $k-\epsilon$  model with the low grid resolution provides excess dissipation of the flow. The comparison of the SHARC solutions to the recording of gauge PB4 is presented in Figure 10 and again shows the two SHARC solutions following similar paths. Both computational results are slightly lower than the experimental stagnation overpressure for most of the history. However, the agreement between the calculations and the experiment is very good.

The most interesting comparisons between the 3-D SHARC calculations and the experiments is at the 22.5  $m$  location for the other 80  $kPa$  shot, Test 8. The stagnation overpressure of the two calculations is compared to the PB19 record in Figure 11. In this figure, the experimental data show signs of highly turbulent jet flow from the 44  $m$  driver at the 22.5  $m$  position. The non-turbulent calculation overpredicts the coherence of the driver jet and predicts stagnation overpressures which are well outside the limits plotted in Figure 11. In fact, the non-turbulent solution has sustained stagnation overpressure levels of over 3000  $kPa$  at certain times in the record. In contrast, the calculation with the  $k-\epsilon$  turbulence model generally follows the path of the experimental data, while still lacking the secondary flow structure.

Finally, the PB4 stagnation overpressure data recorded on Test 8 is compared to the SHARC calculation in Figure 12. This figure shows that the non-turbulent calculation significantly underpredicts the stagnation overpressure at this gauge location between two drivers, an artifact of the artificially strong driver jet flow produced by the non-turbulent

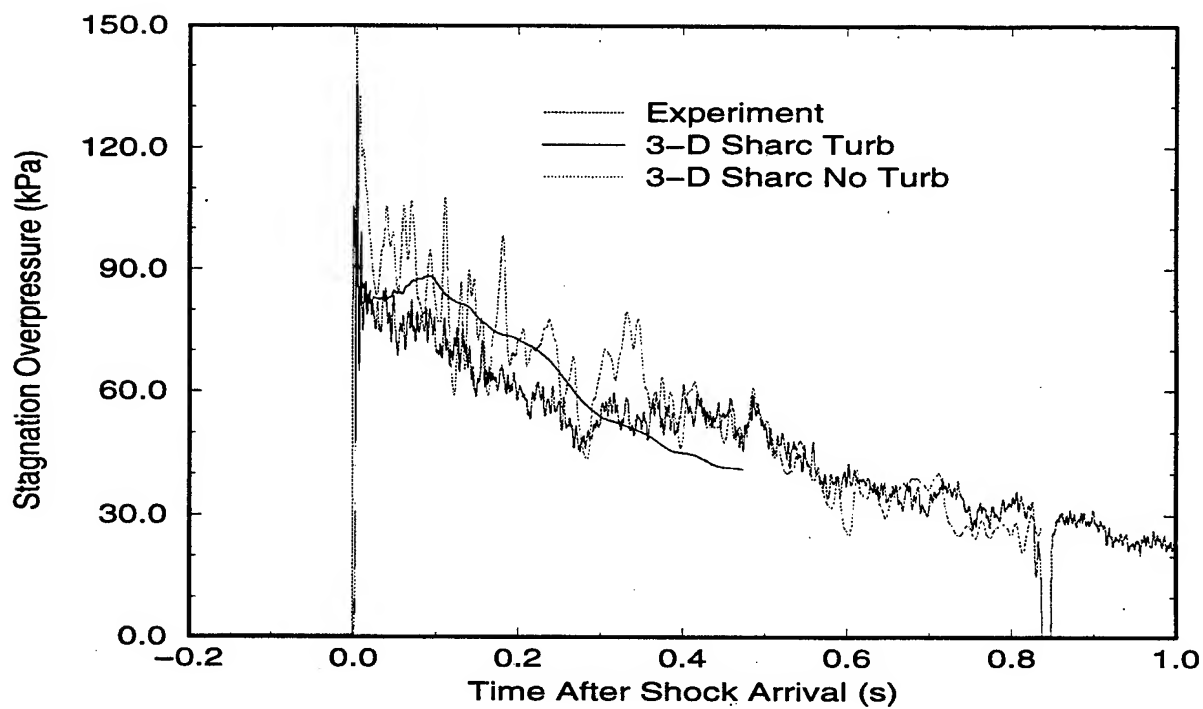


Figure 9. SHARC Simulations of Test 2, Gauge PB19

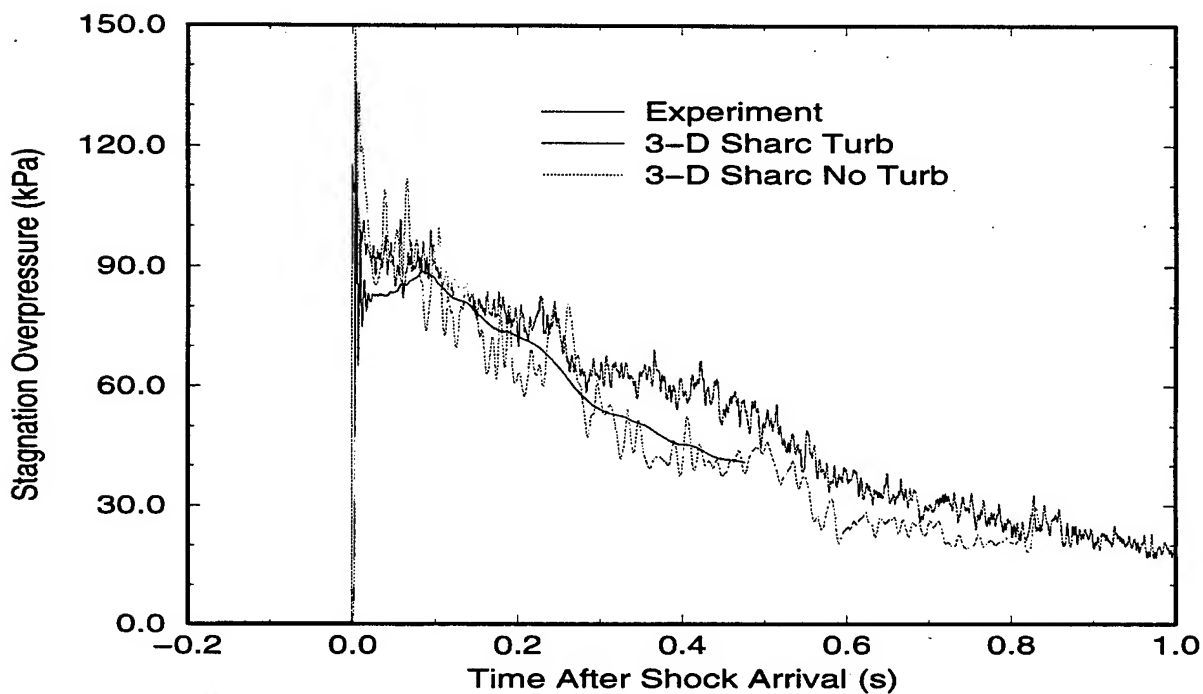


Figure 10. SHARC Simulations of Test 2, Gauge PB4



solution. Consistent with the other figures, the turbulent solution accurately predicts the path of the experimental history, but lacks some of the flow structure.

The excess dissipation of the turbulent solution results in a computed flow field which is uniform at the 22.5 m measurement position. However, the experimental data from Test 8 indicate the presence of some jet flow from the drivers which diffuses prior to reaching the 67.5 m test section.

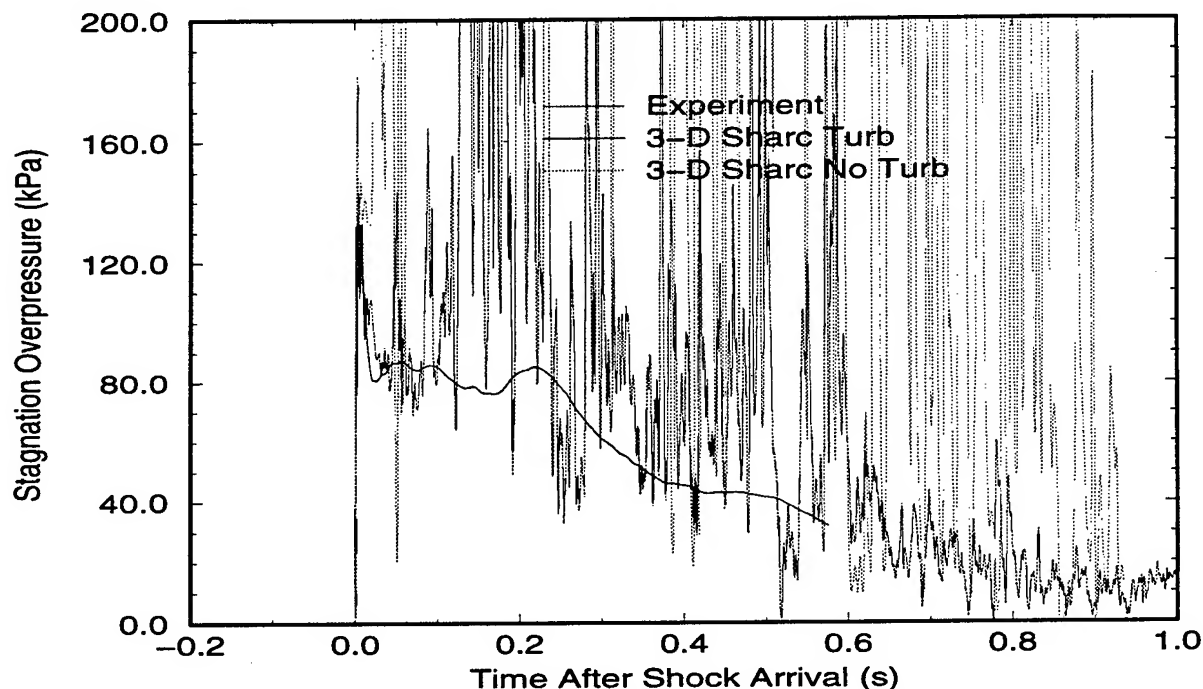


Figure 11. SHARC Simulations of Test 8, Gauge PB19

## 5. USA-RG3 MODEL

The USA-RG3 code model consists of a collection of body conformal grids, or zones, which are combined to define the shape of the drivers and expansion tunnel of the SSGG. Like the 3-D SHARC models, the USA-RG3 model takes advantage of the symmetry of the facility which exists at the vertical center plane of the SSGG. The expansion section is again made artificially long so that disturbances generated at the exit boundary of the model may not arrive at the measurement locations within the period of interest. The USA-RG3 model was designed to allow entrainment of the surrounding ambient air into the expansion section. Figure 13 provides a view of the upstream end of the expansion section of the USA-RG3 model. In this figure, the driver tubes and converging nozzles have been dropped to illustrate the grid definition in the throat sections at the diaphragms. The figure also shows how the shape of the grid defines the surfaces of the diverging nozzles and expansion section. The zones which provide the surrounding ambient air for entrainment are not shown, but the

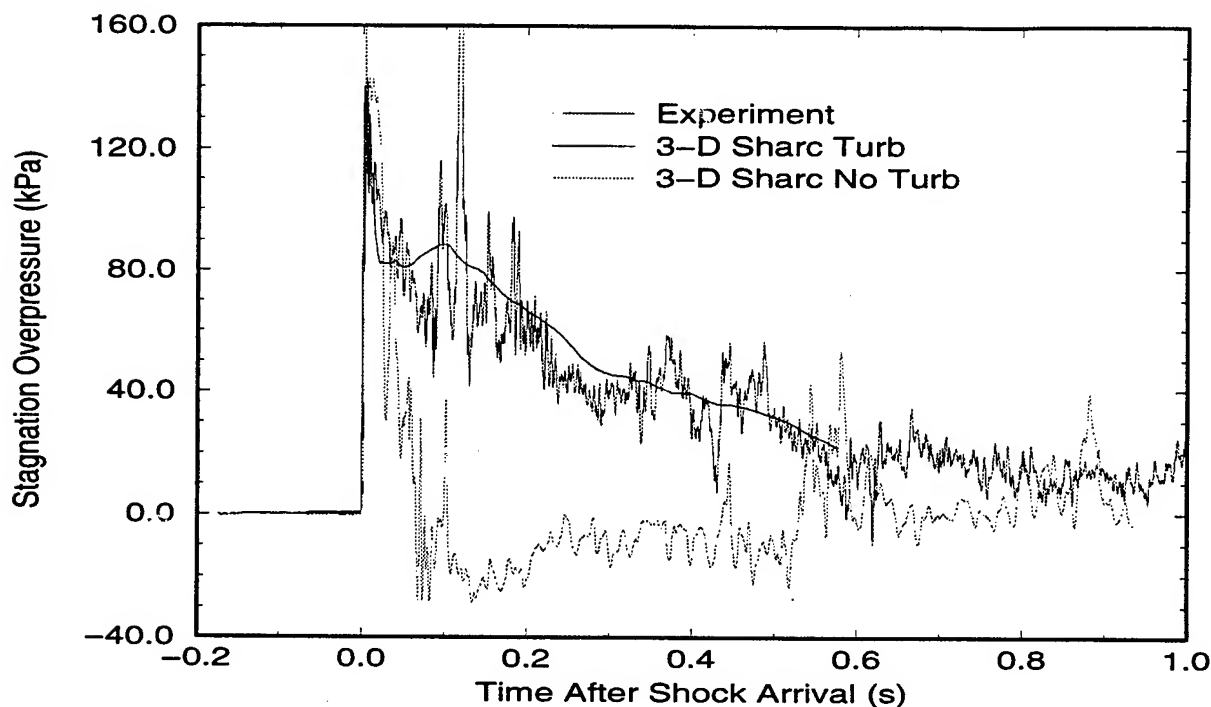


Figure 12. SHARC Simulations of Test 8, Gauge PB4

grid definition at the upstream end of the tunnel for the area between the drivers is evident in the figure.

The multi-grid model contains 21 independent zones, each with its own generalized, curvilinear coordinate system. The interfacing grid points at the zone boundaries are aligned and the flow solver allows flow across these interfaces through communicating boundary condition routines. A total of about 780 thousand grid points are used in the USA-RG3 model of the SSGG. The grid was developed with the greatest concentration of points near the upstream end of the expansion section, and in the converging/diverging nozzle area. Similar to the SHARC model resolution, ten computational cells were placed across the diameter of each throat section. This resolution results in 100 cells within the cross section of each driver at every longitudinal grid point. The implicit solution of the Navier-Stokes equations with  $k-\epsilon$  turbulence modeling involves the solution of 5.5 million simultaneous equations at each time step, and requires about 400MB of core memory.

## 6. SHARC CALCULATIONS MATCHING FLOW UNIFORMITY TESTS

A series of USA-RG3 calculations was performed to match the 20  $kPa$  and 80  $kPa$  shots from the SSGG flow mapping tests. These calculations were executed in a similar manner to the set of SHARC calculations described above. Two calculations were run at each of the shock overpressure levels, one an inviscid flow solution, and the other a viscous solution using the  $k-\epsilon$  turbulence model.

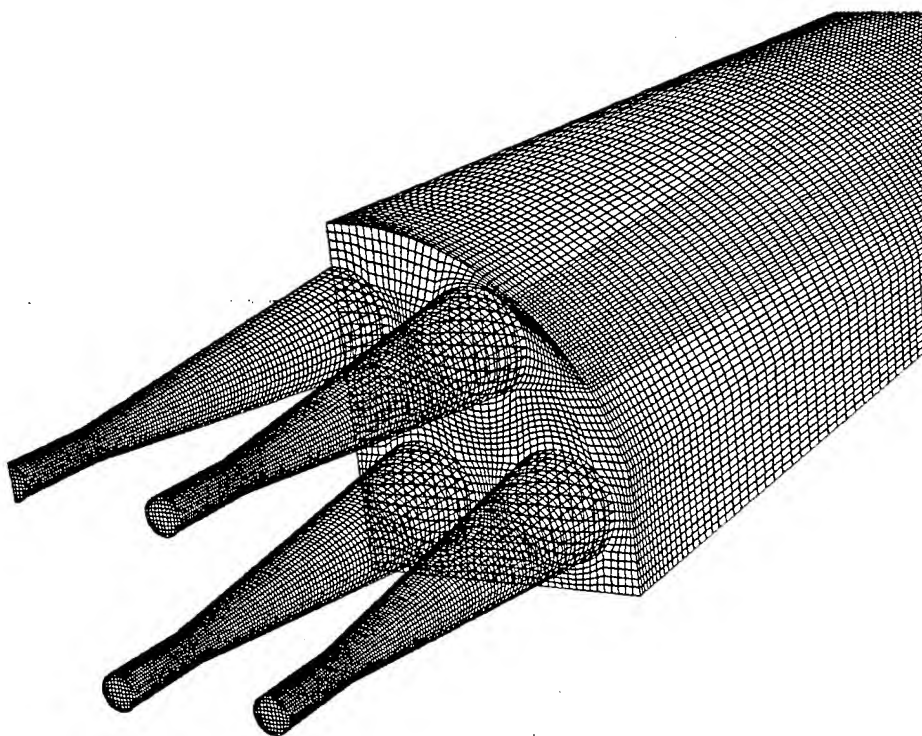


Figure 13. USA-RG3 Model of SSGG

Table 2 provides a summary of some of the details of these calculations. The third column in the table, entitled *Solution Method* describes the set of equations which were used to solve the equations of motion of the fluids. In this column an Euler solution method refers to the solution of the fluid motion equations without the viscous terms utilized. Conversely, N-S +  $k-\epsilon$  in the table describes a Navier-Stokes solution (viscous terms utilized) with the 2-equation  $k-\epsilon$  turbulence model employed. All of the USA-RG3 calculations were run on a Cray C-90 vector supercomputer.

Table 2. Summary of USA-RG3 Calculations

Calculation	Nominal Shock Overpressure (kPa)	Solution Method	Computed Cycles	Flow Time (ms)	CPU Time (hours)
1	20	Euler	8400	919	62
2	20	N-S + $k-\epsilon$	8400	919	115
3	80	Euler	9200	1459	68
4	80	N-S + $k-\epsilon$	9200	1459	126

In Table 2, one can see that the number of cycles and the simulated flow time are common between an Euler solution and its corresponding Navier-Stokes solution. This is different from the SHARC code results in which the turbulent solution required not only

more CPU time per cycle, but also a greater number of cycles to reach the same simulated flow time. As described earlier in the case of the SHARC code, the turbulence model is explicit and the turbulence quantities have an effect on the time step, generally acting to decrease it. In the case of the USA-RG3 code, the solution method is completely implicit. As a result, the time step is not affected by the turbulence model.

### 6.1. USA-RG3 Calculations of 20 kPa Tests

The flow uniformity analysis of Part II of this paper and the discussion of air entrainment earlier in this part both described the significance of the density of the expanded driver gas on the ideal nuclear blast simulation. The results of the USA-RG3 simulation of Tests 1 and 6 help to describe the evolution of the driver gas as it moves downstream in the expansion tunnel and mixes with the entrained air and the tunnel gas. Figures 14 and 15 present illustrations of the density distribution in the shock tube at 172 *ms* and 302 *ms* respectively. In these figures, obtained from the viscous, turbulent solution, density levels are depicted by the shading of various surfaces in the computational domain. The vertical planes in the expansion section area located at 22.5 *m* and 67.5 *m* to indicate the density distribution at the two instrumentation array locations. Grid surfaces which pass through the driver horizontal center planes are also provided to show the longitudinal and lateral motion of the driver gas. Figure 14 shows that at 172 *ms* after flow initiation, the shock front is approaching the 67.5 *m* position (shown in the upper right corner of the figure), but has not yet reached it. The leading edge of the driver gas from the individual drivers has begun to pass through the 22.5 *m* plane and evidence of mixing of the driver gas with the entrained air is evident upstream of the 22.5 *m* location.

Figure 15 shows the density distribution in the computational domain at 302 *ms*. The single, continuous shade at the 67.5 *m* position indicates a uniform distribution of gas density at the test section, further evidence of uniform flow at that location. Regions of slightly elevated density are evident within the driver flow paths at the 22.5 *m* plane. In these elevated regions, the density is approximately 1.35  $\text{kg/m}^3$ , while the density elsewhere at the same cross section is nominally 1.28  $\text{kg/m}^3$ , a variation of about 5%.

The USA-RG3 time history data are compared to the experimental records in the same manner as the SHARC results. The inviscid and viscous solution results for the 20 *kPa* and 80 *kPa* overpressure levels are compared to experimental data from the 67.5 *m* and 22.5 *m* locations in Figures 16 through 23. Again, the PB19 and PB4 gauge locations are the benchmarks against which the computational results are evaluated. The stagnation overpressure from PB19 on Test 1 is compared to the USA-RG3 calculations in Figure 16. This figure shows little difference between the two computational solutions. Both computational results closely follow the experimental data, with the greatest deviation occurring between 75 *ms* and 275 *ms* after shock arrival. The incident static overpressure predicted by the calculations was approximately 17.5 *kPa*, which is below the measured peak of 25 *kPa*.

The reason for the differences in the peak static overpressure lies in the resolution of the computational grid and the formulation of implicit CFD algorithms. Like the SHARC model,

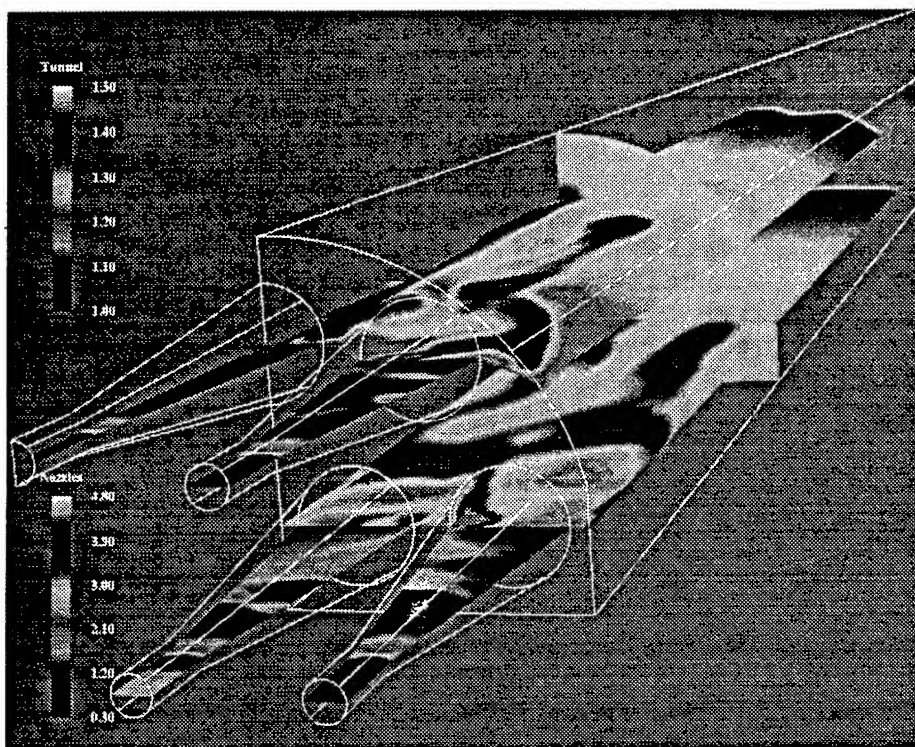


Figure 14. USA-RG3 Viscous Turbulent Solution: Density at 172 *ms*

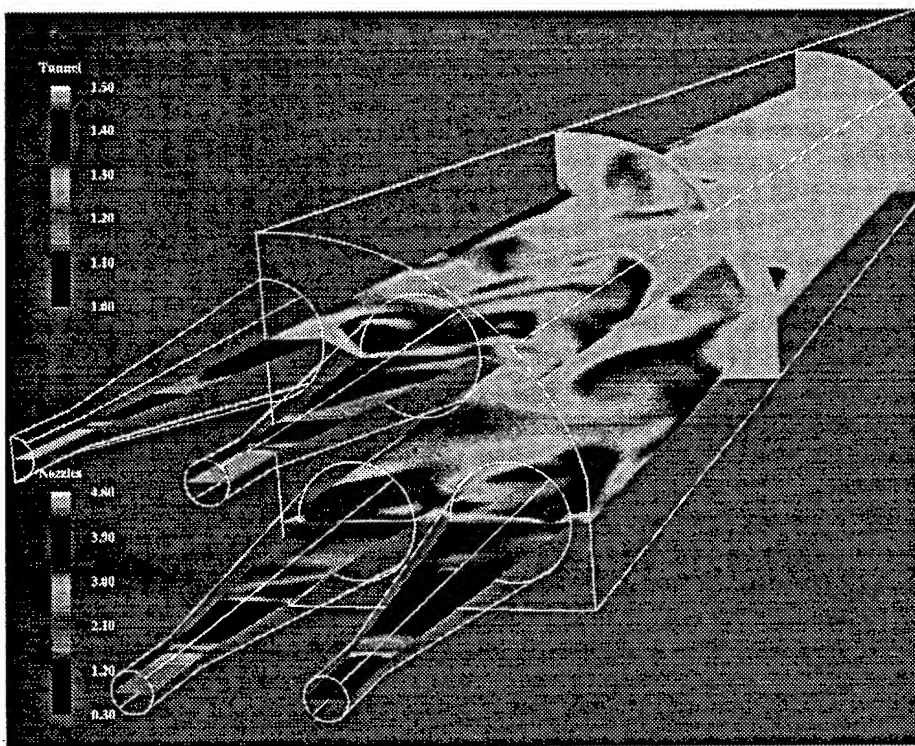


Figure 15. USA-RG3 Viscous Turbulent Solution: Density at 302 *ms*

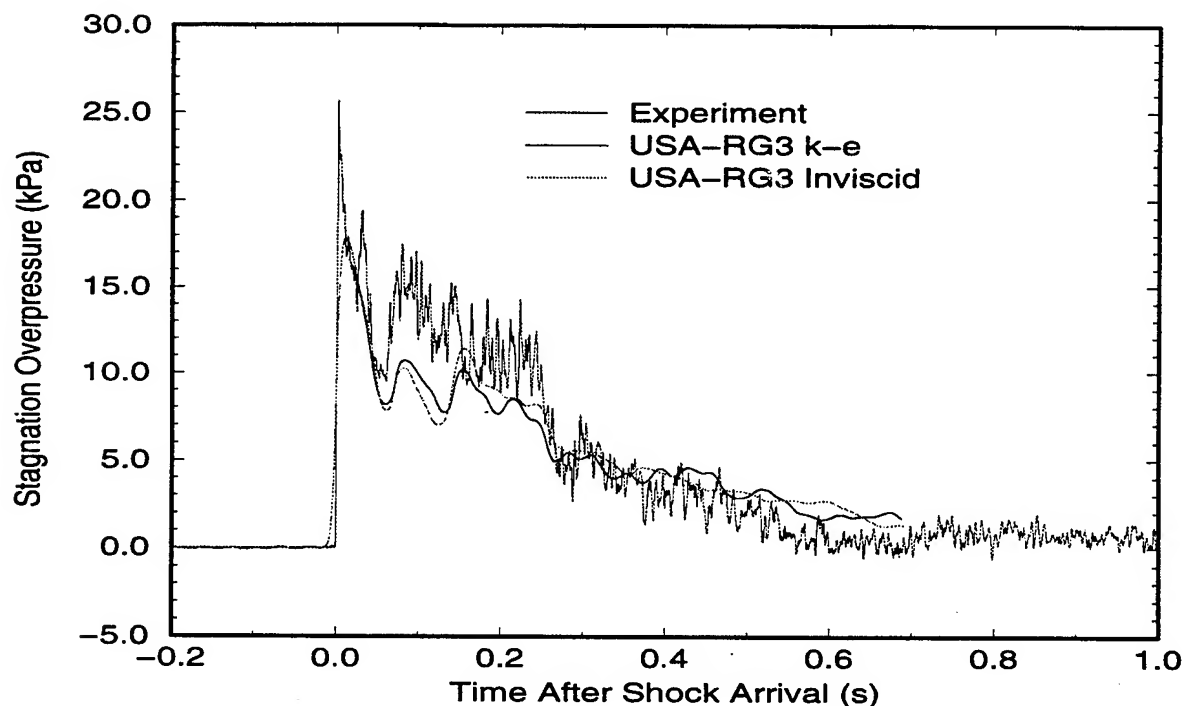


Figure 16. USA-RG3 Simulations of Test 1, Gauge PB19

the grid resolution of the USA-RG3 model is near the minimum necessary to capture the dominant flow characteristics which are present in the SSGG. Increasing the grid resolution to capture more detail in the flow would make the run times unreasonably long.

The time step in implicit codes is determined by the Courant-Friedrichs-Lewy (CFL) stability condition.<sup>25</sup> Because the implicit formulation of the time-marching algorithm casts the entire system of equations into matrix form, the time step is not as strictly limited by the computational cell size, particle velocity and sound speed as in explicit schemes. The formulation of the implicit approach allows larger time steps to be realized by increasing the value of the CFL number used by the code. In each of the USA-RG3 calculations presented here, a CFL number of 10 was used for the entire computation. This value was selected as a compromise between definition of shock structure in the solution and the computer time required to complete the calculations.

This explanation for the reduced incident shock strength is further supported by the fact that the shock front does not have as steep a rise as the experiment or even the explicit SHARC results. To repeat these calculations with an initial CFL number of 1 until the leading shock had propagated past the 67.5 m measurement position, then increasing it to a value of 10 for the remainder of the calculation would probably produce a sharp shock front without significantly increasing the total CPU time required to complete the solutions.

The USA-RG3 predictions of the flow at the PB4 gauge for Test 1 are plotted in Figure 17. These experimental and computational results look very much like those of the previous figure due to the high level of flow uniformity in both the experiment and the cal-

culations. Again, the rounded shock front on the leading edge of the computational records indicates a shock which is spread longitudinally across several computational planes due to the coarseness of the grid and the selected CFL number.

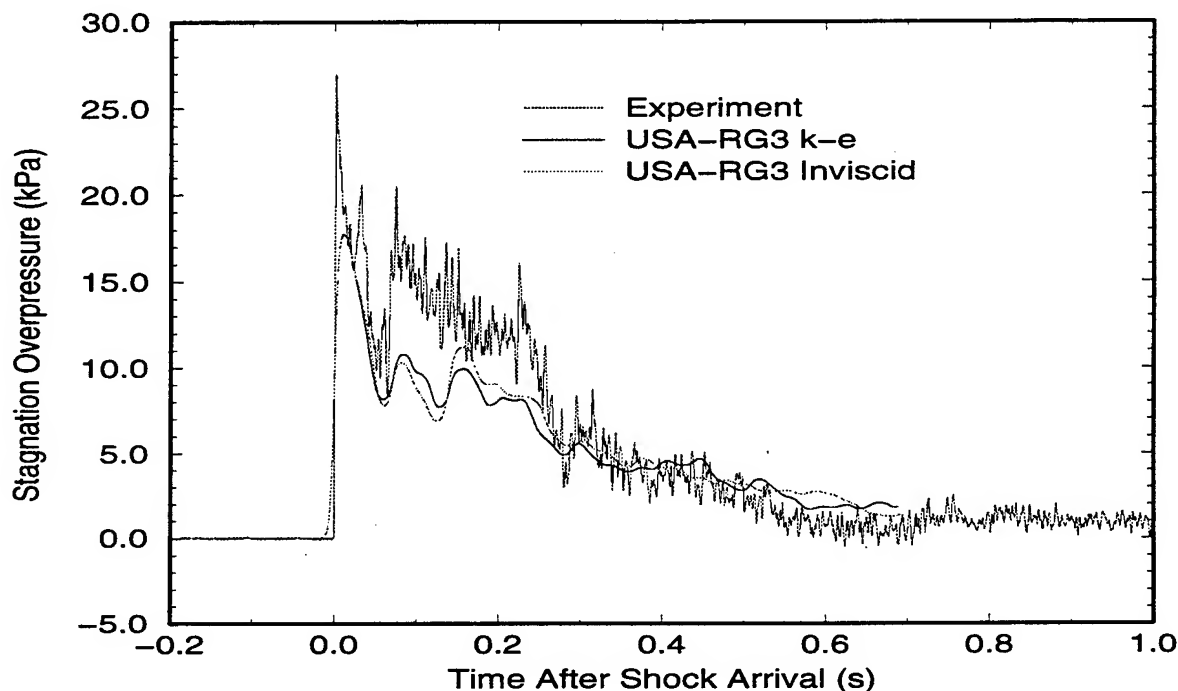


Figure 17. USA-RG3 Simulations of Test 1, Gauge PB4

Figures 18 and 19 show the USA-RG3 predictions of stagnation overpressure at the 22.5 *m* instrumentation array location for Test 6. Both of these figures shows that, closer to the upstream end of the expansion section, the shock front is not as rounded as in the computational results at the 67.5 *m* location. Because the shock front has not traveled as far to reach this measurement position, there has been less opportunity for the solution to spread the shock front across the longitudinal grid planes. The PB19 comparisons in Figure 19 show that, like the SHARC results, the computation did not capture the jet flow effect observed in the path of the 44 *m* driver.

## 6.2. USA-RG3 Calculations of 80 kPa Tests

The simulations of the 80 *kPa* tests are summarized in Figures 20 through 23, with Test 2 comparisons in the first two figures and Test 8 comparisons in the last two. Figures 20 and 21 show that the USA-RG3 code again produced a somewhat rounded shock front. At the PB4 gauge in Figure 21, the predicted peak shock is nearly identical to the experiment, while the predicted shock strength at gauge PB19 is 5% greater than the measured peak. The difference between the peaks at these two gauge locations is in the experimental result, as the computations produce a peak static overpressure of 112 *kPa* uniformly across the 67.5 *m* cross section. The PB4 comparison shows that the computational results closely

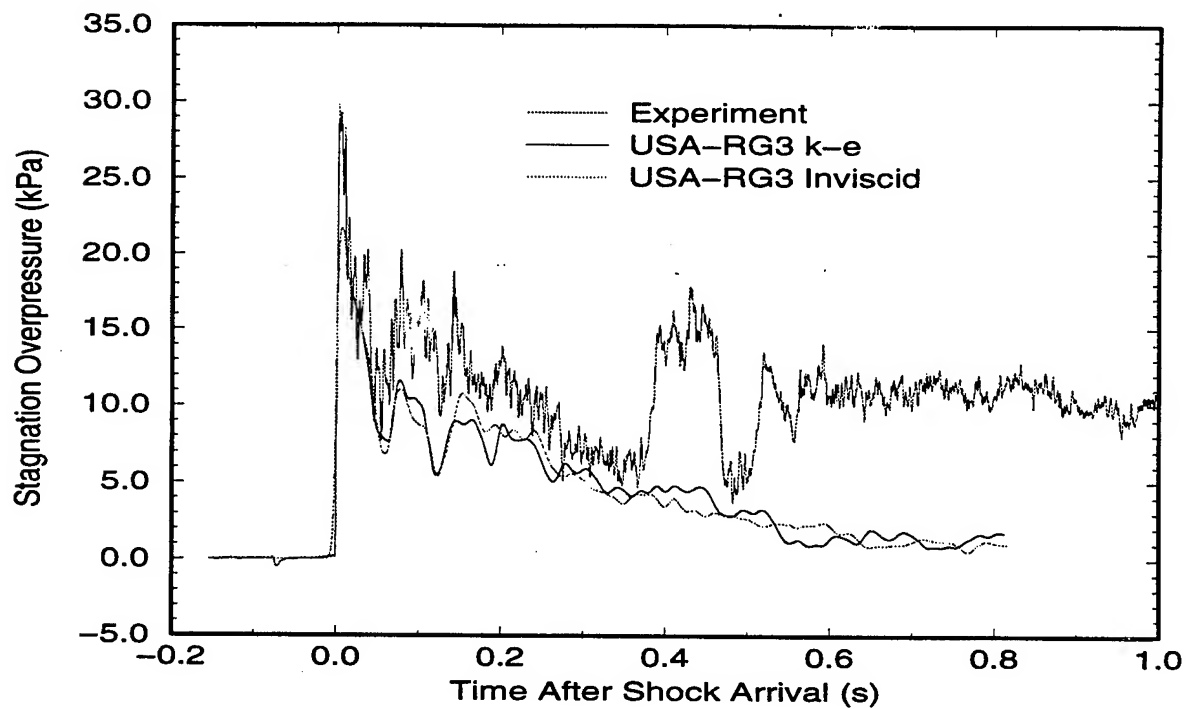


Figure 18. USA-RG3 Simulations of Test 6, Gauge PB19

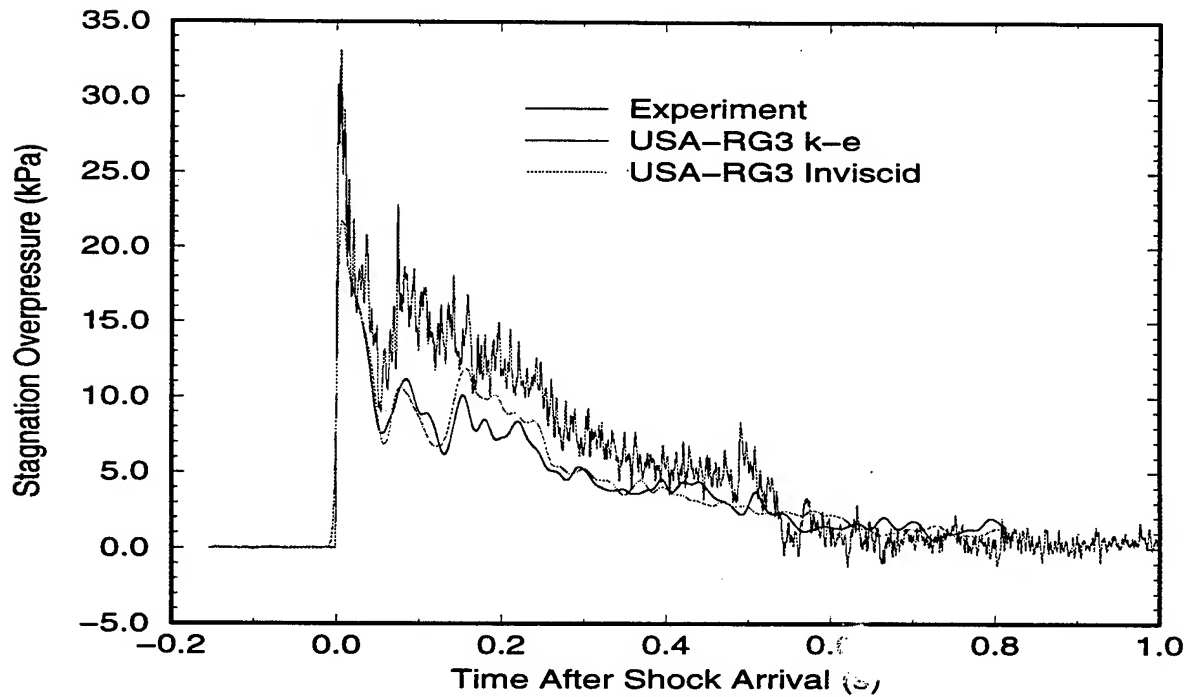
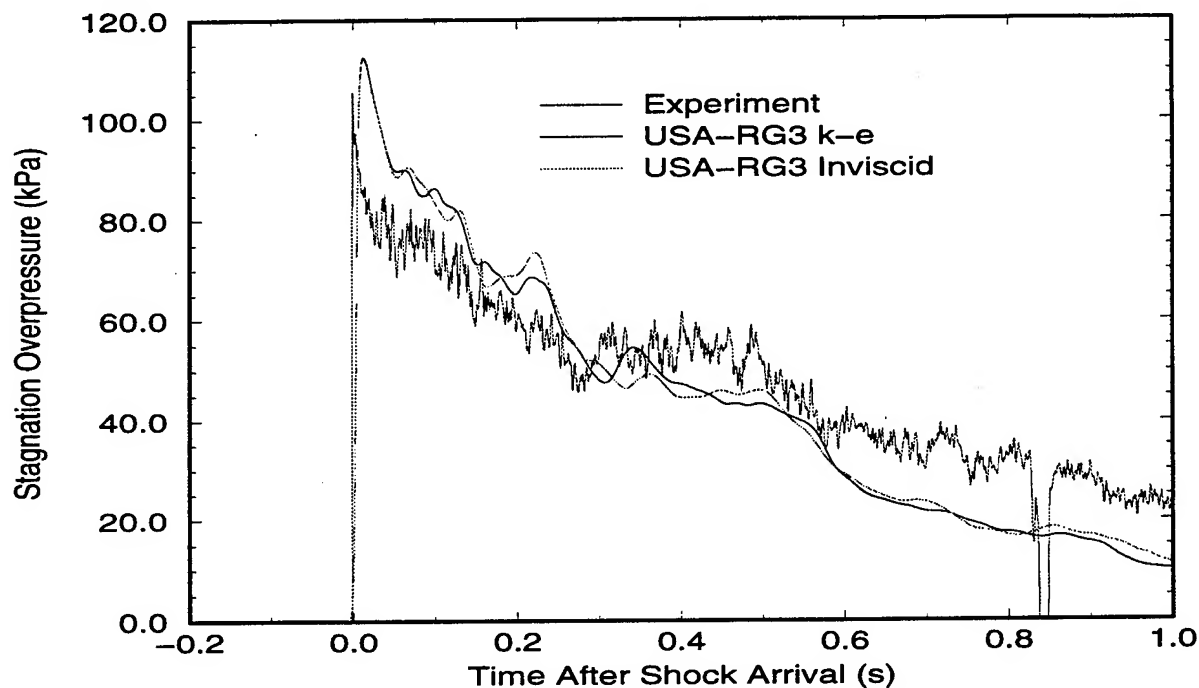


Figure 19. USA-RG3 Simulations of Test 6, Gauge PB4



follow the experiment throughout the entire time of interest, with the computational results slightly lower than the experimental stagnation overpressure. The PB19 comparison shows the computational results indicating a stagnation overpressure which is initially greater than the measured data, then falling slightly below the experimental record at 300 *ms* after shock arrival.



**Figure 20.** USA-RG3 Simulations of Test 2, Gauge PB19

Finally, the stagnation overpressures from gauges PB19 and PB4 from Test 8 are compared to the 22.5 *m* station data in Figures 22 and 23. The PB19 record in the first figure is positioned within the path of the centerline of the 44 *m* driver and shows highly turbulent flow in the jet produced by that driver. The USA-RG3 inviscid and viscous, turbulent predictions both show erratic activity between 75 *ms* and 400 *ms* after shock arrival, but generally do not follow the trend of the experimental data during that time interval. In this figure, the  $k-\epsilon$  turbulence model in the USA-RG3 may behave in the exact opposite manner as the SHARC turbulence model in that it appears to be introducing too little diffusion to the flow field.

The PB4 stagnation overpressure comparison for Test 8 is seen in Figure 23. Here, the experimental data demonstrates only a few, sudden oscillations resulting from the jet flow from the neighboring drivers. The USA-RG3 predictions of stagnation overpressure at this gauge contain some large disturbances between 75 *ms* and 400 *ms* after shock arrival, but otherwise closely follow the path of the experimental record. For both gauge locations examined at the 22.5 *m* test section at the 80 *kPa* overpressure level, the shock front produced by the USA-RG3 calculations have a steep rise and nearly exactly match the peak static overpressure of the experiments.

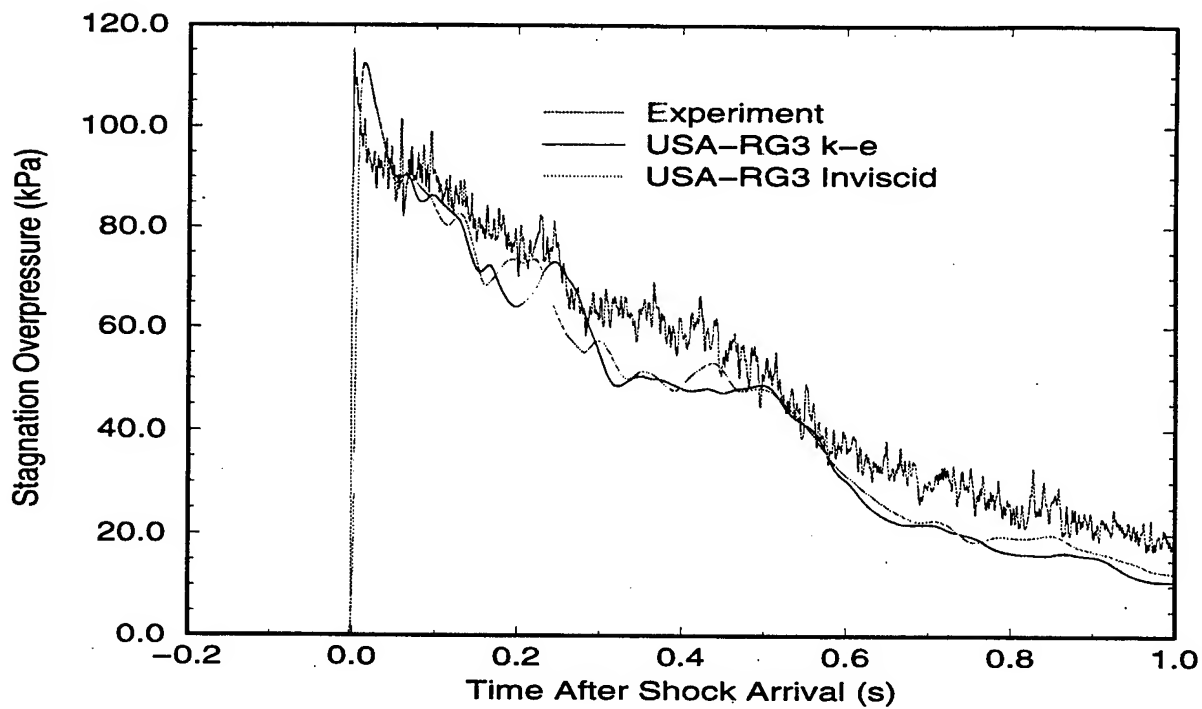


Figure 21. USA-RG3 Simulations of Test 2, Gauge PB4

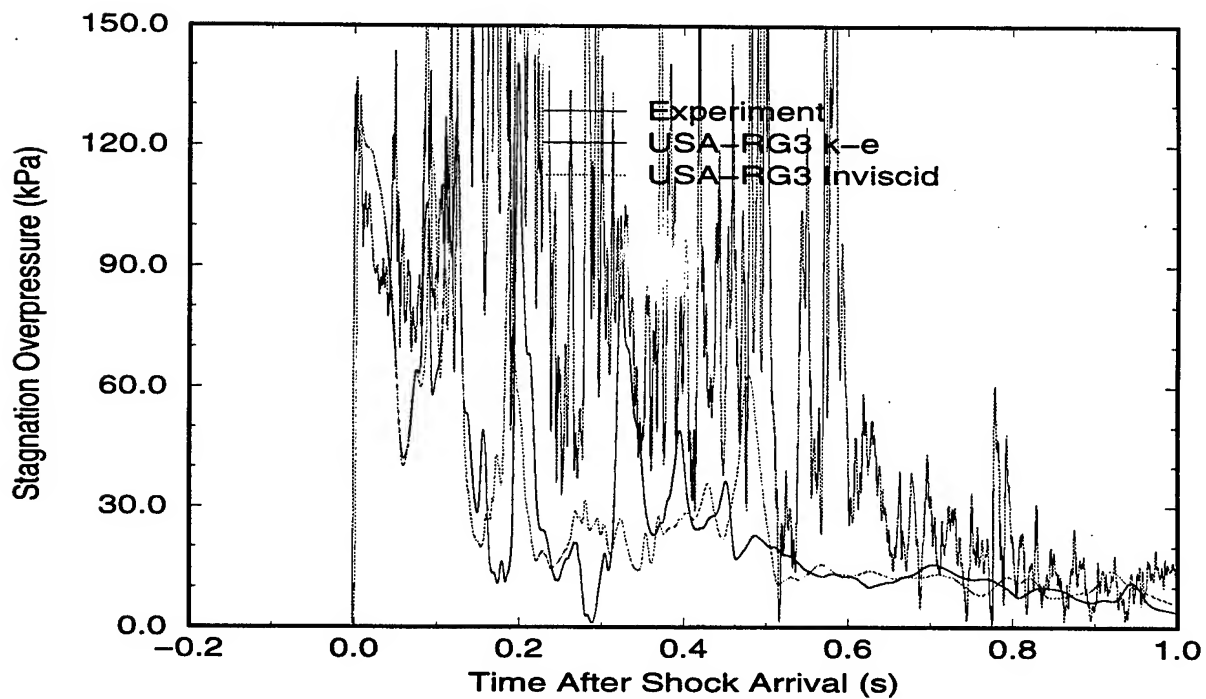


Figure 22. USA-RG3 Simulations of Test 8, Gauge PB19

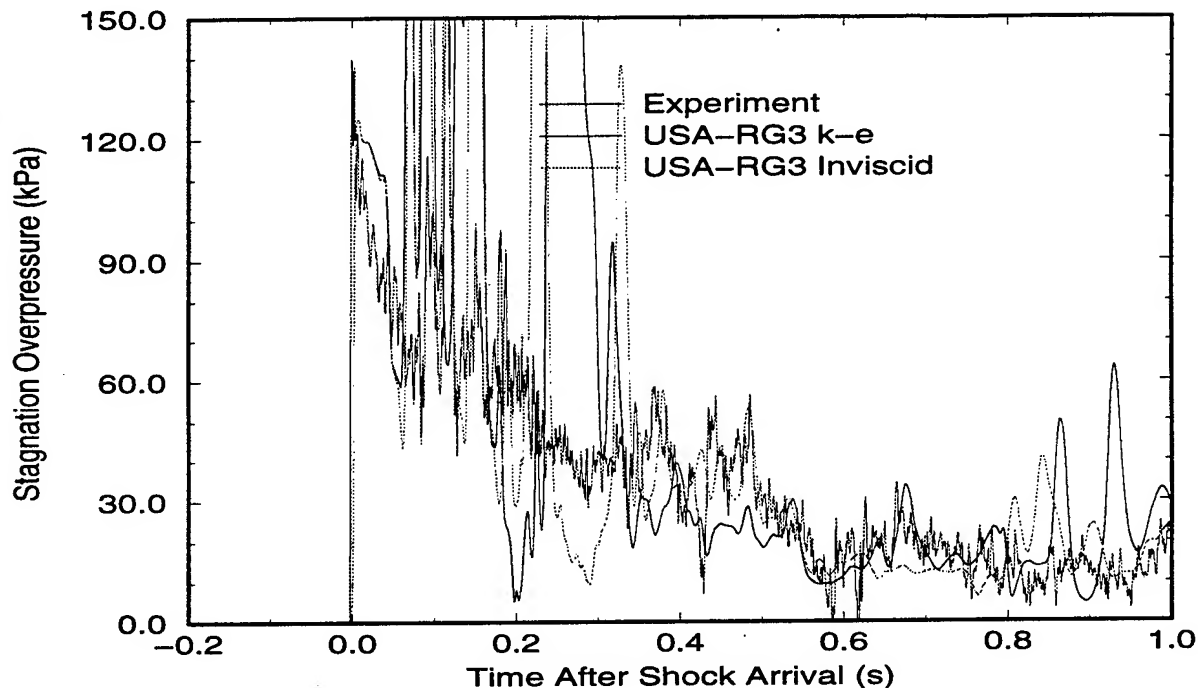


Figure 23. USA-RG3 Simulations of Test 8, Gauge PB4

## 7. SUMMARY

This part of the paper has presented an effort to validate two candidate CFD codes for 3-D modeling of blast effects and phenomena. The USA-RG3 and SHARC codes were employed in a detailed computational investigation which revealed many of the significant features, strengths and weaknesses of these codes. The computational results presented in this paper were selected to illustrate these strengths and weaknesses. The wealth of data produced by these calculations is too voluminous to present it all.

Overall, the CFD codes do an excellent job of predicting the complex, time-dependent flow which exists in the SSGG blast simulator. Additionally, the codes demonstrated the capability to simulate 3-D blast phenomena of interest to ARL and much of the blast effects community. Both of these 3-D codes are in use at ARL for problems that can be reasonably represented in a three-dimensional domain, without resulting in unreasonably long run times.

The calculations presented in this paper also serve to further reinforce the need to adapt these types of CFD codes to scalable, parallel computer platforms in order to obtain significant increases in computational performance. This type of computing technology and robust CFD codes like SHARC and USA-RG3 should make routine 3-D computations of blast effects a reality in the near future.

## REFERENCES

1. Schraml, S.J. and R.J. Pearson. "Small Scale Shock Tube Experiments Using a Computer Controlled Active Rarefaction Wave Eliminator." BRL-TR-3149, U.S. Army Ballistic Research Laboratory, Aberdeen Proving Ground, MD. September 1989.
2. Schraml, S.J. and R.J. Pearson. "Characterization of Flow Distribution in Axisymmetric Shock Tubes." BRL-TR-3353, U.S. Army Ballistic Research Laboratory, Aberdeen Proving Ground, MD. June 1992.
3. Brochure "Simulateur de Souffle à Grand Gabarit." Centre d'Etudes de Gramat, 46500 Gramat, France.
4. S. Gratiot and J.B.G. Monzac. "Le Simulateur de Souffle à Grand Gabarit de Centre d'Etudes de Gramat - Conception, études, performance." Proceedings of the 7<sup>th</sup> International Symposium on the Military Applications of Blast Simulation. Medicine Hat, Alberta, Canada. 13-17 July 1981.
5. A. Cadet and J.B.G. Monzac. "Le Simulateur de Souffle à Grand Gabarit de Centre d'Etudes de Gramat - Description et utilisation opérationnelle." Proceedings of the 7<sup>th</sup> International Symposium on the Military Applications of Blast Simulation. Medicine Hat, Alberta, Canada. 13-17 July 1981.
6. "Shock and blast simulation. Concept and definition of a Large Blast Simulator." Technical Papers T74-27a and T77-13a. Centre d'Etudes de Gramat, 46500 Gramat, France.
7. Gion, E.J. "A Multidriver Shock Tube Model of a Large Blast Simulator." BRL-MR-3757, U.S. Army Ballistic Research Laboratory, Aberdeen Proving Ground, MD. 1989.
8. Loucks, R.B. et al. "Simulation of Non-Ideal Blast with a Shock Tube Exit Jet." Proceedings of the 14<sup>th</sup> International Symposium on the Military Aspects of Blast and Shock. Las Cruces, NM, 10-15 September 1995.
9. Ethridge, N.H. and J.H. Keefer. "Real (Non-Ideal) Surface Effects on Nuclear Explosion Airblast from PRISCILLA-Type Events." Applied Research Associates, Inc. Aberdeen MD. June 1995.
10. Needham, C.E., R.G. Ekler and L.W. Kennedy. "Extended Desert Calculation Results with Comparisons to PRISCILLA Experimental Data and a Near-Ideal Calculation." U.S. Army Research Laboratory Contract Report ARL-CR-235. Aberdeen Proving Ground, MD. July 1995.
11. Ethridge, N.H. "Proposed Design for a Differential Pressure Gage to Measure Dynamic Pressure in Blast Waves." U.S. Army Ballistic Research Laboratory Memorandum Report ARBRL-MR-02814. Aberdeen Proving Ground, MD. 1978.
12. Private conversation with Mr. P.C. Muller. Aberdeen Proving Ground, MD. March 1995.
13. Schraml, S.J. "A Data Parallel Implementation of the BRL-Q1D Code." U.S. Army Ballistic Research Laboratory Technical Report BRL-TR-3389. Aberdeen Proving Ground, MD. June 1992.
14. Schraml, S.J. "Evaluation of a Multiple Instruction / Multiple Data (MIMD) Parallel Computer for CFD Applications." U.S. Army Research Laboratory Technical Report ARL-TR-589. Aberdeen Proving Ground, MD. October 1994.

15. Crepeau, J.E. et al. "SHARC Hydrocode Computations of the PRISCILLA Event." S-Cubed Technical Report SSS-DFR-93-14283. October 1993.
16. Opalka, K.O. "Numerical Simulation of the Flow in a 1:57-Scale Axisymmetric Model of a Large Blast Simulator." U.S. Army Research Laboratory Technical Report ARL-TR-111. Aberdeen Proving Ground, MD. April 1993.
17. Kundu, P.K. "Fluid Mechanics." Academic Press, Inc. San Diego, CA. 1990.
18. Hikida, S., R. Bell, and C. Needham. "The SHARC Codes: Documentation and Sample Problems." S-Cubed Technical Report SSS-R-89-9878. September 1988.
19. Fry, M., R. Durrett, G. Ganong, D. Matuska, M. Stucker, B. Chambers, C. Needham and C. Westmoreland. "The HULL Hydrodynamics Computer Code." U.S. Air Force Weapons Laboratory Technical Report 76-183. September 1977.
20. Barthel, J. "2-D Hydrocode Computations Using a  $k-\epsilon$  Turbulence Model: Model Description and Test Calculations." S-Cubed Technical Report SSS-TR-85-7115. June 1985, (Footnotes added August 1988).
21. Chakravarthy, S., K. Szema, U. Goldberg, J. Gorski and S. Osher. "Application of a New Class of High Accuracy TVD Schemes to the Navier-Stokes Equations." AIAA Paper 85-0165. January 1985.
22. Ramakrishnan, S. and U. Goldberg. "Versatility of an Algebraic Backflow Turbulence Model." AIAA Paper 90-1485. 1990
23. Goldberg, U. and S. Chakravarthy. "Separated Flow Predictions Using a Hybrid  $k-L$ /Backflow Model." AIAA Journal, Volume 28, Number 6. pp. 1005-1009. June 1990.
24. Goldberg, U. and D. Ota. "A  $k-\epsilon$  Near-Wall Formulation for Separated Flows." AIAA Paper 90-1482. 1990.
25. Roache, P.J. "Computational Fluid Dynamics." Hermosa Publishers. Albuquerque, NM. 1972